平成 25（2013）年度　研究成果

著書・総説・発表論文等

著書・総説・発表論文等リスト

著書・総説・解説

1. 永島賢治、櫻井英博、井上和仁
「紅色光合成細菌による水素発生」
光合成のエネルギー利用と環境応用（三宅淳，佐々木健監修）, **2014**, CMC出版, pp.154-162.

2. 川添嘉徳、上村大輔
特集　アカデミアの創薬スクリーニング：分子標的からリード化合物発見への戦略　「エリブリン（ハラヴェン）：海洋天然物からの創薬展開」
細胞工学, **2013**, *32*, 675-681.

3. Ohno, T. Teruya, K. Suenaga, D. Uemura
Apoptosis as a practical target for identifying anticancer agents of marine origin
For. Immunopathol. Dis. Therap., **2013**, *4*, 33-41.

4. 高村浩由、門田功、上村大輔
構造解析を指向したポリオール天然物シンビオジノライドの合成研究
有機合成化学協会誌, **2014**, *72*, 2-13.

5. K. Nomiya, N. C. Kasuga, and A. Takayama, RSC book, in: “Polymeric Materials with Antimicrobial Activity　From Synhtesis to Application” (Ed) by A. Muñoz-Bonilla, M. Cerrada, M. Fernández-García
「Synthesis, structure and antimicrobial activities of polymeric and non-polymeric silver and other metal complexes」
2014, Chapter 7, 156-207.
DOI:10.1039/9781782624998-00156

6. 堀　久男
「フッ素樹脂の最新動向」、第13章「機能性フッ素化合物の分解反応の開発」
澤田英夫監修、シーエムシー出版、2013年4月1日刊行

7. 堀　久男
「排水・汚水処理技術集成」vol.2、第3章総説「化学処理技術」、第１節「フ

ッ素系イオン液体の熱水分解」エヌ・ティー・エス、2013年12月28日刊行

8. 堀　久男
「過塩素酸イオンの環境残留性と対策技術の研究動向」
ぶんせき, **2013**, *8*, 458-463.

9. 堀　久男
「有機フッ素化合物をはじめとする環境負荷物質の分解・無害化反応の開発」
水環境学会誌, **2013**, *36* (9), 331-334.

10. 堀　久男
「有機フッ素化合物の分解反応の開発」
ファルマシア、**2014**, *50* (1), 54-58.

11. 引地 史郎, 中澤 順
錯体化学を基盤とするBio-inspired酸化触媒の開発
化学工業 **2013**, *64*, 756-763.

12. 菅原正・木村榮一 共編
「超分子の化学(化学の指針シリーズ)」
2013年

13. 西本右子
「ベーシックマスター分析化学」
2013年、オーム社　p338−351 第20章　熱分析

発表論文

1. H. Sakuraia, H. Masukawa, M. Kitashima and K. Inoue
Photobiological hydrogen production: Bioenergetics and challenges for its practical application
Journal of Photochemistry and Photobiology C: Photochemistry Reviews **2013,** 17. 1–25.

2. N. Maru, N. Chikaraishi, K. Yokota, Y. Kawazoe, D. Uemura

Jolkinolide F, a Cytotoxic Diterpenoid from *Euphorbia jolkinii*
Chem. Lett. **2013**, *42*, 756-757.

3. H. Takamura, T. Fujiwara, I. Kadota, D. Uemura
Stereoselective synthesis of the C79-C97 fragment of symbiodinolide
Beilstein J. Org. Chem. **2013**, *9*, 1931-1935.

4. N. Maru, T. Inuzuka, K. Yamamoto, M. Kitamura, P. Schupp, K. Yamada, D. Uemura
Relative configuration of luminaolide
Tetrahedron Lett. **2013**, *33*, 4385-4387.

5. R. Wada, T. Kumon, R. Kourist, H. Ohta, D. Uemura, S. Yoshida, K. Miyamoto
Thermally driven asymmetric domino reaction catalyzed by a thermostable esterase and its variants
Tetrahedron Lett. **2013**, *54*, 1921-1923.

6. S. Xu, D. Unabara, D. Uemura, H. Arimoto
Enantioselective Total Synthesis of Pinnaic Acid and Halichlorine
Chem. Asian J. **2013**, *9*, 367-375.

7. T. Sengoku, S. Xu, K. Ogura, Y. Emori, K. Kitada, D. Uemura, H. Arimoto
Total Synthesis of the Antibiotic Kendomycin: A Macrocyclization Using the Tsuji-Trost Etherification
Angew. Chem. Int. Ed. **2014**, 53, in press.

8. S. Aizawa, K. Fukumoto, and T. Kawamoto
Effect of phosphine and phosphine sulfide ligands on the cobalt-catalyzed reductive coupling of 2-iodobutane with *n*-butyl acrylate
Polyhedron **2013**, *62*, 37-41.

9. T. Suzuki, K. Matsuya, T. Kawamoto, and H. Nagao
Synthesis and Structures of Mixed-Valence Oxido-Bridged Diruthenium Complexes Bearing Ethylbis(2-pyridylmethyl)Amine
Eur. J. Inorg. Chem. **2014**, 722-727.

10. H. Osada, A. Ishikawa, Y. Saku, Y. Sakai, Y. Matsuki, S. Matsunaga, and K.

Nomiya
2 : 2-Type complexes of zirconium(IV)/hafnium(IV) centers with mono-lacunary Keggin polyoxometalates: Syntheses and molecular structures of $[(\alpha\text{-}SiW_{11}O_{39}M)_2(\mu\text{-}OH)_2]^{10-}$ (M = Zr, Hf) with edge-sharing octahedral units and $[(\alpha\text{-}SiW_{11}O_{39}M)_2(\mu\text{-}OH)_3]^{11-}$ with face-sharing octahedral units
Polyhedron **2013**, 52, 389-397.

11. Takayama, R. Yoshikawa, S. Iyoku, N. C. Kasuga, and K. Nomiya
Synthesis, structure and antimicrobial activity of *L*-argininesilver(1+) nitrate
Polyhedron **2013**, 52, 844-847.

12. Y. Matsuki, Y. Mouri, Y. Sakai, S. Matsunaga, and K. Nomiya
Monomer and Dimer of Mono-titanium(IV)-Containing α-Keggin Polyoxometalate: Synthesis, Molecular Structures and pH-Dependent Monomer-Dimer Interconversion in Solution
Eur. J. Inorg. Chem. **2013**, 1754-1761.

13. K. Nomiya, K. Ohta, Y. Sakai, T. Hosoya, A. Ohtake, A. Takakura, and S. Matsunaga
Tetranuclear Hafnium(IV) and Zirconium(IV) Cationic Complexes Sandwiched between Two Di-Lacunary Species of α-Keggin Polyoxometalates: Lewis Acid Catalysis of the Mukaiyama-Aldol Reaction
Bull. Chem. Soc. Jpn. **2013**, 86, 800-812.

14. T. Yoshida, S. Matsunaga, and K. Nomiya
Two types of tetranuclear phosphanegold(I) cations as dimers of dinuclear units, $[\{(Au\{P(p\text{-}RPh)_3\})_2(\mu\text{-}OH)\}_2]^{2+}$ (R = Me, F), synthesized by polyoxometalate-mediated clusterization
Dalton Trans. **2013**, 42, 11418-11425.

15. T. Yoshida, S. Matsunaga, and K. Nomiya
Novel Intercluster Compounds Composed of a Tetra{phosphanegold(I)}oxonium Cation and an α-Keggin Polyoxometalate Anion Linked by Three Monomeric Phosphanegold(I) Units
Chem. Lett. **2013**, 42, 1487-1489.

16. Y. Patil, H. Hori, H. Tanaka, T. Sakamoto, B. Ameduri

First radical homopolymerisation of 2-Trifluoromethacrylic acid in water and study of the degradation of the resulting homopolymers
Chemical Communications **2013**, *49*, 6662-6664.

17. H. Hori, Y. Noda, A. Takahashi, T. Sakamoto
Decomposition of perfluorinated ionic liquid anions to fluoride ions in subcritical and supercritical water with iron-based reducing agents
Industrial & Engineering Chemistry Research **2013**, *52*,13622-13628.

18. H. Hori, A. Ishiguro, K. Nakajima, T. Sano, S. Kutsuna, K. Koike
Visible light-induced decomposition of a fluorotelomer unsaturated carboxylic acid in water with a combination of tungsten trioxide and persulfate
Chemosphere **2013**, *93*, 2732-2737.

19. J. Kondo, T. Yamada, C. Hirose, I. Okamoto, Y. Tanaka, A. Ono,
Crystal structure of metallo-DNA duplex containing consecutive Watson-Crick-like T-Hg(II)-T base pairs
Angew. Chem. Int. Ed. **2014**, *53*, 2385-2388.

20. H. Yamaguchi, J. Šebera, J. Kondo, S. Oda, T. Komuro, T. Kawamura, T. Dairaku, Y. Kondo, I. Okamoto, A. Ono, J. V. Burda, C. Kojima, V. Sychrovský and Y. Tanaka,
The structure of metallo-DNA with consecutive thymine–Hg^{II}–thymine base pairs explains positive entropy for the metallo base pair formation
Nucleic Acids Research, in press, doi:10.1093/nar/gkt1344

21. Jakub Šebera, Jaroslav Burda, Michal Straka, Akira Ono,Chojiro Kojima, Yoshiyuki Tanaka, and Vladimír Sychrovský
Formation of a Thymine-HgII-Thymine Metal-Mediated DNA Base Pair: Proposal and Theoretical Calculation of the Reaction Pathway
Chem. Eur. J. **2013**, *19*, 9884–9894.

22. T. Miyao, A. Yoshida, H. Yamada, S. Naito
Mechanistic study of hydrogen occlusion in hollow silica nano-sphere encapsulating iridium metal clusters
J. Molecular Catalysis A, Chemical **2013**, *378*, 174-178.

23. T. Nozawa, Y. Mizukoshi, A. Yoshida, S. Naito
Aqueous phase reforming of ethanol and acetic acid over TiO2 supported Ru catalysts
Applied Catalysis B: Environmental **2014**, *146*, 221-226.

24. J. Nakazawa, S. Terada, M. Yamada, and S. Hikichi
Structural Characterization and Oxidation Reactivity of a Nickel(II) Acylperoxo Complex
J. Am. Chem. Soc. **2013**, *136*, 6010-6013.

25. J. Nakazawa, T. Hori, T. D. P. Stack, and S. Hikichi
Alkane Oxidation by an Immobilized Nickel Complex Catalyst: Structural and Reactivity Differences Induced by Surface Ligand Density on Mesoporous Silica
Chem. Asian J. **2013**, *8*, 1191-1199.

26. J. Nakazawa, A. Yata, T. Hori, T. D. P. Stack, Y. Naruta, and S. Hikichi
Catalytic Alkane Oxidation by Homogeneous and Silica Supported Cobalt Complex Catalysts with a Triazolyl-group Containing Tetradentate Ligand
Chem. Lett. **2013**, *42*, 1197-1199.

27. H. Komatsuzaki, A. Shiota, S. Hazawa, M. Ito, N. Miyamura, N. Miki, Y. Takano, J. Nakazawa, A. Inagaki, M. Akita, and S. Hikichi
Manganese(II) semiquinonato and manganese(III) catecholato complexes with tridentate ligand: Modeling the substrate-binding state of manganese-dependent catechol dioxygenases and reactivity with molecular oxygen
Chem. Asian J. **2013**, *8*, 1115-1119.

28. Ikeda, K. Hoshino, H. Komatsuzaki, M. Satoh, J. Nakazawa, and S. Hikichi
O_2 Activation and External Substrate Oxidation Capability of Co(II)-Semiquinonato Complex
New J. Chem. **2013**, *37*, 2377-2383.

29. Govindachetty Saravanan, Kazuya Nanba, Genki Kobayashi, and Futoshi Matsumoto
Leaching Tolerance of Anodic Pt-based Intermetallic Catalysts for Formic Acid

Oxidation
Electrochim. Acta **2013**, *99*, 15-21.

30. Francis M. Auxilia, Toyokazu Tanabe, Shinsuke Ishihara, Govindachetty Saravanan, Gubbala V. Ramesh, Futoshi Matsumoto, Xu Ya, Katsuhiko Ariga, Arivuoli Dakshanamoorthy, Hideki Abe
Interleaved Mesoporous Copper for the Anode Catalysis in Direct Ammonium Borane Fuel Cells
Journal of Nanoscience and Nanotechnology **2014**, *14*, 4443-4448.

31. G. Ramesh, R. kodiyath, T. Tanabe, T. Fujita, F. Matsumoto, , S. Ishihara, S. Ueda, Y. Yamashita, K. Ariga, H. Abe
Pt_3Nb Intermetallic Nanoparticles: Highly Stable and CO Tolerant Anode Electrocatalyst for the Oxidation of Ethanol and Formic Acid
ChemElectroChem **2014**, in press.

32. G. Takao, G. Saravanan, T. Tanabe, T. Tsuda, M. Miyauchi, G. Kobayashi, H. Abe, and F. Matsumoto
Long-term Stable Oxygen-Reduction Performance of Titania-supported PtPb Nanoparticles
Catalysis Science & Technology **2014**, in press.

33. N. Tsutsui, T. Ohira, T. Okutsu, J. Shinji, S.-H. Bae, B.-J. Kang, M. N. Wilder
Molecular cloning of a cDNA encoding vitellogenesis-inhibiting hormone in the whiteleg shrimp *Litopenaeus vannamei* and preparation of its recombinant peptide using an *E. coli* expression system
Fish. Sci. **2013**, *79*, 357-365.

34. H. Katayama, T. Ohira, H. Nagasawa
Crustacean peptide hormones: structure, gene expression and function
Aqua-BioSci. Monogr. **2013**, *6*, 49-90.

35. Y. Kageyama, N. Tanigake, Y. Kurokome, S. Iwaki, S. Takeda, K. Suzuki, and T. Sugawara
Macroscopic Motion of Supramolecular Assemblies Actuated by Photoisomerization of Azobenzene Derivatives
Chem. Commun. **2013**, *49*, 9386-9388.

36. K. Takakura, T. Yamamoto, K. Kurihara, T. Toyota, K. Ohnuma, and T. Sugawara
Spontaneous Transformation from Micelles to Vesicles Associated with Sequential Conversions of Comprising Amphiphiles within Assemblies
Chem. Commun. **2014**, *50*, 2190-2192.

37. K. Mochida, Y. Funasako, K. Takazawa, M. Takahashi, M. M. Matsushita, and T. Sugawara
Chemical Control of the Monovalent–Divalent Electron-Transfer Phase Transition in Biferrocenium–TCNQ Salts
Chem. Commun. **2014**, in press.

38. T. Okabe, K. Kakishita, H. Simizu, K. Ogawa, Y. Nishimoto, A. Takasaki, T. Suda, M. Fushitani, H. Togawa, M. Sato, R. Yamamoto
Current Status and Application of Woodceramics Made from Biomass
Trans. Mat. Res. Soc. Japan. **2013**, *38*, 2, 191-194.

39. Y. Uehara, E. Shimoda, Y. Iitaka, Y. Nishimoto
Water State in Methyl cellulose Thermo Reversible Hydrogels Containing Salt and Polyethylene Glycol
Trans. Mat. Res. Soc. Japan. **2013**, *38*, 4, 589-592 .

40. T. Matsubara, N. Araida, D. Hayashi, and H. Yamada
Computational Study on the Mechanism of the Electron-Transfer Induced Repair of the (6-4) T-T Photoproduct of DNA by Photolyase: Possibility of a Radical Cation Pathway.
Bull. Chem. Soc. Jpn. **2014**, *87*, 390-399.

41. T. Matsubara and C. Sasamoto,
Computational Study of the Binding Mechanism of Complement C3b with Antigen
Bull. Chem. Soc. Jpn. **2013**, *86*, 1426-1434.

42. N. Watanabe, A. Oguri, M. Horikoshi, H. Takatsuka, H. K. Ijuin, and M. Matsumoto
Chemiexcitation efficiency for the charge-transfer-induced chemiluminescent decomposition of 3-hydroxyphenyl-substituted dioxetanes in an aqueous system
Tetrahedron Lett. **2014**, *55*, 1644-1647.

43. H. Saitoh, H. K. Ijuin, N. Watanabe, and M. Matsumoto
Novel Intramolecular Cyclization of 2-(Buta-1,3-dienyl)benzyl Anions to 6,7(9)-Dihydro-5H-benzocycloheptenyl Anions Leading to Successive Formation of 1,2-Dihydrocyclopropa[a]naphthalenes
Helvetica Chimica Acta. **2013**, *96*, 1704-1713.

報告書・紀要

1. 力石紀子、野宮健司、松永 諭、早津 学、鈴木季直
   2012年度神奈川大学総合理学研究所共同研究助成論文「バクテリア、酵母、カビに対して広い抗菌活性スペクトルを示す新規銀(I)錯体の合成、構造解析と抗菌機構の解明」
   Science J. of Kanagawa University, **2013**, *24*, 31-39.

2. 引地 史郎, 内藤 周弐, 吉田 暁弘, 中澤 順
   環境調和型物質変換及びエネルギープロセス創出の新基盤となるナノ構造触媒の開発
   神奈川大学工学研究所所報 **2013**, 第 36 号, 77-86.

3. 天野　力
   希ガス結晶構造と遮蔽L-Jポテンシャル
   Science Journal of Kanagawa University, **2014**, *25*, 印刷中.

4. 澤田、清水、武井、鈴木、金沢、西本
   環境水からのホウ素及び稀少元素の分離を目的とした試薬フリーな分離濃縮システム
   Science Journal of Kanagawa University. **2013**, *24*, 41-46.

5. 張、西本、本城、久慈
   特殊土砂分離剤の微細構造解析
   Science Journal of Kanagawa University. **2013**, *24*, 101-104.

バイオテクノロジーシリーズ

光合成のエネルギー利用と環境応用

Application of Photosynthesis : Energy and Environment

監修：三宅　淳，佐々木 健
Supervisor : Jun Miyake, Ken Sasaki

HIGH TECHNOLOGY INFORMATION

シーエムシー出版

2　紅色光合成細菌による水素発生

永島賢治[*1]，櫻井英博[*2]，井上和仁[*3]

2.1　はじめに

近年，石油など化石燃料の枯渇問題や原子力発電への不信，さらには地球温暖化など環境問題への懸念の高まりを受け，再生可能エネルギーへの期待は高まる一方である。生物の光合成を通じた太陽光の利用は，こうした期待へ応えるための代表的な課題であることに疑問の余地は無い。このとき，一般に思い浮かべる光合成生物といえば酸素発生型光合成生物である高等植物や藻類であろう。実際に，再生可能エネルギーという言葉が日常になる以前から，特に藻類を利用した炭化水素系燃料生産の研究は連綿と続けられてきており，着実な成果が上がりつつある。最近ではユーグレナ藻（ミドリムシ）を使った航空燃料の生産が話題になるほど，実用化に向けた取り組みも進みつつある。一方で酸素非発生型光合成生物はどうであろう。このグループの生物は全てが原核生物であり，体制や代謝経路の単純さや多様性，独特な光捕集系など，応用研究に数々の魅力を持ち，活発な研究が行われている。しかし，大規模実用化は，発展途上段階にある。本稿では酸素非発生型光合成生物のうち紅色光合成細菌を取り上げ，その光合成の特徴と，エネルギー源としての活用に向けた水素発生の仕組みと実際について解説する。

2.2　紅色光合成細菌の光合成器官

紅色光合成細菌という呼び方は，プロテオバクテリア門に属し，かつ光合成器官を合成する細菌種に対して用いる名称で，「紅色」の文字が示す通り，培養液やコロニーが赤っぽく呈色する種が多い。こうした色は光合成の補助色素として働くスピリロキサンチンやスフェロイデノンなどのカロテノイドによるもので，その組成によってピンク色に見えたり真紅であったりするが，中には緑色に見える種もある。英語表記では“purple” photosynthetic bacteriaである。主要な光合成色素はバクテリオクロロフィルaまたはbで（種によってどちらか一方のみを合成する），これらの色素はタンパク質と結合して800 nm以上の赤外光領域に大きな吸収帯を持つ（図1）。

光合成電子伝達経路は循環的で，光励起された光化学反応中心複合体によってエネルギー準位が高められた電子は細胞膜中のキノンプールを経てシトクロムbc_1複合体へ運ばれ，水溶性の電子伝達タンパクを経て再び光化学反応中心複合体へ運ばれる[1)]。この循環的な電子伝達過程と共役してプロトンが細胞膜の内側から外側へ輸送されてプロトンの濃度勾配を形成し，ATPの合成などに利用している。光化学反応中心複合体は葉緑体などの光化学系2反応中心のものと類似点が

＊1　Kenji Nagashima　㈱科学技術振興機構　さきがけ研究者；神奈川大学
光合成水素生産研究所　客員教授
＊2　Hidehiro Sakurai　神奈川大学　光合成水素生産研究所　客員研究員；
早稲田大学名誉教授
＊3　Kazuhito Inoue　神奈川大学　理学部　生物科学科　教授；光合成水素生産研究所　所長

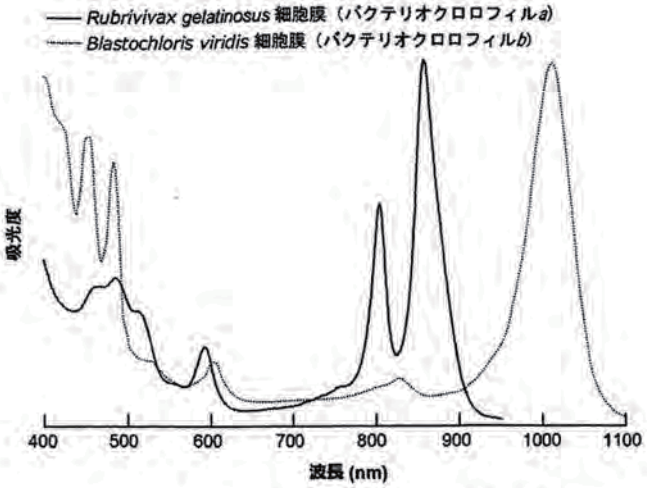

図１　紅色光合成細菌の膜画分の吸収スペクトル

多く，そのコアとなるLおよびMサブユニットは光化学系２反応中心のD1およびD2サブユニットと，それぞれアミノ酸配列で20～30％の相同性を示す。ただし，紅色光合成細菌の反応中心複合体には水を電子供与体として利用するためのMn-Ca-Oクラスターを欠き酸素は発生しない。

紅色光合成細菌の反応中心複合体は細胞膜中で光捕集タンパク（LH1）によって円環状に取り囲まれており，多くの種ではさらにその外側から別の光捕集タンパク（LH2）に囲まれている[2)]。これら光捕集タンパク複合体はバクテリオクロロフィルとカロテノイドを結合し，バクテリオクロロフィル*a*を合成する種では，LH1は870 nm前後，LH2は800および850 nm近辺に大きな吸収帯を持つ（図１）。バクテリオクロロフィル*b*を合成する種では，LH1の吸収帯が1010 nm前後の長波長領域までシフトする（図１）。紅色光合成細菌は，光合成生物の中で，最も長波長の光を利用できる生物である。

2.3　紅色光合成細菌のエネルギー代謝の多様性

紅色光合成細菌の種は，生理学的に古くから紅色イオウ細菌と紅色非イオウ細菌に分けられてきた。紅色イオウ細菌は，より嫌気的な環境に適応しており，硫化水素やチオ硫酸を末端電子供与体として利用する光独立栄養生物である。紅色非イオウ細菌の中にも，その名に反して同様のイオウ代謝を示すものがいるが，両者の違いはイオウ顆粒を細胞内外に蓄積するかしないかであり，この顆粒の有無は，光学顕微鏡で比較的容易に判定できる。16 SrRNAの塩基配列に基づく系統分類では，プロテオバクテリアはα，β，γ，δ，εの５つの綱に分けられており，紅色イオウ細菌はγ-プロテオバクテリア綱に，紅色非イオウ細菌はα-およびβ-プロテオバクテリア綱に分布している。

光合成という分かりやすい特徴を持つため紅色光合成細菌は単系統と思われがちであるが，系統樹上では非光合成細菌と複雑に入り交じった分布を示す。このことはプロテオバクテリアの祖

先種がすでに光合成細菌で，様々な環境に適応・分化する過程で過半の種は光合成能を失ったものと考えられている[3]。プロテオバクテリアはエネルギー代謝に関して多様であり，好気条件下では酸素を末端電子受容体とする酸素呼吸により，嫌気条件下でも硫黄や窒素の化合物や，鉄やセレンなど金属イオンを酸化・還元することによって生育が可能な種が多く分布している。光合成はプロテオバクテリアの多様なエネルギー代謝のうちの一つに過ぎず，実際，紅色非イオウ細菌の多くは暗中でも生育可能で，例えば好気条件下では色素合成は抑制され，もっぱら呼吸により生育する。光合成で生育する際も，通常，炭素源および電子供給源として有機酸などを要求するので，光従属栄養生物と見なされる。

2.4　光合成による水素発生

紅色非イオウ細菌のいくつかの種は，ニトロゲナーゼまたはヒドロゲナーゼの働きにより水素を発生する[4]。ニトロゲナーゼによる場合，窒素→アンモニアの窒素固定反応に付随する反応として，水素イオンの還元により分子状水素が生産される[5]。この反応には電子供与体として還元型フェレドキシン（またはフラボドキシン）と，高エネルギー物質として多量のATPが必要であ

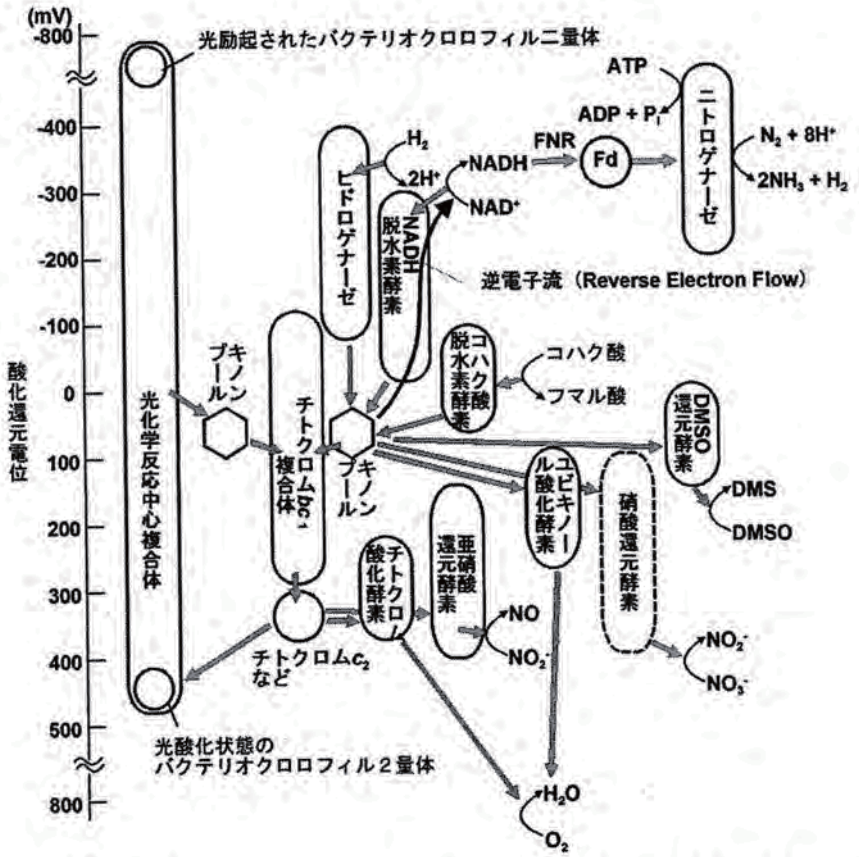

図２　紅色非イオウ光合成細菌細胞内におけるニトロゲナーゼを含むエネルギー代謝（電子伝達）のネットワークと逆電子流

り，これらは光合成によって供給される。ATPは前述した循環的な光合成電子伝達によって形成されたプロトン濃度勾配とATPaseの働きによって合成される。フェレドキシンは主にフェレドキシン-NAD(P)H酸化還元酵素（FNR）によりNAD(P)Hによって還元されるが，紅色細菌の光化学反応系は$NAD(P)^+$やフェレドキシンを直接還元できるほど強力な還元力は形成できない。紅色光合成細菌における光合成によるNADHの生産は，一見すると自由エネルギーが増加する方向の「逆電子流（Reverse Electron Flow）」と呼ばれる電子伝達により行われる（図２）。キノン/キノール（還元型キノン）の酸化還元中点電位は約０mV（ユビキノンの場合）であり，NAD^+/NADHでは－320 mVであるので，通常はキノール→NAD^+の電子移動は起こりにくい。しかし，プロトンの濃度勾配が高レベルに維持されている状態ではNADH脱水素酵素がプロトンの濃度勾配を消費して逆反応を起こし，キノールの電子がNAD^+の還元に使われる。このような熱力学的に不利な電子伝達によるNADHの合成は，鉄酸化細菌や硝化細菌など化学合成独立栄養細菌においても見られる反応である。

図３は紅色光合成細菌*Rhodopsuedomonas palustris*の光合成培養による生育の過程と，気体発生量の関係を調べた結果を示す。使用した培地は比較的富栄養な天然培地（PYS培地：表１）で，

表１　紅色非イオウ光合成細菌の培養液組成

PYS培地		LA培地	
ポリペプトン	0.50%	乳酸ナトリウム	0.50%
酵母エキス（粉末）	0.10%	アスパラギン酸Na	0.10%
コハク酸Na	0.50%	リン酸カリウム溶液	2.00%
基本塩溶液	1.00%	ビタミン混合液	0.10%
		基本塩溶液	1.00%
基本塩溶液		微量元素溶液	
EDTA（3Na）	4.12g	$MnSO_4 \cdot 4H_2O$	5.58g
$FeSO_4 \cdot 7H_2O$	1.11g	$ZnSO_4 \cdot 7H_2O$	1.44g
$MgSO_4 \cdot 7H_2O$	24.65g	$Co(NO_3)2 \cdot 6H_2O$	1.46g
$CaCl_2 \cdot 2H_2O$	2.94g	$CuSO_4 \cdot 5H_2O$	1.26g
NaCl	23.4g	$Na_2MoO_4 \cdot 2H_2O$	1.21g
微量元素溶液	1mL	H_3BO_3	1.55g
以上を蒸留水１Lに溶かす		EDTA(3Na)	20.6g
		以上を蒸留水0.5Lに溶かす	
ビタミン混合液		リン酸カリウム溶液	
ニコチン酸	100mg	KH_2PO_4	75g
チアミン	100mg	K_2HPO_4	78g
ビオチン	5mg	以上を蒸留水１Lに溶かす	
パラアミノ安息香酸	50mg		(pH6.8)
ビタミンB12	1mg		
パントテン酸-Ca	50mg		
ピリドキシン-HCl	50mg		
EDTA（3Na）	200mg		
葉酸	50mg		
以上を蒸留水0.1Lに溶かす			

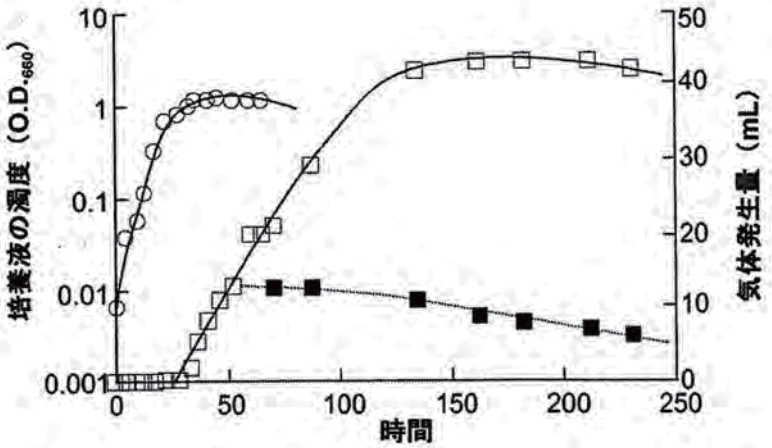

図3　紅色光合成細菌*Rhodopseudomonas palustris* CGA009株の嫌気・光照射培養における増殖と気体発生量の時間経過

○：直径18 mmのガラス試験管中における培養液の濁度（660 nm）を時間に対してプロットした増殖曲線。□：培養液（約30 mL）から発生した気体の蓄積量および，■：培養開始50時間後に遮光した場合の蓄積量。培養は30 mL容（直径18 mm×長さ180 mm）のスクリューキャップ試験管にPYS培地を入れ，0.5 mLのヘッドスペースを残して密閉し，20 cmの距離から100 Wのハロゲンランプで光照射しながら行った。同様に培養して分裂静止期にある菌液を前培養とし，1/100量を新しい培地に加えた時点を培養開始時間とした。試験管のキャップにはブチルゴムが組み込まれており（図4A参照），これに差し込んだ60 mL容のプラスチックシリンジのピストン上昇量を気体発生量（蓄積量）としてプロットした。

紅色非イオウ細菌を光従属栄養条件で培養する際に用いられる標準的な組成である。分裂静止期の細菌を前培養として，その0.3 mLを30 mLの新しい培地へ接種することで培養実験を開始し，30 μmol $m^{-2}s^{-1}$の光子束密度で光を当て，培養液の濁度をモニターしたところ，培養開始直後から指数関数的な増殖を示した後，およそ24時間で静止期へ移行した。指数増殖期には培養からの気体の発生は認められなかったが，培養を続けると，30時間前後から気体の発生が見られるようになり，時間経過とほぼ比例しながら150時間前後まで続いた。この気体をガスクロマトグラフィーで分析したところ，図4に示すように大部分が水素であった。これらのことは，指数増殖期にある細胞は，光エネルギーをもっぱら増殖のために利用していることと，密度効果により細胞の増殖が制限された後は，光合成によって得られる還元力が余剰となり，その還元力を水素生産に振り向けていることを示唆している。水素ガスの発生がある程度進行した培養開始50時間目の試験管をアルミホイルで遮光すると，それ以降の水素ガスの発生が止まることから，光合成が水素生産に利用されていることは明白である。その反応機作は，前述したプロトン駆動力に依存した逆電子流によるNADH→還元型フェレドキシンの蓄積と，それを用いたニトロゲナーゼによる水素イオンの還元反応であると考えられる。

ここで一つ注意しておきたいことは，すべての紅色非イオウ細菌が，図3で例示した*Rps. palustris*と同様な光合成水素生産能を示すわけでは無いということである。むしろ*Rps. palustris*

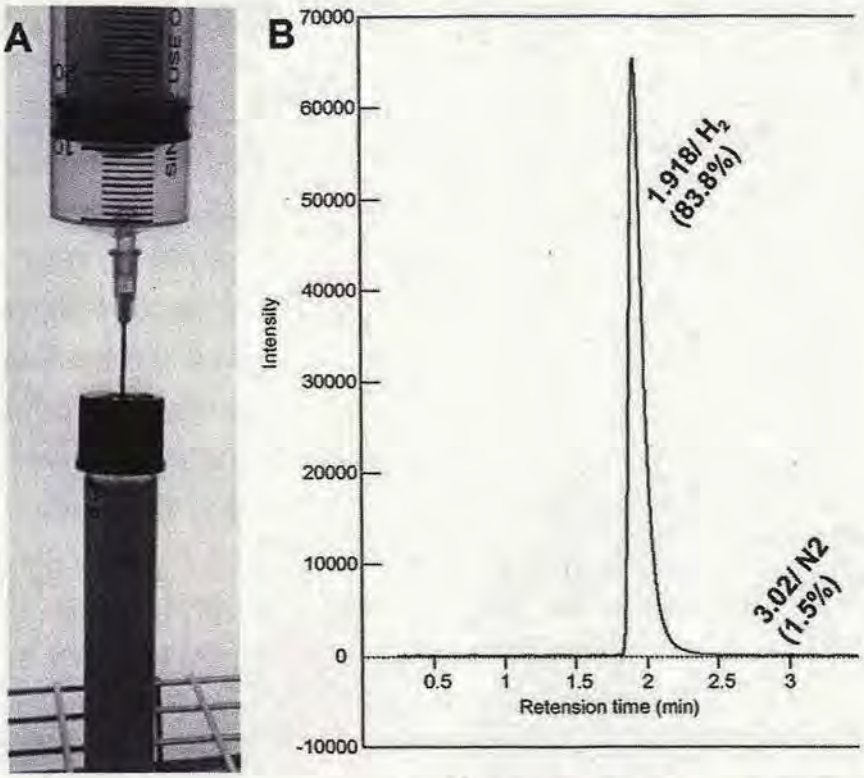

図4　紅色光合成細菌*Rhodopseudomonas palustris* CGA009株の光合成による培養の様子(A)と発生した気体のガスクロマトグラフ分析の結果(B)

は，例外的に水素ガスを発生しやすい種と言い換えた方がよいかもしれない。*Rhodobacter capsulatus*や*Rhodospirillum rubrum*など，紅色非イオウ細菌としては著名な種を含む様々な種を，ここで使用した培地（PYS培地）で同様に培養しても，水素ガスの発生はほとんどみられない。このような違いは恐らく，光合成による余剰な還元力の処理の仕方が種によって異なるという，プロテオバクテリアの多様なエネルギー代謝を反映しているものと考えられる。例えば酪酸その他有機物をポリマー化して貯蔵するなど，水素生産とは違う方法で余剰の還元力を処理しているのであろう。ただし，種によって異なるとは言っても，ニトロゲナーゼを含むエネルギー代謝のネットワークは大抵の紅色光合成細菌に共通して備わっているものであり，むしろ，ある特定の環境条件に置かれたときに電子伝達の複数ある経路のうちどこへ集中するかという酸化・還元のバランスが異なっていると理解すべきであろう。

ニトロゲナーゼの本来の役割は，分子状窒素をアンモニアへ還元すること（窒素固定）であり，その活性あるいは遺伝子発現は，生育環境中のN源の組成，特にアンモニウムイオンの濃度に依存する。たとえば上述の*Rba. capsulatus*をグルタミン酸のみをN源とする合成培地を用いて嫌気・光照射下で培養すると，増殖静止期に達した後，盛んに水素ガスを発生するが，10 mM NH_4Clの添加によってガス発生が停止することが知られている[6]。*Rps. palustris*でも，例示したPYS培地

に20 mMほどの硫安（$(NH_4)_2SO_4$）を加えて培養すると水素ガスの発生はほぼ抑制される。*Rps. palustris*の特殊性は，意図的にアンモニウムイオンを加えない限り，標準的な天然培地に含まれているN源の組成でもニトロゲナーゼの活性が高く維持されるという点にある。著者らは，様々な淡水，海水，土壌環境サンプルから，多数の紅色非イオウ細菌を単離した経験を持つが，*Rps. palustris* CGA009株ように高い水素発生活性を持つものはあまり多くない。

水素を代謝する酵素としてはヒドロゲナーゼがよく知られている。構造・機能の違いにより双方向性ヒドロゲナーゼ（Hox：bidirectional hydrogenase）と取り込み型ヒドロゲナーゼ（Hup：uptake hydogenase）に分けられており，これまでにゲノム解析が行われた紅色光合成細菌のほとんどにHupをコードする遺伝子が見つかっている。Hupの水素代謝は一方向的で，分子状水素を酸化して水素イオンを生成するとともに電子をキノンプールへ取り込む。Hoxは分子状水素の酸化も水素イオンの還元も両方触媒するが，紅色光合成細菌でHoxを持つものはイオウ細菌の*Thiocapsa roseopersicina*など一部の種に限られている。なお，紅色光合成細菌のヒドロゲナーゼの金属クラスターはNiFe型である。これらヒドロゲナーゼ，特にHupは，ニトロゲナーゼによって発生した水素ガスを再吸収してしまうので，光合成による水素生産を目指すとき，その収率を下げてしまう可能性が高い。図3で*Rps. palustris*の培養開始50時間で遮光したとき，水素発生が単に停止するだけでなく，時間とともに少しずつ減少している。これはHupによる水素の回収を示しているものと考えられる。このHupの遺伝子破壊による水素生産増進の試みがしばしばなされてきている。

図5は，β綱の紅色非イオウ細菌*Rubrivivax gelatinosus*を用いた，光合成による水素発生にお

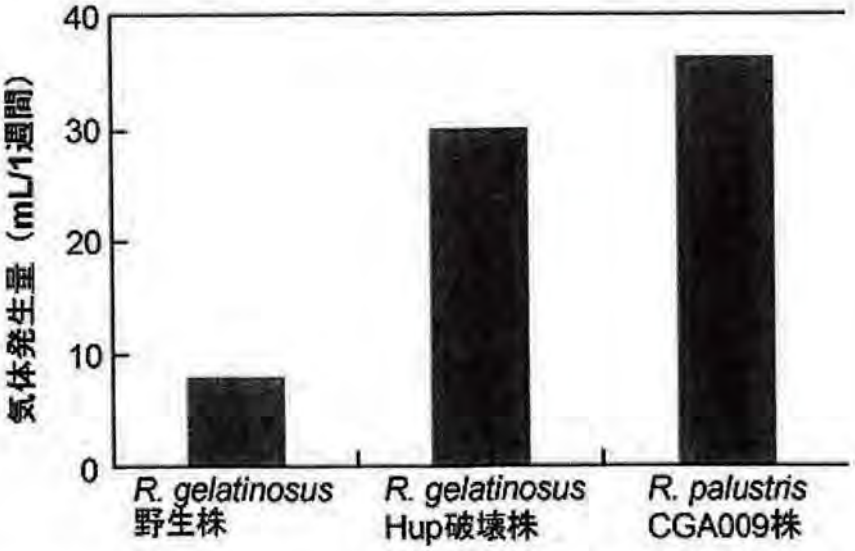

図5　紅色光合成細菌*Rubrivivax gelatinosus*野生株およびHup破壊株の嫌気・光照射培養における気体発生量

培養は図3と同様に行った。ただし培地はSA培地（表1）を使用した。比較のため，同条件で培養した*Rhodopseudomonas palustris* CGA009株の結果も示した。

けるHupの遺伝子破壊の効果を調べた結果である。嫌気・光照射条件下で一週間培養したとき，Hup破壊株は野生株の3倍以上の水素ガスを発生した。このことは，光合成細菌による水素生産を目指すとき，Hup遺伝子の破壊が非常に効果的であることを示している。なお，*Rvi. gelatinosus*はPYS培地（主にポリペプトン，酵母エキス，コハク酸から成る：表1）など一般的組成の天然培地では水素発生を示さないので，この実験ではN源をアスパラギン酸に限定した合成培地（LA培地：表1）を用いてニトロゲナーゼの発現を促進している。比較のため*Rps. palustris*の野生株を同じ培地で培養してみると，*Rvi. gelatinosus*のHup遺伝子破壊株と同等以上の水素ガスを発生した。*Rps. palustris*のHup遺伝子を破壊した場合，さらなる水素発生が見られるのか，あるいはそもそもHupの活性が低い（あるいはタンパク質合成量が少ない）のか，米国のReyら[7]によれば，*Rps. palustris*のCGA009株はHupの発現を制御する遺伝子にフレームシフトがあるためHupの発現量が低いと報告されているので，後者の可能性が高いものと思われる。

2.5　まとめと展望

光合成細菌（特に紅色非イオウ細菌）を水素生産に使う利点として，主に以下の3点が挙げられる。

(1) 光捕集色素としてカロテノイドおよびバクテリオクロロフィル*a*または*b*を用いるため，可視光だけでなく，800 nmから1000 nmにわたる赤外領域の光エネルギーをも活用できる。

(2) 嫌気・光照射条件（光合成条件）下で発生する気体は高純度の水素ガスである。シアノバクテリアや葉緑体と異なり，酸素発生を伴わない。

(3) 体制が単純で増殖速度も速い（100倍に増殖するのに約24時間）。水素発生を増加させるための遺伝子操作も比較的容易である。

(4) 暗発酵では1 molのヘキソースから2～4 molの水素しか生産できないのに対し，理論上は12 mol（実験的には8 mol以上）の水素が生産できる。

光合成生物を使った水素生産は，シアノバクテリアや藻類で活発な研究が続いている。これらの生物を使う利点の一つは末端電子供与体として水を利用できることである。すなわち，いくつかの無機塩さえあれば，あとは水と太陽光だけで水素を生産することができる。一方，紅色非イオウ細菌は基本的に光従属栄養生物であるので，生育にも水素生産にも有機物による電子の供給が必要となる。つまり上記(2)の利点はこの事と引き替えになっている。紅色非イオウ細菌の水素生産への活用は，有機物をいかに低コストで導入できるかがポイントとなろう。この問題に対するアプローチとして，たとえば食品工場の廃水処理と組み合わせることなどが考えられる。食品廃液などの有機物を高濃度に含む廃液のBODを低下させると同時に，水素を発生できるという利点がある。実際に，複雑な組成を持つ有機排水を，高分子有機物の分解能力が高い非光合成細菌と紅色非イオウ細菌*Rhodobacter sphaeroides*を組み合わせて分解し，水素を生産すると同時にBODも下げるという研究報告もなされている。また，光合成生育速度の高い草木，木材，大型藻類などのバイオマスを利用しやすいエネルギー源に変換する研究も行われつつあるが，エタノー

ルやバイオディーゼルと並んで水素もその有力候補である。暗発酵細菌は水素生産速度は高いが，ヘキソース1molあたり2～4molの水素しか生産できないのに対し，紅色細菌ではそれを数倍上まわる水素が生産できるという利点がある。

以上，酸素非発生型生物の光合成もまた，再生可能エネルギーの生産に活用可能[8]であることが少しでもお伝えできていれば幸いである。

文　献

1) J. Lavergne *et al.*, The purple photosynthetic bacteria. (eds. C. N. Hunter *et al.*), Springer, Dordrecht, The Netherlands, pp.509-536 (2009)
2) P. A. Bullough *et al.*, The purple photosynthetic bacteria. (eds. C. N. Hunter *et al.*), Springer, Dordrecht, The Netherlands, pp.155-179 (2009)
3) C. R. Woese, *Microbiol. Rev.*, **51**, 221-271 (1987)
4) H. Sakurai *et al.*, *J. Photochem. Photobiol. C: Photochem. Rev.*, **17**, 1-25 (2013)
5) 増川一ほか，微細藻類によるエネルギー生産と事業展望（監修，竹山春子），シーエムシー出版，pp.80-87 (2012)
6) S. Takakuwa *et al.*, *Arch. Microbiol.*, **136**, 20-25 (1983)
7) F. E. Rey *et al.*, *J. Bacteriol.*, **188**, 6143-6152 (2006)
8) 三宅淳，水素エネルギーシステム，**38**，20-26 (2013)

エリブリン（ハラヴェン）：海洋天然物からの創薬展開

Eribulin（Halaven）: Development of Anticancer Drug from Marine Natural Products

川添嘉徳，上村大輔
Yoshinori Kawazoe, Daisuke Uemura

海洋生物は，私たちの想像をはるかに超えた複雑な構造を持つ天然物を産生する．さらに重要なことは，それらの多くが切れ味鋭い生理活性物質として機能することである．近年上市された抗がん剤であるエリブリンも，そのような海洋性天然物であるハリコンドリンBをリード化合物として開発された．その開発の過程には，天然物の単離と構造決定，その全合成，そして作用機構の解明といった化学と生命科学のエッセンスが凝縮されており，今後の天然物をリード化合物とした創薬におけるモデルケースになると考えられる．

key words　ハリコンドリンB，エリブリン，海洋天然物

はじめに

エリブリン（商品名：ハラヴェン）は，「アントラサイクリン系およびタキサン系抗がん剤を含む少なくとも2種類のがん化学療法による前治療歴のある転移性乳がん」に対する適応で2010年11月に米国FDAにおいて認可された抗悪性腫瘍剤である．その後，2011年1月には欧州，同4月には日本でも承認を受け，現在はスイス，シンガポールにおいても販売されている．この医薬品はクロイソカイメンより単離された海洋天然物ハリコンドリンBをリード化合物としており，その開発は日本においてなされたものである．本稿では，ハリコンドリンBの発見からエリブリンに至る経緯を解説する．海洋性天然物をリードとした創薬に関する理解を深める一助となれば幸いである．

Ⅰ ハリコンドリンB：単離と構造決定

1．日本における海洋性天然物

日本の国土面積は約38万km^2で世界60位に位置するが，排他的経済水域は広大で世界第6位である．さらに，この水域の体積を見ると世界第4位であり，水深5,000m以深の保有体積では世界第一位となる．このような特徴は，島国である日本にとって海洋資源の潜在的な力を物語るものである．

そのような地理的背景に立脚して，天然有機化合物，特に海洋生物由来天然物およびそれらを中心とした生理活性低分子化合物探索の研究分野は，長年にわたり日本が世界を牽引してきた．日本人が関与した代表的な海洋性天然物には，フグ毒のテトロドトキシンや，貝毒オカダ酸，イワスナギンチャク由来の猛毒であるパリトキシンなどが挙げられる．これらは化学構造の複雑さから構造決定も困難を極め，さらに有機合成的にもチャレンジングな標的となっている．特筆すべきは，これら天然物が化学としての研究対象のみならず，切れ味鋭い試薬として生命科学研究においても重要な位置を占めているという事実である．このことは突き詰めれば，医薬品としての利用も示唆する．

2．ハリコンドリン類の単離と構造

海洋性天然物は必ずしも魚や貝によって作り出されるわけではない．多くは海藻に付着する渦鞭毛藻や細菌が真の生産者であると推定されている．つまり，これらが藻食性の魚に摂取され，続いて肉食性の魚に濃縮されていくという機構である．ところで，海綿は日にトン単位の海水を体内に組み入れ，共生微生物を体内に住まわせている．共生微生物の量は想像以上に多く，体の容積の40％を占めるという報告もある．したがって，天然物の真の生産者としての海洋微生物の濃縮体である海綿を材料とすれば，獲得できる天然物の多様性が広がると期待できる．筆者らはこの考えを実践し，容易に大量入手可能なクロイソカイメン（*Halichondria okadai* Kadota）を選び，生理活性物質の探索を行った．

クロイソカイメンは相模湾および房総半島以南の潮溜まりに多く見られ，黒あるいは黒灰色をしている（図1A）．筆者らは神奈川県三浦半島油壺にて採取したクロイソカイメン

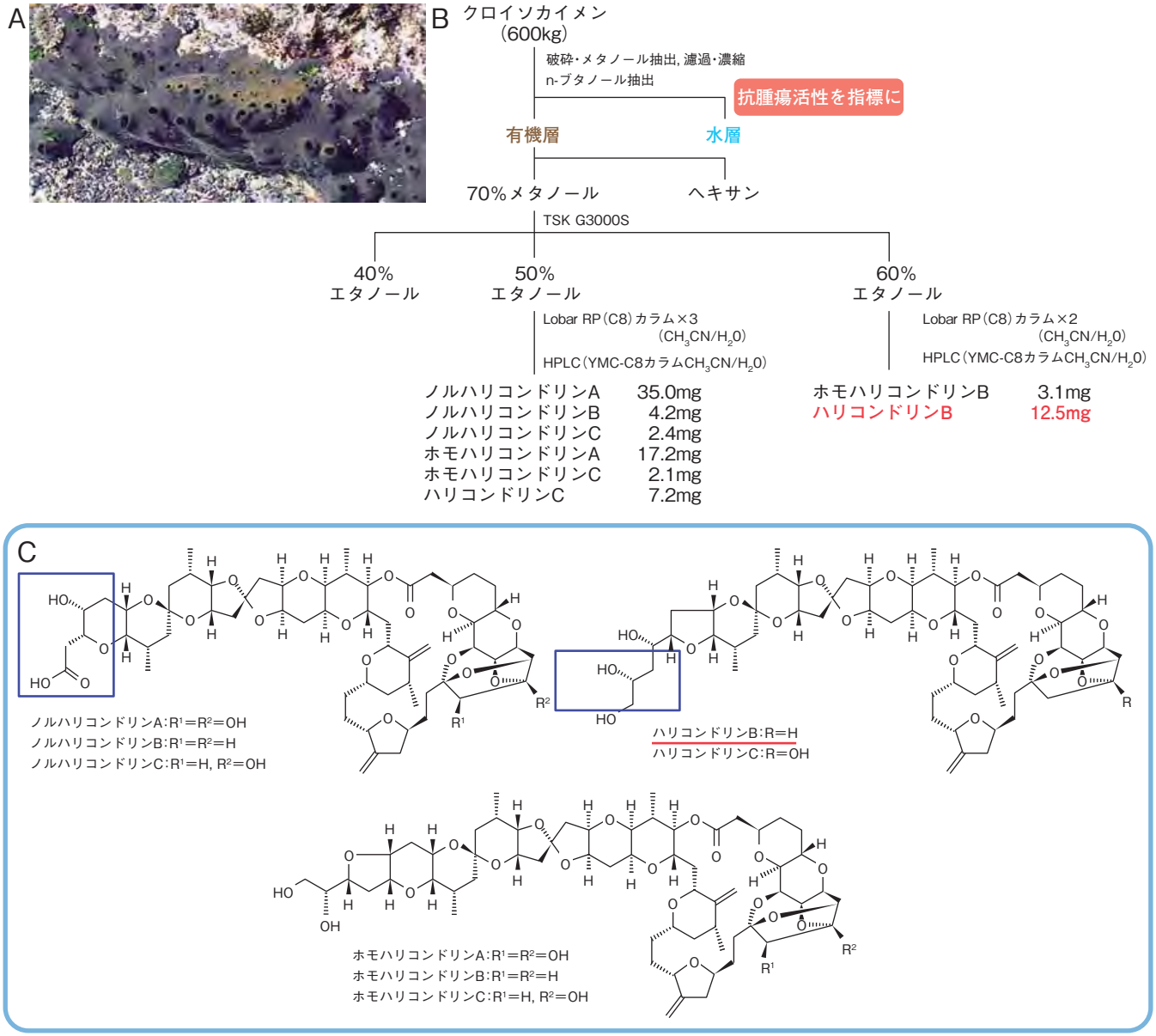

■図1　ハリコンドリン類の単離スキームと化学構造

A：クロイソカイメン*Halichondria okadai*.

B：600kgのクロイソカイメン粗抽出物をB-16メラノーマ細胞に対する抗腫瘍活性を指標に分離を進め，8種類のハリコンドリン類を得た.

C：決定したハリコンドリン類の化学構造.

600kgを用いて，その抽出物をマウスB-16メラノーマ細胞に対する抗腫瘍活性を指標にして生理活性物質の精製を進めた．この海綿にはホスファターゼ阻害活性を有するオカダ酸が比較的多量に含まれていることから，その混入を抑えるように工夫しながらカラム操作を繰り返した（図1B）．その結果，構造的に類似した8種の新規化合物の単離に成功し，これらをハリコンドリン類と名付けた（図1C）[1), 2)]．ハリコンドリン類の分子式と分子量を表1に示す．炭素数59, 60, 61の化合物をそれぞれノルハリコンドリン，ハリコンドリン，ホモハリコンドリンとした．同じ系列における質量の差32および16は，トリシクロ環部分における水酸基の数に由来し，その部分のヒドロキシ基数が2個あるいは1個のものを各々A群，C群とし，1つも有しない化合物をB群とした．

■表1　ハリコンドリン類の分子式と分子量

化合物	分子式	分子量
ノルハリコンドリンA	$C_{59}H_{82}O_{21}$	1126
ノルハリコンドリンB	$C_{59}H_{82}O_{19}$	1094
ノルハリコンドリンC	$C_{59}H_{82}O_{20}$	1110
ハリコンドリンB	$C_{60}H_{86}O_{19}$	1110
ハリコンドリンC	$C_{60}H_{86}O_{20}$	1126
ホモハリコンドリンA	$C_{61}H_{86}O_{21}$	1154
ホモハリコンドリンB	$C_{61}H_{86}O_{19}$	1122
ホモハリコンドリンC	$C_{61}H_{86}O_{20}$	1138

■表2　*in vitro*でのハリコンドリン類のB-16メラノーマに対する細胞毒性

化合物	IC_{50}(ng/mL)
ハリコンドリンB	0.093
ノルハリコンドリンA	5.2
ホモハリコンドリンA	0.26
ハリコンドリンC	0.35
ホモハリコンドリンB	0.10

■表3　*in vivo*でのハリコンドリンBのB-16メラノーマに対する抗腫瘍活性

化合物	用量(mg/kg)	投与方法	MST(日)	T/C(%)
ハリコンドリンB	0	第1～9日(腹腔内投与)	16	
	2.5		32.5	203
	5.0		39	244
	0	第1, 3, 5, 7, 9日(腹腔内投与)	19	
	5.0		37.5	197
	10.0		39.5	208
	0	第1, 5, 9日(腹腔内投与)	18	
	10.0		36.5	203
	20.0		39.5	219
	0	第1, 4, 7, 10日(静脈投与)	17.5	
	10.0		27.5	157

MST；生存期間中央値，T/C；試験群／対照群(Test group/Control group).

Ⅱ　ハリコンドリン類の抗腫瘍活性

1. *in vitro*における活性

表2に*in vitro*でのマウスB-16メラノーマ細胞に対する細胞毒性を示す．構造活性相関について考察してみると，トリシクロ環部分は最も疎水的なB群が良く，ハリコンドリンBおよびホモハリコンドリンBが他に比べて強い活性を示す(それぞれIC_{50}値が0.093ng/mL，0.10ng/mL)．構造式の左末端部分は親水性であるヒドロキシ基の数が多いほうが良く，カルボン酸になるとノルハリコンドリンAのように，極端に弱まる．

2. *in vivo*における活性

ハリコンドリンBのマウス個体における抗腫瘍効果を表3に示す．B-16メラノーマ細胞を移植したマウスにハリコンドリンBを腹腔内投与したところ，低濃度領域でも顕著な効果を示した．この効果は静脈注射によっても再現することができる．さらに，P-388あるいはL-1210という2種類のマウス白血病細胞を用いた動物実験でも，300%を超える延命効果が観察された．加えてマウス個体自身には顕著な毒性を示さなかったことから，ハリコンドリンBは新しい抗がん薬として期待が持たれた．

3. 米国国立がん研究所による抗腫瘍剤探索

ハリコンドリンBの発見と時を前後して，米国国立がん研究所(NCI)では新規抗腫瘍薬の探索が精力的に行われていた．およそ7000個の新規化合物をスクリーニングして複数の候補化合物が得られた．そのほとんどが穏やかな効果しか示さなかった中で，ただ2つの例外があった．その2つがハリコンドリンBとホモハリコンドリンBである[3]．これを契機にNCIでは，特に有望であったハリコンドリンBについて詳細な解析がなされた．この解析には，当時NCIに新たに導入された60-cell line screenを適用して行われている．本法では60種類の異なるヒト腫瘍細胞株に対して目的化合物を様々な濃度で処理し，各々の細胞種に対する作用プロファイルを作成する．それとは別に，およそ200種類からなる作用機構があらかじめわかっている“基準”化合物群の作用プロファイルを用意しておく．この両者を比較することによって，目的化合物の作用機構を解明しようというものである．一連

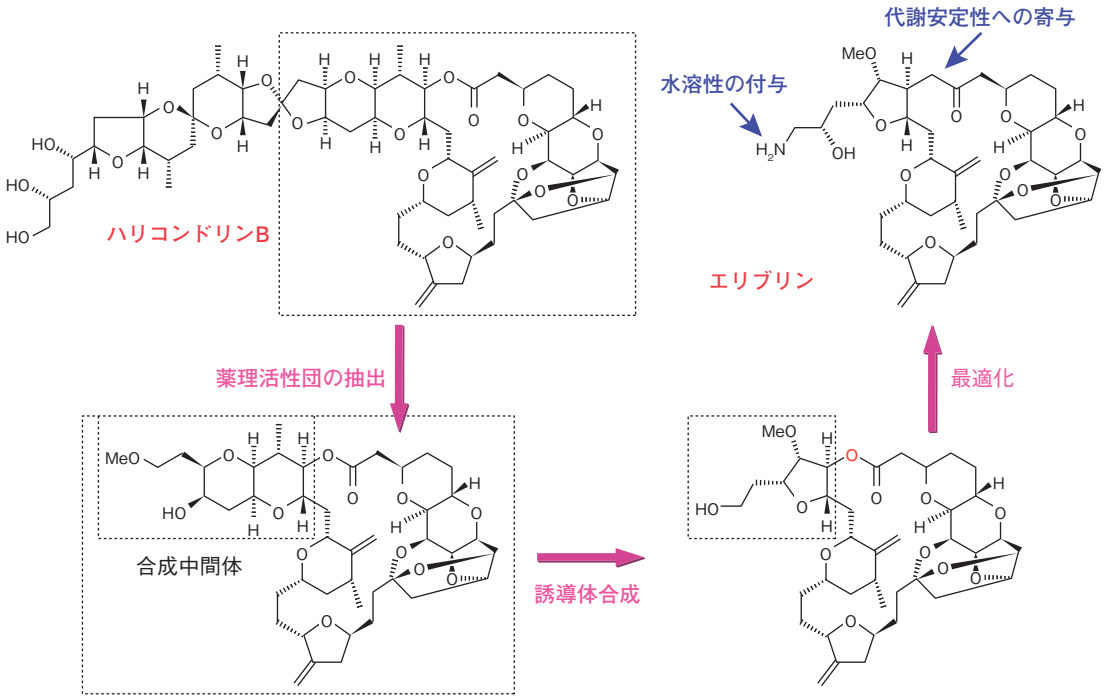

■図2　ハリコンドリンBからエリブリンへ
ハリコンドリンBの全合成を端緒に，この化合物に様々な修飾が加えられ，エリブリンが創製された．

の解析の結果，ハリコンドリンBの作用プロファイルは，コルヒチンやタキソールといったチューブリン結合性の細胞分裂阻害剤のそれと酷似しており，実際に細胞周期をM期に留めることが明らかとなった．同時に，*in vitro*においてチューブリンの重合を阻害することが示されている．

引き続きハリコンドリンBとチューブリンの結合様式が検討されたところ，この天然物はビンブラスチンのチューブリンへの結合を非競合的に阻害すると同時に，コルヒチンのチューブリンへの結合を阻害しないことが明らかとなった．この結果は，ハリコンドリンBがビンブラスチンやコルヒチンとは異なる部位に結合することを示唆する．したがって，ハリコンドリンBの強力な抗腫瘍活性に加えて，そのチューブリンとの相互作用機構が既存のチューブリン結合性細胞分裂阻害剤とは著しく異なることから，この化合物は有望な臨床開発候補と認識されるようになった．しかしながら，さらなる開発研究を進めるうえで1つ問題があった．供給量が極端に少ないのである．600kgの海綿からわずか12.5mgしか得られないため，これ以上の開発研究を行うことは事実上不可能である．このような状況を打破したのが，ハリコンドリンBの有機化学的全合成の達成である．

Ⅲ　ハリコンドリンBの全合成

ハリコンドリン類は，分子中に31～34個の不斉炭素を含む大変複雑な化合物である．このことから，この天然物は有機合成的にも非常に興味深い合成ターゲットとして捉えられていた．事実1986年の構造決定に端を発して，複数のグループがその全合成に着手している．そして1992年，ハーバード大学の岸 義人博士のグループからついにハリコンドリンBの全合成が報告された[4), 5)]．本合成の卓越している点は，ハリコンドリンBの全合成のみならずそれらの実用的供給の確立をも志向していたことである．岸博士らはこの目的のために，大量スケールでも実施可能な新規有機クロムカップリング法（野崎-檜山-岸カップリング反応；NHK反応）を開発し，ハリコンドリンBの合成に応用した．この合成ルートはすべての合成パーツが複数あるハリコンドリンB異性体の中でも最終的にハリコンドリンBのみに収束していくというエレガントなものである．ハリコンドリンBの全合成の報告は現在においてもこの一例のみであり，合成化学の金字塔の1つであると捉えられている．この研究は，ハリコンドリンBの大量供給を可能にしたばかりでなく，後述するように臨床開発において新しい知見を生み出すことに貢献した．

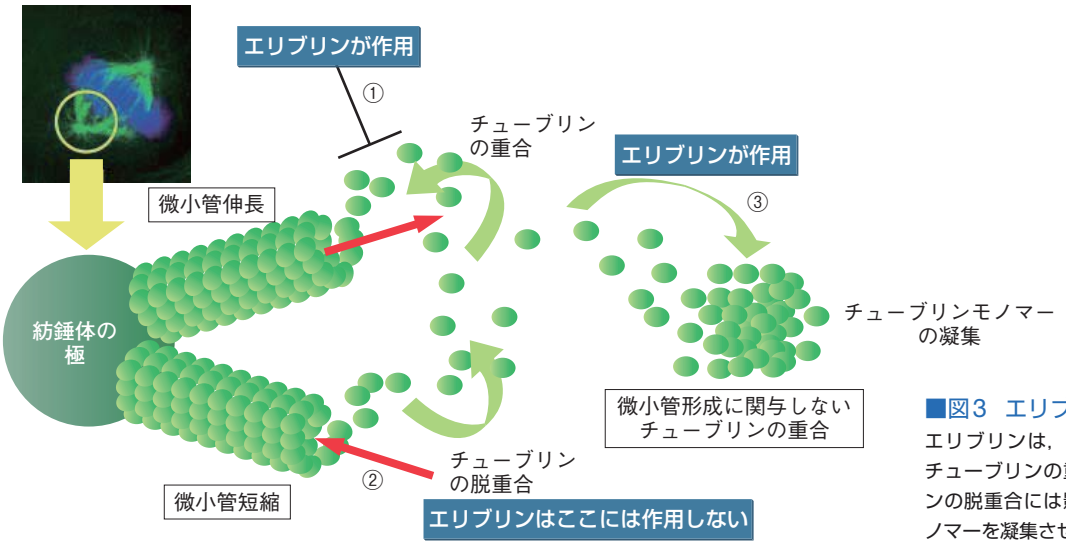

■図3　エリブリンの作用機構
エリブリンは，①微小管の（＋）端に結合してチューブリンの重合を抑制する，②チューブリンの脱重合には影響しない，③チューブリンモノマーを凝集させる，作用を持つ．

Ⅳ ハリコンドリンBからエリブリンへ

1．ハリコンドリンBの活性部位の抽出

一般に医薬品の開発においては，天然物や化合物ライブラリーにおけるヒット化合物そのものが臨床で利用されることはほとんどない．これら医薬品の候補となるリード化合物に対して，活性の増強や不都合な作用の軽減，体内動態や代謝安定性の向上を目的に，種々の化学的修飾を施して最適化がなされる．しかし，ハリコンドリンBは非常に複雑な構造であり，また酸に対して不安定であることから化学修飾の幅も限られている．ところが化学的合成が可能であれば，この限りではない．つまり合成の途上で，将来的な修飾を見据えた足場を導入しておくことが容易にできる．さらには，基本骨格に対して手を入れることも可能である．このような考えのもと，まずはハリコンドリンBの合成中間体に対してその抗がん作用が精査された．その結果，ハリコンドリンB分子全体のうち，右側のラクトン環部分が薬理活性団であることが示された．

2．エリブリンの誕生

こうして見いだされた薬理活性団に対して，数百種類の誘導体を用いた構造活性相関研究が展開された．このような誘導体の中から*in vitro*，*in vivo*モデルにおいて理想とする活性を示した化合物がエリブリンである[6]（図2）．エリブリンの左端のアミノ基は化合物に水溶性を付与し，またラクトンからケトンへの変換によって代謝安定性が向上している．ちなみに，これら一連のエリブリン開発はハーバード大学の岸教授とボストンにあるエーザイ株式会社の研究所でなされたものであり，Eisai Research Instituteの頭文字とチューブリンtubulinを掛け合わせてエリブリン（eribulin）と命名されたものである．

Ⅴ エリブリン

1．エリブリンの作用機構

エリブリンのリード化合物であるハリコンドリンBがチューブリンと結合して微小管の重合を阻害することで細胞分裂を阻止する活性を持つことから，エリブリンのチューブリンに対する作用について興味が持たれ，詳細な解析がなされている[7)~9)]．その要点は次の3つにまとめることができる．つまりエリブリンは，①微小管の伸長途上の（＋）端に結合してさらなる伸長（チューブリンの重合）を阻害する，②逆に微小管の短縮（チューブリンの脱重合）には影響を及ぼさない，③チューブリンモノマーと結合し凝集体を形成させることで微小管への取り込みを抑制する（図3）．以上のことは，電子顕微鏡を用いた微小管繊維の直接観察や，蛍光タンパク質を利用した細胞内微小管の可視化によって，そのダイナミズムを解析するという手法で行われた．このことを裏付けるように，エリブリンで処理した分裂中期の細胞では紡錘糸が顕著に短くなり，染色体は中期板に整列できないことが明らかとなった．その結果，細胞分裂がG2/M期で停止し，アポトーシスによる細胞死が誘導される[10)]．またごく最近では，エリ

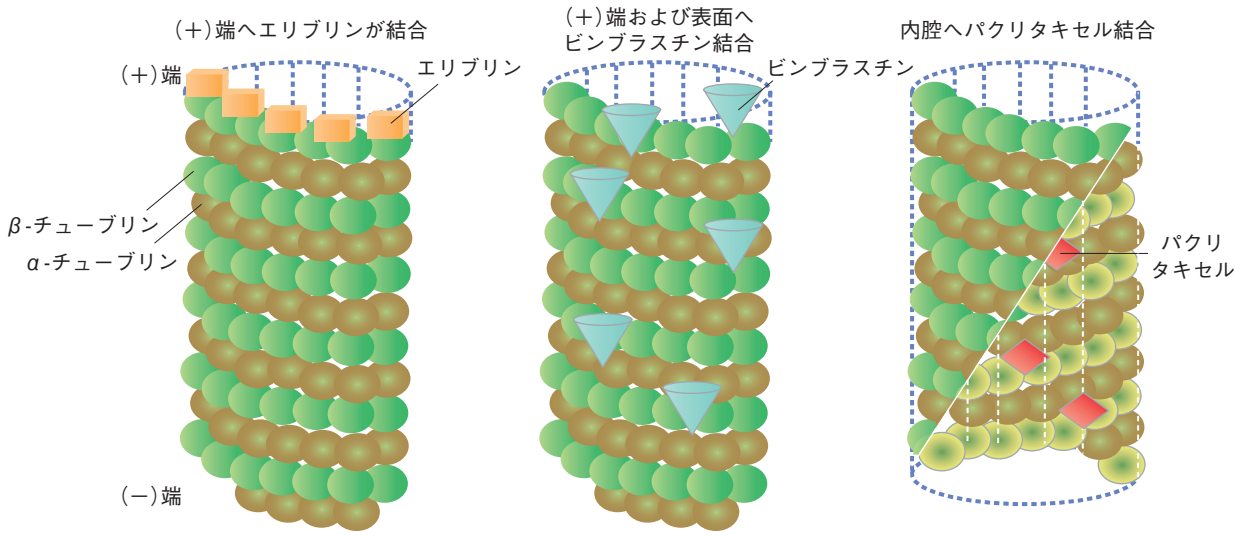

■図4　エリブリン，ビンブラスチン，パクリタキセルのチューブリンへの結合
これら3種のチューブリン結合性抗がん剤は，チューブリンへの結合部位が異なる．エリブリンはチューブリンの(+)端，ビンブラスチンは(+)端および表面，パクリタキセルは内腔にそれぞれ結合する．

ブリンはβ-チューブリンに結合してこのタンパク質の立体構造を変化させるというモデルが提案されている[11]．

エリブリンのこのような作用は，それまでに知られていたチューブリンに作用する分裂阻害剤とは一線を画するものであった．例えば，ビンブラスチンやパクリタキセルは同じく微小管に作用するが，チューブリンの重合と脱重合の双方を阻害する．この微小管ダイナミクスの差は，微小管に対する各々の薬剤の結合部位が異なるためであると説明されている(図4)．このようにエリブリンは，これまでには見られない新規メカニズムを通して抗がん作用を発揮することから，既存のチューブリン結合性抗がん剤に対して耐性を獲得したがんに対しても有効であると考えられ，有望な臨床効果が期待された．

2．エリブリンの臨床試験

このような経過を受けて2002年，第Ⅰ相臨床試験が開始された．本試験で臨床用量が決定され，特に顕著な効果が見られた乳がんに対して2004年に第Ⅱ相，2006年に第Ⅲ相試験が開始，そして2009年これら臨床試験が終了した[12),13)]．その要点は，エリブリン投与群は全生存期間の中央値が13.12カ月であり，治験医師選択療法施行群の10.65カ月を2.5カ月上回ったことである．本試験の重要な点は，対照としてプラセボ(偽薬)ではなく既存の化学療法や放射線療法などの治験医師選択療法が用いられたことである．このことは，本治験がより実践的な臨床現場を反映しており，エリブリンが単剤で延命効果を発揮しうる薬剤であることを示している．本臨床試験の結果を受けて，エリブリンは日米欧において同日に承認申請が行われた．

おわりに

冒頭でも述べたように，エリブリンは日米欧に加えてスイス，シンガポールでも承認を受け，ハラヴェンという製品名で販売が開始された．クロイソカイメンから得られた微量天然物ハリコンドリンBの発見から四半世紀の時を経て，がんの化学療法に新機軸を打ち出す抗腫瘍薬剤が生まれたわけである〔ハラヴェン(Halaven)という製品名はクロイソカイメンの学名*Halichondria okadai*からとられている〕．現在ハラヴェンはさらに14カ国において承認申請中であり，またその適応を拡充すべく非小細胞肺がんや軟部肉腫に対する臨床試験が展開されている．さらに2013年4月には，ハラヴェンが上皮間葉転換に関わる遺伝子群の発現を変動させることが報告された．この結果は，本剤のがん転移抑制効果にも期待を抱かせるものである．

エリブリンはリード化合物ハリコンドリンBと比較すればコンパクトになったとはいえ，分子量が826，さらに分子内に19個もの不斉炭素原子を持つ分子である．このことは2^{19}個，つまり524,288個の立体異性体が存在することを意味する．エリブリンの実用的な合成法も開発され[14)~16)]，現代

化学は総行程64段階の反応を巧みに制御しながら，膨大な異性体のうちのただ1つを年間数kgというスケールで製造することを可能にしている．海洋性天然物は化学構造の複雑さゆえに研究者の興味を掻き立ててきたが，そのことは逆にこれらを医薬品のリード化合物として利用する際の大きな障壁となっていた．エリブリンの商品化成功は，このような障壁をも同時に引き下げることに成功したのではないかと筆者らは感じている．海洋にはまだまだ未知の活性を持つ天然物が豊富に眠っており，それらが有効に活用されることを期待している．

PROFILE 川添嘉徳
■ 神奈川大学天然医薬リード探索研究所 研究員
■ E-mail：ss199164bn@kanagawa-u.ac.jp
京都大学大学院医学研究科修了．博士（医学）．大阪大学医学部，ベイラー医科大学，京都大学化学研究所を経て，2012年より現職．

PROFILE 上村大輔
■ 神奈川大学理学部 化学科 教授
■ E-mail：uemurad@kanagawa-u.ac.jp
名古屋大学大学院理学研究科修了．理学博士．静岡大学教授，名古屋大学教授，慶応大学教授を経て，2011年より現職．名古屋大学名誉教授．金沢大学監事．

文献

1) Uemura D, et al: J Am Chem Soc (1985) 107: 4796-4798
2) Hirata Y, et al: Pure Appl Chem (1986) 58: 701-710
3) Bai RL, et al: J Biol Chem (1991) 266: 15882-15889
4) Aicher TD, et al: J Am Chem Soc (1992) 114: 3162-3164
5) Choi HW, et al: Pure Appl Chem (2003) 75: 1-17
6) Zheng W, et al: Bioorg Med Chem Lett (2004) 14: 5551-5554
7) Towle MJ, et al: Cancer Res (2001) 61: 1013-1021
8) Jordan MA, et al: Mol Cancer Ther (2005) 4: 1086-1095
9) Smith JA, et al: Biochemistry (2010) 49: 1331-1337
10) Kuznetsov G, et al: Cancer Res (2004) 64: 5760-5766
11) Bai R, et al: J Chem Inf Model (2011) 51: 1393-1404
12) Vahdat LT, et al: J Clin Oncol (2009) 27: 2954-2961
13) Cortes J, et al: Lancet (2011) 377: 914-923
14) Namba K, et al: J Am Chem Soc (2004) 126: 7770-7771
15) Namba K, et al: J Am Chem Soc (2005) 127: 15382-15383
16) Kim DS, et al: J Am Chem Soc (2009) 131: 15636-15641

Forum on Immunopathological Diseases and Therapeutics, 4(1):33–41 (2013)

Apoptosis as a Practical Target for Identifying Anticancer Agents of Marine Origin

Osamu Ohno,[1,*] Toshiaki Teruya,[2] Kiyotake Suenaga,[1*] & Daisuke Uemura[3]

[1]Department of Chemistry, Faculty of Science and Technology, Keio University, 3-14-1 Hiyoshi, Yokohama 223-8522, Japan; [2]Faculty of Education, University of Ryukyus, 1 Senbaru, Nishihara, Okinawa 901-0213, Japan; [3]Department of Chemistry, Faculty of Science, Kanagawa University, 2946 Tsuchiya, Hiratsuka 259-1293, Japan

*Address all correspondence to: Osamu Ohno, Department of Chemistry, Faculty of Science and Technology, Keio University, 3-14-1 Hiyoshi, Yokohama 223-8522, Japan, ohno@chem.keio.ac.jp, or Kiyotake Suenaga, Department of Chemistry, Faculty of Science and Technology, Keio University, 3-14-1 Hiyoshi, Yokohama 223-8522, Japan, Email: suenaga@chem.keio.ac.jp

ABSTRACT: Natural products and their synthetic analogs are widely used as anticancer drugs. Many anticancer drugs originated from cytotoxic compounds, and most have been shown to induce apoptosis in cancer cells. Based on the variety of their modes of action, the identification of new cytotoxic compounds may lead to the discovery of new types of drugs. Recently, much attention has been given to the metabolites of marine organisms due to their strong cytotoxicity. For example, eribulin mesylate, a synthetic analog of halichondrin B isolated from *H. okadai* Kadota, has been developed as an anticancer drug. Novel cytotoxic substances, such as halichonines, bisebromoamides, and biselyngbyasides, have been isolated from marine organisms as apoptosis-inducing agents. All of these compounds may possess therapeutic potential, and thus, efforts to identify new apoptosis-inducing agents of marine origin may contribute to the discovery of new pharmaceuticals.

KEY WORDS: anticancer drug, apoptosis, marine organism, bisebromoamide, biselyngbyaside

ABBREVIATIONS: ER: endoplasmic reticulum; **ERK:** extracellular signal regulated protein kinase; **PDGF:** platelet-derived growth factor; **SAR:** structure-activity relationships

I. INTRODUCTION

Cancer accounts for a large number of deaths, approximately 13% of all deaths worldwide, and this number is increasing.[1] There is a constant need for new compounds that can serve as leads for new anticancer drugs. Currently, many naturally occurring compounds and their synthetic analogs have been developed as anticancer drugs, such as doxorubicin, paclitaxel, vinblastine, and etoposide. As these drugs illustrate, many anticancer drugs originated from cytotoxic compounds. Most of the cytotoxic anticancer drugs in current use have been shown to induce apoptosis in cancer cells. The fact that various compounds that interact with different targets induce cell death with common features (e.g., DNA fragmentation, chromatin condensation, cell shrinkage and membrane blebbing) suggests that cytotoxicity is determined by the ability of the cell to engage apoptosis.

Apoptosis, or programmed cell death, is a natural process for removing undesired cells such as those with harmful mutations, unusual detachment, or deviation from cell-cycle control. The deregulation of apoptosis can disrupt the balance between cell proliferation and cell death, which can lead to diseases such as cancer.[2] Apoptosis is usually triggered by intracellular cues such as DNA damage and oxidative stress,

2151-8017/13/$35.00 © 2013 by Begell House, Inc.

and by extracellular cues including death ligand-stimulation, matrix detachment, and lack of growth factors. Two central pathways are involved in the process of apoptosis, one involving the activation of caspase proteases and another involving a mitochondrial pathway. These phenomena can be controlled by some cytotoxic compounds. Many factors participate in the process by which cytotoxic compounds induce apoptosis; however, the regulation of this association may have therapeutic effects. There are various mechanisms of action, such as a loss of membrane integrity, inhibition of metabolic enzymes, blockage of signal transduction, inhibition of DNA replication, inhibition of mitosis, etc. Due to the multitude of these modes of action, the identification of new cytotoxic compounds could be associated with the discovery of new types of drugs.

II. ANTICANCER AGENTS FROM MARINE ORGANISMS

Natural products and their synthetic analogs are widely used as anticancer drugs, as mentioned above. Natural products, especially those from terrestrial plants and microorganisms, have been the most productive source of drug molecules, and such pharmacologically active compounds continue to play an important role in the development of new investigational drugs.[3,4] However, much attention has recently been given to the metabolites of marine organisms due to their strong cytotoxicity.[5] Marine natural products are attractive sources of remarkable bioactive compounds with unique structures.[6,7] Among marine organisms, marine invertebrates have become a focus for the discovery of new drugs. Ecteinascidin-743 (ET-743; Trabectedin) is a marine tetrahydroisoquinoline alkaloid that was isolated from *Ectenascidia turbinata*, a tunicate that grows on mangrove roots throughout the Caribbean sea.[8–10] The mechanism of action of ET-743 has been elucidated: ET-743 binds to the minor groove of DNA, thereby disrupting the cell cycle and inhibiting cell proliferation.[11,12] Recently, ET-743 was approved for use in patients with advanced soft tissue sarcoma (STS) and ovarian cancer in the United States and the European Union.

Marine sponges are also widely known to be a rich source of biologically active and structurally unique secondary metabolites. They take seawater into their bodies, gather food by filtration, and coexist with symbiotic microorganisms; therefore, they may produce many kinds of secondary metabolites.[13] *Halichondria okadai* Kadota (Fig. 1A), a sponge that is abundant in the tidal zone in the Pacific Ocean south of the Boso Peninsula in Japan, contains many compounds that show potential for clinical or biological uses. For example, okadaic acid,[14] halichlorine,[15,16] and halichondrins[17] have already been isolated from this sponge. Halichondrins were isolated based on their cytotoxicity toward mouse melanoma B16 cells.[18] Halichondrin B (Fig. 1B) appears to show significant anticancer activity *in vivo* and was revealed to exert its cytotoxicity through its direct interaction with tubulin.[19]

Based on an analysis of structure–activity relationships (SAR), the right half of the molecule was revealed to be active and was found to induce apoptosis in cancer cells.[20,21] Finally, a synthetic analog of halichondrin B, eribulin mesylate (Halaven™, Fig. 1B) was developed by Kishi *et al.* and Eisai Co., Ltd., and was recently approved for the treatment of patients with metastatic breast cancer in the United States, the European Union, Japan, and many other countries.[22,23] Thus, the identification of new cytotoxic compounds in marine organisms is important for finding new anticancer drugs. As part of the ongoing search for cytotoxic substances from *H. okadai* Kadota, novel sesquiterpene alkaloids, halichonines A, B, and C were recently

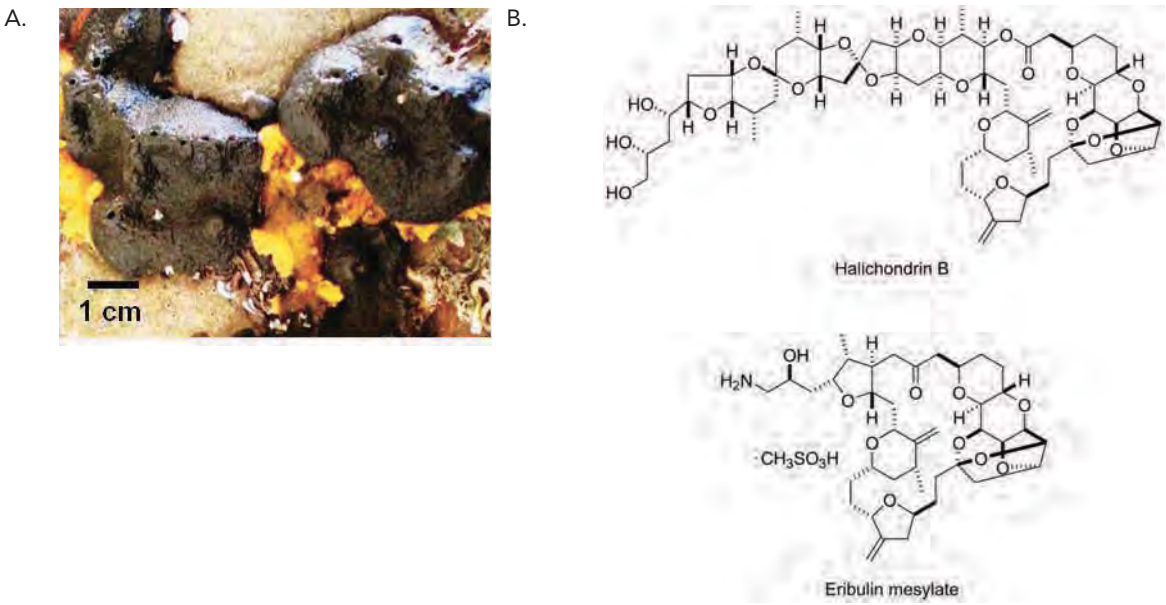

FIGURE 1. Picture of *H. okadai* Kadota (A), and structures of halichondrin B and eribulin mesylate (B).

isolated (Fig. 2).[24] Based on the results of spectroscopic analyses and syntheses, their structures were determined to include a 6,6-bicyclic ring system and two prenylated amine moieties. Halichonines A, B, and C were examined for their cytotoxicity against the mammalian cancer cell lines (L1210 and PC13), and each compound showed moderate activity. In particular, halichonine B induced apoptosis in human leukemia HL60 cells.

FIGURE 2. Structures of halichonines A, B, and C.

Because their mechanisms of action are still unknown, further studies are warranted.

III. MARINE CYANOBACTERIAL CYTOTOXIC METABOLITES

Marine microorganisms are believed to be the true producers of many of the biologically active metabolites that have been isolated from marine invertebrates. In fact, okadaic acid was found in dinoflagellates.[25,26] Dolastatin 10, which was originally isolated from the sea hare *Dolabella auricularia*, has been isolated from the marine cyanobacterium.[27,28] Therefore, marine microorganisms are potential sources of drugs. Cyanobacteria, many of which live in the ocean, are prolific producers of structurally unique and biologically active secondary metabolites.[29] Thus, they have been recognized as a source of pharmaceutical lead compounds.[30] For example, TZT-1027, a synthetic dolastatin 10 analog, is currently being evaluated in phase II clinical trials in several countries.[31] Cryptophycin-309 and

cryptophycin-249, which are derivatives of the terrestrial cyanobacterial peptide cryptophycin-1, have undergone preclinical efficacy studies.[32] Curacins[33] and largazole,[34] which were isolated from marine cyanobacteria, are also clinical candidates for anticancer drugs. In the search for novel biologically active compounds from marine cyanobacteria, novel compounds bisebromoamide, biselyngbyaside, and their analogs have been isolated.[35–39] All of these compounds were isolated as cytotoxic compounds, and their structures were established by spectroscopic analyses, including 2D NMR techniques, and by synthetic studies.

A. Novel Apoptosis-Inducing Agents, Bisebromoamides

Bisebromoamide was isolated from the marine filamentous cyanobacterium *Lyngbya* sp., which was collected at Bise, Okinawa Prefecture, Japan (Figs. 3A, B).[35] Bisebromoamide was found to exhibit strong cytotoxicity toward human epithelial carcinoma HeLa cells. Bisebromoamide was evaluated for its growth-inhibitory activity across a panel of 39 human cancer cell lines (HCC panel),[40] and the average concentration required for 50% growth inhibition (GI_{50}) in the 39 cell lines was 40 nM. Bisebromoamide was confirmed to induce apoptosis in several cancer cell lines.[41] In addition, bisebromoamide was revealed to selectively inhibit the PDGF-induced phosphorylation of ERK in NRK cells. With regard to its anticancer activity, human tumor xenograft tests *in vivo* are now underway. Furthermore, an SAR analysis of bisebromoamide using norbisebromoamide (Fig. 3B) and synthetic derivatives revealed that the ketone, bromine atom, phenolic hydroxyl group, and methyl group on the thiazoline moiety of bisebromoamide are not important for its cytotoxicity.[36] The total synthesis of bisebromoamide has been achieved by both Ye *et al.*[42] and Ma *et al.*[43] Ma *et al.* also carried out an SAR analysis and revealed that the stereochemistry of the methylthiazoline part and the methyl group at the 4-methylproline residue in bisebromoamide have limited influence on its cytotoxicity.

The mode of action of bisebromoamide was studied, and it was revealed that bisebromoamide stabilized actin filaments.[44] Bisebromoamide was demonstrated to enhance the polymerization of monomeric globular actin *in vitro* in a concentration-dependent manner. In addition, fluorescence-conjugated bisebromoamide was synthesized; it localized in a filamentous pattern similar to that of actin filaments in HeLa cells. These results suggest that bisebromoamide targets actin filaments. The actin-targeting agents cytochalasins and jasplakinolide have been well-studied with regard to their apoptosis-inducing activity.

A.

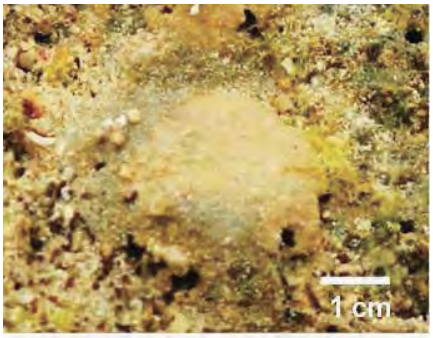

B.

FIGURE 3. Picture of *Lyngbya* sp. (A), and structures of bisebromoamide and norbisebromoamide (B).

The disruption of actin filaments induced by these compounds has been shown to initiate caspase-dependent apoptosis signaling.[45–51] However, the relationship between bisebromoamide-induced actin-stabilization and its apoptosis-inducing activity has not been fully investigated. Because bisebromoamide has potential as a preclinical candidate for use in cancer chemotherapy, further structural and functional analyses might reveal the relationship between actin and other target biomacromolecules of bisebromoamide, which should offer better perspectives for the design and development of new anticancer drugs.

B. Novel Apoptosis-Inducing Agents, Biselyngbyasides

Biselyngbyaside, a new 18-membered macrolide glycoside, was isolated from the marine cyanobacterium *Lyngbya* sp. which was also collected at Bise, Okinawa Prefecture, Japan (Figs. 4A, B, C).[37] Biselyngbyaside exhibited moderate cytotoxicity against HeLa cells. Recently, its novel analogs, biselyngbyolide A[38] and biselyngbyasides B-D,[39] were isolated from the marine cyanobacterium *Lyngbya* sp. which was collected in the Tokunoshima Island, Kagoshima Prefecture, Japan (Fig. 4C). The activity of biselyngbyolide A without a sugar moiety was shown to be approximately 100-fold stronger than that of biselyngbyaside and biselyngbyaside B. Thus, 3-*O*-methylglucoside moieties may reduce cytotoxicity. In contrast, biselyngbyaside C showed less cytotoxicity compared with biselyngbyaside. Therefore, the conjugated diene parts were revealed to be essential for cytotoxicity of biselyngbyasides. In addition, biselyngbyaside, biselyngbyolide A and biselyngbyaside B were determined to exhibit apoptosis-inducing activity against both HeLa cells and HL60 cells. Furthermore, biselyngbyaside and biselyngbyolide A exhibited broad-spectrum cytotoxicity in an HCC panel, indicating that they likely inhibit cancer cell proliferation through a characteristic mechanism. The data-mining tool COMPARE,[40] which may be able to predict the molecular targets of novel bioactive compounds, indicated that biselyngbyaside and biselyngbyolide A were somewhat analogous to thapsigargin.[39] Thapsigargin, an inhibitor of Ca^{2+} influx into endoplasmic reticulum (ER), induces apoptosis toward cancer cells via ER-stress based on its ability to increase intracellular Ca^{2+} concentrations.[52–56] Maintenance of the intracellular Ca^{2+} gradient is essential for various aspects of cellular and physiological functions. Through the analysis of changes in the intracellular Ca^{2+} concentration in HeLa cells, biselyngbyasides were demonstrated to increase the cytosolic Ca^{2+} concentration in the absence of extracellular Ca^{2+}. These studies indicated that biselyngbyasides, like thapsigargin, induce the release of Ca^{2+} from ER, and then induce apoptosis. Thus, it has been hypothesized that biselyngbyasides induce apoptosis toward cancer cells via ER-stress. Because biselyngbyasides exhibited apoptosis-inducing activity in several types of cell lines, cancer cells may generally contain their specific target molecules, which are related to ER stress. Although further investigation is needed, biselyngbyasides may have a therapeutic potential as new anticancer agents.

IV. CONCLUSIONS

Marine organisms are prolific producers of novel biologically active compounds and have been recognized as a source of pharmaceutical lead compounds. Especially, apoptosis-inducing agents of marine origin have the potential to be applied in anticancer drugs. In fact, the anticancer drug eribulin mesylate was developed from halichondrin B, which was isolated from *H. okadai* Kadota. The novel apoptosis-inducing agents halichonines were isolated from the same sponge.

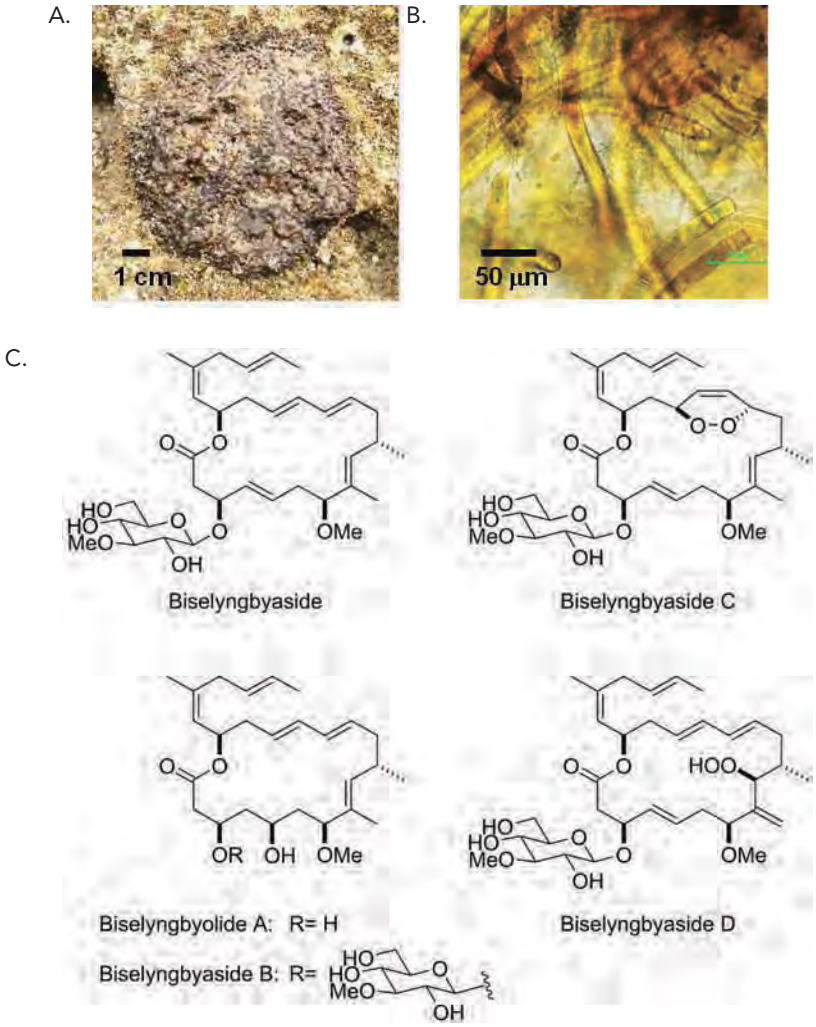

I U . Pictures of *Lyngbya* sp. (A, B), and structures of biselyngbyaside and its analogs (C).

Bisebromoamides and biselyngbyasides were isolated as novel cytotoxic metabolites of the marine cyanobacteria *Lyngbya* sp. Analyses of their biological functions revealed that bisebromoamide targeted actin filaments and exhibited significant apoptosis-inducing activity. Biselyngbyasides were also shown to induce apoptosis toward cancer cells based on their ER-stress-inducing activity. All of these compounds may have therapeutic potential as anticancer drugs. Thus, the search for novel apoptosis-inducing agents from marine organisms should contribute to the discovery of new pharmaceuticals.

AC NO L N S

The authors thank Prof. S. Suda (University of Ryukyus) and Dr. T. Yamori (Japanese Foundation for Cancer Research) for their contributions to the research presented here. Support was provided in part by Grants-in-Aid from the Ministry of Education, Culture, Sports,

Science and Technology of Japan (Grant nos. 19710193, 21221009, 24310160 and 25750386).

NC S

1. Ferlay J, Shin H, Bray F, Forman D, Mathers C, Parkin DM. Estimates of worldwide burden of cancer in 2008: GLOBOCAN 2008. Int J Cancer. 2010;127:2893–2917.
2. Reed JC. Dysregulation of apoptosis in cancer. J Clin Oncol. 1999;17:2941–53.
3. Newman DJ, Cragg GM. Natural products as sources of new drugs over the last 25 years. J Nat Prod. 2007;70:461–77.
4. Butler MS. Natural products to drugs: natural product-derived compounds in clinical trials. Nat Prod Rep. 2008;25:475–561.
5. Molinski TF, Dalisay DS, Lievens SL, Saludes JP. Drug development from marine natural products. Nat Rev Drug Discov. 2009;8:69–85.
6. Uemura D. Bioorganic studies on marine natural products--diverse chemical structures and bioactivities. Chem Rec. 2006;6:235–48.
7. Uemura D. Exploratory research on bioactive natural products with a focus on biological phenomena. Proc Jpn Acad Ser B Phys Biol Sci. 2010;86:190–201.
8. Rinehart KL, Holt TG, Fregeau NL, Stroh JG, Keifer PA, Sun F, Li LH, Martin DG. Ecteinascidins 729, 743, 745, 759A, 759B, and 770 potent antitumor agents from the Caribbean tunicate Ecteinascidia turbinate. J Org Chem. 1990;55:4512–5.
9. Guan Y, Sakai R, Rinehart KL, Wang AHJ. Molecular and crystal structures of ecteinascidins; potent antitumor compounds from the Caribbean tunicate Ecteinascidia turbinate. J Biomol Struct Dyn. 1993;10:793–818.
10. Jimeno JM, Faircloth G, Cameron L, Meely K, Vega E, Gómez JMA, Sousa-Faro F, Rinehart K. Progress in the acquisition of new marine-derived anticancer compounds; development of ecteinascidin-743 (ET-743). Drugs Fut. 1996;21:1155–65.
11. Zewail-Foote M, Hurley LH. Ecteinascidin 743a minor groove alkylator that bends DNA toward the major groove. J Med Chem. 1999;42:2493–7.
12. Pommier Y, Kohlhagen G, Bailly C, Waring M, Mazumder A, Kohn KW. DNA sequence- and structure-selective alkylation of guanine N2 in the DNA minor groove by ecteinascidin 743, a potent antitumor compound from the caribbean tunicate Ecteinascidia turbinate. Biochemistry. 1996;35:13303–9.
13. Vogel G. The inner lives of sponges. Science. 2008;320:1028–30.
14. Tachibana K, Scheuer PJ, Tsukitani Y, Kikuchi H, Van Engen D, Clardy J, Gopichand Y, Schmitz FJ. Okadaic acid, a cytotoxic polyether from two marine sponges of the genus Halichondria. J Am Chem Soc. 1981;103:2469–71.
15. Kuramoto M, Chou T, Yamada K, Chiba T, Hayashi Y, Uemura D. Halichlorine, an inhibitor of VCAM-1 induction from the marine sponge Halichondria okadai Kadota. Tetrahedron Lett. 1996;37:3867–70.
16. Xu S, Yoshimura H, Maru N, Ohno O, Arimoto H, Uemura D. Pinnarine, another member of the halichlorine family. Isolation and preparation from pinnaic acid. J Nat Prod.2011;74:1323-26.
17. Uemura D, Takahashi K, Yamamoto T, Katayama C, Tanaka J, Okumura Y, Hirata Y. Norhalichondrin A: an antitumor polyether macrolide from a marine sponge. J Am Chem Soc. 1985;107:4796–8.
18. Hirata Y, Uemura D. Halichondrins - antitumor polyether macrolides from a marine sponge. Pure Appl Chem. 1986;58:701–10.
19. Bai RL, Paull KD, Herald CL, Malspeis L, Pettit GR, Hamel E. Halichondrin B and homohalichondrin B, marine natural products binding in the vinca domain of tubulin. Discovery of tubulin-based mechanism of action by analysis of differential cytotoxicity data. J Biol Chem. 1991;266:15882–9.
20. Towle MJ, Salvato KA, Budrow J, Wels BF, Kuznetsov G, Aalfs KK, Welsh S, Zheng W, Seletsky BM, Palme MH, Habgood GJ, Singer LA, Dipietro LV, Wang Y, Chen JJ, Quincy DA, Davis A, Yoshimatsu K, Kishi Y, Yu MJ, Littlefield BA. In vitro and in vivo

anticancer activities of synthetic macrocyclic ketone analogues of halichondrin B. Cancer Res. 2001;61:1013–21.

21. Kuznetsov G, Towle MJ, Cheng H, Kawamura T, TenDyke K, Liu D, Kishi Y, Yu MJ, Littlefield BA. Induction of morphological and biochemical apoptosis following prolonged mitotic blockage by halichondrin B macrocyclic ketone analog E7389. Cancer Res. 2004;64:5760-–6.
22. Huyck TK, Gradishar W, Manuguid F, Kirkpatrick P. Eribulin mesylate. Nat Rev Drug Discov. 2011;10:173–4.
23. Newman S. Eribulin, a simplified ketone analog of the tubulin inhibitor halichondrin B, for the potential treatment of cancer. Curr Opin Investig Drugs. 2007;8:1057–66.
24. Ohno O, Chiba T, Todoroki S, Yoshimura H, Maru N, Maekawa K, Imagawa H, Yamada K, Wakamiya A, Suenaga K, Uemura D, Halichonines A, B, and C, novel sesquiterpene alkaloids from the marine sponge Halichondria okadai Kadota. Chem Commun. 2011;47:12453-–5.
25. Dickey RW, Bobzin SC, Faulkner DJ, Bencsath FA, Andrzejewski D. Identification of okadaic acid from a Caribbean dinoflagellate, Prorocentrum concavum. Toxicon. 1990;28:371–7.
26. Koike K, Sato S, Yamaji M, Nagahama Y, Kotaki Y, Ogata T, Kodama M. Occurrence of okadaic acid-producing Prorocentrum lima on the Sanriku coast, northern Japan. Toxicon. 1998;36:2039–42.
27. Pettit GR, Kamano Y, Herald CL, Tuiman AA, Boettner EF, Kizu H, Schmidt JM, Baczynskyj L, Tomer KB, Bontems RJ. The isolation and structure of a remarkable marine animal antineoplastic constituent: dolastatin 10. J Am Chem Soc. 1987;109: 6883–5.
28. Luesch H, Moore RE, Paul VJ, Mooberry PS, Corbett TH. Isolation of dolastatin 10 from the marine cyanobacterium Symploca species VP642 and total stereochemistry and biological evaluation of its analogue symplostatin 1. J Nat Prod. 2001;64:907–10.
29. Gerwick WH, Tan LT, Sitachitta N. Nitrogen-containing metabolites from marine cyanobacteria. In: Cordell G, editor. The Alkaloids. San Diego: Academic Press; 2001. p. 75–184.
30. Tan LT. Bioactive natural products from marine cyanobacteria for drug discovery. Phytochemistry. 2007;68:954–79.
31. Tamura K, Nakagawa K, Kurata T, Satoh T, Nogami T, Takeda K, Mitsuoka S, Yoshimura N, Kudoh S, Negoro S, Fukuoka M. Phase I study of TZT-1027, a novel synthetic dolastatin 10 derivative and inhibitor of tubulin polymerization, which was administered to patients with advanced solid tumors on days 1 and 8 in 3-week courses. Cancer Chemother Pharmacol. 2007;60:285–93.
32. Liang J, Moore RE, Moher ED, Munroe JE, Al-awar RS, Hay DA, Varie DL, Zhang TY, Akins JA, Martinelli MJ, Shih C, Ray JE, Gibson LL, Vasudevan V, Polin L, White K, Kushner J, Simpson C, Pugh S, Corbett TH. Cryptophycins-309, 249 and other cryptophycin analogs: preclinical efficacy studies with mouse and human tumors. Investig New Drugs. 2005;23:213–24.
33. Wipf P, Reeves JT, Day BW. Chemistry and biology of curacin A. Curr Pharm Des. 2004;10:1417–37.
34. Hong J, Luesch H. Largazole: from discovery to broad-spectrum therapy. Nat Prod Rep. 2012;29:449–56.
35. Teruya T, Sasaki H, Fukazawa H, Suenaga K. Bisebromoamide, a potent cytotoxic peptide from the marine cyanobacterium Lyngbya sp.: isolation, stereostructure, and biological activity. Org Lett. 2009;11:5062–5.
36. Sasaki H, Teruya T, Fukazawa H, Suenaga K. Revised structure and structure-activity relationship of bisebromoamide and structure of norbisebromoamide from the marine cyanobacterium Lyngbya sp. Tetrahedron. 2011;67:990–4.
37. Teruya T, Sasaki H, Kitamura K, Nakayama T, Suenaga K. Biselyngbyaside, a macrolide glycoside from the marine cyanobacterium Lyngbya sp. Org Lett. 2009;11: 2421–4.
38. Morita M, Ohno O, Suenaga K. Biselyngbyolide A, a novel cytotoxic macrolide from the marine

cyanobacterium Lyngbya sp. Chem Lett. 2012;41:165–7.

39. Morita M, Ohno O, Teruya T, Yamori T, Inuzuka T, Suenaga K. Isolation and structures of biselyngbyasides B, C, and D from the marine cyanobacterium Lyngbya sp., and the biological activities of biselyngbyasides. Tetrahedron. 2012;68:5984–90.
40. Yamori T, Matsunaga A, Sato S, Yamazaki K, Nakanishi O, Kohno H, Nakajima Y, Komatsu H, Andoh T, Tsuruo T. Potent antitumor activity of MS-247, a novel DNA minor groove binder, evaluated by an in vitro and in vivo human cancer cell line panel. Cancer Res. 1999;59:4042–9.
41. Suzuki K, Mizuno R, Suenaga K, Teruya T, Tanaka N, Kosaka T, Oya M. Bisebromoamide, an extract from Lyngbya species, induces apoptosis through ERK and mTOR inhibitions in renal cancer cells. Cancer Med. 2013;2:32–9.
42. Gao X, Liu Y, Kwong S, Xu Z, Ye T. Total synthesis and stereochemical reassignment of bisebromoamide. Org Lett. 2010;12:3018–21.
43. Li W, Yu S, Jin M, Xia H, Ma D. Total synthesis and cytotoxicity of bisebromoamide and its analogues. Tetrahedron Lett. 2011;52:2124–7.
44. Sumiya E, Shimogawa H, Sasaki H, Tsutsumi M, Yoshita K, Ojika M, Suenaga K, Uesugi M. Cell-morphology profiling of a natural product library identifies bisebromoamide and miuraenamide A as actin filament stabilizers. ACS Chem Biol. 2011;6:425–31.
45. Rubtsova SN, Kondratov RV, Kopnin PB, Chumakov PM, Kopnin BP, Vasiliev JM. Disruption of actin microfilaments by cytochalasin D leads to activation of p53. FEBS Lett. 1998;430:353–7.
46. Suria H, Chau LA, Negrou E, Kelvin DJ, Madrenas J. Cytoskeletal disruption induces T cell apoptosis by a caspase-3 mediated mechanism. Life Sci. 1999;65:2697–707.
47. Yamazaki Y, Tsuruga M, Zhou D, Fujita Y, Shang X, Dang Y, Kawasaki K, Oka S. Cytoskeletal disruption accelerates caspase-3 activation and alters the intracellular membrane reorganization in DNA damage-induced apoptosis. Exp Cell Res. 2000;259:64–78.
48. White SR, Williams P, Wojcik KR, Sun S, Hiemstra PS, Rabe KF, Dorscheid DR. Initiation of apoptosis by actin cytoskeletal derangement in human airway epithelial cells. Am J Respir Cell Mol Biol. 2001;24:282–94.
49. Morley SC, Sun GP, Bierer BE. Inhibition of actin polymerization enhances commitment to and execution of apoptosis induced by withdrawal of trophic support. J Cell Biochem. 2003;88:1066–76.
50. Posey SC, Bierer BE. Actin stabilization by jasplakinolide enhances apoptosis induced by cytokine deprivation. J Biol Chem. 1999;274:4259–65.
51. Odaka C, Sanders ML, Crews P. Jasplakinolide induces apoptosis in various transformed cell lines by a caspase-3-like protease-dependent pathway. Clin Diagn Lab Immunol. 2000;7:947–52.
52. Tsukamoto A, Kaneko Y. Thapsigargin, a Ca2+-ATPase inhibitor, depletes the intracellular Ca2+ pool and induces apoptosis in human hepatoma cells. Cell Biol Int. 1993;17:969–70.
53. Furuya Y, Lundmo P, Short AD, Gill DL, Isaacs JT. The role of calcium, pH, and cell proliferation in the programmed (apoptotic) death of androgen-independent prostatic cancer cells induced by thapsigargin. Cancer Res. 1994;54:6167–75.
54. Middleton JP, Albers FJ, Dennis VW, Raymond JR. Thapsigargin demonstrates calcium-dependent regulation of phosphate uptake in HeLa cells. Am J Physiol. 1990;259:F727–F731.
55. Sekiguchi F, Shimamura K, Akashi M, Sunano S. Effects of cyclopiazonic acid and thapsigargin on electromechanical activities and intracellular Ca2+ in smooth muscle of carotid artery of hypertensive rats. Br J Pharmacol. 1996;118:857–64.
56. Zhou H, Iwasaki H, Nakamura T, Nakamura K, Maruyama T, Hamano S, Ozaki S, Mizutani A, Mikoshiba K. 2-Aminoethyl diphenylborinate analogues: selective inhibition for store-operated Ca2+ entry. Biochem Biophys Res Commun. 2007;352:277–82.

総合論文

構造解明を指向したポリオール天然物シンビオジノライドの合成研究

髙村　浩由[1*]
門田　　功[1*]
上村　大輔[2]

Synthetic Study of the Polyol Natural Product Symbiodinolide toward the Structural Elucidation

Hiroyoshi Takamura*, Isao Kadota*, and Daisuke Uemura

Symbiodinolide is a polyol marine natural product isolated from dinoflagellate *Symbiodinium* sp. This natural product exhibits voltage-dependent N-type Ca^{2+} channel-opening activity at 7 nM and COX-1 inhibition activity at 2 μM. The planar structure of symbiodinolide was elucidated by the detailed 2D NMR analysis. However, the huge and complex molecular structure of this molecule featuring a molecular weight of 2,860 and the presence of 61 chiral centers has hampered the complete stereochemical determination. Herein, we report our synthetic study of symbiodinolide toward the structural elucidation.

Key words: natural product, polyol, symbiodinolide, synthetic study, stereochemistry, structural elucidation

はじめに

生物活性を有する天然有機化合物(天然物)の構造解明は，重要な研究課題の1つである。構造解明は，構造活性相関に関する重要な知見を与え，活性発現部位の特定，分子プローブの設計，生体内標的分子の同定，さらには作用機序の解明への展開が可能となるからである。過去数十年にわたる機器分析の著しい発展に伴い，天然物の構造決定が微量スケールで可能となってきた。しかしながら，対象とする天然物が多官能基化されている場合や巨大分子サイズを有する場合などには，機器分析による構造解析は困難を伴う。このような場合には，化学合成による構造決定が強く要求される[1]。

海洋生物が生産する二次代謝産物は，顕著な生物活性と複雑な化学構造を有する天然物の宝庫であり，有用な医薬シーズとして注目を集めている[2]。海洋天然物のなかでも，ブレベトキシン，ハリコンドリン，マイトトキシン，パリトキシンに代表されるポリエーテルおよびポリオール類は，多様で強力な生物活性と人知を凌駕するほどの複雑な分子構造を有することから，天然物化学，合成化学，生化学，薬理学などの様々な分野で注目を集めている[3]。

シンビオジノライド(1，図1)は，培養された渦鞭毛藻 *Symbiodinium* sp. より単離されたポリオール天然物である[4,5]。本化合物は，7 nM の濃度で電位依存性カルシウムチャネル開口活性を有し，また 2 μM の濃度で COX-1 阻害活性(65% の阻害)を有することが現在までに明らかとなっている。構造解析においては，各種二次元 NMR 測定法を駆使することで，その平面構造が決定されたが，分子量 2,860 および 61 個の不斉中心に特徴付けられた巨大かつ複雑な分子構造を有するため，さらなる解析は困難を極め，全立体構造の解明には至っていない。そこで，シンビオジノライド(1)の立体構造をフラグメントごとに解明することとし，現在までにスキーム1に示す分解反応を行っている。すなわち，1に対しアルカリ加水分解を行ったところ，アミド部位およびエステル部位での結合開裂が進行し，C1'-C25' フラグメントに相当する分解生成物を得ることができた[4]。また，これとは別の分解反応として，ルテニウム触媒を用いたエチレンとのクロスメタセシスを行ったところ，C14-C24 フラグメント，C23-C34 フラグメント，および C33-C42 フラグメントをそれぞれ得ることができた[6]。なお，分解生成物の絶対立体構造はこの段階では未決定であるが，最終決定したものを便宜上記載してある。本稿においては，分解生成物として得られた各フラグメントの合成も含めて，シンビオジノライド(1)の構造解明に向けた合成化学的アプローチについて紹介したい。

[1*] 岡山大学大学院自然科学研究科(700-8530 岡山市北区津島中 3-1-1)
[1*] Graduate School of Natural Science and Technology, Okayama University (3-1-1 Tsushimanaka, Kita-ku, Okayama 700-8530, Japan)
[2] 神奈川大学理学部(259-1293 平塚市土屋 2946)
[2] Faculty of Science, Kanagawa University (2946 Tsuchiya, Hiratsuka 259-1293, Japan)

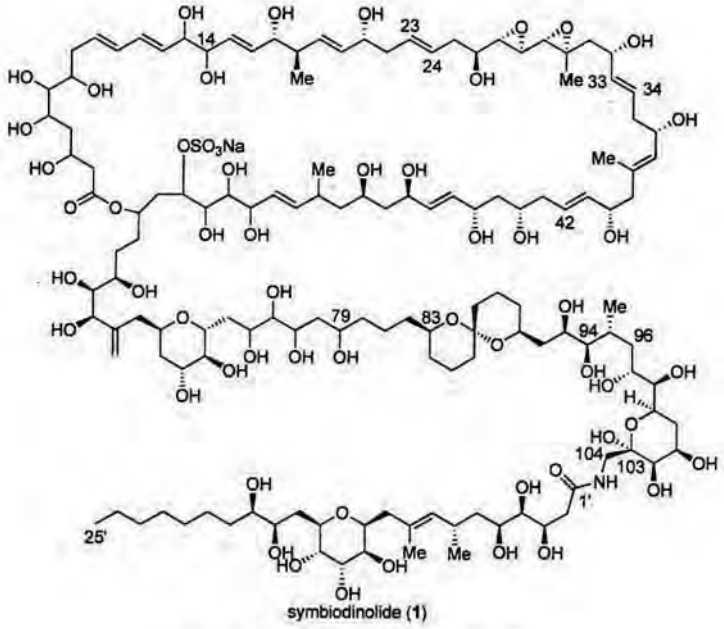

Fig. 1 Structure of symbiodinolide (1).

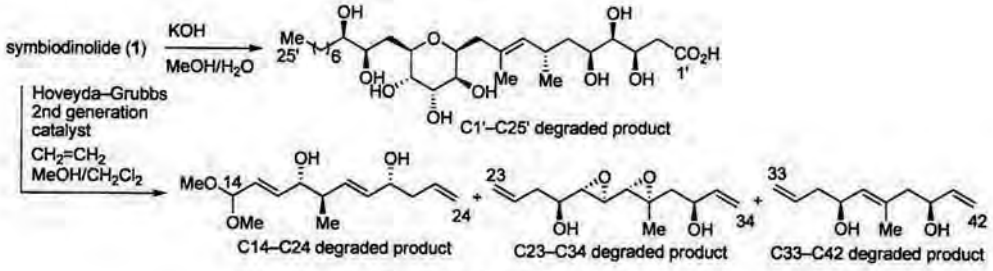

Scheme 1 Degradation of 1.

1. C1'-C25' フラグメントの合成

まずは，C1'-C25' フラグメントの合成に着手することとした。C1'-C25' フラグメント2の逆合成解析をスキーム2に示す。本フラグメントは，左側フラグメント3と右側フラグメント4とを連結し，三置換アルケン部位を構築することで合成することとした。3の左側鎖は，1-nonyne から調製されるリチウムアセチリドとトリフレート5とのカップリングにより導入することとした。三連続酸素官能基部位を有するテトラヒドロピラン5は，ジヒドロピラン6に対する官能基化により合成することとした。一方，右側フラグメント4は D-xylose から合成することとした。

まずは，左側フラグメント18の合成を検討した(スキーム3)。Tri-*O*-acetyl-D-glucal から合成した既知のアルコール7[7] に対し，*N,N*-dimethylacetamide dimethyl acetal を作用させることで Eschenmoser-Claisen 転位を行い，アミド8を得た。続いて，ヨードラクトン化を行い9とした後，sodium methoxide で処

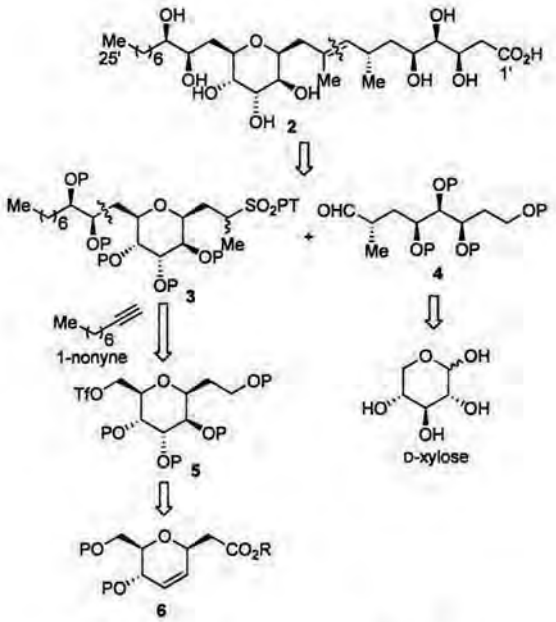

Scheme 2 Retrosynthetic analysis of 2.

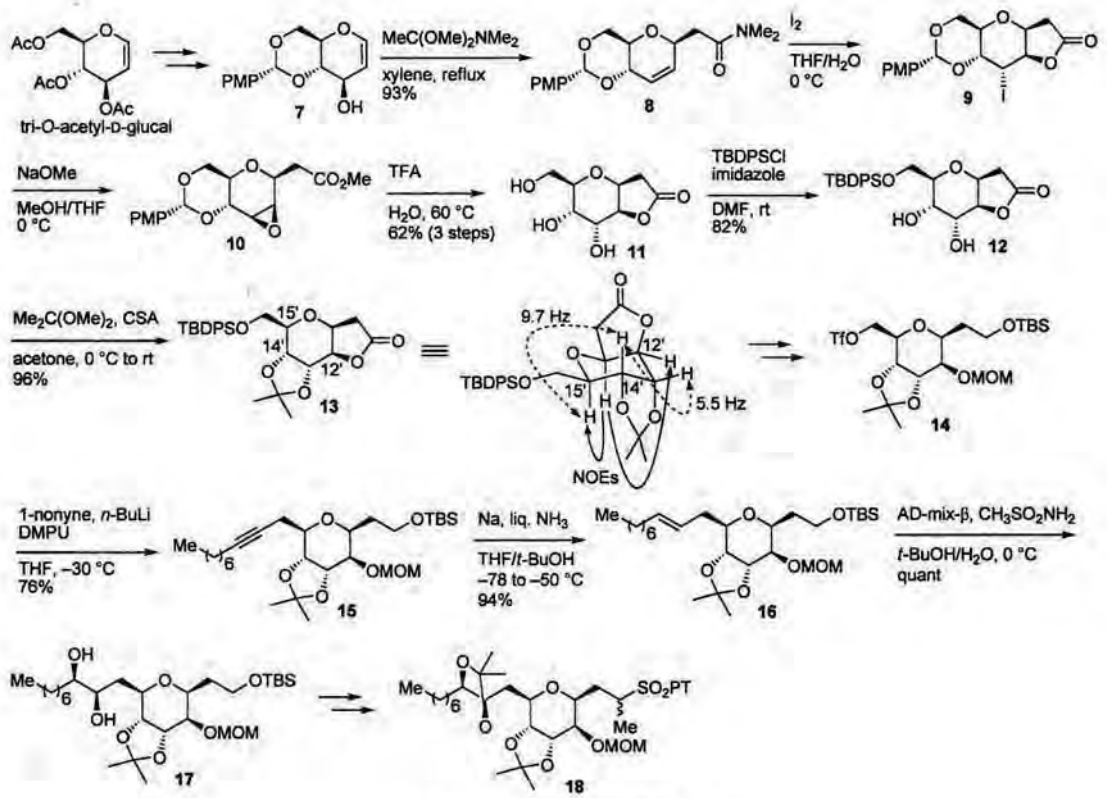

Scheme 3 Synthesis of 18.

理することでエポキシド10とした。10にTFAを作用させることで，位置および立体選択的なエポキシド部位の開環を行いトリオール11とした[8]。この際に生じた1級ヒドロキシ基を保護しシリルエーテル12とした後，アセトナイド保護を行い13とした。ここでテトラヒドロピラン環の立体構造の確認を行った。すなわち，$^{3}J_{14',15'}$が9.7 Hzであることから，H-14'とH-15'がともにアキシアル配置を有していることがわかった。また，$^{3}J_{13',14'}$が5.5 Hzであることから，H-13'とH-14'がそれぞれエクアトリアルおよびアキシアル配置を有することが明らかとなった。さらに，H-11'/H-12'およびH-11'/H-15'にNOE相関が観測されたことから，これらが*syn*の関係にあることがわかった。続いて，さらなる変換を行った。13をトリフレート14へと変換した後，1-nonyneから調製したリチウムアセチリドとのカップリングを行い，アルキン15を収率よく得ることができた[9]。Birch還元の条件を用いることで*trans*-アルケン16とした後，Sharpless不斉ジヒドロキシル化[10]を行い所望の立体化学を有するジオール17を合成した。生じたジオールの保護と右側鎖の変換を行い，左側フラグメント18を合成した。

次に右側フラグメントの合成を行った(スキーム4)。D-Xyloseから合成したカルボン酸19に対し，不斉補助基を導入しイミド20とした後，Evans不斉アルキル化[11]を行うことで所望のメチル化体21を単一生成物として合成した。さらに2段階の操作を行うことで，右側フラグメント22を合成した。

続いて，左右両フラグメントの連結と2への変換を検

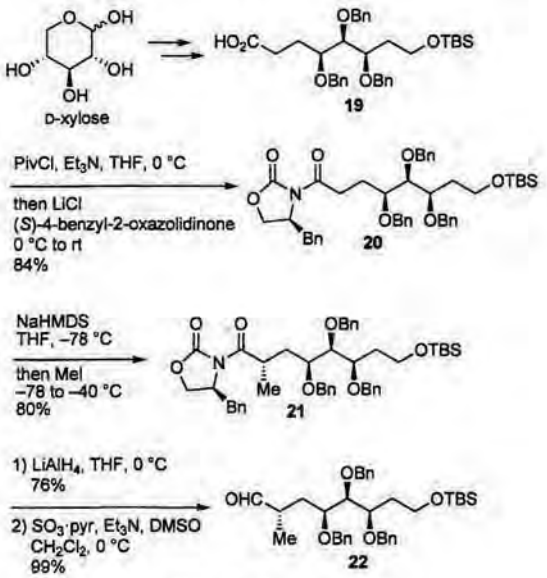

Scheme 4 Synthesis of 22.

討した(スキーム5)。スルホン18をLDAで処理した後，アルデヒド22と反応させることで所望のカップリング成績体23を得た[12]。23の幾何異性については，HaとHbとの間にROE相関が観測されたことにより決定した。TBS基の除去を行った後，段階的な酸化を行いカルボン酸24へと変換した。さらに，ベンジル基を除去しトリオール25とした後，アセトナイド基およびメトキシメチル基の脱保護と，この際に一部生じたラクトンの加水分解を行うことで，C1'-C25'フラグメント2の合成を完了した。合成した2のNMRデータおよび比旋光度が分解生成物のそれらと一致したことから，未解明であった本フラグメントの絶対立体配置が2に示すものであることを明らかにすることができた[13]。

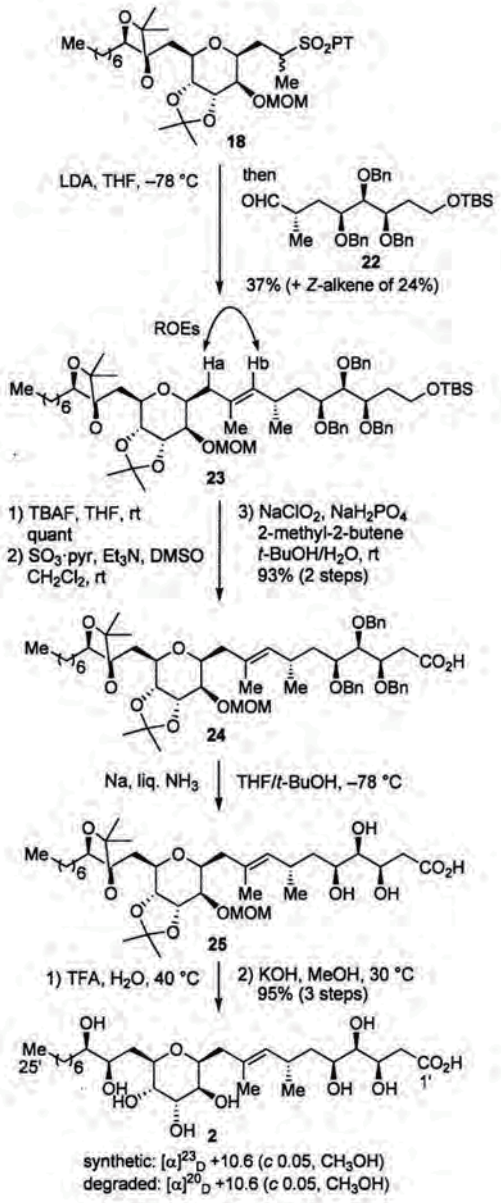

Scheme 5 Synthesis of 2.

2. C14-C24フラグメントの合成

C14-C24フラグメントの合成に着手する前に，まずは本フラグメントの分解生成物に対して改良Mosher法[14]による構造解析を行うこととした。すなわち，分解生成物であるジオールをbis-(*S*)-MTPAエステル(*S*)-26およびbis-(*R*)-MTPAエステル(*R*)-26に変換し，これらの^{1}H NMRにおけるケミカルシフトの差を算出した(図2)。その結果，$\Delta\delta_{S-R}$値の符号が17位の左側でマイナス，21位の右側でプラスとなった。このことにより，17位と21位の立体化学をそれぞれ17*R*および21*R*と決定することができた[15]。そこで次に，18位に関する2つの立体異性体を合成し，合成品データと分解生成物データとを比較することで本フラグメントの絶対立体配置を決定することとした。

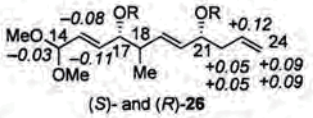

Fig. 2 Chemical shift differences ($\Delta\delta_{S-R}$) of (*S*)- and (*R*)-26. R = MTPA, MTPA = α-methoxy-α-(trifluoromethyl)phenylacetyl.

18位メチル基に関する2つの立体異性体を，できるだけ簡便に合成することを考え，これらを同様の反応を用いて作り分けることとした。具体的には，Crimminsにより報告されている不斉aldol反応[16]を用いることとした。

まずはじめに，(18*R*)-ジオールの合成を検討した。*cis*-2-Butene-1,4-diolから合成した既知のアルデヒド27[17]に対し，1.6当量の四塩化チタンと3.8当量の(−)-sparteine存在下，1.5当量のpropionyl oxazolidinethione 28を反応させたところ，所望のEvansタイプの*syn*-aldol成績体29を単一立体異性体として得ることができた(スキーム6)[16]。この際に生じた17位のオキシメチン部位の立体化学は改良Mosher法[14]により決定した。続いて，18位の立体化学を決定するためにラクトン31へと変換した。すなわち，DIBAL-H還元により不斉補助基を除去した後，Wittig反応によって2炭素増炭し不飽和エステル30とした。水素添加によりアルケン部位を還元後，生じたエステルを対応するジオールへと変換し，TEMPO酸化を行うことでラクトン31を合成した。31において，H-17/H-20α およびCH_3-18/H-20β にNOE相関が観測されたことから，18位の立体配置を決定することができた。

次に29からの変換を行った(スキーム7)。不斉補助基を除去しWeinrebアミドとした後，酸化およびジアステレオ選択的還元を行うことで17位の立体化学を反

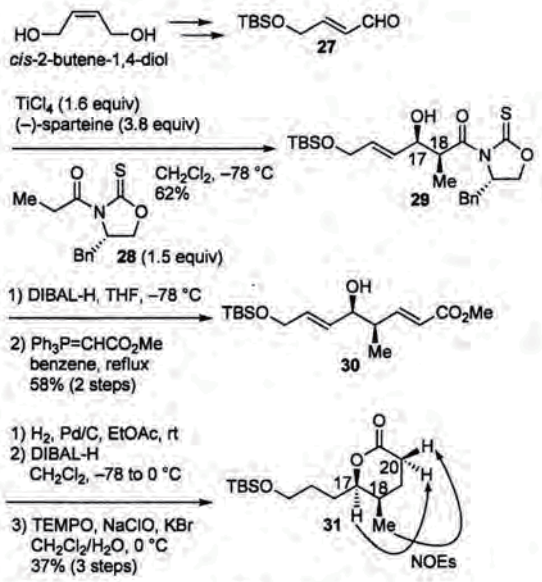

Scheme 6 Synthesis of 29 and its derivatization for the structural elucidation.

転させ，アルコール 32 を得た。32 をアルデヒド 33 へと変換した後，Keck 不斉アリル化の条件[18]にさらすことで所望のホモアリルアルコール 34 を得ることができた。シリルエーテル 34 をアルデヒド 35 へと誘導した後，メタノール中，四塩化チタンを作用させることで TBS 基の除去とメチルアセタール化をワンポットで行い[19]，(18*R*)-ジオール 36 の合成を完了した。

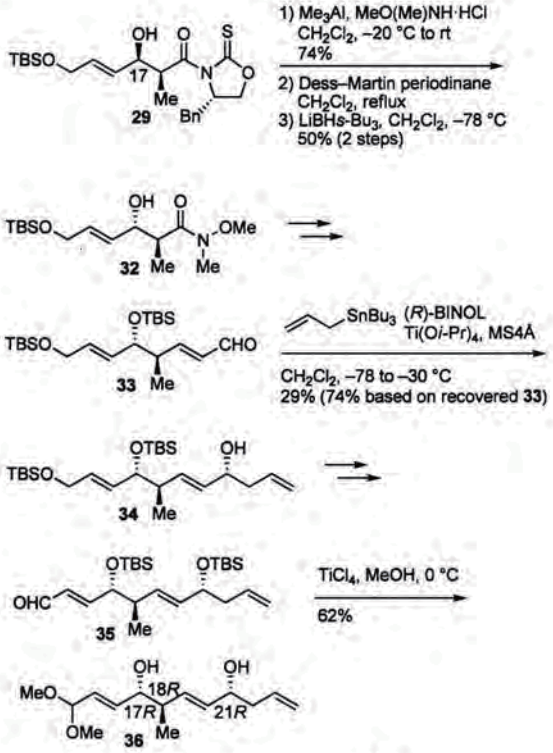

Scheme 7 Synthesis of 36.

続いて，(18*S*)-ジオールの合成を行った(スキーム 8)。先ほどとは条件を変え，4.0 当量の四塩化チタンと 2.2 当量の(−)-sparteine 存在下，2.0 当量の propionyl oxazolidinethione 28 を反応させたところ，non-Evans タイプの *syn*-aldol 成績体 37 を単一生成物として得ることができた[16]。さらに，(18*R*)-ジオール 36 の合成と同様の工程を踏むことで，(18*S*)-ジオール 38 も合成することができた。

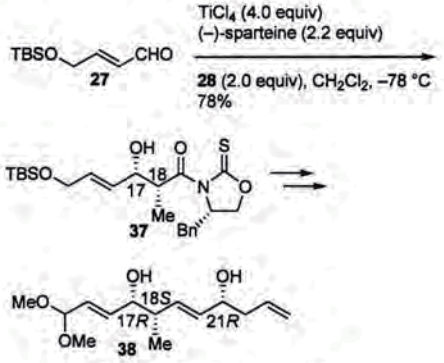

Scheme 8 Synthesis of 38.

次に合成した 2 つのジオール 36 および 38 と分解生成物との NMR データの比較を行った。その結果，(18*R*)-合成品 36 の ^{1}H NMR データは分解生成物データと完全に一致し，(18*S*)-合成品 38 のデータは分解生成物データとは異なることが明らかとなった。特に顕著な違いが見られたのは，17 位および 18 位におけるケミカルシフトであった(図 3)。さらに，合成したジオール 36 から変換した(*S*)- および(*R*)-bis-MTPA エステルの ^{1}H NMR データは，分解生成物から誘導した(*S*)-および(*R*)-bis-MTPA エステルの ^{1}H NMR データとそれぞれ完全に一致した。以上の結果より，本フラグメントは 36 に示すように(17*R*, 18*R*, 21*R*)の絶対立体配置を有し

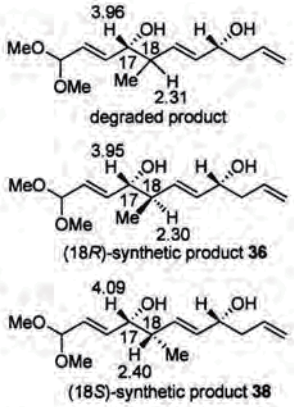

Fig. 3 Chemical shifts in ppm of the H-17 and H-18 of the degraded product and the synthetic products 36 and 38.

ていることを明らかにすることができた[20]。

3. C23-C34 フラグメントの合成

まずは，C23-C34 フラグメントの分解生成物であるジオールに対し，C14-C24 フラグメントの際と同様に改良 Mosher 法[14]を適用した。すなわち，ジオールから誘導した bis-(*S*)-MTPA エステル(*S*)-**39** および bis-(*R*)-MTPA エステル(*R*)-**39** を用いて，^{1}H NMR ケミカルシフトの差を算出したところ，$\Delta\delta_{S-R}$ 値の符号が 26 位の左側でマイナス，32 位の右側でプラスとなった(図 4)[15]。この結果より，26 位および 32 位の絶対立体配置をそれぞれ図 4 に示すように決定することができた。そこで次に，連続する 2 つのエポキシド部位に関する 4 つの立体異性体を合成することとした。

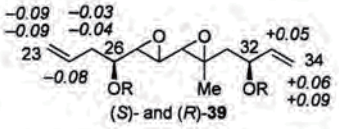

Fig. 4 Chemical shift differences ($\Delta\delta_{S-R}$) of (*S*)- and (*R*)-**39**. R = MTPA. MTPA = α-methoxy-α-(trifluoromethyl)phenylacetyl.

合成標的分子 **43**−**46** の合成計画を**スキーム 9** に示す。アリルアルコール **40** に対し，立体選択的に 29,30-エポキシド部位を導入することで，モノエポキシド **41** および **42** を作り分ける。さらに，**41** と **42** のそれぞれに対し二度目のエポキシ化を施すことで，**43**−**46** をそれぞれ合成することとした。つまり，立体発散的に各種立体異性体を合成する計画である[21]。

標的分子 **43** の合成について説明する。L-Aspartic acid から合成したエポキシド **47**[22] に対し，ethyl propiolate を付加させアルコール **48** とした後，生じたヒドロキシ基を保護し TBS エーテル **49** とした(**スキーム 10**)。アルキニルエステル **49** に対しチオフェノールを共役付加させ，対応する(*Z*)-チオエーテルを得た後，メチルマグネシウムブロミドとヨウ化銅で処理することで，(*E*)-不飽和エステル **50** を単一の幾何異性体として得た[23]。エステル **50** をアリルアルコール **51** へと変換した後，(+)-diethyl tartrate (DET) を用いた Sharpless 不斉エポキシ化[24]を行うことで，所望のエポキシアルコール **52** を合成することができた。**52** を 3 段階の操作により

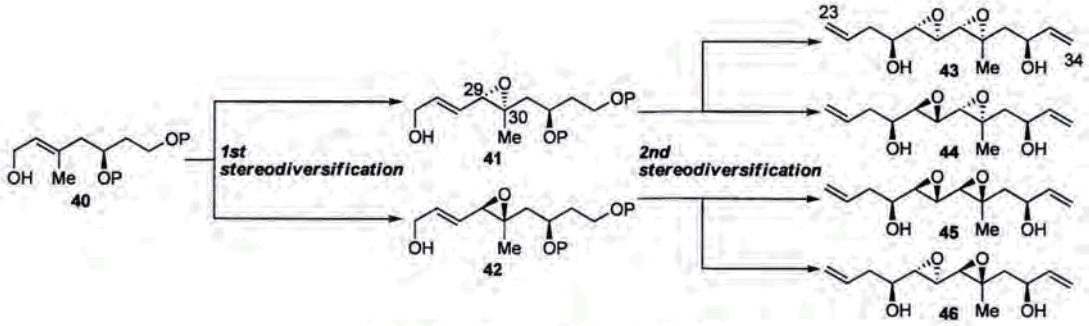

Scheme 9 Synthetic plan of **43**-**46**.

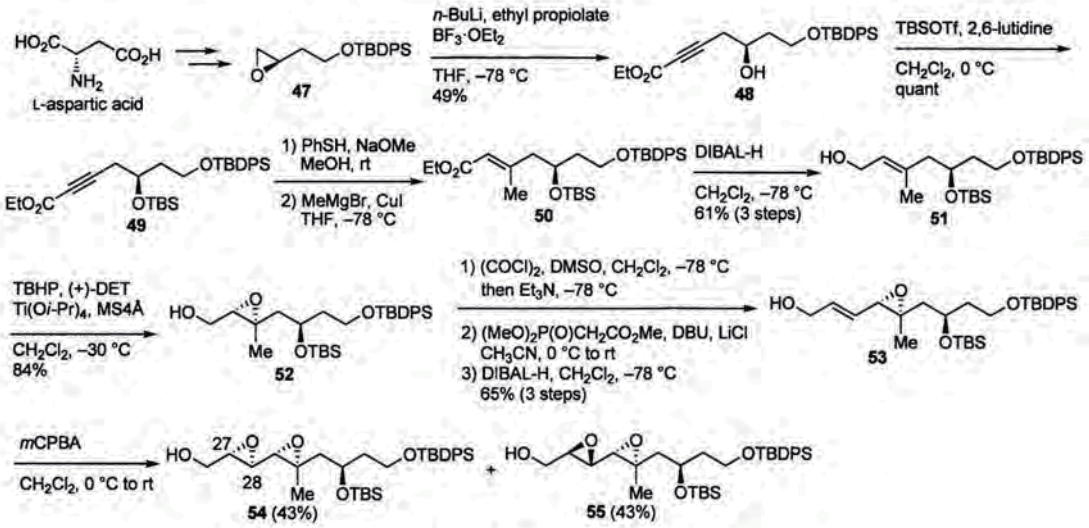

Scheme 10 Synthesis of **54**.

アリルアルコール53へと変換した後，Sharpless条件下でのエポキシ化[24]を行ったが，満足のいく立体選択性を得ることはできなかった。そこで，*m*CPBAによるエポキシ化を行い，ジエポキシド54と55をそれぞれ43%の収率で得た。

ジエポキシド54の27,28-エポキシド部位の立体構造決定は以下のように行った(**スキーム11**)。エポキシアルコール54に対しRed-Alを作用させ1,3-ジオール56とした後[25]，1級ヒドロキシ基を選択的に保護し，続いて生じた2級アルコールをMTPAエステル(*S*)-57および(*R*)-57へと変換した。生じたMTPAエステルにおいて$\Delta\delta_{S-R}$値を算出したところ，26位と27位でプラスの符号を，また29位と31位から34位でマイナスの符号を有することがわかった(**図5**)。このことにより，56の28位の絶対立体化学，言い換えれば54の27,28-エポキシド部位の絶対立体化学を決定することができた。

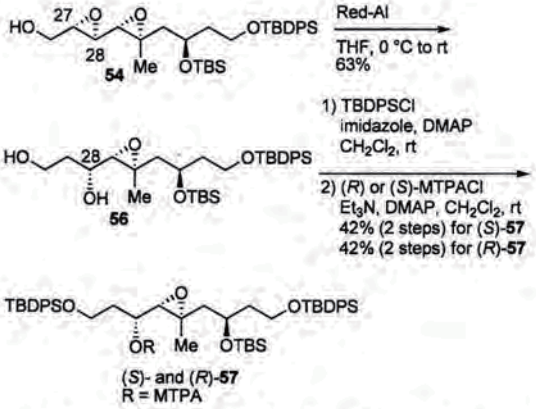

Scheme 11 Derivatization of 54 for the structural elucidation.

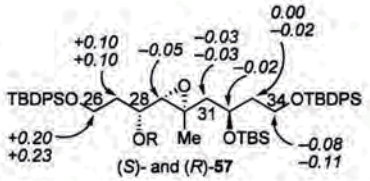

Fig. 5 Chemical shift differences ($\Delta\delta_{S-R}$) of (*S*)- and (*R*)-57. R = MTPA. MTPA = α-methoxy-α-(trifluoromethyl)phenylacetyl.

引き続き54から43への変換を検討した(**スキーム12**)。アルコール54から合成したアルデヒドに対し，Roush試薬58を用いた不斉アリル化[26]を行うことで，所望のホモアリルアルコール59を収率よく得ることができた。続いて，生じたヒドロキシ基のTBS保護とTBDPS基の選択的除去を行うことで，アルコール60とした。Grieco法[27]によりアルケン部位を導入し61とした後，2つのTBS基を除去することで，目的とするジエポキシド43の合成を完了した。

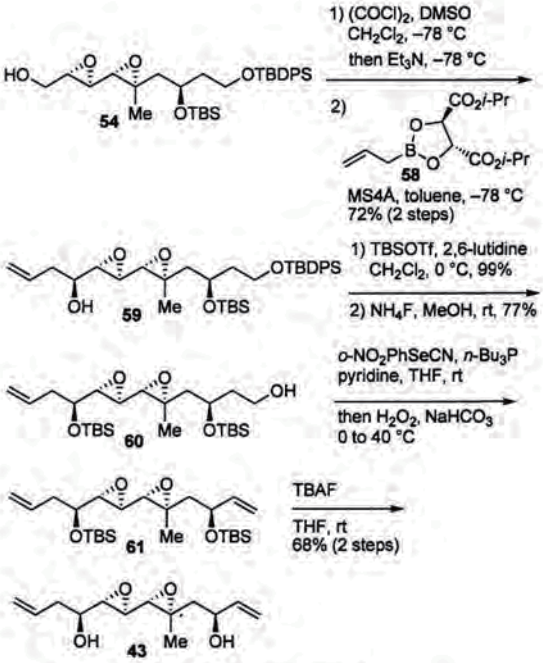

Scheme 12 Synthesis of 43.

さらに，43の合成と同様の工程を踏むことで，残り3つのジエポキシド44−46もそれぞれ合成した。合成完了後，4つの合成品43−46と分解生成物との^{1}H NMRスペクトルの詳細な比較を行ったところ，43のスペクトルのみが分解生成物のそれと一致することがわかった。また，合成品43の比旋光度：$[\alpha]^{24}_{D}$ −14.2(*c* 0.20, CH_3OH)は分解生成物データ：$[\alpha]^{21}_{D}$ −11.2(*c* 0.05, CH_3OH)とよい一致を示したことから，本フラグメントの絶対立体配置は43に示すものであると決定することができた[28]。

4. C33-C42フラグメントの合成

まずは，C33-C42フラグメントの分解生成物であるジオールに対し改良Mosher法[14]を適用した。すなわち，ジオールから誘導したbis-(*S*)-MTPAエステル(*S*)-62およびbis-(*R*)-MTPAエステル(*R*)-62を用いて，^{1}H NMRにおけるケミカルシフトの差を算出したところ，$\Delta\delta_{S-R}$値の符号が，33位から35位においてマイナス，41位と42位においてプラスとなった(**図6**)[15]。このことにより，36位と40位の絶対立体化学を図6の

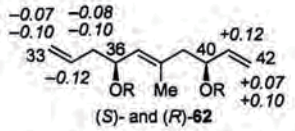

Fig. 6 Chemical shift differences ($\Delta\delta_{S-R}$) of (*S*)- and (*R*)-62. R = MTPA. MTPA = α-methoxy-α-(trifluoromethyl)phenylacetyl.

ように(36*S*, 40*S*)と決定することができた。次に，この構造決定を確認するために，本フラグメントの合成について検討することとした。

既知の方法を用いて，L-aspartic acid より合成したエポキシド 63[29] に対し，ethyl propiolate の付加と生じたヒドロキシ基の保護を行い TBS エーテル 64 を得た(スキーム 13)。64 に対しチオフェノールを共役付加させた後，メチル化を行うことで(*E*)-不飽和エステル 65 を得ることができた[23]。65 をアルデヒド 66 へと変換した後，Keck の不斉アリル化[18] を行い，所望のアリル化体 67 を得た。さらに，生じたヒドロキシ基の保護と TBS 基の選択的脱保護を行い，アルコール 68 とし，アルケン部位の導入[27] とシリル保護基の除去を行い，ジオール 69 の合成を完了した。合成した 69 の ^{1}H NMR スペクトルは，分解生成物のそれと完全に一致した。さらに，合成品 69 から誘導した bis-(*S*)-MTPA エステルおよび bis-(*R*)-MTPA エステルの ^{1}H NMR スペクトルは，分解生成物から誘導された bis-(*S*)-MTPA エステルおよび bis-(*R*)-MTPA エステルのスペクトルとそれぞれ完全に一致した。以上の結果より，本フラグメントは 69 に示すように(36*S*, 40*S*)の立体構造を有していると結論づけることができた[30]。

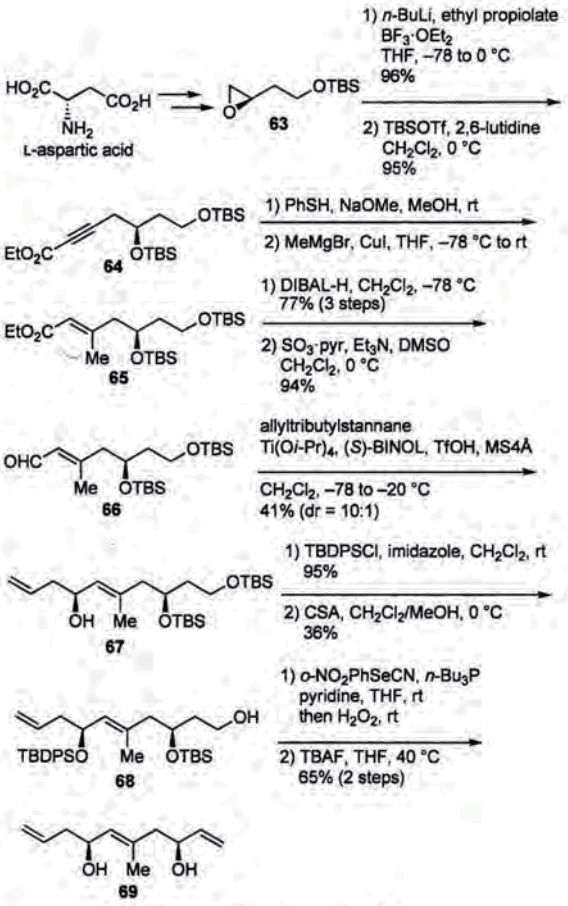

Scheme 13 Synthesis of 69.

5. C79-C96 フラグメントの合成

シンビオジノライド(1)の C83-C103 部位の立体構造は，$^3J_{H,H}$ 分析と NOE 実験により決定されている[1]。本フラグメントに関しては，分解生成物が得られていないため，他のフラグメントの構造決定とは異なるアプローチを用いることとした。具体的には，考え得る立体異性体をすべて合成し，それらの NMR データと天然物の NMR データとを比較することで，合成化学的に立体構造の確認を行うこととした。まずは，決定された立体構造を有する C79-C96 フラグメントの合成について検討することとした。

標的分子 70 の逆合成解析をスキーム 14 に示す。70 はトリフレート 71 とアルキン 72 とをカップリングさせることで得られると考えた。71 のスピロアセタール構造はジヒドロキシケトン 73 から構築することとし，73 はアルキン 74 とエポキシド 75 から合成することとした。

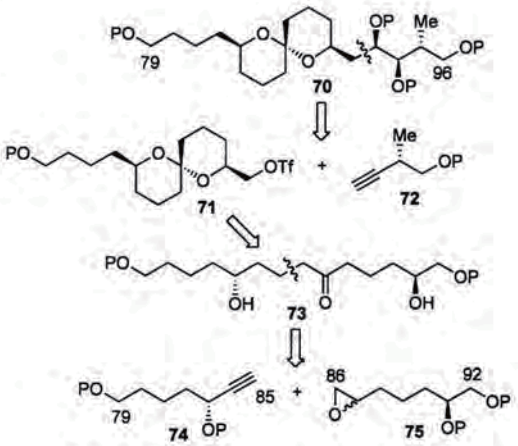

Scheme 14 Retrosynthetic analysis of 70.

C79-C96 フラグメント 88 の合成をスキーム 15 に示す。L-Malic acid から合成した既知のエステル 76[31] に対し DIBAL-H 還元と続くヨウ素化を行い，ヨウ化物 77 とした。続いてラジカル反応によるアリル化を行い 78 とした後，*m*CPBA を作用させることでエポキシド 79 を合成した。次に，別途合成したアルキン 80 とのカップリングを行ったところ，所望のアルコール 81 を 75% の収率で得ることができた。さらに，アルキン部位の還元と酸化を行うことでケトン 82 とした。82 に対しメタノール中 CSA を作用させたところ，3 つの TBS 基の除去と続くスピロアセタール化が速やかに進行し，所望のスピロアセタール 83 を 96% の収率で得ることができた。スピロアセタール 83 は二重アノマー効果が働くこ

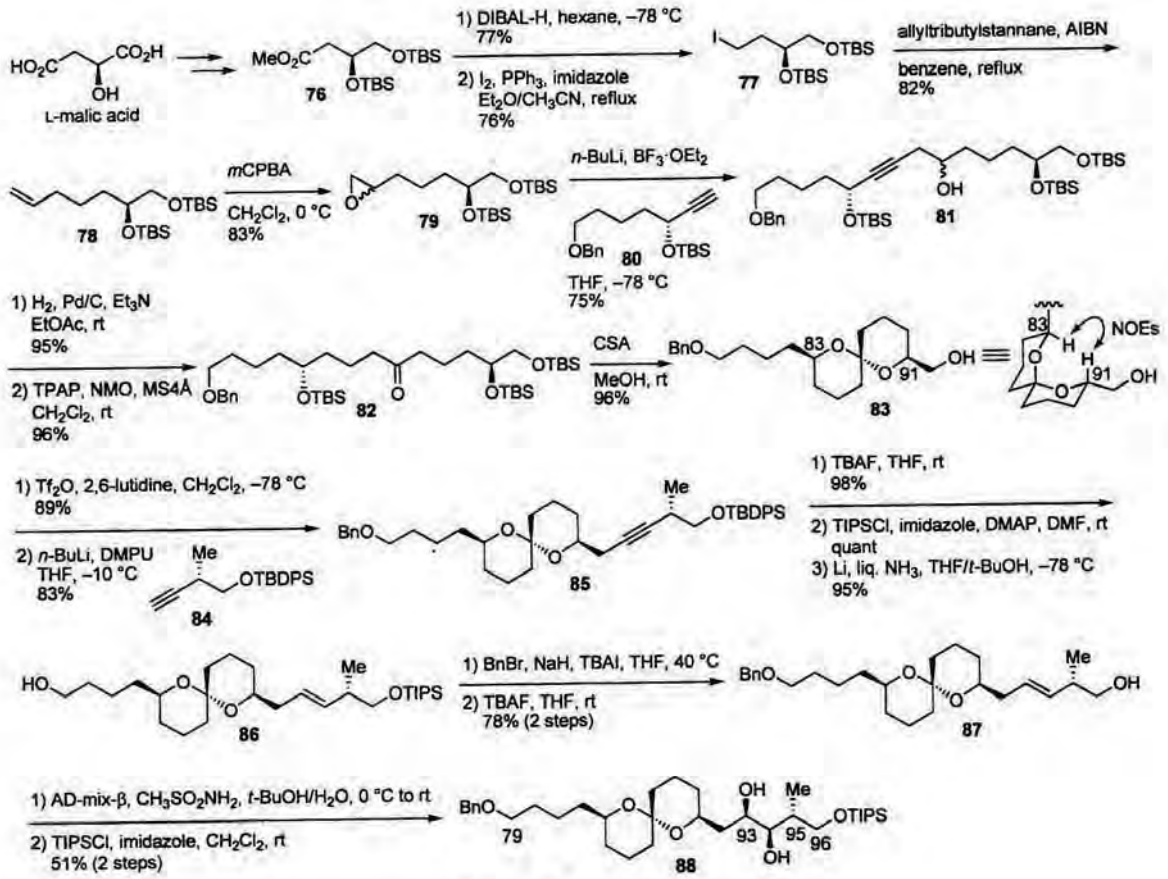

Scheme 15 Synthesis of 88.

とにより熱力学的に最も安定であり，H-83 と H-91 に NOE 相関が観測されたことから，その立体構造を確認した。アルコール 83 を対応するトリフレートへと変換した後，アルキン 84 から調製したリチウムアセチリドと反応させることでカップリング成績体 85 を合成した[9]。85 の TBDPS 基を TIPS 基へと変換した後，Birch 還元により *trans*-アルケン 86 へと変換した。この際に除去されたベンジル基を再度導入した後，TIPS 基を脱保護することでアルコール 87 とし，Sharpless 不斉ジヒドロキシル化[10] と TIPS 保護を行い，C79-C96 フラグメント 88 を合成した[32]。今後は，88 の 93 位から 95 位に関する各種立体異性体を合成し，それらの NMR データと天然物データを比較し，構造解明を行う予定である。

6. C94-C104 フラグメントの合成

C94-C104 フラグメントについても C79-C96 フラグメントと同様に，まずは決定された立体構造を有するフラグメントの合成について検討することとした。

C94-C104 フラグメント 89 の逆合成解析をスキーム 16 に示す。89 の炭素骨格はジチアン 90 とアルデヒド 91 とのカップリングにより構築することとした。91 の 101 位と 102 位の隣接酸素官能基はエノン 92 に対する立体選択的なジヒドロキシル化により導入できると考えた。メチルアセタール 92 の炭素骨格は光学活性なアルコール 93 の Achmatowicz 転位により構築できると考え，93 は市販の furfuryl alcohol から合成することとした。

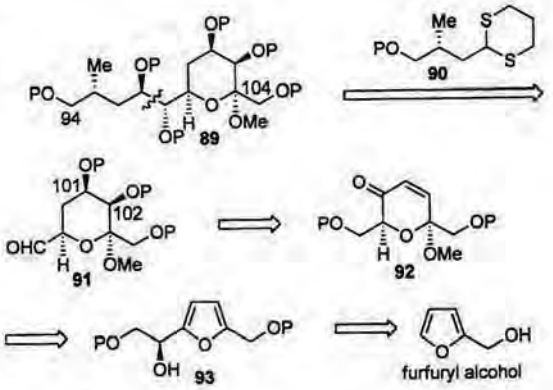

Scheme 16 Retrosynthetic analysis of 89.

まずは，テトラヒドロピラン部位の立体選択的構築を行った（スキーム 17）。Furfuryl alcohol を TBS エーテル 94 へと変換した後，フラン 94 に対する位置選択的なリチオ化と続くアルデヒド 95 との反応を行い，ラセミ体アルコール 96 を得た。96 を対応するケトンへと変換

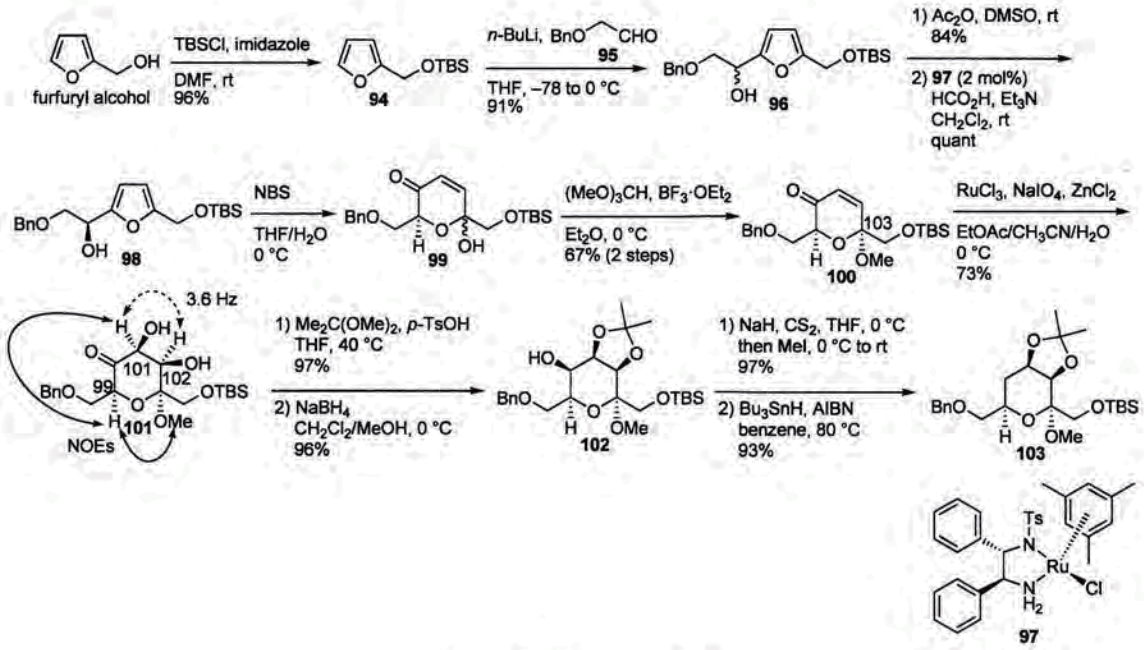

Scheme 17 Synthesis of 103.

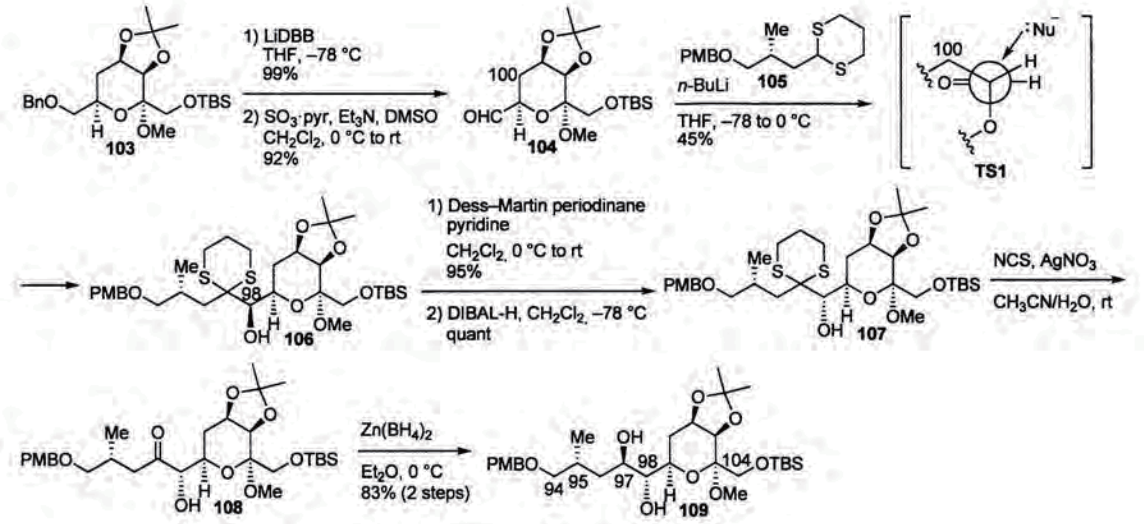

Scheme 18 Synthesis of 109.

した後，野依触媒 97 を用いた不斉水素移動反応[33]を行い，光学活性なアルコール 98 を単一生成物として得ることができた。98 に対し THF/H_2O 中で NBS を作用させることにより Achmatowicz 反応[34]を行い，転位生成物 99 を 1：1 のジアステレオマー混合物として得た。続いてメチルアセタール化を行うことで，100 を 2 段階 67% の収率で得た。次に，エノン 100 に対するジヒドロキシル化の検討を行った。まず，四酸化オスミウムを用いて行ったが，反応は全く進行しなかった。そこで種々検討したところ，電子不足なアルケンに対し有効であると報告されている条件(塩化ルテニウムと過ヨウ素酸ナトリウムと塩化亜鉛の組み合わせ)[35]を適用すると，所望のジオール 101 が単一の立体異性体として得られることがわかった。101 においては，H-99/H-101 および H-99/OCH_3-103 に NOE 相関が観測されたことより，101 位と 103 位の立体化学を決定した。また，$^3J_{101,102}$ が 3.6 Hz であることより，これらのプロトンが *syn* の関係にあることがわかった。続いて，隣接ジオールをアセトナイドへと変換した後，還元を行いアルコール 102 とした。102 を対応する *S*-メチルジチオカーボネートへと変換した後，Barton-McCombie 条件[36]にさらすことでテトラヒドロピラン 103 を合成した。

続いて，側鎖部位導入の検討を行った(**スキーム 18**)。ベンジルエーテル 103 の脱保護を行った後，酸化を行う

ことでアルデヒド104を合成した。次に，別途合成したジチアン105に対しn-BuLiを作用させ対応するアニオン種を発生させた後，アルデヒド104との反応を行うことで，アルコール106を単一の立体異性体として得た。この立体選択性は，TS1に示すFelkin-Anhモデル[37]を経て反応が進行したことによると考えられる。得られたアルコール106を酸化しケトンとした後，DIBAL-Hを用いて還元することで所望の98位の立体化学を有するアルコール107を合成した。ジチオアセタール部位を加水分解した後，生じたα-ヒドロキシケトン108に対しキレート制御型の還元[38]を行い，目的とするジオール109の合成を完了することができた[39]。今後は，95, 97, 98位に関する立体異性体を合成し，合成品と天然物とのNMRデータの比較を行うことで構造解明を進める予定である。

おわりに

本稿では，分子量2,860を有するポリオール海洋天然物シンビオジノライド(1)の構造解明に向けた合成化学的アプローチについて紹介した。現在までに，分解生成物として得られているC1'-C25'フラグメント，C14-C24フラグメント，C23-C34フラグメント，およびC33-C42フラグメントのそれぞれに関して，考え得る立体異性体をすべて合成し，立体構造を解明することができた。また，C79-C96フラグメントとC94-C104フラグメントについては，提出立体構造を有する各フラグメントの合成を完了することができた。今後も，立体構造未解明部位に関して合成を検討し，最終的にはシンビオジノライド(1)の全立体構造を合成化学的に完全解明する予定である[40]。

謝　辞　本研究は上村が高村に発した一言，「高村君，これ，何年で全合成できる？」からスタートしました。この難題に対し，まずは合成化学的に構造を解明することから研究を始めました。時には無理な要求を受けたにもかかわらず，日々の弛まぬ努力により研究成果を出した共同研究者(我々のグループによる発表論文に記載された博士研究員および学生諸氏)に深謝致します。また本研究は，科学研究費補助金，財団法人岡山工学振興会奨励研究助成，ノバルティス研究奨励金，財団法人ウエスコ学術振興財団学術研究費助成，公益信託三菱化学研究奨励基金，加藤記念研究助成，財団法人山陽放送学術文化財団研究助成金，有機合成化学協会塩野義製薬研究企画賞，財団法人薬学研究奨励財団研究助成金，倉田奨励金の助成を受けて行われました。この場を借りてお礼申し上げます。

(2013年6月21日受理)

文　献

1) 化学合成による天然物の構造決定に関する総説：(a)K. C. Nicolaou, S. A. Snyder, *Angew. Chem. Int. Ed.*, **44**, 1012(2005); (b)M. E. Maier, *Nat. Prod. Rep.*, **26**, 1105(2009); (c)T. L. Suyama, W. H. Gerwick, K. L. McPhail, *Bioorg. Med. Chem.*, **19**, 6675(2011)
2) (a)D. Uemura, "*Bioorganic Marine Chemistry*", Vol. 4, ed. by P. J. Scheuer, Springer: Berlin Heidelberg, 1991, p 1; (b)Y. Shimizu, *Chem. Rev.*, **93**, 1685(1993); (c)D. Uemura, *Chem. Rec.*, **6**, 235(2006)
3) (a)T. Yasumoto, M. Murata, *Chem. Rev.*, **93**, 1897(1993); (b)M. Murata, T. Yasumoto, *Nat. Prod. Rep.*, **17**, 293(2000)
4) M. Kita, N. Ohishi, K. Konishi, M. Kondo, T. Koyama, M. Kitamura, K. Yamada, D. Uemura, *Tetrahedron*, **63**, 6241(2007)
5) シンビオジノライド(1)はゾーザンテラトキシン類の構造類縁体である。ゾーザンテラトキシン類の構造決定：(a)H. Nakamura, T. Asari, A. Murai, T. Kondo, K. Yoshida, Y. Ohizumi, *J. Org. Chem.*, **58**, 313(1993); (b)T. Asari, H. Nakamura, A. Murai, Y. Kan, *Tetrahedron Lett.*, **34**, 4059(1993); (c)H. Nakamura, T. Asari, A. Murai, Y. Kan, T. Kondo, K. Yoshida, Y. Ohizumi, *J. Am. Chem. Soc.*, **117**, 550(1995); (d)H. Nakamura, T. Asari, K. Fujimaki, K. Maruyama, A. Murai, Y. Ohizumi, Y. Kan, *Tetrahedron Lett.*, **36**, 7255(1995); (e)H. Nakamura, K. Fujimaki, A. Murai, *Tetrahedron Lett.*, **37**, 3153(1996); (f)H. Nakamura, K. Sato, A. Murai, *Tetrahedron Lett.*, **37**, 7267(1996); (g)H. Nakamura, M. Takahashi, A. Murai, *Tetrahedron: Asymmetry*, **9**, 2571(1998); (h)H. Nakamura, K. Maruyama, K. Fujimaki, A. Murai, *Tetrahedron Lett.*, **41**, 1927(2000)
6) C. Han, D. Uemura, *Tetrahedron Lett.*, **49**, 6988(2008)
7) A. Bartolozzi, S. Pacciani, C. Benvenuti, M. Cacciarini, F. Liguori, S. Menichetti, C. Nativi, *J. Org. Chem.*, **68**, 8529(2003)
8) (a)L. Colombo, G. Casiraghi, A. Pittalis, *J. Org. Chem.*, **56**, 3897(1991); (b)C. Wawrzenczyk, M. Grabarczyk, A. Bialonska, Z. Ciunik, *Tetrahedron*, **59**, 6595(2003)
9) H. Kotsuki, I. Kadota, M. Ochi, *Tetrahedron Lett.*, **31**, 4609(1990)
10) H. C. Kolb, M. S. VanNieuwenhze, K. B. Sharpless, *Chem. Rev.*, **94**, 2483(1994)
11) D. A. Evans, M. D. Ennis, D. J. Mathre, *J. Am. Chem. Soc.*, **104**, 1737(1982)
12) P. R. Blakemore, W. J. Cole, P. J. Kocienski, A. Morley, *Synlett*, **1998**, 26
13) H. Takamura, T. Murata, T. Asai, I. Kadota, D. Uemura, *J. Org. Chem.*, **74**, 6658(2009)
14) I. Ohtani, T. Kusumi, Y. Kashman, H. Kakisawa, *J. Am. Chem. Soc.*, **113**, 4092(1991)
15) 改良Mosher法によるジオールの構造決定：(a)K. Konno, T. Fujishima, Z. Liu, H. Takayama, *Chirality*, **14**, 72(2002); (b)F. Freire, J. M. Seco, E. Quiñoá, R. Riguera, *J. Org. Chem.*, **70**, 3778(2005)
16) (a)M. T. Crimmins, B. W. King, E. A. Tabet, *J. Am. Chem. Soc.*, **119**, 7883(1997); (b)M. T. Crimmins, B. W. King, E. A. Tabet, K. Chaudhary, *J. Org. Chem.*, **66**, 894(2001)
17) J. A. Marshall, A. W. Garofalo, *J. Org. Chem.*, **61**, 8732(1996)
18) G. E. Keck, K. H. Tarbet, L. S. Geraci, *J. Am. Chem. Soc.*, **115**, 8467(1993)
19) A. Clerici, N. Pastori, O. Porta, *Tetrahedron*, **54**, 15679(1998)
20) (a)H. Takamura, Y. Kadonaga, I. Kadota, D. Uemura, *Tetrahedron Lett.*, **51**, 2603(2010); (b)H. Takamura, Y. Kadonaga, I. Kadota, D. Uemura, *Tetrahedron*, **66**, 7569(2010)
21) 天然物の立体発散的合成に関する最近の報告例：(a)B. Schmidt, F. Hölter, *Chem. Eur. J.*, **15**, 11948(2009); (b)T. Kotaki, T. Shinada, K. Kaihara, Y. Ohfune, H. Numata, *Org. Lett.*, **11**, 5234(2009); (c)S. Tamura, T. Ohno, Y. Hattori, N.

Murakami, *Tetrahedron Lett.*, **51**, 1523(2010); (d)D. Urabe, H. Todoroki, K. Masuda, M. Inoue, *Tetrahedron*, **68**, 3210(2012)
22) J. E. Robinson, M. A. Brimble, *Chem. Commun.*, **2005**, 1560
23) (a)S. Kobayashi, T. Mukaiyama, *Chem. Lett.*, **3**, 705(1974); (b)C. J. Hollowood, S. Yamanoi, S. V. Ley, *Org. Biomol. Chem.*, **1**, 1664(2003); (c)F. Ding, M. P. Jennings, *Org. Lett.*, **7**, 2321(2005)
24) (a)T. Katsuki, K. B. Sharpless, *J. Am. Chem. Soc.*, **102**, 5974(1980); (b)R. M. Hanson, K. B. Sharpless, *J. Org. Chem.*, **51**, 1922(1986)
25) J. M. Finan, Y. Kishi, *Tetrahedron Lett.*, **23**, 2719(1982)
26) W. R. Roush, A. E. Walts, L. K. Hoong, *J. Am. Chem. Soc.*, **107**, 8186(1985)
27) P. A. Grieco, S. Gilman, M. Nishizawa, *J. Org. Chem.*, **41**, 1485(1976)
28) T. Murata, M. Sano, H. Takamura, I. Kadota, D. Uemura, *J. Org. Chem.*, **74**, 4797(2009)
29) C. D. Donner, *Tetrahedron Lett.*, **48**, 8888(2007)
30) (a)H. Takamura, Y. Kadonaga, Y. Yamano, C. Han, Y. Aoyama, I. Kadota, D. Uemura, *Tetrahedron Lett.*, **50**, 863(2009); (b)H. Takamura, Y. Kadonaga, Y. Yamano, C. Han, I. Kadota, D. Uemura, *Tetrahedron*, **65**, 7449(2009)
31) T. Yakura, A. Ueki, T. Kitamura, K. Tanaka, M. Nameki, M. Ikeda, *Tetrahedron*, **55**, 7461(1999)
32) H. Takamura, J. Ando, T. Abe, T. Murata, I. Kadota, D. Uemura, *Tetrahedron Lett.*, **49**, 4626(2008)
33) (a)A. Fujii, S. Hashiguchi, N. Uematsu, T. Ikariya, R. Noyori, *J. Am. Chem. Soc.*, **118**, 2521(1996); (b)R. Noyori, S. Hashiguchi, *Acc. Chem. Res.*, **30**, 97(1997)
34) O. Achmatowicz, Jr., P. Bukowski, B. Szechner, Z. Zwierzchowska, A. Zamojski, *Tetrahedron*, **27**, 1973(1971)
35) B. Plietker, M. Niggemann, *J. Org. Chem.*, **70**, 2402(2005)
36) D. H. R. Barton, S. W. McCombie, *J. Chem. Soc., Perkin Trans. 1*, **1975**, 1574
37) A. Mengel, O. Reiser, *Chem. Rev.*, **99**, 1191(1999)
38) T. Nakata, T. Tanaka, T. Oishi, *Tetrahedron Lett.*, **24**, 2653(1983)
39) H. Takamura, K. Tsuda, Y. Kawakubo, I. Kadota, D. Uemura, *Tetrahedron Lett.*, **53**, 4317(2012)
40) シンビオジノライド(1)は立体構造を決定するチャレンジングな分子の1つとして次の論文に紹介されている。T. F. Molinski, B. I. Morinaka, *Tetrahedron*, **68**, 9307(2012)

PROFILE

高村浩由　岡山大学大学院自然科学研究科・助教
〔経歴〕2000年東北大学理学部卒業，2005年東北大学大学院理学研究科博士後期課程修了，同年名古屋大学大学院理学研究科博士研究員，同年同助手，2007年同助教，同年より現職。〔専門〕有機合成化学，天然物合成化学。〔連絡先〕e-mail : takamura@cc.okayama-u.ac.jp

門田 功　岡山大学大学院自然科学研究科・教授
〔経歴〕1988年高知大学理学部卒業，1993年東北大学大学院理学研究科博士後期課程修了，同年東北大学理学部助手，1996年東北大学反応化学研究所講師，2001年東北大学多元物質科学研究所助教授，2004年東北大学大学院理学研究科助教授，2006年より現職。1999年から2000年カリフォルニア大学アーバイン校客員研究員（Scott D. Rychnovsky教授）。〔専門〕有機合成化学。〔連絡先〕e-mail : kadota-i@cc.okayama-u.ac.jp

上村大輔　神奈川大学理学部・教授
〔経歴〕1968年名古屋大学理学部卒業，1973年名古屋大学大学院理学研究科博士後期課程単位取得満期退学，同年名古屋大学理学部助手，1979年静岡大学教養部助教授，1991年同教授，その後，静岡大学理学部教授などを経て1997年名古屋大学大学院理学研究科教授，2008年慶應義塾大学理工学部教授，2011年より現職。名古屋大学名誉教授。〔専門〕天然物有機化学。〔連絡先〕e-mail : uemurad@kanagawa-u.ac.jp

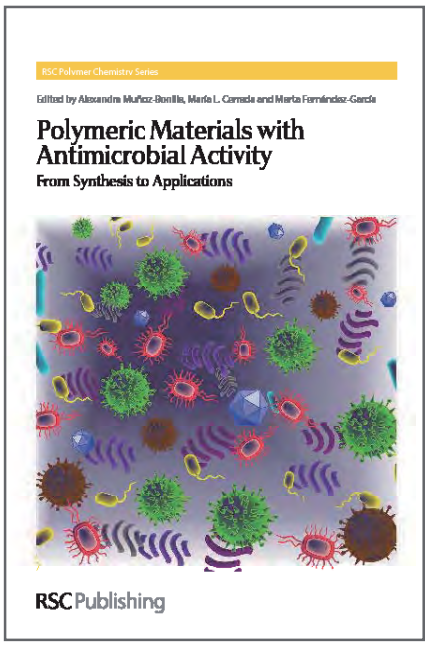

Polymeric Materials with Antimicrobial Activity

From Synthesis to Applications

Edited by Alexandra Muñoz-Bonilla, María Cerrada and Marta Fernández-García

Synopsis

Antimicrobial polymers, materials which prevent microorganism growth, are needed for many everyday applications from food packaging and water treatment to medicine and healthcare. By combining the information of different materials as well as antimicrobial action modes and applications within one source, the book provides a general summary of the field. With contributions from leading scientists the book is suitable for researchers in polymers, chemistry, biology and materials science interested in an overview of antimicrobial polymeric materials as well as the recent advances in their synthesis, properties and applications.

Brief Contents

- Introduction to Antimicrobial Polymeric Materials
- Antimicrobial Activity of Chitosan in Food, Agriculture and Biomedicine
- Synthesis, Antimicrobial Activity and Applications of Polymers with Ammonium and Phosphonium groups
- Water-Soluble Antimicrobial Polymers for Functional Cellulose Fibres and Hygiene Paper Products
- Polymer-Based Synthetic Mimics of Antimicrobial Peptides (SMAMPs) – A New Class of Nature-Inspired Antimicrobial Agents with Low Bacterial Resistance Formation Potential
- Prevention of Hospital and Community Acquired Infections by Using Antibacterial Textiles and Clothing

Series: RSC Polymer Chemistry Series
ISSN: 2044-0790
Publisher: Royal Society of Chemistry
ISBN: 9781849738071
Price: £159.99
Publishing date: 14/11/2013
Target Audience: Professional and scholarly
Format: Hardback
Size: 234 x 156 mm
Pages: 410
BIC: PNNP, TGM

To order

Royal Society of Chemistry
Marston Book Services Ltd
160 Eastern Avenue, Milton Park
Abingdon
Oxfordshire
OX14 4SB, UK
Tel: +44 (0) 1235 465522
Fax: +44 (0) 1235 465555
Email: **enquiries@marston.co.uk**
www.marston.co.uk

USA and Canada
Please contact:
Ingram Publisher Services
Customer Service, Box 631
14 Ingram Blvd
La Vergne, TN 37086, USA
Tel: +1 (866) 400 5351
Fax: +1 (800) 838 1149
Email: **ips@ingramcontent.com**

RSC Publishing

www.rsc.org/books
Registered Charity Number 207890

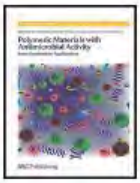

Polymeric Materials with Antimicrobial Activity

Antimicrobial polymers, materials which prevent microorganism growth, are needed for many everyday applications from food packaging and water treatment to medicine and healthcare. By combining the information of different materials as well as antimicrobial action modes and applications within one source, the book provides a general summary of the field. With contributions from leading scientists the book is suitable for researchers in polymers, chemistry, biology and materials science interested in an overview of antimicrobial polymeric materials as well as the recent advances in their synthesis, properties and applications.

View all Chapters | RSC Books Home

CHAPTER 7

Book Chapter

Synthesis, Structure and Antimicrobial Activities of Polymeric and Nonpolymeric Silver and other Metal Complexes

Kenji Nomiya, Noriko Chikaraishi Kasuga and Akihiko Takayama

Copyright Year:2014

Print ISBN: 978-1-84973-807-1
PDF eISBN: 978-1-78262-499-8
DOI:10.1039/9781782624998-00156

« Previous Chapter | Next Chapter »

More

Please choose one of the options provided in the log in section to gain access to this content: ▸▸▸

Abstract | Related Content

In this chapter, we review recent reports of antimicrobial activities of the aqueous silver(I) ion and silver nanoparticles, plus the synthesis, X-ray structures and antimicrobial activities of polymeric and nonpolymeric silver(I) complexes. Herein, we focus on the antimicrobial activities of such silver materials and their mode of action. We also review the structure and antimicrobial activities of other polymeric and nonpolymeric metal complexes. The antimicrobial mechanism of the aqueous silver(I) ion is essentially different from that of silver(I)-sulfur-, nitrogen-, and phosphine-bonding complexes. As for the silver(I) complexes, the coordinating donor atoms significantly determine whether their antimicrobial spectrum is wide or narrow. This is ascribed to the ease of ligand exchange. Thus, by choosing the appropriate ligands it is possible to design silver(I) complexes that show only antibacterial activities, plus both antibacterial and antifungal activities. The antimicrobial behavior of the silver(I) complexes and other metal complexes is also essentially different, i.e. the antimicrobial mechanism is dependent on the metal centers of the complexes.

Log in (Subscriber Access)

Login via Athens or your home institution

Login with your **subscriber** username and password

Subscriber Username*

Password*

Login

Ask your librarian to arrange site-wide access.

Download

PDF

Add PDF to Basket (£25)

Download Citation ?

BibTex Go

フッ素樹脂の最新動向

Current Research Trends of Fluoropolymers

監修：澤田英夫
Supervisor : Hideo Sawada

シーエムシー出版

第13章　機能性有機フッ素化合物の分解反応の開発

堀　久男*

1　はじめに

炭素原子とフッ素原子から形成される有機フッ素化合物は耐熱性，耐薬品性，界面活性などの優れた性質を持ち，我々の生活に欠かすことのできない重要な化学物質である。その種類は低分子化合物から高分子化合物まで多岐にわたる。分子量が百程度の化合物は冷媒などに，数百程度の化合物は界面活性剤や表面処理剤に，数万以上の化合物，すなわちフッ素ポリマーはパッキンなどの汎用品は勿論のこと，イオン交換膜，光ファイバー，レジストなどの先端材料として利用されている。このように高い機能性を持つ一方で，環境残留性や廃棄物の分解処理が困難といった負の側面が近年になって顕在化しつつある。

このような有機フッ素化合物の環境リスクの低減のためには有害性の度合いに応じて排水や廃棄物，さらには汚染地下水・土壌などの無害化を行う必要があるが，炭素・フッ素結合は炭素が形成する共有結合では最強なため容易に分解しない。焼却は可能であるものの，高温が必要であるだけでなく，生成するフッ化水素ガスによる焼却炉材の劣化が著しい。これらの物質をフッ化物イオン（F^-）まで分解できれば，既存の処理技術により環境無害なフッ化カルシウムに変換できる。フッ化カルシウムの鉱物が蛍石で，硫酸処理によりフッ素ポリマーを含む全ての有機フッ素化合物の原料であるフッ化水素酸になるため，産出が特定国（中国）に偏在し，入手に制約が多いフッ素資源の循環利用にも寄与できる（図1）。この場合，穏和な条件でF^-まで分解することが重要である。これまでにも電子線照射やプラズマなどの高エネルギー的な手法を使えばフッ素ポリマーさえも分解することは知られていた。しかしその場合，毒性が非常に高いペルフルオロイソブチレン（$CF_3C(CF_3)CF_2$，PFIB）や温暖化係数が二酸化炭素の数千倍のテトラフルオロ

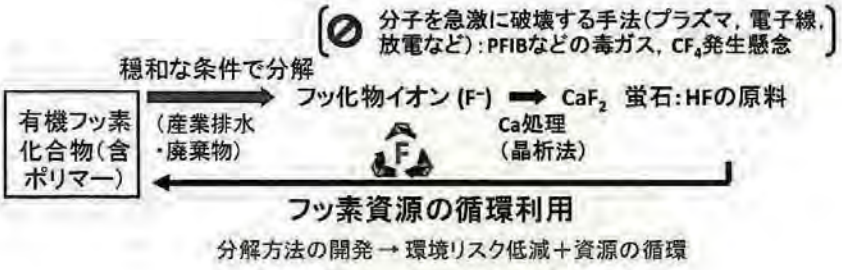

図1　フッ素資源の循環利用スキーム

*　Hisao Hori　神奈川大学　理学部　化学科　教授

メタン（CF_4）などの有害ガスの発生が懸念されている。

以上の背景から我々は主に界面活性剤の構成成分あるいはその原料として用いられてきたペルフルオロアルキルスルホン酸類（PFAS類，一般式$C_nF_{2n+1}SO_3H$）およびペルフルオロカルボン酸類（PFCA類，$C_nF_{2n+1}COOH$，n = 1, 2, 3…），さらにはそれらの代替物質について，ヘテロポリ酸光触媒[1]，ペルオキソ二硫酸イオン（過硫酸イオン，$S_2O_8^{2-}$）＋光照射[2,3]，水・液体二酸化炭素二相系＋光照射[4]，金属粉＋亜臨界水[5~7]，鉄イオン光触媒[8]，$S_2O_8^{2-}$＋温水[9,10]，酸素ガス＋亜臨界水[11]，$S_2O_8^{2-}$＋超音波照射[12]などの種々の反応手法を開発し，F^-までの完全分解，すなわち無機化を達成してきた。最近はこれらの知見を基にフッ素ポリマーの分解にも取り組んでいる[13]。本稿ではそれらの代表例について報告したい。図２に環境中で検出されている典型的なPFAS/PFCA類を示す[14,15]。

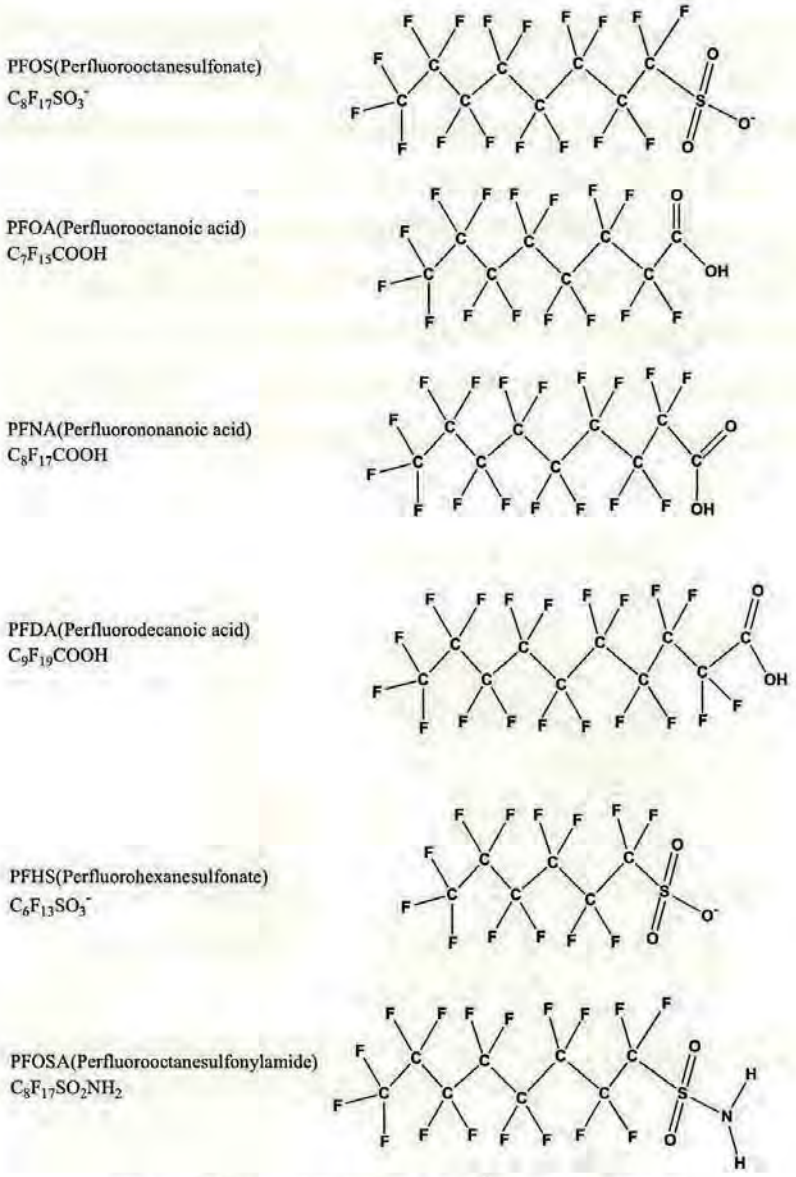

図２　環境中で検出されているPFAS/PFCA類の例

2　鉄粉＋熱水を用いたPFAS類の還元分解

PFAS類は環境水中に存在する有機フッ素化合物の代表的なもので，生体蓄積性が特に問題となっているものがペルフルオロオクタンスルホン酸（$C_8F_{17}SO_3H$，PFOS，PFOSは英語のPerfluorooctanesulfonateの略なので厳密にはペルフルオロオクタンスルホン酸の陰イオン，すなわち$C_8F_{17}SO_3^-$を意味する）である。我々は水中のPFAS類を熱水（亜臨界水，超臨界水）で分解させることを検討した。その結果，鉄粉を還元剤として用いると亜臨界水中で効果的に分解できることを見出した[5]。図3に水の状態図を示す。臨界点（374℃，22.1 MPa）を超える温度・圧力の状態は超臨界水と呼ばれるが，臨界点よりもやや低い領域にある高温，高圧の水（液体）が亜臨界水である。亜臨界水や超臨界水は無極性の有機化合物を溶解し，有機化合物を加水分解するなど，普通の水にはない性質を持っている。

反応は以下のようにして行った。先ず，耐圧容器に不活性ガス雰囲気中でPFOS（カリウム塩）の水溶液（93～372 μM）と鉄粉もしくは他の金属粉（亜鉛，銅，アルミニウム）を入れ，250～350℃の亜臨界水の状態にした。一定時間経過後，室温に戻して成分分析を行った。比較のため金属粉を入れない場合についても実験を行った。金属粉がない場合，水中のPFOS濃度はほとんど減少しなかった。鉄粉を入れた場合にPFOSは最も迅速に分解した。例えばPFOS初期濃度が372 μM，反応温度350℃，圧力23.3 MPaの場合，PFOSは6時間で水中から消失し，同時に水中にはフッ化物イオンが高収率で生成した（図4）。この方法により電子産業界で使用されていた反射防止剤のPFOSや，炭素数2～6のPFAS類（ペルフルオロアルキル基の短いPFAS類はPFOS代替品として導入が進められている）の分解も可能であった。また，超臨界水状態にするとさらに反応は迅速に進行した[6]。

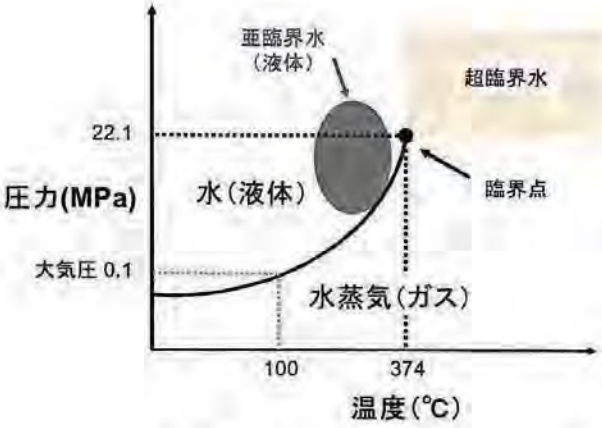

図3　水の状態図

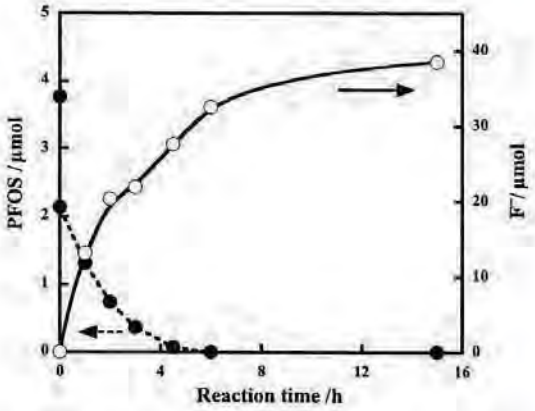

図4　鉄粉を還元剤として用いた亜臨界水反応によるPFOS分解の時間依存性
（PFOS初期濃度 372 μM，処理温度 350℃）

3　ヘテロポリ酸を用いたPFCA類の光触媒分解

PFCA類はPFAS類と並んで環境リスクが懸念されている物質群であり，その典型がペルフルオロオクタン酸（$C_7F_{15}COOH$, PFOA）である。水中のPFCA類はOHラジカルとの反応性が極めて低いため酸化チタン光触媒ではほとんど分解できないが，我々はヘテロポリ酸光触媒$[PW_{12}O_{40}]^{3-}$を用いることでフッ化物イオンと二酸化炭素まで完全に分解させることに成功した[1)]。これはPFCA類に関して光触媒で分解させることに成功した世界初の例である。$[PW_{12}O_{40}]^{3-}$は高い酸化力，強酸性下で安定（pHが1以下でも安定なため分解対象物がPFCA類のような強酸類であっても使用できる），均一系触媒なのでコーキングを起こさない，回収・再利用可能（エーテルと特異的にアダクト形成して相分離する性質を利用して水中から回収できる）といった特徴がある。

光反応は耐フッ素性の装置に炭素数2～9のPFCA類と$[PW_{12}O_{40}]^{3-}$を含む水溶液を導入し，酸素雰囲気下で紫外・可視光を照射することで行った。この方法により，例えばトリフルオロ酢酸（CF_3COOH）の場合，1モルの消失に対して2モルの二酸化炭素と3モルのフッ化物イオンが生成したので物質収支も合っていた。また，テトラフルオロメタン（CF_4）などの環境に有害な物質が発生しないことも確認した。PFOAの場合，反応初期には水中に炭素数が少ないPFCA類（短鎖PFCA類）も検出されたが，長時間照射によりこのような中間体は消失し，フッ素成分はフッ化物イオン，炭素成分は二酸化炭素まで分解した（図5）。この反応は光励起した$[PW_{12}O_{40}]^{3-}$がPFCA類から電子を奪うことで開始されるが，それに伴い$[PW_{12}O_{40}]^{3-}$は1電子還元した状態，すなわち$[PW_{12}O_{40}]^{4-}$になる。この還元種が系内に存在する酸素と反応して元の$[PW_{12}O_{40}]^{3-}$の状態に戻ることで触媒サイクルが形成されている。

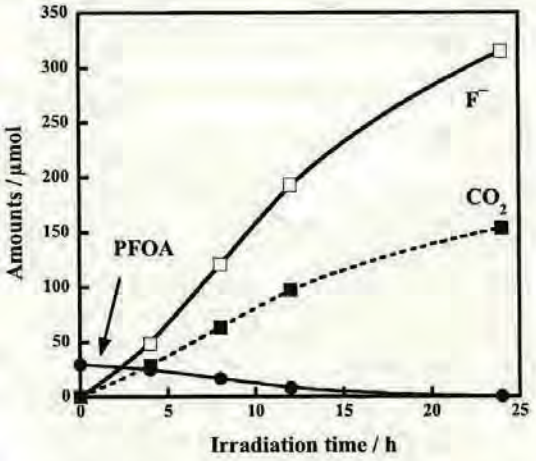

図5　ヘテロポリ酸光触媒によるPFOA分解反応の照射時間依存性
（PFOA初期濃度 1.35 mM）

4　ペルオキソ二硫酸イオンを用いたPFCA類の光酸化分解

上述の方法では200 Wの水銀・キセノン灯を使用した場合，1.35 mMのPFOAを完全に消失させるのに24時間を要する。我々は，より短時間でPFCA類を分解するためにペルオキソ二硫酸イオン（過硫酸イオン，$S_2O_8^{2-}$）を光酸化剤として用いる方法を開発した[2]。

水中の$S_2O_8^{2-}$に紫外光を照射すると酸化力が非常に強い硫酸イオンラジカル（$SO_4^{\bullet-}$）が生成する（(1)式）。$SO_4^{\bullet-}$生成の量子収率は2で非常に効率が高い。発生した$SO_4^{\bullet-}$の酸化還元電位（(2)式の反応に相当）は水中で2.5～3.1 Vであり[16]，OHラジカル（(3)式の場合は1.8 V，(4)式では2.7 V）と同程度か，それ以上である。

$$S_2O_8^{2-} + h\nu \rightarrow 2SO_4^{\bullet-} \quad (1)$$

$$SO_4^{\bullet-} + e^- \leftrightarrow SO_4^{2-} \quad (2)$$

$$\bullet OH + e^- \leftrightarrow OH^- \quad (3)$$

$$\bullet OH + e^- + H^+ \leftrightarrow H_2O \quad (4)$$

そこでPFOA水溶液に$S_2O_8^{2-}$を添加し，光照射して$SO_4^{\bullet-}$を生成させることでPFOAの分解を試みたところ，$[PW_{12}O_{40}]^{3-}$を使用した場合と同じ条件において4時間で消失させることができた（図6，PFOAの消失後も中間体の短鎖PFCA類の分解が続くためF^-とCO_2の生成は続いている）。また，$SO_4^{\bullet-}$は反応後には硫酸イオンになるが，その生成量は使用した$S_2O_8^{2-}$の2倍モルとなった。つまり硫黄分は全て硫酸イオンとして回収可能である。硫酸イオンの処理はカルシウム添加やイオン交換などの確立された方法を用いることができる。この反応は触媒反応ではないため$S_2O_8^{2-}$は消費される一方で再利用はできないが，硫黄化合物は安価であること，反応速度が大きいこと，副生成物は硫酸イオンという処理しやすいものであることは大きな利点である。我々はこの方法

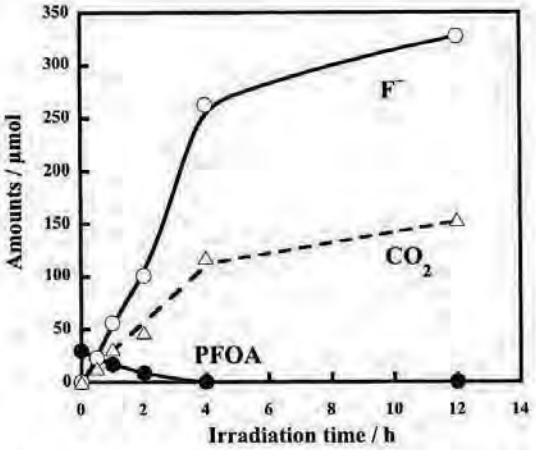

図6　ペルオキソ二硫酸イオンを光酸化剤としたPFOA分解反応の照射時間依存性
（PFOA初期濃度 1.35 mM）

を用いてワックス廃液中のPFCA類や[2]，PFCA類よりも有害性が懸念されるフルオロテロマー不飽和カルボン酸類（$C_nF_{2n+1}CF=CHCOOH$）の分解にも成功している[3]。PFOAよりも炭素数が２つ以上多いPFCA類（PFDA，PFUA）は水中では溶解度が低いため懸濁状となり，コロイド粒子が光を散乱するため光反応が難しくなるが，このような長鎖PFCA類については液体二酸化炭素に特異的に溶解する性質を利用して液体二酸化炭素・水の二相混合系でペルオキソ二硫酸イオンを使用することでフッ化物イオンまで効果的に光分解させることができた[4]。

5　ペルオキソ二硫酸イオンを用いたPFCA類の温水分解

PFCA類については熱水反応も検討した。その結果，$S_2O_8^{2-}$を添加した場合，意外にも80℃程度の低温の熱水，すなわち温水中で最も迅速にフッ化物イオンまで酸化分解できることを明らかにした[9]。反応は耐圧容器に空気雰囲気中でPFCA類と$S_2O_8^{2-}$（カリウム塩）を入れ，密封・加熱することで行った。図７にPFOAと134倍モル過剰の$S_2O_8^{2-}$を入れた温水（80℃）中におけるPFOA分解の時間依存性を示す。$S_2O_8^{2-}$を入れない場合にはPFOA濃度は全く減少しなかったが，$S_2O_8^{2-}$を入れた場合には迅速に減少し，同時に気相中にはCO_2が，水中にはF^-が生成した（図７(A)）。６時間におけるF^-およびCO_2の収率（PFOA初期量中のフッ素量および炭素量に対する値）は77.5％および70.2％であり，効果的に無機化されていることが分かる。水中には微量の短鎖PFCA類も検出され（図７(B)），時間の経過と共により短鎖な化学種の出現と消失が見られた。これはPFOA分解が長鎖種から短鎖種への逐次的な変換を経て進行していることを意味する。

この反応は$S_2O_8^{2-}$の熱分解で生成した硫酸イオンラジカル（$SO_4^{\bullet -}$）がPFOAを酸化することで進行するため，$SO_4^{\bullet -}$は還元してSO_4^{2-}になることが期待される。実際，PFOA分解の進行に伴い水中の$S_2O_8^{2-}$濃度は減少し，SO_4^{2-}が生成した（図８）。全ての反応時間において水中の硫黄の全モル数（SO_4^{2-}のモル数＋$S_2O_8^{2-}$のモル数×２）は$S_2O_8^{2-}$の初期モル数の２倍量と等しかった。このことは水中に安定に存在している硫黄化合物は$S_2O_8^{2-}$とSO_4^{2-}のみであることを意味する。この

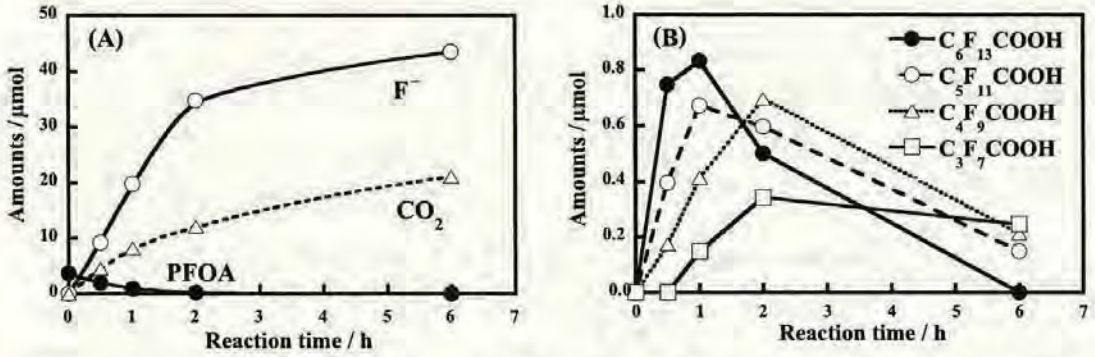

図７　ペルオキソ二硫酸イオンを用いたPFOAの温水分解：(A)PFOA，フッ化物イオンおよび二酸化炭素，および(B)短鎖PFCA類の存在量の時間依存性
（PFOA初期濃度 374 μM）

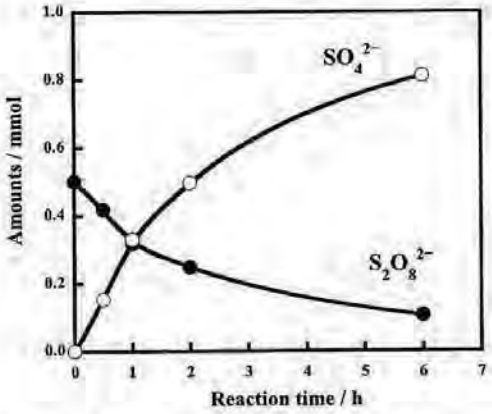

図8　水中のペルオキソ二硫酸イオンと硫酸イオン量の時間依存性

方法を他のPFCA類さらにはPFCA類の代替物質として導入が進みつつあるペルフルオロエーテルカルボン酸類に適用したところ，PFOAの場合と同様にCO_2とF^-までの効果的な分解・無機化が観測された。さらに迅速な分解を期待して反応温度を150℃に上昇させたところ，PFOAの減少速度は低下し，F^-およびCO_2の生成も大幅に減少した（6時間における収率はそれぞれ24.6%および37.0%）。これは150℃のような高温では$SO_4^{\bullet -}$と水との反応が優先してPFOAとの反応が阻害されるためと考えられる。また，150℃では気相中に1H-ペルフルオロアルカン類（$C_nF_{2n+1}H$, $n=4\sim7$）も生成した。以上のことからPFCA類を$S_2O_8^{2-}$により熱水分解させてF^-を効果的に得るためには，意外にも80℃のような低温の熱水（温水）反応が望ましいことが分かった。

6　PFOA代替物質：H-PFCA類の分解

H-PFCA類とはPFCA類の末端のトリフルオロメチル基のフッ素原子の1つを水素原子に置換したものである（一般式$HC_nF_{2n}COOH$）。H-PFCA類は炭素・水素結合を有するためPFCA類よりは分解容易と推測されるが，これまで分解特性の報告は皆無であった。我々は上述の「$S_2O_8^{2-}$＋温水分解法」をH-PFCA類（$n=4\sim8$）に適用し，PFCA類の場合と比較した[10]。

図9に$HC_8F_{16}COOH$の場合の反応の時間依存性を示す。ここで$S_2O_8^{2-}$は$HC_8F_{16}COOH$の初期量（濃度：392 μM）に対して128モル倍用いている。$HC_8F_{16}COOH$は30分で水中から消失した。一方，F^-の生成量は時間と共に増加し，6時間後にはその収率（$HC_8F_{16}COOH$の初期量中の総フッ素量を基準とした値）は98.2%に達し，事実上全てのフッ素成分がF^-まで分解・無機化した。$S_2O_8^{2-}$を添加しない場合，$HC_8F_{16}COOH$は6時間経過しても97.0%が残存し，F^-の収率も0.02%と僅かであった。この結果は$S_2O_8^{2-}$から硫酸イオンラジカル（$SO_4^{\bullet -}$）が発生し，それが$HC_8F_{16}COOH$の酸化分解を起こしていることを意味する。他のH-PFCA類の場合も同様に$S_2O_8^{2-}$を添加することで迅速に分解し，F^-の収率は6時間で96.7～98.2%に達した。80℃では分解が速すぎて速度論的な議論が難しいため反応温度を60℃に下げてみた。その場合でもH-PFCA類は$S_2O_8^{2-}$の共存下

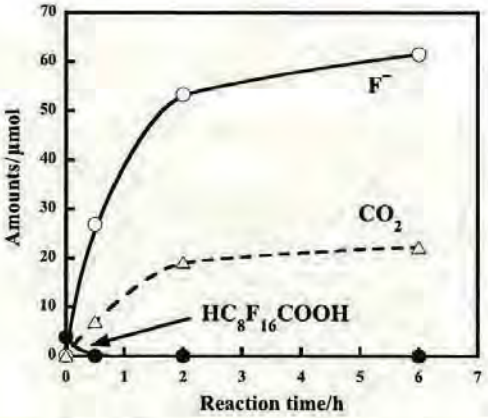

図９　$S_2O_8^{2-}$を用いた$HC_8F_{16}COOH$の温水分解の時間依存性

でF^-まで明白に分解し，分解の初期速度は同じ条件におけるPFCA類の場合の7.1～12.7倍であった。

PFCA類との違いは速度だけでなく，反応の機構にも表れた。反応液のESI-MSスペクトルを測定したところ，PFCA類では出発物質よりもペルフルオロアルキル基が短くなったPFCA類（短鎖PFCA類）が中間体として検出された。その場合，時間の経過と共に長鎖種が消失し，さらに短鎖なPFCA類が現れた。このことはPFCA類では分子末端のカルボキシル基が外れることから分解が進行することを意味する。一方H-PFCA類においては反応途中で出発物質よりもペルフルオロアルキル基が短くなったH-PFCA類は検出されず，代わりに短鎖ペルフルオロジカルボン酸類（一般式$HOOCC_nF_{2n}COOH$）が現れた。このことはH-PFCA類では$SO_4^{\bullet -}$が末端の水素原子が結合している炭素原子に対して求核置換反応を起こすことで反応が開始される，つまりカルボキシル基と反対側の末端から反応が起こることを意味する。生成したペルフルオロジカルボン酸はPFCA類の場合と同様に，末端のカルボキシル基の脱炭酸により分解が進むと考えられる。

7　PFOS代替物質：PFAES類の分解

PFOS/PFOA代替物質としてペルフルオロアルキル基の中にエーテル結合を導入したものがあり，PFAES類はその一種である。PFAES類については酸素ガスを共存させた亜臨界水で効果的に分解できることが分かった[11]。反応は耐圧容器にPFAES類（$C_nF_{2n+1}OC_2F_4SO_3^-$，$n = 2, 3$）の水溶液を入れ，酸素ガスを導入後密封して250～350℃の亜臨界水の状態にすることで行った。比較のため，アルゴン雰囲気下での実験および対応するPFAS類として近年使用が増加しているペルフルオロブタンスルホン酸（$C_4F_9SO_3^-$，PFBS）を用いた実験も行った。

図10に$C_2F_5OC_2F_4SO_3^-$について酸素雰囲気下で反応（350℃）させた場合の分解の時間依存性を示す。水中の$C_2F_5OC_2F_4SO_3^-$の濃度は擬一次反応速度式に従って明白に減少し，F^-，CO_2（図10(A)）およびSO_4^{2-}が生成した（図10(B)）。さらに反応中間体として微量のトリフルオロ酢酸（TFA）お

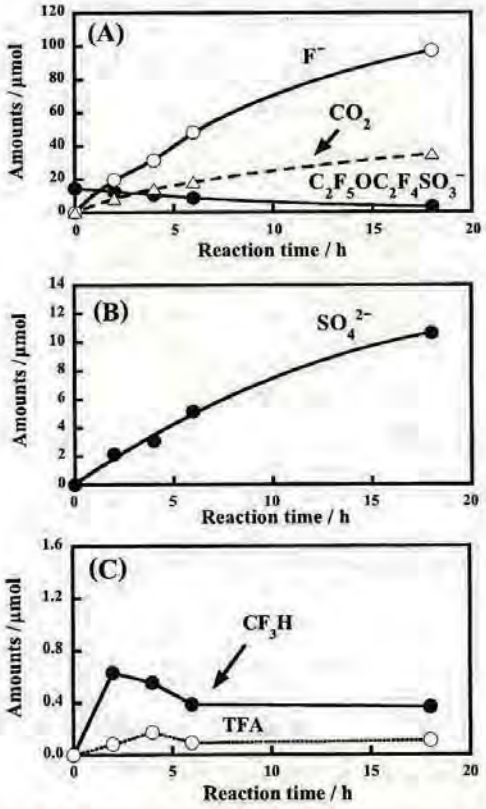

図10　$C_2F_5OC_2F_4SO_3^-$の酸素共存下での亜臨界水分解の時間依存性
（$C_2F_5OC_2F_4SO_3^-$初期濃度 1.46 mM，処理温度 350℃）

よびCF_3Hが検出された（図10(C)）。18時間後のF^-の収率は73.8%であり，効果的に無機化が進行している。またフッ素，炭素および硫黄に関する反応のマスバランスは97.2%，91.5%および94.6%と良好であった。

同じ反応条件において$C_3F_7OC_2F_4SO_3^-$も効果的に無機化された。その減少の擬一次反応速度定数は$C_2F_5OC_2F_4SO_3^-$の場合の1.6倍であり，この反応がペルフルオロアルキル基の長さに依存することが分かった。一方この条件ではPFBSはほとんど分解しなかった。PFBSの分解は上述のように鉄粉を還元剤とした亜臨界水反応でないと進行しない。

$C_2F_5OC_2F_4SO_3^-$の反応をアルゴン雰囲気下で行った場合，$C_2F_5OC_2F_4SO_3^-$の減少の時間依存性は酸素雰囲気下の場合とほぼ同じであったが，生成物の分布が大きく変化した。すなわちF^-，CO_2およびSO_4^{2-}の生成量が大幅に減少する一方で，TFAおよびCF_3Hの生成量が増加した。さらに新たな生成物として$HCF_2SO_3^-$が検出された。このことは酸素ガスが反応中間体の無機化の促進に重要な役割を果たしていることを意味する。

8　フッ素系イオン交換膜の分解・無機化反応

フッ素系イオン交換膜の分解もPFOS分解と同様な方法で達成した。フッ素系イオン交換膜（ポリマー）は造水，浄水，燃料電池，食塩電解など，様々な用途で用いられている機能性材料であるが，その廃棄物は埋め立て処分されているのが現状で，分解処理方法は確立されていない。フッ素系イオン交換膜のうち，ペルフルオロアルキルエーテルスルホン酸を側鎖に持つペルフルオロスルホン酸膜（PFAS膜）については，過酸化水素水やフェントン試薬（$Fe^{2+}+H_2O_2$）による劣化過程を調べた例がある[17]。しかし，それらは燃料電池の耐久性の向上を目的としたもので，廃棄物からフッ素成分を回収するために積極的に分解反応を探索した例はなかった。また，その劣化の過程においてPFCA/PFAS類似物質が生成するという報告もあるのでフッ化物イオンまで完全に無機化することが望ましい。そこで本研究ではPFAS膜について，金属粉を還元剤とした亜臨界水分解で無機化させることを試みた[13]。

試料としては精製したNafion NRE-212（図11）を用いた。この膜（乾燥重量29.8 mg，総フッ素量1.03 mmol）と金属粉（9.60 mmol），および純水（10 ml）を耐圧反応装置に入れ，アルゴン雰囲気下で密封後，250～350℃の亜臨界水状態にした。一定時間経過後，室温に急冷し，水中およびガス相中の反応物を分析した。

表1に300℃で6時間処理した場合の水中の残存ポリマー（水に溶解している）の分子量およびF^-の生成量を示す。金属を添加しない場合，F^-はほとんど生成しなかった（entry 1）。アルミニ

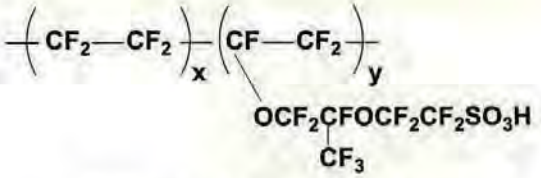

Nafion NRE-212, in Acid Form

図11　使用したペルフルオロスルホン酸膜の構造

表1　PFAS膜の亜臨界水分解における金属の添加効果*

entry	反応圧力 (MPa)	添加金属	水中の残存ポリマーの分子量		F^- (μmol) [収率(%)]
			M_w ($\times 10^5$)	M_w/M_n	
1	8.3	none	1.49	1.27	6.85 [0.67]
2	9.3	Al	1.90	1.27	0.78 [0.08]
3	8.6	Zn	1.70	1.16	22.6 [2.19]
4	8.4	Cu	1.41	1.33	35.7 [3.47]
5	9.4	Fe	1.20	1.32	351 [34.1]

*NRE-212（乾燥重量29.8 mg），金属粉（9.60 mmol），および純水（10 mL）を耐圧容器に入れ，アルゴン雰囲気中300℃で6時間加熱した。

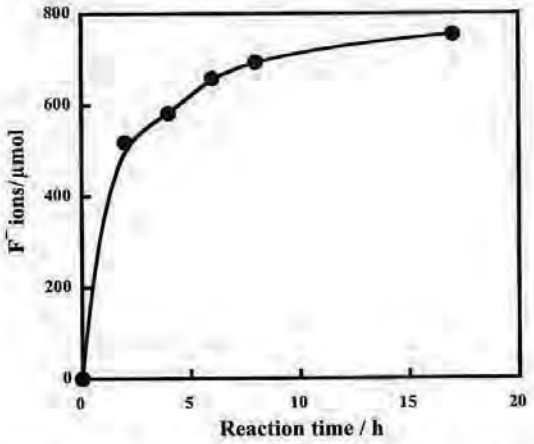

図12　鉄粉＋亜臨界水反応によるPFAS膜の分解におけるF^-生成量の時間依存性
（処理温度 350℃）

ウムを添加した場合，F^-の生成は却って阻害された。亜鉛，銅および鉄の場合には分解促進作用があり，鉄を用いた場合に特に顕著なF^-の生成が見られ，その量は添加しない場合の51倍となった（entry 5）。鉄粉を加えて反応温度を350℃に高めた場合，F^-の生成量はさらに増加し，サイズ排除クロマトグラフィーではもはやポリマーのピークは検出されなくなった。

図12に350℃で鉄粉を添加した場合のF^-生成量の処理時間依存性を示す。17時間後にはF^-の生成量は754 μmolに達した。これは反応前の膜中のフッ素原子のうち，73.2%がF^-に変換されたことを意味し，ポリマーの側鎖のみならず，主鎖 $(CF_2-CF_2)_x$の部分まで効果的に分解できることが分かった。

9　おわりに

以上，我々が行ってきた有機フッ素化合物の分解反応に関して紹介した。フッ素ポリマーについてはイオン交換膜よりもさらに使用量が多いものについて，また低分子の化合物についてもエネルギーデバイス用のイオン液体などとして需要が拡大しているペルフルオロスルホンイミド類などの反応性を調べている。このような取り組みにより新規フッ素材料の環境リスクの低減と資源の循環利用の双方に貢献したいと考えている。

文　　献

1）H. Hori *et al.*, *Environ. Sci. Technol.*, **38**, 6118 (2004)

2) H. Hori *et al.*, *Environ. Sci. Technol.*, **39**, 2383 (2005)
3) H. Hori *et al.*, *Water Res.*, **41**, 2962 (2007)
4) H. Hori *et al.*, *Environ. Sci. Technol.*, **39**, 7692 (2005)
5) H. Hori *et al.*, *Environ. Sci. Technol.*, **40**, 1049 (2006)
6) H. Hori *et al.*, *Chemosphere*, **70**, 800 (2008)
7) H. Hori *et al.*, *Catal. Today*, **196**, 132 (2012)
8) H. Hori *et al.*, *Chemosphere*, **68**, 572 (2007)
9) H. Hori *et al.*, *Environ. Sci. Technol.*, **42**, 7438 (2008)
10) H. Hori *et al.*, *Catal. Today*, **151**, 131 (2010)
11) H. Hori *et al.*, *Chemosphere*, **77**, 1400 (2009)
12) H. Hori *et al.*, *J. Fluorine Chem.*, **141**, 5 (2012)
13) H. Hori *et al.*, *Ind. Eng. Chem. Res.*, **49**, 464 (2010)
14) J. P. Giesy *et al.*, *Environ. Sci. Technol.*, **35**, 146 A (2002)
15) J. W. Martin *et al.*, *Environ. Sci. Technol.*, **38**, 373 (2004)
16) P. Neta *et al.*, *J. Phys. Chem. Ref. Data*, **17**, 1027 (1988)
17) 例えばKadirov *et al.*, *J. Phys. Chem. B*, **109**, 7664 (2005)

排水汚水
処理技術集成 vol.2

別刷り

第 2 編　処理技術研究の最前線

第 3 章　化学処理技術

総説―難分解性有機化合物の処理を中心に―

神奈川大学　　堀　久男

「排水・汚水処理技術集成 vol.2」(2013年12月26日　株式会社エヌ・ティー・エス　刊)

第３章　化学処理技術　総説
―難分解性有機化合物の処理を中心に―

神奈川大学　**堀　久男**

1.　はじめに

化学的手法による排水処理技術は，対象とする物質が有機化合物なのか無機化合物なのか，その物質が溶存している水が用水なのか排水なのかでも相当異なり，研究途上のものまで含めると多種多様にわたる。本書でも多くの具体例が紹介されているので，ここでは難分解性有機化合物の処理に関する代表的な技術についてその原理を中心に解説したい。

2.　促進酸化法

過酸化水素（H_2O_2）やオゾン（O_3）は有機化合物を酸化する能力をもっている。その能力，すなわち酸化力の大小は酸化還元電位により表現される。例えば，H_2O_2 の酸化還元電位は標準水素電極を用いた場合，1.77 V（式(1)の反応に相当），O_3 では 2.07 V（式(2)）[1] となる。この値が正に大きいほど酸化力は高いので，H_2O_2 よりも O_3 の方が酸化力は高いことになる。

$$H_2O_2 + 2H^+ + 2e^- \rightarrow 2H_2O \quad (1)$$

$$O_3 + 2H^+ + + 2e^- \rightarrow O_2 + H_2O \quad (2)$$

促進酸化法（AOP：Advanced Oxidation Process）とは，このような H_2O_2 や O_3 を酸化剤として直接利用するわけではなく，それらを組み合わせたり，それらに紫外線（UV）や超音波などを照射することでヒドロキシラジカル（OH ラジカル）を生成させて，水中の難分解性有機化合物を分解する方法である（**図 1**）。OH ラジカルの酸化還元電位は式(3)で 2.7 V，式(4)で 1.8 V なので，pH などの反応条件を整えれば H_2O_2 や O_3 をそのまま用いた場合よりも高い酸化力を示すことが期待できる。

$$\cdot OH + e^- + H^+ \rightarrow H_2O \quad (3)$$

$$\cdot OH + e^- \leftrightarrow OH^- \quad (4)$$

OH ラジカルは有機化合物に対して電子移動反応，水素引き抜き反応，不飽和結合への付加反応などを起こす[2]。これらの反応により水中の有機化合物の濃度（全有機炭素，TOC：Total Organic Carbon）を低減させることができる。例えば，高橋らは水中のエチレングリコールの分解挙動を O_3 および O_3＋UV の２種の方法で比較している[3]。その結果，O_3 の単独処

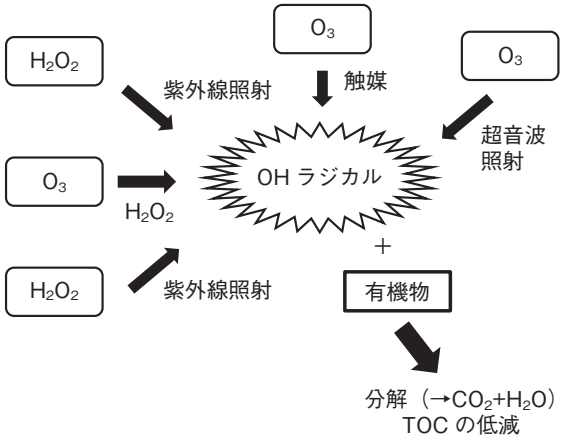

図１　促進酸化法の原理

理ではシュウ酸で分解が止まってしまい TOC がほとんど減少しなかったが，O_3＋UV 法ではホルムアルデヒドを経てギ酸が生成する経路も起こり（**図 2**）[3]，生成したシュウ酸およびギ酸も効果的に分解して TOC が大幅に低減したことを報告している。

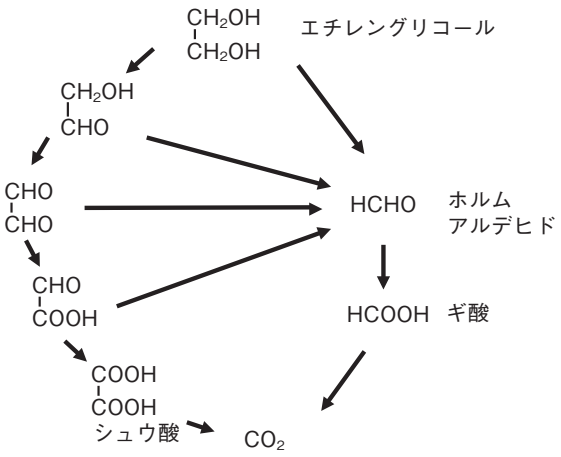

図２　O_3＋UV 法によるエチレングリコール分解の反応経路[3]

3.　フェントン反応

フェントン反応とは酸性の pH 領域で H_2O_2 と Fe^{2+}（硫酸鉄（Ⅱ）を用いる場合が多い）から OH ラジカルを発生させ，種々の有機化合物の分解を行う反応である。Fe^{2+} は H_2O_2 により Fe^{3+} に酸化され，OH ラジカルと OH^- が生成する（式(5)）。この OH ラジカルが有機化合物と反応するわけであるが，式(5)で生成した Fe^{3+} は H_2O_2 と反応して Fe^{2+} とヒドロペルオキシルラジカル（$HO_2\cdot$）が生成し（式(6)），このラジカルも有機化合物に対する酸化剤として作用する。Fe^{2+} はまた H_2O_2 と反応するので触媒的に有機化合物が分解することになる[4]。OH ラジカルの反応性を利用する方法なので促進酸化法の一種と見なすこともできる。

$$Fe^{2+} + H_2O_2 \rightarrow Fe^{3+} + OH\cdot + OH^- \quad (5)$$

$$Fe^{3+} + H_2O_2 \rightarrow Fe^{2+} + HO_2\cdot + H^+ \quad (6)$$

この手法により，土壌中や地下水中のトリクロロエチレンやベンゼンなどの揮発性有機汚染物質（VOC：Volatile Organic Compounds）を分解させた例は数多く報告されている[5)-8)]。

4.　ペルオキソ二硫酸法（過硫酸法）

上述の方法は OH ラジカルの酸化力を利用して有機化合物の分解を行う方法であるが，近年，硫酸イオンラジカル（$SO_4\cdot^-$）を用いて OH ラジカルとの反応性が低い有機化合物の分解を試みることが盛んに検討されている。$SO_4\cdot^-$ の酸化還元電位は（式(7)の反応に相当）は水中で 2.5 ～ 3.1 V であり[9]，OH ラジカル（式(3)の場合は 2.7 V，式(4)では 1.8 V）と同程度か，それ以上である。$SO_4\cdot^-$ はペルオキソ二硫酸イオン（過硫酸イオン）に紫外光を照射して得られる（式(8)）。

$$SO_4\cdot^- + e^- \leftrightarrow SO_4^{2-} \quad (7)$$

$$S_2O_8^{2-} + h\nu \rightarrow 2SO_4\cdot^- \quad (8)$$

水中の難分解性物質として典型的なものに有機フッ素化合物がある。例えば，界面活性剤として使用されてきたペルフルオロカルボン酸類（$C_nF_{2n+1}COOH$，PFCA 類）のうちペルフルオロオクタン酸（$C_7F_{15}COOH$，PFOA）は，近年，生体蓄積性が指摘され世界的に規制が開始されているが，通常の促進酸化法ではほとんど分解できない。筆者らは PFOA 水溶液に $S_2O_8^{2-}$ を添加して紫外光を照射して分解を試みた。その結果，F^- と CO_2 まで分解できることを明ら

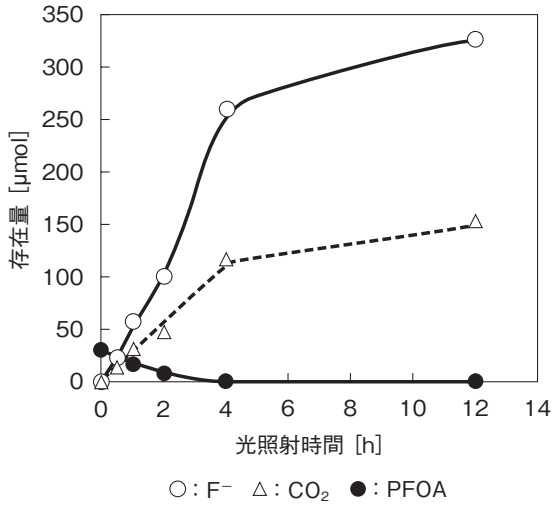

図 3　$S_2O_8^{2-}$を光酸化剤とした PFOA 分解反応の照射時間依存性（PFOA 初期濃度 1.35 mM，$S_2O_8^{2-}$初期濃度 50 mM）[10]

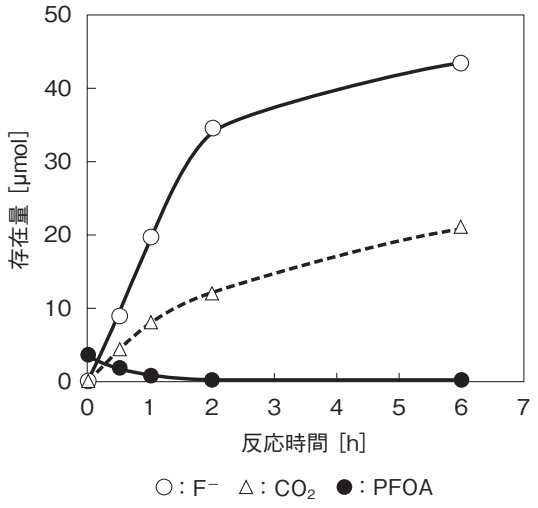

図 4　$S_2O_8^{2-}$を用いた PFOA の温水分解（PFOA 初期濃度 374 μM）[12]

かにした（**図 3**[10]，PFOA の消失後も中間体であるペルフルオロアルキル基（C_nF_{2n+1}）が短い短鎖 PFCA 類の分解が続くため，F^-と CO_2 の生成は続いている）[10]。この反応では $SO_4^{\cdot -}$は硫酸イオンになるが，その生成量は使用した $S_2O_8^{2-}$の 2 倍モルとなった。つまり，硫黄分はすべて硫酸イオンとして回収可能である。この方法で PFCA 類よりも有害性が高いフルオロテロマー不飽和カルボン酸類（$C_nF_{2n+1}CF=CHCOOH$）も分解できた[11]。PFCA 類については $S_2O_8^{2-}$を熱励起することでも分解できる[12]。**図 4**[12] に PFOA と 134 倍モル過剰の $S_2O_8^{2-}$を入れた温水（80 ℃）中における PFOA 分解の時間依存性を示す。$S_2O_8^{2-}$を入れない場合には PFOA 濃度は全く減少しなかったが，$S_2O_8^{2-}$を入れた場合には迅速に減少し，CO_2 と F^-が生成した。

このような方法で，水中や土壌中の PCB や VOC を分解除去した例も報告されている[13)14)]。

5.　超音波分解法

水中に高出力の超音波を照射すると溶解している気泡が圧縮，膨張を繰り返し，断熱的に内崩してミクロな高温高圧場が発生する。そのミクロな場における温度，圧力は数千℃，数百気圧に達し，水は分解して OH ラジカルを生じる。この OH ラジカルや熱の作用により有機化合物を分解させることができる[15)-17)]。例えば，Moriwaki らは上述の PFOA，さらには PFOA 以上に安定なペルフルオロオクタンスルホン酸（$C_8F_{17}SO_3H$，PFOS）が超音波照射で分解することを報告している[18)]。Cheng らは埋立処分場の PFOS 含入地下水に超音波を照射して，反応に及ぼす共存物質の影響を調べている[19)]。筆者らも $S_2O_8^{2-}$と超音波照射を組み合わせて有機フッ素化合物の分解を試みた。例として，$CF_3OC_2F_4OCF_2COOH$（NEDOHA）50 μM に 0 ～ 10 mM の $S_2O_8^{2-}$を添加して超音波照射した場合の水中の NFDOHA 濃度の時間依存性を示す（**図 5**（a））[20)]。$S_2O_8^{2-}$の添加により NFDOHA の分解が促進され，F^-の生成も増加していることが分かる（図 5（b））[20)]。

6. 熱水分解法

有機フッ素化合物のような非常に安定な有機化合物を分解する有力な方法に熱水分解法がある。**図６**に水の状態図を示す。周知のように常圧にある水（液体）を加熱すると100℃で沸騰する。常圧よりも高圧に置かれた水を加熱すると，100℃よりも高温にしないと沸騰しない。22.1 MPaにある水を加熱すると374℃で沸騰するが，それ以上の圧力にさらされた水は加熱しても沸騰という現象が見られない。つまり，沸騰には終点がある。その終点を臨界点（374℃，22.1 MPa）といい，臨界点を超える温度・圧力の状態は超臨界水と呼ばれる。また，臨界点よりもやや低い領域にある高温，高圧の水（液体）は亜臨界水と呼ばれる。この超臨界水や亜臨界水を総称して熱水と呼ぶ。これらの水は高拡散性，低粘性，無極性の有機化合物を溶解する，有機化合物を加水分解するなど，普通の水にはない性質をもっており，トリニトロトルエンやPCBのプラント規模での分解に応用されている[21)22)]。熱水に鉄粉のような還元剤を組み

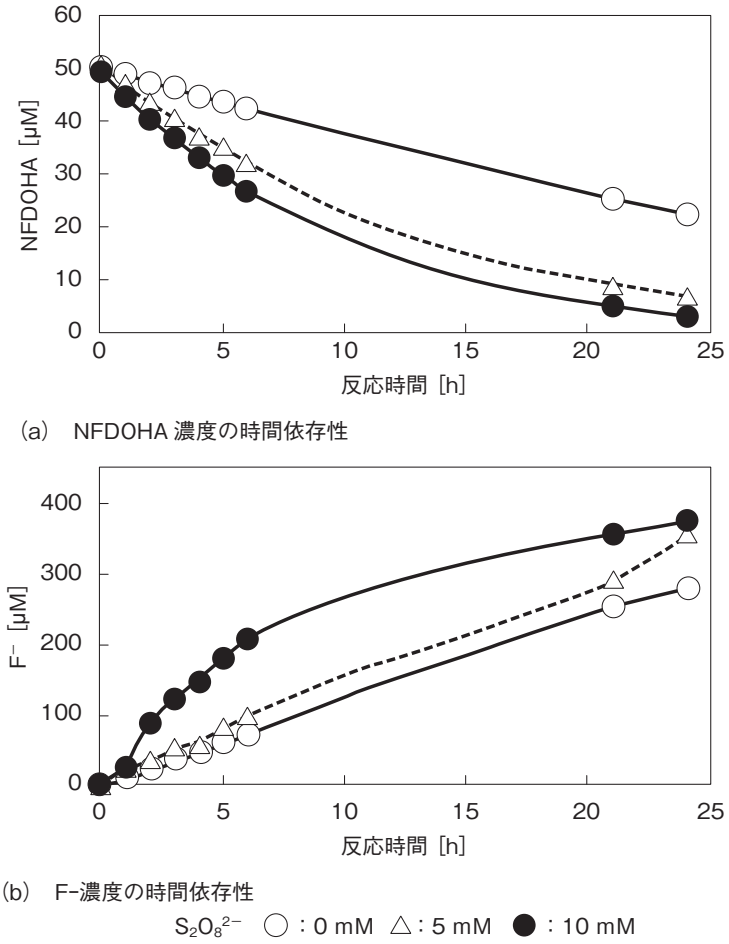

図５　$S_2O_8^{2-}$＋超音波照射による有機フッ素化合物NFDOHAの分解[20)]

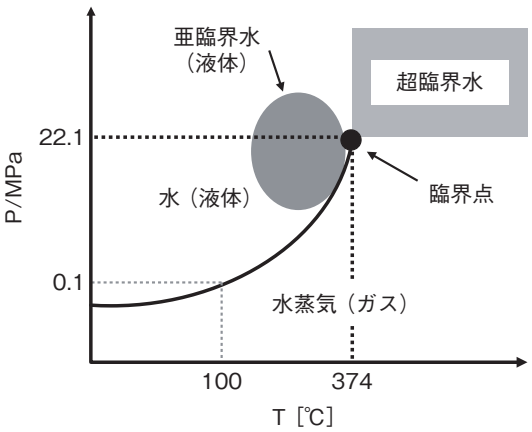

図６　水の状態図（正しいスケールではない）

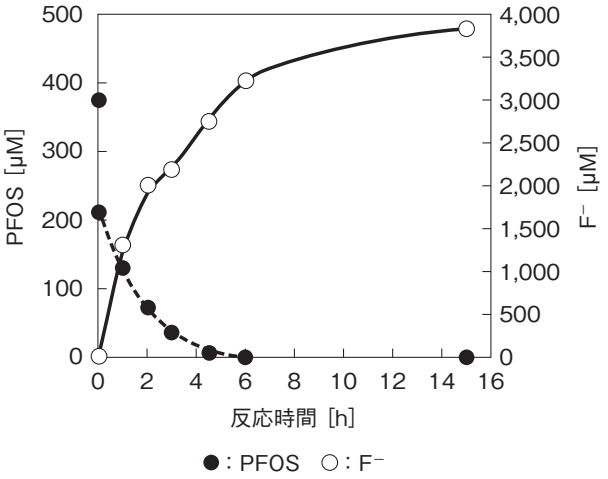

図７　鉄粉＋亜臨界水法によるPFOS分解の処理時間依存性（PFOS初期濃度，372 μM，反応温度350℃）[23)]

合わせることで，有機フッ素化合物を効果的に分解できる。例として，鉄粉を添加して亜臨界水処理した場合の PFOS の分解挙動を**図 7**[23] に示す。PFOS は 6 時間で水中から消失し，同時に F^- が高収率で生成していることが分かる。

文　献

1) W. M. Haynes, Editor in chief：CRC Handbook of Chemistry and Physics, 92nd edition, CRC Press, Boca Raten, Florida (2011).

2) 日本化学会編：活性酸素種の化学，季刊化学総説 7，学会出版センター，東京 (1990).

3) 高橋信行ほか：日本化学会誌，5，763–770 (1988).

4) W. G. Barb et al.：*Trans.Faraday Soc.*, **47**, 591–616 (1951).

5) G. Chen et al.：*J. Hazard. Mater.*, **87**,171–186 (2001).

6) P. T. S. Silva et al.：*J. Hazard.Mater.*, **161**, 967–973 (2009).

7) Z. Tang et al.：*J. Environ. Sci. Health*, Part A：**31**, 2755–2775 (1996).

8) K. R. Weeks et al.：*Soil Sediment Contam.*, **9**, 331–345 (2000).

9) P. Neta et al.：*J. Phys. Chem. Ref. Data*, **17**, 1027–1284 (1988).

10) H. Hori et al.：*Environ. Sci. Technol.*, **39**, 2383–2388 (2005).

11) H. Hori et al.：*Water Res.*, **41**, 2962–2968 (2007).

12) H. Hori et al.：*Environ. Sci. Technol.*, **42**, 7438–7443 (2008).

13) A. Rastogi et al.：*Appl. Catal. B*：*Environ.*, **85**, 171–179 (2009).

14) オルガノ，地下汚染領域の浄化方法，特許第 4405692 号 (2009).

15) Y. G. Adewuyi：*Environ. Sci. Technol.*, **39**, 3409–3420 (2005).

16) Y. G. Adewuyi：*Environ. Sci. Technol.*, **39**, 8557–8570 (2005).

17) Y. T. Dienko et al.：*J. Am. Chem. Soc.*, **121**, 5817–5818 (1999).

18) H. Moriwaki et al.：*Environ. Sci. Technol.*, **39**, 3388–3392 (2005).

19) J. Cheng et al.：*Environ. Sci. Technol.*, **42**, 8057–8063 (2008).

20) H. Hori et al.：*J. Fluirine Chem.*, **141**, 5–10 (2012).

21) S. B. Hawthorne et al.：*Environ. Sci. Technol.*, **34**, 3224–3228 (2000).

22) S. I. Kawasaki et al.：*Process Saf. Environ.*, **84**, 317–324 (2006).

23) H. Hori et al.：*Environ. Sci. Technol.*, **40**, 1049–1054 (2006).

排水汚水
処理技術集成 vol.2

別刷り

第２編　処理技術研究の最前線

第３章　化学処理技術

第１節　フッ素系イオン液体の熱水分解

神奈川大学　　堀　久男

「排水・汚水処理技術集成 vol.2」(2013年12月26日　株式会社エヌ・ティー・エス　刊)

第１節　フッ素系イオン液体の熱水分解

神奈川大学　**堀　久男**

1.　はじめに

フッ素系イオン液体とは，陰イオンと陽イオンからなる塩類でありながら常温付近で液体の物質（イオン液体）のうち，陰イオンを構成するアルキル基の水素原子がすべてフッ素原子に置換された有機フッ素化合物である。それらは有機フッ素化合物に共通な性質，すなわち熱的および化学的に安定であるだけでなく，不揮発性，不燃性，広い電位窓，高イオン電導性，特異な物質溶解能などの性質を有している[1)]。そのため，リチウムイオン電池や固体高分子型燃料電池，湿式太陽電池などの各種エネルギーデバイスの構成材（電解質）をはじめ，ガスクロマトグラフィーの固定相や二酸化炭素吸収材などにも導入されつつある。しかし，これらは炭素のつくる共有結合で，最強の炭素･フッ素結合を有するためきわめて安定である。このため，廃棄物の分解処理技術が確立されていない。焼却は可能であるが，高エネルギーを必要とするだけでなく，生成するフッ化水素ガスが焼却炉材を損傷する問題がある。これらの廃棄物を穏和な条件でフッ化物イオン（F^-）まで分解できれば，既存のカルシウム処理でフッ化カルシウムに変換できる。フッ化カルシウムの鉱物は蛍石で，フッ化水素酸の原料であり，フッ化水素酸からすべての有機フッ素化合物は合成される。したがって，分解技術が確立されることは産出が特定国に偏在し，需給が逼迫しているフッ素資源の循環利用にも貢献できる（**図 1**）。

そこで，筆者らはフッ素系イオン液体の陰イオンの部分をさまざまな還元剤や酸化剤を用いて熱水（亜臨界水および超臨界水）中で分解することを検討した。その結果，零価の鉄（Fe）や酸化鉄（Ⅱ）（FeO）を還元剤として用いることで F^- まで効果的に分解できることを明らかにした[2)]。

2.　実　験

試料としては $(CF_3SO_2)_2N^-$（リチウム塩, 1）および $(C_4F_9SO_2)_2N^-$（カリウム塩, 2）を用いた。

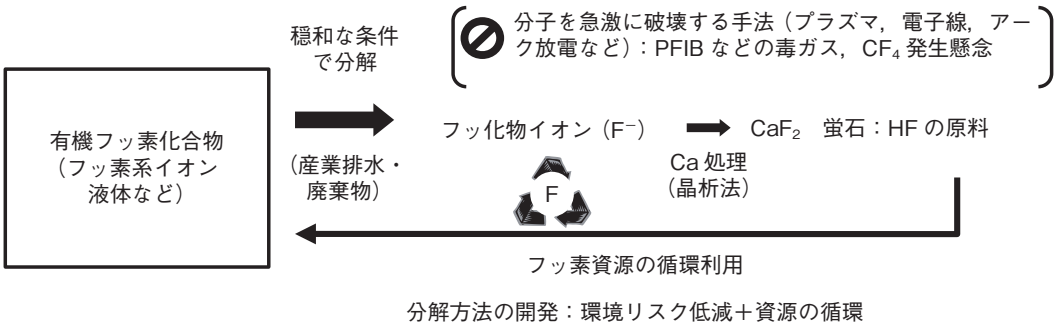

図１　フッ素資源の循環利用スキーム

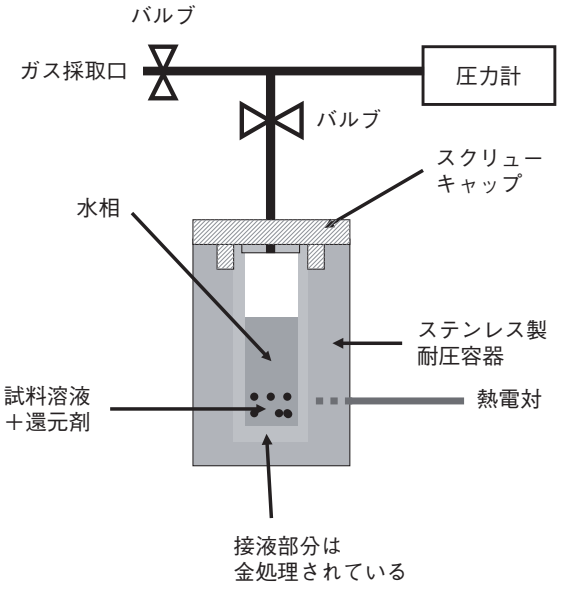

図２　熱水反応装置の概略図

反応はこれらと鉄系の還元剤（Fe，FeO，Fe_3O_4），および純水（10 mL）を耐圧容器に入れ，アルゴン雰囲気中で密閉後，193 ～ 378℃に加熱して行った。反応装置の概略図を**図２**に示す。容器内部は金処理を施しており，容器の構成材料（ステンレス）による試料の汚染を防いでいる。所定の温度で一定時間経過後，室温まで急冷し，液相をイオンクロマトグラフィーおよび高速液体クロマトグラフ質量分析法（LCMS）で，気相をガスクロマトグラフィーおよびガスクロマトグラフ質量分析法（GCMS）で分析した。反応に伴う還元剤の変化は粉末 X 線回折（XRD）で調べた。比較のため還元剤を添加しない反応や，O_2 を酸化剤として用いた反応も行った。

3.　実験結果

表１に 1.62 mM の１を６時間反応させた場合の１の残存率（１の残存モル数/初期モル数）と，生成した F^- の収率（F^- モル数を反応前の１中のフッ素原子のモル数で除した値）を示す。１はアルゴン雰囲気下，純粋な亜臨界水中（344℃）では 98.8 %が残存し，F^- もほとんど生成しなかった（No. 1）。O_2 を用いた場合，１の残存率は 95.4 %，F−収率は 1.11 %となり，反応促進効果はほとんどなかった（No. 2）。このことは，１が酸化分解をきわめて起こしにくいことを意味する。

効果的に分解を起こすために，アルゴン雰囲気下で鉄系の還元剤を用いた反応を行った。Fe を添加して亜臨界水中（344℃）で反応させた場合，１の残存率は 1.35 %まで減少し，F^- 収率は 69.0 %に達した（No. 3）。この値は Fe を添加しない場合の 186 倍であり，顕著な分解促

表１　フッ素系イオン液体（陰イオンの部分）の亜臨界水分解

No.[a]	基質	ガス	還元剤	温度 [℃]	圧力 [MPa]	基質 残存率 [%]	F^- 収率 [%]
1	1[b]	Ar	なし	344	15.9	98.8	0.37
2	1[b]	O_2	なし	345	16.0	95.4	1.11
3	1[b]	Ar	Fe	344	16.5	1.35	69.0
4	1[b]	Ar	FeO	345	15.7	36.8	48.2
5	1[b]	Ar	Fe_3O_4	345	16.0	97.3	3.63
6	2[c]	Ar	なし	346	15.6	17.3	9.50
7	2[c]	Ar	Fe	346	15.4	＜0.16	37.0

a）　液量：10 mL　還元剤添加量：9.60 mmol　反応時間：６時間
b）　初期量：16.2 μmol
c）　初期量：1.62 μmol

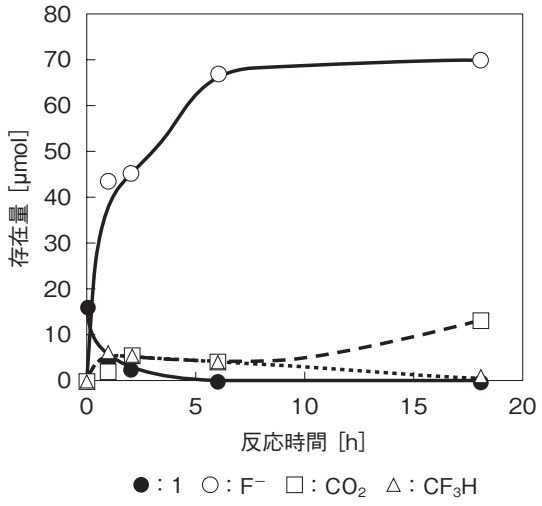

図 3　Fe を用いた場合の 1 の分解の反応時間依存性（反応温度：345℃，1 の初期量：16.2 μmol）

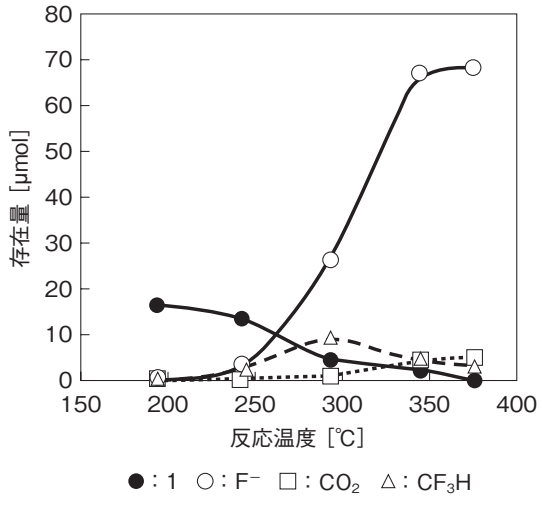

図 4　Fe を用いた場合の 1 の分解の温度依存性（反応時間：6 時間，1 の初期量：16.2 μmol）

進効果があった。345℃で FeO を用いた場合にも Fe には及ばないものの，反応が促進された（No. 4）。一方，Fe_3O_4 を用いた場合にはほとんど効果がなかった（No. 5）。同様の結果は 2 の場合にも見られた（No. 6 と No. 7 を比較）。

図 3 に Fe を添加して 344℃で反応させた場合の 1 および生成物の存在量の時間依存性を示す。水中の 1 の存在量は擬一次反応速度式に従って減少した（速度定数＝0.77 h^{-1}）。同時に F^- の生成量が増加し，18 時間後の F^- 収率は 72.0 %に達した。また，ガス相中には CO_2 と CF_3H が検出された。CF_3H は温暖化係数が高いので，その生成には注意する必要があるが[3]，幸いなことに CF_3H は図から分かるように長時間反応させることでほとんど消失した。このことは，CF_3H が反応中間体であることを意味する。この反応の温度依存性についても調べた（**図 4**）。1 の分解は 243℃ 以上で起こり，375℃の超臨界状態において F^- の生成量は最大となっている。また，CF_3H の生成量は 300℃ 付近で最大となり，それ以上の温度で減少しているので分解していることは間違いな

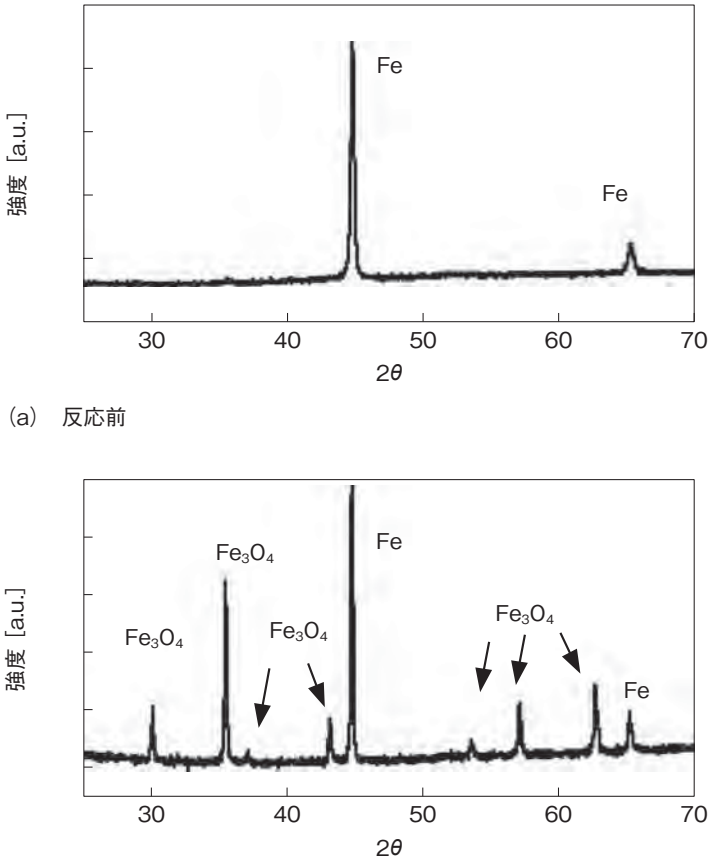

図 5　回収した Fe 粉の XRD パターン

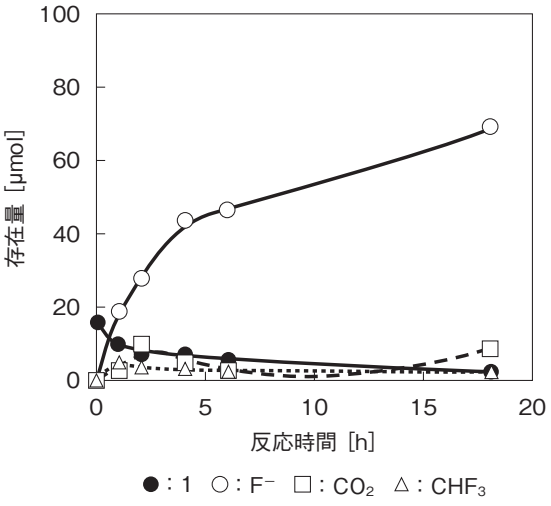

図６　FeO を用いた場合の１の分解の反応時間依存性（反応温度：345℃，１の初期量：16.2 μmol）

い。375℃で反応時間を延長したところ，18 時間で F^- 収率は 76.8 %に達した。

この反応に伴う Fe の変化を XRD 測定で調べた。**図５**に反応前と反応後に回収した Fe 粉の XRD パターンを示す。反応後には Fe_3O_4 のピークが見られた。また，ガス相には水素ガスも検出された。これらの結果は，Fe は１のみならず水とも反応することを意味する。上述のように，Fe_3O_4 には１の反応促進効果はない。したがって，Fe_3O_4 の生成は１の分解を停止させることになる。

図６に１を FeO を用いて 345℃で反応させた場合の反応の時間依存性を示す。Fe の場合とは異なり，１の減少は擬一次反応速度式に従わなかった。また，Fe に比べて初期の反応性は低いものの，意外なことに効果が長時間持続し，最終的に 18 時間における F^- 収率は 71.3 %となり，Fe の場合（72.0 %）と同様であった。何が起こっているのか解明するため反応後に回収した FeO 粉の XRD 測定をしたところ，FeO は短時間で Fe と Fe_3O_4 に変化していた（**図７**）。これは，FeO が亜臨界水中で Fe と Fe_3O_4 に不均化したことを意味する[4)5)]。上述のように Fe_3O_4 には１の反応促進効果はない。したがって，FeO による１の分解においては系内に生成した Fe が１の分解を起こす真の活性種として作用していることが分かる。また，回収した FeO および Fe の XRD パターンから，FeO から生成する Fe の方が，Fe を最初に用いた場合よりも Fe の量は少ないことは明らかである（初期量はどちらも同じモル数である）。にもかかわらず，長時間反応させた後の F^- 収率がほぼ同じになるということは Fe は水とも反応するが，FeO から生成する Fe

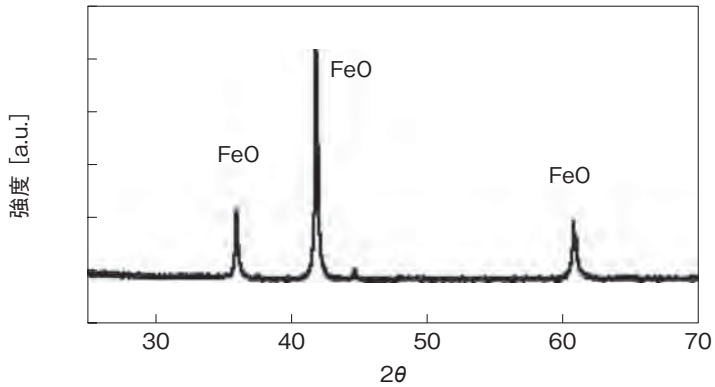

(a)　反応前

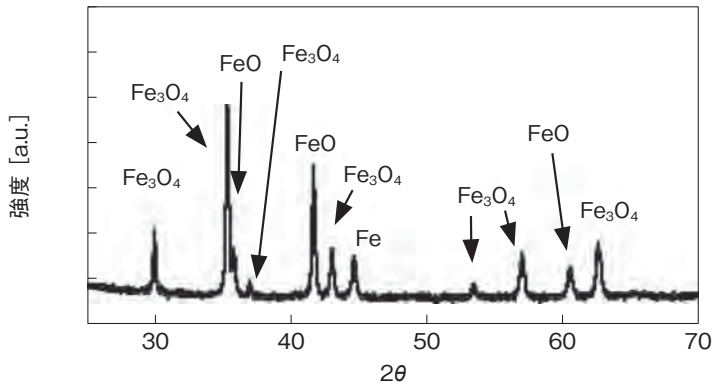

(b)　345℃で１時間反応させた後

図７　回収した FeO 粉の XRD パターン

の方が最初から Fe を用いた場合よりも水との反応に消費されにくく，1 との反応に優先的に使用されることを示唆する。**図 8** に FeO を用いた場合の反応の温度依存性を示す。1 の分解は 300℃ 以上で顕著となったが，その場合に Fe と Fe_3O_4 の不均化が生じていた。378℃においては F^- 収率は 78.0 % となり，最初から Fe を用いた場合（70.6 %）より高くなった。18 時間後には F^- 収率は全条件の中で最高の 85.7 % に達した。

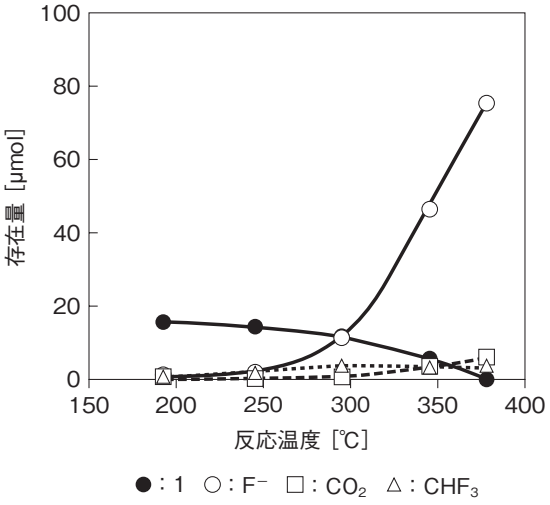

図 8　FeO を用いた場合の 1 の分解の温度依存性（反応時間：6 時間，1 の初期量：16.2 μmol）

4.　おわりに

以上のことから，1 および 2 は Fe あるいは FeO を還元剤として用いることにより，熱水（亜臨界水および超臨界水）中で効果的に F^- まで分解できることを明らかにした。短時間では Fe の方が FeO よりも反応性が高いが，Fe と水との反応も生じて 1 の分解を抑制してしまう。一方，長時間の反応では FeO の方が Fe よりも 1 の分解促進効果が持続し，最終的には Fe を用いた場合よりも高い F^- 収率が得られた。現在，さらに多種多様のフッ素系イオン液体の分解を試みている。

文　献

1) H. Ohno, editor：Electrochemical Aspects of Ionic Liquids, John Wiley & Sons：Hoboken, New Jersey (2011).

2) H. Hori et al.：*Ind. Eng. Chem. Res.*, doi：10.1021/ie4017573 (2013).

3) IPCC Fourth Assessment Report：Climate Change 2007：Working Group I：The Physical Science Basis. Intergovernmental Panel on Climete Change. Geneva, Switzerland. http://www.ipcc.ch/publications_and_data/ar4/wg1/en/ch2s2-10-2.html.

4) L. Broussard et al.：*J. Phys. Chem.*, **73**, 1848-1854 (1969).

5) S. Stølen et al.：*Thermochim. Acta.*, **256**, 91-106 (1995).

ぶんせき

別　刷

No. 8　　2013

過塩素酸イオンの環境残留性と対策技術の研究動向

堀　久男

公益社団法人 日本分析化学会

東京都品川区西五反田1丁目26番2号　五反田サンハイツ304号

解　説

過塩素酸イオンの環境残留性と対策技術の研究動向

近年，火薬等の構成成分である過塩素酸イオンが環境中に残留していることが明らかとなり，その影響が懸念されている。このため水質基準値等が世界的に設定されつつある。そこで本稿では環境中の過塩素酸イオンの発生源や濃度，さらには対策技術の研究動向について，筆者らの例も含めて解説したい。

堀　久　男

1　はじめに

2000年代後半から過塩素酸イオン（ClO_4^-）が環境水[1)~6)]，飲料水や食品[7)~9)]，さらには人体中[10)11)]に広範囲に存在することが明らかとなってきた。ClO_4^-は甲状腺におけるヨウ素の取り込みを抑制する作用があり，多量に摂取した場合に甲状腺の機能を低下させる恐れがある。このため環境分析や生体影響の研究が進むにつれて基準値等が設定されつつある。例えば米国環境保護庁（EPA）は，米国科学アカデミーが勧告した参照用量（reference dose, RfD，生涯毎日暴露を受けてもリスクがない量の推定値）0.7 μg/kg/dayに基づき，2008年10月に飲料水中の暫定基準濃度（health reference level）として15 μg/Lを設定し，現在，最終的な基準濃度の設定に向けた検討を行っている[12)]。我が国においても2009年に水道水に関する要検討項目に「過塩素酸」が追加され，2011年4月1日より目標値25 μg/Lの適用が開始された[13)]。ClO_4^-は塩素のオキソ酸のイオンとしては最も安定で，極めて酸化しにくく，加水分解もしない。嫌気性の微生物により還元されることはあるが，微生物は硝酸塩や硫酸塩を優先的に利用するため，環境中では難分解性物質の範疇（はんちゅう）に入る[14)]。

2　発生源

過塩素酸の塩類は主にロケットやミサイル燃料の推進剤，エアバック，火薬，花火等の構成成分として用いられている。また，リチウム電池の電解質や金属錯体触媒の対アニオン等にも使われている。米国では主にアンモニウム塩が製造されており，1951～1997年までの過塩素酸アンモニウムの生産量は総計395000トンであり，ClO_4^-としての年平均の生産量は7100トンと見積もられている[15)]。我が国では2000～2009年における過塩素酸ナトリウムの生産量は年間1400～1600トンとの推定値があるものの[14)]，経済産業省の実態調査による平成19年度の過塩素酸ナトリウムおよび過塩素酸カリウムの製造（出荷）量はそれぞれ10～100トン未満，100～1000トン未満となっており[16)]，正確な値は不明である。もちろん輸出される分もあり，使用時には分解して大部分が塩化物イオン（Cl^-）になるため，製造量がそのまま環境中へ放出されるわけではない。環境への放出量については米国において，1950年初頭から過塩素酸塩の製造・使用施設からの合計量が15900トンであると推測した例がある[17)]。我が国においては，過塩素酸塩は化学物質把握管理促進法の第一種指定化学物質ではないため，排出量は不明である。「難分解性」という単語からペルフルオロオクタンスルホン酸（PFOS）やペルフルオロオクタン酸（PFOA）のような有機フッ素化合物を思い浮かべる方もいるかもしれないが，ClO_4^-にはPFOS/PFOAとは相当異なる面がある。例えばClO_4^-には自然発生源があり，チリ硝石中に含まれている。チリ硝石は肥料として使用されるが，Urbanskyらは米国で市販されている硝石肥料の2ロット中のClO_4^-を定量したところ，平均で1.5 mg/gおよび1.8 mg/gであったことを明らかにしている[18)]。またテキサス州の乾燥地帯等では特異的に地下水中のClO_4^-濃度が高い地域があるが（>100 μg/L），これも自然発生源に由来している[6)]。さらには大気中でCl^-がオゾンと光反応して生成するとも言われているが，詳細は不明である[19)]。

3　環境残留性（環境，食品，人体中の濃度）

環境中のClO_4^-濃度を報告した文献は多数あるので，ここでは興味深い例のみ取り上げたい。ClO_4^-には上述のように自然発生源がある。そもそもバックグラウンドでどのくらいの濃度があるのか知ることは人為的な発生源への対策を考えるうえで重要である。例えばParkerらは，全米から人為的な発生源（過塩素酸塩の製造・使用箇所）が考えられない326地点から採取し

Perchlorate in the Environment and Its Treatment Technologies.

た地下水を測定している[1]。その結果，検出限界以下（<40 ng/L）が147地点，40 ng/L～120 ng/Lが42地点，120 ng/L～1000 ng/Lが109地点，1000 ng/L～10400 ng/Lが28地点となり，1000 ng/Lを超えた地点はテキサス州の特異的な地域であったと報告している。過塩素酸塩そのものは蒸気圧が低く，揮発することはない。しかしClO_4^-は雨水にも入っている。Rajagopalanらは米国本土，アラスカおよびプエルトリコの26地点で1～3年間かけて採取した1578試料を分析した。その結果，範囲は<5 ng/L（検出限界以下）～102 ng/L，平均値は14.1±13.5 ng/Lであったと報告している[2]。

Kannanらはインドの13地点で採取した環境水について調査した。その結果，範囲は0.02 μg/L以下～6.9 μg/Lとなり，米国での報告値よりも1～2桁低かったと述べている（上述の人為的発生源がない場合と比較したわけではない）[3]。花火大会の影響を調べた例もある。Wuらは米国ニューヨーク州立大学のキャンパス内で行われた独立記念日の花火大会に際し，打ち上げ場所のすぐ近くにある人工池の水中濃度を測定している[4]。大会2日後の濃度は0.11 μg/L～519 μg/Lとなり（採取場所で異なる），大会前より30倍～1480倍高くなっていた。大会後2日～10日で最大値となり，以後擬一次反応速度式に従って（速度定数$k=0.016\ day^{-1}$～$0.039\ day^{-1}$）徐々に減少した。減少の理由については微生物の作用，池にある噴水による飛散，蒸発等を指摘している。また，噴水の飛沫から見物人への暴露量はEPAのRfD値の6％（大人）～32％（乳児）と見積もっている。

産業排水が原因で環境水中の濃度が高くなる場合もある。Kosakaらは利根川流域の河川水や水道水を調べている[5]。調査が行われた2006年当時，利根川にはClO_4^-を含む産業排水が相当量流入していたため利根川上流および支流の碓氷川ではそれぞれ最高で340 μg/Lおよび2300 μg/LのClO_4^-が検出されていた。利根川上流で，排水が直接流入している支流中の濃度は44 μg/L～1500 μg/L，碓氷川の場合，排水中の濃度は15000 μg/L，その排水が流入している支流中の濃度は1100 μg/L～3900 μg/Lであった。また利根川中流～下流域での濃度は10 μg/L～20 μg/L，中流～下流域の水から製造された水道水中の濃度は0.19 μg/L～37 μg/Lであった。最近，大阪府立公衆衛生研究所は水道水源である淀川，猪名川および石川における濃度を測定している[20]。範囲は0.03 μg/L～0.70 μg/Lとなり，これらの流域では特定の発生源が存在しないためか上述の利根川の場合よりもかなり低い。この報告では水道原水と浄水において濃度がほぼ同じであったことも記述している。これはClO_4^-は通常の浄水処理プロセス（オゾン-活性炭処理，活性炭処理，急速・緩速沪過）では除去されないためである[21]。

食品中のClO_4^-についてはDykeらが米国と日本の牛乳中の濃度を比較している[7]。その結果，日本の牛乳54試料の平均値は9.4±2.7 μg/Lで米国食品医薬品局（FDA）が104試料について求めた平均値5.9±1.8 μg/Lより少し高かったと報告している。Gurugeらは日本とスリランカの場合を比較している[8]。日本の牛乳は1.03 μg/L～14.1 μg/Lの範囲であった一方，スリランカの牛乳および粉乳は1.14 μg/L～38.5 μg/Lの範囲であった。Wuらは中国15地点から集めた水道水，地下水，表流水，およびボトル詰め飲料水300試料を分析した[9]。全試料は0.02 μg/L以下～54.4 μg/Lの範囲で，水道水，地下水，表流水およびボトル詰め飲料水の平均値はそれぞれ2.46 μg/L，3.04 μg/L，2.82 μg/L，0.22 μg/Lであった。

人体中のClO_4^-濃度についても近年報告が増えている。Oldiらは米国人84名の血清および血漿（けっしょう）について調査した[10]。血清と血漿の間で有意な差はなく，範囲は0.05 μg/L以下～7.7 μg/L，平均値は0.32 μg/Lであった。発生源が近くにある場合の人体中の濃度がどうなるのか気になるところであるが，Zhangらは世界最大の花火生産国である中国において，主要な生産地である河西省南昌市（Nanchang）の0.4歳～90歳の131名の血液（全血）試料を分析している[11]。その結果，範囲は0.51 μg/L～10.5 μg/L，平均値2.68 μg/Lとなり，濃度は年齢とともに減少すること，大人の場合，米国人より10倍高いレベルであること等を明らかにしている。ここでは血中濃度から暴露量も見積もっているが，平均暴露量は1.12 μg/kg/day（大人）～2.22 μg/kg/day（乳児）の範囲となり，EPAが採用した前述のRfD値0.7 μg/kg/dayを超えている。

4　対策技術の開発状況

4·1　分離技術

以上のような背景により水中のClO_4^-濃度を低減するための技術開発が急がれている。図1に米国におけるClO_4^-の最高濃度の分布を[22]，図2に過塩素酸塩の製造あるいは使用施設の分布を示す[23]。米国では自然発生源はあるものの，高濃度（mg/Lレベル以上）の地域の大半に製造あるいは使用施設が主要な河川の近くに存在していることが分かる。そのような施設からの排水は，1997年以前はなんら処理されることなく下水あるいは河川等の自然水域に放出されていたという[24]。また，我が国では前述の利根川の場合[5]，発生源は過塩素酸塩の製造工場だけでなく，電気分解を行っている工場からの非意図的な排出もあったので，対策はまだ始まったばかりと言えよう。

ClO_4^-の水処理技術には「分離」と「分解」に大別され，「分解」には生物処理と化学処理がある。一般に分離技術としてはイオン交換，膜（逆浸透膜等），沪過，活性炭吸着等の方法があるが，現状ではClO_4^-につい

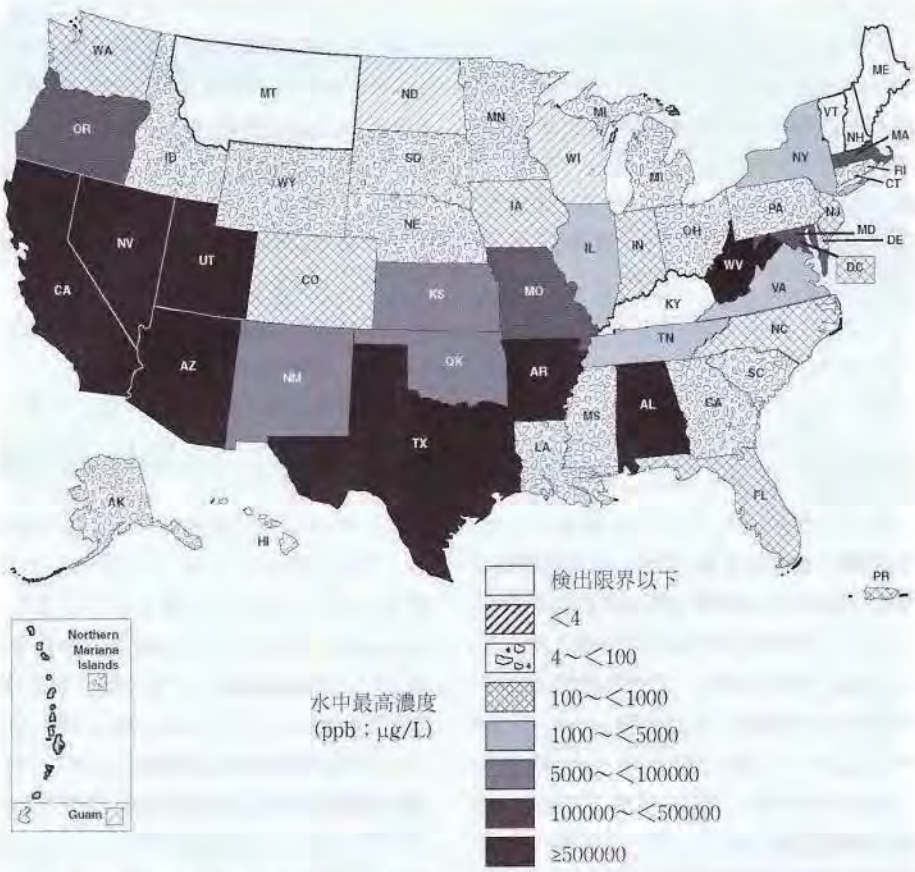

米国会計検査院（GAO）がEPAと国防省（DOD）のデータを基に作成[22]

図1　米国での水（飲料水，表流水，あるいは地下水）中における ClO_4^- 最高濃度の分布（2009年10月時点）

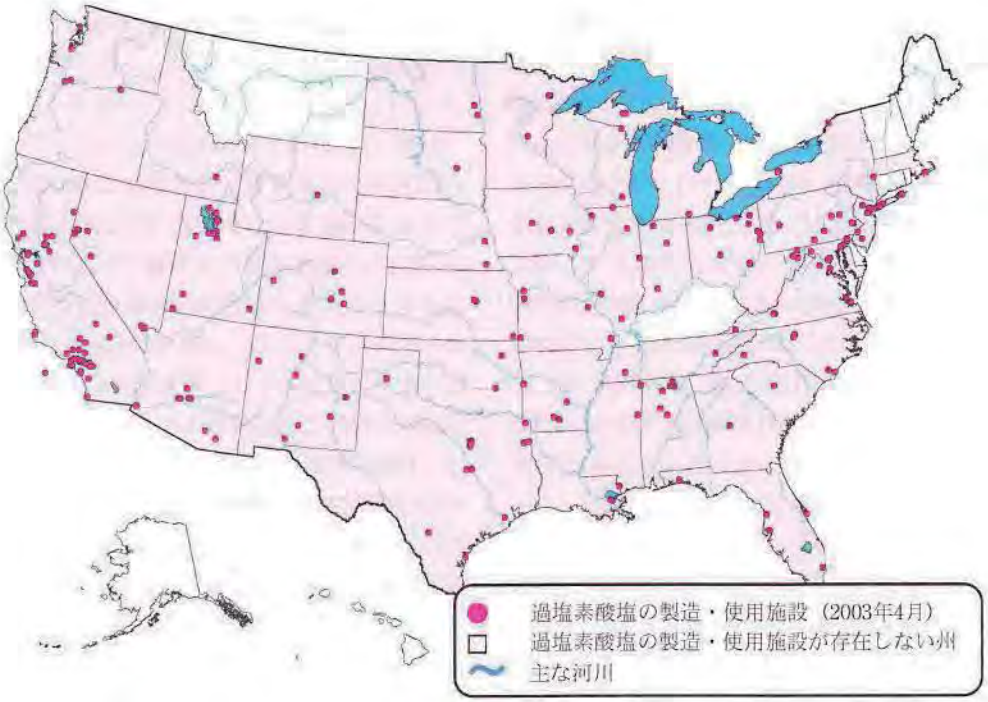

図2　米国における過塩素酸塩の製造・使用施設の分布図（2003年4月時点，EPAによる）[23]

てはイオン交換が最も有効な方法とされている[17]。これは，第四級アンモニウム陽イオンを有する強塩基性の陰イオン交換樹脂において，元々結合している Cl^- が水中の ClO_4^- と置換するという原理に基づいている［式（1）］[25]。

$$R_4N^+Cl^- + ClO_4^- \longrightarrow R_4N^+ClO_4^- + Cl^- \quad \cdots\cdots (1)$$

Gu らはロケットやミサイルの製造企業である Aerojet 社のカリフォルニア州にある工場から発生した汚染水（ClO_4^- を 830 μg/L～890 μg/L 含む）を Purolite 社製 530E で処理している[26]。一般にイオン交換樹脂では特定のイオンに対する選択性が低いことが多いが，この樹脂は ClO_4^- と過テクネチウム酸イオン（TcO_4^-）に対する選択性が優れており，汚染水は ClO_4^- よりはるかに高濃度の硝酸イオンと Cl^-（それぞれ 10 mg/L および 15 mg/L）を含んでいたにもかかわらず，ClO_4^- を問題なく回収できたと述べている。また，使用しているうちに ClO_4^- の吸着量が飽和して破過が起こるが，破過した樹脂を塩化鉄(III)－塩酸溶液（4 M HCl－1 M $FeCl_3$）で再生させている。ただし，イオン交換では水中の ClO_4^- を回収できたとしても，使用済みの樹脂をどう処理するかという問題が出てくる。この報告のように再生が可能でも，再生作業では高濃度の ClO_4^- 溶液が発生する。また，再生させずに廃棄する場合も産廃となってしまい，そのままでは発生源が製造・使用施設から産廃処分場に移るだけになりかねない。ClO_4^- の抜本的な処理のためには無害な化学種，すなわち Cl^- まで分解する必要がある。

4・2　分解技術

水中の ClO_4^- の分解技術で最も多く研究されている方法は生物処理である。これは ClO_4^- を還元する微生物を利用するもので，米国陸空軍はこの方法による処理設備を導入している[24]。この機構は図 3 のように考えられている。ClO_4^- は ClO_4^- 還元酵素により ClO_3^- さらには ClO_2^- へ逐次的に還元され，ClO_2^- は不均化酵素により O_2 と Cl^- へ分解する（ただし，生物処理の文献は単に ClO_4^- の減少のみモニターしている例がほとんどである）。この場合，電子源は主に酢酸塩で，微生物によっては乳酸塩，水素分子，硫化水素等が利用できる場合もある。pH は中性付近が良い。このような微生物は硝酸塩や酸素分子も還元できる。従って ClO_4^- の還元を十分に起こすためには反応場からこのような競合物質をあらかじめ除去する必要がある。微生物には栄養分も与えなくてはならない。数種のビタミンを含むリン酸塩あるいは炭酸水素塩の緩衝液が普通であるが，種類によってはモリブデン，鉄，セレンのような微量の金属が必要な場合もある。酵母抽出物の添加もこれら微生物の繁殖に有効とされている[17]。生物処理はスケールアップも容易であり，上述のとおり，米国では実際に軍事施設から発生した汚染水の処理に使われている。しかし使用する微生物，あるいはそれに関連する微生物の人体に対する影響はほとんど分かっていない。このため飲料水への適用は社会の理解を得ることが大変難しいという指摘もされている[25]。

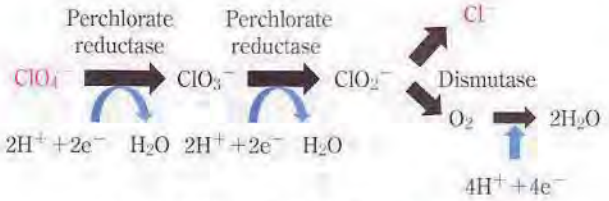

図 3　生物処理による ClO_4^- の分解機構[17]

化学処理で ClO_4^- を分解する報告も最近出始めた。例えばゼロ価の鉄を用いて還元分解を試みた例がある。しかし，この方法では分解速度は非常に遅い。例えば Moore らは初期濃度 0.1 mM の ClO_4^- は 336 時間後も 66 % が残存したと報告している[27]。また Huang らも初期濃度 10.1 μM の ClO_4^- の場合，減少の擬一次反応速度定数（k）は 0.001 h^{-1}～0.004 h^{-1} であったことを報告している[24]。分解速度を高めるために鉄粉にエネルギー源を組み合わせる方法もある。例えば Im らは 254 nm の紫外線照射を併用し，初期濃度 16 μM の ClO_4^- の分解を試みている[28]。しかし，12 時間後にはその 5.6 % が除去されたに過ぎなかった。マイクロ波を照射した例もある。Oh らは 0.5 mM の ClO_4^- に鉄粉を加えてマイクロ波を照射したところ，1 時間で 98 % が除去できたと報告している[29]。しかし，この例では Cl^- の生成についてはなんら触れられていない。この文献に限らず，多くの報告は ClO_4^- の消失のみをモニターしており，Cl^- まで本当に分解しているのか不明であることは大きな問題である。また，鉄以外の金属の検討例もほとんどない。

筆者らは高温高圧水に金属粉を組み合わせて ClO_4^- を Cl^- まで還元分解することを検討した[30]。図 4 に水の状態図を示す。臨界点（374 ℃, 22.1 MPa）を超える温度・圧力の状態は超臨界水と呼ばれるが，臨界点よりも低い領域にある高温，高圧の水（液体）が高温高圧水である。これは pressurized hot water の訳で，余りいい訳とは思えないが勘弁していただきたい。類似した用語に亜臨界水があるが，亜臨界水とは高温高圧水の中でも温度が高い領域（～250 ℃ 以上）を意味する場合が多い。このような水は高拡散性，低粘性，有機物を加水分解する等，普通の水にはない性質を持っている。

反応は以下のようにして行った。まず，耐圧容器に不活性ガス雰囲気中で ClO_4^- の水溶液（101 μM～204 μM）と金属粉を入れ，80 ℃～300 ℃ の高温高圧水の状態に

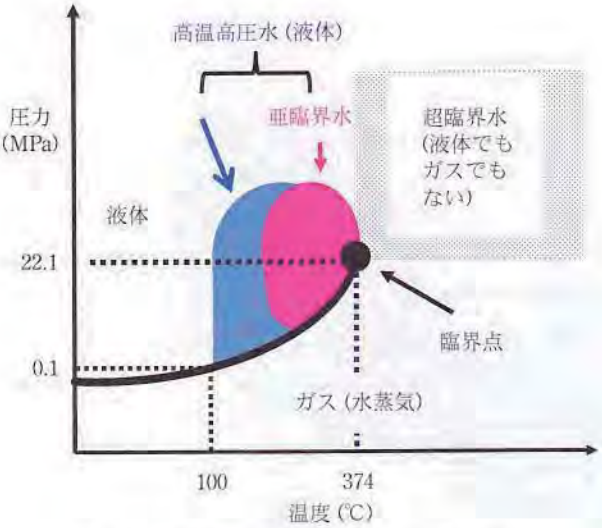

図 4　水の状態図（正しいスケールではない）

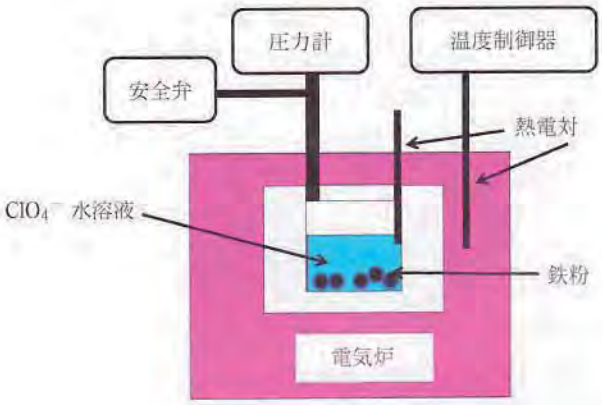

図 5　装置の概略図

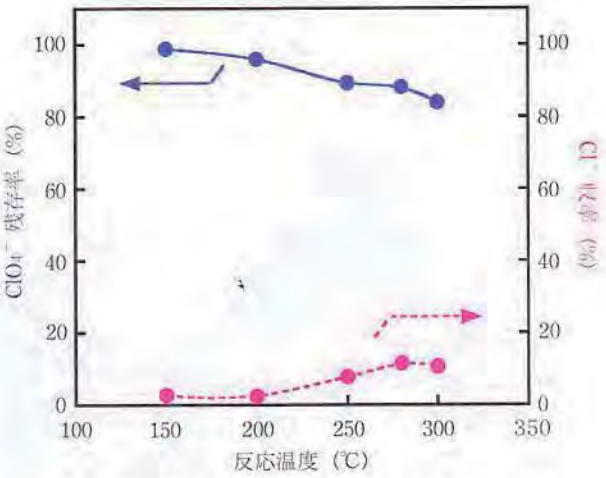

図 6　高温高圧水による ClO_4^- 分解反応の温度依存性（金属無添加）[30]

表 1　高温高圧水を用いた ClO_4^- 分解反応における金属粉の添加効果[30]

No.*1)	金属	ClO_4^- 初期濃度 (μM)	ClO_4^- 残存率 (%)	Cl^- 収率 (%)
1	なし	103	99	3
2	Al	103	93	1
3	Cu	101	86	13
4	Zn	102	51	22
5	Ni	100	46	43
6	Fe	104	<1*2)	85±1

*1) ClO_4^- 水溶液（3.5 mL）と金属粉（0.91 mM）をアルゴン雰囲気中 150 ℃で 6 時間加熱した。
*2) 検出限界以下

した（図 5）。一定時間経過後，室温に戻して成分分析を行った。比較のため金属粉を入れない場合についても実験を行った。金属粉を入れずに ClO_4^- 初期濃度 103 μM で 6 時間反応させた場合の実験結果を図 6 に示す。温度の上昇と共に ClO_4^- の残存率は減少し，Cl^- 収率（ClO_4^- の初期モル数を基にした値）は増加している。しかし，300 ℃においても ClO_4^- の残存率は 84 %，Cl^- 収率は 10 % にとどまっていた。この場合，塩素原子の回収率は 94 % であり，塩素原子を含む化学種は反応溶液中には事実上この 2 種しか存在しないことが分かった。実際，ClO_3^- および ClO_2^- は検出されなかった。反応性を高めるため金属粉を添加して実験を行った。表 1 に 150 ℃で 6 時間反応させた場合の結果を示す。金属粉を添加しない場合，残存率は 99 % でほとんど反応していない（No. 1）。アルミニウムの添加も全く効果がなかった（No. 2）。一方，銅，亜鉛，ニッケル，鉄を添加した場合には明らかに反応促進効果が見られた。特に鉄の場合が優れており，ClO_4^- は検出限界以下（残存率では 1 % 未満），Cl^- 収率は 85 % に達した。図 7 に鉄粉を添加して 150 ℃で処理した場合の反応の時間依存性を示す。ClO_4^- の減少は擬一次反応速度式に従い（k=4.3 h^{-1}），1 時間で検出限界以下になった。一方 Cl^- 収率は 2 時間でほぼ飽和し，最終的に 6 時間で 85 % に達した。また，反応に伴い，鉄は Fe_3O_4 に酸化す

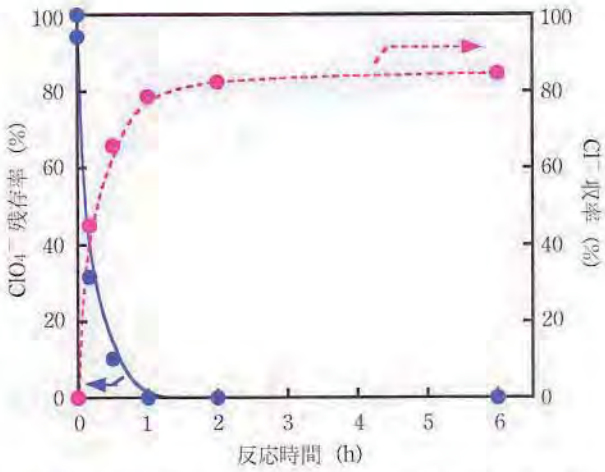

図 7　鉄粉を添加した高温高圧水による ClO_4^- 分解反応の時間依存性[30]

ることがX線回折測定から分かった。この方法を花火大会後の環境水の分解に適用してみた。試料は前述の米国ニューヨーク州立大学のものである。この試料は5.22 μM の ClO_4^- を含んでいたが，それよりはるかに高濃度の Cl^-（472 μM）および SO_4^{2-}（130 μM）を含んでいた。そのような共存物質の存在にかかわらず，反応後の ClO_4^- 濃度は 0.03±0.01 μM まで減少し，99 % 以上の ClO_4^- の除去に成功した。

5 おわりに

以上，ClO_4^- の環境残留性と対策技術の研究動向について概説した。ClO_4^- が環境水はもとより，食品や人体等に地球規模でどこにでも存在することが明らかとなったのはここ10年ほどの間であるが，環境動態については自然発生源もあるため謎が多い。例えば大気中や土壌中の挙動についてはほとんど分かっていない。また，対策技術のうち，分解方法に関する研究例は生物処理に偏っている。化学処理の報告は少なく，中でも Cl^- への迅速かつ高効率な無機化を達成した例は筆者らの方法を除いてほとんどない。ClO_4^- の環境リスクの低減のために，これらの課題に多くの研究者が取り組むことが望まれる。

文　献

1) D. R. Parker, A. L. Seyfferth, B. K. Reese : *Environ. Sci. Technol.*, **42**, 1465 (2008).
2) S. Rajagopalan, T. Anderson, S. Cox, G. Harvey, Q. Cheng, W. A. Jackson : *Environ. Sci. Technol.*, **43**, 616 (2009).
3) K. Kannan, M. L. Praamsma, J. F. Oldi, T. Kunisue, R. K. Sinha : *Chemosphere*, **76**, 22 (2009).
4) Q. Wu, J. F. Oldi, K. Kannan : *Environ. Toxicol. Chem.*, **30**, 2449 (2011).
5) K. Kosaka, M. Asami, Y. Matsuoka, M. Kamoshita, S. Kunikane : *Water Res.*, **41** 3474 (2007).
6) S. Rajagopalan, T. A. Anderson, L. Fahlquist, K. A. Rainwater, M. Ridley, W. A. Jackson : *Environ. Sci. Technol.*, **40**, 3156 (2006).
7) J. V. Dyke, K. Ito, T. Obitsu, Y. Hisamatsu, P. K. Dasgupta, B. C. Blount : *Environ. Sci. Technol.*, **41**, 88 (2007).
8) K. S. Guruge, Q. Wu, K. Kannan : *J. Environ. Monit.*, **13**, 2312 (2011).
9) Q. Wu, T. Zhang, H. W. Sun, K. Kannan : *Arch. Environ. Contam. Toxicol.*, **58**, 543 (2010).
10) J. F. Oldi, K. Kannan : *Chemosphere*, **77**, 43 (2009).
11) T. Zhang, Q. Wu, H. W. Sun, J. Rao, K. Kannan : *Environ. Sci. Technol.*, **44**, 6947 (2010).
12) US EPA, Drinking water : regulatory determination on perchlorate. Federal Register, **76** (29), 7762 (2011).
13) 厚生労働省，水質基準に関する省令等の一部改正等について，平成23年1月28日，http://wwwhourei.mhlw.go.jp/hourei/doc/tsuchi/T110131H0010.pdf（2013年4月2日最終確認）.
14) 環境省，化学物質の環境リスク評価第9巻第1編，平成23年3月，http://www.env.go.jp/chemi/report/h23-01/pdf/chpt1/1-2-2-04.pdf（2013年4月2日最終確認）.
15) P. K. Dasgupta, J. V. Dyke, A. B. Kirk, W. A. Jackson : *Environ. Sci. Technol.*, **40**, 6608 (2006).
16) 経済産業省，化学物質の製造・輸入量に関する実態調査，平成19年度結果，http://www.meti.go.jp/statistics/sei/kagaku/result-2.html（2013年4月2日最終確認）.
17) N. Bardiya, J. H. Bae : *Microbiol. Res.*, **166**, 237 (2011).
18) E. T. Urbansky, S. K. Brown, M. L. Magnuson, C. A. Kalty : *Environ. Pollut.*, **112**, 299 (2001).
19) P. K. Dasgupta, P. K. Martinelango, W. A. Jackson, T. A. Anderson, K. Tian, R. W. Tock, S. Rajagopalan : *Environ. Sci. Technol.*, **39**, 1569 (2005).
20) 大阪府立公衆衛生研究所メールマガジン第108号，2012年8月31日，http://www.iph.pref.osaka.jp/merumaga/back/108-2.html（2013年4月2日最終確認）.
21) 高木総吉，安達史恵，宮野啓一，吉田直志，小川有理，Hui Li，北川幹也，関口陽子，足立伸一，田辺信介：環境化学，**21**，251 (2011).
22) US GAO, PERCHLORATE. Occurrence Is Widespread but at Varying Levels; Federal Agencies Have Taken Some Actions to Respond to and Lessen Releases. GAO-10-769, October 2010. http://www.gao.gov/assets/310/308652.pdf（2013年4月2日最終確認）.
23) US EPA, Transmittal of Perchlorate Maps and Table, April, 2003. http://www.epa.gov/ncea/perchlorate/references/documents/ref008.pdf（2013年4月2日最終確認）.
24) H. Huang, G. A. Sorial : *Environ. Eng. Sci.*, **24**, 917 (2007).
25) R. Srinivasan, G. A. Sorial : *Sep. Purif. Technol.*, **69**, 7 (2009).
26) B. Gu, G. M. Brown, C. C. Chiang : *Environ. Sci. Technol.*, **41**, 6277 (2007).
27) A. M. Moore, C. H. de Leon, T. M. Young : *Environ. Sci. Technol.*, **37**, 3189 (2003).
28) J. K. Im, H. S. Son, K. D. Zoh : *J. Hazard. Mater.*, **192**, 457 (2011).
29) S. Y. Oh, P. C. Chiu, B. J. Kin, D. K. Cha : *J. Hazard. Mater.*, **B129**, 304 (2006).
30) H. Hori, T. Sakamoto, T. Tanabe, M. Kasuya, A. Chino, Q. Wu, K. Kannan : *Chemosphere*, **89**, 737 (2012).

堀　久男（Hisao Hori）
神奈川大学理学部化学科（〒259-1293 平塚市土屋2946）。慶應義塾大学大学院理工学研究科応用化学専攻後期博士課程修了。工学博士。≪現在の研究テーマ≫環境負荷物質の分解・無害化，再資源化反応システムの開発。≪主な著書≫"国内外におけるPFOS/PFOAの最新規制動向と対応策"（技術情報協会）。≪趣味≫小動物の飼育，寺巡り，茶道。
E-mail : h-hori@kanagawa-u.ac.jp

有機フッ化化合物をはじめとする
環境負荷物質の分解・無害化反応の開発

堀　　久　男

水環境学会誌　第36巻 第9号（2013）
pp. 331～334　別刷
公益社団法人　日本水環境学会

有機フッ化化合物をはじめとする環境負荷物質の分解・無害化反応の開発*

堀　　久男

1．はじめに

炭素・フッ素結合から形成される有機フッ素化合物は耐熱性，耐薬品性，界面活性等の優れた性質を持ち，多く産業で使われている。中でもペルフルオロアルキルスルホン酸類（PFAS 類，$C_nF_{2n+1}SO_3H$）やペルフルオロカルボン酸類（PFCA 類，$C_nF_{2n+1}COOH$），およびそれらの誘導体は表面処理剤や乳化剤の原料や構成成分として用いられてきた[1)]。ところが 2000 年頃からペルフルオロオクタンスルホン酸（$C_8F_{17}SO_3H$，PFOS）やペルフルオロオクタン酸（$C_7F_{15}COOH$，PFOA）といった一部の化合物が環境水中や野生生物中に存在していることが明らかとなった。PFOS/PFOA については規制の進行にともない代替物質への転換が進み，リスク評価の対象も現在では代替物質が中心になっているが，代替物質も有機フッ素化合物であり環境残留性は変わらない。このような有機フッ素化合物の環境リスクの低減のためには有害性に応じて産業排水・廃棄物の分解・無害化を行う必要があるが，これらはオゾン，過酸化水素＋紫外線照射等の促進酸化法ではほとんど分解できない。焼却は可能であるが，高温が必要であるだけでなく，生成するフッ化水素ガスによる炉材の劣化が著しい。これらの物質をフッ化物イオン（F^-）まで分解できれば，既存の処理技術により環境無害なフッ化カルシウムに変換できる。フッ化カルシウムは硫酸処理によりフッ素ポリマーを含むすべての有機フッ素化合物の原料であるフッ化水素酸になるため，産出が特定国に偏在し，入手難の状況が続いているフッ素資源の循環利用にも寄与できる（図１）。この場合，穏和な条件で F^- まで分解することが重要である。これまでにも電子線照射やプラズマ等の高エネルギー的な手法を使えばフッ素ポリマーさえも分解することは知られていた。しかしその場合，ペルフルオロイソブチレン（PFIB）やテトラフルオロメタン（CF_4）等の有害ガスが発生する懸念がある[2)]。

以上の背景から我々は PFAS/PFCA 類やそれらの代替物質，さらには二次生成物について，ヘテロポリ酸光触媒[3~7)]，ペルオキソ二硫酸イオン（$S_2O_8^{2-}$）＋光照射[8~10)]，金属粉＋亜臨界水[11~13)]，鉄イオン光触媒[14)]，$S_2O_8^{2-}$ ＋温水[15, 16)]，酸素ガス＋亜臨界水[17)]，$S_2O_8^{2-}$ ＋超音波照射[18)]等の手法により F^- までの分解，すなわち無機化を達成してきた。近年はこれらの知見を基にイオン交換膜[19)]や表面処理用のフッ素ポリマー[20)]，さらには過塩素酸イオン[21)]等の新規環境リスク懸念物質の分解方法の開発にも取り組んでいる。本稿ではそれらの代表的な例について報告したい。

2．PFAS 類および関連物質の分解

2.1　鉄粉＋亜臨界水

水中の PFAS 類について熱水（亜臨界水，超臨界水）分解を検討した[11~13)]。図２に水の状態図を示す。臨界点（374℃，22.1 MPa）を超える温度・圧力の状態は超臨界水と呼ばれるが，臨界点よりもやや低い領域にある

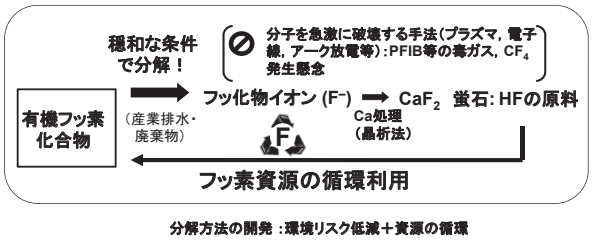

図１　フッ素資源の循環利用スキーム

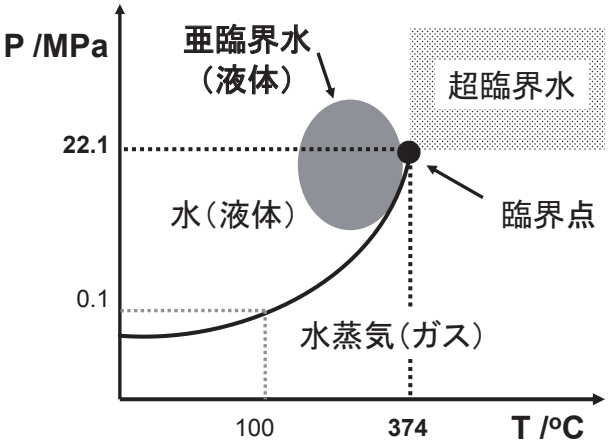

図２　水の状態図（正しいスケールではない）

Hisao Hori
平成２年　慶應義塾大学大学院理工学研究科応用科学専攻後期博士課程修了
同年　㈱東芝研究開発センター研究員
５年　通商産業省工業技術院資源環境技術総合研究所研究員
６年　同主任研究官
９年　マックス・プランク研究所客員研究員（科学技術庁長期在外研究員併任）
16年　㈱産業技術総合研究所環境管理技術研究部門研究グループ長
22年　神奈川大学理学部教授・産業技術総合研究所招聘型客員研究員(兼務)
工学博士
化学・バイオつくば賞

＊ Development of Decomposition Techniques for Environmentally Persistent Chemicals

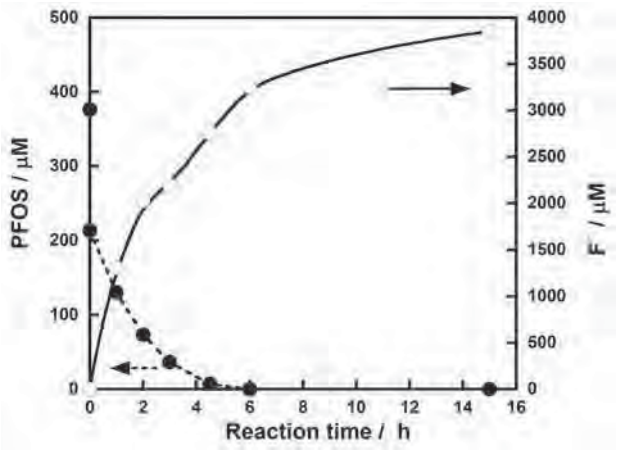

図３　鉄粉を還元剤として用いた亜臨界水反応によるPFOS分解の反応時間依存性[11]

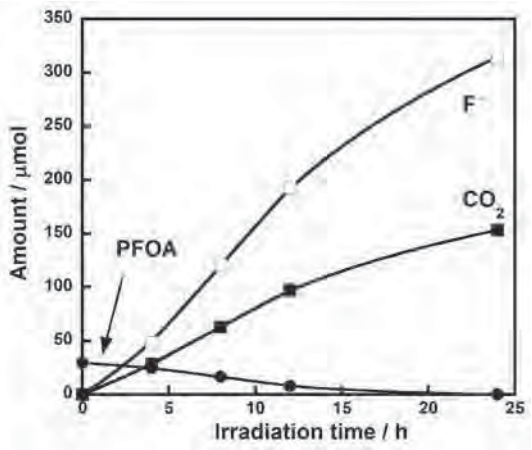

図４　ヘテロポリ酸光触媒によるPFOA分解反応の照射時間依存性（PFOA初期濃度1.35 mM）[5]

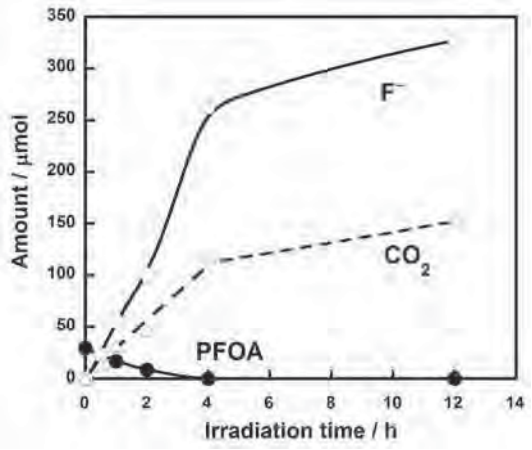

図５　$S_2O_8^{2-}$を光酸化剤としたPFOA分解反応の照射時間依存性[8]

高温，高圧の水（液体）が亜臨界水である。亜臨界水や超臨界水は無極性の有機化合物を溶解し，有機化合物を加水分解する等，普通の水にはない性質を持っている。

反応は耐圧容器に不活性ガス雰囲気中でPFOS水溶液（93～372 μM）と鉄粉もしくは他の金属粉を入れ，加熱することで行った。金属粉がない場合，水中のPFOS濃度はほとんど減少しなかった。鉄粉を入れた場合にPFOSは最も迅速に分解した。例えばPFOS初期濃度が372 μM，反応温度350 ℃の場合，PFOSは６時間で水中から消失し，同時にF^-が高収率で生成した（図３）。この方法により反射防止剤中のPFOSや，炭素数２～６の短鎖PFAS類（PFOS代替品）も分解できた。

２.２　酸素ガス＋亜臨界水

PFOS代替物質としてペルフルオロアルキル基の中にエーテル結合を導入したペルフルオロアルキルエーテルスルホン酸類（PFAES類）がある。PFAES類については酸素ガスを共存させた亜臨界水反応でF^-，CO_2およびSO_4^{2-}まで効果的に分解することができた[17]。反応を無酸素条件で行った場合，PFAES類の減少の時間依存性は酸素雰囲気の場合とほぼ同じであったが，F^-，CO_2およびSO_4^{2-}の生成量が大幅に減少した。このことは酸素ガスが反応中間体の無機化に重要な役割を果たしていることを意味する。

３．PFCA類および関連物質の分解

３.１　ヘテロポリ酸光触媒

水中のPFCA類は通常の促進酸化法ではほとんど分解できないが，我々はヘテロポリ酸$[PW_{12}O_{40}]^{3-}$を用いることでF^-とCO_2まで分解させることに成功した[3~7]。これはPFCA類を光触媒分解させた世界初の例である。光反応はPFCA類と$[PW_{12}O_{40}]^{3-}$を含む水溶液を耐フッ素性の反応装置に入れ，酸素雰囲気下で紫外・可視光を照射することで行った。この方法により，例えばトリフルオロ酢酸の場合，１モルの消失に対して２モルのCO_2と３モルのF^-が生成したので物質収支も合っていた[3]。また，CF_4等の有害ガスも発生しなかった。PFOAの場合，反応初期には水中に短鎖PFCA類も検出されたが，長時間照射により消失してF^-とCO_2まで分解した（図４）[5]。この反応は光励起した$[PW_{12}O_{40}]^{3-}$がPFCA類から電子を奪うことで開始されるが，それにともない$[PW_{12}O_{40}]^{3-}$は還元種$[PW_{12}O_{40}]^{4-}$となる。この還元種が酸素と反応して$[PW_{12}O_{40}]^{3-}$に戻ることで触媒サイクルが形成されている。

３.２　$S_2O_8^{2-}$＋光照射

上述の方法では200 Wの水銀・キセノン灯を使用した場合，1.35 mMのPFOAを完全に消失させるのに24時間を要した。より短時間でPFCA類を分解するために$S_2O_8^{2-}$を用いる方法を開発した[8]。

水中の$S_2O_8^{2-}$に紫外光を照射すると硫酸イオンラジカル（$SO_4^{\bullet-}$）が生成する（１式）。$SO_4^{\bullet-}$の酸化還元電位（２式の反応に相当）は水中で2.5～3.1 Vであり[22]，OHラジカル（３式の場合は1.8 V，４式では2.7 V）と同程度か，それ以上である。

$$S_2O_8^{2-} + h\nu \rightarrow 2SO_4^{\bullet-} \quad (1)$$
$$SO_4^{\bullet-} + e^- \leftrightarrow SO_4^{2-} \quad (2)$$
$$^{\bullet}OH + e^- \leftrightarrow OH^- \quad (3)$$
$$^{\bullet}OH + e^- + H^+ \leftrightarrow H_2O \quad (4)$$

そこでPFOA水溶液に$S_2O_8^{2-}$を添加し，光照射してPFOAの分解を試みたところ$[PW_{12}O_{40}]^{3-}$を使用した場合と同じ条件において４時間で消失させることができた（図５，PFOAの消失後も中間体である短鎖PFCA類の分解が続くためF^-とCO_2の生成は続いている）。また

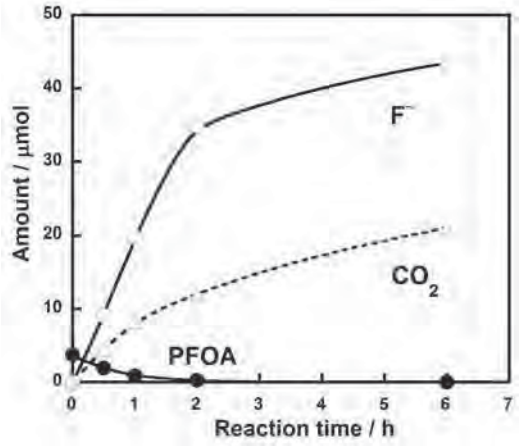

図6　$S_2O_8^{2-}$を用いたPFOAの温水分解（PFOA初期濃度374 μM）[15]

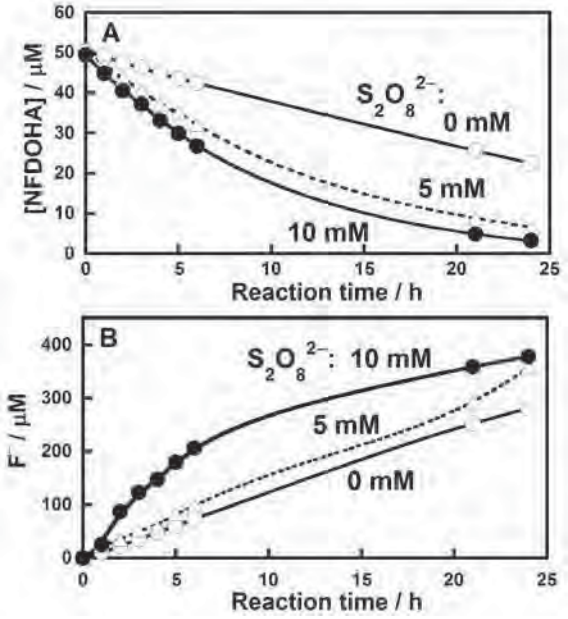

図7　$S_2O_8^{2-}$＋超音波照射によるNFDOHAの分解[18]

$SO_4^{\bullet-}$は反応後にはSO_4^{2-}になるが，その生成量は使用した$S_2O_8^{2-}$の２倍モルとなった。つまり硫黄分はすべてSO_4^{2-}として回収可能である。この方法でワックス廃液中のPFCA類や[8]，PFCA類よりも有害性が高いフルオロテロマー不飽和カルボン酸類[9]も分解できた。PFOAよりも炭素数が２つ以上多く，難溶性の長鎖PFCA類については液体二酸化炭素・水の二相混合系で$S_2O_8^{2-}$を使用することで効果的に分解させることができた[10]。

3.3　$S_2O_8^{2-}$＋温水

PFCA類については$S_2O_8^{2-}$を添加した熱水反応も検討した。その結果，意外にも80 ℃程度の低温の熱水，すなわち温水中で最も迅速にF^-まで分解できた[15]。図6にPFOAと134倍モル過剰の$S_2O_8^{2-}$を入れた温水（80 ℃）中におけるPFOA分解の時間依存性を示す。$S_2O_8^{2-}$を入れない場合にはPFOA濃度は全く減少しなかったが，$S_2O_8^{2-}$を入れた場合には迅速に減少し，CO_2とF^-が生成した。この方法で他のPFCA類さらにはPFCA類の代替物質であるペルフルオロエーテルカルボン酸類（ペルフルオロアルキル基の中にエーテル結合を導入した化合物，PFECA類）やヒドロペルフルオロカルボン酸類[16]

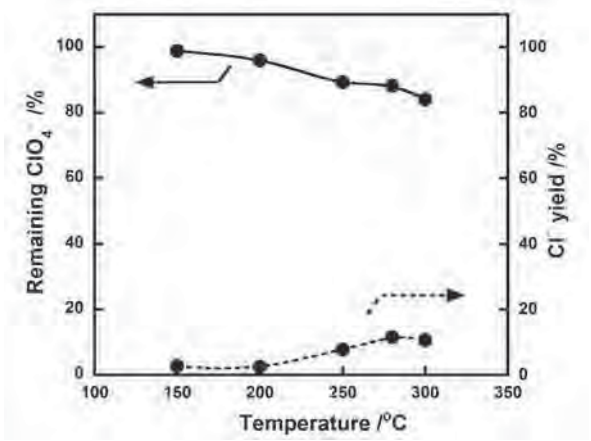

図8　熱水によるClO_4^-分解反応の温度依存性（金属無添加）[21]

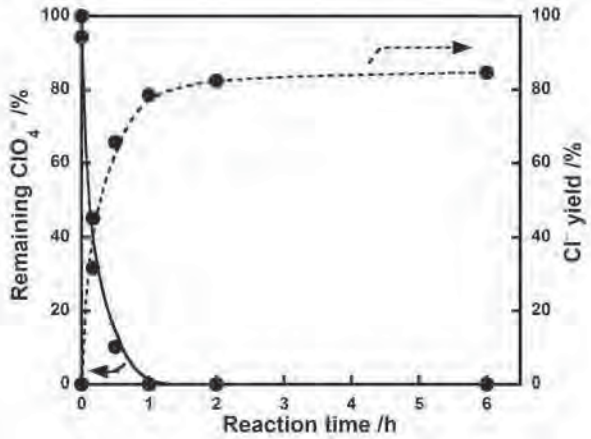

図9　鉄粉を添加した熱水によるClO_4^-分解反応の時間依存性[21]

もCO_2とF^-まで効果的に分解・無機化できた。

3.4　$S_2O_8^{2-}$＋超音波照射

ここでは$S_2O_8^{2-}$と超音波照射を組み合わせてPFECA類を迅速に分解させることを試みた[18]。例として$CF_3OC_2F_4OCF_2COOH$（NFDOHA）50 μMに0～10 mMの$S_2O_8^{2-}$を添加して超音波照射した場合の水中のNFDOHA濃度の時間依存性を示す（図７A）。$S_2O_8^{2-}$の添加によりNFDOHAの分解が促進され，F^-の生成も増加している（図７B）。10 mM添加した場合，F^-収率は24時間で84.8%となった。$S_2O_8^{2-}$による分解反応の促進は他の炭素数５～10のPFECA類においても見られ，$S_2O_8^{2-}$の初期濃度が10 mMの場合，減少の速度定数は$S_2O_8^{2-}$がない場合の2.5～3.9倍となった。これは超音波照射で生成するミクロな高温高圧場において$S_2O_8^{2-}$が$SO_4^{\bullet-}$に熱分解し，これがPFECA類の脱炭酸を誘起するためと考えられる。

４．過塩素酸イオンの分解

過塩素酸イオン（ClO_4^-）はエンジンの推進剤やエネルギーデバイスの電解質等の様々な用途に使われているが，近年環境影響が懸念されつつある。ClO_4^-は凝集沈殿等の既存の水処理技術の適用が極めて難しい。イオン交換樹脂での回収は可能であるが，回収物は廃棄物となってしまう。そこでClO_4^-を熱水中で金属を還元剤としてCl^-まで分解することを検討した[21]。金属粉を入れずにClO_4^-

初期濃度 103 μM で６時間反応させた場合の実験結果を図８に示す。温度の上昇と共に ClO_4^- の残存率は減少し，Cl^- 収率は増加したが 300℃においても ClO_4^- の残存率は 84%，Cl^- 収率は 10%にとどまった。一方，金属粉を添加するととくに鉄粉の場合に ClO_4^- が顕著に分解することが分かった。図９に鉄粉を添加して 150 ℃に加熱した場合の反応の時間依存性を示す。ClO_4^- は擬一次反応速度式に従って減少し（速度定数：4.3 h^{-1}），１時間で検出限界以下になった。一方 Cl^- 収率は２時間でほぼ飽和し，最終的に６時間で 85%に達した。この方法を米国での花火大会後の環境水の分解に適用してみた。この試料は 5.22 μM の ClO_4^- を含んでいたが，それよりはるかに高濃度の Cl^-（472 μM）と SO_4^{2-}（130 μM）を含んでいた。そのような共存物質の存在にもかかわらず，反応後の ClO_4^- 濃度は 0.03 ± 0.01 μM まで減少し，99%以上の ClO_4^- を除去することができた。

５．おわりに

以上，我々が行ってきたこれまでの取り組みについて紹介した。フッ素ポリマーについてはさらに使用量が多いものについて，また低分子の化合物についても需要が拡大しているイオン液体等の反応性を調べており，結果については１年以内に公表したいと考えている。

謝　辞

本研究は環境省公害防止等試験研究費，日本学術振興会科学研究費補助金基盤研究Ｂ（５件），および旭硝子株式会社の支援を受けて行われた。関係各位に感謝する。

参　考　文　献

1）堀 久男ほか（2008）国内外におけるPFOS/PFOAの最新規制動向と対応策，第１～３章，技術情報協会，東京.

2）例えばPacansky, J. and Waltman, R. J. (1991) Electron beam irradiation of poly (perfluoro ethers) : Identification of gaseous products as a result of main chain scission, *J. Phys. Chem.*, **95**, 1512–1518.

3）Hori, H., Takano, Y., Koike, K., Takeuchi, K. and Einaga, H. (2003) Decomposition of environmentally persistent trifluoroacetic acid to fluoride ions by a homogeneous photocatalyst in water, *Environ. Sci. Technol.*, **37**, 418–422.

4）Hori, H., Takano, Y., Koike, K., Kutsuna, S., Einaga, H. and Ibusuki, T. (2003) Photochemical decomposition of pentafluoropropionic acid to fluoride ions with a water-soluble heteropolyacid photocatalyst, *Appl. Catal. B: Environ.*, **46**, 333–340.

5）Hori, H., Hayakawa, E., Einaga, H., Kutsuna, S., Koike, K., Ibusuki, T., Kitagawa, H. and Arakawa, R. (2004) Decomposition of environmentally persistent perfluorooctanoic acid in water by photochemical approaches, *Environ. Sci. Technol.*, **38**, 6118–6124.

6）Hori, H., Yamamoto, A., Koike, K., Kutsuna, S., Murayama, M., Yoshimoto, A. and Arakawa, R. (2008) Photocatalytic decomposition of a perfluoroether carboxylic acid by tungstic heteropolyacids in water, *Appl. Catal. B, Environ.*, **82**, 58–66.

7）Hori, H., Ishida, K., Inoue, N., Koike, K. and Kutsuna, S. (2011) Photocatalytic mineralization of hydroperfluorocarboxylic acids with heteropolyacid $H_4SiW_{12}O_{40}$ in water, *Chemosphere*, **82**, 1129–1134.

8）Hori, H., Yamamoto, A., Hayakawa, E., Taniyasu, S., Yamashita, N., Kutsuna, S., Kitagawa, H. and Arakawa, R. (2005) Efficient decomposition of environmentally persistent perfluorocarboxylic acids using persulfate as a photochemical oxidant, *Environ. Sci. Technol.*, **39**, 2383–2388.

9）Hori, H., Yamamoto, A., Koike, K., Kutsuna, S., Osaka, I. and Arakawa, R. (2007) Persulfate-induced photochemical decomposition of a fluorotelomer unsaturated carboxylic acid in water, *Water Res.*, **41**, 2962–2968.

10）Hori, H., Yamamoto, A. and Kutsuna, S. (2005) Efficient photochemical decomposition of long-chain perfluorocarboxylic acids by means of an aqueous/liquid CO_2 biphasic system, *Environ. Sci. Technol.*, **39**, 7692–7697.

11）Hori, H., Nagaoka, Y., Yamamoto, A., Sano, T., Yamashita, N., Taniyasu, S., Kutsuna, S., Osaka, I. and Arakawa, R. (2006) Efficient decomposition of environmentally persistent perfluorooctanesulfonate and related fluorochemicals using zerovalent iron in subcritical water, *Environ. Sci. Technol.*, **40**, 1049–1054.

12）Hori, H., Nagaoka, Y., Sano, T. and Kutsuna, S. (2008) Iron-induced decomposition of perfluorohexanesulfonate in sub- and supercritical water, *Chemosphere*, **70**, 800–806.

13）Hori, H., Sakamoto, T., Kimura, Y. and Takai, A. (2012) Iron-induced efficient mineralization of a cyclic perfluoroalkyl surfactant in subcritical and supercritical water, *Catal. Today*, **196**, 132–136.

14）Hori, H., Yamamoto, A., Koike, K., Kutsuna, S., Osaka, I. and Arakawa, R. (2007) Photochemical decomposition of environmentally persistent short-chain perfluorocarboxylic acids in water mediated by iron (II) / (III) redox reactions, *Chemosphere*, **68**, 572–578.

15）Hori, H., Nagaoka, Y., Murayama, M. and Kutsuna, S. (2008) . Efficient decomposition of perfluorocarboxylic acids and alternative fluorochemical surfactants in hot water, *Environ. Sci. Technol.*, **42**, 7438–7443.

16）Hori, H., Murayama, M., Inoue, N., Ishida, K. and Kutsuna, S. (2010) Efficient mineralization of hydroperfluorocarboxylic acids with persulfate in hot water, *Catal. Today*, **151**, 131–136.

17）Hori, H., Murayama, M. and Kutsuna, S. (2009) Oxygen-induced efficient mineralization of perfluoroalkylether sulfonates in subcritical water, *Chemosphere*, **77**, 1400–1405.

18）Hori, H., Nagano, Y., Murayama, M., Koike, K. and Kutsuna, S. (2012) Efficient decomposition of perfluoroether carboxylic acids in water with a combination of persulfate oxidant and ultrasonic irradiation, *J. Fluorine Chem.*, **141**, 5–10.

19）Hori, H., Murayama, M., Sano, T. and Kutsuna, S. (2010) Decomposition of perfluorinated ion-exchange membrane to fluoride ions using zerovalent metals in subcritical water, *Ind. Eng. Chem. Res.*, **49**, 464–471.

20）Patil, Y., Hori, H. Tanaka, H., Sakamoto, T. and Ameduri, B. (2013) First radical homopolymerisation of 2-trifluoromethacrylic acid in water and study of the degradation of the resulting homopolymers, *Chem.Commun.*, **49**, 6662–6664.

21）Hori, H., Sakamoto, T., Tanabe, T., Kasuya, M., Chino, A. Wu, Q. and Kannan, K. (2012) Metal-induced decomposition of perchlorate in pressurized hot water, *Chemosphere*, **89**, 737–742.

22）Neta, P. Huie, R. E. and Ross, A. B. (1988) Rate constants for reactions of inorganic radicals in aqueous solution, *J. Phys. Chem. Ref. Data*, **17**, 1027–1284.

ファルマシア

別刷

公益社団法人
日本薬学会
The Pharmaceutical Society of Japan

有機フッ素化合物の分解反応の開発

堀　久男 Hisao HORI　神奈川大学理学部教授

1 はじめに

有機フッ素化合物は耐熱性，耐薬品性，界面活性等の優れた性質を持つ.[1] このため様々なところで使われているが，近年になって環境残留性や生体蓄積性，さらには廃棄物の分解処理が困難といった負の側面が顕在化しつつある．環境中で検出されているのは主に界面活性剤として用いられてきたペルフルオロアルキルスルホン酸類(PFAS類，$C_nF_{2n+1}SO_3H$)やペルフルオロカルボン酸類(PFCA類，$C_nF_{2n+1}COOH$)，およびそれらの誘導体である．中でもペルフルオロオクタンスルホン酸($C_8F_{17}SO_3H$，PFOS)やペルフルオロオクタン酸($C_7F_{15}COOH$，PFOA)といった化合物は生体蓄積性が高いため，使用や排出に関する規制(自主規制も含む)が世界的に進行している．

このような有機フッ素化合物の環境リスクの低減のためには，有害性の度合いに応じて排水や廃棄物の無害化を行う必要があるが，炭素・フッ素結合は炭素が形成する共有結合では最強なため容易に分解しない．焼却は可能であるものの，高温が必要であるだけでなく，生成するフッ化水素ガスが焼却炉材を損傷する問題がある．

これらの物質をフッ化物イオン(F^-)まで分解できれば，既存の処理技術により環境無害なフッ化カルシウムに変換できる．フッ化カルシウムの鉱物は蛍石で，硫酸処理によりフッ素ポリマーを含むすべての有機フッ素化合物の原料であるフッ化水素酸になるため，フッ素資源の循環利用にも寄与できる(図1)．これまでにも電子線照射やプラズマ等の高エネルギー的な手法を使えば，フッ素ポリマーでさえ分解できることは知られていた．しかしその場合，毒性が非常に高いペルフルオロイソブチレン($CF_3C(CF_3)CF_2$，PFIB)や温暖化係数が二酸化炭素の数千倍のテトラフルオロメタン(CF_4)等の有害ガスの発生が懸念されている.[2]

以上の背景から，我々はPFCA類やPFAS類，さらにはそれらの誘導体について種々の比較的穏和な反応手法を開発し，F^-までの完全分解，すなわち無機化を達成してきた．本稿ではそれらについて，他の研究者の報告例も交えて報告したい．

2 ヘテロポリ酸を用いたPFCA類の光触媒分解

PFOAをはじめとするPFCA類は，OHラジカルとの反応性が極めて低いため通常の促進酸化法※1

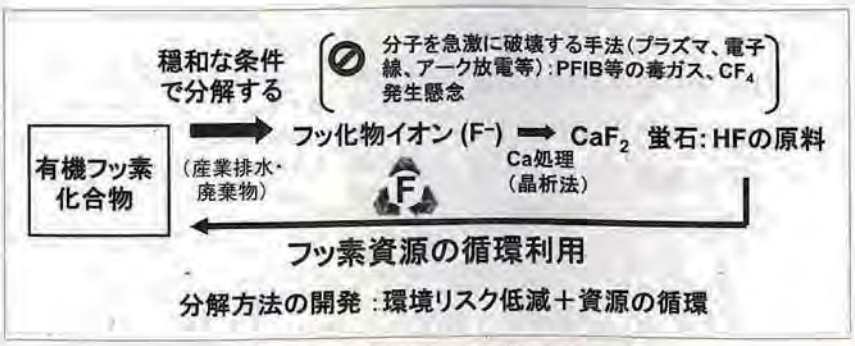

図1　フッ素資源の循環利用スキーム

※1　促進酸化法についての用語解説は，59頁参照．

ではほとんど分解できないが，我々はヘテロポリ酸光触媒$[PW_{12}O_{40}]^{3-}$を用いることで，F^-とCO_2まで分解させることに成功した．[3~7] これはPFCA類を光触媒で分解させることに成功した，世界初の例である．$[PW_{12}O_{40}]^{3-}$は高酸化力，強酸性下で安定(pHが1以下でも安定なため，分解対象物がPFCA類のような強酸類であっても使用できる)，均一系触媒なのでコーキング(触媒表面を生成物が覆って光反応が阻害される現象)を起こさないといった特徴がある．

光反応は，耐フッ素性の装置に炭素数2～9のPFCA類と$[PW_{12}O_{40}]^{3-}$を含む水溶液を導入し，酸素雰囲気下で紫外・可視光を照射することで行った．PFOAの場合，反応初期には水中に炭素数が少ないPFCA類(短鎖PFCA類)も検出されたが，長時間照射によりこのような中間体は消失した．この反応は光励起した$[PW_{12}O_{40}]^{3-}$がPFCA類から電子を奪うことで開始されるが，それに伴い$[PW_{12}O_{40}]^{3-}$は1電子還元した状態，すなわち$[PW_{12}O_{40}]^{4-}$になる．この還元種が系内に存在する酸素と反応して，元の$[PW_{12}O_{40}]^{3-}$の状態に戻ることで触媒サイクルが形成される．

3 ペルオキソ二硫酸イオン(光酸化剤)を用いたPFCA類の分解

前項の方法では，200 Wの水銀・キセノン灯を使用した場合，1.35 mMのPFOAを完全に消失させるのに24時間を要する．我々は，より短時間でPFCA類を分解するためにペルオキソ二硫酸イオン(過硫酸イオン，$S_2O_8^{2-}$)を光酸化剤として用いる方法を開発した．[8]

水中の$S_2O_8^{2-}$に紫外光を照射すると酸化力が非常に強い硫酸イオンラジカル($SO_4^{\bullet-}$)が生成する(式1)．$SO_4^{\bullet-}$生成の量子収率は2で非常に効率が高い．発生した$SO_4^{\bullet-}$の酸化還元電位(式2の反応に相当)は水中で2.5～3.1 Vであり，[9] OHラジカル(式3の場合は1.8 V，式4では2.7 V)と同程度か，それ以上である．

$$S_2O_8^{2-} + h\nu \rightarrow 2\,SO_4^{\bullet-} \quad (1)$$

$$SO_4^{\bullet-} + e^- \leftrightarrow SO_4^{2-} \quad (2)$$

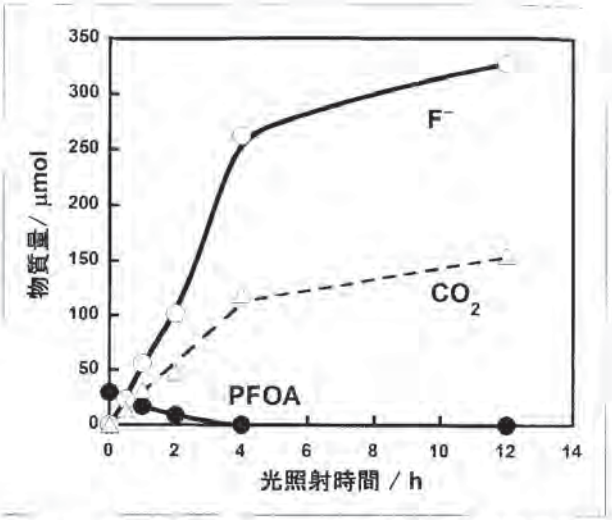

図2 $S_2O_8^{2-}$を光酸化剤としたPFOA分解反応の照射時間依存性

PFOA初期濃度1.35 mM[9]，PFOAの消失後も中間体の短鎖PFCA類の分解が続くためF^-とCO_2の生成は続いている．

$$\bullet OH + e^- \leftrightarrow OH^- \quad (3)$$

$$\bullet OH + e^- + H^+ \leftrightarrow H_2O \quad (4)$$

そこでPFOA水溶液に$S_2O_8^{2-}$を添加し，光照射して$SO_4^{\bullet-}$を生成させることでPFOAの分解を試みたところ，$[PW_{12}O_{40}]^{3-}$を使用した場合と同じ条件において4時間で消失させることができた(図2)．また，$SO_4^{\bullet-}$は反応後にはSO_4^{2-}になるが，その生成量は使用した$S_2O_8^{2-}$の2倍モルとなった．つまり，硫黄分はすべてSO_4^{2-}として回収可能である．この反応は触媒反応ではないため$S_2O_8^{2-}$は消費される一方で再利用はできないが，硫黄化合物は安価であること，反応速度が大きいこと，副生成物はSO_4^{2-}という処理しやすいものであることは大きな利点である．我々はこの方法を用いて，PFCA類よりも有害性が懸念されるフルオロテロマー不飽和カルボン酸類($C_nF_{2n+1}CF=CHCOOH$)の分解にも成功している．[10]

4 ペルオキソ二硫酸イオンを用いたPFCA類の温水分解

$S_2O_8^{2-}$を用いた反応については上述のような光化学的手法のみならず，高温水(熱水)を用いた反応も検討した．その結果，意外にも80℃程度の低温の熱水，すなわち温水中で最も迅速にF^-まで酸化分

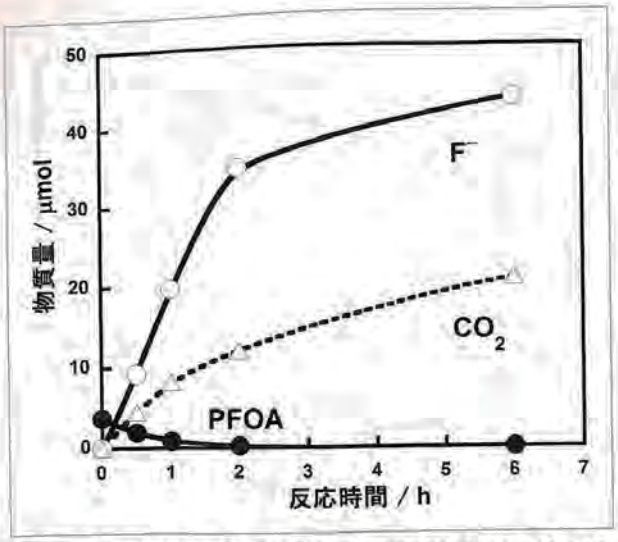

図3　$S_2O_8^{2-}$を用いたPFOAの温水分解(PFOA初期濃度374 μM)[11]

解できることを明らかにした.[11] 反応は耐圧容器に空気雰囲気中でPFCA類と$S_2O_8^{2-}$(カリウム塩)を入れ，密封・加熱することで行った．図3にPFOAと134倍モル過剰の$S_2O_8^{2-}$を入れた温水(80℃)中におけるPFOA分解の時間依存性を示す．$S_2O_8^{2-}$を入れない場合にはPFOA濃度は全く減少しなかったが，$S_2O_8^{2-}$を入れた場合には迅速に減少し，同時に気相中にはCO_2が，水中にはF^-が生成した．さらに迅速な分解を期待して反応温度を150℃に上昇させたところ，PFOAの減少速度は低下し，F^-およびCO_2の生成も大幅に減少した．これは150℃のような高温では，$SO_4^{\bullet-}$と水との反応が優先してPFOAとの反応が阻害されるためと考えられる．この方法で他のPFCA類，さらにはPFCA類の代替物質であるペルフルオロエーテルカルボン酸類やヒドロペルフルオロカルボン酸類[12]も分解できた．

5 鉄イオンを用いたPFCA類の光触媒分解

PFCA類については，鉄イオンの酸化還元反応を利用することでもF^-とCO_2まで分解できることを明らかにした.[13] 反応はPFCA類とFe^{3+}を含む水溶液を光反応装置内に入れ，O_2ガスを充満した後に紫外・可視光(220～460 nm)を照射して行った．アルゴン雰囲気の場合，分解反応は大幅に抑制され，同時に水相中の鉄イオンのうちFe^{2+}の割合が93.3%に達した．この結果は，O_2はFe^{2+}のFe^{3+}への再酸化過程に必要であることを意味している．

近年，PFCA類を光化学的手法で分解する報告例が増えている．例えばZhaoらはバンドギャップが広いβ-Ga_2O_3光触媒を用いてPFOAを分解している.[14] また，PanchangamらはTiO_2光触媒と超音波照射を組み合わせてPFOAを分解している.[15]

6 鉄粉＋熱水を用いたPFAS類の還元分解

水中のPFAS類は，上述の酸化的な手法では全く分解しなかった．そこで熱水(亜臨界水,※2 超臨界水)中で還元分解させることを検討した．その結果，鉄粉を還元剤として用いることで，亜臨界水中で効果的に分解できた.[16]

反応は以下のようにして行った．まず，耐圧容器に不活性ガス雰囲気中でPFOS(カリウム塩)の水溶液(93～372 μM)と鉄粉もしくは他の金属粉(亜鉛，銅，アルミニウム)を入れ，250～350℃の亜臨界水の状態にした．一定時間経過後，室温に戻して成分分析を行った．比較のため，金属粉を入れない場合についても実験を行った．金属粉がない場合，水中のPFOS濃度はほとんど減少しなかった．鉄粉を入れた場合に，PFOSは最も迅速に分解した．例えばPFOS初期濃度が372 μM，反応温度350℃，圧力23.3 MPaの場合，PFOSは6時間で水中から消失し，同時に水中にはF^-が高収率で生成した(図4)．

この方法により，電子産業界で使用されていた反射防止剤のPFOSや，炭素数2～6のPFAS類(PFOS代替品)，さらにはペルフルオロスルホンイミド[17]の分解も可能であった．また，超臨界水状態にすると更に反応は迅速に進行した.[18]

PFAS関連物質の中には，より簡単に分解できるものもある．例えば，PFOS代替物質としてペルフルオロアルキル基の中にエーテル結合を導入したペルフルオロアルキルエーテルスルホン酸類(PFAES類)があるが，これらは酸素ガスを共存させた亜臨界水反応でF^-，CO_2およびSO_4^{2-}まで効果的に分解

※2　亜臨界水についての用語解説は，59頁参照．

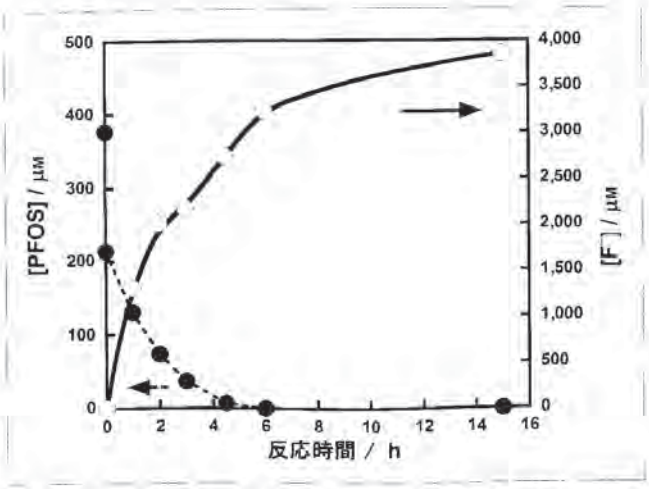

図4　鉄粉を還元剤として用いた亜臨界水反応による PFOS 分解の時間依存性[18]

できた.[19] 反応を無酸素条件で行った場合，PFAES 類の減少の時間依存性は酸素雰囲気の場合とほぼ同じであったが，F^-，CO_2 および SO_4^{2-} の生成量が大幅に減少した．このことは，酸素ガスが反応中間体の無機化に重要な役割を果たしていることを意味する．

7　超音波照射による PFAS/PFCA 類の分解

水中に高出力の超音波を照射するとミクロな高温高圧場が発生し，そこで生じる OH ラジカルや熱の作用で溶解している有機物を分解することができる．この方法を有機フッ素化合物に適用した報告例がある．例えば Moriwaki らは，純水中の PFOS および PFOA が超音波照射で分解することを報告しているが，PFOS の分解に伴い PFOA が生成することも観察しているので注意が必要である.[20] Cheng らは埋立処分場の PFOS 含入地下水に超音波を照射して，反応に及ぼす共存物質の影響を調べている.[21] 我々も $S_2O_8^{2-}$ と超音波照射を組み合わせてペルフルオロエーテルカルボン酸類の分解を試みた．その結果，$S_2O_8^{2-}$ の添加が当該物質の分解を促進することを見いだしている.[22]

8　フッ素系イオン交換膜の分解

フッ素系イオン交換膜の分解も，前述の PFOS

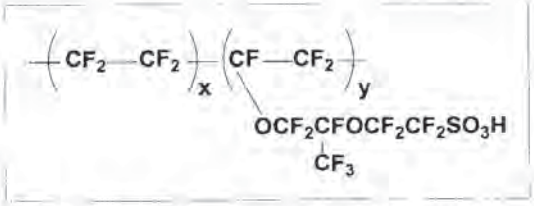

図5　実験に用いたフッ素系イオン交換膜
(ナフィオン　NRE-212)

の場合と同様の方法で達成した．フッ素系イオン交換膜(ポリマー)は造水，浄水，燃料電池，食塩電解等，様々な用途で用いられている機能性材料であるが，その廃棄物は埋め立て処分されているのが現状で，分解処理方法は確立されていない．フッ素系イオン交換膜のうち，ペルフルオロアルキルエーテルスルホン酸を側鎖に持つペルフルオロスルホン酸膜については，過酸化水素水やフェントン試薬(Fe^{2+} $+H_2O_2$)による劣化過程を調べた例がある.[23] しかし，それらは燃料電池の耐久性の向上を目的としたもので，廃棄物からフッ素成分を回収するために積極的に分解反応を探索した例はなかった．また，その劣化の過程において PFCA/PFAS 類似物質が生成するという報告もあるので，F^- まで完全に無機化することが望ましい．そこで本研究ではこのような膜について金属粉を還元剤とした亜臨界水反応で分解することを試みた.[24]

試料としては図5のポリマーを用いた．この膜(乾燥重量 29.8 mg，総フッ素量 1.03 mmol)と金属粉(9.60 mmol)および純水(10 mL)を耐圧反応装置に入れ，アルゴン雰囲気下で密封後，250～350℃の亜臨界水状態にした．一定時間経過後，室温に急冷し，水中およびガス相中の反応物を分析した．

その結果，金属を添加しない場合，F^- はほとんど生成しなかった．アルミニウムを添加した場合，F^- の生成はかえって阻害された．亜鉛，銅および鉄の場合には分解促進作用があり，鉄を用いた場合に特に顕著な F^- の生成が見られた．鉄粉を加えて 350℃ で反応させたところ，17 時間後には F^- の生成量は 754 μmol に達した．これは反応前の膜中のフッ素原子うち，73.2% が F^- に変換されたことを意味し，ポリマーの側鎖のみならず，主鎖 $(CF_2\text{-}CF_2)_x$ の部分まで効果的に分解できることが分かった．

9 おわりに

以上，有機フッ素化合物の分解反応に関して紹介した．我々はフッ素ポリマーについては更に使用量が多いものについて，また低分子の化合物についてもエネルギーデバイス用のフッ素系イオン液体の反応性を調べている．[25] このような取り組みにより，新規フッ素材料の環境リスクの低減と資源の循環利用の双方に貢献したいと考えている．

参考文献

1) 澤田英夫監修，"フッ素樹脂の最近動向，" シーエムシー，東京，2013.
2) Pacansky J., Waltman R. J., *J. Phys. Chem.*, 95, 1512–1518 (1991).
3) Hori H. *et al.*, *Environ. Sci. Technol.*, 37, 418–422 (2003).
4) Hori H. *et al.*, *Appl. Catal. B: Environ.*, 46, 333–340 (2003).
5) Hori H. *et al.*, *Environ. Sci. Technol.*, 38, 6118–6124 (2004).
6) Hori H. *et al.*, *Appl. Catal. B, Environ.*, 82, 58–66 (2008).
7) Hori H. *et al.*, *Chemosphere*, 82, 1129–1134 (2011).
8) Hori H. *et al.*, *Environ. Sci. Technol.*, 39, 2383–2388 (2005).
9) Neta P. *et al.*, *J. Phys. Chem. Ref. Data*, 17, 1027–1284 (1988).
10) Hori H. *et al.*, *Water Res.*, 41, 2962–2968 (2007).
11) Hori H. *et al.*, *Environ. Sci. Technol.*, 42, 7438–7443 (2008).
12) Hori H. *et al.*, *Catal. Today*, 151, 131–136 (2010).
13) Hori H. *et al.*, *Chemosphere*, 68, 572–578 (2007).
14) Zhao B., Zhang P., *Catal. Commun.*, 10, 1184–1187 (2009).
15) Panchangam S. S. *et al.*, *Chemosphere*, 75, 654–660 (2009).
16) Hori H. *et al.*, *Environ. Sci. Technol.*, 40, 1049–1054 (2006).
17) Hori H. *et al.*, *Catal. Today*, 196, 132–136 (2012).
18) Hori H. *et al.*, *Chemosphere*, 70, 800–806 (2008).
19) Hori H. *et al.*, *Chemosphere*, 77, 1400–1405 (2009).
20) Moriwaki H. *et al.*, *Environ. Sci. Technol.*, 39, 3388–3392 (2005).
21) Cheng J. *et al.*, *Environ. Sci. Technol.*, 42, 8057–8063 (2008).
22) Hori H. *et al.*, *J. Fluirine Chem.*, 141, 5–10 (2012).
23) Kadirov M. K. *et al.*, *J. Phys. Chem. B*, 109, 7664–7670 (2005).
24) Hori H. *et al.*, *Ind. Eng. Chem. Res.*, 49, 464–471 (2010).
25) Hori H *et al.*, *Ind. Eng. Chem. Res.*, 52, 13622–13628 (2013).

Book Review
新刊紹介

薬学生・薬剤師のための 知っておきたい病気100 (第2版)

日本薬学会　編
東京化学同人／B6・340頁・2,940円

「多くの医師は限られた領域の疾患に関しては深い知識をもつものの，専門外の疾患に関しては浅い知識しかなく」．本書のまえがきで，編集委員長で医師でもある上田先生が書いている．日本薬学会が編集するこの本は，副題に「薬学生・薬剤師のための」と銘打つことからも分かるように，薬剤師業務において知っておくべき病態と主な薬物治療に関してまとめたものである．

内容は大きく3部に分かれ，第Ⅰ部の「病態」で様々な病気が体の部位別に解説され，続く第Ⅱ部「症候」では患者の状態からどのような病気が疑われるかを，最後の第Ⅲ部「薬剤性障害」で注意するべき薬剤障害をまとめている．個々の病気では，まずどのような治療法があるかを述べた後に，薬物療法に用いられる薬剤の作用機序やその組み合わせなどが記載されている．分かりにくい部分は治療法をアルゴリズムにした図表を加えるなど，病気と薬剤の関係をイメージしやすくする工夫が随所に見られる．前立腺の病気や乳がん，更年期障害などは「男性の疾患」「女性の疾患」の項にそれぞれ分類されているのも理解の一助となる．

一方，感染症に関しては，例えば肺炎が「肺と気道疾患」に，副鼻腔炎が「耳・鼻・喉疾患」にと，疾患部位別に分けて記載されているため，やや全体のイメージがつかみにくい．第Ⅰ部の最後に「感染症」の項があり，ここまでの記載で漏れているウイルス感染症などをまとめている．この中に呼吸器や尿路感染症などの概略があれば，より理解しやすいのではないか．

充実した内容がコンパクトにまとめられており，B6判で持ち歩きやすいサイズである．前述のまえがきで，上田先生は国家試験受験までに本書を5回通読することを提案している．かなり厳選してまとめたのだろうが，それでも本書をほぼすべて頭に入れることは大変な作業だ．ただ，スペシャリストである医師とタッグを組む臨床薬剤師は，やはり薬物治療に関してゼネラリストであることが求められる．薬剤師の職務に関する責任の重さを，再確認した次第である．

佐藤康夫　Yasuo SATO

錯体化学を基盤とするBio-inspired酸化触媒の開発

引地史郎[*1]・中澤　順[*2]

1. はじめに

グリーンケミストリーに対する関心が高まる中，高い反応選択性を示し，かつエネルギー消費が少ない上に廃棄物の環境に対する負荷が小さい生体内反応の機構を，触媒や反応プロセスの設計に活かしていく“bio-inspired chemistry”は，近年ますます進展している．とりわけ生体内での酸素代謝過程における有機化合物への酸素添加反応は，極めて穏和な条件下における高効率な反応であり，人工的に同様なプロセスを達成することは多くの化学者達の夢である．

生体内における炭化水素への酸素添加反応は，主に鉄・銅などの遷移金属を活性中心とする酸素添加酵素により触媒されている．酵素の特異な反応特性は，アミノ酸やポルフィリンなどの補欠分子族によって精密に立体および電子的特性が制御された金属配位場（金属錯体）[1]と，その周囲を取り巻く三次元反応場空間によりもたらされる．筆者らは，これら酵素の特徴を取り入れて設計された高機能触媒，すなわち人工酵素の開発を目指している（図1）．具体的には精密分子設計に基づ

*1 Shiro Hikichi　神奈川大学工学部物質生命化学科　教授　博士（工学）
*2 Jun Nakazawa　同上　特別助教　博士（理学）
Development of Bio-inspired Oxidation Catalysts Based on Coordination Chemistry

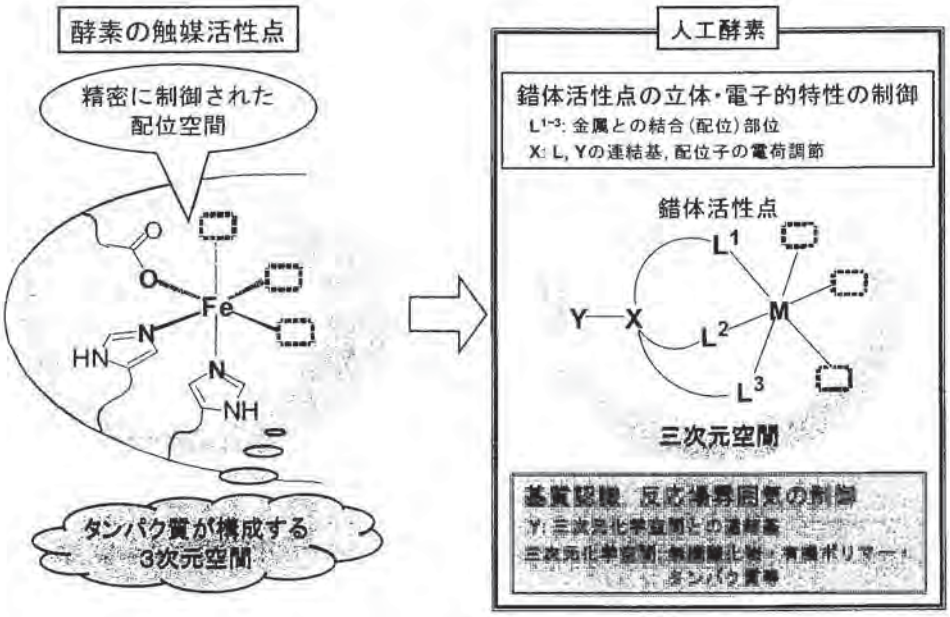

図1　人工酵素のコンセプト

く配位空間の制御を軸とした錯体分子触媒の開発と，無機材料と錯体触媒分子の複合化による新規固体触媒の開発を推進している[2]．以下本稿では精密な分子設計が容易に行えるアニオン性キレート配位子を用いた，ニッケル錯体触媒によるアルカン水酸化機構の解明を目指した研究について解説する．さらにニッケル錯体触媒を固体担体上に固定することにより不均一系触媒反応に展開した結果について解説する．

2．ニッケル錯体触媒による有機過酸を酸化剤とする触媒的アルカン水酸化反応

2．1　酸化触媒と酸素錯体の化学

アルカンのアルコールへの変換（選択的水酸化）を触媒する酸化酵素における酸化活性種は，遷移金属中心（鉄や銅）に配位した活性酸素種である．そこで酵素反応の機構解明や触媒設計のための知見を得るといった学術的な見地，および温和な条件での選択酸化反応の実現を目指した実用的な見地の両面から，遷移金属錯体触媒による酸素分子の還元的活性化や，過酸化物等の効率的活性化を経た触媒反応系の構築が検討されてきた．酸化剤の活性化過程で生じる金属-酸化剤付加体の多くは熱的に不安定な化学種であるが，この不安定種の化学的特性についての知見は，触媒反応機構の直接的な理解につながるのみならず，これを更なる分子設計にフィードバックすることで，より高性能な触媒開発につながることが期待される[3]．

ところでニッケルはその酸化還元特性に基づいて，有機合成化学および生体内反応における種々の触媒反応を司る重要な金属種であるが，合成化学的な酸化反応への適用例は少なく，またアルカンの酸化反応を触媒する酵素の活性点には現在まで見出されていない．しかし酸素添加酵素の触媒活性点となっている銅や鉄に関する研究を発展させる形で，周期表において銅に隣接するニッケルについても，活性酸素種との相互作用に関する化学への興味が近年高まっている．特に複核Ni(III)-架橋ジオキソ種がアルキル基からの水素引き抜き反応に高い活性を示すことが明らかになって以来，ニッケル-活性酸素錯体の特異な酸化活性に注目が集まるようになった[4]．近年になり大阪大学の伊東やその他の研究グループにより，ニッケル錯体触媒による過安息香酸（=*meta*-chloroperbenzoic acid；*m*CPBA）を酸化剤とするアルカン水酸化反応が，温和な条件できわめて高選択的に進行することが報告された[5]．*m*CPBAは有機合成化学における汎用的な酸化剤であり，高温であれば触媒不在でもアルカンの酸化が進行するが，これはO-O結合の開裂によって生じたフリーラジカル種が活性種であるために反応選択性はきわめて低い．しかし適切な触媒と組み合わせることで，温和な条件でも酸化反応が進行するようになり，かつ触媒の構造や電子的特性に応じた反応選択性が発現する．代表的なアルカン水酸化酵素であるCytochrome P-450のモデル化合物である鉄ポルフィリン錯体では，*m*CPBAとの反応により鉄中心にアシルペルオキシドイオンが配位した錯体が生じ，さらにそのO-O結合のイオン的開裂により生成した高原子価鉄-オキソ種が真の酸化活性種として機能することが知られている．一方ニッケル錯体と*m*CPBAの反応においてもニッケル-アシルペルオキシド錯体の形成を経て反応が進行するものと推定されている．しかし既報のニッケル錯体触媒による反応において，反応中間体は一切検出されておらず，反応機構に関する提案は推測の域を出ない[5]．そこで筆者らは，置換基の導入により錯体金属中心の立体および電子的特性を自在に制御することが可能なキレート配位子Tp^R（**図２**）[6]を有するニッケル(II)錯体を用いて，錯体の分子構造と触媒特性の相関の解明，および反応中間体を検出・同定に基づく反応機構の考察を行うこととした．

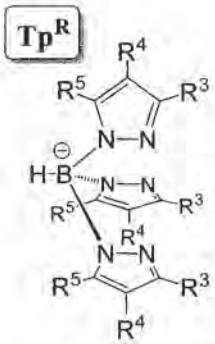

R of Tp^R	R^3	R^4	R^5
iPr2	iPr	H	iPr
iPr2,Br	iPr	Br	iPr
Me2	Me	H	Me
Me2,Br	Me	Br	Me
CF3,Me	CF_3	H	Me

図2　アニオン性キレート配位子Tp^Rの構造と置換基

2．1．1　金属支持配位子の分子設計と触媒特性

まず既報の触媒と同様，シクロヘキサンに対する酸化触媒活性を検討したところ，金属支持配位子(=Tp^R)の立体および電子的特性が触媒活性発現の鍵となっていることが明らかとなった[7]．触媒前駆体には，*m*CPBAとの脱水縮合によるニッケル-アシルペルオキシド付加体の形成が速やかに進行することが期待されるニッケル(II)-ヒドロキソ錯体[$(Ni^{II}Tp^R)_2(\mu\text{-}OH)_2$]を用いた．錯体形成時に金属中心をかさ高いイソプロピル(iPr)基が覆うTp^{iPr2}を配位子とする錯体が触媒活性を示さないのに対し，立体障害が小さいメチル(Me)基が金属近傍に位置するTp^{Me2}を配位子とする錯体は，高選択的に対応するアルコール(シクロヘキサノール)を与えた．さらに立体的な環境を維持したまま電子状態にのみ摂動を加えるためにTp^{Me2}のピラゾリル基の4位(図2におけるR^4)に電子吸引基である臭素(Br)を導入した$Tp^{Me2,Br}$を配位子とする錯体では，反応速度は低下するものの生成物に占めるアルコールの選択性が向上した．なお触媒活性を示さないTp^{iPr2}を配位子とする錯体では，ニッケル近傍のイソプロピル基が酸化されていることが判明した．

さらに基質をメチルシクロヘキサンとしたところ，触媒不在の場合にはC-H結合開裂エネルギーが低い3級炭素部位が選択的に酸化されることとは対照的に，Tp^{Me2}および$Tp^{Me2,Br}$錯体を触媒とすることで，C-H結合開裂エネルギーが高いものの立体障害が小さい2級炭素部位の酸化が優先した(**表1**)．以上の結果は，錯体分子中の立体的に込み合ったニッケル中心上に発生した活性種により酸化反応が進行していることを意味しており，金属支持配位子の精密分子設計によって，より高度な反応選択性(位置選択性や立体選択性)の発現が期待できる．

表1　メチルシクロヘキサンに対する酸化活性

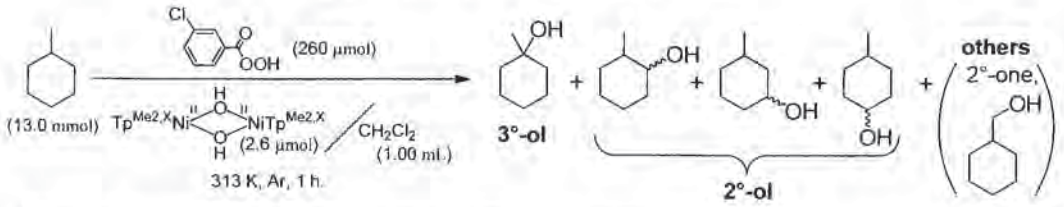

X of $Tp^{Me2,X}$	Products / μmol						3°-ol: 2°-ol	TON
	OH	OH	OH	OH	2-ones	OH		
H	74.7	47.1	61.6	27.9	4.6	0.9	35 : **65**	**43**
Br	72.3	45.6	62.4	29.6	3.8	0.8	34 : **66**	**42**
No catalyst	6.1	0.9	0.9	0	0	0	**77** : 23	2 [b]
No cat. (353K) [a]	153.6	10.4	11.5	6.6	2.4	0.2	**84** : 16	36 [b]

[a] Without CH_2Cl_2, 2 h.　[b] based on 5.2 μmol of virtual nickel catalyst

2．1．2　ニッケル(II)-アシルペルオキソ中間体の同定とその反応特性の解明

低温でのニッケル(II)-ヒドロキソ錯体と*m*CPBAの反応をUV-visや*in situ* IRスペクトルにより追跡したところ，ニッケル(II)-アシルペルオキシド付加体 [Ni^{II}(OOC(=O)C_6H_4Cl)Tp^R] が生成していることが確認できた．このアシルペルオキソ錯体の安定性は，触媒特性と同様にTp^Rに導入した置換基の立体的なかさ高さおよび電子的特性に支配されており，外部から基質が接近できない程にかさ高いイソプロピル基がニッケル中心を覆い，かつ電子吸引基である臭素が導入されている$Tp^{iPr2,Br}$を配位子とする錯体が最も安定であった．しかしいずれの錯体も溶液状態で−40℃以上では分解してしまい，単離には至らなかった[7]．

ニッケル(II)-アシルペルオキソ錯体の本質的な反応特性を理解するためには，アシルペルオキソ錯体そのもの単離する必要がある．そこで金属支持配位子(Tp^R)の分子設計によって，外部基質に対する反応性を維持したまま安定化を図ることを計画した．置換基の特性について精査し，適度な立体的なかさ高さと電子吸引性に基づく安定化効果が期待され，さらには酸化耐性にも優れるトリフルオロメチル(CF_3)基がニッケル中心を覆う$Tp^{CF3,Me}$を選択した．これにより得られたアシルペルオキソ錯体 [Ni^{II}(OOC(=O)C_6H_4Cl)$Tp^{CF3,Me}$] は，基質不在であれば期待通り室温においても安定であり，単離およびX線単結晶構造解析による分子構造の決定に成功した(**図3**)[8]．

単離したアシルペルオキソ錯体のさまざまな基質に対する酸化特性を速度論的解析および反応生成物分析により検討した．興味深いことに，ニッケル(II)-アシルペルオキソ錯体は1,4-シクロヘキサジエンや9,10-ジヒドロアントラセン，キサンテン，フルオレンといった基質の活性メチレン部位からの水素原子引き抜き活性を示した．アシルペルオキソ錯体の消失速度は錯体濃度と基質濃度の両方に依存する2次反応であったが，一連の活性メチレン化合物に対する反応速度と，各基質のC-H結合解離エネルギーの間には相関はなく，立体障害が小さくニッケルに配位したアシルペルオキシドに接近しやすいと考えられる1,4-シクロヘキサジエンとの反応が最も早かった．したがってアシルペルオキソ錯体は，O-O結合を開裂することなく直接脂肪族炭化水素を酸化することが明らかとなった．その一方，シクロヘキサンを基質とした場合，対応する酸化生成物は得られたものの，アシルペルオキソ錯体の消失速度は錯体濃度のみに依存した1次反応であってシクロヘキサンの濃度には依存していなかった．これはC-H結合解離エネルギーが高い炭化水素の場合には，アシルペルオキソ錯体が直接の活性種ではないことを意味しており，ニッケルに配位したアシルペルオキシドのO-O結合開裂により生じた高原子価ニッケル-オキソ(あるいはニッケル(II)-酸素ラジカル)種[9]が活性種となっているものと考えられる．以上より，ニッケル(II)-アシルペルオキソ錯体は基質に応じて活性種，あるいは活性種の前駆体となることが明らかとなった(**図4**)[8]．

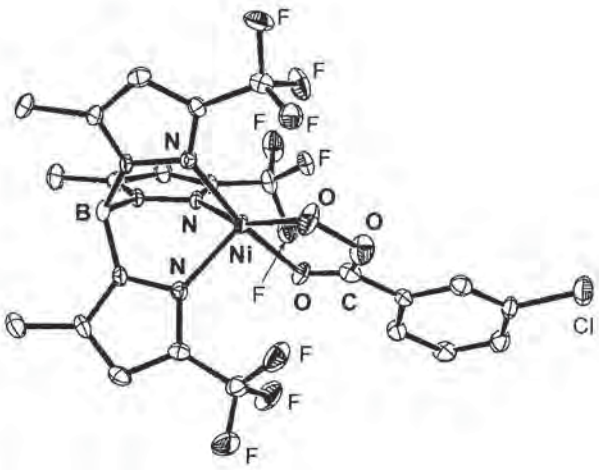

図3　ニッケル(II)-アシルペルオキソ錯体の分子構造

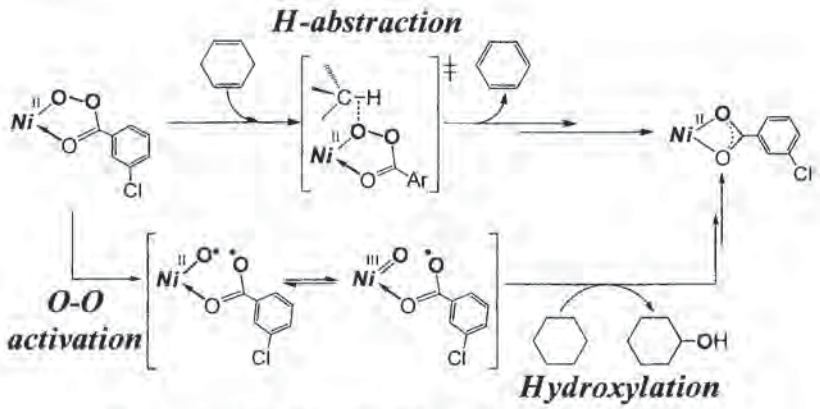

図4　ニッケル(II)-アシルペルオキソ錯体の脂肪族 C-H 酸化機構

2. 2　固定化錯体触媒への展開

酵素において，金属錯体活性点を取り巻く三次元空間反応場は，基質認識能や電子伝達・雰囲気(親水性・疎水性)の制御といった反応促進や触媒安定化に関わる重要な因子である．すなわち配位子により形成される配位圏だけでなく，それを取り囲む周辺環境の構造や性質も考慮する必要があるが，これには規則的な三次元構造を有し，かつ化学修飾による親和性の制御やさまざまな機能の付与が可能な固体表面の活用が有効であると考えられる．また金属錯体触媒は溶液内での化学平衡や錯体分子間での不均化反応により失活してしまう場合があるが，これを防ぐには，固体表面への錯体分子の固定化が有効であると考えられる．特に液相中では不活性な配位飽和種が生成してしまうような場合でも，配位子を固体表面に適当な間隔を保って固定できれば，活性な配位不飽和錯体が担体表面で形成され，しかもその間隔を制御することで錯体触媒活性点の構造制御(単核金属種と多核金属種の創り分け)も期待できる(**図5**)．さらに固体の特性を活かして，同一担体上に機能の異なる金属錯体を固定化した触媒デバイスの構築も可能になると考えられる．以上のような発想の下，筆者らは錯体分子触媒の固定化錯体触媒への展開を検討している．

2. 2. 1　固定化錯体触媒の設計

錯体触媒の担体への固定化に伴い触媒活性や機能が大きく変化してしまうことがある．その要因の一部として金属支持配位子部の構造・性質と，担体への固定状態が挙げられ，その解決には，①配位子と担体が安定な共有結合により連結されることや，②触媒活性点となる金属上の配位不飽和座と担体表面が直接相互作用しないこと，といった条件を満たした上で，③配位子間を適切な間隔を保って固定し，孤立した錯体触媒活性点として機能させる必要があると考えた．

そこで筆者らは有機アジド基修飾メソ多孔体シリカゲル($SBA\text{-}N_3$)を担体とすること

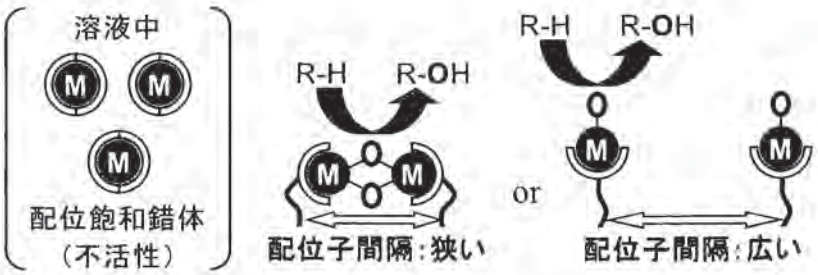

図5　固定化錯体触媒における配位子の間隔と錯体種の構造

を計画した[10]．アジド基はアルキン類とのHuisugen [3+2] 環化付加反応(クリック反応)により1,2,3-トリアゾールに変換できる．よって金属支持配位子中に末端アルキン部位を導入できれば，SBA-N_3の有機アジド基とのクリック反応によって担体上への共有結合を介した固定化が達成できる．またここで用いたSBA-N_3は，テトラエトキシシラン($Si(OEt)_4$)に対して任意の量(ケイ素モル比，x%；x=0.5，1.0，2.0，4.0)の3-アジドプロピルトリエトキシシラン($N_3CH_2CH_2CH_2Si(OEt)_3$)を添加したシラノールエステル混合物を，鋳型となるポリマーミセルの存在下で加水分解・脱水縮合することにより構築したSBA-15類縁体であるが，このone-pot法により調製したSBA-N_3-xでは，有機アジド基の修飾量が原料シラノールエステルの仕込み比xにより制御できるだけでなく，有機アジド基の分布がランダムであるという特徴を持つ．シリカゲル担体の化学修飾法としては，純粋な担体に対して有機官能基化シラノールエステルを作用させるpost-synthesis法が一般的であるが，この方法では担体表面の残留シラノール(Si-OH)基とシラノールエステルの縮合反応だけではなくシラノールエステルどうしの縮合も同時に起こりやすく，有機官能基がランダムに分散し難い．

このSBA-N_3-xに固定する配位子には，末端アルキン構造への誘導が容易なビス(ピリジルメチル)アミン構造を基本骨格とするものを用いた．これは，伊東らにより最初に報告されたアルカン水酸化触媒として機能するニッケル錯体の金属支持配位子トリス(ピリジルメチル)アミン(=TPA)[5a]のピリジル基の1個をプロパルギル基に置換したものである．また，担体固定時にクリック反応により生成するトリアゾリル基は，配位子と担体をつなぐリンカーとしての機能を担うだけではなく，状況によっては金属配位基となることも想定している．なお配位子固定後の担体にヘキサメチルジシラザン($(Me_3Si)_2NH$)を作用させることで，表面に残存して金属イオンと相互作用する可能性のある水酸基をトリメチルシリル($SiMe_3$)基で不活性化したSBA*-**L**-xへと誘導した(図6)．これに酢酸ニッケルを作用することによりニッケル錯体固定化触媒Ni/SBA*-**L**-xとした．

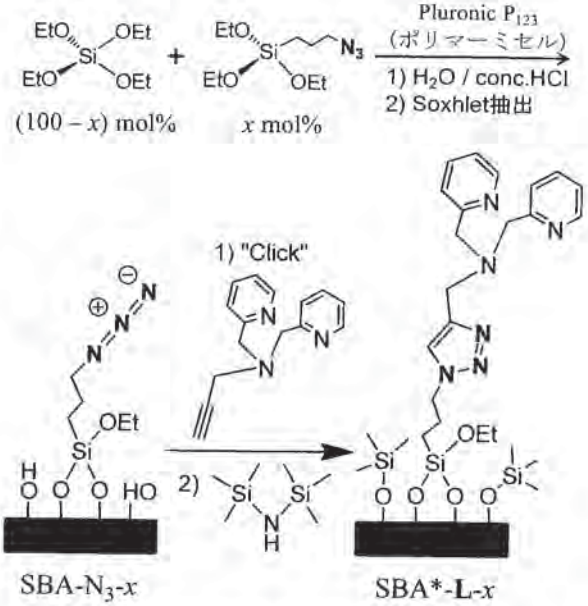

図6　配位子固定化担体SBA*-**L**-xの調製

2．2．2　担体上の配位子固定密度と触媒特性の相関

調製したNi/SBA*-**L**-xの配位子担持量は，SBA-N_3-x調製時のアジド基仕込み比率xに応じて単調に変化していたが，ニッケルイオン担持量は配位子担持量に応じて異なり，x=0.5～2ではほぼ**L**：Ni=1：1であるのに対してx=4のものでは**L**：Ni=2：1に近くなった(表2)．ところでSBA-N_3-xに替えて*tert*-ブチルアジド(tBuN$_3$)との反応により得た配位子$\mathbf{L}^{t\mathrm{Bu}}$を用いて別途ニッケル錯体を合成したところ，条件に応じて**L**：Ni=1：1である$[Ni(\mathbf{L}^{t\mathrm{Bu}})(OAc)_2(OH_2)]$ (= Ni/$\mathbf{L}^{t\mathrm{Bu}}$)および**L**：Ni=2：1の組成からなる$[Ni(\mathbf{L}^{t\mathrm{Bu}})_2](BF_4)_2$(=Ni/2$\mathbf{L}^{t\mathrm{Bu}}$)が得られた．両者の分子構造を解析したところ，どちらの錯体においてもトリアゾリル基はニッケルに配位していないことが判明し，Ni/SBA-**L**-xに

表2　Ni/SBA*-L-x の配位子およびニッケル担持量

x of SBA*-L-x / %	0.5	1	2	4
BET比表面積 / $m^2 \cdot g^{-1}$	590	602	423	302
Lの担持量 / $mmol \cdot g^{-1}$	0.072	0.13	0.25	0.33
Niの担持量 / $mmol \cdot g^{-1}$	0.08	0.14	0.22	0.19
L:Ni	0.9:1	0.9:1	1.1:1	1.7:1

表3　固定化錯体触媒の酸化活性

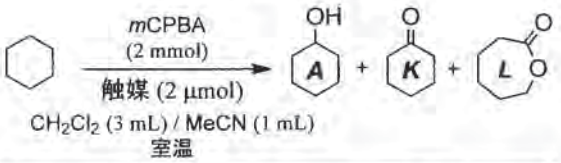

触媒	反応時間 / h	TON		
		A	*K*	*L*
Ni/TPA	1	587	69	no data
Ni/$\mathbf{L}^{t\mathrm{Bu}}$	1	599	56	25
Ni/2$\mathbf{L}^{t\mathrm{Bu}}$	1	647	56	20
Ni/SBA*-L-0.5	3	534	17	34
Ni/SBA*-L-1	3	377	14	22
Ni/SBA*-L-2	3	261	10	11
Ni/SBA*-L-4	3	251	10	10

おいても同様な錯体種が担体表面に形成されていることが推測された[11].

これらの触媒について，*m*CPBA を酸化剤とするシクロヘキサン酸化活性を比較することで，担体上の配位子固定密度が触媒活性に及ぼす影響を検討した(**表3**)．別途合成した錯体 Ni/$\mathbf{L}^{t\mathrm{Bu}}$ を触媒とした液相均一系反応は速やかに進行し，反応開始から1時間後にシクロヘキサノールの生成量が金属あたりの触媒回転数(TON)に換算して約600回に達したところで反応が停止した．これは伊東が報告している TPA を配位子とするニッケル錯体と同等の反応性である．一方，固定化触媒では反応速度は低下していたが，特筆すべきは配位子担持量に応じて活性が異なっていたことである．生成物の比率は配位子担持量によらず Ni/$\mathbf{L}^{t\mathrm{Bu}}$やTPA 錯体の場合と大きく変化していないことから，反応メカニズムは同一であると考えられる．したがって配位子

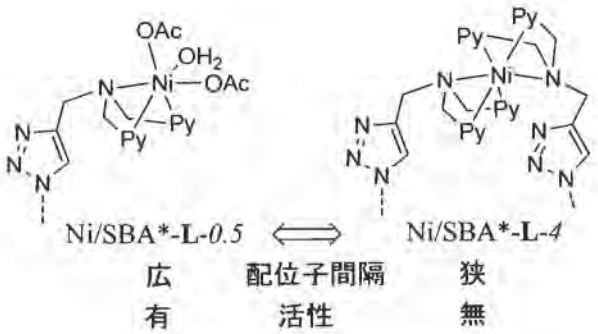

図7　Ni/SBA*-L-x の推定活性点構造

固定量が少ない場合($x = 0.5$, 1, 2)には，Ni/$\mathbf{L}^{t\mathrm{Bu}}$ と同様な孤立した錯体触媒活性点が構築されているために溶液中と同様な反応性を維持していたものの，配位子固定量が多い Ni/SBA*-L-4.0 では，L : Ni が 2 : 1 に近いことから，担体表面には不活性な錯体種 $[\mathrm{Ni}(\mathbf{L})_2]^{2+}$ が多く形成しているものと考えられる(**図7**)．ところで L : Ni = 2 : 1 である錯体 Ni/2$\mathbf{L}^{t\mathrm{Bu}}$ は液相均一系反応において Ni/$\mathbf{L}^{t\mathrm{Bu}}$ と全く同様な触媒活性を示したことから，溶液中では $[\mathrm{Ni}(\mathbf{L}^{t\mathrm{Bu}})_2]^{2+}$ における $\mathbf{L}^{t\mathrm{Bu}}$ は置換活性であると考えられる．しかし Ni/SBA-L-4.0 では L が担体に固定されたことで運動性が低下して平衡状態が大きく変化したために，担体表面に形成された $[\mathrm{Ni}(\mathbf{L})_2]^{2+}$ は置換不活性であり触媒活性点とはなりえなかったものと推測される[11].

3. おわりに

本稿で紹介したニッケル錯体触媒を用いる有機過酸を酸化剤とするアルカン水酸化反応は，高価な *m*CPBA を酸化剤としていること

からバルクプロセスには適用できず，現状では基礎研究の域を出ない．しかし均一系触媒反応の機構解明の過程で得られた，金属支持配位子の立体および電子的特性と触媒特性および反応中間体の安定性の相関といった知見は，金属錯体触媒の精密分子設計によって位置および立体選択的なアルカン水酸化が達成できる可能性を示唆するものであり，ファインケミカルズへの展開が期待されよう．

また不均一系触媒反応に適用可能な固定化錯体触媒については，担体や配位子についても用途に合わせた設計を行っていく必要があることが明らかになった．本稿で紹介したニッケル錯体触媒の場合，担体上の配位子固定密度が高すぎると活性低下を招くのに対し，中心金属をコバルトに替えると逆の結果が得られている[12]．これは金属種に応じた配位平衡の違いによるものであるが，液-固界面（不均一系）と溶液状態（均一系）では平衡挙動が異なってくることも触媒特性の支配因子となっている．また本稿では詳細な解説は割愛したが，担体表面の構造（分子レベルでの平滑さ）と触媒活性の相関[13]や，錯体触媒の分子構造を損なうことなく担体に固定するための金属支持配位子の分子設計のポイント[14]等も明らかになりつつある．これらを踏まえた触媒設計を行うことで，液相均一系では得難い錯体触媒活性点を有する人工酵素を構築することを目指している．

参考文献

1）(a) 引地史郎，固体物理，**43**，733 (2008); (b) 引地 史郎，触媒，**46**，262 (2004).

2）引地史郎，中澤 順，触媒，**52**，243 (2010).

3）(a) B. Meunier, ed., "*Biomimetic Oxidations Catalyzed by Transition Metal Complexes*"; Imperial College Press: London (2000); (b) L. Que, Jr, W.B. Tolman, *Nature*, **455**, 333 (2008).

4）(a) 引地史郎，化学工業 **53**，410 (2002); (b) S. Hikichi, M. Yoshizawa, Y. Sasakura, H. Komatsuzaki, Y. Moro-oka, M. Akita, *Chem. Eur. J.*, **7**, 5011 (2001); (c) S. Itoh, H. Bandoh, M. Nakagawa, S. Nagatomo, T. Kitagawa, K.D. Karlin, S. Fukuzumi, *J. Am. Chem. Soc.*, **123**, 11168 (2001); (d) M. Suzuki, *Acc. Chem. Res.* **40**, 609 (2007); (e) M.T. Kieber-Emmons, C.G. Riordan, *Acc. Chem. Res.* **40**, 618 (2007); (f) J. Cho, R. Sarangi, J. Annaraj, S.Y. Kim, M. Kubo, T. Ogura, E.I. Solomon, W. Nam, *Nature Chem.*, **1**, 568 (2009); (g) S. Hikichi, H. Okuda, Y. Ohzu, M. Akita, *Angew. Chem. Int. Ed.*, **48**, 188 (2009); (h) S. Hikichi, C. Kobayashi, M. Yoshizawa, M. Akita, *Chem. Asian J.*, **5**, 2086 (2010); (i) J. Nakazawa, H. Ogiwara, Y. Kashiwazaki, A. Ishii, N. Imamura, Y. Samejima, S. Hikichi, *Inorg. Chem.*, **50**, 9933 (2011); (j) S. Yao, M. Driess, *Acc. Chem. Res.*, **45**, 276 (2012).

5）(a) T. Nagataki, Y. Tachi and S. Itoh, *Chem. Commun.*,, 4016 (2006); (b) T. Nagataki, K. Ishii, Y. Tachi and S. Itoh, *Dalton Trans.*, 1120 (2007); (c) T. Nagataki and S. Itoh, *Chem Lett.*, **36**, 748 (2007); (d) M. Balamurugan, R. Mayilmurugan, E. Sureshb and M. Palaniandavar, *Dalton Trans.*, **40**, 9413 (2011).

6）(a) M. Akita, S. Hikichi, *Bull. Chem. Soc. Jpn.*, **75**, 1657 (2002); (b) S. Trofimenko, "*Scorpionates – The Coordination Chemistry of Polypyrazolylborate Ligands*", Imperial College Press, London (1999); (c) C. Pettinari, "*Scorpionates II: Chelating Borate Ligans*", Imperial College Press, London (2008).

7）S. Hikichi, K. Hanaue, T. Fujimura, H. Okuda, J. Nakazawa, Y. Ohzu, C. Kobayashi, M. Akita, *Dalton Trans.*, **42**, 3346 (2013).

8）J. Nakazawa, S. Terada, M. Yamada, S. Hikichi, *J. Am. Chem. Soc.*, **135**, 6010 (2013).

9）F. F. Pfaff, F. Heims, S. Kundu, S. Mebs and K. Ray, *Chem. Commun.*, **48**, 3730 (2012).

10）(a) J. Nakazawa, T.D. P. Stack, *J. Am. Chem. Soc.*, **130**, 14360 (2008); J. Nakazawa, B.J. Smith, T.D. P. Stack, *J. Am. Chem. Soc.*, **134**, 2750 (2012).

11）J. Nakazawa, T. Hori, T.D. P. Stack, S. Hikichi, *Chem. Asian J.*, **8**, 1191 (2013).

12）J. Nakazawa, A. Yata, T. Hori, T.D.P. Stack, Y. Naruta, S. Hikichi, *Chem. Lett.*, doi:10.1246/cl.130464 (Advance Publication on the web June 22, 2013).

13）T. Akashi, J. Nakazawa, S. Hikichi, *J. Mol. Catal. A: Chem.*, **371**, 42 (2013).

14）S. Hikichi, M. Kaneko, Y. Miyoshi, N. Mizuno, K. Fujita, M. Akita, *Top. Catal.*, **52**, 845 (2009).

ISBN978-4-7853-3226-6
C3043 ¥2400E
9784785332266
定価（本体2400円＋税）
1923043024002

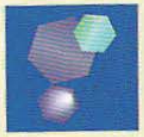

化学の指針シリーズ

超分子の化学

菅原 正
木村 榮一
共編

裳華房

化学の指針シリーズ
編集委員会 井上祥平・伊藤 翼・岩澤康裕
大橋裕二・西郷和彦・菅原 正

超分子の化学

菅原 正 木村 榮一 共編
菅原 正 村田 滋 堀 顕子 執筆

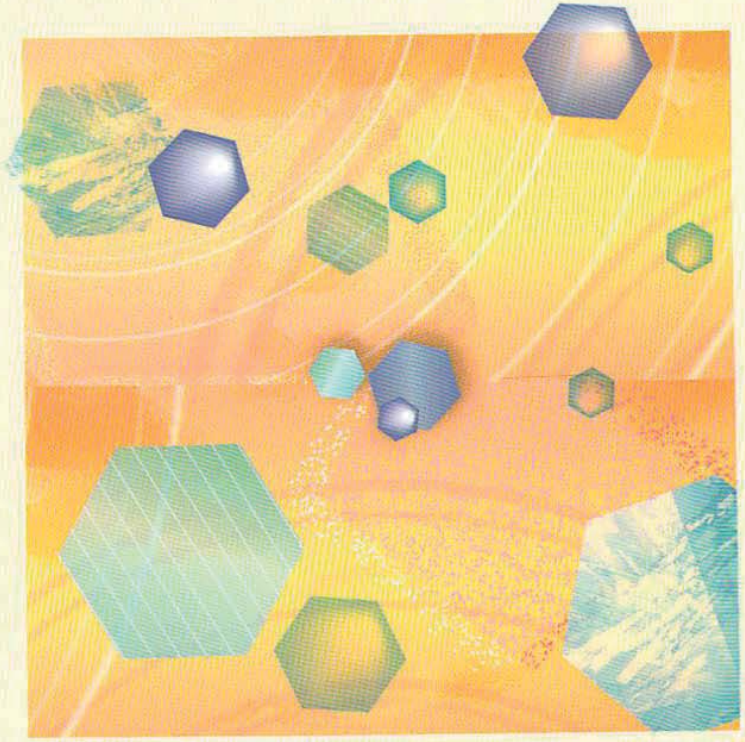

裳華房

化学の本だな

BOOK REVIEW

超分子化学の複雑さをシンプルな原理に立ち返って解説

超分子の化学
(化学の指針シリーズ)
菅原 正，木村榮一 編
菅原 正，村田 滋，堀 顕子 著
A5判，226頁，定価2520円
(裳華房)

超分子化学には，相間移動触媒や分子機械などのように，分子の組合せにより個々の分子の性質を超えた機能が発現するという面白さがある．超分子の複雑な構造やそれらが示す独特の現象には興味をそそられるものが多くあり，実際それらを概観できる本はすでにいくつか刊行されている．しかし，本書はそのような本とは趣旨が少し異なり，分子集合体の分野で活躍している著者らが，超分子の形成やその機能発現の「しくみ」の部分に焦点を当てて，超分子の化学を論じたものである．

化学者は，原子集合体である分子を，「もの」の理を知る最小単位として捉えている．経験豊富な化学者であれば，分子の構造(化学構造式)を見ただけで，その分子のもつ特徴を予測することができる．たとえば色素の設計は，分子軌道法が発達する以前から行われてきた．一方，分子が集合化すると，単分子とはまた違った性質が現れることもよく知られている．液晶はその代表例であり，分子集合体ならではの光学特性を発揮する物質である．そして超分子は，分子が集まったときにその特徴が際立つような物質である．

超分子は，化合物に抱く常識的なイメージを超えるものをわれわれに与えてくれる．超分子化学の先駆けとなったクラウンエーテルは，無機物である過マンガン酸カリウムをベンゼンに溶解させ，溶液を紫色に染めるといえば，驚く方もおられるのではないだろうか．クラウンエーテルの発見後，カテナンやロタキサンなどの物質も合成され，その特徴的な分子の動きを利用した分子機械，分子コンピュータという概念も生みだされている．

ところで，本書では超分子を「分子が集合体を形成することで，単独の分子からは想像もつかない性質や機能を示すもの」と定義している．そのため，クラウンエーテル，カテナン，ロタキサンなどの一般的な超分子に留まらず，分子性導電体や生体関連分子にまで話が及んでおり，その守備範囲はとても広い．にもかかわらず散漫な印象を与えないのは，一貫して超分子の形成や機能の「原理」を大切にする姿勢を崩していないからであろう．本書を読めば，超分子化学を理解するうえでの物理化学の大切さに気づかされるはずである．

超分子化学にはいろいろな役割がある．機能の多様性をうまく利用した新材料の開発や生命現象の分子論的理解などの研究は，今後もさかんに行われていくであろう．複雑さに特徴がある超分子化学の根底にはシンプルなしくみが存在する．本書はそれを知る機会を与えてくれる良書である．

評者：久保孝史
(大阪大学大学院理学研究科)

売れすじ理工書Best10 (5月1～31日，ジュンク堂書店京都店調べ)

1. 『統計学が最強の学問である データ社会を生き抜くための武器と教養』 西内啓 著，ダイヤモンド社，定価1680円
2. 『井田寛子の気象キャスターになりたい人へ伝えたいこと』 井田寛子 著，成山堂書店，定価1680円
3. 『研究発表のためのスライドデザイン 「わかりやすいスライド」作りのルール』 宮野公樹 著，講談社，定価945円
4. 『調査報告 チェルノブイリ被害の全貌』 アレクセイ・V．ヤブロコフ 他著，星川 淳 監訳，定価5250円
5. 『「死ぬのが怖い」とはどういうことか』 前野隆司 著，講談社，定価1575円
6. 『からだの中の外界 腸のふしぎ 最大の免疫器官にして第二のゲノム格納庫』 上野川修一 著，講談社，定価903円
7. 『この世はウソでできている』 池田清彦 著，新潮社，定価1260円
8. 『人類20万年 遥かなる旅路』 アリス・ロバーツ 著，野中香方子 訳，文藝春秋，定価1995円
9. 『ポケット図鑑 日本の昆虫1400 ②トンボ・コウチュウ・ハチ』 槐 真史 編，伊丹市昆虫館 監修，文一総合出版，定価1050円
10. 『ABC予想入門』 黒川信重，小山信也 著，PHP研究所，定価945円

2. **SPring-8（スプリング・エイト，Super Photon Ring 8GeV）**
http://www.spring8.or.jp/ja/

3. **ICDD ホームページ**
http://www.icdd.com/
○X線回折に関してはICDD（International Centre for Diffraction Data）にX線回折の講習会案内，粉末X線回折データ，デンバーX線会議など国際会議の案内が掲載されている．

4. **日本分析化学会ホームページ**
・日本分析化学会（http://www.jsac.jp/）
・X線分析研究懇談会（http://www.nims.go.jp/xray/xbun/）
○日本分析化学会X線分析研究懇談会の「研究懇談会」またはX線分析研究懇談会へ．X線分析討論会，X線回折講習会，「X線分析の進歩誌」など．

5. **アグネ技術センターホームページ**
・アグネ技術センター（www.agne.co.jp）
・X線分析の進歩誌（http://www.agne.co.jp/books/xray_index.htm）
○アグネ技術センター「X線分析の進歩誌」のバックナンバーの目次

6. **日本中性子科学会ホームページ**
http://www.jsns.net/jp/
○日本中性子科学会，国内中性子散乱施設の利用窓口一覧

第20章 熱分析法

本章について

熱重量測定（thermogravimetry：TG）と示差熱分析（differential thermal analysis：DTA），示差走査熱量測定（differential scanning calorimetry：DSC）は分析化学でよく用いられる熱分析手法である．TGでは，試料を温度変化させた際の質量の変化を測定するが，不活性雰囲気で測定すれば酸化を抑えた条件下での揮発性成分の揮発や有機成分の熱分解などが観測され，その後，空気中や酸素を含んだ雰囲気に切り替えると，さらに酸化分解が測定され，灰分が残る．質量減に伴う熱の出入りや発生気体を分析すればさらに情報が得られることになる．DTA，DSCでは試料の相転移や反応温度が，DSCではさらにその際の熱量，比熱の情報も得られる．本章では，TG，DTA，DSCの原理，装置，測定法，応用例を概説する．また初心者に参考となる標準物質や公定法についても触れる．

第20章

熱分析法

20.1 熱分析

迅速性と極微量での超高感度の分析技術が求められるのが最近の動向ではあるが，熱分析は分析手法としては，時間がかかり，mg 以上と比較的多くの試料を必要とし，感度もあまり高くない．分析と物性測定の中間に位置する手法ともいえる．一方で材料や環境関連分野において多用される手法でもある．熱分析とは，「物質の温度を一定のプログラムによって変化させながら，その物質のある物理的性質を温度（または時間）の関数として測定する一連の技法の総称」であり，物質にはその反応生成物も含まれる．広い意味では「温度変化させて測定する機器分析すべて」といえるが，以下にはこのうち分析化学で一般に用いられる手法として，**熱重量測定**（thermogravimetry：**TG**，TGA と表す場合もある）および**示差熱分析**（differential thermal analysis：**DTA**），**示差走査熱量測定**（differential scanning calorimetry：**DSC**）を中心に述べる．**表 20.1** に主な熱分析手法と得られる情報を示した．

「一定のプログラム」には，一定昇降温速度で制御する等速度熱分析（constant rate thermal analysis）のほか，正弦波や矩形波・三角波などの温度振動を加える測定も DSC を中心に多くなっている（温度変調 DSC）．また，物質の物理的性質の変化速度を制御するために，温度を制御する「試料制御熱分析（sample controlled thermal analysis：SCTA）または速度制御熱分析（controlled rate

表 20.1　主な熱分析手法と得られる情報

物理量（対象）	測定法	得られる情報
質量	熱重量測定：TG 発生気体分析：EGA	吸脱着，酸化，熱分解，蒸発，気化など 発生ガスの分析，反応，吸脱着，揮発など
温度	示差熱分析：DTA	転移温度，反応温度など
エンタルピー	示差走査熱量測定：DSC	転移温度・熱量，熱容量，反応温度・熱量
寸法	熱膨張測定	膨張係数，転移温度など
力学的特性	熱機械分析：TMA 動的粘弾性測定：DMA	膨張係数，転移温度，軟化温度など 弾性率，分子運動，緩和現象など

thermal analysis：CRTA)」と呼ばれる手法も，TG を中心に市販の装置にも装備されるようになってきた．この方法は微分信号を制御することにより，変化速度が一定になるように制御するものであり，複数の反応が連続して起こる場合に有効であり，分解能が向上するほか，新しい応用が期待されている．

熱分析装置は一般に，温度制御部，加熱炉部，物理量測定・変換部，制御システム部およびデータ処理部から構成され，制御システム部とデータ処理部は各装置に共通であることが多い．

最近は微小領域や微小試料での熱測定が AFM（原子間力顕微鏡）を利用した装置などで行われるようになってきている．

20.2 熱重量測定

20.2.1 熱重量測定で何が分かるか

標準試料にも使われることが多いシュウ酸カルシウム一水和物（$CaC_2O_4 \cdot H_2O$）を例に考えてみよう．空気中で加熱するとはじめに結晶水が脱離し，無水物となる．その後，一酸化炭素（CO）が脱離し，炭酸カルシウム（$CaCO_3$）となり，さらに

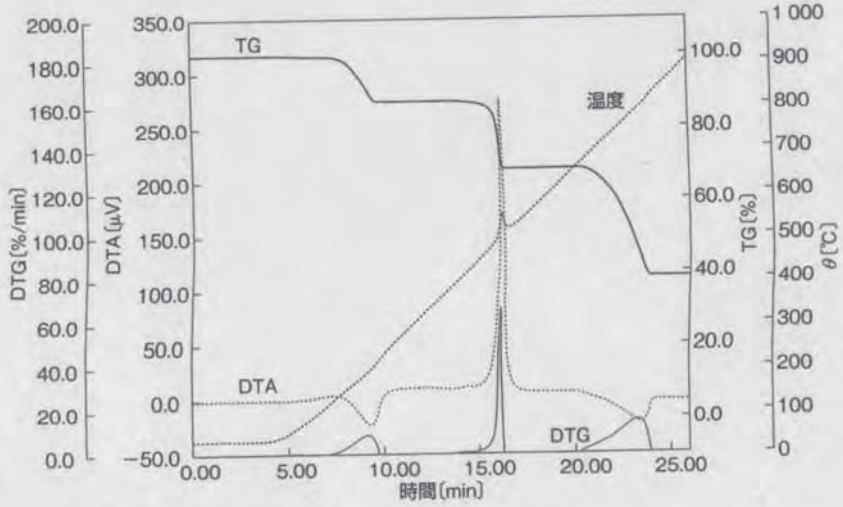

図 20.1　$CaC_2O_4H_2O$ の TG/DTA 測定結果

加熱すると酸化カルシウム（CaO）となる．**図 20.1** に空気中でのシュウ酸カルシウム一水和物の TG－DTA 測定結果を示した．式(20.1) で示した 3 段階に対応する質量減が観測される．測定結果では熱分解に伴う熱の出入り（DTA）も合わせて示してあるが，2 段目の質量減では発生した CO がすぐに空気中の酸素と化合して二酸化炭素となるため，大きな発熱ピークが観測されている．

$$CaC_2O_4 \cdot H_2O \longrightarrow CaC_2O_4 \longrightarrow CaCO_3 \longrightarrow CaO \qquad (20.1)$$

20.2.2 熱重量測定装置

試料の質量を温度または時間に対して連続的に測定する熱天秤と，熱天秤からの電気信号を制御する質量測定回路から構成される．熱天秤の構造は天秤と試料部との位置関係により，吊り下げ型，上皿型，水平型などに分類される．**図 20.2** に TG 装置の概略図を，**図 20.3** には各 TG 装置の名称と構造の概略を示した．装置は 1 000℃以上まで測定でき，高温での測定の際に生じるさまざまな要因による誤差を少なくするために基準物質を同時に測定する差動式を採ることが多い．

差動式の TG では DTA と同時測定できる装置が多い．質量変化量を微分することで微分熱重量（DTG）曲線が得られ，質量変化が連続して起こる場合などに有用である．DTG 信号を参照し，"質量の変化速度" を制御する SCTA では反応が起こっていない温度範囲では，設定した温度プログラムに従って試料温度が制御さ

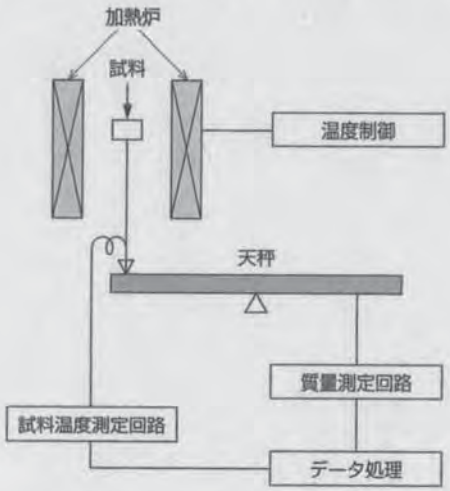

図 20.2 TG 装置の概略図

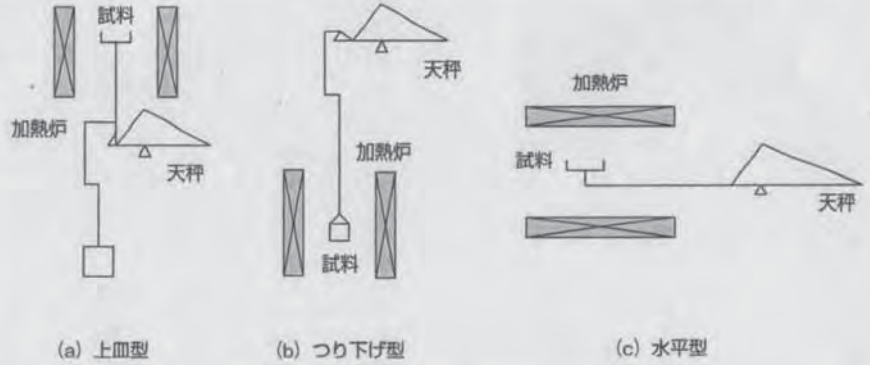

図 20.3 各種 TG 装置の名称と構造

れ，反応が開始すると DTG 信号を参照しながらプログラムに従って試料温度が制御される．SCTA ではこの他に等速度法や速度ジャンプ法，速度振動法などの制御方法がある．さらに測定中に発生したガス（発生気体）を逐次 IR（赤外吸収スペクトル）や MS（質量分析）に導入して分析する TG/IR，TG/MS などの**発生気体分析**（evolved gas analysis：EGA）も行われている．

20.2.3 熱重量測定の実際

測定温度範囲と試料の特性から試料容器の材質を選択し，基準物質として一般に同量程度の α アルミナを用いて，パージガスとして空気，窒素またはアルゴンを流しながら昇温測定する．試料は浅い容器に薄く，広く均一に詰め，一般には蓋はしない．試料量と昇温速度は測定結果を見て増減する．測定条件が決まったら装置が正しく作動していることを，標準試料を使って同一条件で測定して確かめる．

20.2.4 熱重量測定で用いられる標準物質

測定値の信頼性を確保するためには，温度目盛りと測定する物理量の校正が必要であり，熱重量測定では，温度と質量の校正となる．DTA との同時測定装置では，DSC，DTA と同様に純金属の融解温度を利用することができる．一方，TG 単独の装置では，天秤部の上方あるいは下方に磁石を置き，強磁性物質（Ni などの金属あるいは Ni-Co 合金など）試料を昇温測定する．キュリー温度（常磁性体に変化する温度）において，強磁性物質は磁石に引きつけられなくなるので，天秤部の下方に磁石をおいた場合は，見かけの質量増加が，天秤部の上方に磁石をおいた場

合は質量減少が生じることになる．

吊り下げ型の天秤では，温度校正用に用いられる純金属の線材におもりをつけて試料部に吊り下げ，純金属の融解によりおもりが落下する温度で校正することができる．**表 20.2** に 1 気圧のもとでの純金属の融点の例を示した．**図 20.4** には Al と Ag および Ni63/Co37 合金を同一試料容器に入れて磁石を装着した TG/DTA で測定した結果を示した．TG 曲線には Ni63/Co37 のキュリー温度付近で見かけの質量増加が観測され，DTA 曲線には 660℃付近に Al の融解による吸熱ピークと 960℃付近に Ag の融解による吸熱ピークがそれぞれ観測される．これらの校正に用いる標準試料は 99.99％以上の純物質を使用するが，認証標準物質もいくつかの

表 20.2　1 気圧のもとでの純金属の融点の例

金属	融点〔℃〕
In	156.61
Sn	231.9681
Pb	327.5
Zn	419.58
Al	660.37
Ag	961.93
Au	1064.43

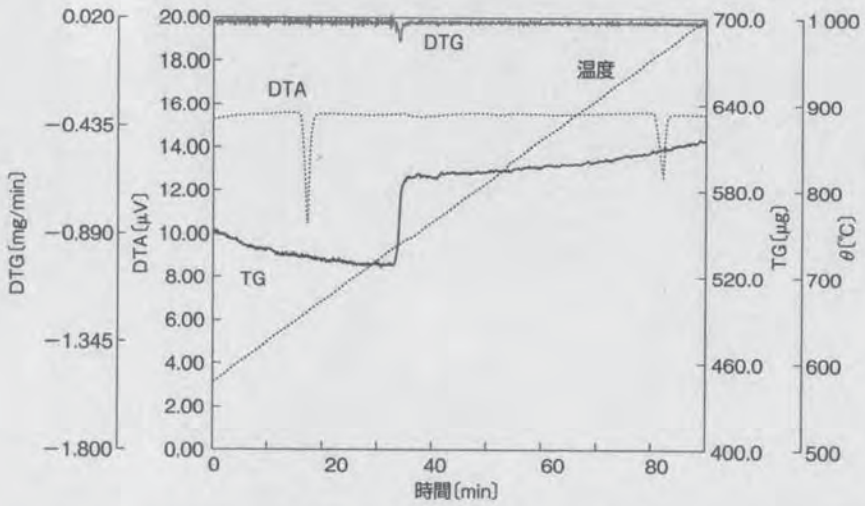

図 20.4　Al，Ag，Ni63/Co37 の TG/DTA 測定結果

国家計量標準研究機関から供給されている．

TG 信号（質量）校正は，簡便法として試料部に基準分銅を加除し，そのときの質量変化によるが，より実際的な校正として熱分解による質量変化が既知の物質の測定結果を用いることもできる．第 16 改正日本薬局方では，基準分銅による校正を第一次校正とし，第二次校正として測定中の雰囲気ガスによる浮力および対流などの質量測定への影響を除くために，シュウ酸カルシウム一水和物標準品を 10 mg 用いて，5℃ /min で 250℃まで乾燥空気または窒素一定流量下（つり下げ形 40 mL/min，その他 100 mL/min）で昇温測定することとしている．

20.2.5　熱重量測定の応用例

熱重量測定は温度を変化させた際に質量が変化する現象すべてを対象とするため，測定対象とする物質は多岐にわたる．また製造工程で発生するガスや室内空気汚染物質の吸脱着評価など環境面で利用される測定手法でもある．さらに材料や製品の劣化解析には不可欠な手法である．**図 20.5** は備長炭に吸着した *p*-キシレンと香料の脱離過程を測定した TG-MS のデータである．香料の方が低温から脱離していることが分かる．**図 20.6** には汎用ポリマーであるポリエチレングリコールを 1～20℃ /min の各昇温速度で測定した結果を重ねて示した．昇温速度が速くなるに従って熱分解温度が高温側にずれていくのが分かる．このような結果を用いて材料の寿命予測などを行うこともある．

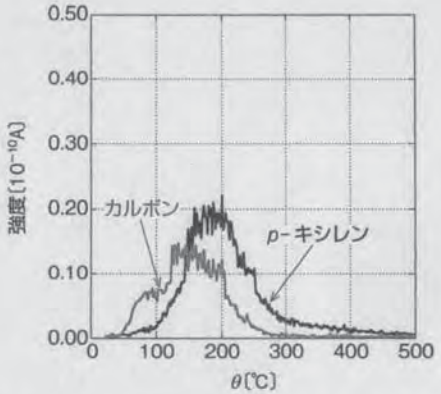

図 20.5　備長炭に吸着したカルボン（香料）と *p*-キシレンの TG-MS 測定結果の例

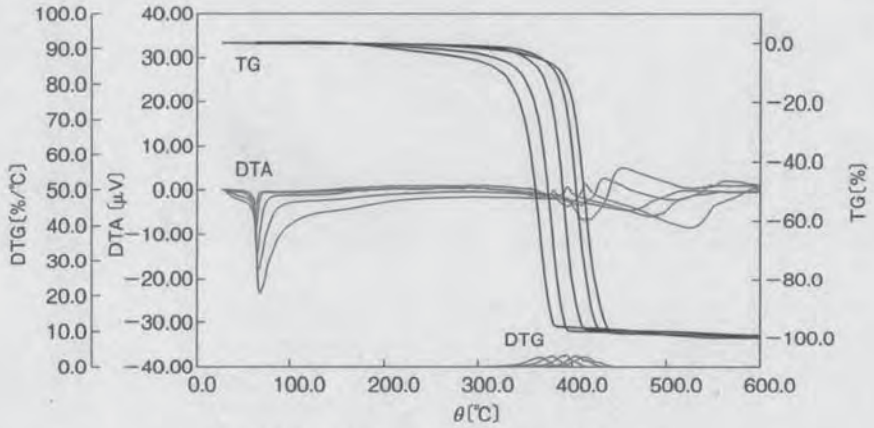

図 20.6 PEG6000 の TG/DTA 測定結果

（昇温速度 1，2，5，10，20℃/min）

20.2.6 熱重量測定を用いる公定法の例

熱重量測定は日本工業規格（**JIS**）や日本薬局方に採用されている．JIS には基本規格（用語，記号，単位などを規定したもの），方法規格（試験，分析，検査および測定の方法などを規定したもの），製品規格（製品の形状，寸法，材質，品質，性能，機能などを規定したもの）があり，毎年約 10 000 件が制定・改正・見直しがなされている．化学分野の JIS は 1 700 件以上と最大の件数であるが，なかでもゴム・プラスチックは件数が多い．商取引以外でも製品や原料の分析の際に JIS に制定されている分析法が参考になることは多い．熱重量測定を用いる分析法の JIS はゴム，プラスチック，分野で規定されている．2005 年に改正された熱分析通則では用語の定義，装置構成，操作方法，データの質の管理についての詳細が規定されている．**表 20.3** に熱重量測定を用いた測定法に関する JIS を通則とともに示した．

第 16 改正日本薬局方には，一般試験法の物理的試験法に「2.52 熱分析法」の記載があり，DTA，DSC と TG が取り上げられ，装置・操作法・装置の構成について記載されている．TG は「2.41 乾燥減量試験法」の別法として，また揮発性成分が水分のみの場合は「2.48 水分測定法」の別法として用いることができる．

表 20.3 熱分析通則と TG を用いた JIS の例

規格 No.	名称
JIS K 0129	熱分析通則
JIS K 6226-1	ゴム－熱重量測定による加硫ゴムおよび未加硫ゴム組成の求め方（定量）－ 第1部：ブタジエンゴム，エチレンプロピレンゴムおよびターポリマー，ブチルゴム，イソプレンゴム，スチレンブタジエンゴム
JIS K 6226-2	ゴム－熱重量測定による加硫ゴムおよび未加硫ゴム組成の求め方（定量）－ 第2部：アクリロニトリルブタジエンゴム（NBR，XNBR，HNBR）およびハロゲン化ブチルゴム
JIS K 7120	プラスチックの熱重量測定方法

20.3 示差熱分析・示差走査熱量測定

20.3.1 示差熱分析・示差走査熱量測定で何が分かるか

ミネラルウォーターなどの PET ボトルを例に考えてみよう．徐々に加熱していくと柔らかくなり，さらに加熱を続けると 260℃位で融解する．融解した PET 試料は急冷して再度加熱するとどうなるだろうか．**図 20.7** には DSC の測定例を示

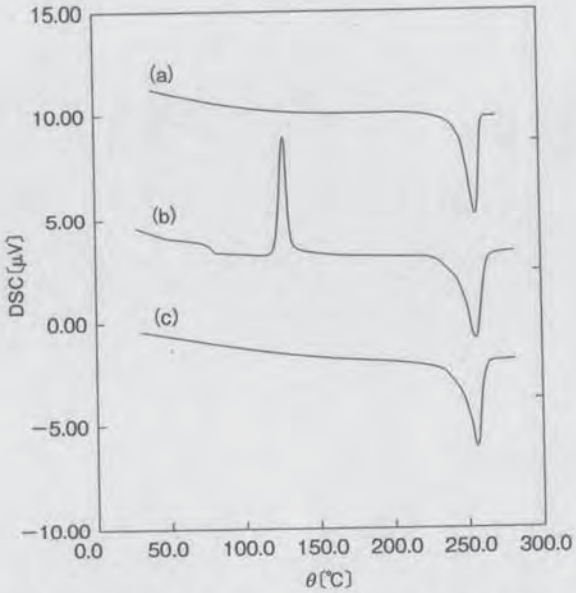

図 20.7 熱履歴の異なった PET の DSC 曲線

(a) 切り出し後未処理，(b) 融解後急冷，(c) 融解後炉内徐冷

した．切り出した試料を測定すると，260℃付近での融解による吸熱ピークのみが明瞭に観測されるが，融解後急冷した試料では70～80℃にかけてのガラス転移によるベースラインの吸熱側へのシフト，130℃付近での結晶化による発熱ピークも明瞭に観測される．融解後徐冷した試料では融解ピークのみが明瞭に観測され，熱履歴を反映した測定データが得られることが分かる．

20.3.2 示差熱分析装置・示差走査熱量計

図20.8にはDTA装置の概略と，PET測定時の加熱炉・試料・基準物質温度変化およびそのとき得られるDTA曲線を示した．装置は試料と基準物質との間の温度差および試料の温度を測定する測温部からなる．測温部には熱電対が使用されることが多い．DSC装置には，入力補償DSC装置と熱流束DSC装置がある．**図20.9**に入力補償DSC装置と熱流束DSC装置の概略を示した．

入力補償DSC装置は試料と基準物質の温度を測定する測温部，試料および基準物質に加える熱エネルギーの発生源，試料および基準物質の温度が等しくなるように制御する熱量補償回路から構成されている．一方，熱流束DSC装置は試料と基準物質との間の温度差および試料の温度を測定する測温部から構成され，試料と基準物質の温度差は単位時間当たりの熱エネルギーの入力差に比例するようになって

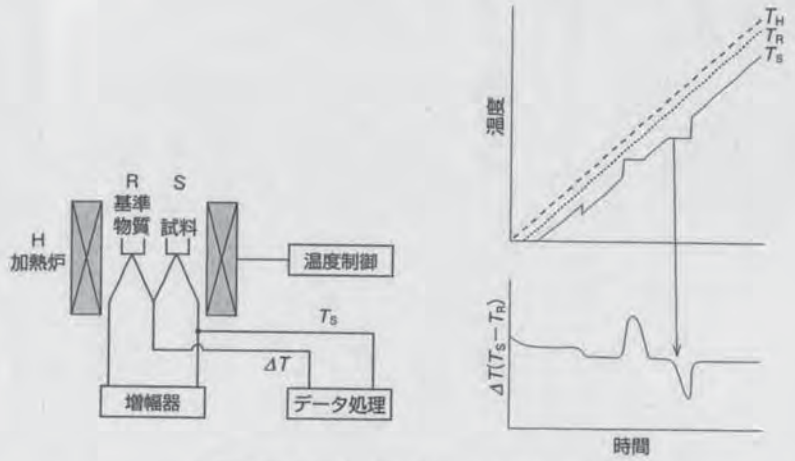

図20.8 DTA装置の概略と測定原理

DTA装置の概略（左）とPET測定時の加熱炉・試料・基準物質温度変化（右上）とDTA曲線（右下）

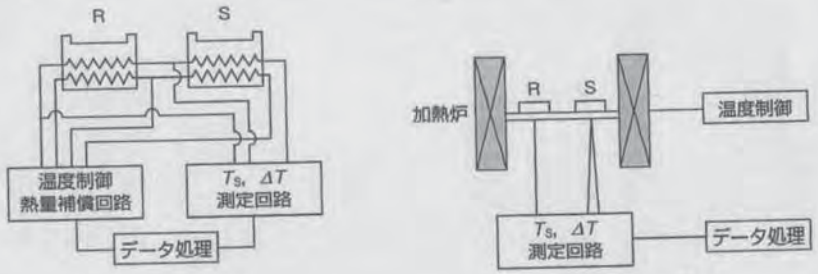

(a) 入力補償DSC　(b) 熱流束DSC

図20.9 DSC装置の概略

いるため，熱量の定量性があるDTA，DSC信号の変化量を微分することで微分DTA（またはDSC）曲線が得られ，変化が見やすくなることが多い．またX線回折やFT-IRと同時測定できる装置もある．

20.3.3 示差熱分析・示差走査熱量測定の実際

測定目的・測定温度範囲と試料の特性から試料容器の材質を選択する．溶液試料や揮発性の試料では密封型の試料容器を用いる．**表20.4**にDSCで用いられる試料容器の例を示した．基準物質としては測定温度範囲で変化のない物質を用い，固体試料ではαアルミナが用いられることが多く，溶液試料では溶媒を用いることもある．試料は浅い容器に薄く，広く均一に詰め，容器底面に押さえつけるように

表20.4 DSC，DTAで用いられる試料容器の例

種類	材質（耐圧10^5Pa）	用途
開放型	Al	通常のDSC測定に用いる，600℃以下
	Pt	600℃以上，金属の測定は合金生成に注意 Ptの触媒作用に注意
	アルミナ	600℃以上，Ptと反応性のある試料に用いる，熱伝導悪い
	石英	
密閉型	Al（30）	溶液，分解ガスを発生する試料に用いる
	Ag（50）	水溶液やAlと反応する試料に用いる
	SUS（50）	Al，Agと反応する試料，危険物（自己反応性）に用いる
簡易密封型	Al（3）	分解ガスを発生する試料に用いる
	表面処理Al（3）	水分を含む試料に用いる

し，一般に蓋をして，窒素やアルゴンなどを一定流量で流しながら測定する．試料量と昇降温速度は測定結果を見て増減する．測定条件が決まったら装置が正しく作動していることを，標準試料を使って同一条件で測定して確かめる．示差走査熱量測定では一般に測定温度範囲を熱分解温度以下とする．

20.3.4 示差熱分析，示差走査熱量測定で用いられる標準物質

熱重量測定の項で述べた純金属の融解温度が用いられることが多いが，示差走査熱量測定では熱量の校正も必要となる．さらに室温以下の測定を行うことも多いため，低温で使用できる標準物質も必要となる．**表 20.5** には DSC 用標準物質の例を示した．この他にも安息香酸やナフタレンなどの純度のよい有機物質が用いられることもある．これらの標準物質は認証標準物質として代表的な国家標準機関である NIST *1（USA），PTB *2（ドイツ），LGC *3（英国），NMIJ *4/AIST *5（日本）などから供給されている．いずれも保管に気をつけ，純金属では表面層をのぞいて使用する．

表 20.5 DSC 校正用の標準物質の例

物質	相転移温度	相転移エンタルピー
In（融解）	156.61 ℃	3 296 J mol^{-1}
Sn（融解）	231.92 ℃	7 187 J mol^{-1}
Pb（融解）	327.47 ℃	4 765 J mol^{-1}
Zn（融解）	419.53 ℃	7 103 J mol^{-1}
Al（融解）	660.22 ℃	10 827 J mol^{-1}
シクロヘキサン（固-固）	−86.97 ℃	6 264 J mol^{-1}
シクロヘキサン（融解）	6.71 ℃	2 492 J mol^{-1}

20.3.5 示差熱分析・示差走査熱量測定の応用例

融解などの相転移に基づく試料の熱的な変化の温度，DSC ではそのエネルギー変化の大きさの測定に用いられるため，測定対象は有機・無機化合物，金属，高分子，ゴム，生体分子，医薬品，食品，生物試料など多岐にわたる．また比熱の測定や，医薬品など有機物質の純度の測定にも用いられる．比熱測定用，純度測定用の標準物質も NIST から供給されている．

*1 NIST（National Institute of Standards and Technology：米国国立標準技術研究所）
*2 PTB（Physikalisch-Technische Bundesanstalt：ドイツ物理工学研究所）
*3 LGC（Laboratory of the Government Chemist：英国政府化学研究所）
*4 NMIJ（National Metrology Institute of Japan：計量標準総合センター）
*5 AIST（National Institute of Advanced Industrial Science and Technology：産業技術総合研究所）

20.3.6 示差走査熱量測定を用いる公定法の例

DSC を用いる測定法の JIS はプラスチック，ゴム，金属分野に多い．**表 20.6** に JIS の例を示した．JIS では試料の採取や測定条件について詳細に定められていることが多い．例えば試験片は，JIS K 7121，7122，7123 では，直径または各片の長さが 0.5 mm 以下の場合はそのまま使用し，それ以上の場合は 0.5 mm 以下に切断する．厚さが 0.5 mm 以下のシートおよびフィルムは容器に合わせて無理なく入るように切断し，薄く切れるものは 0.5 mm 以下の厚さに切った後，容器に合わせて無理なく入るように切断する．

質量は①融解，結晶化温度の測定では約 5 mg を，ガラス転移温度の測定では約 10 mg をそれぞれ 0.1 mg まで，②転移熱の測定では 5〜10 mg を 0.01 mg まで，③比熱容量の測定では 5〜15 mg を 0.01 mg までそれぞれはかり取ることとなっている．JIS K 6240 では試料の中心部を取り出し，10〜20 mg をはかり取ることとなっている．さらに JIS K 7121，7122，7123 では，容器への充填方法についても詳細な記述がある．これらの記述は試験片相互，試験片と容器，容器とホルダーとの熱接触をよくするために重要な事項であり，初心者にとって大変参考になる記述である．

表 20.6 DSC を用いた JIS の例

規格 No.	名称
JIS H 7101	形状記憶合金の変態点測定方法
JIS H 7151	アモルファス金属の結晶化温度測定方法
JIS K 6240	原料ゴム−示差走査熱量測定（DSC）によるガラス転移温度の求め方
JIS K 7095	炭素繊維強化プラスチックの熱分析によるガラス転移温度測定法
JIS K 7121	プラスチックの転移温度測定法
JIS K 7122	プラスチックの転移熱測定方法
JIS K 7123	プラスチックの比熱容量測定方法
JIS R 1672	長繊維強化セラミックス複合材料の示差走査熱量法による比熱容量測定方法
JIS Z 3198-1	鉛フリーはんだ試験方法−第1部：溶融温度範囲測定方法

演習問題

Q.1 DSC測定において以下の各操作を行った．正誤を○×で示し，その理由を述べよ．

(1) ピークが小さかったので試料量を減らした．
(2) ピークが小さかったので試料と容器の密着性を上げた．
(3) 隣接する2つのピークが一部が重なっていたのでピークの分離をよくするために走査速度を速くした．

Q.2 シュウ酸カルシウム一水和物のTG測定を1000℃まで行ったところ，3段階の質量減が観測された．それぞれどのような反応に対応する質量減か，また各段階における質量%を予測せよ．

Q.3 熱分析で用いる試料容器について記した以下の(1)～(4)について間違っているものを選び，その理由を述べよ．

(1) 1000℃までTG測定するためにはAlの試料容器を用いるのがよい．
(2) DSCでは一般に試料容器に蓋をしないで測定する．
(3) 試料および生成物と反応しない材質の試料容器を選択する．
(4) できるだけ熱伝導性のよい試料容器を選択する．

Q.4 TG測定について述べた以下の(1)～(3)について間違っているものを選びその理由を述べよ．

(1) TG測定では測定温度範囲が広いので，測定目的にかかわらずなるべく早い昇温速度で測定するのがよい．
(2) TG測定を行う際，腐食性のガスが発生しないことが分かっているので，パージガスを流さずに測定した．
(3) 詳細が不明な金属の測定をTGで行う際にアルミナ製の試料容器を用いた．

Q.5 DSCを用いるプラスチックのJISでは試料の厚さを0.5 mm以下とすることと記されているが，この理由を述べよ．

参考図書

1. 小澤丈夫，吉田博久 編：最新熱分析，講談社サイエンティフィック（2005）
2. 日本熱測定学会 編：熱量測定・熱分析ハンドブック 第2版，丸善（2010）
3. 日本化学会 編：第5版実験化学講座6 －温度・熱，圧力－，丸善（2006）

4. 日本分析化学会 編，齋藤一弥，森川淳子 著：分析化学実技シリーズ 機器分析 編 13，熱分析，共立出版（2012）

ウェブサイト紹介

1. **日本熱測定学会**
   http://www.netsu.org/j+/hpmain0.html

2. **日本熱物性学会**
   http://www.netsubussei.jp/index.html

3. **産総研 NMIJ（計量標準総合センター）**
   http://www.nmij.jp/
   ○標準物質についての情報．

4. **ICTAC（国際熱測定連合）**
   http://www.ictac.org/

5. **JISC（日本工業標準調査会）**
   http://www.jisc.go.jp/
   ○JISの検索ができる．

Journal of Photochemistry and Photobiology C: Photochemistry Reviews 17 (2013) 1–25

Contents lists available at SciVerse ScienceDirect

Journal of Photochemistry and Photobiology C: Photochemistry Reviews

journal homepage: www.elsevier.com/locate/jphotochemrev

Invited review

Photobiological hydrogen production: Bioenergetics and challenges for its practical application

Hidehiro Sakurai[a,*], Hajime Masukawa[b], Masaharu Kitashima[c], Kazuhito Inoue[c]

[a] Research Institute for Photobiological Hydrogen Production, Kanagawa University, Tsuchiya, Hiratsuka, Kanagawa 259-1293, Japan
[b] JST, PRESTO, 4-1-8 Honcho, Kawaguchi, Saitama 332-0012, Japan
[c] Department of Biological Sciences, Kanagawa University, Tsuchiya, Hiratsuka, Kanagawa 259-1293, Japan

ARTICLE INFO

Article history:
Received 30 January 2013
Received in revised form 25 May 2013
Accepted 30 May 2013
Available online 10 June 2013

Keywords:
Chlamydomonas
Cyanobacteria
Hydrogen
Photosynthesis
Purple bacteria

ABSTRACT

Photobiological production of hydrogen is considered to be one of the most promising technologies for replacing or complementing fossil fuel-derived energy. This review focuses on the bioenergetics of photobiological hydrogen production by various phototrophs, namely purple non-sulfur bacteria, green sulfur bacteria, cyanobacteria, and green algae. We discuss the improvements in hydrogen production efficiency and the advances in related technologies that are needed before phototrophs can be used for economically-viable hydrogen production. We also discuss some technological aspects such as the cost of nutrients and bioreactors, which should be taken into consideration in designing future plans for the application of photobiological hydrogen production.

© 2013 Elsevier B.V. All rights reserved.

Contents

1. Introduction 02
2. Energy conversion in photochemical reactions and enzymes of H_2 production 03
   2.1. Photochemical reaction centers and linked e^- transport systems 03
   2.2. Ferredoxin and flavodoxin 04
   2.3. Quinone pools 04
   2.4. Electron transport chains 04
   2.5. Proton-motive force and ATP synthesis 04
      2.5.1. Membrane-bound ATP synthase 04
      2.5.2. H^+/ATP ratio in ATP synthesis 05
      2.5.3. Transhydrogenase and NADPH/$NADP^+$, NADH/NAD^+ redox couples 05
      2.5.4. Hydrogen and NAD(P)H 05
   2.6. The enzymes of H_2 production 06
      2.6.1. Hydrogenases 06
      2.6.2. Nitrogenase 07
3. H_2 production by living organisms 08
   3.1. Purple bacteria 08
      3.1.1. Photobiological H_2 production by purple non-sulfur bacteria 08
      3.1.2. N_2ase-based H_2 production with various organic substances serving as e^- sources 08
      3.1.3. Comparison with dark fermentative H_2 production 09
      3.1.4. Ferredoxin/flavodoxin reduction in PNS bacteria 10
      3.1.5. Optimizing photobiological H_2 production by purple non-sulfur bacteria 10

Abbreviations: BChl, bacteriochlorophyll; Chl, chlorophyll; Fd, ferredoxin; Fld, flavodoxin; FNR, ferredoxin-$NADP^+$ reductase; H_2ase, hydrogenase; N_2ase, nitrogenase; Ndh, NADH dehydrogenase; MQ, menaquinone; MQH_2, menaquinol; pmf, proton-motive force; PNS, purple non-sulfur; PQ, plastoquinone; PQH_2, plastoquinol; PS I, photosystem I; PS II, photosystem II; PTOX, plastoquinol terminal oxidase; RC, reaction center; UQ, ubiquinone; UQH_2, ubiquinol.

* Corresponding author. Tel.: +81 463 59 4111; fax: +81 463 58 9684.
E-mail address: sakurai@waseda.jp (H. Sakurai).

1389-5567/$20.00 © 2013 Elsevier B.V. All rights reserved.
http://dx.doi.org/10.1016/j.jphotochemrev.2013.05.001

3.2. Green sulfur bacteria 12
3.3. Cyanobacteria 13
3.3.1. Heterocyst-forming cyanobacteria 13
3.3.2. Filamentous non-heterocystous cyanobacteria 13
3.3.3. Unicellular cyanobacteria 13
3.3.4. H_2ase-based H_2 production by cyanobacteria 16
3.4. Green algae 16
3.4.1. *Chlamydomonas* 16
4. Need for further improvements 17
4.1. Energy conversion efficiency 17
4.2. A selection of proposed strategies for improving photobiological H_2 production 18
4.2.1. Improvement of H_2ase 18
5. Need for cost reductions 19
5.1. Bioreactors and storage 19
5.2. Cost of nutrients 20
5.2.1. Filling gas for N_2-based H_2 production 20
6. Future prospects 20
6.1. Achieving the target of solar energy conversion to H_2 20
6.1.1. Using the price of corn to gauge the performance of modern agriculture 20
6.1.2. Targeting improved photobiological H_2 production efficiency by optimizing solar energy conversion 20
6.1.3. Targeting H_2 price 21
7. Concluding remarks 21
Acknowledgments 21
References 21

Hidehiro Sakurai is an Emeritus Professor, Waseda University, Tokyo, and a Guest Research Fellow, Research Institute for Photobiological Hydrogen Production, Kanagawa University, Hiratsuka, Japan. He was graduated from the Department of Botany, and the Graduate Course of Biochemistry and Biophysics, University of Tokyo (PhD. 1966). He was a Professor, Department of Biology, School of Education, Waseda University (1976-2006). He stayed in Dr. A. San Pietro's laboratory for one year in the late 1970s. In Waseda University, he was the Director of the Environmental Safety Center (1995-1999) and the Director of the Research Institute for a Sustainable Future. He was a Guest Professor, Kanagawa University (2006-2012). His research areas include: photophosphorylation, photosystem I (iron-sulfur clusters), green sulfur bacteria (reaction center, electron transport components, and inorganic sulfur metabolism), and photobiological hydrogen production by cyanobacteria.

Hajime Masukawa is a researcher at JST, PRESTO and a visiting researcher at Kanagawa University. He received his Dr. Sci. degree in Waseda University in 2003. He graduated from Waseda University, Department of Physics, Science and Engineering in 1998. His research interests include photobiological hydrogen production by nitrogenase of cyanobacteria and regulation of heterocyst differentiation.

Masaharu Kitashima is a researcher at Research Institute for Integrated Science, Kanagawa University. He graduated from Department of Biological Sciences, Faculty of Science, Kanagawa University (BSc, MSc) and obtained Ph.D. degree in Biological Sciences from Kanagawa University (2012). His main research area is photobiological hydrogen production by cyanobacteria.

Kazuhito Inoue is a professor of Department of Biological Sciences and a director of Research Institute of Photobiological Hydrogen Production at Kanagawa University, Hiratsuka, Japan. He received his B. Sc. in 1984 and Ph. D degree in 1989 from Waseda University. He was appointed research associate of Department of Biological Sciences at Kanagawa University in 1989, and promoted associate professor in 1999. Since 2005, he has been a professor at Kanagawa University. He also worked as a visiting scientist at Indiana University at Bloomington (1993-1994, and 1996), and a visiting associate professor (2002-2006) and visiting professor (2006-2008) at The University of Tokyo. His research interest concerns with photosynthetic electron transport system as well as biosynthesis of photosynthetic pigments.

1. Introduction

The global human population has an acute need for renewable energy sources in order to mitigate the global climate change caused by increasing green-house gases in the atmosphere and to keep up with the dwindling fossil fuel supplies. According to one of the scenarios presented in the Intergovernmental Panel on Climate Change's (IPCC) 4th Assessment Report "Climate Change" [327], in order to mitigate the dangerous effects of anthropogenic warming, we must reduce global CO_2 emission from fossil fuels by about 50% of present levels by 2050. The more economically-advanced countries will be required to achieve more severe reductions. An upcoming 5th Assessment Report by the IPCC is scheduled to be published in 2014 and will provide more in-depth analyses. In order to achieve the significant reductions of CO_2 emissions called for in the IPCC report, the adoption of large-scale solar energy-based technologies seems to be among the most promising strategies (Table 1) in terms of meeting energy demands.

Considering that our current consumption of fossil fuels is about 20 times greater than our energy derived from foods, we cannot expect much additional energy production from agricultural land-based energy crops. Even if we had additional arable land available to produce energy crops alongside food crops, and energy crops were as productive as food crops in terms of the quantity of available energy, this theoretical energy crop production would meet only 5% of our current fossil fuel energy demand. Therefore, even with new crops grown exclusively for energy production, the amount of energy feasibly produced from our agricultural lands

Table 1
Global energy consumption.

Items	(10^{18} J yr^{-1})	Ratio[b]	Ratio[c]
Fossil fuel energy consumption (2010)[a]	431	1	20
Solar energy received on Earth' surface	2700000	6300	120000
Human digestive energy intake[d]	22	0.05	1

[a] IEA 2012 Key World Energy Statistics [328].
[b] Ratio to Fossil fuel energy consumption (2010).
[c] Ratio to Human digestive energy intake.
[d] World population: 7100000000, Digestive energy: 2000 kcal/day.

simply cannot replace the energy currently derived from fossil fuels. Some additional energy from land-based crops may be available via the improved utilization of current agricultural waste such as stovers from row crops and other by-products from forestry. Mariculture-raised phototrophs may be another available energy source [1,2].

Photobiologically-produced hydrogen (H_2) is considered to be an attractive renewable energy source candidate for a number of reasons: (1) The amount of solar energy is vast in quantity, (2) Fuel cells powered by H_2 are expected to be energetically the most efficient for power generation with minimal pollution; the final by-product is H_2O, and (3) In contrast to electricity produced by windmills, H_2 is easily stored and transported from overseas. In response to the immediate needs for renewable energy sources and given the promise of technologically and economically feasible large-scale photobiological H_2 production, there has been a marked increase in the number of research projects and accompanying publications devoted to the topic of photobiologically-produced H_2 [3–13].

Phototrophs utilize solar energy for H_2 production either with H_2O as the e^- donor (autotrophic photobiological H_2 production) or with various organic substances such as saccharides, organic acids, etc. (heterotrophic photobiological H_2 production). The organic substrates are derived from photosynthetic products, and the entire process is carbon neutral because CO_2 has been absorbed in the preceding reactions of photosynthesis. Since the early proposals of renewable photobiological H_2 energy production [14–16], much progress has been made in photobiological H_2 production with research focusing on optimization through the use of various types of organisms under a variety of production schemes. However, additional research and development of the biological aspects as well as the supporting energy production technology is needed before photobiological H_2 production is put into actual practice. This review considers photobiological H_2 production utilizing living phototrophic organisms. The artificial photobiological H_2 production strategies that utilize some parts of photosynthesis incorporated into processed materials, for example artificial films with embedded phototrophic microorganisms or inorganic substrates embedded with reaction centers, etc., [17–21] will not be considered in principle.

2. Energy conversion in photochemical reactions and enzymes of H_2 production

2.1. Photochemical reaction centers and linked e^- transport systems

Light energy absorbed by antenna pigments such as chlorophylls (Chl), bacteriochlorophylls (BChl), carotenoids, phycobilins (present in cyanobacteria), etc., is transferred by excitation energy transfer to the primary e^- donors (P840, P700, P680, P870, etc., which are dimers of Chls or BChls bound to proteins [22]) of the reaction centers (RCs), and finally converted to redox energy. RCs are composed of pigment protein complexes binding several e^- transfer cofactors. The RCs are divided into two groups, namely Type I and Type II, according to their functional characteristics and the e^- carriers bound to them (Fig. 1, Table 2).

Type I include the RCs found in green sulfur bacteria [23], heliobacteria [23], and Photosystem I (PS I) [24–26] found in cyanobacteria, and chloroplasts of algae and land plants, etc. Type II includes the RCs found in purple bacteria [27], and green

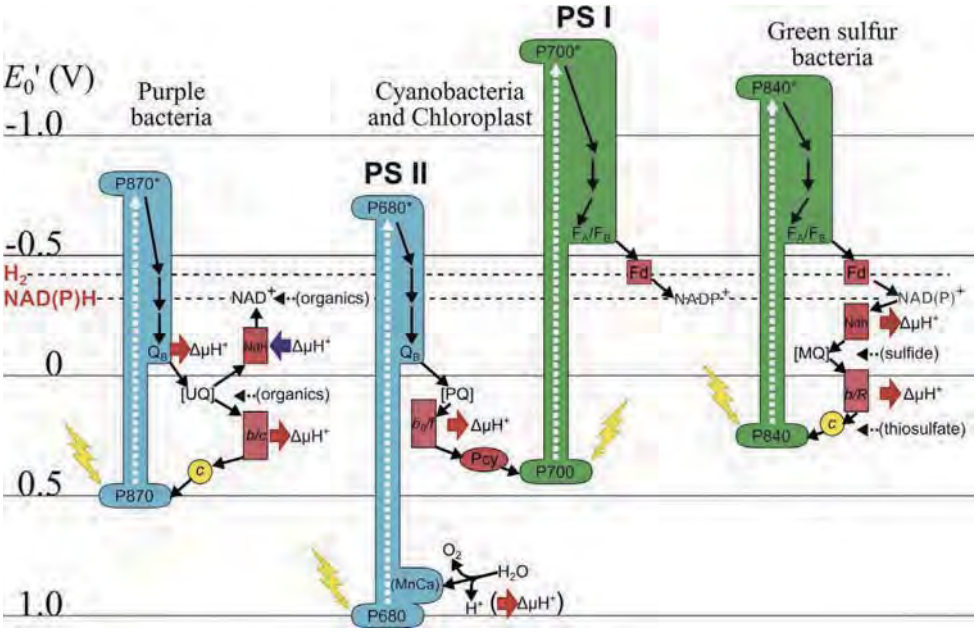

Fig. 1. Reaction centers and e^- transport systems of phototrophic microorganisms. Type I reaction center (green), Type II reaction center (blue), $\Delta\mu H^+$: proton-motive force, *b*/*c*: cytochrome *b*/*c* complex, *c*: cytochrome *c*, F_A/F_B: iron-sulfur cluster A and B bound to the reaction center, Fd: ferredoxin, MnCa: water oxidizing cluster of Mn_4-Ca-O_5, MQ: menaquinone, Ndh: NADH dehydrogenase, P870, P840, P680, and P700: special chlorophyll or bacteriochlorophyll pairs in the reaction center, with*: excited special pairs. Pcy: plastocyanin, PQ: plastoquinone, Q_B: quinone temporarily bound to the reaction center, UQ: ubiquinone. For chlorophyll, bacteriochlorophyll, and quinones bound to the reaction centers, see [22].

Table 2
Components of reaction centers and photosynthetic electron transport chains.

	Organisms/Organelle	RC special pair (pigments)	Redox energy (eV)	Bound e^- acceptors	External e^- acceptor	Immediate e^- donor to RC special pair
Type I	Green sulfur bacteria	P840 (BChl a')$_2$	1.48	Chl *a*, MQ, Fe-$S_{X,A,B}$	Fd	cyt *c* (bound)
(PS I)	Cyanobacteria	P700 (Chl *a* and Chl a')	1.74	Chl *a*, PhylloQ, Fe-$S_{X,A,B}$	Fd/Fld	Plastocyanon/cyt c_6 (soluble)
(PS I)	Chloroplasts	P700 (Chl *a* and Chl a')	1.74	Chl *a*, PhylloQ, Fe-$S_{X,A,B}$	Fd/Fld	Plastocyanin (soluble)
Type II	Purple bacteria	P870 (BChl *a*)$_2$	1.44	BPheo *a*, $UQ_{A,B}$	UQ	cyt *c* (soluble or bound)
(PS II)	Cyanobacteria and chloroplasts	P680 (Chl *a*)$_2$	1.78	Pheo *a*, $PQ_{A,B}$	PQ	Mn_4-Ca-O_5 cluster (bound)

Abbreviations: Bpheo, bacteriopheophytin; Chl, chlorophyll; Fd, ferredoxin; Fe-S, iron-sulfur cluster; Fld, flavodoxin; MQ, menaquinone; Pheo, pheophytin; UQ, ubiquinone. For BChl a' and Chl a', epipers of Bchl *a* and Chl *a*, see [22].

filamentous bacteria (*Chloroflexaceae*), Photosystem II (PS II) found in cyanobacteria, and chloroplasts of algae and land plants, etc. [24,28–31] (Fig. 1). The amino acid sequences of the RC proteins are homologous across species within the same type of RC. Among various species of RCs, the oxidation–reduction potential (E_0') difference generated by the photochemical reaction is a function of the absorption wavelength (λ) of the primary donors: $hc\,\lambda^{-1}$, where *h* is the Planck's constant and *c* is the speed of light (about 3×10^8 m s^{-1}). For example, P700 generates a redox potential difference of 1.77 eV, or about 171 kJ mol^{-1} (for energy conversion of photosynthesis, see [32]).

2.2. Ferredoxin and flavodoxin

The photochemical reaction of Type I RC reduces a low potential iron-sulfur protein ferredoxin (Fd), which in turn donates e^-s to a variety of different molecules, depending on the species, examples include Fd-$NADP^+$ oxidoreductase (also called Fd-$NADP^+$ reductase, FNR[1]), some types of hydrogenase (H_2ase), nitrogenases (N_2ase), thioredoxin reductase, nitrite reductase, etc. In purple bacteria, cyanobacteria and green algae, a flavoprotein called flavodoxin (Fld) with FMN as the cofactor is sometimes present as an apparent replacement for Fd [33]. The redox potential at pH 7 (E_0') of Fd isolated from spinach is about −0.43 V [34], low enough to be directly used as the e^- donors in H_2 production by FeFe-type hydrogenase (H_2ase, Section 2.6.2), and in reduction of $NADP^+$ by FNR. In the N_2ase reaction, the redox potential of Fd or Fld need not be so low, and in fact some microorganisms have Fd and/or Fld with slightly higher redox potentials with a maximum of about −0.3 V (E_0') [35], some of which are induced under nitrogen-deficient conditions (see Section 2.6.2). Two types of Fds were isolated from the nitrogen fixing *Anabaena variabilis*; Fd isolated from N_2ase containing cells (heterocysts) showed higher activity than Fd isolated from ordinary cells (also called vegetative cells) in the N_2ase assay with NADPH as the e^- source [36–38]. In some *Anabaena* strains, Fld mediates e^- transfer from NADPH to N_2ase [37].

2.3. Quinone pools

In photosynthetic membranes, some quinones occur as diffusible e^- carriers and thus link together various membrane-bound e^- transport components such as Type II RCs, NADH dehydrogenase, succinate dehydrogenase, cyt *b*/*c* complex, etc. The concentration of quinones in the membranes is much greater than the e^- transporting complexes discussed above, and these quinones are often referred to as bulk quinones or quinone pools (Fig. 1). The species of quinones present in the pools differ among organisms and organelles: ubiquinone (UQ) is found in the cytoplasmic membranes (sometimes intracellular membranes depending on the species) of purple bacteria and in the inner mitochondrial membrane of algae, plastoquinone (PQ) in the intracellular membranes of cyanobacteria and chloroplast thylakoid membranes of eukaryotic algae, and menaquinone (MQ) in the cytoplasmic membranes of green sulfur bacteria [39]. UQ and PQ are benzoquinones with E_0' values of about 0–0.1 V, while MQ is a naphtoquinone with an E_0' value of about −0.1 V (for a review of the chemistry of quinone, see [40]). The redox potentials of UQ or PQ reduced by Type II RC are not low enough to directly reduce Fd and $NAD(P)^+$.

2.4. Electron transport chains

The low-potential e^-s generated by photochemical RCs are sequentially transferred via e^- transport chains (Fig. 1), with some components of the e^- transport chain being integral to the membrane, and other components extrinsic to the membrane or even soluble. The low-potential e^-s are used as the source reducing power in various reactions and for generating the proton-motive force (pmf, see below). The redox energy of 1 eV is equivalent to 96.5 kJ mol^{-1}.

2.5. Proton-motive force and ATP synthesis

2.5.1. Membrane-bound ATP synthase

ATP is essential for many cell functions including cell maintenance and division. In photosynthetic organisms, most of the ATP is synthesized by membrane-bound ATP synthase linked to the e^- transport chains of photosynthesis (photophosphorylation) and respiration (oxidative phosphorylation). The enzyme that catalyzes ATP synthesis ($ADP + Pi = ATP + H_2O$, $\Delta G^{\circ\prime} = 30.5$ kJ) is called membrane-bound ATP synthase, H^+-ATPase, or F_oF_1-ATP synthase (CF_oCF_1 in chloroplasts). Homologues of the mitochondrial membrane-bound ATP synthases are found in the cytoplasmic membranes of bacteria, intracellular (also called thylakoid) membranes of cyanobacteria, thylakoid membranes of chloroplasts, etc. The enzyme is composed of part F_1 peripheral membrane protein (subunit composition: $\alpha_3\beta_3\gamma\delta\varepsilon$) that plays a catalytic function and part F_o (subunit composition $ab_2c_{8\text{-}15}$), an intrinsic membrane protein that forms a H^+ channel [41].

Some portion of the energy available from the redox reactions is transformed into the electro-chemical potential of H^+ (pmf) across the energy transducing membranes according to P. Mitchell's chemi-osmotic theory [42,43] (for a review, see [44]). The energy of the pmf is used for:

[1] This is different from the Crp/Fnr family of transcriptional regulators found in *E. coli*, etc.

- ATP synthesis by the membrane-bound ATP synthase,
- pmf-driven uphill transfer of e^-s (also called energy-dependent reversal of e^- transport, e.g., reversal of NADH dehydrogenase (Ndh)),
- $NADP^+$ reduction from NADH (pmf-dependent transhydrogenase, Thg) [45],
- Fd reduction from NADH by Rnf [46] (Section 3.1.4.1)
- Fd reduction from NADH by Fix [47] (Section 3.1.4.2), and
- active transport, etc.

The pmf (measured in kJ) is expressed as the function of the membrane potential ($\Delta\psi$ in volt) and the pH difference (ΔpH in a pH unit) across the membrane where pmf = −2.3 ΔpH + 96.5 $\Delta\psi$ kJ per mol of H^+. We will further denote the p and n sides, which, respectively, become more positive or negative in electrical potential upon energization of the membrane. The p side and the n side, respectively, are the periplasmic side and the cytosolic side of cell membranes of photosynthetic bacteria, the lumen side and the stroma side of thylakoid membranes of chloroplasts, and the intermembrane space side and the matrix side of mitochondria. In some organisms, instead of pmf, the electrochemical potential of Na^+ drives various energy-linked reactions across the membranes [48].

2.5.2. H^+/ATP ratio in ATP synthesis

As described above, H^+-ATP synthase [41] is composed of the integral membrane protein part F_o (ab_2c_n, where c differs among species with n = 8–15, [44,49]) and the peripheral membrane part F_1 attached to F_o. The enzyme synthesizes ATP with the consumption of pmf by a rotational mechanism [50,51]. The ratio of H^+/ATP has yet to be conclusively determined, and may differ among species and organelles even within the same species. The c subunit constitutes a H^+ channel, whose function may be inhibited by dicyclohexyl carbodiimide (DCCD) via covalent modification of the functionally important aspartyl residue. The γ subunit is the axis of rotation, with the torque presumably generated by H^+ moving through the c subunits. The catalytic reaction occurs on the $\alpha_3\beta_3$ hexamer by the binding change mechanism [41]. Based on this binding change mechanism model, it is logical to postulate that one full turn of the γ rotation driven by the H^+ movement through the c subunit synthesizes 3 ATP consuming H^+s, whose number is equal to that of the c subunit. F_oF_1 complexes have been crystallized [52] and analyzed by X-ray crystallography, followed by reports from a variety of species and organelles [49]. The number n of the c subunit determined experimentally thus far seems to differ between 8 and 15 depending on the species and the organelles with n equaling: 8 from bovine mitochondria, 10 from yeast mitochondria, 14 from spinach chloroplasts, etc. [44,49]. These ratios imply that the expected value of H^+/ATP ratio is between 2.7 and 5 depending on the source of ATP synthase. Petersen et al. [49] reconstituted the F_oF_1 ATP synthase from yeast mitochondria (c = 10, or c/β = 3.3) and from spinach chloroplasts (c = 14, or c/β = 4.7) into liposomes, determined the H^+/ATP ratio, and obtained a value of 2.9 ± 0.2 for the mitochondrial enzyme and 3.9 ± 0.3 for the chloroplast enzyme. Their results indicate that the values of experimentally obtained H^+/ATP ratio depends on the stoichiometry of the c-subunit, although this may not simply be a function of the number of c subunits.

In photosynthetic organisms, ATP is required for various reactions such as the assimilation of carbon in photosynthesis, N_2ase reaction, membrane transport of metabolites, etc. Because the value of the H^+/ATP ratio is not fixed, it is impossible to estimate with much certainty the theoretical maximum solar energy conversion efficiency to H_2. In calculating the theoretical maximum energy conversion efficiencies for this paper, we tentatively adopt the values of 3, 4, and 5 (see below and Table 5).

2.5.3. Transhydrogenase and NADPH/$NADP^+$, NADH/NAD^+ redox couples

Both NADPH and NADH are used in a variety of enzymatic reactions as coenzymes, and the redox potentials of the two couples are about the same (E_0' = −0.32 V). However, many organisms use them differentially, typically using NADH for catabolic reactions and NADPH for anabolic reactions. Often within the same cell or organelle the NADPH/$NADP^+$ ratio is kept high, while the NADH/NAD^+ ratio is kept low. These states are attained in part through the activities of metabolic reactions; for example the chloroplast FNR, the *Escherichia coli* glucose-6-phosphate-dehydrogenase which preferentially uses NADPH/$NADP^+$ as the reaction partner, and other organisms where lactate dehydrogenase uses NADH/NAD^+. In mitochondria and purple bacteria [53], membrane-bound nicotinamide transhydrogenase transfers e^-s from NADH to $NADP^+$, driven by consumption of pmf [45,54], which enables the organelles and cells to keep the NADPH/$NADP^+$ ratio at a high level and the NADH/NAD^+ ratio at a low level. In rat mitochondria, the ratio of [NADPH]·[NAD^+]/[$NADP^+$]·[NADH] (i.e., ([NADPH]/[$NADP^+$])/([NADH]/[NAD^+]) can reach a value of up to 500 (for a summary and thermodynamical considerations of transhydrogenase, see [55]).

2.5.4. Hydrogen and NAD(P)H

The redox potential E_h of a redox couple is expressed as:

$$E_h = E_0 + \frac{RT}{nF}\ln\left(\frac{[\mathrm{Ox}]}{[\mathrm{Red}]}\right),$$

where E_0 is the standard redox potential, R is the gas constant, n is the number of e^-s participating in the reaction, T is the absolute temperature, and F is Faraday's constant. At 25 °C (298 K),

$$E_h = E_0 + \frac{0.06}{n}\log\left(\frac{[\mathrm{Ox}]}{[\mathrm{Red}]}\right).$$

As for the reaction formula of $2H^+$ (aq) + $2e^-$ → H_2 (g), we have

$$E_h = E_0 + \frac{RT}{2F}\ln\left(\frac{[H^+]^2}{[H_2]}\right) = E_0 + \frac{RT}{F}\ln[H^+] - \frac{RT}{2F}\ln[H_2].$$

Note. When the reaction is expressed as $H^+ + e^-$ → 1/2 H_2, we have the same result:

$$E_h = E_0 + \frac{RT}{F}\ln\left(\frac{[H^+]}{[H_2]^{1/2}}\right) = E_0 + \frac{RT}{F}\ln[H^+] - \frac{RT}{2F}\ln[H_2].$$

In the above reaction, E_0 = 0 at [H^+] = 1 M (pH zero), by definition, and [H_2] is the partial pressure of H_2 (p_{H_2}) in atm (101325 Pa). At 25 °C (298 K), we have $E_h = 0 - 0.06\,\mathrm{pH} + RT/2F\ \ln p_{H_2}$. At p_{H_2} of 1 atm, E_h is a function of the pH of the compartment where the hydrogenase is located: at pH 0, 5, 6, 7, or 8, it is 0, −0.3, −0.36, −0.42, or −0.48 V, respectively. The E_h is also a function of the p_{H_2}, and at pH 7 when the p_{H_2} is 1 (100%), 0.1, 0.01, or 0.001 atm, the E_h (expressed as E_0', please note the ′) is about −0.42, −0.39, −0.36, or −0.33 V, respectively.

As for the reaction formula of $NAD(P)^+$ (aq) + H^+ (aq) + $2e^-$ → NAD(P)H (aq), E_h at pH 7 (E_0') = −0.32 V at 298 K, we have, E_0' = −0.32 + 0.03 log([$NAD(P)^+$]/[NAD(P)H] + 0.03 log([H^+]/10^{-7}) = −0.32 + 0.03 log([$NAD(P)^+$]/[NAD(P)H] − 0.03 (pH−7). When the [NAD(P)H]/[$NAD(P)^+$] ratio is 0.1, 1, or 10, the E_h is about −0.29, −0.32, or −0.35 V at pH 7, and about −0.26, −0.29, or −0.32 V at pH 6, respectively.

From the above calculations, at pH 7 and 6 when the [NAD(P)H]/[$NAD(P)^+$] is 10 (−0.35 V and −0.32 V, respectively), the H_2 concentration (p_{H_2}) in equilibrium does not exceed 1% and 10%

(v/v), respectively. The back reaction (H_2 absorption) becomes significant, when H_2 concentration exceeds several percentages. Apart from cell physiology and the pH dependence of enzymatic activity, the more acidic the compartment where the H_2ase is located, the more favorable conditions are energetically for H_2 production. Because there is an upper limit for the H_2 concentration attained by the activity of NAD(P)H-linked hydrogenase (Section 2.6.1.2), the H_2 accumulation levels are also limited [56].

2.6. The enzymes of H_2 production

The enzymes that catalyze H_2 production in phototrophic organisms are either hydrogenase (H_2ase) or nitrogenase (N_2ase).

2.6.1. Hydrogenases

The feasibility of photoproducing H_2 was demonstrated a long time ago using an artificial system composed of H_2ase from *Clostridium*, chloroplasts and Fd from spinach [57]. Various aspects of H_2ases have been extensively reviewed [6,58–65].

H_2ase is the enzyme that catalyzes the following simple reaction:

$$2H^+ + 2e^- \rightleftarrows H_2.$$

H_2ases are metalloenzymes and are classified into two main classes based on the metallic co-factor of their active centers: [FeFe]-H_2ase (also called Fe-H_2ase or Fe-only H_2ase) and [NiFe]-H_2ase (see below). On the basis of physiological functions, H_2ases can be further divided into bi-direactional H_2ases and uptake H_2ases.

The bi-directional H_2ases (sometimes called reversible H_2ase) catalyze either evolution or uptake of H_2 depending on the redox state of the immediate e^- donors (Fd_{red}/Fld_{red} or NADPH) within the cellular compartments, and on the partial pressure of H_2. Bidirectional H_2ases found in phototrophic organisms are divided into two groups: the first is [FeFe]-H_2ase found in green algae with reduced or oxidized Fd/Fld as the reaction partner, and the second is [NiFe]-H_2ase found in cyanobacteria and photosynthetic bacteria with NAD(P)H/NAD(P)$^+$ as the reaction partner. These two groups of bidirectional H_2ases are of different phylogenetic origins.

The uptake H_2ase (Hup) found in photosynthetic bacteria and cyanobacteria belongs to the [NiFe]-H_2ase; it absorbs H_2 and feeds e^- to the quinone pool. Because the uptake H_2ase catalyzes the essentially unidirectional uptake of H_2, it naturally interferes with N_2ase-based H_2 production (see Section 2.6.2). Although the physiological function differs, the [NiFe]-type uptake H_2ase and NAD(P)H/NAD(P)$^+$-linked bi-directional H_2ase share similarity in the amino acid sequences of their catalytic proteins and in the 3-D structures of the metal cluster [63]. However, they differ in the composition and number of subunit proteins that constitute the H_2ase complexes.

The catalytic centers of the both types of H_2ase are generally sensitive to O_2.

2.6.1.1. [FeFe] hydrogenase. [FeFe]-H_2ase is typically found in chloroplasts of green algae, and catalyzes the reversible reaction with Fd/Fld as the reaction partner as described above [66]. Because the redox potential (E_0') of Fd is around −0.43 V and because PS I produces electronegative reducing power (E_0') of around −0.55 to −0.6 V, there are no redox potential constraints for photobiological H_2 production in green algae. In order for photobiological H_2 production to occur in green algae, in addition to the expression of H_2ase, there must be an adequate intracellular supply of Fd_{red}/Fld_{red} as many other enzyme activities are also linked to Fd_{red}/Fld_{red} (e.g. FNR, nitrate reductase, antimycin A-sensitive cyclic e^- transport around PS I, etc., see below and Fig. 9). Compared with other H_2-producing enzymes, [FeFe]-H_2ase has the highest activity with a turnover rate of 6000–9000 s^{-1} [3]. By comparison, [NiFe]-type bi-directional H_2ase has a turnover rate of about 100 s^{-1} and 450–600 s^{-1}, in the direction of H_2 evolution and uptake, respectively, and N_2ase, about 6.4 s^{-1} [3].

The catalytic metal cluster of the [FeFe]-H_2ase is extremely sensitive to O_2, and when the catalytic cluster is inactivated, the protein is eliminated by degradation. After translation of the [FeFe]-H_2ase genes, the participation of 3 proteins is required for formation of an active [FeFe]-cluster on the nascent polypeptide [67,68]. Because [FeFe]-H_2ase is sensitive to O_2 and O_2 is a product of photosynthesis, optimal photobiological H_2 production in these species will require that either O_2 production via photosynthesis is minimized or the O_2 produced is promptly consumed. In the green alga *Chlamydomonas*, sulfur deprivation in the culture medium leads to a gradual decrease in PS II activity and the production of H_2 mainly from stored starch (see Section 3.4.1).

2.6.1.2. [NiFe] H_2ases. [NiFe]-H_2ases are found in photosynthetic bacteria and cyanobacteria, and are one of three major types, differing by physiological function [58,59,62,63]: (1) bi-directional H_2ase (cyanobacterial enzyme sometimes called Hox) catalyzing a reversible reaction with NAD(P)$^+$/NAD(P)H as the reaction partner, (2) uptake H_2ase (called Hup) catalyzing practically unidirectional absorption of H_2, in many cases with a *b*-type cytochrome as the e^- acceptor from the [NiFe] catalytic center, and (3) H_2-sensing H_2ase activating the gene expression of the former two in the presence of H_2. The NiFe binding sites of this group of H_2ase show a certain degree of similarity in 3-D structure, and also in amino acid sequences [62]. After translation of the [NiFe]-H_2ase genes, the participation of 7 proteins is required for formation of an active [NiFe]-cluster on the nascent polypeptide [68,69].

Among these [NiFe]-H_2ases, only bi-directional H_2ase is a viable candidate for biological H_2 production. However, because the redox potential of NADPH is about −0.32 V (E_0'), the maximal concentration of H_2 produced by the bi-directional [NiFe]-type H_2ase is limited under normal pressure as discussed in Section 2.5.4. Although the molecular activity of bidirectional [NiFe]-H_2ase is lower than that of [FeFe]-H_2ase, an advantage of the [NiFe]-H_2ase is that the inactivated catalytic cluster can be reconstituted in the presence of H_2 or NAD(P)H without the synthesis of the structural protein. The Fe of the catalytic center of [NiFe]-H_2ase binds CN and CO as the ligands as in [FeFe]-H_2ase, although the phylogenetic origins and structures of the catalytic centers of the two differ. After translation of the [NiFe]-H_2ase genes, the interaction of a variety of proteins is required for formation of an active [NiFe]-cluster on the nascent polypeptide. A total of 7 proteins (6 Hyp proteins and one additional) are required [69,70] and the total inactivation of any one of them leads to elimination of [NiFe] H_2ase activity.

The *hup* genes encoding uptake H_2ase are distributed throughout most of the N_2-fixing PNS bacteria and cyanobacteria. The *hox* genes encoding bidirectional H_2ase are found in some of the unicellular and filamentous cyanobacteria, but are apparently absent in others (see below).

2.6.1.3. Physiological roles of H_2ases. The physiological roles of the uptake H_2ase Hup are either to use H_2 from the environment as the e^- donors for various synthetic pathways (hydrogenotrophy) or for recovery of H_2 as the energy source that is produced in N_2ase reactions.

The physiological roles of bi-directional H_2ase are: to absorb H_2 from the environment as the e^- donors for oxidative chains, to evolve H_2 in order to drive metabolic pathways for ATP synthesis (e.g., in fermentation), or to avoid accumulation of reducing power on the e^- acceptor sides of e^- transport chain in oxygenic

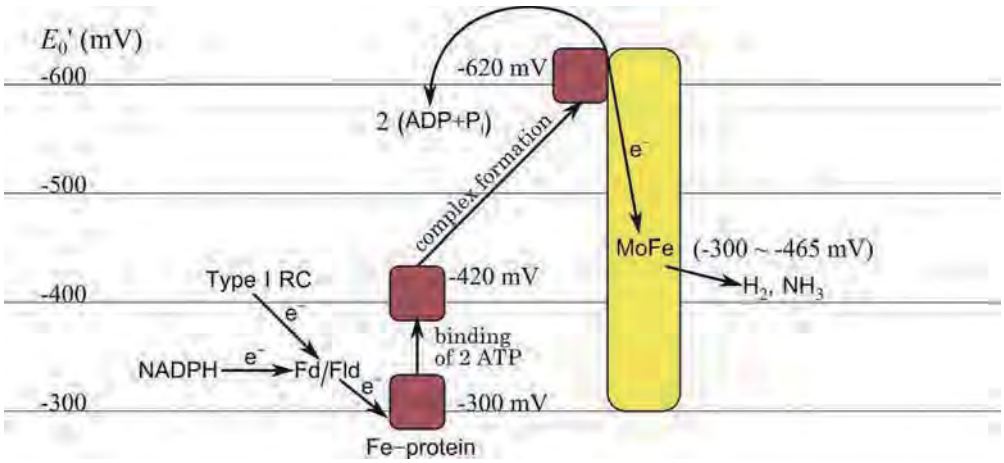

Fig. 2. Redox potential changes of clusters in nitrogenase proteins. The N_2ase reaction is catalyzed by the interaction of two separate proteins (collectively called N_2ase): the Fe protein (reddish brown) and the MoFe protein (yellow). The E_0' of free Fe-protein is around −300 mV, and it decreases to about −420 mV upon binding 2 ATP per Fe-protein. Upon further binding of Fe-protein-ATP_2 complex with MoFe-protein, the E_0' of Fe-protein still decreases to about −620 mV [35,79,80].

phototrophs. While H_2 production in these cases seems to be a waste of acquired energy, it likely has a physiological function under certain conditions. For example, when excess e^- accumulate on the e^- acceptor side of PS I as Fd_{red} and reduced RC-bound iron-sulfur clusters, these reduced components react with O_2 to generate the active oxygen species super oxide (O_2^-) which damages various cell components [71], including the iron-sulfur clusters of PS I [72]. In addition, on the reducing side of PS II under reducing conditions but in the presence of transient O_2, retention of excited energy on chlorophyll molecules leads to formation of triplet chlorophyll, which reacts with ordinary (triplet) O_2 to produce singlet O_2, a highly active oxygen species that damages various cellular components including PS II itself [71]. Accordingly, oxygenic organisms have developed various means to decrease the accumulation of excess e^- in photosynthetic e^- transport chains, and also to detoxify active oxygen species. It has been proposed that bidirectional H_2ase functions as a sort of "emergency valve" for excess e^-, thus mitigating the formation of damaging reactive oxygen species [73].

Collectively, these results suggest that the bi-directional H_2ase functions as a valve for low-potential e^-s generated during the light reactions of photosynthesis, thus preventing a "slowing down" of e^- transport caused by reactive oxygen species. This hypothesis is supported by growth curves demonstrating that the cyanobacterium *Nostoc punctiforme* bi-directional H_2ase mutant needs more time to adapt to changing light intensities [74].

2.6.2. Nitrogenase

N_2ase is an enzyme of N_2 fixation, found only in some prokaryotes including purple non-sulfur (PNS) bacteria, green sulfur bacteria, some cyanobacteria strains, etc. N_2ase catalyzes the unidirectional production of H_2 as the inevitable by-product of N_2 fixation with substantial energy input in the form of ATP [75]. Thus, N_2ase is a candidate enzyme for photobiological H_2 production. N_2ase catalyzes the reaction under optimal conditions for N_2 fixation:

$$N_2 + 8e^- + 8H^+ + 16ATP \rightarrow H_2 + 2NH_3 + 16(ADP + P_i) \quad \text{(Eq.1)}$$

whereas, in the absence of N_2 (e.g., under Ar), all e^-s are allocated to H_2 production:

$$2e^- + 2H^+ + 4ATP \rightarrow H_2 + 4(ADP + P_i) \quad \text{(Eq.2)}$$

The merit of using N_2ase in photobiological H_2 production is that it catalyzes an essentially unidirectional production of H_2, and furthermore that the cells lacking H_2ase activity can accumulate H_2 for a long time even in the presence of O_2.

The typical, and most widely distributed and well-characterized N_2ase contains molybdenum (Mo-N_2ase), and is expressed under conditions of combined nitrogen deprivation in the presence of Mo. The N_2ase reaction is catalyzed by the interaction of two separate proteins (collectively called N_2ase): the Fe protein (encoded by *nifH*) and the MoFe protein (encoded by *nifD* and *nifK*). The homodimeric Fe protein, also called dinitrogenase reductase, contains a single [4Fe-4S] cluster per dimer that accepts e^- from Fd_{red} or Fld_{red} and in turn donates the e^- to the MoFe protein in an ATP-dependent manner requiring 2 ATP per e^- (Fig. 2). The MoFe protein also called dinitrogenase contains a [8Fe-7S] P-cluster and the FeMo cofactor (FeMo-co; $MoFe_7S_9C$-homocitrate) that binds and reduces N_2 and H^+ [76–78].

Some prokaryotes have other type(s) of N_2ases called V-N_2ase (encoded by *vnf* gene cluster) and Fe-only N_2ase (encoded by *anf* gene cluster) in addition to Mo-N_2ase. These other N_2ases are sometimes called alternative N_2ases and are similar to a certain extent to the Mo-type N_2ase in amino acid sequence, but can be divided into distinct subgroups [81,82]. V-N_2ase and Fe-only N_2ase are expressed in the absence of Mo, but in the presence of V and in the absence of both Mo and V, respectively. In terms of the "e^- allocation coefficient" that is the ratio of (total e^- fixed in NH_3) to (total e^- used in the reaction catalyzed by N_2ase), the alternative N_2ases are less efficient in fixing N_2 and conversely, can be more efficient in producing H_2 than the Mo-N_2ase [83–85]. The general chemical equation for these types of N_2ase is:

$$N_2 + (6+2n)e^- + (6+2n)H^+ + 2(6+2n)ATP \rightarrow nH_2 + 2NH_3 + 2(6+2n)(ADP + P_i) \quad (n \geq 1.0) \quad \text{(Eq.3)}$$

Thus in the presence of N_2, one would expect greater efficiency of photobiological H_2 production by the alternative N_2ases rather than the conventional Mo-N_2ases. Based on information from the genomic sequence data bases, purple non-sulfur (PNS) bacteria have Mo-N_2ase, and some V-N_2ase. The PNS bacterium *Rhodopseudomonas palustris* CGA009 appears to have all three types of N_2ase [86]. Some N_2-fixing cyanobacteria contain both Mo- and V-N_2ases [87–89], but the existence of a strain containing the Fe-only type enzyme has not yet been reported. The cyanobacterium *Anabaena variabilis* contains two Mo- and one V-N_2ases. One of the Mo-N_2ase is expressed in the heterocysts, the cell specialized for N_2 fixation (see Section 3.3.1), and the other is

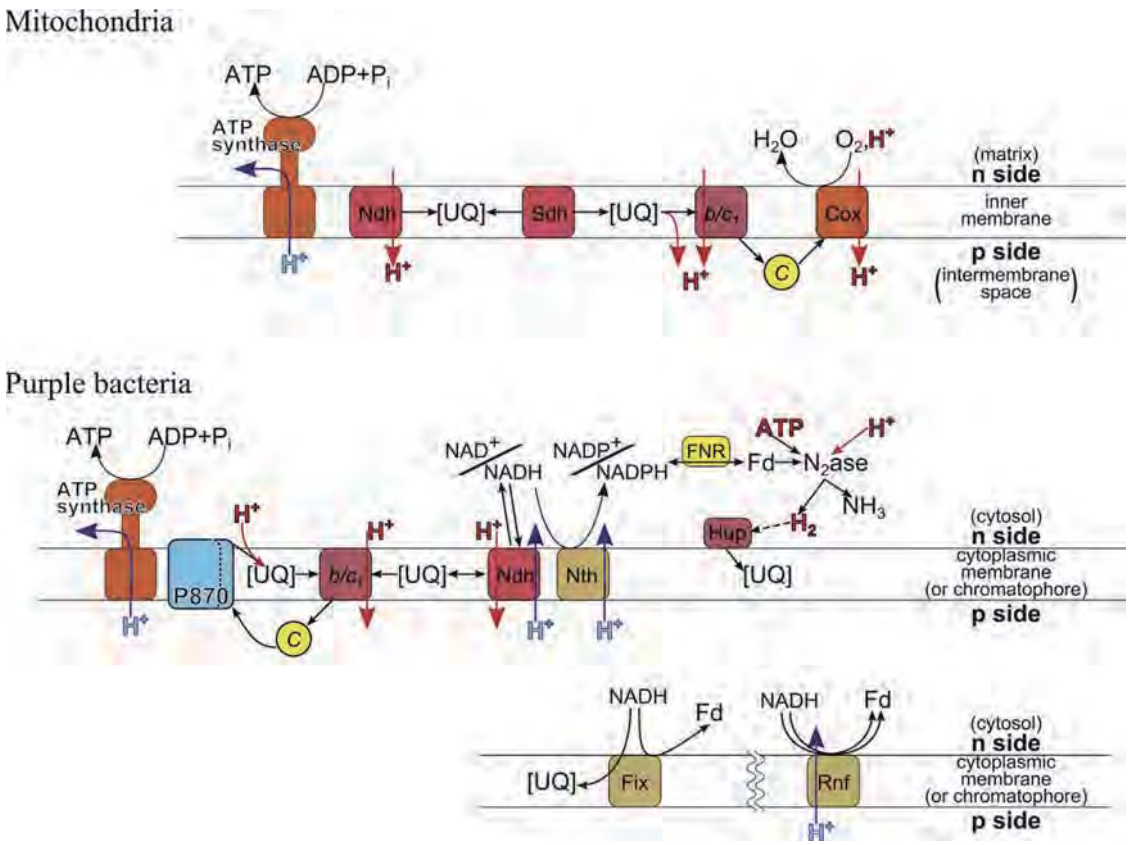

Fig. 3. Electron transport system of mitochondria and purple bacteria. Upper part: mitochondria (animal or yeast). Middle and lower parts: some PNS bacteria. H^+ with a red arrow: formation of proton-motive force, H^+ with a blue arrow: consumption of proton-motive force. b/c_1: cytochrome b/c_1 complex, *c*: cytochrome *c*, Cox: cytochrome *c* oxidase, Fd: ferredoxin, Fix: Fix complex (present in some strains), FNR: ferredoxin-$NADP^+$ oxidoreductase, Hup: uptake hydrogenase, N_2ase: nitrogenase, Ndh: NADH dehydrogenase [93], Nth: nicotineamide transhydrogenase, P870: reaction center [92], Rnf: Rnf complex (present in some strains), Sdh: succinate dehydrogenase, UQ: ubiquinone. See, for RC [27], pmf generation by RC [94], cyt *b*/*c* complex and pmf generation [91,95]. For details, see text.

expressed in ordinary (vegetative) cells under anaerobic conditions [90].

The E_0' of the cluster in the Fe-protein from *Azotobacter vinelandii* is −290 mV, and the E_0' is lowered to −430 mV upon binding two ATP [35]. The E_0' of the cluster in the Fe-protein (Fe-protein-ATP_2) is further lowered to about −620 mV, low enough to drive N_2 fixation as well as H_2 production, by complex formation with the MoFe-protein (dinitrogenase) accompanied by ATP hydrolysis [80] (reviewed in [79]) (Fig. 2).

3. H_2 production by living organisms

3.1. Purple bacteria

3.1.1. Photobiological H_2 production by purple non-sulfur bacteria

Purple bacteria [27] constitute a group of Gram-negative pink to purplish-brown bacteria that contain Type II RC, which cannot use H_2O as the e^- donor in contrast with organisms like cyanobacteria, algae and land plants that contain PS II. This is because the oxidant generated by the photochemical reaction of Type II RCs of purple bacteria is not strong enough to extract e^- from H_2O (Fig. 1). The primary donor of the RC is a dimer of BChl *a* (BChl *b*, in some strains), and the major antenna pigments are protein-bound BChls and carotenoids. The oxidized primary donor is reduced by either soluble or membrane-bound cyt *c* in most of the RCs. The RC, energy transducing e^- transport chains, and ATP synthase are localized in cytoplasmic membranes (Fig. 3). In certain species, some parts of the membranes lodge into the cytoplasm and protrude further to form intracellular membrane vesicles with the F_1 portion of the H^+-ATP catalytic domain facing into the cytoplasm (n side).

The major groups of bacteria that contain this type of RC are PNS bacteria (PNS genera *Rhodobacter*, *Rhodospirillum*, *Rhodopseudomonas*, etc.), purple sulfur bacteria (*Chromatia*, *Allochromatia*), green filamentous bacteria (*Chloroflexaci*), etc. This review focuses on PNS bacteria, because they are the most commonly used purple bacteria for studies of photobiological H_2 production (for H_2 production by PNS bacteria, see [5,96–99]).

3.1.2. N_2ase-based H_2 production with various organic substances serving as e^- sources

The PNS *Rhodospirillum rubrum* was found to produce H_2 upon illumination under He or Ar, but not under N_2 [100], and the activity was later attributed to N_2ase [101]. In many PNS bacteria, various organic substances are metabolized through dark fermentation pathways (Section 3.1.3) to reduce either NAD^+ or UQ. In PNS bacteria, N_2ase activity is induced by combined-nitrogen deficiency. In the absence of N_2 (under He, Ar, or no gas), all the e^-s are allocated to H_2 production in the N_2ase reaction. N_2ase requires ATP and Fd_{red} [102] and/or Fld_{red} [103]. ATP is supplied by photophosphorylation, and the Fd_{red}/Fld_{red} is supplied by different pathways, depending on the species and cell physiology, possibly involving one or more of the following: (1) Rnf pathway (from NADH to Fd), (2) Fix pathway (from NADH to Fd), (3) pmf-dependent transhydrogenase followed by FNR (from NADH to NADPH, and to Fd). Electrons for NAD^+ reduction are supplied from UQH_2 by the pmf-driven uphill

transfer of e^- through NADH dehydrogenase (Ndh, Fig. 3). Because the E_0' of the Fe-protein of N_2ase is not so electronegative (about −300 mV [35] compared to the E_0' of H_2 at −420 mV)), N_2ase is able to recruit e^-s from various metabolic pathways via Fd_{red} or Fld_{red}. *Rhodobacter capsulatus* Fd gene located upstream of the *nif* gene was expressed in *E. coli* and the protein had E_0' of −220 mV, which did not function *in vitro* as an e^- donor to N_2ase [104].

3.1.3. Comparison with dark fermentative H_2 production

Dark fermentative H_2 production is typically studied using some species of enterobacteria such as *Escherichia* and some members of Gram-positive spore-forming *Clostridium* growing on organic-based media. Although the metabolic pathways leading to H_2 production in these bacteria are not fully elucidated, the maximum stoichiometric amount of H_2 produced by the dark fermentation from glucose under normal pressure is generally assumed to be about 2 (mol/mol) for *Enterobacteriaceae* and 4 for *Clostridiaceae* with various organic acids such as acetate, propionate, pyruvate, succinate, butylate, etc., as the end products. However, some PNS bacteria frequently produce more than 7 mol H_2/mol of hexose in the light, based on their photosynthetic machinery and N_2ase (see Table 3). In assessing the potential yield of H_2 from organic compounds, the importance of metabolic network-wide balancing of reducing equivalents should be taken into account [105–109].

PNS bacteria are comprised of a phylogenetically diverse range of strains. The species of organic substances that PNS bacteria can efficiently use differ as do the resulting rates of metabolic reactions. For the majority of PNS strains used in laboratory experiments, the preferred substrates are organic acids such as malate, succinate, butyrate, pyruvate, etc., but not acetate. PNS strains using saccharide substrates such as glucose, starch, etc. typically have lower rates of metabolic reactions than do strains using organic acids.

The standard free energy changes (ΔG°) of formate, acetate and pyruvate for H_2 production are [110]:

Reaction (1) $\text{formate}^- + H_2O = HCO_3{}^- + H_2 \quad (\Delta G^{\circ\prime} = +1.3\,\text{kJ})$

Reaction (2) $\text{acetate}^- + 4H_2O = 2HCO_3{}^- + 4H_2 + H^+$

$(\Delta G^{\circ\prime} = +104.6\,\text{kJ})$

Reaction (3) $\text{acetate}^- + 4H_2 + 2H_2O = HCO_{3^-} + \text{pyruvate}^- + 3H_2$

$(\Delta G^{\circ\prime} = +151.7\,\text{kJ})$

Reaction (4) $\text{pyruvate}^- + 2H_2 = \text{acetate}^- + HCO_3{}^- + H^+ + H_2$

$(\Delta G^{\circ\prime} = -47.3\,\text{kJ})$

Direct H_2 production from acetate is bioenergetically unfavorable. Oxidation of pyruvate can be linked to ATP synthesis ($\Delta G^{\circ\prime}$ = +30.5 kJ. Total ΔG° = −47.3 kJ + 30.5 kJ = −16.8 kJ). In enterobacteria such as *E. coli*, the main reaction pathway of H_2 production with glucose as the substrate may be described as:

Reaction (5) pyruvate formate lyase :
$\text{pyruvate}^- + \text{CoA} = \text{formate}^- + \text{acetyl-CoA}$, and

Reaction (6) formate hydrogen lyase-hydrogenase complex :

$\text{formate}^- + H^+ = CO_2 + H_2$

Reaction (7) phosphate acetyl transferase, and acetate kinase :

$\text{acetyl} - \text{CoA} + \text{Pi} = \text{acetyl phosphate} + \text{CoA}$,

and $\text{acetyl phosphate} + \text{ADP} = \text{acetate} + \text{ATP}$.

Even when formate is secreted extracellularly without further metabolism, the cells are still able to produce ATP (Reaction 5 and 7).

As a consideration for future practical applications, it should be noted that when the gas total pressure was decreased from 1 atm to 0.5 atm, the molar yield of H_2 by *Enterobacteria cloacae* increased from 1.9 mol to 3.9 mol/mol glucose [111], indicating that the H_2 yield is greatly affected by the H_2 partial pressure of the environment (see Section 2.5.4).

Members of the genus *Clostridia* have pyruvate-Fd oxidoreductase, and the pathway is described as:

(1) pyruvate-Fd oxidoreductase: $\text{pyruvate}^- + 2Fd_{ox} + \text{CoASH} = \text{acetyl-CoA} + 2Fd_{red} + CO_2$.
(2) H_2ase: $2Fd_{red} + 2H^+ = 2Fd_{ox} + H_2$.

Under atmospheric pressure, some members of the family *Clostridia* maximally evolve more than 2 but less than 4 H_2 per glucose. The mechanism of the apparent additional H_2 pathway is not fully elucidated, and the participation of Rnf (Section 3.1.4.1)

Table 3
Some examples of photobiological H_2 production by coculture or two-stage culture including PNS bacteria.

Type of culture	Fermentative bacteria	PNS bacteria	Substrate	Total H_2 yield (mol/mol hexose)	Special remarks	References
Coculture						
	Lactobacillus delbrueckii	*Rhodobacter sphaeroides*	Glucose	7.1		[132]
	Clostridium butylicum	*Rhodobacter sphaeroides*	Glucose	7.0		[130]
	Cellulomonas sp.	*Rhodobacter capsulatus*	Cellulose	4.3		[129]
	Caldicellulolosiruptor saccahrolyticus	*Rhodobacter capsulatus*	Beet molasses	6.9		[135]
2-Stage						
	Closteridium pasteurianum	*Rhodopseudomonas palstris*	Sucrose	7.1	90% COD removal (sucrose)	[134]
	Clostridium butyricum and *Enterobacter aerogenes*	*Rhodobacter* sp.	Starch mining waste	7.2		[131]
	activated sludge	*Rhodobacter sphaeroides*	Olive mill waste	Not applicable	52% COD removal	[133]

For an extensive review, see [99].

or Fix (Section 3.1.4.2) pathways (see below) for some species is conceivable.

3.1.4. Ferredoxin/flavodoxin reduction in PNS bacteria

3.1.4.1. Ion-motive Fd-NAD$^+$ oxidoreductase, Rnf. From *Rhodobacter capsulatus*, Schmehl et al. [46] identified homologs of a *nif* gene cluster encoding N_2ase-related genes. The *R. capsulatus nif* gene cluster was shown to have homologs in *Azotobacter vinelandii*. At the time of the report, the functions of the *R. capsulatus* gene products were unknown. When one of the products of the genes in *rnf* (for *R*hodobacter *n*itrogen *f*ixing) gene cluster was disrupted, the *in vivo* N_2ase activity of *R. capsulatus* was greatly decreased, but not totally abolished, and the authors concluded that the products of the genes function in e^- transport to N_2ase. Similarly, RnfABCDEG from *Acetobacterium woodii* is a membrane protein complex that reversibly transports e^- from NADH to Fd via the electrochemical potential of Na^+ (or generation of the potential in the reverse reaction) [112]. The pumped cation species is Na^+ in *Acetobacterium woodii* [48], but most likely H^+ in *Rhodobacter capsulatus*. The enzyme complex works reversibly, and oxidation of Fd_{red} by NAD^+ is accompanied by Na^+ (or H^+) extracellular transport (reviewed in [113]). The *rnf* gene clusters have been found in some *Escherichia and Clostridium* strains, the purple sulfur bacterium *Allochromatium vinosum*, and some PNS bacteria. Of the PNS bacterial strains whose entire genomes have been sequenced, 5 strains of *Rhodobacter* (alphaproteobacteria) and one strain *Rubrivivax gelatinosus* (betaproteobacterium) [114] contain the *rnf* gene cluster, but it appears to be absent in 7 strains of *Rhodopseudomonas* and 4 strains of *Rhodospirillum*. Among green sulfur bacteria, 4 out of 5 *Chlorobium* strains have the *rnf* gene cluster, but 2 strains of *Chlorobaculum* do not. Some *Clostridium* strains have the *rnf* gene cluster, and others apparently lack it, as reported in the KEGG (Kyoto Encyclopedia of Genes and Genomes) database [115,329]. The *rnf* gene cluster is apparently entirely absent in cyanobacteria (>40) strains examined thus far and the green alga *Chlamydomonas reinhardtii* (1 strain) in the KEGG database [115,329]. In yet another variation, the acetogenic bacterium *Acetobacterium woodii* fixes CO_2 with H_2 as the e^- donor. In *A. woodii*, HydABCD H_2ase reduces Fd, and Fd_{red} is in turn oxidized by a sodium-motive Rnf complex, reducing NAD^+ and generating the Na^+ electrochemical potential which is used to drive ATP synthesis. In some PNS bacteria, Rnf complex requires both Fd_{ox} and NADH, generating Fd_{red} and NAD^+ in a 1:1 stoichiometry in e^-.

3.1.4.2. FixABCX pathway. Edgren [47] reported the importance of *fixABCX* genes to e^- transport in the N_2ase reaction in *Rhodospirillum rubrum*, a species lacking *rnf* genes. In a more detailed analysis, the bacterium has been reported to have two pathways of e^- transport to N_2ase, with the Fix pathway appearing to be the minor one operating under heterophototrophic conditions. It seems that a pyruvate:ferredoxin oxidoreductase, encoded by the *nifJ* gene, may play a central role under anaerobic conditions in the dark in this strain [116]. The biochemical function of the membrane-bound FixABCX was not known at that time, but Hermann et al. [117] later proposed that e^-s from NADH (carrying 2 e^-s) are bifurcated, one going to Fd/Fld (endergonic), and the other to quinone (exergonic).

3.1.5. Optimizing photobiological H_2 production by purple non-sulfur bacteria

3.1.5.1. Inactivation of H_2ase. Many of the PNS bacteria have N_2ase and uptake H_2ase (Hup). In these bacteria, the N_2ase enzymes may serve as viable candidates for H_2 production systems. In order to express N_2ase, the N/C ratio of culture media should not be high, the N_2 in the gas phase should be low or initially zero (no gas in the head space), and the main components of the produced gas should be H_2 and CO_2. The presence of Hup activity, which reabsorbs the H_2 produced, lowers the yield of H_2. The strains lacking H_2ase activity, either selected from the environment or following chemical mutagenesis, or constructed through genetic engineering, have been shown to have significantly improved photobiological H_2 production. For example, a mutant deficient in H_2ase activity was obtained by ethylmethylsulfonate (EMS) mutagenesis of *Rhodopseudomonas capsulata* [118]. In other examples, inactivation of uptake H_2ase genes in *Rhodopseudomonas capsulata* by transposon mutagenesis was reported [119] and an uptake H_2ase and poly-hydroxybutylate synthase deficient mutant of *Rhodobacter sphaeroides* was reported to have improved H_2 productivity [120]. Other molecular targets for improved H_2 production include HypF, shown to be essential for the cluster formation of NiFe-H_2ase [69]. A *hypF*-deficient mutant of the purple sulfur phototrophic bacterium *Thiocapsa roseopersicina* created by transposon mutagenesis, showed dramatic increases in its H_2 evolution capacity under nitrogen-fixing conditions [121]. Thus inactivation of H_2ase activity enhances photobiological H_2 production activity by PNS bacteria such as *R. capsulata*. For expression of H_2ase genes in PNS bacteria, see [122].

3.1.5.2. Acceleration of photobiological H_2 production from various organic sources by coculture and two-stage culture. While many PNS bacteria can efficiently use various short-chain organic acids as the e^- donors for growth, in contrast their growth rates are rather low on media containing saccharides and complex organic substances that might be more desirable for use in photobiological H_2 production systems. Some other microorganisms degrade complex organic substances at much higher rates, yielding various organic acids, but the H_2 yields from organic substances are modest (maximally 4 mol H_2/mole glucose) [123]. Accordingly, coculture (also called mixed culture) of PNS bacteria with fermentative bacteria seems to be suitable for increasing the overall rate as well as the yield of H_2. Similarly, the two-stage process begins with a dark fermentation stage followed by a second stage of photofermentation in the PNS bacteria (Fig. 4, Table 3) [99,124–128].

One of the merits of the two-stage process is that culture conditions can be manipulated to support the growth of two otherwise culturally incompatible organisms. Specifically, the culture conditions may be optimized for the first stage organism and then shifted to support the growth requirements of the second stage organism. For example, the both the pH of the medium and the culture temperature can be optimized for growth of thermophilic fermentative bacteria in the first stage and then medium pH and culture temperature can be shifted to support the growth of mesophilic PNS bacteria in the second stage. The shortcoming of the two-stage process is that accumulating acids, which are continuously removed in coculture by PNS bacteria, can limit the catalytic activities of the first-stage microbes [136]. There are practical limitations of both the coculture and the two-stage process systems, even though the metabolic activities of dark fermentation microbes are generally much higher than those of the PNS bacteria [137]. In order for either of these systems to achieve economically viable rates of energy production, further improvements are needed in the conversion efficiency of H_2 per substrate, as well as in the rates of H_2 production [99].

Two examples of coculture are: *Rhodospirillum rubrum* with *Klebsiella pneumonia* with glucose or hydrolyzed cellulose as substrates [138]; and coculture of *Clostridium* and *Rhodopseudomonas* which produced 1.1 mol H_2 in the dark and 7.0 mol H_2/mol glucose in the light [130]. Taken together, cocultures using PNS bacterial strains with inactivated Hup activity can lead to enhanced photobiological H_2 production. In another coculture system composed of the cellulose-fermenting, dark fermentation bacterium *Cellulomonas* and either mutant (H_2ase-negative) or wild-type *Rhodopseudomonas capsulata*, the system containing the H_2ase

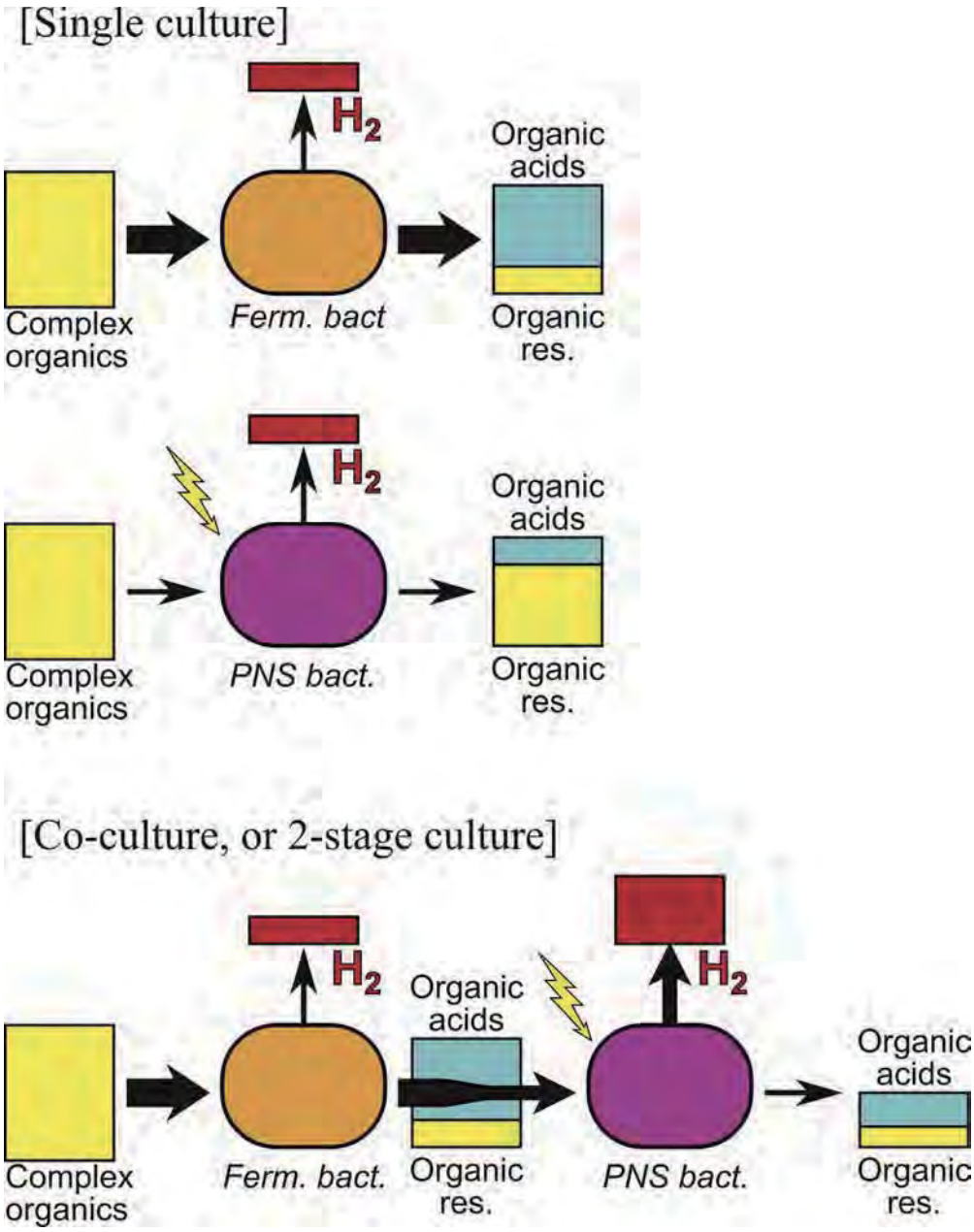

Fig. 4. Schematic illustration of improvement in H_2 production by coculture or 2-stage culture of fermentative bacteria and purple non-sulfur bacteria. Upper part: Fermentative bacteria decompose various organic substances at a high rate producing large amounts of organic acids, but the amount of produced H_2 is not high. Middle part: PNS bacteria decompose only a portion of organic substances, and the amount of produced H_2 is not high. Lower part: In coculture or 2-stage culture, fermentative bacteria produce a large amount of organic acids, which is efficiently used by PNS bacteria. Total amount of H_2 produced is higher than the sum of those in the former two systems, and the amount of organic acids and organic residues are substantially decreased.

mutant bacteria showed an increased level of H_2 evolution at 4.6–6.2 and compared to the wild-type at 1.2–4.3 mol per mol of glucose equivalent, respectively [129].

3.1.5.3. Selection of PNS bacteria with improved organic acid utilization for H_2 production. Acetate is one of the major products of dark fermentation in various bacterial strains, and thus cannot be a substrate for H_2 production by dark fermentation due to thermodynamic constraints (Section 3.1.3). Furthermore, for most PNS bacteria, acetate is a rather poor substrate for the reactions of photobiological H_2 production. However, there is variability among PNS bacterial strains with some being capable of achieving highly efficient rates of photobiological H_2 production using acetate. For example, *Rhodopseudomonas* sp. decreased the acetate concentration from 1.5 g l^{-1} to about 0 in 47 h accompanied by H_2 production [139].

As fermentation by dark fermentative bacteria produces various organic acids, selection of PNS bacterial strains that are capable of using a variety of organic acids as substrates for H_2 production will be useful. Furthermore, these strains of bacteria can decrease BOD in waste water. Two examples are: 2.1–2.5 (mol H_2/mol acetate) (sludge, mainly *Rhodobacter capsulatus*), 402–474 ml H_2/g volatile suspended solid day^{-1} [139]; and 2.7 (mol H_2/mol acetate) (*Rhodobacter sphaeroides*) with COD removal of >80% (>80% succinate lactate, >70% butylate, malate, pyruvate, >60% acetate, propionate) [140]. More examples of H_2 production

Table 4
Some examples of H_2 production from acetate and other acids by PNS bacteria.

PNS bacterium	Substrate	mol H_2/mol acid	References
Rhodopseudomonas sp. 2613	Acetate	2.7	[142]
Rhodopseudomonas palustris P4	Acetate	2.4–2.8	[143]
Rhodobacter capsulatus	Acetate	2.5	[140]
Rhodopseudomonas sp.	Acetate	2.9	[139]
Rhodobacter sphaeroides ZX-5	Acetate	2.8	[141]
ibid	Succinate	6.3	ibid
Rhodobacter capsulatus	Acetate + propionate + butylate	(45%)	[144]

Table 5
Quantum requirement for production of 1 molecule H_2 via N_2ase by PNS bacteria and GSB.

	Path	Quanta	H^+ (pmf)	e^- donor	Product/e^- donor	Additional H^+ requirement	Total H^+ requirement[a] for 4ATP and $2Fd_{red}$ (and required quanta)		
							$3H^+$/ATP	$4H^+$/ATP	$5H^+$/ATP
PNS bacteria	A	1	3	UQH_2	(cyclic)				
	B			(from substrate)	UQH_2	6[b]	18	22	26
					(Quantum requirement)		(6)	(7.3)	(8.7)
	C			(from substrate)	NADH	2[c]	14	18	22
					(Quantum requirement)		(3.7)	(6)	(7.3)
GSB	A	1	4		(cyclic)				
	B	1	2	H_2S	Fd_{red}	0	10	14	18
					(Quantum requirement)		(4.5)	(5.5)	(6.5)
	C	1	0	$H_2S_2O_3$	Fd_{red}	0	12	16	20
					(Quantum requirement)		(5)	(6)	(7)

[a] Calculated for the 3 values of H^+/ATP ratio (see text).
[b] $UQH_2 \rightarrow$ [Ndh ($2H^+/e^-$)] $\rightarrow$ NADH $\rightarrow$ [Nth (H^+/e^-)] $\rightarrow$ NADPH $\rightarrow$ [FNR] $\rightarrow$ Fd_{red} (see text).
[c] NADH $\rightarrow$ [Nth (H^+/e^-)] $\rightarrow$ NADPH $\rightarrow$ [FNR] $\rightarrow$ Fd_{red} (see text).

from acetate and other acids by PNS bacteria are shown in Table 4.

3.1.5.4. Light energy conversion efficiency (from organic acids to H_2). In PNS bacteria, photobiological H_2 production is closely linked to pmf, and the estimated minimum number of quanta required for H_2 production and the light conversion efficiencies assuming that N_2ase allocates all the e^- to H_2 production (Eq. (2), Section 2.6.2) are shown in Table 5.

3.1.5.5. Some schemes for improvement of H_2 production. Rey et al. [145] described *Rhodpseudomonas palstris* mutants that produce H_2 in high N/C medium, presumably because the expression of N_2ase genes in these mutants was not repressed in the presence of combined nitrogen.

Introduction of the [FeFe]-H_2ase gene from the PNS bacterium *Rhodospirillum rubrum* into *Rhodobacter sphaeroides* resulted in enhanced photobiological H_2 production with pyruvate as the substrate [146]. The effects were modest, and given the limitations of the e^- transport system of PNS bacteria (Figs. 1 and 3), it seems unlikely that this photobiological H_2 production scheme can be substantially improved even with various organic acids as substrates.

Kars and Gündüz have discussed various schemes for the improvement of PNS bacteria-based H_2 production systems using genetic engineering [147].

3.2. Green sulfur bacteria

Green sulfur bacteria (GSB) are strictly anaerobic, Gram-negative bacteria that utilize various sulfur compounds such as sulfide, elemental sulfur, thiosulfate, etc. as e^- donors [148,149]. They have Type I RC similar to cyanobacteria and green algae, which generate strong reducing power, capable of directly reducing Fd [23,150,151]. The enzyme FNR from GSB is phylogenetically distinct from the FNRs of chloroplasts and cyanobacteria, with the discrimination between $NADP^+$ and NAD^+ being less strict for the GSB FNR [152] as compared to chloroplast and cyanobacteria FNRs. Heliobacteria [153] have Type I photosystems [23], and are unique in that they belong to *Firmicutus* (Gram-positive bacteria). Although the genome of *Heliobacterium modesticaldum* contains N_2ase genes, heliobacteria will not be further considered in this review because of the limited number of published reports.

GSB fix N_2 [153,154], and assimilate carbon by a reverse TCA cycle [155,156]. *Chlorobaculum tepidum* (formerly *Chlorobium tepidum*) uses only a limited number of organic compounds such as acetate and pyruvate, and the photoheterotrophic growth rates using these organic acids are low [157]. The genome of *C. tepidum* contains N_2ase and [NiFe]-type uptake H_2ase (Hup) genes [158], and various aspects of its metabolic pathways have been discussed [159]. Although the presence of N_2ase activity in GSB has been known for some time [154,160], research and development efforts on this group of bacteria for H_2 production have been minimal. Coculture (this case, also known as syntrophic culture) of the marine green sulfur bacterium *Chlorobium vibrioforme* with the sulfur-reducing bacterium *Desulfuromonas acetoxidans* produced H_2 under light [161]. The latter bacterium uses elemental sulfur as the terminal e^- acceptor, and reduces it to sulfide with acetate as the e^- donor (sulfur respiration). *Chlorobium* uses sulfide as the e^- donor, and produces H_2 by N_2ase with elemental sulfur as the intermediate product, which normally is further oxidized to sulfate as the final product [149]. Because GSB can directly reduce Fd by photosynthetic e^- transport, they may be good candidates for photobiological H_2 production from organic waste by coculture.

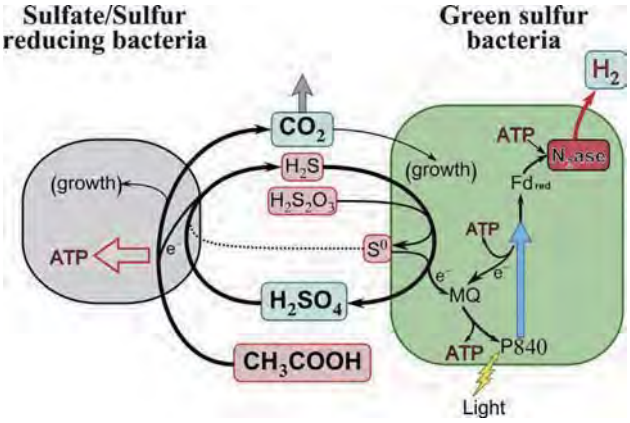

Fig. 5. H_2 production system by coculture of green sulfur bacteria and sulfate/sulfur oxidizing bacteria. Fd: ferredoxin, MQ: menaquinone, N_2ase: nitrogenase, P840: the reaction center, S^0: zero-valence sulfur or elemental sulfur.

Although *D. acetoxidans* uses elemental sulfur and not sulfate as the e^- acceptor [161], the use of sulfate-reducing bacteria as the partner of a coculture with GSB is promising for H_2 production, with removal of both organic waste and reduced sulfur compounds (Fig. 5). As many of the sulfate/sulfur-reducing bacteria and GSB contain uptake H_2ases, these activities should be eliminated for efficient H_2 photobiological production. For theoretical maximum efficiency of H_2 production, see Table 5.

3.3. Cyanobacteria

Cyanobacteria are prokaryotes that have oxygenic photosynthetic activity like eukaryotic green algae. They have chlorophyll *a* but not *b*, and the major antennas are pigment-protein complexes called phycobilins (phycocyanin, allophycocyanin, etc.). Some cyanobacteria have uptake H_2ase (Hup), [NiFe]-type bidirectional H_2ase (called Hox in cyanobacteria), and N_2ase. Hox and N_2ase can be used as the enzymes of H_2 production (there are various summaries and reviews listed in the citations; for a short summary of H_2 production research before 2002 [4] and thereafter [162–170], for H_2ase [171], for reviews on H_2ase and N_2ase [172], for evolution of nitrogen fixing cyanobacteria [173], for large-scale H_2 production using mariculture raised cyanobacteria [1,2]). Various aspects of the biological roles of Hox in cyanobacteria have been reviewed [174].

3.3.1. Heterocyst-forming cyanobacteria

This group of cyanobacteria has been frequently studied for photobiological H_2 production and are considered to be especially good candidates for optimization of photobiological H_2 production. Because much is known about their cell differentiation [175–178], they are amenable to standard molecular biological techniques [179], and the whole genome sequence of *Anabaena*/*Nostoc* sp. PCC 7120 [180] has been available to researchers for a number of years now.

Heterocyst-forming cyanobacteria reconcile two incompatible processes, namely oxygenic photosynthesis and the O_2-sensitive N_2ase reaction, by spatially separating them [173]. In response to combined-nitrogen deprivation, some filamentous N_2-fixing cyanobacteria (e.g., *Anabaena* and *Nostoc* sp.) develop differentiated cells called heterocysts [177,178], in a ratio of approximately one heterocyst per 10–20 photosynthesizing vegetative cells. Heterocysts are the site of nitrogen fixation, functioning to provide a microanaerobic environment, allowing the O_2-labile N_2ases to function in aerobic environments. Heterocysts lack O_2-evolving PS II activity, show an increased rate of respiration (for terminal oxidases, see [181–184]), and are surrounded by a thick cell envelope composed of glycolipids and polysaccharides that impede the entry of O_2 [175,178]. Vegetative cells perform oxygenic photosynthesis and fix CO_2 to synthesize organic substances such as saccharides [176]. Heterocysts obtain saccharides in the form of sucrose from vegetative cells, and the sucrose is then utilized in the N_2ase reaction as the source of e^- and, in turn, provides the vegetative cells with fixed nitrogen in the form of glutamine [36]. The cooperation between vegetative cells and heterocysts in the N_2ase reaction, and plausible routes of saccharide metabolism are shown in Fig. 6.

Since the entire genome sequence of *Anabaena*/*Nostoc* sp. PCC 7120 has been available [180], genome-wide gene expression studies of heterocyst development revealed many genes that were up- and down-regulated during heterocyst development [185]. Several genes are involved in differentiation and patterning of heterocysts [175,178] and mutations of some of them have shown to increase the frequency of heterocysts [177,186]. Since it can be expected that greater numbers of heterocysts may increase the rates of H_2 production as well as N_2 fixation, it will be worthwhile to study the effect of increased heterocysts on H_2 production.

Many of these types of cyanobacterial strains have Hup and some (but not all) of them have Hox [89,187,188]. Notably, the presence of Hup activity is considered to be a great obstacle to developing large-scale N_2ase-based H_2 production based on these organisms. Hup deficient mutants obtained by chemical mutagenesis [189] or genetic engineering [162,190–194] had no H_2-absorbing activity, and consequently showed greater photobiological H_2 production activity. Because N_2ase catalyzes an essentially unidirectional evolution of H_2, ΔHup mutant cells of *Nostoc* sp. were able to accumulate H_2 to a concentration of 29% (v/v) over several days in the presence of evolved O_2 [194].

3.3.2. Filamentous non-heterocystous cyanobacteria

There have been a relatively small number of published reports on photobiological H_2 production for this group of cyanobacteria, accordingly the discussion here is limited. Non-heterocystous cyanobacteria such as *Trichodesmium* and *Oscillatoria* fix N_2 and produce H_2 in the light with O_2 evolution. In contrast to heterocyst forming cyanobacteria that spatially separate N_2ase in heterocysts from O_2 evolving vegetative cells, these types of strains do not develop morphologically discernible heterocysts. One member of the group, *Trichodesmium*, is ubiquitous in tropical and subtropical seas and is known to be an important contributor to global N and C cycling. Thus, this group has potentially unique physiological mechanisms for sustaining O_2-evolving photosynthesis in the presence of an O_2-sensitive N_2ase reaction. Some groups of researchers postulate based on immune-electron microscopy [195] or fluorescence microscopy observations [196] that N_2ase in *Trichodesmium* is temporally localized in a subset of contiguous cells. In addition, the cells could turn photosynthesis on and off within 10–15 min (as measured by O_2-evolution) under continuous illumination [196].

The other study on *Trichodesmium* cells has used high-resolution mass spectroscopy to quantitatively Image ^{13}C and ^{15}N uptake. In this study, transient inclusion of ^{15}N and ^{13}C into discrete subcellular bodies identified as cyanophycin granules was observed [197]. A cyanophycin granule [198] is a nitrogen reserve polymer composed mainly of arginine and aspartate, which is formed when the rate of combined nitrogen supply exceeds that of organic compounds generated by photosynthesis. The appearance of the granules in the light indicates that these cells actively fix N_2 in a temporal fashion. The granules were not confined to a subset of contiguous cells, but randomly distributed. This observation is congruent with immune-electron microscopy observations where N_2ase proteins were seen almost uniformly distributed throughout the cells on filaments [199–201]. The maximal CO_2 fixation rates were detected

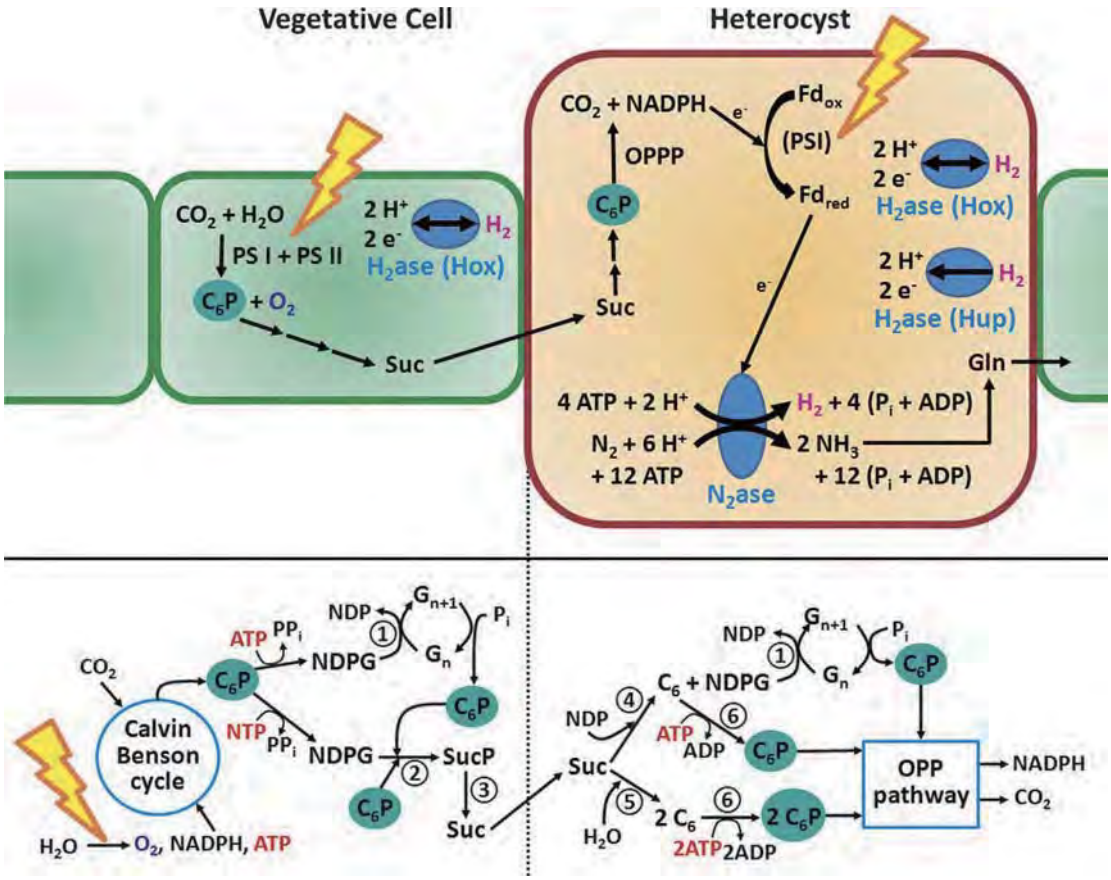

Fig. 6. H_2 metabolism in heterocyst forming cyanobacteria. Upper part: Metabolite exchange between vegetative cells and heterocysts. Lower part: Metabolic pathways of saccharides. C_6P: hexose phosphate, Fd: ferredoxin, G_n and G_{n+1}: glycogen with the number (n) and ($n+1$) of glucose residues, H_2ase: hydrogenase, Hox: bidirectional H_2ase, Hup: uptake H_2ase, N_2ase: nitrogenase, NDP: nucleoside diphosphate (ADP or UDP), NDPG: nucleoside diphosphate glucose (ADPG or UDPG), OPP pathway: oxidative pentose phosphate pathway, Suc: sucrose, SucP: sucrose phosphate. Enzymes: ① glycogen synthase, ② sucrose phosphate synthase, ③ sucrose-phosphate phosphatase, ④ sucrose synthase, ⑤ invertase, and ⑥ hexokinase. In the right, for producing 2 C_6P, sucrose synthase ④ pathway requires 1 ATP, and invertase pathway ⑤ requires 2 ATP.

in the morning, compared with maximal N_2 fixation rates in the afternoon, suggesting that CO_2 and N_2 fixation in *Trichodesmium* is regulated in part by temporal factors [197]. *Trichodesmium* cells are known to accumulate glycogens [202] indicating that under combined nitrogen deprivation conditions, the carbon assimilation exceeds what is needed for growth. Finzi-Hart et al. [197] speculated that *Trichodesmium* uses these dynamic storage bodies to uncouple CO_2 and N_2 fixation from the dynamics of overall growth, and that increased O_2-consumption activities within individual cells enable them to temporally segregate the biochemically incompatible processes of CO_2 and N_2 fixation.

Other adaptive strategies have been reported for other strains in this group, including an *Oscillatoria* sp. from the sea, where N_2ase activity was mainly expressed in the dark, indicating a diurnal rhythm [203]. A filamentous non-heterocystous *Oscillatoria* sp. strain Miami BG7 with high photobiological H_2 production activity selected from a marine environment was found to be devoid of H_2ase activity and capable of active photobiological H_2 production under Ar at 260 μmol mg Chl^{-1} h^{-1} [204].

3.3.3. Unicellular cyanobacteria

The majority of nitrogen fixing unicellular cyanobacteria strains have Hup, with some of them bidirectional H_2ase (Hox) [162,164,170,172].

3.3.3.1. N_2ase based H_2 production. Unicellular N_2 fixing cyanobacteria occur in some strains of the genera *Cyanothece*, *Synechococcus*, *Gloeothece*, etc. In order to maintain both O_2-sensitive N_2ase and O_2 evolving photosynthesis within the same microorganism, unicellular N_2 fixing cyanobacteria have adopted the main strategy whereby the two activities are temporally separated: O_2 evolving photosynthesis occurs during the day, and N_2 fixation occurs during the night [205–209] accompanied by N_2ase specific gene expression during the night [210] and photosynthesis specific gene expression in the light [211–213]. During the early night, active respiration removes O_2 and produces ATP required for N_2ase by oxidative phosphorylation. From recent genome-wide gene expression profiling studies in *Cyanothece* sp., many genes related to N_2 fixation and also to uptake H_2ase genes (*hups*) appear to be expressed mainly in the dark period, while genes related to photosynthesis appear to be expressed mainly in the light period. In some species, however, the regulation of expression of the N_2 fixation and uptake H_2ase genes as measured in the whole culture is more as tightly regulated than the expression of the photosynthesis-related genes [213]. These circadian patterns of expression [214] are likely modulated at the molecular level by Kai proteins [215,216]. In some species, circadian H_2 production from the culture still occurs in the light, even under continuous illumination [209]. Temporal cessation of oxygenic photosynthetic carbon assimilation seems to occur in some portion of cells as described for the non-heterocyst forming filamentous cyanobacteria (Section 3.3.2) [197] (Fig. 7).

Some of the *Cyanothece* strains photoheterotrophically produce H_2 in the presence of glycerol, with rates reported as high as 300

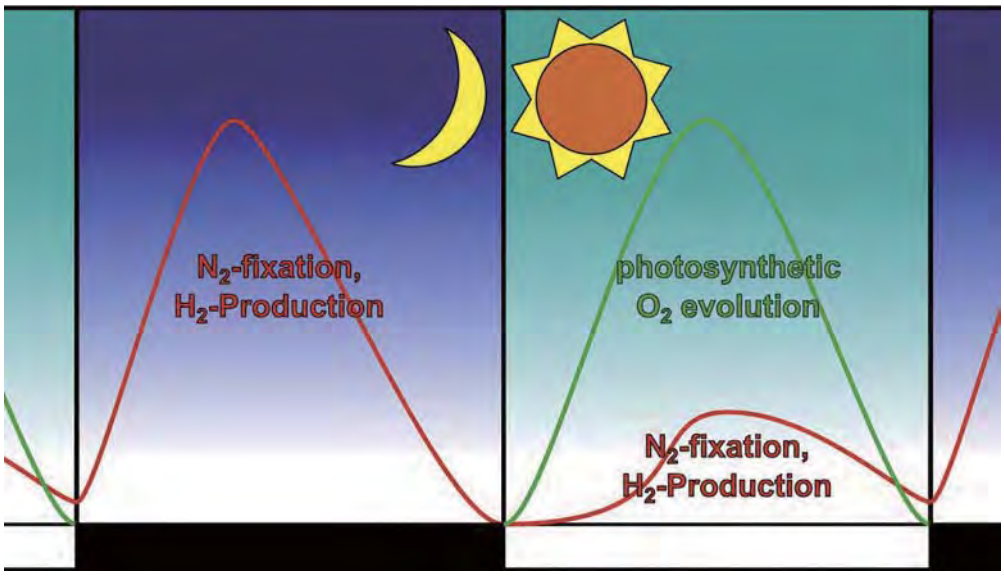

Fig. 7. Schematic illustration of H_2 production by unicellular cyanobacteria via temporal separation of oxygenic photosynthesis and N_2ase. Schematic illustration of circadian rhythm of H_2 production and oxygenic photosynthesis. In the majority of cells, N_2ase and H_2 production activities are high in the night, but some portions of cells evolve H_2 in the day time.

Table 6
Some records of the rates of H_2 production by oxygenic phototrophs.

Phototrophs	Strains	e^- donor(s)	Rate (μmol mg Chl^{-1} h^{-1})	Light intensity	Duration	Comments	References
Cyanobacteria	Cyanobacterium						
Unicellular	*Synechococcus* sp. Miami BG 043511		About 140	25 W m^{-2} (PAR)	1 d	Accumulation	[222]
	Cyanothece sp. strain ATCC 51142	50 mM glycerol + H_2O	300	30 μmol m^{-2} s^{-1}	About 24 h	Accumulation	[217]
	Cyanothece sp. strain ATCC 51142	50 mM glycerol + H_2O	465	100 μmol m^{-2} s^{-1}	12 h	Accumulation	[218]
	Cyanothece sp. strain ATCC 51142	H_2O	370	100 μmol m^{-2} s^{-1}	12 h	Accumulation	ibid
	Cyanothece sp. strain ATCC 51142	H_2O	400	140 μmol m^{-2} s^{-1}	a few h	Accumulation	[219]
	Cyanothece sp. strain ATCC 51142	H_2O	125	140 μmol m^{-2} s^{-1}	over 100 h	Accumulation	ibid
Heterocystous	*A. cylindrica* B-629	H_2O	320	400 W m^{-2}	1 d	Ar flow	[220]
	Anabaena sp. PCC 7120 ΔHup	H_2O	53	70 W m^{-2}	1 h	Accumulation	[225]
	Anabaena sp. PCC 7120 ΔHup	H_2O	63	152 μmol m^{-2} s^{-1}	1 d	Accumulation	[227]
	A. variabilis PK84 (H_2ase-deficient)	H_2O	168	140 μmol m^{-2} s^{-1}	0.5 h	Accumulation	[223]
	A. variabilis ATCC 29413 AVM13 Δ*hup*	H_2O	About 135	100 μmol m^{-2} s^{-1}	4 h	Accumulation	[162]
	Anabaena sp. PCC 7120 AMC 414	H_2O	About 110	100 μmol m^{-2} s^{-1}	4 h	Accumulation	ibid
	Anabaena sp. PCC 7120 ΔHup	H_2O	About 80	200 μmol m^{-2} s^{-1}	1 h	Accumulation	[194]
	Nostoc sp. PCC 7422 ΔHup	H_2O	About 100	200 μmol m^{-2} s^{-1}	1 h	Accumulation	ibid
Filamentous non-heterocystous	*Oscillatori*a sp. Miami BG7	H_2O (some portion from stored glycogen)	260	2 × 30 W fluorescent lamp	About 2 d	Accumulation	[221]
Green algae	Green algae						
	Chlamydomonas reinhardtii	Acetate + H_2O	5.94	300 μmol m^{-2} s^{-1}	3 h	Synchronized cells	[224]
	Chlamydomonas reinhardtii	Acetate + H_2O	4	285 μmol m^{-2} s^{-1}	A few d	Gel-immobilized	[226]
	Chlamydomonas reinhardtii (D1 mutant)	Acetate + H_2O	27.5	2 × 140 μmol m^{-2} s^{-1}	About 24 h	Accumulation	[228]

[217], 465 [218], and photoautotrophically 400 μmol mg Chl^{-1} h^{-1} [219] (see Table 6).

3.3.4. H_2ase-based H_2 production by cyanobacteria

A unicellular non-nitrogen-fixing *Synechocystis* mutant deficient in type I NADH dehydrogenase showed increased photobiological H_2 production activity catalyzed by NiFe-H_2ase compared to the wild-type, although the activity was low [229]. Non-N_2 fixing *Gloeocapsa alpicola* produced H_2 in the dark accompanied by acetate production [230]. A two-stage H_2 production scheme using H_2ase by non-N_2 fixing *Anthrospira* (formerly *Spirulina*) has been proposed [231]. In the 1st stage: accumulation of starch, in the 2nd stage: dark fermentative H_2 production by [NiFe]-H_2ase. Because dark fermentation depends on NAD(P)H-linked H_2ase, it will be challenging to increase the H_2 yield per glucose residue in starch (see Section 2.5.4).

Ferreira et al. [232] performed LCA analysis of two-stage H_2 production by heterocystous cyanobacterium *Nostoc* sp. followed by dark fermentation by enterobacteria. They estimated the cost of H_2 from a laboratory-scale H_2 production scheme partly based on theoretical calculations, and concluded that with technical improvements, the system could be economically viable. However, the target value of production is 0.1 kg H_2 per kg biomass (roughly equivalent to 9 mol H_2 per mol glucose), which will be a challenging target to meet using dark fermentation of enterobacteria (see Section 3.1.3).

Using cyanobacteria cells as the feed stocks, a three-stage H_2 production scheme has been presented; Stage 1: growth of cyanobacteria, Stage 2: dark fermentation, and Stage 3: photofermentation by PNS bacteria [99].

3.4. Green algae

It has been 70 years since Gaffron and Rubin [233] found that cells of the green alga *Scenedesmus obliquus* kept under anaerobic conditions for several hours could evolve H_2 upon subsequent illumination. However, the H_2 evolution activity was very low and short-lived. Unicellular green algae such as *Chlamydomonas* and *Scenedesmus* have bi-directional [FeFe]-H_2ase, but no N_2ase. The most widely-studied green algae for H_2 production is *Chlamydomonas reinhardtii*, and a number of review articles have been published in recent years [6,8,10,234,235,237,239,241].

3.4.1. Chlamydomonas

In *Chlamydomonas*, the [FeFe]-H_2ase is located in the chloroplast [62,238], where it is highly active with a turnover rate of 6000–9000 s^{-1} [3], but it is extremely sensitive to O_2. When the catalytic metal cluster in the matured H_2ase is inactivated by O_2, cells cannot reconstruct the cluster, and H_2ase must be renewed starting from protein synthesis. Accordingly, the key challenge of using green algae for H_2 production is how to reconcile the requirement of O_2-evolving photosynthesis with H_2 production that is sensitive to O_2. Under sulfur-deficient growth conditions, the light-saturated PS I activity was unaffected by sulfur deprivation (S-deprivation), whereas the PS II partial reaction rate was reduced by more than 50% after 1 day [243], with the participation sac1 gene for the acclimination [240].

3.4.1.1. Sustained H_2 production by sulfur starvation. Melis et al. [242], using *Chlamydomonas*, succeeded in separating the O_2-evolving photosynthesis stage from the subsequent photobiological H_2-production stage for more than 120 h by simply transferring the cells from a S-replete medium to a S-deprived medium. This report led to further studies of the various aspects of photobiological H_2 production utilizing *Chlamydomonas*. The entire process of H_2 production can be summarized as follows [224,236,243]:

(Stage 1) Growth of cells by ordinary photosynthesis accompanied by O_2 evolution in S-replete medium and internal stores of saccharides, etc.
(Stage 2) Transfer of cells to S-deprived medium resulting in a gradual decrease of PS II, because the D1 protein of PS II is continuously inactivated by illumination and in the absence of S-containing amino acids the D1 protein cannot be efficiently replenished. Consequently, the cells cease to multiply and there is breakdown of various proteins notably Rubisco, along with the accumulation of a large quantity of starch in chloroplasts.
(Stage 3) After 10–15 h of anaerobiosis, algal cells induce the reversible [FeFe]-H_2ase in the chloroplast stroma and after about 20 h, cells began to continuously evolve H_2 for several days consuming substantial amounts of internal starch and protein [243]. When the reserve starch is exhausted, the H_2 production ceases. In the H_2 production stage, the apparent O_2 production ceased [244]. For reviews of early studies on algal biological H_2 production, see [245–247].

Subsequent studies further revealed the details of H_2 production by *Chlamydomonas*. Although the apparent O_2 evolution ceases upon S-deprivation, PS II is not totally inactivated. With the remaining low level of PS II activity, photo-produced O_2 is removed by active mitochondrial respiration as well as by chloroplast metabolic pathways that consume starch and other reserves [248,249]. The e$^-$s for photobiological H_2 production largely depend on both PS II and PS I activities and on non-photochemical catabolic activities with e$^-$ fed from organic reserves to PQ and NAD(P)$^+$ [248–252] (Figs. 8 and 9).

Chlamydomonas contains two mechanisms that apparently allow the cells to overcome long-term anaerobiosis; pyruvate-formate lyase activity (Section 3.1.3), seldom found in eukaryotic algae, and a fermentative carbon degradation pathway [236,250]. For anaerobic microorganisms, fermentation produces most of the cellular ATP supply. With glucose as the substrate, yeast (ethanol

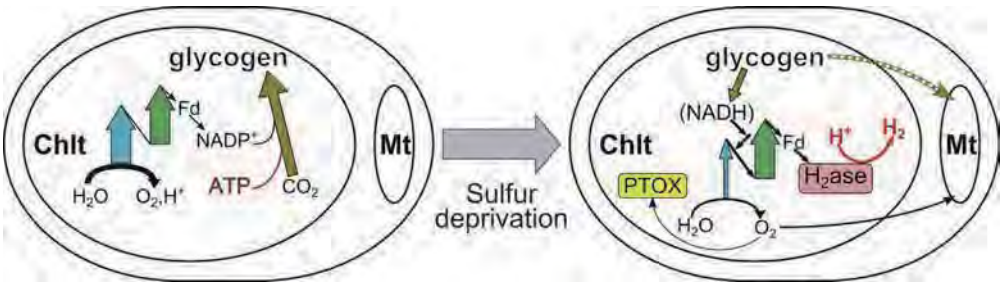

Fig. 8. H_2 production by S-deprived *Chlamydomonas*. Left: S-replete cells accumulate organic substances by ordinary photosynthesis. In the transition stage (not shown in the figure), S-deprived cells accumulate large amounts of starch by photosynthesis and by degradation of existing cell materials such as PS II proteins, etc. Right: The cells still have low PS II activity, and O_2 produced is consumed by mitochondria and also by chloroplast alternative oxidase (PTOX) [248].

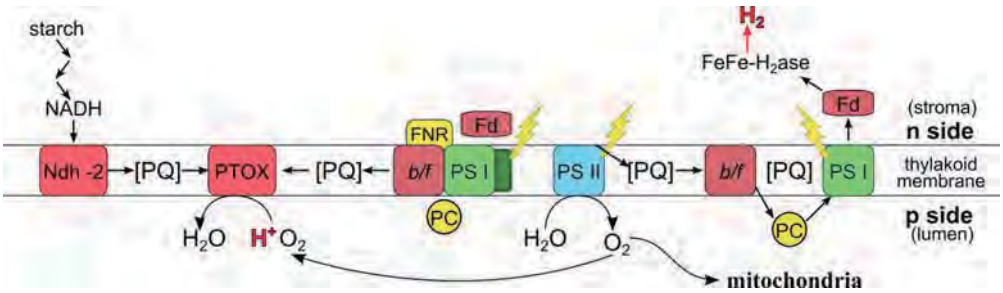

Fig. 9. Reaction center and linked e^- transport system in *Chlamydomonas*. In the middle of the figure, some portion of PS I forms a protein super-complex composed of PS I with its own light-harvesting complex (LHCI), the cytochrome *b*|*f* complex (Cyt *b*|*f*), FNR, the integral membrane protein PGRL1, etc. contributes to a part of the cyclic e^- transport system around PS I [256]. The latter may involve antimycin A-sensitive Fd-mediated system [34] directly or indirectly involving PGR5 protein [253]. When PQ is fully reduced, e^-s from organic substances as well as from PS II are used for H_2 production with H^+ as the e^- acceptor. These processes on the whole contribute to synthesis of ATP required for the maintenance of cell functions (for details, see text). Ndh-2 (type-2 NADH-PQ oxidoreductase, which does not generate pmf in contrast with Ndh-1 typically found in bacteria as well as in animal and yeast mitochondria) [254,255], mediates reduction of PQ using NADH derived from organic substrates. For discussion of cyclic pathway, see [257,258], *b*|*f*: cytochrome *b*|*f* complex, Fd: ferredoxin, Ndh: Type-2 NADH dehydrogenase, PTOX: plastoquinol terminal oxidase.

as the end product) and lactic acid bacteria (lactic acid as the end product) synthesize net 2 ATP per glucose molecule. In *Chlamydomonas*, the glycolytic pathway synthesizes 2 ATP per glucose with pyruvate and NADH as the intermediary products. When pyruvate is cleaved by pyruvate:Fd oxidoreductase or pyruvate-formate lyase, an additional 2 ATP are synthesized from acetyl phosphate via acetyl-CoA leaving NADH and Fd_{red} for the former and NADH and formate for the latter (Section 3.1.3). In order for ATP formation to continue, NADH and Fd_{red} need to be eliminated either by further fermentation (e.g., to butylate, propionate) or by H_2 evolution through H_2ase in the light. As evidence of this biochemical pathway, a *Chlamydomonas* mutant with a disrupted pyruvate-formate lyase gene showed a decreased H_2 production activity in the light, but not in the dark [259]. The growth media for laboratory experiments usually contain acetate, but completely photoautotrophic H_2 production is also possible in media devoid of acetate [260].

Since the whole genome sequence of *Chlamydomonas reinhardtii* has been available [261], in depth studies on a variety of projects related to H_2 production are underway. From studies using genome, transcriptome, and metabolome data, the switching of the above-described stages is accompanied by dramatic changes in the gene expression and metabolic patterns of the cells [262,263]. The ability of *Chlamydomonas* to produce H_2 by S-deprivation seems to be intimately related to the activity of this organism to survive frequently encountered anaerobic periods in the natural environment [264,265]. Under anaerobic conditions, one metabolic route of degradation of pyruvate in the mitochondria seems to be via pyruvate-formate lyase, phosphotransacetylase and acetate kinase, producing ATP, instead of acetyl-CoA that is fed to the TCA cycle in aerobic metabolism [266]. The *Chlamydomonas* mutant cells that have no [FeFe]-H_2ase activity accumulated higher amount of succinate compared to the wild-type cells under anaerobic conditions [267].

It should be noted that not every unicellular green algae has the capacity to photobiologically evolve H_2 by S-deprivation [268]. The photobiological H_2 production activity and H_2 activity of 4 green algal strains was compared with *C. reinhardtii*, and some of them showed higher and other lower activities [269]. The authors concluded that unique anaerobic acclimation strategies have evolved in distinct green algae, resulting in differential levels of H_2ase activity and species-specific patterns of NADH reoxidation during anoxia. For a description of H_2 production activity screening methodology from naturally occurring green algae, see [270].

The rate of H_2 production is generally not so high, and various strategies for further improvement have been discussed [234].

3.4.1.2. Two-stage and three-stage H_2 production systems using green algal biomass. Benemann [271] proposed a two-stage indirect H_2 production scheme: first growing algae without H_2 production in open ponds, followed by H_2 production by dark fermentation. He proposed this scheme, because the algae growth rate is high, and H_2 production rate is low (Section 5.1). Tekucheva and Tsygankov [99] proposed a three-stage H_2 production system adding a photofermentation stage by PNS bacteria to the above scheme (Section 3.1.5).

4. Need for further improvements

4.1. Energy conversion efficiency

Although much progress has been made in understanding the biological and biochemical basis of photobiological H_2 production across many different organisms, the knowledge has yet to be put into practical use. If photobiological H_2 production is to be developed as the source of large-scale renewable energy, achieving improvements in light energy conversion efficiency and in rates of H_2 production are essential (for discussion of needed improvements, see [13,272]).

For comparison purposes, the values of the minimum quantum requirement for H_2 production by PNS bacteria and GSB are shown in Table 5. Depending on the e^- donor (NAD^+- or UQ-reducing substrate) and H^+/ATP ratio (3, 4, or 5), the values of the minimum quantum requirement by PNS bacteria are calculated to be between 3.7 and 8.7. Assuming that PNS bacteria utilize 400–900 nm light with the mean value of energy 184 kJ mol^{-1} (650 nm light), the theoretical maximum light energy conversion efficiency into H_2 (286 kJ mol^{-1}, (HHV) see Table 8) is calculated to be between 17.9 and 42.0%. Assuming that 400–900 nm light comprises 61% of the total solar radiation in energy, the maximum solar energy conversion efficiency is calculated to be between 10.9 and 25.6%.

Similarly, depending on the e^- donors (sulfide or thiosulfate) and H^+/ATP ratio (3, 4, or 5), the values of the minimum quantum requirement for H_2 production by GSB are calculated to be between 4.5 and 7.0. Assuming that GSB utilize light of 400–870 nm with the mean value of energy 189 kJ mol^{-1} (635 nm light), the theoretical maximum light energy conversion efficiency into H_2 is calculated to be between 21.6 and 33.6%. Assuming that 400–870 nm light comprises 59% of the total solar radiation, the maximum solar energy conversion efficiency is calculated to be between 12.7 and 19.8%.

For N_2ase-based photoautotrophic H_2 production by cyanobacteria, Sakurai and Masukawa [1] calculated values by assuming an H^+/ATP ratio of between 3 and 4, the maximum energy conversion

efficiency between 13.9 and 16.3% for 550 nm light and between 6.3 and 7.3% vs. the total solar radiation, respectively. For H_2ase-based photoautotrophic H_2 production by green algae (starch accumulation followed by its decomposition and PSI photoreaction), the maximum energy conversion efficiencies have been calculated to be 22% vs. 550 nm light and 9.9% vs. the total solar radiation, respectively.

Under field conditions, the maximal photosynthesis efficiencies of land plants are estimated to be 3.5% and 4.3% for C3 and C4 plants, respectively [273] (Compare with the theoretical maximum values of 12.5% (vs. total solar radiation, 27.6×0.45) and 9.3–11% (vs. total solar radiation, $(20.7–24.5) \times 0.45$) for C3 and C4 plants, respectively [1]). These values are about 28% and 39–46% of the theoretical maximum efficiencies for C3 and C4 plants, respectively. In bioreactors using microphototrophs, the composition of gases such as CO_2, N_2, Ar, etc., can be optimized for H_2 production, and wild-type or genetically selected or genetically engineered strains can be grown without resource competition from other organisms. Thus, using bioreactors for photobiological H_2 production appears to be a better strategy than relying on variable field conditions for attaining the higher actual/theoretical efficiency ratios.

4.2. A selection of proposed strategies for improving photobiological H_2 production

4.2.1. Improvement of H_2ase

4.2.1.1. Introduction of heterologous H_2ase and identification of some candidate H_2ases that could be targeted for improvement in H_2ase-based H_2 production. The bidirectional H_2ase present in some strains of cyanobacteria is [NiFe]-H_2ase with NAD(P)H/NAD(P)$^+$ as the reaction partner. Because [FeFe]-H_2ase receives e^- from low-potential Fd_{red}/Fld_{red} and because its molecular activity is higher than [NiFe]-H_2ase [3], introduction of the [FeFe]-H_2ase gene from *Clostridium pasteurianum* into the cyanobacterium *Synechococcus* sp. resulted in the production of active [FeFe]-H_2ase [132]. This result was surprising because the structure of the metal cluster of [FeFe]-H_2ase differs somewhat from that of [NiFe]-H_2ase. Although both H_2ases bind CN and CO as ligands in the catalytic metal cluster, the H_2ase maturation proteins required for the catalytic cluster formation differ between the two. It seems that cyanobacterial [NiFe]-H_2ase maturation proteins [69] substitute the role of [FeFe]-H_2ase counterparts of *Clostridium* [67].

In order to overcome the O_2-lability of H_2ase, some other candidate H_2ases for heterologous incorporation into phototrophs are presented below:

- [NiFe]-H_2ase from *Ralstonia eutropha* is reported to be O_2-tolerant [274,275].
- H_2ase from the aerobic hyperthermophilic archaeon *Aeropyrum camini* retained 75% of its initial activity after a 168 h of air exposure, and showed a half-life of 48 h at 90 °C [276].
- Membrane-associated H_2ase from the deep-sea Epsilonproteobacterium *Hydrogenimonas thermophila* was partially purified, and the preparation retained 37% of its initial activity after 72 h of air exposure [277].
- [NiFeSe]-H_2ase from *Desulfomicrobium baculatum* is a selenocysteine enzyme, and a highly efficient H_2 cycling catalyst. Although traces of O_2 (much less than 1%) rapidly and completely remove H_2 oxidation activity, the enzyme sustains partial activity for H_2 production even in the presence of 1% O_2 in the atmosphere [278].
- [NiFe]-H_2ase from the aerobic H_2 oxidizer *Ralstonia eutropha* is highly resistant to O_2, and binds one additional unprecedented [4Fe-3S] cluster [279].

Thermotolerant H_2ases have been reviewed [280], and introduction of heterologous H_2ases have been discussed [68,281].

4.2.1.2. Engineering of a putative gas channel of H_2ase. Recent studies of the 3-D structure of various H_2ases have shown that the catalytic metal clusters appear to be embedded inside the protein. Putative channels for entering/exiting H_2 and O_2 have been identified [282–284]. As the molecular size of O_2 is slightly larger than that of H_2, one intriguing strategy for improving the H_2ase would be to increase the specificity of the gas channel by introducing a more bulky residue(s) via site-directed mutagenesis. This strategy is supported by studies of *Desulfovibrio fructose*, in which both valine and leucine residues were replaced by methionine residues, and resulted in decreased susceptibility to O_2 inactivation [285] (see also, [286–288]).

4.2.1.3. Truncated antenna. Phototrophic microorganisms contain an abundance of antenna pigments that contribute to the individual organisms survival and propagation under fluctuating conditions, including low light. However, in a mass culture of phototrophic microorganisms, the high concentration of antenna pigments decreases the light utilization efficiency of the culture as a whole because cells near the surface absorb the majority of light energy and thus cannot efficiently use it for photosynthesis. This is due to rate limitations of the processes following the initial photochemistry in RCs ("dark reaction": photophosphorylation, carbon assimilation, etc.).

Various authors have speculated that based on theoretical considerations, a lower light harvesting pigment content should result in higher photosynthetic productivity under high light intensity [15,289], (for a review [290]). There have been several published studies that support this concept. A mutant of the cyanobacterium *Synechocystis* deficient in the antenna pigment phycocyanin was created by nitrosoguanidine mutagenesis, and the photosynthetic activity of the culture was found to be 20–30% higher than that of the wild-type [291,292]. A mutant of the purple bacterium *Rhodobacter sphaeroides* created by UV irradiation had a smaller antenna size than that of the parent strain, and the H_2 evolution rate of the mutant cell suspension was 1.5 times higher than that of the wild-type strain [293]. The antenna pigment content can be changed by growing algae under different light intensities. The green alga *Dunaliella salina* cells grown under high light with decreased antenna Chl content showed higher photosynthetic activity at high light intensities than the cells grown under low light with larger antenna size [294]. A mutant of the green alga *Chlamydomonas reinhardtii* with truncated antenna was created by DNA insertional mutagenesis, and the culture of the strain showed greater solar energy conversion efficiencies under high light intensities [295].

Thus, the truncation of antenna pigments appears to be an effective strategy for improving photobiological H_2 production activity for a variety of phototrophic organisms [226,235,296,297] (reviewed in [290]).

4.2.1.4. Selection of promising strains followed by metabolic engineering. For the 4 groups of phototrophs described above, the entire genome sequence is available for at least several strains within each group. Based on information from genome-wide gene expression, and proteomic and metabolomic studies, the limiting steps in the metabolic networks leading to H_2 production will soon be identified in strains of model organisms. Selection of strains with desirable traits such as high photosynthetic activity under outdoor field conditions, followed by targeted metabolic engineering [298–301] will likely be pursued as a strategy for improvement in

Table 7
Some reports of light energy conversion efficiency to H_2 by various phototrophs.

Phototrophs	Main substrate	Efficiency (%)	Light intensity ($W\,m^{-2}$)	Light intensity ($\mu mol\,m^{-2}\,s^{-1}$)	Light source	Duration of time	Comments	References
PNS bacteria								
Rhodobacter sphaeroides	Lactate	7.9	50 (total rad.)		Xe	1–2 h	Agar-immobilized	[302]
ibid		6.2	75 (total rad.[a])		Xe-based Solar simulator	1–2 h		ibid
ibid		About 2	1000 (total rad.)		Xe-based Solar simulator	1–2 h		ibid
Rhodopseudomonas sp.	Acetate	6.2		43	Halogen/tungstem	about 200 h		[139]
Rhodospirillum rubrum		7.5	3 (870 nm)		Infrered lamp	a few min		[303]
GS bacteria								
Chlorobium vibrioforme		8.6	3 (812 nm)		Infrered lamp	a few min		[303]
Cyanobacteria								
Synechococcus sp. Miami BG043511	Carbohydrates	5.5	17 (PAR[b])		Fluorescent tube	4 h		[222]
H_2O		2.6	17 (PAR)			24 h		ibid
Nostoc sp. PCC 7422, ΔHup	H_2O	3.7	18 (PAR)		Fluorescent tube	6 d		[194]
Anabaena sp. TU37-1	H_2O	2.4	22 (PAR)		Fluorescent tube	12 h		[304]
Anabaena variabilis PK84 (H_2ase-deficient)	H_2O	0.029–0.094	max. 850 (total rad.)		Outdoors	40 d	June–July, London	[305]
Anabaena sp. PCC 7120 (uptake H_2ase-deficient)	H_2O	0.042	max. 850 (total rad.)		Outdoors	1 d	August, London	[74]
Green algae								
Chlamydomonas reinhardtii	H_2O + acetate	0.36		120		1 h	Gel-immobilized	[306]
ibid	ibid	0.24		200		1 h	Suspension	ibid
Chlamydomonas reinhardtii	H_2O + acetate	0.4		19 (PAR)	Fluorescent tube	240 h	Gel-immobilized	[226]

[a] total rad.: total radiation.
[b] PAR: photosynthetically active radiation (400–700 nm for oxygenic phototrophs).

the near future [269]. Some reports of the light energy conversion efficiencies to H_2 by oxygenic phototrophs are tabulated in Table 7.

5. Need for cost reductions

Research efforts aimed at identifying and optimizing renewable energy production in various phototrophs have increased in recent years, but the most important question that remained to be answered is that of feasibility; specifically if phototroph-based systems will be able to produce net energy in the future at reasonable costs? In the following discussion, we highlight the important cost considerations for photobiological H_2 production. Life cycle assessment of biohydrogen production by photosynthetic processes has been described [307].

5.1. Bioreactors and storage

Amos [330] estimated the cost of H_2-based photobiological H_2 production by the green alga *Chlamydomonas*, and pointed out that if the price of the bioreactor exceeds \$100 per m^2, then the system will not be economically viable. Various types of bioreactors for outdoor use have been proposed (e.g. [228,305,308–312], but many of them are designed for the research-scale evaluation of photobiological H_2 productivity and are not designed to minimize costs.

Benemann [271] proposed a two-stage indirect H_2 production scheme: first growing algae without H_2 production in open ponds, followed by H_2 production by dark fermentation. He proposed this scheme, because from the cost analysis of open pond and photobiological H_2 production bioreactor, he found that the cost of the former is \$5 m^{-2} and that of the latter about \$130 at that time of the publication. Melis [234] inferred based on their unpublished results that construction materials and operational costs of a photobioreactor (including materials, fertilizer, personnel, etc.) can be as low as \$1.67 m^{-2}, recurring every 2 months of continuous operation. However, the actual materials and the structure of the bioreactor are not described.

Prince and Kheshgi [313] enumerated various technical issues that need to be addressed to make photobiologically produced H_2 economically viable, with one of them being the need for inexpensive H_2-barrier bioreactors. They suggested the use of H_2 barrier plastic bags as part of an economically feasible system. Elaborating on this idea, Sakurai et al. [1,2] have proposed the use of large flexible H_2 barrier plastic bioreactors (e.g., 25 m × 200 m) floating on the ocean surface for photobiological H_2 production by fresh water phototrophs. In this system, the bags will spontaneously spread over the sea surface due to the difference in densities of the medium and sea water. H_2-barrier plastic bags for laboratory use with a H_2 permeability P_m of about 20–90 $cm^3\,m^{-2}\,d^{-1}\,atm^{-1}$ are commercially available [314]. The leak of H_2 produced over 60 days from such a plastic bioreactor with a H_2 P_m value of

Table 8
H_2 energy (HHV) conversion table.[a]

	MJ	kWh	kCal	kOe
kg H_2	142	39.4	34×10^3	3.4
m^3 H_2	12.7	3.55	3.06×10^3	0.306

kOe (kilo oil equivalent) = 10×10^3 kcal.
1 m^3 H_2 (STP) = 0.08988 g.
H_2 energy.
$H_2 + 1/2O_2 = H_2O$.
ΔH (HHV: higher heating value, the product is liquid water) = -286 kJ mol^{-1}.
ΔH (LHV: lower heating value, the product is vapor) = -242 kJ mol^{-1}.
$\Delta G = -242$ kJ mol^{-1}.
[a] Ref. [326] and other sources.

50 cm^3 m^{-2} d^{-1} atm^{-1} is calculated to be less than 0.2% of the produced H_2 (based on the following assumptions; H_2 production at an energy conversion efficiency of 1.2%, solar energy: 1500 kWh m^{-2}, initial gas (mainly Ar) 0.5 m^3 m^{-2}) [314]. Similar types of bags have been used for photobiological H_2 production by PNS bacteria trapped in nanoporous latex coated materials [315].

Amos [330] also pointed out the importance of reducing storage costs. At 25 °C, the energy content of 1 m^3 H_2 at 1 atm is less than 0.3 kg of crude oil (Table 8), and cost reduction of storage is essential for practical applications of photobiological H_2 production. The purification and storage issues have been discussed [316].

5.2. Cost of nutrients

Clarens et al. [317] performed a life cycle analysis of the production of biomass by green algae based upon their life cycle model: Briefly, a mass culture of algae is grown with bubbling of CO_2 in open ponds using a raceway configuration in 3 sites in USA,, followed by harvesting. Their analysis indicated that the environmental burden of producing energy exceeded the produced biomass energy. They calculated that in order to produce 1.0 unit of biomass energy, more energy is expended than gained at the current levels of productivity (total of about 1.1–1.2 unit, consisting of about 0.5 unit for nutrients (fertilizers), about 0.35 unit for CO_2, about 0.2–0.35 unit for water, and about 0.1 unit for the energy needs of the operation). Their LAC analysis has influenced biofuel R&D efforts such as biodiesel oil production by the green alga *Botryococcus* that requires total harvesting of cells. In order to deal with the energy input costs, various improvements are proposed including the use of eutrophic waste water or flue gas from coal power plants, etc.

It seems that photobiological H_2 production has an advantage over other photobiological energy production systems such as biodiesel production, because the cultures can produce H_2 for a long time without harvesting the cells. For systems using PNS bacteria, the cost of nutrients is not an insurmountable problem, because readily available nutrient-rich waste products from agriculture, forestry, drainage, etc., can be used to support culture growth with only minor additions of deficient nutrients needed to support the growth of bacteria. The cost of nutrients is further alleviated in photobiological H_2 production systems using oxygenic phototrophs as they can evolve H_2 for a long time without harvesting the cells and without changing the culture medium. For example, *Chlamydomonas* cells, after H_2 production by sulfur deprivation, resume H_2 production by adding sulfate followed by accumulation of starch by ordinary photosynthesis [10]. In another example, cyanobacteria have been reported to produce H_2 for 60 days without changing the culture medium [331].

5.2.1. Filling gas for N_2-based H_2 production

This potential limitation is not a critical issue for H_2 production by PNS bacteria, because removing gas from the initial culture will lead to production of H_2 and CO_2 as the main products. It is important for N_2ase-based H_2 production by cyanobacteria with H_2O as the substrate, and the products are H_2 and O_2 in about 2:1 ratio. High concentrations of O_2 may decrease the N_2ase activity even if cyanobacteria have developed various measures to cope with O_2. In order to alleviate the harmful effects of high concentrations of O_2, the bioreactors for cyanobacterial H_2 production are usually filled with Ar plus low concentrations of CO_2. This is usually necessary, because high concentrations of N_2 lead to a lowering of N_2ase activity in the short term due to sufficient intracellular levels of combined nitrogen by N_2 fixation. Some site-directed N_2ase mutants evolve H_2 under N_2 at levels approaching what has been attained under Ar. This is likely because their N_2ases are impaired in N_2 fixation activity without losing the H_2 evolving activity [318,319]. Use of these mutants in production systems will result in reducing costs, as Ar would not be needed. Although the mutants require combined nitrogen to support growth, the cost reduction of gas will surpass the cost of nutrients, because they can produce H_2 for a long time without changing the culture media.

6. Future prospects

6.1. Achieving the target of solar energy conversion to H_2

6.1.1. Using the price of corn to gauge the performance of modern agriculture

As an example of an economically sustainable agricultural production model, corn production in the USA can be considered as the benchmark to guide development of large-scale photobiological H_2 production. In the USA, the energy conversion efficiency from solar energy to corn grain is estimated to be roughly about 0.3%. Corn has traded at 1.4–6.2 cents per kWh in these 10 years [332]:

I Yield of corn
a. Annual corn yield: about 150 (in 2010 and 2011) and 130 bushels $acre^{-1}$ (in 2012, due to drought) [333].
b. 1 bushel of corn: about 900 ounces in weight, and 1 ounce of corn: 119 kcal in nutritional energy.
c. Solar energy (assumed): about 1500 kWh m^{-2} yr^{-1}, and 1 acre: 4047 m^2.
II Calculation of Energy conversion efficiency in 2010 and 2011, at about 150 bushels $acre^{-1}$:

$$\frac{150 \times 900 \times 119 \times 4.2 \times 103 \times J}{4047 \times 1500 \times 103 \times 3600 \times J} = 0.33\% (0.28\% \text{ in } 2012).$$

Assuming an efficiency of about 0.3% as the annual energy conversion efficiency, the efficiency limited to the growing season (from spring to autumn) into corn is roughly estimated at about 0.5%, and at this efficiency, an economical production of 1.4–6.2 cents per kWh is achieved. The low cost production of corn has been attained through the confluence of many factors, beginning with the selection of suitable crops for a given region, by improvements in breeding, horticulture, various related technologies, social infrastructure, etc. It should be pointed out that the scale of agriculture land needed to support the corn-growing farmer is about several km^2 or larger. Levin et al. [137] calculated the scale of a bioreactor necessary to support H_2 fuel cells.

6.1.2. Targeting improved photobiological H_2 production efficiency by optimizing solar energy conversion

Several authors have proposed relatively high target values for the efficiency of solar energy conversion by oxygenic phototrophs. For example, Benemann [271] targeted about 10% for a mass culture

of green algae. Blankenship et al. [21] discussed various possibilities for improving the efficiency above the currently observed high efficiency values of 3.5% for C3 plants and 4.3% for C4 plants under field conditions [273]. Rupprecht [320] discussed the necessity for improving the energy conversion efficiency of *Chlamydomonas* to 7%, and has proposed improvements by systems biology.

We conclude that using corn production as a model, it seems reasonable to set the efficiency of 1–1.5% as the interim target for photobiological H_2 production by oxygenic phototrophs. In the near future, if we are able to photobiologically produce H_2 at 1.2% that results in 18 kWh m^{-2} yr^{-1} (assumption: solar energy of 1500 kWh m^{-2} yr^{-1}), and if the crude H_2 is purified and transported to the final destination with an energy recovery of 50% (net 9 kWh m^{-2} yr^{-1}) with the advancement of related technologies, we will be able to replace 50% (the present level) of the fossil fuel consumption by using the sea surface, equivalent to 1.3% of the Earth's total surface area (equivalent to about 85% of the Australian continent) [2].

Although relatively high photoautotrophic H_2 production efficiencies of 2.7–3.6% vs. PAR (translated to 1.2–1.5% vs. solar radiation, assuming that PAR comprises 45% of the solar radiation) are reported from laboratory experiments using cyanobacteria, these experiments were done under low light intensities of less than 10% of full sun light intensities [194,304]. Under outdoor conditions, the highest efficiency reported thus far is only about 0.1% for cyanobacteria [305]. The theoretical maximum energy conversion efficiency by N_2ase-based H_2 production by cyanobacteria is estimated to be 6.3–7.3% [1]. The energy conversion efficiency of H_2ase-based H_2 production by *Chlamydomonas* is reported to be 0.36% [306] (compared to the theoretical maximum efficiencies of 22% vs. PAR and 9.9% vs. total solar radiation (Section 4.1). Although the metabolic networks for S-starved *Chlamydomonas* are not certain at this time, the theoretical maximum efficiency seems to be roughly around 10% or less. For both cyanobacteria and green algae, much improvement in the solar energy conversion efficiency to H_2 is required.

For PNS bacteria, the H_2 photobiological production efficiencies from organic acids of about 6–8% in laboratory experiments are occasionally reported (Table 7). In the future, the most promising roles for large-scale photobiological H_2 by PNS bacteria will be in cocultures or two-stage cultures with dark fermentation bacteria (see above) utilizing wastes derived of agricultural and forestry by-products [321,322]. For example, the perennial grass *Miscanthus* shows relatively high photosynthetic productivity [323], and the thermophilic bacterium *Thermotoga* produced 0.3 L $H_2/L_{culture}$. In the two-stage system, further treatment of the effluent by *Rhodobacter capsulatus* increased the total yield to 1.0 L $H_2/L_{culture}$ [324].

In the coculture or two-stage fermentation, not only the improved efficiency, but also increased rates of photobiological H_2 production can be realized. In these coculture systems, dark fermentation bacteria can degrade organic materials into organic acids much faster than they are utilized by PNS bacteria for H_2 production [99,136].

6.1.3. Targeting H_2 price

In the Annual Progress Report, DOE, USA, [334] set a milestone target price for H_2 produced by photosynthetic organisms and by dark fermentative organisms at \$4/kg H_2 (about 10.1 cents/kWh, Table 8). The final goal of \$2–\$3/kg H_2 (about 5.0–7.6 cents/kWh) was presented by USDE and NREL, and the potential for renewable H_2 production in USA including solar panels, etc. was discussed [325,334].

Although there are many uncertainties for the future implementation of photobiological H_2 production, some preliminary cost analyses have been presented. In a review article, Melis [235] presented a preliminary estimate of the future production cost (without storage) of \$1.38/kg H_2 (about 3.4 cents kWh^{-1}) on the assumption that *Chlamydomonas* produces H_2 at 20 g H_2 m^{-2} day^{-1} (about 300 kWh m^{-2} yr^{-1}). Considering the solar energy received in the Arizona desert is around 2600 kWh m^{-2} yr^{-1}, the assumed photobiological H_2 production rate in this scenario may be rather high. Sakurai et al. [2] presented a calculation of a preliminary future H_2 price of 26.4 cent kWh^{-1} if mariculture-raised cyanobacteria produce H_2 at a 1.2% energy conversion efficiency (solar to H_2) (18 kWh m^{-2} yr^{-1}) and if the crude H_2 is purified and delivered to ports as pure H_2 at an energy recovery of 50%, possible with advancements of related technologies. These preliminary calculations and assumptions used indicate that there are many problems to overcome before photobiologically produced H_2 can be put into actual use.

7. Concluding remarks

In spite of the many biological and technological challenges to overcome, photobiological production of H_2 remains one of the leading contenders for renewable energy. The proof of concept demonstration of H_2 production at acceptable rates under outdoor conditions will be important and among the challenges to be addressed by researchers in this field. In the future, even small-scale photobiological H_2 production may contribute not only to production of renewable energy, but also to protection of the environment by decreasing BOD in organic-rich waste water and to local economies. We also should think carefully about the development of large-scale and economical photobiological H_2 production, which may make meaningful contributions in mitigating climate change and also provide new opportunities for employment. In order to put photobiological H_2 production into actual use, much biological and technological progress is required.

Acknowledgments

We thank Drs. KVP Nagashima, K. Ohki, M. Ghirardi for informations on PNS bacteria, *Trichodesmium*, and *Chlamydomonas*, respectively, and Dr. S. Carlson for carefully reading the manuscript. This work was supported in part by grant-in aid for Scientific Research on Innovative Areas (No. 24107004) and Strategic Research Base Development Program for Private Universities from MEXT, Japan (to KI), Grant-in-aid-for Scientific-Research (21380200) from MEXT Japan (to HS), by JST, PRESTO (to HM), and by a donation from LiteraMed, *K.K.* (to KI).

References

[1] H. Sakurai, H. Masukawa, Mar. Biotechnol. 9 (2007) 128–145.
[2] H. Sakurai, H. Masukawa, M. Kitashima, K. Inoue, Adv. Exp. Med. Biol. 675 (2010) 291–303.
[3] P.C. Hallenbeck, J.R. Benemann, Int. J. Hydrogen Energy 27 (2002) 1185–1193.
[4] F.A.L. Pinto, O. Troshina, P. Lindblad, Int. J. Hydrogen Energy 27 (2002) 1209–1215.
[5] N. Basak, D. Das, World J. Microb. Biot. 23 (2007) 31–42.
[6] M.L. Ghirardi, M.C. Posewitz, P.-C. Maness, A. Dubini, J. Yu, M. Seibert, Annu. Rev. Plant Biol. 58 (2007) 71–91.
[7] S.M. Kotay, D. Das, Int. J. Hydrogen Energy 33 (2008) 258–263.
[8] M.L. Ghirardi, A. Dubini, J. Yu, P.C. Maness, Chem. Soc. Rev. 38 (2009) 52–61.
[9] S.I. Allakhverdiev, V. Thavasi, V.D. Kreslavski, S.K. Zharmukhamedov, V.V. Klimov, S. Ramakrishna, D.A. Los, M. Mimuro, H. Nishihara, R. Carpentier, J. Photochem. Photobiol. C 11 (2010) 101–113.
[10] M.L. Ghirardi, P. Mohanty, Curr. Sci. India 98 (2010) 499–507.
[11] H.S. Lee, W.F.J. Vermaas, B.E. Rittmann, Trends Biotechnol. 28 (2010) 262–271.
[12] E. Eroglu, A. Melis, Bioresour. Technol. 102 (2011) 8403–8413.
[13] K. Srirangan, M.E. Pyne, C.P. Chou, Bioresour. Technol. 102 (2011) 8589–8604.
[14] M. Gibbs, A. Hollaender, B. Kok, L.O. Krampits, A. San Pietro, Proceedings of the Workshop on Bio-solar Conversion, Indiana University, Workshop held at Bethesda, MD, 1974.
[15] S. Lien, A. San Pietro, Inquiry into Biophotolysis of Water to Produce Hydrogen. Report to NSF/RANN, 1976.

[16] P.F. Weaver, S. Lien, M. Seibert, Sol. Energy 24 (1980) 3–45.
[17] B. Esper, A. Badura, M. Rögner, Trends Plant Sci. 11 (2006) 543–549.
[18] J. Barber, Chem. Soc. Rev. 38 (2009) 185–196.
[19] A. Magnuson, M. Anderlund, O. Johansson, P. Lindblad, R. Lomoth, T. Polivka, S. Ott, K. Stensjö, S. Styring, V. Sundström, L. Hammarström, Acc. Chem. Res. 42 (2009) 1899–1909.
[20] C.E. Lubner, P. Knörzer, P.J.N. Silva, K.A. Vincent, T. Happe, D.A. Bryant, J.H. Golbeck, Biochemistry 49 (2010) 10264–10266.
[21] R.E. Blankenship, D.M. Tiede, J. Barber, G.W. Brudvig, G. Fleming, M. Ghirardi, M.R. Gunner, W. Junge, D.M. Kramer, A. Melis, T.A. Moore, C.C. Moser, D.G. Nocera, A.J. Nozik, D.R. Ort, W.W. Parson, R.C. Prince, R.T. Sayre, Science 332 (2011) 805–809.
[22] S. Ohashi, T. Iemura, N. Okada, S. Itoh, H. Furukawa, M. Okuda, M. Ohnishi-Kameyama, T. Ogawa, H. Miyashita, T. Watanabe, S. Itoh, H. Oh-oka, K. Inoue, M. Kobayashi, Photosynth. Res. 104 (2010) 305–319.
[23] S.P. Romberger, J.H. Golbeck, Photosynth. Res. 104 (2010) 333–346.
[24] N. Nelson, C.F. Yocum, Annu. Rev. Plant Biol. 57 (2006) 521–565.
[25] R. Fromme, I. Grotjohann, P. Fromme, in: G. Renger (Ed.), Primary Processes of Photosynthesis—Part 2: Principles and Apparatus, RSC Publishing, Cambridge, UK, 2007, pp. 111–146.
[26] P. Sétif, W. Leibl, in: G. Renger (Ed.), Primary Processes of Photosynthesis—Part 2: Principles and Apparatus, RSC Publishing, Cambridge, UK, 2007, pp. 147–191.
[27] C.N. Hunter, F. Daldal, M. Thurnauer, J.T. Beatty, The Purple Phototrophic Bacteria, Springer, Netherlands, 2008.
[28] J. Barber, Biochem. Soc. Trans. 34 (2006) 619–631.
[29] G. Renger, T. Renger, Photosynth. Res. 98 (2008) 53–80.
[30] Y. Umena, K. Kawakami, J.R. Shen, N. Kamiya, Nature 473 (2011), 55–U65.
[31] K. Kawakami, Y. Umena, N. Kamiya, J.R. Shen, J. Photochem. Photobiol. B 104 (2011) 9–18.
[32] O. Kruse, J. Rupprecht, J.H. Mussgnug, G.C. Dismukes, B. Hankamer, Photochem. Photobiol. Sci. 4 (2005) 957–970.
[33] R.M. Smillie, Biochem. Biophys. Res. Commun. 20 (1965) 621–629.
[34] K. Tagawa, H.Y. Tsujimoto, D.I. Arnon, Proc. Natl. Acad. Sci. U. S. A. 49 (1963) 567–572.
[35] W.N. Lanzilotta, M.J. Ryle, L.C. Seefeldt, Biochemistry 34 (1995) 10713–10723.
[36] B. Schrautemeier, H. Böhme, FEBS Lett. 184 (1985) 304–308.
[37] M. Fillat, G. Sandmann, C. Gomez-Moreno, Arch. Microbiol. 150 (1988) 160–164.
[38] P. Razquin, S. Schmitz, M.L. Peleato, M.F. Fillat, C. Gómez-Moreno, H. Böhme, Photosynth. Res. 43 (1995) 35–40.
[39] N. Frankenberg, C. HagerBraun, U. Feiler, M. Fuhrmann, H. Rogl, N. Schneebauer, N. Nelson, G. Hauska, Photochem. Photobiol. 64 (1996) 14–19.
[40] B. Nowicka, J. Kruk, Biochim. Biophys. Acta, Bioenerg. 1797 (2010) 1587–1605.
[41] P.D. Boyer, Annu. Rev. Biochem. 66 (1997) 717–749.
[42] P. Mitchell, Nature 191 (1961) 144–148.
[43] P. Mitchell, Biol. Rev. Camb. Philos. Soc. 41 (1966) 445–502.
[44] W. Junge, in: G. Renger (Ed.), Primary Processes of Photosynthesis, Part 2: Principles and Apparatus, RSC Publishing, Cambridge, 2008, pp. 447–487.
[45] J. Rydström, A.T. da Cruz, L. Ernster, Eur. J. Biochem. 17 (1970) 56–62.
[46] M. Schmehl, A. Jahn, A.M.Z. Vilsendorf, S. Hennecke, B. Masepohl, M. Schuppler, M. Marxer, J. Oelze, W. Klipp, Mol. Gen. Genet. 241 (1993) 602–615.
[47] T. Edgren, S. Nordlund, J. Bacteriol. 186 (2004) 2052–2060.
[48] W. Laubinger, P. Dimroth, Biochemistry 27 (1988) 7531–7537.
[49] J. Petersen, K. Förster, P. Turina, P. Gräber, Proc. Natl. Acad. Sci. U.S.A. 109 (2012) 11150–11155.
[50] H. Noji, R. Yasuda, M. Yoshida, K. Kinosita, Nature 386 (1997) 299–302.
[51] R. Yasuda, H. Noji, M. Yoshida, K. Kinosita, H. Itoh, Nature 410 (2001) 898–904.
[52] D. Stock, A.G.W. Leslie, J.E. Walker, Science 286 (1999) 1700–1705.
[53] D.L. Keister, N.J. Yike, Biochem. Biophys. Res. Commun. 24 (1966) 519–525.
[54] J.B. Jackson, FEBS Lett. 545 (2003) 18–24.
[55] J.B. Hoek, J. Rydström, Biochem. J. 254 (1988) 1–10.
[56] A. Veit, M.K. Akhtar, T. Mizutani, P.R. Jones, Microb. Biotechnol. 1 (2008) 382–394.
[57] J.R. Benemann, N.M. Weare, Science 184 (1974) 174–175.
[58] R. Cammack, M. Frey, R.W. Robson, Hydrogen as a Fuel, Taylor & Francis, London, 2001.
[59] P.M. Vignais, B. Billoud, J. Meyer, FEMS Microbiol. Rev. 25 (2001) 455–501.
[60] P.M. Vignais, A. Colbeau, Curr. Issues. Mol. Biol. 6 (2004) 159–188.
[61] J.C. Fontecilla-Camps, A. Volbeda, C. Cavazza, Y. Nicolet, Chem. Rev. 107 (2007) 4273–4303.
[62] P.M. Vignais, B. Billoud, Chem. Rev. 107 (2007) 4206–4272.
[63] K.A. Vincent, A. Parkin, F.A. Armstrong, Chem. Rev. 107 (2007) 4366–4413.
[64] C. Schwarz, Z. Poss, D. Hoffmann, J. Appel, Adv. Exp. Med. Biol. 675 (2010) 305–348.
[65] D.H. Kim, M.S. Kim, Bioresour. Technol. 102 (2011) 8423–8431.
[66] J. Meyer, Cell. Mol. Life Sci. 64 (2007) 1063–1084.
[67] P.W. King, M.C. Posewitz, M.L. Ghirardi, M. Seibert, J. Bacteriol. 188 (2006) 2163–2172.
[68] C.M. English, C. Eckert, K. Brown, M. Seibert, P.W. King, Dalton Trans. (2009) 9970–9978.
[69] A. Böck, P.W. King, M. Blokesch, M.C. Posewitz, Adv. Microb. Physiol. 51 (2006) 1–71.
[70] R. Böhm, M. Sauter, A. Böck, Mol. Microbiol. 4 (1990) 231–243.
[71] K. Asada, Annu. Rev. Plant Physiol. Plant Mol. Biol. 50 (1999) 601–639.
[72] K. Inoue, H. Sakurai, T. Hiyama, Plant Cell Physiol. 27 (1986) 961–968.
[73] J. Appel, S. Phunpruch, K. Steinmüller, R. Schulz, Arch. Microbiol. 173 (2000) 333–338.
[74] P. Lindblad, K. Christensson, P. Lindberg, A. Fedorov, F. Pinto, A. Tsygankov, Int. J. Hydrogen Energy 27 (2002) 1271–1281.
[75] L.C. Seefeldt, B.M. Hoffman, D.R. Dean, Annu. Rev. Biochem. 78 (2009) 701–722.
[76] O. Einsle, F.A. Tezcan, S.L.A. Andrade, B. Schmid, M. Yoshida, J.B. Howard, D.C. Rees, Science 297 (2002) 1696–1700.
[77] K.M. Lancaster, M. Roemelt, P. Ettenhuber, Y.L. Hu, M.W. Ribbe, F. Neese, U. Bergmann, S. DeBeer, Science 334 (2011) 974–977.
[78] T. Spatzal, M. Aksoyoglu, L.M. Zhang, S.L.A. Andrade, E. Schleicher, S. Weber, D.C. Rees, O. Einsle, Science 334 (2011) 940.
[79] R.Y. Igarashi, L.C. Seefeldt, Crit. Rev. Biochem. Mol. Biol. 38 (2003) 351–384.
[80] W.N. Lanzilotta, L.C. Seefeldt, Biochemistry 36 (1997) 12976–12983.
[81] R.R. Eady, Coord. Chem. Rev. 237 (2003) 23–30.
[82] B.E. Smith, Adv. Inorg. Chem. 47 (1999) 159–218.
[83] F.B. Simpson, R.H. Burris, Science 224 (1984) 1095–1097.
[84] R.R. Eady, R.L. Robson, T.H. Richardson, R.W. Miller, M. Hawkins, Biochem. J. 244 (1987) 197–207.
[85] K. Schneider, U. Gollan, M. Drottboom, S. Selsemeier-Voigt, A. Müller, Eur. J. Biochem. 244 (1997) 789–800.
[86] F.W. Larimer, P. Chain, L. Hauser, J. Lamerdin, S. Malfatti, L. Do, M.L. Land, D.A. Pelletier, J.T. Beatty, A.S. Lang, F.R. Tabita, J.L. Gibson, T.E. Hanson, C. Bobst, J.L.T.Y. Torres, C. Peres, F.H. Harrison, J. Gibson, C.S. Harwood, Nat. Biotechnol. 22 (2004) 55–61.
[87] T. Thiel, J. Bacteriol. 175 (1993) 6276–6286.
[88] G. Boison, C. Steingen, L.J. Stal, H. Bothe, Arch. Microbiol. 186 (2006) 367–376.
[89] H. Masukawa, X.H. Zhang, E. Yamazaki, S. Iwata, K. Nakamura, M. Mochimaru, K. Inoue, H. Sakurai, Mar. Biotechnol. 11 (2009) 397–409.
[90] T. Thiel, E.M. Lyons, J.C. Erker, A. Ernst, Proc. Natl. Acad. Sci. U.S.A. 92 (1995) 9358–9362.
[91] P. Mitchell, J. Theor. Biol. 62 (1976) 327–367.
[92] A.J. Hoff, J. Deisenhofer, Phys. Rep. 287 (1997) 1–247.
[93] S.M. Herter, C.M. Kortluke, G. Drews, Arch. Microbiol. 169 (1998) 98–105.
[94] M.Y. Okamura, M.L. Paddock, M.S. Graige, G. Feher, Biochim. Biophys. Acta, Bioenerg. 1458 (2000) 148–163.
[95] J.L. Cape, M.K. Bowman, D.M. Kramer, Trends Plant Sci. 11 (2006) 46–55.
[96] H. Koku, I. Eroğlu, U. Gündüz, M. Yücel, L. Türker, Int. J. Hydrogen Energy 27 (2002) 1315–1329.
[97] B. Masepohl, P.C. Hallenbeck, Adv. Exp. Med. Biol. 675 (2010) 49–70.
[98] V. Gadhamshetty, A. Sukumaran, N. Nirmalakhandan, Crit. Rev. Env. Sci. Tec. 41 (2011) 1–51.
[99] D.N. Tekucheva, A.A. Tsygankov, Appl. Biochem. Microbiol. 48 (2012) 319–337.
[100] H. Gest, M.D. Kamen, Science 109 (1949) 558–559.
[101] P. Hillmer, H. Gest, J. Bacteriol. 129 (1977) 732–739.
[102] D.C. Yoch, D.I. Arnon, W.V. Sweeney, J. Biol. Chem. 250 (1975) 8330–8336.
[103] M.A. Cusanovich, D.E. Edmondson, Biochem. Biophys. Res. Commun. 45 (1971) 327–336.
[104] J. Armengaud, C. Meyer, Y. Jouanneau, Biochem. J. 300 (1994) 413–418.
[105] T. Fuhrer, U. Sauer, J. Bacteriol. 191 (2009) 2112–2121.
[106] K. Nath, D. Das, Appl. Microbiol. Biotechnol. 65 (2004) 520–529.
[107] P.C. Hallenbeck, Water Sci. Technol. 52 (2005) 21–29.
[108] P.C. Hallenbeck, D. Ghosh, Trends Biotechnol. 27 (2009) 287–297.
[109] M. Hambourger, G.F. Moore, D.M. Kramer, D. Gust, A.L. Moore, T.A. Moore, Chem. Soc. Rev. 38 (2009) 25–35.
[110] R.K. Thauer, K. Jungermann, K. Decker, Bacteriol. Rev. 41 (1977) 100–180.
[111] B. Mandal, K. Nath, D. Das, Biotechnol. Lett. 28 (2006) 831–835.
[112] V. Müller, F. Imkamp, E. Biegel, S. Schmidt, S. Dilling, Ann. N. Y. Acad. Sci. 1125 (2008) 137–146.
[113] E. Biegel, S. Schmidt, J.M. González, V. Müller, Cell. Mol. Life Sci. 68 (2011) 613–634.
[114] S. Nagashima, A. Kamimura, T. Shimizu, S. Nakamura-Isaki, E. Aono, K. Sakamoto, N. Ichikawa, H. Nakazawa, M. Sekine, S. Yamazaki, N. Fujita, K. Shimada, S. Hanada, K.V.P Nagashima, J. Bacteriol. 194 (2012) 3541–3542.
[115] M. Kanehisa, S. Goto, M. Hattori, K.F. Aoki-Kinoshita, M. Itoh, S. Kawashima, T. Katayama, M. Araki, M. Hirakawa, Nucleic Acids Res. 34 (2006) D354–D357.
[116] T. Edgren, S. Nordlund, FEMS Microbiol. Lett. 260 (2006) 30–35.
[117] G. Herrmann, E. Jayamani, G. Mai, W. Buckel, J. Bacteriol. 190 (2008) 784–791.
[118] S. Takakuwa, J. Odom, J. Wall, Arch. Microbiol. 136 (1983) 20–25.
[119] A. Colbeau, A. Godfroy, P.M. Vignais, Biochimie 68 (1986) 147–155.
[120] M.S. Kim, J.S. Baek, J.K. Lee, Int. J. Hydrogen Energy 31 (2006) 121–127.
[121] B. Fodor, G. Rákhely, A.T. Kovács, K.L. Kovács, Appl. Environ. Microbiol. 67 (2001) 2476–2483.
[122] P. Vignais, in: C.N. Hunter, F. Daldal, M. Thurnauer, J.T. Beatty (Eds.), The Purple Phototrophic Bacteria, Springer, Netherlands, 2008, pp. 743–757.
[123] P.C. Hallenbeck, Int. J. Hydrogen Energy 34 (2009) 7379–7389.
[124] C.M. Lee, P.C. Chen, C.C. Wang, Y.C. Tung, Int. J. Hydrogen Energy 27 (2002) 1309–1313.
[125] M.D. Redwood, L.E. Macaskie, Int. J. Hydrogen Energy 31 (2006) 1514–1521.
[126] Y.Z. Tao, Y. Chen, Y.Q. Wu, Y.L. He, Z.H. Zhou, Int. J. Hydrogen Energy 32 (2007) 200–206.
[127] H. Argun, F. Kargi, I.K. Kapdan, Int. J. Hydrogen Energy 33 (2008) 7405–7412.
[128] K. Nath, M. Muthukumar, A. Kumar, D. Das, Int. J. Hydrogen Energy 33 (2008) 1195–1203.
[129] J.M. Odom, J.D. Wall, Appl. Environ. Microbiol. 45 (1983) 1300–1305.

[130] J. Miyake, X.Y. Mao, S. Kawamura, J. Ferment. Technol. 62 (1984) 531–535.
[131] H. Yokoi, R. Maki, J. Hirose, S. Hayashi, Biomass Bioenerg. 22 (2002) 389–395.
[132] Y. Asada, M. Tokumoto, Y. Aihara, M. Oku, K. Ishimi, T. Wakayama, J. Miyake, M. Tomiyama, H. Kohno, Int. J. Hydrogen Energy 31 (2006) 1509–1513.
[133] E. Eroglu, I. Eroglu, U. Gunduz, L. Turker, M. Yucel, Int. J. Hydrogen Energy 31 (2006) 1527–1535.
[134] C.-Y. Chen, M.-H. Yang, K.-L. Yeh, C.-H. Liu, J.-S. Chang, Int. J. Hydrogen Energy 33 (2008) 4755–4762.
[135] E. Ozgur, A.E. Mars, B. Peksel, A. Louwerse, M. Yucel, U. Gunduz, P.A.M. Claassen, I. Eroglu, Int. J. Hydrogen Energy 35 (2010) 511–517.
[136] T.V. Laurinavichene, B.F. Belokopytov, K.S. Laurinavichius, A.N. Khusnutdinova, M. Seibert, A.A. Tsygankov, Int. J. Hydrogen Energy 37 (2012) 8800–8810.
[137] D.B. Levin, L. Pitt, M. Love, Int. J. Hydrogen Energy 29 (2004) 173–185.
[138] H.H. Weetall, B.P. Sharma, C.C. Detar, Biotechnol. Bioeng. 23 (1981) 605–614.
[139] M.J. Barbosa, J.M.S. Rocha, J. Tramper, R.H. Wijffels, J. Biotechnol. 85 (2001) 25–33.
[140] H.H.P. Fang, H. Liu, T. Zhang, Int. J. Hydrogen Energy 30 (2005) 785–793.
[141] Y.Z. Tao, Y.L. He, Y.Q. Wu, F.H. Liu, X.F. Li, W.M. Zong, Z.H. Zhou, Int. J. Hydrogen Energy 33 (2008) 963–973.
[142] X.Y. Mao, J. Miyake, S. Kawamura, Anglais 64 (1986) 245–249.
[143] Y.K. Oh, E.H. Seol, M.S. Kim, S. Park, Int. J. Hydrogen Energy 29 (2004) 1115–1121.
[144] X.Y. Shi, H.Q. Yu, Int. J. Hydrogen Energy 31 (2006) 1641–1647.
[145] F.E. Rey, E.K. Heiniger, C.S. Harwood, Appl. Environ. Microbiol. 73 (2007) 1665–1671.
[146] E.J. Kim, M.K. Lee, M.S. Kim, J.K. Lee, Int. J. Hydrogen Energy 33 (2008) 1516–1521.
[147] G. Kars, U. Gündüz, Int. J. Hydrogen Energy 35 (2010) 6646–6656.
[148] N.U. Frigaard, D.A. Bryant, in: R. Hell, C. Dahl, L.T. D. Knaff (Eds.), Sulfur Metabolism in Phototrophic Organisms, Springer, Netherlands, 2008, pp. 337–355.
[149] H. Sakurai, T. Ogawa, M. Shiga, K. Inoue, Photosynth. Res. 104 (2010) 163–176.
[150] G. Hauska, T. Schoedl, H. Remigy, G. Tsiotis, Biochim. Biophys. Acta, Bioenerg. 1507 (2001) 260–277.
[151] P. Sétif, D. Seo, H. Sakurai, Biophys. J. 81 (2001) 1208–1219.
[152] D. Seo, H. Sakurai, Biochim. Biophys. Acta, Protein Struct. Mol. Enzimol. 1597 (2002) 123–132.
[153] H. Gest, J. Favinger, Arch. Microbiol. 136 (1983) 11–16.
[154] E.S. Lindstrom, S.R. Tove, P.W. Wilson, Science 112 (1950) 197–198.
[155] M.C. Evans, B.B. Buchanan, D.I. Arnon, Proc. Natl. Acad. Sci. U.S.A. 55 (1966) 928–934.
[156] F.R. Tabita, Photosynth. Res. 80 (2004) 315–332.
[157] T.M. Wahlund, C.R. Woese, R.W. Castenholz, M.T. Madigan, Arch. Microbiol. 159 (1991) 81–90.
[158] J.A. Eisen, K.E. Nelson, I.T. Paulsen, J.F. Heidelberg, M. Wu, R.J. Dodson, R. Deboy, M.L. Gwinn, W.C. Nelson, D.H. Haft, E.K. Hickey, J.D. Peterson, A.S. Durkin, J.L. Kolonay, F. Yang, I. Holt, L.A. Umayam, T. Mason, M. Brenner, T.P. Shea, D. Parksey, W.C. Nierman, T.V. Feldblyum, C.L. Hansen, M.B. Craven, D. Radune, J. Vamathevan, H. Khouri, O. White, T.M. Gruber, K.A. Ketchum, J.C. Venter, H. Tettelin, D.A. Bryant, C.M. Fraser, Proc. Natl. Acad. Sci. U.S.A. 99 (2002) 9509–9514.
[159] N.U. Frigaard, A.G.M. Chew, H. Li, J.A. Maresca, D.A. Bryant, Photosynth. Res. 78 (2003) 93–117.
[160] O.I. Keppen, N.V. Lebedeva, S.A. Petukhov, Y.V. Rodionov, Microbiology (Moscow, Russ. Fed.) 54 (1985) 28–32.
[161] R. Warthmann, H. Cypionka, N. Pfennig, Arch. Microbiol. 157 (1992) 343–348.
[162] K. Schutz, T. Happe, O. Troshina, P. Lindblad, E. Leitao, P. Oliveira, P. Tamagnini, Planta 218 (2004) 350–359.
[163] S. Dawar, H. Masukawa, P. Mohanty, H. Sakurai, Proc. Indian Natl. Sci. Acad. 72 (2006) 213–224.
[164] P. Tamagnini, E. Leitao, P. Oliveira, D. Ferreira, F. Pinto, D.J. Harris, T. Heidorn, P. Lindblad, FEMS Microbiol. Rev. 31 (2007) 692–720.
[165] A.A. Tsygankov, Appl. Biochem. Microbiol. 43 (2007) 250–259.
[166] S.A. Angermayr, K.J. Hellingwerf, P. Lindblad, M.J.T. de Mattos, Curr. Opin. Biotechnol. 20 (2009) 257–263.
[167] H. Bothe, O. Schmitz, M.G. Yates, W.E. Newton, Microbiol. Mol. Biol. Rev. 74 (2010) 529–551.
[168] H. Bothe, O. Schmitz, M.G. Yates, W. Newton, in: G.A. Peschek, C. Obinger, G. Renger (Eds.), Bioenergetic Processes of Cyanobacteria, Springer, Netherlands, 2011, pp. 137–157.
[169] P. Hallenbeck, in: P.C. Hallenbeck (Ed.), Microbial Technologies in Advanced Biofuels Production, Springer, US, 2012, pp. 15–28.
[170] A. Tiwari, A. Pandey, Int. J. Hydrogen Energy 37 (2012) 139–150.
[171] J. Appel, in: R. Burnap, W. Vermaas (Eds.), Functional Genomics and Evolution of Photosynthetic Systems, Springer, Netherlands, 2012, pp. 357–381.
[172] P. Tamagnini, R. Axelsson, P. Lindberg, F. Oxelfelt, R. Wünschiers, P. Lindblad, Microbiol. Mol. Biol. Rev. 66 (2002) 1–20.
[173] I. Berman-Frank, P. Lundgren, P. Falkowski, Res. Microbiol. 154 (2003) 157–164.
[174] D. Carrieri, K. Wawrousek, C. Eckert, J. Yu, P.C. Maness, Bioresour. Technol. 102 (2011) 8368–8377.
[175] C.P. Wolk, A. Ernest, J. Elhai, in: D.A. Bryant (Ed.), The Molecular Biology of Cyanobacteria, Springer (Kluwer Academic Publishers), Dordrecht, The Netherlands, 1994, pp. 769–823.
[176] V. Mariscal, E. Flores, Adv. Exp. Med. Biol. 675 (2010) 123–135.
[177] K. Kumar, R.A. Mella-Herrera, J.W. Golden, Cold Spring Harb. Perspect. Biol. 2 (2010).
[178] E. Flores, A. Herrero, Nat. Rev.-Microbiol. 8 (2010) 39–50.
[179] J. Elhai, C.P. Wolk, Methods Enzymol. 167 (1988) 747–754.
[180] T. Kaneko, Y. Nakamura, C.P. Wolk, T. Kuritz, S. Sasamoto, A. Watanabe, M. Iriguchi, A. Ishikawa, K. Kawashima, T. Kimura, Y. Kishida, M. Kohara, M. Matsumoto, A. Matsuno, A. Muraki, N. Nakazaki, S. Shimpo, M. Sugimoto, M. Takazawa, M. Yamada, M. Yasuda, S. Tabata, DNA Res. 8 (2001) 205–213.
[181] G. Schmetterer, A. Valladares, D. Pils, S. Steinbach, M. Pacher, A.M. Muro-Pastor, E. Flores, A. Herrero, J. Bacteriol. 183 (2001) 6429–6434.
[182] K.M. Jones, R. Haselkorn, J. Bacteriol. 184 (2002) 2491–2499.
[183] A. Valladares, A. Herrero, D. Pils, G. Schmetterer, E. Flores, Mol. Microbiol. 47 (2003) 1239–1249.
[184] M. Paumann, G. Regelsberger, C. Obinger, G.A. Peschek, Biochim. Biophys. Acta, Bioenerg. 1707 (2005) 231–253.
[185] S. Ehira, M. Ohmori, N. Sato, DNA Res. 10 (2003) 97–113.
[186] J.C. Meeks, E.L. Campbell, M.L. Summers, F.C. Wong, Arch. Microbiol. 178 (2002) 395–403.
[187] P. Tamagnini, O. Troshina, F. Oxelfelt, R. Salema, P. Lindblad, Appl. Environ. Microbiol. 63 (1997) 1801–1807.
[188] M. Ludwig, R. Schulz-Friedrich, J. Appel, J. Mol. Evol. 63 (2006) 758–768.
[189] L.E. Mikheeva, O. Schmitz, S.V. Shestakov, H. Bothe, Z. Naturforsch. C 50 (1995) 505–510.
[190] T. Happe, K. Schutz, H. Bohme, J. Bacteriol. 182 (2000) 1624–1631.
[191] H. Masukawa, M. Mochimaru, H. Sakurai, Appl. Microbiol. Biotechnol. 58 (2002) 618–624.
[192] P. Lindberg, K. Schutz, T. Happe, P. Lindblad, Int. J. Hydrogen Energy 27 (2002) 1291–1296.
[193] C.D. Carrasco, S.D. Holliday, A. Hansel, P. Lindblad, J.W. Golden, J. Bacteriol. 187 (2005) 6031–6038.
[194] F. Yoshino, H. Ikeda, H. Masukawa, H. Sakurai, Mar. Biotechnol. 9 (2007) 101–112.
[195] S.J. Lin, S. Henze, P. Lundgren, B. Bergman, E.J. Carpenter, Appl. Environ. Microbiol. 64 (1998) 3052–3058.
[196] I. Berman-Frank, P. Lundgren, Y.B. Chen, H. Kupper, Z. Kolber, B. Bergman, P. Falkowski, Science 294 (2001) 1534–1537.
[197] J.A. Finzi-Hart, J. Pett-Ridge, P.K. Weber, R. Popa, S.J. Fallon, T. Gunderson, I.D. Hutcheon, K.H. Nealson, D.G. Capone, Proc. Natl. Acad. Sci. U.S.A. 106 (2009) 6345–6350.
[198] R.D. Simon, Proc. Natl. Acad. Sci. 68 (1971) 265–267.
[199] H.W. Paerl, J.C. Priscu, D.L. Brawner, Appl. Environ. Microbiol. 55 (1989) 2965–2975.
[200] K. Ohki, J. Oceanogr. 64 (2008) 211–216.
[201] Y. Taniuchi, A. Murakami, K. Ohki, Aquat. Microb. Ecol. 51 (2008) 237–247.
[202] C.H. Johnson, S.S. Golden, Ann. Rev. Microbiol. 53 (1999) 389–409.
[203] L. Stal, W. Krumbein, Arch. Microbiol. 143 (1985) 67–71.
[204] S. Kumazawa, A. Mitsui, Appl. Environ. Microbiol. 50 (1985) 287–291.
[205] P.M. Mullineaux, A.E. Chaplin, J.R. Gallon, J. Gen. Microbiol. 129 (1983) 1689–1696.
[206] A. Mitsui, S. Kumazawa, A. Takahashi, H. Ikemoto, S. Cao, T. Arai, Nature 323 (1986) 720–722.
[207] K.J. Reddy, J.B. Haskell, D.M. Sherman, L.A. Sherman, J. Bacteriol. 175 (1993) 1284–1292.
[208] M.A. Schneegurt, D.M. Sherman, S. Nayar, L.A. Sherman, J. Bacteriol. 176 (1994) 1586–1597.
[209] N. Grobbelaar, T.C. Huang, H.Y. Lin, T.J. Chow, FEMS Microbiol. Lett. 37 (1986) 173–177.
[210] B. Bergman, J.R. Gallon, A.N. Rai, L.J. Stal, FEMS Microbiol. Rev. 19 (1997) 139–185.
[211] J. Stöckel, E.A. Welsh, M. Liberton, R. Kunnvakkam, R. Aurora, H.B. Pakrasi, Proc. Natl. Acad. Sci. U.S.A. 105 (2008) 6156–6161.
[212] L.A. Sherman, H. Min, J. Toepel, H.B. Pakrasi, Adv. Exp. Med. Biol. 675 (2010) 275–290.
[213] J. Toepel, E. Welsh, T.C. Summerfield, H.B. Pakrasi, L.A. Sherman, J. Bacteriol. 190 (2008) 3904–3913.
[214] G.G. Dong, S.S. Golden, Curr. Opin. Microbiol. 11 (2008) 541–546.
[215] T. Kondo, T. Mori, N.V. Lebedeva, S. Aoki, M. Ishiura, S.S. Golden, Science 275 (1997) 224–227.
[216] H. Ito, M. Mutsuda, Y. Murayama, J. Tomita, N. Hosokawa, K. Terauchi, C. Sugita, M. Sugita, T. Kondo, H. Iwasaki, Proc. Natl. Acad. Sci. U.S.A. 106 (2009) 14168–14173.
[217] H.T. Min, L.A. Sherman, Appl. Environ. Microbiol. 76 (2010) 4293–4301.
[218] A. Bandyopadhyay, J. Stöckel, H.T. Min, L.A. Sherman, H.B. Pakrasi, Nat. Commun. 1 (2010).
[219] M.R. Melnicki, G.E. Pinchuk, E.A. Hill, L.A. Kucek, J.K. Fredrickson, A. Konopka, A.S. Beliaev, Mbio 3 (2012).
[220] J.C. Weissman, J.R. Benemann, Appl. Environ. Microbiol. 33 (1977) 123–131.
[221] S. Kumazawa, A. Mitsui, Int. J. Hydrogen Energy 6 (1981) 339–348.
[222] S. Kumazawa, A. Mitsui, Biotechnol. Bioeng. 44 (1994) 854–858.
[223] D.A. Sveshnikov, N.V. Sveshnikova, K.K. Rao, D.O. Hall, FEMS Microbiol. Lett. 147 (1997) 297–301.
[224] S. Kosourov, A. Tsygankov, M. Seibert, M.L. Ghirardi, Biotechnol. Bioeng. 78 (2002) 731–740.
[225] H. Masukawa, M. Mochimaru, H. Sakurai, Int. J. Hydrogen Energy 27 (2002) 1471–1474.

[226] S.N. Kosourov, M.L. Ghirardi, M. Seibert, Int. J. Hydrogen Energy 36 (2011) 2044–2048.
[227] A.E. Marques, A.T. Barbosa, J. Jotta, M.C. Coelho, P. Tamagnini, L. Gouveia, Biomass Bioenergy 35 (2011) 4426–4434.
[228] A. Scoma, L. Giannelli, C. Faraloni, G. Torzillo, J. Biotechnol. 157 (2012) 613–619.
[229] L. Cournac, G. Guedeney, G. Peltier, P.M. Vignais, J. Bacteriol. 186 (2004) 1737–1746.
[230] O. Troshina, L. Serebryakova, M. Sheremetieva, P. Lindblad, Int. J. Hydrogen Energy 27 (2002) 1283–1289.
[231] G.M. Ananyev, N.J. Skizim, G.C. Dismukes, J. Biotechnol. 162 (2012) 97–104.
[232] A.F. Ferreira, A.C. Marques, A.P. Batista, P.A.S.S. Marques, L. Gouveia, C.M. Silva, Int. J. Hydrogen Energy 37 (2012) 179–190.
[233] H. Gaffron, J. Rubin, J. Gen. Physiol. 26 (1942) 219–240.
[234] A. Melis, Plnta 226 (2007) 1075–1086.
[235] A. Melis, M. Seibert, M. Ghirardi, in: R. León, A. Galván, E. Fernández (Eds.), Transgenic Microalgae as Green Cell Factories, Springer, New York, 2007, pp. 110–121.
[236] A. Hemschemeier, S. Fouchard, L. Cournac, G. Peltier, T. Happe, Planta 227 (2008) 397–407.
[237] A. Tsygankov, in: P.C. Hallenbeck (Ed.), Microbial Technologies in Advanced Biofuels Production, Springer, US, 2012, pp. 29–51.
[238] T. Happe, B. Mosler, J.D. Naber, Eur. J. Biochem. 222 (1994) 769–774.
[239] S.T. Stripp, T. Happe, Dalton Trans. (2009) 9960–9969.
[240] J.P. Davies, F.H. Yildiz, A. Grossman, EMBO J. 15 (1996) 2150–2159.
[241] M. Ghiraldi, S. Kosourov, P. Maness, S. Smolinski, M. Seibert, in: M.C. Flickinger (Ed.), Encyclopedia of Industrial Biotechnology: Bioprocess, Bioseparation, and Cell Technology, John Wiley & Sons, New York, 2010, pp. 1–14.
[242] A. Melis, L.P. Zhang, M. Forestier, M.L. Ghirardi, M. Seibert, Plant Physiol. 122 (2000) 127–135.
[243] L.P. Zhang, T. Happe, A. Melis, Planta 214 (2002) 552–561.
[244] S. Kosourov, M. Seibert, M.L. Ghirardi, Plant Cell Physiol. 44 (2003) 146–155.
[245] M.L. Ghirardi, J.P. Zhang, J.W. Lee, T. Flynn, M. Seibert, E. Greenbaum, A. Melis, Trends Biotechnol. 18 (2000) 506–511.
[246] T. Happe, A. Hemschemeier, M. Winkler, A. Kaminski, Trends Plant Sci. 7 (2002) 246–250.
[247] A. Melis, T. Happe, Photosynth. Res. 80 (2004) 401–409.
[248] T.K. Antal, T.E. Krendeleva, T.V. Laurinavichene, V.V. Makarova, M.L. Ghirardi, A.B. Rubin, A.A. Tsygankov, M. Seibert, Biochim. Biophys. Acta, Bioenerg. 1607 (2003) 153–160.
[249] S. Fouchard, A. Hemschemeier, A. Caruana, K. Pruvost, J. Legrand, T. Happe, G. Peltier, L. Cournac, Appl. Environ. Microbiol. 71 (2005) 6199–6205.
[250] A. Hemschemeier, T. Happe, Biochem. Soc. Trans. 33 (2005) 39–41.
[251] F. Mus, L. Cournac, W. Cardettini, A. Caruana, G. Peltier, Biochim. Biophys. Acta, Bioenerg. 1708 (2005) 322–332.
[252] A. Hemschemeier, J. Jacobs, T. Happe, Eukaryot. Cell 7 (2008) 518–526.
[253] T. Shikanai, Annu. Rev. Plant Biol. 58 (2007) 199–217.
[254] F. Jans, E. Mignolet, P.A. Houyoux, P. Cardol, B. Ghysels, S. Cuine, L. Cournac, G. Peltier, C. Remacle, F. Franck, Proc. Natl. Acad. Sci. U.S.A. 105 (2008) 20546–20551.
[255] C. Desplats, F. Mus, S. Cuine, E. Billon, L. Cournac, G. Peltier, J. Biol. Chem. 284 (2009) 4148–4157.
[256] M. Iwai, K. Takizawa, R. Tokutsu, A. Okamuro, Y. Takahashi, J. Minagawa, Nature 464 (2010), 1210–U1134.
[257] G. Peltier, D. Tolleter, E. Billon, L. Cournac, Photosynth. Res. 106 (2010) 19–31.
[258] A. Hemschemeier, T. Happe, Biochim. Biophys. Acta 1807 (2011) 919–926.
[259] G. Philipps, D. Krawietz, A. Hemschemeier, T. Happe, Plant J. 66 (2011) 330–340.
[260] A.A. Tsygankov, S.N. Kosourov, I.V. Tolstygina, M.L. Ghirardi, M. Seibert, Int. J. Hydrogen Energy 31 (2006) 1574–1584.
[261] S.S. Merchant, S.E. Prochnik, O. Vallon, E.H. Harris, S.J. Karpowicz, G.B. Witman, A. Terry, A. Salamov, L.K. Fritz-Laylin, L. Maréchal-Drouard, W.F. Marshall, L.H. Qu, D.R. Nelson, A.A. Sanderfoot, M.H. Spalding, V.V. Kapitonov, Q.H. Ren, P. Ferris, E. Lindquist, H. Shapiro, S.M. Lucas, J. Grimwood, J. Schmutz, P. Cardol, H. Cerutti, G. Chanfreau, C.L. Chen, V. Cognat, M.T. Croft, R. Dent, S. Dutcher, E. Fernández, H. Fukuzawa, D. González-Ballester, D. González-Halphen, A. Hallmann, M. Hanikenne, M. Hippler, W. Inwood, K. Jabbari, M. Kalanon, R. Kuras, P.A. Lefebvre, S.D. Lemaire, A.V. Lobanov, M. Lohr, A. Manuell, I. Meir, L. Mets, M. Mittag, T. Mittelmeier, J.V. Moroney, J. Moseley, C. Napoli, A.M. Nedelcu, K. Niyogi, S.V. Novoselov, I.T. Paulsen, G. Pazour, S. Purton, J.P. Ral, D.M. Riaño-Pachón, W. Riekhof, L. Rymarquis, M. Schroda, D. Stern, J. Umen, R. Willows, N. Wilson, S.L. Zimmer, J. Allmer, J. Balk, K. Bisova, C.J. Chen, M. Elias, K. Gendler, C. Hauser, M.R. Lamb, H. Ledford, J.C. Long, J. Minagawa, M.D. Page, J.M. Pan, W. Pootakham, S. Roje, A. Rose, E. Stahlberg, A.M. Terauchi, P.F. Yang, S. Ball, C. Bowler, C.L. Dieckmann, V.N. Gladyshev, P. Green, R. Jorgensen, S. Mayfield, B. Mueller-Roeber, S. Rajamani, R.T. Sayre, P. Brokstein, I. Dubchak, D. Goodstein, L. Hornick, Y.W. Huang, J. Jhaveri, Y.G. Luo, D. Martínez, W.C.A. Ngau, B. Otillar, A. Poliakov, A. Porter, L. Szajkowski, G. Werner, K.M. Zhou, I.V. Grigoriev, D.S. Rokhsar, A.R. Grossman, C. Annotation, J.A. Team, Science 318 (2007) 245–251.
[262] F. Mus, A. Dubini, M. Seibert, M.C. Posewitz, A.R. Grossman, J. Biol. Chem. 282 (2007) 25475–25486.
[263] M. Timmins, W.X. Zhou, J. Rupprecht, L. Lim, S.R. Thomas-Hall, A. Doebbe, O. Kruse, B. Hankamer, U.C. Marx, S.M. Smith, P.M. Schenk, J. Biol. Chem. 284 (2009) 23415–23425.
[264] A.R. Grossman, C. Catalanotti, W.Q. Yang, A. Dubini, L. Magneschi, V. Subramanian, M.C. Posewitz, M. Seibert, New Phytol. 190 (2011) 279–288.
[265] A.R. Grossman, D. González-Ballester, S. Bailey, S.J. Karpowicz, S.S. Merchant, Functional Genomics and Evolution of Photosynthetic Systems, Springer, Netherlands, 2012, pp. 139–176.
[266] A. Atteia, R. van Lis, G. Gelius-Dietrich, A. Adrait, J. Garin, J. Joyard, N. Rolland, W. Martin, J. Biol. Chem. 281 (2006) 9909–9918.
[267] A. Dubini, F. Mus, M. Seibert, A.R. Grossman, M.C. Posewitz, J. Biol. Chem. 284 (2009) 7201–7213.
[268] M. Winkler, A. Hemschemeier, C. Gotor, A. Melis, T. Happe, Int. J. Hydrogen Energy 27 (2002) 1431–1439.
[269] J.E. Meuser, G. Ananyev, L.E. Wittig, S. Kosourov, M.L. Ghirardi, M. Seibert, G.C. Dismukes, M.C. Posewitz, J. Biotechnol. 142 (2009) 21–30.
[270] M. Timmins, S.R. Thomas-Hall, A. Darling, E. Zhang, B. Hankamer, U.C. Marx, P.M. Schenk, J. Exp. Bot. 60 (2009) 1691–1702.
[271] J.R. Benemann, J. Appl. Phycol. 12 (2000) 291–300.
[272] Y.K. Oh, S.M. Raj, G.Y. Jung, S. Park, Bioresour. Technol. 102 (2011) 8357–8367.
[273] X.-G. Zhu, S.P. Long, D.R. Ort, Annu. Rev. Plant Biol. 61 (2010) 235–261.
[274] T. Burgdorf, O. Lenz, T. Buhrke, E. van der Linden, A.K. Jones, S.P.J. Albracht, B. Friedrich, J. Mol. Microbiol. Biotechnol. 10 (2005) 181–196.
[275] T. Goris, A.F. Wait, M. Saggu, J. Fritsch, N. Heidary, M. Stein, I. Zebger, F. Lendzian, F.A. Armstrong, B. Friedrich, O. Lenz, Nat. Chem. Biol. 7 (2011) 310–318.
[276] H. Nishimura, Y. Sako, J. Biosci. Bioeng. 108 (2009) 299–303.
[277] H. Nishimura, Y. Kitano, T. Inoue, K. Nomura, Y. Sako, Biosci., Biotechnol., Biochem. 74 (2010) 1624–1630.
[278] A. Parkin, G. Goldet, C. Cavazza, J.C. Fontecilla-Camps, F.A. Armstrong, J. Am. Chem. Soc. 130 (2008) 13410–13416.
[279] J. Fritsch, P. Scheerer, S. Frielingsdorf, S. Kroschinsky, B. Friedrich, O. Lenz, C.M.T. Spahn, Nature 479 (2011), 249–U134.
[280] J.O. Eberly, R.L. Ely, Crit. Rev. Microbiol. 34 (2008) 117–130.
[281] L. Girbal, G. von Abendroth, M. Winkler, P.M. Benton, I. Meynial-Salles, C. Croux, J.W. Peters, T. Happe, P. Soucaille, Appl. Environ. Microbiol. 71 (2005) 2777–2781.
[282] J. Cohen, K. Kim, P. King, M. Seibert, K. Schulten, Structure 13 (2005) 1321–1329.
[283] P.P. Liebgott, F. Leroux, B. Burlat, S. Dementin, C. Baffert, T. Lautier, V. Fourmond, P. Ceccaldi, C. Cavazza, I. Meynial-Salles, P. Soucaille, J.C. Fontecilla-Camps, B. Guigliarelli, P. Bertrand, M. Rousset, C. Léger, Nat. Chem. Biol. 6 (2010) 63–70.
[284] P.P. Liebgott, A.L. de Lacey, B. Burlat, L. Cournac, P. Richaud, M. Brugna, V.M. Fernandez, B. Guigliarelli, M. Rousset, C. Léger, S. Dementin, J. Am. Chem. Soc. 133 (2011) 986–997.
[285] S. Dementin, F. Leroux, L. Cournac, A.L. de Lacey, A. Volbeda, C. Léger, B. Burlat, N. Martinez, S. Champ, L. Martin, O. Sanganas, M. Haumann, V.M. Fernandez, B. Guigliarelli, J.C. Fontecilla-Camps, M. Rousset, J. Am. Chem. Soc. 131 (2009) 10156–10164.
[286] T. Buhrke, O. Lenz, N. Krauss, B. Friedrich, J. Biol. Chem. 280 (2005) 23791–23796.
[287] M.L. Ghirardi, P. King, S. Kosourov, M. Forestier, L. Zhang, M. Seibert, in: A.F. Collings, C. Critchley (Eds.), Artificial Photosynthesis: From Basic Biology to Industrial Application, Wiley-VCH, Weinheim, 2005, pp. 213–227.
[288] T. Lautier, P. Ezanno, C. Baffert, V. Fourmond, L. Cournac, J.C. Fontecilla-Camps, P. Soucaille, P. Bertrand, I. Meynial-Salles, C. Léger, Faraday Discuss. 148 (2011) 385–407.
[289] B. Kok, in: M. Gibbs, A. Hollaender, B. Kok, L.O. Krampitz, A. San Pietro (Eds.), Proceedings of the Workshop on Bio-Solar Hydrogen Conversion, Bethesda, Maryland, 1973, pp. 22–30.
[290] A. Melis, Plant Sci. 177 (2009) 272–280.
[291] Y. Nakajima, R. Ueda, J. Appl. Phycol. 9 (1997) 503–510.
[292] Y. Nakajima, S. Fujiwara, H. Sawai, M. Imashimizu, M. Tsuzuki, Plant Cell Physiol. 42 (2001) 992–998.
[293] L. Vasilyeva, M. Miyake, E. Khatipov, T. Wakayama, M. Sekine, M. Hara, E. Nakada, Y. Asada, J. Miyake, J. Biosci. Bioeng. 87 (1999) 619–624.
[294] A. Melis, J. Neidhardt, J.R. Benemann, J. Appl. Phycol. 10 (1998) 515–525.
[295] J.E.W. Polle, J.R. Benemann, A. Tanaka, A. Melis, Planta 211 (2000) 335–344.
[296] J.E.W. Polle, S. Kanakagiri, E. Jin, T. Masuda, A. Melis, Int. J. Hydrogen Energy 27 (2002) 1257–1264.
[297] S.D. Tetali, M. Mitra, A. Melis, Planta 225 (2007) 813–829.
[298] P.M. Vignais, J.P. Magnin, J.C. Willison, Int. J. Hydrogen Energy 31 (2006) 1478–1483.
[299] J. Mathews, G.Y. Wang, Int. J. Hydrogen Energy 34 (2009) 7404–7416.
[300] K. McNeely, Y. Xu, N. Bennette, D.A. Bryant, G.C. Dismukes, Appl. Environ. Microbiol. 76 (2010) 5032–5038.
[301] R.L. Chang, L. Ghamsari, A. Manichaikul, E.F.Y. Hom, S. Balaji, W.Q. Fu, Y. Shen, T. Hao, B.O. Palsson, K. Salehi-Ashtiani, J.A. Papin, Mol. Syst. Biol. 7 (2011).
[302] J. Miyake, S. Kawamura, Int. J. Hydrogen Energy 12 (1987) 147–149.
[303] R. Warthmann, N. Pfennig, H. Cypionka, Appl. Microbiol. Biotechnol. 39 (1993) 358–362.
[304] S. Kumazawa, H. Asakawa, Biotechnol. Bioeng. 46 (1995) 396–398.
[305] A.A. Tsygankov, A.S. Fedorov, S.N. Kosourov, K.K. Rao, Biotechnol. Bioeng. 80 (2002) 777–783.
[306] M.L. Ghirardi, Indian J. Biochem. Biophys. 43 (2006) 201–210.

[307] F. Romagnoli, D. Blumberga, I. Pilicka, Int. J. Hydrogen Energy 36 (2011) 7866–7871.
[308] T. Otsuki, S. Uchiyama, K. Fujiki, S. Fukunaga, in: O. Zaborsky, J. Benemann, T. Matsunaga, J. Miyake, A. San Pietro (Eds.), BioHydrogen, Springer, US, 1999, pp. 369–374.
[309] M. Janssen, J. Tramper, L.R. Mur, R.H. Wijffels, Biotechnol. Bioeng. 81 (2003) 193–210.
[310] J. Rupprecht, B. Hankamer, J.H. Mussgnug, G. Ananyev, C. Dismukes, O. Kruse, Appl. Microbiol. Biotechnol. 72 (2006) 442–449.
[311] C.N. Dasgupta, J.J. Gilbert, P. Lindblad, T. Heidorn, S.A. Borgvang, K. Skjanes, D. Das, Int. J. Hydrogen Energy 35 (2010) 10218–10238.
[312] K. Kumar, C.N. Dasgupta, B. Nayak, P. Lindblad, D. Das, Bioresour. Technol. 102 (2011) 4945–4953.
[313] R.C. Prince, H.S. Kheshgi, Crit. Rev. Microbiol. 31 (2005) 19–31.
[314] M. Kitashima, H. Masukawa, H. Sakurai, K. Inoue, Biosci., Biotechnol., Biochem. 76 (2012) 831–833.
[315] J.L. Gosse, B.J. Engel, J.C.H. Hui, C.S. Harwood, M.C. Flickinger, Biotechnol. Prog. 26 (2010) 907–918.
[316] D.B. Levin, R. Chahine, Int. J. Hydrogen Energy 35 (2010) 4962–4969.
[317] A.F. Clarens, E.P. Resurreccion, M.A. White, L.M. Colosi, Environ. Sci. Technol. 44 (2010) 1813–1819.
[318] H. Masukawa, K. Inoue, H. Sakurai, C.P. Wolk, R.P. Hausinger, Appl. Environ. Microbiol. 76 (2010) 6741–6750.
[319] P.D. Weyman, B. Pratte, T. Thiel, FEMS Microbiol. Lett. 304 (2010) 55–61.
[320] J. Rupprecht, J. Biotechnol. 142 (2009) 10–20.
[321] I.K. Kapdan, F. Kargi, Enzyme Microb. Technol. 38 (2006) 569–582.
[322] X.M. Guo, E. Trably, E. Latrille, H. Carrere, J.P. Steyer, Int. J. Hydrogen Energy 35 (2010) 10660–10673.
[323] E.A. Heaton, F.G. Dohleman, S.P. Long, Global Change Biol. 14 (2008) 2000–2014.
[324] B. Uyar, M. Schumacher, J. Gebicki, M. Modigell, Bioprocess Biosyst. Eng. 32 (2009) 603–606.
[325] J. Turner, G. Sverdrup, M.K. Mann, P.C. Maness, B. Kroposki, M. Ghirardi, R.J. Evans, D. Blake, Int. J. Energ. Res. 32 (2008) 379–407.
[326] K. Yamaji (Ed.), Hydrogen Energy Society, Japan Soc. Energy and Resources, Ohsaka, 2008 (in Japanease).
[327] http://ipcc.ch/publications_and_data/ar4/syr/en/contents.html, : IPCC, Climate Change AR4, Synthesis Report.
[328] http://www.iea.org/publications/freepublications/publication/kwes.pdf, : IEA 2012 Key World Energy Statistics [accessed January 25, 2013].
[329] http://www.genome.jp/kegg/catalog/org_list.html, : KEGG Organisms [accessed January 25, 2013].
[330] W.A. Amos, http://www.nrel.gov/docs/fy04osti/35593.pdf, Updated Cost Analysis of Photobiological Hydrogen Production from *Chlamydomonas reinhardtii* Green Algae Report to N.R.E. Laboratory [accessed January 25, 2013].
[331] M. Kitashima, H. Masukawa, H. Sakurai, K. Inoue, https://www.jstage.jst.go.jp/article/jspp/2011/0/2011_0_0298/_article, Effects of CO_2 concentration on photobiological H_2 accumulation by cyanobacteria, and the use of gas-barrier bags, Abstract of the Annual Meeting of JSPP (March 16-18, 2012, Kyoto) P0298 [accessed January 25, 2013].
[332] http://www.nass.usda.gov/Charts_and_Maps/Agricultural_Prices/pricecn.asp, : USDA (corn price) [accessed January 25, 2013].
[333] http://usda01.library.cornell.edu/usda/current/CropProdSu/CropProdSu-01-11-2013.pdf, : USDA (Corn production) [accessed January 25, 2013].
[334] B.D. James, G.N. Baum, J. Perez, K.N. Baum, http://www1.eere.energy.gov/hydrogenandfuelcells/pdfs/46674.pdf, Technoeconomic boundary analysis of biological pathways to hydrogen production, Report to N.R.E. Laboratory, (2009 Aug) [accessed January 25, 2013].

doi:10.1246/cl.130280
Published on the web July 5, 2013

Jolkinolide F, a Cytotoxic Diterpenoid from *Euphorbia jolkinii*

Norihito Maru,* Noriko Chikaraishi, Keisuke Yokota, Yoshinori Kawazoe, and Daisuke Uemura*
Faculty of Science, Kanagawa University, Hiratsuka, Kanagawa 259-1293

(Received March 31, 2013; CL-130280; E-mail: maru@bio.keio.ac.jp)

A new diterpenoid, jolkinolide F (**1**), was isolated from roots of *Euphorbia jolkinii*. The planar structure of **1** was elucidated by spectroscopic analysis, and its stereochemistry was determined by NOESY spectroscopic data and X-ray data analysis. **1** showed cytotoxicity against mammalian cells.

Many *Euphorbia* species are known to be toxic or medicinal plants worldwide. When the aerial parts of these plants are broken or cut, they exude milky sap which has various biological effect in humans and animals, including skin inflammation, irritation, and tumor promotion. *Euphorbia jolkinii* grows along warm beaches in Japan and Taiwan and produces biologicaly active terpenoids, called jolkinolides[1–4] and jolkinols,[5] as secondary metabolites. These compounds have been reported to exhibit cytotoxicity, antibacterial activity, antiviral activity, and antitumor activity. Structures of these jolkinolides and their analogs[6,7] are characterized by an abietan backbone with α,β-unsaturated γ-lactone and various oxidation patterns. In this paper we describe the isolation, structure determination, and bioactivity of a new jolkinolide-type diterpene.

The roots of *Euphorbia jolkinii* (600 g, wet weight), collected on the coast of Wakayama Prefecture, Japan, were extracted with 80% ethanol (3 L) for 14 days. The extract was filtered, concentrated, and partitioned between EtOAc and H_2O. The material obtained from the EtOAc portion was subjected to fractionation using silica gel (chloroform–methanol), a preparative TLC (chloroform–methanol) and reversed-phase HPLC (Develosil ODS-HG-5, 70% aqueous methanol) to give 2 mg of jolkinolide F (**1**) (Chart 1).

Jolkinolide F (**1**)[8] was isolated as colorless prisms with a molecular formula of $C_{20}H_{28}O_3$ on the basis of HRESIMS at m/z 317.21288 $[M + H]^+$ (calcd for $C_{20}H_{29}O_3$, 317.21167). IR absorption at 3460 and 1736 cm^{-1} suggested the presence of hydroxy and ester functional groups. NMR analyses of ^1H, ^{13}C, DEPT, and HMQC showed that **1** is an abietane terpenoid containing four singlet methyls, six methylenes, three methynes, and seven quaternary carbons including one ester carbon (Table 1). The chemical sifts of 77.5 ppm at the quaternary carbon C9 and 77.2 ppm at the methyne C12 suggest hydroxy groups or ethers. The COSY correlations allowed us to connect three series of proton–proton spin systems: H1–H2–H3, H5–H6–H7, and H11–H12. The weak correlation on COSY and small coupling constant ($J = 1.8$ Hz) at H7a and H14 also suggested the connection of three range bond between C7 and C14. The HMBC correlations from H7 to C8 and H14 to C8 were consistent with the presence of a C8–C14 trisubstituted olefin and a connection at C8–C7. The HMBC correlations from methyl H20 to carbonyl C16, olefinic carbons C13 and C15 allowed us to construct a tetrasubstituted olefin, which those from H11/H14 to C13 and from H12 to C16 revealed an

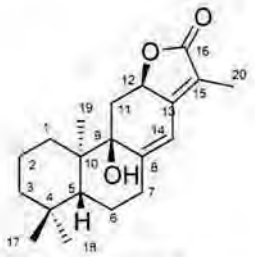

jolkinolide F

Chart 1.

Table 1. NMR data for **1** in $CDCl_3$

Position	$^{13}C^{a,b}$	$^1H^c$	Multi (J_H)^d
1	32.0t	1.55	m
2	18.8t	1.24	m
3	33.5t	1.33	m
4	41.5s		
5	46.2d	1.85	m
6a	23.5t	1.34	m
6b		1.65	m
7a	32.9t	2.30	dq (13.2, 1.8)
7b		2.69	tdd (13.2, 5.1, 1.6)
8	153.1s		
9	77.5s		
10	44.5s		
11a	39.4t	1.33	t (12.9)
11b		3.10	dd (12.9, 6.0)
12	77.2d	4.88	dd (12.9, 6.0)
13	155.0s		
14	115.5d	6.36	d (1.8)
15	117.5s		
16	174.8s		
17	34.0q	0.94	s
18	22.2q	0.87	s
19	17.6q	0.99	s
20	8.3q	1.85	s
9-OH		ND	

[a]Recorded at 100 MHz. [b]Multiplicity was based on the HMQC spectrum. [c]Recorded at 400 MHz. [d]Coupling constants (Hz) are in parentheses.

$\alpha,\beta,\gamma,\delta$-unsaturated γ-lactone. Therefore, a tertiary alcohol was shown to exist at C9. Three singlet methyls were connected to C5 and C1 or C3 via quaternary carbons C4 or C10 as indicated by HMBC correlations from H17 and H18 to C3, C4, and C5, and from H19 to C1, C5, and C10. The HMBC correlations from H19 and H11 to C9 showed a series of bonds C11–C9–C10, and

 © 2013 The Chemical Society of Japan

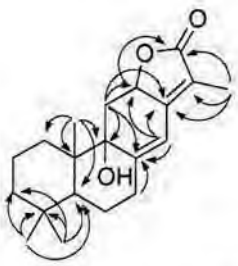

Figure 1. HMBC study of jolkinolide F.

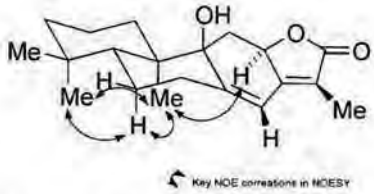

Figure 2. Relative stereochemistry of jolkinolide F from NOESY.

those from H11 to C8 constructed a fused ring of C5 to C14 (Figure 1).

The relative stereochemistry of **1** was elucidated by an analysis of NOESY correlations (Figure 2). The NOESY correlations between H18 and H6a, H19 and H6a, H19 and H18, and H19 and H12 showed that H12 was located on the same side as axial methyls and this orientation suggested that the hydroxy group at C9 was also axial but on the other side of the molecule.

Finally, the structure was determined by X-ray crystallographic analysis[9] (Figure 3). The X-ray structure confirmed that the OH group at C9 is β-oriented on the abietane backbone, while Me19, Me20, H6a, and H12 are α-oriented.

The biological activity of compound **1** was examined with regard to cytotoxicity against HL60 human leukemia cells and HeLa human cervical carcinoma cells. After incubation, **1** showed an IC_{50} of 15.2 µM against HL60 cells and weak toxicity ($IC_{50} > 100$ µM) against HeLa cells.

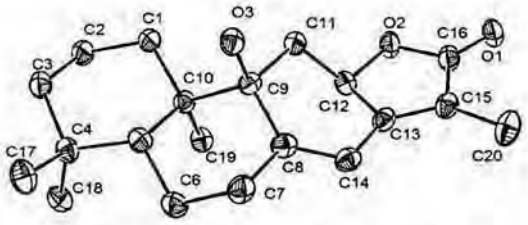

Figure 3. ORTEP drawing of jolkinolide F.

In conclusion, the novel diterpenoid jolkinolide F (**1**) was isolated from roots of *Euphorbia jolkinii*. The structure of **1** was determined by spectroscopic analyses and X-ray crystallographic analysis. **1** showed cytotoxicity against human tumor cells.

This work was supported in part by a Grant-in-Aid for Scientific Research (No. 21221009) from JSPS.

References and Notes

1 D. Uemura, Y. Hirata, *Tetrahedron Lett.* **1972**, *13*, 1387.
2 D. Uemura, Y. Hirata, *Chem. Lett.* **1974**, 819.
3 H. Kigoshi, T. Ichino, K. Yamada, Y. Ijuin, S. F. Makita, D. Uemura, *Chem. Lett.* **2001**, 518.
4 K. Suenaga, Y. Takayanagi, M. Yamaura, H. Kigoshi, *Chem. Lett.* **2004**, *33*, 918.
5 D. Uemura, K. Nobuhara, Y. Nakayama, Y. Shizuri, Y. Hirata, *Tetrahedron Lett.* **1976**, *17*, 4593.
6 Y. Shizuri, S. Kosemura, S. Yamamura, S. Ohba, M. Ito, Y. Saito, *Chem. Lett.* **1983**, 65.
7 N. Crespi-Perellino, L. Garofano, E. Arlandini, V. Pinciroli, A. Minghetti, F. F. Vincieri, B. Danieli, *J. Nat. Prod.* **1996**, *59*, 773.
8 $[\alpha]_D^{20}$ −114.2 (*c* 0.1, $CHCl_3$); IR (neat): 3460, 1736, 1670, 1603, 1458 cm^{-1}; ^1H NMR and ^{13}C NMR: (Table 1); HRESIMS *m/z*: $[M+H]^+$ found 317.21288, calcd for $C_{20}H_{29}O_3$ (+1.21 mmu).
9 Crystal data for **1**: orthorhombic, $P2_12_12_1$, $a = 7.351(1)$ Å, $b = 9.809(2)$ Å, $c = 23.441(5)$ Å, $V = 1690.3(5)$ Å$_3$, $Z = 4$, $D_{calcd} = 1.24$ mg cm^{-3}. $T = 120$ K, R (Rw) = 0.082 (0.083) based on 3099 reflections $\{I > 0.00\sigma(I)\}$ and 214 variable parameters.

© 2013 The Chemical Society of Japan

Beilstein Journal
of Organic Chemistry

Stereoselective synthesis of the C79–C97 fragment of symbiodinolide

Hiroyoshi Takamura*[1], Takayuki Fujiwara[1], Isao Kadota*[1] and Daisuke Uemura[2]

Letter

Open Access

Address:
[1]Department of Chemistry, Graduate School of Natural Science and Technology, Okayama University, 3-1-1 Tsushimanaka, Kita-ku, Okayama 700-8530, Japan and [2]Department of Chemistry, Faculty of Science, Kanagawa University, 2946 Tsuchiya, Hiratsuka 259-1293, Japan

Email:
Hiroyoshi Takamura* - takamura@cc.okayama-u.ac.jp; Isao Kadota* - kadota-i@cc.okayama-u.ac.jp

* Corresponding author

Keywords:
Julia–Kocienski olefination; polyol marine natural product; Sharpless asymmetric dihydroxylation; spiroacetalization; symbiodinolide

Beilstein J. Org. Chem. **2013,** *9,* 1931–1935.
doi:10.3762/bjoc.9.228

Received: 18 July 2013
Accepted: 03 September 2013
Published: 25 September 2013

This article is part of the Thematic Series "Natural products in synthesis and biosynthesis".

Guest Editor: J. S. Dickschat

© 2013 Takamura et al; licensee Beilstein-Institut.
License and terms: see end of document.

Abstract

Symbiodinolide is a polyol marine natural product with a molecular weight of 2860. Herein, a streamlined synthesis of the C79–C97 fragment of symbiodinolide is described. In the synthetic route, a spiroacetalization, a Julia–Kocienski olefination, and a Sharpless asymmetric dihydroxylation were utilized as the key transformations.

Findings

A 62-membered polyol marine natural product, symbiodinolide (**1**, Figure 1), was isolated from the 80% aqueous ethanol extract of the cultured symbiotic dinoflagellate *Symbiodinium* sp. in 2007 [1]. Symbiodinolide shows voltage-dependent N-type Ca^{2+} channel-opening activity at 7 nmol/L and COX-1 inhibitory effect at 2 µmol/L (65% inhibition). Furthermore, **1** ruptures the tissue surface of the acoel flatworm *Amphiscolops* sp. at 2.5 µmol/L. The entire planar structure of **1** was established by the detailed 2D NMR spectroscopic analysis. However, the complete stereostructural determination of **1** with its 61 chirality centres and a molar mass of 2860 has been an unsolved issue. Therefore, in order to complete the configurational elucidation of **1**, we are now investigating its chemical degradation [1-3] and chemical synthesis of the fragments [4-11].

Previously, we reported the stereoselective synthesis of the spiroacetal C79–C96 fragment [4], which is summarized in Scheme 1. Triflate **2** was reacted with the lithium acetylide prepared from alkyne **3** to give the desired coupling product **4**. The TBDPS ether **4** was transformed to TIPS ether **5** because of the lability of the TBDPS protecting group under the following Birch conditions. The alkyne **5** was subjected to the Birch reduction to afford the *trans*-alkene **6**, wherein the benzyl

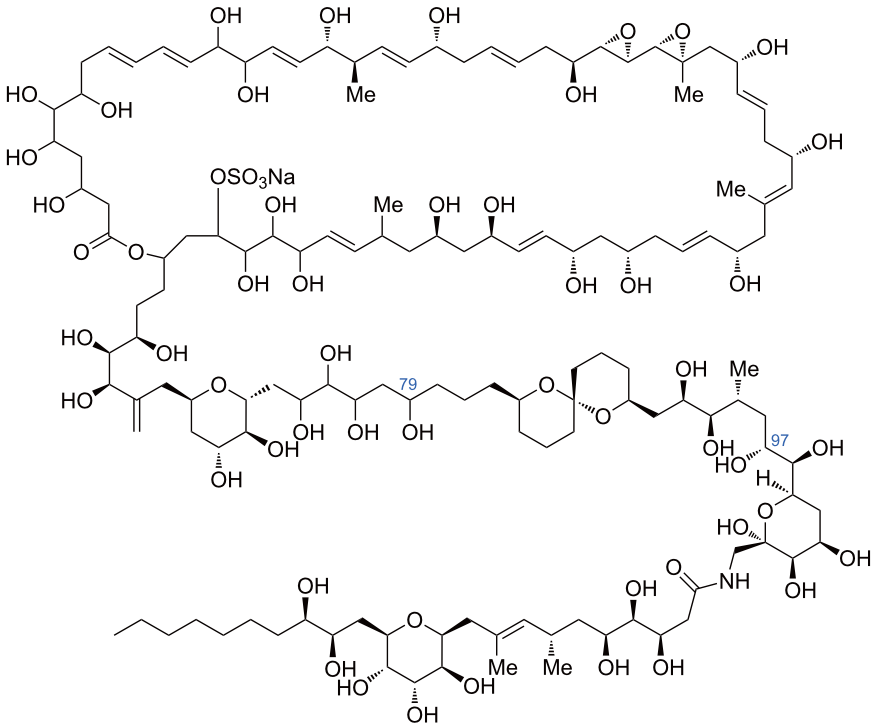

Figure 1: Structure of symbiodinolide (**1**).

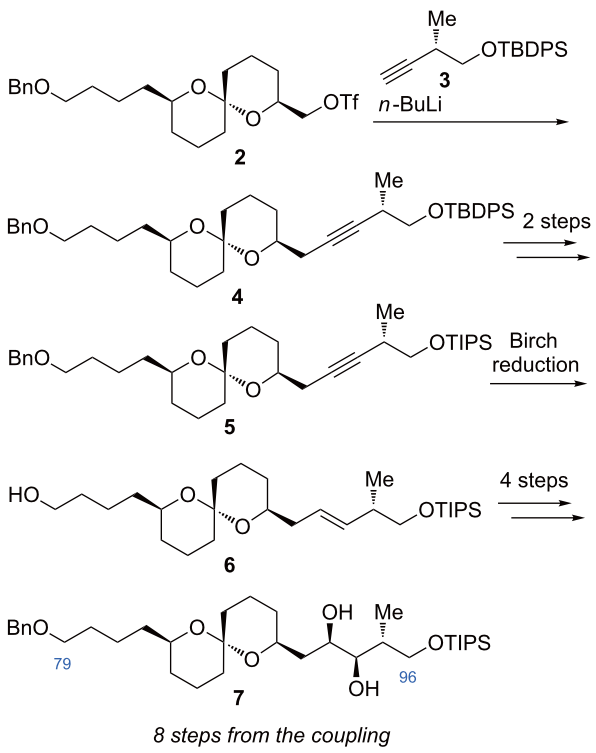

Scheme 1: Our previous synthesis of the C79–C96 fragment **7**.

moiety was deprotected. The alkene **6** was derivatized to the spiroacetal C79–C96 fragment **7** in four steps including the benzyl protection and Sharpless asymmetric dihydroxylation (AD). Although the desired spiroacetal fragment **7** was synthesized stereoselectively, the transformation starting with the coupling between **2** and **3** to the final product **7** needed eight steps. Therefore, we decided to examine the more efficient synthesis of the spiroacetal fragment. Herein, we report the improved synthesis of the spiroacetal fragment by utilizing Julia–Kocienski olefination as the coupling reaction.

The new retrosynthetic analysis of the C79–C97 fragment **8** is described in Scheme 2. We envisaged that the diol **8** could be synthesized by the Julia–Kocienski olefination [12-14] between aldehyde **9** and 1-phenyl-1*H*-tetrazol-5-yl (PT)-sulfone **10** and subsequent Sharpless AD [15], wherein the target molecule **8** could be prepared in two steps from the coupling. The carbon framework of **9** could be constructed through the stereoselective spiroacetalization of dihydroxyketone **11**.

First, we commenced the stereocontrolled synthesis of aldehyde **20** (Scheme 3). Treatment of epoxide **13**, which was prepared from L-aspartic acid (**12**) by the known procedure [8], with 3-butenylmagnesium bromide/CuI [16] provided the corresponding secondary alcohol. Protection of the alcohol with

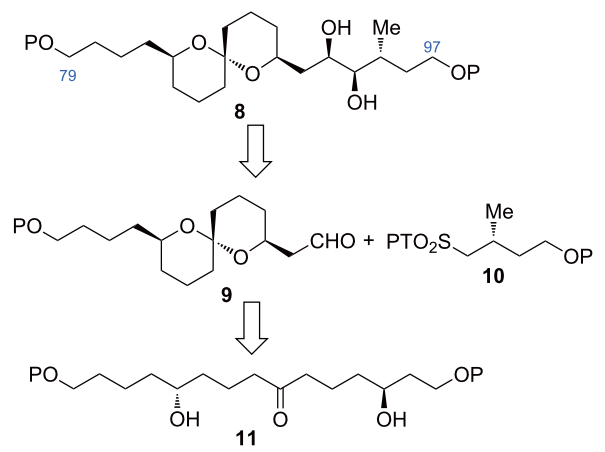

Scheme 2: Retrosynthetic analysis of the C79–C97 fragment **8**.

TBSCl afforded TBS ether **14** in 91% yield in two steps. Alkene **14** was reacted with *m*-CPBA to produce epoxide **15** as a 1:1 diastereomeric mixture. Epoxide **15** was coupled with alkyne **16** [4] in the presence of *n*-BuLi/$BF_3{\cdot}OEt_2$ [17] to give the desired product **17** in 92% yield from **15**. Hydrogenation of the alkyne moiety of **17** followed by TPAP oxidation [18] yielded ketone **18**. Removal of the three TBS protecting groups and subsequent stereoselective spiroacetalization were performed in one-pot with CSA in MeOH to provide spiroacetal **19** as a single stereoisomer [19,20]. The stereochemistry of **19** was elucidated by the observed NOE correlations between H-83 and H-91 as indicated by an arrow. The plausible rationale for the stereoselective formation of **19** is the thermodynamic stability due to the double anomeric effect. Oxidation of the alcohol **19** with $SO_3{\cdot}$pyr/Et_3N/DMSO [21] afforded aldehyde **20**.

Next, we carried out the synthesis of PT-sulfones **23** and **24** which were the coupling partners of the aldehyde **20** (Scheme 4). The synthesis started from commercially available methyl (*S*)-3-hydroxy-2-methylpropanoate (**21**), which was converted to alcohol **22** by the known method [22]. Alcohol **22** was treated with 1-phenyl-1*H*-tetrazole-5-thiol/DEAD/PPh_3 to furnish the corresponding PT-sulfide, which was oxidized with

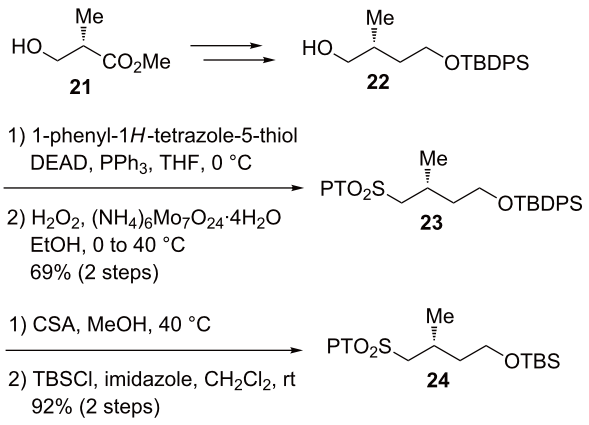

Scheme 4: Synthesis of PT-sulfones **23** and **24**.

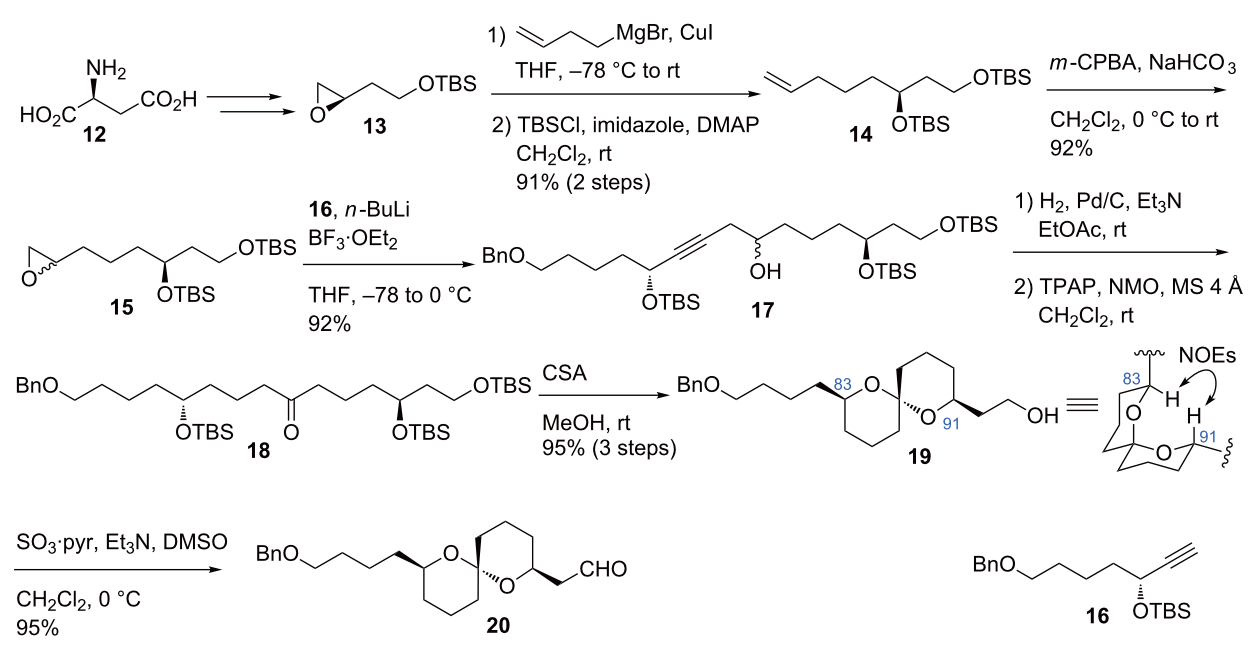

Scheme 3: Synthesis of aldehyde **20**.

H_2O_2/Mo(VI) [23] to yield PT-sulfone **23**. The TBDPS protecting group of **23** was transformed to the TBS group in two steps to provide PT-sulfone **24**.

With the coupling precursors aldehyde **20** and PT-sulfones **23** and **24** in hand, we next examined the Julia–Kocienski olefination [12-14] of these compounds (Table 1). Deprotonation of the PT-sulfone **23** with KHMDS, followed by addition of the aldehyde **20**, gave rise to the desired coupling product (*E*)-**25** along with (*Z*)-**25** in 27% combined yield at a 3.5:1 diastereomeric ratio (Table 1, entry 1). When NaHMDS was used as the base, the chemical yield was improved to 77%, however, the *E*/*Z* ratio was decreased to 1.3:1 (Table 1, entry 2). When LDA was used as the base, the chemical yield and diastereomeric ratio were increased to 98% and 2.6:1, respectively (Table 1, entry 3). Reaction of PT-sulfone **24** using LDA gave the coupling products (*E*)- and (*Z*)-**26** in 86% yield, wherein the diastereomeric ratio was increased to 5.0:1 (Table 1, entry 4). The configurations of the coupling products were elucidated by their coupling constants between H-93 and H-94 (15.3 Hz in (*E*)-**25** and (*E*)-**26**, 10.7 Hz in (*Z*)-**25** and (*Z*)-**26**). Finally, the desired alkene (*E*)-**26** was subjected to the Sharpless AD [15] with AD-mix-β to furnish the C79–C97 fragment **27** in 72% yield as a single diastereomer (Scheme 5). The configuration of the resulting two vicinal hydroxy groups at C93 and C94 of **27** were unambiguously confirmed by the modified Mosher method, respectively (see Supporting Information File 1).

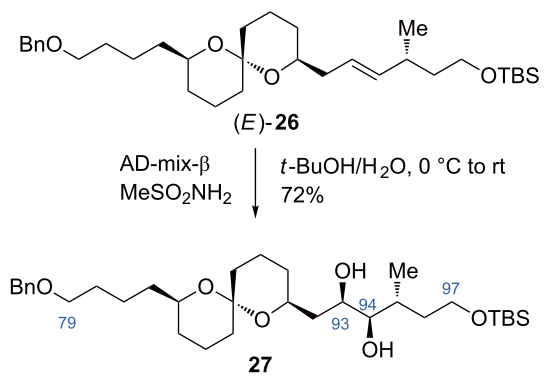

Scheme 5: Synthesis of the C79–C97 fragment **27**.

In conclusion, we have achieved the stereoselective synthesis of the C79–C97 fragment. The synthetic route has featured a stereoselective spiroacetalization, a Julia–Kocienski olefination, and a Sharpless asymmetric dihydroxylation. This synthesis of the spiroacetal fragment, wherein the two-step sequence was conducted and the overall yield was 52% from the coupling, has been improved over the previous synthesis wherein the eight-step transformation was needed and the overall yield was 31% from the coupling. Further synthetic effort of symbiodinolide toward the complete structural elucidation is currently underway and will be reported in due course.

Table 1: Julia–Kocienski olefination between aldehyde **20** and PT-sulfones **23** and **24**.

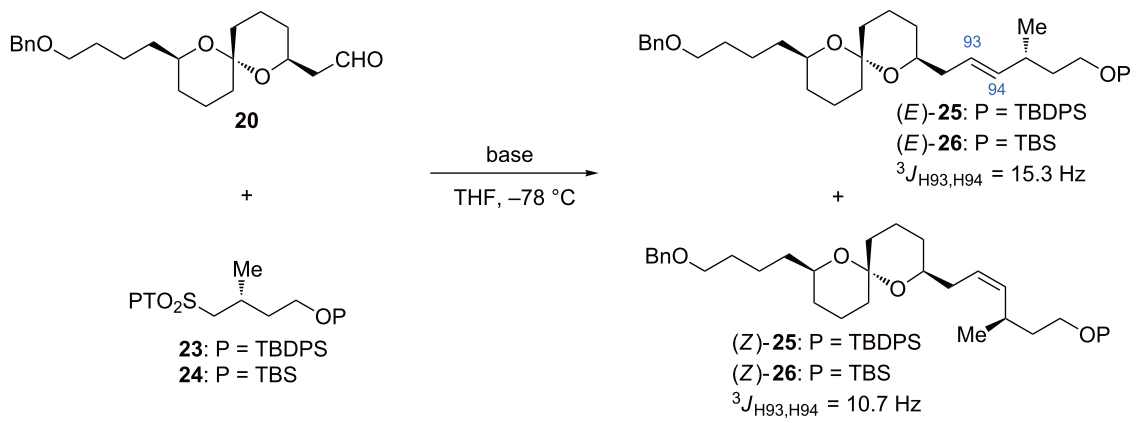

Entry	PT-Sulfone	Base	Yield (%)[a]	Ratio (*E*:*Z*)[b]
1	**23**	KHMDS	27	3.5:1
2	**23**	NaHMDS	77	1.3:1
3	**23**	LDA	98	2.6:1
4	**24**	LDA	86	5.0:1

[a]Isolated yield from **20**. [b]Determined by ^{1}H NMR spectroscopy.

Supporting Information

Supporting Information File 1

Experimental procedures, spectroscopic data, and NMR spectra of all new compounds.
[http://www.beilstein-journals.org/bjoc/content/supplementary/1860-5397-9-228-S1.pdf]

Acknowledgements

We are grateful to Mr. Yohei Kawakubo (Okayama University) for valuable discussions. We acknowledge The Kurata Memorial Hitachi Science and Technology Foundation, The Research Foundation for Pharmaceutical Sciences, and The Society of Synthetic Organic Chemistry, Japan (Shionogi Award in Synthetic Organic Chemistry, Japan) for financial supports. This research was supported by a Grant-in-Aid for Scientific Research (No. 24710250) from the Japan Society for the Promotion of Science (JSPS).

References

1. Kita, M.; Ohishi, N.; Konishi, K.; Kondo, M.; Koyama, T.; Kitamura, M.; Yamada, K.; Uemura, D. *Tetrahedron* **2007,** *63,* 6241–6251. doi:10.1016/j.tet.2007.02.093
2. Han, C.; Uemura, D. *Tetrahedron Lett.* **2008,** *49,* 6988–6990. doi:10.1016/j.tetlet.2008.09.118
3. Han, C.; Yamano, Y.; Kita, M.; Takamura, H.; Uemura, D. *Tetrahedron Lett.* **2009,** *50,* 5280–5282. doi:10.1016/j.tetlet.2009.07.014
4. Takamura, H.; Ando, J.; Abe, T.; Murata, T.; Kadota, I.; Uemura, D. *Tetrahedron Lett.* **2008,** *49,* 4626–4629. doi:10.1016/j.tetlet.2008.05.078
5. Murata, T.; Sano, M.; Takamura, H.; Kadota, I.; Uemura, D. *J. Org. Chem.* **2009,** *74,* 4797–4803. doi:10.1021/jo900546k
6. Takamura, H.; Murata, T.; Asai, T.; Kadota, I.; Uemura, D. *J. Org. Chem.* **2009,** *74,* 6658–6666. doi:10.1021/jo901162v
7. Takamura, H.; Kadonaga, Y.; Yamano, Y.; Han, C.; Aoyama, Y.; Kadota, I.; Uemura, D. *Tetrahedron Lett.* **2009,** *50,* 863–866. doi:10.1016/j.tetlet.2008.11.056
8. Takamura, H.; Kadonaga, Y.; Yamano, Y.; Han, C.; Kadota, I.; Uemura, D. *Tetrahedron* **2009,** *65,* 7449–7456. doi:10.1016/j.tet.2009.07.019
9. Takamura, H.; Kadonaga, Y.; Kadota, I.; Uemura, D. *Tetrahedron Lett.* **2010,** *51,* 2603–2605. doi:10.1016/j.tetlet.2010.03.014
10. Takamura, H.; Kadonaga, Y.; Kadota, I.; Uemura, D. *Tetrahedron* **2010,** *66,* 7569–7576. doi:10.1016/j.tet.2010.07.045
11. Takamura, H.; Tsuda, K.; Kawakubo, Y.; Kadota, I.; Uemura, D. *Tetrahedron Lett.* **2012,** *53,* 4317–4319. doi:10.1016/j.tetlet.2012.06.005
12. Blakemore, P. R.; Cole, W. J.; Kocieński, P. J.; Morley, A. *Synlett* **1998,** 26–28. doi:10.1055/s-1998-1570
13. Aïssa, C. *Eur. J. Org. Chem.* **2009,** 1831–1844. doi:10.1002/ejoc.200801117
14. Blakemore, P. R. *J. Chem. Soc., Perkin Trans. 1* **2002,** 2563–2585. doi:10.1039/B208078H
15. Kolb, H. C.; VanNieuwenhze, M. S.; Sharpless, K. B. *Chem. Rev.* **1994,** *94,* 2483–2547. doi:10.1021/cr00032a009
16. Paterson, I.; Anderson, E. A.; Dalby, S. M.; Lim, J. H.; Maltas, P.; Loiseleur, O.; Genovino, J.; Moessner, C. *Org. Biomol. Chem.* **2012,** *10,* 5861–5872. doi:10.1039/c2ob25100k
17. Yamaguchi, M.; Hirao, I. *Tetrahedron Lett.* **1983,** *24,* 391–394. doi:10.1016/S0040-4039(00)81416-1
18. Ley, S. V.; Norman, J.; Griffith, W. P.; Marsden, S. P. *Synthesis* **1994,** 639–666. doi:10.1055/s-1994-25538
19. Perron, F.; Albizati, K. F. *Chem. Rev.* **1989,** *89,* 1617–1661. doi:10.1021/cr00097a015
20. Aho, J. E.; Pihko, P. M.; Rissa, T. K. *Chem. Rev.* **2005,** *105,* 4406–4440. doi:10.1021/cr050559n
21. Parikh, J. R.; Doering, W. v. E. *J. Am. Chem. Soc.* **1967,** *89,* 5505–5507. doi:10.1021/ja00997a067
22. Kurosawa, S.; Mori, K. *Eur. J. Org. Chem.* **2000,** 955–962. doi:10.1002/(SICI)1099-0690(200003)2000:6<955::AID-EJOC955>3.0.CO;2-Y
23. Schultz, H. S.; Freyermuth, H. B.; Buc, S. R. *J. Org. Chem.* **1963,** *28,* 1140–1142. doi:10.1021/jo01039a512

License and Terms

This is an Open Access article under the terms of the Creative Commons Attribution License (http://creativecommons.org/licenses/by/2.0), which permits unrestricted use, distribution, and reproduction in any medium, provided the original work is properly cited.

The license is subject to the *Beilstein Journal of Organic Chemistry* terms and conditions: (http://www.beilstein-journals.org/bjoc)

The definitive version of this article is the electronic one which can be found at:
doi:10.3762/bjoc.9.228

Tetrahedron Letters 54 (2013) 4385–4387

Contents lists available at SciVerse ScienceDirect

Tetrahedron Letters

journal homepage: www.elsevier.com/locate/tetlet

Relative configuration of luminaolide

Norihito Maru [a,*], Toshiyasu Inuzuka [b], Keita Yamamoto [a], Makoto Kitamura [c], Peter J. Schupp [c], Kaoru Yamada [a], Daisuke Uemura [a,*]

[a] Faculty of Science, Kanagawa University, Hiratsuka 259-12, Japan
[b] Division of Instrumental Analysis, Life Science Research Center, Gifu University, 1-1 Yanagido, Gifu 501-1193, Japan
[c] Institute for Chemistry and Biology of the Marine Environment, Terramare, Carl-von-Ossietzky University Oldenburg, Wilhelmshaven, Germany

ARTICLE INFO

Article history:
Received 31 March 2013
Revised 25 May 2013
Accepted 30 May 2013
Available online 15 June 2013

Keywords:
Luminaolide
Coral larvae
Enhancer
Stereochemistry
JBCA method

ABSTRACT

The coral metamorphosis-enhancing compound luminaolide was isolated from the crustose coralline algae (CCA) *Hydrolithon reinboldii*, and was shown to 34-membered macrodiolide skeleton. The relative configuration of luminaolide was established based on ^{1}H–^{1}H coupling constants, steric information from ROESY and a *J*-based configuration analysis using long-range ^{1}H–^{13}C coupling constants.

© 2013 Elsevier Ltd. All rights reserved.

Luminaolide (**1**) was isolated from the crustose coralline algae (CCA) *Hydrolithon reinboldii* as a novel compound that enhanced the metamorphosis of scleractinian coral larvae. [1,2] The settlement and metamorphosis of many marine invertebrates, including coral, are known to be influenced by CCA, and in some species CCA inhibit recruitment. However, limited information is available on the external chemical cues that act as natural inducers of larval metamorphosis.[3,4] The isolation, larval metamorphosis activity, and planar structure of **1** have been reported previously.[1] In this letter, we present the result of a stereochemical study of macrodiolide **1**.

Luminaolide (**1**) was purified as a white amorphous solid from the extract of the CCA H. *reinboldii*, by bio-assay-guided isolation using reversed-phase HPLC and preparative TLC. The planar structure was determined based on the result of spectroscopic analyses. (Fig. 1).

The relative configuration of the dihydropyran moiety (C7–C11) was determined from ROESY correlations. The ROESY correlations between H6b (δ_H 1.90) and H11 (δ_H 3.55) showed that C6 and H11 are in a diaxial orientation and half-chair conformation on the dihydropyran ring. Therefore, the relative configurations were deduced to be 7*R** and 11*S** (Fig. 2).

The conformation assignments for the macrocyclic moiety and its side chain were first analyzed on the assumption that the carbon chain has a zigzag conformation. For C3–C7, a series of **3** alternate stereocenters, C3, C5, and C7, were elucidated based on $^{3}J_{H,H}$ values and ROESY correlations. For C3–C4, an *anti* orientation at H3 (δ_H 4.07)/H4b (δ_H 1.85) was revealed by the observation of a large $^{3}J_{H3,H4b}$ value (9.8 Hz). The ROESY correlation between H3 and H4a (δ_H 1.46) followed this relationship. For C4–C5, the ROESY correlation at H4b/H5 (δ_H 3.73) and 5-OCH_3 (δ_H 3.40)/H4a, the small $^{3}J_{H4b,H5}$ value (3.4 Hz) established a *gauche* orientation at H4b/H5. For C5–C6, the observation of a large $^{3}J_{H5,H6a}$ value (7.5 Hz) indicated that H5 and H6a (δ_H 1.68) are in an *anti* orientation. The ROESY correlation between protons at 5-OCH_3 (δ_H 3.40) and H6a, 5-OCH_3 and H7 (δ_H 4.45), and H6a and H7 determined relative configurations as 3*S** and 5*S** (Fig. 3).

The side chain C20–C30 was separated into two contiguous stereocenters, C20–C22 and C26–C28, by the ethylene-carbonyl chain C23–C25. For C26–C27, the observation of a large $^{3}J_{H26,H27}$ value (9.2 Hz) indicated that H26 (δ_H 2.76) and H27 (δ_H 3.30) are in an *anti* orientation. For C27–C28, a *gauche* orientation at H27/H28 (δ_H 2.46) was revealed by the observation of a small $^{3}J_{H27,H28}$ value (2.6 Hz). The ROESY correlations between H26 and 27-OCH_3 (δ_H 3.34), H27 and 26-CH_3 (δ_H 0.95), H27 and H28, and 27-OCH_3 and 28-CH_3 (δ_H 1.17) showed that the relative configurations were 26*S**, 27*S** and 28*R** (Fig. 4).

For C20–C21, an *anti* orientation at H20 (δ_H 1.80)/H21 (δ_H 2.85) was revealed by the observation of a large $^{3}J_{H20,H21}$ value (7.8 Hz). The ROESY correlation between H20 and 21-OCH_3 (δ_H 3.44) showed that the configuration of H20/21-OCH_3 was *gauche*. For C21–C22, the observation of a small $^{3}J_{H21,H22}$ value (3.2 Hz) indicated that H21 and H22 (δ_H 1.74) are in a *gauche* orientation.

* Corresponding authors. Tel.: +81 463 59 4111; fax: +81 463 58 9684.
E-mail addresses: n-maru@kanagawa-u.ac.jp (N. Maru), uemurad@kanagawa-u.ac.jp (D. Uemura).

0040-4039/$ - see front matter © 2013 Elsevier Ltd. All rights reserved.
http://dx.doi.org/10.1016/j.tetlet.2013.05.143

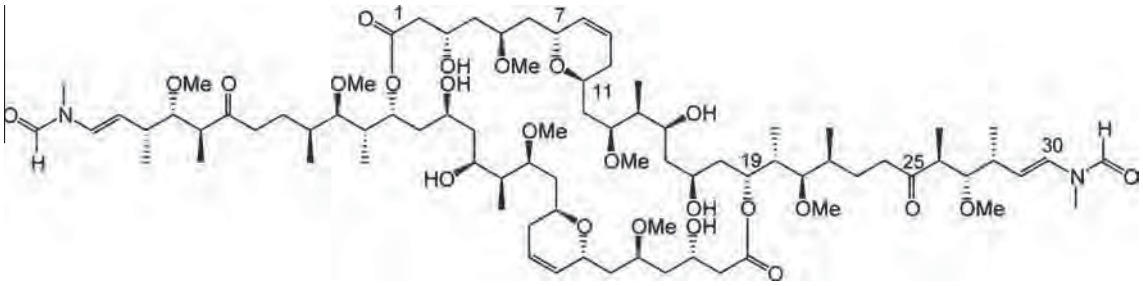

Figure 1. Structure of luminaolide. Stereochemistry of C3–C22 and C26–C28 fragments are independent.

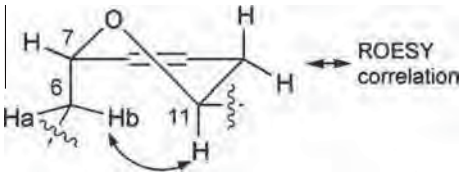

Figure 2. Relative configuration of C7–C11.

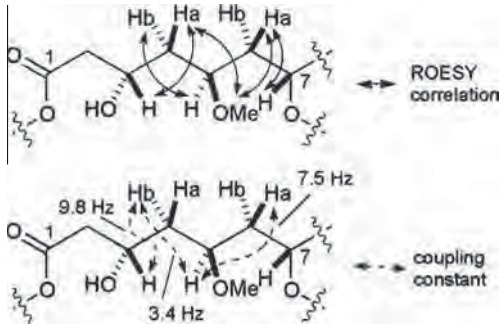

Figure 3. Relative configuration of C3–C7.

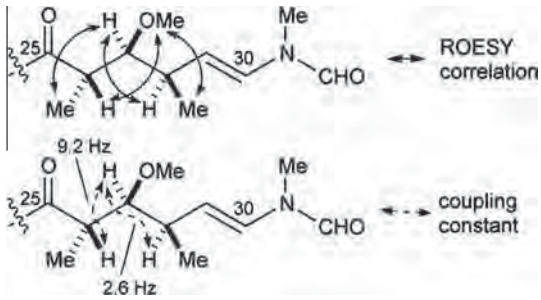

Figure 4. Relative configuration of C26–C28.

The ROESY correlation between H20 and H22, 21-OCH_3 and 22-CH_3 (δ_H 0.97), and H21 and H22 revealed that 21-OCH_3 and 22-CH_3 are in a *gauche* orientation. Therefore, the relative configuration of C20–C23 was deduced to be 20*R**, 21*R**, and 22*S** (Fig. 5).

For C11–C19, the ROESY correlations at H11/H14 (δ_H 1.51) and H15 (δ_H 3.62)/H18b (δ_H 1.95) suggested that the carbon chain is not in a zigzag formation. Therefore, we applied the *J*-based configuration analysis (JBCA) method[5] with a ROESY analysis for this section. The JBCA method has been used to elucidate the relative configurations of various compounds. Although JBCA is used for acyclic compounds, some fragments of large-ring macrolides are considered to have sufficiently flexible molecular structures. In fact, the relative configurations of medium- and large-ring macrolides have been elucidated using JBCA.[6,7] For the JBCA analysis, $^{2/3}J_{H,C}$ values are required in addition to $^3J_{H,H}$ values. We obtained coupling constant values by using the homo-*J*-resolved ^{1}H NMR method and *J*-resolved HMBC method.[8]

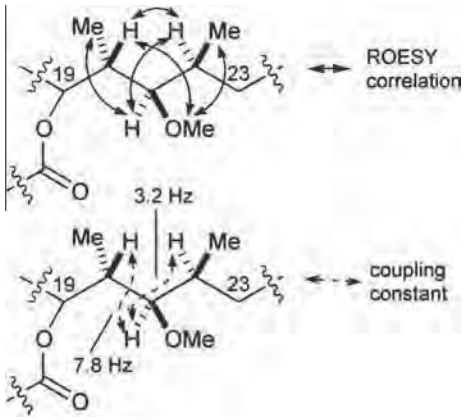

Figure 5. Relative configuration of C20–C22.

For C11–C12, the ROESY correlations between H11 and H12a (δ_H 1.64), and H10 (δ_H 1.97) and H12a/H12b (δ_H 1.82) revealed that H11 and H12a are in a *gauche* orientation, H11 and H12b are in an *anti* orientation, and H12a/b and C10 are both in a *gauche* orientation. For C12–C13, the observation of a large $^3J_{H12a,H13}$ value (10.6 Hz) indicated that H12a and H13 (δ_H 3.92) are in an *anti* orientation, and a large $^3J_{H12b,C14}$ value (7.7 Hz) indicated that H12b and C14 (δ_C 43.82) are in an *anti* orientation. For C13–C14, *gauche* orientations at H13/H14 and C12/H14 are shown in a small $^3J_{H13,H14}$ value (2.4 Hz) and the ROESY correlations at H12a/H14. A large $^3J_{H13,14-CH_3}$ value (6.9 Hz) indicated that H13 and 14-CH_3 (δ_H 0.82) are in an *anti* orientation. For C14–C15, a small value of $^2J_{H14,C15}$ (<3 Hz) indicated an *anti* orientation at H14/OH15, and *gauche* orientations at H14/C16 (δ_C 43.34) and H15 (δ_H 3.62)/14-CH_3 were revealed by small values of $^3J_{H14,C16}$ (<3 Hz) and $^3J_{H15,14-CH3}$ (<3 Hz). For C15–C16, the observation of a small value of $^2J_{C15,H16b}$ (<3 Hz) inferred that H16b (δ_H 1.74) and OH15 are in an *anti* orientation, and small values of $^3J_{C14,H16a}$ (<3 Hz) and $^3J_{C14,H16b}$ (<3 Hz) revealed that H16a (δ_H 1.71)/C14 and H16b/C14 had *gauche* orientations. Additionally, the ROESY correlations between H15 and H16b indicated a *gauche* orientation at H15/H16b. For C16–C17, a large $^2J_{H16a,C17}$ value (6.2 Hz) and a small $^2J_{H16b,C17}$ value (<2 Hz) showed that H16a and OH17 are in a *gauche* orientation, while in an *anti* orientation at H16b and OH17. The observation of a large $^3J_{H16a,C18}$ value (7.6 Hz) showed an *anti* orientation at H16a and C18 (δ_C 42.29), and a small $^3J_{H16b,C18}$ value (<3 Hz) revealed a *gauche* orientation at H16b and C18. For C17–C18, an *anti* orientation at H17 and H18a (δ_H 1.44) were indicated in a large $^3J_{H17,H18a}$ value (9.0 Hz). The ROESY correlations at H18b/H15 revealed that H18b and C16 are in a *gauche* orientation. For

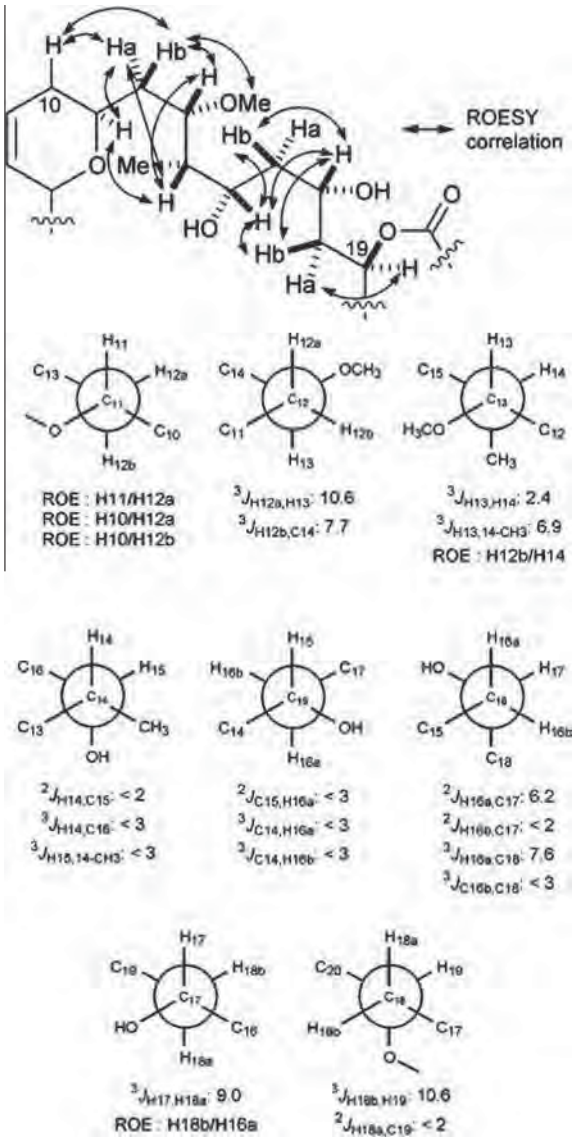

Figure 6. Relative configurations and projections of C11–C19.

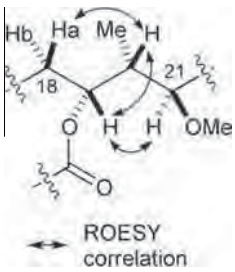

Figure 7. Relative configuration of C18–C20.

the C18–C19, the observation of a large $^3J_{H18b,H19}$ value (10.6 Hz) indicated that H18b and H19 (δ_H 5.62) are in an *anti* orientation, and a small $^2J_{H18a,C19}$ value (<2 Hz) indicated that H18a and O19 are in an *anti* orientation. Thus, the relative configurations of C12–C19 were deduced to be 13*S**, 14*S**, 15*S**, 17*S**, and 19*R** (Fig. 6).

Finally, for C19–C20, the ROESY correlations at H19/H20, H19/H21, and H18b/H20 were associated with the asymmetry of C3–C19 and C20–C22 (Fig. 7). The stereochemical relation between the fragments of two fragments, C3–C22 and C26–C28 and their absolute configurations are currently under investigation.

Another biological activity of compound **1** was examined with regard to cytotoxicity against B16 mouse melanoma cells. After incubation, **1** showed an IC_{50} of 0.7 μM. Meanwhile, **1** enhanced metamorphosis activity by 42-fold in *Leptastrea purpurea* larva at 16.6 nM.

Acknowledgment

This work was supported in part by a Grant-in-Aid for Scientific Research (No. 21221009) from JSPS.

References and notes

1. Kitamura, M.; Schupp, P. J.; Nakano, Y.; Uemura, D. *Tetrahedron Lett.* **2009**, *50*, 6606.
2. Uemura, D.; Kita, M.; Arimoto, H.; Kitamura, M. *Pure Appl. Chem.* **2009**, *81*, 1093.
3. Kitamura, M.; Koyama, T.; Nakano, Y.; Uemura, D. *Chem. Lett.* **2005**, *34*, 1272.
4. Kitamura, M.; Koyama, T.; Nakano, Y.; Uemura, D. *J. Exp. Mar. Biol. Ecol.* **2007**, *152*, 639.
5. Matsumori, N.; Kaneno, D.; Murata, M.; Nakamura, H.; Tachibana, K. *J. Org. Chem.* **1999**, *64*, 866.
6. Morinaka, B. I.; Molinski, T. F. *Org. Lett.* **2011**, *13*, 6338.
7. Kawahara, T.; Izumikawa, M.; Takagi, M.; Shin-ya, K. *Org. Lett.* **2012**, *14*, 4435.
8. Furihata, K.; Tashiro, M.; Seto, H. *Magn. Reson. Chem.* **2009**, *47*, 814.

Tetrahedron Letters 54 (2013) 1921–1923

Contents lists available at SciVerse ScienceDirect

Tetrahedron Letters

journal homepage: www.elsevier.com/locate/tetlet

Thermally driven asymmetric domino reaction catalyzed by a thermostable esterase and its variants

Reina Wada [a], Takashi Kumon [a], Robert Kourist [b], Hiromichi Ohta [a], Daisuke Uemura [a], Shosuke Yoshida [a], Kenji Miyamoto [a,*]

[a] Department of Biosciences and Informatics, Keio University, 3-14-1 Hiyoshi, Kohoku-ku, Yokohama, Kanagawa 223-8522, Japan
[b] Junior Professorship for Microbial Biotechnology, Ruhr Universität Bochum, Universitätstr. 150, 44780 Bochum, Germany

ARTICLE INFO

Article history:
Received 14 December 2012
Revised 15 January 2013
Accepted 18 January 2013
Available online 29 January 2013

Keywords:
Domino reaction
Thermostable esterase
α-Arylpropionates
Thermal spontaneous decarboxylation
Active site

ABSTRACT

We have developed a thermally driven domino reaction for the synthesis of (*S*)-α-arylpropionates (profens) using a thermostable esterase from *Sulfolobus tokodaii* strain 7. Stereoselectivity was improved considerably by engineering of the active site. Stereoselective decarboxylation at the active site of an esterase is a new reaction for the synthesis of optically active carboxylic acids.

Crown Copyright © 2013 Published by Elsevier Ltd. All rights reserved.

Climate change and the future limitation of energy and resources create a high demand for efficient, sustainable, synthetic strategies under the green chemistry philosophy.[1] One approach to this is the minimization of resources dedicated to the work-up and purification of compounds. Domino reactions, where several bond-forming and bond-breaking steps take place in one pot under the same reaction conditions, provide a highly efficient strategy. These reactions improve the synthetic efficiency by decreasing the number of operations and thus the amount of chemicals and solvents required. The application of enzymes in multistep reactions permits the use of excellent stereoselectivity and mild reaction conditions usually associated with enzymes.[2] Akai et al. reported the first example of lipase-catalyzed enantioselective esterification followed by an intramolecular Diels–Alder reaction, a sequence which gave products with up to 99% enantiomeric excess (ee).[3]

We have recently identified a thermostable esterase gene (ST0071) from the thermophilic archeon *Sulfolobus tokodaii* by an in silico screening of the total genome.[4] Esterase (Est0071) expressed from the putative gene is highly similar to esterases with a so-called GGG(A)X motif in their active sites. This motif has been associated with the ability of GGG(A)X hydrolases to convert sterically demanding tertiary alcohols.[5] Indeed, Est0071 shows activity toward several arylaliphatic tertiary alcohols, albeit with low enantioselectivity (not published). Moreover, it is known that several of these esterases have excellent enantioselectivity toward bulky malonate diesters (**1**).[6]

The hydrolysis reaction can be used to synthesize malonic acid monoesters (**2**) in asymmetrization with 100% theoretical yield. In contrast to mesophilic enzymes, Est0071 can catalyze this reaction at temperatures above 70 °C. Under these reaction conditions, the monoester is spontaneously cleaved to the α-arylpropionic acid ester (**4**). If decarboxylation occurs at the active site it may be stereoselective. This prompted us to attempt an enantioselective domino reaction to produce the pharmacologically important compound naproxen (**5b**). If the chiral environment of the enzyme causes the product to be optically pure, the stereospecific outcome should depend to some degree on the choice of amino acids at the active site, thus creating the opportunity to optimize enantioselectivity by protein engineering (see Table 2).

Initially, we examined whether this esterase could catalyze the hydrolysis of prochiral malonate diesters (**1a**) at room temperature. As anticipated, cell-free extract of Est0071 catalyzed the hydrolysis of prochiral diesters to the corresponding monoesters ((*S*)-**2a**) with excellent stereoselectivity (99% ee) and 96% yield. Interestingly, the enantiopreference of Est0071 is the opposite to that of pig liver esterase, which forms the (*R*)-enantiomer with 96% ee.[6] Under high temperatures of 50–70 °C, the monoester (**2a**) was cleaved to the racemic ester (**4a**).[4] As the esterase shows excellent enantioselectivity, the decrease in optical purity was attributed to racemization during decarboxylation. Variations in

* Corresponding author. Tel.: +81 45 566 1786; fax: +81 45 566 1783.
E-mail address: kmiyamoto@bio.keio.ac.jp (K. Miyamoto).

0040-4039/$ - see front matter Crown Copyright © 2013 Published by Elsevier Ltd. All rights reserved.
http://dx.doi.org/10.1016/j.tetlet.2013.01.080

pH between 6 and 9 and temperature between 50 and 70 °C had no influence on the ee of the product. Nevertheless, the optical purity of **5a** was increased to 48% ee when His-tag purified enzyme was employed in the reaction. In addition, no decarboxylation of **2a** occurred without Est0071 (data not shown). These observations led us to assume that cleavage of the carboxyl group might take place at the active site of Est0071. Accordingly, the chiral environment of the active site induces stereoselective decarboxylation. As both steps occur in an enantioselective manner, the reaction is a one-enzyme three-step domino reaction (see Fig. 1).

To obtain a better understanding of the reaction mechanisms, several of the compounds considered to be intermediates were subjected to reaction with Est0071. We considered two possible reaction courses (Fig. 2). In the first pathway shown as Path A, a half-ester is first hydrolyzed to prochiral phenylmalonic acid (**6a**). Diacid (**6a**) is then decarboxylated to the corresponding monoacid (**5a**). In this pathway, decarboxylation of malonic acid is the selectivity-determining step. To confirm this assumption, we incubated phenylmalonate with Est0071 at 70 °C. We found that decarboxylation proceeded with or without esterase at almost the same rate, and that both products (**5a**) were racemic. Moreover, it is known that the esterase-catalyzed hydrolysis of the second ester of malonic acid esters is slow. Based on these observations, a reaction via a prochiral dicarboxylic acid intermediate is unlikely. In the second proposed pathway (Path B), decarboxylation of the half-ester (**2a**) is followed by hydrolysis. In this pathway, a monoester (**2a**) is decarboxylated to an optically active ester **4a**. The esterase then hydrolyzes **4a** to the corresponding acid (**5a**). In order to test this possibility, the reaction intermediate was analyzed. In the beginning of the reaction, the diester disappeared immediately, and the half ester (**2a**) generated. After that, the carboxylic acid (**5a**) was formed gradually. Next, both (*R*)-**4a** and (*S*)-**4a** were subjected to the reaction. We found that the hydrolysis rates of both enantiomers were nearly identical. If Path B is correct, the decarboxylation product must be an optically active ester. However, the ester (**4a**) could not be isolated because the ester hydrolysis rate was faster than that of decarboxylation. Therefore, the decarboxylation is a rate-determining step. Adding the racemic monoester (**2a**) as a substrate to the reaction led to the formation of optically enriched (*S*)-**5a** (45% ee). Selectivity was almost the same as the reaction using the optically active half-ester (48% ee).

These results indicated that the intermediate of the domino reaction should be planar (**3**). After hydrolysis forms the (*S*)-enantiomer of the monoester (**2a**), decarboxylation is stereoselective or at least preserves the absolute configuration to some extent. Accordingly, protonation occurs mainly from one side of the planar enolate intermediate. This mechanism strongly resembles that of arylmalonate decarboxylase, which catalyzes the enantioselective

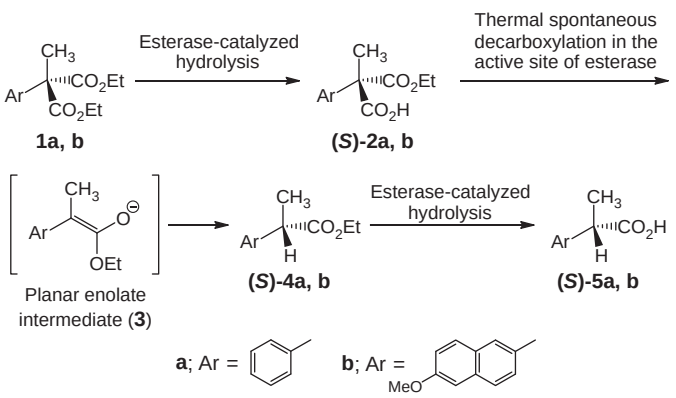

Figure 1. Esterase-catalyzed asymmetric domino reaction.

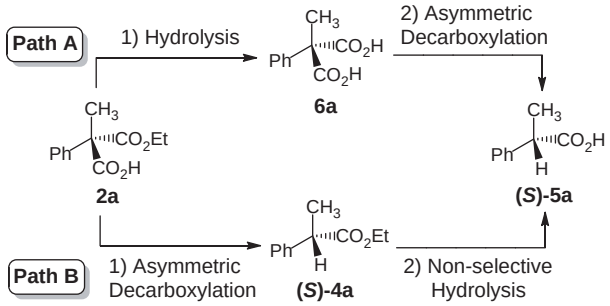

Figure 2. Two possible reaction courses.

decarboxylation of malonate (**6a**) and proceeds via a prochiral intermediate.[7–9] In this two-step reaction, the formation of the enolate is the rate determining step, and the direction of the addition of the proton decides the absolute configuration of the product. It is also important to note that the optically active ester (**4a**) is hydrolyzed to the corresponding acid in a non-selective manner. Interestingly, the esterase-catalyzed reaction forms (*S*)-enantiomers, while arylmalonate decarboxylase is (*R*)-specific.

These findings encouraged us to increase the stereoselectivity of the domino reaction by protein engineering. Directed evolution efficiently improves the enantioselectivity of esterases.[10] Unfortunately, no high-throughput assay for determining the optical purity of **5** was available. It is rather difficult to predict the amino acid substitutions for rational engineering of stereoselectivity because the exact role of active-site amino acids in the decarboxylation mechanism remains unknown. Therefore, we chose a semi-rational approach. A combination of structural considerations for generating small, high-quality libraries has been shown to be effective for improving esterases.[10] A homology model of Est0071 based

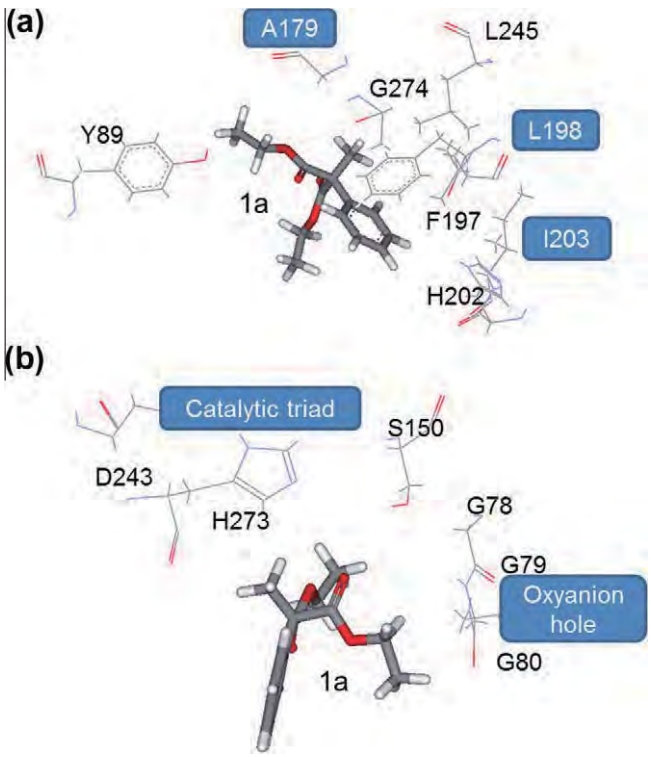

Figure 3. (a) Residues of the active site pocket of Est0071 with potential impact on the conversion of phenylmalonate diethyl ester (**1a**); (b) catalytic triad (D243, H273 and S150) and oxyanion hole (G78, G78, and G80) of Est0071.

Table 1
Enantioselectivity of Est0071 and its variants[a]

Variant	Conversion (%)	ee[b] (%)	Configuration
A179M/L198Y	37	80	*S*
A179M/L198E	43	77	*S*
I203R	5	74	*S*
A179K	56	70	*S*
I203E	15	67	*S*
A179M/L198S	35	66	*S*
Wild-type	85	48	*S*

[a] Reaction conditions: pH 7, 70 °C, 48 h.
[b] The ee values were determined by chiral-phase HPLC.

Table 2
Asymmetric synthesis of naproxen (**5b**)[a]

Variant	Conversion (%)	ee (%)	Configuration
A179K	>99	64	*S*
I203R	>99	63	*S*
I203E	>99	52	*S*
A179M/198Y	>99	31	*S*
A179M/198E	>99	18	*S*
Wild-type	>99	21	*S*

[a] Reaction conditions: pH 7, 70 °C, 48 h.

on the X-ray structure of an esterase from *Archaeoglobus fulgidus* (PDB 1JJI) was the basis for the identification of three amino acid residues around the substrate binding site (Fig. 3).

Residues 179, 198, and 203 are situated in close proximity to the catalytic triad. These positions were simultaneously altered by mutagenic polymerase chain reaction with primers bearing the NNK codon. A library of 200 clones was constructed. The number of clones was not sufficient for full coverage, but helped to ensure the potential impact of the residues on the outcome of decarboxylation. All clones were expressed in *Escherichia coli* and purified by His-tag affinity chromatography. After purification, all variants were active in the hydrolysis of *p*-nitrophenyl butyrate at room temperature. In the domino reaction at 70 °C, 69 variants showed activity. Using these positive mutants, we next confirmed the stereoselectivity of the domino reaction by HPLC [12].

All variants showed (*S*)-selectivity. Interestingly, 6 variants showed increased stereoselectivity compared to the wild-type enzyme (Table 1). The best variants (A179 M/L198Y) showed 80% ee, at conversions around 37%. The variants with improved selectivity had hydrophobic residues such as leucine replaced with polar arginine, serine, glutamate, or lysine.

The enantioselective domino reaction was applied to the synthesis of (*S*)-naproxen (**5b**). The conversion of **1b** was much faster than that of **1a**. This can be explained by the higher stability of the putative prochiral intermediate, based on better delocalization of the charge on the naphthyl ring system. The effects of the amino acid substitutions differed remarkably from the findings using **1a** as the substrate. Variant A179 M/L198Y, which produced **5a** with 80% ee, catalyzed the formation of **5b** with 31% ee. In contrast, A179 K gave rise to (*S*)-**5b** with good optical purity (64% ee).

We developed the first enzymatic domino reaction for the synthesis of optically active (*S*)-profens. A mechanistic analysis of the reaction showed that it proceeds via enantioselective hydrolysis of the malonic acid ester to the monoester. Cleavage of the carboxyl group at the active site of the enzyme leads to the formation of the prochiral intermediate, which is then protonated to give the enantioenriched monoacid. Engineering of the active site gave rise to a variant with good stereoselectivity. As the esterase-catalyzed domino reaction does not need external cofactors and allows a theoretical yield of 100%, it offers clear advantages over alternative enzymatic routes.[11] The esterase-catalyzed domino reaction is thus an important step on the road toward the sustainable synthesis of optically active profens.

References and notes

1. Poliakoff, M.; Licence, P. *Nature* **2007**, *450*, 810–812.
2. Burda, E.; Hummel, W.; Gröger, H. *Angew. Chem., Int. Ed.* **2008**, *47*, 9551–9554.
3. Akai, S.; Tanimoto, K.; Kita, Y. *Angew. Chem., Int. Ed.* **2004**, *43*, 1407–1410.
4. (a) Suzuki, Y.; Miyamoto, K.; Ohta, H. *FEMS Microbiol. Lett.* **2004**, *236*, 97–102; Esterase (Est0071) is commercially available from Enzymicals AG (Germany), http://www.enzymicals.com/.
5. Kourist, R.; Bornscheuer, U. T. *Appl. Microbiol. Biotechnol.* **2011**, *191*, 505–517.
6. Domínguez de María, P.; García-Burgos, C. A.; Bargeman, G.; van Gemert, R. W. *Synthesis* **2007**, *10*, 1439–1452.
7. Miyamoto, K.; Ohta, H. *J. Am. Chem. Soc.* **1990**, *112*, 4077–4078.
8. Miyamoto, K.; Tsuchiya, S.; Ohta, H. *J. Am. Chem. Soc.* **1992**, *114*, 6256–6257.
9. Ijima, Y.; Matoishi, K.; Terao, Y.; Doi, N.; Yanagawa, H.; Ohta, H. *Chem. Commun.* **2005**, 877–879.
10. Kourist, R.; Jochens, H.; Bartsch, S.; Kuipers, R.; Padhi, S. K.; Gall, M.; Bottcher, D.; Joosten, H. J.; Bornscheuer, U. T. *ChemBioChem* **2010**, *11*, 1635–1643.
11. Kourist, R.; Domínguez de Maria, P.; Miyamoto, K. *Green Chem.* **2011**, *13*, 2607–2618.
12. *Typical procedure:* Two hundred microliters of 50 mM substrate (**1a** or **1b**) solution in CH_3CN was added to 4 ml of 400 mM HEPES–NaOH buffer (pH 7). To the resulting solution, 1 ml of Est007 solution (25 μg/ml) was added and the mixture was stirred for 48 h at 70 °C. The reaction was stopped by addition of 2 ml of 2 M HCl. The products were extracted with 5 ml diisopropyl ether. The organic layer (4 ml) was concentrated in vacuo, and to this was added 400 μl diisopropyl ether, 100 μl methanol, and an excess amount of Me_3SiMeN_2 in hexane. The solution was vortexed and allowed to stand at room temperature for 30 min. Enatiomeric excess of methyl ester of **5a** and **5b** was determined by HPLC analysis using CHRALCEL OJ (Daicel Corporation, Japan). To determine the conversion rate, 500 μl of the reaction mixture was transferred to the tube, and the reaction was stopped by addition of 200 μl of CH_3CN containing 2% CF_3CO_2H. The products were extracted with EtOAc which contains diethyl phthalate as an internal standard. The conversion rate of the products was determined by reverse phase HPLC using COSMOSIL 5C18-PAQ (Nakarai Tesque, Inc., Japan).

DOI: 10.1002/asia.201301248

Enantioselective Total Synthesis of Pinnaic Acid and Halichlorine

Shu Xu,[a] Daisuke Unabara,[a] Daisuke Uemura,[b] and Hirokazu Arimoto*[a]

Abstract: The enantioselective total synthesis of the bioactive marine natural products pinnaic acid and halichlorine is reported in detail. Our total synthesis features the construction of the five-membered ring and C9 and C13 stereogenic centers through a palladium-catalyzed trimethylenemethane [3+2] cyclization; the installation of the nitrogen atom through a regioselective Beckmann rearrangement of a poorly reactive ketone; the stereoselective cyclization of the spiro ring through a four-step, one-pot hydrogenation–cyclization; and efficient connection of the sterically hindered lower chain through a reduced-pressure cross olefin metathesis reaction.

Keywords: cyclization · metathesis · natural products · stereoselectivity · total synthesis

Introduction

In 1996, one of us reported the isolation of a novel class of marine natural products represented by pinnaic acid (**1**)[1] and halichlorine (**2**).[2] Compound **1** was obtained from the Okinawan bivalve *Pinna muricata*. It inhibits a cytosolic 85 kDa phospholipase ($cPLA_2$)[3] in vitro.[1] Compounds that inhibit $cPLA_2$ have been targeted as anti-inflammatory agents. Compound **2** was obtained from the black marine sponge *Halichondria okadai* Kadota, and shows bioactivity for reducing the induced mRNA expression of adhesion molecules (VCAM-1, ICAM-1, E-selectin)[4] and induced monocyte (U937) adhesion to endothelial cells by attenuating NF-κB activity,[2,5] which may be useful for treating atherosclerosis. Compound **2** also inhibits L-type Ca^{2+} channels in vascular smooth muscle cells, making it promising as an antihypertensive agent.[6]

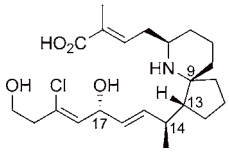

Pinnaic acid (**1**)

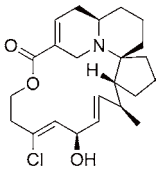

Halichlorine (**2**)

The architectural 6-aza-spiro[4.5]decane structures of these two molecules are even more impressive than their bioactivities. They have attracted considerable attention in the synthetic chemistry community and have been the topic of specific reviews[7] and a large number of synthetic studies.[8] However, significant problems still exist and, since Danishefsky's first total synthesis of both chiral molecules,[9] only two asymmetric total syntheses of **1** from our[10] and Zhao's group,[11] and one asymmetric recent total synthesis of **2** from Clive's group,[12] have been reported. Construction of the contiguous stereogenic centers at C9, C13, and C14 is a challenge, and thus, many reported examples, including the elegant total synthesis by Heathcock and Christie,[13] involved the preparation of only the spiro framework in racemic form. Another significant problem is the addition of the side chains to the spiro core. All of the reported total syntheses suffered low yields for the lower-chain connection and/or poor selectivity in the subsequent C17 stereogenic center installation.[9–13] In fact, none of the formal total syntheses reported to date, attempted this chain connection.[14]

In continuation of earlier reports,[10] we herein disclose our recent efforts, which have culminated in the enantioselective total synthesis of **1** and **2**. Our total synthesis features 1) construction of the five-membered ring and C9 and C13 stereogenic centers through a palladium-catalyzed trimethylenemethane (TMM) [3+2] cyclization; 2) installation of the nitrogen atom through a regioselective Beckmann rearrangement of a poorly reactive ketone by using a modified reaction protocol; 3) stereoselective cyclization of the spiro ring through a one-pot, four-step hydrogenation–cyclization; and 4) efficient connection of the sterically hindered lower chain through a reduced-pressure cross olefin metathesis reaction.

[a] Dr. S. Xu, D. Unabara, Prof. Dr. H. Arimoto
Graduate School of Life Sciences
Tohoku University, 2-1-1 Katahira
Sendai 980-8577 (Japan)
Fax: (+81) 22-217-6204
E-mail: arimoto@biochem.tohoku.ac.jp

[b] Prof. Dr. D. Uemura
Department of Chemistry, Faculty of Science
Kanagawa University, Hiratsuka 259-1293 (Japan)

Supporting information for this article is available on the WWW under http://dx.doi.org/10.1002/asia.201301248.

© 2014 Wiley-VCH Verlag GmbH & Co. KGaA, Weinheim

Results and Discussion

Retrosynthetic Analysis of 1 and 2

Because of the abovementioned difficulty with the installation of the lower chain, we planned to employ olefin metathesis to form the C15=C16 bond. Thus, the C17 center could be preinstalled in the lower-chain fragment with definite stereochemistry. Because **1** and **2** are proposed to be biosynthetically related[15] and share the same structural backbone, the common intermediate **3** was designed and expected to lead to **1** through cross metathesis with the upper-chain unit **4** (A = hydrogen) and chiral lower-chain unit **5** (Scheme 1). By using the same compound **5** and a modified upper-chain unit (A = leaving group), intermediate **3** could also afford tetraene **6**; a precursor designed to provide **2** through a one-pot double ring-closing metathesis (RCM) process.

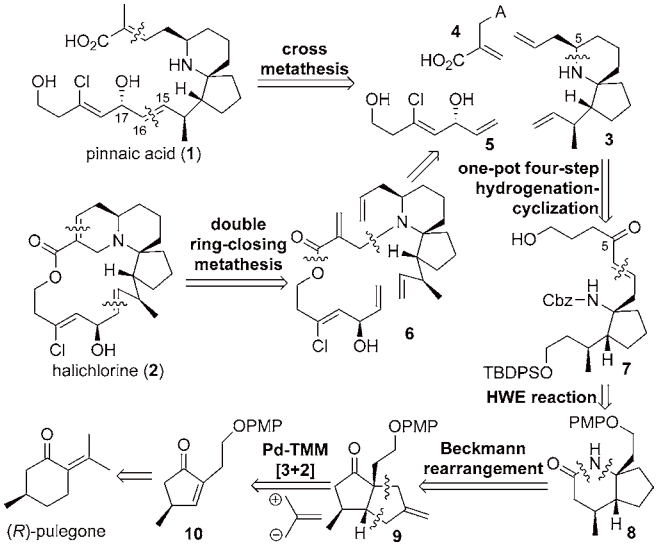

Scheme 1. Retrosynthetic analysis of **1** and **2**. Cbz = carboxybenzyl, TBDPS = *tert*-butyldiphenylsilyl, PMP = *p*-methoxyphenyl.

The spiro core of **3** was expected to be prepared from the unsaturated ketone **7** through a diastereoselective, one-pot, four-step hydrogenation–cyclization developed in our previous synthetic studies.[10c] Intermediate **7** could be formed from compound **8** through a Horner–Wadsworth–Emmons olefination (HWE reaction). The nitrogen atom of **8** would be installed through a regioselective Beckmann rearrangement from the bicyclic ketone **9**, which could be synthesized by Pd-TMM [3+2] cyclization.[16] This cyclization was anticipated to occur from the opposite face of the adjacent methyl group in cyclopentenone **10** to construct the three contiguous stereogenic centers diastereoselectively. The chiral compound **10** could be prepared from commercially available (*R*)-(+)-pulegone.

Preparation of Chiral Building Block 10

From the retrosynthetic analysis, (*S*)-2-alkyl-4-methylcyclopent-2-enone (**10**) was our first target. When this study was initiated, there were no reports on methods for preparation of this type of building block in chiral form.[17] Thus, a short route from (*R*)-(+)-pulegone was designed by using Dieckmann condensation[18] and Tsuji's decarboxylation–dehydrogenation[19] reactions.

Ozonolysis[20] of technical grade (*R*)-pulegone[21] cleanly gave the dicarboxylic acid **11**, which was esterified to afford diallyl ester **12** in 89% yield (2 steps, 40 gram scale, Scheme 2). Our synthesis of **11** is superior to other literature procedures[22] because of the metal-free conditions and easy workup. Dieckmann condensation[18] of **12** with potassium metal as the base gave the mixed enolates **13a** and **13b** (≈2:1), which in situ reacted with the iodide **14** to afford a mixture of **15** and **16**. The combination of the potassium salt and alkyl iodide provided the best *C*- (**15a**, **b**) to *O*-alkylation (**16a**, **b**) ratio (≈9:1), as expected based on hard and soft acids and bases (HSAB) theory.[23] Because the byproducts **16a** and **16b** interrupted the subsequent palladium-catalyzed reaction and were difficult to separate from compounds **15a** and **15b**, hydrolysis was employed to transform them into the corresponding protonated compounds **13a** and **13b**. The hydrolyzed mixture was then subjected to Tsuji decarboxylation–dehydrogenation,[19] which afforded compound **10** in 49% yield (3 steps, 20 gram scale), together with isolated byproduct **17** derived from **13b**. The yield of this decarboxylation–dehydrogenation was largely depen-

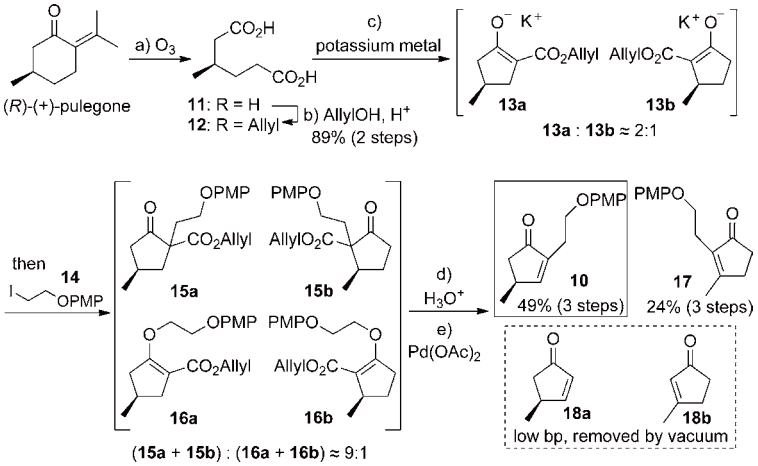

Scheme 2. Synthesis of the chiral building block **10**: a) O_3, 0 °C, HOAc, H_2O, EtOAc; b) AllylOH, H_2SO_4 (cat.), Dean–Stark, reflux, 89% (2 steps); c) K, AllylOH, PhMe, reflux; then **14**, reflux; d) HCl (aq), acetone, RT; e) $Pd(OAc)_2$ (5 mol%), MeCN (4 M), 90 °C, 49% (3 steps).

 © 2014 Wiley-VCH Verlag GmbH & Co. KGaA, Weinheim

dent on the concentration; a higher concentration favored a higher conversion and fewer byproducts. However, neat conditions led to a decrease in the yield owing to the difficulty in achieving efficient stirring.

Pd-TMM [3+2] Cyclization

With the chiral building block **10** in hand, we attempted the key Pd-TMM [3+2] cyclization (Scheme 3).[16] As anticipated, compound **10** reacted with the TMM precursor **19** highly selectively, and only the diastereomer **9** was detected (80% yield).[23] The configuration of the C9 and C13 centers was verified by NOE analysis of **9**.

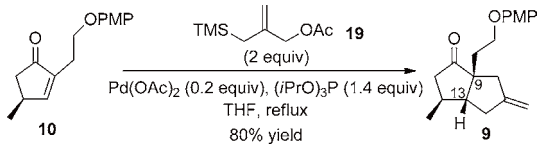

Scheme 3. Key Pd-TMM [3+2] cyclization of compound **10**. THF = tetrahydrofuran, TMS = trimethylsilyl.

Beckmann Rearrangement with a Modified MSH Manipulation

For installation of the nitrogen atom, the Schmidt reaction[24] and Beckmann rearrangement[25] were tested with substrate **9** (Table 1). Schmidt conditions (Table 1, entry 1) led to a complex mixture. The standard two-step Beckmann procedure with NH_2OH[25a] (Table 1, entry 2) proceeded well, but only with 3:1 regioselectivity, presumably owing to weak stereocontrol during formation of the oxime. Thus, a hindered nitrogen reagent, MSH,[25b,c] was tested (Table 1, entries 3–7). As expected, only the desired isomer **20** was detected. However, the conversion of the reaction was never clean and sometimes not reproducible. Although larger amounts of MSH did provide higher conversion, the enhancement of the yield was limited. A literature screen revealed that all reported MSH–Beckmann rearrangements employed highly reactive substrates (sterically unhindered ketones or strained cyclobutanones), and the solution of MSH/dichloromethane was added to the solution of the ketone substrate. However, we observed that MSH rapidly self-decomposed in dichloromethane at room temperature particularly at high concentrations, and sometimes the solution refluxed on its own.[26] This self-decomposition may compete with the formation of the desired oxime when using hindered low-reactive substrates. Thus, to avoid decomposition of MSH, the experimental procedure was modified to involve the direct addition of solid MSH to the solution of ketone **9** (Table 1, entry 7). Gratifyingly, this approach led to clean, full, and reproducible conversion of **9** to **20** in 85% yield on a 5 gram scale.

Table 1. Nitrogen atom installation in compound **9**.[a]

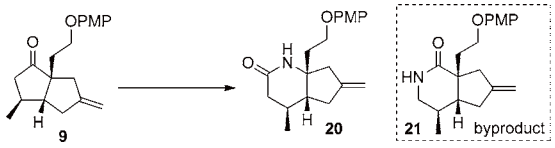

Entry	Conditions	Results[b]
1	NaN_3 (5.0 equiv), $MeSO_3H$, $MeOCH_2CH_2OMe$, RT	complex mixture
2	i) $NH_2OH{\cdot}HCl$ (5 equiv), DABCO (1.1 equiv), MeOH, RT ii) TsCl (1.2 equiv), NaOH (aq), acetone, reflux	84% in 2 steps (**20**/**21**=3:1)
3	MSH (1.0 equiv), CH_2Cl_2, RT; then silica gel	**20** (35%), **9** (50%)
4	MSH (1.5 equiv), MS 4Å, alumina, CH_2Cl_2, RT	**20** (43%), **9** (57%)
5	MSH (5.0 equiv), CH_2Cl_2, RT; then silica gel	**20** (60%), **9** (1%)
6	MSH (10.0 equiv), CH_2Cl_2, RT; then silica gel	**20** (63%), **9** (0%)
7	MSH (1.5 equiv, solid), CH_2Cl_2, RT; then silica gel	**20** (85%), **9** (0%)

[a] DABCO = 1,4-diazabicyclo[2.2.2]octane, Ts = *p*-toluenesulfonyl, MSH = *O*-mesitylenesulfonylhydroxylamine, MS 4Å = 4 Å molecular sieves. [b] Yield of isolated product.

Preparation of 28 and Subsequent One-Pot, Four-Step Hydrogenation–Cyclization

For the synthesis of the spiro core, cleavage of the *exo*-olefin bond was required (Table 2). Ozonolysis of compound **20** smoothly afforded ketone **22**. However, the next deoxygenation reaction proved to be troublesome. The thioacetal–Raney nickel method (Table 2, entry 1) led to partial removal of PMP (plausibly through benzene-ring hydrogenation and hydrolysis). The NH_2NHTs–$NaBH_4$ method[27] (Table 2, entry 2) decomposed the lactam ring. The NH_2NHTs–$NaBH_3CN$ method[28] (Table 2, entry 3) only gave a modest yield. Although the Yamamura-modified Clemmensen reduction[29] (Table 2, entry 4) worked well, it was not reproducible on a larger scale owing to the poor solubility of **22** in Et_2O. Finally, the use of a combination of TMSCl and H_2O in THF afforded a reproducibly good result on the gram scale (Table 2, entry 5). Notably, Yamamura et al. reported that a solution of HCl in THF was not suitable for this transformation.[29b] Based on these results, we also developed a one-pot ozonolysis–Clemmensen reduction process[30] that provided **8** directly from **20** in 72% yield.

Protection of **8** with Cbz led to compound **24** (Scheme 4). The next reductive ring opening was first attempted with $NaBH_4$,[31] which proceeded well, but was contaminated with a small amount of solvolyzed byproduct.[23] Thus, $LiBH_4$ in the aprotic solvent THF was tested, which yielded **25** quantitatively. Next, protection with TBDPS, removal of PMP, Parikh–Doering oxidation, and the HWE reaction with **27** afforded spiro-cyclization precursor **28** as the single *trans* isomer.[32]

Our one-pot hydrogenation–cyclization[10] is a powerful protocol for constructing the piperidine ring of **1** and **2** with the desired C5 configuration (Scheme 4). It consists of four

 © 2014 Wiley-VCH Verlag GmbH & Co. KGaA, Weinheim

Table 2. Cleavage of the *exo*-olefin bond of **20**.

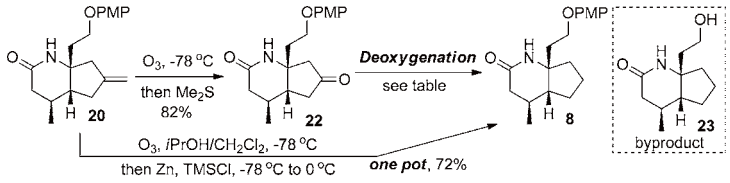

Entry	Conditions	Results[a] ([%])
1	i) $HSCH_2CH_2SH$, $TiCl_4$, −15 °C, CH_2Cl_2; ii) Raney nickel, EtOH, reflux	**8** (35), **23** (17)
2	i) NH_2NHTs, MeOH, reflux; ii) $NaBH_4$, MeOH, reflux	decomposed
3	i) NH_2NHTs, MeOH, reflux; ii) $NaBH_3CN$, TsOH, THF, reflux	**8** (60)
4	activated Zn, HCl (sat. in Et_2O), 0 °C	**8** (80), low reproducibility
5	Zn, TMSCl-H_2O (5:2), THF, 5 °C	**8** (86), reproducible on gram scale

[a] Yield of isolated product. For two-step procedures, the yield is the overall yield.

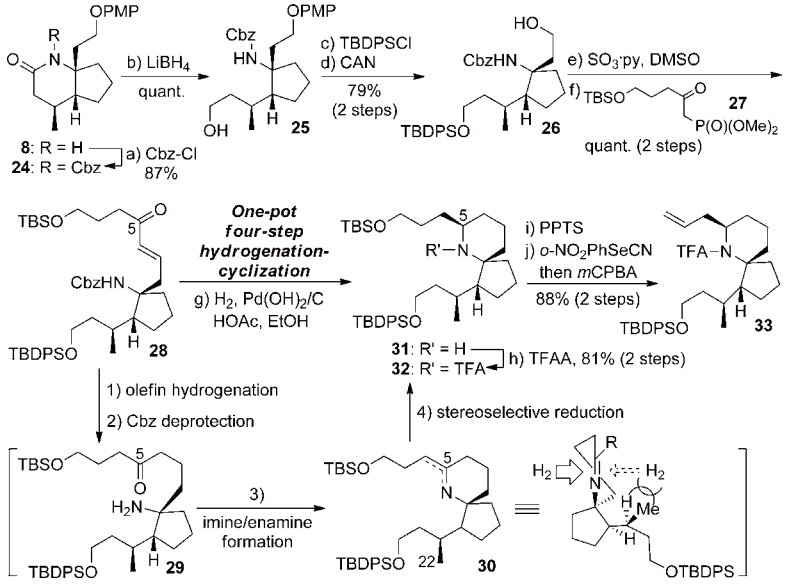

Scheme 4. Preparation of the spiro core: a) NaH, CbzCl, THF, reflux, 87%; b) $NaBH_4$, LiBr, THF, 50 °C, quant.; c) TBDPSCl, DMAP, Et_3N, CH_2Cl_2, RT; d) CAN, MeCN, H_2O, 0 °C, 79% (2 steps); e) SO_3·py, Et_3N, DMSO, RT; f) **27**, Et_3N, LiCl, THF, 30 °C, quant. (2 steps); g) H_2, $Pd(OH)_2/C$ (20 mol%), HOAc (2 equiv), EtOH, 25 °C; h) TFAA, iPr_2NEt, CH_2Cl_2, 0 °C, 81% (2 steps); i) PPTS, EtOH, 25 °C; j) *o*-$NO_2PhSeCN$, nBu_3P, THF, RT; then *m*CPBA, RT, 88% (2 steps). CAN = $(NH_4)_2Ce(NO_3)_6$, DMAP = 4-dimethylaminopyridine, py = pyridine, DMSO = dimethylsulfoxide, TBS = *tert*-butyldimethylsilyl, TFAA = trifluoroacetic anhydride, TFA = trifluroacetyl, PPTS = pyridium *p*-toluenesulfonate, *m*CPBA = *m*-chloroperbenzoic acid.

consecutive transformations: 1) saturation of the olefin, 2) removal of the Cbz group, 3) intramolecular cyclic imine and/or enamine formation, and 4) stereoselective reduction of the imine/enamine intermediate. The stereoconformation of **30** clearly demonstrated that attack from the right side (which is also the β face of **30**) would be disfavored because of steric hindrance of the C22 methyl group. Similar reductive cyclizations have since then also been conducted by others.[11,13] In our earlier studies,[10b–d] when this reaction was carried out under neutral or acidic conditions with a catalytic amount of HOAc,[33] typically 50 mol% of palladium catalyst was required to obtain reproducible results. Careful examination of the reaction conditions revealed that the basic amino group of product **31** seemed to be the reason for the high catalyst loading; it may deter the Cbz hydrogenolysis step.[34] Thus, when excess HOAc was used, only 20 mol% of the palladium catalyst was sufficient to cleanly and reproducibly afford the desired diastereomer **31**. Next, TFA protection of the amino group, selective removal of TBS,[35] and Grieco elimination[36] led to terminal olefin **33**, which exhibited NOE correlations that confirmed the desired stereochemistry at C5.

Synthesis of the Lower-Chain Fragment

As mentioned in the Introduction, the stereoselective construction of the C17 center is difficult during or after installation of the lower chain. Therefore, we decided to construct the C17 stereogenic center in the lower-chain fragment before the coupling reaction. After failed attempts with Sharpless desymmetrization and Brown asymmetric allylation,[23] the Corey–Bakshi–Shibata (CBS) method[37] became our method of choice (Scheme 5). Prechiral ketone **36** was readily prepared from butynol **34** through TBDPS protection, addition to acrolein,[38] and IBX oxidation.[39] For the asymmetric reduction, the commercially available (*R*)-Me-CBS chiral catalyst was used. After initially suffering from low reproducibility, a procedure involving the slow addition of 0.6 equivalents of $Me_2S{\cdot}BH_3$ in THF to a premixed solution of **36** and 0.1 equivalents of Me–CBS in THF ensured an acceptable yield with 90% *ee*. Notably, Noyori asymmetric transfer hydrogenation[40] gave no reaction with substrate **36**. To the best of our knowledge, our result was the first example of the catalytic asymmetric reduction of an alkenyl–alkynyl–ketone substrate. Next, installation of chlorine by using the Red-Al/NCS method provided the chiral C15–C21 fragment **37a** in a total of just five steps from inexpensive, commercially available starting materials. The enantiomeric excess (*ee*) of **37a** was confirmed again to ensure that no racemization occurred during

 © 2014 Wiley-VCH Verlag GmbH & Co. KGaA, Weinheim

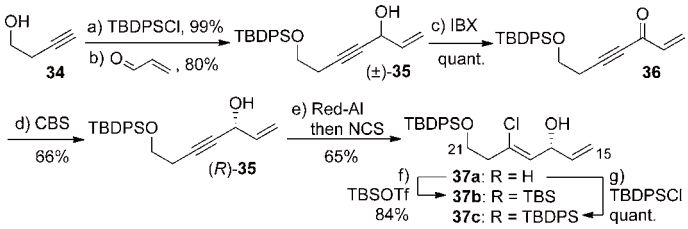

Scheme 5. Preparation of the lower-chain fragment through CBS asymmetric reduction: a) TBDPSCl, Et_3N, DMAP, CH_2Cl_2, RT, 99%; b) *n*BuLi, LiBr, THF, RT; then acrolein, −78°C, 80% (95% brsm); c) IBX, EtOAc, reflux, quant.; d) (*R*)-Me-CBS (0.1 equiv), $BH_3{\cdot}Me_2S$ (0.6 equiv), THF, −40°C, 66% (90% *ee*); e) Red-Al, THF, RT; then NCS, −78°C, 65% (90% *ee*); f) TBSOTf, Et_3N, CH_2Cl_2, RT, 84%; g) TBDPSCl, Et_3N, DMAP, CH_2Cl_2, RT, quant. CBS = Corey–Bakshi–Shibata catalyst, brsm = based on recovered starting material, IBX = 2-iodoxybenzoic acid, Red-Al = sodium bis(2-methoxyethoxy) aluminum hydride, NCS = *N*-chlorosuccinimide, Tf = trifluoromethanesulfonyl.

the chlorination step. Protection of **37a** with TBS and TBDPS afforded **37b** and **37c**, respectively.

Cross Olefin Metathesis for the Total Synthesis of 1

For the synthesis of **1**, the upper chain was connected to compound **33** through a cross olefin metathesis reaction (Scheme 6). With the less reactive counterpart, **38**, as the solvent and 8 mol% Hoveyda–Grubbs II catalyst,[41] 81% yield of olefin **41** was obtained exclusively in the desired *E* configuration, together with 5% yield of homodimer **42**. With the Grubbs II catalyst,[42] phenyl-substituted byproduct **43** was also detected. When isolated **42** and **43** were subjected again to the above metathesis conditions, they reached an equilibrium with **41**, but we did not pursue this approach for preparative purposes. Removal of TBDPS and Grieco elimination generated the terminal olefin **44**.

The cross metathesis of **44** was tested with the lower-chain units **37a–c** (Table 3). Four carbon–carbon double bonds exist in the substrates. The two tri-substituted double bonds were expected[43] and proved to be inert under the tested conditions. However, the monosubstituted olefin in compound **44** showed unexpected lower reactivity than that in lower-chain unit **37**. The group of Grubbs summarized experience-based rules for the cross olefin metathesis.[43] They categorized olefin substrates into four types with different reactivity and predicted the products and reaction difficulty according to the "types" of the substrates. Thus, according to Grubbs' theory, the terminal olefin in compound **44** should be a "Type I substrate" (the most reactive category, fast homodimerization), and the secondary allylic alcohols **37** (protected and unprotected) should be "Type II substrates" (less reactive, slow homodimerization). However, under all of our tested conditions, the dimer of **44** was never detected and the dimer of TBS-protected **37b** always appeared in considerable quantities (the free alcohol **37a** decomposed under the reaction condition, entry 1). Thus, substrate **44** is less reactive than **37b** for cross metathesis and should belong to Grubbs' "Type III substrate" (least reactive, no homodimerization). The low reactivity of **44** is thought to be due to high steric hindrance from the nearby spiro core. It is well known that for cross metathesis between Type II and Type III olefins, a large excess of the Type III olefin is required to suppress the competing dimerization of Type II olefins.[43] However, this approach was not feasible for our substrates because Type III olefin **44** is much more precious than the readily prepared lower-chain unit **37**. Therefore, as shown in Table 3, entries 2–4, even

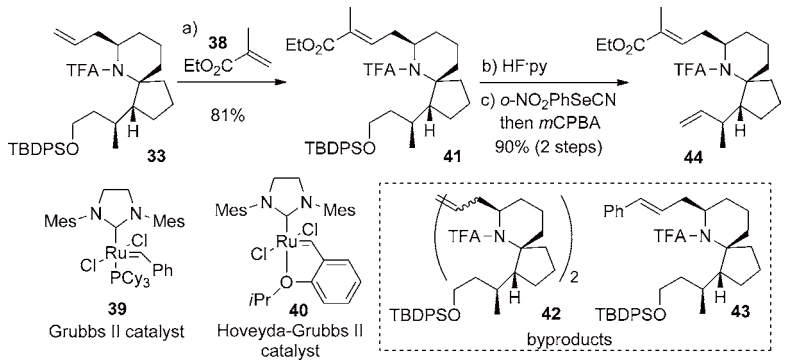

Scheme 6. Cross metathesis installation of the upper chain and preparation of **44**: a) **40** (8 mol%), **38**/toluene (1:1), 100°C, 81%; b) $HF{\cdot}(py)_x$, py, 45°C; c) *o*-NO_2PhSeCN, nBu_3P, THF, RT; then *m*CPBA, RT, 90% (2 steps). Mes = mesityl, Cy = cyclohexyl.

Table 3. Cross metathesis installation of the lower chain of **1**.

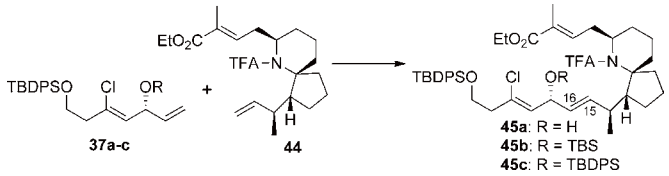

Entry	**37** ([equiv])	Cat. ([mol%])	Conditions	Results ([%])[a]
1	**37a** (6.2)	**39** (20)	PhMe, 90°C, 6 h	**45a** (0), **44** (90)
2	**37b** (6.8)	**40** (20)	neat, 90°C, 12 h	**45b** (7), **44** (80)
3	**37b** (4.0)	**39** (50)	neat, 90°C, 6 h	**45b** (20), **44** (70)
4	**37b** (5.5)	**39** (80)	PhMe, 90°C, 24 h	**45b** (40), **44** (42)
5	**37c** (5.0)	**39** (44)	neat, 90°C, 10 h	**45c** (5), **44** (90)
6	**37c** (5.0)	**39** (29)	neat, 90°C, 20 mmHg, 6.5 h	**45c** (100), **44** (0)
7	**37c** (6.0)	**39** (50)	$C_6H_3Cl_3$,[b] 90°C, 20 mmHg, 22 h	**45c** (69), **44** (0)

[a] Yield of isolated product. [b] 1,2,4-Triclorobenzene, which is a high-boiling-point solvent (215°C, 1 atm).

 © 2014 Wiley-VCH Verlag GmbH & Co. KGaA, Weinheim

when excess **37b** was used, the conversion of **44** was low and 80 mol% of catalyst had to be employed to afford a moderate yield, as reported in our preliminary communication (Table 3, entry 4).[10a]

To avoid undesired homodimerization, the cross metathesis using TBDPS-protected **37c** was attempted (Table 3, entries 5–7). Compound **37c** is bulkier around the olefin than TBS-protected **37b**. As expected, it showed lower metathesis reactivity and only tiny amounts of its dimer could be detected. However, owing to the low reactivity of both **37c** and **44**, the conversion of the reaction remained low (Table 3, entry 5). Thus, forcing conditions were applied with reduced pressure for removal of the in situ generated ethylene and styrene (Table 3, entries 6 and 7). To our delight, under these conditions, full conversion was achieved, and the fully protected pinnaic acid **45c** was obtained in quantitative yield under neat conditions (Table 3, entry 6). The use of high vacuum was reported originally by the group of Grubbs for the dimerization of unhindered terminal olefins[44a] and recently by the groups of Schrock[44b] and Grubbs[44c] to achieve *cis*-selective metathesis. It should be noted that under all of the conditions tested for our substrates, only the desired *trans* isomer (C15=C16 bond) of **45** was formed.

Deprotection of **45c** successively with HF·py (2× TBDPS), $NaBH_4$ (TFA amide), and basic hydrolysis (ethyl ester), afforded chiral **1** in its sodium salt form (66%, 2 steps, Scheme 7), which was identical to the synthetic racemic sodium salt of **1**[13] based on a comparison of the ^{1}H NMR spectra.

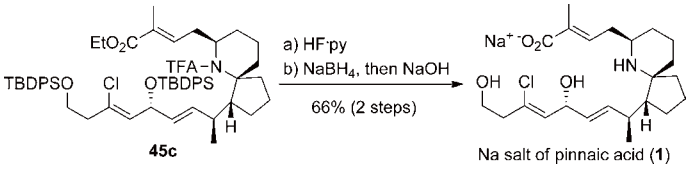

Scheme 7. Synthesis of **1** by deprotection of **45c**: a) HF·(py)$_x$, py, 25°C; b) $NaBH_4$, EtOH, 25°C; then NaOH (aq), 25°C to 40°C, 66% (2 steps).

Macrocyclic RCM toward 2

In Scheme 1, tetraene **6** was designed as the precursor for **2** through two RCMs: a six-membered RCM and a macrocyclic RCM. Because the lower-chain metathesis showed lower reactivity than the upper-chain reaction in the total synthesis of **1**, it was expected that the two RCMs could be achieved in one pot. Thus, the six-membered RCM in the presence of C15=C16 terminal olefin was first explored by using model compound **48** (Scheme 8), which was readily prepared from **32** through double silyl deprotection, double Grieco elimination, removal of TFA, and alkylation with the upper-chain unit **47**. The RCM of **48** was tested with Hoveyda–Grubbs II catalyst **40** (10 mol%, 60°C in toluene, similar conditions to those used by the Kibayashi group[14a]). However, the desired product **49** was not detected at all and compound **48** was fully converted into the C3=C15 RCM product **50**. This

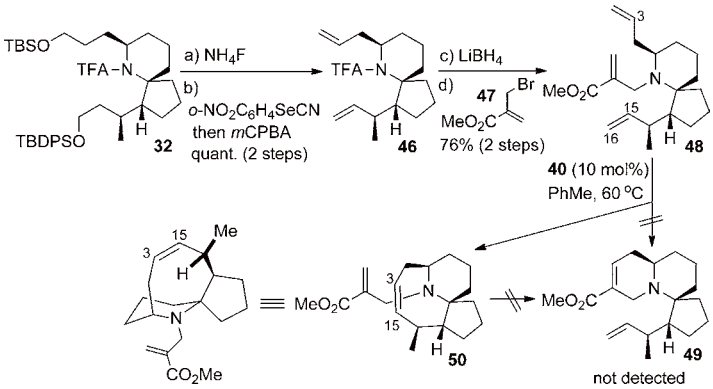

Scheme 8. Preparation of compound **48** and its RCM: a) NH_4F, MeOH, 60°C; b) *o*-$NO_2PhSeCN$, nBu_3P, THF, RT; then *m*CPBA, RT, quant. (2 steps); c) $LiBH_4$, THF, 50°C; d) **47**, K_2CO_3, MeCN, 80°C, 76% (2 steps).

unexpected cyclization is thought to occur because of the spatially neighboring C3 and C15 centers protruding from the spiro core. All attempts to transform **48** or **50** into the desired **49** by using a variety of metathesis conditions failed. Therefore, we changed our idea from the one-pot RCM strategy to a stepwise RCM strategy.

The stepwise RCM strategy commenced with compound **33** (Scheme 9), which smoothly afforded compound **53** after removal of TFA, alkylation with bromide **51**, and six-membered RCM. Next, removal of TBDPS, Grieco elimination, acidic hydrolysis of the *tert*-butyl ester, and condensation with lower-chain unit **54** by using the Shiina reagent[45] provided the macrocyclic RCM precursor **55**. However, precursor **55** proved to be inert to metathesis conditions,[23] and surprisingly, contrary to our experience in the study of the cross metathesis of **1**, the TBS-protected lower chain was less reactive than the C15 olefin. It is well known that free amino groups usually inhibit metathesis through coordination to the ruthenium atom in the catalyst.[46] However, with substrates **48** and **52**, metathesis did occur in the presence of tertiary amines. Thus, it was reasoned that, for substrate **55**,

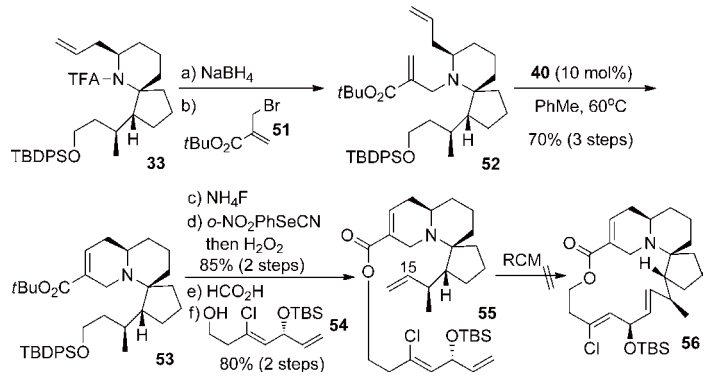

Scheme 9. Preparation of compound **55** and its RCM: a) $NaBH_4$, EtOH, RT; b) **51**, K_2CO_3, MeCN, 90°C; c) NH_4F, MeOH, 60°C; d) *o*-$NO_2PhSeCN$, nBu_3P, THF, RT; then H_2O_2, RT, 85% (2 steps); e) HCO_2H, RT; f) **54**, MNBA, DMAP, RT, CH_2Cl_2, 80% (2 steps). MNBA = 2-methyl-6-nitrobenzoic anhydride.

 © 2014 Wiley-VCH Verlag GmbH & Co. KGaA, Weinheim

coordination of both the decalin nitrogen and C15 olefin to the ruthenium atom might form a stable complex and deactivate the catalyst.

Revised Strategy for the Total Synthesis of 2

Given the above results, we speculated that for the synthesis of **2** the lower-chain metathesis must be carried out with protection of the amino group, and therefore, before the upper-chain RCM reaction. Thus, the retrosynthesis of **2** was revised to macrolactonization, RCM, and alkylation, which led to the key intermediate **58**, possibly prepared by cross metathesis of compounds **37c** and **59** (Scheme 10).

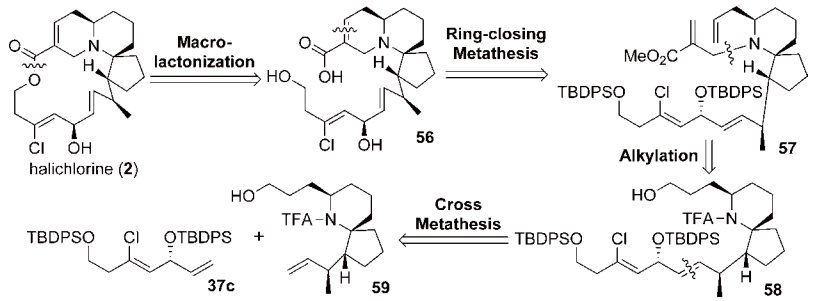

Scheme 10. Revised retrosynthetic analysis of **2**.

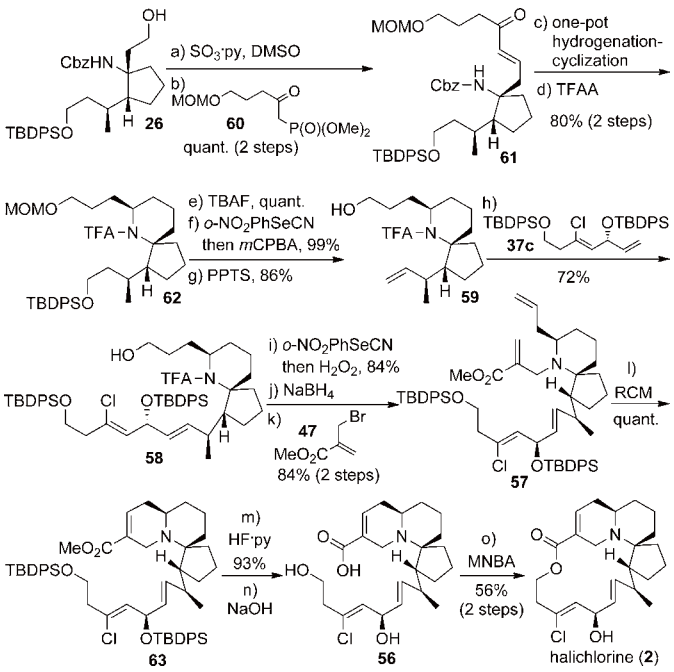

Scheme 11. Total synthesis of **2**: a) SO_3·py, Et_3N, DMSO, RT; b) **60**, Et_3N, LiCl, THF, 30 °C, quant. (2 steps); c) H_2, $Pd(OH)_2/C$ (20 mol %), HOAc (2 equiv), EtOH, RT; d) TFAA, *i*Pr_2NEt, CH_2Cl_2, 0 °C, 80 % (2 steps); e) TBAF, THF, 0 °C, quant.; f) *o*-$NO_2PhSeCN$, *n*Bu_3P, THF, RT; then *m*CPBA, RT, 99 %; g) PPTS, *t*BuOH, 90 °C, 86 %; h) **37c** (4.3 equiv), **40** (28 mol %), PhMe, static vacuum, 60 °C, 72 %; i) *o*-$NO_2PhSeCN$, *n*Bu_3P, THF, RT; then H_2O_2, RT, 84 %; j) $NaBH_4$, EtOH, 30 °C; k) **47**, K_2CO_3, MeCN, 60 °C, 84 % (2 steps); l) **39** (10 mol %), CH_2Cl_2, reflux, quant.; m) HF·$(py)_x$/py (1:3), RT, 93 %; n) NaOH, THF, MeOH, H_2O, 50 °C; o) MNBA, DMAP, THF, RT, 56 % (2 steps). MOM = methoxymethyl, TBAF = tetra-*n*-butylammonium fluoride.

Compound **59** was prepared from the synthetic intermediate **26** (Scheme 11) through a sequence that including a Parikh–Doering oxidation, the HWE reaction with **60** (quantitative, 2 steps), our key one-pot hydrogenation–cyclization, TFA protection (80 %, 2 steps), TBDPS deprotection (quantitative), Grieco elimination (99 %), and MOM deprotection (86 %). The cross metathesis of **59** then proceeded smoothly with the lower-chain unit **37c** under static vacuum conditions[44] to afford compound **58** in 72 % yield. Next, Grieco elimination (84 %), deprotection of TFA, and alkylation with bromo-substituted upper-chain unit **47** (84 %, 2 steps) gave compound **57**. Six-membered RCM of **57** under the conditions reported by Kibayashi et al.[14a] afforded the tricyclic compound **63** (quantitative). Deprotection of the two TBDPS groups (93 %), basic hydrolysis of the methyl ester, and Shiina macrolactonization[45b] (56 %, 2 steps) completed the total synthesis of **2**.

Conclusion

We described the enantioselective total synthesis of **1** and **2** in detail. From a new chiral building block, **10**, the azaspiro core was constructed stereoselectively by using Pd-TMM [3+2] cyclization, a modified MSH–Beckmann rearrangement, and a one-pot four-step hydrogenation–cyclization. The C17 center was preinstalled to the lower-chain fragment through catalytic CBS reduction. The lower-chain connection was achieved effectively through reduced-pressure cross metathesis of sterically hindered olefins. In addition, during our synthetic journey, a TMSCl-modified Yamamura–Clemmensen reduction and its use in a one-pot procedure to cleave olefins to alkanes were also developed.

Experimental Section

The synthetic procedures and characterization of the compounds studied herein can be found in the Supporting Information.

Acknowledgements

We are grateful for the financial support of Grants-in-Aid for Scientific Research (16GS0206 and 16310150) from the JSPS.

[1] T. Chou, M. Kuramoto, Y. Otani, M. Shikano, K. Yazawa, D. Uemura, *Tetrahedron Lett.* **1996**, *37*, 3871–3874.
[2] a) M. Kuramoto, T. Chou, K. Yamada, T. Chiba, Y. Hayashi, D. Uemura, *Tetrahedron Lett.* **1996**, *37*, 3867–3870; b) H. Arimoto, I. Hayakawa, M, Kuramoto, D. Uemura, *Tetrahedron Lett.* **1998**, *39*, 861–862.

 © 2014 Wiley-VCH Verlag GmbH & Co. KGaA, Weinheim

[3] G. Y. Sun, P. B. Shelat, M. B. Jensen, Y. He, A. Y. Sun, A. Simonyi, *NeuroMol. Med.* **2010**, *12*, 133–148.
[4] J. M. Cook-Mills, M. E. Marchese, H. Abdala-Valencia, *Antioxid. Redox Signaling* **2011**, *15*, 1607–1638.
[5] Y. Tsubosaka, T. Murata, K. Yamada, D. Uemura, M. Hori, H. Ozaki, *J. Pharmacol. Sci.* **2010**, *113*, 208–213.
[6] Y. Tsubosaka, T. Murata, K. Kinoshita, K. Yamada, D. Uemura, M. Hori, H. Ozaki, *Eur. J. Pharmacol.* **2010**, *628*, 128–131.
[7] a) D. L. J. Clive, M. Yu, J. Wang, V. S. C. Yeh, S. Kang, *Chem. Rev.* **2005**, *105*, 4483–4514; b) G. Dake, *Tetrahedron* **2006**, *62*, 3467–3492; c) C. Kibayashi, S. Aoyagi, *J. Synth. Org. Chem. Jpn.* **2011**, *69*, 1006–1019.
[8] a) S. P. Keen, S. M. Weinreb, *J. Org. Chem.* **1998**, *63*, 6739–6741; b) M. J. Martín-López, F. Bermejo, *Tetrahedron* **1998**, *54*, 12379–12388; c) S. Lee, Z. Zhao, *Org. Lett.* **1999**, *1*, 681–683; d) S. Lee, Z. Zhao, *Tetrahedron Lett.* **1999**, *40*, 7921–7924; e) J. L. Koviach, C. J. Forsyth, *Tetrahedron Lett.* **1999**, *40*, 8529–8532; f) M. Shindo, Y. Fukuda, K. Shishido, *Tetrahedron Lett.* **2000**, *41*, 929–932; g) D. L. Wright, J. P. Schulte II, M. A. Page, *Org. Lett.* **2000**, *2*, 1847–1850; h) J. D. White, P. R. Blakemore, E. A. Korf, A. F. T. Yokochi, *Org. Lett.* **2001**, *3*, 413–415; i) W. Yokota, M. Shindo, K. Shishido, *Heterocycles* **2001**, *54*, 871–885; j) T. Ito, N. Yamazaki, C. Kibayashi, *Synlett* **2001**, *10*, 1506–1510; k) S. Ciblat, J.-L. Canet, Y. Troin, *Tetrahedron Lett.* **2001**, *42*, 4815–4817; l) K. Takasu, H. Ohsato, M. Ihara, *Org. Lett.* **2003**, *5*, 3017–3020; m) Y. Matsumura, S. Aoyagi, C. Kibayashi, *Org. Lett.* **2003**, *5*, 3249–3252; n) P. B. Hurley, G. R. Dake, *Synlett* **2003**, *14*, 2131–2134; o) G. R. Dake, M. D. B. Fenster, P. B. Hurley, B. O. Patrick, *J. Org. Chem.* **2004**, *69*, 5668–5675; p) L. G. Arini, P. Szeto, D. L. Hughes, R. A. Stockman, *Tetrahedron Lett.* **2004**, *45*, 8371–8374; q) T. Huxford, N. S. Simpkins, *Synlett* **2004**, *13*, 2295–2298; r) K. S. Feldman, A. L. Perkins, K. M. Masters, *J. Org. Chem.* **2004**, *69*, 7928–7932; s) A. L. de Sousa, R. A. Pilli, *Org. Lett.* **2005**, *7*, 1617–1619; t) E. Roulland, A. Chiaroni, H.-P. Husson, *Tetrahedron Lett.* **2005**, *46*, 4065–4068; u) D. G. Hilmey, L. A. Paquette, *Org. Lett.* **2005**, *7*, 2067–2069; v) D. G. Hilmey, J. C. Gallucci, L. A. Paquette, *Tetrahedron* **2005**, *61*, 11000–11009; w) H. Kim, J. H. Seo, K. J. Shin, D. J. Kim, D. Kim, *Heterocycles* **2006**, *70*, 143–146; x) S. H. Yang, V. Caprio, *Synlett* **2007**, 1219–1222; y) P. B. Hurley, G. R. Dake, *J. Org. Chem.* **2008**, *73*, 4131–4138; z) R. J. Bahde, S. D. Rychnovsky, *Org. Lett.* **2008**, *10*, 4017–4020; aa) G. E. Keck, S. A. Heumann, *Org. Lett.* **2008**, *10*, 4783–4786; ab) S. H. Yang, G. R. Clark, V. Caprio, *Org. Biomol. Chem.* **2009**, *7*, 2981–2990; ac) I. D. Jenkins, F. Lacrampe, J. Ripper, L. Alcaraz, P. Van Le, G. Nikolakopoulos, P. A. de Leone, R. H. White, R. J. Quinn, *J. Org. Chem.* **2009**, *74*, 1304–1313; ad) S. M. Amorde, I. T. Jewett, S. F. Martin, *Tetrahedron* **2009**, *65*, 3222–3231; ae) A. C. Flick, M. J. A. Caballero, H. I. Lee, A. Padwa, *J. Org. Chem.* **2010**, *75*, 1992–1996; af) J. J. Sahn, D. L. Comins, *J. Org. Chem.* **2010**, *75*, 6728–6731; ag) J. C. Killen, J. Leonard, V. K. Aggarwal, *Synlett* **2010**, *4*, 579–582; ah) B. Stevenson, W. Lewis, J. Dowden, *Synlett* **2010**, 672–674; ai) F. D. Ferrari, A. J. Ledgard, R. Marquez, *Tetrahedron* **2011**, *67*, 4988–4994; aj) Y. Kurosaki, K. Shirokane, T. Oishi, T. Sato, N. Chida, *Org. Lett.* **2012**, *14*, 2098–2101; ak) A. C. Flick, A. Padwa, *J. Sulfur Chem.* **2013**, *34*, 88–103.
[9] a) D. Trauner, J. B. Schwarz, S. J. Danishefsky, *Angew. Chem.* **1999**, *111*, 3756–3758; *Angew. Chem. Int. Ed.* **1999**, *38*, 3542–3545; b) M. W. Carson, G. Kim, M. F. Hentemann, D. Trauner, S. J. Danishefsky, *Angew. Chem.* **2001**, *113*, 4582–4584; *Angew. Chem. Int. Ed.* **2001**, *40*, 4450–4452; c) M. W. Carson, G. Kim, S. J. Danishefsky, *Angew. Chem.* **2001**, *113*, 4585–4588; *Angew. Chem. Int. Ed.* **2001**, *40*, 4453–4456; d) D. Trauner, S. J. Danishefsky, *Tetrahedron Lett.* **1999**, *40*, 6513–6516; e) D. Trauner, D. G. Churchill, S. J. Danishefsky, *Helv. Chim. Acta* **2000**, *83*, 2344–2351.
[10] a) S. Xu, H. Arimoto, D. Uemura, *Angew. Chem.* **2007**, *119*, 5848–5851; *Angew. Chem. Int. Ed.* **2007**, *46*, 5746–5749; b) I. Hayakawa, H. Arimoto, D. Uemura, *Heterocycles* **2003**, *59*, 441–444; c) H. Arimoto, S. Asano, D. Uemura, *Tetrahedron Lett.* **1999**, *40*, 3583–3586; d) I. Hayakawa, H. Arimoto, D. Uemura, *Chem. Commun.* **2004**, 1222–1223.
[11] a) H. Wu, H. Zhang, G. Zhao, *Tetrahedron* **2007**, *63*, 6454–6461; b) H. L. Zhang, G. Zhao, Y. Ding, B. Wu, *J. Org. Chem.* **2005**, *70*, 4954–4961.
[12] a) D. Z. Liu, H. P. Acharya, M. L. Yu, J. Wang, V. S. C. Yeh, S. Z. Kang, C. Chiruta, S. M. Jachak, D. L. J. Clive, *J. Org. Chem.* **2009**, *74*, 7417–7428; b) D. L. J. Clive, V. S. C. Yeh, *Tetrahedron Lett.* **1999**, *40*, 8503–8507; c) D. L. J. Clive, J. Wang, M. Yu, *Tetrahedron Lett.* **2005**, *46*, 2853–2855; d) M. Yu, D. L. J. Clive, V. S. C. Yeh, S. Kang, J. Wang, *Tetrahedron Lett.* **2004**, *45*, 2879–2881; e) D. L. J. Clive, M. Yu, Z. Li, *Chem. Commun.* **2005**, 906–908.
[13] H. Christie, C. H. Heathcock, *Proc. Natl. Acad. Sci. USA* **2004**, *101*, 12079–12084.
[14] a) Y. Matsumura, S. Aoyagi, C. Kibayashi, *Org. Lett.* **2004**, *6*, 965–968; b) R. B. Andrade, S. F. Martin, *Org. Lett.* **2005**, *7*, 5733–5735; c) Y. Yamamoto, Y. Yasuda, H. Nasu, K. Tomioka, *Org. Lett.* **2009**, *11*, 2007–2009; d) C. Gignoux, A. F. Newton, A. Barthelme, W. Lewis, M. L. Alcarazb, R. A. Stockman, *Org. Biomol. Chem.* **2012**, *10*, 67–69; e) R. Liu, O. Gutierrez, D. J. Tantillo, J. Aubé, *J. Am. Chem. Soc.* **2012**, *134*, 6528–6531.
[15] a) M. Kuramoto, H. Arimoto, D. Uemura, *Mar. Drugs* **2004**, *2*, 39–54; b) S. Xu, H. Yoshimura, N. Maru, O. Ohno, H. Arimoto, D. Uemura, *J. Nat. Prod.* **2011**, *74*, 1323–1326.
[16] a) S. Yamago, E. Nakamura, *Org. React.* **2002**, *61*, 1–217; b) B. M. Trost, *Pure Appl. Chem.* **1988**, *60*, 1615–1626; c) R. Baker, R. B. Keen, *J. Organomet. Chem.* **1985**, *285*, 419–427.
[17] a) M. Schelwies, P. Dübon, G. Helmchen, *Angew. Chem.* **2006**, *118*, 2526–2529; *Angew. Chem. Int. Ed.* **2006**, *45*, 2466–2469; b) M. Schelwies, P. Dübon, G. Helmchen, *Chem. Eur. J.* **2008**, *14*, 6722–6733.
[18] B. T. Becicka, F. L. Koerwitz, G. J. Drtina, N. C. Baenziger, D. F. Wiemer, *J. Org. Chem.* **1990**, *55*, 5613–5619.
[19] a) J. Tsuji, *Pure Appl. Chem.* **1986**, *58*, 869–878; b) J. Tsuji, M. Nisar, I. Shimizu, I. Minami, *Synthesis* **1984**, 1009.
[20] W. G. Dauben, H. G. Wight, G. A. Boswell, *J. Org. Chem.* **1958**, *23*, 1787–1788.
[21] (*R*)-Pulegone was purchased from Aldrich (>85% purity). Its exact purity may depend on the lots received. However, the impurities are not (*S*)-pulegone, but other chiral or achiral substrates; see also ref. [32].
[22] a) D. Yang, C. Zhang, *J. Org. Chem.* **2001**, *66*, 4814–4818; b) L. M. Jackman, R. L. Webb, H. C. Yick, *J. Org. Chem.* **1982**, *47*, 1824–1831.
[23] See the Supporting Information for details.
[24] N. Gálvez, M. Moreno-Mañas, R. M. Sebastián, A. Vallribera, *Tetrahedron* **1996**, *52*, 1609–1616.
[25] a) R. T. Conley, M. C. Annis, *J. Org. Chem.* **1962**, *27*, 1961–1964; b) Y. Tamura, J. Minamikawa, M. Ikeda, *Synthesis* **1977**, 1–17; c) Y. Tamura, H. Fujiwara, K. Sumoto, M. Ikeda, Y. Kita, *Synthesis* **1973**, 215–216.
[26] The plausible self-decomposition mechanism was presumed to be as follows:

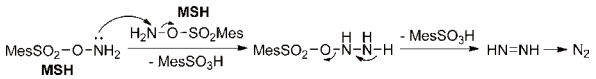

[27] L. Caglioti, *Organic Syntheses*, *Coll. Vol. 6*, 62–67.
[28] G. R. Krow, D. A. Shaw, B. Lynch, W. Lester, S. W. Szczepanski, R. Raghavachari, A. E. Derome, *J. Org. Chem.* **1988**, *53*, 2258–2262.
[29] a) S. Yamamura, M. Toda, Y. Hirata, *Organic Syntheses*, *Coll. Vol. 6*, 289–292; b) M. Toda, M. Hayashi, Y. Hirata, S. Yamamura, *Bull. Chem. Soc. Jpn.* **1972**, *45*, 264–266.
[30] S. Xu, T. Toyama, J. Nakamura, H. Arimoto, *Tetrahedron Lett.* **2010**, *51*, 4534–4537.
[31] T. Fukuyama, J. J. Nunes, *J. Am. Chem. Soc.* **1988**, *110*, 5196–5198.
[32] The high optical purity of our synthetic route was confirmed by measuring the *ee* of the derivative of compound **25**,[10a] which proved that the original (*R*)-pulegone was optically pure and no racemization occurred in our synthetic route.

 © 2014 Wiley-VCH Verlag GmbH & Co. KGaA, Weinheim

[33] With excess HOAc, the one-pot hydrogenation of the substrate in our previous study[10b] sometimes led to byproduct **A** through the following plausible mechanism:

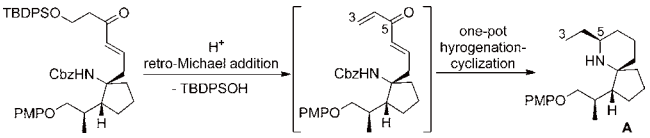

[34] B. P. Czech, R. A. Bartsch, *J. Org. Chem.* **1984**, *49*, 4076–4078.
[35] C. Prakash, S. Saleh, I. A. Blair, *Tetrahedron Lett.* **1989**, *30*, 19–22.
[36] P. Grieco, Y. Masaki, D. Boxler, *J. Am. Chem. Soc.* **1975**, *97*, 1597–1599.
[37] E. J. Corey, C. J. Helal, *Angew. Chem.* **1998**, *110*, 2092–2118; *Angew. Chem. Int. Ed.* **1998**, *37*, 1986–2012.
[38] J. Mulzer, M. Berger, *J. Org. Chem.* **2004**, *69*, 891–898.
[39] J. D. More, N. S. Finney, *Org. Lett.* **2002**, *4*, 3001–3003.
[40] K. Matsumura, S. Hashiguchi, T. Ikariya, R. Noyori, *J. Am. Chem. Soc.* **1997**, *119*, 8738–8739.
[41] S. B. Garber, J. S. Kingsbury, B. L. Gray, A. H. Hoveyda, *J. Am. Chem. Soc.* **2000**, *122*, 8168–8179.
[42] M. Scholl, S. Ding, C. W. Lee, R. H. Grubbs, *Org. Lett.* **1999**, *1*, 953–956.
[43] A. K. Chatterjee, T. L. Choi, D. P. Sanders, R. H. Grubbs, *J. Am. Chem. Soc.* **2003**, *125*, 11360–11370.
[44] a) H. E. Blackwell, D. J. O'Leary, A. K. Chatterjee, R. A. Washenfelder, D. A. Bussmann, R. H. Grubbs, *J. Am. Chem. Soc.* **2000**, *122*, 58–71; b) S. J. Meek, R. V. O'Brien, J. Llaveria, R. R. Schrock, A. H. Hoveyda, *Nature* **2011**, *471*, 461–466; c) B. K. Keitz, K. Endo, M. B. Herbert, R. H. Grubbs, *J. Am. Chem. Soc.* **2011**, *133*, 9686–9688.
[45] a) I. Shiina, R. Ibuka, M. Kubota, *Chem. Lett.* **2002**, 286–287; b) I. Shiina, M. Kubota, R. Ibuka, *Tetrahedron Lett.* **2002**, *43*, 7535–7539.
[46] G. C. Fu, S. T. Nguyen, R. H. Grubbs, *J. Am. Chem. Soc.* **1993**, *115*, 9856–9857.

Received: September 12, 2013
Published online: October 17, 2013

 © 2014 Wiley-VCH Verlag GmbH & Co. KGaA, Weinheim

Natural Products

DOI: 10.1002/anie.201400305

Total Synthesis of the Antibiotic Kendomycin: A Macrocyclization Using the Tsuji–Trost Etherification**

*Tetsuya Sengoku, Shu Xu, Kenji Ogura, Yoshinori Emori, Kenji Kitada, Daisuke Uemura, and Hirokazu Arimoto**

Abstract: *A highly stereocontrolled, convergent total synthesis of kendomycin [(−)-TAN2162], an ansa-macrocyclic antibiotic, is reported. The key of the strategy is an unprecedented Tsuji–Trost macrocyclic etherification, followed by a transannular Claisen rearrangement to construct the 18-membered carbocyclic framework. The oxa-six- and five-membered rings were also stereoselectively constructed respectively by a cascade oxidative cyclization at an unfunctionalized benzylic position and using a one-pot epoxidation/5-exo-tet epoxide opening.*

Kendomycin [(−)-TAN2162; **1**; for structure see Scheme 1] is an ansa-macrocyclic polyketide comprising a quinone methide chromophore, and was originally isolated as an antagonist for the endothelin receptor,[1] and as an antiosteoporotic agent.[2] Zeeck and Bode reported that **1** exhibited not only cytotoxic effects against a number of human tumor cell lines but also a strong antibacterial activity against both Gram-positive and Gram-negative bacteria, notably methicillin-resistant *Staphylococcus aureus* (MRSA) and vancomycin intermediate *S. aureus* (VISA) Mu50 strain.[3] The architectural structure and multiple biological activities of **1** have attracted significant interest in the past decade from biological,[4] biosynthetic,[5] and chemically synthetic[6] perspectives.

The macrocyclic carbon framework of **1** represents a major challenge for an efficient chemical synthesis. Among all the achieved total syntheses and formal total syntheses, several macrocyclization strategies, including C-glycosydation,[7a] ring-closing metathesis (RCM),[7b,c,e,f,8] the Barbier reaction,[7d] photo-Fries rearrangement,[7e,f] Dötz benzannulation,[7g] and Prins reaction[7h] have been reported, albeit in modest yields. We have attempted an RCM strategy for the macrocyclization at the C13–C14 double bond of **1**.[8] Unfortunately, the unnatural *Z* diastereomer was the predominant product. However, in our studies the Claisen rearrangement was found to work as a powerful tool for the introduction of a carbon substituent at the highly hindered C20a position.[8a] We finally found that the macrocyclic etherification/Claisen rearrangement combination could be used for the construction of kendomycin's carbon framework.

The retrosynthetic analysis of **1** is outlined in Scheme 1. It could be derived from **2** through aromatic oxidation and oxidative removal of the terminal hydroxymethyl group. The five-membered ring of **2** could possibly be constructed selectively by a 5-*exo* cyclization of the phenol and the neighboring olefin of **3**. The macro-carbocycle of **3** was envisioned to be derived from the transannular Claisen rearrangement of the allyl aryl ether **4**, which comes from hydroquinone **5** using a selective macrocyclization at the less hindered hydroxy group by means of Tsuji–Trost etherifica-

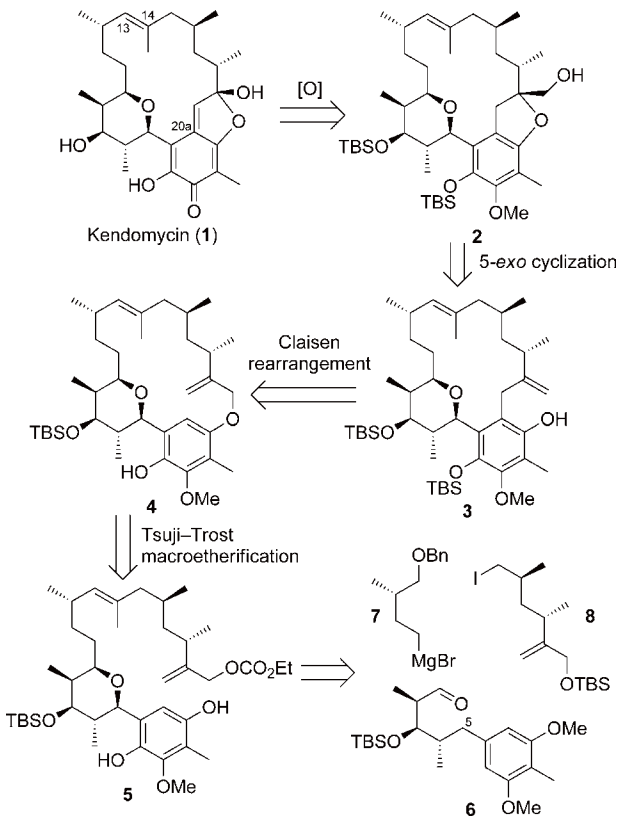

Scheme 1. Retrosynthetic analysis. TBS = *tert*-butyldimethylsilyl.

[*] Dr. T. Sengoku,[§] [+] Dr. S. Xu,[+] K. Ogura, Y. Emori, K. Kitada, Prof. Dr. H. Arimoto
Graduate School of Life Sciences, Tohoku University
2-1-1 Katahira, Sendai 980-8577 (Japan)
E-mail: arimoto@biochem.tohoku.ac.jp
Homepage: http://www.agri.tohoku.ac.jp/bunseki/index-j.html
Prof. Dr. D. Uemura
Department of Chemistry, Faculty of Science, Kanagawa University
Hiratsuka 259-1293 (Japan)

[§] Current address: Department of Materials Science, Faculty of Engineering, Shizuoka University, Shizuoka 432-8561 (Japan)

[+] These authors contributed equally to this work.

[**] We are grateful for the financial support of Grants-in-Aid for Scientific Research (Nos.18032010 and 21310136) from the JSPS. T.S. acknowledges the JSPS for the Research Fellowships for Young Scientists.

Supporting information for this article is available on the WWW under http://dx.doi.org/10.1002/anie.201400305.

© 2014 Wiley-VCH Verlag GmbH & Co. KGaA, Weinheim

tion. The macrocyclization precursor **5** would be prepared convergently from the aldehyde **6**, alkylmagnesium **7**, and iodide **8**. The tetrahydropyran ring could be cyclized diastereoselectively at the unfunctionalized C5-position by a Ag_2O-triggered cascade reaction, as we have previously reported.[8a]

We have previously reported on the preparation of the C1–C13 segment of **1**,[8a] and herein, we present a modified scalable synthetic route (Scheme 2). The modified route

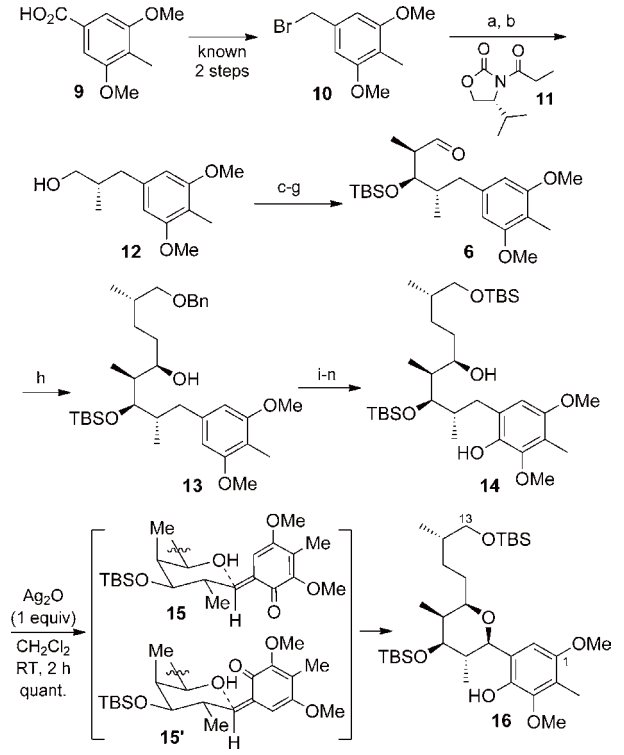

Scheme 2. Synthesis of C1–C13 segment **16**: a) **11**, NaHMDS, THF, −60 °C; b) $LiAlH_4$, THF, −78 °C to 0 °C, 82 % (2 steps); c) $(COCl)_2$, DMSO, Et_3N, CH_2Cl_2, −78 °C to 0 °C; d) (*R*,*R*)-[(*E*)-2-butenyl]diisopropyl tartrate boronate, 4 Å M.S., PhMe, −78 °C, 77 % (2 steps); e) TBSOTf, 2,6-lutidine, CH_2Cl_2, 0 °C, quant.; f) OsO_4 (cat.), NMO, acetone/H_2O (4:1), RT; g) $NaIO_4$, EtOH/H_2O (1:1), RT, 93 % (2 steps); h) **7**, −78 °C, THF, quant. (d.r. 15:1); i) H_2, $Pd(OH)_2$/C, EtOAc, RT; j) TBSCl, DMAP, Et_3N, CH_2Cl_2, RT, 85 % (2 steps); k) HBr_3·Py, K_2CO_3, Py, 0 °C to RT; l) ethyl vinyl ether, PPTS, RT, quant. (2 steps); m) *n*BuLi, $B(OMe)_3$, THF, −78 °C to RT, then 30 % H_2O_2 aq., Na_2CO_3, RT, 90 %; n) PPTS, *n*PrOH, RT, 99 %. DMAP = 4-(*N*,*N*-dimethylamino)pyridine, DMSO = dimethylsulfoxide, HMDS = hexamethyldisilazide, M.S. = molecular sieves, NMO = *N*-methylmorpholine *N*-oxide, PPTS = pyridinium *p*-toluenesulfonate, Py = pyridine, Tf = trifluoromethanesulfonyl, THF = tetrahydrofuran.

commenced with the commercially available benzoic acid **9**, which was easily converted into the aryl bromide **10** with a two-step procedure.[9] Evans asymmetric alkylation[10] and reduction furnished the *S*-alcohol **12** with more than 99 % *ee*, which was determined using the modified Mosher's method.[11] Swern oxidation and Roush crotylation[12] afforded a single diastereomer containing the three desired contiguous stereogenic centers, which was further transformed to aldehyde **6**. Nucleophilic addition of the Grignard compound **7**[13] to **6** gave a 15:1 diastereomer mixture of the secondary alcohol **13**, favoring the expected Felkin–Anh-type product. This selectivity is higher than our previous result (5.5:1) which was obtained using a similar alkyllithium nucleophile.[8a] After introduction of a phenolic hydroxy group to the aromatic ring, **14** was stereoselectively cyclized at the unfunctionalized benzylic position under phenol oxidation conditions (Ag_2O[14]) and quantitatively afforded the tetrahydropyran **16** as a single diastereomer. The excellent selectivity was thought to be due to the chair-form oxa-Michael-addition transition-state **15** or **15′** with the bulky quinone methide in an equatorial position. This result also proposed another possibility for the unclear biosynthetic mechanism of kendomycin's pyran ring formation.[5] With this modified route, **16** was obtained on a 3 gram scale.

The conversion of phenol **16** into **5** is shown in Scheme 3. After a manipulation of the protecting groups, Swern oxidation and Corey–Fuchs protocol furnished the alkyne **17**. Hydrozirconation with the Schwartz reagent[15] and subsequent iodination proceeded with high regioselectivity (9:1) along with removal of a MOM ether. The regioisomers **18** and **18′** were not easily separable from each other, and

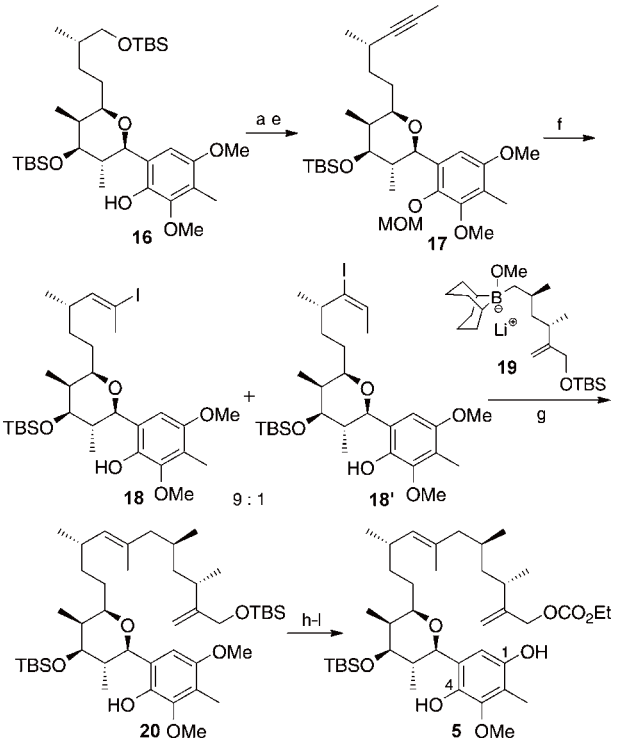

Scheme 3. Synthesis of the macrocyclization precursor **5**: a) MOMCl, NaH, THF, RT; b) PPTS, THF/MeOH (1:1), RT, 92 % (2 steps); c) $(COCl)_2$·DMSO, Et_3N, CH_2Cl_2, −78 °C; d) CBr_4, PPh_3, Et_3N, CH_2Cl_2, −78 °C, 72 % (2 steps); e) *n*BuLi, MeI, THF, −78 °C to RT, 98 %; f) [$HZrCp_2Cl$], PhH, RT, then I_2; g) **8** (2 equiv), *t*BuLi, Et_2O, −78 °C, then MeO-9-BBN, THF, −78 °C to RT, then **18** + **18′**, [Pd-$(dppf)_2Cl_2$]·CH_2Cl_2 (20 mol %), 3 M K_3PO_4 aq., DMF, RT, 87 % (2 steps); h) MOMCl, NaH, THF, RT, 95 %; i) PPTS, THF/MeOH (1:1), RT, 73 %; j) $ClCO_2Et$, Py, RT, 94 %; k) $(NH_4)_2Ce(NO_3)_6$, MeCN/H_2O (2:1), RT; l) $Na_2S_2O_4$, MeCN/H_2O (1:1), 0 °C, quant. (2 steps). BBN = borabicyclo[3.3.1]nonane, Cp = cyclopentadienyl, DMF = *N*,*N*-dimethylformamide, dppf = 1,1′-bis(diphenylphosphino)ferrocene, MOM = methoxymethyl.

 © 2014 Wiley-VCH Verlag GmbH & Co. KGaA, Weinheim

were thus used as a mixture for the Suzuki–Miyaura cross-coupling reaction[16] with boranate **19**. The boranate was prepared by lithiation and transmetalation of **8**.[17] The desired coupling product **20** was isolated in 87% yield (two steps). Protection of **20** with MOMCl, selective removal of the terminal TBS group, carbonate formation, and exposure of the two hydroxy groups of the *p*-hydroquinone yielded the Tsuji–Trost cyclization precursor **5**.

The examination of the key palladium-catalyzed Tsuji–Trost cyclization is shown in Table 1. Although the Tsuji–Trost reaction is a well-established synthetic protocol,[18] to the best of our knowledge, the macroetherification with this reaction has not been reported in total synthesis studies of natural products. More challenging is that our substrate, **5**, is actually a hydroquinone which contains two hydroxy nucleophiles, and is sensitive to oxidation, which may render the reaction more complicated. However, to avoid the tedious and poorly selective protecting strategy for the hindered C4-OH group, we decided to perform the cyclization with both free hydroxy groups. Eventually, it was found that the desired macrocyclic ether **4** was obtained with $[Pd_2(dba)_3]$ and dppb at room temperature in THF,[19] though the regioisomer **4′** was the major product (entry 1). Solvent effects were later found to have great influence on the regioselectivity, with CH_2Cl_2 giving the best result (**4**/**4′** = 10:1, entries 5 and 6). Notably, when the concentration of **5** was higher than 10 mM, intermolecular coupling became significant. Other palladium catalysts such as $[Pd(PPh_3)_4]$ or $Pd(OAc)_2$ gave either no reaction or decomposed byproducts.[20] Although the solvent has been shown to play a key role in the ion-pairing in the Tsuji–Trost reaction,[21] the specific reason for the selectivity in this study is still not clear.

After obtaining the 18-membered macrocyclic ether, we next attempted a ring contraction through a Claisen rearrangement[22] (Scheme 4). We have reported this transformation with an acyclic substrate in refluxing Me_2NPh.[8a] This time, after TBS protection of the phenol **4** and heating at 205 °C in Et_2NPh (a more stable solvent), **21** was smoothly converted into the desired carbocyclic **3** in 99% yield.[23] Next, several strategies (iodoetherification, oxymercuration, etc.) were attempted to cyclize the five-membered ring of kendomycin. Eventually, epoxidation and subsequent intramolecular epoxide opening proved to be most efficient. Thus, after alkene epoxidation with *m*CPBA in CH_2Cl_2, the 5-*exo*-tet cyclization proceeded smoothly by just adding a protic solvent, MeOH, and furnished predominately one diastereomer of **22**. Since the upper trisubstituted alkene was also epoxidized during the process, a subsequent deoxygenation[7b,c,24] afforded the compound **2** in 82% yield (two steps) as a single diastereomer. Next a hypervalent-iodine-promoted β-fragmentation of the alkoxyl radical removed the terminal hydroxymethyl group, and presumably provided an unstable intermediate *tert*-iodide, which was gradually eliminated to give the benzofuran **23**. This elimination process was accelerated by the addition of a small amount of water. The compound **23** has the same skeleton as intermediates obtained by the groups of Lee[7a] and Mulzer.[7e,f] Finally, the selective removal of the phenolic TBS group, oxidation, and acidic rearrangement of the resulting *o*-quinone, with the simultaneous TBS removal, accomplished the total synthesis of kendomycin.

In summary, we have achieved the total synthesis of the antibiotic kendomycin (**1**) by using a highly stereocontrolled convergent strategy. The key step of this synthetic route is the

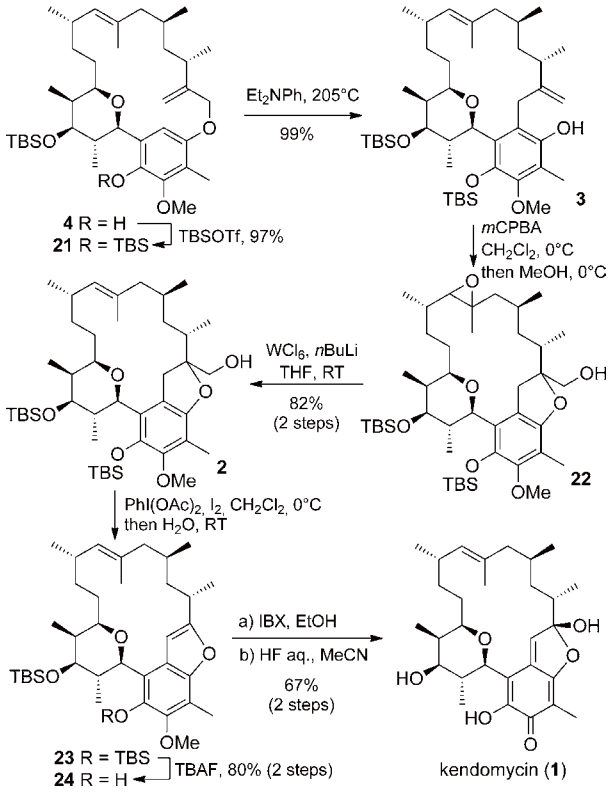

Scheme 4. Complete total synthesis of **1**. *m*CPBA = *m*-chloroperoxybenzoic acid, TBAF = tetra-*n*-butylammonium fluoride.

Table 1: Regioselective macrocyclization using Tsuji–Trost etherification.[a]

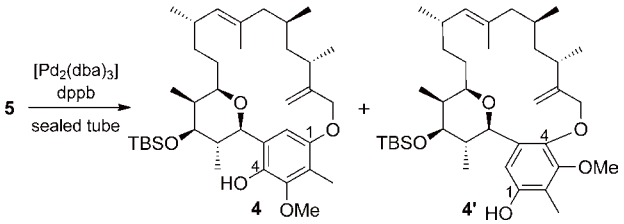

Entry	$[Pd_2(dba)_3]$ (equiv)	dppb (equiv)	Solvent	*T* [°C]	**4**/**4′**[b]	Yield **4** [%][c]
1	0.15	0.4	THF	RT	1:3[d]	–
2	0.5	2	toluene	RT	1:1	–
3	1.1	20	DMF	60	3:5	–
4	0.2	1.6	$(ClCH_2)_2$	70	–[e]	–
5	0.4	10	CH_2Cl_2	50	10:1	80
6	0.14	0.86	CH_2Cl_2	70	10:1	71

[a] The reaction was performed with 1–5 mM of **5** in the dark in a sealed tube. [b] Determined by ^1H NMR analysis of the crude reaction mixture. [c] Yield of the isolated product. [d] Approximately 20% of the starting material remained. [e] Only starting material recovered. dba = dibenzylideneacetone, dppb = 1,4-bis(diphenylphosphino)butane.

© 2014 Wiley-VCH Verlag GmbH & Co. KGaA, Weinheim

palladium-catalyzed regioselective Tsuji–Trost macroetherification/transannular Claisen rearrangement sequence to construct the macrocyclic framework. Other synthetic features include the tetrahydropyran installation by stereoselective nucleophilic addition to an aldehyde and a Ag_2O-triggered stereoselective cyclization and the establishment of a five-membered ring by one-pot epoxidation/5-*exo*-tet cyclization process.

Received: January 11, 2014
Published online: ■■ ■■, ■■■■

Keywords: antibiotics · macrocycles · natural products · palladium · total synthesis

[1] a) Y. Funahashi, T. Ishimaru, N. Kawamura, JP Patent 08231551, **1996**; b) Y. Funahashi, N. Kawamura, T. Ishimaru, JP Patent 08231552, **1996**.
[2] M. H. Su, M. I. Hosken, B. J. Hotovec, T. L. Johnston, US Patent 5728727, **1998**.
[3] H. B. Bode, A. Zeeck, *J. Chem. Soc. Perkin Trans. 1* **2000**, 323–328.
[4] a) Y. A. Elnakady, M. Rohde, F. Sasse, C. Backes, A. Keller, H.-P. Lenhof, K. J. Weissman, R. Müller, *ChemBioChem* **2007**, *8*, 1261–1272; b) C. O. Janssen et al., *Bioorg. Med. Chem. Lett.* **2008**, *18*, 5771–5773 (see the Supporting Information for all authors).
[5] a) H. B. Bode, A. Zeeck, *J. Chem. Soc. Perkin Trans. 1* **2000**, 2665–2670; b) S. C. Wenzel, H. B. Bode, I. Kochems, R. Müller, *ChemBioChem* **2008**, *9*, 2711–2721.
[6] For reviews, see: a) H. J. Martin, T. Magauer, J. Mulzer, *Angew. Chem.* **2010**, *122*, 5746–5758; *Angew. Chem. Int. Ed.* **2010**, *49*, 5614–5626; b) D. Bicchielli, Y. Borguet, L. Delaude, A. Demonceau, I. Dragutan, V. Dragutan, M. Hans, C. Jossifov, F. Nicks, Q. Willem, *Curr. Org. Synth.* **2012**, *9*, 397–405; c) M. Shan, L. Wang, Q. Zhang, G. A. O'Dooherty, *Chemtracts* **2009**, *22*, 1–17.
[7] For total syntheses, see: a) Y. Yu, H. Men, C. Lee, *J. Am. Chem. Soc.* **2004**, *126*, 14720–14721; b) A. B. Smith III, E. F. Mesaros, E. A. Meyer, *J. Am. Chem. Soc.* **2005**, *127*, 6948–6949; c) A. B. Smith III, E. F. Mesaros, E. A. Meyer, *J. Am. Chem. Soc.* **2006**, *128*, 5292–5299; d) J. T. Lowe, J. S. Panek, *Org. Lett.* **2008**, *10*, 3813–3816; e) T. Magauer, H. J. Martin, J. Mulzer, *Angew. Chem.* **2009**, *121*, 6148–6152; *Angew. Chem. Int. Ed.* **2009**, *48*, 6032–6036; f) T. Magauer, H. J. Martin, J. Mulzer, *Chem. Eur. J.* **2010**, *16*, 507–519; g) K. Tanaka, M. Watanabe, K. Ishibashi, H. Matsuyama, Y. Saikawa, M. Nakata, *Org. Lett.* **2010**, *12*, 1700–1703; For formal total syntheses, see: h) K. B. Bahnck, S. D. Rychnovsky, *J. Am. Chem. Soc.* **2008**, *130*, 13177–13181; i) K. B. Bahnck, S. D. Rychnovsky, *Chem. Commun.* **2006**, 2388–2390.
[8] a) T. Sengoku, H. Arimoto, D. Uemura, *Chem. Commun.* **2004**, 1220–1221; b) T. Sengoku, D. Uemura, H. Arimoto, *Chem. Lett.* **2007**, *36*, 726–727.
[9] S. R. Kasibhatla, K. D. Hong, M. F. Boehm, M. A. Biamonte, L. Zhang, US Patent 20050113340A1, **2005**.
[10] D. A. Evans, M. D. Ennis, D. J. Mathre, *J. Am. Chem. Soc.* **1982**, *104*, 1737–1739.
[11] J. M. Seco, E. Quinoa, R. Riguera, *Chem. Rev.* **2004**, *104*, 17–118.
[12] W. R. Roush, A. D. Palkowitz, K. Ando, *J. Am. Chem. Soc.* **1990**, *112*, 6348–6359.
[13] The bromide precursor of the alkylmagnesium **7** was prepared one step from the corresponding alcohol. For a three-step synthesis of the alcohol from commercially available starting materials, see: a) T. J. Donohoe, T. J. C. O'Riordan, M. Peifer, C. R. Jones, T. J. Miles, *Org. Lett.* **2012**, *14*, 5460–5463; b) A. W. van Zijl, F. López, A. J. Minnaard, B. L. Feringa, *J. Org. Chem.* **2007**, *72*, 2558–2563.
[14] S. R. Angle, K. D. Turnbull, *J. Am. Chem. Soc.* **1989**, *111*, 1136–1138.
[15] D. W. Hart, T. F. Blackburn, J. Schwartz, *J. Am. Chem. Soc.* **1975**, *97*, 679–680.
[16] a) N. Miyaura, A. Suzuki, *Chem. Rev.* **1995**, *95*, 2457–2483; b) J. A. Marshall, B. A. Johns, *J. Org. Chem.* **1998**, *63*, 7885–7892.
[17] For the synthesis of **8**, see the Supporting Information.
[18] B. M. Trost, M. L. Crawley, *Chem. Rev.* **2003**, *103*, 2921–2943.
[19] a) C. Damez, J.-R. Labrosse, P. Lhoste, D. Sinou, *Synthesis* **2001**, 1456–1458; b) G. Wang, D. Niu, T.-L. Qiu, L. T. Phan, Z. Chen, A. Polemeropoulos, Y. S. Or, *Org. Lett.* **2004**, *6*, 4455–4458; c) C. Goux, P. Lhoste, D. Sinou, *Synlett* **1992**, 725–727.
[20] Among the byproducts, the quinone **A** and methylenedioxy arene **B** were structurally determined. **A** was speculated to derive from oxidation of the hydroquinone **5** by high-valence palladium intermediates. **B** might be generated from **A** by a light-triggered transformation. For similar examples, see: C. Thommen, C. K. Jana, M. Neuburger, K. Gademann, *Org. Lett.* **2003**, *5*, 1390–1393, and references therein.

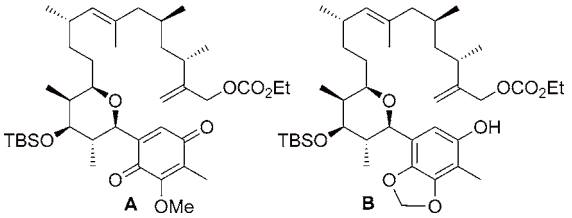

[21] L. A. Evans, N. Fey, J. N. Harvey, D. Hose, G. C. Lloyd-Jones, P. Murray, A. G. Orpen, R. Osborne, G. J. J. Owen-Smith, M. Purdie, *J. Am. Chem. Soc.* **2008**, *130*, 14471–14473.
[22] E. A. Ilardi, C. E. Stivala, A. Zakarian, *Chem. Soc. Rev.* **2009**, *38*, 3133–3148.
[23] In a recent total synthesis of kendomycin (Ref. [7g]), Nakata's group applied a set of reaction conditions, similar to our previously reported method, on a substrate which was more acidic than **21**. In their case, Ac_2O had to be used for the in situ trap of the Claisen product to avoid further decomposition. In our substrate case, no decomposition was observed.
[24] K. B. Sharpless, M. A. Umbreit, M. T. Nieh, T. C. Flood, *J. Am. Chem. Soc.* **1972**, *94*, 6538–6540.

 © 2014 Wiley-VCH Verlag GmbH & Co. KGaA, Weinheim

Communications

Natural Products

T. Sengoku, S. Xu, K. Ogura, Y. Emori, K. Kitada, D. Uemura, H. Arimoto* ——— ▮▮▮▮–▮▮▮▮

Total Synthesis of the Antibiotic Kendomycin: A Macrocyclization Using the Tsuji–Trost Etherification

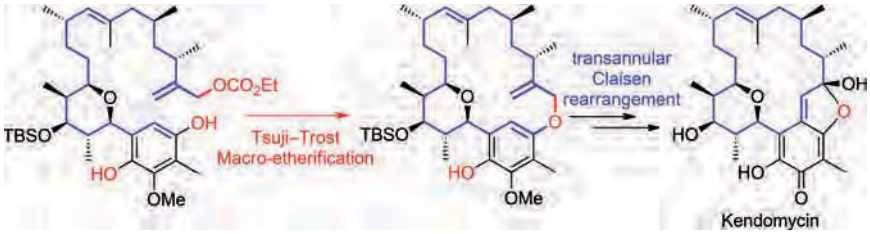

A new construct: The asymmetric total synthesis of the antibiotic kendomycin was accomplished by using a highly stereocontrolled convergent route. The key feature of the synthetic strategy is the construction of an 18-membered carbocycle based on an intramolecular Tsuji–Trost etherification/transannular Claisen rearrangement sequence. TBS = *tert*-butyldimethylsilyl.

© 2014 Wiley-VCH Verlag GmbH & Co. KGaA, Weinheim

Polyhedron 62 (2013) 37–41

Contents lists available at SciVerse ScienceDirect

Polyhedron

journal homepage: www.elsevier.com/locate/poly

Effect of phosphine and phosphine sulfide ligands on the cobalt-catalyzed reductive coupling of 2-iodobutane with *n*-butyl acrylate

Sen-ichi Aizawa [a,*], Koichi Fukumoto [a], Tatsuya Kawamoto [b]

[a] Graduate School of Science and Engineering, University of Toyama, 3190 Gofuku, Toyama 930-8555, Japan
[b] Department of Chemistry, Faculty of Science, Kanagawa University, 2946 Tsuchiya, Hiratsuka, Kanagawa 259-1293, Japan

ARTICLE INFO

Article history:
Received 22 April 2013
Accepted 3 June 2013
Available online 20 June 2013

Keywords:
Cobalt-catalyzed reductive coupling
Activated alkene
Oxidative addition driven mechanism
Phosphine sulfide ligand

ABSTRACT

Tris[2-(diphenylphosphino)ethyl]phosphine disulfide (pp_3S_2), in which two terminal phosphino groups are selectively sulfidated, was prepared by utilizing the selective sulfidation reaction of $[PdI(pp_3)]I$. Co(II) complexes with bidentate, tridentate and tetradentate phosphines and pp_3S_2 were prepared from anhydrous CoI_2. X-ray crystal analyses revealed that the reaction of CoI_2 with 1 equivalent of 1,2-bis(diphenylphosphino)ethane (p_2) gave rise to partial oxidation of p_2 to give the dicationic octahedral $[Co(p_2O_2)_2(CH_3CN)_2]^{2+}$ ($p_2O_2 = p_2$ dioxide) and dianionic p_2O-bridged tetrahedral dinuclear $[CoI_3(p_2O)CoI_3]^{2-}$ ($p_2O = p_2$ monooxide) complexes, while the reaction with 2 equivalents of p_2 gave the square-pyramidal $[CoI(p_2)_2]^+$ complex. The catalytic activity for the Co-catalyzed coupling reaction of 2-iodobutane with *n*-butyl acrylate was compared using multidentate phosphines and phosphine sulfides as ligands, and the efficiency of the phosphine sulfides was shown. The tendency for multidentate phosphine to deactivate the Co-catalysis can substantiate an oxidative addition driven mechanism in which the multidentate ligand should interfere with the formation of the alkyl halide Co(III) adduct and subsequent coordination of an alkene.

© 2013 Elsevier Ltd. All rights reserved.

1. Introduction

Carbon–carbon bond formation reactions by transition metal catalysts are now quite versatile and indispensable in organic syntheses. In particular, direct C–H bond transformation is a highly attractive strategy because of the commonness of C–H bonds [1]. Although some of the second row transition metal catalysts, such as Rh, Pd and Ru complexes, have proven to be highly effective in the direct coupling processes [2], the development of new cost-effective catalysts is significant for industrial use. In line with the above challenge, several Co-catalyzed reactions using a Grignard reagent have been reported, where a radical generation mechanism was proposed [3]. However, these catalytic reactions cannot be used for the coupling of an alkyl halide with an electron-withdrawing alkene because Grignard reagents are quite reactive to the activated alkene. Recently, Cheng et al. reported efficient Co-catalyzed C_{sp^3}-C_{sp^3} bond forming reactions of primary, secondary and tertiary alkyl halides with electron-withdrawing alkenes under mild conditions without Grignard reagents [4], and they proposed an oxidative addition driven mechanism in which an alkene is bound to a Co(III) adduct formed by the oxidative addition of Co(I) with an alkyl halide. Although PPh_3 or bidentate phosphines were used for the bound ligand in that work, the steric and electronic properties of the ligand on the Co center should be quite significant factors affecting the catalytic activity in the oxidative addition driven mechanism. Thus, in the present report, the steric and electronic effects of ligands are investigated by using some sterically different multidentate phosphines and more π-accepting and polarizable phosphine sulfides, which are electronically more efficient for the oxidative addition–reductive elimination mechanism in the Pd(0) catalytic cycle [5]. The observed differences in the catalytic activity provide further insight into the reaction mechanism of the catalytic cycle from the view point of coordination chemistry.

2. Experimental

2.1. Reagents

Tris[2-(diphenylphosphino)ethyl]phosphine (pp_3, Aldrich), bis[2-(diphenylphosphino)ethyl]phenylphosphine (p_3, Aldrich), 1,2-bis(diphenylphosphino)ethane (p_2, Wako), anhydrous cobalt(II) iodide (Kishida Chemical), tetrakis(acetonitrile)palladium(II) tetrafluoroborate ($[Pd(CH_3CN)_4](BF_4)_2$, Aldrich), tetra(*n*-butyl) ammonium iodide (Wako), sulfur (Wako), zinc powder (Wako),

* Corresponding author. Tel./fax: +81 76 445 6980.
E-mail address: saizawa@eng.u-toyama.ac.jp (S.-i. Aizawa).

0277-5387/$ - see front matter © 2013 Elsevier Ltd. All rights reserved.
http://dx.doi.org/10.1016/j.poly.2013.06.013

2-iodobutane (Tokyo Chemical), *n*-butyl acrylate (Kishida Chemical) and dibenzyl ether (Kishida Chemical) were used for the preparation and catalytic reactions without further purification.

2.2. Preparation

2.2.1. Tris[2-(diphenylphosphino)ethyl]phosphine disulfide (pp_3S_2)

The disulfide complex [$PdI_2(pp_3S_2)$] was prepared by the reaction of [$PdI(pp_3)$]I [6] (0.362 g, 0.351 mmol) with sulfur (0.0225 g, 0.702 mmol) in degassed chloroform (ca. 10 cm^3) under N_2 at 40 °C for 3 days. The reaction solution was concentrated to a small volume, and to this was added diethyl ether. The resultant yellow solid was filtered and air-dried. Yield: 0.28 g (70%). *Anal.* Calc. for $C_{42}H_{42}I_2P_4S_2Pd{\cdot}0.5CHCl_3$: C, 44.20; H, 3.71; N, 0.00; S, 5.55. Found: C, 44.48; H, 3.75; N, 0.00; S, 5.57%. $^{31}P\{^1H\}$ NMR ($CHCl_3$) δ: 44.4 (d, 2P, sulfide), 70.0 (d, 1P, terminal), 78.1 (m, 1P, center); $^3J_{P(sulfide)-P(center)}$ = 55.0 Hz, $^3J_{P(terminal)-P(center)}$ = 17.8 Hz.

The disulfide Pd(II) complex prepared above, [$PdI_2(pp_3S_2)$]·0.5$CHCl_3$ (0.190 g, 0.165 mmol), and pp_3 (0.122 g, 0.182 mmol) were dissolved in degassed chloroform (ca. 5 cm^3) and reacted under N_2 at 50 °C for 1 day. The formed red pp_3 complex [$PdI(pp_3)$]I [6] was removed by silica gel column chromatography with chloroform as the eluent. The ^{31}P NMR spectrum of the concentrated colorless eluate indicated that the eluate contained unreacted pp_3 and dissociated free pp_3S_2. The concentrated chloroform eluate was mixed with an aqueous solution of $K_2[PdCl_4]$ to form red [$PdCl(pp_3)$]Cl [6,7] in the chloroform layer. Aqueous $K_2[PdCl_4]$ was added until the ^{31}P NMR signals of pp_3 completely disappeared, showing only the signals of pp_3S_2 and [$PdCl(pp_3)$]Cl [6,7]. Then, the red Pd(II) complex was removed by silica gel column chromatography, eluting with chloroform. The colorless eluate was concentrated and to this was added diethyl ether to obtain pure pp_3S_2. Yield: 0.049 g (40%). *Anal.* Calc. for $C_{42}H_{42}P_4S_2{\cdot}0.5H_2O$: C, 67.82; H, 5.82; N, 0.00; S, 8.62. Found: C, 67.81; H, 5.67; N, 0.00; S, 8.36%. $^{31}P\{^1H\}$ NMR ($CHCl_3$) δ: −19.7 (q, 1P, center), −13.1 (d, 1P, terminal), 44.4 (d, 2P, sulfide); $^3J_{P(center)-P(terminal)}$ = 27.5 Hz, $^3J_{P(center)-P(sulfide)}$ = 30.7 Hz.

2.2.2. [$CoI(p_2)_2$]I (**1**)

Anhydrous CoI_2 (0.0510 g, 0.163 mmol) and p_2 (0.130 g, 0.326 mmol) were dissolved in degassed THF and reacted under N_2 at room temperature for 2 h. The reaction solution was concentrated under N_2, and to this was added degassed diethyl ether to obtain the resultant brown solid by filtration. The solid was recrystallized from chloroform, and single crystals suitable for an X-ray analysis were obtained. Yield: 0.13 g (55%). *Anal.* Calc. for $C_{52}H_{48}P_4CoI_2$ (**1**)·$CHCl_3$: C, 50.82; H, 3.94; N, 0.00. Found: C, 50.58; H, 3.87; N, 0.00%.

2.2.3. [$Co(p_2O_2)_2(CH_3CN)_2$][$CoI_3(p_2O)CoI_3$] (**2**)

This complex salt was obtained by a procedure similar to that described for **1**, using 1 equivalent of p_2 instead of 2 equivalents. Single crystals suitable for an X-ray analysis were obtained by recrystallization from acetonitrile. Yield: 0.050 g (40%). *Anal.* Calc. for $C_{82}H_{78}N_2O_5P_6Co_3I_6$ (**2**): C, 42.91; H, 3.42; N, 1.22. Found: C, 42.67; H, 3.45; N, 1.09%.

2.2.4. [$CoI(p_2O_2)_2$]I (**3**)

This bis(P_2O_2) complex was obtained by a procedure similar to that described for **1**, using P_2O_2 prepared by the oxidation of p_2 with 10% aqueous H_2O_2 in chloroform instead of P_2. Yield: 0.16 g (65%). *Anal.* Calc. for $C_{64}H_{60}O_4P_4CoI_2$ (**3**)·$3C_4H_4O$: C, 55.79; H, 4.39; N, 0.00; S, 0.00. Found: C, 55.90; H, 4.37; N, 0.07; S, 0.00%.

2.2.5. [$CoI_2(L)$] (L = pp_3 (**4**), p_3 (**5**), and pp_3S_2 (**6**))

These phosphine and phosphine disulfide complexes were obtained by a procedure similar to that described for **1**, using 1 equivalent of pp_3 for **4**, p_3 for **5** and pp_3S_2 for **6** instead of 2 equivalents of p_2. Yields: 0.14 g (74%) for **4**, 0.10 g (63%) for **5** and 0.16 g (72%) for **6**. *Anal.* Calc. for $C_{42}H_{42}P_4CoI_2$ (**4**)·1.5$CHCl_3$: C, 44.94; H, 3.77; N, 0.00; S, 0.00. Found: C, 44.82; H, 3.88; N, 0.04; S, 0.00%. *Anal.* Calc. for $C_{34}H_{33}P_3CoI_2$ (**5**)·$CHCl_3$: C, 43.49; H, 3.55; N, 0.00; S, 0.00. Found: C, 44.19; H, 3.60; N, 0.00; S, 0.00%. *Anal.* Calc. for $C_{42}H_{42}P_4S_2CoI_2$ (**6**)·$2C_4H_4O$·1.5$CHCl_3$: C, 45.39; H, 3.81; N, 0.00; S, 4.71. Found: C, 45.16; H, 3.88; N, 0.08; S, 4.59%.

2.2.6. [$CoI(pp_3)$] (**7**)

This Co(I) complex was obtained by a procedure similar to that described in the literature [8]. $^{31}P\{^1H\}$ NMR ($CHCl_3$) δ: 59.5 (d, 3P, terminal), 157.9 (q, 1P, center); $^3J_{P(center)-P(terminal)}$ = 37.2 Hz.

2.3. Crystal structure determination

The measurements for **1**·3$CHCl_3$ and **2** were made on a Rigaku Mercury CCD X-ray diffractometer using graphite-monochromated Mo Kα (λ = 0.71075 Å) radiation at 200 K. Cell parameters were refined using the program CRYSTALCLEAR (Rigaku and MSC, version 1.3, 2001) and the collected data were reduced using the program CRYSTALSTRUCTURE (Rigaku and MSC, version 3.8, 2006). Empirical absorption corrections were applied. The structures were solved by direct methods using SIR 92 [9] and refined by full-matrix least-squares techniques using SHELXL-97 [10]. All non-hydrogen atoms for **1**·3$CHCl_3$ and **2** were refined anisotropically and hydrogen atoms were included in calculated positions. The structure of **2** contains CoI_3 moieties disordered over two different orientations for I1 and three different orientations for I2, I3, I4, I5, and I6[1].

2.4. General procedure for the cobalt-catalyzed coupling reaction

Reactions of *n*-butyl acrylate (0.128 g, 1.00 mmol) with 2-iodobutane (0.184 g, 1.00 mmol) were carried out in a sealed tube containing degassed acetonitrile (2 cm^3), the cobalt catalyst (0.040 mmol), zinc powder (0.164 g, 2.50 mmol), water (0.018 g, 1.0 mmol) and dibenzyl ether (0.015 g, 0.075 mmol) under N_2 at 80 °C. The yields were calculated by the ^1H NMR intensity of the methylene protons of the formed *n*-butyl-4-methylhexanoate on the basis of the intensity of the methylene protons of dibenzyl ether contained as an internal reference and followed as a function of time.

2.5. Measurements

^{31}P and ^1H NMR spectra for solutions were recorded on a JEOL JNM-A400 FT-NMR spectrometer operating at 160.70 and 399.65 MHz, respectively. In order to determine the chemical shifts of the ^{31}P NMR signals, a 3-mm-o.d. NMR tube containing the sample solution was coaxially mounted in a 5-mm-o.d. NMR tube containing deuterated water as a lock solvent and phosphoric acid as a reference.

[1] Crystal data for **1**·3$CHCl_3$: $C_{55}H_{51}Cl_9CoI_2P_4$, M_r = 1467.62, triclinic, space group $P\bar{1}$, a = 14.4437(15) Å, b = 20.182(2) Å, c = 20.612(2) Å, α = 93.404(3)° β = 91.004(3)° γ = 93.107(3)° V = 5987.8(11) $Å^3$, Z = 4, ρ_{calcd} = 1.628 Mg m^{-3}, crystal size 0.26 × 0.23 × 0.12 mm^3, F(000) = 2908, μ(Mo Kα) = 1.862 mm^{-1}, GOF = 1.080, 26866 independent reflections (R_{int} = 0.0588). The final R indicates were R_1 = 0.0635 ($I > 2\sigma(I)$) and wR_2 = 0.1641 (all data). Crystal data for **2**: $C_{82}H_{78}Co_3I_6N_2O_5P_6$, M_r = 2295.47, monoclinic, space group $P2_1$, a = 11.583(3) Å, b = 20.038(5) Å, c = 20.039(5) Å, β = 105.090(8)° V = 4491(2) $Å^3$, Z = 2, ρ_{calcd} = 1.698 Mg m^{-3}, crystal size 0.25 × 0.10 × 0.05 mm^3, F(000) = 2226, μ(Mo Kα) = 2.764 mm^{-1}, GOF = 1.117, 20075 independent reflections (R_{int} = 0.0577). The final R indicates were R_1 = 0.0819 ($I > 2\sigma(I)$) and wR_2 = 0.1411 (all data).

3. Results and discussion

3.1. Synthesis

The selective sulfidation of two terminal phosphino groups of the tetradentate tris[2-(diphenylphosphino)ethyl]phosphine (pp_3) was reported previously for the five-coordinated trigonal-bipyramidal Pd(II) complex, [PdCl(pp_3)]Cl [11]. The disulfide complex exists in equilibrium between the five-coordinate pseudo-trigonal-bipyramidal complex and the four-coordinate square-planar one with two pendant phosphine sulfide groups in chloroform [11a]. In this work, such reactivity of the pp_3 complex was applied to the preparation of pp_3S_2 (pp_3 disulfide) (Scheme 1). The selective sulfidation of two terminal phosphino groups of pp_3 was carried out with [PdI(pp_3)]I instead of the corresponding chloro complex, [PdCl(pp_3)]Cl. The obtained disulfide complex exhibited ^{31}P NMR behavior similar to that of the chloro complex, with broadening of the signals, suggesting an equilibrium between the five and four coordinate structures as observed for the chloro complex [11a]. The pp_3S_2 ligand was successfully dissociated from the Pd(II) complex by competitive coordination of pp_3 to form the more stable five coordinate [PdI(pp_3)]I [6]. The reason for use of the iodo complex instead of the chloro one is that the electron-accepting ability of the iodo ligand is greater than that of chloro one, which may promote coordination of phosphine σ donors to form the five coordinate pp_3 complex [6], and accordingly the pp_3S_2 ligand may dissociate more easily from the pp_3S_2 complex. Furthermore, taking advantage of the stability of the five-coordinate Pd(II) complex with the tetradentate pp_3 ligand compared to the pp_3S_2 complex equilibrated between the four and five-coordinate structures, unreacted pp_3 was successfully removed from the mixture of free pp_3 and pp_3S_2 by complexation with $K_2[PdCl_4]$, followed by separation with a silica gel column (see Section 2).

For a comparison of the catalytic activity of the Co(II) complexes with different bound ligands, the preparation of the 1:1 complexes with a phosphine or phosphine chalcogenide was attempted. However, the reaction of anhydrous CoI_2 with 1 equiv of 1,2-bis(diphenylphosphino)ethane (p_2) gave rise to partial oxidation of p_2, probably during recrystallization, to give **2** which consists of the dicationic octahedral bis(p_2O_2) complex, $[Co(p_2O_2)_2(CH_3CN)_2]^{2+}$ (p_2O_2 = p_2 dioxide), and the dianionic p_2O-bridged dinuclear tetrahedral complex, $[CoI_3(p_2O)CoI_3]^{2-}$ (p_2O = p_2 monooxide), in which p_2O does not act as a bidentate chelate (see below). This fact indicates that the 1:1 complex, $[CoI_2(p_2)]$, is not stable because the p_2 chelate bite distance is too small to give the tetrahedral Co(II) complex (see below). Consequently, the 1:2 complexes were prepared using 2 equivalents of p_2 or p_2O_2 to give **1** and **3**.

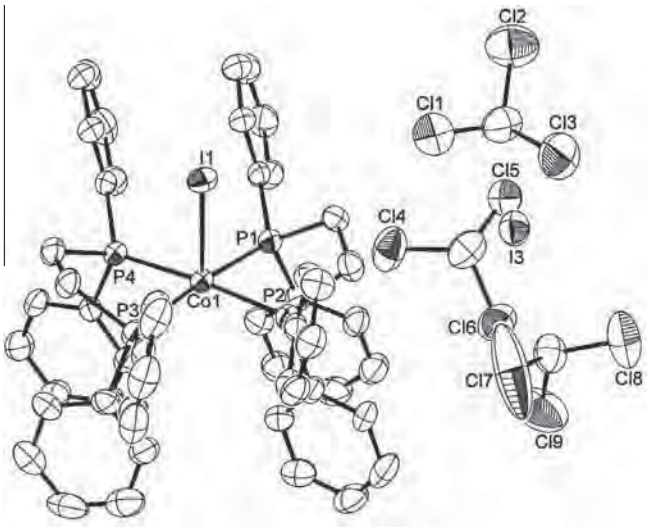

Fig. 1. ORTEP diagram of **1**·3CHCl$_3$.

3.2. Crystal structure

The perspective views of **1**·3CHCl$_3$ and **2** are shown in Figs. 1 and 2, respectively. The bis(p_2) complex **1**, prepared with a 1:2 CoI_2/p_2 ratio, takes a five-coordinate square-pyramidal geometry with one iodide group in the apical position. The other iodide ion is surrounded by three chloroform molecules. The chelate bite angles of the p_2 bidentate ligands are considerably smaller than 90° (P1-Co1-P2 = 82.09(5)° and P3-Co1-P4 = 81.57(5)°). This structure indicates that the five-membered chelate of p_2 is too small to form a regular square plane for the Co(II) centre. It is obvious that formation of a tetrahedral geometry, expected for the mono(p_2) complex $[CoI_2(p_2)]$, would give rise to further distortion because the chelate bite angle should be 109° for a regular tetrahedral geometry.

Complex **2**, which was obtained from a 1:1 CoI_2/p_2 ratio, consists of the dicationic octahedral complex $[Co(p_2O_2)_2(CH_3CN)_2]^{2+}$ and the dianionic p_2O-bridged dinuclear complex with two tetrahedral $Co(II)I_3$ moieties linked by phosphino and phosphine oxide groups. The complex cation takes a nearly regular octahedral geometry in which the chelate bite angles of the p_2O_2 ligands are almost 90° (89.6–90.7°). This is attributed to the flexibility and steric adjustability of the seven-membered p_2O_2 chelate. Though large deviations of the bond distances and angles were observed in the two distorted tetrahedral Co(II) moieties, the averaged I–Co–I bond angles for the phosphine complex moiety (114.1°) and the phosphine oxide complex moiety (113.8°) are obviously larger than

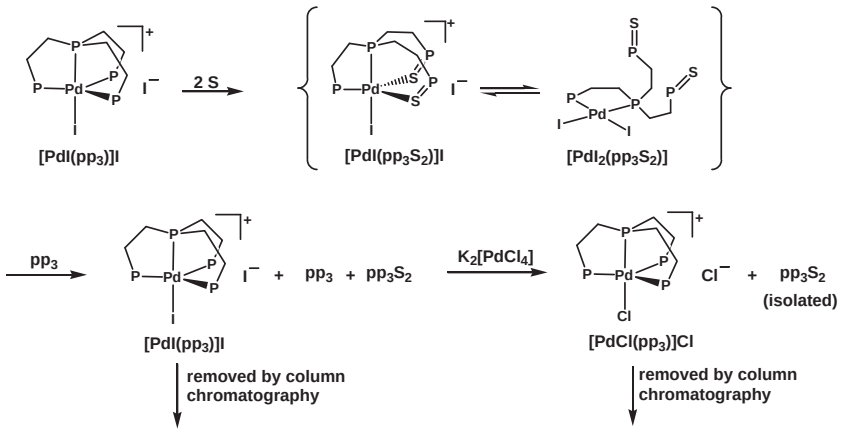

Scheme 1. Isolation of pp3S2.

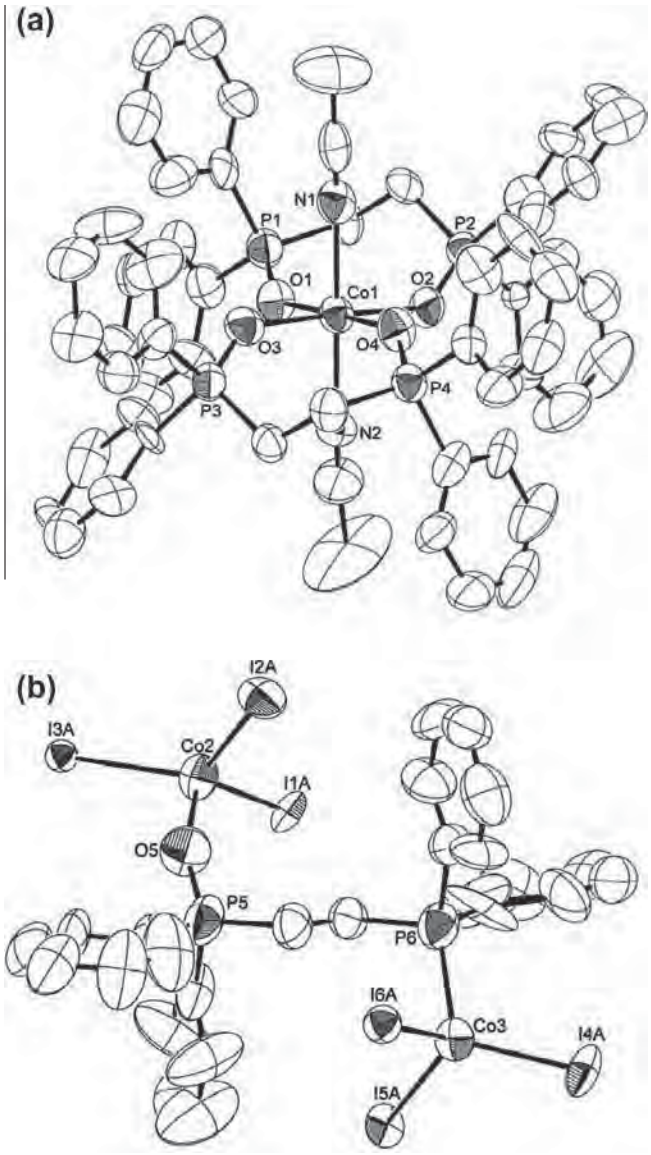

Fig. 2. ORTEP diagram of **2** showing $[Co(p_2O_2)_2(CH_3CN)_2]^{2+}$ (a) and $[CoI_3(p_2O)CoI_3]^{2-}$ (b), individually.

the averaged I–Co–P (103.5°) and I–Co–O (104.7°) bond angles, due to the repulsion between the large iodide anions. It should be noted that the averaged Co–I bond distance for the phosphine complex moiety (2.52 Å) is considerably shorter than that for the phosphine oxide complex moiety (2.61 Å), in spite of the larger steric bulkiness of the diphenylphosphino group in the coordination sphere compared to the phosphine oxide group. Such a difference in bond distances may suggest that the electron donation of the soft diphenylphosphino group to the hard tetrahedral Co(II) ion is relatively weaker than that of the hard phosphine oxide group, resulting in smaller electronic repulsion on the Co(II) center with a phosphino group rather than that with a phosphine oxide group. This is consistent with the fact that the Co–P distance in the tetrahedral Co(II) moiety in **2** (2.463(5) Å) is significantly longer than the averaged Co–P distance of the five-coordinate Co(II) complex **1** (2.283 Å), though the ionic radius of four-coordinate tetrahedral Co(II) should be smaller than those for five- or six-coordinate Co(II). On the other hand, the Co–O distance in the tetrahedral Co(II) moiety in **2** (1.892(8) Å) is reasonably shorter than the averaged Co–O distance in the six-coordinate octahedral Co(II) moiety in **2** (2.036 Å).

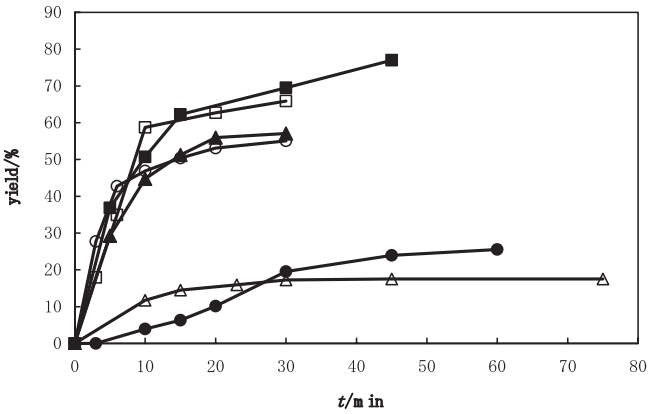

Fig. 3. Change in the yield of butyl-4-methylhexanoate with time in the cobalt-catalyzed coupling reaction using **1** (○), **3** (●), **4** (△), **5** (▲), **6** (□) and a mixture of CoI_2 and pp_3S_4 (■).

3.3. Cobalt-catalyzed coupling reaction

The catalytic activities of the p_2, pp_3 and bis[2-(diphenylphosphino)ethyl]phenylphosphine (p_3,) phosphine complexes, **1**, **4** and **5**, and the pp_3S_2 phosphine sulfide complex **6** for the cobalt-catalyzed coupling reaction of an alkyl halide with an alkene were compared using 2-iodobutane and *n*-butyl acrylate as the substrates. The changes in the yield of the formed *n*-butyl-4-methylhexanoate are plotted in Fig. 3. If an excess of *n*-butyl acrylate (more than 2 equivalents) and more Co catalyst (0.1 equivalents) were used, as described in the literature [4], a much higher yield was obtained for each ligand. However, in the present experiments, equimolar amounts of substrates and 0.04 equivalents of the Co catalysts were used in order to make the difference in the activity clearer. The catalytic activity of the phosphine sulfide complex **6** is definitely higher than those of the phosphine complexes **1**, **4** and **5**. The efficiency of phosphine sulfides was also shown by the reaction with a mixture of pp_3S_4 (pp_3 tetrasulfide) [5a] and CoI_2 (Fig. 3). Among the phosphine complexes, complex **4**, with the tetradentate phosphine ligand pp_3, showed the lowest activity, and the bidentate phosphine, p_2, does not deactivate the catalysis even in the case of the bis(p_2) complex **1**. On the other hand, the phosphine oxide group gives rise to deactivation, as observed for the reaction using the bis(p_2O_2) complex **3** as an analogue of **1**.

Phosphines have been reported to be quite versatile ligands so far, especially for Pd catalyzed coupling reactions [12]. However, phosphines are usually susceptible to oxidation to give inactive Pd black and addition of excess phosphines inhibits the catalytic reactions by blocking the substrate coordination. More recently, it has been reported that phosphine sulfides are more effective ligands for some Pd catalyzed C–C coupling reactions because phosphine sulfides can stabilize the active Pd(0) species, even in the air, and do not interfere with the oxidative addition of Pd(0) and subsequent coordination of substrates on Pd(II) [5]. The nature of P=X (X = O, S, Se) bonds has been extensively discussed and reviewed over the years [13]. In line with these discussions, the π accepting ability of the P=S bond of phosphine sulfides can stabilize low-valent metal centers to promote the generation of the catalytically active species. Also the polarizability of the P=S bond can be effective for coordination to higher positively charged metal ions, so as not to interfere with the oxidative addition of the active species. Furthermore, because phosphine sulfides are weak σ donors, forming relatively weak σ bonds, the coordination of another substrate and subsequent migration on the oxidized metal center are not blocked. The polarization of P=S bonds by coordination is observed even in the solid state, that is the P=S distances for coordinated p_2S_2 and pOp_2S_3 ligands (2.009–2.018 Å for $[PdCl_2(p_2S_2)]$ [14],

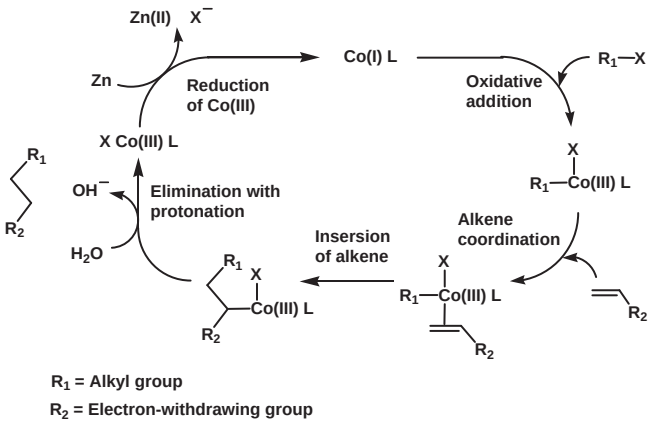

Scheme 2. Oxidative addition driven mechanism.

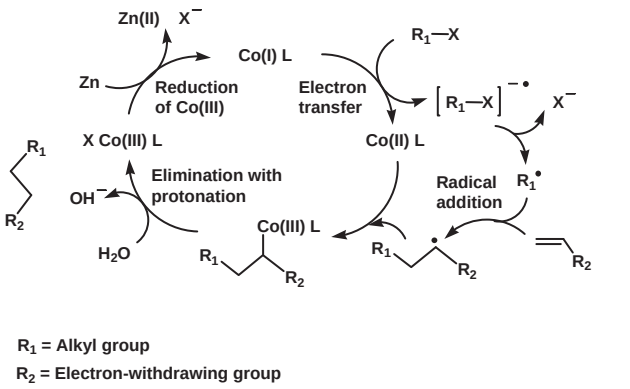

Scheme 3. Radical generation mechanism.

1.984–2.005 Å for $[Pd(p_2S_2)_2](BF_4)_2$ [5b] and 2.005–2.011 Å for $[Pd_3Cl_6(pp_3S_3)_2]$ [15]) are definitely elongated compared with those in the free phosphine sulfide, e.g. pp_3S_4 (1.957–1.958 Å) [16], while such a difference in bond distances is not clearly observed for phosphine oxides (1.449–1.518 Å for the bound P=O in **6** and 1.473–1.487 Å for the pendant P=O in $[Pd(4\text{-}ClC_6H_4S)(pp_3O)]^+$ and $[Pd(4\text{-}ClC_6H_4S)_2(pp_3O_2)]$ [17]). The present comparison of the catalytic activities also indicates the efficiency of phosphine sulfides in the case of the Co(I)/Co(III) catalytic cycle. On the other hand, the phosphine oxide p_2O_2 deactivated the Co catalyst, probably due to the poor π accepting ability resulting in destabilization of the Co(I) active species.

Two different reaction mechanisms for the catalytic cycle were proposed recently [4]. One is an oxidative addition driven mechanism (Scheme 2) in which the oxidative addition of a Co(I) species with an alkyl halide gives the alkyl Co(III) intermediate, followed by coordination of an alkene. The alkene is then inserted into the Co-alkyl bond, protonation gives the final reductive coupling product and reduction of the Co(III) species by zinc powder regenerates the active Co(I) species. The other is a radical generation mechanism (Scheme 3) in which electron transfer from a low-valent Co(I) species to an alkyl halide generates an alkyl radical, followed by radical addition to the acrylate, trapping by the Co(II) species to give the Co(III) intermediate. Subsequent protonation gives the final product, and reduction of Co(III), similar to the oxidative addition driven mechanism, regenerates the Co(I) species. It is obvious that the active catalyst is the Co(I) complex, generated by reduction of the Co(II) species with zinc powder, because the coupling product, *n*-butyl-4-methylhexanoate, was stoichiometrically formed by the reaction of the Co(I) complex **7** without zinc powder. Deactivation of complex **4** with the tetradentate pp_3 compared to the bis(p_2) complex **1** may be attributed to blocking the formation of the alkyl halide adduct and subsequent coordination of an alkene by the robust coordination structure with the tetradentate ligand. On the other hand, the tetradentate phosphine sulfides pp_3S_2 and pp_3S_4 do not interfere with the substrate coordination, probably due to partial dissociation of the weakly σ-donating phosphine sulfide groups on Co(III). These results are consistent with an oxidative addition driven mechanism with alkene coordination to the alkyl halide adduct.

Acknowledgments

This research was supported by Grant-in-Aid for Scientific Research (No. 23550068) from the Japan Society for the Promotion of Science.

Appendix A. Supplementary data

CCDC 923329 and 923330 contain the supplementary crystallographic data for **1** and **2**, respectively. These data can be obtained free of charge via http://www.ccdc.cam.ac.uk/conts/retrieving.html, or from the Cambridge Crystallographic Data Centre, 12 Union Road, Cambridge CB2 1EZ, UK; fax: +44 1223 336 033; or e-mail: deposit@ccdc.cam.ac.uk.

References

[1] (a) D. Alberico, M.E. Scott, M. Lautens, Chem. Rev. 107 (2007) 174;
(b) M. Miura, T. Satoh, Top. Organomet. Chem. 14 (2005) 55;
(c) L.-C. Campeau, K. Fagnou, Chem. Commun. (2006) 1253;
(d) I.Y. Seregin, V. Gevorgyan, Chem. Soc. Rev. 36 (2007) 1173;
(e) J. Ellman, Science 316 (2007) 1131.
[2] (a) S. Proch, R. Kempe, Angew. Chem., Int. Ed. 46 (2007) 3135;
(b) M. Lafrance, K. Fagnou, J. Am. Chem. Soc. 128 (2006) 16496;
(c) L. Ackermann, P. Novàk, R. Vicente, N. Hofmann, Angew. Chem., Int. Ed. 48 (2009) 6045;
(d) M. Tobisu, I. Hyodo, N. Chatani, J. Am. Chem. Soc. 131 (2009) 12070.
[3] (a) Y. Ikeda, T. Nakamura, H. Yorimitsu, K.J. Oshima, Am. Chem. Soc. 124 (2002) 6514;
(b) T. Fujioka, T. Nakamura, H. Yorimitsu, K. Oshima, Org. Lett. 4 (2002) 2257;
(c) H. Ohmiya, T. Tsuji, H. Yorimitsu, K. Oshima, Chem. Eur. J. 10 (2004) 5640.
[4] P. Shukla, Y.-C. Hsu, C.-H.J. Cheng, Org. Chem. 71 (2006) 655.
[5] (a) S. Aizawa, A. Majumder, Y. Yokoyama, M. Tamai, D. Maeda, A. Kitamura, Organometallics 28 (2009) 6067;
(b) S. Aizawa, M. Kondo, R. Miyatake, M. Tamai, Inorg. Chim. Acta 360 (2007) 2809.
[6] S. Aizawa, T. Iida, S. Funahashi, Inorg. Chem. 35 (1996) 5163.
[7] D. Fernández, M.I. G.-Seijo, T. Kégl, G. Petőcz, L. Kollár, M.E. G.-Fernández, Inorg. Chem. 41 (2002) 4435.
[8] (a) C.A. Ghilardi, S. Midollini, L. Sacconi, Inorg. Chem. 14 (1975) 1790;
(b) W.H. Hohman, D.J. Kountz, D.W. Meek, Inorg. Chem. 25 (1986) 616.
[9] A. Altomare, G. Cascarano, C. Giacovazzo, A. Guagliardi, M.C. Burla, G. Polidori, M. Camalli, J. Appl. Crystallogr. 27 (1994) 435.
[10] G.M. Sheldrick, SHELXL97, Program for Crystal Structure Refinement, University of Göttingen, Germany, 1997.
[11] (a) S. Aizawa, T. Hase, T.J. Wada, Organomet. Chem. 692 (2007) 813;
(b) S. Aizawa, T. Kawamoto, Y. Asai, C.J. Ishimura, Organomet. Chem. 695 (2010) 1253.
[12] (a) J. Tsuji, Palladium Reagents and Catalysts, Wiley, Chichester, 1995;
(b) R.F. Heck, Palladium Reagents in Organic Synthesis, VCH, Weinheim, 1996;
(c) A.J. Suzuki, Organomet. Chem. 576 (1999) 147;
(d) I.P. Beletskaya, A.V. Cheprakov, Chem. Rev. 100 (2000) 3009.
[13] (a) A. Streitwieser Jr., A. Rajca, R.S. McDowell, R.J. Glaser, Am. Chem. Soc. 109 (1987) 4184;
(b) D.G. Gilheany, Chem. Rev. 94 (1994) 1339;
(c) A.E. Reed, P.R.J. Schleyer, Am. Chem. Soc. 112 (1990) 1434;
(d) M.W. Schmidt, S. Yabushita, M.S.J. Gordon, Phys. Chem. 88 (1984) 382;
(e) P.A. Schultz, R.P.J. Messmer, Am. Chem. Soc. 115 (1993) 10925;
(f) P.A. Schultz, R.P.J. Messmer, Am. Chem. Soc. 115 (1993) 10938;
(g) J.A. Dobado, H. Martínez-García, J.M. Molina, M.R.J. Sundberg, Am. Chem. Soc. 120 (1998) 8461.
[14] T.S. Labana, R. Verma, A. Singh, M. Shikha, A. Castineiras, Polyhedron 21 (2002) 205.
[15] S. Aizawa, T. Kawamoto, S. Nishigaki, A.J. Sasaki, Organomet. Chem. 696 (2011) 2471.
[16] B. Deb, P.P. Sarmah, K. Saikia, A.L. Fuller, R.A.M. Randall, A.M.Z. Slawin, J.D. Woollins, D.K.J. Dutta, Organomet. Chem. 696 (2011) 3279.
[17] S. Aizawa, T. Kawamoto, K. Saito, Inorg. Chim. Acta 357 (2004) 2191.

EurJIC European Journal of Inorganic Chemistry
ChemPubSoc Europe
FULL PAPER

DOI:10.1002/ejic.201301070

Synthesis and Structures of Mixed-Valence Oxido-Bridged Diruthenium Complexes Bearing Ethylbis(2-pyridylmethyl)amine

CLUSTER ISSUE

Tomoyo Suzuki,[a] Kazuhiro Matsuya,[a] Tatsuya Kawamoto,[b] and Hirotaka Nagao*[a]

Keywords: Oxido ligands / Mixed-valent compounds / Redox chemistry / Ruthenium / Tridentate ligands

Trihalogenoruthenium(III) complexes bearing an ethylbis(2-pyridylmethyl)amine (ebpma) ligand, *fac*-[$Ru^{III}X_3$(ebpma)] (X = Cl, Br), were reduced by zinc in acetone that contained halogeno acid to afford a reddish-orange solution. Two kinds of dinuclear complexes were synthesized from the solution. After removing the remaining zinc and adding counterions such as PF_6^- and BF_4^- with water, the solution was allowed to stand under air until the color of the solution changed. New oxido-bridged dinuclear complexes of mixed-valence Ru^{III}–Ru^{IV} [{$Ru^{III,IV}X_2$(ebpma)}$_2$(μ-O)]Y (X = Cl, Y = PF_6, [**1**]PF_6; Y = BF_4, [**1**]BF_4; X = Br, Y = PF_6, [**2**]PF_6; Y = BF_4, [**2**]BF_4), which showed a similar framework to the reported water oxidation catalysts, were obtained as deep-colored solids. In the reaction without addition of extra water, a different mixed-valence dinuclear complex of Ru^{II}–Ru^{III} [{$Ru^{II,III}$(ebpma)}$_2$(μ-Cl)$_3$]$^{2+}$, for which the metal centers were triply bridged by three chlorides, was formed. The synthetic procedures are useful for the development of multinuclear frameworks that function as molecular catalysts for redox reactions such as water oxidation.

Introduction

Reduction and oxidation reactions are important processes for the activation and conversion of inert molecules to more useful materials. Metal complexes play important roles in redox reactions and have been widely investigated in connection with material- and energy-conversion systems such photosynthesis.[1] Water oxidation is one of the important processes for artificial photosynthesis, and various types of catalysts based on metal complexes with mononuclear and dinuclear frameworks have been developed.[2,3] In dinuclear complexes, bridging moieties are related to their electronic interaction between metal centers, redox behaviors, and reactivities. Oxido-bridged diruthenium complexes, such as the so-called blue dimer [{$Ru^{III,III}$(bpy)$_2$(H$_2$O)}$_2$(μ-O)]$^{4+}$ (bpy = 2,2′-bipyridyl), are first homogeneous catalysts and have attracted much interest as a catalyst for water oxidation.[2,4–6] The blue dimer has been actively investigated with respect to its electronic structure and properties. For oxido-bridged diruthenium complexes, it has been suggested that the higher oxidation states of Ru^{IV}–Ru^{IV}, Ru^{IV}–Ru^{V}, and Ru^{V}–Ru^{V} are important species in the water oxidation reactions. However, these complexes were too unstable for investigations on their structure and reactivity. The Ru^{III}–Ru^{III} and Ru^{III}–Ru^{IV} oxidation-state complexes have been investigated with regard to their structure and reactivity.[4,7,8] To create diruthenium frameworks and synthesize stable dinuclear complexes that show higher oxidation states such as Ru^{III}–Ru^{IV}, flexible tridentate ethylbis(2-pyridylmethyl)amine (ebpma),[9,10] as shown in Figure 1, was used as a supporting ligand.

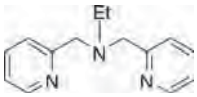

Figure 1. Tridentate ethylbis(2-pyridylmethyl)amine (ebpma).

In this study, new oxido-bridged diruthenium complexes bearing ebpma ([**1**]Y and [**2**]Y) have been synthesized, fully characterized, and their structures have been determined. These complexes have a novel mixed-valence state of Ru^{III} and Ru^{IV}. Their dinuclear frameworks were formed by means of reduction of the ruthenium center and dissociation of ligand(s) by using the Ru^{III} complex *fac*-[$Ru^{III}X_3$(ebpma)], similar to the previously reported dimerization reaction to afford triply bridged diruthenium complexes.[10]

Results and Discussion

Synthesis and Characterization of Oxido-Bridged Complexes

fac-[$Ru^{III}X_3$(ebpma)] (X = Cl or Br) was reduced by zinc in acetone containing aqueous HX. After addition of water

[a] Department of Materials and Life Sciences, Sophia University, 7-1 Kioicho, Chiyodaku, Tokyo 102-8554 Japan
E-mail: h-nagao@sophia.ac.jp
http://www.sophia.ac.jp
[b] Department of Chemistry, Kanagawa University, Hiratsuka, Kanagawa 259-1293, Japan
http://www.kanagawa-u.ac.jp
Supporting information for this article is available on the WWW under http://dx.doi.org/10.1002/ejic.201301070.

© 2014 Wiley-VCH Verlag GmbH & Co. KGaA, Weinheim

and NH_4PF_6 or NH_4BF_4 as a counter anion, the solutions were left standing under air at room temperature for 1 d to give deep orange or red crystals. The obtained complexes were characterized as the diruthenium complexes bridged by an oxido ligand in a mixed-valence state of Ru^{III}–Ru^{IV}, $[\{Ru^{III,IV}X_2(ebpma)\}_2(\mu\text{-}O)]PF_6\cdot(CH_3)_2CO$ [X = Cl ([**1**]-PF_6) or Br ([**2**]PF_6)] in approximately 60% yields. Spectral and electrochemical properties together with $\Delta\tilde{\nu}_{1/2}$ and K_c values (see below) are summarized in Table 1.

Table 1. Spectral and electrochemical properties.

	[**1**]PF_6	[**2**]PF_6
UV/Vis/NIR absorption bands		
λ [nm]	460 (17540)	500 (16490)
(ε [$M^{-1}cm^{-1}$])	1189 (380)	1196 (460)
Half bandwidths at half-maximum of NIR absorption bands		
$\Delta\tilde{\nu}_{1/2}$(found) [cm^{-1}]	3796	3714
$\Delta\tilde{\nu}_{1/2}$(calcd.) [cm^{-1}]	4408	4395
Redox potential		
$E1$ [V]	0.74	0.74
$E2$ [V]	–0.46	–0.39
$E3$ [V]	–1.39	–1.32
K_c	2.0×10^{20}	1.3×10^{19}

Since both diruthenium complexes as PF_6 salts, [**1**]PF_6 and [**2**]PF_6, were not sufficiently soluble in water and organic solvents usually used for electrochemistry, the BF_4 salts, [**1**]BF_4 and [**2**]BF_4, were synthesized in similar manners; the solubilities of the BF_4 salts were slightly higher than that of the PF_6 salts. Results of FAB MS showed molecular-ion peaks at m/z = 816 and 994 for the Cl and Br complexes, respectively, and other fragment peaks, thus indicating dissociation of halogeno ligands and/or ebpma without decomposition of their oxido-bridged dinuclear framework. Effective magnetic moments (μ_{eff}) of [**1**]PF_6 and [**2**]PF_6 at room temperature were 1.67 and 1.65 B.M., respectively, thus indicating the presence of one unpaired electron on two ruthenium centers. X-band ESR spectra were measured at both 77 K and room temperature. No ESR signals were observed for the solid state of both [**1**]BF_4 and [**2**]BF_4 at room temperature and 77 K. A broad and weak signal was observed at g = 2.54 in the frozen solution of [**2**]BF_4 in acetone/toluene at 77 K (Figure S1 in the Supporting Information), whereas for [**1**]BF_4, an ESR signal was not observed. UV/Vis and near-infrared (NIR) spectra of both [**1**]PF_6 and [**2**]PF_6 in acetonitrile are shown in Figure 2. A strong ligand-to-metal charge-transfer (LMCT) band at 460 nm for the Cl complex (black line) and 500 nm for the Br complex (gray line) were observed in the visible region. In the near-infrared region, weak broad intervalence charge transfer (IVCT) bands, that were characteristic of the mixed-valence complexes, were observed at 1189 and 1196 nm, respectively. Both dinuclear ruthenium complexes were characterized by X-ray crystallography.

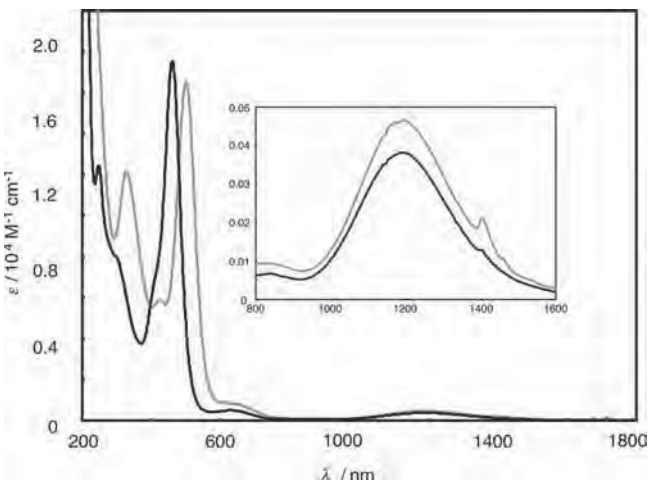

Figure 2. UV/Vis/NIR spectra of $[\{Ru^{III,IV}X_2(ebpma)\}_2(\mu\text{-}O)]PF_6$ ([**1**]PF_6, black line; [**2**]PF_6, gray line) in CH_3CN.

Structures of Oxido-Bridged Complexes

Single crystals of both Cl and Br complexes, [**1**]PF_6 and [**2**]PF_6, suitable for X-ray structural analysis were obtained by recrystallization from acetone solutions. The complexes crystallized with one acetone molecule in the unit cell.[11,12] The two ruthenium centers are bridged by the oxido ligand, and the geometries of both ruthenium centers were slightly distorted octahedral with one bridging oxido, two halogeno, and three nitrogen atoms of the ebpma ligand. The ebpma ligand coordinates in a facial configuration around each ruthenium center. The structure of $[\{Ru^{III,IV}Cl_2(ebpma)\}_2(\mu\text{-}O)]^+$ is shown in Figure 3 and that of $[\{Ru^{III,IV}Br_2(ebpma)\}_2(\mu\text{-}O)]^+$ in Figure S3 of the Supporting Information. The structures of both Cl and Br complexes are similar to each other within differences between the chlorido and bromido ligands. Bond lengths and angles are summarized in Table 2. The bond lengths between Ru

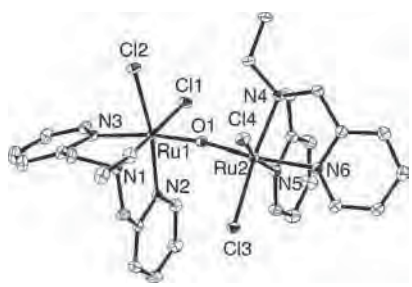

Figure 3. Structure of $[\mathbf{1}]^+$ with thermal ellipsoids at 50% probability. Hydrogen atoms are omitted for clarity.

Table 2. Selected bond lengths [Å] and angles [°].

	[**1**]PF_6	[**2**]PF_6
Ru–O	1.8248(19), 1.8200(19)	1.829(3), 1.826(3)
Ru–N(py)	*trans* toward the oxido:	
	2.095(3), 2.103(3)	2.108(4), 2.112(4)
	cis toward the oxido:	
	2.075(3), 2.064(3)	2.085(4), 2.072(4)
Ru–N(amine)	2.123(3), 2.129(3)	2.132(4), 2.151(4)
Ru–O–Ru	166.82(12)	167.70(17)

© 2014 Wiley-VCH Verlag GmbH & Co. KGaA, Weinheim

and O and the bond angles of Ru–O–Ru [1.8248(19), 1.8200(19) Å, and 166.82(12)° for the Cl complex, and 1.829(3), 1.826(3) Å, and 167.70(17)° for the Br complex] are in good agreement with those of previously reported Ru^{III}–Ru^{IV} mixed-valence oxido-bridged diruthenium complexes.[7,8] The Ru–O distances are shorter than those of Ru^{III}–Ru^{III} oxido-bridged diruthenium complexes[13–20] and are longer than those of Ru^{IV}–Ru^{IV} complexes.[21–26] The metric parameters of the ebpma ligand are similar to those of the previously reported complexes.[9,10] The Ru–N(py) (py = pyridine) distances *trans* with respect to the oxido ligand are slightly longer than those of the *cis* position.

Mixed-Valence State of Oxido-Bridged Complexes

Cyclic voltammograms of [**1**]PF_6 in acetonitrile show three waves as shown in Figure 4. A reversible oxidation wave, and two reversible and irreversible reduction waves were observed at *E*1, *E*2, and *E*3.

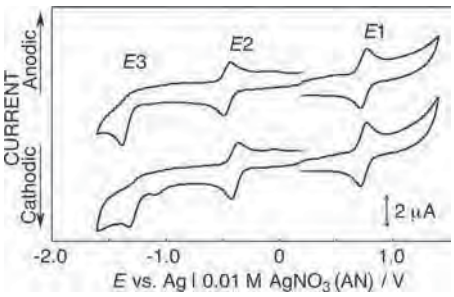

Figure 4. Cyclic voltammograms of [**1**]PF_6 and [**2**]PF_6 [3.0×10^{-4} M; [**1**]PF_6 (upper) and [**2**]PF_6 (lower)] in acetonitrile containing 0.1 M tetrabutylammonium hydroxide (TBAH) at room temperature with a scan rate of 100 mV s^{-1}.

These values of *E*1, *E*2, and *E*3 for the Cl and the Br complexes are shown in Table 1. Two reversible oxidation and reduction waves at *E*1 and *E*2 are assigned to Ru^{IV}–Ru^{IV}/Ru^{III}–Ru^{IV} and Ru^{III}–Ru^{IV}/Ru^{III}–Ru^{III} processes, respectively. These two reversible waves were confirmed to be one-electron reaction processes by analysis using hydrodynamic voltammetry (HDV) and controlled potential electrolysis (CPE) shown in Figures S4A and S5A of the Supporting Information. The wide differences between the redox potentials of the reversible Ru^{IV}–Ru^{IV}/Ru^{III}–Ru^{IV} and Ru^{III}–Ru^{IV}/Ru^{III}–Ru^{III} couples, $\Delta E = E1 - E2$, for both Cl and Br complexes indicate the stability of the mixed-valence state of Ru^{III}–Ru^{IV}.[26] The values of comproportionation constant K_c, calculated by ΔE, is 2.0×10^{20} for complex **1** and 1.3×10^{19} for complex **3**. These K_c values are similar to those of reported Ru–O–Ru complexes of Ru^{III}–Ru^{IV} and larger than those of Ru^{II}–Ru^{III}[4] and that of the triply chlorido- and methoxido-bridged Ru^{II}–Ru^{III} mixed-valence complex with ebpma, $[\{Ru^{II,III}(ebpma)\}_2(\mu\text{-Cl})(\mu\text{-OCH}_3)_2]^{2+}$.[10] In addition to the large K_c value, half bandwidths at half-maximum, $\Delta\tilde{\nu}_{1/2}$(calcd.), were estimated according to Hush's theory: 4408 cm^{-1} for [**1**]PF_6 and 4395 cm^{-1} for [**2**]PF_6 (Table 1). The experimental half bandwidths (3796 cm^{-1} for [**1**]PF_6 and 3714 cm^{-1} for [**2**]PF_6) are smaller than the theoretical values. These results of analysis of IVCT bands could be interpreted as the result of strong electronic coupling. Both Cl and Br complexes are classified as Class III according to the Robin–Day classification of mixed-valence states.[27]

Redox Behaviors of Oxido-Bridged Complexes

These oxido-bridged complexes of Ru^{III}–Ru^{IV} were electrochemically oxidized and reduced by CPE in acetonitrile at room temperature and –40 °C, and the ensuing reactions were monitored by cyclic voltammetry (CV) to investigate relationships between reactivities and oxidation states of the metal centers. The oxidative CPE experiments for both [**1**]BF_4 and [**2**]BF_4 at 0.85 V reveal that the oxidation waves at 0.74 V are assigned to one-electron oxidation processes from Ru^{III}–Ru^{IV} to Ru^{IV}–Ru^{IV}. The oxidized forms Ru^{IV}–Ru^{IV} of both complexes were stable under CPE experimental conditions (Figures S4B and S5B in the Supporting Information). For [**1**]BF_4, the UV/Vis spectrum also reversibly changed between Ru^{III}–Ru^{IV} and Ru^{IV}–Ru^{IV} states with isosbestic points using an optical transparent thin-layer electrode (OTTLE) cell as shown in Figure S4C of the Supporting Information.

Changes in cyclic voltammograms of [**1**]BF_4 during reductive CPE experiments are shown in Figure 5; those of [**2**]BF_4 are in Figure S7B of the Supporting Information.

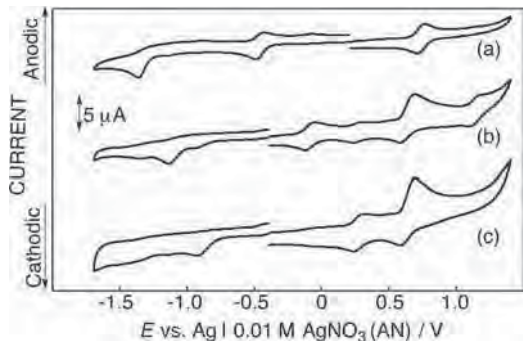

Figure 5. Change in the cyclic voltammograms during reductive CPE of [**1**]BF_4 (5.0×10^{-4} M) in acetonitrile: (a) before CPE, (b) after one-electron reduction at –0.5 V, and (c) after standing for 1 d.

The first reversible reduction waves of the original complexes, observed at –0.46 V for the Cl complexes and –0.39 V for the Br complexes, were confirmed to be one-electron processes by changes in HDV during CPE at –0.5 V (Figures S6A and S7A in the Supporting Information). During one-electron reduction by CPE, three waves of the original complex decreased, and three new waves appeared at more positive potentials around 1.1, –0.1, and –1.1 V with the appearance of another new wave around 0.7 V, which was assigned to an oxidation wave of Cl^- as shown in Figure 5b. One-electron-reduced forms Ru^{III}–Ru^{III} of both Cl and Br complexes were unstable at room temperature and changed into new complexes that kept their dinuclear frameworks to afford Ru^{III}–Ru^{III} complexes. Observation of the oxidation wave of Cl^- at 0.7 V

© 2014 Wiley-VCH Verlag GmbH & Co. KGaA, Weinheim

and positive shifts of the waves for [**1**]BF_4 indicate that dissociation of the Cl ligand(s) and coordination of acetonitrile to the ruthenium center(s) occur. After the samples had stood for 1 d, these waves were shifted to further positive potentials, and there was a further increase in the Cl oxidation wave (Figure 5c and Figure S7c in the Supporting Information). These results reveal that substitution of Cl ligands was made possible by reduction to the Ru^{III}–Ru^{III} state to give the $\{Cl_{2-n}(CH_3CN)_nRu^{III}(\mu\text{-}O)Ru^{III}Cl_{2-m}(CH_3CN)_m\}^{(n+m)+}$ moiety (n, m = 0–2). Attempts to synthesize a new oxido-bridged complex under several different conditions were unsuccessful. Reversible spectral changes with an oxidation state between Ru^{III}–Ru^{IV} and Ru^{III}–Ru^{III} of the central metals for [**1**]BF_4 were observed using an OTTLE cell as shown in Figure 6. The strong LMCT band at 460 nm disappeared, and a new metal-to-ligand charge-transfer (MLCT) band appeared at 604 nm with electrochemical reduction of [**1**]BF_4. The spectrum of the Ru^{III}–Ru^{IV} complex was reversibly regenerated by oxidation from the Ru^{III}–Ru^{III} to the Ru^{III}–Ru^{IV} state, thus indicating that the Ru^{III}–Ru^{III} state was stable for this experimental period (ca. 10 min). These characteristic bands for the Ru^{III}–Ru^{IV} and the Ru^{III}–Ru^{III} complexes are similar to those for $[(bpy)_2(H_2O)Ru^{III}(\mu\text{-}O)Ru^{IV}(bpy)_2(OH)]^{4+}$ and $[\{Ru^{III,III}(bpy)_2(H_2O)\}_2(\mu\text{-}O)]^{4+}$.[4–6,19]

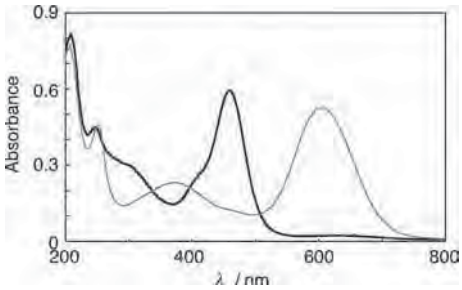

Figure 6. UV/Vis spectra of [**1**]BF_4 (2.50×10^{-4} M; black line) in acetonitrile and after reduction using an OTTLE cell (gray line).

Further reduction of both [**1**]BF_4 and [**2**]BF_4 to the Ru^{II} state were carried out by CPE at –40 °C (Figures S8 and S9 in the Supporting Information). The one-electron-reduced form was generated by CPE at –0.40 V and was stable under electrochemical conditions at –40 °C as shown in Figures S8b and S9b in the Supporting Information. For further reduction of the one-electron-reduced form, the Ru^{III}–Ru^{III} state, at –1.60 V, two moles of electrons based on the amount of the starting compounds [**1**]BF_4 and [**2**]BF_4 were consumed. The reduced complexes slightly changed to new complexes that showed redox waves around 0 and 0.6 V with the oxidation wave of Cl^- around 0.7 V. According to the redox potential, the reduction product around 0.6 V seemed to be a mononuclear ruthenium(II) complex such as $[Ru^{II}Cl(NCCH_3)_2(ebpma)]^+$.[9] When comparing CV-profile changes during these CPE experiments for both Cl and Br complexes at room temperature and –40 °C, the Br complex was more reactive than the Cl complex.

Catalytic activities of both compounds [**1**]PF_6 and [**2**]PF_6 for the water oxidation reaction were examined by CV of an acetonitrile solution with the addition of H_2O as shown in Figure S10 of the Supporting Information. Although significant current increases were not observed, the change in the current using the Br complex [**2**]PF_6 was slightly higher than that of the Cl complex [**1**]PF_6.

Formation of Oxido-Bridged Diruthenium Frameworks

The present oxido-bridged dinuclear ruthenium complexes of Ru^{III}–Ru^{IV} seemed to be formed by means of formation and substitution of the triply bridged halogeno complex, $[\{Ru^{II,II}(ebpma)\}_2(\mu\text{-}X)_3]^+$ (X = Cl, Br), and oxidation in acetone solutions with or without water as shown in Scheme 1. In the reduction of $[Ru^{III}Cl_3(ebpma)]$ in acetone by Zn with hydrochloric acid, an orange solution was generated at the early stage of the reaction. H_2O was added to the solution, and the solution was allowed to stand for 1 d to yield complex **1** by addition of NH_4PF_6 as a precipitant. In the absence of H_2O, a dark blue solution was obtained after the sample had stood for 2 h, and the deep blue complex was isolated by addition of NH_4PF_6. This deep blue complex $[\{Ru^{II,III}(ebpma)\}_2(\mu\text{-}Cl)_3]^{2+}$ has a diruthenium framework, the ruthenium centers of which are bridged by three Cl ligands. The structure is similar to that of the reported diruthenium complex $[\{Ru^{II,III}(ebpma)\}_2(\mu\text{-}Cl)(\mu\text{-}OCH_3)_2]^{2+}$.[10] Compounds [**1**]$PF_6$ and [**2**]PF_6 were also synthesized by reduction of $[\{Ru^{II,III}(ebpma)\}_2(\mu\text{-}Cl)_3]^+$ and standing under air in the presence of H_2O. A brown complex was isolated from the orange solution by the addition of NH_4PF_6 and H_2O as a poor solvent. The isolated brown complex was unstable, and the color of the complex in the solid state quickly changed to green under air. CV of the obtained orange complex showed two reversible waves at –0.14 and 0.84 V, the same as that of $[\{Ru^{II,III}(ebpma)\}_2(\mu\text{-}Cl)_3]^{2+}$ in CH_3CN, whereas their rest potentials were different from each other (Figure S11 in the Supporting Information). Thus, the brown complex was identified as a triply chlorido-bridged diruthenium complex of Ru^{II}–Ru^{II}, $[\{Ru^{II,II}(ebpma)\}_2(\mu\text{-}Cl)_3]^+$.

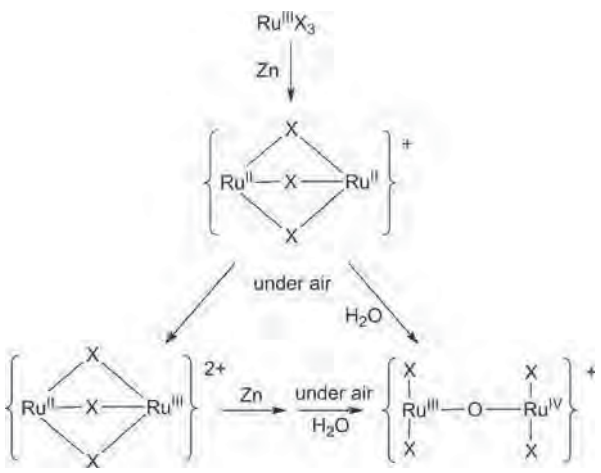

Scheme 1. Formation of $[\{Ru^{III,IV}X_2(ebpma)\}_2(\mu\text{-}O)]^+$.

© 2014 Wiley-VCH Verlag GmbH & Co. KGaA, Weinheim

Conclusion

Oxido-bridged diruthenium complexes of Ru^{III}–Ru^{IV} were synthesized through the formation of $[\{Ru^{II,II}(ebpma)\}_2(\mu\text{-}X)_3]^+$ (X = Cl, Br) and reaction with H_2O followed by oxidation under air. The properties of both Cl and Br complexes are similar to each other within differences in the nature between Cl^- and Br^- ligands. The reactivity of the Br complex is slightly higher than that of the Cl complex. Although significant catalytic activities of both Cl and Br complexes for the water oxidation reaction were not observed by cyclic voltammetry of an acetonitrile solution with the addition of H_2O, the catalytic activity of the Br complex was slightly higher than that of the Cl complex, as shown in Figure S10 of the Supporting Information. Whereas the Ru–O–Ru framework is stable in the Ru^{III}–Ru^{IV} and Ru^{IV}–Ru^{IV} oxidation states, reduction to the one-electron-reduced form, the Ru^{III}–Ru^{III} state, affords a new complex in which the chlorido ligand(s) was substituted. Further reduction to the Ru^{II} state induces decomposition of the Ru–O–Ru framework. These results indicate that stabilization of higher oxidation states such as Ru^{III}–Ru^{IV} and Ru^{IV}–Ru^{IV} is important for the development of a homogeneous water oxidation catalyst. The Ru^{III}–Ru^{IV} species would be one of the important complexes for understanding the catalytic function of the oxido-bridged dinuclear complex. Attempts to prepare new oxido-bridged dinuclear ruthenium complexes by substitution of the halogeno ligands of $[\{Ru^{III,IV}X_2(ebpma)\}_2(\mu\text{-}O)]^+$ (X = Cl, Br) under various conditions and by reduction of the metal center are under investigation.

Experimental Section

Measurements: IR spectra were recorded with a Perkin–Elmer FT-2000 FTIR spectrophotometer using samples prepared as KBr disks. Elemental analyses were carried out with a Perkin–Elmer 2400-II. Magnetic-susceptibility measurements were carried out at room temperature with a Sherwood Scientific Magway MSB MK1 balance. X-band ESR spectra were measured with a JEOL JES-FA300 ESR spectrometer at both 77 K and room temperature. UV/Vis/NIR spectra were obtained with a Shimadzu MultiSpec-1500 diode array spectrophotometer and a JASCO V-570. CV, normal pulse voltammetry (NPV), and differential pulse voltammetry (DPV) were carried out on acetonitrile solutions that contained tetraethylammonium perchlorate (TEAP; 0.1 M) from Nakarai Tesque, Ltd., tetra(*n*-butyl)ammonium hexafluorophosphate (TBAH; 0.1 M), or tetra(*n*-butyl)ammonium tetrafluoroborate (TBAT; 0.1 M) as supporting electrolyte with a platinum disk working electrode (ϕ = 1.6 mm) and an $Ag/AgNO_3$ (0.01 M) reference electrode with a BAS 100B/W electrochemical analyzer. HDV was carried out with a rotating platinum-disk working electrode (ϕ = 3.0 mm) and a BAS RDE-2 rotating electrode. Electrochemical reduction and oxidation were performed by the controlled potential electrolysis (CPE) technique. CPE was carried out in a three-compartment cell with a platinum-gauze working electrode in the first compartment, an auxiliary electrode in the second compartment, and a reference electrode in the third compartment with a Huso Polarograph Model 312 and 343B digital coulometer. At the end of each measurement, ferrocene was added as an internal standard to correct redox potentials.

$[\{Ru^{III,IV}Cl_2(ebpma)\}_2(\mu\text{-}O)]PF_6\cdot(CH_3)_2CO$ {[1]$PF_6\cdot(CH_3)_2CO$}: *fac*-$[RuCl_3(ebpma)]$ (102 mg, 0.23 mmol) was suspended in acetone (15 cm^3) that contained hydrochloric acid (0.12 cm^3). Zinc powder was added, and the mixed solution was stirred for 4 h to give an orange solution. After removing the remaining zinc, water (2 cm^3) and NH_4PF_6 (55 mg, 0.34 mmol) as a precipitant were added. The reddish-orange solution was allowed to stand under air at room temperature for 1 d. The deep-orange product obtained was collected by filtration, washed with ethanol and diethyl ether, and dried under vacuum. $[\{RuCl_2(ebpma)\}_2(\mu\text{-}O)]PF_6$ was recrystallized several times from acetone. Yield: 64 mg, 57%. $[\{RuCl_2(ebpma)\}_2O]PF_6\cdot(CH_3)_2CO$ (1017.60): calcd. C 36.59, H 3.96, N 8.26; found C 36.52, H 4.16, N 8.09. FAB MS: *m*/*z* = 816 [M – PF_6], 781 [M – Cl – PF_6], 674 [M – 4 Cl – PF_6]. Electrochemical properties (CV in CH_3CN): E_{pa} = –1.39 V ($Ru^{III,III}/Ru^{II,II}$), $E_{1/2}$ = –0.46 V ($Ru^{III,IV}/Ru^{III,III}$), $E_{1/2}$ = 0.74 V ($Ru^{IV,IV}/Ru^{III,IV}$) versus $Ag/AgNO_3(CH_3CN)$ (0.01 M). μ_{eff} = 1.67 B.M. Thermogravimetric analysis showed a gentle mass loss of approximately 6–8% at 100–200 °C.

$[\{Ru^{III,IV}Cl_2(ebpma)\}_2(\mu\text{-}O)]BF_4\cdot2(CH_3)_2CO$ {[1]$BF_4\cdot2(CH_3)_2CO$}: The complex was synthesized by a procedure similar to that for [**1**]-PF_6, but NH_4BF_4 (118 mg, 1.13 mmol) was used as precipitant. Yield: 93 mg, 70%. $[\{RuCl_2(ebpma)\}_2O]BF_4\cdot2(CH_3)_2CO$ (1017.52): calcd. C 39.49, H 4.38, N 8.50; found C 39.35, H 4.50, N 8.40.

$[\{Ru^{III,IV}Br_2(ebpma)\}_2(\mu\text{-}O)]PF_6\cdot(CH_3)_2CO$ {[1]$PF_6\cdot(CH_3)_2CO$} and $[\{Ru^{III,IV}Br_2(ebpma)\}_2(\mu\text{-}O)]BF_4\cdot2H_2O$ {[2]$BF_4\cdot2H_2O$}: These complexes were synthesized by the same procedure as for the chlorido complex but using *fac*-$[RuBr_3(ebpma)]$ (68 mg, 0.12 mmol) and hydrobromic acid (0.10 cm^3). Yield: 77 mg, 73% for the PF_6 salt and 47 mg, 69% for the BF_4 salt. $[\{RuBr_2(ebpma)\}_2O]PF_6\cdot(CH_3)_2CO$ (1195.41): calcd. C 31.15, H 3.37, N 7.03; found C 31.26, H 3.56, N 6.98. FAB MS: *m*/*z* = 994 [M – PF_6], 913 [M – Br – PF_6], 834 [M – 2 Br – PF_6]. Electrochemical properties (CV in CH_3CN): E_{pa} = –1.32 V ($Ru^{III,III}/Ru^{II,II}$), $E_{1/2}$ = –0.39 V ($Ru^{III,IV}/Ru^{III,III}$), $E_{1/2}$ = 0.74 V ($Ru^{IV,IV}/Ru^{III,IV}$) versus $Ag/AgNO_3(CH_3CN)$ (0.01 M). μ_{eff} = 1.65 B.M. $[\{RuBr_2(ebpma)\}_2O]BF_4\cdot2H_2O$ (1115.20): calcd. C 30.16, H 3.43, N 7.54; found C 30.06, H 3.42, N 7.08.

$[\{Ru^{II,III}(ebpma)\}_2(\mu\text{-}Cl)_3](PF_6)_2$: *fac*-$[RuCl_3(ebpma)]$ (150 mg, 0.35 mmol) was suspended in acetone (15 cm^3) that contained hydrochloric acid (0.5 cm^3). Zinc powder was added, and the mixed solution was stirred for 4 h to give an orange solution. After removing the remaining zinc, the solution was allowed to stand under air at room temperature for 2 h until the color changed to dark blue. NH_4PF_6 (300 mg, 1.84 mmol) was added to the solution as a precipitant. The deep blue product obtained was collected by filtration, washed with water, ethanol and diethyl ether, and dried under vacuum. Yield: 155 mg, 85%. $[\{Ru(ebpma)\}_2Cl_3](PF_6)_2$ (1053.04): calcd. C 31.94, H 3.25, N 7.98; found C 32.17, H 3.39, N 7.63. FAB MS: *m*/*z* = 765 [M – 2 PF_6]. Electrochemical properties (CV in CH_3CN): $E_{1/2}$ = –0.14 V ($Ru^{II,III}/Ru^{II,II}$), $E_{1/2}$ = 0.84 V ($Ru^{III,III}/Ru^{II,III}$) versus $Ag/AgNO_3(CH_3CN)$ (0.01 M). μ_{eff} = 1.94 B.M.

X-ray Crystallography: Single crystals of [**1**]$PF_6\cdot(CH_3)_2CO$ and [**2**]$PF_6\cdot(CH_3)_2CO$ were obtained by recrystallization from the acetone solution and then vapor diffusion of diethyl ether into the solution or slow concentration of the acetone solution. Intensity data were collected with a Rigaku Mercury CCD diffractometer using graphite-monochromated Mo-K_α radiation (0.71075 Å). All the calculations were carried out using the Crystal Structure software package.[28] Structures were solved by direct methods, expanded using Fourier techniques, and refined using full-matrix least-

© 2014 Wiley-VCH Verlag GmbH & Co. KGaA, Weinheim

squares techniques on F^2 using SHELXL97.[29] The crystallographic data are summarized in Table S1 of the Supporting Information, selected bond lengths and angles are in Table S2 of the Supporting Information, and structures of the complex cations are shown in Figures S2 and S3 of the Supporting Information. CCDC-955811 {[**1**]PF_6·$(CH_3)_2CO$ measured at 93 K}, -956150 {[**1**]PF_6·$(CH_3)_2CO$ measured at 298 K}, -955812 {[**2**]PF_6·$(CH_3)_2CO$ measured at 93 K}, and -956150 {[**2**]PF_6·$(CH_3)_2CO$ measured at 298 K} contain the supplementary crystallographic data for this paper. These data can be obtained free of charge from The Cambridge Crystallographic Data Centre via www.ccdc.cam.ac.uk/data_request/cif.

Supporting Information (see footnote on the first page of this article): ESR, X-ray crystallography, electrochemical behaviors, and UV/Vis/NIR data.

Acknowledgments

We thank Prof. R. Miyamoto at Hirosaki University for a helpful discussion of ESR measurements.

[1] a) T. J. Meyer, M. H. V. Huynh, H. H. Thorp, *Angew. Chem.* **2007**, *119*, 5378; *Angew. Chem. Int. Ed.* **2007**, *46*, 5284 and references cited therein; b) K. Arifin, E. J. Majlan, W. R. W. Daud, M. B. Kassim, *Int. J. Hydrogen Energy* **2012**, *37*, 3066.
[2] For example: a) C. W. Chronister, R. A. Binstead, J. Ni, T. J. Meyer, *Inorg. Chem.* **1997**, *36*, 3814; b) J. K. Hurst, J. Zhou, Y. Lei, *Inorg. Chem.* **1992**, *31*, 1010.
[3] For example: a) C. D. Giovanni, L. Vaquer, X. Sala, J. Benet-Buchholz, A. Llobet, *Inorg. Chem.* **2013**, *52*, 4335, and references cited therein; b) Y. Jiang, F. Li, B. Zhang, X. Li, X. Wang, F. Huang, L. Sun, *Angew. Chem. Int. Ed.* **2013**, *52*, 3398.
[4] J. W. Jurss, J. J. Concepcion, J. M. Butler, K. M. Omberg, L. M. Baraldo, D. G. Thompson, E. L. Lebeau, B. Hornstein, J. R. Schoonover, H. Jude, J. D. Thompson, D. M. Dattelbaum, R. C. Rocha, J. L. Templeton, T. J. Meyer, *Inorg. Chem.* **2012**, *51*, 1345.
[5] F. Liu, J. J. Concepcion, J. W. Jurss, T. Cardolaccia, J. L. Templeton, T. J. Meyer, *Inorg. Chem.* **2008**, *47*, 1727.
[6] J. K. Hurst, J. L. Cape, A. E. Clark, S. Das, C. Qin, *Inorg. Chem.* **2008**, *47*, 1753.
[7] A. D. Ryabov, R. Le Lagadec, H. Estevez, R. A. Toscano, S. Hemandez, L. Alexandrova, V. S. Kurova, A. Fischer, C. Sirlin, M. Pfeffer, *Inorg. Chem.* **2005**, *44*, 1626.
[8] J. R. Schoonover, J.-F. Ni, L. Roecker, P. S. White, T. J. Meyer, *Inorg. Chem.* **1996**, *35*, 5885.
[9] a) J. Mola, I. Romero, M. Rodriguez, F. Bozoglian, A. Poater, M. Solâ, T. Parella, J. Benet-Buchholz, X. Fontrodona, A. Llobet, *Inorg. Chem.* **2007**, *46*, 10707; b) J. Mola, M. Rodríguez, I. Romero, A. Llobet, T. Parella, A. Poater, M. Duran, M. Solá, J. Benet-Buchholz, *Inorg. Chem.* **2006**, *45*, 10520.
[10] K. Matsuya, S. Fukui, Y. Hoshino, H. Nagao, *Dalton Trans.* **2009**, 7876, and references cited therein.
[11] Crystallographic data for [{$Ru^{III,IV}Cl_2$(ebpma)}$_2$(μ-O)$_3$]-PF_6·$(CH_3)_2CO$: monoclinic, $P2_1/n$, a = 9.6494(8) Å, b = 14.8044(11) Å, c = 27.2349(19) Å, b = 92.073(5)°, V = 3888.1(5) Å^3, Z = 4, T = 93 K, 38106 reflections collected, 8892 unique (R_{int} = 0.0472), $R1$ = 0.0371, wR_2 = 0.0884 [$I > 2\sigma(I)$], GOF = 1.075.
[12] Crystallographic data for [{$Ru^{III,IV}Br_2$(ebpma)}$_2$(μ-O)$_3$]-PF_6·$(CH_3)_2CO$: monoclinic, $P2_1/n$, a = 9.7159(6) Å, b = 15.1126(9) Å, c = 27.2953(17) Å, b = 92.882(3)°, V = 4002.8(5) Å^3, Z = 4, T = 93 K, 39290 reflections collected, 9165 unique (R_{int} = 0.0340), $R1$ = 0.0427, wR_2 = 0.1122 [$I > 2\sigma(I)$], GOF = 1.091.
[13] W.-Z. Wang, X. Liu, D.-Z. Liao, Z.-H. Jiang, S.-P. Yan, G.-L. Wang, *Inorg. Chem. Commun.* **2002**, *5*, 1007.
[14] E. L. Lebeau, S. A. Aseyemi, T. J. Meyer, *Inorg. Chem.* **1998**, *37*, 6476.
[15] C. Koshi, K. Umakoshi, Y. Sasaki, *Chem. Lett.* **1997**, 1155.
[16] O. Ishitani, P. S. White, T. J. Meyer, *Inorg. Chem.* **1996**, *35*, 2167.
[17] R. Schneider, T. Weyhermüller, K. Wieghardt, *Inorg. Chem.* **1993**, *32*, 4925.
[18] J. Emerson, M. J. Clarke, W.-L. Ying, D. R. Sabadi, *J. Am. Chem. Soc.* **1993**, *115*, 11799.
[19] J. A. Gilbert, D. S. Eggleston, W. R. Murphy, Jr., D. A. Geselowitz, S. W. Gersten, D. J. Hodgson, T. J. Meyer, *J. Am. Chem. Soc.* **1985**, *107*, 3855.
[20] D. W. Phelps, E. M. Kahn, D. J. Hodgson, *Inorg. Chem.* **1975**, *14*, 2486.
[21] J.-L. Zhang, C.-M. Che, *Chem. Eur. J.* **2005**, *11*, 3899.
[22] E. Gallo, A. Caselli, F. Ragaini, S. Fantauzzi, N. Masciocchi, A. Sironi, S. Cenini, *Inorg. Chem.* **2005**, *44*, 2039.
[23] S. K. Tyrlik, M. Kisielinska, J. C. Huffman, *Trans. Annu. Meet. Orthop. Res. Soc. Trans. Met. Chem.* **1995**, *20*, 413.
[24] J. P. Collman, C. E. Barnes, P. J. Brothers, T. J. Collins, T. Ozawa, J. C. Gallucci, J. A. Ibers, *J. Am. Chem. Soc.* **1984**, *106*, 5151.
[25] H. Masuda, T. Taga, K. Osaki, H. Sugimoto, M. Mori, H. Ogoshi, *Bull. Chem. Soc. Jpn.* **1982**, *55*, 3887.
[26] H. Masuda, T. Taga, K. Osaki, H. Sugimoto, M. Mori, H. Ogoshi, *J. Am. Chem. Soc.* **1981**, *103*, 2199.
[27] *Mixed Valency Systems – Applications in Chemistry, Physics and Biology* (Ed.: K. Prassides), Kluwer Academic Publishers, Dordrecht, **1991**.
[28] *Crystal Structure 4.0.1, Single Crystal Structure Analysis Software*, Molecular Structure Corp. and Rigaku Corp., The Woodlands, TX and Rigaku, Tokyo, **2010**.
[29] G. Sheldrick, *SHELXL97, Program for Structure Refinement*, University of Göttingen, Germany, **1997**.

Received: August 19, 2013
Published Online: November 5, 2013

© 2014 Wiley-VCH Verlag GmbH & Co. KGaA, Weinheim

Polyhedron 52 (2013) 389–397

Contents lists available at SciVerse ScienceDirect

Polyhedron

journal homepage: www.elsevier.com/locate/poly

2:2-Type complexes of zirconium(IV)/hafnium(IV) centers with mono-lacunary Keggin polyoxometalates: Syntheses and molecular structures of $[(\alpha\text{-}SiW_{11}O_{39}M)_2(\mu\text{-}OH)_2]^{10-}$ (M = Zr, Hf) with edge-sharing octahedral units and $[(\alpha\text{-}SiW_{11}O_{39}M)_2(\mu\text{-}OH)_3]^{11-}$ with face-sharing octahedral units

Hironori Osada, Akio Ishikawa, Yoshio Saku, Yoshitaka Sakai, Yusuke Matsuki, Satoshi Matsunaga, Kenji Nomiya *

Department of Chemistry, Faculty of Science, Kanagawa University, Hiratsuka, Kanagawa 259-1293, Japan

ARTICLE INFO

Article history:
Available online 1 September 2012

We dedicate this paper to Professor Alfred Werner on the 100th anniversary of his Nobel Prize in Chemistry.

Keywords:
Polyoxometalates (POMs)
Zr^{IV} and Hf^{IV} atoms
Sandwiched structure
Face-sharing
X-ray structure analysis

ABSTRACT

This paper describes the syntheses and crystal structures of a set of novel 2:2-type Zr^{IV}/Hf^{IV}-containing Keggin complexes with edge-sharing and face-sharing linkages prepared under different pH conditions, each consisting of di-Zr^{IV}/Hf^{IV} cluster cations sandwiched between two mono-lacunary α-Keggin polyoxometalates (POMs) with an Si heteroatom, i.e., $(Et_2NH_2)_{10}[(\alpha\text{-}SiW_{11}O_{39}M)_2(\mu\text{-}OH)_2]\cdot 4H_2O$ (M = Zr, **Zr-edge**; Hf, **Hf-edge**) and $(Et_2NH_2)_{11}[(\alpha\text{-}SiW_{11}O_{39}M)_2(\mu\text{-}OH)_3]\cdot 15H_2O$ (M = Zr, **Zr-face**; Hf, **Hf-face**). The two central Zr and Hf atoms of the **Zr-edge** and **Hf-edge** are linked by two μ-OH groups, i.e., an edge-sharing linkage, whereas those of the **Zr-face** and **Hf-face** are linked by three μ-OH groups, i.e., a face-sharing linkage. Previously reported Zr/Hf-containing POM dimers were generally linked by edge-sharing $M(OH)_2M$ (M = Zr, Hf) bonds. Therefore, the present **Zr-face** and **Hf-face** are the first examples of Zr/Hf-containing POM dimers linked in a face-sharing fashion.

© 2012 Elsevier Ltd. All rights reserved.

1. Introduction

The coordination chemistry of polyoxometalates (POMs) with d^0 transition metals has been particularly well documented in the past few decades. Indeed, the d^0 transition metal derivatives of polyoxoanions have attracted considerable attention in the fields of catalysis, surface science, and materials science because POMs are often considered as molecular analogs of oxides in terms of structure [1–19]. In the Group IV (d^0) metal ion-containing POMs, the Zr/Hf atoms function very similarly to each other but show quite different behavior from the Ti atom [20]. The Zr and Hf atoms in the group IV metals, compared with the Ti atom (ionic radius 0.75 Å and a maximum coordination number of 6 in POMs), have larger ionic radii (approximately 0.85 Å) and show higher coordination numbers (6, 7, and 8). Therefore, if they are incorporated into the POMs, a wide variety of molecular structures are anticipated. Furthermore, Lewis acid catalysis in the coordinatively unsaturated complexes of Zr and Hf atoms is also anticipated.

Following the development of Ti^{IV}-containing POMs, there has been a dramatic advance in recent years in studies on various types of Zr^{IV}/Hf^{IV} complexes in combination with several lacunary POMs [21–54]. For example, the following have been reported as Zr^{IV}/Hf^{IV} sandwich-structured complexes with the same compositions and formulas: mono-nuclear, 8-coordinate metal complexes sandwiched between two mono-lacunary α-Keggin- and α_2-Dawson-type POMs, i.e., $[M(\alpha\text{-}PW_{11}O_{39})_2]^{10-}$ (M = Hf, Zr; the Keggin 1:2 complexes) and $[M(\alpha_2\text{-}P_2W_{17}O_{61})_2]^{16-}$ (the Dawson 1:2-type complexes), respectively [34,46]; di- and tetra-nuclear 7-coordinate metal complexes sandwiched between two γ-Keggin silicotungstates, i.e., $[\{M(H_2O)\}_2(\mu\text{-}OH)_2(\gamma\text{-}SiW_{10}O_{36})_2]^{10-}$ and $[\{M(H_2O)\}_4(\mu_4\text{-}O)(\mu\text{-}OH)_6(\gamma\text{-}SiW_{10}O_{36})_2]^{8-}$ (M = Hf, Zr), respectively [38]; tetra-nuclear two 7-coordinate and two 8-coordinate metal complexes with two β-Keggin silicotungstates, i.e., $[Zr_4(\mu_3\text{-}O)_2(OH)_2(H_2O)_4(\beta\text{-}SiW_{10}O_{37})_2]^{10-}$ [31]; hexa-nuclear three 7-coordinate and three 8-coordinate metal complexes formed with three β-Keggin silicotungstates, i.e., $[Zr_6O_2(OH)_4(H_2O)_3(\beta\text{-}SiW_{10}O_{37})_3]^{14-}$ [31]; tetra-nuclear 7-coordinate metal complexes with acetate ligands sandwiched between two di-lacunary Keggin-type POMs, i.e., $[Zr_4(OH)_6(CH_3CO_2)_2(\alpha\text{-}PW_{10}O_{37})_2]^{10-}$ [51] and $[Hf_4(OH)_6(CH_3CO_2)_2(x\text{-}PW_{10}O_{37})_2]^{12-}$ (x = α, β) [52], respectively; and hexa-nuclear 6-peroxo metal complexes formed with three γ-Keggin silicotungstates, i.e., $[M_6(O_2)_6(\mu\text{-}OH)_6(\gamma\text{-}SiW_{10}O_{36})_3]^{18-}$ (M = Hf, Zr) [40,45]. Recently, three 6-coordinate prismatic Hf^{IV} and Zr^{IV} ions, i.e., the $[M_3(\mu\text{-}OH)_3]^{9+}$ cluster cations (M = Hf, Zr) sandwiched between two tri-lacunary α-Keggin POMs, or $[M_3(\mu\text{-}OH)_3$

* Corresponding author.
E-mail address: nomiya@kanagawa-u.ac.jp (K. Nomiya).

0277-5387/$ - see front matter © 2012 Elsevier Ltd. All rights reserved.
http://dx.doi.org/10.1016/j.poly.2012.08.062

$(A\text{-}\alpha\text{-}PW_9O_{34})_2]^{9-}$ (the Keggin 3:2 complexes), were reported [47]; the analogous tri-nuclear 6-coordinate Zr^{IV} cluster compound $[Zr_3(\mu\text{-}OH)_3(A\text{-}\beta\text{-}SiW_9O_{34})_2]^{11-}$ has previously been reported [24]. The di-nuclear, 7-coordinate Hf and Zr cluster cations sandwiched between two mono-lacunary α-Keggin POMs and between two mono-lacunary α-Dawson POMs, i.e., $[\{\alpha\text{-}PW_{11}O_{39}M(H_2O)\}_2(\mu\text{-}OH)_2]^{8-}$ (M = Hf, Zr; the Keggin 2:2 complexes) [48,53] and $[\{\alpha_2\text{-}P_2W_{17}O_{61}M(H_2O)\}_2(\mu\text{-}OH)_2]^{14-}$ (the Dawson 2:2 complexes) [50,53], respectively, and the tetra-nuclear 7-coordinate metal cluster cation species $[M_4(\mu_3\text{-}O)_2(\mu\text{-}OH)_2(H_2O)_4]^{10+}$ (M = Zr [27], Hf [49]) sandwiched between two di-lacunary Dawson POMs, i.e., $[M_4(\mu_3\text{-}O)_2(\mu\text{-}OH)_2(H_2O)_4(P_2W_{16}O_{59})_2]^{14-}$ (the Dawson 4:2 complexes), have also been reported. As a molybdo-POM, the 8-coordinate Hf complex, i.e., $\{Hf[PMo_{12}O_{40}][(NH_4)PMo_{11}O_{39}]\}^{5-}$, has also recently been reported [41].

Most Ti-substituted Keggin POMs are isolated as oligomers formed by corner-sharing Ti–O–Ti bonds. Meanwhile, Zr/Hf-containing α-Keggin/α-Dawson POMs are usually isolated as di-, tri-, tetra-Zr/Hf cluster cations sandwiched between two lacunary POMs, the cluster cations of which are formed by edge-sharing $M(OH)_2M$ (M = Zr, Hf) bonds [20]. For example, the Keggin 2:2 and the Dawson 2:2 complexes, i.e., $[\{\alpha\text{-}PW_{11}O_{39}M(H_2O)\}_2(\mu\text{-}OH)_2]^{8-}$ and $[\{\alpha_2\text{-}P_2W_{17}O_{61}M(H_2O)\}_2(\mu\text{-}OH)_2]^{14-}$ (M = Zr, Hf), respectively, are composed of two mono-Zr- and Hf-substituted POM units $[\alpha\text{-}PW_{11}O_{39}M]$ and $[\alpha_2\text{-}P_2W_{17}O_{61}M]$ linked via two μ-OH groups [48,50].

In this work, we prepared a set of novel 2:2-type Zr^{IV}/Hf^{IV}-containing Keggin complexes with edge-sharing and face-sharing linkages under different pH conditions, each consisting of di-Zr^{IV}/Hf^{IV} cluster cations sandwiched between two mono-lacunary α-Keggin POMs with an Si heteroatom, i.e., $(Et_2NH_2)_{10}[(\alpha\text{-}SiW_{11}O_{39}M)_2(\mu\text{-}OH)_2]\cdot 4H_2O$ (M = Zr, **Zr-edge**; Hf, **Hf-edge**) and $(Et_2NH_2)_{11}[(\alpha\text{-}SiW_{11}O_{39}M)_2(\mu\text{-}OH)_3]\cdot 15H_2O$ (M = Zr, **Zr-face**; Hf, **Hf-face**). We successfully determined their molecular structures by X-ray crystallography. Two central Zr and Hf atoms of the **Zr-edge** and the **Hf-edge** were linked by two μ-OH groups, i.e., an edge-sharing linkage, whereas those of the **Zr-face** and the **Hf-face** were linked by three μ-OH groups, i.e., a face-sharing linkage. The Zr/Hf-containing POM dimers reported so far are usually linked by edge-sharing $M(OH)_2M$ (M = Zr, Hf) bonds [20]. Therefore, the **Zr-face** and the **Hf-face** are the first examples of Zr/Hf-containing POM dimers linked in a face-sharing fashion.

2. Experimental

2.1. Synthesis

2.1.1. Materials

The following reactants were used as received: 1 M aqueous HCl solutions (quantitative analysis grade), 0.1 and 1 M aqueous KOH solutions (quantitative analysis grade), EtOH, Et_2O, Et_2NH_2Cl, zirconium(IV) dichloride oxide octahydrate, hafnium(IV) dichloride oxide octahydrate (Wako), and D_2O (Isotec). The precursor or mono-lacunary α-Keggin POM with heteroatom Si and the 2:2-type Zr^{IV}-containing Keggin POM, $K_8[\alpha\text{-}SiW_{11}O_{39}]\cdot 15H_2O$ [55] and $(Et_2NH_2)_8[\{\alpha\text{-}PW_{11}O_{39}Zr(H_2O)\}_2(\mu\text{-}OH)_2]\cdot 9H_2O$ [48], respectively, were prepared according to the literature and identified by FTIR, thermogravimetric (TG)/differential thermal analyses (DTA), ^{29}Si NMR, and ^{31}P NMR.

2.1.2. Preparation of sample mixture of *Zr-edge* and *Zr-face*

$ZrCl_2O\cdot 8H_2O$ (0.258 g, 0.80 mmol) was dissolved in 20 mL of water, and the solution was stirred vigorously in a water bath at >90 °C for 1 min. To the hot solution was added 2.61 g (0.80 mmol) of solid $K_8[\alpha\text{-}SiW_{11}O_{39}]\cdot 15H_2O$, followed by stirring for 30 min. This solution was stirred at >90 °C (pH 7.3). To the colorless solution was added 2.0 g (18.2 mmol) of Et_2NH_2Cl, followed by stirring for 1 min. The colorless solution was slowly evaporated at r.t. After 2 days, colorless, clear needle crystals formed, which were collected on a membrane filter (JG 0.2 μm), washed with EtOH (30 mL × 3) and Et_2O (50 mL × 3), and dried *in vacuo* for 2 h. This crystalline sample was a mixture of **Zr-edge** and **Zr-face** and the obtained yield was 1.45 g.

2.1.3. Synthesis of $(Et_2NH_2)_{10}[(\alpha\text{-}SiW_{11}O_{39}Zr)_2(\mu\text{-}OH)_2]\cdot 4H_2O$ (*Zr-edge*)

The sample mixture (2.5 g) was dissolved in 10 mL of water. This solution (pH 7.1) was slowly adjusted to pH 4.5 with a 1 M aqueous HCl solution and slowly evaporated at r.t. After 1 day, colorless, clear prismatic crystals formed, which were collected on a membrane filter (JG 0.2 μm), washed with EtOH (30 mL × 3) and Et_2O (50 mL × 3), and dried *in vacuo* for 2 h. The yield was 1.83 g (47.5% based on $K_8[\alpha\text{-}SiW_{11}O_{39}]\cdot 15H_2O$).

The crystalline samples were soluble in water and DMSO but insoluble in diethyl ether and ethanol. *Anal.* Calc. for $C_{40}H_{130}N_{10}O_{84}Si_2W_{22}Zr_2$ or $(Et_2NH_2)_{10}[(\alpha\text{-}SiW_{11}O_{39}Zr)_2(\mu\text{-}OH)_2]\cdot 4H_2O$: C, 7.53; H, 2.05; N, 2.20. Found: C, 7.60; H, 1.61; N, 2.33%.

TG/DTA under atmospheric conditions: a weight loss of 1.25% due to dehydration was observed at below 166.9 °C; calc. 1.13% for a total of four water molecules. A weight loss of 11.44% was observed between 166.9 and 500.0 °C with an exothermic peak at 381.2 °C; calc. 11.62% for a total of 10 $Et_2NH_2^+$ cations. Selected IR (KBr): 1624 w, 1471 w, 1454 w, 1433 w, 1387 w, 1363 vw, 1198 vw, 1159 vw, 1061 w, 1045 w, 1001 w, 957 m, 906 vs, 877 m, 789 vs, 692 m, 663 m, 642 m, 540 m, 525 m, 507 m cm^{-1}. Solution ^{29}Si NMR (22.2 °C, D_2O): δ −85.47 ppm. Solid-state ^{29}Si CPMAS NMR (r.t.): δ −83.89 ppm.

2.1.4. Synthesis of $(Et_2NH_2)_{11}[(\alpha\text{-}SiW_{11}O_{39}Zr)_2(\mu\text{-}OH)_3]\cdot 15H_2O$ (*Zr-face*)

The sample mixture (2.5 g) was dissolved in 10 mL of water. This solution was slowly adjusted to pH 9.5 with a 1 M aqueous KOH solution and slowly evaporated at r.t. After 7 days, colorless, clear prismatic crystals formed, which were collected on a membrane filter (JG 0.2 μm), washed with EtOH (30 mL × 3) and Et_2O (50 mL × 3), and dried *in vacuo* for 2 h. The yield was 1.85 g (45.9% based on $K_8[\alpha\text{-}SiW_{11}O_{39}]\cdot 15H_2O$).

The crystalline samples were soluble in water and DMSO but insoluble in diethyl ether and ethanol. *Anal.* Calc. for $C_{44}H_{165}N_{11}O_{96}Si_2W_{22}Zr_2$ or $(Et_2NH_2)_{11}[(\alpha\text{-}SiW_{11}O_{39}Zr)_2(\mu\text{-}OH)_3]\cdot 15H_2O$: C, 7.93; H, 2.49; N, 2.31. Found: C, 7.86; H, 2.18; N, 2.37%.

TG/DTA under atmospheric conditions: a weight loss of 3.94% due to dehydration was observed at below 169.8 °C; calc. 4.05% for a total of fifteen water molecules. A weight loss of 11.57% was observed between 169.8 and 500.0 °C with an exothermic peak at 374.4 °C; calc. 12.23% for a total of eleven $Et_2NH_2^+$ cations. Selected IR (KBr): 1620 w, 1471 w, 1454 w, 1390 w, 1362 vw, 1312 vw, 1275 vw, 1196 vw, 1159 vw, 1062 w, 1047 w, 1000 m, 956 m, 903 s, 786 vs, 586 w, 541 m, 526 m, 504 m, 478 w, 461 w, 403 w cm^{-1}. Solution ^{29}Si NMR (25.9 °C, D_2O) δ −85.51 ppm. Solid-state ^{29}Si CPMAS NMR (r.t.): δ −84.09 ppm.

2.1.5. Preparation of sample mixture of *Hf-edge* and *Hf-face*

In the synthesis of the sample mixture of **Hf-edge** and **Hf-face**, $HfCl_2O\cdot 8H_2O$ was used in place of $ZrCl_2O\cdot 8H_2O$ with almost the same work-up. A sample mixture of **Hf-edge** and **Hf-face** was obtained as a yield of 1.67 g.

*2.1.6. Synthesis of $(Et_2NH_2)_{10}[(\alpha\text{-}SiW_{11}O_{39}Hf)_2(\mu\text{-}OH)_2]\cdot 4H_2O$ (**Hf-edge**)*

The sample mixture (2.5 g) was dissolved in 10 mL of water. This solution was slowly adjusted to pH 4.5 with a 1 M aqueous HCl solution and slowly evaporated at r.t. After 1 day, colorless, clear prismatic crystals formed, which were collected on a membrane filter (JG 0.2 μm), washed with EtOH (30 mL × 3) and Et_2O (50 mL × 3), and dried *in vacuo* for 2 h. Yield 1.98 g (56.1% based on $K_8[\alpha\text{-}SiW_{11}O_{39}]\cdot 15H_2O$).

The crystalline samples were soluble in water and DMSO but insoluble in diethyl ether and ethanol. *Anal.* Calc. for $C_{40}H_{130}N_{10}O_{84}Si_2W_{22}Hf_2$ or $(Et_2NH_2)_{10}[(\alpha\text{-}SiW_{11}O_{39}Hf)_2(\mu\text{-}OH)_2]\cdot 4H_2O$: C, 7.33; H, 2.00; N, 2.14. Found: C, 7.37; H, 1.54; N, 2.28%.

TG/DTA under atmospheric conditions: a weight loss of 1.11% due to dehydration was observed at below 168.6 °C; calc. 1.10% for a total of four water molecules. A weight loss of 11.04% was observed between 168.6 and 500.0 °C with an exothermic peak at 381.5 °C; calc. 11.31% for a total of 10 $Et_2NH_2^+$ cations. Selected IR (KBr): 1622 w, 1471 w, 1452 w, 1430 w, 1390 w, 1363 vw, 1198 vw, 1159 vw, 1061 w, 1045 w, 1001 w, 957 m, 906 vs, 877 m, 791 vs, 702 m, 671 w, 646 w, 542 m, 523 m, 509 m cm^{-1}. Solution ^{29}Si NMR (21.4 °C, D_2O): δ −85.69 ppm. Solid-state ^{29}Si CPMAS NMR (r.t.): δ −84.09 ppm.

*2.1.7. Synthesis of $(Et_2NH_2)_{11}[(\alpha\text{-}SiW_{11}O_{39}Hf)_2(\mu\text{-}OH)_3]\cdot 15H_2O$ (**Hf-face**)*

The sample mixture (2.5 g) was dissolved in 10 mL of water. This solution was slowly adjusted to pH 9.5 with a 1 M aqueous KOH solution and slowly evaporated at r.t. After 7 days, colorless, clear prismatic crystals formed, which were collected on a membrane filter (JG 0.2 μm), washed with EtOH (30 mL × 3) and Et_2O (50 mL × 3), and dried *in vacuo* for 2 h. Yield 1.91 g (54.2% based on $K_8[\alpha\text{-}SiW_{11}O_{39}]\cdot 15H_2O$).

The crystalline samples were soluble in water and DMSO but insoluble in diethyl ether and ethanol. *Anal.* Calc. for $C_{44}H_{165}N_{11}O_{96}Si_2W_{22}Hf_2$ or $(Et_2NH_2)_{11}[(\alpha\text{-}SiW_{11}O_{39}Hf)_2(\mu\text{-}OH)_3]\cdot 15H_2O$: C, 7.72; H, 2.43; N, 2.25. Found: C, 7.76; H, 1.83; N, 2.42%.

TG/DTA under atmospheric conditions: a weight loss of 3.93% due to dehydration was observed at below 197.3 °C; calc. 3.95% for a total of fifteen water molecules. A weight loss of 9.78% was observed between 197.3 and 500.0 °C with an exothermic peak at 361.6 °C; calc. 11.92% for a total of eleven $Et_2NH_2^+$ cations. Selected IR (KBr): 1626 m, 1471 w, 1456 w, 1390 w, 1363 vw, 1198 vw, 1159 vw, 1063 w, 1045 w, 1003 w, 957 m, 906 vs, 877 m, 791 vs, 700 m, 665 m, 644 m, 542 m, 523 m, 509 m cm^{-1}. Solution ^{29}Si NMR (21.2 °C, D_2O) δ −85.69 ppm. Solid-state ^{29}Si CPMAS NMR (r.t.): δ −84.28 ppm.

2.1.8. Control experiment: attempting to prepare the phosphotungstate Keggin 2:2-type complex linked in a face-sharing fashion

The pH of the solution (pH 4.2) containing the Keggin 2:2-type complex with heteroatom P, i.e., $(Et_2NH_2)_8[\{\alpha\text{-}PW_{11}O_{39}Zr(H_2O)\}_2(\mu\text{-}OH)_2]\cdot 9H_2O$, (0.75 g, 0.12 mmol) dissolved in 15 mL water at 70 °C, was adjusted to 4.5, 5.5, 6.5, 7.5, 8.5 and finally 9.5. ^{31}P NMR spectra were measured (Fig. 6): pH 4.2 (−13.55 ppm), pH 4.5 (−13.51, −14.52, −14.61 ppm), pH 5.5 (−13.46, −14.53, −14.61 ppm), pH 6.5 (−13.41, −14.52, −14.62 ppm), pH 7.5 (−13.40, −14.51, −14.60 ppm), pH 8.5 (2.67 ppm), pH 9.5 (2.76 ppm).

2.2. Instrumentation/analytical procedures

CHN elemental analyses were carried out with a Perkin Elmer 2400 CHNS Elemental Analyzer II. Infrared spectra were recorded on a JASCO 4100 FTIR spectrometer in KBr disks at room temperature. TG and DTA were acquired using a Rigaku Thermo Plus 2 series TG/DTA TG 8120 instrument. ^{29}Si NMR (78.0 MHz) spectra in D_2O solution were recorded in 5-mm outer diameter tubes on a JEOL JNM ECA 400 FT-NMR spectrometer with a JEOL ECA-400 NMR data-processing system and on a JEOL JNM ECP 500 FT-NMR spectrometer with a JEOL ECP-500 NMR data-processing system. The ^{29}Si NMR spectra were referenced to an internal standard of DSS. ^{31}P NMR (160.0 MHz) spectra in a D_2O solution were recorded in 5-mm outer diameter tubes on a JEOL JNM-ECA-400 FT-NMR spectrometer with a JEOL ECA-400 NMR data-processing system. The ^{31}P NMR spectra were referenced to an external standard of 25% H_3PO_4 in H_2O in a sealed capillary. The ^{31}P NMR signals with the usual 85% H_3PO_4 were shifted to +0.544 ppm from our data with 25% H_3PO_4. Solid-state ^{29}Si CPMAS NMR (59.0 MHz) spectra were recorded in 6-mm outer diameter rotors on a JEOL JNM-ECP-300 FT-NMR spectrometer with a JEOL ECP-300 NMR data-processing system and were referenced to an external standard of polydimethylsilane (δ = −34.0 ppm). Powder X-ray diffraction (PXRD) was carried out on a RIGAKU Ultima IV and characterization instrument using Cu Kα radiation.

Table 1
Crystallographic data for **Zr-edge**, **Zr-face**, **Hf-edge**, and **Hf-face**.

	Zr-edge	**Zr-face**	**Hf-edge**	**Hf-face**
Formula	$C_{40}H_{120}N_{10}O_{86}Si_2W_{22}Zr_2$	$C_{44}H_{132}N_{11}O_{94}Si_2W_{22}Zr_2$	$C_{40}H_{120}Hf_2N_{10}O_{86}Si_2W_{22}$	$C_{44}H_{132}Hf_2N_{11}O_{93}Si_2W_{22}$
Formula weight	6400.78	6602.93	6575.32	6761.47
Color, shape	colorless, prismatic	colorless, prismatic	colorless, prismatic	colorless, prismatic
Crystal system	triclinic	monoclinic	triclinic	monoclinic
Space group	$P\bar{1}$	$P2(1)/c$	$P\bar{1}$	$P2(1)/c$
T (K)	120	90	120	120
a (Å)	12.2571(9)	13.5533(8)	12.2527(11)	13.6619(5)
b (Å)	13.5084(10)	45.823(3)	13.4995(12)	45.6954(17)
c (Å)	20.1586(15)	21.5559(13)	20.1314(18)	21.5558(8)
α (°)	79.7940(10)	90	79.7620(10)	90
β (°)	86.3960(10)	99.7050(10)	86.3360(10)	99.6130(10)
γ (°)	65.7590(10)	90	65.7310(10)	90
V (Å^3)	2995.1(4)	13195.8(14)	2987.1(5)	13268.0(8)
Z	1	4	1	4
D_{calc} (g cm^{-3})	3.549	3.324	3.655	3.385
F_{000}	2854	11844	2918	12068
GOF	0.956	1.064	1.059	1.050
R_1 ($I > 2.00\sigma(I)$))	0.0443	0.0457	0.0592	0.0503
R (all data)	0.0636	0.0599	0.0623	0.0700
wR_2 (all data)	0.1288	0.1024	0.1747	0.1448

2.3. X-ray crystallography

Single crystals with dimensions of $0.15 \times 0.08 \times 0.04\ mm^3$ for **Zr-edge**, $0.28 \times 0.08 \times 0.04\ mm^3$ for **Zr-face**, $0.20 \times 0.19 \times 0.03\ mm^3$ for **Hf-edge**, $0.29 \times 0.10 \times 0.07\ mm^3$ for **Hf-face** were mounted on cryoloops using liquid paraffin (Paratone-N) and cooled by a stream of cooled N_2 gas. All measurements were made on a Bruker SMART APEX CCD diffractometer at 90 K with a graphite monochromated Mo Kα radiation (λ = 0.71073 Å). The intensity data were automatically collected for Lorentz and polarization effects during integration. The structures were solved by direct methods (SHELXS-97) [56] followed by a subsequent difference Fourier calculation and refined by a full-matrix, least-squares procedure on F^2 (SHELXL-97) [57]. Absorption corrections were performed with SADABS (empirical absorption correction) [58]. The compositions and formulae of the POM containing many countercations and many hydrated water molecules were determined by CHN elemental analysis and TG analysis. As with other structural investigations of crystals of highly hydrated large polyoxometalate complexes, it was not possible to locate every diethylammonium countercation and hydrated water molecule for all the complexes. This frequently encountered situation is attributed to extensive disorder of the cations and many of the hydrated water molecules. The details of the crystallographic data for **Zr-edge**, **Zr-face**, **Hf-edge**, and **Hf-face** are listed in Table 1.

3. Results and discussion

3.1. Synthesis and compositional characterization

The diethylammonium salts of the di-zirconium(IV) and di-hafnium(IV) cluster cations sandwiched between the two mono-lacunary Keggin POMs with heteroatom Si linked in an edge-sharing fashion and a face-sharing fashion, $(Et_2NH_2)_{10}[(\alpha\text{-}SiW_{11}O_{39}Zr)_2(\mu\text{-}OH)_2]\cdot 4H_2O$ (**Zr-edge**) and $(Et_2NH_2)_{11}[(\alpha\text{-}SiW_{11}O_{39}Zr)_2(\mu\text{-}OH)_3]\cdot 15H_2O$ (**Zr-face**), were obtained in 47.5% and 45.9% yields, respectively. First, the mixed sample of **Zr-edge** and **Zr-face** was obtained by a 1:1-M ratio reaction of the separately prepared $K_8[\alpha\text{-}SiW_{11}O_{39}]\cdot 15H_2O$ with $ZrCl_2O\cdot 8H_2O$ in water without pH adjustment (pH 7.3), following by stirring the solution at 90 °C. From this solution, two types of crystals having different shapes were formed. This mixed sample of **Zr-edge** and **Zr-face** was dissolved in water (pH 7.1). When the solution was adjusted to pH 4.5 with a 1 M aqueous HCl solution and evaporated slowly, the crystalline sample of **Zr-edge** was obtained. On the other hand, from the solution adjusted to pH 9.5 with a 1 M aqueous KOH solution, the crystals of **Zr-face** were formed. The Hf analogs, **Hf-edge** and **Hf-face**, were obtained by procedures and conditions similar to the **Zr-edge** and **Zr-face** syntheses. Each crystalline sample was characterized by CHN elemental analysis, FTIR, TG/DTA, solution and solid-state ^{29}Si NMR, and X-ray crystallography.

The formation of the mixtures of **M-edge** and **M-face** (M = Zr, Hf) can be represented by the sum of Eqs. (1) and (2).

$$2[\alpha\text{-}SiW_{11}O_{39}]^{8-} + 2MCl_2O + 2H^+ \rightarrow [(\alpha\text{-}SiW_{11}O_{39}M)_2(\mu\text{-}OH)_2]^{10-} + 4Cl^- \quad (1)$$

$$2[\alpha\text{-}SiW_{11}O_{39}]^{8-} + 2MCl_2O + 2H_2O \rightarrow [(\alpha\text{-}SiW_{11}O_{39}M)_2(\mu\text{-}OH)_3]^{11-} + 4Cl^- + OH^- \quad (2)$$

When the sample mixture solution was adjusted to pH 4.5, **M-face** in the solution was converted into **M-edge** by the reaction with H^+ (Eq. (3)). In this way a pure sample of M-edge can be obtained.

$$[(\alpha\text{-}SiW_{11}O_{39}M)_2(\mu\text{-}OH)_3]^{11-} + H^+ \rightarrow [(\alpha\text{-}SiW_{11}O_{39}M)_2(\mu\text{-}OH)_2]^{10-} + H_2O \quad (3)$$

On the other hand, adjusting to pH 9.5 using a 1 M KOH solution, **M-edge** in the solution was converted into **M-face** by the insertion of OH^- for the $M(\mu\text{-}OH)_2M$ bonds (Eq. (4)).

$$[(\alpha\text{-}SiW_{11}O_{39}M)_2(\mu\text{-}OH)_2]^{10-} + OH^- \rightarrow [(\alpha\text{-}SiW_{11}O_{39}M)_2(\mu\text{-}OH)_3]^{11-} \quad (4)$$

M-edge and **M-face** (M = Zr, Hf) have different charges, i.e., **M-edge** is 10− and **M-face** is 11−, due to the difference in the number of bridged $\mu\text{-}OH^-$ groups. Therefore, the number of counter cations is also different, and the CHN elemental analyses of these compounds showed a clear difference. The data we found were in good accord with the calculated values for the formulae with 10 Et_2NH_2 cations, two μ-OH groups, and four crystalline water molecules for **M-edge**, and for the formulae with eleven Et_2NH_2 cations, three μ-OH groups and fifteen crystalline water molecules for **M-face**.

In the TG/DTA measurements carried out under atmospheric conditions, the weight losses of 1.25% observed at below 166.9 °C for **Zr-edge** (Fig. S8) and 1.11% observed at below 168.6 °C for **Hf-edge** (Fig. S10) corresponded to ca. four water molecules for both, and the weight losses of 3.94% observed at below 169.8 °C for **Zr-face** (Fig. S9) and 3.93% observed at below 197.3 °C for **Hf-face** (Fig. S11) corresponded to ca. 15 water molecules for both, all of which were consistent with the elemental analyses data.

The four FTIR spectra of **Zr-edge**, **Zr-face** (Fig. 1 and Fig. S1), **Hf-edge**, and **Hf-face** (Figs. S2 and S3), measured in KBr disks, showed the characteristic bands of the Keggin POM framework (1500–750 cm^{-1}). The bands were very similar to each other and almost coincident within the experimental error.

The powder X-ray diffractions (PXRD) of **Zr-edge**, **Zr-face** (Fig. S12), **Hf-edge**, and **Hf-face** (Fig. S13) were measured. The PXRD patterns did not agree with the PXRD patterns simulated from the respective single-crystal X-ray data, because several hydrated water molecules were lost during the measurement of PXRD and the crystal structures were changed. In the meantime, clear difference in the PXRD patterns of **M-edge** and **M-face**

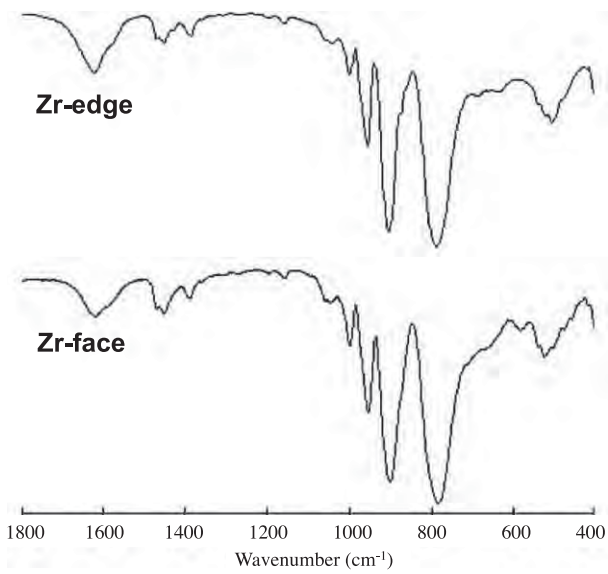

Fig. 1. The FTIR spectra in the polyoxoanion region (1200–400 cm^{-1}), measured in KBr disks, of $(Et_2NH_2)_{10}[(\alpha\text{-}SiW_{11}O_{39}Zr)_2(\mu\text{-}OH)_2]\cdot 4H_2O$ (**Zr-edge**) and $(Et_2NH_2)_{11}[(\alpha\text{-}SiW_{11}O_{39}Zr)_2(\mu\text{-}OH)_3]\cdot 15H_2O$ (**Zr-face**).

appeared. Thus, **M-edge** and **M-face** can be distinguished and purity of the bulk materials was confirmed.

3.2. Structural analyses

3.2.1. Molecular structures of M-edge (M = Zr and Hf)

The molecular structure of polyoxoanion **Zr-edge**, its polyhedral representation, and the partial structure around the Zr_2 centers are shown in Fig. 2a, b, and c, respectively. Selected bond lengths (Å) and angles (°) around the Zr_2 centers in **Zr-edge** are given in Table 2.

The composition and formula of **Zr-edge**, which contains 10 diethylammonium countercations and four hydrated water molecules, were determined by CHN elemental analysis and TG/DTA analysis. In X-ray crystallography, one polyoxoanion, five diethylammonium cations, and three hydrated water molecules per formula unit were identified in the crystal structure.

X-ray crystallography of **Zr-edge** revealed that two polyhedral Zr units were linked in an edge-sharing fashion, i.e., two mono-Zr-substituted α-Keggin POM units [α-$SiW_{11}O_{39}Zr$] were linked via two μ-OH groups (O1M) [Zr–O average 2.130 Å] (Fig. 2a, b, and c). Bond valence sum (BVS) calculations [59–62] have strongly suggested that the oxygen atoms (O1M) are protonated, i.e., they are ascribed to the OH^- groups (the BVS value of O1M is 1.160). Each Zr atom is bonded to four oxygen atoms (O(16), O(22), O(23), O(28)) of the lacunary site in each $SiW_{11}O_{39}$ unit (Fig. 2c) [Zr–O average 2.086 Å]. Thus, two Zr atoms can be considered as 6-coodinate and the whole symmetry of the molecule is shown with approximate C_i symmetry. The Zr–Zr distance is 3.577 Å.

The 2:2-type Zr^{IV}-containing Keggin POMs related to the present **Zr-edge**, a di-zirconium(IV) cation species sandwiched between two mono-lacunary Keggin POMs with heteroatom P, i.e., $(Et_2NH_2)_8[\{\alpha\text{-}PW_{11}O_{39}Zr(H_2O)\}_2(\mu\text{-}OH)_2]\cdot 7H_2O$ (**Et_2NH_2-2**) and $(n\text{-}Bu_4N)_8[(\alpha\text{-}PW_{11}O_{39}Zr)_2(\mu\text{-}OH)_2]$ (**OK-2**), have been reported by our group [48] and Kholdeeva's group [32], respectively. Both of these 2:2-type POMs were also linked in an edge-sharing fashion; however, the coordination environment around the Zr center in the previous **Et_2NH_2-2** was different from that of the present **Zr-edge** and Kholdeeva's **OK-2**. In the case of **Zr-edge** and **OK-2**, the 6-coordinate geometry around the Zr center was accomplished by bonding with two bridging μ-OH and four terminal oxygen atoms in the mono-lacunary site of the Keggin POM and without any coordinating water molecules. The **Et_2NH_2-2** which was previously reported by us contained one water molecule coordinating to each Zr atom, resulting in the 7-coordination environment around the Zr center. On the other hand, the orientation of the two lacunary Keggin units of **Zr-edge** was similar to that of **Et_2NH_2-2**; however, it was different from that of **OK-2**. The two lacunary Keggin units of **Zr-edge** and **Et_2NH_2-2** oriented in the opposite direction; therefore, the whole symmetry of these molecules is shown with approximate C_i symmetry. **OK-2** had two lacunary Keggin units oriented in the same direction, resulting in the approximate C_{2h} symmetry. [*Note:* It has been erroneously described in the text to be C_s symmetry. We have checked it using the CIF file downloaded from the ESI of Ref. [32]].

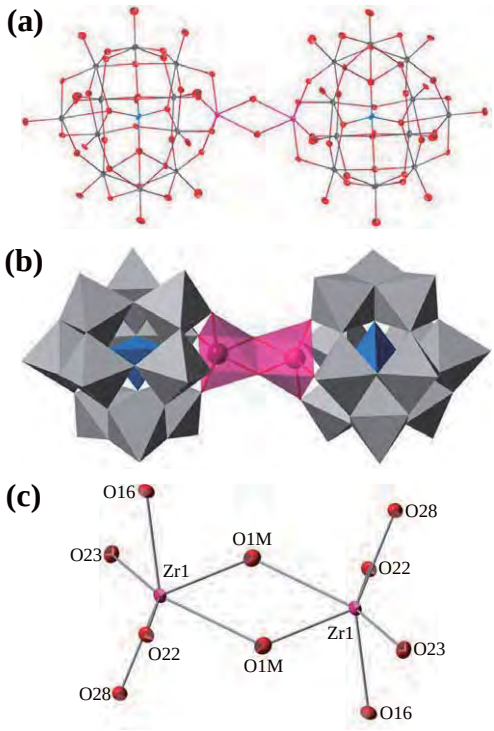

Fig. 2. (a) Molecular structure of the polyoxoanion $[(\alpha\text{-}SiW_{11}O_{39}Zr)_2(\mu\text{-}OH)_2]^{10-}$ in **Zr-edge**, (b) its polyhedral representation, and (c) the partial structure around the Zr_2 center.

Table 2
Selected bond lengths (Å) and angles (°) around the Zr^{IV} center in **Zr-edge**.

Lengths			
Zr(1)–O(1M)	2.137(10)	Zr(1)–O(16)	2.073(10)
Zr(1)–O(1M)#	2.123(11)	Zr(1)–O(22)	2.084(9)
Average	2.130	Zr(1)–O(23)	2.113(9)
		Zr(1)–O(28)	2.073(10)
		average	2.086
Angles			
Zr(1)–O(1M)–Zr(1)#	114.2(4)	O(1M)–Zr(1)–Zr(1)#	32.8(3)
		O(1M)#–Zr(1)–Zr(1)#	33.0(3)
O(1M)–Zr(1)–O(1M)#	65.8(4)	average	32.9

Symmetry operators: $-x+2$, $-y+1$, $-z$.

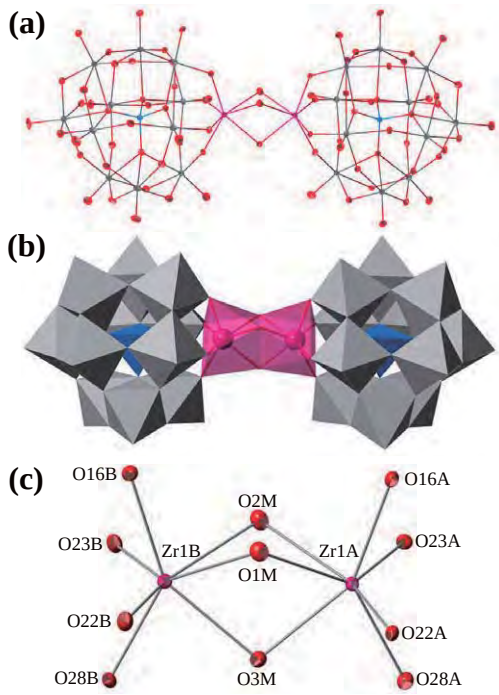

Fig. 3. (a) Molecular structure of the polyoxoanion $[(\alpha\text{-}SiW_{11}O_{39}Zr)_2(\mu\text{-}OH)_3]^{11-}$ in **Zr-face**, (b) its polyhedral representation, and (c) the partial structure around the Zr_2 center.

X-ray crystallography revealed that the molecular structure of **Hf-edge** was isostructural with that of **Zr-edge** (see Fig. S4 and Table S1).

3.2.2. Molecular structures of M-face (M = Zr and Hf)

The molecular structure of polyoxoanion **Zr-face**, its polyhedral representation, and the partial structure around the Zr_2 centers are shown in Fig. 3a, b, and c, respectively. Selected bond lengths (Å) and angles (°) around the Zr_2 centers in **Zr-face** are given in Table 3.

The composition and formula of **Zr-face**, which contains 11 diethylammonium countercations and fifteen hydrated water molecules, were determined by CHN elemental analysis and TG/DTA analysis. In X-ray crystallography, one polyoxoanion, eleven diethylammonium cations and thirteen hydrated water molecules per formula unit were identified in the crystal structure.

X-ray crystallography of **Zr-face** revealed that two polyhedral Zr units were linked in a face-sharing fashion, i.e., two mono-Zr-substituted α-Keggin POM units [α-$SiW_{11}O_{39}Zr$] were linked via three μ-OH groups (O1M, O2M, O3M) [Zr-O average 2.188 Å] (Fig. 3a, b, and c). To the best of our knowledge, it is the first example of a sandwiched compound of POMs containing group IV metals with a face-sharing linkage. BVS calculations have strongly suggested that the oxygen atoms (O1M, O2M, O3M) are protonated, i.e., they are ascribed to the OH^- groups (the BVS value of O1M is 0.876, O2M 0.947, and O3M 1.175). Each Zr atom (Zr1A, Zr1B) is bonded to four oxygen atoms (O16A, O22A, O23A, O28A; O16B, O22B, O23B, O28B) of the lacunary site in each $SiW_{11}O_{39}$ unit (Fig. 3c) [Zr–O average 2.126 Å]. Thus, two Zr atoms can be considered as 7-coordinate.

Two $SiW_{11}O_{39}Zr$ units were slightly twisted away from each other (torsion angle between O16A–Zr1A–Zr1B plane and Zr1A–Zr1B–O16B plane, 3.579°; O22A–Zr1A–Zr1B plane and Zr1A–Zr1B–O22B plane, 4.323°; O23A–Zr1A–Zr1B plane and Zr1A–Zr1B–O23B, 3.445°; O28A–Zr1A–Zr1B plane and Zr1A–Zr1B–O28B plane, 3.621°; average 3.742°), and the two enantiomers of the $[(\alpha\text{-}SiW_{11}O_{39}Zr)_2(\mu\text{-}OH)_3]^{11-}$ anion were defined by the relative twist direction. Therefore, the whole symmetry of **Zr-face** is shown with approximate C_1 symmetry. The $[(\alpha\text{-}SiW_{11}O_{39}\text{-}Zr)_2(\mu\text{-}OH)_3]^{11-}$ anions of **Zr-face** were detected as two sets of enantiomeric pairs of two different units in the unit cell. The Zr–Zr distance of **Zr-face** was much shorter than that of **Zr-edge** due to the effect of the face-sharing connection (**Zr-face**, 3.282 Å; **Zr-edge**, 3.577 Å). Unlike the edge-sharing analogs **Zr-** and **Hf-edge**, the two mono-lacunary Keggin units oriented in the same direction. This orientation mode was similar to that of Kholdeeva's **OK-2**.

X-ray crystallography revealed that the molecular structure of **Hf-face** was isostructural with that of **Zr-face** (see Fig. S5 and Table S2).

Table 3
Selected bond lengths (Å) and angles (°) around the Zr^{IV} center in **Zr-face**.

Lengths			
Zr(1A)–O(1M)	2.252(7)	Zr(1A)–O(16A)	2.134(7)
Zr(1A)–O(2M)	2.186(7)	Zr(1A)–O(22A)	2.120(7)
Zr(1A)–O(3M)	2.109(7)	Zr(1A)–O(23A)	2.136(7)
Zr(1B)–O(1M)	2.216(7)	Zr(1A)–O(28A)	2.133(7)
Zr(1B)–O(2M)	2.224(7)	Zr(1B)–O(16B)	2.124(7)
Zr(1B)–O(3M)	2.141(7)	Zr(1B)–O(22B)	2.130(7)
Average	2.188	Zr(1B)–O(23B)	2.114(7)
		Zr(1B)–O(28B)	2.120(7)
		average	2.126
Angles			
Zr(1A)–O(1M)–Zr(1B)	94.5(2)	O(1M)–Zr(1A)–O(2M)	67.4(3)
Zr(1A)–O(2M)–Zr(1B)	96.2(3)	O(1M)–Zr(1A)–O(3M)	68.2(3)
Zr(1A)–O(3M)–Zr(1B)	101.1(3)	O(2M)–Zr(1A)–O(3M)	73.7(3)
Average	97.3	O(1M)–Zr(1B)–O(2M)	67.4(3)
		O(1M)–Zr(1B)–O(3M)	68.3(3)
		O(2M)–Zr(1B)–O(3M)	72.4(3)
		average	69.6

3.3. Solution ^{29}Si NMR and solid-state ^{29}Si CPMAS NMR

The solution ^{29}Si NMR spectra of **Zr-edge** and **Zr-face** in D_2O showed only one resonance for each at −85.47 and −85.51 ppm, respectively (Fig. 4). The solid-state ^{29}Si CPMAS NMR spectra of the crystalline sample of **Zr-edge** and **Zr-face** showed a single broad signal for each at −83.89 and −84.09 ppm, respectively (Fig. 5). Although in both solution and solid-state ^{29}Si CPMAS NMR spectra, only one signal was observed which should correspond to one solid-state structure as determined by X-ray crystallography, these chemical shifts hardly reflect a difference in solid-state structure due to the very small difference in their

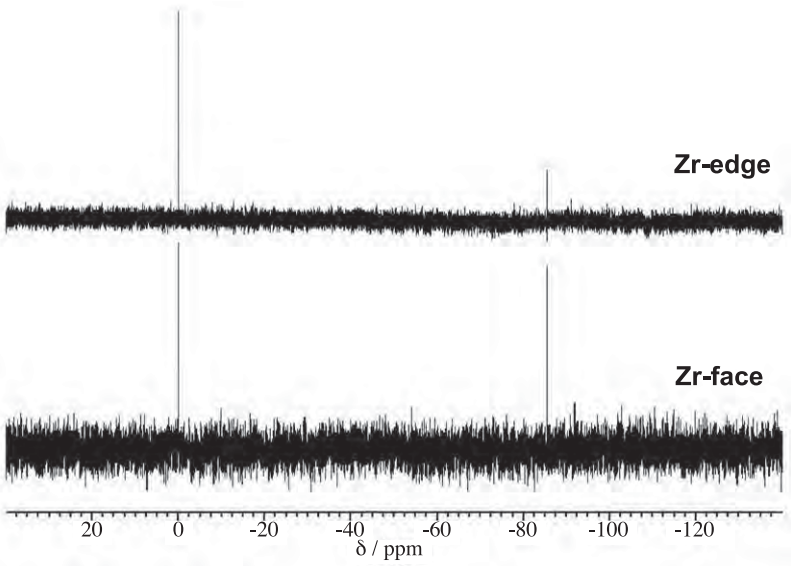

Fig. 4. Solution ^{29}Si NMR spectra of **Zr-edge** and **Zr-face** dissolved in D_2O.

molecular structures. As a matter of fact, the solid-state ^{29}Si CPMAS NMR spectrum of a 3:4 M-ratio mixed sample of **Zr-edge** and **Zr-face**, which were separately prepared and then mixed, also showed only one signal at −83.85. Therefore, **Zr-edge** and **Zr-face** were difficult to identify by solution and solid-state ^{29}Si NMR spectra.

Solution ^{29}Si NMR spectra of both **Hf-edge** and **Hf-face** in D_2O showed only one resonance at −85.69 ppm (Fig. S6). The solid-state ^{29}Si CPMAS NMR spectra of the crystalline sample of **Hf-edge** and **Hf-face** showed a single broad signal for each at −84.09 and −84.28 ppm, respectively (Fig. S7). The tendency for the ^{29}Si NMR resonances of the Hf compounds to appear in a higher field

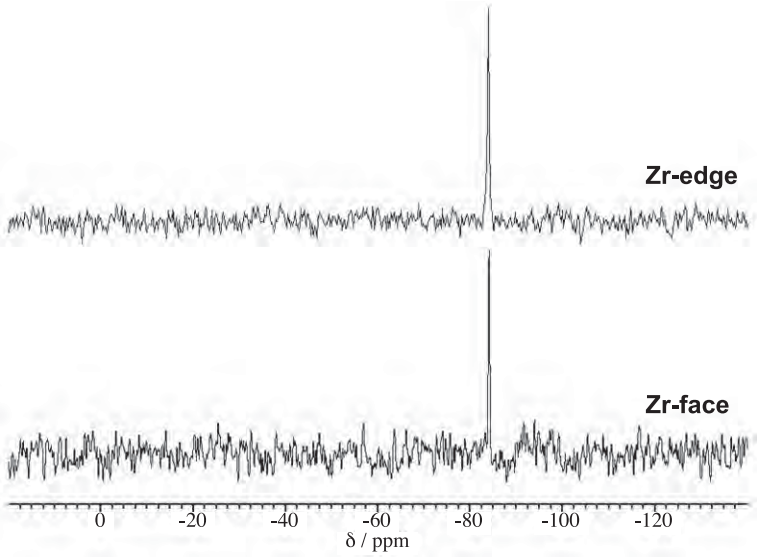

Fig. 5. Solid-state ^{29}Si CPMAS NMR spectra of **Zr-edge** and **Zr-face**.

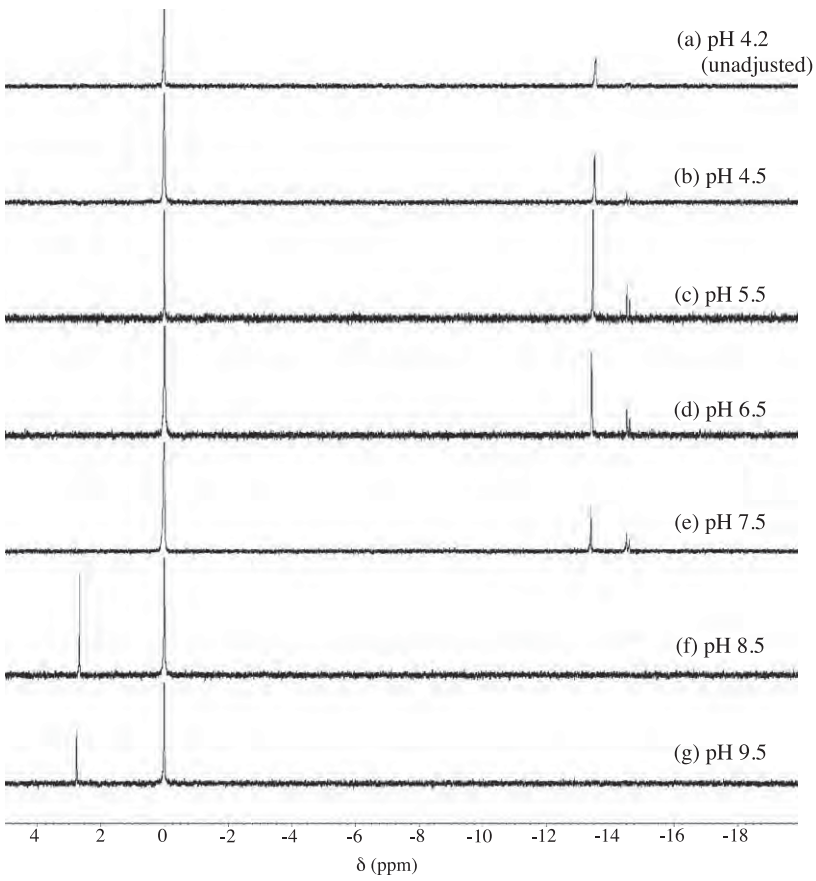

Fig. 6. ^{31}P NMR of the solutions of the Keggin 2:2-type complex with heteroatom P, $[\{\alpha\text{-}PW_{11}O_{39}Zr(H_2O)\}_2(\mu\text{-}OH)_2]^{8-}$ (**Et_2NH_2-2**), in which pH was changed: pH (a) 4.2 (unadjusted); (b) 4.5; (c) 5.5; (d) 6.5; (e) 7.5; (f) 8.5; (g) 9.5.

than those of the Zr compounds is consistent with the recently reported ^{31}P NMR resonances of Zr- and Hf-containing POMs: $[M_3(\mu\text{-}OH)_3(A\text{-}\alpha\text{-}PW_9O_{34})_2]^{9-}$ in D_2O (M = Hf, Zr) at −11.45 and −10.85 ppm, respectively [47]; $[M(\alpha\text{-}PW_{11}O_{39})_2]^{10-}$ in D_2O at −14.67 and −14.77 ppm for M = Hf and at −14.57 and −14.65 ppm for M = Zr [48]; $[M(\alpha_2\text{-}P_2W_{17}O_{61})_2]^{16-}$ in D_2O at −9.25 and −13.82 ppm for M = Hf and at −9.20 and −13.81 ppm for M = Zr [48].

3.4. Attempting to prepare the phosphotungstate Keggin 2:2-type complex linked in a face-sharing fashion, $[(\alpha\text{-}PW_{11}O_{39}Zr)_2(\mu\text{-}OH)_3]^{9-}$

The Zr/Hf cluster cations sandwiched between α-Keggin phosphotungstate POMs are usually linked with edge-sharing $M(OH)_2M$ (M = Zr, Hf) bonds. We tried to prepare the 2:2-type Zr complexes sandwiched between α-Keggin phosphotungstate in a face-sharing fashion by alkalification. Thus, we have examined the pH-dependent ^{31}P NMR of the 2:2-type Zr complex sandwiched between two α-Keggin phosphotungstates in an edge-sharing fashion. The pH of the aqueous solution (pH 4.2) of the Keggin 2:2-type complex with heteroatom P, i.e., $[\{\alpha\text{-}PW_{11}O_{39}Zr(H_2O)\}_2(\mu\text{-}OH)_2]^{8-}$ (**Et_2NH_2-2**) [48], was adjusted to 4.5, 5.5, 6.5, 7.5, 8.5 and finally 9.5, and ^{31}P NMR spectra were measured (Fig. 6). ^{31}P NMR spectra in the unadjusted sample (pH 4.2) showed a singlet signal at −13.55 ppm, which can be assigned to the Keggin 2:2-type complex in an edge-sharing fashion. In the pH range of 4.5–7.5, other signals were observed in addition to the signal of the 2:2-type complex. These signals can be tentatively assigned to the 1:2-type complex, $[M(\alpha\text{-}PW_{11}O_{39})_2]^{10-}$ and the proton-dissociation species of the coordination water molecules. We previously reported that the 2:2-type complexes $[\{\alpha\text{-}PW_{11}O_{39}M(H_2O)\}_2(\mu\text{-}OH)_2]^{8-}$ undergo a conversion to the 1:2-type complexes $[M(\alpha\text{-}PW_{11}O_{39})_2]^{10-}$ in solution under less acidic conditions [48]. However, in more basic conditions, no peaks due to POM were observed, and the peak of the decomposition product appeared in a lower field region (ca. 2.7 ppm). This fact suggests that the 2:2-type Keggin POM in a face-sharing fashion can be formed only if the heteroatom is Si because the POM with heteroatom Si is resistant to base.

4. Conclusion

We have prepared a set of novel 2:2-type Zr^{IV}/Hf^{IV}-containing Keggin complexes with edge-sharing and face-sharing linkages under different pH conditions, each consisting of di-Zr^{IV}/Hf^{IV} cluster cations sandwiched between two mono-lacunary α-Keggin POMs with heteroatom Si, i.e., $(Et_2NH_2)_{10}[(\alpha\text{-}SiW_{11}O_{39}M)_2(\mu\text{-}OH)_2]\cdot 4H_2O$ (M = Zr, **Zr-edge**; Hf, **Hf-edge**) and $(Et_2NH_2)_{11}[(\alpha\text{-}SiW_{11}O_{39}M)_2(\mu\text{-}OH)_3]\cdot 15H_2O$ (M = Zr, **Zr-face**; Hf, **Hf-face**). We successfully determined their molecular structures by X-ray crystallography. When the solution was adjusted to pH 4.5 with a 1 M aqueous HCl solution, **Zr-edge** or **Hf-edge** was crystallized. On the other hand, from a solution adjusted to pH 9.5 with a 1 M aqueous KOH solution, the crystals of **Zr-face** or **Hf-face** were formed. Two central Zr and Hf atoms of **Zr-edge** and **Hf-edge** were linked by two μ-OH groups, i.e., an edge-sharing linkage, whereas those of **Zr-face** and **Hf-face** were linked by three μ-OH groups, i.e., a face-sharing linkage. **Zr-face** and **Hf-face** are the first examples of Zr/Hf-containing POM dimers linked in a face-sharing fashion. In the case of heteroatom P, the 2:2-type Zr^{IV}-containing Keggin POM decomposed in basic conditions. Therefore, the 2:2-type Keggin POM in a face-sharing fashion can be prepared only if the heteroatom is Si due to its basic resistance. From the viewpoint of catalysis, Zr^{IV}/Hf^{IV}-containing POMs have attracted much attention [20]. Oxidation catalysis for H_2O_2-based epoxidation of olefins by the present 2:2-type Keggin POM in a face-sharing fashion is in progress.

Acknowledgments

This work was supported by a Grant-in-Aid for Scientific Research (C) No. 22550065 from the Ministry of Education, Culture, Sports, Science and Technology, Japan.

Appendix A. Supplementary data

CCDC 875058, 875059, 875060, and 875061 contain the supplementary crystallographic data for **Zr-edge**, **Zr-face**, **Hf-edge**, and **Hf-face**, respectively. These data can be obtained free of charge via http://www.ccdc.cam.ac.uk/conts/retrieving.html, or from the Cambridge Crystallographic Data Centre, 12 Union Road, Cambridge CB2 1EZ, UK; fax: (+44) 1223-336-033; or e-mail: deposit@ccdc.cam.ac.uk. Supplementary data associated with this article can be found, in the online version, at http://dx.doi.org/10.1016/j.poly.2012.08.062.

References

[1] M.T. Pope, Heteropoly and Isopoly Oxometalates, Springer-Verlag, New York, 1983.
[2] V.W. Day, W.G. Klemperer, Science 228 (1985) 533.
[3] M.T. Pope, A. Müller, Angew. Chem., Int. Ed. 30 (1991) 34.
[4] C.L. Hill, C.M. Prosser-McCartha, Coord. Chem. Rev. 143 (1995) 407.
[5] T. Okuhara, N. Mizuno, M. Misono, Adv. Catal. 41 (1996) 113.
[6] C.L. Hill, J. Mol. Catal. A: Chem. 114 (1996) 1. A series of 34 papers in a volume devoted to polyoxoanions in catalysis.
[7] C.L. Hill, Chem. Rev. 98 (1998) 1.
[8] R. Neumann, Prog. Inorg. Chem. 47 (1998) 317.
[9] M.T. Pope, A. Müller (Eds.), Polyoxometalate Chemistry from Topology via Self-Assembly to Applications, Kluwer Academic Publishers, Netherlands, 2001.
[10] T. Yamase, M.T. Pope (Eds.), Polyoxometalate Chemistry for Nano-Composite Design, Kluwer Academic Publishers, Netherlands, 2002.
[11] M.T. Pope, Polyoxoanions: synthesis and structure, Comprehensive Coordination Chemistry II, vol. 4, Elsevier Science, New York, 2004, p. 635.
[12] C.L. Hill, Polyoxometalates: reactivity, Comprehensive Coordination Chemistry II, vol. 4, Elsevier Science, New York, 2004, p. 679.
[13] C.L. Hill, J. Mol. Catal. A: Chem. 262 (2007) 1. A series of 32 recent papers in a volume devoted to polyoxometalates in catalysis.
[14] A. Proust, R. Thouvenot, P. Gouzerh, Chem. Commun. (2008) 1837.
[15] B. Hasenknopf, K. Micoine, E. Lacôte, S. Thorimbert, M. Malacria, R. Thouvenot, Eur. J. Inorg. Chem. (2008) 5001.
[16] D. Laurencin, R. Thouvenot, K. Boubekeur, F. Villain, R. Villanneau, M.-M. Rohmer, M. Benard, A. Proust, Organometallics 28 (2009) 3140.
[17] D.-L. Long, R. Tsunashima, L. Cronin, Angew. Chem., Int. Ed. 49 (2010) 1736.
[18] A. Dolbecq, E. Dumas, C.R. Mayer, P. Mialane, Chem. Rev. 110 (2010) 6009.
[19] C.P. Pradeep, D.-L. Long, L. Cronin, Dalton Trans. 39 (2010) 9443.
[20] K. Nomiya, Y. Sakai, S. Matsunaga, Eur. J. Inorg. Chem. (2011) 179.
[21] R. Villanneau, H. Carabineiro, X. Carrier, R. Thouvenot, P. Herson, F. Lemos, E.R. Ribeiro, M.J. Che, Phys. Chem. B 108 (2004) 12465.
[22] H. Carabineiro, R. Villanneau, X. Carrier, P. Herson, F. Lemos, E.R. Ribeiro, A. Proust, M. Che, Inorg. Chem. 45 (2006) 1915.
[23] R.J. Errington, S.S. Petkar, P.S. Middleton, W. McFarlane, W. Clegg, R.A. Coxall, W. Harrington, J. Am. Chem. Soc. 129 (2007) 12181.
[24] R.G. Finke, B. Rapko, T.J.R. Weakley, Inorg. Chem. 28 (1989) 1573.
[25] E.V. Radkov, V.G. Young Jr., R.H. Beer, J. Am. Chem. Soc. 121 (1999) 8953.
[26] A.J. Gaunt, I. May, D. Collison, M. Helliwell, Acta Crystallogr., Sect. C 59 (2003) i65.
[27] A.J. Gaunt, I. May, D. Collison, K.T. Holman, M.T. Pope, J. Mol. Struct. 656 (2003) 101.
[28] A.J. Gaunt, I. May, D. Collison, O.D. Fox, Inorg. Chem. 42 (2003) 5049.
[29] X. Fang, T.M. Anderson, Y. Hou, C.L. Hill, Chem. Commun. (2005) 5044.
[30] X. Fang, T.M. Anderson, C.L. Hill, Angew. Chem., Int. Ed. 44 (2005) 3540.
[31] B.S. Bassil, M.H. Dickman, U. Kortz, Inorg. Chem. 45 (2006) 2394.
[32] O.A. Kholdeeva, G.M. Maksimov, R.I. Maksimovskaya, M.P. Vanina, T.A. Trubitsina, D.Y. Naumov, B.A. Kolesov, N.S. Antonova, J.J. Carbo, J.M. Poblet, Inorg. Chem. 45 (2006) 7224.
[33] O.A. Kholdeeva, R.I. Maksimovskaya, J. Mol. Catal. A: Chem. 262 (2007) 7.
[34] M.N. Sokolov, E.V. Chubaroba, E.V. Peresypkina, A.V. Virovets, V.P. Fedin, Russ. Chem. Bull., Int. Ed. 56 (2007) 220.
[35] S. Yamaguchi, Y. Kikukawa, K. Tsuchida, Y. Nakagawa, K. Uehara, K. Yamaguchi, N. Mizuno, Inorg. Chem. 46 (2007) 8502.
[36] X. Fang, C.L. Hill, Angew. Chem., Int. Ed. 46 (2007) 3877.
[37] Y. Hou, X. Fang, C.L. Hill, Chem. Eur. J. 13 (2007) 9442.

[38] Y. Kikukawa, S. Yamaguchi, K. Tsuchida, Y. Nakagawa, K. Uehara, N. Mizuno, J. Am. Chem. Soc. 130 (2008) 5472.
[39] N. Leclerc-Laronze, J. Marrot, M. Haouas, F. Taulelle, E. Cadot, Eur. J. Inorg. Chem. (2008) 4920.
[40] B.S. Bassil, S.S. Mal, M.H. Dickman, U. Kortz, H. Oelrich, L. Walder, J. Am. Chem. Soc. 130 (2008) 6696.
[41] R. Copping, L. Jonasson, A.J. Gaunt, D. Drennan, D. Collison, M. Helliwell, R.J. Pirttijarvi, C.J. Jones, A. Huguet, D.C. Apperley, N. Kaltsoyannis, I. May, Inorg. Chem. 47 (2008) 5787.
[42] S.S. Mal, N.H. Nsouli, M. Carraro, A. Sartorel, G. Scorrano, H. Oelrich, L. Walder, M. Bonchio, U. Kortz, Inorg. Chem. 49 (2010) 7.
[43] C. Jahier, S.S. Mal, U. Kortz, S. Nlate, Eur. J. Inorg. Chem. (2010) 1559.
[44] R. Villanneau, D. Racimor, E. Messner-Henning, H. Rousselière, S. Picart, R. Thouvenot, A. Proust, Inorg. Chem. 50 (2011) 1164.
[45] M. Carraro, N. Nsouli, H. Oelrich, A. Sartorel, A. Sorarù, S.S. Mal, G. Scorrano, L. Walder, U. Kortz, M. Bonchio, Chem. Eur. J. 17 (2011) 8371.
[46] C.N. Kato, A. Shinohara, K. Hayashi, K. Nomiya, Inorg. Chem. 45 (2006) 8108.
[47] Y. Saku, Y. Sakai, A. Shinohara, K. Hayashi, S. Yoshida, C.N. Kato, K. Yoza, K. Nomiya, Dalton Trans. (2009) 805.
[48] K. Nomiya, Y. Saku, S. Yamada, W. Takahashi, H. Sekiya, A. Shinohara, M. Ishimaru, Y. Sakai, Dalton Trans. (2009) 5504.
[49] Y. Saku, Y. Sakai, K. Nomiya, Inorg. Chem. Commun. 12 (2009) 650.
[50] Y. Saku, Y. Sakai, K. Nomiya, Inorg. Chim. Acta 363 (2010) 967.
[51] W. Zhang, S.-X. Liu, C.-D. Zhang, R.-K. Tan, F.-J. Ma, S.-J. Li, Y.-Y. Zhang, Eur. J. Inorg. Chem. (2010) 3473.
[52] A.S. Assran, S.S. Mal, N.V. Izarova, A. Banerjee, A. Suchopar, M. Sadakane, U. Kortz, Dalton Trans. 40 (2011) 2920.
[53] M.N. Sokolov, N.V. Izarova, E.V. Peresypkina, A.V. Virovets, V.P. Fedin, Russ. Chem. Bull., Int. Ed. 58 (2009) 507.
[54] M.N. Sokolov, N.V. Izarova, E.V. Peresypkina, D.A. Mainichev, V.P. Fedin, Inorg. Chim. Acta 362 (2009) 3756.
[55] A. Tézé, G. Hervé, Inorg. Synth. 27 (1990) 89.
[56] G.M. Sheldrick, Acta Crystallogr., Sect. A 46 (1990) 467.
[57] G.M. Sheldrick, SHELXL-97 Program for Crystal Structure Refinement, University of Göttingen, Göttingen, Germany, 1997.
[58] G.M. Sheldrick, SADABS, University of Göttingen, Göttingen, Germany, 1996.
[59] I.D. Brown, D. Altermatt, Acta Crystallogr., Sect. B 41 (1985) 244.
[60] I.D. Brown, R.D. Shannon, Acta Crystallogr., Sect. A 29 (1973) 266.
[61] I.D. Brown, Acta Crystallogr., Sect. B 48 (1992) 553.
[62] I.D. Brown, J. Appl. Crystallogr. 29 (1996) 479.

Polyhedron 52 (2013) 844–847

Contents lists available at SciVerse ScienceDirect

Polyhedron

journal homepage: www.elsevier.com/locate/poly

Synthesis, structure and antimicrobial activity of *L*-argininesilver(1+) nitrate

Akihiko Takayama, Rie Yoshikawa, Sayuri Iyoku, Noriko Chikaraishi Kasuga, Kenji Nomiya *

Department of Chemistry (formerly, Department of Materials Science), Faculty of Science, Kanagawa University, Tsuchiya, Hiratsuka, Kanagawa 259-1293, Japan

ARTICLE INFO

Article history:
Available online 20 July 2012

This paper is dedicated to Professor Alfred Werner on the 100th Anniversary of the award of his Nobel prize in Chemistry in 1913.

Keywords:
Silver(I) complexes
Arginine
Ag...Ag contacts
Self-assembly
Coordination polymers
Hydrogen bonding
Antimicrobial activities

ABSTRACT

A chiral coordination polymer of *L*-argininesilver(1+) nitrate, $\{\{[Ag(L\text{-Harg})](NO_3)\}_2\cdot H_2O\}_n$ (**1**) was prepared by vapor diffusion using a water-methanol mixed solution containing $AgNO_3$ and neutral *L*-arginine (*L*-Harg) as the inner solution and ether as the external solvent, followed by characterization by CHN analysis, FTIR, TG/DTA, single-crystal X-ray analysis and (^1H and ^{13}C) NMR spectroscopy. In the crystal, each silver(I) ion was coordinated by N_{amino} of one *L*-Harg and $O_{carboxy}$ of the other. Linear polymer chains consisting of repeating N_{amino}–Ag–$O_{carboxy}$ bonding units were connected by Ag...Ag (3.0440(5) Å) interaction and intermolecular hydrogen bonding to form a grid-like sheet. The sheets were connected by hydrogen bonds and electrostatic interaction between guanidium groups and NO_3^-. The antimicrobial activities of **1** against selected bacteria, yeasts and molds were evaluated by minimum inhibitory concentration (MIC). Complex **1** inhibited growth of four bacteria (*Escherichia coli*, *Pseudomonas aeruginosa*, *Bacillus subtilis*, and *Staphylococcus aureus*) and a yeast (*Saccharomyces cerevisiae*) moderately, the spectrum of which is different from that of $AgNO_3$.

© 2012 Elsevier Ltd. All rights reserved.

1. Introduction

The medicinal applications of coinage metal (Cu, Ag and Au) complexes have been established for years [1] and among them silver(I) complexes have been known to show antimicrobial activity [2]. It has been said that discovering new compounds that work against Gram-negative bacteria but simultaneously are not toxic to humans is difficult [3]. Fortunately, silver(I) complexes with natural amino-acid ligands have been shown to exhibit low toxicity towards human skin [4], and, in fact, silver(I) histidinate formulated with some additives has been practically used [5]. Notably, silver(I) complexes have been reported to show a different antimicrobial spectrum against microorganisms compared to the activity of the ligand itself and the hydrated silver(I) ion [6]. From the viewpoints of (1) model complexes for silver(I)–protein interaction, (2) the anticipated wider spectrum of antimicrobial activities and (3) structure–activity correlation, we focused on the silver(I) complexes of amino-acid ligands with both N and O donor atoms and without an S atom [7–9], and examined the antimicrobial activity of the silver(I) coordination polymer with *L*-argaine.

L-Arginine (*L*-Harg), i.e., (*S*)-2-amino-5-guanidinopentanoic acid, is one of the 20 most common natural α-amino acids, and is also known as playing an important role as a precursor of nitric oxide, urea, ornithine and agmatine [10]. It is classified as a basic amino acid because the distal end is capped by a guanidium group (p*K*a of 12.5) [11]. The conjugation between double bonds and nitrogen lone pairs in a guanidium group makes this compound a positively charged amino acid and also enables the formation of multiple hydrogen bonds. Although the behavior of arginine toward metal ions represents an important and useful subject of research [12–26], only a few investigations have been reported so far on the structures of metal complexes of arginine [15,22,25,26]. Our preliminary experiments have shown that there are many types of silver(I) complexes with *L*-arginine ligand, depending upon the reaction conditions such as the starting silver(I) source e.g., $AgNO_3$, Ag_2O, Ag_2SO_4, $Ag(CH_3CO_2)$ etc., the starting molar ratios of silver(I) and *L*-arginine, and pH and so on.

In this paper, we report the preparation and first crystal structure of a polymeric silver(I) complex with *L*-arginine, $\{\{[Ag(L\text{-Harg})](NO_3)\}_2\cdot H_2O\}_n$ (**1**) and its antimicrobial activity evaluated by minimum inhibitory concentration (MIC). We compared the results with those of other N- and O-coordinating silver(I) complexes having related amino acid ligands.

2. Experimental

2.1. Materials and measurements

The following reagent-grade chemicals were used as received: $AgNO_3$, Et_2O, dimethyl sulfoxide (DMSO), EtOH, $CHCl_3$, CH_2Cl_2,

Abbreviation: *L*-Harg, neutral *L*-arginine ligand with zwitter ionic structure.

* Corresponding author. Tel.: +81 463 59 4111; fax: +81 463 58 9684.
E-mail address: nomiya@kanagawa-u.ac.jp (K. Nomiya).

0277-5387/$ - see front matter © 2012 Elsevier Ltd. All rights reserved.
http://dx.doi.org/10.1016/j.poly.2012.07.031

MeOH, EtOAc, CH_3CN, and acetone (Wako); *L*-arginine (*L*-Harg) (Ajinomoto Co. Inc.); 4,4-dimethyl-4-silapentane-1-sulfonic acid (DSS) (Aldrich); and D_2O (99.9 D atom%, Isotec).

CHN elemental analyses were performed using a Perkin–Elmer PE2400 series II CHNS/O analyzer. Thermogravimetric (TG) and differential thermal analyses (DTA) were performed under air with a temperature ramp of 4 °C min^{-1} using a Rigaku Thermo Plus 2 TG 8120 instrument between 30 and 200 °C. Infrared spectra were recorded on a JASCO FT-IR 4100 spectrometer in KBr disks at room temperature. ^1H and $^{13}C\{^1H\}$ NMR spectra in solution were recorded at ambient temperature on a JEOL ECP500 NMR spectrometer. ^1H and $^{13}C\{^1H\}$ NMR spectra of the complexes were measured in a D_2O solution with reference to an internal DSS.

2.2. Preparation of $\{\{[Ag(L\text{-}Harg)](NO_3)\}_2\cdot H_2O\}_n$ (**1**)

To a solution of 85 mg (0.50 mmol) of $AgNO_3$ in 5 mL of water was added 86 mg (0.49 mmol) of *L*-Harg in 15 mL of water. Immediately, a white suspension was formed. After 30 min of stirring, 80 mL of MeOH was added to the suspension, and the mixture was filtered off through a folded filter paper (Whatman No. 5). Crystallization was carried out by vapor diffusion of an internal aqueous solution of the clear filtrate with diethyl ether as the external solvent. Colorless platelet crystals were formed in five days of standing at ambient temperature, which were washed with ether (30 mL × 2) and dried in vacuo for 2 h (30 mg, 17% yield). The crystals obtained were characterized as below. *Anal.* Calc. for $C_{12}H_{30}N_{10}O_{11}Ag_2$ or $\{\{[Ag(L\text{-}Harg)](NO_3)\}_2\cdot H_2O\}$ as a monomer unit: C, 20.41; H, 4.28; N, 19.83. Found: C, 20.69; H, 4.01; N, 19.85%. TG/DTA data: no weight loss was observed before decomposition temperature. Decomposition began at around 141 °C with an endothermic peak at 179 °C. Prominent IR bands in the 1800–400 cm^{-1} region (KBr disk): 1671 s, 1560 s, 1472 m, 1384 vs, 1214 w, 1121 w, 1100 w, 1038 w, 1008 w, 824 w, 658 m, 604 m, 565 m, 462 w cm^{-1}. ^1H NMR (D_2O, 26.5 °C): δ 1.59–1.81 ($C\underline{H}_2$, two multiplets, 4H), 3.21 ($C\underline{H}_2$, t, 2H), and 3.51 ($C\underline{H}$, t, 1H) ppm. ^{13}C NMR (D_2O, 27.8 °C): δ 27.04 (C4), 35.01 and 43.58 (C3 and C5), 59.12 (C2), 159.56 (C6), 182.91 (C1) ppm. The colorless crystals changed to brown within a few days. ^{109}Ag NMR measurement was unsuccessful because of insufficient solubility in D_2O.

2.3. X-ray crystallography

A single crystal of silver(I) complex **1** was mounted on a loop and used for the measurements of precise cell constants and the collection of intensity data at 100 K on a Bruker Smart APEX CCD diffractometer. The structures were solved by direct methods, followed by difference Fourier calculation and were refined by full-matrix least-squares on F^2 using a SHELXTL program package [27]. All non-hydrogen atoms were refined anisotropically. The hydrogen atoms were placed geometrically or found on a difference Fourier-map and were treated using a riding model. The crystal data and structural refinement of complex **1** are summarized in Table 1.

2.4. Antimicrobial activity

The antimicrobial activities of *L*-argininesilver(1+) nitrate were estimated by minimum inhibitory concentration (MIC: μg mL^{-1}) in water, as described elsewhere [28].

3. Results and discussion

Preparation of complex **1** was carried out by using a mixture of $AgNO_3$ and *L*-arginine (*L*-Harg) as the inner water-methanol mixed solution and ether as an external solvent at room temperature, and colorless, platelet crystals of **1** were obtained in 17% (30 mg scale) yield. The composition and molecular formula of **1** were consistent with elemental analysis and FTIR. X-ray structure analysis revealed that *L*-argininesilver(1+) nitrate **1** formed a coordination polymer. In the polymer, each silver(I) ion was bound to the N_{amino} atom (N1) of one arginine ligand and to the $O_{carboxy}$ atom ($O1^{iii}$) of the other, i.e., the N–Ag–O bonding units were repeated, as shown in Fig. 1a [Ag1–N1 and Ag1–$O1^{iii}$ distances are 2.1440(19) and 2.152(2) Å, respectively; N1–Ag1–$O1^{iii}$ angle 169.07(8)°, Table 2].

Silver(I) complexes formed by amino acids with N and O donor atoms and without an S atom have been classified into four types (I–IV) based on the bonding modes of the silver(I) center [7]. Type I contains only Ag–O bonds, as observed in $\{[Ag_2(D\text{-}Hasp)(L\text{-}$

Table 1
Crystallographic data for $\{\{[Ag(L\text{-}Harg)](NO_3)\}_2\cdot H_2O\}_n$ (**1**).

Empirical formula	$C_{12}H_{30}O_{11}N_{10}Ag_2$
Formula weight	704.18
Crystal system	monoclinic
T (K)	90
Space group	$C2$(No.5)
a (Å)	12.6657(15)
b (Å)	7.5091(9)
c (Å)	12.9366(16)
α (°)	90
β (°)	100.570(2)
γ (°)	90
V (Å^3)	1209.5(3)
Z	2
D_{calc} (g cm^{-3})	1.94
μ (mm^{-1})	1.69
No. of reflections total	4356
Unique	2548
Goodness-of-fit (GOF)	1.157
No. of observations [$I > 2\sigma(I)$]	2543
R_{int}	0.0217
R	0.0187
R_w	0.0539

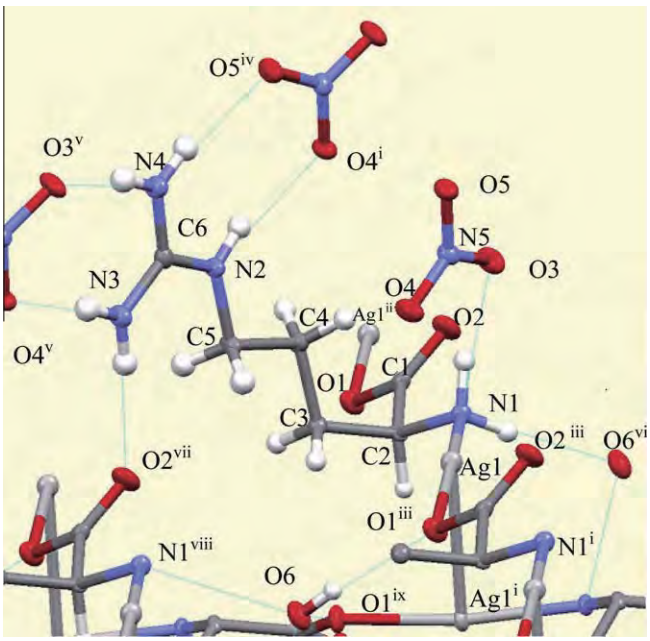

Fig. 1a. Molecular structure of the local coordination around silver(I) centers of $\{\{[Ag(L\text{-}Harg)](NO_3)\}_2\cdot H_2O\}_n$ **1** with 50% probability ellipsoids (symmetry operations: i = –x, y, 1–z; ii = 0.5+x, 0.5+y, z; iii = –0.5+x, –0.5+y, z; iv = –x, y, –z, v = –x, –1+y, –z; vi = x, 1+y, z; vii = –1+x, y, z; viii = x, 1–y, z; ix = 0.5–x, –0.5–y, 1–z).

Table 2
Selected distances (Å) and angles (°) for $\{\{[Ag(L\text{-Harg})]_2(NO_3)\}_2\cdot H_2O\}_n$ (**1**).

$\{\{[Ag(L\text{-Harg})](NO_3)\}_2\cdot H_2O\}_n$			
Ag1–N1	2.152(2)	N1–Ag1–O1^{iii}	169.07(8)
Ag1–O^{iii}	2.1440(19)	Ag1^{i}–Ag1–O1	84.38(5)
Ag1–Ag1^{i}	3.0440(5)	Ag1^{i}–Ag1–N1	85.35(6)
C6–N2	1.331(4)		
C6–N3	1.324(3)		
C6–N4	1.339(3)		
N1…O3	3.047(3)		
N1…O6^{vi}	3.001(4)		
N2…O4	2.902(3)		
N3…O2^{vii}	2.976(3)		
N3…O4^{v}	2.941(3)		
N4…O3	2.956(3)		
N4…O5	2.952(4)		

Symmetry operations: i = –x, y, 1–z; ii = 0.5+x, 0.5+y, z; iii = –0.5+x, –0.5+y, z; iv = –x, y, –z; v = –x, –1+y, –z; vi = x, 1+y, z; vii = –1 + x, y, z.

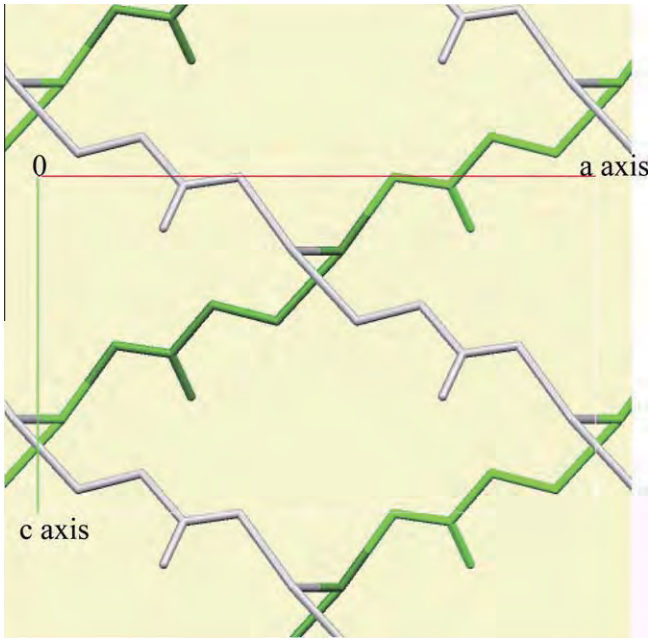

Fig. 1b. View of a grid-like sheet of the polymer backbones (containing only Ag1, C1, C2, N1, O1 and O2) of **1** with 50% probability ellipsoids. Colors of chains were changed by symmetry operations. (Colour online.)

Hasp)]·1.5$H_2O\}_n$, $\{[Ag(\beta\text{-ala})]NO_3\}_2$ [29], $[Ag(Hglygly)]NO_3$ [30]. In type II, the two-coordinate O–Ag–O and N–Ag–N bonding units are alternately repeated, as found in $\{[Ag(gly)]_2\cdot H_2O\}_n$. The two-coordinate N–Ag–O bonding units are repeated in type III, as seen in $\{[Ag(L\text{-asn})]\}_n$ [7], and complexes that contain only Ag–N bonds

Fig. 1c. View of the grid-like sheets (green), NO_3^- (blue) and hydrated water molecules (red) of **1** with 50% probability ellipsoids along the b axis. (Colour online.)

belong to type IV, as found in silver(I) histidinates [8,9]. Thus, complex **1** belongs to type III. The other $O_{carboxy}$ atom (O2) did not take part in the coordination of silver(I). Another N–Ag–O bonding chain (N1^{i}–Ag1^{i}–O1^{ix}) is located in a skew position of the former polymer chain, as shown in Fig. 1a and also they are displayed in green and white lines in Fig. 1b. Van der Waals contact was observed between Ag1 and Ag1^{i} (3.0440(5) Å) [31,32]. A hydrated water molecule (O6^{vi}) connects polymer chains through hydrogen bonds between N_{amino} groups (N1 and N1^{i}). As a result, linear N–Ag–O chains of green and white are arranged in a grid-like sheet shown in Fig. 1b running perpendicular to the *c* axis. Neither the terminal guanidium groups nor NO_3^- participate in coordination to the silver(I) center as seen in Fig. 1a, but they form multiple hydrogen bonds. Five hydrogen atoms of the guanidium group form hydrogen bonds with two NO_3^- (O4^{iv}, O5^{iv}, O3^{v} and O4^{v}) and an $O_{carboxy}$ atom (O2^{vii}). At the same time, NO_3^- groups (the blue groups in Fig. 1c) connect the grid-like sheets (shown in green chains) electrostatically through positively charged guanidium groups. NO_3^- also interacted weakly with the silver(I) of an adjacent coordination polymer chain. These multiple interactions between sheets would be a reason why **1** is a sparingly soluble complex in water. The difference in polymeric chain of structure between $[Ag(L\text{-asn})]_n$ and **1** is caused by bulkiness and the charge distribution of substituent groups [7] see Chart 1.

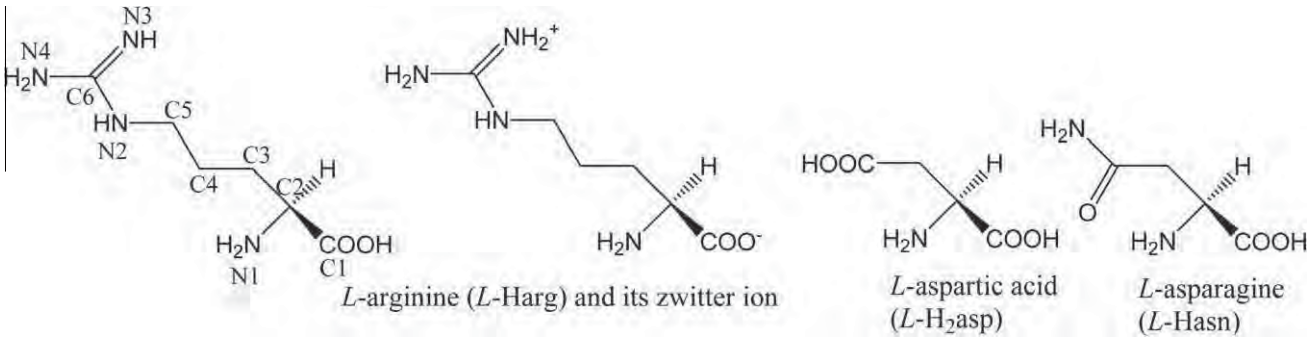

Chart 1. Scheme of *L*-arginine (*L*-Harg) with atomic numbering, its zwitter ion and related amino acids.

Table 3
Antimicrobial activities of $\{\{[Ag(L\text{-Harg})](NO_3)\}_2\cdot H_2O\}_n$ **1**, $AgNO_3$ and a related complex evaluated by minimum inhibitory concentration (MIC; μg mL^{-1}).

	L-Harg	$AgNO_3$[a]	$\{\{[Ag(L\text{-Harg})](NO_3)\}_2\cdot H_2O\}_n$ (**1**)	$\{[Ag(L\text{-asn})]\}_n$[b]
Escherichia coli	>1000	6	125	31.3
Bacillus subtilis	>1000	>1600	125	250
Staphylococcus aureus	>1000	100	125	250
Pseudomonas aeruginosa	>1000	6	62.5	62.5
Candida albicans	>1000	>1600	>1000	125
Saccharomyces cerevisiae	>1000	1600	125	62.5
Aspergillus niger	>1000	>1600	>1000	62.5
Penicillium citrinum	>1000	>1600	>1000	62.5

[a] Ref. [33].
[b] Ref. [7].

Changes of signals of arginine were observed in the 1D NMR spectra of **1** (^1H and ^{13}C NMR) upon coordination. However, in the both ^1H and ^{13}C NMR spectra of **1**, little shifts were observed for the signals located close to the guanidium group, which was in good agreement with the structure of **1** in the crystal, revealing that the guanidium groups did not coordinate to silver(I) .

The antimicrobial activities of the silver(I) complexes are listed in Table 3. The antimicrobial activities of complex **1** and $AgNO_3$ against selected bacteria (*Escherichia coli*, *Bacillus subtilis*, *Staphylococcus aureus* and *Pseudomonas aeruginosa*), yeasts (*Candida albicans* and *Saccharomyces cerevisiae*) and molds (*Aspergillus niger* and *Penicillium citrinum*) were evaluated by minimum inhibitory concentration (MIC), as shown in Table 3. Complex **1** inhibited the growth of four bacteria (*E. coli*, *P. aeruginosa*, *B. subtilis*, and *S. aureus*) and a yeast (*S. cerevisiae*) moderately. Complex **1** showed a wider spectrum of antimicrobial activities compared to those of hydrated Ag^+ ($AgNO_3$) [33], which exhibited effective activities against two Gram-negative bacteria. The key factors which lead to a wide spectrum of antimicrobial activities are (1) the ease of ligand replacement and (2) the N–Ag–O binding mode of complex **1**, which also supports the nature of the atom that coordinates with the silver(I) center plus its bonding properties (rather than the solubility, charge, chirality, or degree of polymerization of the complexes) [34]. The antimicrobial activities of **1** were less effective in comparison with those of $\{[Ag(L\text{-asn})]\}_n$, although both silver(I) complexes belong to the same type III having O–Ag–N polymer structure. This may be caused by the multiple-bonded sheet structure of **1**.

4. Conclusions

In summary, a coordination polymer, $\{\{[Ag(L\text{-Arg})](NO_3)\}_2\cdot H_2O\}_n$, **1**, was prepared by vapor diffusion and was well-characterized by CHN analysis, FTIR, single-crystal X-ray analysis and (^1H and ^{13}C) NMR spectroscopy. In the crystal, each silver(I) ion was coordinated by N_{amino} of one *L*-Harg and $O_{carboxy}$ of the other. Linear polymers consisting of repeating N_{amino}–Ag–$O_{carboxy}$ bonding units were connected by Ag...Ag (3.0440(5) Å) interactions and intermolecular hydrogen bonding to form a grid-like sheet of polymer chains. Multiple hydrogen bonds and electrostatic interaction were formed between guanidium groups and NO_3^-. The antimicrobial activities of **1** against selected bacteria, yeasts and molds, evaluated by MIC, revealed that N and O bonding of complex **1** inhibited the growth of four bacteria (*E. coli*, *P. aeruginosa*, *B. subtilis*, and *S. aureus*) and a yeast (*S. cerevisiae*) moderately, which was slightly different from those of hydrated silver(I) ion and $\{[Ag(L\text{-asn})]\}_n$.

Acknowledgements

Financial support from Ajinomoto Co. Ltd. is acknowledged.

Appendix. A. Supplementary data

Supplementary data CCDC 880566 contains the supplementary crystallographic data for $\{\{[Ag(L\text{-Harg})](NO_3)\}_2\cdot H_2O\}_n$ (**1**). These data can be obtained free of charge via http://www.ccdc.cam.ac.uk/conts/retrieving.html, or from the Cambridge Crystallographic Data Centre, 12 Union Road, Cambridge CB2 1EZ, UK; fax: (+44) 1223-336-033; or e-mail: deposit@ccdc.cam.ac.uk.

References

[1] C.F. Shaw III, Chem. Rev. 99 (1999) 2589.
[2] A. Kascatan-Nebioglu, M.J. Panzner, C.A. Tessier, C.L. Cannon, W.J. Youngs, Coord. Chem. Rev. 251 (2007) 884.
[3] S. Silver, FEMS Microbiol. Rev. 27 (2003) 341.
[4] K.J. Williams, R.P. Bax, Curr. Opin. Invest. Drugs 10 (2009) 157.
[5] S. Arai, T. Kubota, M. Yabe, K. Nomiya, (2009) WO 2009098850.
[6] S. Ahmad, A.A. Isab, S. Ali, A.R. Al-Arfaj, Polyhedron 25 (2006) 1633.
[7] K. Nomiya, H. Yokoyama, J. Chem. Soc., Dalton Trans. (2002) 2483.
[8] N.C. Kasuga, Y. Takagi, S. Tsuruta, W. Kuwana, R. Yoshikawa, K. Nomiya, Inorg. Chim. Acta 368 (2011) 44.
[9] K. Nomiya, S. Takahashi, R. Noguchi, S. Nemoto, T. Takayama, M. Oda, Inorg. Chem. 39 (2000) 3301.
[10] S.M. Morris Jr., Am. J. Clin. Nutr. 83 (2006) 508S.
[11] K.A. Shug, W. Linder, Chem. Rev. 105 (2005) 67.
[12] A. Taurins, Can. J. Res. 28B (1950) 762.
[13] D.J. Perkins, Biochem. J. 55 (1953) 649.
[14] S.P. Datta, A.K. Grzybowski, J. Chem. Soc. (1959) 1091.
[15] H. Maeda, A. Odani, T. Yamazaki, T. Yajima, O. Yamauchi, Inorg. Chem. 32 (1993) 1111.
[16] O. Yamauchi, A. Odani, Pure Appl. Chem. 8 (1996) 469.
[17] R.C. Santana, R.O. Cunha, J.F. Carbalho, I. Vencato, R. Calvo, J. Inorg. Biochem. 99 (2005) 415.
[18] M. Antonilli, E. Bottari, M.R. Festa, L. Gentile, Ann. Chim. 97 (2007) 1257.
[19] M.W. Forbes, M.F. Bush, N.C. Polfer, J. Oomens, R.C. Dunbar, E.R. Williams, R.A. Jockusch, J. Phys. Chem. A 111 (2007) 11759.
[20] M.F. Bush, J. Oomens, R.J. Saykally, E.R. Williams, J. Am. Chem. Soc. 130 (2008) 6463.
[21] M. Remko, D. Fitz, B.M. Rode, J. Phys. Chem. A 112 (2008) 7652.
[22] A.K. Patra, T. Bhowmick, S. Roy, S. Ramakumar, A.R. Chakravatry, Inorg. Chem. 48 (2009) 2932.
[23] E. Bottari, M.R. Festa, L. Gentile, J. Chem. Eng. Data 56 (2011) 1903.
[24] T. Darbre, M. Machuqueiro, Chem. Commun. (2003) 1090.
[25] C.D.L. Saunders, L.E. Longbardi, N. Burford, M.D. Lumsden, U. Werner-Zwanzinger, B. Chen, R. McDonald, Inorg. Chem. 50 (2011) 2700.
[26] A. Alagha, D.A. Brown, M. Elawad, H. Muller-Bunz, H. Nimir, A.I. Yanovsky, K.B. Nolan, Inorg. Chim. Acta 377 (2011) 185.
[27] G.M. Sheldrick, SHELXTL, Version 5.10, Bruker Analytical X-ray Systems, Madison, WI, USA, 1997.
[28] K. Nomiya, K. Tsuda, N.C. Kasuga, J. Chem. Soc., Dalton Trans. (1998) 1653.
[29] M.E. Kamwaya, E. Papavinasam, S.G. Teoh, R.K. Rajaram, Acta Crystallogr., Sect. C 40 (1984) 1318.
[30] C.B. Acland, H.C. Freeman, Chem. Commun. (1971) 1016.
[31] A.F. Wells, Structural Inorganic Chemistry, fourth ed., Oxford University Press, London, 1975. pp. 1015.
[32] A. Bondi, J. Phys. Chem. 68 (1964) 441.
[33] K. Nomiya, Y. Kondoh, K. Onoue, N.C. Kasuga, H. Nagano, M. Oda, T. Sudoh, S. Sakuma, J. Inorg. Biochem. 58 (1995) 255.
[34] K. Nomiya, I. Azumaya, N.C. Kasuga, T. Kato, Curr. Top. Biochem. Res. 10 (2008) 1.

EurJIC European Journal of Inorganic Chemistry
ChemPubSoc Europe
ULL A

DOI:10.1002/ejic.201201290

Monomer and Dimer of Mono-titanium(IV)-Containing α-Keggin Polyoxometalates: Synthesis, Molecular Structures, and pH-Dependent Monomer–Dimer Interconversion in Solution

CLUSTER ISSUE

Yusuke Matsuki,[a] Yuki Mouri,[a] Yoshitaka Sakai,[a] Satoshi Matsunaga,[a] and Kenji Nomiya*[a]

Dedicated to Professor Michael T. Pope on the occasion of his 80th birthday

Keywords: Polyoxometalates / Titanium / Tungsten

Powder and crystalline samples of the monomer $(Et_2NH_2)_5[\alpha\text{-}PW_{11}TiO_{40}]\cdot 2H_2O$ (EtN-**1**) and a crystalline sample of the μ-oxo dimer $(Et_2NH_2)_8[(\alpha\text{-}PW_{11}TiO_{39})_2O]\cdot 6H_2O$ (EtN-**2**) of mono-titanium(IV)-containing α-Keggin polyoxometalates (POMs) were prepared and characterized by elemental analysis, thermogravimetry/differential thermal analysis (TG/DTA), FTIR, single-crystal X-ray crystallography, and solid-state cross-polarization magic angle spinning (CPMAS) ^{31}P NMR and solution (^{31}P and ^{183}W) NMR spectroscopy. The molecular structure of the dimeric polyoxoanion with a μ-oxo group in **2** was determined for the first time. The monomer–dimer equilibrium in solution was clarified by pH-varied ^{31}P NMR spectroscopy.

Introduction

Polyoxometalates (POMs) are molecular metal oxide clusters that have attracted considerable attention in the fields of catalysis, medicine, surface science, materials science, and nanotechnology because POMs are often considered to be molecular analogues of metal oxides in terms of structural analogy.[1] The ionic radius of Ti^{IV} (0.75 Å) is close to that of W^{VI} (0.74 Å), which suggests that Ti^{IV} should fit nicely into the POM framework. Thus, site-selective substitution of W^{VI} atoms in POMs with Ti^{IV} atoms is particularly interesting because of the formation of multicenter active sites with corner- or edge-sharing TiO_6 octahedra and also the generation of oligomeric species through Ti–O–Ti bonds.[2–6] A number of catalytic reactions of titanium(IV)-containing POMs have also been reported so far.[1g,1m,3] Oxidation catalysis by peroxo and hydroperoxo species of Ti-containing Keggin POMs has been extensively studied.[3]

The dimerization process in Lindqvist and Keggin POMs (i.e., the mechanism of formation of the μ-oxo dimer) has been discussed by using DFT studies,[7] in which the most probable thermodynamic mechanism for the smaller clusters has been proposed: first, the formation of a protonated monomer, the protonation site of which is the O atom of a terminal M=O bond; second, the formation of di-μ-hydroxo intermediate from the M–OH species (this requires +28 kcal mol^{-1}); and the final step, formation of the μ-oxo dimer by loss of a water molecule from the di-μ-hydroxo intermediate.

The tri-titanium(IV)-substituted Dawson POM "$[P_2W_{15}Ti_3O_{62}]^{12-}$" has been realized through the formation of several tetrameric species[4] [e.g., the tetrameric Dawson Ti–O–Ti-bridged anhydride form without bridging μ_3-$Ti(H_2O)_3$ octahedral groups (the nonbridging Dawson tetramer)], which has an encapsulated Cl^- anion in the central cavity {i.e., $[\{\alpha\text{-}1,2,3\text{-}P_2W_{15}Ti_3O_{57.5}(OH)_3\}_4Cl]^{25-}$},[4b–4d] an encapsulated NH_4^+ cation species {i.e., $[(\alpha\text{-}1,2,3\text{-}P_2W_{15}Ti_3O_{60.5})_4(NH_4)]^{35-}$},[4g] and also the tetrameric Dawson species with bridging μ_3-$Ti(H_2O)_3$ groups (the bridging Dawson tetramer) with an encapsulated anion X $[\{\alpha\text{-}1,2,3\text{-}P_2W_{15}Ti_3O_{59}(OH)_3\}_4\{\mu_3\text{-}Ti(H_2O)_3\}_4X]^{21-}$ (X = Cl, Br, I, NO_3).[4a,4d,4e]

The dimeric mono-titanium(IV)-substituted Dawson POM {i.e., the μ-oxo Dawson dimer $[(\alpha_2\text{-}P_2W_{17}TiO_{61})_2(\mu\text{-}O)]^{14-}$ and its protonated species $[(\alpha_2\text{-}P_2W_{17}TiO_{61})(\alpha_2\text{-}P_2W_{17}TiO_{61}H)(\mu\text{-}O)]^{13-}$} has been structurally charac-

[a] Department of Chemistry, Faculty of Science, Kanagawa University, Hiratsuka, Kanagawa 259-1293, Japan
Homepage: http://professor.kanagawa-u.ac.jp/sci/chemistry/prof05.html

Supporting information for this article is available on the WWW under http://dx.doi.org/10.1002/ejic.201201290.

© 2013 Wiley-VCH Verlag GmbH & Co. KGaA, Weinheim

terized by single-crystal X-ray crystallography.[5] In the latter, the protonation site is the surface Ti–O–W site of one of the two Dawson units, but not the μ-oxo site, and therefore, two Dawson units became inequivalent. The monomeric form $K_8[\alpha_2\text{-}P_2W_{17}TiO_{62}]\cdot 18H_2O$ was also prepared. pH-varied ^{31}P NMR spectroscopic measurements showed the presence of monomer–dimer equilibrium in solution; that is, the predominant species in aqueous solutions are the monomeric species at pH 7.0, the μ-oxo dimer at pH 1.0–3.0, and the monoprotonated species at pH 0.5, the protonation site of which is the surface Ti–O–W site of one of the two Dawson units.

In terms of the Keggin derivatives, tri-titanium(IV)-1,2,3- and di-titanium(IV)-1,2-substituted Keggin POMs have been isolated as tri-μ-oxo dimers {e.g., $[(\beta\text{-}1,2,3\text{-}SiW_9Ti_3O_{37})_2O_3]^{14-}$,[2a] $[(\alpha\text{-}1,2,3\text{-}GeW_9Ti_3O_{37})_2O_3]^{14-}$,[2b] $[(\beta\text{-}1,2,3\text{-}GeW_9Ti_3O_{37})_2O_3]^{14-}$,[2c] and $[(\alpha\text{-}1,2,3\text{-}PW_9Ti_3O_{37})_2O_3]^{12-}$}[2e] and as a di-μ-oxo dimer {e.g., $[(\alpha\text{-}1,2\text{-}PW_{10}Ti_2O_{38})_2O_2]^{10-}$}.[2d] Furthermore, di-titanium(IV)-substituted γ-Keggin silicotungstate and germanotungstate {i.e., $[\{\gamma\text{-}SiTi_2W_{10}O_{36}(OH)_2\}_2O_2]^{8-}$[2f] and $[\{\gamma\text{-}GeTi_2W_{10}O_{36}(OH)_2\}_2O_2]^{8-}$}[2g] have also been prepared as a dimeric species, whereas a di-titanium(IV)-1,5-substituted β-Keggin POM has been isolated as a tetrameric species, $[\{\beta\text{-}Ti_2SiW_{10}O_{39}\}_4]^{24-}$.[2h] In addition, cyclic tri-titanium(IV)-substituted Keggin trimers such as $[(\alpha\text{-}Ti_3PW_9O_{38})_3(PO_4)]^{18-}$,[2i] $[(\alpha\text{-}Ti_3SiW_9O_{37}OH)_3\{TiO_3(OH_2)_3\}]^{17-}$,[2i] and $\{K[\{Ge(OH)O_3\}(GeW_9Ti_3O_{38}H_2)_3]\}^{14-}$[2j] have recently been reported.

As to the titanium(IV)-substituted Keggin POMs, however, it should be noted that no structural determination through X-ray crystallography of the mono-titanium(IV)-containing POMs has been reported. Concerned with such POMs, Kholdeeva's group has reported the preparation and characterization of the μ-hydroxo dimer $(Bu_4N)_7[(PTiW_{11}O_{39})_2(\mu\text{-}OH)]$ (H**1**) formed in acidic MeCN from the monomeric species Keggin POM $(Bu_4N)_5[PTiW_{11}O_{40}]$ (**2**), and pH-dependent interconversion between them.[6a] The same research group has also reported the μ-oxo dimer $(Bu_4N)_8[(PTiW_{11}O_{39})_2(\mu\text{-}O)]$ (μ-oxo dimer **1**) and three monomeric derivatives $(Bu_4N)_4[PTi(L)W_{11}O_{39}]$ {L = OH, OMe, and OAr [ArOH = 2,3,6-trimethylphenol (TMP)]}, which have been synthesized starting from the μ-hydroxo dimer $(Bu_4N)_7[(PTiW_{11}O_{39})_2(\mu\text{-}OH)]$ (H**1**) or the heteropolyacid $H_5PW_{11}TiO_{40}\cdot 12H_2O$.[6b] In these studies, however, the molecular structures of the μ-hydroxo dimer and the μ-oxo dimer have not been determined through X-ray crystallography.

In this work, we have prepared and characterized the monomeric Keggin POM $(Et_2NH_2)_5[\alpha\text{-}PW_{11}TiO_{40}]\cdot 2H_2O$ (EtN-**1**) and the μ-oxo Keggin dimer $(Et_2NH_2)_8[(\alpha\text{-}PW_{11}TiO_{39})_2O]\cdot 6H_2O$ (EtN-**2**), and also confirmed a monomer–dimer equilibrium in solution by pH-varied ^{31}P NMR spectroscopy. Furthermore, we have successfully determined the molecular structure of μ-oxo dimeric polyoxoanion **2** by X-ray crystallography. Herein, we report full details of the synthesis and characterization of EtN-**1** and EtN-**2**.

Results and Discussion

Synthesis and Characterization

The monomer and dimer of the titanium(IV)-substituted Keggin POM have been significantly discussed.[6] However, their X-ray structures have not been reported so far, because the crystals suitable for X-ray crystallography have never been obtained. In this work, we successfully prepared and crystallized the monomer in the presence of NaOAc. The dimer was also crystallized from the monomer under acidic conditions of pH 1.0 and the X-ray structure was determined.

In the presence of NaOAc, a 1:1 molar ratio reaction of mono-lacunary Keggin POM $K_7[PW_{11}O_{39}]\cdot 8H_2O$ with $TiCl_4$ in an aqueous solution and the addition of excess amounts of solid Et_2NH_2Cl produced the diethylammonium salt of the monomeric Keggin POM, $(Et_2NH_2)_5[\alpha\text{-}PW_{11}TiO_{40}]\cdot 2H_2O$ (EtN-**1**). Monomer EtN-**1** was dissolved in an H_2O/MeOH (1:1 v/v) mixed solvent, and the solution was adjusted to pH 1.0 with a 1 M aqueous HCl solution, followed by stirring for 2 days at room temperature. The solution was evaporated slowly, and after 3 days, colorless, clear plate crystals of the dimer Keggin POM, $(Et_2NH_2)_8[(\alpha\text{-}PW_{11}TiO_{39})_2O]\cdot 6H_2O$ (EtN-**2**), were obtained. These compounds were characterized by CHN elemental analysis, FTIR, thermogravimetry/differential thermal analysis (TG/DTA), X-ray crystallography, and solution and solid-state cross-polarization magic angle spinning (CPMAS) ^{31}P NMR and solution ^{183}W NMR spectroscopy.

The number of water molecules was determined by TG/DTA measurements under atmospheric conditions and elemental analysis. In the TG/DTA, weight losses of 1.15% observed at below 199.3 °C for EtN-**1** (Figure S1 in the Supporting Information) and 1.84% observed at below 122.5 °C for EtN-**2** (Figure S2 in the Supporting Information) corresponded to approximately two water molecules and approximately six water molecules, respectively, which were consistent with the data from elemental analyses.

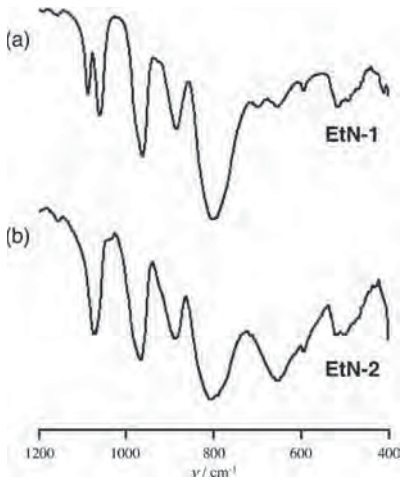

Figure 1. The FTIR spectra in the polyoxoanion region (1200–400 cm^{-1}), measured in KBr disks, of (a) $(Et_2NH_2)_5[\alpha\text{-}PW_{11}TiO_{40}]\cdot 2H_2O$ (EtN-**1**) and (b) $(Et_2NH_2)_8[(\alpha\text{-}PW_{11}TiO_{39})_2O]\cdot 6H_2O$ (EtN-**2**).

© 2013 Wiley-VCH Verlag GmbH & Co. KGaA, Weinheim

The solid FTIR spectrum of monomer EtN-**1** (Figure 1, a) measured in a KBr disk showed prominent bands in the polyoxometalate region (1200–400 cm^{-1}) at 1090, 1062, 964, 886, and 801 cm^{-1}, which originated from mono-lacunary Keggin POM, $[PW_{11}O_{39}]^{7-}$. These are the characteristic vibration bands of the Keggin-type "$PW_{12}O_{40}^{3-}$".[8] The Ti–O–Ti vibration band of the inter-Keggin units was not observed at around 650 cm^{-1}. The P–O vibration band was observed as split peaks at 1090 and 1062 cm^{-1}. The FTIR spectrum of dimer EtN-**2** measured in a KBr disk also showed prominent bands in the polyoxometalate region (1200–400 cm^{-1}) at 1075, 968, 889, 807, and 654 cm^{-1}. The Ti–O–Ti vibration band of the inter-Keggin units in EtN-**2** was observed at 654 cm^{-1}, which was consistent with the X-ray crystallography data (see below). The P–O vibration band of EtN-**2** was observed as a single peak at 1075 cm^{-1}.

Molecular Structures of Dimeric EtN-2 and Monomeric EtN-1

The molecular structure of polyoxoanion **2** in EtN-**2** and its polyhedral representation are shown in Figure 2 (a and b), respectively. Selected bond lengths [Å] and angles [°] around the titanium(IV) centers in **2** are listed in Table 1, whereas other bond lengths [Å] and angles [°] for the Keggin unit (Table S1) and bond valence sum (BVS) calculations (Table S2) are given in the Supporting Information.

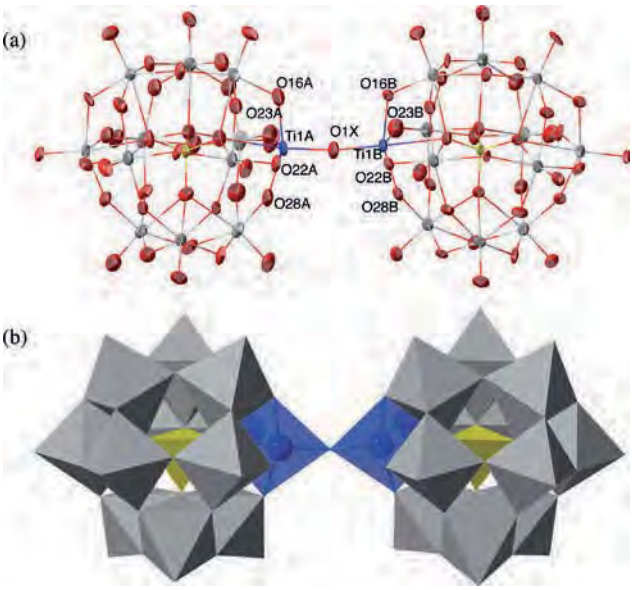

Figure 2. (a) Molecular structure of the polyoxoanion $[(\alpha\text{-}PW_{11}TiO_{39})_2O]^{8-}$ (**2**) in EtN-**2** and (b) its polyhedral representation.

The composition and formula of EtN-**2**, which contains eight diethylammonium countercations and six hydrated water molecules, were determined by CHN elemental analysis and TG/DTA analysis. In X-ray crystallography, one polyoxoanion that contained two Keggin units, five diethylammonium cations, and three hydrated water molecules per formula unit was identified in the crystal structure.

X-ray crystallography of EtN-**2** revealed that six-coordinate geometry around each Ti center was accomplished by bonding with five oxygen atoms in the mono-lacunary site

Table 1. Selected bond lengths [Å] and angles [°] around the Ti^{IV} center in $[(\alpha\text{-}PW_{11}TiO_{39})_2O]^{8-}$ (**2**).

Ti–O bond lengths			
Ti(1A)–O(1X)	1.794(12)	Ti(1B–O(1X)	1.782(11)
Ti(1A)–O(16A)	1.934(14)	Ti(1A)–O(23A)	1.912(13)
Ti(1A)–O(22A)	1.943(12)	Ti(1A)–O(28A)	1.904(13)
Ti(1B)–O(16B)	1.933(11)	Ti(1B)–O(23B)	1.893(10)
Ti(1B)–O(22B)	1.947(11)	Ti(1B)–O(28B)	1.906(12)
Ti(1A)–O(36A)	2.361(12)	Ti(1B)–O(36B)	2.343(11)
Ti–O–Ti angle			
Ti(1A)–O(1X)–Ti(1B)	169.9(9)		

of the Keggin POM and the bridging oxygen atom (μ-O). Here the bonding between the titanium atom and the oxygen atom coordinated to the P atom [O(36A)–Ti(1A) 2.361(12) Å, O(36B)–Ti(1B) 2.343(11) Å] is incorporated in the coordination. The two Keggin units are crystallographically independent due to the slight twist between each Keggin unit, thus resulting in the overall C_1 symmetry of the polyoxoanion molecule in the solid state. However, in solution, the twist was averaged, thus resulting in overall C_{2v} symmetry. Therefore, the six-line ^{183}W NMR spectrum in D_2O/CD_3CN (1:3 v/v) was observed with a relative intensity ratio of 2:2:1:2:2:2 (Figure 6; see below). The Ti–O–Ti bonding moiety and the eleven W atoms in the Keggin unit exhibited conventional octahedral coordination polyhedra (Figure 2, b). Structural analysis revealed that **2** was composed of two mono-titanium(IV)-substituted Keggin POM subunits "$[\alpha\text{-}PW_{11}TiO_{39}]^{3-}$" linked through one μ-oxo group. The bond angle of the Ti–O–Ti moiety [Ti(1A)–O(1X)–Ti(1B) 169.9(9)°] and the inter-Keggin unit Ti–Ti distance [Ti(1A)–Ti(1B) 3.562 Å] in **2** can be compared with those of the previously reported di- and tri-titanium(IV)-substituted dimeric Ti–O–Ti-bridged anhydride forms (Figure 3); that is, (i) the Ti–O–Ti angles between the two Keggin units (135.7, 136.3°) in the di-titanium(IV)-substituted dimer, $[(\alpha\text{-}1,2\text{-}PW_{10}Ti_2O_{38})_2O_2]^{10-}$ (Figure 3, b),[2d] and (ii) the Ti–O–Ti angles between the two Keggin units (130.2, 130.9, 131.3°) in the tri-titanium(IV)-substituted dimer, $[(\alpha\text{-}1,2,3\text{-}PW_9Ti_3O_{37})_2O_3]^{12-}$ (Figure 3, c).[2e] The angle of the intermolecular Ti–O–Ti moiety of **2** was more of a linear alignment, and the inter-Keggin unit Ti–Ti distance of **2** was longer than those of the previously reported di- and tri-Ti^{IV}-substituted Keggin dimers. The bond lengths of the Ti–O–Ti moiety [O(1X)–Ti(1A) 1.794(12) Å, O(1X)–Ti(1B) 1.782(11) Å] in **2** were slightly shorter than those of di- and tri-titanium(IV)-substituted Keggin dimers {1.80(2)–1.84(2) Å for $[(\alpha\text{-}1,2\text{-}PW_{10}Ti_2O_{38})_2O_2]^{10-}$, 1.80(1)–1.86(1) Å for $[(\alpha\text{-}1,2,3\text{-}PW_9Ti_3O_{37})_2O_3]^{12-}$}.

The bond valence sum (BVS) value of the bridging oxygen atom [O(1X)], which was calculated on the basis of the observed bond lengths in **2** (Table S2 in the Supporting Information), strongly suggested that the bridging oxygen atom [O(1X)] was not protonated (i.e., ascribed to O^{2-}). As for the other oxygen atoms in the Keggin units of **2**, there

© 2013 Wiley-VCH Verlag GmbH & Co. KGaA, Weinheim

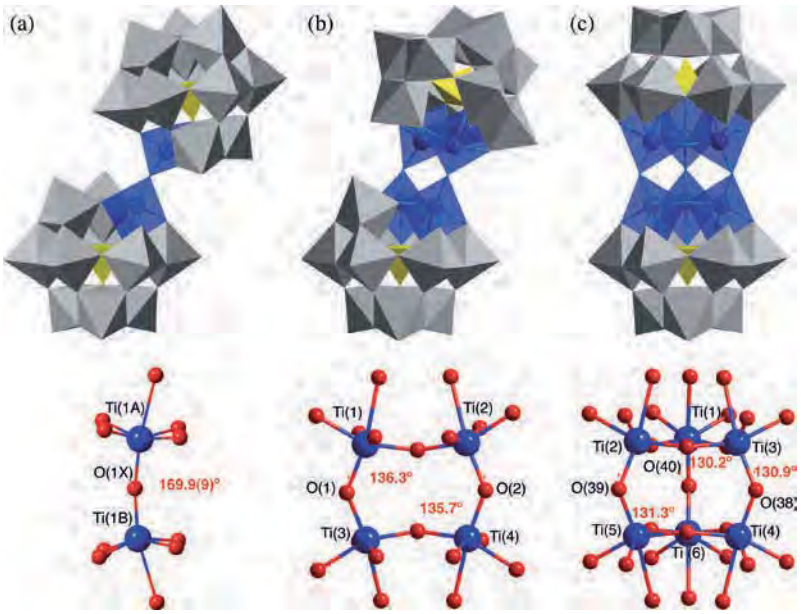

Figure 3. Structures and partial structures around the Ti center of (a) mono-titanium(IV)-substituted dimer, $[(\alpha\text{-}PW_{11}TiO_{39})_2O]^{8-}$ (this work), (b) di-titanium(IV)-substituted dimer, $[(\alpha\text{-}1,2\text{-}PW_{10}Ti_2O_{38})_2O_2]^{10-}$,[2d] and (c) tri-titanium(IV)-substituted dimer, $[(\alpha\text{-}1,2,3\text{-}PW_9Ti_3O_{37})_2O_3]^{12-}$.[2e]

was also no protonation in any of them. The BVS values of other elements in **2** reasonably corresponded to the formal valences of O^{2-}, Ti^{4+}, W^{6+}, and P^{5+} (Table S2 in the Supporting Information).

The crystal structure of **1** in EtN-**1** was successfully determined (Figure S3 in the Supporting Information) and had the same structure as the saturated Keggin POM. However, it was not possible to determine the mono-Ti^{IV} site due to the high symmetry of the Keggin structure. Nevertheless, from this X-ray structural analysis, we were able to confirm that **1** was not a dimeric structure but rather a monomeric structure.

Solid-State ^{31}P CPMAS NMR Spectroscopy

Solid-state ^{31}P CPMAS NMR spectroscopy of EtN-**1** and EtN-**2** showed a single broad signal due to Keggin units at δ = –12.96 and –13.21 ppm, respectively (Figure 4), which should be consistent with X-ray crystallography. Solid-state ^{31}P NMR spectra of EtN-**1** and EtN-**2** corresponded to solution ^{31}P NMR spectra in D_2O/DMSO (10:1 v/v) in a similar region.

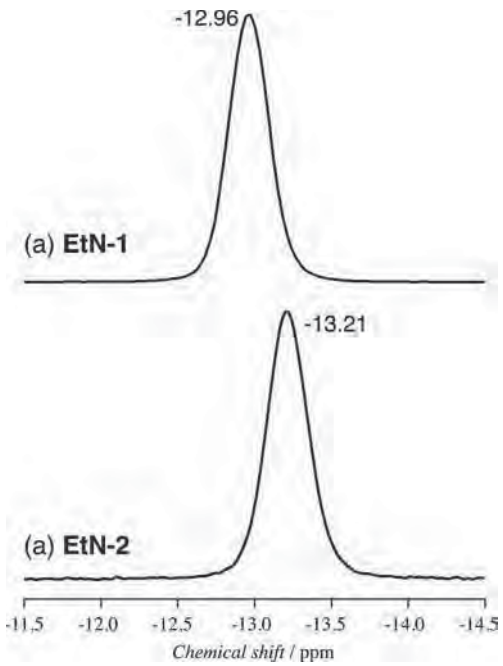

Figure 4. Solid-state ^{31}P CPMAS NMR spectra of (a) $(Et_2NH_2)_5[\alpha\text{-}PW_{11}TiO_{40}]\cdot 2H_2O$ (EtN-**1**), and (b) $(Et_2NH_2)_8[(\alpha\text{-}PW_{11}TiO_{39})_2O]\cdot 6H_2O$ (EtN-**2**).

Solution (^{31}P and ^{183}W) NMR and pH-Varied ^{31}P NMR Spectroscopy

The ^{31}P NMR spectrum of EtN-**1** in D_2O/DMSO (10:1 v/v; Figure 5, a) showed only one resonance at δ = –13.71 ppm, thus showing the formation of a single phosphorus-containing species and that the molecular structure of **1** in the solid state was maintained in solution. On the other hand, the ^{31}P NMR spectrum of EtN-**2** in D_2O/DMSO (10:1 v/v; Figure 5, b) showed two peaks at δ = –13.72 and –13.79 ppm, in which the downfield resonance was assigned to monomeric species **1**, and the upfield resonance was assigned to dimeric species **2**. When 1 M aqueous HCl (50 µL) was added to this NMR spectroscopy sample tube, only one resonance due to dimer **2** was observed at δ = –13.78 ppm (Figure 5, c). These ^{31}P NMR spectra indicate that monomer **1** and dimer EtN-**2** in solution are strongly dependent on pH.

© 2013 Wiley-VCH Verlag GmbH & Co. KGaA, Weinheim

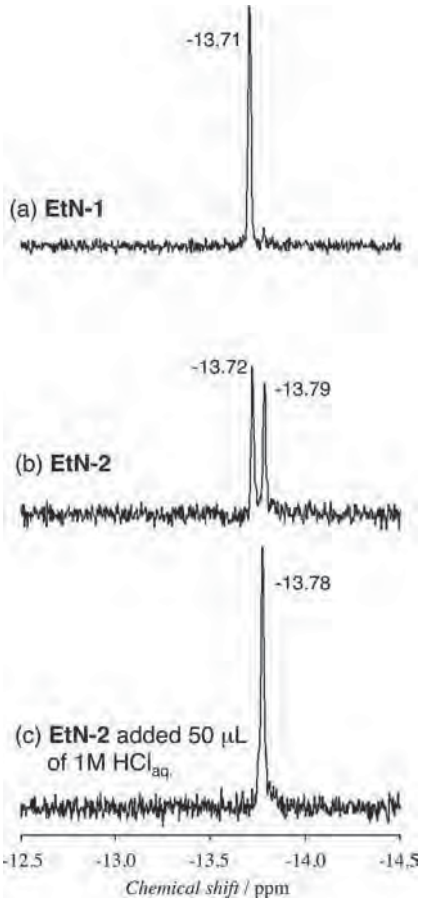

Figure 5. Solution ^{31}P NMR spectra of (a) $(Et_2NH_2)_5[\alpha\text{-}PW_{11}TiO_{40}]\cdot 2H_2O$ (EtN-**1**), and (b) $(Et_2NH_2)_8[(\alpha\text{-}PW_{11}TiO_{39})_2O]\cdot 6H_2O$ (EtN-**2**) dissolved in a solvent mixture of D_2O/DMSO (10:1 v/v), and (c) the solution of (b) to where 50 µL of 1 M aqueous HCl were added.

The ^{183}W NMR spectrum of EtN-**1** measured in D_2O/CD_3CN (1:3 v/v) (Figure 6, a) showed a six-line spectrum at δ = –69.55 (2 W), –101.34 (2 W), –110.11 (1 W), –114.31 (2 W), –117.89 (2 W) and –124.53 (2 W) ppm. The peaks at around δ = –69.55 and –110.11 ppm were observed as doublets due to ^{183}W-^{31}P coupling.[9] This NMR spectrum, consistent with a C_s symmetric compound, indicates that the solid-state structure of **1** is maintained in solution. The ^{183}W NMR spectrum of EtN-**2** in D_2O/CD_3CN (1:3 v/v) (Figure 6, b) showed a six-line spectrum at δ = –99.20 (2 W), –99.36 (2 W), –101.30 (1 W), –105.81 (2 W), –116.74 (2 W) and –117.16 (2 W) ppm. In the solid state, the whole symmetry of the molecule is shown with approximate C_1 symmetry. However, the six-line ^{183}W NMR spectrum indicated the overall C_{2v} symmetry in solution, because the twist between each Keggin unit was averaged.

The pH-varied ^{31}P NMR spectra were also measured using monomeric species EtN-**1** as the starting material. The pH of the H_2O/DMSO (10:1 v/v) solution (pH 3.2) of monomer EtN-**1** was adjusted to 2.0, 1.5, 1.0, and finally to 0.5 by 6 and 1 M aqueous HCl solutions, and the ^{31}P NMR spectra were measured (Figure 7). ^{31}P NMR spectra in the unadjusted sample (pH 3.2) showed a single signal at

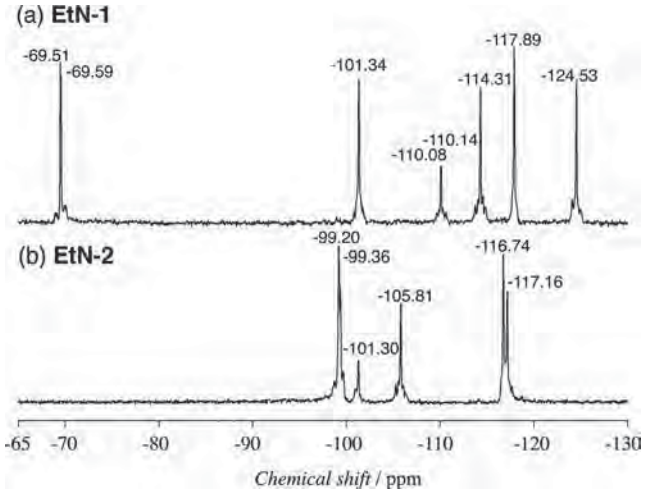

Figure 6. Solution ^{183}W NMR spectra in D_2O/CD_3CN (1:3 v/v) of (a) $(Et_2NH_2)_5[\alpha\text{-}PW_{11}TiO_{40}]\cdot 2H_2O$ (EtN-**1**) and (b) $(Et_2NH_2)_8[(\alpha\text{-}PW_{11}TiO_{39})_2O]\cdot 6H_2O$ (EtN-**2**).

δ = –13.72 ppm, which can be assigned to the monomeric Ti-containing Keggin POM **1**. In the pH range of 2.0–1.0, the signal of dimeric Ti-containing Keggin POM **2** was observed in addition to the signal of monomer **1**. At pH 0.5,

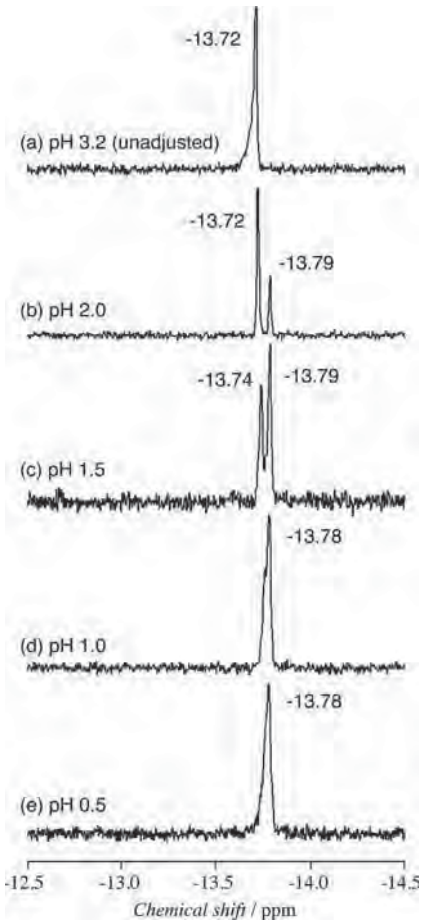

Figure 7. pH-varied ^{31}P NMR spectra of $(Et_2NH_2)_5[\alpha\text{-}PW_{11}TiO_{40}]\cdot 2H_2O$ (EtN-**1**) in H_2O/DMSO (10:1 v/v); pH (a) 3.2 (unadjusted); (b) 2.0; (c) 1.5; (d) 1.0; (e) 0.5 ppm.

© 2013 Wiley-VCH Verlag GmbH & Co. KGaA, Weinheim

the signal of only dimer **2** was observed. Therefore, dimeric species **2** was the predominant species in solution. The tendency for the ^{31}P NMR spectroscopic resonances of monomeric **1** to appear in a higher field than that of dimer **2** is consistent with the solid-state ^{31}P CPMAS NMR spectra of EtN-**1** and EtN-**2**. Thus, interconversion between the monomer and the dimer can be controlled by the pH of the solutions. The pH-varied ^{31}P NMR spectra of the mono-Ti^{IV}-substituted Dawson analogues reported previously[5] {i.e., $K_{14}[(\alpha_2\text{-}P_2W_{17}TiO_{61})_2(\mu\text{-}O)]\cdot 55H_2O$} in aqueous solutions showed that the monomer at pH 7.0, the dimer at pH 1.0–3.0, and the mono-protonated species of the dimer at pH 0.5 were the predominant species in the solutions. The present mono-Ti^{IV}-substituted Keggin POM denoted the same tendency as the Dawson analogue, that is, the mono-Ti^{IV}-substituted POM was present as a dimeric form under acidic conditions, but as a monomeric form under less acidic conditions. Unlike the Dawson analogues, the mono-protonated species of the dimer was not found in the pH range of 3.2–0.5.

Conclusion

In this work, we prepared and characterized the monomer Keggin POM $(Et_2NH_2)_5[\alpha\text{-}PW_{11}TiO_{40}]\cdot 2H_2O$ (EtN-**1**) and the μ-oxo Keggin dimer $(Et_2NH_2)_8[(\alpha\text{-}PW_{11}TiO_{39})_2O]\cdot 6H_2O$ (EtN-**2**). The molecular structure of μ-oxo dimeric polyoxoanion **2** was successfully determined for the first time by single-crystal X-ray crystallography. Structural analysis revealed that **2** was composed of two mono-titanium(IV)-substituted Keggin POM subunits "$[\alpha\text{-}PW_{11}TiO_{39}]^{3-}$" linked through one μ-oxo group. The BVS value of the bridging oxygen atom [O(1X)] of **2** has strongly suggested that it is not protonated. The pH-varied ^{31}P NMR spectra revealed that monomer **1** and dimer **2** in solution were strongly dependent upon pH, and therefore, the interconversion between them can be controlled by the pH of the solutions. Unlike the Dawson analogues, the mono-protonated species of the dimer was not found in the pH range of 3.2–0.5. These facts also provide significant information about acid catalysis by the Keggin mono-titanium(IV)-substituted POMs.

Experimental Section

Materials: The following reactants were used as received: NaOAc, Et_2NH_2Cl, MeOH, EtOH, Et_2O, DMSO, CH_3CN, $TiCl_4$ (Wako); D_2O, CD_3CN (Isotec). The precursor $K_7[\alpha\text{-}PW_{11}O_{39}]\cdot 8H_2O$ was prepared and identified by FTIR, TG/DTA, and ^{31}P NMR spectroscopy.[10]

Instrumentation/Analytical Procedures: CHN elemental analyses were carried out with a Perkin–Elmer 2400 CHNS Elemental Analyzer II. Infrared spectra were recorded with a JASCO 4100 FTIR spectrometer in KBr disks at room temperature. TG and DTA were acquired with a Rigaku Thermo Plus 2 series TG/DTA TG 8120 instrument. ^{31}P NMR (160 MHz) spectra in a D_2O solution were recorded in 5 mm outer diameter tubes with a JEOL JNM-ECS 400 FT-NMR spectrometer and a JEOL ECS-400 NMR spectroscopic data processing system and were referenced with an external standard of 25% H_3PO_4 in H_2O in a sealed capillary. The ^{31}P NMR spectroscopic signals with the usual 85% H_3PO_4 are shifted by +0.544 ppm from our data with 25% H_3PO_4. The ^{183}W NMR (20 MHz) spectra were recorded in 10 mm outer diameter tubes with a JEOL JNM-ECP 500 FT-NMR spectrometer equipped with a JEOL NM-50 T10L low-frequency tunable probe and a JEOL ECP-500 NMR spectroscopic data processing system. The ^{183}W NMR spectra measured in D_2O were referenced with an external standard of a saturated Na_2WO_4/D_2O solution. The ^{183}W NMR spectroscopic signals were shifted by –0.787 ppm by using a 2 M Na_2WO_4 solution as a reference instead of the saturated Na_2WO_4 solution. Solid-state CPMAS ^{31}P NMR (120 MHz) spectra were recorded in 6 mm outer diameter tubes with a JEOL JNM-ECP 300 FT-NMR spectrometer with a JEOL ECP-300 NMR spectroscopic data processing system and were referenced to an external standard of $(NH_4)_2HPO_4$. Chemical shifts are reported as negative for resonances upfield of $(NH_4)_2HPO_4$ (δ = 1.60).

Synthesis of the Monomeric POM, $(Et_2NH_2)_5[PW_{11}TiO_{40}]\cdot 2H_2O$ (EtN-1): NaOAc (0.11 g, 1.34 mmol) was added to a solution of $K_7[PW_{11}O_{39}]\cdot 8H_2O$ (2.0 g, 0.65 mmol) dissolved in water (20 mL). After stirring for 15 min in an ice bath, a colorless solution of $TiCl_4$ (ca. 0.08 mL, ca. 0.7 mmol) was added at a rate of one drop per 2 s. The solution was stirred for 1 h in a water bath at 80 °C, followed by filtration. Et_2NH_2Cl (3.0 g, 27.4 mmol) was added to the filtrate at once. The white powder formed was collected with a glass filter (P40, or G 4.0), washed with EtOH (10 mL three times) and Et_2O (10 mL three times), and then dried under vacuum for 2 h. At this stage, the white powder was obtained in a yield of 1.59 g {77.7% relative to $(Et_2NH_2)_5[PW_{11}TiO_{40}]\cdot 2H_2O$}, which was very soluble in water and a solvent mixture of water/DMSO (10:1 v/v) and water/CH_3CN (1:3 v/v), soluble in MeOH, sparingly soluble in EtOH, but insoluble in Et_2O. IR (KBr) (polyoxometalate region): $\tilde{\nu}$ = 1635 (w), 1576 (w), 1472 (w), 1456 (w), 1428 (w), 1396 (w), 1388 (w), 1362 (vw), 1307 (vw), 1275 (vw), 1192 (vw), 1159 (vw), 1090 (m), 1062 (m), 964 (s), 886 (m), 801 (vs), 699 (m), 656 (m), 594 (m), 515 (m), 492 (m) cm^{-1}. ^{31}P NMR [23.2 °C, D_2O/DMSO (10:1 v/v)]: δ = –13.71 ppm. Solid-state ^{31}P NMR: δ = –12.96 ppm. ^{183}W NMR [room temp., D_2O/CD_3CN (1:3 v/v)]: δ = –69.51, –69.59 (2 W), –101.34 (2 W), –110.08, –110.14 (1 W), –114.31 (2 W), –117.89 (2 W), –124.53 (2 W) ppm. TG/DTA under atmospheric conditions: a weight loss of 1.15%, due to dehydration of solvated water molecules, was observed at below 199.3 °C; calcd. 1.14% for x = 2 in $(Et_2NH_2)_5[PW_{11}TiO_{40}]\cdot xH_2O$. A weight loss of 10.98%, due to decomposition of Et_2NH_2 cations, was observed between 199.3 and 500 °C with an exothermic peak at 359.1 °C. Calcd. for $(Et_2NH_2)_5[PW_{11}TiO_{40}]\cdot 2H_2O$ or $C_{20}H_{64}N_5O_{42}P_1W_{11}Ti_1$: C 7.63, H 2.05, N 2.22; found: C 7.70, H 1.83, N 2.15.

pH-Varied ^{31}P NMR Spectroscopy: The monomeric powder sample of $(Et_2NH_2)_5[PW_{11}TiO_{40}]\cdot 2H_2O$ (EtN-**1**; 0.6 g, 0.19 mmol) was dissolved in a solvent mixture of water and DMSO (9.9 mL, 10:1 v/v). The pH of the solution (pH 3.2) was adjusted to 2.0, 1.5, 1.0, and 0.5, using 6 and 1 M aqueous HCl solutions and their ^{31}P NMR spectra were measured (Figure 7). The solutions of pH 3.2, 2.0, 1.5, and 1.0 were colorless and clear, but the solution of pH 0.5 was not clear (cloudy or a bit suspended).

Crystallization of the Monomeric Species (EtN-1): EtN-**1** (2.0 g, 0.64 mmol) was added to a solution of Et_2NH_2Cl (0.20 g, 1.82 mmol) and NaOAc (0.15 g, 1.83 mmol) dissolved in water (30 mL). The colorless, clear solution was slowly evaporated at room temperature. After 3 d, colorless, clear column crystals were deposited, which were collected by a glass frit (P16, or G 3.5),

© 2013 Wiley-VCH Verlag GmbH & Co. KGaA, Weinheim

washed with EtOH (20 mL two times) and Et_2O (20 mL two times), and dried under vacuum for 2 h. White powder, obtained in a yield of 1.42 g {71.3% relative to $(Et_2NH_2)_5[PW_{11}TiO_{40}]\cdot 0.4H_2O$}, was very soluble in water and a solvent mixture of water/CH_3CN (1:3 v/v), soluble in MeOH, sparingly soluble in EtOH, but insoluble in Et_2O. IR (KBr) (polyoxometalate region): $\tilde{\nu}$ = 1630 (w), 1603 (w), 1573 (w), 1472 (w), 1453 (w), 1427 (w), 1389 (w), 1362 (vw), 1327 (vw), 1306 (vw), 1275 (vw), 1192 (vw), 1159 (vw), 1090 (m), 1062 (m), 964 (s), 886 (m), 799 (vs), 700 (m), 655 (m), 594 (m), 515 (m), 491 (m) cm^{-1}. ^{31}P NMR [23.3 °C, D_2O/DMSO (10:1 v/v)]: δ = –13.70 ppm. TG/DTA under atmospheric conditions: a weight loss of 0.23%, due to dehydration of solvated water molecules, was observed at below 57.5 °C; calcd. 0.23% for x = 0.4 in $(Et_2NH_2)_5[PW_{11}TiO_{40}]\cdot xH_2O$. A weight loss of 10.22%, due to decomposition of Et_2NH_2 cations, was observed between 57.5 and 500 °C with exothermic peaks at 322.6 and 372.2 °C. Calcd. for $(Et_2NH_2)_5[PW_{11}TiO_{40}]\cdot 0.4H_2O$ or $C_{20}H_{60.8}N_5O_{40.4}P_1W_{11}Ti_1$: C 7.70, H 1.96, N 2.25; found C 7.80, H 1.87, N 2.22.

Crystallization of the Dimeric Species (EtN-2): The monomeric species $(Et_2NH_2)_5[PW_{11}TiO_{40}]\cdot 2H_2O$ (EtN-**1**; 0.5 g, 0.16 mmol) was dissolved in a solvent mixture of MeOH/water (10 mL, 1:1 v/v), with the pH of the solution being 4.9–5.3. The pH was adjusted to 1.0 by using 1 M aqueous HCl, followed by stirring for 2 d. The white suspension formed was filtered by a membrane filter (JG 0.2 µm). The colorless, clear filtrate was slowly evaporated at room temperature. After 3 d, colorless, clear plate crystals were deposited, which were collected by a glass frit (G 4.0), washed with EtOH (20 mL two times) and Et_2O (20 mL two times), and dried under vacuum for 2 h. The white powder, obtained in a yield of 0.32 g {65.3% relative to $(Et_2NH_2)_8[(PW_{11}TiO_{39})_2O]\cdot 6H_2O$}, was very soluble in a solvent mixture of water/DMSO (10:1 v/v) and water/CH_3CN (1:3 v/v), less soluble in water, and insoluble in EtOH and Et_2O. IR (KBr) (polyoxometalate region): $\tilde{\nu}$ = 1620 (w), 1469 (w), 1451 (w), 1389 (w), 1205 (vw), 1158 (vw), 1075 (m), 968 (s), 889 (m), 807 (vs), 654 (s) [intermolecular Ti–O–Ti], 594 (m), 520 (m), 499 (m) cm^{-1}. ^{31}P NMR [23.2 °C, D_2O/DMSO (10:1 v/v)]: δ = –13.72, –13.79 ppm. ^{31}P NMR [23.0 °C, D_2O/DMSO (10:1 v/v), after addition of 1 M aqueous HCl (0.05 mL, 50 µmol)]: δ = –13.78 ppm. Solid-state ^{31}P NMR: δ = –13.21 ppm. ^{183}W NMR [room temp., D_2O/CD_3CN (1:3 v/v)]: δ = –99.20 (2 W), –99.36 (2 W), –101.30 (1 W), –105.81 (2 W), –116.74 (2 W), –117.16 (2 W) ppm. TG/DTA under atmospheric conditions: a weight loss of 1.84%, due to dehydration of solvated water molecules, was observed at below 122.5 °C; calcd. 1.75% for x = 6 in $(Et_2NH_2)_8[(PW_{11}TiO_{39})_2O]\cdot xH_2O$. A weight loss of 9.40%, due to decomposition of Et_2NH_2 cations, was observed between 122.5 and 500 °C with endothermic peaks at 40.5 and 60.6 °C and an exothermic peak at 371.5 °C. Calcd. for $(Et_2NH_2)_8[(PW_{11}TiO_{39})_2O]\cdot 6H_2O$ or $C_{32}H_{108}N_8O_{85}P_2W_{22}Ti_2$: C 6.23, H 1.77, N 1.82; found C 6.31, H 2.28, N 1.78.

X-ray Crystallography: A colorless column crystal of EtN-**1** ($0.28 \times 0.07 \times 0.05$ mm^3) and a colorless plate crystal of EtN-**2** ($0.20 \times 0.10 \times 0.04$ mm^3) were surrounded by liquid paraffin (Paratone-N) to prevent its degradation. Data collection was carried out with a Bruker SMART APEX CCD diffractometer at 100 K in a range of $3.56° < 2\theta < 56.70°$ (EtN-**1**) and $3.62° < 2\theta < 55.00°$ (EtN-**2**). The intensity data were automatically corrected for Lorentz and polarization effects during integration. The structure was solved by direct methods (SHELXS-97[11a] for EtN-**1** and SIR2004[12] for EtN-**2**), followed by subsequent difference Fourier calculation and refined by a full-matrix least-squares procedure on F^2 (SHELXL-97).[11b] Absorption correction was performed with SADABS (empirical absorption correction).[11c] High-level alerts in the checkCIF report are due to the disorder of many hydrated water molecules and countercations. The compositions and formulae of the POMs that contained many countercations and many hydrated water molecules were determined by CHN elemental analysis and TG analysis. In general, it is not possible in X-ray crystallography to determine the location of the hydrogen atoms of hydrated water molecules due to extensive disorder of the countercations and the hydrate water molecules. Such features are frequently encountered and common in POM crystallography.

Crystal Data for EtN-1: $O_{44}PW_{12}$; M_r = 2941.17; triclinic, space group $P\bar{1}$; a = 11.8449(14) Å, b = 11.8552(14) Å, c = 13.0038(15) Å; α = 104.547(2)°, β = 104.450(2)°, γ = 116.313(2)°; V = 1440.8(3) $Å^3$; Z = 1; $D_{calcd.}$ = 3.390 $g\,cm^{-3}$; μ(Mo-K_α) = 23.947 mm^{-1}; $R1$ = 0.0897, $wR2$ = 0.2297 (for all data), R_{int} = 0.0385, $R1$ = 0.0675, $wR2$ = 0.2073; GOF = 1.074 {19883 total reflections, 7148 unique reflections [$I > 2\sigma(I)$]}.

Crystal Data for EtN-2: $C_{20}H_{60}N_5O_{82}P_2Ti_2W_{22}$; M_r = 5909.19; triclinic, space group $P\bar{1}$; a = 11.6856(11) Å, b = 21.196(2) Å, c = 21.463(2) Å; α = 86.9960(10)°, β = 79.4420(10)°, γ = 78.1580(10)°; V = 5114.2(8) $Å^3$; Z = 2; $D_{calcd.}$ = 3.837 $g\,cm^{-3}$; μ(Mo-K_α) = 24.903 mm^{-1}; $R1$ = 0.0781, $wR2$ = 0.1475 (for all data), R_{int} = 0.0658, $R1$ = 0.0565, $wR2$ = 0.1358; GOF = 1.052 {60352 total reflections, 23161 unique reflections [$I > 2\sigma(I)$]}.

CCDC-906701 (for EtN-**1**) and -906699 (for EtN-**2**) contain the supplementary crystallographic data for this paper. These data can be obtained free of charge from The Cambridge Crystallographic Data Centre via www.ccdc.cam.ac.uk/data_request/cif.

Supporting Information (see footnote on the first page of this article): TG/DTA data for EtN-**1** and EtN-**2** (Figures S1 and S2); the molecular structure and polyhedral representation of **1** in EtN-**1** (Figure S3); bond lengths and angles for **2** in EtN-**2** (Table S1); and BVS calculations of Ti and O around Ti for **2** in EtN-**2**.

Acknowledgments

This work was supported by the Japan Society for the Promotion of Science through a Grant-in-Aid for Scientific Research (C) (JSPS KAKENHI Grant Number 22550065) and by the Ministry of Education, Culture, Sports, Science and Technology of Japan (Strategic Research Base Development Program for Private Universities).

[1] a) M. T. Pope, A. Müller, *Angew. Chem.* **1991**, *103*, 56; *Angew. Chem. Int. Ed. Engl.* **1991**, *30*, 34–48; b) M. T. Pope, *Heteropoly and Isopoly Oxometalates*, Springer Verlag, New York, **1983**; c) V. W. Day, W. G. Klemperer, *Science* **1985**, *228*, 533–541; d) C. L. Hill (Ed.), *Chem. Rev.* **1998**, *98*, 1–390; e) T. Okuhara, N. Mizuno, M. Misono, *Adv. Catal.* **1996**, *41*, 113–252; f) C. L. Hill, C. M. Prosser-McCartha, *Coord. Chem. Rev.* **1995**, *143*, 407–455; g) a series of 34 papers in a volume devoted to polyoxoanions in catalysis: C. L. Hill (Ed.), *J. Mol. Catal. A* **1996**, *114*, 1–371; h) R. Neumann, *Prog. Inorg. Chem.* **1998**, *47*, 317–370; i) M. T. Pope, A. Müller Editors (Eds.), *Polyoxometalate Chemistry from Topology via Self-Assembly to Applications*, Kluwer Academic Publishers, The Netherlands, **2001**; j) T. Yamase, M. T. Pope (Eds.), *Polyoxometalate Chemistry for Nano-Composite Design*, Kluwer Academic Publishers, The Netherlands, **2002**; k) M. T. Pope, in: *Comprehensive Coordination Chemistry II* (Ed.: A. G. Wedd), Elsevier Science, New York, **2004**, vol. 4, p. 635; l) C. L. Hill in *Comprehensive Coordination Chemistry II* (Ed.: A. G. Wedd), Elsevier Science, New York, **2004**, vol. 4, p. 679; m) a series of 32 papers was published in a volume devoted to polyoxometalates in catalysis: C. L. Hill, *J. Mol. Catal. A* **2007**, *262*, 1; n) B. Hasenknopf, K. Micoine,

© 2013 Wiley-VCH Verlag GmbH & Co. KGaA, Weinheim

E. Lacôte, S. Thorimbert, M. Malacria, R. Thouvenot, *Eur. J. Inorg. Chem.* **2008**, 5001–5013; o) A. Proust, R. Thouvenot, P. Gouzerh, *Chem. Commun.* **2008**, 1837–1852; p) D. Laurencin, R. Thouvenot, K. Boubekeur, F. Villain, R. Villanneau, M.-M. Rohmer, M. Benard, A. Proust, *Organometallics* **2009**, *28*, 3140–3151; q) D.-L. Long, R. Tsunashima, L. Cronin, *Angew. Chem.* **2010**, *122*, 1780; *Angew. Chem. Int. Ed.* **2010**, *49*, 1736–1758; r) A. Dolbecq, E. Dumas, C. R. Mayer, P. Mialane, *Chem. Rev.* **2010**, *110*, 6009–6048; s) C. P. Pradeep, D.-L. Long, L. Cronin, *Dalton Trans.* **2010**, *39*, 9443–9457; t) K. Nomiya, Y. Sakai, S. Matsunaga, *Eur. J. Inorg. Chem.* **2011**, 179–196.

[2] a) Y. Lin, T. J. R. Weakley, B. Rapko, R. G. Finke, *Inorg. Chem.* **1993**, *32*, 5095–5101; b) T. Yamase, T. Ozeki, H. Sakamoto, S. Nishiya, A. Yamamoto, *Bull. Chem. Soc. Jpn.* **1993**, *66*, 103–108; c) T. Yamase, X. O. Cao, S. Yazaki, *J. Mol. Catal. A* **2007**, *262*, 119–127; d) K. Nomiya, M. Takahashi, J. A. Widegren, T. Aizawa, Y. Sakai, N. C. Kasuga, *J. Chem. Soc., Dalton Trans.* **2002**, 3679–3685; e) K. Nomiya, M. Takahashi, K. Ohsawa, J. A. Widegren, *J. Chem. Soc., Dalton Trans.* **2001**, 2872–2878; f) Y. Goto, K. Kamata, K. Yamaguchi, K. Uehara, S. Hikichi, N. Mizuno, *Inorg. Chem.* **2006**, *45*, 2347–2356; g) R. Tan, D. Li, H. Wu, C. Zhang, X. Wang, *Inorg. Chem. Commun.* **2008**, *11*, 835–836; h) F. Hussain, B. S. Bassil, L.-H. Bi, M. Reicke, U. Kortz, *Angew. Chem.* **2004**, *116*, 3567; *Angew. Chem. Int. Ed.* **2004**, *43*, 3485–3488; i) G. A. Al-Kadamany, F. Hussain, S. S. Mal, M. H. Dickman, N. Leclerc-Laronze, J. Marrot, E. Cadot, U. Kortz, *Inorg. Chem.* **2008**, *47*, 8574–8576; j) Y. H. Ren, S. X. Liu, R. G. Cao, X. Y. Zhao, J. F. Cao, C. Y. Gao, *Inorg. Chem. Commun.* **2008**, *11*, 1320–1322.

[3] a) K. Hayashi, C. N. Kato, A. Shinohara, Y. Sakai, K. Nomiya, *J. Mol. Catal. A* **2007**, *262*, 30–35; b) O. A. Kholdeeva, T. A. Trubitsina, R. I. Maksimovskaya, A. V. Golovin, W. A. Neiwert, B. A. Kolosov, X. López, J. M. Poblet, *Inorg. Chem.* **2004**, *43*, 2284–2292; c) C. N. Kato, K. Hayashi, S. Negishi, K. Nomiya, *J. Mol. Catal. A* **2007**, *262*, 25–29; d) C. N. Kato, S. Negishi, K. Yoshida, K. Hayashi, K. Nomiya, *Appl. Catal.* **2005**, *292*, 97–104; e) J. Gong, Q. J. Shan, D. R. Wang, R. N. Hua, L. Y. Qu, *J. Electroanal. Chem.* **1998**, *455*, 39–44; f) O. A. Kholdeeva, T. A. Trubitsina, M. N. Timofeeva, G. M. Maksimov, R. I. Maksimovskaya, V. Rogov, *J. Mol. Catal. A* **2005**, *232*, 173–178; g) O. A. Kholdeeva, *Top. Catal.* **2006**, *40*, 229–243.

[4] a) Y. Sakai, K. Yoza, C. N. Kato, K. Nomiya, *Chem. Eur. J.* **2003**, *9*, 4077–4083; b) Y. Sakai, K. Yoza, C. N. Kato, K. Nomiya, *Dalton Trans.* **2003**, 3581–3586; c) K. Nomiya, Y. Arai, Y. Shimizu, M. Takahashi, T. Takayama, H. Weiner, T. Nagata, J. A. Widegren, R. G. Finke, *Inorg. Chim. Acta* **2000**, *300–302*, 285–304; d) Y. Sakai, Y. Kitakoga, K. Hayashi, K. Yoza, K. Nomiya, *Eur. J. Inorg. Chem.* **2004**, 4646–4652; e) Y. Sakai, S. Yoshida, T. Hasegawa, H. Murakami, K. Nomiya, *Bull. Chem. Soc. Jpn.* **2007**, *80*, 1965–1974; f) U. Kortz, S. S. Hamzeh, N. A. Nasser, *Chem. Eur. J.* **2003**, *9*, 2945–2952; g) Y. Sakai, S. Ohta, Y. Shintoyo, S. Yoshida, Y. Taguchi, Y. Matsuki, S. Matsunaga, K. Nomiya, *Inorg. Chem.* **2011**, *50*, 6575–6583.

[5] S. Yoshida, H. Murakami, Y. Sakai, K. Nomiya, *Dalton Trans.* **2008**, 4630–4638.

[6] a) O. A. Kholdeeva, G. M. Maksimov, R. I. Maksimovskaya, L. A. Kovaleva, M. A. Fedotov, V. A. Grigoriev, C. L. Hill, *Inorg. Chem.* **2000**, *39*, 3828–3837; b) O. A. Kholdeeva, T. A. Trubitsina, G. M. Maksimov, A. V. Golovin, R. I. Maksimovskaya, *Inorg. Chem.* **2005**, *44*, 1635–1642; c) G. M. Maksimov, R. I. Maksimovskaya, O. A. Kholdeeva, M. A. Fedotov, V. I. Zaikovskii, V. G. Vasil'ev, S. S. Arzumanov, *J. Struct. Chem.* **2009**, *50*, 618–627.

[7] X. López, I. A. Weinstock, C. Bo, J. P. Sarasa, J. M. Poblet, *Inorg. Chem.* **2006**, *45*, 6467–6473.

[8] a) C. Rocchiccioli-Deltcheff, R. Thouvenot, R. Franck, *Spectrochim. Acta A* **1976**, *32*, 587–597; b) C. Rocchiccioli-Deltcheff, M. Fournier, R. Franck, *Inorg. Chem.* **1983**, *22*, 207–216; c) R. Thouvenot, M. Fournier, R. Franck, C. Rocchiccioli-Deltcheff, *Inorg. Chem.* **1984**, *23*, 598–605.

[9] G. Lenoble, B. Hasenknopf, R. Thouvenot, *J. Am. Chem. Soc.* **2006**, *128*, 5735–5744.

[10] S. Aoki, T. Kurashina, Y. Kasahara, T. Nishijima, K. Nomiya, *Dalton Trans.* **2011**, *40*, 1243–1253.

[11] a) G. M. Sheldrick, *Acta Crystallogr., Sect. A* **1990**, *46*, 467–473; b) G. M. Sheldrick, *SHELXL-97, Program for Crystal Structure Refinement*, University of Göttingen, Germany, **1997**; c) G. M. Sheldrick, *SADABS*, University of Göttingen, Germany, **1996**.

[12] M. C. Burla, R. Caliandro, M. Camalli, B. Carrozzini, G. L. Cascarano, L. De Caro, C. Giacovazzo, G. Polidori, R. Spagna, *J. Appl. Crystallogr.* **2005**, *38*, 381–388.

Received: October 24, 2012
Published Online: January 23, 2013

 © 2013 Wiley-VCH Verlag GmbH & Co. KGaA, Weinheim

 © 2013 The Chemical Society of Japan

Selected Papers

Tetranuclear Hafnium(IV) and Zirconium(IV) Cationic Complexes Sandwiched between Two Di-Lacunary Species of α-Keggin Polyoxometalates: Lewis Acid Catalysis of the Mukaiyama–Aldol Reaction

Kenji Nomiya,* Kazuaki Ohta, Yoshitaka Sakai, Taka-aki Hosoya, Atsushi Ohtake, Akira Takakura, and Satoshi Matsunaga

Department of Chemistry, (formerly Department of Materials Science), Faculty of Science, Kanagawa University, Hiratsuka, Kanagawa 259-1293

Received January 22, 2013; E-mail: nomiya@kanagawa-u.ac.jp

The syntheses, X-ray structures, and homogeneous Lewis acid catalytic activities for the Mukaiyama–aldol reaction of four tetranuclear Hf^{IV} and Zr^{IV} cluster cations, which are sandwiched between two 1,2-di-lacunary α-Keggin polyoxometalates (POMs) and between two 1,4-di-lacunary POMs, are described, i.e., $[[\{M(H_2O)\}_2\{M(H_2O)_2\}_2(\mu\text{-}OH)_3(\mu_3\text{-}OH)_2](\alpha\text{-}1,2\text{-}PW_{10}O_{37})_2]^{7-}$ (M = Hf **1** and M = Zr **2**) and $[\{M_4(H_2O)_4(\mu\text{-}OH)_2(\mu_3\text{-}O)_2\}(\alpha\text{-}1,4\text{-}PW_{10}O_{37})_2]^{8-}$ (M = Hf **3** and M = Zr **4**), respectively. Evaluated was homogeneous Lewis acid catalysis of the Mukaiyama–aldol reaction in aqueous/CH_3CN mixed media at room temperature under air by water-soluble sodium or lithium salts of sandwich-structured Hf/Zr-containing Keggin and Dawson POMs. In particular, the sodium salts of tetranuclear Hf/Zr cluster cations sandwiched between two di-lacunary α-Keggin POMs, i.e., **Na-1**–**Na-4**, showed the highest activities, compared with other cluster cations. The present POM-based sandwich-structured compounds gave products with high stereoselectivity, i.e., high *anti*-selectivity, regardless of high or low activities. The excellent stabilities of **Na-1**–**Na-4** as catalysts, i.e., with no reduced activities, were confirmed even after reusing several times.

The coordination chemistry of polyoxometalates (POMs) with d^0 transition metals has been particularly well documented in the past few decades. Indeed, the d^0 transition metal derivatives of polyoxoanions have attracted considerable attention in the fields of catalysis, surface science, and materials science, since POMs are often considered as molecular analogues of oxides in terms of structural analogy.[1] In POMs containing Group IV (d^0) metal ions, the Zr/Hf atoms function very similarly to each other, but show quite different behavior from the Ti atom.[2] The Zr and Hf atoms in Group IV metals, compared with the Ti atom (ionic radius 0.75 Å and a maximum coordination number of 6 in POM), have larger ionic radii (ca. 0.85 Å) and show higher coordination numbers (6, 7, and 8) and, therefore, if they are incorporated in POMs, a wide variety of molecular structures are anticipated. Most Ti-substituted Keggin POMs are isolated as oligomers formed by corner-sharing Ti–O–Ti bonds, whereas Zr/Hf-containing α-Keggin/α-Dawson POMs are usually isolated as di-, tri-, and tetra-Zr/Hf cluster cations sandwiched between two lacunary POMs, the cluster cations of which are formed by edge-sharing $M(OH)_2M$ (M = Zr and Hf) bonds.[2]

Following the development of Ti^{IV}-containing POMs, there has been a dramatic advance in recent years in studies on various types of Hf^{IV}/Zr^{IV} complexes in combination with several POMs.[3–5] For example, the followings have been reported as Hf^{IV}/Zr^{IV} sandwich-structured complexes with the same compositions and formulas: mononuclear, 8-coordinate metal complexes sandwiched between two mono-lacunary α-Keggin- and α_2-Dawson-type POMs, i.e., $[M(\alpha\text{-}PW_{11}O_{39})_2]^{10-}$ (M = Hf and Zr; the Keggin 1:2 complexes) and $[M(\alpha_2\text{-}P_2W_{17}O_{61})_2]^{16-}$ (the Dawson 1:2-type complexes), respectively,[4k,5a] di- and tetranuclear 7-coordinate metal complexes sandwiched between two γ-Keggin silicotungstates $[\{M(H_2O)\}_2(\mu\text{-}OH)_2(\gamma\text{-}SiW_{10}O_{36})_2]^{10-}$ and $[\{M(H_2O)\}_4(\mu_4\text{-}O)(\mu\text{-}OH)_6(\gamma\text{-}SiW_{10}O_{36})_2]^{8-}$ (M = Hf and Zr), respectively,[4o] and tetranuclear two 7-coordinate and two 8-coordinate metal complexes with two β-Keggin silicotungstates $[Zr_4(\mu_3\text{-}O)_2(OH)_2(H_2O)_4(\beta\text{-}SiW_{10}O_{37})_2]^{10-}$ and hexanuclear three 7-coordinate and three 8-coordinate metal complexes formed with three β-Keggin silicotungstates $[Zr_6O_2(OH)_4(H_2O)_3(\beta\text{-}SiW_{10}O_{37})_3]^{14-}$,[4h] and hexanuclear 6-peroxo metal complexes formed with three γ-Keggin silicotungstates $[M_6(O_2)_6(\mu\text{-}OH)_6(\gamma\text{-}SiW_{10}O_{36})_3]^{18-}$ (M = Hf and Zr).[4q,4v] Recently, three 6-coordinate prismatic Hf^{IV} and Zr^{IV} ions, i.e., the $[M_3(\mu\text{-}OH)_3]^{9+}$ cluster cations (M = Hf and Zr) sandwiched between two tri-lacunary α-Keggin POMs, or $[M_3(\mu\text{-}OH)_3(A\text{-}\alpha\text{-}PW_9O_{34})_2]^{9-}$ (the Keggin 3:2 complexes), were reported;[5b] the analogous trinuclear 6-coordinate Zr^{IV} cluster compound $[Zr_3(\mu\text{-}OH)_3(A\text{-}\beta\text{-}SiW_9O_{34})_2]^{11-}$ has previously been reported.[4a] The dinuclear, 7-coordinate Hf and Zr cluster cations sandwiched between two mono-lacunary α-Keggin POMs and between two mono-lacunary α-Dawson POMs, i.e., $[\{\alpha\text{-}PW_{11}O_{39}M(\mu\text{-}OH)(H_2O)\}_2]^{8-}$ (M = Hf and

Published on the web April 27, 2013; doi:10.1246/bcsj.20130016

Zr; the Keggin 2:2 complexes)[5c] and $[\{\alpha_2\text{-}P_2W_{17}O_{61}M(\mu\text{-}OH)(H_2O)\}_2]^{14-}$ (the Dawson 2:2 complexes),[5e] respectively, and the tetranuclear 7-coordinate metal cluster cation species $[M_4(\mu_3\text{-}O)_2(\mu\text{-}OH)_2(H_2O)_4]^{10+}$ (M = Zr[4d] and Hf[5d]) sandwiched between two di-lacunary Dawson POMs (POMs), i.e., $[M_4(\mu_3\text{-}O)_2(\mu\text{-}OH)_2(H_2O)_4(P_2W_{16}O_{59})_2]^{14-}$ (the Dawson 4:2 complexes), have also been reported. As a molybdo-POM, the 8-coordinate Hf complex, i.e., $[Hf\{PMo_{12}O_{40}\}\{(NH_4)PMo_{11}O_{39}\}]^{5-}$, has also recently been reported.[4r]

It should be noted that several examples of central-cluster cations with the same structure, being sandwiched between different lacunary POM units, are found: the $[Zr_4(H_2O)_4(\mu\text{-}OH)_2(\mu_3\text{-}O)_2]^{10+}$ cation is sandwiched between two $[\beta\text{-}SiW_{10}O_{37}]^{10-}$ POMs[4h] and the same cluster cation is also sandwiched between two $[P_2W_{16}O_{59}]^{12-}$ POMs.[4d]

As to application, Lewis acid catalysis of unsaturated coordination complexes of Zr and Hf atoms can be anticipated,[1o,4o,6] while that of Ti-containing POMs cannot. Malacria's group has reported Lewis acid catalysis of the Mannich reaction, Mukaiyama–aldol reaction, Diels–Alder reaction and so on using a combination of mono-lacunary α_1-Dawson POM and lanthanoide series (La^{3+}, Eu^{3+}, Sm^{3+}, and Yb^{3+}) and Hf^{4+} and Zr^{4+} cations, which relatively favor 1:1 complexes over sandwich 1:2 complexes in aqueous solution.[1o,6] Their work is based on sandwich 1:2 and dimeric 2:2 structures precluding or decreasing catalytic activity—relative to the 1:1 complex—because they have no or few free sites for complexation of substrates.[1o,4o,6] The Mukaiyama–aldol reaction has been recognized as a facile and valuable method for the synthesis of (β-hydroxy)carbonyl compounds, and a wide variety of catalysts are known to accelerate the reaction.[7] Herein, we are interested in whether the Hf/Zr sandwich complexes such as 1:2, 2:2, and 4:2 complexes of Keggin- and Dawson-type POMs preclude or decrease catalytic activity, because many Hf/Zr sandwich complexes have available sites for interaction with substrates, i.e., as sites of terminal water molecules coordinated to Hf and Zr centers.

We have recently reported the structural characterization and preliminary catalytic studies of two types of novel tetranuclear Hf/Zr clusters sandwiched between two 1,2-di-lacunary α-Keggin POMs and between two 1,4-di-lacunary α-Keggin POMs (the Keggin 4:2 complexes), i.e., $[[\{M(H_2O)\}_2\{M(H_2O)_2\}_2(\mu\text{-}OH)_3(\mu_3\text{-}OH)_2](\alpha\text{-}1,2\text{-}PW_{10}O_{37})_2]^{7-}$ (M = Hf **1** and M = Zr **2**) and $[\{M_4(H_2O)_4(\mu\text{-}OH)_2(\mu_3\text{-}O)_2\}(\alpha\text{-}1,4\text{-}PW_{10}O_{37})_2]^{8-}$ (M = Hf **3** and M = Zr **4**), respectively.[8]

In the present work, the two sets of POMs, cesium salts of **1** and **2** (abbreviated as **Cs-1** and **Cs-2**, respectively), and dimethylammonium salts of **3** and **4** (abbreviated as **MeN-3** and **MeN-4**, respectively), were rigorously characterized by complete elemental analysis, TG/DTA, FTIR, solid-state and solution ^{31}P NMR, and X-ray crystallography. In this work, we also examined homogeneous Lewis acid catalysis of the Mukaiyama–aldol reaction of silyl enol ether with benzaldehyde in aqueous/CH_3CN media, together with *syn*/*anti*-stereoselectivity of the reaction product, i.e., 3-hydroxy-2-methyl-1,3-diphenylpropan-1-one, at room temperature under air, using water-soluble sodium or lithium salts of **1**–**4** as well as various sandwich-structured Hf/Zr-containing Keggin and Dawson POMs.

Herein, we report full details of the synthesis and structure of **Cs-1**/**Cs-2**, and **MeN-3**/**MeN-4**, and discuss their homogeneous Lewis acid catalysis of the Mukaiyama–aldol reaction by water-soluble POMs containing **Na-1**–**Na-4**.

Experimental

Materials. The following reagents were used as received: Amberlite IR120B NA, 0.1, 1, and 6 M aqueous HCl solutions (quantitative analysis grade), benzaldehyde, toluene, MeOH, EtOH, Et_2O, CH_3CN, Me_4NCl, Me_2NH_2Cl, CsCl, Na_2CO_3, pyridine, 2,6-di-*tert*-butylpyridine, zirconium(IV) sulfate tetrahydrate (all from Wako); D_2O (Isotec); hafnium(IV) chloride, hafnium(IV) sulfate (Aldrich). The precursors or the trilacunary Keggin POMs, $Na_9[A\text{-}PW_9O_{34}]\cdot 16H_2O$ and $Na_9[B\text{-}PW_9O_{34}]\cdot 16H_2O$ were prepared according to the literature[9a] and identified with FTIR, TG/DTA and ^{31}P NMR. One of the substrates of the Mukaiyama–aldol reaction (silyl enol ether), (*Z*)-1-phenyl-1-trimethylsiloxy-1-propene, was prepared according to the literature[9b] and identified by (^1H, ^{13}C) NMR.[6f,9c]

Instrumentation/Analytical Procedures. Complete elemental analyses were carried out by Mikroanalytisches Labor Pascher (Remagen, Germany). The samples were dried at room temperature under 10^{-3}–10^{-4} Torr overnight before analysis. Infrared spectra were recorded on a Jasco 4100 FTIR spectrometer in KBr disks at room temperature. Thermogravimetric (TG) and differential thermal analyses (DTA) were acquired using a Rigaku Thermo Plus 2 series TG/DTA TG 8120 instrument. ^{31}P NMR (161.70 MHz) spectra were recorded in 5-mm outer diameter tubes on a JEOL JNM-EX 400 FT-NMR spectrometer with a JEOL EX-400 NMR data processing system. ^{31}P NMR spectra were measured with reference to an external standard of 25% H_3PO_4 in H_2O in a sealed capillary. ^{31}P NMR data with the usual 85% H_3PO_4 reference are shifted to +0.544 ppm from our data. Chemical shifts are reported as negative for resonances upfield of 25% H_3PO_4 (δ 0). Solid-state ^{31}P CPMAS NMR (121.00 MHz) spectra were recorded in 6-mm outer diameter rotors on a JEOL JNM-ECP 300 FT-NMR spectrometer with a JEOL ECP-300 NMR data processing system and were referenced to an external standard of $(NH_4)_2HPO_4$. Chemical shifts were reported as negative for resonances upfield of $(NH_4)_2HPO_4$ (δ 1.60).

Syntheses of $Cs_7[[\{Hf(H_2O)\}_2\{Hf(H_2O)_2\}_2(\mu\text{-}OH)_3(\mu_3\text{-}OH)_2](\alpha\text{-}1,2\text{-}PW_{10}O_{37})_2]\cdot 10H_2O$ (Cs-1). To a colorless clear solution of 0.96 g (3.0 mmol) of $HfCl_4$ dissolved in 20 mL of water was added 6 mL of 6 M aqueous HCl solution. To the vigorously stirred, colorless, clear solution, 2.0 g (0.73 mmol) of solid $Na_9[A\text{-}PW_9O_{34}]\cdot 16H_2O$ was added instantly, followed by stirring overnight at room temperature. To the clear solution, 8.0 g (73.0 mmol) of Me_4NCl was added. After stirring for 30 min, the precipitated white powder was collected on a membrane filter (JG 0.2 µm), washed with EtOH (10 mL × 2) and then with Et_2O (50 mL × 2). This powder obtained in ca. 1.5 g yield was added to 20 mL of a 0.1 M aqueous HCl solution. After stirring for 1 h at room temperature, the resulting suspension was filtered through a membrane filter (JG 0.2 µm). The colorless clear filtrate was passed through a cation-exchange resin column [Amberlite IR120B NA, 50 mL] of the Na^+ form at a rate of 2 drops per second. Moreover, 100 mL of water was passed through the column. The combined solution was evapo-

rated to ca. 10 mL of the volume by rotary evaporation at 35 °C. The pH (ca. 5) of the solution was adjusted to 1.0 by adding a 6 M aqueous HCl solution. To the colorless solution, 2.0 g (11.9 mmol) of CsCl was added, followed by stirring for 1 h. The precipitated white powder was collected on a membrane filter (JG 0.2 μm), washed with EtOH (10 mL × 2) and Et_2O (50 mL × 3) and dried in vacuo for 2 h. At this stage, a white powder sample was obtained in 28.5% (0.65 g scale) yield.[10]

Crystallization. A 0.3-g powder sample was dissolved in 7 mL of a pH-2.0 HCl acidic aqueous solution in a water bath at 50 °C. The colorless solution was filtered through a folded filter paper (Whatman #5), and the filtrate was slowly evaporated at room temperature. After 2 days, colorless, clear, granular crystals formed, which were collected on a membrane filter (JG 0.2 μm), washed with EtOH (10 mL × 2) and Et_2O (50 mL × 3) and dried in vacuo for 2 h. Yield 56.7% (0.17 g scale). The crystalline samples were soluble in water (more soluble in an acidic aqueous solution), but insoluble in diethyl ether and ethanol. Microanalysis: Calculated values were fitted within allowed errors for all $x = 0$–2 in $Cs_7[\{Hf_4(H_2O)_x(OH)_5\}(\alpha\text{-}1,2\text{-}PW_{10}O_{37})_2]$. Calcd for $x = 0$ or $H_5O_{79}P_2Hf_4Cs_7W_{20}$: H, 0.08; O, 19.00; P, 0.93; Hf, 10.73; Cs, 13.99; W, 55.27%; calcd for $x = 2$ or $H_9O_{81}P_2Hf_4Cs_7W_{20}$: H, 0.14; O, 19.38; P, 0.93; Hf, 10.68; Cs, 13.91; W, 54.98%. Found: H, 0.34; O, 18.0; P, 0.91; Hf, 10.6; Cs, 13.7; W, 55.5; Na, <0.001; total 99.05%. A weight loss of 3.69% (weakly solvated or adsorbed water) was observed during the course of drying at room temperature at 10^{-3}–10^{-4} Torr overnight before analysis, suggesting the presence of 14 water molecules. TG/DTA under atmospheric conditions: a weight loss of 4.07% due to dehydration was observed at below 199.5 °C with endothermic peaks at 51.7 and 100.5 °C and with an exothermic peak at 247.0 °C; calcd 4.15% for a total of 16 water molecules, i.e., 6 water molecules coordinated to hafnium(IV) atoms plus $x = 10$ in $Cs_7[[\{Hf(H_2O)\}_2\{Hf(H_2O)_2\}_2(\mu\text{-}OH)_3(\mu_3\text{-}OH)_2](\alpha\text{-}1,2\text{-}PW_{10}O_{37})_2]\cdot xH_2O$. IR (KBr) (polyoxometalate region): 1109 s, 1069 s, 1039 s, 951 vs, 892 s, 804 vs, br, 688 w, 520 w cm^{-1}. Solid-state ^{31}P CPMAS NMR: δ −13.82. ^{31}P NMR (23.4 °C, D_2O): δ −13.71. ^{31}P NMR (22.1 °C, 0.1 M aqueous HCl solution): δ −13.42.

Synthesis of $Cs_7[[\{Zr(H_2O)\}_2\{Zr(H_2O)_2\}_2(\mu\text{-}OH)_3(\mu_3\text{-}OH)_2](\alpha\text{-}1,2\text{-}PW_{10}O_{37})_2]\cdot 10H_2O$ (Cs-2). $Zr(SO_4)_2\cdot 4H_2O$ (0.522 g, 1.47 mmol) was dissolved in 20 mL of water. To it, 5 mL of a 6 M aqueous HCl solution was dropwise added using a burette at a rate of ca. 0.25 mL per minute. To the vigorously stirred, colorless, clear solution, 2.0 g (0.73 mmol) of solid $Na_9[A\text{-}PW_9O_{34}]\cdot 16H_2O$ was added instantly. After stirring for 30 min at room temperature, 2.0 g (18.2 mmol) of Me_4NCl was added, followed by stirring for 30 min. The white powder which formed was collected on a membrane filter (JG 0.2 μm), washed with EtOH (10 mL × 2) and then Et_2O (50 mL × 2). This powder, obtained in ca. 1.6 g yield, was added to 10 mL of water, followed by stirring for 30 min at room temperature. The resulting suspension was filtered through a membrane filter (JG 0.2 μm). The colorless, clear filtrate was passed through a cation-exchange resin column [Amberlite IR120B NA, 50 mL] of the Na^+ form at a rate of 2 drops per second. Moreover, 100 mL of water was passed through the column. The combined solution was evaporated to ca. 10 mL of the volume by rotary evaporation at 35 °C. The pH (ca. 5) of the solution was adjusted to 2.0 by adding a 1 M aqueous HCl solution. To the colorless solution, CsCl (0.5 g, 2.97 mmol) was added, followed by stirring for 30 min. The precipitated white powder was collected on a membrane filter (JG 0.2 μm), washed with EtOH (10 mL × 2) and Et_2O (50 mL × 3) and dried in vacuo for 2 h. At this stage, a white powder sample was obtained in 18.0% (0.39 g scale) yield.

Crystallization. A 0.5-g powder sample was dissolved in 20 mL of an HCl acidic aqueous solution at pH 2.0 in a water bath at 50 °C. The colorless solution was filtered through a folded filter paper (Whatman #5), and the filtrate was slowly evaporated at room temperature. After 2 weeks, colorless, clear, granular crystals were deposited and collected on a membrane filter (JG 0.2 μm), washed with EtOH (10 mL × 2) and Et_2O (50 mL × 3) and dried in vacuo for 2 h. Yield 34.0% (0.17 g scale). The crystalline samples were soluble in water (more soluble in an acidic aqueous solution), but insoluble in diethyl ether and ethanol. Microanalysis: Calculated values were fitted within allowed errors for all $x = 0$–2 in $Cs_7[\{Zr_4(H_2O)_x(OH)_5\}(\alpha\text{-}1,2\text{-}PW_{10}O_{37})_2]$. Calcd for $x = 0$ or $H_5O_{79}P_2Zr_4Cs_7W_{20}$: H, 0.08; O, 20.05; P, 0.98; Zr, 5.79; Cs, 14.76; W, 58.33%; calcd for $x = 2$ or $H_9O_{81}P_2Zr_4Cs_7W_{20}$: H, 0.14; O, 20.44; P, 0.98; Zr, 5.76; Cs, 14.68; W, 58.00%. Found: H, 0.36; O, 19.4; P, 1.01; Zr, 5.84; Cs, 14.5; W, 58.7; Na, <0.001; total 99.81%. A weight loss of 3.76% (weakly solvated or adsorbed water) was observed during the course of drying at room temperature at 10^{-3}–10^{-4} Torr overnight before analysis, suggesting the presence of 14 water molecules. TG/DTA under atmospheric conditions showed a weight loss of 4.28% due to loss of water molecules at below 199.7 °C with endothermic peaks at 53.9 and 98.0 °C and with an exothermic peak at 237.6 °C; calcd 4.37% for a total of 16 water molecules, i.e., 6 water molecules coordinated to zirconium(IV) atoms plus $x = 10$ in $Cs_7[[\{Zr(H_2O)\}_2\{Zr(H_2O)_2\}_2(\mu\text{-}OH)_3(\mu_3\text{-}OH)_2](\alpha\text{-}1,2\text{-}PW_{10}O_{37})_2]\cdot xH_2O$. IR (KBr) (polyoxometalate region): 1107 s, 1068 s, 1038 s, 951 vs, 892 s, 801 vs, br, 678 w, 512 w cm^{-1}. Solid-state ^{31}P CPMAS NMR: δ −13.21. ^{31}P NMR (22.9 °C, D_2O): δ −13.28. ^{31}P NMR (22.7 °C, 0.1 M aqueous HCl solution): δ −12.82.

Cs-2 can also be synthesized by the reaction of $ZrCl_4$ and $Na_9[A\text{-}PW_9O_{34}]\cdot 16H_2O$ with almost the same work-ups as **Cs-1**.

Synthesis of $(Me_2NH_2)_8[\{Hf_4(H_2O)_4(\mu\text{-}OH)_2(\mu_3\text{-}O)_2\}(\alpha\text{-}1,4\text{-}PW_{10}O_{37})_2]\cdot 9H_2O$ (MeN-3). Solid $Hf(SO_4)_2\cdot 4H_2O$ (1.00 g, 2.26 mmol) was dissolved in 20 mL of water in a water bath at 50 °C. The pH (ca. 0.7) of the colorless solution was adjusted to 1.4–1.5 by adding solid Na_2CO_3, followed by stirring for 15 min in an ice-bath. To it, vigorously stirred in an ice-bath, 2.0 g (0.73 mmol) of solid $Na_9[B\text{-}PW_9O_{34}]\cdot 16H_2O$ was slowly added over more than 10 min. To that, 1.5 g (18.4 mmol) of Me_2NH_2Cl was added, followed by stirring for 30 min at room temperature. The white suspension was filtered through a membrane filter (JG 0.2 μm). Also, 1.0 g (12.3 mmol) of Me_2NH_2Cl was added to the colorless filtrate and then stirred overnight at room temperature. The white powder which formed was collected on a membrane filter (JG 0.2 μm), washed with H_2O 3 mL, EtOH (10 mL × 3) and Et_2O (50 mL × 2) and dried in vacuo for 2 h. At this stage, the crude product of the dimethylammonium salt was obtained in a yield of ca. 0.8 g.

Crystallization. This powder (0.76 g) was dissolved in 5 mL of water in a water bath at 50 °C. The colorless solution was slowly evaporated at room temperature. After 4 days, colorless, clear, plate crystals formed, which were collected on a membrane filter (JG 0.2 μm), washed with EtOH (10 mL × 2) and Et_2O (50 mL × 3) and dried in vacuo for 2 h. The crystals were obtained in 3.0% yield (0.07 g scale). Found: C, 3.25; H, 1.18; N, 1.74%. Calcd for $C_{16}H_{92}N_8O_{91}P_2Hf_4W_{20}$ or $(Me_2NH_2)_8[\{Hf_4(H_2O)_4(\mu\text{-}OH)_2(\mu_3\text{-}O)_2\}(\alpha\text{-}1,4\text{-}PW_{10}O_{37})_2]\cdot 9H_2O$: C, 3.05; H, 1.47; N, 1.78%. TG/DTA under atmospheric conditions showed a weight loss of 3.78% due to loss of water at below 131.0 °C with an endothermic peak at 115.3 °C; calcd 3.71% for a total of 13 water molecules, i.e., 4 water molecules coordinated to hafnium(IV) atoms plus $x = 9$ in $(Me_2NH_2)_8[\{Hf_4(H_2O)_4(\mu\text{-}OH)_2(\mu_3\text{-}O)_2\}(\alpha\text{-}1,4\text{-}PW_{10}O_{37})_2]\cdot xH_2O$. IR(KBr) (polyoxometalate region): 1465 m, 1436 w, 1412 w, 1392 w, 1079 s, 1044 s, 1017 m, 949 vs, 879 s, 790 vs, 635 m, 589 w, 510 m, 489 w, 429 w, 416 w cm^{-1}. Solid-state ^{31}P CPMAS NMR: δ −11.13. ^{31}P NMR (17.3 °C, D_2O): δ −11.68.

Synthesis of $(Me_2NH_2)_8[\{Zr_4(H_2O)_4(\mu\text{-}OH)_2(\mu_3\text{-}O)_2\}(\alpha\text{-}1,4\text{-}PW_{10}O_{37})_2]\cdot 9H_2O$ (MeN-4). The pH (ca. 0.9) of a solution of $Zr(SO_4)_2\cdot 4H_2O$ (0.79 g, 2.22 mmol) dissolved in 20 mL of water was adjusted to 1.6 by adding solid Na_2CO_3. To the vigorously stirred, colorless solution, 2.0 g (0.73 mmol) of solid $Na_9[B\text{-}PW_9O_{34}]\cdot 16H_2O$ was slowly added over more than 10 min. This solution was stirred for 15 min at room temperature. To it, 1.0 g (12.3 mmol) of Me_2NH_2Cl was added, followed by stirring for 5 min at room temperature. The solution was allowed to stand for 9 h in a refrigerator at 4 °C. The white powder which precipitated was filtered off through a membrane filter (JG 0.2 μm). The colorless filtrate was slowly evaporated at room temperature. After 3 days, colorless, clear, plate crystals formed and were collected on a membrane filter (JG 0.2 μm), washed with EtOH (20 mL × 3) and Et_2O (50 mL × 3) and dried in vacuo for 2 h. The crystals, obtained in 18.7% (0.18 g scale) yield, were soluble in water, but insoluble in diethyl ether and ethanol. Found: C, 3.42; H, 1.27; N, 1.86%. Calcd for $C_{16}H_{92}N_8O_{91}P_2Zr_4W_{20}$ or $(Me_2NH_2)_8[\{Zr_4(H_2O)_4(\mu\text{-}OH)_2(\mu_3\text{-}O)_2\}(\alpha\text{-}1,4\text{-}PW_{10}O_{37})_2]\cdot 9H_2O$: C, 3.23; H, 1.56; N, 1.88%. TG/DTA under atmospheric conditions: a weight loss of 3.91% due to loss of water was observed at below 160.5 °C with an endothermic peak at 125.0 °C; calcd 3.93% for a total of 13 water molecules, i.e., 4 water molecules coordinated to zirconium(IV) atoms plus $x = 9$ in $(Me_2NH_2)_8[\{Zr_4(H_2O)_4(\mu\text{-}OH)_2(\mu_3\text{-}O)_2\}(\alpha\text{-}1,4\text{-}PW_{10}O_{37})_2]\cdot xH_2O$. IR(KBr) (polyoxometalate region): 1465 m, 1435 w, 1412 w, 1392 w, 1251 w, 1228 w, 1077 s, 1043 s, 1016 m, 950 vs, 880 s, 799 vs, 641 m, 614 m, 588 w, 545 m, 512 m, 489 w, 414 w cm^{-1}. Solid-state ^{31}P CPMAS NMR: δ −10.76. ^{31}P NMR (16.2 °C, D_2O): δ −10.86.

Syntheses of Precatalysts Na-1 to Na-4. The water-soluble sodium salts **Na-1**, **Na-2**, **Na-3**, and **Na-4** as precatalysts for the Mukaiyama–aldol reaction were obtained and characterized by FTIR, TG/DTA, and solid-state ^{31}P CPMAS and solution ^{31}P NMR, as described below.[11] The compounds **Na-1** to **Na-4** were obtained as pure powder samples, but not crystalline samples. In fact, their powder XRD patterns were not obtained.

Na-1: POM **Cs-1** (0.5 g, 0.07 mmol) was dissolved in 20 mL of water in a water bath at 60 °C. The colorless, clear solution was passed through a cation-exchange resin column [Amberlite IR120B NA, 50 mL] of the Na^+ form at a rate of 2 drops per second, and 100 mL of water was also passed through the column. The combined solution was evaporated with a rotary evaporator at 40 °C and dried in vacuo for 2 h. Yield 73.2% (0.33 g scale). The powder samples were soluble in water and acetonitrile. TG/DTA under atmospheric conditions showed a weight loss of 8.55% due to dehydration at below 459.9 °C with an endothermic peak at 59.6 °C; calcd 8.67% for a total of 31 water molecules, i.e., 6 water molecules coordinated to hafnium(IV) atoms plus $x = 25$ in $Na_7[[\{Hf(H_2O)\}_2\text{-}\{Hf(H_2O)_2\}_2(\mu\text{-}OH)_3(\mu_3\text{-}OH)_2](\alpha\text{-}1,2\text{-}PW_{10}O_{37})_2]\cdot xH_2O$. IR (KBr) (polyoxometalate region): 1105 s, 1068 s, 1038 s, 953 vs, 895 s, 816 vs, br, 686 w, 522 w cm^{-1}. ^{31}P NMR (22.6 °C, D_2O): δ −13.48. Solid-state ^{31}P CPMAS NMR: δ −12.85.

Na-2: POM **Cs-2** (0.4 g, 0.06 mmol) was dissolved in 20 mL of water in a water bath at 60 °C. The colorless, clear solution was passed through a cation-exchange resin column [Amberlite IR120B NA, 50 mL] of the Na^+ form at a rate of 2 drops per second, after which 100 mL of water was passed through the column. The combined solution was evaporated with a rotary evaporator at 40 °C and dried in vacuo for 2 h. Yield 87.5% (0.32 g scale). The powder samples were soluble in water and acetonitrile. TG/DTA under atmospheric conditions showed a weight loss of 9.29% due to loss of water molecules at below 467.1 °C with endothermic peaks at 45.1 and 66.1 °C; calcd 9.16% for a total of 31 water molecules, i.e., 6 water molecules coordinated to zirconium(IV) atoms plus $x = 25$ in $Na_7[[\{Zr(H_2O)\}_2\{Zr(H_2O)_2\}_2(\mu\text{-}OH)_3(\mu_3\text{-}OH)_2]\text{-}(\alpha\text{-}1,2\text{-}PW_{10}O_{37})_2]\cdot xH_2O$. IR (KBr) (polyoxometalate region): 1101 s, 1066 s, 1039 s, 955 vs, 891 s, 806 vs, br, 675 w, 663 w, 592 w cm^{-1}. ^{31}P NMR (22.5 °C, D_2O): δ −12.86 (main), −13.17 (minor), ^{31}P NMR (24.0 °C, 0.1 M HCl (aq)): δ −12.95, ^{31}P NMR (23.2 °C, D_2O/CD_3CN (200 μL/450 μL)): δ −12.31. Solid-state ^{31}P CPMAS NMR: δ −11.50.

Na-3: POM **MeN-3** (0.55 g, 0.092 mmol) and a cation-exchange resin [Amberlite IR120B NA, 50 mL] of the Na^+ form were added to 50 mL of water (batch method). After stirring for 1 h at room temperature, a cation-exchange resin [Amberlite IR120B NA, 50 mL] of the Na^+ form was filtered off through a membrane filter (JG 0.2 μm). The colorless, clear filtrate was evaporated by a rotary evaporator at 30 °C and dried in vacuo for 2 h. Yield 72.1% (0.41 g scale). The powder samples were soluble in water and acetonitrile. TG/DTA under atmospheric conditions revealed a weight loss of 5.09% due to loss of water molecules at below 500 °C with an endothermic peak at 76.4 °C; calcd 5.22% for a total of 18 water molecules, i.e., 4 water molecules coordinated to hafnium(IV) atoms plus $x = 14$ in $Na_8[\{Hf_4(H_2O)_4(\mu\text{-}OH)_2(\mu_3\text{-}O)_2\}(\alpha\text{-}1,4\text{-}PW_{10}O_{37})_2]\cdot xH_2O$. IR (KBr) (polyoxometalate region): 1074 s, 1045 s, 954 s, 892 s, 783 vs, 625 s, 587 s, 547 s, 504 s, 410 s cm^{-1}. ^{31}P NMR (24.0 °C, D_2O): δ −11.60. Solid-state ^{31}P CPMAS NMR: δ −11.04.

Na-4: POM **MeN-4** (0.57 g, 0.096 mmol) and a cation-exchange resin [Amberlite IR120B NA, 50 mL] of the Na^+ form were added to 50 mL of water (batch method). After stirring for 1 h at room temperature, a cation-exchange resin

[Amberlite IR120B NA, 50 mL] of the Na^+ form was filtered off through a membrane filter (JG 0.2 μm). The colorless, clear filtrate was evaporated by a rotary evaporator at 30 °C and dried in vacuo for 2 h. Yield 66.3% (0.38 g scale). The powder samples were soluble in water and acetonitrile. TG/DTA under atmospheric conditions displayed a weight loss of 7.48% due to loss of water molecules at below 500 °C with an endothermic peak at 63.9 °C; calcd 7.52% for a total of 21 water molecules, i.e., 4 water molecules coordinated to zirconium(IV) atoms plus $x = 17$ in $Na_8[\{Zr_4(H_2O)_4(\mu\text{-}OH)_2(\mu_3\text{-}O)_2\}(\alpha\text{-}1,4\text{-}PW_{10}O_{37})_2]\cdot xH_2O$. IR (KBr) (polyoxometalate region): 1072 s, 1044 s, 954 s, 891 s, 785 vs, 605 s, 588 s, 542 s, 503 s, 411 s cm^{-1}. ^{31}P NMR (22.2 °C, D_2O): δ −10.81. Solid-state ^{31}P CPMAS NMR: δ −10.38.

By a similar method, the sodium salts of other Keggin POMs and the lithium salts of Dawson POMs, used for the catalysis of the Mukaiyama–aldol reaction, were obtained through the ion-exchange resins from known POMs.[2,4d,5d,5e]

Mukaiyama–Aldol Reaction. The sodium salts **Na-1**, **Na-2**, **Na-3**, and **Na-4** as precatalysts (0.025 mmol) were dissolved in a solvent mixture of acetonitrile/water (4.5 mL/2.0 mL) in a round-bottom flask. To it were added benzaldehyde (51 μL, 0.50 mmol), silyl enol ether (113 μL, 0.50 mmol) and toluene (100 μL, 0.94 mmol) as an internal reference for HPLC analysis. The dispersed solution was stirred for 24 h at room temperature. During stirring for several hours, the dispersed solution became a homogeneous, colorless solution. Then 100 μL of the solution were put into a 10-mL volumetric flask, diluted with MeOH to 10 mL, and 5 μL of the colorless, clear solution were analyzed by HPLC, Shimadzu LC-20AD (column: VP-ODS with a size of 150 L × 4.6; detector: Shimadzu SPD-20A, 260 nm ABS). The *syn*/*anti* ratio of aldol as product, i.e., 3-hydroxy-2-methyl-1,3-diphenylpropan-1-one, was determined by ^1H NMR and HPLC.

Reuse Experiments of Na-1, Na-3, and Na-4: 1st–4th Reuse for Mukaiyama–Aldol Reaction. The solution after 24 h reaction in the 1st run (Entries 1, 6, and 9, Table 5) was evaporated until all of the acetonitrile was removed by a rotary evaporator at 30 °C, resulting in separation of two layers. To it was added a solvent mixture of 10 mL of dichloromethane and 10 mL of water, stirred for a few min and transferred into a separatory funnel. The organic layer from the two layers was separated off and the aqueous layer was washed with dichloromethane (10 mL × 3). The residual aqueous layer was transferred to a round bottom flask, evaporated to dryness by rotary evaporation at 40 °C, and further dried in vacuo for 30 min. This material was dissolved in a solvent mixture of acetonitrile/water (4.5 mL/2.0 mL) and the colorless clear solution was used for the 2nd run experiment (Entries 2, 7, and 10, Table 5). This procedure was repeated for 3–5 runs (Entries 3–5, 8, and 11, Table 5). After the 5th run (Entry 5, Table 5), white powder of 0.14 g was recovered (recovery rate; 88%).

X-ray Crystallography. Full details of X-ray crystallographic data of **Cs-1**, **Cs-2**, **MeN-3**, and **MeN-4** are described in Supporting Information (Figures S1–S4, Tables S1–S12) because the structural characterization were briefly reported in a previous paper.[8]

The crystal structure investigation may be obtained from the Fachinformationszentrum Karlsruhe, 76344 Eggenstein-Leopoldshafen, Germany (fax: (+49)7247-808-666); e-mail: crysdata@fiz-karlsruhe.de, by quoting depository number CSD-424498 (formula/code: yos011s) for **Cs-1** and CSD-424497 (formula/code: yos007s) for **Cs-2**. CCDC reference numbers 874376 (formula/code: yos017s) for **MeN-3** and 874375 (formula/code: yos016s) for **MeN-4** contain supplementary crystallographic data for this paper. These data can be obtained free of charge at www.ccdc.cam.ac.uk/conts/retrieving.html (or from Cambridge Crystallographic Data Center, 12 Union Road, Cambridge CB2 1EZ, UK.; Fax: +44-1223-336-033; E-mail: deposite@ccdc.cam.ac.uk).

Results and Discussion

Synthesis and Compositional Characterization. The cesium salts of tetrahafnium(IV) and tetrazirconium(IV) cluster cations sandwiched between two di-1,2-lacunary Keggin POMs, $Cs_7[[\{Hf(H_2O)\}_2\{Hf(H_2O)_2\}_2(\mu\text{-}OH)_3(\mu_3\text{-}OH)_2](\alpha\text{-}1,2\text{-}PW_{10}O_{37})_2]\cdot 10H_2O$ (**Cs-1**) and $Cs_7[[\{Zr(H_2O)\}_2\{Zr(H_2O)_2\}_2(\mu\text{-}OH)_3(\mu_3\text{-}OH)_2](\alpha\text{-}1,2\text{-}PW_{10}O_{37})_2]\cdot 10H_2O$ (**Cs-2**), were obtained as analytically pure, colorless crystals in 16.2% and 6.1% yields, respectively. Compounds **Cs-1** and **Cs-2** were prepared by the 1:4 molar ratio reaction of $[A\text{-}PW_9O_{34}]^{9-}$ with $HfCl_4$ and the 1:2 molar ratio reaction of $[A\text{-}PW_9O_{34}]^{9-}$ with $Zr(SO_4)_2\cdot 4H_2O$, respectively, in stronger HCl-acidic solutions (pH ca. 0), both followed by changing the counterion first to Me_4N^+, then to Na^+ and finally to Cs^+. The low yield of **Cs-1** (16.2%) and **Cs-2** (6.1%) mainly came from the three fold exchange work-ups of the counter cation for purification and crystallization. Crystallization of **Cs-1** and **Cs-2** was carried out by slow evaporation of the aqueous HCl acidic solutions. The crystalline samples were characterized by complete elemental analysis, including Cs and O analyses, FTIR, TG/DTA, solid-state ^{31}P CPMAS and solution ^{31}P NMR in a D_2O and 0.1 M aqueous HCl solution, and X-ray crystallography.

The formation of polyoxoanions **1** and **2** can be represented in eq 1.

$$2[A\text{-}PW_9O_{34}]^{9-} + 4M^{4+} + 9H_2O + 2WO_4^{2-} \rightarrow [[\{M(H_2O)\}_2\{M(H_2O)_2\}_2(\mu\text{-}OH)_3(\mu_3\text{-}OH)_2](\alpha\text{-}1,2\text{-}PW_{10}O_{37})_2]^{7-} \quad (M = \text{Hf } \mathbf{1}, \text{Zr } \mathbf{2}) + H^+ \tag{1}$$

As to the synthetic reaction using $[A\text{-}PW_9O_{34}]^{9-}$, it should be noted that the trinuclear hafnium(IV) and zirconium(IV) complexes sandwiched between two Keggin tri-lacunary POMs, $[M_3(\mu\text{-}OH)_3(A\text{-}\alpha\text{-}PW_9O_{34})_2]^{9-}$ (M = Hf and Zr) have been prepared by the 1:3 molar ratio reactions of $[A\text{-}PW_9O_{34}]^{9-}$ with $Hf(SO_4)_2$ and $Zr(SO_4)_2$ in aqueous acidic solutions (pH 1.2) at 80–90 °C, followed by refluxing.[5b] The key points of the synthesis of the M_3 clusters and the present M_4 clusters are as follows: (1) the M_3 clusters were prepared by 1:3 molar ratio reactions in pH 1.2 solutions, (2) the Hf_4 cluster (**Cs-1**) was prepared by 1:4 molar ratio reaction in a pH ca. 0 solution, and (3) the Zr_4 cluster (**Cs-2**) was prepared by 1:2 molar ratio reaction in a pH ca. 0 solution. The M_4 clusters are sandwiched between two di-lacunary Keggin units, although the tri-lacunary Keggin POMs are used as starting materials. The di-lacunary Keggin units should be in situ generated by decomposition and subsequent reactions of the tri-lacunary Keggin POMs. Therefore, lower pH may be required to synthesize the present M_4 clusters.

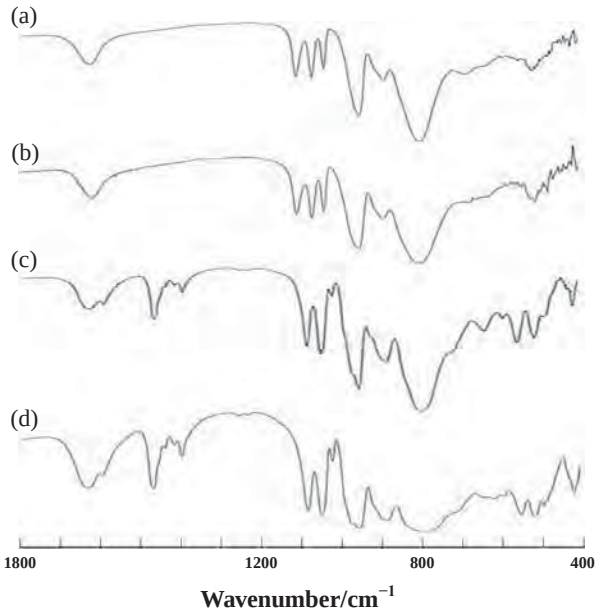

Figure 1. FTIR spectra in the polyoxoanion region (1800–400 cm^{-1}), measured as KBr disks, of (a) $Cs_7[[\{Hf(H_2O)\}_2\{Hf(H_2O)_2\}_2(\mu\text{-}OH)_3(\mu_3\text{-}OH)_2](\alpha\text{-}1,2\text{-}PW_{10}O_{37})_2]\cdot 10H_2O$ (**Cs-1**), (b) $Cs_7[[\{Zr(H_2O)\}_2\{Zr(H_2O)_2\}_2(\mu\text{-}OH)_3(\mu_3\text{-}OH)_2](\alpha\text{-}1,2\text{-}PW_{10}O_{37})_2]\cdot 10H_2O$ (**Cs-2**), (c) $(Me_2NH_2)_8[\{Hf_4(H_2O)_4(\mu\text{-}OH)_2(\mu_3\text{-}O)_2\}(\alpha\text{-}1,4\text{-}PW_{10}O_{37})_2]\cdot 9H_2O$ (**MeN-3**), and (d) $(Me_2NH_2)_8[\{Zr_4(H_2O)_4(\mu\text{-}OH)_2(\mu_3\text{-}O)_2\}(\alpha\text{-}1,4\text{-}PW_{10}O_{37})_2]\cdot 9H_2O$ (**MeN-4**).

The two samples, **Cs-1** and **Cs-2**, for elemental analysis, were dried at room temperature under a vacuum of 10^{-3}–10^{-4} Torr overnight. All elements (H, O, P, W, Cs, and Hf or Zr) were observed for a total analysis of 99.05% for **Cs-1** and 99.81% for **Cs-2**, and Na analysis of <0.001% found for both POMs revealed no contamination of the sodium ions from the precursors. The analytical data we found were in good accord with the calculated values for the formulas within the allowed errors for 0–2 hydrated water molecules (see Experimental section). The weight losses observed during drying before analysis were 3.69% for **Cs-1** and 3.76% for **Cs-2**, both of which corresponded to approximately 14 weakly solvated and/or adsorbed water molecules. Thus, the elemental analyses showed a presence of a total of 14–16 water molecules for both samples under atmospheric conditions.

On the other hand, in the TG/DTA measurements carried out under atmospheric conditions, the weight losses of 4.07% observed at below 199.5 °C for **Cs-1** and 4.28% observed at below 199.7 °C for **Cs-2** corresponded to approximately 16 water molecules for both. Thus, the total of 16 water molecules observed by TG/DTA measurements under atmospheric conditions, assigned as 10 solvated and/or adsorbed water molecules plus 6 water molecules coordinated to Hf or Zr atoms, are in good agreement with a total of 14–16 water molecules found by elemental analyses. The formulas presented herein are based on the results of TG/DTA measurements.

The FTIR spectra (Figures 1a and 1b) of **Cs-1** and **Cs-2**, measured in KBr disks, showed the characteristic bands of the Keggin POM framework,[12] which were very similar to each other and almost coincidental within experimental error.

The dimethylammonium salts of tetrahafnium(IV) and tetrazirconium(IV) cluster cations sandwiched between two di-1,4-lacunary Keggin POMs, $(Me_2NH_2)_8[\{Hf_4(H_2O)_4(\mu\text{-}OH)_2(\mu_3\text{-}O)_2\}(\alpha\text{-}1,4\text{-}PW_{10}O_{37})_2]\cdot 9H_2O$ (**MeN-3**) and $(Me_2NH_2)_8[\{Zr_4(H_2O)_4(\mu\text{-}OH)_2(\mu_3\text{-}O)_2\}(\alpha\text{-}1,4\text{-}PW_{10}O_{37})_2]\cdot 9H_2O$ (**MeN-4**), were obtained as analytically pure, colorless crystals in 3.0% and 18.7% yields, respectively. The powder sample of **MeN-3** was prepared by the 1:3 molar ratio reaction of $[B\text{-}PW_9O_{34}]^{9-}$ with $Hf(SO_4)_2\cdot 4H_2O$ in aqueous acidic solution (pH ca. 1.4–1.5) in an ice bath, followed by changing the counter ion to $Me_2NH_2^+$. The $Me_2NH_2^+$ salt of **3** was crystallized by slow evaporation of the solution. Compound **MeN-4** was also prepared by the 1:3 molar ratio reaction of $[B\text{-}PW_9O_{34}]^{9-}$ with $Zr(SO_4)_2\cdot 4H_2O$ in an aqueous acidic solution (pH ca. 1.6), after adding Me_2NH_2Cl, and the crystalline sample was obtained by slow evaporation. Both crystalline samples were characterized by CHN elemental analysis, FTIR, TG/DTA, solution ^{31}P NMR in a D_2O and X-ray crystallography.

The formation of polyoxoanions **3** and **4** can be represented in eq 2.

$$2[B\text{-}PW_9O_{34}]^{9-} + 4M^{4+} + 6H_2O + 2WO_4^{2-} \rightarrow [\{M_4(H_2O)_4(\mu\text{-}OH)_2(\mu_3\text{-}O)_2\}(\alpha\text{-}1,4\text{-}PW_{10}O_{37})_2]^{8-} \quad (M = \text{Hf } \mathbf{3}, \text{Zr } \mathbf{4}) + 2H^+ \tag{2}$$

In the TG/DTA measurements carried out under atmospheric conditions, the weight losses of 3.78% observed at below 131.0 °C for **MeN-3** and those of 3.91% observed at below 160.5 °C for **MeN-4** corresponded to approximately 13 water molecules for both. Thus, the total of 13 water molecules observed by TG/DTA measurements under atmospheric conditions, assigned as 9 solvated and/or adsorbed water molecules plus 4 water molecules coordinated to Hf or Zr atoms, are in good agreement with the total of 13 water molecules found by CHN elemental analyses.

The FTIR spectra (Figures 1c and 1d) of **MeN-3** and **MeN-4**, measured in KBr disks, showed the characteristic bands of the Keggin POM framework,[12] which were very similar to each other and almost coincidental within experimental error. The two intense P–O vibrational bands due to di-1,4-lacunary Keggin POMs are in contrast to the three intense P–O bands in **Cs-1** and **Cs-2**.

Molecular Structures. X-ray crystallography revealed that the central Hf_4 cluster cation moiety in **1**, i.e., $[\{Hf(H_2O)\}_2\{Hf(H_2O)_2\}_2(\mu\text{-}OH)_3(\mu_3\text{-}OH)_2]^{11+}$, was sandwiched between two α-Keggin 1,2-di-lacunary POMs, $[\alpha\text{-}1,2\text{-}PW_{10}O_{37}]^{9-}$ (Figure 2a). The central Hf_4 cluster cation unit was composed of two 8-coordinate Hf polyhedra (Hf1A and Hf1B) with one coordinated water molecule (O1X and O2X were coordinated to Hf1A and Hf1B, respectively) and two 7-coordinate Hf polyhedra (Hf2A and Hf2B) with two coordinated water molecules (O3X and O4X were coordinated to Hf2A; O5X and O6X were coordinated to Hf2B). Four Hf polyhedra were linked through 3 μ-OH (O7X, O9X, and O11X) and 2 μ_3-OH groups (O8X and O10X) (Tables S1, S2, and S9, Figure S1).

The molecular structure of Zr-analogue **2** in **Cs-2** was isostructural with that of **1** (Tables S3, S4, and S10, Figure S2).

X-ray crystallography revealed that the central Hf_4 cluster cation moiety in **3**, i.e., $[Hf_4(H_2O)_4(\mu\text{-}OH)_2(\mu_3\text{-}O)_2]^{10+}$, was

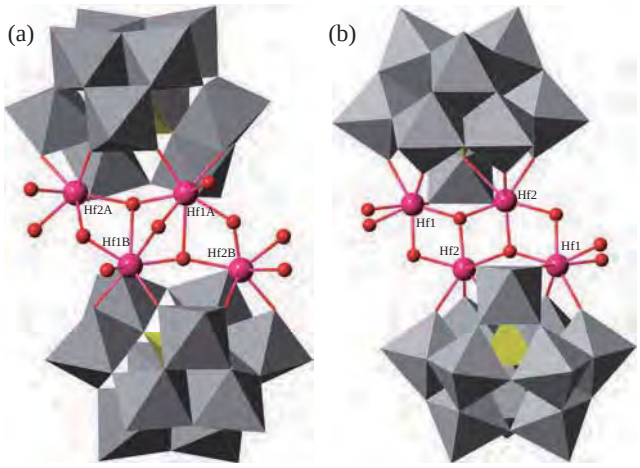

Figure 2. Molecular structures of the polyoxoanion (a) $[[\{Hf(H_2O)\}_2\{Hf(H_2O)_2\}_2(\mu\text{-}OH)_3(\mu_3\text{-}OH)_2](\alpha\text{-}1,2\text{-}PW_{10}O_{37})_2]^{7-}$ (**1**) in **Cs-1** and (b) $[\{Hf_4(H_2O)_4(\mu\text{-}OH)_2(\mu_3\text{-}O)_2\}(\alpha\text{-}1,4\text{-}PW_{10}O_{37})_2]^{8-}$ (**3**) in **MeN-3**.

sandwiched between two α-Keggin 1,4-di-lacunary POMs, $[\alpha\text{-}1,4\text{-}PW_{10}O_{37}]^{9-}$ (Figure 2b). The central Hf_4 cluster cation unit of **3** was different from those of **1** and **2**. In contrast to the Hf_4 cluster moiety in **1** with two 7-coordinate and two 8-coordinate Hf atoms, the central Hf_4 cluster cation unit in **3** is composed of only 7-coordinate Hf atoms (Hf1 and Hf2). Four Hf polyhedra were linked through 2 μ-OH groups (O1M) and 2 $\mu_3\text{-}O^{2-}$ atoms (O2M) (Tables S5, S6, and S11, Figure S3). The Hf1 atom is accompanied by 2 coordinated water molecules (O1W and O2W: the BVS of O1W and O2W are 0.388 and 0.397, respectively), whereas no water molecule is observed on the Hf2 atom.

The molecular structure of Zr-analogue **4** in **MeN-4** was isostructural with that of **3** (Tables S7, S8, and S12, Figure S4).

Solid-State ^{31}P CPMAS and Solution ^{31}P NMR. Solid-state ^{31}P CPMAS NMR of the crystalline samples of **Cs-1** and **Cs-2** showed a single ^{31}P resonance due to the two equivalent 1,2-di-lacunary α-Keggin units, as shown in X-ray crystallography, at −13.82 and −13.21 ppm, respectively (Figures 3a and 3b). The difference in the chemical shifts reflects that of the tetra-nuclear Hf and Zr clusters.

Solid-state ^{31}P CPMAS NMR of the crystalline samples of **MeN-3** and **MeN-4** also showed a single ^{31}P resonance due to the two equivalent 1,4-di-lacunary α-Keggin units, as shown in X-ray crystallography, at −11.13 and −10.76 ppm, respectively (Figures 3c and 3d).

The solid-state ^{31}P CPMAS NMR spectra of **Cs-1** and **Cs-2** correspond to the solution ^{31}P NMR spectra in D_2O (at −13.71 and −13.28 ppm, respectively, Figures 4a and 4b), and the solid-state ^{31}P NMR of **MeN-3** and **MeN-4** correspond to the solution ^{31}P NMR in D_2O (−11.68 and −10.84 ppm, respectively, Figures 4c and 4d), indicating that the solid-state sandwich structures are maintained in solution. These spectra also demonstrate the purity and single-product nature of these compounds. Solution ^{31}P NMR spectra of the sandwich-structured Keggin POMs reflect the differences in both the central Hf/Zr clusters and the lacunary Keggin POM units; the 4:2 complexes, 1:2 complexes, 2:2 complexes, and 3:2 complexes

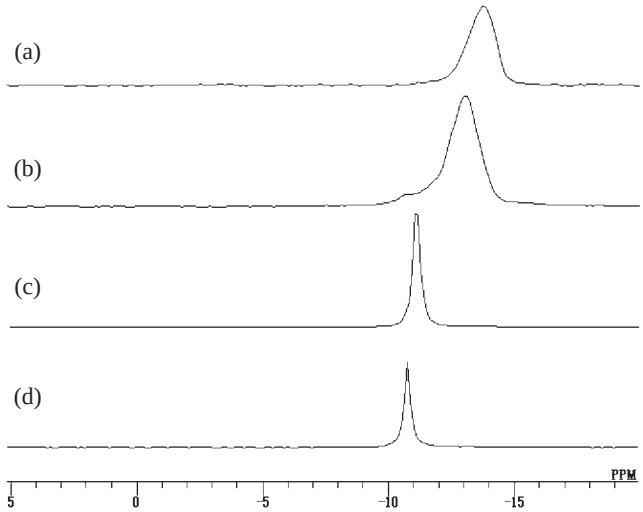

Figure 3. Solid-state ^{31}P CPMAS NMR spectra of (a) $Cs_7[[\{Hf(H_2O)\}_2\{Hf(H_2O)_2\}_2(\mu\text{-}OH)_3(\mu_3\text{-}OH)_2](\alpha\text{-}1,2\text{-}PW_{10}O_{37})_2]\cdot 10H_2O$ (**Cs-1**), (b) $Cs_7[[\{Zr(H_2O)\}_2\{Zr(H_2O)_2\}_2(\mu\text{-}OH)_3(\mu_3\text{-}OH)_2](\alpha\text{-}1,2\text{-}PW_{10}O_{37})_2]\cdot 10H_2O$ (**Cs-2**), (c) $(Me_2NH_2)_8[\{Hf_4(H_2O)_4(\mu\text{-}OH)_2(\mu_3\text{-}O)_2\}(\alpha\text{-}1,4\text{-}PW_{10}O_{37})_2]\cdot 9H_2O$ (**MeN-3**), and (d) $(Me_2NH_2)_8[\{Zr_4(H_2O)_4(\mu\text{-}OH)_2(\mu_3\text{-}O)_2\}(\alpha\text{-}1,4\text{-}PW_{10}O_{37})_2]\cdot 9H_2O$ (**MeN-4**).

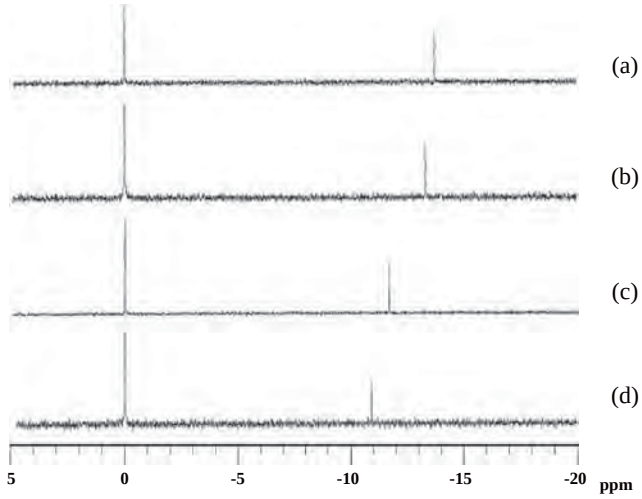

Figure 4. Solution ^{31}P NMR spectra in D_2O of (a) $Cs_7[[\{Hf(H_2O)\}_2\{Hf(H_2O)_2\}_2(\mu\text{-}OH)_3(\mu_3\text{-}OH)_2](\alpha\text{-}1,2\text{-}PW_{10}O_{37})_2]\cdot 10H_2O$ (**Cs-1**), (b) $Cs_7[[\{Zr(H_2O)\}_2\{Zr(H_2O)_2\}_2(\mu\text{-}OH)_3(\mu_3\text{-}OH)_2](\alpha\text{-}1,2\text{-}PW_{10}O_{37})_2]\cdot 10H_2O$ (**Cs-2**), (c) $(Me_2NH_2)_8[\{Hf_4(H_2O)_4(\mu\text{-}OH)_2(\mu_3\text{-}O)_2\}(\alpha\text{-}1,4\text{-}PW_{10}O_{37})_2]\cdot 9H_2O$ (**MeN-3**), and (d) $(Me_2NH_2)_8[\{Zr_4(H_2O)_4(\mu\text{-}OH)_2(\mu_3\text{-}O)_2\}(\alpha\text{-}1,4\text{-}PW_{10}O_{37})_2]\cdot 9H_2O$ (**MeN-4**).

(Table 1). Comparison within each pair of complexes shows the differences in the clusters of Hf and Zr.

The chemical shifts of **Cs-1** and **Cs-2** in D_2O (−13.71 and −13.28 ppm, respectively) were found in a higher field than those in a 0.1 M aqueous HCl solution (−13.42 and −12.82 ppm, respectively). The tetranuclear cluster structure may be present in a different state in D_2O and the 0.1 M HCl solution. It should also be noted that the opposite tendency has been observed in the 2:2 complex; ^{31}P NMR resonances of the dinuclear Hf and Zr complexes in D_2O observed at −13.76 and

Table 1. Solution ^{31}P NMR and Solid-State ^{31}P CPMAS NMR

Entry			Complex type	Chemical shift [ppm] in D_2O	Solid-state CPMAS
1	$Cs_7[[\{Zr(H_2O)\}_2\{Zr(H_2O)_2\}_2(\mu\text{-}OH)_3(\mu_3\text{-}OH)_2](\alpha\text{-}1,2\text{-}PW_{10}O_{37})_2]\cdot 10H_2O$	(**Cs-2**)	4:2-type	−13.28	−13.21
2	$Na_7[[\{Zr(H_2O)\}_2\{Zr(H_2O)_2\}_2(\mu\text{-}OH)_3(\mu_3\text{-}OH)_2](\alpha\text{-}1,2\text{-}PW_{10}O_{37})_2]\cdot 25H_2O$	(**Na-2**)	4:2-type	−12.86, −13.17[a)]	−11.50
3	$Cs_7[[\{Hf(H_2O)\}_2\{Hf(H_2O)_2\}_2(\mu\text{-}OH)_3(\mu_3\text{-}OH)_2](\alpha\text{-}1,2\text{-}PW_{10}O_{37})_2]\cdot 10H_2O$	(**Cs-1**)	4:2-type	−13.71	−13.82
4	$Na_7[[\{Hf(H_2O)\}_2\{Hf(H_2O)_2\}_2(\mu\text{-}OH)_3(\mu_3\text{-}OH)_2](\alpha\text{-}1,2\text{-}PW_{10}O_{37})_2]\cdot 25H_2O$	(**Na-1**)	4:2-type	−13.48	−12.85
5	$(Me_2NH_2)_8[\{Zr_4(H_2O)_4(\mu\text{-}OH)_2(\mu_3\text{-}O)_2\}(\alpha\text{-}1,4\text{-}PW_{10}O_{37})_2]\cdot 9H_2O$	(**MeN-4**)	4:2-type	−10.84	−10.76
6	$Na_8[\{Zr_4(H_2O)_4(\mu\text{-}OH)_2(\mu_3\text{-}O)_2\}(\alpha\text{-}1,4\text{-}PW_{10}O_{37})_2]\cdot 21H_2O$	(**Na-4**)	4:2-type	−10.81	−10.38
7	$(Me_2NH_2)_8[\{Hf_4(H_2O)_4(\mu\text{-}OH)_2(\mu_3\text{-}O)_2\}(\alpha\text{-}1,4\text{-}PW_{10}O_{37})_2]\cdot 9H_2O$	(**MeN-3**)	4:2-type	−11.68	−11.13
8	$Na_8[\{Hf_4(H_2O)_4(\mu\text{-}OH)_2(\mu_3\text{-}O)_2\}(\alpha\text{-}1,4\text{-}PW_{10}O_{37})_2]\cdot 14H_2O$	(**Na-3**)	4:2-type	−11.60	−11.04
9	$(Et_2NH_2)_{10}[Zr(\alpha\text{-}PW_{11}O_{39})_2]\cdot 7H_2O$		1:2-type	−14.57, −14.65	
10	$(Et_2NH_2)_{10}[Hf(\alpha\text{-}PW_{11}O_{39})_2]\cdot 2H_2O$		1:2-type	−14.67, −14.77	
11	$(Et_2NH_2)_8[\{\alpha\text{-}PW_{11}O_{39}Zr(\mu\text{-}OH)(H_2O)\}_2]\cdot 7H_2O$		2:2-type	−13.49	
12	$(Et_2NH_2)_8[\{\alpha\text{-}PW_{11}O_{39}Hf(\mu\text{-}OH)(H_2O)\}_2]\cdot 7H_2O$		2:2-type	−13.76	
13	$(Et_2NH_2)_7H_2[Zr_3(\mu\text{-}OH)_3(A\text{-}\alpha\text{-}PW_9O_{34})_2]\cdot 12H_2O$		3:2-type	−10.85	
14	$(Et_2NH_2)_7H_2[Hf_3(\mu\text{-}OH)_3(A\text{-}\alpha\text{-}PW_9O_{34})_2]\cdot 11H_2O$		3:2-type	−11.45	

a) δ −12.86 ppm (main), δ −13.17 ppm (minor) in D_2O; δ −12.95 ppm in 0.1 M aqueous HCl solution; δ −12.31 ppm in D_2O/CD_3CN (200 μL/450 μL).

Table 2. Keggin POM-Catalyzed Mukaiyama–Aldol Reaction

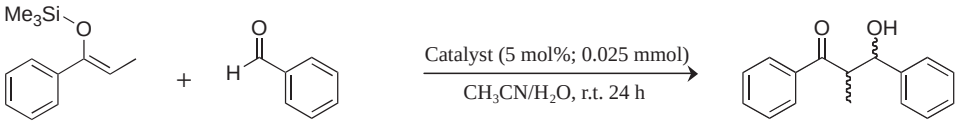

0.5 mmol 0.5 mmol

Entry	Keggin POM-based catalysts	Complex type	Total yield/%	TON	*syn*:*anti* ratio
1	$Na_{10}[Zr(\alpha\text{-}PW_{11}O_{39})_2]\cdot 15H_2O$	1:2	15	3.0	20:80
2	$Na_{10}[Hf(\alpha\text{-}PW_{11}O_{39})_2]\cdot 15H_2O$	1:2	33	6.6	18:82
3	$Na_8[\{\alpha\text{-}PW_{11}O_{39}Zr(\mu\text{-}OH)(H_2O)\}_2]\cdot 12H_2O$	2:2	42	8.4	20:80
4	$Na_8[\{\alpha\text{-}PW_{11}O_{39}Hf(\mu\text{-}OH)(H_2O)\}_2]\cdot 11H_2O$	2:2	42	8.4	19:81
5	$Na_9[Zr_3(\mu\text{-}OH)_3(A\text{-}\alpha\text{-}PW_9O_{34})_2]\cdot 31H_2O$	3:2	15	3.0	19:81
6	$Na_9[Hf_3(\mu\text{-}OH)_3(A\text{-}\alpha\text{-}PW_9O_{34})_2]\cdot 18H_2O$	3:2	13	2.6	20:80
7	$Na_7[[\{Zr(H_2O)\}_2\{Zr(H_2O)_2\}_2(\mu\text{-}OH)_3(\mu_3\text{-}OH)_2](\alpha\text{-}1,2\text{-}PW_{10}O_{37})_2]\cdot 25H_2O$ (**Na-2**)	4:2	75	15	14:86
8	$Na_7[[\{Hf(H_2O)\}_2\{Hf(H_2O)_2\}_2(\mu\text{-}OH)_3(\mu_3\text{-}OH)_2](\alpha\text{-}1,2\text{-}PW_{10}O_{37})_2]\cdot 25H_2O$ (**Na-1**)	4:2	87	17	15:85
9	$Na_8[\{Zr_4(\mu\text{-}OH)_2(\mu_3\text{-}O)_2(H_2O)_4\}(\alpha\text{-}1,4\text{-}PW_{10}O_{37})_2]\cdot 21H_2O$ (**Na-4**)	4:2	89	18	12:88
10	$Na_8[\{Hf_4(\mu\text{-}OH)_2(\mu_3\text{-}O)_2(H_2O)_4\}(\alpha\text{-}1,4\text{-}PW_{10}O_{37})_2]\cdot 14H_2O$ (**Na-3**)	4:2	88	18	13:87
11	$Na_{12}[(\alpha\text{-}1,2,3\text{-}PW_9Ti_3O_{37})_2O_3]\cdot 20H_2O$	6 (Ti):2	trace	—	—

−13.49 ppm, respectively, have shown a slight shift to a lower field than those in a 0.1 M aqueous HCl solution (−13.86 and −13.55 ppm, respectively). This fact has been explained by the dissociation of the proton from the coordinated water in D_2O.[5c]

Solution ^{31}P NMR of **Na-1** to **Na-4** in D_2O can be compared with those of **Cs-1**, **Cs-2**, **MeN-3**, and **MeN-4** (Table 1). ^{31}P NMR spectrum of **Na-2** showed two peaks at −12.86 (major) and −13.17 (minor) ppm. These two peaks of ^{31}P NMR of **Na-2** were changed to a single peak (−12.95 ppm) by addition of an acid, indicating that the major peak at −12.86 ppm was due to the protonated species of **Na-2**. Probably, **Na-1** and **Na-2** show different acidity in aqueous solution.

In order to confirm the solution structures of **Na-1** to **Na-4**, the solid-state ^{31}P NMR were also measured. The solid-state ^{31}P NMR of **Cs-1**, **Cs-2**, **MeN-3**, and **MeN-4**, which should be consistent with X-ray structure, were found to be consistent with those of **Na-1** to **Na-4**. The latter were consistent with their solution ^{31}P NMR. Thus, in **Na-1** to **Na-4**, the sandwich structures are maintained in solution. Further, the difference of the catalytic activities of Keggin and Dawson POMs with sandwich structures indirectly suggest that the solid state structures are maintained in solution (see the section of Catalysis).

Catalysis of Mukaiyama–Aldol Reaction. The results of the Mukaiyama–aldol reaction between silyl enol ether (0.5 mmol) and benzaldehyde (0.5 mmol), carried out using water-soluble Zr and Hf sandwich Keggin and Dawson POMs (5 mol %; 0.025 mmol) as precatalysts in a CH_3CN/water mixed solvent (4.5 mL/2.0 mL) at room temperature and in air, are summarized in Tables 2 and 3 [Note: See Ref. 11 as to the precatalysts used here]. These reaction conditions are subtly different from those of Malacria's papers, in which excess amounts (0.75 mmol[6f] and 2.5 mmol[6h]) of silyl enol ether, benzaldehyde (0.5 mmol), and Hf/Zr-containing α_1-Dawson $[P_2W_{17}O_{61}]^{10-}$ POMs (20 mmol %; 0.1 mmol) were

Table 3. Dawson POM-Catalyzed Mukaiyama–Aldol Reaction[a)]

Entry	Dawson POM-based catalysts	Complex type	Total yield /%	TON	*syn*:*anti* ratio	Ref
1	$Li_6[\alpha_2\text{-}P_2W_{17}O_{61}Zr(H_2O)_3]\cdot 19H_2O$[2]	1:1	68	14	10:90	This work
2	$Li_{14}[\{\alpha_2\text{-}P_2W_{17}O_{61}Zr(\mu\text{-}OH)(H_2O)\}_2]\cdot nH_2O$[5e]	2:2	23	4.6	13:87	This work
3	$Li_{14}[\{\alpha_2\text{-}P_2W_{17}O_{61}Hf(\mu\text{-}OH)(H_2O)\}_2]\cdot nH_2O$[5e]	2:2	35	7.0	11:89	This work
4	$Li_{14}[Zr_4(\mu_3\text{-}O)_2(\mu\text{-}OH)_2(H_2O)_4(P_2W_{16}O_{59})_2]\cdot 34H_2O$[4d]	4:2	18	3.6	13:87	This work
5	$Li_{14}[Hf_4(\mu_3\text{-}O)_2(\mu\text{-}OH)_2(H_2O)_4(P_2W_{16}O_{59})_2]\cdot 34H_2O$[5d]	4:2	5.4	1.1	16:84	This work
6	$TBA_5K[\alpha_1\text{-}Hf(H_2O)_4P_2W_{17}O_{61}]$	1:1	85	4.3	48:52	6f
7	$TBA_5K[\alpha_1\text{-}Zr(H_2O)_4P_2W_{17}O_{61}]$	1:1	92	4.6		6h

a) Reaction conditions: amounts for Entries 1–5, catalysts 0.025 mmol, benzaldehyde 0.5 mmol, silyl enol ether 0.5 mmol; solvent: CH_3CN/water (4.5 mL/2.0 mL), reaction time: 24 h, at room temperature, in air. For Entry 6, catalyst 0.1 mmol, benzaldehyde 0.5 mmol; silyl enol ether 0.75 mmol; solvent: dry CH_3CN, reaction time: 24 h, at room temperature. For Entry 7, silyl enol ether 2.5 mmol.

Table 4. Yields, TONs, and Stereoselectivities of the Mukaiyama–Aldol Product by Varied Amounts of Precatalysts, **Na-3** and **Na-4**[a)]

Entry	Keggin POM-based catalysts	Amount of precatalyst /mmol	Total yield /%	TON	*syn*:*anti* ratio
1	$Na_8[\{Zr_4(\mu\text{-}OH)_2(\mu_3\text{-}O)_2(H_2O)_4\}(\alpha\text{-}1,4\text{-}PW_{10}O_{37})_2]\cdot 21H_2O$ (**Na-4**)	0.025	89	18	12:88
2	**Na-4**	0.012	71	30	13:87
3	**Na-4**	0.0048	70	73	13:87
4	**Na-4**	0.0024	47	98	14:86
5	$Na_8[\{Hf_4(\mu\text{-}OH)_2(\mu_3\text{-}O)_2(H_2O)_4\}(\alpha\text{-}1,4\text{-}PW_{10}O_{37})_2]\cdot 14H_2O$ (**Na-3**)	0.025	94	19	13:87
6	**Na-3**	0.013	85	33	13:87
7	**Na-3**	0.0050	62	62	12:88
8	**Na-3**	0.0023	37	80	12:88

a) Reaction conditions: amounts for Entries 1–8, benzaldehyde 0.5 mmol, silyl enol ether 0.5 mmol; solvent: CH_3CN/water (4.5 mL/2.0 mL), reaction time: 24 h, at room temperature, in air.

Table 5. Yields, TONs, and Stereoselectivities of the Mukaiyama–Aldol Product after Reuse of Precatalysts **Na-1**, **Na-3**, and **Na-4** Several Times[a)]

Entry	Keggin POM-based catalysts	Time /h	Total yield /%	TON	*syn*:*anti* ratio
1	$Na_7[[\{Hf(H_2O)\}_2\{Hf(H_2O)_2\}_2(\mu\text{-}OH)_3(\mu_3\text{-}OH)_2](\alpha\text{-}1,2\text{-}PW_{10}O_{37})_2]\cdot 25H_2O$ (**Na-1**)	24	92	18	15:85
2	after the 1st reuse	24	93	19	15:85
3	after the 2nd reuse	24	92	18	15:85
4	after the 3rd reuse	24	90	18	15:85
5	after the 4th reuse	24	91	18	15:85
6	$Na_8[\{Zr_4(\mu\text{-}OH)_2(\mu_3\text{-}O)_2(H_2O)_4\}(\alpha\text{-}1,4\text{-}PW_{10}O_{37})_2]\cdot 21H_2O$ (**Na-4**)	24	89	18	12:88
7	after the 1st reuse	29	86	17	13:87
8	after the 2nd reuse	31	84	17	13:87
9	$Na_8[\{Hf_4(\mu\text{-}OH)_2(\mu_3\text{-}O)_2(H_2O)_4\}(\alpha\text{-}1,4\text{-}PW_{10}O_{37})_2]\cdot 14H_2O$ (**Na-3**)	24	94	19	13:87
10	after the 1st reuse	24	91	18	13:87
11	after the 2nd reuse	24	94	19	13:87

a) Reaction conditions: amounts for Entries 1, 6, and 9, 0.025 mmol; benzaldehyde 0.5 mmol; silyl enol ether 0.5 mmol; solvent: CH_3CN/water (4.5 mL/2.0 mL), at room temperature, in air. The results of Entries 1, 6, and 9 are obtained by different lots of the catalysts in Entries 8, 9, and 10 in Table 2.

used in a dry CH_3CN solvent.[6f,6h] Tables 4 and 5 show the effects by varied amounts of precatalysts and their stability as catalysts, respectively. Table 6 shows the effect of the addition of pyridine and 2,6-di-*tert*-butylpyridine, suggesting that the reaction mechanism was due to Lewis acid catalysis.

(1) Catalysis by Keggin POMs. The Zr and Hf cluster cations sandwiched between two lacunary Keggin POMs showed various activities (Entries 1–10, Table 2). Aldol as product, i.e., 3-hydroxy-2-methyl-1,3-diphenylpropan-1-one, was obtained with high *anti*-selectivity (*syn*/*anti* = 20/80–12/88). The Lewis acid catalytic activities (Table 2) of the Mukaiyama–aldol reaction by the water-soluble sodium salts of the Keggin sandwich POMs were found in the order of the product yields: the 4:2 complexes (Entries 7–10, Table 2) > the 2:2 complexes (Entries 3 and 4, Table 2) > the 1:2 complexes (Entries 1 and 2, Table 2) > the 3:2 complexes (Entries 5 and 6, Table 2). The sandwich-structured POMs used here were air- and water-stable, and their Lewis acid catalysis was found with high activities and

Table 6. Inhibition of the Mukaiyama–Aldol Reaction

Entry[a)]	Catalyst	Additive	Yield/%	TON	*syn*:*anti* ratio
1	**Na-1**	—	87	17	15:85
2	**Na-1**	2,6-di-*tert*-butylpyridine	85	17	14:86
3	**Na-1**	pyridine	35	7.0	17:83
4	**Na-2**	—	75	15	14:86
5	**Na-2**	2,6-di-*tert*-butylpyridine	66	13	18:82
6	**Na-2**	pyridine	10	2.0	24:76
7	**Na-3**	—	88	18	13:87
8	**Na-3**	2,6-di-*tert*-butylpyridine	64	13	15:85
9	**Na-3**	pyridine	15	3.0	20:80
10	**Na-4**	—	89	18	12:88
11	**Na-4**	2,6-di-*tert*-butylpyridine	70	14	14:86
12	**Na-4**	pyridine	28	5.6	17:83
13	α_1-Dawson/Hf[b)]	—	100	5	
14	α_1-Dawson/Hf[b)]	2,6-di-*tert*-butylpyridine	6	0.3	
15	α_1-Dawson/Hf[b)]	pyridine	5	0.25	
16	α_1-Dawson/Zr[c)]	—	92	4.6	
17	α_1-Dawson/Zr[c)]	2,6-di-*tert*-butylpyridine	0	0	
18	α_1-Dawson/Zr[c)]	pyridine	16	0.8	

a) Entries 13–18 are cited from Ref. 6h. b) $(Bu_4N)_5K[\alpha_1\text{-Hf}(H_2O)_4P_2W_{17}O_{61}]$. c) $(Bu_4N)_5K[\alpha_1\text{-Zr-}(H_2O)_4P_2W_{17}O_{61}]$.

excellent stereoselectivities. The reaction sites will be the sites of the water molecules coordinated to the Hf/Zr atoms within the sandwiched clusters, because such sites can interact with the aldehyde oxygen atom of the substrate. The tetranuclear Hf/Zr complexes, i.e., the 4:2 complexes, showed higher activities (Entries 7–10, Table 2) than the 2:2 complexes (Entries 3 and 4, Table 2). These results are attributable to the fact that the former complexes have 4–6 available reaction sites as terminal water molecules, while the latter have only 2 sites. The 3:2 complexes showed the lowest activities, because the central trinuclear clusters have no available site for interaction with the substrate. Among the sandwich structured-POMs, it was found that the Keggin 4:2 complexes showed high activities, while the 1:2 complexes showed low activities (Entries 1 and 2, Table 2). With regard to the apparent activities of the Keggin 1:2 complexes, the following points should be noted. Since the 1:2 complexes are composed of saturated coordinated Hf/Zr atoms, i.e., 8-coordinate Hf/Zr atoms, they should not have any activities, i.e., the 1:2 complexes are not true catalysts. Since 1:2 complexes are readily converted to 2:2 complexes (composed of dinuclear 7-coordinate Hf/Zr atoms) under acidic conditions,[5c] the converted 2:2 complexes will act as true catalysts. On the other hand, the dimeric form of the trititanium(IV)-substituted Keggin POM, $[(\alpha\text{-1,2,3-}PW_9Ti_3O_{37})_2O_3]^{12-}$, did not show any activity in the Mukaiyama–aldol reaction (Entry 11, Table 2). Titanium(IV) atoms occupying in the lacunary sites of the POM do not work as Lewis acid catalysts, whereas $TiCl_4$ in organic solvents works as a general Lewis acid catalyst.[7a] The titanium(IV) atoms in $[(\alpha\text{-1,2,3-}PW_9Ti_3O_{37})_2O_3]^{12-}$ take 6-coordinate composed of the lacunary POM site as a 5-coordinate ligand and one terminal OH group, and thus they cannot further accept an electron pair of the Lewis base. In case of the Keggin-sandwiched POMs, these results indicate that the Hf/Zr sandwich structures do not necessarily preclude or decrease catalytic activity, and the existence of the free sites for complexation of substrates is important. Furthermore, the sandwiched Keggin structures induced the *anti*-selectivity of the products (vide infra).

(2) Stereoselectivity of the product. The high *anti*-selectivity of the products found here is in contrast to the *syn*-selectivity of the products obtained by general Lewis acid catalysts, for example, $TiCl_4$ (−78 °C, CH_2Cl_2), and mononuclear complexes such as $Sc(OTf)_3$, $Bi(OTf)_3$, and $Sn(OTf)_2$ bearing chiral bipyridine or chiral diamine ligands.[7a–7d] *anti*-Selective Mukaiyama–aldol reactions using a chiral zirconium catalyst containing bulky ligands such as (*R*)-3,3′-I_2BINOL have been reported.[7f] The sandwich structure of the present POMs still has available reaction sites and the presence of large POM moieties can significantly participate in the interaction of the Hf/Zr sites with aldehyde and subsequent nucleophilic attack of silyl enol ether. Because the high *anti*-selectivity of the products was found here regardless of Keggin (Table 2) or Dawson (Table 3) POMs, it is concluded that the high *anti*-selectivity is characteristic of the POM-based catalysis. However, at present its mechanism is still unclear. The high *anti*-selectivity of the products was also confirmed by reactions using aldehydes such as *p*-tolualdehyde and *p*-methoxybenzaldehyde other than benzaldehyde.

(3) Issue of water and reaction system. Although the reaction system contained water that comes from the solvent system and the solvated water molecules of the precatalysts, remarkably reduced activities were not found due to the hydrolysis of silyl enol ether. In fact, the highest activities found here (Entries 7–10, Table 2) were comparable to those of the Hf/Zr-containing $[\alpha_1\text{-}P_2W_{17}O_{61}]^{10-}$ POMs reported by Malacria et al. (Entries 6 and 7, Table 3), the reactions of which were carried out in dry CH_3CN.[6f,6h] Furthermore, our reaction conditions in the CH_3CN/water system were found to have some merit in the elimination of the TMS group and subsequent protonation leading to the final product, because the overall reac-

tions take place without the addition of any acids, such as HCl, as in other reported Mukaiyama–aldol reactions in aqueous media.[7g,7h] Probably, the water molecules coordinated to the higher charge Hf^{IV}/Zr^{IV} atoms will function as a Brønsted acid for hydrolysis of the intermediate. This is in contrast to the reactions of Malacria's group carried out in dry CH_3CN,[6f,6h] in which they have used aq. HCl for desilylation or in order to eliminate the TMS group and obtain the final product by protonation. This is also in contrast to the general Lewis acid reactions catalyzed by $TiCl_4$, $Sc(OTf)_3$ etc., in which protonic acids or water are added.[7a–7d]

The present reactions should also be compared with the results by heterogeneous catalysts such as mesoporous aluminosilicate,[7e] in which the final product is not a (β-hydroxy)-carbonyl compound, but a β-siloxy ketone, because the protonation step is lacking.

(4) Catalysis by Dawson POMs. Lewis acid activities in the Mukaiyama–aldol reaction by the water-soluble lithium salts of the sandwich Dawson POMs, under conditions similar to the Keggin POM-based reactions, were found in the order of the 1:1 complex (Entry 1, Table 3) > the 2:2 complexes (Entries 2 and 3, Table 3) > the 4:2 complexes (Entries 4 and 5, Table 3), all kept with high *anti*-selectivity.

The apparent activity by the 1:1 complex (Entry 1, Table 3) does not simply come only from the monomeric, open-structured POM, because it can be readily changed to the 2:2 complex and the 1:2 complex.[5e] The true activity by the 1:1 complex itself may be comparable to those of Malacria's results (Entries 6 and 7, Table 3). It should be noted that the high *anti*-selectivity of the product is kept in the case of catalysis by the 1:1 complex (see the discussion (2) described above).

The lowest activities of the Dawson 4:2 complexes (Entries 4 and 5, Table 3) should be compared with the highest activities of the Keggin 4:2 complexes (Entries 9 and 10, Table 2), because the structures of the central tetranuclear cluster cations are quite the same. It is suggested that the Dawson POM moieties will strongly restrict interaction between aldehyde and the central Hf/Zr cluster ion, and/or subsequent nucleophilic attack by silyl enol ether. This may also be the reason why the activities of the 4:2 complexes (Entries 4 and 5, Table 3) are lower than those of the 2:2 complexes (Entries 2 and 3, Table 3), despite the former having many more available reaction sites than the latter. However, the high *anti*-selectivity of the product indicates that the reaction mechanism is the same in the catalysis by the present Dawson and Keggin POMs.

(5) Amounts of catalysts. The yields, TONs and stereoselectivities by varied amounts of precatalysts, i.e., the 4:2 complexes **Na-3** and **Na-4**, are summarized in Table 4 (Entries 1–8). The varied amounts of precatalysts (0.025–0.0024 mmol) resulted in yields of 47–89% and TONs of 18–98; the *syn*:*anti* selectivities were unchanged (14:86–12:88). These results showed that the sandwich-structured precatalysts were stable under the reactions. These yields and TONs are superior to those of the open-structured Hf/Zr-containing α_1-Dawson POMs (Entries 6 and 7, Table 3).

(6) Reuse of catalysts. The yields, TONs and stereoselectivities found after reusing precatalysts **Na-1**, **Na-3**, and **Na-4** several times are shown in Table 5 (Entries 1–11). The activities and selectivities were unchanged, for example, even after 4th reuse of **Na-1** (Entry 5, Table 5). Thus, it is also concluded that these sandwich-structured Hf/Zr compounds are very stable as catalysts even in water-containing reaction systems.

(7) Reaction mechanism. The Mukaiyama–aldol reaction was examined in the presence or absence of additives, i.e., pyridine and 2,6-di-*tert*-butylpyridine. Malacria's group has recently pointed out the fact that (1) both bases are strong enough to capture protons and should inhibit any Brønsted acid-catalyzed reaction, (2) pyridine also binds to metal centers, thus inhibiting Lewis acid-catalyzed reactions, but (3) 2,6-di-*tert*-butylpyridine is highly hindered and should coordinate less to the Lewis acid centers located in the POMs, and its effect on Lewis acid catalysis is expected to be weak.[6h]

Our reaction solutions were white suspensions composed of POM catalysts (**Na-1**–**Na-4**: 0.025 mmol), benzaldehyde (0.5 mmol), silyl enol ether ((*Z*)-1-phenyl-1-trimethylsiloxy-1-propene, 0.5 mmol), pyridine (0.1 mmol) or 2,6-di-*tert*-butylpyridine (0.1 mmol), toluene (0.94 mmol) in a mixed solvent (CH_3CN 4.5 mL/H_2O 2.0 mL). During stirring at room temperature for several hours, the suspensions became homogeneous, colorless, clear solutions. After a reaction time of 24 h, the solutions were analyzed by HPLC. The results are summarized in Table 6.

The 2,6-di-*tert*-butylpyridine influenced all of the reaction outcomes less, regardless of the metal center (Entries 2, 5, 8, and 11, Table 6), whereas pyridine significantly decreased the outcomes of all the reactions (Entries 3, 6, 9, and 12, Table 6). Thus, the Mukaiyama–aldol reactions by **Na-1**–**Na-4** proceed through substrate complexation, i.e., Lewis acid catalysis. An easy deprotonation of coordinated water molecules in the POM/Hf or POM/Zr complexes, which has been indicated by DFT calculations,[6h] does not play an important role in our reaction mechanism.

Our results based on Lewis acid catalysis are quite different from the mechanism based on the indirect Brønsted catalysis proposed by Malacria et al. for Mukaiyama–aldol reaction by α_1-Dawson complexes, $(Bu_4N)_5K[\alpha_1\text{-}M(H_2O)_4P_2W_{17}O_{61}]$ (M = Hf, Zr).[6f] In the latter, nearly complete inhibition of the reaction was observed in all the cases in which both pyridine and 2,6-di-*tert*-butylpyridine were included.

The high *anti*-selectivity of the products in the catalysis by our Keggin and Dawson POMs with the sandwich structure suggests that the POM moieties which comprise the sandwich structure also significantly take part in the nucleophilic attack by silyl enol ether in the transition state, but not only the central Hf/Zr cluster cation moieties.

(8) Comparison with the catalysis by $[\alpha_1\text{-}L(H_2O)P_2W_{17}O_{61}]$ reported by Malacria's group. First, although the reaction conditions are subtly different from those of Malacria's papers, in which dry CH_3CN was used as solvent, the present reactions can be compared with the reactions by the $[\alpha_1\text{-}L(H_2O)\text{-}P_2W_{17}O_{61}]$ catalysts reported by Malacria's group,[6f] because they think that the dimeric species is of low activity. Second, the stereoselectivity in the present Keggin and Dawson POM-based catalysis is in contrast to that in the catalysis by the open-structured α_1-Dawson POMs of Hf atoms, in which the products were reported as those with comparable or slightly higher *syn*-selective ratios (*syn*:*anti* ratios = 48:52, 56:44,

60:40, 55:45, and 66:34).[6f] As to the stereoselectivity of the product, Malacria et al. have also reported *syn*:*anti* = 25:75 for the Keggin POM catalyst $(TBA)_{3.7}K_{0.3}[\alpha\text{-Hf(OH)PW}_{11}O_{39}]$[6f] and *syn*:*anti* = 48:52 for the α_1-Dawson/Hf POM.[6f]

Conclusion

Four tetranuclear Hf^{IV} and Zr^{IV} cluster cations, sandwiched between two 1,2-di-lacunary α-Keggin polyoxometalates (POMs) and between two 1,4-di-lacunary POMs, i.e., $[[\{M(H_2O)\}_2\{M(H_2O)_2\}_2(\mu\text{-OH})_3(\mu_3\text{-OH})_2](\alpha\text{-1,2-PW}_{10}O_{37})_2]^{7-}$ (M = Hf **1** and M = Zr **2**) and $[\{M_4(H_2O)_4(\mu\text{-OH})_2(\mu_3\text{-O})_2\}(\alpha\text{-1,4-PW}_{10}O_{37})_2]^{8-}$ (M = Hf **3** and M = Zr **4**), respectively, were synthesized and rigorously characterized by complete elemental analysis, TG/DTA, FTIR, solid-state and solution ^{31}P NMR, and X-ray crystallography. Homogeneous Lewis acid catalysis by the water-soluble sodium salts of the Hf/Zr-containing sandwich-structured Keggin POMs **Na-1**–**Na-4** was evaluated for the Mukaiyama–aldol reaction of silyl enol ether with benzaldehyde in aqueous/CH_3CN media, together with *syn*/*anti*-stereoselectivity of the reaction product, i.e., 3-hydroxy-2-methyl-1,3-diphenylpropan-1-one, at room temperature under air. In this work, we have interest in whether the Hf/Zr sandwich-structured POM complexes truly preclude or decrease catalytic activity, because Malacria's group thinks that the dimeric POM species is of low activity.[6f]

The water-soluble sodium salts of the Keggin sandwich POMs **Na-1**–**Na-4** were air- and water-stable, and their Lewis acid catalysis was found with high activities. The catalytic activities by **Na-1**–**Na-4** were superior to those of the Dawson analogues and other sandwich-structured Keggin POMs. It should be noted that all of the POM-based sandwich-structured compounds showed high *anti*-selectivity of the products, regardless of high and low activities. The excellent stabilities of **Na-1**–**Na-4** as catalysts, i.e., no reduced activities, were confirmed even after reusing several times. The effect of the addition of pyridine and 2,6-di-*tert*-butylpyridine showed that the present reactions are exclusively due to Lewis acid catalysis. Furthermore, the high *anti*-selectivities of the reaction products and the fact that the catalytic activities by Keggin POMs are superior to those by Dawson analogues with the same structured central cluster cations suggest that not only the central cluster cation moieties, but also the polyoxoanion moieties should significantly participate in the Mukaiyama–aldol reaction mechanism. The presence of large POM moieties should significantly contribute to the interaction of the Hf/Zr sites with aldehyde and subsequent nucleophilic attack of silyl enol ether, but its mechanism is unclear at present. A more detailed mechanism will be reported in due course.

This work was supported by JSPS KAKENHI Grant number 22550065 and also by the Strategic Research Base Development Program for Private Universities of the Ministry of Education, Culture, Sports, Science and Technology of Japan.

Supporting Information

Molecular structures of **Cs-1** (Figure S1), **Cs-2** (Figure S2), **MeN-3** (Figure S3), and **MeN-4** (Figure S4), bond lengths and angles for **Cs-1**, **Cs-2**, **MeN-3**, and **MeN-4** (Tables S2, S4, S6, and S8, respectively), selected bond lengths and angles around the cluster cation moiety for them (Tables S1, S3, S5, and S7), bond valence sum calculations of the Hf and O atoms for **Cs-1** and **MeN-3** (Tables S9 and S11) and those of the Zr and O atoms for **Cs-2** and **MeN-4** (Tables S10 and S12). This material is available free of charge on the Web at http://www.csj/jp/journals/bcsj/.

References

1 a) M. T. Pope, *Heteropoly and Isopoly Oxometalates*, Springer-Verlag, New York, **1983**. b) V. W. Day, W. G. Klemperer, *Science* **1985**, *228*, 533. c) M. T. Pope, A. Müller, *Angew. Chem., Int. Ed. Engl.* **1991**, *30*, 34. d) C. L. Hill, C. M. Prosser-McCartha, *Coord. Chem. Rev.* **1995**, *143*, 407. e) T. Okuhara, N. Mizuno, M. Misono, *Adv. Catal.* **1996**, *41*, 113. f) A series of 34 papers in a volume devoted to Polyoxometalates in Catalysis ed. by C. L. Hill: *J. Mol. Catal. A: Chem.* **1996**, *114*, Issues 1–3. g) Special issue on Polyoxometalates: *Chem. Rev.* **1998**, *98*, Issue 1. h) R. Neumann, in *Progress in Inorganic Chemistry*, ed. by K. D. Karlin, John Wiley & Sons, Inc., Hoboken, NJ, USA, **2007**, Vol. 47. doi:10.1002/9780470166482.ch3. i) *Polyoxometalate Chemistry from Topology via Self-Assembly to Applications*, ed. by M. T. Pope, A. Müller, Kluwer Academic Publishers, Netherlands, **2001**. doi:10.1007/0-306-47625-8. j) *Polyoxometalate Chemistry for Nano-Composite Design*, ed. by T. Yamase, M. T. Pope, Kluwer Academic Publishers, Netherlands, **2002**. doi:10.1007/b105365. k) M. T. Pope, in *Transition Metal Groups 3–6* in *Comprehensive Coordination Chemistry II*, ed. by J. A. McCleverty, T. J. Meyer, Elsevier Science, New York, **2003**, Vol. 4, pp. 635–678. doi:10.1016/B0-08-043748-6/03035-8. l) C. L. Hill, in *Transition Metal Groups 3–6* in *Comprehensive Coordination Chemistry II*, ed. by J. A. McCleverty, T. J. Meyer, Elsevier Science, New York, **2003**. Vol. 4, pp. 679–759. doi:10.1016/B0-08-043748-6/03036-X. m) A series of 32 recent papers in a volume devoted to Polyoxometalates in Catalysis ed. by C. L. Hill: *J. Mol. Catal. A: Chem.* **2007**, *262*, Issues 1–2. n) A. Proust, R. Thouvenot, P. Gouzerh, *Chem. Commun.* **2008**, 1837. o) B. Hasenknopf, K. Micoine, E. Lacôte, S. Thorimbert, M. Malacria, R. Thouvenot, *Eur. J. Inorg. Chem.* **2008**, 5001. p) D. Laurencin, R. Thouvenot, K. Boubekeur, F. Villain, R. Villanneau, M.-M. Rohmer, M. Bénard, A. Proust, *Organometallics* **2009**, *28*, 3140. q) D.-L. Long, R. Tsunashima, L. Cronin, *Angew. Chem., Int. Ed.* **2010**, *49*, 1736. r) A. Dolbecq, E. Dumas, C. R. Mayer, P. Mialane, *Chem. Rev.* **2010**, *110*, 6009. s) C. P. Pradeep, D.-L. Long, L. Cronin, *Dalton Trans.* **2010**, *39*, 9443.

2 K. Nomiya, Y. Sakai, S. Matsunaga, *Eur. J. Inorg. Chem.* **2011**, 179.

3 a) R. Villanneau, H. Carabineiro, X. Carrier, R. Thouvenot, P. Herson, F. Lemos, F. R. Ribeiro, M. Che, *J. Phys. Chem. B* **2004**, *108*, 12465. b) H. Carabineiro, R. Villanneau, X. Carrier, P. Herson, F. Lemos, F. R. Ribeiro, A. Proust, M. Che, *Inorg. Chem.* **2006**, *45*, 1915. c) R. J. Errington, S. S. Petkar, P. S. Middleton, W. McFarlane, W. Clegg, R. A. Coxall, W. Harrington, *J. Am. Chem. Soc.* **2007**, *129*, 12181.

4 a) R. G. Finke, B. Rapko, T. J. R. Weakley, *Inorg. Chem.* **1989**, *28*, 1573. b) E. V. Radkov, V. G. Young, Jr., R. H. Beer, *J. Am. Chem. Soc.* **1999**, *121*, 8953. c) A. J. Gaunt, I. May, D. Collison, M. Helliwell, *Acta Crystallogr., Sect. C* **2003**, *59*, i65. d) A. J. Gaunt, I. May, D. Collison, K. T. Holman, M. T. Pope, *J. Mol. Struct.* **2003**, *656*, 101. e) A. J. Gaunt, I. May, D. Collison, O. D. Fox, *Inorg. Chem.* **2003**, *42*, 5049. f) X. Fang, T. M.

Anderson, Y. Hou, C. L. Hill, *Chem. Commun.* **2005**, 5044. g) X. Fang, T. M. Anderson, C. L. Hill, *Angew. Chem., Int. Ed.* **2005**, *44*, 3540. h) B. S. Bassil, M. H. Dickman, U. Kortz, *Inorg. Chem.* **2006**, *45*, 2394. i) O. A. Kholdeeva, G. M. Maksimov, R. I. Maksimovskaya, M. P. Vanina, T. A. Trubitsina, D. Yu. Naumov, B. A. Kolesov, N. S. Antonova, J. J. Carbó, J. M. Poblet, *Inorg. Chem.* **2006**, *45*, 7224. j) O. A. Kholdeeva, R. I. Maksimovskaya, *J. Mol. Catal. A: Chem.* **2007**, *262*, 7. k) M. N. Sokolov, E. V. Chubarova, E. V. Peresypkina, A. V. Virovets, V. P. Fedin, *Russ. Chem. Bull.* **2007**, *56*, 220. l) S. Yamaguchi, Y. Kikukawa, K. Tsuchida, Y. Nakagawa, K. Uehara, K. Yamaguchi, N. Mizuno, *Inorg. Chem.* **2007**, *46*, 8502. m) X. Fang, C. L. Hill, *Angew. Chem., Int. Ed.* **2007**, *46*, 3877. n) Y. Hou, X. Fang, C. L. Hill, *Chem.—Eur. J.* **2007**, *13*, 9442. o) Y. Kikukawa, S. Yamaguchi, K. Tsuchida, Y. Nakagawa, K. Uehara, K. Yamaguchi, N. Mizuno, *J. Am. Chem. Soc.* **2008**, *130*, 5472. p) N. Leclerc-Laronze, J. Marrot, M. Haouas, F. Taulelle, E. Cadot, *Eur. J. Inorg. Chem.* **2008**, 4920. q) B. S. Bassil, S. S. Mal, M. H. Dickman, U. Kortz, H. Oelrich, L. Walder, *J. Am. Chem. Soc.* **2008**, *130*, 6696. r) R. Copping, L. Jonasson, A. J. Gaunt, D. Drennan, D. Collison, M. Helliwell, R. J. Pirttijarvi, C. J. Jones, A. Huguet, D. C. Apperley, N. Kaltsoyannis, I. May, *Inorg. Chem.* **2008**, *47*, 5787. s) S. S. Mal, N. H. Nsouli, M. Carraro, A. Sartorel, G. Scorrano, H. Oelrich, L. Walder, M. Bonchio, U. Kortz, *Inorg. Chem.* **2010**, *49*, 7. t) C. Jahier, S. S. Mal, U. Kortz, S. Nlate, *Eur. J. Inorg. Chem.* **2010**, 1559. u) R. Villanneau, D. Racimor, E. Messner-Henning, H. Rousselière, S. Picart, R. Thouvenot, A. Proust, *Inorg. Chem.* **2011**, *50*, 1164. v) M. Carraro, N. Nsouli, H. Oelrich, A. Sartorel, A. Sorarù, S. S. Mal, G. Scorrano, L. Walder, U. Kortz, M. Bonchio, *Chem.—Eur. J.* **2011**, *17*, 8371.

5 a) C. N. Kato, A. Shinohara, K. Hayashi, K. Nomiya, *Inorg. Chem.* **2006**, *45*, 8108. b) Y. Saku, Y. Sakai, A. Shinohara, K. Hayashi, S. Yoshida, C. N. Kato, K. Yoza, K. Nomiya, *Dalton Trans.* **2009**, 805. c) K. Nomiya, Y. Saku, S. Yamada, W. Takahashi, H. Sekiya, A. Shinohara, M. Ishimaru, Y. Sakai, *Dalton Trans.* **2009**, 5504. d) Y. Saku, Y. Sakai, K. Nomiya, *Inorg. Chem. Commun.* **2009**, *12*, 650. e) Y. Saku, Y. Sakai, K. Nomiya, *Inorg. Chim. Acta* **2010**, *363*, 967.

6 a) M. Sadakane, M. H. Dickman, M. T. Pope, *Inorg. Chem.* **2001**, *40*, 2715. b) Q.-H. Luo, R. C. Howell, M. Dankova, J. Bartis, C. W. Williams, W. D. Horrocks, Jr., V. G. Young, Jr., A. L. Rheingold, L. C. Francesconi, M. R. Antonio, *Inorg. Chem.* **2001**, *40*, 1894. c) C. Zhang, R. C. Howell, Q.-H. Luo, H. L. Fieselmann, L. J. Todaro, L. C. Francesconi, *Inorg. Chem.* **2005**, *44*, 3569. d) C. Boglio, G. Lemière, B. Hasenknopf, S. Thorimbert, E. Lacôte, M. Malacria, *Angew. Chem.* **2006**, *118*, 3402; C. Boglio, G. Lemière, B. Hasenknopf, S. Thorimbert, E. Lacôte, M. Malacria, *Angew. Chem., Int. Ed.* **2006**, *45*, 3324. e) C. Boglio, G. Lenoble, C. Duhayon, B. Hasenknopf, R. Thouvenot, C. Zhang, R. C. Howell, B. P. Burton-Pye, L. C. Francesconi, E. Lacôte, S. Thorimbert, M. Malacria, C. Afonso, J.-C. Tabet, *Inorg. Chem.* **2006**, *45*, 1389. f) C. Boglio, K. Micoine, P. Rémy, B. Hasenknopf, S. Thorimbert, E. Lacôte, M. Malacria, C. Afonso, J.-C. Tabet, *Chem.—Eur. J.* **2007**, *13*, 5426. g) C. Boglio, B. Hasenknopf, G. Lenoble, P. Rémy, P. Gouzerh, S. Thorimbert, E. Lacôte, M. Malacria, R. Thouvenot, *Chem.—Eur. J.* **2008**, *14*, 1532. h) N. Dupré, P. Rémy, K. Micoine, C. Boglio, S. Thorimbert, E. Lacôte, B. Hasenknopf, M. Malacria, *Chem.—Eur. J.* **2010**, *16*, 7256.

7 a) T. Mukaiyama, K. Narasaka, K. Banno, *Chem. Lett.* **1973**, 1011. b) S. Ishikawa, T. Hamada, K. Manabe, S. Kobayashi, *J. Am. Chem. Soc.* **2004**, *126*, 12236. c) S. Kobayashi, T. Ogino, H. Shimizu, S. Ishikawa, T. Hamada, K. Manabe, *Org. Lett.* **2005**, *7*, 4729. d) T. Mukaiyama, S. Kobayashi, H. Uchiro, I. Shiina, *Chem. Lett.* **1990**, 129. e) S. Ito, H. Yamaguchi, Y. Kubota, M. Asami, *Chem. Lett.* **2009**, *38*, 700. f) Y. Yamashita, H. Ishitani, H. Shimizu, S. Kobayashi, *J. Am. Chem. Soc.* **2002**, *124*, 3292. g) J. Jankowska, J. Paradowska, B. Rakiel, J. Mlynarski, *J. Org. Chem.* **2007**, *72*, 2228. h) Y. Mei, P. Dissanayake, M. J. Allen, *J. Am. Chem. Soc.* **2010**, *132*, 12871.

8 K. Nomiya, N. C. Kasuga, S. Matsunaga, Y. Sakai, T. Hasegawa, T. Kimura, *Sci. J. Kanagawa Univ.* **2010**, *21*, 43.

9 a) P. J. Domaille, G. Hervéa, A. Téazéa, *Vanadium(V) Substituted Dodecatungstophosphates* in *Inorganic Syntheses*, ed. by A. P. Ginsberg, John Wiley & Sons, Inc., Hoboken, NJ, USA, **2007**, Vol. 27. doi:10.1002/9780470132586.ch17. b) H.-J. Li, H.-Y. Tian, Y.-C. Wu, Y.-J. Chen, L. Liu, D. Wang, C.-J. Li, *Adv. Synth. Catal.* **2005**, *347*, 1247. c) S. Nagayama, S. Kobayashi, *J. Am. Chem. Soc.* **2000**, *122*, 11531.

10 Complete elemental analysis and TG/DTA data of powder sample of **Cs-1**, abbreviated as **Cs-1pow**, suggested its formula and composition to be $Cs_8[\{Hf_4(H_2O)_5(OH)_6\}(\alpha\text{-}1,2\text{-}PW_{10}O_{37})_2]\cdot 11H_2O$ (**Cs-1pow**). The number of coordinated water molecules in **Cs-1pow**, 5, is different from that of the crystalline sample **Cs-1**, 6 (see Preparation of **Cs-1** in Experimental section). The crystalline sample (**Cs-1**) was obtained by crystallization of the powder sample (**Cs-1pow**) under HCl-acidic conditions (pH 2.0).

11 Brønsted acidity of the water molecules coordinated to Hf atoms may be different in the two samples, i.e., the crystalline sample **Cs-1** and the powder sample **Cs-1pow**. Silyl enol ether is more hydrolyzed by the stronger Brønsted acid. By passing **Cs-1** and **Cs-1pow** through a cation-exchange resin column in the Na^+ form, they have been changed to **Na-1** and **Na-1pow**, respectively. As a matter of fact, the HPLC analysis suggested that silyl enol ether is much more hydrolyzed by **Na-1** than by **Na-1pow**, indicating that **Na-1** is a stronger Brønsted acid than **Na-1pow**. This is the reason why the activity of Lewis acid catalysis by **Na-1** is much lower than that by **Na-1pow**. Thus, the catalytic data by **Na-1pow** are presented as the results.

12 a) C. Rocchiccioli-Deltcheff, R. Thouvenot, R. Franck, *Spectrochim. Acta, Part A* **1976**, *32*, 587. b) C. Rocchiccioli-Deltcheff, M. Fournier, R. Franck, R. Thouvenot, *Inorg. Chem.* **1983**, *22*, 207. c) R. Thouvenot, M. Fournier, R. Franck, C. Rocchiccioli-Deltcheff, *Inorg. Chem.* **1984**, *23*, 598.

Dalton Transactions

RSC Publishing

PAPER

Cite this: *Dalton Trans.*, 2013, **42**, 11418

Two types of tetranuclear phosphanegold(I) cations as dimers of dinuclear units, $[\{(Au\{P(p\text{-}RPh)_3\})_2(\mu\text{-}OH)\}_2]^{2+}$ (R = Me, F), synthesized by polyoxometalate-mediated clusterization†

Takuya Yoshida, Satoshi Matsunaga and Kenji Nomiya*

Received 30th May 2013,
Accepted 6th June 2013

DOI: 10.1039/c3dt51412a

www.rsc.org/dalton

Novel intercluster compounds $[\{(Au\{P(p\text{-}RPh)_3\})_2(\mu\text{-}OH)\}_2]_3[\alpha\text{-}PM_{12}O_{40}]_2\cdot n$EtOH (R = Me, M = W for **1**; R = Me, M = Mo for **2**; R = F, M = Mo for **3**) were synthesized by the polyoxometalate (POM)-mediated clusterization of monomeric phosphanegold(I) complexes, and unequivocally characterized by elemental analysis, TG/DTA, FTIR, X-ray crystallography, and ^{1}H and ^{31}P{^{1}H} NMR. In each cluster cation, two digold(I) units, $\{Au\{P(p\text{-}RPh)_3\})_2(\mu\text{-}OH)\}^+$, dimerized to form the tetragold(I) cluster cation by interdimer aurophilic interactions, *i.e.*, a dimer of dinuclear units, and these cations showed different forms of structural dimerization, *i.e.*, a crossed-edge arrangement for **1** and **2** and a parallel-edge arrangement for **3**, depending upon the substituent on the aryl group of triarylphosphanes. The dimerization of digold(I) cations was affected by not only the type of the POMs, but also the phosphane ligand of the monomeric phosphanegold(I) precursors.

Introduction

Polyoxometalates (POMs) are discrete metal oxide clusters that are of current interest as soluble metal oxides and for their applications in catalysis, medicine, and materials science.[1] The preparation of POM-based materials is therefore an active field of research. One of the intriguing aspects of POMs is that their combination with cluster cations or macrocations has resulted in the formation of various intercluster compounds that are interesting from the viewpoints of conducting research on ionic crystals, crystal growth, crystal engineering, structure, sorption properties, and so on. In many compounds, POMs have been combined with separately prepared Au cluster cations.[2]

Recently, we unexpectedly found the clusterization of monomeric phosphanegold(I) $[Au(PR_3)]^+$ units during the course of carboxylate elimination of a monomeric phosphanegold(I) carboxylate, [Au(*RS*-pyrrld)(PPh_3)] (*RS*-Hpyrrld = (*RS*)-2-pyrrolidone-5-carboxylic acid), in the presence of the free-acid form of the α-Keggin POM, $H_3[\alpha\text{-}PW_{12}O_{40}]\cdot 7H_2O$.[3a] This reaction resulted in the formation of a tetrakis{triphenylphosphanegold(I)}oxonium cation, *i.e.*, $[\{Au(PPh_3)\}_4(\mu_4\text{-}O)]^{2+}$, as countercations of POM anions. In addition, we also found that the reaction of [Au(*RS*-pyrrld)(PPh_3)] with the sodium salt of the α-Keggin POM, $Na_3[\alpha\text{-}PW_{12}O_{40}]\cdot 9H_2O$, gave a heptakis{triphenylphosphanegold(I)}dioxonium cation, *i.e.*, $[\{\{Au(PPh_3)\}_4(\mu_4\text{-}O)\}\{\{Au(PPh_3)\}_3(\mu_3\text{-}O)\}]^{3+}$, with the α-Keggin POM anion.[3b] The formation of such tetragold(I) and heptagold(I) cluster cations was strongly dependent upon the bulkiness and charge density of the POMs, and the POMs appeared to act as a template in the clusterization of phosphanegold(I) cations.

The field of element-centered gold clusters $[E(AuL)_n]^{m+}$ (L = group 13–17 elements)[4–8] has been extensively studied by the groups of Schmidbaur[4a,b,7] and Laguna;[4c,6i,j] their findings included $[E(AuPPh_3)_4]^{2+}$ (E = S, Se),[6i,j] the angular flexibility of the Au–E–Au angles,[4a,b] and new structural findings, *i.e.*, the tetrahedral bonding of $[N(AuL)_4]^+$ and the pyramidal bondings of $[As(AuL)_4]^+$ and $[P(AuL)_4]^+$.[7] In addition, several phosphanegold(I) complexes have been known to serve as effective homogeneous catalysts for organic synthesis.[9a–f] For example, $[\{Au(PPh_3)\}_3(\mu_3\text{-}O)]BF_4$[5d,e,9g–j] has been used as an effective catalyst for a Claisen rearrangement of propargyl vinyl ethers,[9a–f] and such a complex has also been used as a precursor for the synthesis of novel metal complexes.[10] Conceivably, the oxonium cations, $[\{Au(PR_3)\}_3(\mu_3\text{-}O)]^+$, are sources of the catalytically active $[Au(PR_3)]^+$ species.

The aurophilic interaction is the driving force for the oligomerization of many phosphanegold(I) cluster cations in the

Department of Chemistry (formerly Department of Materials Science), Faculty of Science, Kanagawa University, 2946, Tsuchiya, Hiratsuka, Kanagawa 259-1293, Japan. E-mail: nomiya@kanagawa-u.ac.jp

†Electronic supplementary information (ESI) available: Molecular structure of **2**, syntheses of the phosphanegold(I) precursors. CCDC 940031–940033. For ESI and crystallographic data in CIF or other electronic format see DOI: 10.1039/c3dt51412a

This journal is © The Royal Society of Chemistry 2013

solid state, resulting in the dimer-of-multinuclear phosphanegold(I) clusters.[5a,d–g,6c–h,8b,c] For example, trigold(I) oxonium cations $[\{Au(PR_3)\}_3(\mu_3\text{-}O)]^+$ have been reported to exhibit different forms of structural dimerization depending upon the bulkiness of phosphane ligands, resulting in the hexagold(I) cation as a dimer of trinuclear units $[\{\{Au(PR_3)\}_3(\mu_3\text{-}O)\}_2]^{2+}$.[5d–g] The previously described heptagold(I) dioxonium cation, *i.e.*, $[\{\{Au(PPh_3)\}_4(\mu_4\text{-}O)\}\{\{Au(PPh_3)\}_3(\mu_3\text{-}O)\}]^{3+}$, was regarded as an assembly of the tetragold(I) unit $\{\{Au(PPh_3)\}_4(\mu_4\text{-}O)\}$ and the trigold(I) unit $\{\{Au(PPh_3)\}_3(\mu_3\text{-}O)\}$ induced by intercationic aurophilic interactions.[3b] This class of compounds is of interest as a source of useful aurating agents, and the POM-mediated clusterization of the phosphanegold(I) complexes provides effective synthetic routes for novel phosphanegold(I) cluster cations by a combination of the phosphanegold(I) carboxylate and different POMs. In fact, the previously described heptagold(I) cluster has been isolated only by the POM-mediated clusterization method.[3b]

In this paper, we report the syntheses and characterizations of novel intercluster compounds $[\{(Au\{P(p\text{-}RPh)_3\})_2(\mu\text{-}OH)\}_2]_3[\alpha\text{-}PM_{12}O_{40}]_2\cdot n$EtOH (R = Me, M = W for **1**; R = Me, M = Mo for **2**; R = F, M = Mo for **3**), which were synthesized by the POM-mediated clusterization of the monomeric phosphanegold(I) complexes. We successfully determined their molecular structures by X-ray crystallography. In each cluster cation, two digold(I) units dimerized to form the tetragold(I) cluster cation as a dimer of dinuclear units by interdimer aurophilic interactions, and these cations showed different forms of structural dimerization, *i.e.*, a crossed-edge arrangement for **1** and **2** and a parallel-edge arrangement for **3**. The parallel-edge tetragold(I) cation in **3** has not been synthesized by the conventional method, but can only be synthesized by the POM-mediated clusterization method.

Results and discussion

Synthesis and composition characterization

The intercluster compounds between the dimer of triaryl phosphanegold(I) hydroxo dimers and the α-Keggin POM anion were obtained as **1** in 78.0% (0.078 g scale) yield and as **3** in 27.9% (0.071 g scale) yield. These compounds were prepared by reactions between [Au(*RS*-pyrrld)(P(*p*-RPh))] (R = Me for **1** and **2**, R = F for **3**) in CH_2Cl_2 and the free-acid forms of Keggin POMs in mixed EtOH–H_2O solvents, *i.e.*, $H_3[\alpha\text{-}PM_{12}O_{40}]\cdot nH_2O$ (M = W, n = 7 for **1**; M = Mo, n = 14 for **2** and **3**), at r.t. Their crystallizations were carried out by slow evaporation. The molecular formulae of the intercluster compounds **1** and **3** prepared here were consistent with the obtained results of X-ray crystallography, elemental analysis, thermogravimetric and differential thermal analyses (TG/DTA), Fourier transform infrared (FTIR), and solution $^{31}P\{^1H\}$ nuclear magnetic resonance (NMR) spectra. In the case of compound **2**, an unknown greenish powder was also formed as a byproduct in addition to yellow plate crystals of **2**. Because manual separation of the byproduct was not possible, bulk chemical analysis of **2** was not performed, and only the crystal structure was determined by single-crystal structural analysis.

The formation of **1** and **2** is represented in eqn (1) and that of **3** is represented in eqn (2).

$$12[Au(RS\text{-pyrrld})\{P(p\text{-MePh})_3\}] + 2H_3[\alpha\text{-}PM_{12}O_{40}] + 6H_2O \rightarrow [\{(Au\{P(p\text{-MePh})_3\})_2(\mu\text{-OH})\}_2]_3[PM_{12}O_{40}]_2 + 12RS\text{-Hpyrrld}\ (\mathrm{M = W\ for\ \mathbf{1}, Mo\ for\ \mathbf{2}}) \quad (1)$$

$$12[Au(RS\text{-pyrrld})\{P(p\text{-FPh})_3\}] + 2H_3[\alpha\text{-}PMo_{12}O_{40}] + 6H_2O \rightarrow [\{(Au\{P(p\text{-FPh})_3\})_2(\mu\text{-OH})\}_2]_3[PMo_{12}O_{40}]_2 + 12RS\text{-Hpyrrld} \quad (2)$$

X-ray crystallography of **1**, **2**, and **3** showed the formation of discrete intercluster compounds between $[\{(Au\{P(p\text{-RPh})_3\})_2(\mu\text{-OH})\}_2]^{2+}$ (R = Me for **1** and **2**, F for **3**) and a saturated Keggin POM (Molecular structures of **1**, **2**, and **3**).

Compounds **1**, **2**, and **3** showed the same composition and formulae except the substituent on the aryl group of triarylphosphanes. When [Au(*RS*-pyrrld)(P(*o*-RPh)$_3$)] (R = H and Me) was used in reactions with the free-acid form of α-Keggin POMs such as $H_n[XM_{12}O_{40}]\cdot yH_2O$ (X = P, Si; M = W, Mo), the oxonium-centered tetragold(I)phosphane cations $[\{Au(PR_3)\}_4(\mu_4\text{-}O)]^{2+}$ were obtained.[3a] In addition, the heptagold(I)phosphane cation, $[\{Au(PPh_3)\}_7O_2]^{3+}$, was formed by the reaction of [Au(*RS*-pyrrld)(PPh$_3$)] with the sodium salt of an α-Keggin POM, $Na_3[PW_{12}O_{40}]\cdot 9H_2O$.[3b] In the present study, the reactions of [Au(*RS*-pyrrld){P(*p*-RPh)$_3$}] (R = Me, F) with $H_3[\alpha\text{-}PM_{12}O_{40}]\cdot nH_2O$ (M = W, Mo) provided the tetragold(I) cluster cation as a dimer of dinuclear units, $[\{(Au\{P(p\text{-RPh})_3\})_2(\mu\text{-OH})\}_2]^{2+}$ (R = Me for **1** and **2**; F for **3**). Therefore, the POM-mediated clusterization of the monomeric phosphanegold(I) complexes depends upon not only the POMs, but also the phosphane ligand of the monomeric phosphanegold(I) precursors.

In the TG/DTA measurements performed under atmospheric conditions, the weight loss of 0.55% observed at temperatures less than 258.3 °C for **1** corresponded to *ca.* one EtOH molecule, and that of 1.40% observed at temperatures less than 223.4 °C for **3** corresponded to *ca.* three EtOH molecules, all of which were consistent with the elemental analysis results.

The solid-state FTIR spectra of **1** and **3** showed the characteristic vibrational bands on the basis of coordinating PR_3 ligands (R = Me for **1**, F for **3**). The FTIR spectra also showed prominent vibrational bands owing to the α-Keggin tungsto-POMs (1079, 978, 896, and 820 cm^{-1}) for **1** and the α-Keggin molybdo-POMs (1062, 957, 879, and 799 cm^{-1}) for **3**.[13] In these spectra, the carbonyl vibrational bands of the anionic (*RS*)-pyrrld ligand in the [Au(*RS*-pyrrld)(P(*p*-RPh)$_3$)] (R = Me for **1**, at 1699 and 1637 cm^{-1}; F for **3**, at 1697 and 1634 cm^{-1}) precursors disappeared, suggesting that the carboxylate ligand was eliminated. Elimination of the carboxylate ligand was also confirmed by ^1H NMR in DMSO-d_6. The carboxylate plays only the role of a leaving group. In fact, not only pyrrolidone

carboxylate, but also other carboxylates such as 5-oxotetrahydrofuran-2-carboxylate and acetylglycinate can serve as the leaving groups in the formation of the tetraphosphanegold(I) clusters in the presence of POMs.[3a]

Molecular structures of 1, 2, and 3

Single-crystal X-ray analysis revealed that **1** crystallizes in the cubic *Ia*$\bar{3}$*d* space group and is composed of three tetragold(I) cluster cations, *i.e.*, $[\{(Au\{P(p\text{-}MePh)_3\})_2(\mu\text{-}OH)\}_2]^{2+}$, and two saturated α-Keggin POMs $[\alpha\text{-}PW_{12}O_{40}]^{3-}$ as counteranions (Fig. 1a).

The tetragold(I) cluster cation in **1** can be regarded as the dimerization of digold(I) units $\{(Au\{P(p\text{-}MePh)_3\})_2(\mu\text{-}OH)\}^+$. The digold(I) unit consists of two $Au\{P(p\text{-}MePh)_3\}$ monomer subunits linked by a μ-OH ligand and is triangular in shape. Two digold(I) units dimerize to form the tetragold(I) cluster cation, $[\{(Au\{P(p\text{-}MePh)_3\})_2(\mu\text{-}OH)\}_2]^{2+}$, by interdimer aurophilic interactions (Au1–Au1′, 2.991 Å) in a crossed-edge arrangement, leading to a tetrahedral array of the four gold(I) atoms (Fig. 1b). This interdimer Au–Au distance was longer than the Au–Au separation of metallic gold (2.88 Å) but was shorter than twice the van der Waals radius of gold (3.32 Å). In

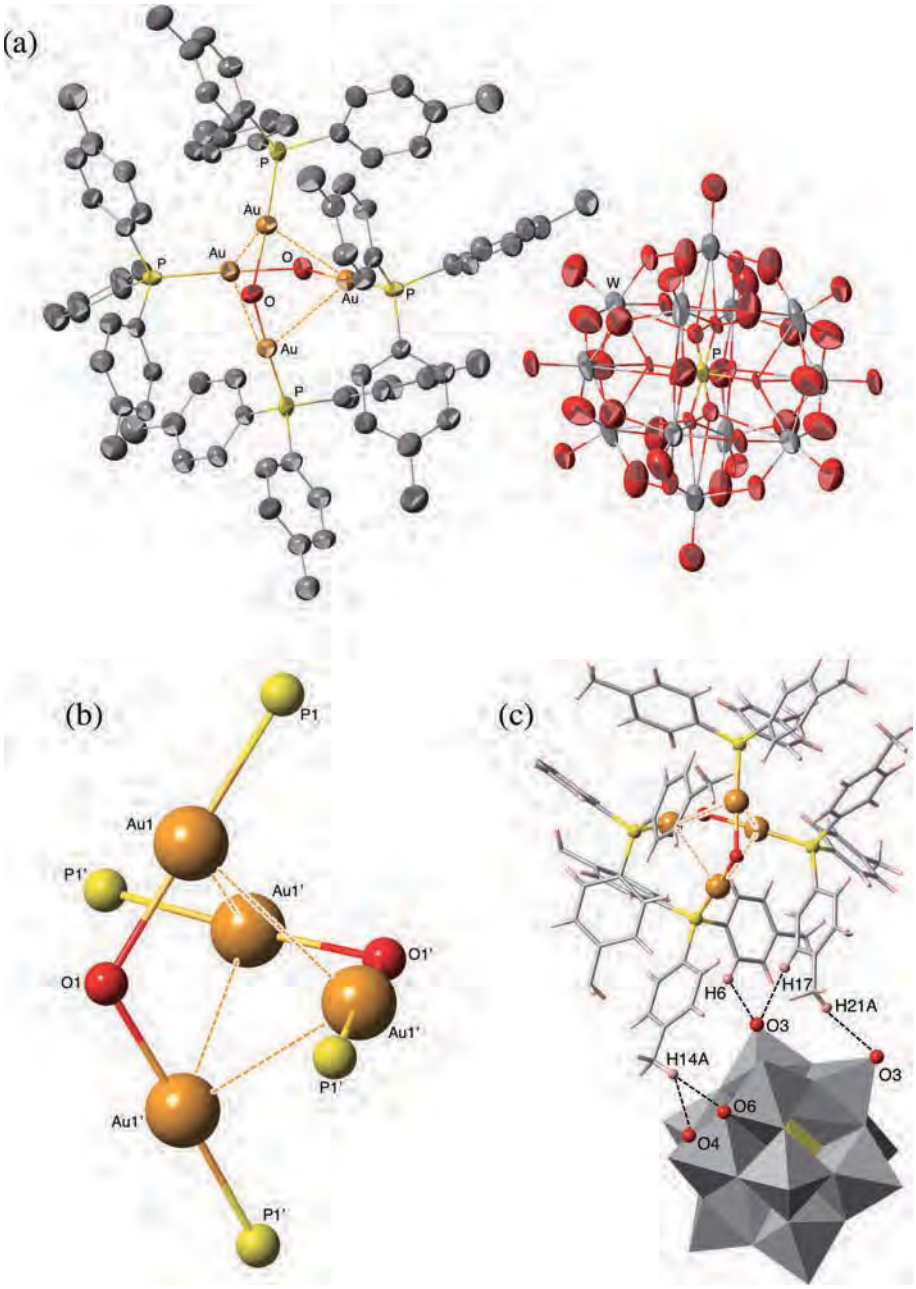

Fig. 1 (a) Molecular structure of $[\{(Au\{P(p\text{-}MePh)_3\})_2(\mu\text{-}OH)\}_2]_3[\alpha\text{-}PW_{12}O_{40}]_2\cdot EtOH$ (**1**); (b) the partial structure around the tetragold(I) cluster core of **1** in a crossed-edge arrangement; and (c) the short interactions between the tetragold(I) unit and the α-Keggin POM unit.

 This journal is © The Royal Society of Chemistry 2013

comparison, the intradimer Au–Au distance was 3.554 Å, indicating the absence of any significant aurophilic interactions in each dimer. The Au1–O1–Au1′ bond angle is 116.1°. A crossed-edge tetragold(I) cation similar to that observed in **1** has been reported for $[(\{Au(PPh_3)\}_2(\mu\text{-}OH))_2](TfO)_2$,[5a] and its interdimer Au–Au distances were reported to be 3.1035–3.2798 Å. These distances are longer than that of compound **1** (2.991 Å), indicating stronger aurophilic interactions in **1**. Hydrogen bonding between the μ-OH and the TfO^- anion was observed in the reported $[(\{Au(PPh_3)\}_2(\mu\text{-}OH))_2](TfO)_2$, whereas for compound **1**, no interaction was observed between the tetragold(I) core and the Keggin POM unit. However, hydrogen bonding between the peripheral phosphane ligands and the oxygen atoms of Keggin POMs was found in **1** (O3···H6, 2.420 Å; O3···H17, 2.551 Å; O3···H21A, 2.692 Å; O4···H14A, 2.643 Å; O6···H14A, 2.688 Å; Fig. 1c). Other related compounds are the halide-bridged tetragold(I) cations with a crossed-edge arrangement, $[(\{Au(PR)\}_2(\mu\text{-}X))_2](SbF_6)_2$ (X = Cl, Br, I; R = Ph_3, $\{(MeO)_2C_6H_3\}Ph_2$).[8b,c] These compounds showed an anion-dependent monomer–dimer conversion, *i.e.*, the compounds exist as tetragold(I) dimers with large SbF_6^- anions, whereas they occur as digold(I) monomers with small anions such as BF_4^- or ClO_4^-. The Keggin POM anion is much larger than the SbF_6^-, BF_4^-, and ClO_4^- anions; therefore, the fact that compound **1** exists as tetragold(I) dimers is consistent with the previously described anion dependency.

X-ray crystallography revealed that the molecular structure of **2** is isostructural with that of **1** except that the addenda metal atoms of Keggin POM units are Mo (Fig. S1†).

Single-crystal X-ray analysis revealed that **3** crystallizes in the triclinic $P\bar{1}$ space group and is composed of three tetragold(I) cluster cations, *i.e.*, $[\{(Au\{P(p\text{-}FPh)_3\})_2(\mu\text{-}OH)\}_2]^{2+}$, two saturated α-Keggin POMs $[\alpha\text{-}PMo_{12}O_{40}]^{3-}$ as counteranions, and four solvated ethanol molecules (Fig. 2a).

As with compound **1**, the digold(I) unit consists of two Au-$\{P(p\text{-}FPh_3\}$ monomers linked by a μ-OH ligand, and the two digold(I) units dimerize by interdimer aurophilic interactions (Au1–Au2′, 3.280 Å; Au3–Au4′, 3.197 Å; Au5–Au6′, 3.192 Å) to form the tetragold(I) cluster cation $[\{(Au\{P(p\text{-}FPh)_3\})_2(\mu\text{-}OH)\}_2]^{2+}$. There were three crystallographically independent tetragold(I) cations in the unit cell. Unlike compound **1**, the digold(I) cations of **3** dimerized in a parallel-edge arrangement, leading to a rectangular array of the four gold(I) atoms (Fig. 2b). The Au–(μ-OH)–Au angles in each digold(I) dimer are 92.216° (Au1–O1–Au2), 91.700° (Au3–O2–Au4), and 98.572° (Au5–O3–Au6), and these angles are narrower than that in **1** (116.1°). Because of these narrow angles, the intradimer Au–Au distances of the digold(I) unit are shorter (2.996 for Au1–Au2, 2.998 for Au3–Au4, and 3.152 for Au5–Au6 Å) than that of **1**, indicating that the aurophilic interactions are also present in the digold(I) units. Notably, interactions between the tetragold(I) core and the Keggin POM unit were observed in compound **3** (Fig. 2c). The Keggin POM interacts with each crystallographically independent tetragold(I) cation (Au1, Au2, and O1 interact with edge-sharing oxygen atoms O34, O36, and O35; Au3, Au4, and O2 interact with edge-sharing oxygen atoms O25, O13, and O14; Au5 interacts with edge-sharing oxygen O11; Au6 and O3 interact with corner-sharing oxygen atoms O11 and O7; the short distances between O1, O2, O3 and O36, O25, O7 indicate the existence of a hydrogen bonding), resulting in a 2D sheet structure (Fig. 2c). The short contact between the fluorine atoms of the phosphane ligands of tetragold(I) cations and the oxygen atoms of Keggin POM units was not observed.

A parallel-edge tetragold(I) cation similar to that observed in **3** has been reported for the thiolate-bridged tetragold(I) cations $[(\{Au(PR^1)\}_2(\mu\text{-}SR^2))_2]^{2+}$ (R^1 = Ph, Me; R^2 = CMe_3, 2-$H_2NC_6H_4$, CH_2CMe_3, 4-MeC_6H_4, 2,3,4,6-tetraacetyl-1-thio-D-glucopyranosato).[6c–h] To the best of our knowledge, compound **3** is the first example of a hydroxide-bridged tetragold(I) cation dimerized in a parallel-edge arrangement.

Many trigold(I) oxonium cations have been reported, and these cations show different forms of structural dimerization depending upon the phosphane ligands, resulting in the hexagold(I) cations.[5d–f] For example, the rectangular-type hexagold(I) cations were favored with bulkier phosphane ligands such as PPh_3 and $PMePh_2$, whereas trimers were favored with smaller ligands such as PMe_3 dimerized in a tetrahedral arrangement. Theoretical studies also support these results.[5g] The present crossed- and parallel-edge tetragold(I) cations may also be regarded as analogs with the loss of $\{AuPR_3\}^+$ moieties from each trimer of the tetrahedral and rectangular cations, respectively. In the case of the tetragold(I) cations presented here, the crossed-edge tetragold(I) cations in **1** and **2**, *i.e.*, the analog of the tetrahedral type, are formed even with bulkier ligands such as $P(p\text{-}MePh)_3$. On the other hand, the digold(I) cation with a smaller ligand such as $P(p\text{-}FPh)_3$ formed the parallel-edge tetragold(I) cation in **3**, *i.e.*, the analog of rectangular cations. Our results indicate that the dimerization of digold(I) cations may be affected by not only the bulkiness of the phosphane ligand, but also the interactions between the digold(I) cations, including the phosphane ligand and the POM anion.

Solution $^{31}P\{^1H\}$ NMR

The solution $^{31}P\{^1H\}$ NMR spectrum of **1** in DMSO-d_6 showed two sharp signals at −14.72 and 23.06 ppm because of the α-Keggin POM and $P(p\text{-}MePh)_3$ ligands, respectively, of the gold(I) cluster. The signal of the $P(p\text{-}MePh)_3$ ligands at 23.06 ppm shifted to a higher field from the signal observed at 25.35 ppm of the $[Au(RS\text{-}pyrrld)\{P(p\text{-}MePh)_3\}]$ precursor. The solution $^{31}P\{^1H\}$ NMR spectrum of **3** showed a sharp peak at 24.14 ppm because of $P(p\text{-}FPh)_3$ ligands of the gold(I) cluster, and three peaks from 0 to −3.5 ppm due to the α-Keggin POM (−3.43 ppm) and decomposition species of the Keggin POM (−0.58 and −1.90 ppm).

The tendency for the $^{31}P\{^1H\}$ NMR spectroscopic resonances of the oligomeric phosphanegold(I) clusters **1** and **3** to appear in a higher field than that of the monomeric phosphanegold(I) precursor is consistent with the previously reported NMR results for other phosphanegold(I) clusters.[3]

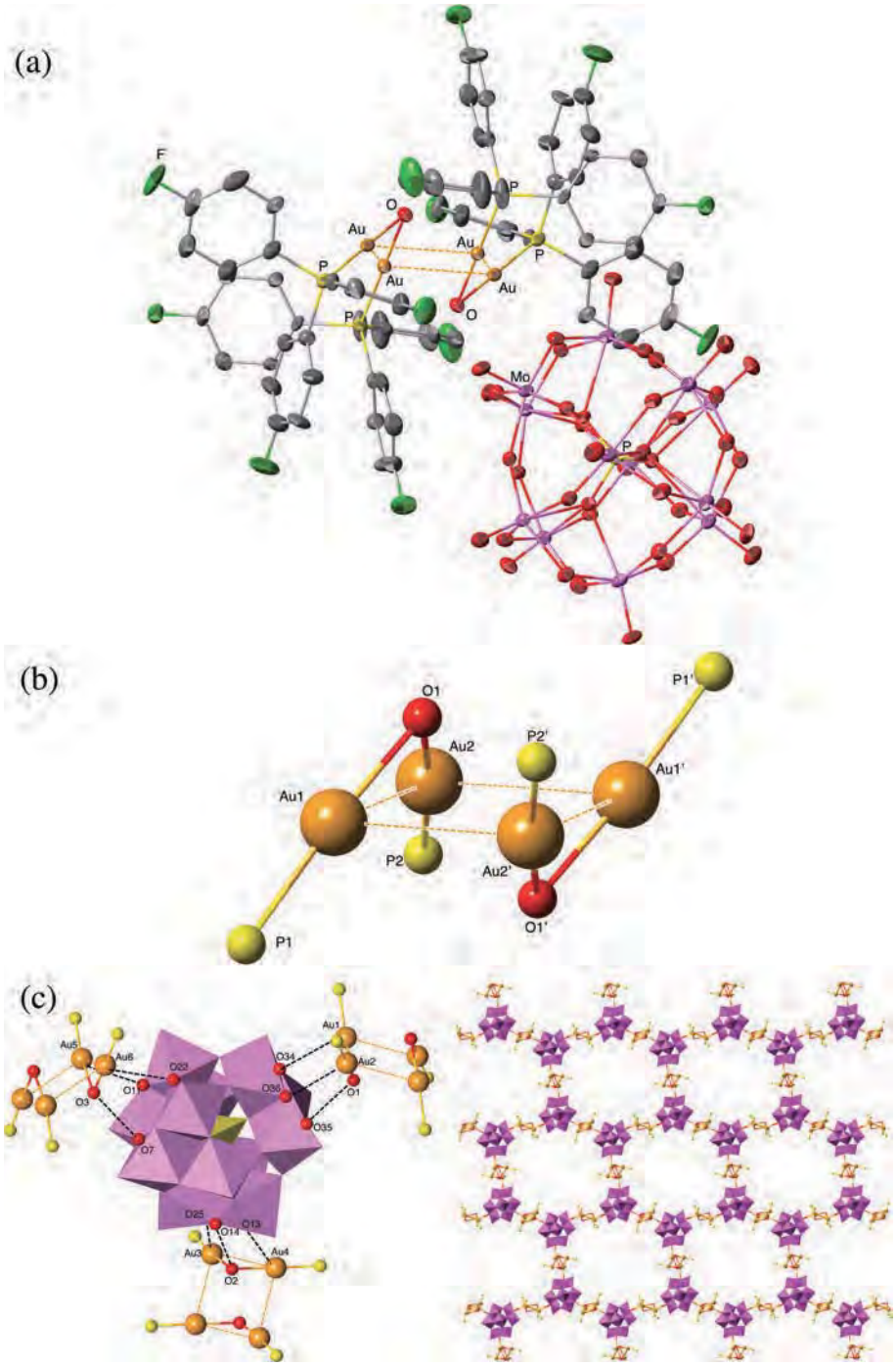

Fig. 2 (a) Molecular structure of $[\{(Au\{P(p\text{-}FPh)_3\})_2(\mu\text{-}OH)\}_2]_3[\alpha\text{-}PMo_{12}O_{40}]_2\cdot 3EtOH$ (**3**); (b) the partial structure around the tetragold(I) cluster core of **3** in a parallel-edge arrangement; and (c) the short interactions between the tetragold(I) unit and the α-Keggin POM unit, and the 2D sheet structure is also shown.

Conclusion

In this study, we prepared and characterized novel intercluster compounds by the POM-mediated clusterization of monomeric phosphanegold(I) complexes. In each cluster cation, two digold(I) units dimerized to form the tetragold(I) cluster cation by interdimer aurophilic interactions, and these cations show different forms of structural dimerization depending upon the substituent on the aryl group of triarylphosphanes, *i.e.*, a crossed-edge arrangement for the $P(p\text{-}MePh)_3$ ligand (**1** and **2**) and a parallel-edge arrangement for the $P(p\text{-}FPh)_3$ ligand (**3**). Our results indicate that the dimerization of digold(I) cations may be affected by not only the type of POM, but also the phosphane ligand of the monomeric phosphanegold(I) precursors. In addition, the dimerization of digold(I) cations may be affected by the interactions between the digold(I) cations,

 This journal is © The Royal Society of Chemistry 2013

including interactions between the phosphane ligands and the POM anions. These facts provide significant information about the synthesis of phosphanegold(I) cluster cations by the POM-mediated clusterization method.

Experimental

Materials

The following reactants were used as received: EtOH, CH_2Cl_2, Et_2O (all from Wako), and DMSO-d_6 (Isotec). With respect to the α-Keggin POM, $H_3[\alpha\text{-}PW_{12}O_{40}]\cdot 7H_2O$ was derived from a separately prepared sodium salt using the ether extraction method and was identified by FTIR, TG/DTA, and solution ^{31}P NMR spectroscopy.[11a] The [Au(*RS*-pyrrld){P(*p*-RPh)$_3$}] (R = Me, F) precursors were synthesized using P(*p*-RPh)$_3$ (R = Me, F) with the same previously reported procedure used to prepare [Au(*RS*-pyrrld)(PPh$_3$)][11b] and characterized by CHN elemental analysis, FTIR, TG/DTA, and (^{1}H, ^{13}C{^{1}H}, and ^{31}P{^{1}H}) NMR spectroscopy (ESI).

Instrumentation/analytical procedures

CHN elemental analyses were performed with a Perkin-Elmer 2400 CHNS Elemental Analyzer II. IR spectra were recorded on a Jasco 4100 FTIR spectrometer in KBr disks at r.t. TG/DTA analyses were performed using a Rigaku Thermo Plus 2 series TG/DTA TG 8120 instrument. ^{1}H NMR (500.00 MHz) and ^{31}P{^{1}H} NMR (202.00 MHz) spectra of samples in DMSO-d_6 solutions contained in 5-mm-outer-diameter tubes were recorded on a JEOL JNM-ECP 500 FT-NMR spectrometer equipped with a JEOL ECP-500 NMR data processing system. The ^{1}H NMR spectra were referenced to an internal standard of tetramethylsilane. The ^{31}P{^{1}H} NMR spectra were referenced to an external standard of 25% H_3PO_4 in H_2O in a sealed capillary tube. The ^{31}P NMR data with the usual 85% H_3PO_4 reference are shifted by +0.544 ppm from our chemical shifts.

Syntheses

[{(Au{P(*p*-MePh)$_3$})$_2$(μ-OH)}$_2$]$_3$[α-PW$_{12}$O$_{40}$]$_2$·EtOH (1). A solution of [Au(*RS*-pyrrld){P(*p*-MePh)$_3$}] (0.189 g, 0.300 mmol) dissolved in 25 mL of CH_2Cl_2 was slowly added to a clear solution of $H_3[\alpha\text{-}PW_{12}O_{40}]\cdot 7H_2O$ (0.150 g, 0.050 mmol) dissolved in 15 mL of an EtOH–H_2O (5 : 1, v/v) mixed solvent. After stirring for 1 h at r.t., the resulting pale yellow translucent solution was concentrated to 15 mL with a rotary evaporator at 30 °C. A yellow-white powder was collected on a membrane filter (JG 0.2 μm), washed with H_2O (20 mL × 2), EtOH (20 mL × 2) and Et_2O (20 mL × 2), and dried *in vacuo* for 2 h. At this stage, the yellow-white powder was obtained in a yield of 0.26 g.

Crystallization

The yellow-white powder (0.100 g) was dissolved in 20 mL of a CH_2Cl_2–EtOH (3 : 1, v/v) mixed solvent and was filtered through a folded filter paper (Whatman no. 5). The clear pale yellow filtrate was slowly evaporated at r.t. in the dark. After 5 days, orange block crystals were formed and collected on a membrane filter (JG 0.2 μm), washed with EtOH (20 mL × 2) and Et_2O (20 mL × 2), and dried *in vacuo* for 2 h. Yield: 0.078 g (78.0%). The crystalline samples were soluble in DMSO and sparingly soluble in CH_2Cl_2, but were insoluble in H_2O, EtOH, and Et_2O. Found: C, 25.80; H, 2.14%. Calcd for $C_{254}H_{264}O_{87}P_{14}W_{24}Au_{12}$ or [{(Au{P(*p*-tolyl)$_3$})$_2$(μ-OH)}$_2$]$_3$[α-PW$_{12}$O$_{40}$]$_2$·EtOH: C, 25.60; H, 2.23%. TG/DTA under atmospheric conditions: a weight loss of 0.55% because of desorption of EtOH was observed at temperatures less than 258.3 °C; calcd 0.39% for one EtOH molecule. IR (KBr): 1597 w, 1444 w, 1397 w, 1309 vw, 1188 w, 1104 m, 1079 s, 978 s, 896 s, 820 vs, 802 vs, 706 w, 648 w, 633 w, 620 w, 529 m, 510 m cm^{-1}. ^{31}P{^{1}H} NMR (25.8 °C, DMSO-d_6): δ −14.73, 23.06 ppm. ^{1}H NMR (24.9 °C, DMSO-d_6): δ 1.06 (t, J = 6.9 Hz, CH_3CH$_2$OH solvate), 2.27 (s, *Me*), 7.14–7.32 (m, *Ph*) ppm.

[{(Au{P(*p*-MePh)$_3$})$_2$(μ-OH)}$_2$]$_3$[α-PMo$_{12}$O$_{40}$]$_2$ (2). A solution of [Au(*RS*-pyrrld){P(*p*-MePh)$_3$}] (0.252 g, 0.400 mmol) dissolved in 25 mL of CH_2Cl_2 was slowly added to a clear solution of $H_3[\alpha\text{-}PMo_{12}O_{40}]\cdot 14H_2O$[11c] (0.104 g, 0.050 mmol) dissolved in 15 mL of an EtOH–H_2O (5 : 1, v/v) mixed solvent. After stirring for 1 h at r.t., only CH_2Cl_2 was evaporated, and the resulting precipitate was separated by filtration on a membrane filter (JG 0.2 μm). The resulting yellow powder was washed with H_2O (20 mL × 2), EtOH (20 mL × 2) and Et_2O (20 mL × 2), and dried *in vacuo* for 2 h. At this stage, the yellow powder was obtained in a yield of 0.210 g.

Crystallization

The yellow powder (0.100 g) was dissolved in 20 mL of a CH_2Cl_2–EtOH (3 : 1, v/v) mixed solvent and filtered through a folded filter paper (Whatman no. 5). The clear yellow filtrate was slowly evaporated at r.t. in the dark. After 2 days, yellow block crystals were formed. Because an unknown greenish powder was also formed as a byproduct in addition to yellow block crystals of **2** and their manual separation was not possible, bulk chemical analysis of **2** was not performed; the crystal structure, however, was determined by single-crystal X-ray structural analysis.

[{(Au{P(*p*-FPh)$_3$})$_2$(μ-OH)}$_2$]$_3$[α-PMo$_{12}$O$_{40}$]$_2$·3EtOH (3). A solution of [Au(*RS*-pyrrld){P(*p*-FPh)$_3$}] (0.192 g, 0.300 mmol) dissolved in 30 mL of CH_2Cl_2 was slowly added to a clear solution of $H_3[\alpha\text{-}PMo_{12}O_{40}]\cdot 14H_2O$ (0.104 g, 0.050 mmol) dissolved in 15 mL of an EtOH–H_2O (5 : 1, v/v) mixed solvent. After stirring for 1 h at r.t., the reaction solution was filtered through a membrane filter (JV 0.1 μm). The resulting yellow-orange translucent solution was slowly evaporated at r.t. in the dark. After 7 days, yellow plate crystals were formed and collected on a membrane filter (JG 0.2 μm), washed with EtOH (20 mL × 2) and Et_2O (20 mL × 2), and dried *in vacuo* for 2 h. Yield: 0.071 g (27.9%). The crystalline samples were soluble in DMSO and sparingly soluble in CH_2Cl_2; they were insoluble in H_2O, EtOH, and Et_2O. Found: C, 26.29; H, 1.37%. Calcd for $C_{222}H_{168}O_{89}P_{14}Au_{12}Mo_{24}$ or [{(Au{P(*p*-FPh)$_3$})$_2$(μ-OH)}$_2$]$_3$[α-PMo$_{12}$O$_{40}$]$_2$·3EtOH: C, 26.55; H, 1.69%. TG/DTA under atmospheric conditions: a weight loss of 1.40% because of desorption of EtOH was observed at temperatures less than 223.4 °C; calcd 1.38%

Table 1 Crystallographic data for **1**, **2**, and **3**

	1	**2**	**3**
Formula	$C_{252}H_{258}Au_{12}O_{86}P_{14}W_{24}$	$C_{252}H_{258}Au_{12}Mo_{24}O_{86}P_{14}$	$C_{224}H_{174}Au_{12}F_{36}Mo_{24}O_{90}P_{14}$
Formula weight	11 872.16	9762.32	10 089.37
Color, shape	Orange, block	Yellow, block	Yellow, plate
Crystal system	Cubic	Cubic	Triclinic
Space group	$Ia\bar{3}d$	$Ia\bar{3}d$	$P\bar{1}$
T/K	100(2)	100(2)	100(2)
a/Å	44.4487(9)	44.1632(9)	17.2850(14)
b/Å			22.6003(19)
c/Å			22.6840(18)
α/°			75.933(2)
β/°			80.236(2)
γ/°			78.267(2)
V/Å^3	87 817(3)	86 135(3)	8348.5(12)
Z	8	8	1
D_{calc}/g cm^{-3}	1.796	1.506	2.007
F_{000}	43 136	36 992	4728
GOF	1.159	1.099	1.044
R_1 ($I > 2.00\sigma(I)$)	0.0921	0.0638	0.0544
R (all data)	0.1140	0.1252	0.0877
wR_2 (all data)	0.2367	0.2350	0.1638

for three EtOH molecules. IR (KBr): 1589 s, 1496 s, 1396 w, 1302 vw, 1278 vw, 1238 m, 1161 m, 1103 w, 1062 m, 1013 vw, 957 s, 879 m, 799 vs, 709 w, 640 w, 618 w, 534 m, 451 w, 442 w cm^{-1}. $^{31}P\{^1H\}$ NMR (27.0 °C, DMSO-d$_6$): δ −3.43, 24.14 (main), −1.90, −0.58, −0.16, 41.09 (minor) ppm. ^{1}H NMR (25.9 °C, DMSO-d$_6$): δ 1.09 (t, J = 7.0 Hz, CH_3CH$_2$OH solvate), 3.39 (q, J = 7.0 Hz, CH$_3$CH_2OH solvate), 7.40–7.66 (m, *Ph*) ppm.

X-ray crystallography

Single crystals with dimensions of 0.23 × 0.21 × 0.12 mm^3 for **1**, 0.11 × 0.11 × 0.08 mm^3 for **2**, and 0.18 × 0.09 × 0.02 mm^3 for **3** were mounted on cryoloops using liquid paraffin and cooled by a stream of cooled N_2 gas. All measurements were performed on a Bruker SMART APEX CCD diffractometer at 100 K; the diffractometer was equipped with a graphite-monochromated Mo Kα radiation source (λ = 0.71073 Å). The intensity data were automatically collected for Lorentz and polarization effects during integration. The structures were solved by direct methods (SHELXS-97)[12a] followed by a subsequent difference Fourier calculation; the structures were refined by a full-matrix least-squares procedure on F^2 (SHELEXL-97).[12b] Absorption corrections were performed with SADABS (empirical absorption correction).[12c] The compositions and formulae of the POMs containing many solvated molecules were determined by CHN elemental analysis, TG analysis, and ^{1}H NMR analysis. As with other structural investigations of crystals of highly solvated, large polyoxometalate complexes, every solvated EtOH molecule for all of the complexes could not be located. This frequently encountered situation is attributed to extensive disorder of the solvated EtOH molecules. The central PO_4 group of compounds **1** and **2** is crystallographically disordered, which leads to the observation of a cube instead of a tetrahedron. This observation is common for Keggin anions lying on an element of symmetry. The details of the crystallographic data for **1**, **2**, and **3** are listed in Table 1.

Acknowledgements

This study was supported by JSPS KAKENHI grant number 22550065 and by the Strategic Research Base Development Program for Private Universities of the Ministry of Education, Culture, Sports, Science and Technology of Japan.

References

1 (*a*) M. T. Pope and A. Müller, *Angew. Chem., Int. Ed. Engl.*, 1991, **30**, 34–48; (*b*) M. T. Pope, *Heteropoly- and Isopolyoxometalates*, Springer-Verlag, New York, 1983; (*c*) V. W. Day and W. G. Klemperer, *Science*, 1985, **228**, 533; (*d*) C. L. Hill, *Chem. Rev.*, 1998, **98**, 1; (*e*) T. Okuhara, N. Mizuno and M. Misono, *Adv. Catal.*, 1996, **41**, 113; (*f*) C. L. Hill and C. M. Prosser-McCartha, *Coord. Chem. Rev.*, 1995, **143**, 407; (*g*) A series of 34 recent papers in a volume devoted to Polyoxoanions in Catalysis, ed. C. L. Hill, *J. Mol. Catal. A: Chem.*, 1996, 114, 1; (*h*) R. Neumann, *Prog. Inorg. Chem.*, 1998, **47**, 317; (*i*) *Polyoxometalate Chemistry from Topology via Self-Assembly to Applications*, ed. M. T. Pope and A. Müller, Kluwer Academic Publishers, Netherlands, 2001; (*j*) *Polyoxometalate Chemistry for Nano-Composite Design*, ed. T. Yamase and M. T. Pope, Kluwer Academic Publishers, Netherlands, 2002; (*k*) M. T. Pope, Polyoxo anions: synthesis and structure, in *Comprehensive Coordination Chemistry II*, ed. A. G. Wedd, Elsevier Science, New York, 2004, vol. 4, p. 635; (*l*) C. L. Hill, Polyoxometalates: reactivity, in *Comprehensive Coordination Chemistry II*, ed. A. G. Wedd, Elsevier Science, New York, 2004, vol. 4, p. 679; (*m*) A series of 32 recent papers in a volume devoted to Polyoxometalates in Catalysis, ed. C. L. Hill, *J. Mol. Catal. A: Chem.*, 2007, vol. 262, 1; (*n*) A. Proust, R. Thouvenot and P. Gouzerh, *Chem. Commun.*, 2008, 1837;

 This journal is © The Royal Society of Chemistry 2013

(*o*) B. Hasenknopf, K. Micoine, E. Lacôte, S. Thorimbert, M. Malacria and R. Thouvenot, *Eur. J. Inorg. Chem.*, 2008, 5001; (*p*) D. Laurencin, R. Thouvenot, K. Boubekeur, F. Villain, R. Villanneau, M.-M. Rohmer, M. Benard and A. Proust, *Organometallics*, 2009, **28**, 3140; (*q*) D.-L. Long, R. Tsunashima and L. Cronin, *Angew. Chem., Int. Ed.*, 2010, **49**, 1736; (*r*) K. Nomiya, Y. Sakai and S. Matsunaga, *Eur. J. Inorg. Chem.*, 2011, 179.

2 (*a*) M. Schulz-Dobrick and M. Jansen, *Eur. J. Inorg. Chem.*, 2006, 4498; (*b*) M. Schulz-Dobrick and M. Jansen, *Inorg. Chem.*, 2007, **46**, 4380; (*c*) M. Schulz-Dobrick and M. Jansen, *Z. Anorg. Allg. Chem.*, 2007, **633**, 2326.

3 (*a*) K. Nomiya, T. Yoshida, Y. Sakai, A. Nanba and S. Tsuruta, *Inorg. Chem.*, 2010, **49**, 8247; (*b*) T. Yoshida, K. Nomiya and S. Matsunaga, *Dalton Trans.*, 2012, **41**, 10085.

4 (*a*) H. Schmidbaur, *Chem. Soc. Rev.*, 1995, **24**, 391; (*b*) H. Schmidbaur and A. Schier, *Chem. Soc. Rev.*, 2008, **37**, 1931; (*c*) M. C. Gimeno and A. Laguna, *Chem. Soc. Rev.*, 2008, **37**, 1952.

5 (*a*) Y. Tang and B. Yu, *RSC Adv.*, 2012, **2**, 12686; (*b*) S. Gaillard, A. M. Z. Slawin and S. P. Nolan, *Chem. Commun.*, 2010, **46**, 2742; (*c*) R. S. Ramón, S. Gaillard, A. Poater, L. Cavallo, A. M. Z. Slawin and S. P. Nolan, *Chem.–Eur. J.*, 2011, **17**, 1238; (*d*) A. N. Nesmeyanov, E. G. Perevalova, Y. T. Struchkov, M. Y. Antipin, K. I. Grandberg and V. P. Dyadchenko, *J. Organomet. Chem.*, 1980, **201**, 343; (*e*) Y. Yang, V. Ramamoorthy and P. R. Sharp, *Inorg. Chem.*, 1993, **32**, 1946; (*f*) K. Angermaier and H. Schmidbaur, *Inorg. Chem.*, 1994, **33**, 2069; (*g*) S.-C. Chung, S. Krüger, H. Schmidbaur and N. Rösch, *Inorg. Chem.*, 1996, **35**, 5387; (*h*) H. Schmidbaur, S. Hofreiter and M. Paul, *Nature*, 1995, **377**, 503.

6 (*a*) S. Hofreiter, M. Paul and H. Schmidbaur, *Chem. Ber.*, 1995, **128**, 901; (*b*) P. G. Jones and C. Thöne, *Chem. Ber.*, 1991, **124**, 2725; (*c*) J. Chen, T. Jiang, G. Wei, A. A. Mohamed, C. Homrighausen, J. A. Krause Bauer, A. E. Bruce and M. R. M. Bruce, *J. Am. Chem. Soc.*, 1999, **121**, 9225; (*d*) A. A. Mohamed, J. Chen, A. E. Bruce and M. R. M. Bruce, *Inorg. Chem.*, 2003, **42**, 2203; (*e*) S. Wang and J. P. Fackler Jr., *Inorg. Chem.*, 1990, **29**, 4404; (*f*) A. Battisti, O. Bellina, P. Diversi, S. Losi, F. Marchetti and P. Zanello, *Eur. J. Inorg. Chem.*, 2007, 865; (*g*) J. M. López-de-Luzuriaga, A. Sladek, W. Schneider and H. Schmidbaur, *Chem. Ber./Recl.*, 1997, **130**, 641; (*h*) A. Sladek and H. Schmidbaur, *Chem. Ber.*, 1995, **128**, 907; (*i*) F. Canales, M. C. Gimeno, P. G. Jones and A. Laguna, *Angew. Chem., Int. Ed.*, 1994, **33**, 769; (*j*) F. Canales, C. Gimeno, A. Laguna and M. D. Villacampa, *Inorg. Chim. Acta*, 1996, **244**, 95.

7 (*a*) E. Zeller, H. Beruda, A. Kolb, P. Bissinger, J. Riede and H. Schmidbaur, *Nature*, 1991, **352**, 141; (*b*) H. Schmidbaur, *Z. Naturforsch., B: Chem. Sci.*, 2008, **63**, 853.

8 (*a*) P. G. Jones and G. M. Sheldrick, *Acta Crystallogr., Sect. B: Struct. Crystallogr. Cryst. Chem.*, 1980, **36**, 1486; (*b*) A. Hamel, N. W. Mitzel and H. Schmidbaur, *J. Am. Chem. Soc.*, 2001, **123**, 5106; (*c*) H. Schmidbaur, A. Hamel, N. W. Mitzel, A. Schier and S. Nogai, *Proc. Natl. Acad. Sci. U. S. A.*, 2002, **99**, 4916.

9 (*a*) A. Fürstner and P. W. Davies, *Angew. Chem., Int. Ed.*, 2007, **46**, 3410; (*b*) A. S. K. Hashmi, *Chem. Rev.*, 2007, **107**, 3180; (*c*) E. Jiménez-Núñez and A. M. Echavarren, *Chem. Rev.*, 2008, **108**, 3326; (*d*) D. J. Gorin, B. D. Sherry and F. D. Toste, *Chem. Rev.*, 2008, **108**, 3351; (*e*) P. Mauleón, J. L. Krinsky and F. D. Toste, *J. Am. Chem. Soc.*, 2009, **131**, 4513; (*f*) K. Sakaguchi, T. Okada, T. Shinada and Y. Ohfune, *Tetrahedron Lett.*, 2008, **49**, 25; (*g*) H. Schmidbaur, A. Kolb, E. Zeller, A. Schier and H. Beruda, *Z. Anorg. Allg. Chem.*, 1993, **619**, 1575; (*h*) L. G. Kuz'mina, A. V. Churakov, G. G. Sadikov and J. A. K. Howard, *Crystallogr. Rep.*, 2003, **48**, 61; (*i*) K. Angermaier and H. Schmidbaur, *Inorg. Chem.*, 1994, **33**, 2069; (*j*) T. Mathieson, A. Schier and H. Schmidbaur, *Z. Naturforsch., B: Chem. Sci.*, 2000, **55**, 1000.

10 (*a*) A. Singh, U. Anandhi, M. A. Cinellu and P. R. Sharp, *Dalton Trans.*, 2008, 2314; (*b*) A. Singh and P. R. Sharp, *Inorg. Chim. Acta*, 2008, **361**, 3159; (*c*) A. Blumenthal, H. Beruda and H. Schmidbaur, *J. Chem. Soc., Chem. Commun.*, 1993, 1005.

11 (*a*) S. Aoki, T. Kurashina, Y. Kasahara, T. Nishijima and K. Nomiya, *Dalton Trans.*, 2011, **40**, 1243; (*b*) R. Noguchi, A. Hara, A. Sugie and K. Nomiya, *Inorg. Chem. Commun.*, 2006, **9**, 355. The representation of H_2pyrrld is changed to Hpyrrld; thus, the formulation of [Au(*RS*-Hpyrrld)(PPh_3)] used so far is also changed to [Au(*RS*-pyrrld)(PPh_3)]; (*c*) E. O. North and W. Haney, *Inorg. Synth.*, 1939, **1**, 127.

12 (*a*) G. M. Sheldrick, *Acta Crystallogr., Sect. A: Fundam. Crystallogr.*, 1990, **46**, 467; (*b*) G. M. Sheldrick, *SHELXL-97 program for crystal structure refinement*, University of Göttingen, Göttingen, Germany, 1997; (*c*) G. M. Sheldrick, *SADABS*, University of Göttingen, Göttingen, Germany, 1996.

13 R. Thouvenot, M. Fournier, R. Franck and C. Rocchiccioli-Deltcheff, *Inorg. Chem.*, 1984, **23**, 598.

This journal is © The Royal Society of Chemistry 2013

Novel Intercluster Compounds Composed of a Tetra{phosphanegold(I)}oxonium Cation and an α-Keggin Polyoxometalate Anion Linked by Three Monomeric Phosphanegold(I) Units

Takuya Yoshida, Satoshi Matsunaga, and Kenji Nomiya*
Department of Chemistry, Faculty of Science, Kanagawa University, Hiratsuka, Kanagawa 259-1293

(Received August 7, 2013; CL-130728; E-mail: nomiya@kanagawa-u.ac.jp)

The novel intercluster compounds composed of a tetrakis{triphenylphosphanegold(I)}oxonium cation and an α-Keggin polyoxometalate (POM) linked by three monomeric triphenylphosphanegold(I) units, were synthesized. A single peak was observed in the solution $^{31}P\{^{1}H\}$ NMR for these clusters, which is consistent with rapid exchange of the phosphanegold(I) units in the tetra{phosphanegold(I)}oxonium cluster cation with the three monomeric phosphanegold(I) species linked to the POM. Importantly, these compounds may be relevant transition states or intermediates in POM-mediated tetra{phosphanegold(I)}oxonium cluster formation.

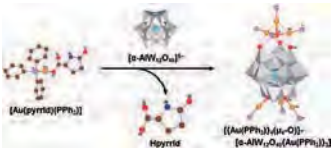

REPRINTED FROM

Chemistry Letters

Vol.42 No.12 2013 p.1487–1489
CMLTAG
December 5, 2013

The Chemical Society of Japan

Published on the web August 31, 2013; doi:10.1246/cl.130728

doi:10.1246/cl.130728
Published on the web August 31, 2013

Novel Intercluster Compounds Composed of a Tetra{phosphanegold(I)}oxonium Cation and an α-Keggin Polyoxometalate Anion Linked by Three Monomeric Phosphanegold(I) Units

Takuya Yoshida, Satoshi Matsunaga, and Kenji Nomiya*
Department of Chemistry, Faculty of Science, Kanagawa University, Hiratsuka, Kanagawa 259-1293

(Received August 7, 2013; CL-130728; E-mail: nomiya@kanagawa-u.ac.jp)

Using highly negatively charged Keggin polyoxometalates (POMs), $[\alpha\text{-}XW_{12}O_{40}]^{5-}$ (X = Al and B), novel intercluster compounds composed of a tetrakis{triphenylphosphanegold(I)}-oxonium cation and an α-Keggin POM linked by three monomeric triphenylphosphanegold(I) units were prepared. A single peak was observed in the solution $^{31}P\{^1H\}$ NMR for these clusters, which is consistent with rapid exchange of the phosphanegold(I) units in the tetra{phosphanegold(I)}oxonium cluster cation with the three monomeric phosphanegold(I) species linked to the POM. Importantly, these compounds may be relevant transition states or intermediates in POM-mediated tetra{phosphanegold(I)}oxonium cluster formation.

The reaction of polyoxometalates (POMs) with cluster cations or macrocations has yielded a diverse set of intercluster compounds. Preparation of these compounds, many of which have interesting structure and sorption properties, has informed how they crystallize and has allowed for the controlled crystal engineering of these materials.[1,2] Intercluster compounds are commonly prepared by the reaction of separately prepared metal cluster cations with POMs.[1,2]

Recently, we discovered the clusterization of monomeric phosphanegold(I) units, $[Au(PR_3)]^+$, during the course of carboxylate elimination of a monomeric phosphanegold(I) carboxylate, [Au(*RS*-pyrrld)(PPh_3)] (*RS*-Hpyrrld: *RS*-2-pyrrolidone-5-carboxylic acid),[3] in the presence of the free-acid form of the Keggin POM, $H_3[\alpha\text{-}PW_{12}O_{40}]\cdot 7H_2O$. This reaction resulted in the formation of a novel intercluster compound, composed of a tetrakis{triphenylphosphanegold(I)}oxonium cluster cation and the Keggin POM anion, with the formula $[\{Au(PPh_3)\}_4(\mu_4\text{-}O)]_3[\alpha\text{-}PW_{12}O_{40}]_2$.[4a] The tetra{phosphanegold(I)}oxonium cluster cation, $[\{Au(PR_3)\}_4(\mu_4\text{-}O)](BF_4)_2$, as the BF_4^- salt, has been previously synthesized via an alternative method by the Schmidbaur group.[5a] We have also prepared the heptakis{triphenylphosphanegold(I)}dioxonium cluster cation, $[\{\{Au(PPh_3)\}_4(\mu_4\text{-}O)\}\{\{Au(PPh_3)\}_3(\mu_3\text{-}O)\}]^{3+}$, by the reaction of [Au(*RS*-pyrrld)(PPh_3)] with the sodium salt of the Keggin POM, $Na_3[\alpha\text{-}PW_{12}O_{40}]\cdot 9H_2O$.[4b] Also, the novel intercluster compounds, $[\{(Au\{P(p\text{-}RPh)_3\})_2(\mu\text{-}OH)\}_2]_3[\alpha\text{-}PM_{12}O_{40}]_2\cdot n$EtOH (R = Me, M = W; R = Me, M = Mo; R = F, M = Mo) have been recently synthesized using the POM-mediated clusterization of monomeric phosphanegold(I) complexes.[4c] These reactions are influenced by the acidity, bulkiness, and high-charge density of the POM and substituents of phosphane ligand.

Element-centered gold clusters, $[E(AuL)_n]^{m+}$ have been studied extensively by Schmidbaur[6a–6d] and Laguna.[6e] For example, a trigold(I)oxonium cluster, $[\{Au(PMe_3)\}_3(\mu_3\text{-}O)]^+$, was found to be a structural motif for chalcogen-centered gold clusters, in that the monomeric units are aggregated through crossed edges.[6b] Element-centered gold clusters are also apt models for the isolobal protic species $[H_3O]^+$ and $[H_4O]^{2+}$, which are currently of interest.[7] In terms of applications, several phosphanegold(I) complexes have been shown to be effective homogeneous catalysts.[8] For example, $[\{Au(PPh_3)\}_3(\mu_3\text{-}O)]BF_4$[5b,5c] effectively catalyzes the Claisen rearrangement of propargyl vinyl ethers.[9] It is hypothesized that the oxonium cation, $[\{Au(PPh_3)\}_3(\mu_3\text{-}O)]^+$, is a source of the catalytically active species, $[Au(PR_3)]^+$.[8f] $[\{Au(PPh_3)\}_3(\mu_3\text{-}O)]BF_4$ has also been utilized as a precursor for the synthesis of novel metal complexes.[10]

The POM-mediated clusterization of monomeric phosphanegold(I) complexes provides an effective synthetic route for the preparation of novel phosphanegold(I) cluster cations, and a library of clusters can be built by the combination of phosphanegold(I) carboxylate with various POMs. However, the clusterization mechanism of the monomeric phosphanegold(I) unit in the presence of the Keggin POMs is still unclear. Herein, we report the synthesis and characterization of two novel intercluster compounds $[\{Au(PPh_3)\}_4(\mu_4\text{-}O)][\alpha\text{-}XW_{12}O_{40}\{Au(PPh_3)\}_3]\cdot 3$EtOH (X = Al (**1**) and B (**2**)), which are composed of a tetrakis{triphenylphosphanegold(I)}oxonium cluster cation, a saturated, negatively charged Keggin POM anion, and three monomeric phosphanegold(I) units linked through OW_2 oxygen atoms of edge-shared WO_6 octahedra. These compounds appear to be intermediates in the formation of the tetra{phosphanegold(I)}oxonium cluster cation from the monomeric phosphanegold(I) units in the presence of the free-acid form of the Keggin POM,[4a] because the solid-state and solution ^{31}P NMR measurements revealed a rapid exchange of phosphanegold(I) with the tetra{phosphanegold(I)}oxonium cluster cation and the three monomeric phosphanegold(I) units linked to the POM.

The novel intercluster compounds were prepared and crystallized by the liquid–liquid diffusion reaction of [Au(*RS*-pyrrld)(PPh_3)] in CH_2Cl_2 with the free-acid form of the highly negatively charged Keggin POM, $H_5[\alpha\text{-}XW_{12}O_{40}]\cdot nH_2O$ (X = Al, $n = 12$; X = B, $n = 14$) in EtOH/H_2O at room temperature (7:1 Au:POM mole ratio). Compounds **1** and **2** were isolated in 51.9% (0.324 g scale) and 44.8% (0.279 g scale) yields, respectively. Synthesis and characterization of the precursors and compounds **1** and **2** are given in Supporting Information.[11]

The chemical equation for the preparation of **1** and **2** is shown in eq 1.

$$7[Au(RS\text{-pyrrld})(PPh_3)] + H_5[\alpha\text{-}XW_{12}O_{40}] + H_2O \rightarrow [\{Au(PPh_3)\}_4(\mu_4\text{-}O)][\alpha\text{-}XW_{12}O_{40}\{Au(PPh_3)\}_3] \quad (X = Al\ (\mathbf{1})\ \text{and}\ B\ (\mathbf{2})) + 7RS\text{-Hpyrrld} \tag{1}$$

Solid-state FT-IR of **1** and **2** showed the characteristic vibrational bands associated with coordinating triphenylphosphane ligands. The carbonyl vibrational bands of the anionic

 © 2013 The Chemical Society of Japan

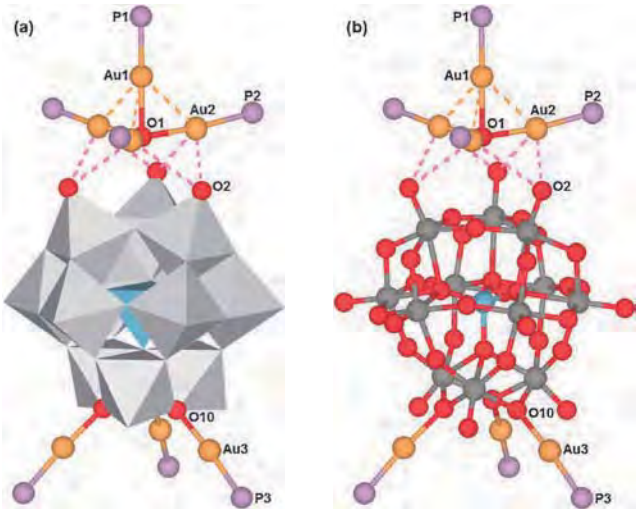

Figure 1. Molecular structure of $[\{Au(PPh_3)\}_4(\mu_4\text{-}O)][\alpha\text{-}AlW_{12}O_{40}\{Au(PPh_3)\}_3]\cdot 3EtOH$ (**1**). (a) Polyhedral representation and (b) ball-and-stick model.

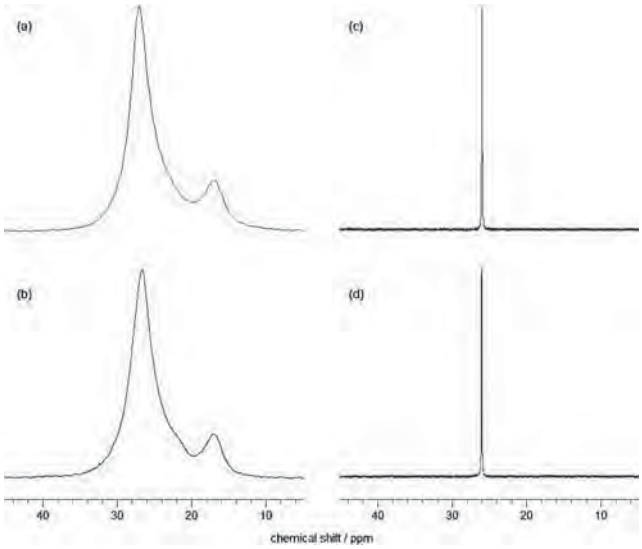

Figure 2. Solid-state CPMAS ^{31}P NMR spectrum of (a) **1** and (b) **2** and the $^{31}P\{^1H\}$ NMR spectrum in DMSO-d_6 of (c) **1** and (d) **2**.

RS-pyrrld ligand in [Au(*RS*-pyrrld)(PPh_3)], present before the reaction, disappeared, suggesting elimination of the carboxylate ligand. Elimination of this ligand was also confirmed by ^1H NMR.

The molecular structures of **1** and **2** were determined by X-ray crystallography; however, it was not possible to define the positions of the phenyl groups due to extensive disorder. Crystal data and selected bond lengths and angles of **1** and **2** are given in Supporting Information.[11] Compound **1** is composed of one tetra{phosphanegold(I)}oxonium cluster cation, $[\{Au(PPh_3)\}_4(\mu_4\text{-}O)]^{2+}$, one Keggin POM anion, $[\alpha\text{-}AlW_{12}O_{40}]^{5-}$, and three monomeric phosphanegold(I) units linked to the OW_2 oxygen atoms of edge-shared WO_6 octahedra of the POM. The tetra{phosphanegold(I)}oxonium cluster cation in **1** adopts a trigonal-pyramidal structure composed of three short edges associated with the Au1 atom, Au1–Au2 2.8929(14) Å, and a triangular plane of the Au2, Au2′, and Au2″ atoms with longer edge lengths (Au2–Au2′: 3.583 Å; Figure 1). The three edges associated with the Au1 atom are longer than the Au–Au separation of metallic gold (2.88 Å),[12a] but shorter than twice the van der Waals radius for gold (3.32 Å).[12b] The bridged-oxygen atom (μ_4-O) was placed within the basal plane composed of the Au2, Au2′, and Au2″ atoms (Au–O–Au: 119.3(3)°), resulting in a point group of C_{3v} for the tetra{phosphanegold(I)}oxonium cluster cation. The distorted tetra{phosphanegold(I)}oxonium cluster cation in **1** is similar to that of the previously reported tetra{phosphanegold(I)}oxonium cluster cation, $[\{Au(PPh_3)\}_4(\mu_4\text{-}O)]^{2+}$, as the counter ion of the POM.[4a] The three gold(I) atoms, Au2, Au2′, and Au2″, in the tetra{phosphanegold(I)}oxonium cluster cation, interact with the terminal oxygen atoms of the Keggin POM (Au2–O2: 3.160 Å). These interactions may contribute to a stabilization of the tetra{phosphanegold(I)}oxonium cluster structure on the Keggin POM.

Three monomeric phosphanegold(I) units link to the OW_2 oxygen atoms of edge-shared WO_6 octahedra of the Keggin POM opposite the tetra{phosphanegold(I)}oxonium cluster cation. The Au–Au distance between the coordinating monomeric phosphanegold(I) units is relatively long (Au3–Au3′: 5.379 Å), indicating no aurophilic interaction among these units. Although an intermolecular interaction such as "phenyl embraces"[13] may be suggested among an apical phosphanegold(I) unit in the tetra{phosphanegold(I)}oxonium cluster cation and the three phosphanegold(I) units at the bottom, it is unclear because of extensive disorder of the phenyl groups.

Since the POM-mediated clusterization of the monomeric phosphanegold(I) units is strongly regulated by the acidity and the negative charge of the POM,[4] the structures obtained may be intermediate states, and it is likely that the POM acts as a template for the formation of the tetra{phosphanegold(I)}oxonium cluster cation. The dynamic behavior of these coordinating phosphanegold(I) units is also supported by solid-state and solution ^{31}P NMR. Compound **2** is isostructural with **1**, with the difference being the heteroatom in the Keggin POM (B vs. Al).

Solid-state CPMAS ^{31}P NMR of **1** showed two broad signals at 17.0 and 27.1 ppm, with relative intensities of 1:6, originating from the inequivalent triphenylphosphane groups (Figure 2a). The peak at 17.0 ppm is assignable to one apical triphenylphosphane group in the tetra{phosphanegold(I)}oxonium cluster cation, and the signal at 27.1 ppm is assignable to the three basal triphenylphosphane groups in the tetra{phosphanegold(I)}oxonium cluster cation and three monomeric phosphanegold(I) units linked to the POM. Interestingly, the solution $^{31}P\{^1H\}$ NMR spectrum of **1** in DMSO-d_6 displayed only one sharp singlet at 26.00 ppm (Figure 2c). The presence of a singlet can be explained by the rapid exchange of phosphanegold(I) units among the tetra{phosphanegold(I)}oxonium cluster cation, the three monomeric phosphanegold(I) units linked to the Keggin POM, and the monomeric $[Ph_3PAu(DMSO)]^+$ cation present in solution. This exchange is likely a result of the weak Au–O bonds between the monomeric phosphanegold(I) units and the Keggin POM. The monomeric phosphanegold(I) units linked to the POM may indicate a transient state in the formation of the tetra{phosphanegold(I)}oxonium cluster cation from

 © 2013 The Chemical Society of Japan

monomeric phosphanegold(I) units. Compound **1** showed low solubility even in DMSO and DMF, and further information in solution by temperature-dependent ^{31}P NMR was not obtained.

The same behavior was observed for compound **2**. The solid-state CPMAS ^{31}P NMR spectrum of **2** showed two broad signals at 17.0 and 26.7 ppm, with a relative intensity ratio of 1:6 (Figure 2b). In the solution ^{31}P{^{1}H} NMR spectrum, a singlet was observed at 26.08 ppm (Figure 2d), which is an averaged signal due to the rapid exchange process in solution.

In summary, the clusterization of monomeric phosphanegold(I) units to form the new compounds $[\{Au(PPh_3)\}_4(\mu_4\text{-}O)][\alpha\text{-}XW_{12}O_{40}\{Au(PPh_3)\}_3]\cdot 3EtOH$ (X = Al (**1**) and B (**2**)) was achieved by the reaction of phosphanegold(I) carboxylate with free-acid forms of Keggin POMs. These compounds, prepared using negatively charged Keggin POM (5−) with the heteroatoms Al^{3+} and B^{3+}, appear to be intermediates in the formation of the tetra{phosphanegold(I)}oxonium cluster cation. The present work establishes that in addition to the POM acidity (proton vs. sodium), the high negative charge of the POM (5− vs. 3− or 4−) determines its reactivity. It should be also noted that the OW_2 oxygen atoms of edge-shared WO_6 octahedra in the Keggin POM act as multicentered active binding sites[14] for the monomeric phosphanegold(I) cations generated from the elimination of the carboxylate ligands in the presence of the POM. This work shows that clusterization is strongly dependent upon the POM, and it provides fundamental details about the molecular architecture of POM-mediated element-centered gold clusters.

This work was supported by JSPS KAKENHI Grant number 22550065 and also by the Strategic Research Base Development Program for Private Universities of the Ministry of Education, Culture, Sports, Science and Technology of Japan.

References and Notes

1 M. Schulz-Dobrick, M. Jansen, *Eur. J. Inorg. Chem.* **2006**, 4498.

2 S. Uchida, N. Mizuno, *Coord. Chem. Rev.* **2007**, *251*, 2537.

3 R. Noguchi, A. Hara, A. Sugie, K. Nomiya, *Inorg. Chem. Commun.* **2006**, *9*, 355.

4 a) K. Nomiya, T. Yoshida, Y. Sakai, A. Nanba, S. Tsuruta, *Inorg. Chem.* **2010**, *49*, 8247. b) T. Yoshida, K. Nomiya, S. Matsunaga, *Dalton Trans.* **2012**, *41*, 10085. c) T. Yoshida, S. Matsunaga, K. Nomiya, *Dalton Trans.* **2013**, *42*, 11418.

5 a) H. Schmidbaur, S. Hofreiter, M. Paul, *Nature* **1995**, *377*, 503. b) A. N. Nesmeyanov, E. G. Perevalova, Y. T. Struchkov, M. Y. Antipin, K. I. Grandberg, V. P. Dyadchenko, *J. Organomet. Chem.* **1980**, *201*, 343. c) Y. Yang, V. Ramamoorthy, P. R. Sharp, *Inorg. Chem.* **1993**, *32*, 1946.

6 a) H. Schmidbaur, A. Schier, *Chem. Soc. Rev.* **2012**, *41*, 370. b) K. Angermaier, H. Schmidbaur, *Inorg. Chem.* **1994**, *33*, 2069. c) K. Angermaier, H. Schmidbaur, *Chem. Ber.* **1994**, *127*, 2387. d) H. Schmidbaur, A. Schier, *Chem. Soc. Rev.* **2008**, *37*, 1931. e) M. C. Gimeno, A. Laguna, *Chem. Soc. Rev.* **2008**, *37*, 1952.

7 a) H. G. Raubenheimer, H. Schmidbaur, *Organometallics* **2012**, *31*, 2507. b) E. S. Stoyanov, G. Gunbas, N. Hafezi, M. Mascal, I. V. Stoyanova, F. S. Tham, C. A. Reed, *J. Am. Chem. Soc.* **2012**, *134*, 707.

8 a) D. J. Gorin, F. D. Toste, *Nature* **2007**, *446*, 395. b) A. S. K. Hashmi, *Chem. Rev.* **2007**, *107*, 3180. c) Z. Li, C. Brouwer, C. He, *Chem. Rev.* **2008**, *108*, 3239. d) A. S. K. Hashmi, M. Rudolph, *Chem. Soc. Rev.* **2008**, *37*, 1766. e) D. J. Gorin, B. D. Sherry, F. D. Toste, *Chem. Rev.* **2008**, *108*, 3351. f) H. Schmidbaur, A. Schier, *Z. Naturforsch., B: Chem. Sci.* **2011**, *66*, 329. g) M. Rudolph, A. S. K. Hashmi, *Chem. Soc. Rev.* **2012**, *41*, 2448.

9 a) B. D. Sherry, F. D. Toste, *J. Am. Chem. Soc.* **2004**, *126*, 15978. b) B. D. Sherry, L. Maus, B. N. Laforteza, F. D. Toste, *J. Am. Chem. Soc.* **2006**, *128*, 8132. c) K. Sakaguchi, T. Okada, T. Shinada, Y. Ohfune, *Tetrahedron Lett.* **2008**, *49*, 25. d) P. Mauleón, J. L. Krinsky, F. D. Toste, *J. Am. Chem. Soc.* **2009**, *131*, 4513.

10 a) A. Blumenthal, H. Beruda, H. Schmidbaur, *J. Chem. Soc., Chem. Commun.* **1993**, 1005. b) A. Singh, U. Anandhi, M. A. Cinellu, P. R. Sharp, *Dalton Trans.* **2008**, 2314. c) A. Singh, P. R. Sharp, *Inorg. Chim. Acta* **2008**, *361*, 3159.

11 Supporting Information is available electronically on the CSJ-Journal Web site, http://www.csj.jp/journals/chem-lett/index.html.

12 a) A. F. Wells, *Structural Inorganic Chemistry*, 4th ed., Clarendon Press, Oxford, **1975**, p. 1020. b) A. Bondi, *J. Phys. Chem.* **1964**, *68*, 441.

13 a) I. Dance, M. Scudder, *Chem.—Eur. J.* **1996**, *2*, 481. b) I. Dance, M. Scudder, *J. Chem. Soc., Dalton Trans.* **2000**, 1579.

14 a) M. Filowitz, R. K. C. Ho, W. G. Klemperer, W. Shum, *Inorg. Chem.* **1979**, *18*, 93. b) W. H. Knoth, R. L. Harlow, *J. Am. Chem. Soc.* **1981**, *103*, 4265.

 © 2013 The Chemical Society of Japan

ChemComm

RSC Publishing

COMMUNICATION

View Article Online
View Journal | View Issue

Published on 28 May 2013. Downloaded by Kanagawa University on 28/06/2013 01:40:52.

Cite this: *Chem. Commun.*, 2013, **49**, 6662

Received 2nd April 2013,
Accepted 24th May 2013

DOI: 10.1039/c3cc42395f

www.rsc.org/chemcomm

First radical homopolymerisation of 2-trifluoromethacrylic acid in water and study of the degradation of the resulting homopolymers†

Yogesh Patil,[a] Hisao Hori,[b] Hirotaka Tanaka,[b] Takehiko Sakamoto[b] and Bruno Ameduri*[a]

The radical homopolymerisation of 2-trifluoromethacrylic acid (MAF) initiated by $Na_2S_2O_8$ in water, under the influence of pH, led to original water soluble surfactants, the decomposition of which was investigated. The value of the square of the propagation rate constant to the termination rate constant, k_p^2/k_{te}, of MAF was 4×10^{-3} l mol^{-1} s^{-1} at 80 °C.

2-Trifluoromethacrylic acid (MAF) is an industrial monomer synthesized in three steps from 3,3,3-trifluoropropene and mainly used as a precursor of different derivatives, monomers and copolymers.[1] Many surveys developed by Narita report that the homopolymerisation of MAF can be successfully achieved using an anionic initiator.[2] In contrast, the radical homopolymerisation of MAF or MAF-ester failed.[1,3–8] In this study, the failure to polymerize was ascribed mainly due to (i) an inefficient propagation step due to the small interaction of the low energy singly occupied molecular orbital (SOMO) and the lowest unoccupied molecular orbital (LUMO) of the acrylate, (ii) the higher *e*-values of fluorinated vinyl monomers than those of non-fluorinated analogues, (iii) the highest electronegativity of fluorine atoms that induces a high electron-withdrawing inductive effect that would reduce the electron density of the vinyl group and (iv) the strong acidic nature of the MAF monomer ($pK_a = 2.1$).[9] As a matter of fact, itaconic acid is difficult to homopolymerize but recent studies have shown that under certain basic conditions, this acidic monomer is able to homopolymerize.[10] Hence, it was of interest to investigate the influence of the pH value on the homopolymerisation of MAF. Besides, perfluorooctanesulfonate ($C_8F_{17}SO_3^-$) and perfluorooctanoic acid ($C_7F_{15}COOH$), which have been widely used as surface treatment agents in the industry until the mid-2000s, are on the way to being banned, because of their persistency, toxicity and bioaccumulation. Thus, US environmental protection agency and European REACH regulations seek alternative fluorochemical surfactants.[11] For the industrial application of fluorochemical surfactants, their degradation behaviour is challenging. Elucidation of the degradation of fluorochemicals would be desired not only for the reduction of the environmental impact, but also for the development of a waste treatment technology instead of incineration (since the decomposition of fluorochemicals by incineration requires high temperatures and produces hazardous HF gas, which damages the walls of incinerators). Hence, it would be ideal if they could be mineralized into F^- ions because F^- ions can combine with Ca^{2+} ions to form CaF_2 as a raw material for synthesis of hydrofluoric acid, which has been facing an increasing global demand.

Recently, performing reactions under pressurized hot water (PHW) has been recognized as an innovative and environmentally benign reaction technique.[12] Recently, practical-plant-scale decomposition of hazardous chemicals in PHW was demonstrated,[13,14] and mineralisation of fluorochemicals such as perfluoroalkylsulfonates,[15,16] perfluoroalkylether sulfonates,[17] cyclic perfluoroalkanesulfonylamide,[18] and perfluorinated ion-exchange membranes[19] was also achieved *via* oxidation or reduction processes in PHW. Thus, the present communication deals with (i) the homopolymerisation of MAF in water initiated under radical conditions without any surfactant (Scheme 1) and (ii) the degradation study of poly(MAF) in PHW leading to CaF_2 by addition of $Ca(OH)_2$ to the reaction system.

The results of the homopolymerisation of MAF initiated by sodium persulphate are summarized in Table 1. The reaction temperature was chosen to be 80 °C for which $Na_2S_2O_8$ has a half life of 1 h. Preliminary blank runs (runs 1 and 2, Table 1) showed that at acidic pH (2 and 5) appreciable amounts of the polymer could not be produced under the adopted reaction conditions. In contrast, at higher pH (8–9, neutralised with NaOH), a good yield and high monomer conversion was observed (run 3, Table 1). It is remarkable that the highest yield (95%) and conversion of monomer (97%) ascertained in this preliminary run are yet higher with respect

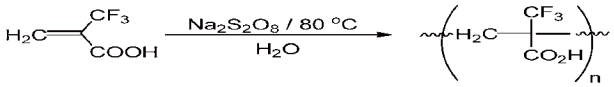

Scheme 1 Radical homopolymerisation of 2-trifluoromethacrylic acid (MAF) initiated by persulphate salts in water.

[a] *Ingénierie et Architectures Macromoléculaires, Institut Charles Gerhardt UMR 5253, 8, rue de l'École Normale, 34296 Montpellier Cedex1, France. E-mail: bruno.ameduri@enscm.fr*

[b] *Department of Chemistry, Faculty of Science, Kanagawa University, 2946 Tsuchiya, Hiratsuka 259-1293, Japan*

† Electronic supplementary information (ESI) available: ^{1}H NMR spectrum, kinetic curve and TGA of poly(MAF) homopolymer; experimental section. See DOI: 10.1039/c3cc42395f

This journal is © The Royal Society of Chemistry 2013

Published on 28 May 2013. Downloaded by Kanagawa University on 28/06/2013 01:40:52.

Table 1 Homopolymerisation of 2-trifluoromethacrylic acid (MAF) initiated by $Na_2S_2O_8$ (2 mmol) at 80 °C for 16 hours

Run	pH	Solvent (60 mL)	Press (bar)	Conv. (%)	Yield (%)	M_n	$Đ$
1	2	Water	0	0	—	—	—
2	5	Water	0	0	—	—	—
3	9	Water	0	97	95	4000	2.8
4	2	Water	30	0	—	—	—
5	9	Water	30	98	85	4200	2.9
6	9	CH_3CN	0	66	64	3200	2.8
7[a]	9	Water	0	49	26	9000	3.3
8[b]	9	Water	0	98	96	4500	2.9

[a] $Na_2S_2O_8$ = 1 mmol. [b] Neutralised with KOH.

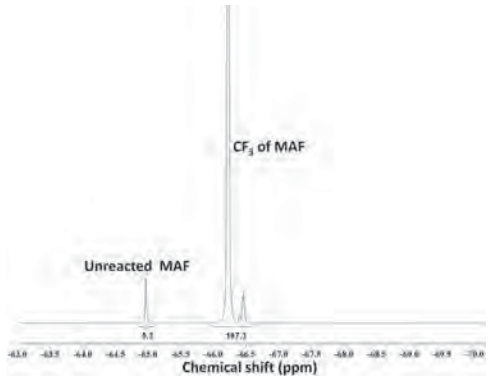

Fig. 1 ^{19}F NMR spectrum of poly(2-trifluoromethacrylic acid) (run 3 Table 1) recorded in D_2O at room temperature.

to those of the anionic initiators[2] and represent the best result for the first time in the radical homopolymerisation of MAF.

Polymer characterization using ^1H NMR (Fig. S1, ESI†) and ^{19}F NMR spectroscopy (Fig. 1) evidenced that the basic polymerisation took place with sharp formation of poly(MAF) with a higher conversion and no side reactions. Characteristic signals in ^1H NMR spectra from 6.5 to 6.7 ppm and at 3.4 ppm are assigned to ethylenic protons and CH_2 of MAF, respectively. The ^{19}F NMR spectra exhibit signals at −64.8 (I_1) and −66.8 (I_2) assigned to the CF_3 group of unreacted MAF and MAF units, respectively.[8] By comparing I_1 and I_2 integrals of both peaks, the conversion rate of MAF was assessed from eqn (1).[8b]

$$\text{MAF conversion (\%)} = I_2/(I_1 + I_2) \quad (1)$$

Besides the acidic factor of MAF, we studied the effect of pressure on polymerisation (runs 4 and 5 Table 1). Usually hydrostatic pressure is known to favourably affect the propagation–depropagation equilibrium during polymerisation and consequently this increases the rate of polymerisation.[20] However, even at high pressure (30 bar N_2) but at acidic pH (run 4 Table 1) no polymer could be obtained. In contrast, when the pH was basic, PMAF was obtained in fair amount (run 5 Table 1) but was still low when compared to PMAF produced without pressure. Thus, it is necessary to maintain basic conditions since the COO^- anion enhances the density of the double bond p electron of MAF (instead of an acid since the pK_a of MAF is 2.1). A significant decrease in yield as well as monomer conversion were noted when acetonitrile (AN) (run 6, Table 1) was used as the solvent, and the initiator concentrations decreased (run 7, Table 1). A similar yield, conversion and characteristics of PMAF were observed when MAF was neutralised with both KOH (run 8, Table 1) and NaOH (run 3, Table 1).

For kinetic study, ^{19}F NMR spectroscopy was used to monitor the MAF conversion (eqn (1)) and Fig. S2 (ESI†) shows the ^{19}F NMR spectra of the total product mixture in D_2O at different reaction times for experiment 3 (Table 1). The evolution of MAF conversion appeared to be linear *versus* time (Fig. S3, ESI†) allowing the determination of k_p^2/k_{te}. Once integrated, eqn (S1) (ESI†) leads to the Tobolsky's law (eqn (S2), ESI†). Thus, plotting $\ln([M]_0/[M])$ *versus* $[1 - \exp(-k_d \times t/2)]$ led to a straight line, the slope of which was directly related to the k_p^2/k_{te} value (Fig. S4, ESI†), by choosing k_d and an efficiency of 2.8×10^{-3} min^{-1} and 0.5[21] for $Na_2S_2O_8$ in water at 80 °C. Hence, the k_p^2/k_{te} value obtained for MAF homopolymerisation at 80 °C was 4×10^{-3} l mol^{-1} s^{-1} which is lower than the values found for two similar hydrogenated monomers: acrylic acid (56×10^6 l mol^{-1} s^{-1})[21,22] and methacrylic acid (32×10^6 l mol^{-1} s^{-1})[21,23] at 25 °C. The molar masses and polydispersity indices of poly(MAF) homopolymers were assessed using size exclusion chromatography with poly(acrylic acid) standards in aqueous buffer. They ranged between 4000 to 9000 g mol^{-1} and from 2.8 to 3.3 (Fig. S5, ESI†). In addition, their thermal stabilities were assessed using thermogravimetric analysis (TGA) under an oxygen atmosphere. Poly(MAF) started to decompose from 150 °C with 10% of weight loss while sharp decomposition was achieved at 250 °C (Fig. S6, ESI†). The glass transition temperature (T_g) of these polymers ranged between 30 and 35 °C (Fig. S7, ESI†).

These poly(MAF) oligomers were water soluble and may act as surfactants, and it was worth investigating their decomposition under pressurized hot water, PHW. The effect of temperature on the decomposition of poly(MAF)-H was achieved by PHW reactions under oxygen.[24] The initial polymer contained 439 μmol of the fluorine atoms, as measured using combustion ion-chromatography. When the reaction was carried out at 80 °C, 91.8 μmol of F^- was detected in the reaction solution (Fig. 2). This value corresponds to a F^- yield [(moles of F^- formed)/(moles of initial fluorine atoms in the polymer, *i.e.*, 439 μmol)] of 20.9%. Raising the reaction temperature increased the reactivity. The F^- formation became prominent above 250 °C, at which point the F^- yield reached 93.4%. Therefore, mineralisation of the fluorine component in the initial poly(MAF)-H to F^- was well achieved. A further increase in the temperature resulted in almost the same F^- formation: when the reaction was carried out at 350 °C, the highest tested temperature, the F^- yield was 92.0%. In the gas phase, CO_2 was detected as a major product. The CO_2 formation increased with increasing temperature, and showed a saturation tendency above 250 °C (plateau in Fig. 2). When the reaction was carried out at 350 °C, the formed CO_2 reached

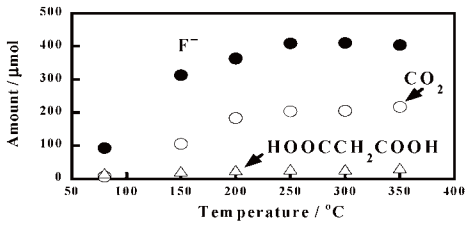

Fig. 2 Effect of temperature on the decomposition of poly(MAF)-H with O_2 for 6 h. An aqueous solution (10 mL) containing poly(MAF)-H (30 mg) was transferred into the reactor, which was pressurized with O_2 (0.60 MPa), then the reactor temperature was raised.

Published on 28 May 2013. Downloaded by Kanagawa University on 28/06/2013 01:40:52.

217 μmol. On the other hand, the moles of carbon atoms in the initial poly(MAF)-H was 634 μmol based on the elementary analysis. Hence, the CO_2 yield [(moles of CO_2 formed)/(moles of carbon atoms in the initial polymer)] was 34.2%, which was considerably lower than the corresponding F^- yield (92.0%). This finding indicated that carbon-containing species bearing no fluorine atom, other than CO_2, were formed. GC/MS measurement was carried out for the gas phase after the reaction at 350 °C to assess the gaseous products, and C_2H_4 and C_2H_6 were detected. However, these amounts were nearly trace level: 0.02 μmol and 0.01 μmol for C_2H_4 and C_2H_6, respectively, suggesting that additional hydrocarbon species were mainly present in the reaction solution but not in the gas phase. Consistently, ATR-IR spectra of the reaction solutions showed broad peaks around 1600–1750 cm^{-1}, which can be assigned to COOH groups. Therefore, we employed ion-chromatography to quantify organic acids in the reaction solutions, and found that at least malonic acid, $HOOCCH_2COOH$, was present as a major product. The amount of $HOOCCH_2COOH$ gradually increased with increasing temperature, and reached 32 μmol at 350 °C (Fig. 2).

To eliminate possible degradation under oxidative conditions, the reaction system was changed from O_2 to argon. The effect of temperature on the decomposition of poly(MAF)-H in PHW under argon is shown in Fig. S8 (ESI†). The temperature dependence of the F^- formation was similar to that with O_2 (Fig. 2). When the reaction was carried out at 350 °C with argon, the F^- yield reached 90.4%, which is slightly lower (92.0%) than that obtained when the reaction was carried out in the presence of O_2.

These results indicate that the mineralisation of the fluorine component in poly(MAF)-H was almost unaffected by the nature of gas. The effect of temperature on the formation of $HOOCCH_2COOH$ (Fig. S8, ESI†) was also similar to that observed in previous experiments carried out under O_2 (Fig. 2): the amount of $HOOCCH_2COOH$ reached 27 μmol, while the corresponding value with O_2 was 32 μmol. In contrast, a significant difference in the result ascribed to the gas was observed in the CO_2 formation. The reactions with argon resulted in lower CO_2 formation at higher temperatures (250–350 °C, compare Fig. 2 and Fig. S8, ESI†). This result indicates that O_2 plays some role in the mineralisation of the carbon component of poly(MAF-H) to CO_2. The decomposition of poly(MAF)-K in PHW was also examined. As for poly(MAF)-H, F^-, CO_2 and $HOOCCH_2COOH$ were detected as major products. The effect of the temperature on the formation of these products from reactions with O_2 is shown in Fig. S9 (ESI†).

The amount of F^- increased with increasing temperature, and the F^- yield reached 98.4% at 250 °C. This result indicates that mineralisation of the fluorine component of poly(MAF)-K occurred efficiently in subcritical water in the presence of O_2, as well as poly(MAF)-H. In addition, almost complete mineralisation of the fluorine component of poly(MAF)-K was also observed when the reaction was carried out under an argon atmosphere (Fig. S10, ESI†). The temperature dependence of the formation of $HOOCCH_2COOH$ was also similar to that in the presence of O_2. When the reactions were carried out under argon, CO_2 formation was lower than that released under O_2 (Fig. S9 and S10, ESI†), which indicates that O_2 plays a role in the mineralisation of poly(MAF)-K, similar to poly(MAF)-H.

To examine whether CaF_2 was formed in the present reaction, a similar reaction involving $Ca(OH)_2$ was performed as above. When the aqueous solution of poly(MAF)-H was heated at 350 °C for 6 h under O_2 in the presence of a stoichiometric amount of $Ca(OH)_2$, a white precipitate was observed. The XRD pattern of the collected powder indicated that this species was X-ray spectrometrically pure CaF_2 (Fig. S11, ESI†). The molar amount of CaF_2 was 168 μmol, in which the amount of fluorine atoms was 336 μmol. On the other hand, the amount of fluorine atoms in the initial poly(MAF)-H was 439 μmol. Therefore, 76.5% of the fluorine atoms in the initial polymer were transformed to CaF_2.

In conclusion, for the first time, the radical homopolymerisation of a highly electron-withdrawing acidic monomer (MAF) was successfully carried out under pH conditions in water. The value of the square of the propagation rate to the termination rate of MAF, k_p^2/k_{te}, was 4×10^{-3} l mol^{-1} s^{-1} at 80 °C. The decomposition of poly(MAF)-H and poly(MAF)-K in PHW in the presence of O_2 or argon was assessed and the fluorine components of these chemicals were almost completely mineralized to F^- ions after treatment above *ca.* 250 °C for 6 h. When the aqueous solution of poly(MAF)-H was heated with the stoichiometric amount of $Ca(OH)_2$ at 350 °C for 6 h under O_2, X-ray spectrometrically pure CaF_2 was obtained in *ca.* 77% yield.

Notes and references

1 Y. Patil and B. Ameduri, *Prog. Polym. Sci.*, 2013, **38**, 703–739.
2 T. Narita, *Prog. Polym. Sci.*, 1999, **24**, 1095–1148.
3 (*a*) H. Ito, M. D. Miller and C. G. Willson, *Macromolecules*, 1982, **15**, 915–920; (*b*) H. Ito, B. Giese and R. Engelbrecht, *Macromolecules*, 1984, **17**, 2204–2205.
4 (*a*) S. Iwatsuki, A. Kondo and H. Harashima, *Macromolecules*, 1984, **17**, 2473–2479; (*b*) S. Iwatsuki, T. Itoh and T. Iida, *J. Polym. Sci., Part A: Polym. Chem.*, 1994, **32**, 1389–1392.
5 Q. Xu and H. L. Frisch, *J. Polym. Sci., Part A: Polym. Chem.*, 1994, **32**, 2803–2807.
6 M. Aglietto, E. Passaglia, L. M. di Mirabello, C. Botteghi, S. Paganelli, U. Matteoli and G. Menchi, *Macromol. Chem. Phys.*, 1995, **196**, 2843–2853.
7 K. T. McElroy, S. T. Purrington, C. L. Bumgardner and J. P. Burgess, *J. Fluorine Chem.*, 1999, **95**, 117–120.
8 (*a*) Y. Patil, T. Ono and B. Ameduri, *ACS Macro Lett.*, 2012, **1**, 315–320; (*b*) Y. Patil and B. Ameduri, *Polym. Chem.*, 2013, **4**, 2783–2799.
9 E. P. C. Lai and S. Y. Feng, *Microchem. J.*, 2003, **75**, 159–168.
10 Y. Durant, M. Cao and M. Chirat, *US Pat.*, 2009/0022436, 2009; Y. Durant, M. Cao and M. Chirat, *US Pat.*, 2010/0016153, 2010, (to itaconics).
11 (*a*) *New Chemical Review of Alternatives for PFOA and Related Chemicals*, US Environmental Protection Agency, Washington, DC, USA; (*b*) A. Zaggia and B. Ameduri, *Curr. Opin. Colloid Interface Sci.*, 2012, **17**, 188–195.
12 *Chemical Synthesis Using Supercritical Fluids*, ed. P. G. Jessop and W. Leitner, Wiley VCH, Weinheim, Germany, 1999.
13 S. B. Hawthorne, A. J. M. Lagadec, D. Kalderis, A. V. Lilke and D. J. Miller, *Environ. Sci. Technol.*, 2000, **34**, 3224–3228.
14 S. I. Kawasaki, T. Oe, N. Anjoh, T. Nakamori, A. Suzuki and K. Arai, *Process Saf. Environ. Prot.*, 2006, **84**, 317–324.
15 H. Hori, Y. Nagaoka, A. Yamamoto, T. Sano, N. Yamashita, S. Taniyasu, S. Kutsuna, I. Osaka and R. Arakawa, *Environ. Sci. Technol.*, 2006, **40**, 1049–1054.
16 H. Hori, Y. Nagaoka, T. Sano and S. Kutsuna, *Chemosphere*, 2008, **70**, 800–806.
17 H. Hori, M. Murayama and S. Kutsuna, *Chemosphere*, 2009, **77**, 1400–1405.
18 H. Hori, T. Sakamoto, Y. Kimura and A. Takai, *Catal. Today*, 2012, **196**, 132–136.
19 H. Hori, M. Murayama, T. Sano and S. Kutsuna, *Ind. Eng. Chem. Res.*, 2010, **49**, 464–471.
20 (*a*) J. Rzayev and J. Penelle, *J. Polym. Sci., Part A: Polym. Chem.*, 2001, **40**, 836–843; (*b*) J. Rzayev and J. Penelle, *Angew. Chem., Int. Ed.*, 2004, **43**, 1691–1694.
21 J. Brandrup and E. H. Immergut, *Polymer Handbook*, New York, 3rd edn, 1989.
22 T. M. Karaputadse, A. I. Kurilova, D. A. Topchiev and V. A. Kabanov, *Vysokomol. Soedin., Ser. A*, 1972, **14**, 323.
23 N. N. Bashenova, B. A. Egorov and Y. D. Semchikov, *Dokl. Akad. Nauk SSSR*, 1979, **245**, 621.
24 The reaction time was 6 h and the initial poly(MAF)-H was 30 mg.

 This journal is © The Royal Society of Chemistry 2013

I&EC research
Industrial & Engineering Chemistry Research

Article

pubs.acs.org/IECR

Decomposition of Perfluorinated Ionic Liquid Anions to Fluoride Ions in Subcritical and Supercritical Water with Iron-Based Reducing Agents

Hisao Hori,* Yoshinari Noda, Akihiro Takahashi, and Takehiko Sakamoto

Department of Chemistry, Faculty of Science, Kanagawa University, 2946 Tsuchiya, Hiratsuka, Kanagawa 259-1293, Japan

ABSTRACT: Decomposition of perfluorinated ionic liquid anions $[(CF_3SO_2)_2N]^-$ and $[(C_4F_9SO_2)_2N]^-$ in subcritical and supercritical water was investigated with the aim of developing a technique to recover the fluorine component from ionic liquid wastes. Addition of zerovalent iron to the reaction system dramatically increased the yield of F^-: when the reaction of $[(CF_3SO_2)_2N]^-$ was carried out at 344 °C for 6 h, the F^- yield was 69.0%, which is 186 times the yield without iron. Increasing the temperature and reaction time in the presence of zerovalent iron further increased the yield: when $[(CF_3SO_2)_2N]^-$ and zerovalent iron were heated in supercritical water at 375 °C for 18 h, 76.8% of the fluorine content in the initial $[(CF_3SO_2)_2N]^-$ was transformed into F^-. $[(CF_3SO_2)_2N]^-$ also decomposed in the presence of FeO, which underwent in situ disproportionation to form zerovalent iron, which acted as the reducing agent. Although the FeO-induced decomposition of $[(CF_3SO_2)_2N]^-$ was initially slower than the zerovalent iron-induced decomposition, after prolonged reaction (18 h) at 378 °C, the F^- yield of the former reaction reached 85.7%, which was the highest yield obtained. This result suggests that the zerovalent iron that formed in situ reacted preferentially with the substrate, as opposed to water.

INTRODUCTION

Ionic liquids (ILs) have been widely investigated as reaction and extraction media for green chemistry applications.[1,2] Furthermore, there has been increasing interest in the electrochemical applications of ILs, mainly as electrolytes safer than organic solvents.[3] In particular, perfluorinated IL anions are being introduced in many electrochemical devices, including lithium-ion batteries, polymer electrolyte membrane fuel cells, and dye-sensitized solar cells, owing to their nonflammability, high thermal stability, wide electrochemical windows, high ion conductivity, and low viscosity.[3−6] Wider use of ILs will require that waste treatment be established. Incineration is one method for decomposing these chemicals. However, incineration requires high temperatures to break the strong C−F bonds, and hydrogen fluoride gas is formed, which can seriously damage the firebrick of an incinerator. In addition, these anions do not biodegrade under either aerobic or anaerobic conditions,[7] which indicates that conventional microbial degradation processes are not applicable for treatment of waste ILs. If perfluorinated IL anions could be decomposed to F^- by means of environmentally benign techniques, the well-established protocol for treatment of F^- could be used, whereby Ca^{2+} is added to the system to form CaF_2, which is a raw material for hydrofluoric acid. Thus, the development of such a method would allow the recycling of fluorine, the global demand for which is increasing.

Reactions in subcritical and supercritical water have been recognized as an innovative and environmentally benign waste-treatment technique, owing to the high diffusivity and low viscosity of these media, as well as their ability to hydrolyze many organic compounds.[8] Subcritical water is defined as hot water with sufficient pressure to maintain the liquid state, and supercritical water is defined as water at temperatures and pressures higher than the critical point, 374 °C and 22.1 MPa. Recently, such water was used for pilot- and practical-plant-scale decomposition of hazardous compounds such as trinitrotoluene[9] and polychlorinated biphenyls.[10] We previously demonstrated that a perfluorosulfonic acid membrane polymer for fuel cells is efficiently decomposed in subcritical water in the presence of metals.[11]

In this study, we investigated the decomposition of two typical perfluorinated IL anions, $[(CF_3SO_2)_2N]^-$ and $[(C_4F_9SO_2)_2N]^-$, in subcritical and supercritical water in the presence of an oxidizing agent (O_2) or an iron-based reducing agent (zerovalent iron, FeO, or Fe_3O_4). The latter conditions (except Fe_3O_4) effectively decomposed the anions to F^-. This is the first report not only on the decomposition of perfluorinated IL anions in subcritical and supercritical water but also on a technique aimed at waste treatment that successfully achieves the efficient formation of F^- ions from the anions.

EXPERIMENTAL SECTION

Materials. Bis(trifluoromethanesulfonyl)imide ($[(CF_3SO_2)_2N]^-$, >99.5%) and bis(nonafluorobutanesulfonyl)-imide ($[(C_4F_9SO_2)_2N]^-$, >99%) were obtained from SynQuest Laboratories (Alachua, FL) and Mitsubishi Material Electronic Chemicals (Akita, Japan) as lithium and potassium salts, respectively. Zerovalent iron (>99.9%, <53 μm), FeO (>99.9%, <180 μm), and Fe_3O_4 (>99.9%, <150 μm) powders were purchased from Kojundo Chemical Laboratory (Saitama, Japan) and used as received. Argon (99.99%), O_2 (99.999%), CO_2 (0.995%)/N_2, and CF_3H (0.971%)/N_2 gases were

Received: June 3, 2013
Revised: August 22, 2013
Accepted: August 26, 2013
Published: August 26, 2013

ACS Publications © 2013 American Chemical Society

Table 1. Decomposition of Perfluorinated IL Anions in Subcritical Water under Various Reaction Conditions

entry[a]	substrate	gas	iron-based reducing agent	temp (°C)	press (MPa)	remaining substrate (%)	F^- yield (%)[e]
1	$[(CF_3SO_2)_2N]^-$[b]	Ar	none	344	15.9	98.8	0.37
2	$[(CF_3SO_2)_2N]^-$[b]	O_2	none	345	16.0	95.4	1.11
3	$[(CF_3SO_2)_2N]^-$[b]	Ar	Fe	344	16.5	1.35	69.0
4	$[(CF_3SO_2)_2N]^-$[b]	O_2	Fe	343	15.5	1.84	39.6
5	$[(CF_3SO_2)_2N]^-$[b]	Ar	FeO	345	15.7	36.8	48.2
6	$[(CF_3SO_2)_2N]^-$[b]	Ar	Fe_3O_4	345	16.0	97.3	3.63
7	$[(C_4F_9SO_2)_2N]^-$[c]	Ar	none	346	15.6	17.3	9.50
8	$[(C_4F_9SO_2)_2N]^-$[c]	Ar	Fe	346	15.4	<0.16[d]	37.0

[a]An aqueous solution (10 mL) containing the substrate and additive (9.60 mmol) was introduced into the reactor, which was pressurized with argon or oxygen (0.60 MPa) and then heated for 6 h. [b]Initial amount, 16.2 μmol. [c]Initial amount, 1.62 μmol. [d]Below the detection limit. [e]F^- yield (%) = [(moles of F^- formed)/(moles of fluorine content in initial substrate)] × 100.

purchased from Taiyo Nippon Sanso (Tokyo, Japan). Standard gas mixtures, N_2O (1.0%)/air, and C_2H_4 (1.0%)/air were prepared from N_2O and C_2H_4 (99.5%, GL Sciences, Tokyo, Japan), respectively. Other reagents were of high purity and were obtained from Wako Pure Chemical Industries (Osaka, Japan).

Reaction Procedures. Reactions were carried out in a stainless steel high-pressure reactor (35.1 mL volume) equipped with a thermocouple and a stainless steel screw cap. The screw cap was connected to a pressure gauge for measuring the pressure in the reactor and to a sampling port for analyzing gaseous products. A gold vessel (24.6 mL, 2.8 cm i.d.) was fitted into the reactor to prevent contamination from the reactor material. In a typical run using $[(CF_3SO_2)_2N]^-$, an argon-saturated aqueous (Milli-Q) solution (10 mL) containing $[(CF_3SO_2)_2N]^-$ (16.2 μmol, 1.62 mM) and zerovalent iron powder (9.60 mmol) was introduced into the gold vessel, and the reactor was pressurized to 0.60 MPa with argon and sealed. The reactor was placed in an oven, and the reactor temperature was raised to the desired value (193−375 °C) and held there for a specified time (e.g., 6 h), after which the reactor was quickly cooled to room temperature. The reaction solution was subjected to ion chromatography, high-performance liquid chromatography/mass spectrometry (LC/MS), and electrospray ionization (ESI)-MS. The gas phase was subjected to gas chromatography (GC)/MS and GC, and the solid phase (iron) was subjected to X-ray diffractometry (XRD). We also conducted control experiments in the absence of zerovalent iron, with other iron-based reducing agents (FeO and Fe_3O_4), under O_2 instead of argon, and with another IL anion, $[(C_4F_9SO_2)_2N]^-$.

Analysis. An ion-chromatography system (IC-2001, Tosoh, Tokyo, Japan) consisting of an automatic sample injector (30-μL injection volume), a degasser, a pump, a guard column (TSKguard column Super IC-A, 4.6-mm i.d., 1.0-cm length, Tosoh), a separation column (TSKgel Super IC-Anion, 4.6-mm i.d., 15-cm length, Tosoh), a column oven (40 °C), and a conductivity detector with a suppressor device was used to measure the F^- concentrations. The mobile phase was an aqueous solution containing $Na_2B_4O_7$ (6 mM), H_3BO_3 (15 mM), and $NaHCO_3$ (0.2 mM), and the flow rate was 0.8 mL min^{-1}.

The concentrations of the IL anions were quantified by means of an ion-chromatography system (IC-2010, Tosoh). The separation column was a Tosoh TSKgel Super Anion HS column (4.6 mm i.d., 10 cm length); the mobile phase was an aqueous solution containing acetonitrile (39%), $NaHCO_3$ (7 mM), and Na_2CO_3 (7 mM); and the flow rate was 0.8 mL min^{-1}. The detection limits for $[(CF_3SO_2)_2N]^-$ and $[(C_4F_9SO_2)_2N]^-$ were 0.17 μM (48 μg L^{-1}) and 0.27 μM (157 μg L^{-1}), respectively, and were calculated from a signal-to-noise ratio of 3.

An LC/MS system (LCMS-2010 EV, Shimadzu, Kyoto, Japan) with a separation column (TSKgel ODS-80TSQA) was used to identify the intermediates in the reaction solutions. The mobile phase was a mixture (50:50, v/v) of methanol and aqueous CH_3COONH_4 (1 mM, adjusted to pH 4.0 with acetic acid), and the flow rate was 0.2 mL min^{-1}. Analyses were carried out in negative-ion mode, and the electrospray probe voltage was 4.50 kV. ESI-MS was also carried out without the separation column in the LC/MS system with methanol as the mobile phase.

The products in the gas phase were analyzed by GC/MS (QP2010 SE, Shimadzu) with a fused silica capillary column (Rt-Q-BOND, Restek, Bellefonte, PA, USA). The carrier gas was helium, and the oven temperature was held constant at 30 °C. A GC system (GC 323, GL Sciences, Tokyo, Japan) with a thermal conductivity detector was also used. The column was packed with active carbon (60/80 mesh), and the carrier gas was argon. The oven and detector temperatures were 110 and 130 °C, respectively. Changes in iron-based reducing agents that occurred during the reactions were determined by XRD with Cu Kα radiation (Multiflex, Rigaku, Tokyo, Japan). X-ray photoelectron spectroscopy (XPS) measurements were also carried out at Nissan Arc (Yokosuka, Japan), with a Quantum-2000 instrument (Physical Electronics, Eden Prairie, MN, USA) with Al Kα radiation.

■ RESULTS AND DISCUSSION

Reactions in Subcritical Water in the Absence or Presence of an Iron-Based Reducing Agent. The results for reactions of perfluorinated IL anions in subcritical water at 343−346 °C and at a constant reaction time of 6 h are summarized in Table 1. When the initial amount of $[(CF_3SO_2)_2N]^-$ was 16.2 μmol (i.e., the concentration in the initial aqueous solution was 1.62 mM) and the reaction was performed under argon without any additive (entry 1), most (98.8%) of the initial substrate remained after the reaction, and the yield of F^- was only 0.37%. This observation indicates that $[(CF_3SO_2)_2N]^-$ was stable in pure subcritical water, reflecting the anion's high thermal and chemical stability. In an attempt to facilitate the decomposition of $[(CF_3SO_2)_2N]^-$, we first examined the possibility of using O_2 to induce oxidative decomposition. However, introduction of 0.60 MPa (4.99 mmol) of O_2 only slightly enhanced the decomposition of $[(CF_3SO_2)_2N]^-$: 95.4% of the initial substrate remained, and

the F^- yield was low (1.11%, entry 2), even though the molar amount of introduced O_2 was 308 times that of the initial substrate (16.2 μmol).

Next, we examined the decomposition of $[(CF_3SO_2)_2N]^-$ in the presence of iron-based reducing agents. When the reaction was carried out in the presence of zerovalent iron (9.60 mmol) under an argon atmosphere, the amount of the $[(CF_3SO_2)_2N]^-$ substrate dramatically decreased to 1.35% of the initial amount (entry 3). Simultaneously, the F^- yield reached 69.0%, which is 186 times the yield without iron (entry 1). On the other hand, when the reaction was carried out in the presence of zerovalent iron under O_2, the amount of remaining substrate (1.84%, entry 4) was similar to that under argon, while the F^- yield (39.6%, entry 4) was much lower than that under argon. This fact indicates that the presence of O_2 suppresses the mineralization of the substrate to F^- induced by iron.

Addition of FeO also enhanced the decomposition of the substrate, although the enhancement was not as great as that observed with zerovalent iron: the amount of residual $[(CF_3SO_2)_2N]^-$ was 36.8%, and the F^- yield was 48.2% (entry 5). In contrast, Fe_3O_4 did not enhance the decomposition of the substrate: 97.3% of the initial $[(CF_3SO_2)_2N]^-$ remained, and the F^- yield was only 3.63% (entry 6).

The reactivity of $[(C_4F_9SO_2)_2N]^-$ in subcritical water differed somewhat from that of $[(CF_3SO_2)_2N]^-$. After 6 h of reaction, the amount of $[(C_4F_9SO_2)_2N]^-$ decreased to 17.3% even in pure subcritical water, although the F^- yield remained low (9.50%, entry 7). This fact suggests that although the initial step of the decomposition of $[(C_4F_9SO_2)_2N]^-$ proceeded in pure subcritical water, the subsequent steps leading to F^- formation did not. The decomposition of $[(C_4F_9SO_2)_2N]^-$ was enhanced by zerovalent iron: the proportion of remaining substrate decreased to <0.16% of the initial amount (below the detection limit of ion chromatography), and the F^- yield increased to 37.0% (entry 8), which was 3.9 times the yield without iron.

Decomposition in the Presence of Zerovalent Iron. Among the iron-based reducing agents tested, zerovalent iron gave the highest F^- yields, so we further investigated the decomposition of $[(CF_3SO_2)_2N]^-$ to F^- with zerovalent iron at various reaction times and temperatures (Figure 1). In addition to analyzing the solution-phase products, we also analyzed the gas-phase products. When the reaction was carried out at 344 °C for 6 h, H_2 made up 42.7% of the total gas after the reaction, corresponding to 3.38 mmol of H_2. The formation of this large amount of H_2 indicates that zerovalent iron reacted not only with $[(CF_3SO_2)_2N]^-$ but also with subcritical water. As described later, zerovalent iron transformed to Fe_3O_4 in our reaction condition (eq 1).

$$3Fe + 4H_2O \rightarrow Fe_3O_4 + 4H_2 \quad (1)$$

According to eq 1, the amount of H_2 observed here (3.38 mmol) indicates that 2.54 mmol of the zerovalent iron was consumed by the reaction with H_2O. This value was much larger than the initial amount of $[(CF_3SO_2)_2N]^-$ (16.2 μmol).

Besides H_2, small amounts of CO_2 and CF_3H were detected. The reaction-time dependences of the amount of remaining $[(CF_3SO_2)_2N]^-$ and the amounts of CO_2, CF_3H, and F^- at 344 °C are shown in Figure 1a. The amount of $[(CF_3SO_2)_2N]^-$ in the reaction solution decreased with increasing reaction time, following pseudo-first-order kinetics with a rate constant of 0.77 h^{-1}, and the decrease in the amount of substrate was

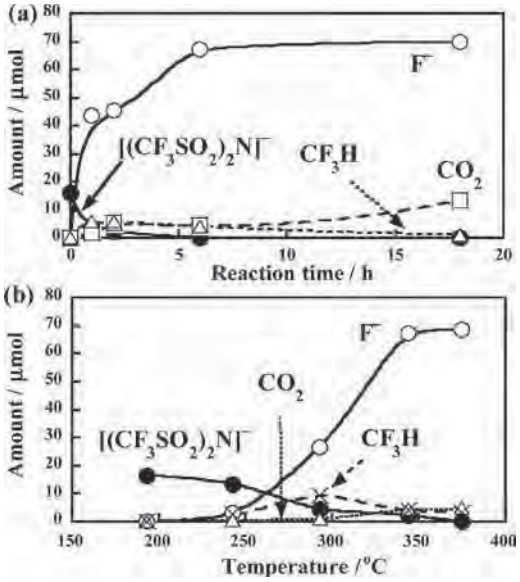

Figure 1. (a) Reaction-time and (b) temperature dependence of $[(CF_3SO_2)_2N]^-$ decomposition in the presence of iron: detected molar amounts of $[(CF_3SO_2)_2N]^-$, F^-, CO_2, and CF_3H. An aqueous solution (10 mL) of $[(CF_3SO_2)_2N]^-$ (16.2 μmol, 1.62 mM) and zerovalent iron powder (9.60 mmol) were introduced into the reactor, which was pressurized with argon (0.60 MPa) and (a) heated at 344 °C for 1−18 h or (b) heated at 193−375 °C for 6 h.

accompanied by an increase in the amount of F^-. After 6 h, the amount of $[(CF_3SO_2)_2N]^-$ in the reaction solution decreased to 0.22 μmol, indicating that 98.7% of the initial amount disappeared. At the same time, the F^- amount reached 67.1 μmol, which corresponds to a F^- yield of 69.0%. At a prolonged reaction time, F^- formation became saturated: after 18 h, the F^- amount reached 70.0 μmol (72.0% yield). In contrast, the amount of the minor product CF_3H in the gas phase increased during the first 1 h of the reaction and then decreased. By 18 h, CF_3H had almost disappeared. This result indicates that the CF_3H that formed decomposed under the reaction conditions. The disappearance of CF_3H is advantageous because this species is a greenhouse gas with a global-warming potential of 14,800 for a time horizon of 100 years.[12]

We also investigated the temperature dependence of the reaction at a constant reaction time of 6 h (Figure 1b). At 193 °C, no decomposition of $[(CF_3SO_2)_2N]^-$ was observed. Substrate decomposition was observed at above 243 °C, and decomposition increased with increasing temperature, resulting in increasing F^- formation. At 375 °C, the temperature at which the water reached the supercritical state, the substrate completely disappeared from the reaction solution, and 68.6 μmol of F^- formed (70.6% yield). Prolonged reaction at 375 °C increased the amount of F^- formed: after 18 h, the F^- yield reached 76.8%.

The reaction-time and reaction-temperature dependences of the decomposition of $[(C_4F_9SO_2)_2N]^-$ in the presence of zerovalent iron are shown in Figure 2. When the reaction was carried out at 346 °C, the substrate disappeared from the reaction solution within 1 h, and the decrease in the amount of substrate was accompanied by increases in the amounts of F^- and CO_2 (Figure 2a). In this case, no formation of CF_3H was observed. After disappearance of the substrate, the amounts of F^- and CO_2 continued to increase. This result suggests that

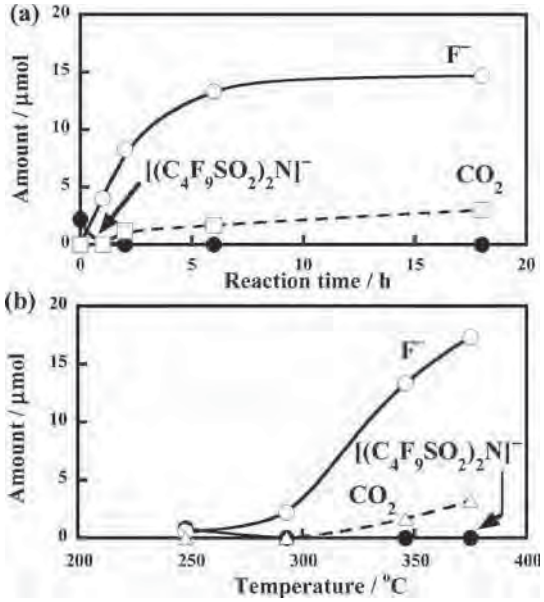

Figure 2. (a) Reaction-time and (b) temperature dependence of $[(C_4F_9SO_2)_2N]^-$ decomposition in the presence of iron: detected molar amounts of $[(C_4F_9SO_2)_2N]^-$, F^-, and CO_2. An aqueous solution (10 mL) of $[(C_4F_9SO_2)_2N]^-$ (1.62 μmol; 0.16 mM) and zerovalent iron powder (9.60 mmol) were introduced into the reactor, which was pressurized with argon (0.60 MPa) and (a) heated at 346 °C for 1−18 h or (b) heated at 248−375 °C for 6 h.

some reaction intermediate(s) produced F^- and CO_2 during this period. After 18 h, the amount of F^- reached 14.7 μmol (50.4% yield). Although $[(C_4F_9SO_2)_2N]^-$ disappeared faster than $[(CF_3SO_2)_2N]^-$ (Figure 1a), the F^- yield from $[(C_4F_9SO_2)_2N]^-$ at 18 h was lower than that from $[(CF_3SO_2)_2N]^-$ (72.0%). The temperature dependence of the reaction of $[(C_4F_9SO_2)_2N]^-$ is shown in Figure 2b. When the reaction was carried out at 248 °C, the proportion of remaining substrate decreased to 52.2% of the initial amount, but little F^- or CO_2 formed. However, F^- and CO_2 formed at temperatures above ~300 °C. At 375 °C, 17.3 μmol of F^- formed (59.3% yield). Prolonged reaction at 375 °C slightly increased the amount of F^- formed: after 18 h, the F^- yield reached 60.9%.

To detect reaction intermediates, we analyzed reaction solutions by LC/MS. When $[(CF_3SO_2)_2N]^-$ was decomposed in the presence of zerovalent iron, the total-ion mass chromatograms of several reaction solutions showed a peak that yielded signals at m/z 148, which corresponds to $CF_3SO_2NH^-$. No peak for $CF_3SO_3^-$, which has an m/z value of 149 and a different retention time, was observed. The presence of $CF_3SO_2NH^-$ clearly indicates that the decomposition of $[(CF_3SO_2)_2N]^-$ proceeded through cleavage of the N−S bond. The reaction-time dependence at 344 °C of the LC/MS peak intensity for $CF_3SO_2NH^-$ is shown in Figure 3. The peak intensity increased during the initial stage of the reaction (<1 h) and then decreased, indicating that the formed $CF_3SO_2NH^-$ decomposed under the reaction conditions. In other words, $CF_3SO_2NH^-$ was a reaction intermediate. A similar phenomenon was also observed during the reaction of $[(C_4F_9SO_2)_2N]^-$ in the presence of zerovalent iron. The ESI-MS spectra of the reaction solutions of $[(C_4F_9SO_2)_2N]^-$ before and after heating for 6 h are shown in Figure 4. Before the reaction, the spectrum showed a single peak (at m/z 580),

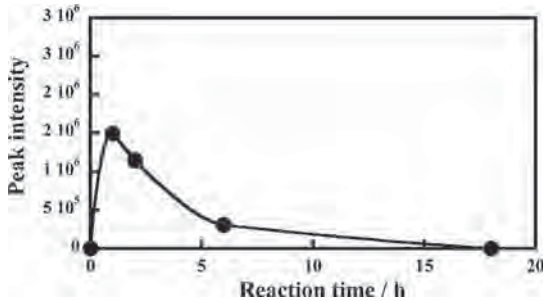

Figure 3. Reaction-time dependence of the intensity of the LC/MS peak for $CF_3SO_2NH^-$. The reaction conditions were the same as those described in the caption of Figure 1a.

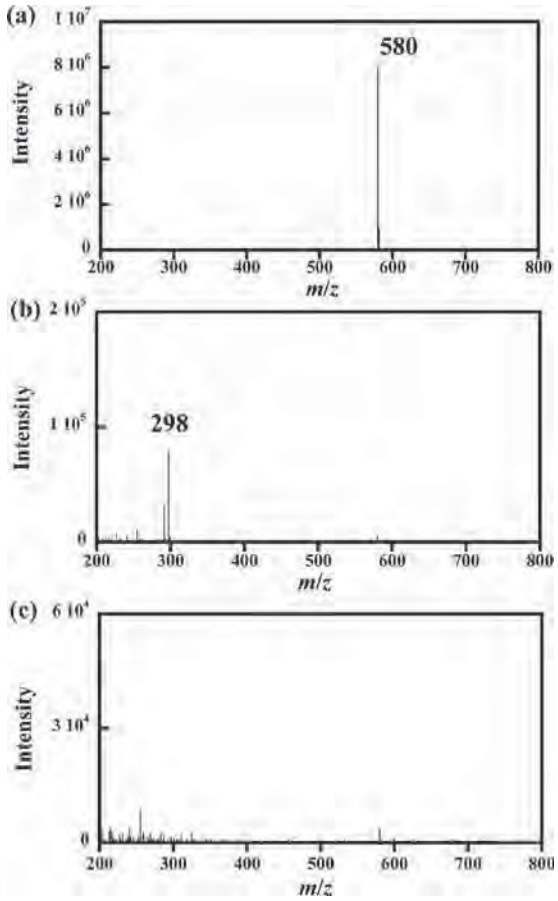

Figure 4. ESI-MS spectra of the reaction solutions (a) before heating and after heating at (b) 346 and (c) 375 °C for 6 h. The reaction conditions were the same as those described in Figure 2b.

corresponding to the initial anion $[(C_4F_9SO_2)_2N]^-$ (Figure 4a). When the reaction was carried out at 346 °C for 6 h in the presence of zerovalent iron, the resulting reaction solution showed a peak at m/z 298, which was assigned to $C_4F_9SO_2NH^-$ (Figure 4b). Raising the reaction temperature to 375 °C led to the disappearance of the peak (Figure 4c). These results clearly indicate that $C_4F_9SO_2NH^-$ was a reaction intermediate.

To elucidate the changes in zerovalent iron during reactions, we compared the XRD patterns of the iron powder before and after reaction of $[(CF_3SO_2)_2N]^-$ at 375 °C for 6 h (Figures 5a

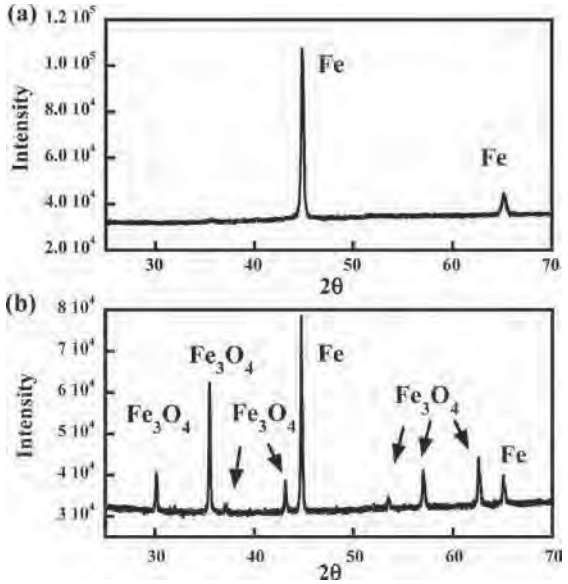

Figure 5. XRD patterns of the iron powder (a) before and (b) after reaction. For the measurement of pattern (b), an aqueous solution (10 mL) of $[(CF_3SO_2)_2N]^-$ (16.2 μmol; 1.62 mM) and zerovalent iron powder (9.60 mmol) were introduced into the reactor, which was pressurized with argon (0.60 MPa) and heated at 375 °C for 6 h, after which the iron powder was recovered.

and 5b, respectively). The pattern of the recovered iron powder showed peaks that were assigned to Fe_3O_4, indicating that the zerovalent iron was oxidized to Fe_3O_4 as $[(CF_3SO_2)_2N]^-$ decomposed: the formation of Fe_3O_4 suppressed the decomposition of the substrate because this iron species had almost no reactivity toward the substrate, as shown in entry 6 in Table 1.

As for the fate of sulfur atoms in the substrate during the iron-induced reaction, we detected SO_4^{2-} in the reaction solution. However, the amount was considerably lower than the amount of sulfur atoms in the substrate: for example, the reaction of $[(CF_3SO_2)_2N]^-$ (16.2 μmol) at 344 °C for 6 h (entry 3 in Table 1) resulted in 0.34 μmol of SO_4^{2-}. This fact suggests that most of the formed SO_4^{2-} remained on the iron surface. We also surveyed the nitrogen-containing products, and GC/MS measurement indicated that NO, NO_2, and N_2O did not form during the iron-induced mineralization of $[(CF_3SO_2)_2N]^-$. However, when the reaction was carried out under O_2 (entry 2 in Table 1), a trace amount of N_2O (0.42 μmol) was detected.

Decomposition in the Presence of FeO. As described above, zerovalent iron induced efficient decomposition of the IL anions in subcritical and supercritical water. However, the iron reacted not only with the substrate (and reaction intermediates) but also with subcritical and supercritical water to form Fe_3O_4, which was unreactive toward the substrate.

Iron(II) oxide undergoes disproportionation to Fe and Fe_3O_4 at higher temperatures (>257 °C) (eq 2),[13,14] although to our knowledge this reaction has not been reported in subcritical or supercritical water:

$$4FeO \rightarrow Fe + Fe_3O_4 \quad (2)$$

If the disproportionation did occur in subcritical or supercritical water, zerovalent iron would form in situ, and the formed iron might be preferentially consumed by reaction with the substrate than with water. To test this possibility, we carried out the reaction of $[(CF_3SO_2)_2N]^-$ in the presence of FeO, despite the fact that its reactivity at 345 °C for 6 h was lower than that of zerovalent iron (compare entries 3 and 5 in Table 1).

The reaction-time dependences of the amounts of remaining $[(CF_3SO_2)_2N]^-$ and the amounts of the products formed at 345 °C are shown in Figure 6a. The amount of $[(CF_3SO_2)_2N]^-$

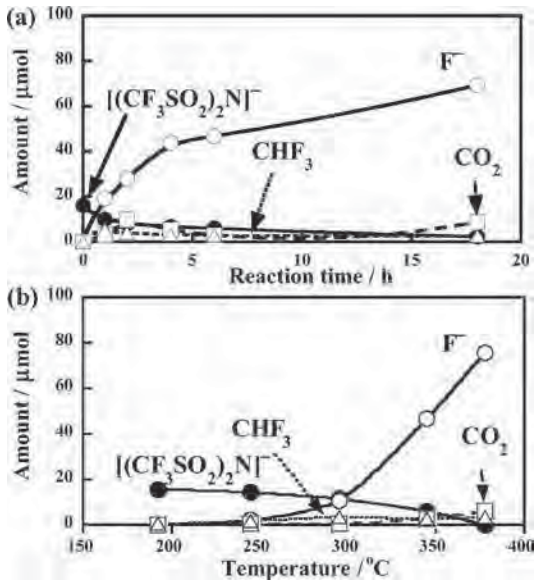

Figure 6. (a) Reaction-time and (b) temperature dependence of $[(CF_3SO_2)_2N]^-$ decomposition in the presence of FeO in subcritical water: detected molar amounts of $[(CF_3SO_2)_2N]^-$, F^-, CO_2 and CF_3H. An aqueous solution (10 mL) of $[(CF_3SO_2)_2N]^-$ (16.2 μmol; 1.62 mM) and FeO powder (9.60 mmol) were introduced into the reactor, which was pressurized with argon (0.60 MPa) and (a) heated at 345 °C for 1−18 h or (b) heated at 193−378 °C for 6 h.

in the reaction solution decreased with increasing reaction time, but the decrease of $[(CF_3SO_2)_2N]^-$ did not follow pseudo-first-order kinetics. This is not surprising, because the disproportionation of FeO to Fe and Fe_3O_4 occurred simultaneously during this period, as shown in the XRD pattern of the recovered FeO powder (Figure 7b). After 6 h, the XRD pattern of the recovered FeO powder from the reaction mixture showed only peaks assignable to zerovalent iron and Fe_3O_4 (Figure 7c). As the reaction time was extended beyond 6 h, the amount of $[(CF_3SO_2)_2N]^-$ continued to decrease, and the amount of F^- continued to increase (Figure 6a). Because Fe_3O_4 did not decompose $[(CF_3SO_2)_2N]^-$ (as mentioned above), the decomposition of the substrate observed after 6 h of reaction must have been induced by zerovalent iron. That is, the iron that formed in situ acted as the real reducing agent for the decomposition of the substrate. Although during the initial reaction period (~6 h), the decomposition of $[(CF_3SO_2)_2N]^-$ proceeded more slowly in the presence of FeO than in the presence of zerovalent iron, the F^- amount reached 69.3 μmol (71.3% yield) after 18 h, at which time the yield was almost the same as the yield observed when zerovalent iron was present from the beginning of the reaction (72.0%). Compared to the XRD pattern of the recovered solid after 345 °C for 6 h (Figure 7c) with that of the solid recovered after the same reaction conditions conducted with zerovalent iron (the pattern was almost the same as Figure 5b), the amount of zerovalent iron

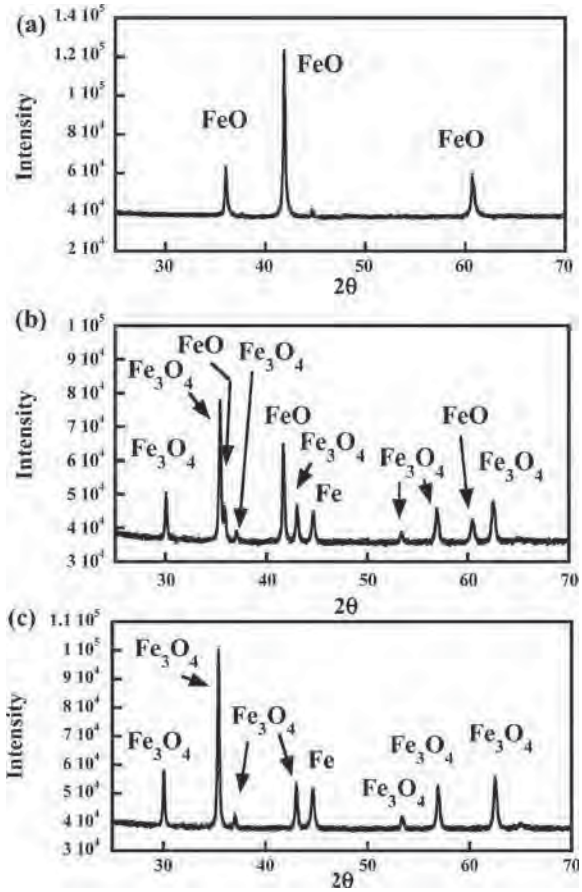

Figure 7. XRD patterns of the FeO powder (a) before and (b, c) after reactions at 345 °C. An aqueous solution (10 mL) of $[(CF_3SO_2)_2N]^-$ (16.2 μmol, 1.62 mM) and FeO powder (9.60 mmol) were introduced into the reactor, which was pressurized with argon (0.60 MPa) and heated for (b) 1 h or (c) 6 h, after which the solid was recovered.

produced in situ from FeO must have been much lower than the remaining amount when zerovalent iron was used (the initial amounts of added FeO and zerovalent iron were the same, 9.60 mmol). Nevertheless the two reaction conditions resulted in almost the same F^- yields after a long reaction time (18 h). This fact suggests that the zerovalent iron formed in situ from the disproportionation of FeO reacted preferentially with the substrate. Consistently, the amounts of H_2 were almost constant (0.31−0.33 mmol) during the FeO-induced decomposition of $[(CF_3SO_2)_2N]^-$ at 345 °C (Figure 6a). The temperature dependence of the reaction of $[(CF_3SO_2)_2N]^-$ in the presence of FeO is shown in Figure 6b. Decomposition of the substrate increased substantially at above ~300 °C, at which temperature the disproportionation of FeO was clearly observed. At 378 °C, F^- formation reached 75.8 μmol (78.0% yield), which is higher than the yield when zerovalent iron was present from the beginning of the reaction (70.6%). Prolonged reaction further increased the F^- yield. The reaction of $[(CF_3SO_2)_2N]^-$ in the presence of FeO at 378 °C for 18 h afforded a F^- yield of 85.7%, the highest yield among all the reaction conditions tested. As for the fate of carbon in the substrate, we detected CO_2 and CF_3H (as described above) and also detected a trace of C_2H_4 (below the quantification limit) in the gas phase. However, the carbon recovery (the molar ratio of total carbon content in the CO_2 and CF_3H formed to that in the initial substrate before reaction) was 52.3% after the reaction at 378 °C for 18 h in the presence of FeO, which led to the highest F^- yield. This fact suggests that the rest of the carbon-containing species were mainly present on the surface of the FeO used.

To detect the possible presence of the fluorine-containing species on the surface of the recovered FeO powder after the reaction at 378 °C for 18 h, we measured the XPS spectrum for the region corresponding to the binding energy of the F(1s) core electrons. The spectrum showed a dominant peak around 684 eV, which can be assigned to negatively charged monovalent fluorine, F^- (Figure 8). This result indicates that

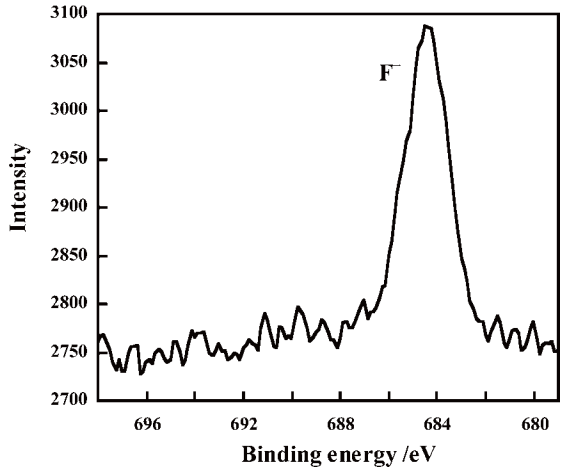

Figure 8. XPS spectrum [(F(1s) region] of the recovered FeO powder after reaction at 378 °C for 18 h. An aqueous solution (10 mL) of $[(CF_3SO_2)_2N]^-$ (16.2 μmol, 1.62 mM) and FeO powder (9.60 mmol) were introduced into the reactor, which was pressurized with argon (0.60 MPa) and heated, after which the solid was recovered.

F^- ions are present not only in the reaction solution but also on the surface of the FeO used. If species containing fluorine−carbon bonds are present on the surface, the peak corresponding to fluorine bonded to carbon (F−C) should appear around 689 eV. The absence of the F−C peak in the XPS spectrum indicates that this reaction completely mineralized the substrate on the solid surface.

■ CONCLUSION

We investigated the decomposition of IL anions $[(CF_3SO_2)_2N]^-$ and $[(C_4F_9SO_2)_2N]^-$ in subcritical and supercritical water. Addition of zerovalent iron to the reaction system dramatically accelerated the decomposition of these anions to F^-. When $[(CF_3SO_2)_2N]^-$ and zerovalent iron were allowed to react at 375 °C for 18 h, 76.8% of the fluorine content in the initial $[(CF_3SO_2)_2N]^-$ was transformed into F^-. During the iron-induced reactions, $CF_3SO_2NH^-$ was detected as an intermediate, indicating that the decomposition was initiated by N−S bond cleavage. Zerovalent iron also enhanced the yield of F^- from the reaction of $[(C_4F_9SO_2)_2N]^-$. The decomposition of $[(CF_3SO_2)_2N]^-$ was also enhanced in the presence of FeO, which underwent in situ disproportionation to form Fe_3O_4 and zerovalent iron, which acted as the real reducing agent for the substrate. Although $[(CF_3SO_2)_2N]^-$ decomposed more slowly in the presence of FeO than in the presence of zerovalent iron during the initial reaction period, the F^- yield of the former reaction reached 85.7% after a

prolonged reaction time (18 h, 378 °C). This yield was higher than that obtained when zerovalent iron was added at the beginning of the reaction.

Further application of this method to perfluorinated ILs with several organic cations is being investigated in our laboratory.

■ AUTHOR INFORMATION

Corresponding Author

*Phone: +81-463-59-4111. Fax: +81-463-58-9688. E-mail: h-hori@kanagawa-u.ac.jp.

Notes

The authors declare no competing financial interest.

■ ACKNOWLEDGMENTS

This work was supported in part by a Grant-in-Aid for Scientific Research from the Japan Society for the Promotion of Sciences (JSPS).

■ REFERENCES

(1) Jessop, P. G. Searching for green solvents. *Green Chem.* **2011**, *13*, 1391.

(2) *Ionic Liquids in Synthesis*; Wasserscheid, P., Welton, T., Eds.; Wiley-VCH: Weinheim, Germany, 2007.

(3) *Electrochemical Aspects of Ionic Liquids*; Ohno, H., Ed.; Wiley: Hoboken, NJ, 2011.

(4) Valencia, H.; Kohyama, M.; Tanaka, S.; Matsumoto, H. First-principles study of EMIM-FAFSA molecule adsorption on a Li(100) surface as a model for Li-Ion battery electrodes. *J. Phys. Chem. C* **2012**, *116*, 8493.

(5) Ong, S. P.; Andreussi, O.; Wu, Y.; Marzari, M.; Ceder, G. Electrochemical windows of room-temperature ionic liquids from molecular dynamics and density functional theory calculations. *Chem. Mater.* **2011**, *23*, 2979.

(6) Sakaebe, H.; Matsumoto, H.; Tatsumi, K. Application of room temperature ionic liquids to Li batteries. *Electrochim. Acta* **2007**, *53*, 1048−1054.

(7) Neumann, J.; Cho, C. W.; Steudte, S.; Köser, J.; Uerdingen, M.; Thöming, J.; Stolte, S. Biodegradability of fluoroorganic and cyano-based ionic liquid anions under aerobic and anaerobic conditions. *Green Chem.* **2012**, *14*, 410.

(8) *Chemical Synthesis Using Supercritical Fluids*; Jessop, P. G., Leitner, W., Eds.; Wiley-VCH: Weinheim, Germany, 1999.

(9) Hawthorne, S. B.; Lagadec, A. J. M.; Kalderis, D.; Lilke, A. V.; Miller, D. J. Pilot-scale destruction of TNT, RDX, and HMX on contaminated soils using supercritical water. *Environ. Sci. Technol.* **2000**, *34*, 3224.

(10) Kawasaki, S.-I.; Oe, T.; Anjoh, N.; Nakamori, T.; Suzuki, A.; Arai, K. Practical supercritical water reactor for destruction of high concentration polychlorinated biphenyls (PCB) and dioxin waste streams. *Process Saf. Environ. Prot.* **2006**, *84*, 317.

(11) Hori, H.; Murayama, M.; Sano, T.; Kutsuna, S. Decomposition of perfluorinated ion-exchange membrane to fluoride ions by using zerovalent metals in subcritical water. *Ind. Eng. Chem. Res.* **2010**, *49*, 464.

(12) *IPCC Fourth Assessment Report: Climate Change 2007*: Working Group I: The Physical Science Basis. Intergovernmental Panel on Climete Change. Geneva, Switzerland. http://www.ipcc.ch/publications_and_data/ar4/wg1/en/ch2s2-10-2.html (accessed June 1, 2013).

(13) Broussard, L. Disproportionation of wustite. *J. Phys. Chem.* **1969**, *73*, 1848.

(14) Stølen, S.; Glöcker, R.; Grønvold, F. Nearly stoichiometric iron monoxide formed as a metastable intermediate in a two-stage disproportionation of quenched wüstite. Thermodynamic and kinetic aspects. *Thermochim. Acta* **1995**, *256*, 91.

Author's personal copy

Chemosphere 93 (2013) 2732–2737

Contents lists available at ScienceDirect

Chemosphere

journal homepage: www.elsevier.com/locate/chemosphere

Visible light-induced decomposition of a fluorotelomer unsaturated carboxylic acid in water with a combination of tungsten trioxide and persulfate

Hisao Hori [a,b,*], Atsushi Ishiguro [a], Kohei Nakajima [a], Taizo Sano [b], Shuzo Kutsuna [b], Kazuhide Koike [b]

[a] Department of Chemistry, Faculty of Science, Kanagawa University, 2946 Tsuchiya, Hiratsuka 259-1293, Japan
[b] National Institute of Advanced Industrial Science and Technology (AIST), AIST Tsukuba West, 16-1 Onogawa, Tsukuba 305-8569, Japan

HIGHLIGHTS

- $C_3F_7CF{=}CHCOOH$ was not decomposed by visible light and either TiO_2 or WO_3 under O_2.
- Irradiation in the presence of WO_3 and $K_2S_2O_8$ clearly decomposed $C_3F_7CF{=}CHCOOH$.
- The photochemical decomposition of $C_3F_7CF{=}CHCOOH$ was greater under argon than under O_2.
- Under O_2, formed H_2O_2 may have interfered with the photochemical decomposition.

GRAPHICAL ABSTRACT

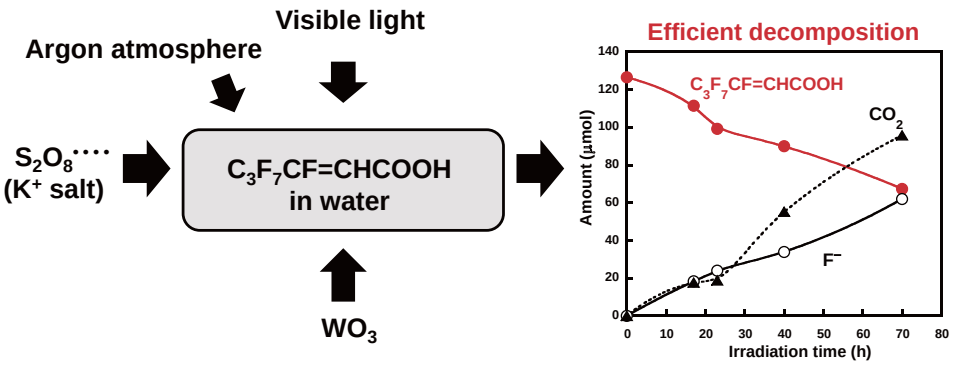

ARTICLE INFO

Article history:
Received 20 May 2013
Received in revised form 1 September 2013
Accepted 4 September 2013
Available online 7 October 2013

Keywords:
Fluorine
Surfactant
Degradation
Peroxodisulfate
Photocatalyst

ABSTRACT

Photochemical decomposition of a fluorotelomer unsaturated carboxylic acid, $C_3F_7CF{=}CHCOOH$ ( ), in the presence of WO_3 and an electron acceptor ($S_2O_8^{2-}$ or H_2O_2) in water under visible-light irradiation was investigated. Under an O_2 atmosphere, was not decomposed either by TiO_2 (P25) or WO_3 alone. A combination of WO_3 and H_2O_2 also resulted in almost no decomposition of . In contrast, irradiation in the presence of a combination of WO_3 and $S_2O_8^{2-}$ (potassium salt) efficiently decomposed to F^-, CO_2, C_3F_7COOH, and C_2F_5COOH. The decomposition of was affected by the counter cation of $S_2O_8^{2-}$: the decomposition extent was higher with $K_2S_2O_8$ than with $(NH_4)_2S_2O_8$. The decomposition of was further enhanced when the reaction in the presence of WO_3 and $K_2S_2O_8$ was carried out under an argon atmosphere. Under O_2, the amount of H_2O_2 formed in the reaction solution was an order of magnitude higher than the amount formed under argon. This fact suggests that the decrease in the decomposition of under O_2 can be ascribed to the formation of H_2O_2, which consumed $S_2O_8^{2-}$ and SO_4^{-}.

© 2013 Elsevier Ltd. All rights reserved.

Perfluorocarboxylic acids (PFCAs; $C_nF_{2n+1}COOH$) and related chemicals have been used as emulsifying agents and surface treatment agents because of their high surface-active effect, high thermal and chemical stability, and high light transparency (Schultz et al., 2003). Since it became clear that PFCAs with long perfluoroalkyl chains (n 6), such as perfluorooctanoic acid ($C_7F_{15}COOH$), bioaccumulate in the environment, efforts have been made to eliminate them from facility emissions (US EPA, 2013). Under the circumstances, there has been increasing interest in photochemical degradation of these chemicals in water (Hori et al., 2004, 2005, 2007a,b, 2011; Dillert et al., 2007; Zhao and

* Corresponding author at: Department of Chemistry, Faculty of Science, Kanagawa University, 2946 Tsuchiya, Hiratsuka 259-1293, Japan. Tel.: +81 463 59 4111; fax: +81 463 58 9688.
E-mail address: h-hori@kanagawa-u.ac.jp (H. Hori).

0045-6535/$ - see front matter © 2013 Elsevier Ltd. All rights reserved.
http://dx.doi.org/10.1016/j.chemosphere.2013.09.024

Author's personal copy

μ

=

μ

μ

°

=

°

1

Author's personal copy

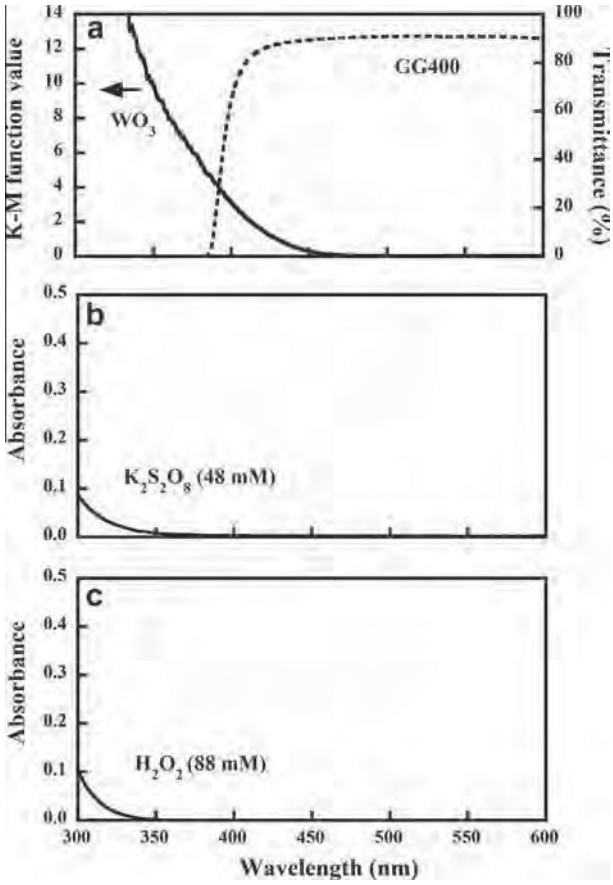

1

Author's personal copy

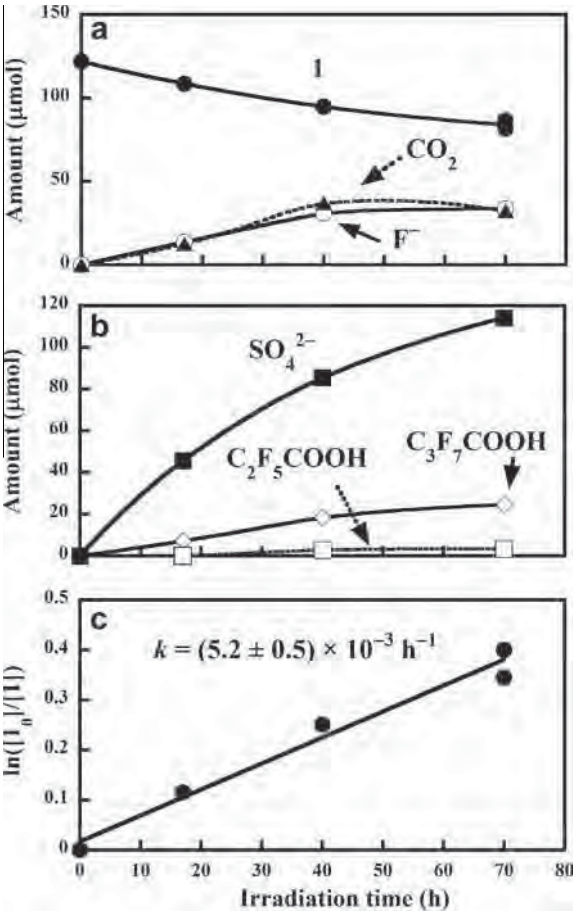

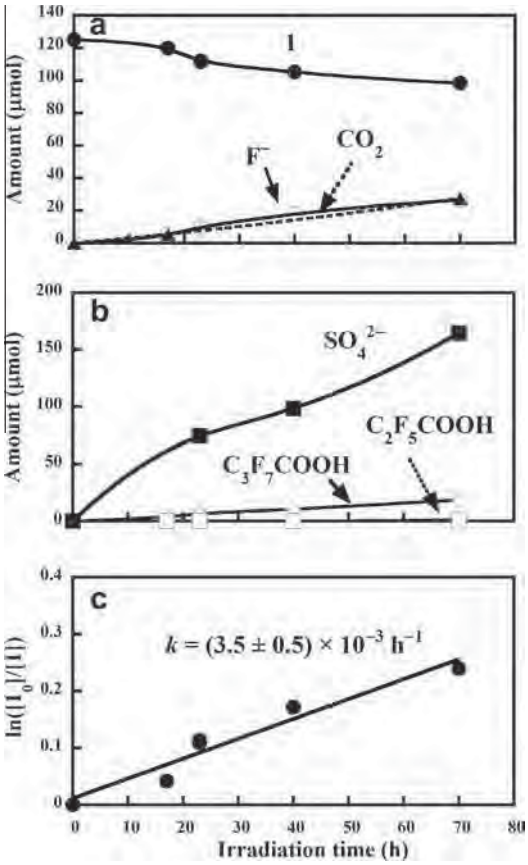

μ

Author's personal copy

=

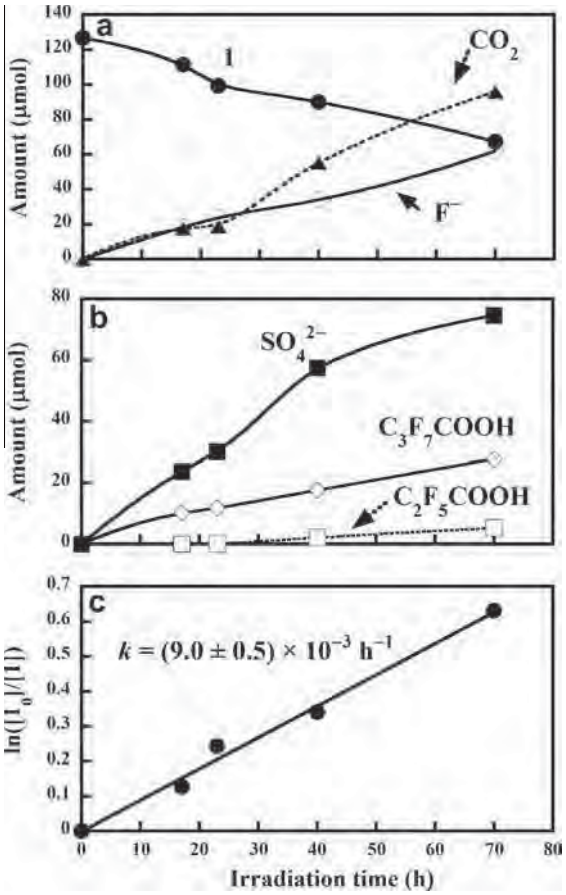

μ

μ

Author's personal copy

β

Abstract:

°

= = = = = = = = =
= =

°

= = +
+ + =

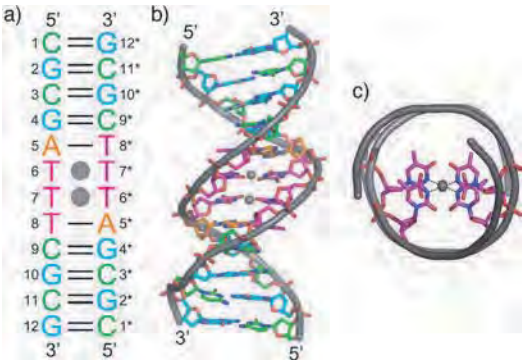
a)
5' 3'
1 C = G 12*
2 G = C 11*
3 C = G 10*
4 G = C 9*
5 A — T 8*
6 T T 7*
7 T T 6*
8 T — A 5*
9 C = G 4*
10 G = C 3*
11 C = G 2*
12 G = C 1*
3' 5'
b)
5' 3'
3' 5'
c)

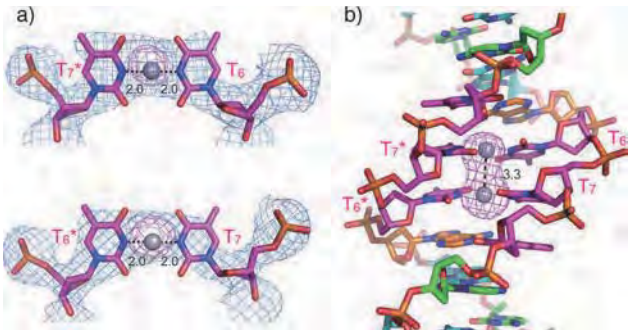
a)
b)
T7*
T6
2.0
2.0
T6*
T7
3.3

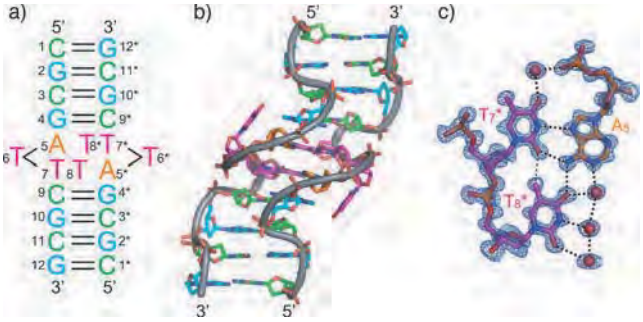
a)
b)
c)
5'
3'
T7*
A5
T8*

Keywords:

Nucleic Acids Research Advance Access published December 26, 2013

Downloaded from http://nar.oxfordjournals.org/ at Kanagawa University on January 16, 2014

Downloaded from http://nar.oxfordjournals.org/ at Kanagawa University on January 16, 2014

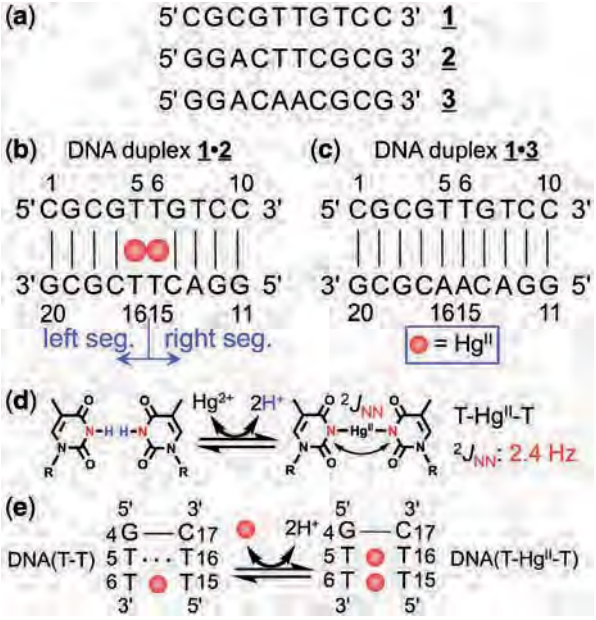

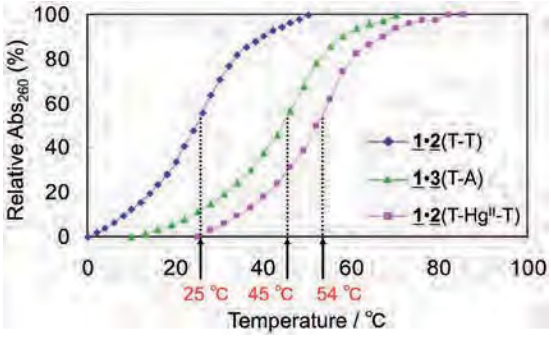

Downloaded from http://nar.oxfordjournals.org/ at Kanagawa University on January 16, 2014

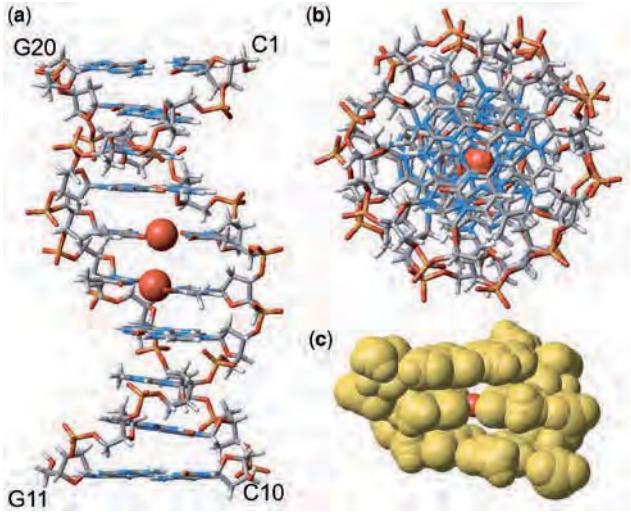

Downloaded from http://nar.oxfordjournals.org/ at Kanagawa University on January 16, 2014

Downloaded from http://nar.oxfordjournals.org/ at Kanagawa University on January 16, 2014

Downloaded from http://nar.oxfordjournals.org/ at Kanagawa University on January 16, 2014

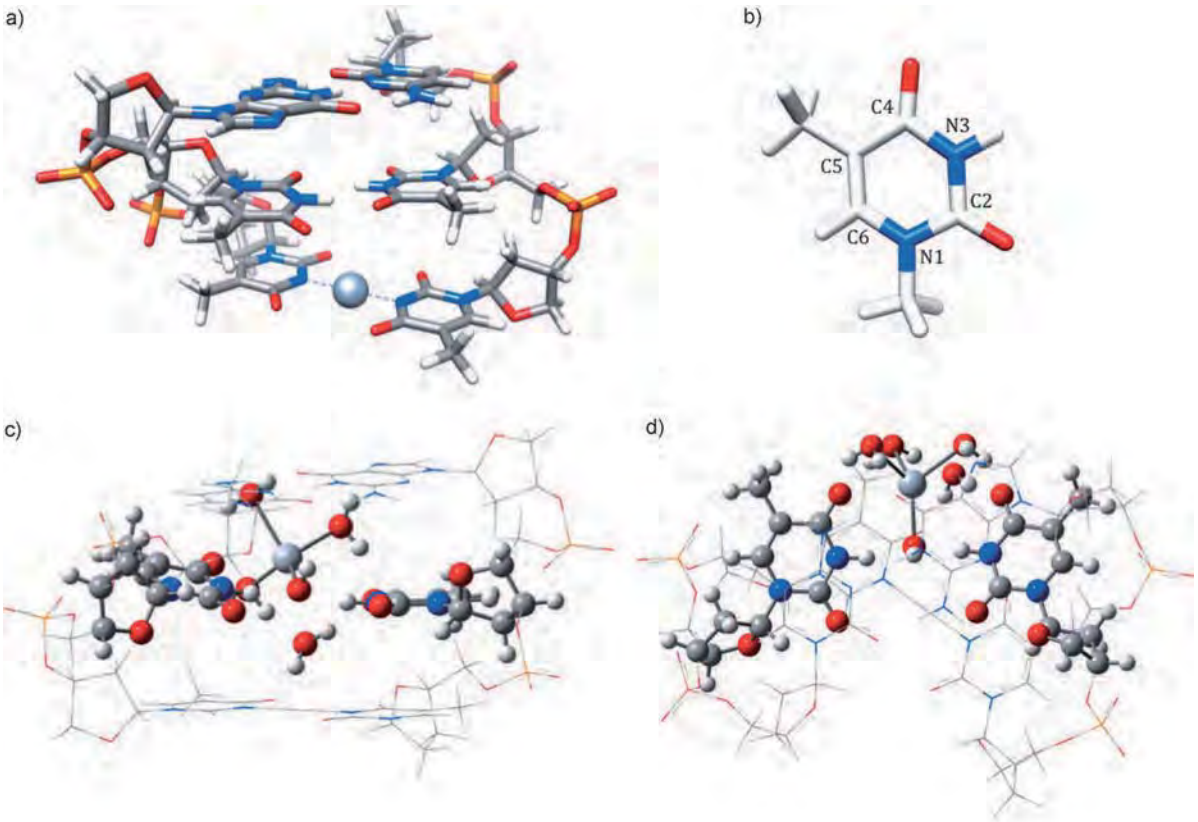
a)
b)
C4
N3
C5
C2
C6
N1
c)
d)

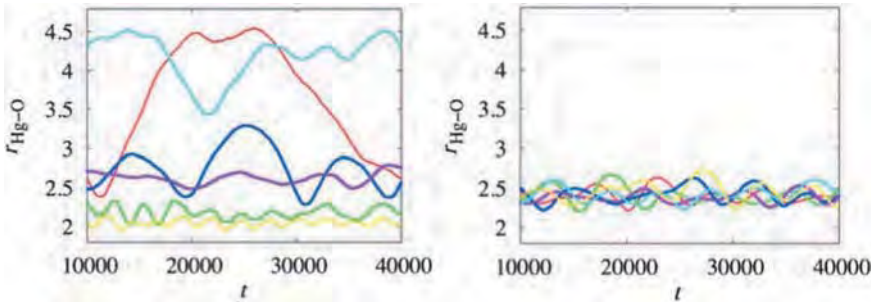
4.5
4
3.5
3
2.5
2
r_{Hg-O}
10000
20000
30000
40000
t

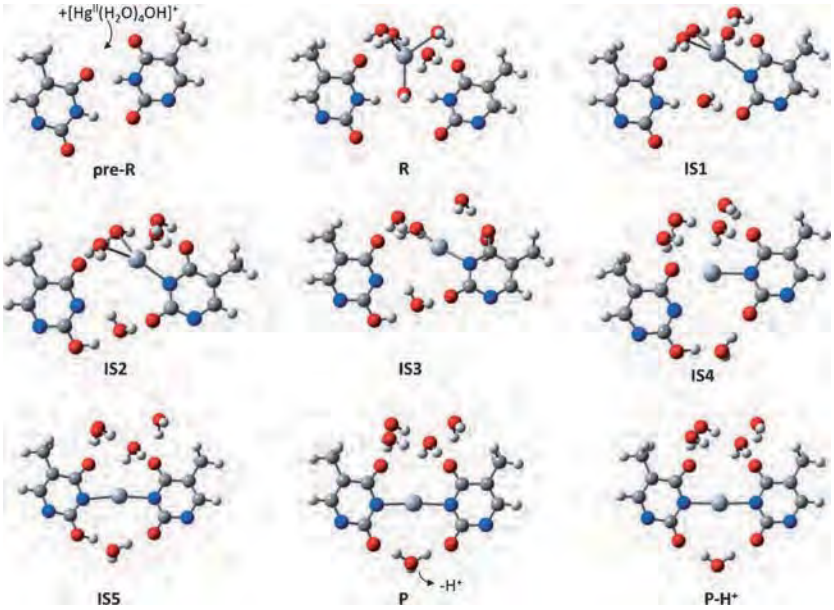
+[Hg^II(H2O)4OH]+
pre-R
R
IS1
IS2
IS3
IS4
IS5
P
-H+
P-H+

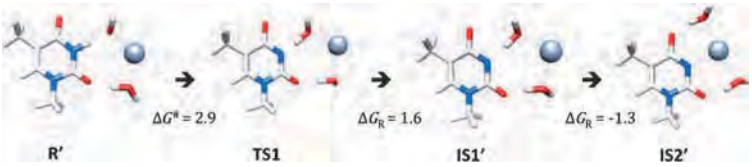
ΔG‡ = 2.9
ΔGR = 1.6
ΔGR = -1.3
R'
TS1
IS1'
IS2'

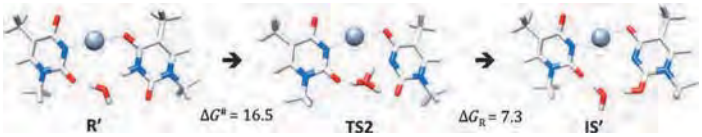
R'
ΔG‡ = 16.5
TS2
ΔG_R = 7.3
IS'

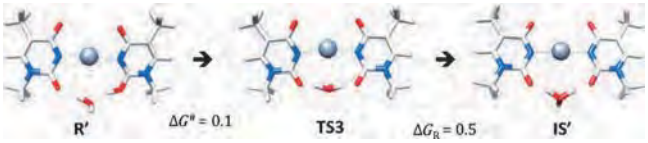
R'
ΔG‡ = 0.1
TS3
ΔG_R = 0.5
IS'

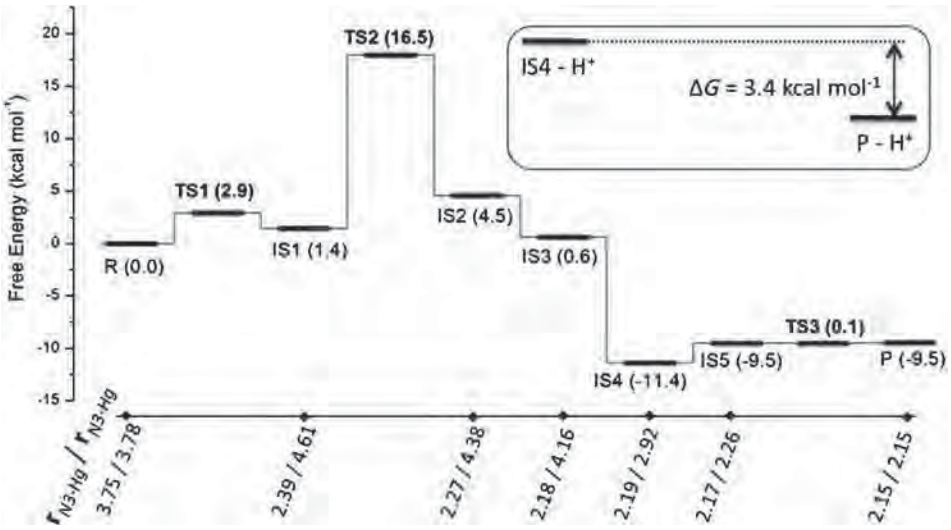
Free Energy (kcal mol⁻¹)
20
15
10
5
0
-5
-10
-15
TS2 (16.5)
TS1 (2.9)
IS1 (1.4)
IS2 (4.5)
IS3 (0.6)
IS4 (-11.4)
IS5 (-9.5)
TS3 (0.1)
P (-9.5)
R (0.0)
IS4 - H⁺
ΔG = 3.4 kcal mol⁻¹
P - H⁺
r N3-Hg / r N3-Hg
3.75 / 3.78
2.39 / 4.61
2.27 / 4.38
2.18 / 4.16
2.19 / 2.92
2.17 / 2.26
2.15 / 2.15

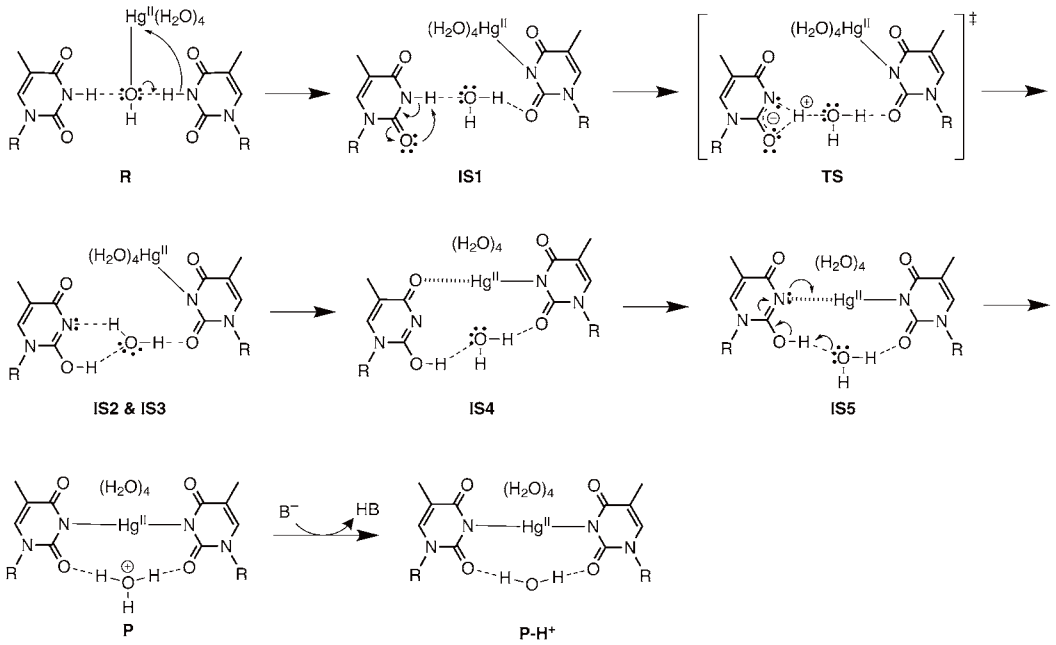
R
IS1
TS
IS2 & IS3
IS4
IS5
P
P-H+
B−
HB

Contents lists available at SciVerse ScienceDirect

journal homepage: www.elsevier.com/locate/molcata

*

ARTICLE INFO

ABSTRACT

1. Introduction

2. Experimental

*

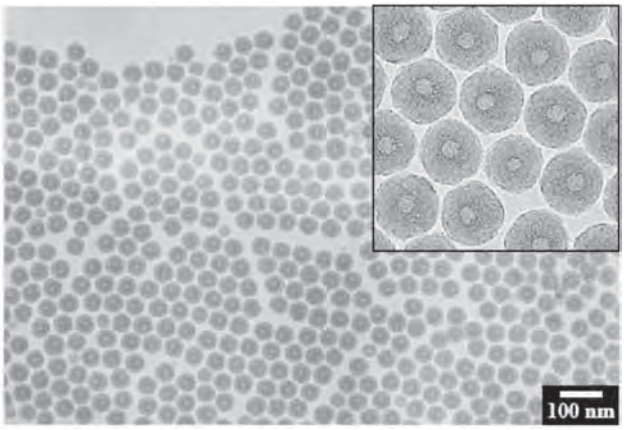

Fig. 1.

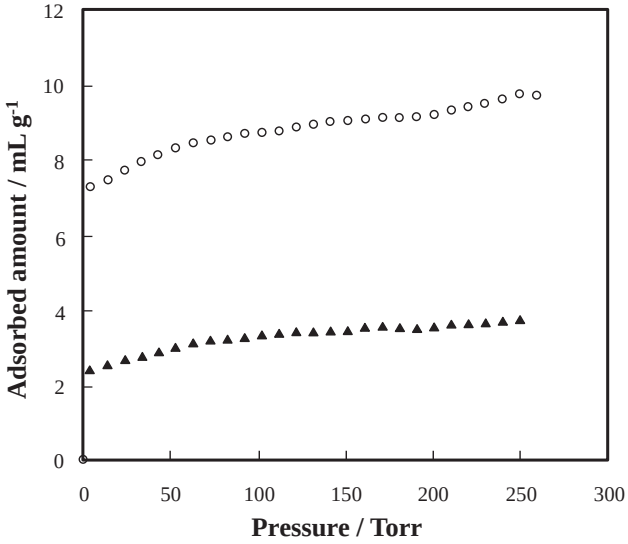

Fig. 2.

3. Results and discussion

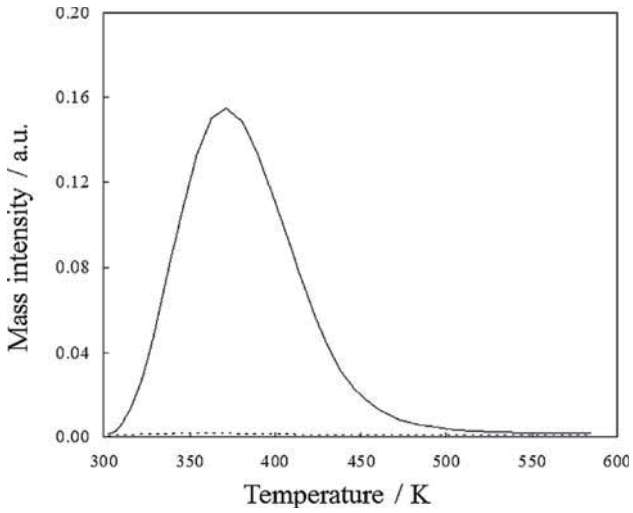

Fig. 3.

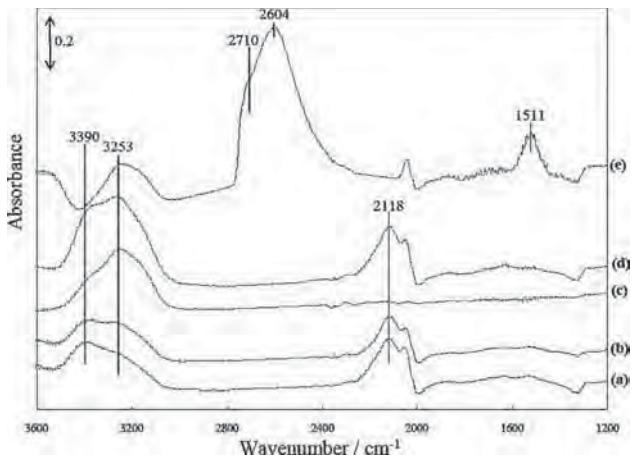

Fig. 4.

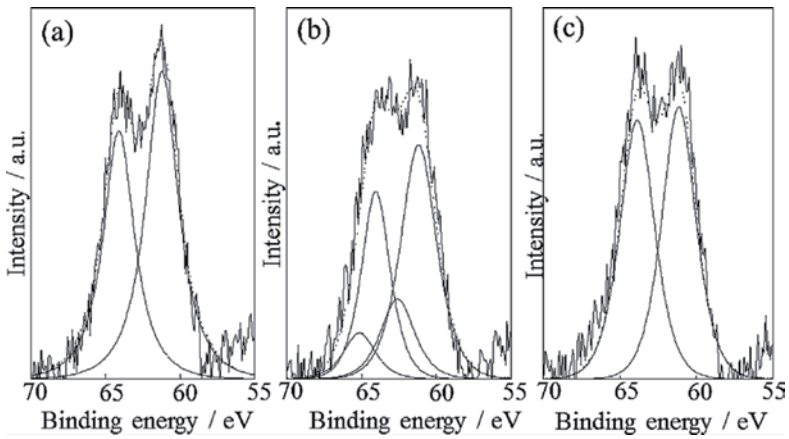

Fig. 5.

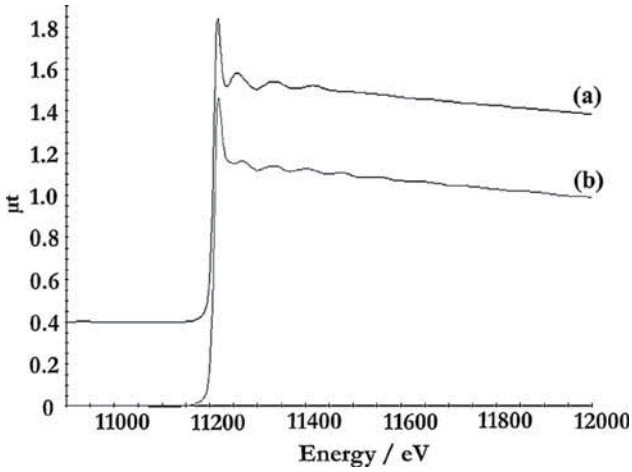
1.8
1.6
1.4
1.2
1.0
0.8
0.6
0.4
0.2
0
μt
(a)
(b)
11000
11200
11400
11600
11800
12000
Energy / eV

Fig. 6.

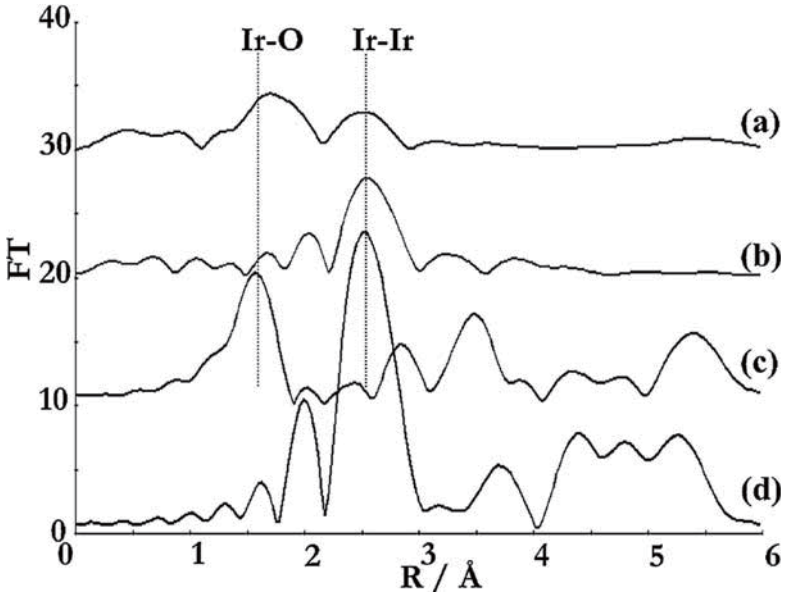
40
30
20
10
0
FT
Ir-O
Ir-Ir
(a)
(b)
(c)
(d)
0
1
2
3
4
5
6
R / Å

Fig. 7.

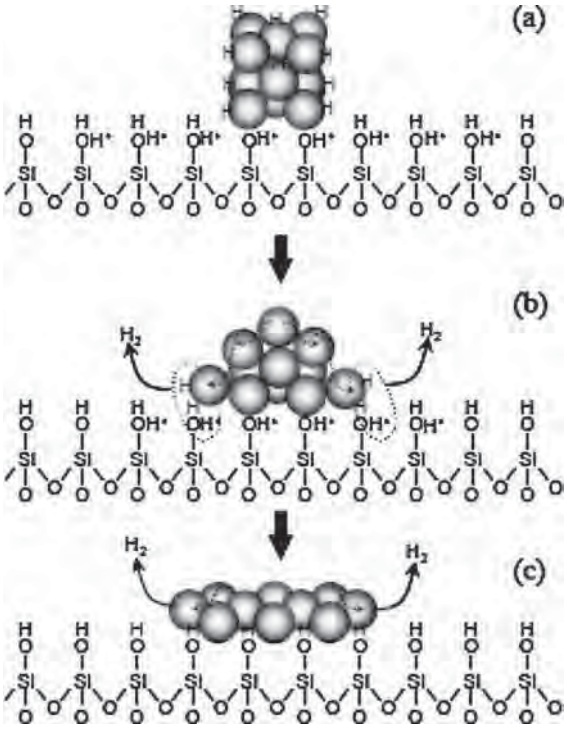

Scheme 1.

4. Conclusion

Acknowledgments

References

Contents lists available at SciVerse ScienceDirect

journal homepage: www.elsevier.com/locate/apcatb

ARTICLE INFO

ABSTRACT

1. Introduction

Table 1

2. Experimental

3. Results and discussion

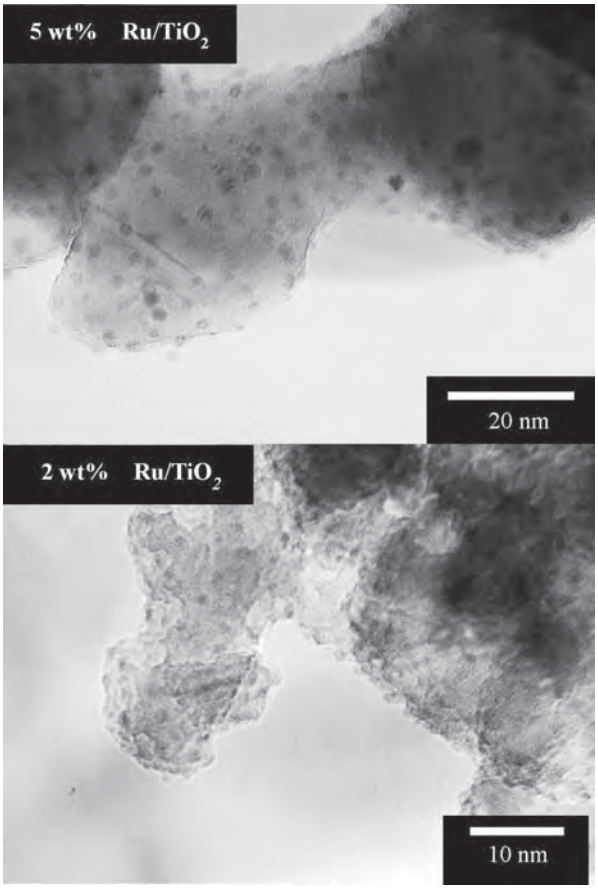
5 wt% Ru/TiO2
20 nm
2 wt% Ru/TiO2
10 nm

Fig. 1.

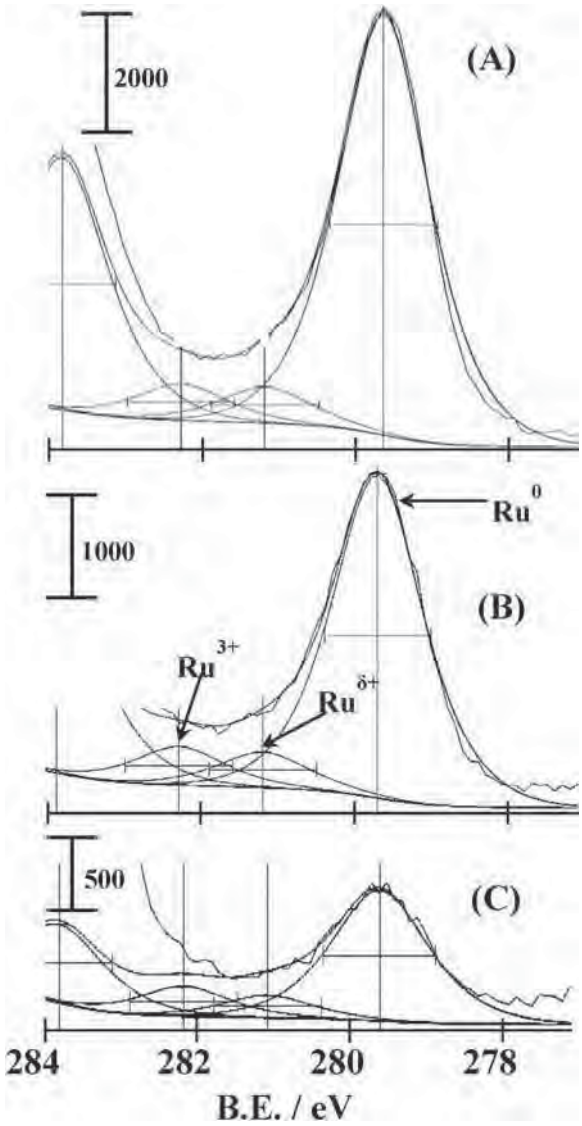
2000
(A)
1000
Ru0
(B)
Ru3+
Ruδ+
500
(C)
284
282
280
278
B.E. / eV

Fig. 2.

Table 2

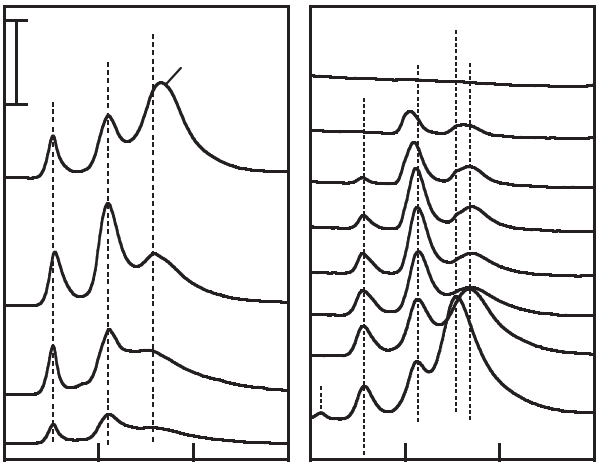

Fig. 3.

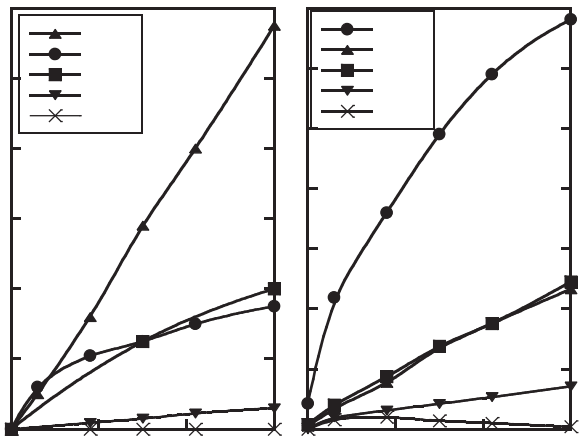

Fig. 4.

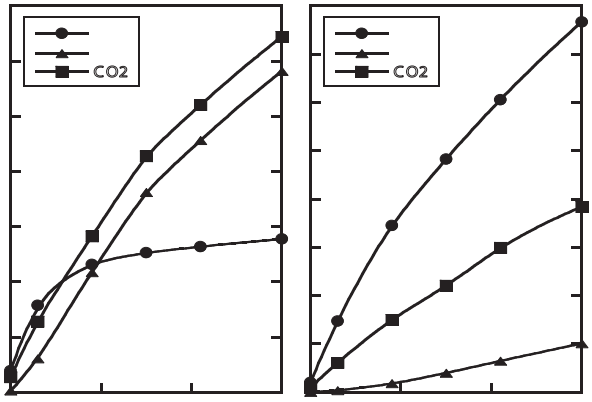

Fig. 5.

Table 3

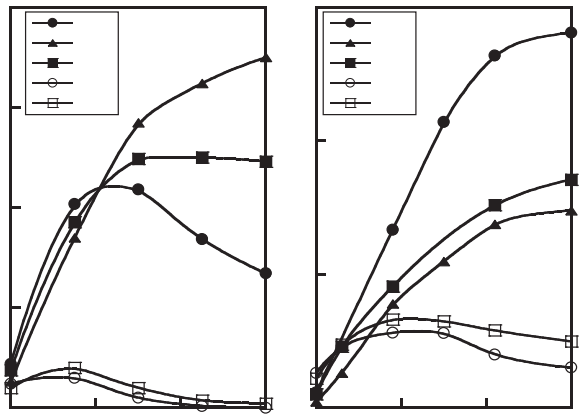

Fig. 6.

4. Conclusions

Acknowledgment

References

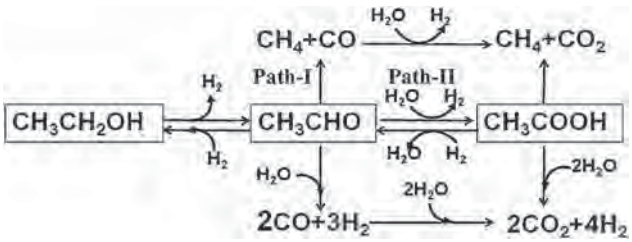

Fig. 7.

JACS
JOURNAL OF THE AMERICAN CHEMICAL SOCIETY
Communication
pubs.acs.org/JACS

Structural Characterization and Oxidation Reactivity of a Nickel(II) Acylperoxo Complex

Jun Nakazawa,* Shota Terada, Masaki Yamada, and Shiro Hikichi*

Department of Material and Life Chemistry, Kanagawa University, 3-27-1 Rokkakubashi, Kanagawa-ku, Yokohama 221-8686, Japan

ABSTRACT: The nickel(II)–acylperoxo complex [Ni-(Tp^{CF_3Me})(^{2}-*m*CPBA)] (**1**^{CF_3Me}) [Tp^{CF_3Me} = hydrotris(3-tri uoromethyl-5-methylpyrazolyl)borate, *m*CPBA = *m*-chloroperbenzoate] was isolated and fully characterized. The electrophilic oxygenation ability of **1**^{CF_3Me} toward sul des and ole ns was con rmed. The Michaelis–Menten-type behavior of thioanisole oxygenation indicates the existence of a pre-equilibrium of substrate association in the reaction. In addition, **1**^{CF_3Me} retains H-atom abstraction ability for hydrocarbons with activated methylene C–H bonds (e.g., uorene). The oxidations of styrenes and these readily oxidizable hydrocarbons follow second-order kinetics, rst-order each with respect to **1**^{CF_3Me} and substrate. The lack of clear acceleration in the decay of **1**^{CF_3Me} in the presence of substrates with high C–H bond dissociation energies (e.g., cyclohexane) suggests that another reaction pathway contributes through the O–O-cleaved intermediate.

Organic peroxycarboxylic acids, such as *m*-chloroperbenzoic acid (H*m*CPBA) and peracetic acid, are versatile oxidants and extensively utilized reagents for organic substrate oxygenation. H*m*CPBA has enough reactivity for O-atom transfer toward various organic compounds, including non-activated hydrocarbons, without the use of a catalyst. However, the combination of a transition-metal catalyst and H*m*CPBA leads to regio- and chemoselective oxygenation. In the catalytic process, it is considered that an initially formed metal–acylperoxo complex is a precursor to the actual active oxidants, namely, high-valent metal–oxo species formed via homolytic or heterolytic O–O bond cleavages.[1] In the case of heme iron complexes, the metal–acylperoxo species themselves also work as O-atom transfer reagents toward ole ns.[2,3] As a result, the chemical properties of *m*CPBA complexes of redox-active transition metals have attracted much attention. To date, fully characterized *m*CPBA complexes are still scarce. Especially, the substrate-oxidizing abilities of non-heme metal–*m*CPBA complexes remain to be clari ed. The transfer of O atoms from Cu–*m*CPBA complexes to phosphine has been reported. However, these copper complexes are not very reactive.[4]

Recently, the selective hydroxylation of cyclohexane catalyzed by Ni(II) complexes with H*m*CPBA has been reported.[5] While we were examining the reactivity of the active oxygen complexes of nickel with tridentate Tp^R ligands, where Tp^R denotes a substituted hydrotris(pyrazolyl)borate and R lists the non-hydrogen substituents (R = iPr$_2$, iPr$_2$Br, Me$_2$, and Me$_2$Br; see Chart 1), we detected thermally unstable Ni(II)–acylperoxo intermediates [Ni^{II}(Tp^R)(*m*CPBA)] (**1**^{R}).[6] The

Chart 1. Abbreviations for the Tp^R Ligands

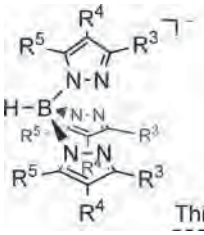

Tp^R	R^3	R^4	R^5
Tp^{iPr2}	iPr	H	iPr
Tp^{iPr2Br}	iPr	Br	iPr
Tp^{Me2}	Me	H	Me
Tp^{Me2Br}	Me	Br	Me
This work Tp^{CF3Me}	CF$_3$	H	Me

acylperoxo complexes **1**^{R} were formed by reaction of the dinuclear bis(-hydroxo)nickel(II) complexes [(Ni^{II}Tp^R)$_2$(-OH)$_2$] (**2**^{R}) with stoichiometric amounts of H*m*CPBA (Scheme 1, route A). The thermal stability of **1**^{R} depends on

Scheme 1. Preparation of Tp^{R}Ni^{II} Complexes

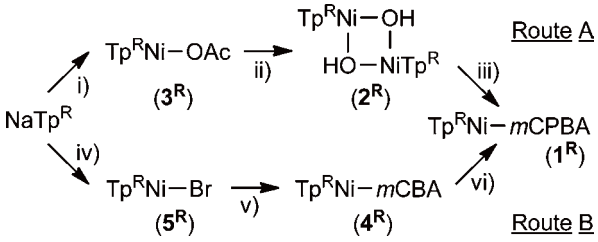

[a] *m*CBA and *m*CPBA indicate *m*-chlorobenzoate and *m*-chloroperbenzoate, respectively. Reaction conditions: (i) Ni(OAc)$_2$; (ii) NaOH; (iii) H*m*CPBA; (iv) NiBr$_2$; (v) K*m*CBA; (vi) H*m*CPBA.

the electronic nature of the R^4 group on the Tp ligand: the complex **1**^{Me_2Br} bearing the electron-withdrawing bromine group is more stable than the nonbrominated derivative **1**^{Me_2}. Interestingly, the acylperoxo species **1**^{R} have the potential to abstract a hydrogen atom from the aliphatic C–H group, as evidenced by the kinetic isotope e ect during the self-decomposition of **1**^{R} in CH_2Cl_2/CD_2Cl_2. We have not been able to isolate **1**^{R} to date. Not only does its structure remain to be characterized, but the nature of its oxidizing abilities toward various external substrates other than alkanes remains to be clari ed. In this work, we characterized in detail the molecular

Received: February 25, 2013
Published: April 5, 2013

ACS Publications © 2013 American Chemical Society

structure and external substrate oxidizing behavior of a Ni(II)−*m*CPBA complex.

Our strategy for the isolation of a Ni(II)−*m*CPBA complex involved controlling the properties of the Ni-supporting Tp^R ligand. As mentioned above, the incorporation of electron-withdrawing groups (EWGs) on the pyrazolyl rings of Tp^R enhances the stability of **1**. In addition, steric hindrance and chemical stability (i.e., resistance to oxidation) of the substituent groups on Tp^R are critical. Bulky alkyl groups (e.g., isopropyl groups) at the R^3 position of the pyrazolyl rings wrap the O−O moiety of the metal-bound acylperoxide, stabilizing **1** and hindering the reaction with external substrates. Moreover, C−H bonds of the R^3 substituents are oxidized by a proximal oxidant (i.e., metal-bound acylperoxide or further activated species generated via O−O breaking) through intramolecular reaction. Therefore, in this study hydrotris(3-trifluoromethyl-5-methylpyrazolyl)borate (Tp^{CF_3Me}) was employed as the Ni-supporting ligand because the proximal trifluoromethyl groups exhibit an electron-withdrawing nature, high oxidation resistance, and moderate steric hindrance. The versatility of Tp^{CF_3Me} for the stabilization of metal−dioxygen species was revealed by the $Cu_2(\ -\ ^2{:}\ ^2\text{-}O_2)$ complex reported by Gorun and co-workers.[7]

Our first attempt to synthesize an acylperoxo complex with Tp^{CF_3Me} ($\mathbf{1}^{CF_3Me}$) in a manner similar to that used to form the reported $\mathbf{1}^{R}$ (i.e., dehydrative condensation between the Ni(II)−hydroxo species and H*m*CPBA; route A in Scheme 1)[6] failed because of the insolubility of the putative Ni(II)−hydroxo complex $\mathbf{2}^{CF_3Me}$ formed by the reaction of the Ni(II)−acetato complex $[Ni^{II}(Tp^{CF_3Me})(OAc)]$ ($\mathbf{3}^{CF_3Me}$) with aqueous NaOH. Therefore, we selected an *m*-chlorobenzoate (*m*CBA) complex, $[Ni^{II}(Tp^{CF_3Me})(mCBA)]$ ($\mathbf{4}^{CF_3Me}$), as a precursor to $\mathbf{1}^{CF_3Me}$ because exchange of the *m*CBA ligand with *m*CPBA on the Ni(II) center might occur during the turnover process in catalytic alkane oxidation by Ni/*m*CPBA systems (route B in Scheme 1).[5] $\mathbf{4}^{CF_3Me}$ was prepared from bromido complex $\mathbf{5}^{CF_3Me}$ by ligand exchange with K*m*CBA.[8] As we expected, the reaction of $\mathbf{4}^{CF_3Me}$ with a small excess (~2 equiv) of H*m*CPBA in CH_2Cl_2 at −40 °C allowed a perfect conversion to $\mathbf{1}^{CF_3Me}$. Monitoring of the UV−vis spectral changes revealed an increase in absorbance at 375 nm, which was attributed to $\mathbf{1}^{CF_3Me}$, as the 408 nm band of $\mathbf{4}^{CF_3Me}$ decreased with an isosbestic point at 395 nm. Surprisingly, this titration experiment was reproducible at room temperature, indicating the high thermal stability of the formed $\mathbf{1}^{CF_3Me}$ [Figure S2 in the Supporting Information (SI)].

After the volatiles were removed from the reaction mixture of H*m*CPBA (2.7 equiv) and $\mathbf{4}^{CF_3Me}$ in CH_2Cl_2, the dissociated H*m*CBA and the remaining excess H*m*CPBA were washed out with H_2O and EtOH. The agreement between the UV−vis spectra of the redissolved isolated solid and the final species in the above-mentioned titration in CH_2Cl_2 suggests that isolation was achieved (Figure S4). Recrystallization of the resulting green-blue solid from CH_2Cl_2/*n*-hexane yielded a single crystal of $\mathbf{1}^{CF_3Me}$ suitable for X-ray analysis (Figure 1 and Table S3 in the SI).[8,9] The oxidation state of the Ni center is +2, and $\mathbf{1}^{CF_3Me}$ is a neutral complex, as evidenced by the absence of any counterions in the crystal lattice. The Ni center in $\mathbf{1}^{CF_3Me}$ is supported by a donor set containing three N atoms and two O atoms. The O−O bond length [1.443(3) Å] falls in the typical range for peroxide O−O lengths (Figure S4).[3,4a,10] The coordination mode of *m*CPBA is ^{2}, as indicated by the bond lengths of the percarboxylate moiety [Ni1−O1, Ni−O3, and

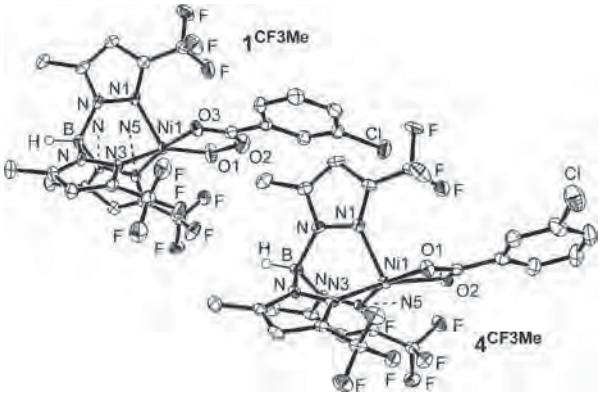

Figure 1. ORTEP diagrams of the complexes $\mathbf{1}^{CF_3Me}$ and $\mathbf{4}^{CF_3Me}$ with 50% thermal ellipsoids. H atoms on the carbon backbones have been omitted for clarity.

O3 C16 = 1.914(2), 2.040(2), and 1.223(3) Å, respectively]. The Ni−N(Tp) lengths in $\mathbf{1}^{CF_3Me}$ [Ni1−N1, Ni1−N3, and Ni1−N5 = 2.037(2), 2.041(2), and 2.058(2) Å, respectively] are comparable to those in $\mathbf{4}^{CF_3Me}$, where the Ni center is supported by the tridentate Tp^{CF_3Me} ligand and the ^{2}-binding *m*CBA ligand. The geometry of the nickel center of $\mathbf{1}^{CF_3Me}$ is slightly distorted from square-pyramidal (= 0) toward trigonal-bipyramidal (= 1), as indicated by its value of 0.26. The Ni−*m*CPBA site is fully surrounded by CF_3 groups. These structural characteristics are consistent with the following observed spectroscopic properties:[8] Paramagnetically shifted ^{1}H NMR signals of $\mathbf{1}^{CF_3Me}$ assignable to the protons of the Tp^{CF_3Me} and *m*CPBA ligands support the high-spin configuration (S = 1) of the distorted five-coordinate Ni(II) center (Figures S5 and S6). Coordination of the carbonyl moiety of the acylperoxo ligand leads to a red shift of the $_{C\ O}$ vibration to 1644 cm^{-1} in the IR spectrum, as found in the previously reported Tp^R derivatives (i.e., for $\mathbf{1}^{Me2}$ in CH_2Cl_2 solution at −40 °C, $_{C\ O}$ = 1646 cm^{-1}) (Figures S7−S9).[4,6,11]

The oxidation reactivity of the isolated Ni(II)−acylperoxo complex $\mathbf{1}^{CF_3Me}$ for external substrates in aprotic solvents ($CF_3C_6H_5$, toluene, benzene) was studied by kinetic analysis using UV−vis spectroscopy and product analysis using GC (Scheme 2).[8] Without any substrate, the complex $\mathbf{1}^{CF_3Me}$ was thermally robust even at 70 °C in benzene (first-order rate constant = 1.63 × 10^{-5} s^{-1}), while $\mathbf{1}^{Me2}$ decomposed below −20 °C.[12] This thermal stability of $\mathbf{1}^{CF_3Me}$ is a result of the steric protection around the Ni center and the electron-withdrawing nature of the CF_3 groups in the Tp^{CF_3Me} ligand. However, $\mathbf{1}^{CF_3Me}$ behaved as an O-atom transfer reagent toward nucleophiles such as phosphine and sulfide under mild conditions. A reaction solution containing 10 equiv of thioanisole stoichiometrically formed MeS(O)Ph (96%) and MeS(O)$_2$Ph (1%), and the use of 10 equiv of PPh_3 gave O PPh_3 (103%), as determined by GC analyses (yields based on $\mathbf{1}^{CF_3Me}$; Table S4). In fact, the decay of $\mathbf{1}^{CF_3Me}$ was accelerated even at −40 °C in the presence of excess thioanisole. The pseudo-first-order reaction rate constant (k_{obs}) for the decay of $\mathbf{1}^{CF_3Me}$ became saturated as the concentration of thioanisole increased, implying that the reaction of $\mathbf{1}^{CF_3Me}$ and thioanisole proceeds through a Michaelis−Menten-type mechanism (Scheme 2 and Figures S10−S12).[13] A Lineweaver−Burk-type plot (1/[thioanisole] vs $1/k_{obs}$) gave values of the association equilibrium constant K_{on}

Scheme 2. Oxidation of Various Substrates Using 1^{CF_3Me} as the Stoichiometric Oxidant

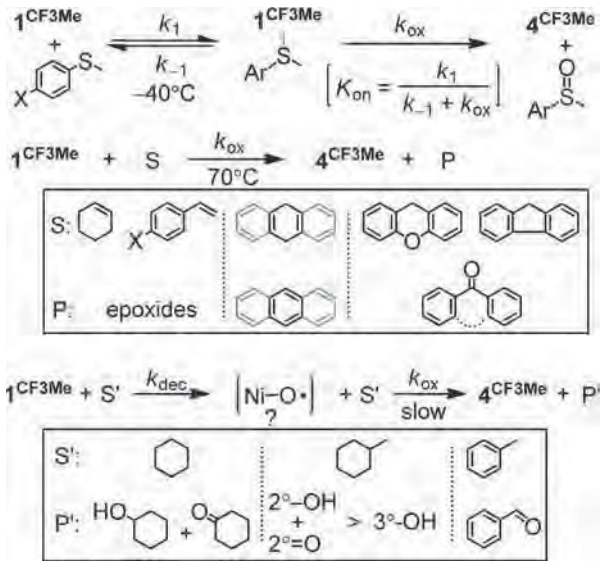

for the formation of a substrate adduct of 1^{CF_3Me} and the rate constant k_{ox} for the subsequent sulfoxide formation (Figure 2a).

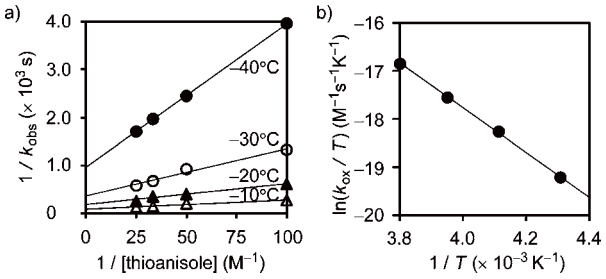

Figure 2. Plots of (a) $1/k_{ox}$ vs 1/[thioanisole] (Lineweaver–Burk plot) and (b) $\ln(k_{ox}/T)$ vs $1/T$ (Eyring plot) for the reaction of 1^{CF_3Me} (1 mM) with thioanisole (5–40 mM) at −40 to −10 °C in toluene under Ar. The Eyring plot gave H = 38.5 kJ mol^{-1} and S = −191 J K^{-1} mol^{-1}.

The negative value of S (−191 J K^{-1} mol^{-1}) derived from the Eyring plot suggested that the O-atom transfer from the Ni-bound acylperoxide to the S atom occurs directly (Figure 2b). The reactions of 1^{CF_3Me} with other para-substituted thioanisoles ($MeSC_6H_4$–X; X = Br, Me, OMe) exhibited similar reaction pro les. Linear correlations between the substituent constants and the K_{on} and k_{ox} values, with negative values of the Hammett reaction constants , indicated that the higher Lewis basicity of the substrate enhances the formation of the 1^{CF_3Me}·$MeSC_6H_4$–X adduct and that the Ni-bound acylperoxide shows an electrophilic nature (Figures S13 and S14).

The Ni(II)–acylperoxide complex 1^{CF_3Me} also behaves as an electrophilic O-atom transfer reagent toward alkenes. Reactions of 1^{CF_3Me} with 10 equiv of cyclohexene and styrene in $CF_3C_6H_5$ at 70 °C yielded the corresponding epoxides in 66 and 92% yield, respectively. The formation of small amounts of 2-cyclohexen-1-ol (4%)/2-cyclohexen-1-one (6%) and benzaldehyde (3%), respectively, might suggest the involvement of a small extent of H-atom abstraction (Table S4). The reactions of 1^{CF_3Me} with a series of para-substituted styrenes (H_2C CHC_6H_4–X; X = Br, H, Me, OMe) exhibited second-order kinetics (Figures S15–S20). The negative value of S (−110 J K^{-1} mol^{-1}) for the oxidation of styrene (X = H) indicates that the reaction proceeds through an associative transition state. The time course of changes in the UV–vis spectral pattern showed an isosbestic point, which may imply conversion from 1^{CF_3Me} to 4^{CF_3Me} without any intermediate. Also, the electrophilic nature of 1^{CF_3Me} was evidenced by a negative value (−1.35) derived from the Hammett plot of versus log k_{ox} (k_{ox} = second-order rate constant) at 90 °C.

Remarkably, 1^{CF_3Me} can oxidize hydrocarbon substrates with activated methylene C–H bonds, such as 1,4-cyclohexadiene (CHD), 9,10-dihydroanthracene (DHA), xanthene, and uorene, obeying second-order kinetics (Figures S21–S28). In the UV–vis spectrum of 1^{CF_3Me} in the presence of a large excess of CHD, the 4^{CF_3Me} band at 408 nm increased concomitantly with the consumption of 1^{CF_3Me}. No signi cant features were found at around 800 nm in our system; we attribute this result to the absence of putative high-valent Ni–O species arising from the cleavage of the acylperoxide O–O bond.[14] The negative S values for the reactions of the compounds with activated methylene C–H bonds indicated that 1^{CF_3Me} works as the direct oxidant without an O–O-bond-cleaved intermediate (Figures S29–S32). The values of the second-order rate constants and C–H bond dissociation energies (BDEs) of these substrates are not correlated, which might be attributable to the steric e ects of the CF_3 groups around the Ni center of 1^{CF_3Me}: less hindered CHD is more easily accessible to the acylperoxide ligand of 1^{CF_3Me}, leading to a faster reaction than with hindered DHA, although the latter has a lower BDE (Figure S33). It must be noted that no clear acceleration of the decay of **1** was observed in the presence of 1000 equiv of cyclohexane in benzene. The product analysis of the reaction of 1^{CF_3Me} and methylcyclohexane indicated that the reaction proceeded in the somewhat sterically crowded coordination sphere of the Ni center (Table S4).[6] Therefore, in the case of large-BDE substrates such as cyclohexane, another reaction pathway through the O–O-cleaved intermediates [i.e., high-valent Ni–O or Ni(II)–oxyl species] is dominant.

In conclusion, we have succeeded in fully characterizing the Ni(II)–acylperoxo complex. This thermally robust acylperoxide compound works as an O-atom transfer reagent toward nucleophilic sul des and ole ns and also is a genuine oxidant toward activated aliphatic C–H bonds.

■ ASSOCIATED CONTENT

Supporting Information

Experimental procedures, characterization data, and kinetic data. This material is available free of charge via the Internet at http://pubs.acs.org.

■ AUTHOR INFORMATION

Corresponding Author

jnaka@kanagawa-u.ac.jp; hikichi@kanagawa-u.ac.jp

Notes

The authors declare no competing nancial interest.

■ ACKNOWLEDGMENTS

This work was supported in part by a Cooperative Research Program, "Network Joint Research Center for Materials and Devices" (2011169, 2012216, and 2012348), a Scienti c

Frontier Research Project, and a Strategic Development of Research Infrastructure for Private Universities grant from the Ministry of Education, Culture, Sports, Science, and Technology of Japan. S.H. and J.N. also thank Kanagawa University for its nancial support.

■ REFERENCES

(1) Formation of reactive non-heme Fe O species through O−O activation of putative Fe−*m*CPBA complexes: (a) De Oliveira, F. T.; Chanda, A.; Banerjee, D.; Shan, X.; Mondal, S.; Que, L., Jr.; Bominaar, E. L.; Munck, E.; Collins, T. J. *Science* **2007**, *315*, 835. (b) Lee, S. H.; Han, J. H.; Kwak, H.; Lee, S. J.; Lee, E. Y.; Kim, H. J.; Lee, J. H.; Bae, C.; Lee, S. N.; Kim, Y.; Kim, C. *Chem Eur. J.* **2007**, *13*, 9393. (c) Ray, K.; Lee, S. M.; Que, L., Jr. *Inorg. Chim. Acta* **2008**, *361*, 1066. (d) van den Berg, T. A.; de Boer, J. W.; Browne, W. R.; Roelfes, G.; Feringa, B. L. *Chem. Commun.* **2004**, 2550. (e) Kodera, M.; Shimakoshi, H.; Kano, K. *Chem. Commun.* **1996**, 1737. (f) Kitajima, N.; Ito, M.; Fukui, H.; Moro-oka, Y. *J. Am. Chem. Soc.* **1993**, *115*, 9335.

(2) Proposals for heme-Fe(III)−*m*CPBA species working as oxidants: (a) Suzuki, N.; Higuchi, T.; Nagano, T. *J. Am. Chem. Soc.* **2002**, *124*, 9622−9628. (b) Nam, W.; Lim, M. H.; Lee, H. J.; Kim, C. *J. Am. Chem. Soc.* **2000**, *122*, 6641−6647. (c) Lee, K. A.; Nam, W. *J. Am. Chem. Soc.* **1997**, *119*, 1916−1922.

(3) The molecular structure and substrate oxidation abilities of the related peracetatoiron(III) complex have been reported: Zhang, X.; Furutachi, H.; Tojo, T.; Tsugawa, T.; Fujinami, S.; Sakurai, T.; Suzuki, M. *Chem. Lett.* **2011**, *40*, 515.

(4) (a) Ghosh, P.; Tyeklar, Z.; Karlin, K. D.; Jacobson, R. R.; Zubieta, J. *J. Am. Chem. Soc.* **1987**, *109*, 6889. (b) Sanyal, I.; Ghosh, P.; Karlin, K. D. *Inorg. Chem.* **1995**, *34*, 3050. (c) Kitajima, N.; Fujisawa, K.; Moro-oka, Y. *Inorg. Chem.* **1990**, *29*, 357.

(5) (a) Nagataki, T.; Ishii, K.; Tachi, Y.; Itoh, S. *Dalton Trans.* **2007**, 1120. (b) Nagataki, T.; Itoh, S. *Chem. Lett.* **2007**, *36*, 748. (c) Nagataki, T.; Tachi, Y.; Itoh, S. *Chem. Commun.* **2006**, 4016. (d) Balamurugan, M.; Mayilmurugan, R.; Suresh, E.; Palaniandavar, M. *Dalton Trans.* **2011**, *40*, 9413.

(6) Hikichi, S.; Hanaue, K.; Fujimura, T.; Okuda, H.; Nakazawa, J.; Ohzu, Y.; Kobayashi, C.; Akita, M. *Dalton Trans.* **2013**, *42*, 3346.

(7) Stabilization of Cu_2(- ^{2}: ^{2}-O_2) species by Tp^{CF_3Me} has been reported: (a) Hu, Z.; Williams, R. D.; Tran, D.; Spiro, T. G.; Gorun, S. M. *J. Am. Chem. Soc.* **2000**, *122*, 3556. (b) Hu, Z.; George, G. N.; Gorun, S. M. *Inorg. Chem.* **2001**, *40*, 4812.

(8) See the Supporting Information.

(9) Crystal Information Files for $\mathbf{5}^{CF_3Me}$, $\mathbf{4}^{CF_3Me}$, and $\mathbf{1}^{CF_3Me}$ have been deposited with the Cambridge Crystallographic Data Centre (CCDC-924706−8).

(10) O−O bond lengths in Fe−percarbonates and Ni−alkylperoxides: (a) Hashimoto, K.; Nagatomo, S.; Fujinami, S.; Furutachi, H.; Ogo, S.; Suzuki, M.; Uehara, A.; Maeda, Y.; Watanabe, Y.; Kitagawa, T. *Angew. Chem., Int. Ed.* **2002**, *41*, 1202. (b) Hikichi, S.; Okuda, H.; Ohzu, Y.; Akita, M. *Angew. Chem., Int. Ed.* **2009**, *48*, 188. (c) Hikichi, S.; Kobayashi, C.; Yoshizawa, M.; Akita, M. *Chem. Asian J.* **2010**, *5*, 2086.

(11) IR assignment of porphyrin-Fe−*m*CPBA: Groves, J. T.; Watanabe, Y. *Inorg. Chem.* **1987**, *26*, 785.

(12) The thermal stability of $\mathbf{1}^{CF_3Me}$ is comparable to that of H*m*CPBA.

(13) Ligand exchange with the terminal O atom of *m*CPBA during the initial association process can be excluded because no immediate decrease in the peroxide-to-Ni ligand-to-metal charge-transfer band of $\mathbf{1}^{CF_3Me}$ at 375 nm was observed in the UV−vis spectrum after the addition of thioanisole.

(14) Pfaff, F. F.; Heims, F.; Kundu, S.; Mebs, S.; Ray, K. *Chem. Commun.* **2012**, *48*, 3730.

=

=

+

+

=

WILEY
ONLINE LIBRARY

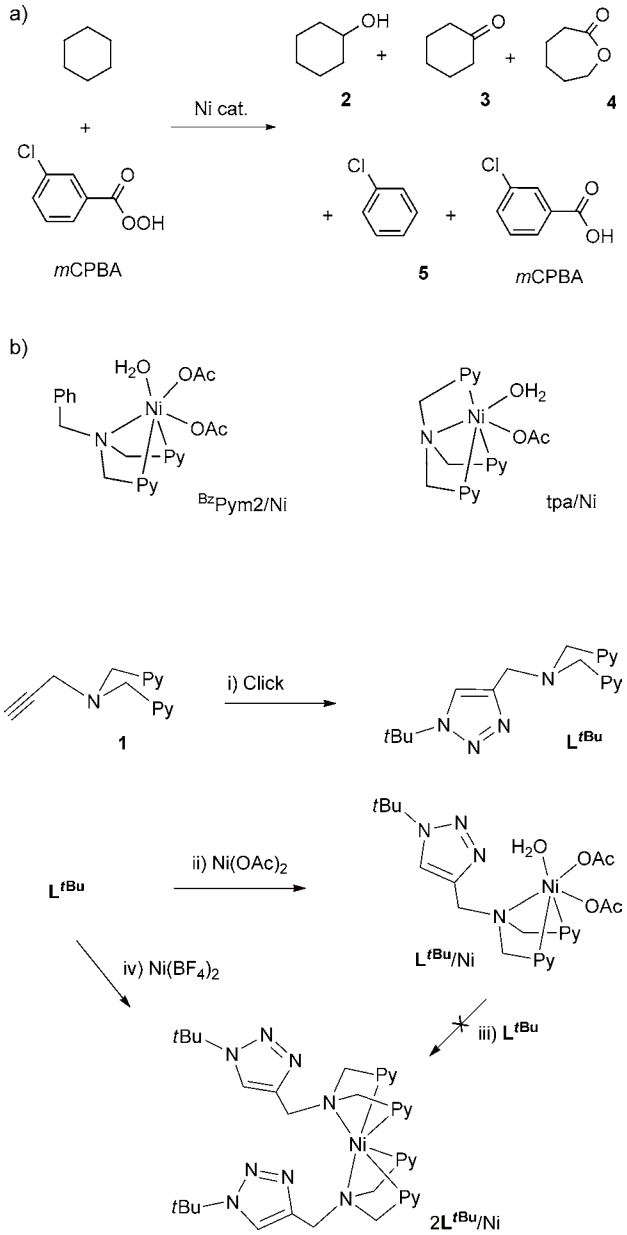

ビスピリジルメチルアミン配位子 **L** の担持量 (x) を制御した固定化錯体触媒 SBA*-**L**-x/Ni を調製し，その均一系モデル錯体 $[Ni(\mathbf{L}^{tBu})(OAc)_2(OH_2)]$ ($\mathbf{L}^{tBu}$/Ni) および $[Ni(\mathbf{L}^{tBu})_2](BF_4)_2$ についても合成・構造決定した．固定化錯体の **L**/M 比率より，配位子担持量の増加に伴って担体上の錯体種が $[Ni\mathbf{L}(X)_n]$ から $[Ni\mathbf{L}_2]$ へ変化することが示唆された．*m*CPBA を酸化剤とするシクロヘキサンの酸化反応に対して，均一および固定化錯体触媒の活性を評価した．$\mathbf{L}^{tBu}$/Ni は既報の tpa/Ni 錯体と同様の高い活性を示した．一方固定化錯体触媒は配位子担持量の増大に伴い活性が低下した．この結果は担体上における配位子量が錯体種の構造および反応活性を制御する上で重要な要素であることを示している．

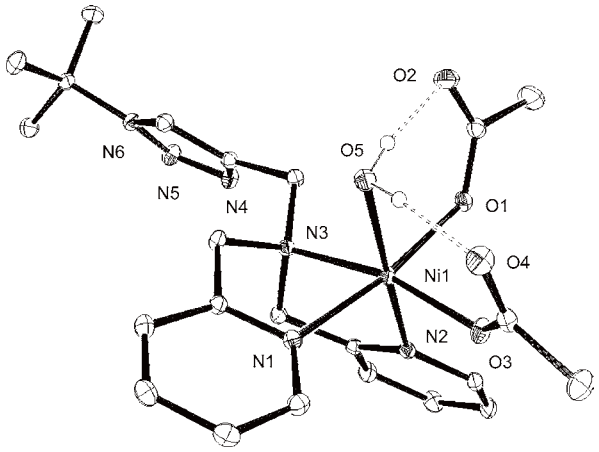
O2
O5
N6
N5
N4
N3
O1
Ni1
O4
N2
N1
O3

°

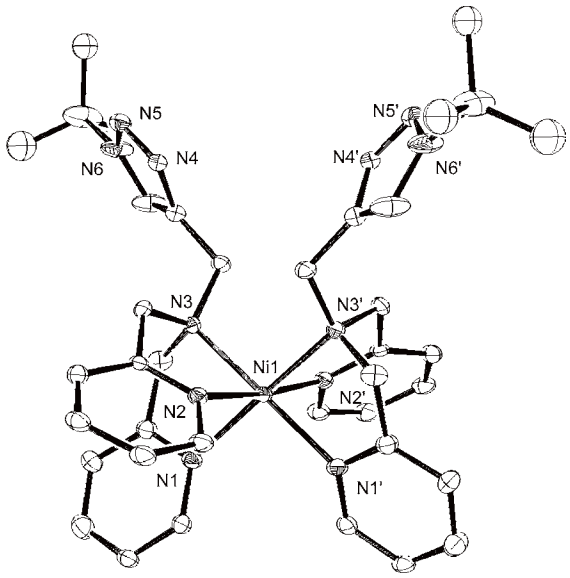
N5
N5'
N6
N4
N4'
N6'
N3
N3'
Ni1
N2
N2'
N1
N1'

°

, ,
, ,
, ,

, ,
, ,
, ,

=

=

=

,

=

=

=

=

=

=

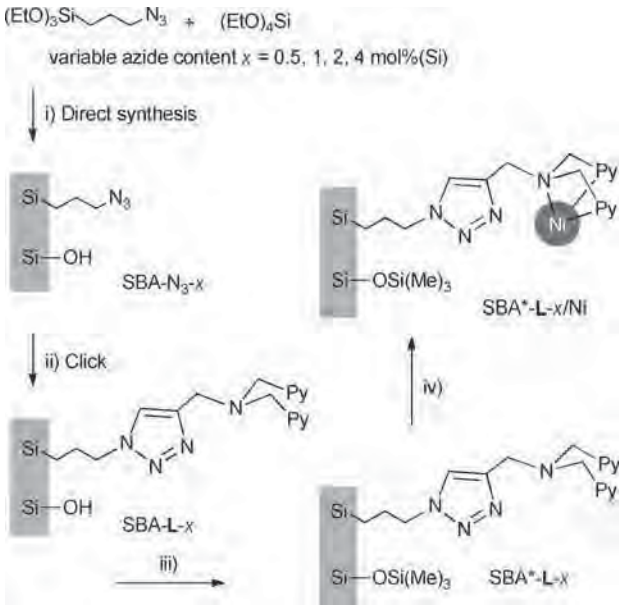
(EtO)3Si
N3
+
(EtO)4Si
variable azide content x = 0.5, 1, 2, 4 mol%(Si)
i) Direct synthesis
Si
N3
Si—OH
SBA-N3-x
ii) Click
Py
Py
N
Si
N
N
N
Si—OH
SBA-L-x
iii)
iv)
Ni
Si—OSi(Me)3
SBA*-L-x/Ni
SBA*-L-x

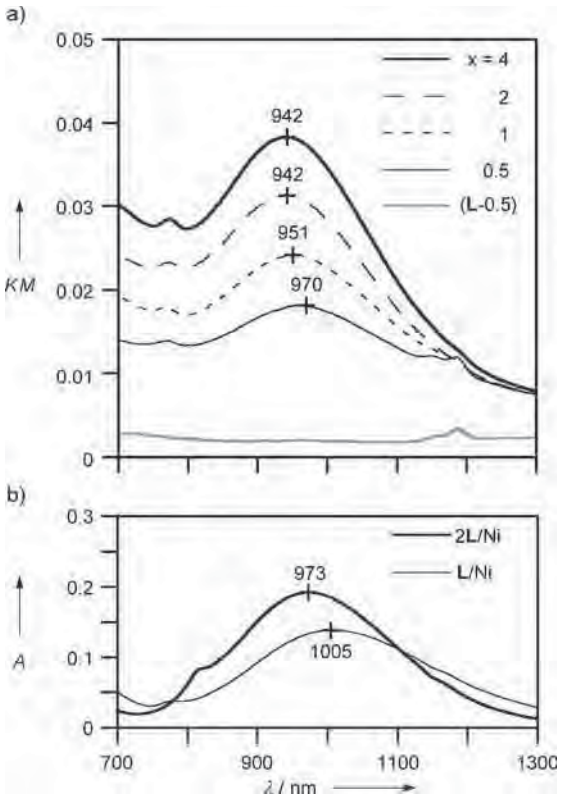
a)
0.05
0.04
0.03
0.02
0.01
0
KM
x = 4
2
1
0.5
(L-0.5)
942
942
951
970
b)
0.3
0.2
0.1
0
A
2L/Ni
L/Ni
973
1005
700
900
1100
1300
λ / nm

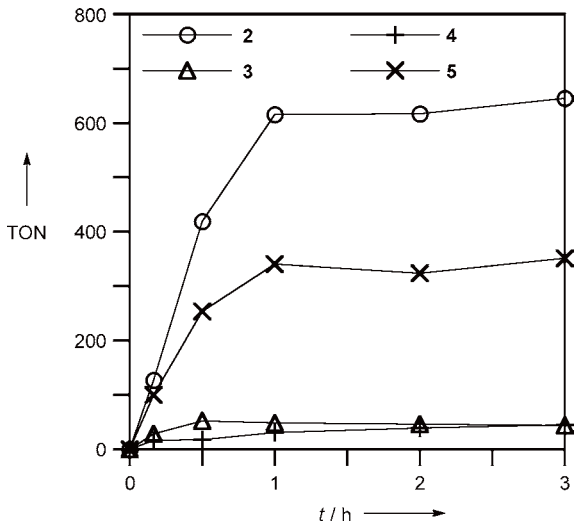
800
600
400
200
0
TON
2
4
3
5
0
1
2
3
t / h

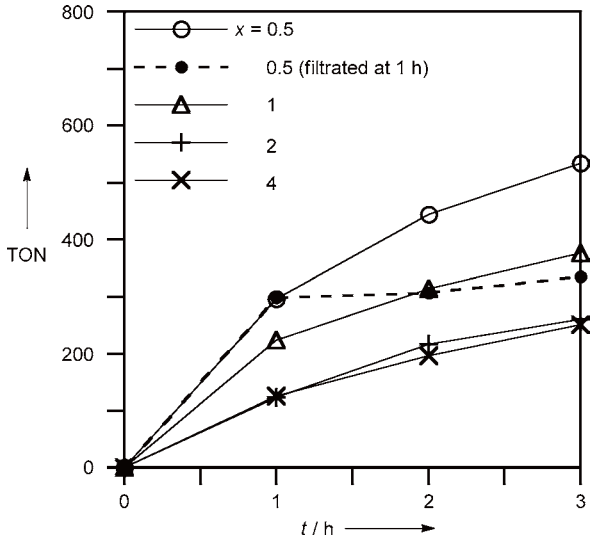
800
600
400
200
0
TON
0
1
2
3
t / h
x = 0.5
0.5 (filtrated at 1 h)
1
2
4

。

。

。

>

。

doi:10.1246/cl.130464
Published on the web June 22, 2013

Catalytic Alkane Oxidation by Homogeneous and Silica-supported Cobalt(II) Complex Catalysts with a Triazolyl Group-containing Tetradentate Ligand

Jun Nakazawa,*[1] Akinori Yata,[1] Tomoaki Hori,[1] T. Daniel P. Stack,[2] Yoshinori Naruta,[3] and Shiro Hikichi*[1]
[1]*Department of Material and Life Chemistry, Kanagawa University, 3-27-1 Rokkakubashi, Kanagawa-ku, Yokohama, Kanagawa 221-8686*
[2]*Department of Chemistry, Stanford University, 333 Campus Drive, Stanford, California, 94305-5080, USA*
[3]*Institute for Materials Chemistry and Engineering, Kyushu University, 6-10-1 Hakozaki, Higashi-ku, Fukuoka 812-8581*

(Received May 17, 2013; CL-130464; E-mail: jnaka@kanagawa-u.ac.jp)

Homogeneous and heterogeneous cobalt complex catalysts with bis(pyridylmethyl)(triazolylmethyl)amine ligand were prepared. Although simple cobalt salts catalyze cyclohexane oxidation with *m*CPBA, the cyclohexane selectivity increases upon coordination of tetradentate ligands. In the heterogeneous catalysis, the yield and selectivity of cyclohexanol are improved with an increase in the ligand density on the silica support due to the suppression of metal leaching.

Partial and selective oxidation of alkane remains a challenging reaction. To overcome this issue, the development and understanding of metal-based oxidants are considered important.[1–3] Accordingly, Itoh and co-workers have reported the catalytic oxidation of alkanes (e.g., cyclohexane) by metal complexes with a tpa (= tris(2-pyridylmethyl)amine) ligand and acetate coligands (Figure 1).[4,5] Among the tpa complexes of divalent nickel, cobalt, iron, and manganese, the nickel(II) complex shows the highest conversion, with good selectivity of alcohol over ketone. The cobalt(II)–tpa complex exhibits the highest alcohol selectivity with moderate conversion, although a longer reaction time is needed. In terms of nickel(II)–tpa complexes, the roles of the tpa ligand and the acetate coligand have been investigated.[6,7] Other nickel(II) complexes have also been reported as *m*CPBA-activating catalysts, and related nickel–oxygen complexes such as nickel(II)–acylperoxo and nickel(III)–oxygen species have been characterized by some research groups, including ourselves.[8–10] In contrast, examples of *m*CPBA-activating cobalt complexes remain scarce, and the role of the ligands as well as the reaction mechanism of the cobalt catalysts remains to be clarified.[11–17] Meanwhile, we have been investigating heterogenized metal complex catalysts.[18–22] We have recently prepared triazolyl group-containing poly(pyridyl)amine ligands, *N,N*-bis(2-pyridylmethyl)-*N*-[(1-*R*-1*H*-1,2,3-triazol-4-yl)methyl]amine, of which *R* is *tert*-butyl (= $\mathbf{L}^{t\text{-Bu}}$) for a homogeneous complex catalyst, while it is a linker to silica gel (= SBA*-**L**-*x*, *x* denotes the content of a ligand tether in mol % of silicon atom) for a heterogenized complex catalyst.[23] The nickel catalysts with these ligands exhibit cyclohexane oxygenation activity with *m*CPBA, and the catalytic performances of the heterogenized catalysts depend on the loading density of **L** on the surface of the silica support. In this work, we have prepared homogeneous and heterogeneous cobalt(II) complex catalysts in order to clarify the role of **L** and the trend of catalyses depending on the central metal ion.

A homogeneous catalyst $[Co^{II}(OAc)\mathbf{L}^{t\text{-Bu}}](BPh_4)$ (= $\mathbf{L}^{t\text{-Bu}}$/Co) was prepared from $Co(OAc)_2{\cdot}4H_2O$ and $\mathbf{L}^{t\text{-Bu}}$ with the treatment of $NaBPh_4$ in methanol according to the reported procedure of $[Co(OAc)(tpa)](BPh_4)$ (= tpa/Co).[4,24] The molecular structure of $\mathbf{L}^{t\text{-Bu}}$/Co was revealed by X-ray crystallography (Figure 2).[25] In addition to the bidentate coordination of an acetate anion, the tetradentate coordination structure of $\mathbf{L}^{t\text{-Bu}}$ is similar to the reported tpa/Co complex.[26] In addition, the strongly coordinating acetate O1 atom (Co1–O1 2.001, Co1–O2 2.438 Å) is located in a trans position to the tertiary amine N3 (Co1–N3 2.292 Å), as observed in tpa/Co. We have previously reported the molecular structures of the related nickel(II) complexes, $[Ni^{II}(OAc)_2(\mathbf{L}^{t\text{-Bu}})(H_2O)]$ (= $\mathbf{L}^{t\text{-Bu}}$/Ni) and $[Ni(\mathbf{L}^{t\text{-Bu}})_2](BF_4)_2$ (= $\mathbf{L}^{t\text{-Bu}}{}_2$/Ni).[23] In both nickel complexes, the $\mathbf{L}^{t\text{-Bu}}$ ligand coordinates to the nickel centers not by the triazole nitrogen but by the three nitrogen donors of the bis(pyridylmethyl)amine unit at facial positions. This tridentate coordination induces the formation of $\mathbf{L}^{t\text{-Bu}}{}_2$/Ni.

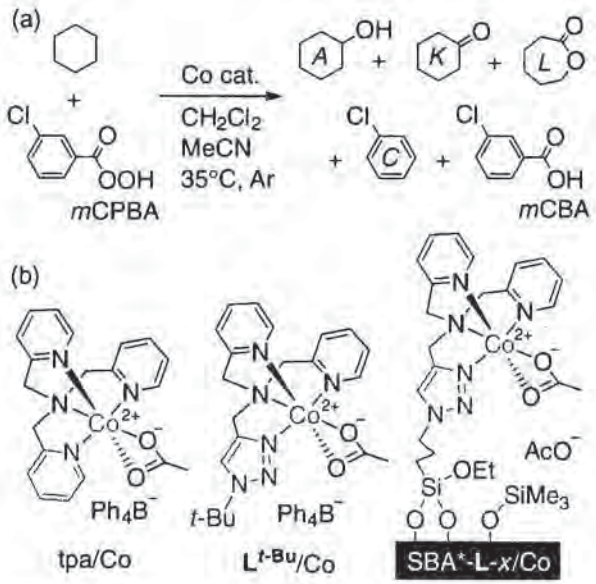

Figure 1. Cyclohexane oxidation with *m*CPBA catalyzed by cobalt(II) complex catalysts (a). Molecular structures of homogeneous and silica-immobilized complexes having tetradentate ligands (b).

Heterogenized cobalt complex catalyst was prepared by the procedure for the corresponding nickel catalyst.[23,24] The ligand-immobilized mesoporous silica gels, SBA*-**L**-*x* ($x = 0.5$ and 4 mol % of silicon atoms), were treated with a MeOH solution of $Co(OAc)_2{\cdot}4H_2O$ to obtain the SBA*-**L**-*x*/Co catalysts. Cobalt loadings on the catalysts were determined by atomic absorption

© 2013 The Chemical Society of Japan

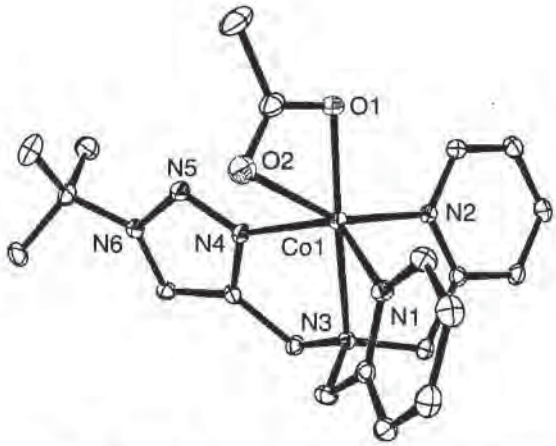

Figure 2. Molecular structure of $[Co(OAc)(\mathbf{L}^{t\text{-}Bu})](BPh_4)$. Hydrogen atoms on the carbon backbone and BPh_4 anion are omitted for clarity. Thermal ellipsoids are drawn for a 30% probability level. Co1–O1 2.001(1), Co1–O2 2.438(2), Co1–N1 2.065(2), Co1–N2 2.079(2), Co1–N3 2.292(1), Co1–N4 2.051(2) Å.

Table 1. Ligand and metal loadings on the immobilized catalysts

Catalyst	L /mmol g^{-1}	Co /mmol g^{-1}	Co (recovered) /mmol g^{-1} [a]
SBA*-**L**-0.5/Co	0.080	0.080	0.034
SBA*-**L**-4/Co	0.316	0.225	0.162

[a]After usage for the oxidation catalysis.

analysis of the KOH-digested solution (Table 1). The molar ratios of the ligand and cobalt on the two immobilized catalysts were different (**L**:Co ca. 1:1 in SBA*-**L**-0.5/Co and 1.6:1 in SBA*-**L**-4/Co), as was found in the nickel catalysts. Assuming that the coordination structure of the immobilized cobalt centers is the same as that of $\mathbf{L}^{t\text{-}Bu}$/Co, some free ligand sites remain on the SBA*-**L**-4/Co.

The cyclohexane oxidation catalysis with *m*CPBA oxidant was initially examined on the homogeneous catalysts (Table 2 and Figure S8).[24] Generally, this type of cyclohexane oxidation yields cyclohexanol (*A*) with its overoxidation products, cyclohexanone (*K*) and caprolactone (*L*). The reactivity of catalysts for the oxidation was evaluated by the product formation turnover number (= TON) and the alcohol selectivity $A/(K+L)$ at 35 °C. The oxidation did not proceed catalytically in the absence of a catalyst or the presence of nickel acetate. In the presence of $\mathbf{L}^{t\text{-}Bu}$/Ni catalyst, the reaction proceeded within 1 h to give a high TON (599) and selectivity (7.4) for *A*.[23] This result showed clear reactivity enhancement of the nickel center upon coordination of the $\mathbf{L}^{t\text{-}Bu}$ ligand. In the case of cobalt, simple cobalt(II) salts such as $CoCl_2$, $Co(NO_3)_2$, and $Co(OAc)_2$ catalyzed the oxidation with moderate TON and with an alcohol selectivity range of 2.3 to 4.5, as has been previously reported for catalysis with the use of $Co(ClO_4)_2$.[27] On the other hand, both cobalt complexes with the tetradentate ligands ($\mathbf{L}^{t\text{-}Bu}$/Co and tpa/Co) showed higher TON and alcohol selectivity than simple cobalt salts. It is noteworthy that the catalysis with the

Table 2. Product TON in cyclohexane oxidation catalyzed by homogeneous and immobilized cobalt complex catalysts with *m*CPBA[a]

Catalyst	*t*/h	TON				$A/(K+L)$
		A	*K*	*L*	*C*	
None[b]	3	8	5	0	15	1.8
$Ni(OAc)_2$	3	18	7	0	11	2.6
$CoCl_2$	0.5	515	221	4	511	2.3
$Co(NO_3)_2$	0.5	331	66	8	255	4.5
$Co(OAc)_2$	0.5	368	80	7	277	4.2
tpa/Co[c]	1[d]	300	16	nd	nd	18.8
	3	ca. 600	nd	nd	nd	nd
$\mathbf{L}^{t\text{-}Bu}$/Co	2	604	98	14	459	5.4
SBA*-**L**-0.5/Co	3	577	138	6	377	4.0
SBA*-**L**-4/Co	3	745	80	25	582	7.1
SBA*-**L**-4/Co[e]	3	533	191	13	432	2.6

[a]Catalyst 2 μmol, cyclohexane 15 mmol, *m*CPBA 2 mmol in CH_2Cl_2 (3 mL)/MeCN (1 mL) at 35 °C for 3 h under Ar. [b]Values based on 2 μmol of virtual catalyst. [c]From ref 4, at room temperature for 1 h. nd: no data. [d]The reaction is in progress. [e]The catalyst was removed at 15 min.

tetradentate ligands required a longer reaction time (2–3 h) than that with simple salts (within 30 min). A major difference in reactivity of $\mathbf{L}^{t\text{-}Bu}$/Co from tpa/Co is the reduction in alcohol selectivity. Based on the similar molecular structures of the two complexes, the reactivity difference may be caused by coordination properties of the triazole moiety. In the nickel(II) complexes, $[Ni^{II}(OAc)_2(\mathbf{L}^{t\text{-}Bu})(H_2O)]$ and $[Ni(\mathbf{L}^{t\text{-}Bu})_2]^{2+}$, the triazole group does not coordinate to the nickel(II) centers.[23] Thus, the coordinating triazolyl side arm on the cobalt center may be capable of replacement with *m*CPBA or *m*CBA (= *m*-chlorobenzoic acid, by-product) molecules under the oxidation catalysis. A large quantity of chlorobenzene (*C*), which is a side product from *m*CPBA via homolytic cleavage of the peroxide O–O bond, was detected in all cases with homogeneous cobalt catalysts.

Cyclohexane oxidation with heterogeneous cobalt complex catalysts was carried out (Table 2 and Figure 3). The ligand-dense catalyst, SBA*-**L**-4/Co, showed a higher product TON and alcohol selectivity than did SBA*-**L**-0.5/Co catalyst. This reactivity trend of the cobalt system was opposite to that of the related nickel system.[23] The lowest loading Ni catalyst, SBA*-**L**-0.5/Ni, showed high reactivity (TON = 534, and selectivity = 10.5 for *A* after 3 h), similar to that for the related homogeneous catalyst $\mathbf{L}^{t\text{-}Bu}$/Ni. An increase in the loading of SBA*-**L**-*x*/Ni catalysts resulted in a decrease in TON while maintaining the high selectivity for alcohol. This tendency of the nickel systems may be due to the coordination of an excess ligand to form an inert $\mathbf{L}^{t\text{-}Bu}{}_2$/Ni species that has no coordination site for the oxidant. After catalysis, cobalt loadings on both recovered catalysts were analyzed (Table 2). More than half the amount of cobalt ion was leached from SBA*-**L**-0.5/Co during the catalysis or workup process, and the leached amount was much higher than that from SBA*-**L**-4/Co. To investigate this leaching process, a filtration test was applied for the heterogeneous catalysis with SBA*-**L**-4/Co. 15 min after initiation of the catalysis, the catalyst was removed by filtration (Advantech

 © 2013 The Chemical Society of Japan

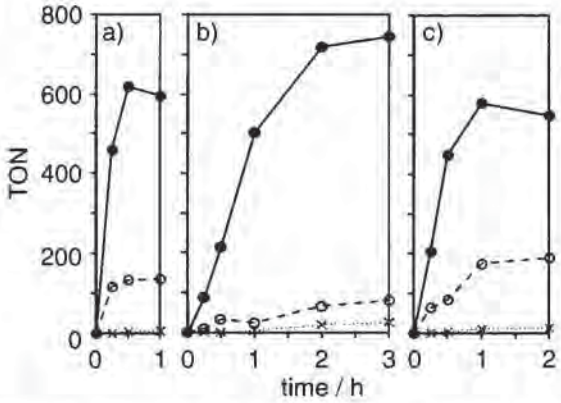

Figure 3. Time course of cyclohexanol (filled circle), cyclohexanone (open circle), and ε-caprolactone (cross) formations in cyclohexane oxidation reaction with *m*CPBA catalyzed by SBA*-**L**-0.5/Co (a), SBA*-**L**-4/Co (b), and catalyst removal of SBA*-**L**-4/Co at 15 min (c). Reaction conditions: Catalyst 2 μmol, cyclohexane 15 mmol, *m*CPBA 2 mmol in CH_2Cl_2 (3 mL)/MeCN (1 mL) at 35 °C under Ar.

PTFE syringe filter), and the product formation in this solution was then monitored for 3 h. The reaction was found to remain in progress for 2 h after the filtration, although with a reduction in the alcohol selectivity. This result indicates that the eluted cobalt ion shows similar reactivity to that of the homogeneous simple cobalt salts. Due to the higher local ligand density and the existence of some free ligand sites on the silica surface, SBA*-**L**-4/Co retains its cobalt ion more tightly, resulting in the highest yield of cyclohexanol among the catalysts we prepared. It remains unclear, however, whether the leaching mechanism involves oxidation, protonation, or an exchange of **L** by the excess quantity of *m*CPBA oxidant during the reaction.

In conclusion, we prepared homogeneous and heterogeneous cobalt complex catalysts with a tpa-type ligand, which contains a triazole group. Coordination of the ligand improved the yield and selectivity of cyclohexanol in the cyclohexane oxidation with *m*CPBA. The ligand-dense environment on the silica surface prevented metal elution, thus improving the catalytic reactivity. Finally, the reactivity trend of the immobilized cobalt system, depending on the ligand density, was the reverse of that of the related nickel system. These results demonstrate the importance of site density control appropriate to the type of metal ion utilized in the development of immobilized complex catalysts.

This work was supported in part by a Cooperative Research Program of "Network Joint Research Center for Materials and Devices" (No. 2012348) and by a Strategic Development of Research Infrastructure for Private Universities from the Ministry of Education, Culture, Sports, Science and Technology of Japan. S.H. and J.N. also thank Kanagawa University for financial support.

References and Notes

1 T. Newhouse, P. S. Baran, *Angew. Chem., Int. Ed.* **2011**, *50*, 3362.
2 R. Giri, B.-F. Shi, K. M. Engle, N. Maugel, J.-Q. Yu, *Chem. Soc. Rev.* **2009**, *38*, 3242.
3 M. M. Díaz-Requejo, P. J. Pérez, *Chem. Rev.* **2008**, *108*, 3379.
4 T. Nagataki, Y. Tachi, S. Itoh, *Chem. Commun.* **2006**, 4016.
5 T. Nagataki, K. Ishii, Y. Tachi, S. Itoh, *Dalton Trans.* **2007**, 1120.
6 T. Nagataki, S. Itoh, *Chem. Lett.* **2007**, *36*, 748.
7 M. Balamurugan, R. Mayilmurugan, E. Suresh, M. Palaniandavar, *Dalton Trans.* **2011**, *40*, 9413.
8 F. F. Pfaff, F. Heims, S. Kundu, S. Mebs, K. Ray, *Chem. Commun.* **2012**, *48*, 3730.
9 S. Hikichi, K. Hanaue, T. Fujimura, H. Okuda, J. Nakazawa, Y. Ohzu, C. Kobayashi, M. Akita, *Dalton Trans.* **2013**, *42*, 3346.
10 J. Nakazawa, S. Terada, M. Yamada, S. Hikichi, *J. Am. Chem. Soc.* **2013**, *135*, 6010.
11 S. Hikichi, M. Akita, Y. Moro-oka, *Coord. Chem. Rev.* **2000**, *198*, 61.
12 S. Hikichi, H. Komatsuzaki, N. Kitajima, M. Akita, M. Mukai, T. Kitagawa, Y. Moro-oka, *Inorg. Chem.* **1997**, *36*, 266.
13 S. Hikichi, C. Kobayashi, M. Yoshizawa, M. Akita, *Chem.—Asian J.* **2010**, *5*, 2086.
14 S. Hikichi, H. Komatsuzaki, M. Akita, Y. Moro-oka, *J. Am. Chem. Soc.* **1998**, *120*, 4699.
15 S. Hikichi, H. Okuda, Y. Ohzu, M. Akita, *Angew. Chem., Int. Ed.* **2009**, *48*, 188.
16 S. Hikichi, M. Yoshizawa, Y. Sasakura, M. Akita, Y. Moro-oka, *J. Am. Chem. Soc.* **1998**, *120*, 10567.
17 S. Hikichi, M. Yoshizawa, Y. Sasakura, H. Komatsuzaki, Y. Moro-oka, M. Akita, *Chem.—Eur. J.* **2001**, *7*, 5011.
18 T. J. Terry, G. Dubois, A. Murphy, T. D. P. Stack, *Angew. Chem., Int. Ed.* **2007**, *46*, 945.
19 T. J. Terry, T. D. P. Stack, *J. Am. Chem. Soc.* **2008**, *130*, 4945.
20 J. Nakazawa, T. D. P. Stack, *J. Am. Chem. Soc.* **2008**, *130*, 14360.
21 S. Hikichi, M. Kaneko, Y. Miyoshi, N. Mizuno, K. Fujita, M. Akita, *Top. Catal.* **2009**, *52*, 845.
22 J. Nakazawa, B. J. Smith, T. D. P. Stack, *J. Am. Chem. Soc.* **2012**, *134*, 2750.
23 Alkane oxidation reactivity of related homogeneous and heterogeneous nickel complexes with $\mathbf{L}^{t\text{-}\mathbf{Bu}}$ and SBA*-**L**-*x*: J. Nakazawa, T. Hori, T. D. P. Stack, S. Hikichi, *Chem.—Asian J.* **2013**, *8*, 1191.
24 See Supporting Information. Supporting Information is available electronically on the CSJ-Journal Web site, http://www.csj.jp/journals/chem-lett/index.html.
25 Crystal data for $[Co(OAc)(\mathbf{L}^{t\text{-}\mathbf{Bu}})](BPh_4)$: $C_{45}H_{51}BCoN_6O_2$, $fw = 773.63\ g\ mol^{-1}$, triclinic $P\bar{1}$ (No. 2), $a = 11.120(3)$, $b = 13.206(3)$, $c = 14.592(4)$ Å, $\alpha = 91.811(1)$, $\beta = 102.361(4)$, $\gamma = 109.947(4)°$, $V = 1954.9(9)$ Å^3, $Z = 2$, $T = 113$ K, $\mu = 0.487\ mm^{-1}$, $D_{calcd} = 1.314\ g\ cm^{-3}$. Number of unique reflections = 8905, number of reflections included in the refinement = 8031 ($I > 2\sigma(I)$), $R = 5.48$ (all data), 5.01 ($I > 2\sigma(I)$), $R_w = 10.70$ (all data), 10.14 ($I > 2\sigma(I)$). GOF = 1.138. Crystallographic data reported in this manuscript have been deposited with Cambridge Crystallographic Data Centre as supplementary publication no. CCDC-898169. Copies of the data can be obtained free of charge via http://www.ccdc.cam.ac.uk/conts/retrieving.html (or from the Cambridge Crystallographic Data Centre, 12, Union Road, Cambridge, CB2 1EZ, U.K.; fax: +44 1223 336033; or deposit@ccdc.cam.ac.uk).
26 Selected bond lengths in $[Co(tpa)(OAc)](BPh_4)$ from ref 4: Co–N1 (4° amine) 2.234(2), Co–O1 (C–O, trans to 4° amine) 2.043(2), Co–O2 (C=O, trans to Py N3) 2.376(2), Co–N2 (Py, trans to Py N4) 2.086(2), Co–N3 (Py)2.081(2), Co–N4 (Py) 2.096(2) Å.
27 W. Nam, J. Y. Ryu, I. Kim, C. Kim, *Tetrahedron Lett.* **2002**, *43*, 5487.

 © 2013 The Chemical Society of Japan

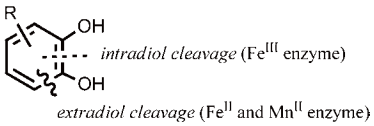

=

=

+

+

WILEY
ONLINE LIBRARY

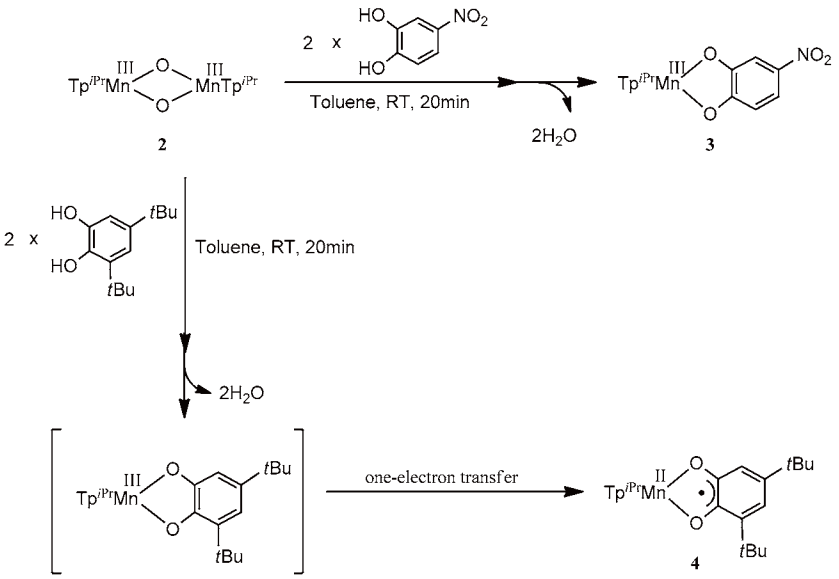
2 x
HO
NO2
HO
Toluene, RT, 20min
2H2O
2
3
2 x
HO
tBu
HO
tBu
Toluene, RT, 20min
2H2O
one-electron transfer
4

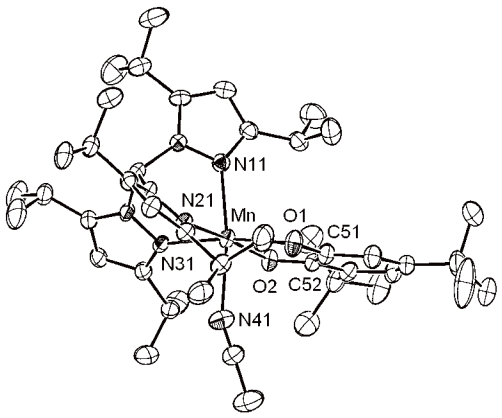
N11
N21
Mn
O1
C51
N31
O2
C52
N41

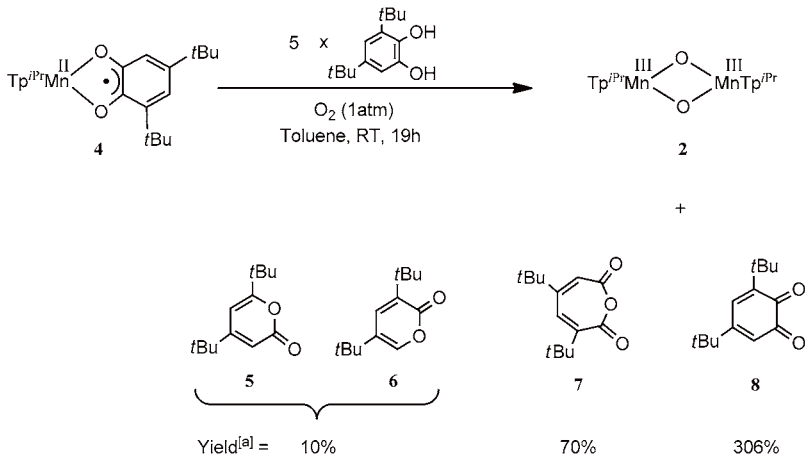
Tp^{iPr}Mn
II
tBu
tBu
4
5 x
tBu
OH
tBu
OH
O$_2$ (1atm)
Toluene, RT, 19h
III
III
Tp^{iPr}Mn
MnTp^{iPr}
2
+
5
6
7
8
Yield[a] =
10%
70%
306%

M

NJC

RSC Publishing

PAPER

O_2 activation and external substrate oxidation capability of a Co(II)–semiquinonato complex

Cite this: *New J. Chem.*, 2013, **37**, 2377

Atsushi Ikeda, Kazuya Hoshino, Hidehito Komatsuzaki, Minoru Satoh, Jun Nakazawa and Shiro Hikichi*

The synthesis, characterization and catalytic oxidizing activity of a cobalt(II)–semiquinonato complex with hydrotris(3,5-dimethyl-1-pyrazolyl)borate (=Tp^{Me2}) have been investigated. The cobalt(II)–semiquinonato complex can be synthesized by two alternative routes; (i) dehydrative condensation of a cobalt(II)–hydroxo complex with 3,5-di-*tert*-butylcatechol and following O_2 oxidation, or (ii) one-electron oxidation of catechol by a dinuclear cobalt(III)-bis(μ-oxo) complex. The synthesized cobalt(II)–semiquinonato complex can bind O_2 at low temperatures and catalyzes the oxidation of *ortho*- and *para*-hydroquinones to the corresponding benzoquinones concomitant with the generation of hydrogen peroxide. The resulting H_2O_2 is utilized as an oxidant for the epoxidation of allyl alcohol catalyzed by peroxotungstate. Aerobic oxidation of benzyl alcohol to the corresponding aldehyde is also promoted by the cobalt(II)–semiquinonato complex.

www.rsc.org/njc

Introduction

1

Results and discussion

Synthesis and characterization of the cobalt(II)–semiquinonato complex 1

1

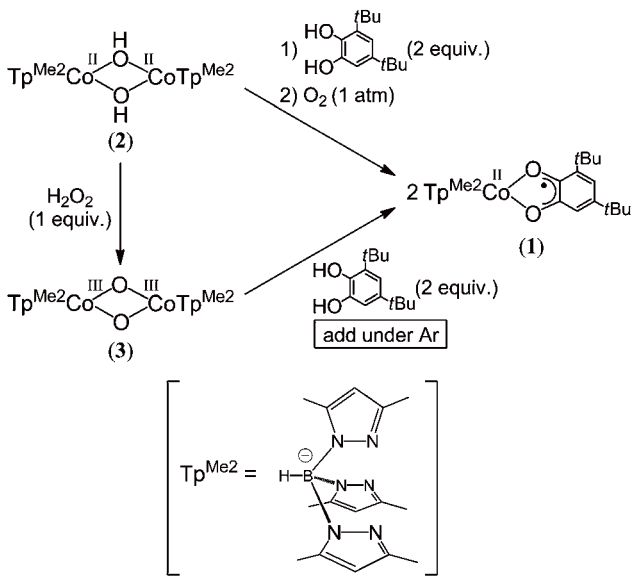

Scheme 1 1

μ 2 1

1

1

1

1

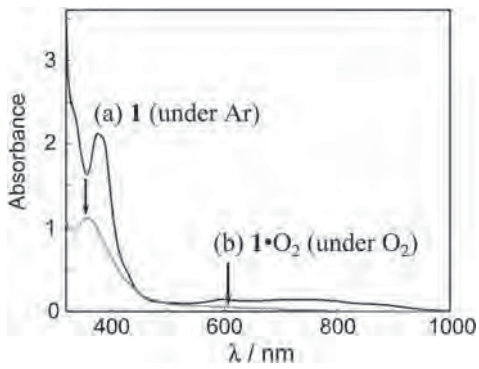

Fig. 1 1 *in situ*

1 1 1

1

1

μ μ

3

3

1

1

3 3

μ

1

1

1 1

1

1

1

1

P

1

1

S

1

4

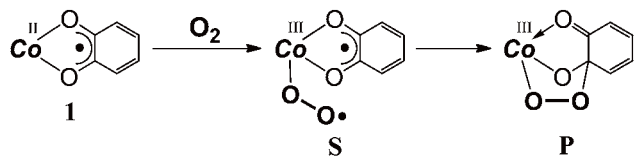

Scheme 2 1

 This journal is © The Royal Society of Chemistry and the Centre National de la Recherche Scientifique 2013

4

μ

5

5 1

4 5

1

1

1 1

1

Hydroquinone oxidation and concomitant H_2O_2 generation catalyzed by 1

1

1

1

1

1

η μ

6

1

1

6

2

1

Table 1 1[a]

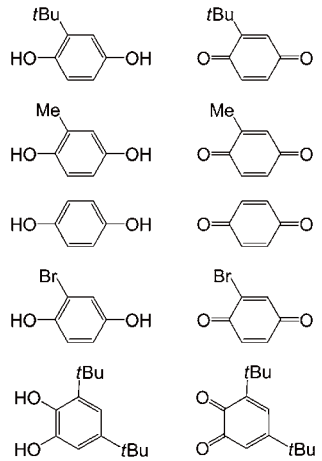

>

1 μ

Table 2 1[a]

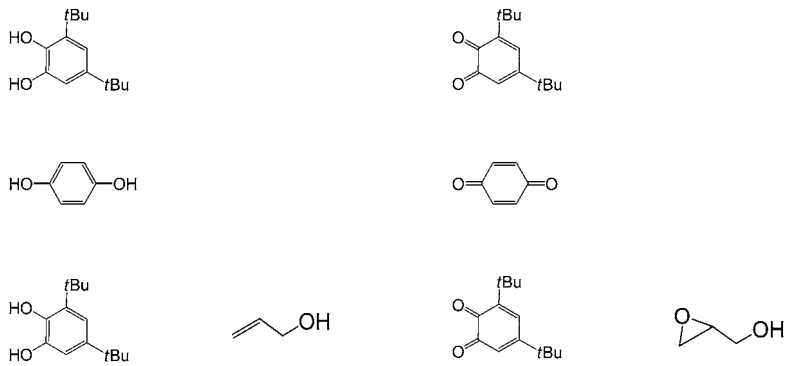

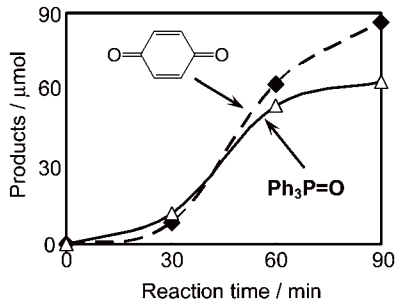

Fig. 2 *para*
1 1 µ
µ

2 >
1

2
1
2 1

P

S
1

1

Alcohol oxidation capability

1
1

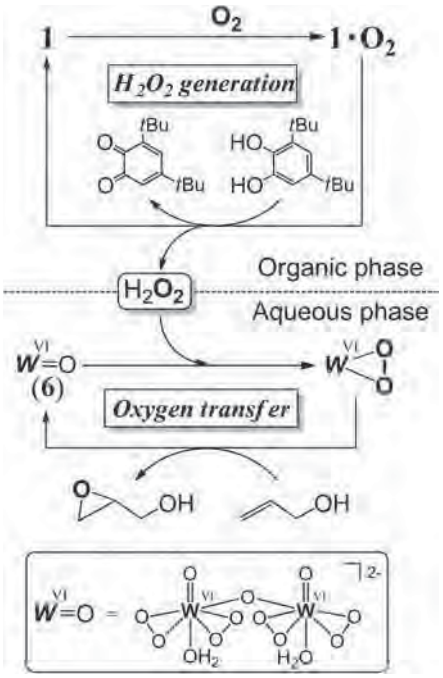

Scheme 3 1 5

 This journal is © The Royal Society of Chemistry and the Centre National de la Recherche Scientifique 2013

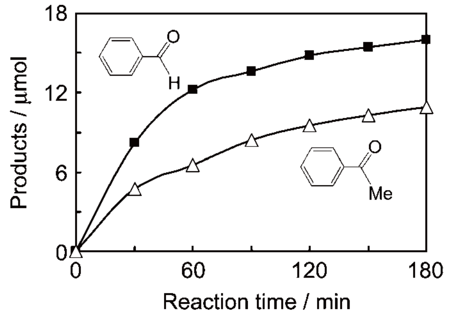

Fig. 3
1 1 μ μ

1
1
1
1
1
1

1

1
1
–
1
– –
1 –

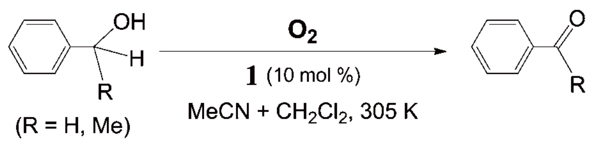

Experimental section

General

1 **2**
μ **3**
η μ ·
6

μ

μ

Synthesis of the Co(II)–semiquinonato complex [Co^{II}(DTBSQ)(Tp^{Me_2})] (1)

2

1
2 **1** –
– –

Conclusion

1

References

– –

Catalytic oxidation

1 μ

58

97

H_2O_2 detection experiment

455

103

1 μ **104**

316

40

107

–

78

Co-oxidation of -hydroquinone and Ph_3P with O_2 catalyzed by 1 **51**

1 μ μ **50**

μ **50**

327

104

μ μ

35

Co-oxidation of $DTBCH_2$ and allylalcohol with O_2

1 μ **6** **12**

η μ · μ **8**

12

46

50

Acknowledgements

50

37

48

49

 This journal is © The Royal Society of Chemistry and the Centre National de la Recherche Scientifique 2013

52 30
29
45
113
31
348
39
39
39
47
36
345
7
292
38
47
121 14
33 15
128
37
46
16
134 38
144 9

Contents lists available at SciVerse ScienceDirect

journal homepage: www.elsevier.com/locate/electacta

ARTICLE INFO

ABSTRACT

1. Introduction

2. Experimental

μ

3. Results and discussion

μ

μ

μ

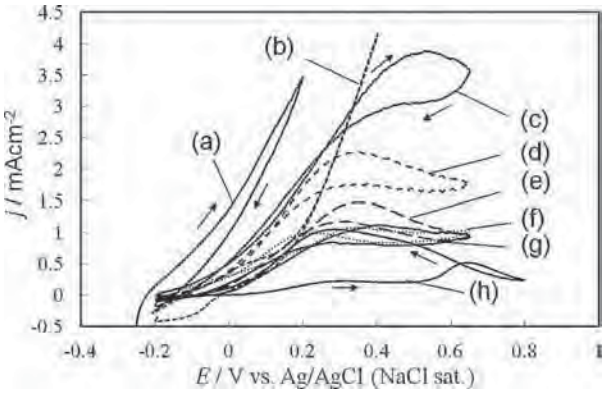

Fig. 1.

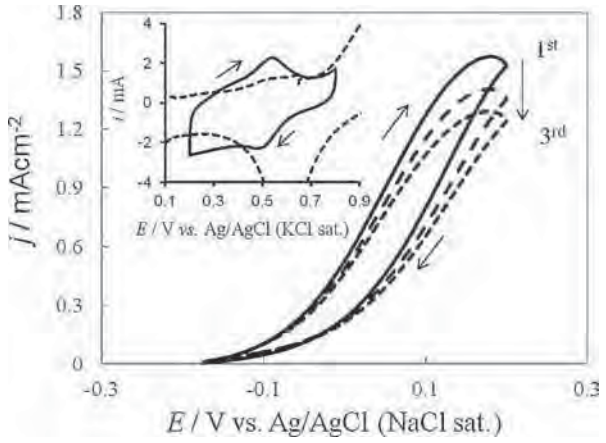

Fig. 2.

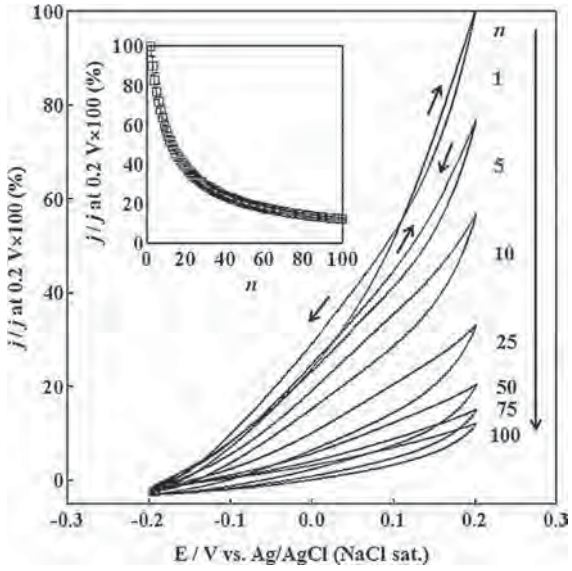

Fig. 3.

Table 1

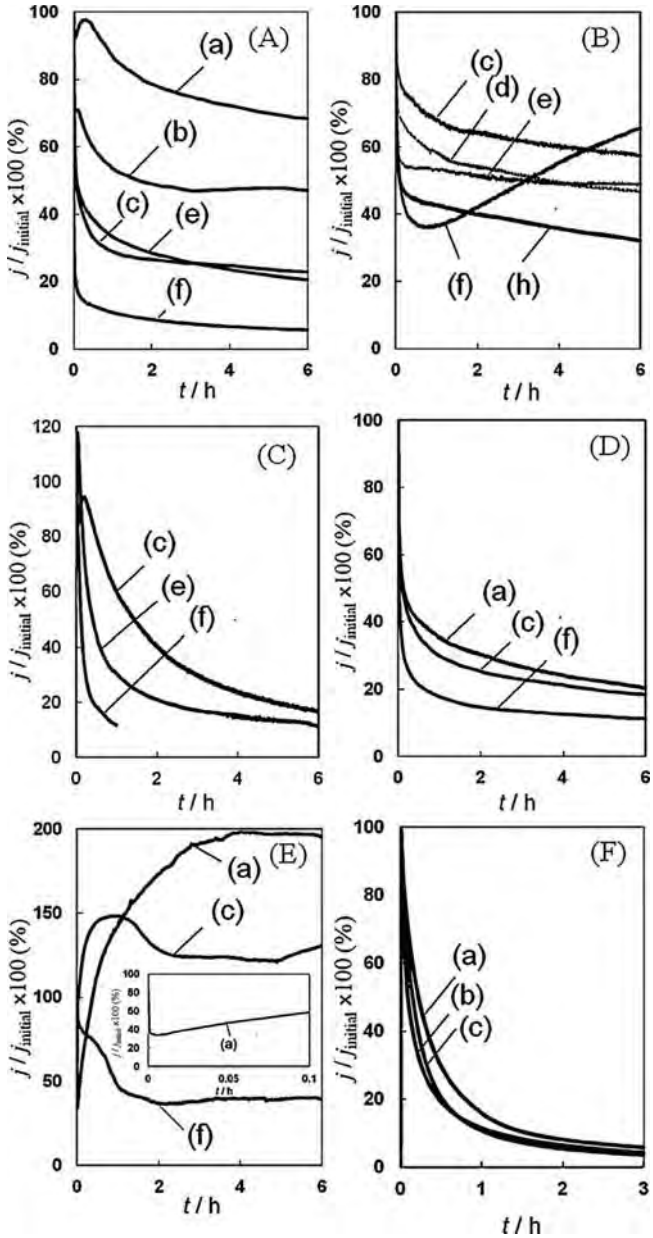

Fig. 4.

μ

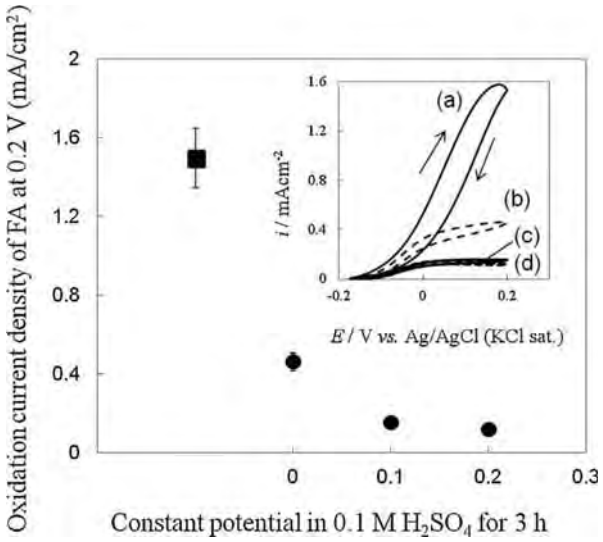
Oxidation current density of FA at 0.2 V (mA/cm²)
Constant potential in 0.1 M H₂SO₄ for 3 h
i / mAcm⁻²
E / V vs. Ag/AgCl (KCl sat.)
(a)
(b)
(c)
(d)

Fig. 6.

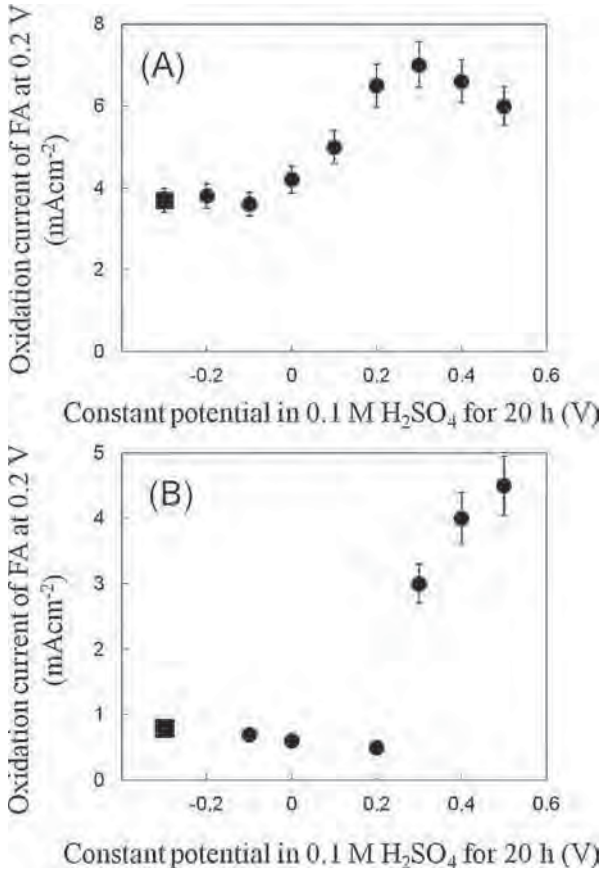
(A)
Oxidation current of FA at 0.2 V (mAcm⁻²)
Constant potential in 0.1 M H₂SO₄ for 20 h (V)
(B)
Oxidation current of FA at 0.2 V (mAcm⁻²)
Constant potential in 0.1 M H₂SO₄ for 20 h (V)

Fig. 5.

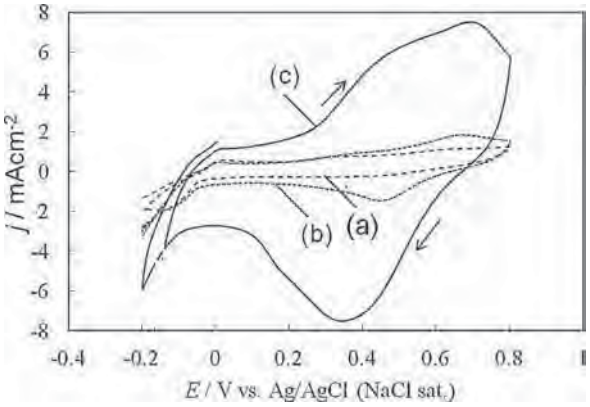

Fig. 7.

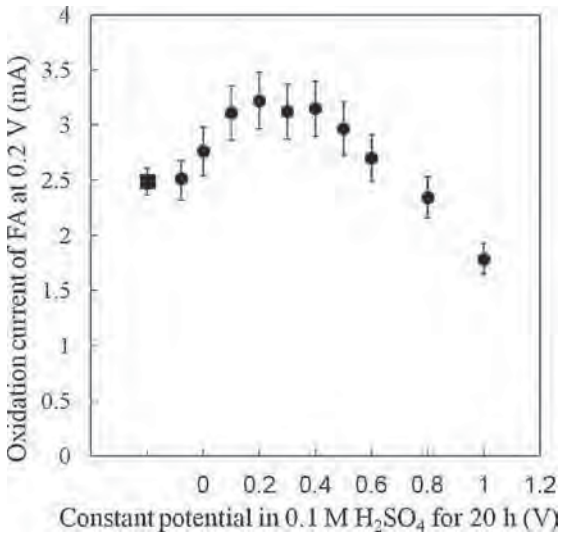

Fig. 8.

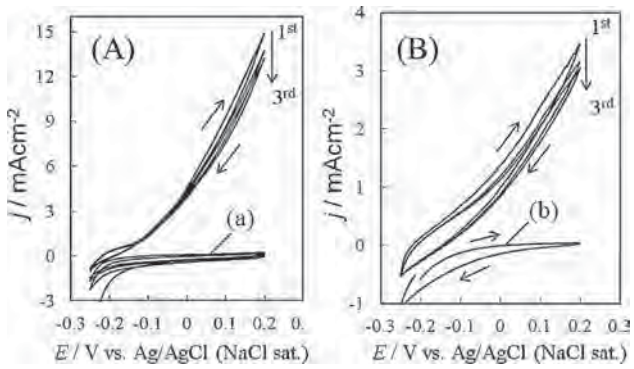

Fig. 9.

4. Conclusions

Acknowledgments

References

Delivered by Publishing Technology to: Tohoku University
IP: 130.34.113.201 On: Mon, 17 Feb 2014 08:30:31
Copyright: American Scientific Publishers

Delivered by Publishing Technology to: Tohoku University
IP: 130.34.113.201 On: Mon, 17 Feb 2014 08:30:31
Copyright: American Scientific Publishers

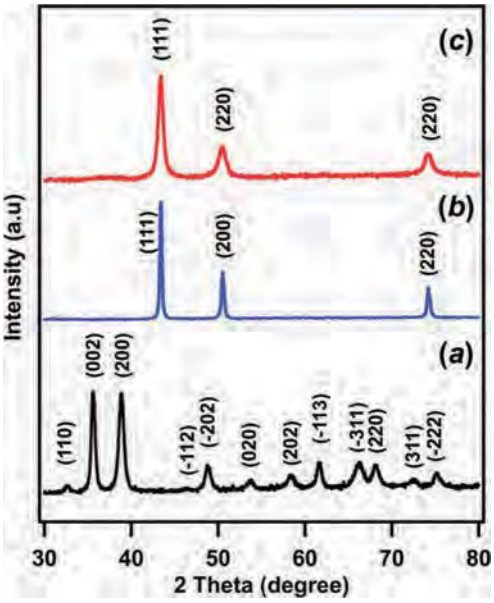

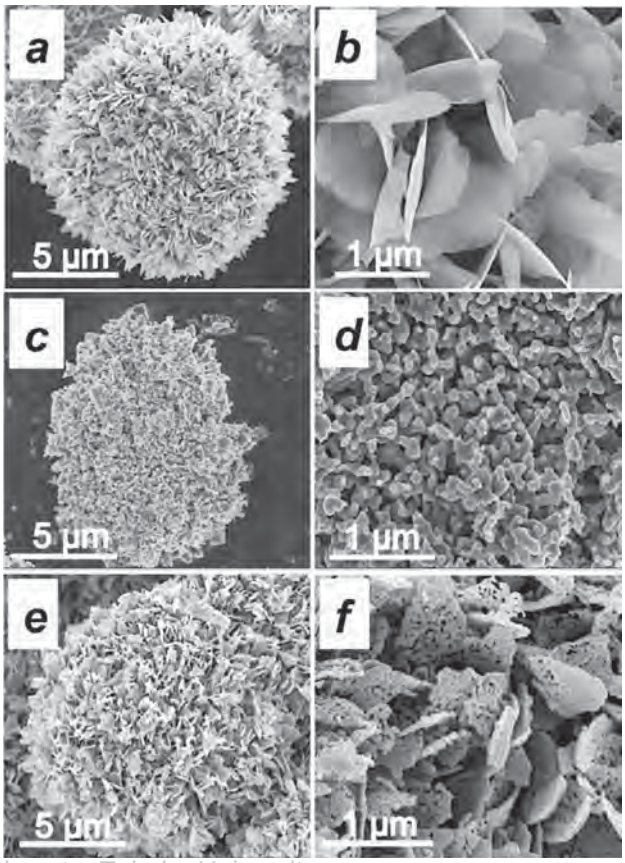

Delivered by Publishing Technology to: Tohoku University
IP: 130.34.113.201 On: Mon, 17 Feb 2014 08:30:31
Copyright: American Scientific Publishers

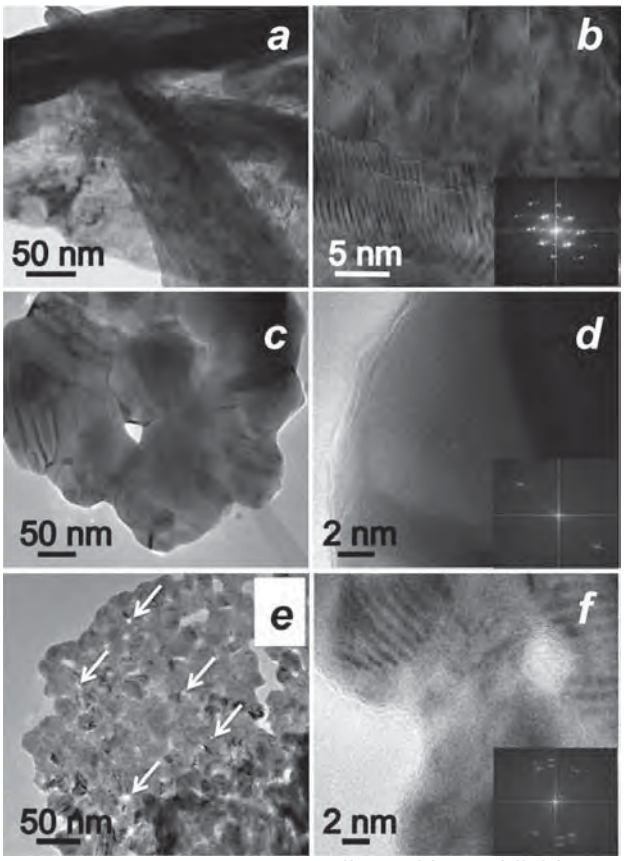

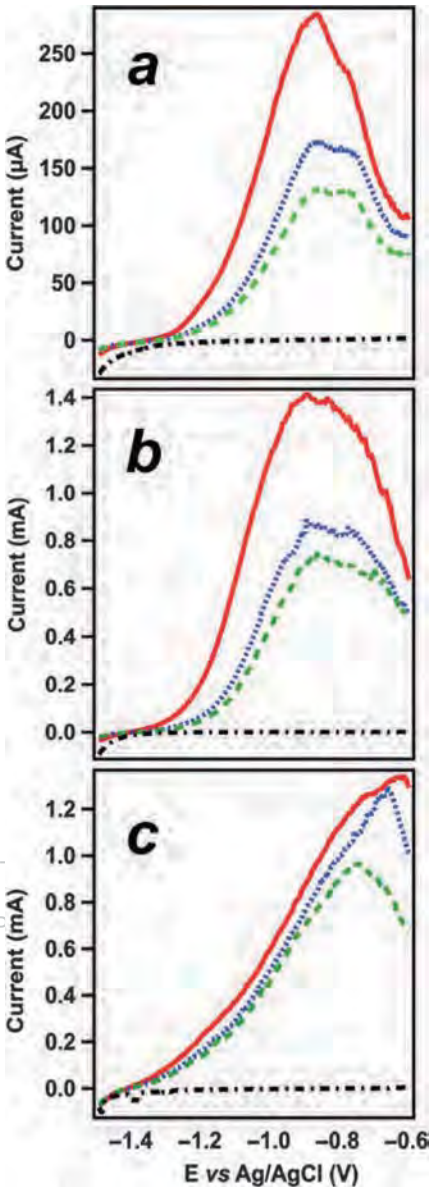

Delivered by Publishing Technology to:
IP: 130.34.113.201 On: Mon, 17 Feb
Copyright: American Scientific P

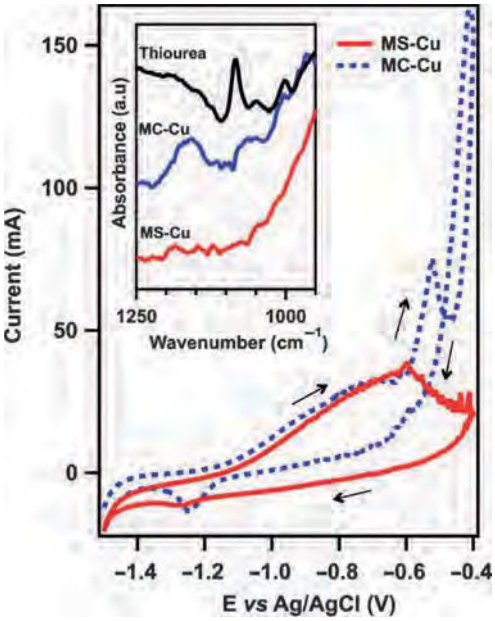

Delivered by Publishing Technology to: Tohoku University
IP: 130.34.113.201 On: Mon, 17 Feb 2014 08:30:31
Copyright: American Scientific Publishers

Delivered by Publishing Technology to: Tohoku University
IP: 130.34.113.201 On: Mon, 17 Feb 2014 08:30:31
Copyright: American Scientific Publishers

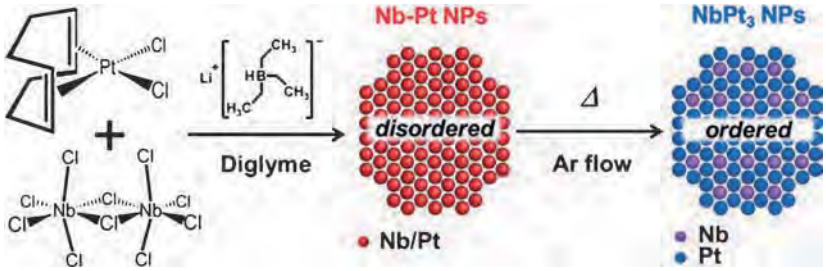
Nb-Pt NPs
NbPt3 NPs
Diglyme
disordered
Δ
Ar flow
ordered
Nb/Pt
Nb
Pt

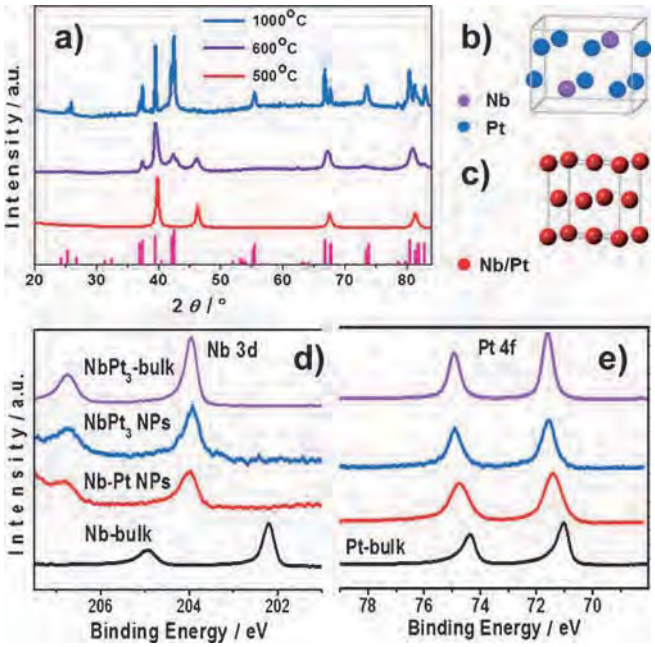
a)
1000°C
600°C
500°C
Intensity / a.u.
2θ / °
b)
Nb
Pt
c)
Nb/Pt
d)
Nb 3d
NbPt3-bulk
NbPt3 NPs
Nb-Pt NPs
Nb-bulk
Binding Energy / eV
e)
Pt 4f
Pt-bulk
Binding Energy / eV

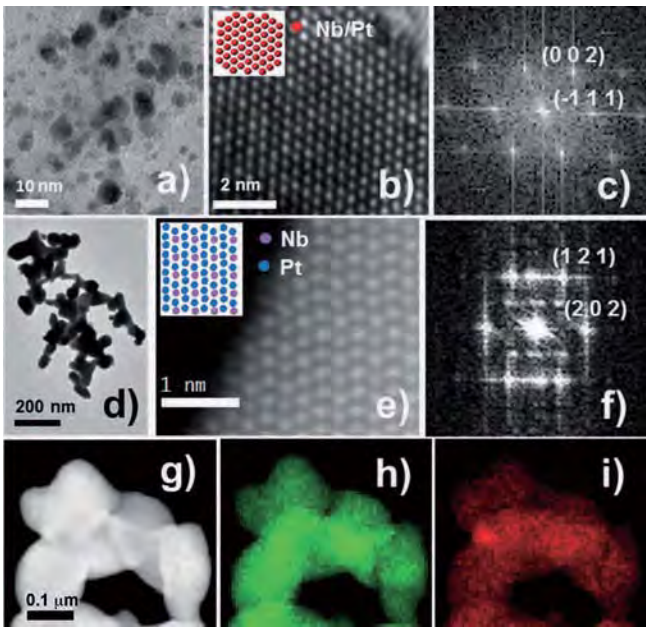
10 nm
a)
Nb/Pt
2 nm
b)
(0 0 2)
(-1 1 1)
c)
200 nm
d)
Nb
Pt
1 nm
e)
(1 2 1)
(2 0 2)
f)
g)
0.1 µm
h)
i)

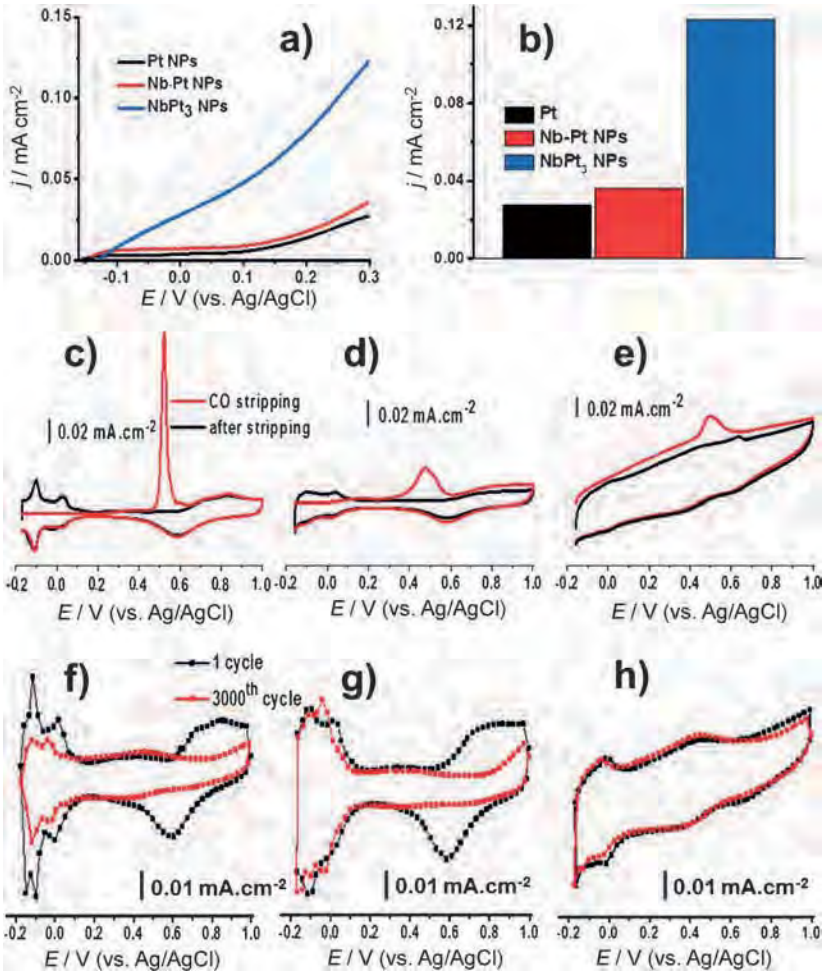

+

M

–

–

– +

– +

–

M

These are not the final page numbers!

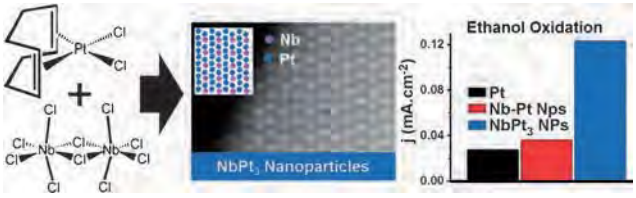
Nb
Pt
NbPt3 Nanoparticles
Ethanol Oxidation
j (mA.cm-2)
0.12
0.08
0.04
0.00
Pt
Nb-Pt Nps
NbPt3 NPs

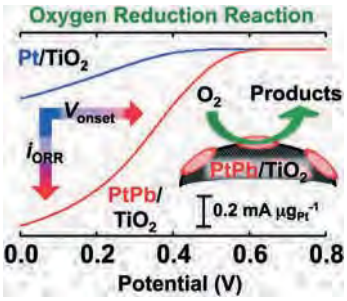
Oxygen Reduction Reaction
Pt/TiO2
Vonset
iORR
O2
Products
PtPb/TiO2
PtPb/
TiO2
0.2 mA μgPt-1
0.0
0.2
0.4
0.6
0.8
Potential (V)

[redacted]

<

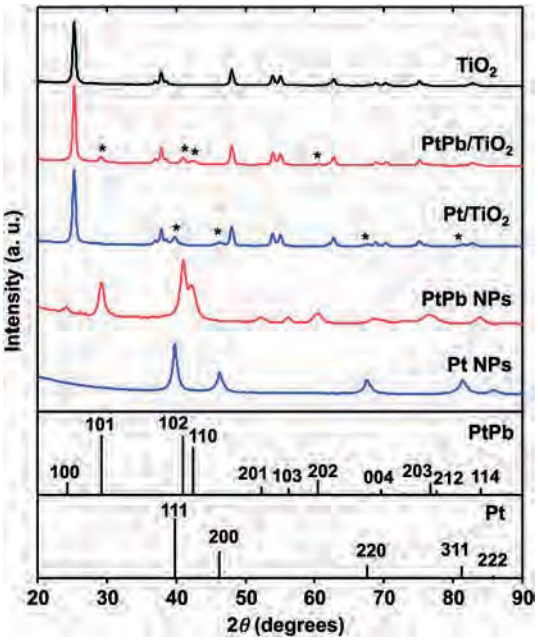
TiO2
PtPb/TiO2
Pt/TiO2
PtPb NPs
Pt NPs
Intensity (a. u.)
PtPb
100
101
102
110
201
103
202
004
203
212
114
Pt
111
200
220
311
222
20
30
40
50
60
70
80
90
2θ (degrees)

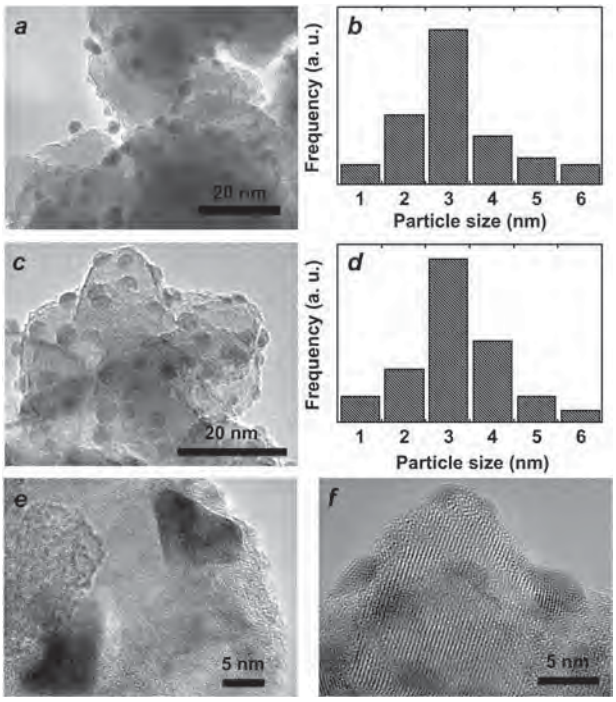
a
20 nm
b
Frequency (a. u.)
1
2
3
4
5
6
Particle size (nm)
c
20 nm
d
Frequency (a. u.)
1
2
3
4
5
6
Particle size (nm)
e
5 nm
f
5 nm

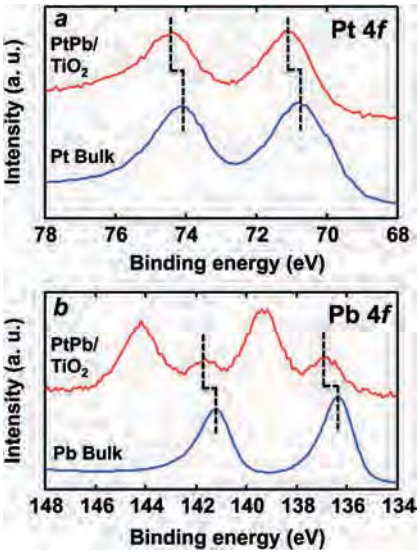
a
Pt 4f
PtPb/
TiO2
Pt Bulk
Intensity (a. u.)
78 76 74 72 70 68
Binding energy (eV)
b
Pb 4f
PtPb/
TiO2
Pb Bulk
Intensity (a. u.)
148 146 144 142 140 138 136 134
Binding energy (eV)

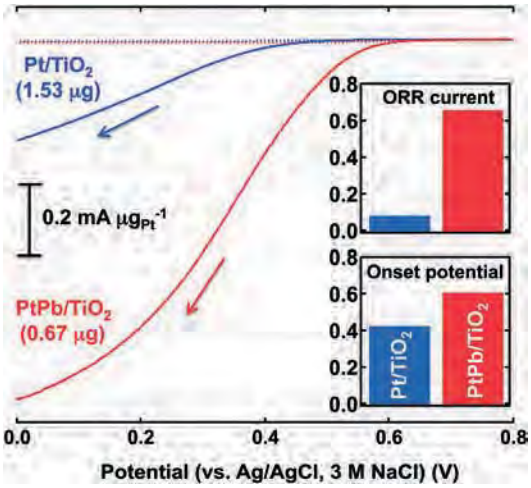
Pt/TiO2
(1.53 μg)
0.2 mA μgPt-1
PtPb/TiO2
(0.67 μg)
ORR current
Onset potential
Pt/TiO2
PtPb/TiO2
0.0 0.2 0.4 0.6 0.8
Potential (vs. Ag/AgCl, 3 M NaCl) (V)

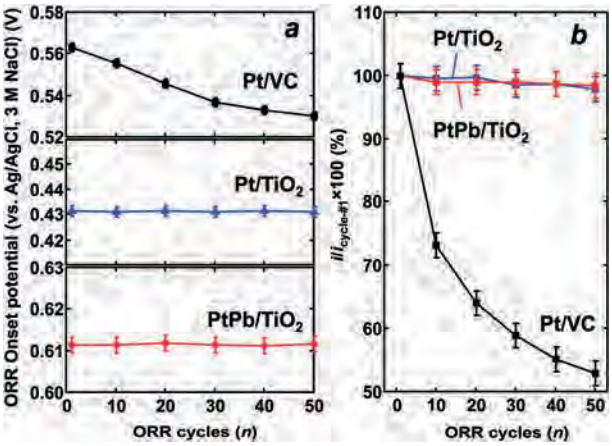
a
Pt/VC
Pt/TiO2
PtPb/TiO2
ORR Onset potential (vs. Ag/AgCl, 3 M NaCl) (V)
ORR cycles (n)
b
Pt/TiO2
PtPb/TiO2
Pt/VC
i/i_cycle-#1×100 (%)
ORR cycles (n)

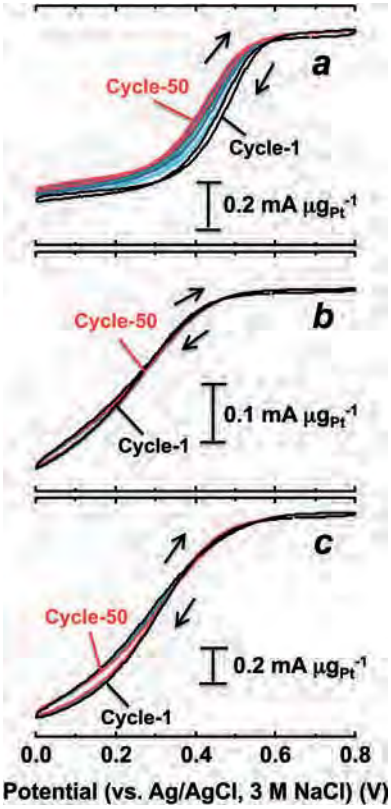
a
Cycle-50
Cycle-1
0.2 mA μg_Pt^-1
b
Cycle-50
Cycle-1
0.1 mA μg_Pt^-1
c
Cycle-50
Cycle-1
0.2 mA μg_Pt^-1
Potential (vs. Ag/AgCl, 3 M NaCl) (V)

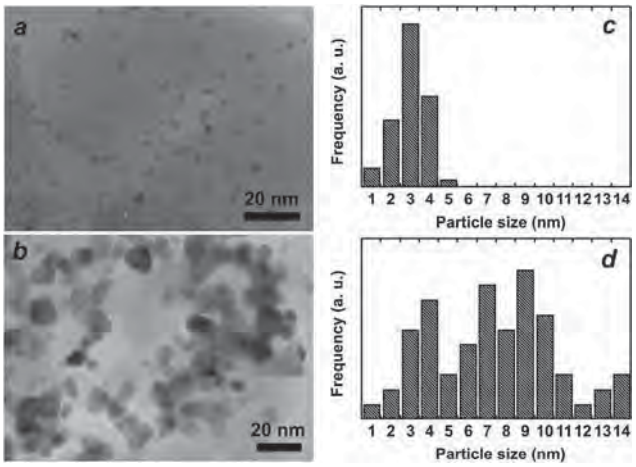
a
20 nm
b
20 nm
c
Frequency (a. u.)
1 2 3 4 5 6 7 8 9 10 11 12 13 14
Particle size (nm)
d
Frequency (a. u.)
1 2 3 4 5 6 7 8 9 10 11 12 13 14
Particle size (nm)

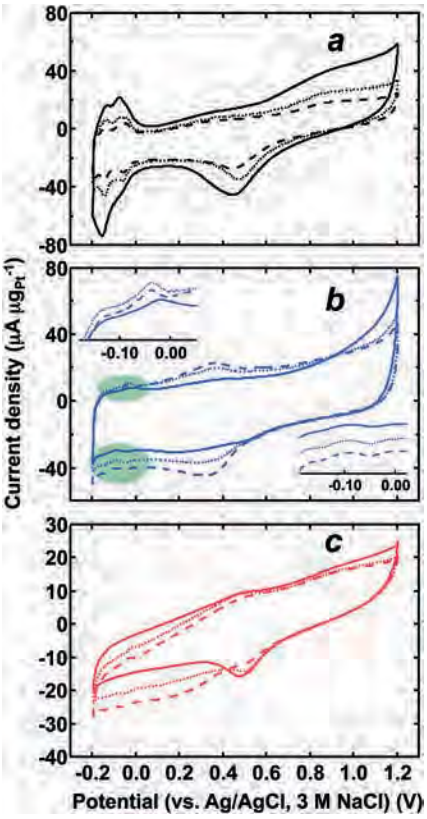
a
b
c
-0.10 0.00
Current density (μA μg$_{Pt}^{-1}$)
Potential (vs. Ag/AgCl, 3 M NaCl) (V)

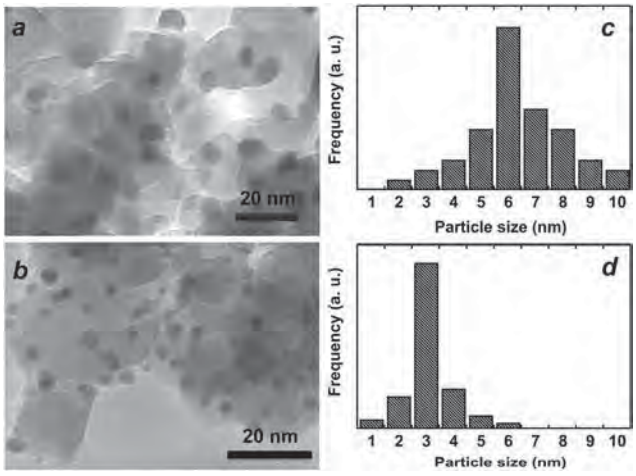
a
20 nm
b
20 nm
c
Frequency (a. u.)
1 2 3 4 5 6 7 8 9 10
Particle size (nm)
d
Frequency (a. u.)
1 2 3 4 5 6 7 8 9 10
Particle size (nm)

©

°

μ

μ

```
CTGCCTTCGAGGTCGCAGTCACAGTCGCCAGCTGCTCATACTCTGAACTCTTGACACAGACTGCTCGCCATGACAGCCTTTCGCTTGATG  90
                                                                    M  T  A  F  R  L  M
                                                                 -22

GCCGTGGCCCTGGTGGTGGTCGTGGCGTGCTCGACGACCTGGGCTCGCTCCGCCGAGGAGTCGTCGTCCCCCGTGGCCTCCCTCATCAGG 180
A  V  A  L  V  V  V  V  A  C  S  T  T  W  A  R  S  A  E  E  S  S  S  P  V  A  S  L  I  R
                                         -1  1                                          15

GGCCGCAGCCTCAGCAAGCGAGCAAACTTCGACCCTTCCTGCACGGGCGTCTACGACCGGGAGCTCCTGGGGAGGCTGAGCCGCCTCTGC 270
G  R  S  L  S  K  R  A  N  F  D  P  S  C  T  G  V  Y  D  R  E  L  L  G  R  L  S  R  L  C
                                                                                         45

GACGACTGCTACAACGTGTTTCGCGAGCCCAAGGTGGCCACGGAGTGCAGGAGCAACTGCTTCTACAACCCCGTGTTCGTCCAGTGCCTG 360
D  D  C  Y  N  V  F  R  E  P  K  V  A  T  E  C  R  S  N  C  F  Y  N  P  V  F  V  Q  C  L
                                                                                         75

GAGTACCTGATTCCGGCCGACCTGCACGAGGAGTACCAAGCCCTCGTGCAGACGGTGGGCAAGTAGGCTCGCTCGACCTGCCACGACCTC 450
E  Y  L  I  P  A  D  L  H  E  E  Y  Q  A  L  V  Q  T  V  G  K  *
                                                          96

GCCCCGCGCACTCACGCCAACGGCCAGAAGACACAGAGAGGATTTCAGGATTTGTTTCTGGCTAACTGGTGTATTTTATCGACCCTGCTC 540
GGATTTTGATATGATTTCTCATGTCCTAAATTGTGATGAATCTCTAAATGAAGTGTGTTGGAAT(A)n                        621
```

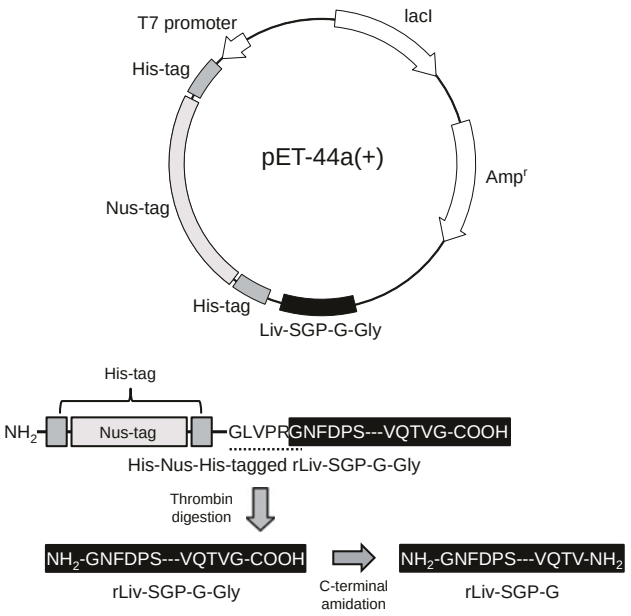

β

μ

μ

μ

α

μ

°

μ

°

°

β

β

μ

μ μ μ

μ

μ

β

μ μ μ

μ

μ

β

○ ○ ○

○

β

μ

β

β

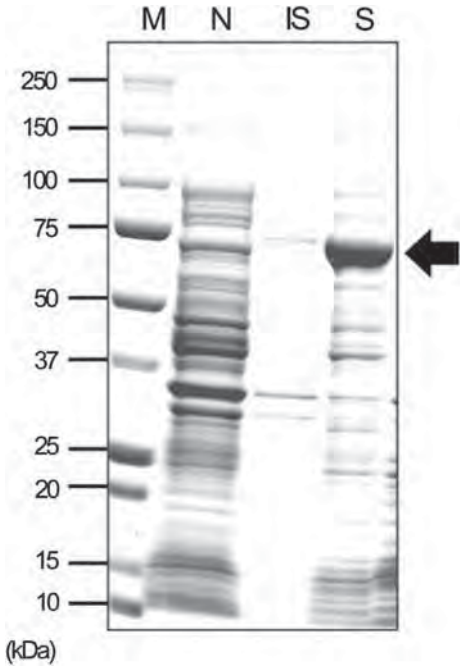

β

β

μ

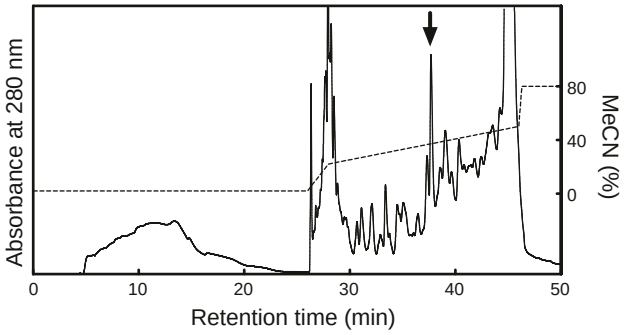
Absorbance at 280 nm
MeCN (%)
80
40
0
0
10
20
30
40
50
Retention time (min)

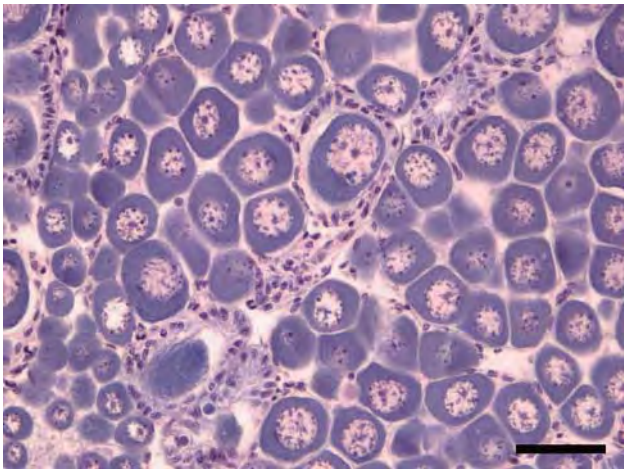

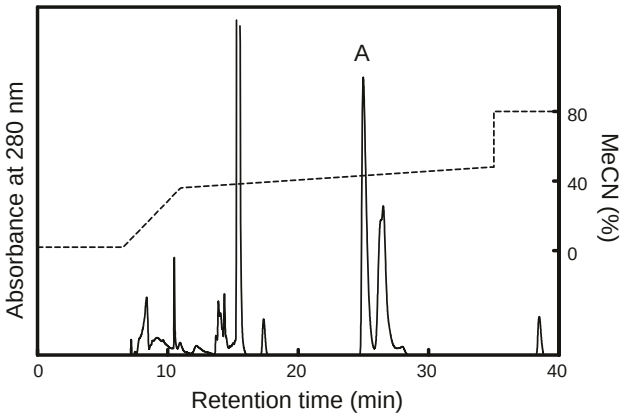
A
Absorbance at 280 nm
MeCN (%)
80
40
0
0
10
20
30
40
Retention time (min)

μ

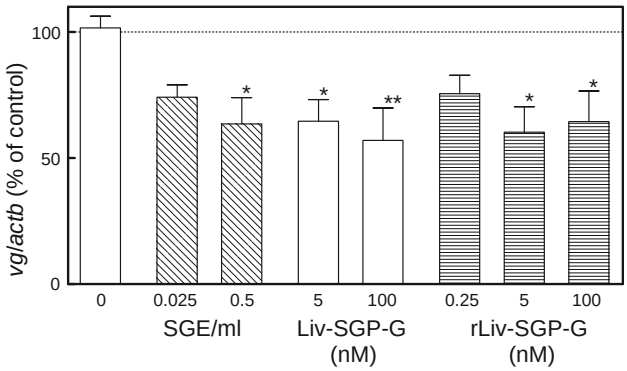
vg/actb (% of control)
100
50
0
*
*
**
*
*
0
0.025
0.5
5
100
0.25
5
100
SGE/ml
Liv-SGP-G
(nM)
rLiv-SGP-G
(nM)

β

α

α

α

Aqua-BioScience Monographs, Vol. 6, No. 2, pp. 49-90 (2013) www.terrapub.co.jp/onlinemonographs/absm/

Crustacean Peptide Hormones: Structure, Gene Expression and Function

Hidekazu Katayama[1†], Tsuyoshi Ohira[2†] and Hiromichi Nagasawa[3*]

[1]*Department of Applied Biochemistry*
School of Engineering
Tokai University
Hiratsuka, Kanagawa 259-1292, Japan
[2]*Department of Biological Sciences*
Faculty of Science
Kanagawa University
Hiratsuka, Kanagawa 259-1293, Japan
[3]*Department of Applied Biological Chemistry*
Graduate School of Agricultural and Life Sciences
The University of Tokyo
Bunkyo-ku, Tokyo 113-8657, Japan
*e-mail: anagahi@mail.ecc.u-tokyo.ac.jp

Abstract
Homeostasis, growth and reproduction in crustaceans are under endocrine control as is established in other animals. The identification of crustacean hormones and elucidation of mechanisms of hormonal regulation have been pursued extensively. Mechanisms are found to be partly similar to, but also considerably different from those in insects, although both groups of animals are arthropods. Molting in insects, for example, is positively regulated by prothoracicotropic hormone (PTTH), which is secreted by the brain/corpora allata complex and stimulates the prothoracic glands to promote the synthesis and secretion of ecdysteroids. On the other hand, molting in crustaceans is negatively regulated by molt-inhibiting hormone (MIH), which is secreted by the X-organ/sinus gland complex and suppresses the Y-organs from synthesizing ecdysteroids during the intermolt period. Therefore, it is rather difficult to fully elucidate physiological mechanisms in crustaceans based only on the results obtained in insects. Using experimental evidence, we have thus far looked into the roles of crustacean eyestalk hormones and androgenic gland hormone (AGH). Various eyestalk hormones have been isolated from the sinus glands and characterized: e.g., crustacean hyperglycemic hormone (CHH), MIH, vitellogenesis-inhibiting hormone (VIH), red pigment concentrating hormone (RPCH) and pigment dispersing hormone (PDH). CHH, MIH and VIH are structurally similar, forming the CHH-family. Insects also possess molecules similar to CHH, RPCH and PDH, but their functions are different. In addition, AGH has been studied mainly using terrestrial isopods. Here, we describe the present state of our understanding of the structure and function of these peptide hormones, and discuss future perspectives.

Received on May 10, 2012
Accepted on November 13, 2012
Online published on September 10, 2013

Keywords
- androgenic gland hormone
- *Armadillidium vulgare*
- crustacean hyperglycemic hormone
- eyestalk
- insulin-like androgenic gland factor
- *Marsupenaeus* (*Penaeus*) *japonicus*
- molt-inhibiting hormone
- pigment dispersing hormone
- red pigment concentrating hormone
- sinus gland
- vitellogenesis-inhibiting hormone

1. Introduction

Approximately 25,000 species of crustaceans have so far been identified and recorded on Earth, and most of these species live in freshwater or seawater, while a small number of species dwell on land. Some crustacean species including shrimps and crabs are of commercial importance in fisheries and aquaculture, while others play a key role as intermediates in the food chain, linking phytoplanktons and fishes within the aquatic ecosystem. Modern shrimp culture was first established in Japan over 50 years ago using the kuruma prawn *Marsupenaeus* (formerly *Penaeus*) *japonicus*, which is one of the most important commercial species in Japan, and the aquaculture technique has now spread to many countries, especially in tropical and subtropical

†These authors contributed equally to this work.

© 2013 TERRAPUB, Tokyo. All rights reserved.
doi:10.5047/absm.2013.00602.0049

regions. At present, Japan is one of the largest shrimp-importing countries in the world, totaling over 200,000 tons per year. Considerable quantities of shrimp, mainly the tiger prawn, *Penaeus monodon*, had formerly been imported from Taiwan about 20 years ago, but Taiwan was later replaced by various southeast Asian countries due to a sudden decrease in shrimp production in Taiwan in relation to a serious viral disease outbreak. Despite the worldwide importance of shrimp culture as an industry, insufficient knowledge exists concerning basic mechanisms of growth and reproduction in crustaceans. Since crustaceans belong to the arthropods, it may appear that they are similar to insects in all aspects. Crustaceans do resemble insects in many ways, but still differ from them considerably, for example, in terms of control of body color, molting systems, neurosecretory systems, calcification of the exoskeleton, sexual differentiation, control of blood carbohydrate levels and so forth. Thus, it is necessary to understand many peculiar phenomena at the molecular level, and one way to do so is by characterizing hormones related to those phenomena.

Blood carbohydrates in crustaceans consist principally of glucose, while trehalose is found in insects. The existence of a hyperglycemic factor in crustacean eyestalks has been known since Abramowitz and his colleagues first demonstrated that the injection of extracts of eyestalks into crabs caused an increase in hemolymph glucose levels (Abramowitz *et al.* 1944). Mechanisms of carbohydrate homeostasis in crustaceans are thus quite different from those in insects. The physiological and biochemical properties of the hyperglycemic factor have been extensively investigated (reviewed by Keller 1992). Crustacean hyperglycemic hormone (CHH) was first characterized in the shore crab *Carcinus maenas* (Kegel *et al.* 1989). CHHs are always the major neuropeptides in the crustacean sinus gland and therefore have been characterized in many decapod and isopod species (Santos and Keller 1993). Recent studies have revealed that CHHs are also involved in various processes such as ion transport at the gills and water uptake for the purpose of enlarging body size after molting (Chung *et al.* 1999; Spanings-Pierrot *et al.* 2000).

Crustaceans as well as many other arthropod species characteristically shed the exoskeleton during growth, because the calcified hard exoskeleton interferes with growth. An eyestalk hormone responsible for molting was discovered as early as 1905 (Zeleny 1905), but its chemical identification was first accomplished using the American lobster *Homarus americanus* only about 20 years ago (Chang *et al.* 1990). In the 1960's, the structure of the molting hormone in insects was determined after many years of effort by a German research group; it was found to be a highly hydroxylated steroid (Hoppe and Huber 1965), which is synthesized from cholesterol. Soon after this structural determination, crustaceans were also found to use the same compound in molting (Hampshire and Horn 1966). Thus, insects and crustaceans utilize a common steroid, referred to as ecdysteroid, for the purpose of molting. However, the regulation of molting hormone production by the prothoracic glands in insects is different from that by the Y-organs in crustaceans; in insects, the prothoracic glands are positively regulated by prothoracicotropic hormone (PTTH) secreted by the brain/corpora allata complex (Kawakami *et al.* 1990), while in crustaceans, the Y-organs are negatively regulated by molt-inhibiting hormone (MIH) secreted from the X-organ/sinus gland complex (Keller 1992). Therefore, there seems to be some diversity in regulatory systems of molting in arthropods. This difference is not yet well understood, and differences in signal transduction systems from hormone reception to biosynthesis of molting hormone should be clarified in the future. Recently, some biosynthetic enzymes involved in the biosynthetic pathway from cholesterol to ecdysone have been characterized at the cDNA level in both insects (Gilbert 2004; Truman 2005; Rewitz and Gilbert 2008) and crustaceans (Rewitz and Gilbert 2008; Asazuma *et al.* 2009).

Vitellogenesis is an essential physiological event in the reproduction of oviparous animals. Various nutrients including carbohydrates, proteins, lipids, minerals, and vitamins necessary for embryonic development are accumulated in the oocytes during this process. In crustaceans, vitellogenesis is negatively regulated by a neuropeptide, vitellogenesis-inhibiting hormone (VIH), which is synthesized in and secreted from the X-organ/sinus gland complex in the eyestalks. When we started to study on *M. japonicus* VIHs, peptides designated as VIHs had been purified and characterized from only two crustacean species, the American lobster *H. americanus* (Soyez *et al.* 1991) and the terrestrial isopod *Armadillidium vulgare* (Gréve *et al.* 1999). In *H. americanus*, two VIH isoforms (Hoa-VIH-I and -II) were isolated and had an identical sequence of 77 amino acid residues (Soyez *et al.* 1991). They may occur via the transformation of an L-amino acid residue to a D-amino acid residue in either sequence through post-translational modifications (Soyez *et al.* 1994). Hoa-VIH-I and *A. vulgare* VIH (Arv-VIH) were shown to inhibit the onset of vitellogenesis in an *in vivo* bioassay, and therefore are generally accepted to be VIHs. In *Penaeus semisulcatus*, vitellogenesis was inhibited by some CHHs purified from the sinus glands of *M. japonicus*, and therefore the CHHs of these shrimps may have dual functions of hyperglycemic and vitellogenesis-inhibiting activities (Khayat *et al.* 1998).

It was found that CHH is structurally similar to MIH, forming a peptide family designated as the CHH-family (Keller 1992). Many peptides belonging to the CHH-family have been characterized from various crustacean species and also from insects (Audsley *et*

doi:10.5047/absm.2013.00602.0049 © 2013 TERRAPUB, Tokyo. All rights reserved.

al. 1992; Endo *et al.* 2000) and a spider (Gasparini *et al.* 1994). VIH and mandibular organ-inhibiting hormone (MOIH), which inhibits the synthesis of methyl farnesoate by the mandibular organs (Wainwright *et al.* 1996), are also produced in the eyestalk of crustaceans, and are included as members of the CHH-family. Ion transport peptide (ITP) was characterized in a locust (Audsley *et al.* 1992), and low molecular weight protein (LMWP) was found in spider venom (Gasparini *et al.* 1994). Therefore, CHH-family peptides are likely to play various roles in arthropods. CHH-family peptides have not yet been discovered in any animals other than arthropods, and are therefore considered to be molecules unique to the arthropods.

Many crustaceans have the ability to alter body color in order to adapt to their surrounding background, and this alteration is accomplished by specialized cells called chromatophores. Body color changes result from dispersion or concentration of movable pigment granules in the chromatophores, which in crustaceans include four types: erythrophores, xanthophores, leucophores and melanophores. To date, red pigment concentrating hormone (RPCH) and pigment dispersing hormone (PDH), which are produced by and released from the X-organ/sinus gland complex in the eyestalk, are well known as chromatophore-regulating neuropeptides (Keller 1992). RPCH was first isolated and sequenced from the pink shrimp *Pandalus borealis* (Fernlund and Josefsson 1972). This molecule is an octapeptide with an amidated C-terminus, and was the first neuropeptide to be characterized not only in crustaceans but also in invertebrates. Later, adipokinetic hormones (AKHs) in insects were found to be structurally related to RPCH (Mordue and Stone 1976; Gäde 1991). Thus, a large family of AKH/RPCH peptides was established. PDH was originally identified as distal retinal pigment hormone (DRPH), and was isolated from *P. borealis* and sequenced (Fernlund 1976). PDH consists of 18 amino acid residues with an amidated C-terminus. Thus far, PDHs have been shown to exist widely not only in crustaceans but also in insects (Rao and Riehm 1993). Homologous peptides to PDH in insects are known as pigment dispersing factors (PDFs), and some reports suggest that PDFs may play an important role in the regulation of circadian rhythms in insects (Park and Hall 1998; Park *et al.* 2000).

Sex determination and sexual differentiation in vertebrates have been studied extensively, and have been clarified to be under both genetic and hormonal regulations. In contrast, in invertebrates little is known about sex determination and sexual differentiation with the exception of the fruit fly, in which there is no hormonal regulation (Schütt and Nöthiger 2000). The mechanism of sexual differentiation in crustaceans seems to be considerably different from that in insects, and crustaceans seem to be more similar to vertebrates than to insects with respect to being under endocrine regulation (Charniaux-Cotton 1967). Androgenic gland hormone (AGH), which is produced by the androgenic glands (AGs) and is responsible for sexual differentiation in crustaceans, was discovered in 1954 (Charniaux-Cotton 1954). Since then, many efforts have been made to isolate and characterize AGH. In 1999, AGH was successfully isolated from the terrestrial isopod *A. vulgare*, and its structure was determined to be an insulin-like heterodimeric peptide having an *N*-linked glycan (Martin *et al.* 1999; Okuno *et al.* 1999).

In this monograph, we will present our findings on purification, structural determination, cDNA cloning, gene expression and intrinsic functioning of these crustacean peptide hormones, and discuss future perspectives of crustacean molecular endocrinology.

2. Eyestalk peptide hormones I: CHH-family peptides

It has been shown that various types of neuropeptides are produced in the crustacean eyestalks (Keller 1992). Most of these are synthesized in the X-organ and transferred to the sinus gland, from which they are released into the hemolymph. Among these, the amino acid sequences of four neuropeptides, CHH, MIH, VIH and MOIH, are similar, forming a peptide family referred to as the CHH-family (Keller 1992). CHH-family peptides are mostly 72 to 78 amino acid residues long having six conserved cysteine residues that form three intramolecular disulfide bonds. It is believed that they have evolved from a common ancestral molecule. CHH-family peptides have been isolated not only from decapod and isopod crustaceans, but also from insects (Audsley *et al.* 1992) and a spider (Gasparini *et al.* 1994).

2-1. CHH

2-1A. Bioassay and purification

A CHH was first isolated and sequenced from the shore crab *C. maenas* (Kegel *et al.* 1989). Thereafter, the amino acid sequences of CHHs in various decapod species have been determined (reviewed by Santos and Keller 1993). However, no information concerning the structure of CHH in shrimps or prawns was available when we started to study crustacean eyestalk hormones. Therefore, we began purifying CHH molecules from the sinus glands of the kuruma prawn *M. japonicus* and determining their structures (Yang *et al.* 1995, 1996, 1997; Yang 1997; Nagasawa *et al.* 1999).

In our research, an *in vivo* injection bioassay using *M. japonicus* was performed essentially according to methods described previously (Leuven *et al.* 1982), but slightly modified as described below (Yang *et al.* 1995, 1996, 1997). Glucose levels in the hemolymph of normal prawns were 220 ± 30 μg/mL. They dramatically decreased to 35 ± 10 μg/mL 2 d (day) after bilateral

doi:10.5047/absm.2013.00602.0049 © 2013 TERRAPUB, Tokyo. All rights reserved.

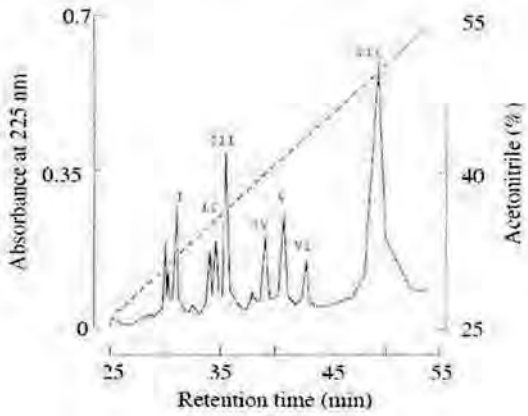

Fig. 1. Reversed-phase HPLC elution profile of extracts from 300 sinus glands of the kuruma prawn *Marsupenaeus japonicus*. Column: Asahi-Pak ODP-50 (4.6 × 150 mm). Solvent: linear gradient of 0–55% acetonitrile in 0.05% trifluoroacetic acid (TFA). Flow rate: 1 mL/min. Detection: absorbance at 225 nm. Temperature: 40°C. The concentration of acetonitrile is indicated by dashed line. Reprinted from Yang, Structures and functions of peptide hormones in the sinus gland of the kuruma prawn *Penaeus japonicus*, PhD Thesis, The University of Tokyo, © 1997, with permission from Wei-Jun Yang.

Table 1. Biological activities of Pej-SGP-I to -VII.

	Activity	
	CHH	MIH
Pej-SGP-I	++	–
Pej-SGP-II	+	–
Pej-SGP-III	+++	–
Pej-SGP-IV	–	+++
Pej-SGP-V	+++	+
Pej-SGP-VI	+++	+
Pej-SGP-VII	+++	nd

CHH, crustacean hyperglycemic hormone; MIH, molt-inhibiting hormone; nd, not determined.

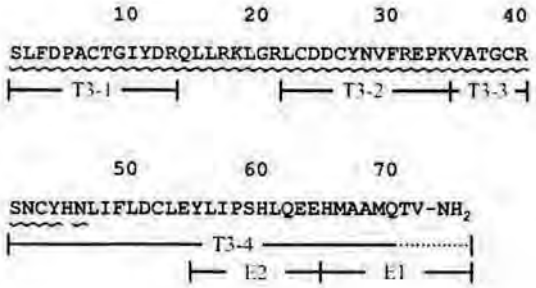

Fig. 2. Amino acid sequencing analyses of Pej-SGP-III. Wavy line, residues identified by N-terminal sequencing; T3-1, -2, -3 and -4, tryptic peptides connected together by three disulfide bonds; E1 and E2, endoproteinase Glu-C peptides. Reprinted from *Aquaculture*, **135**, Yang *et al.*, Amino acid sequences of a hyperglycaemic hormone and its related peptides from the Kuruma prawn, *Penaeus japonicus*, 205–212, © 1995, with permission from Elsevier.

eyestalk ablation. To determine the appropriate time for hemolymph sampling following injection, a time-course experiment was conducted. After the injection of each CHH into eyestalk-ablated prawns, glucose levels were measured. The levels increased with time, reached a maximum within 2 h (hour) after injection, and decreased gradually thereafter. Thus, we drew up the conditions of a bioassay for hyperglycemic activity as follows.

Live kuruma prawns were obtained at a fish market in Tokyo, Japan and were kept in an aquarium at 20°C during the experiment. Samples dissolved in 100 μL of saline solution were injected into prawns (average body weight, 20 g) whose eyestalks had been ablated 2 d prior to the injection experiments. The hemolymph (200 μL each) was taken just prior to injection and 2 h after injection. Hemolymph glucose levels were determined using the glucose oxidase peroxidase method (Papadopoulos and Hess 1960). Hyperglycemic activity was assessed by the increase of hemolymph glucose levels following injection.

In order to purify *M. japonicus* CHH molecules, peptides were extracted from the sinus glands and fractionated by a single run of reversed-phase HPLC (Yang *et al.* 1995, 1996, 1997; Yang 1997; Nagasawa *et al.* 1999). A typical chromatogram from 300 sinus glands is shown in **Fig. 1**. Seven peak materials were designated as Pej-SGP-I to -VII in the order of elution. Hyperglycemic activities of the seven peaks were assessed by the methods described above, revealing that Pej-SGP-I, II, III, V, VI and VII showed considerable hyperglycemic activity. In contrast, Pej-SGP-IV exhibited almost no hyperglycemic activity, whereas it showed strong molt-inhibiting activity (**Table 1**), as described in Subsection 2-2A. Therefore, in *M. japonicus*, Pej-SGP-I, II, III, V, VI and VII are considered to be CHHs, whereas Pej-SGP-IV is considered to be an MIH.

2-1B. Structural determination

Next, we focused on the structural determination of the seven Pej-SGPs. The seven peak materials were reduced, carboxymethylated, and subsequently subjected to N-terminal amino acid sequence analysis (Yang *et al.* 1995, 1996, 1997; Yang 1997; Nagasawa *et al.* 1999). As a result, more than 43 amino acid residues for each peptide were identified. The N-terminal amino acid sequences of Pej-SGP-I, II, III, V,

doi:10.5047/absm.2013.00602.0049 © 2013 TERRAPUB, Tokyo. All rights reserved.

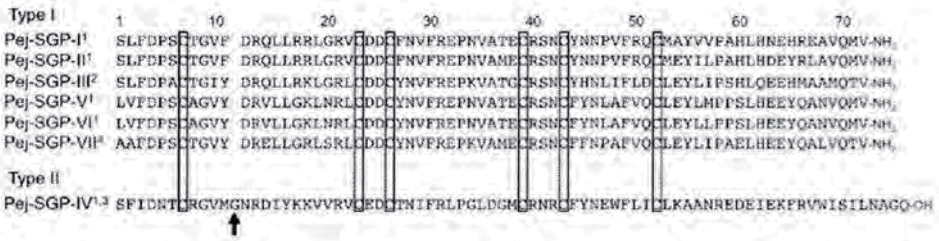

Fig. 3. Comparisons between amino acid sequences of CHH-family peptides purified from the sinus glands of *Marsupenaeus japonicus*. Open boxes represent as conserved six cystein residues. An arrow indicates an insertion of a Gly residue at position 12. [1]Yang *et al.*, 1997; [2]Yang *et al.*, 1995; [3]Yang *et al.*, 1996; [4]Nagasawa *et al.*, 1999.

VI and VII were highly similar to each other and slightly less similar to the known CHHs from other crustaceans. In contrast, Pej-SGP-IV was more similar to *C. maenas* MIH and *H. americanus* VIH than to Pej-SGP-I, II, III, V, VI, VII and the known CHHs. These results showed good agreement with those of the bioassays as described above.

Since Pej-SGP-III is an abundant CHH molecule in the sinus glands of *M. japonicus*, further structural analysis of this peptide was first performed (Yang *et al.* 1995). Trypsin digestion of the intact Pej-SGP-III afforded a peptide fragment named T3 (**Fig. 2**). This fragment consisted of four peptide chains, among which three sequences (T3-1, -2 and -3) were easily assigned based on the N-terminal sequence. The fourth peptide (T3-4) starting from Ser^{41} was assigned by subtracting the above three sequences from the total. T3-4 was considered to be a C-terminal peptide, but the residues could be identified up to the 70th residue and, judging from the mass spectral data, two more unidentified residues probably remained at the C-terminus.

In order to determine the C-terminal sequence, the intact Pej-SGP-III was digested with endoproteinase Glu-C. Four major fragment peptides named E1–E4 were obtained. E1 was found by sequence analysis to be a C-terminal fragment, and one more residue, Thr^{71}, could be identified. Thus, there remained only a C-terminal unidentified residue. The high resolution FAB mass spectrum of E1 showed a protonated molecular ion peak at *m/z* 887.43. The only possibility for the C-terminal residue which could satisfy this value was Val with an amidated structure (calculated value, 887.42). Thus the complete amino acid sequence of Pej-SGP-III was unambiguously determined (**Fig. 2**).

Subsequently, the complete amino acid sequences of the remaining five CHHs, Pej-SGP-I, II, V, VI and VII (Yang *et al.* 1997; Yang 1997; Nagasawa *et al.* 1999), and the MIH, Pej-SGP-IV (see Subsection 2-2B), were also determined similarly to the structural characterization of Pej-SGP-III. Amino acid sequences of the seven peptides are shown in **Fig. 3**. These peptides showed considerable sequence similarity to the CHH-family peptides characterized previously, and especially were found to have the conserved six cysteine residues which are involved in the formation of three disulfide bridges. Therefore, the seven peptides are thought to be members of the CHH-family peptide in *M. japonicus*. CHH-family peptides are divided into two subtypes based on the absence (type I) or presence (type II) of a glycine residue at position 12 in the mature peptide. According to this grouping, the six CHHs (Pej-SGP-I, II, III, V, VI and VII) can be classified into type I and the MIH (Pej-SGP-IV) belongs to type II. This classification is consistent with previous studies in that all of the known CHH molecules are classified as type I, and MIH, MOIH and VIH molecules are classified as type II (Lacombe *et al.* 1999).

2-1C. Immunohistochemical localization

In order to elucidate the localization of cells producing CHH-family peptides in *M. japonicus*, we developed five specific antibodies against Pej-SGP-I, -II, -III, -IV and -V (Shih *et al.* 1997, 1998). Immunohistochemical studies using these antibodies showed that neurosecretory cells of Pej-SGP-III and IV were located in the same cluster of the medulla terminalis ganglionic X-organ (MTGX), and that three kinds of neurosecretory cells stained with an anti-Pej-SGP-III antiserum and/or an anti-Pej-SGP-IV antiserum were present (**Figs. 4a, b**). The number of neurosecretory cells which were stained with both antisera was much smaller than that of neurosecretory cells which were stained with one antiserum only. Co-localization of two CHH-family peptides has been reported in previous studies on CHH- and VIH-producing cells using immunohistochemistry and *in situ* hybridization in *Homarus gammarus* (Rotllant *et al.* 1993) and *H. americanus* (De Kleijn *et al.* 1992). In contrast, no co-localization of MIH and CHH was observed at either the mRNA or peptide level in *C. maenas* (Klein *et al.* 1993).

The diagrammatic localization of neurosecretory cells stained with the five antibodies is shown in **Fig. 5**. Pej-SGP-I cells were found in the three clusters. The first cluster was in the medulla interna ganglionic X-

doi:10.5047/absm.2013.00602.0049 © 2013 TERRAPUB, Tokyo. All rights reserved.

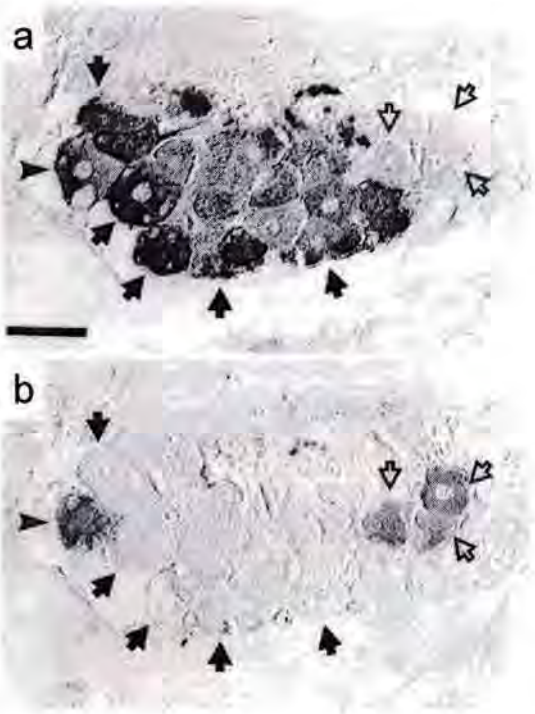

Fig. 4. Pej-SGP-III- and Pej-SGP-IV-immunopositive neurosecretory cells. (a) Pej-SGP-III-immunopositive neurosecretory cells in the medulla terminalis ganglionic X-organ (MTGX). (b) Pej-SGP-IV-immunopositive neurosecretory cells in the MTGX. Arrows indicate Pej-SGP-III (➡), Pej-SGP-IV (⇨) and Pej-SGP-III and -IV (➢) neurosecretory cells. Scale bar represents 50 μm. Reprinted with permission from *Zool. Sci.*, **15**, Shih *et al.*, Immunohistochemical identification of hyperglycemic hormone- and molt-inhibiting hormone-producing cells in the eyestalk of the kuruma prawn, *Penaeus japonicus*, 389–397, Fig. 4, © 1998, Zoological Society of Japan.

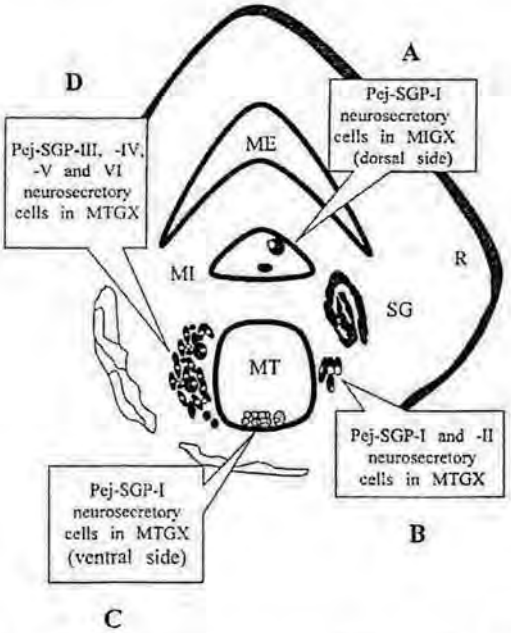

Fig. 5. Schematic representation of the right eyestalk in the kuruma prawn *Marsupenaeus japonicus*, showing the localization of neurosecretory cells (horizontal section). ME, medulla externa; MI, medulla interna; MT, medulla terminalis; SG, sinus gland; MIGX, medulla interna ganglionic X-organ; MTGX, medulla terminalis ganglionic X-organ; R, rerinula. Reprinted from Kawashima and Kikuyama (eds)., *Proceedings of the XIII International Congress of Comparative Endocrinology*, Shih *et al.*, Immunohistochemical localization of crustacean hyperglycemic hormones (CHHs) and a molt-inhibiting hormone (MIH) in the eyestalk of *Penaeus japonicus*, 87–91, © 1997, with permission from Monduzzi Editore, Bologna.

organ (MIGX) (Position A in **Fig. 5**). The second cluster was in the MTGX near to the sinus gland (Position B in **Fig. 5**). The third cluster was also in the MTGX, but located at the ventral side of the medulla terminalis (MT) near to the root of the eyestalk (Position C in **Fig. 5**). Pej-SGP-II cells were found in the MTGX near to the sinus gland (Position B in **Fig. 5**). Pej-SGP-V cells existed in the MTGX opposite to the sinus gland, being of the same cluster as those of Pej-SGP-III and IV (Position D in **Fig. 5**). As far as we know, the neurosecretory cells of CHH-family peptides in crustaceans are known to exist in the same cluster of the MTGX located at the opposite side of the sinus gland (Jaros and Keller 1979). Therefore, the results of our study are the first to show that not all of the CHH-family peptides are produced in the same cell cluster. Different patterns of localization of these neurosecretory cells for *M. japonicus* CHH-family peptides may imply that they have different physiological and regulatory roles.

2-1D. cDNA cloning

When we started our studies on CHHs of the kuruma prawn *M. japonicus*, cDNAs encoding CHHs had been isolated from the shore crab *C. maenas* (Weidemann *et al.* 1989), the American lobster *H. americanus* (De Kleijn *et al.* 1995), and the crayfish *Orconectes limosus* (De Kleijn *et al.* 1994a). A common structure for these CHH precursors was demonstrated by cDNA sequence analysis. The CHH precursors consisted of a signal peptide, a CHH precursor-related peptide (CPRP), and a CHH. The CPRPs were 33–38 residues long and structurally conserved. The CPRPs had been purified from sinus glands of the above three crustacean species (Tensen *et al.* 1991), but their biological function had not yet been clarified. Moreover, there was no information concerning the structure of CHH precursor

doi:10.5047/absm.2013.00602.0049 © 2013 TERRAPUB, Tokyo. All rights reserved.

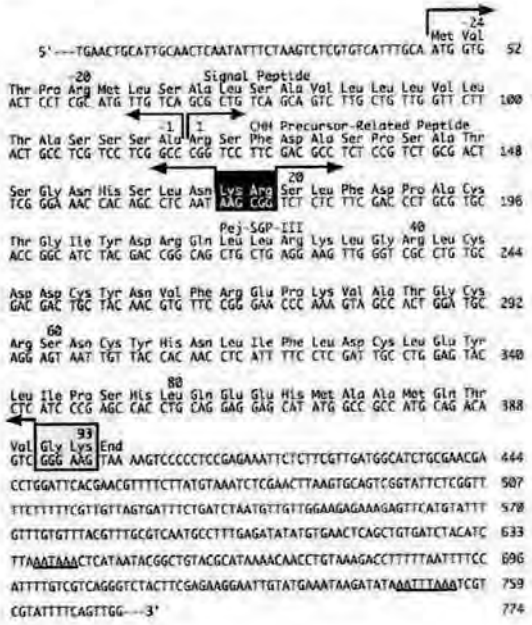

Fig. 6. Nucleotide sequence of a cDNA encoding a Pej-SGP-III precursor in the kuruma prawn *Marsupenaeus japonicus* and its deduced amino acid sequence. Amino acid numbering starts at the N-terminal residue of the propeptide of Pej-SGP-III with the presumptive signal peptide indicated by negative numbers. The black box indicates the putative dibasic cleavage site between Pej-SGP-III and CHH precursor-related peptide (CPRP). The light gray box indicates the putative amidation signal. The putative polyadenylation signals are underlined. The sequence has been deposited in the DNA Data Bank of Japan (accession No. D87864). Reprinted with permission of John Wiley & Sons, Inc. from *Mol. Mar. Biol. Biotechnol.*, **6**, Ohira *et al.*, Cloning and sequence analysis of a cDNA encoding a crustacean hyperglycemic hormone from the Kuruma prawn *Penaeus japonicus*, 59–63, Fig. 1, © 1997, Wiley-Liss, Inc., a Wiley Company.

in shrimps or prawns at that time. Therefore, we attempted to isolate a cDNA encoding a precursor of Pej-SGP-III, which was the first CHH to be characterized among the six CHHs in *M. japonicus* (Ohira *et al.* 1997a).

Total RNA isolated from the eyestalk of *M. japonicus* was subjected to RT-PCR to obtain a cDNA fragment encoding Pej-SGP-III. The reaction product was used as a probe to screen an eyestalk cDNA library, and subsequently three clones encoding a Pej-SGP-III precursor were isolated. The nucleotide sequence of one of the cDNA clones is shown in **Fig. 6**. An open reading frame (ORF) of 354 bp was found, and this ORF was conceptually translated into a putative protein of 117 amino acid residues. As expected, the sequence of Ser^{20}–Val^{91} of this protein was identical to that of Pej-SGP-III. This segment Ser^{20}–Val^{91} was flanked C-terminally by Gly^{92}–Lys^{93} and followed by a stop codon. Val^{91} of the mature Pej-SGP-III is amidated (Yang *et al.* 1995); Lys^{93}, therefore, is expected to be removed from the precursor, and Gly^{92} might be the amide donor to Val^{91}. Segment Met^{-24}–Ala^{-1} had a highly hydrophobic core (Met^{-19}–Leu^{-7}) and therefore was likely to constitute a signal peptide (Von Heijne 1986). The remaining sequences of Arg^{1}–Asn^{17} and Lys^{18}–Arg^{19} were thought to be a putative CPRP and a putative dibasic cleavage site, respectively. This cDNA also included a 5′ flanking sequence (46 bp) and a 3′ untranslated region (374 bp) containing a consensus polyadenylation signal site and a variant one (AATTTAAA) 132 bp and 16 bp upstream from poly (A) tail, respectively.

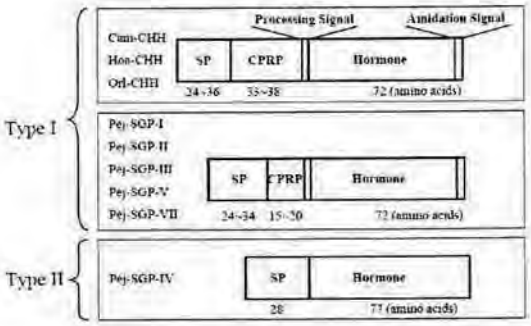

Fig. 7. Schematic representation of the organization of CHH-family peptide precursors. Cam-CHH, *Carcinus maenas* CHH; Hoa-CHH, *Homarus americanus* CHH; Orl-CHH, *Orconectes limosus* CHH; Pej-SGP-I, II, III, V and VII, *Marsupenaeus japonicus* CHHs; Pej-SGP-IV, *M. japonicus* MIH; SP, signal peptide; CPRP, CHH precursor-related peptide.

Following the cDNA cloning of the Pej-SGP-III, nucleotide sequences of cDNAs encoding other CHHs in *M. japonicus* were determined. cDNA clones of Pej-SGP-I, V, and VII were isolated by the same methods as those for Pej-SGP-III (Ohira *et al.* 1997b). A Pej-SGP-II cDNA was amplified by RT-PCR coupled with 5′- and 3′-RACE (Ohira 2000). Although we looked for a Pej-SGP-VI cDNA, unfortunately it could not be cloned. Nucleotide sequences of those cDNAs encoding Pej-SGP-I, II, V, and VII are presently accessible through public DNA databases (their accession Nos. AB007507, AB035724, AB007508, and AB007509).

The schematic organization of CHH precursors in *M. japonicus* and other species are shown in **Fig. 7**. The manner of organization of the five precursors was identical with that of *C. maenas*, *H. americanus*, and *O. limosus*, but differed from that of a Pej-SGP-IV precursor, which is an MIH in *M. japonicus* (see Subsection 2-2B). The CHH-family peptides can therefore be grouped into two types as previously mentioned. Also,

doi:10.5047/absm.2013.00602.0049 © 2013 TERRAPUB, Tokyo. All rights reserved.

the precursors of the two types have a distinct organization: type I precursors such as CHHs in *C. maenas*, *H. americanus*, and *O. limosus* consist of a signal peptide, a CPRP and a mature hormone, whereas type II precursors lack a CPRP (reviewed by De Kleijn and Van Herp 1995). It has already been mentioned that Pej-SGP-I, II, III, V, VI and VII are grouped into type I, whereas only Pej-SGP-IV is classified into type II based on amino acid sequence of mature hormones (see Subsection 2-2B). Therefore, the results revealed by cDNA cloning of the five CHHs are consistent with the previous results, because CPRP were found in the five precursors (**Fig. 7**).

The five CPRPs in *M. japonicus* (15–20 residues) were significantly shorter than those in *C. maenas*, *H. americanus*, and *O. limosus* (33–38 residues). The primary structures of the CPRPs were conserved among *C. maenas*, *H. americanus* and *O. limosus*, suggesting a common biological function. The CPRPs in Pej-SGP-I, II, III, V and VII, however, showed low sequence similarity to those in other crustacean species. These observations would argue against the possibility that the CPRPs in *M. japonicus* have the same function as the CPRPs in other crustacean species.

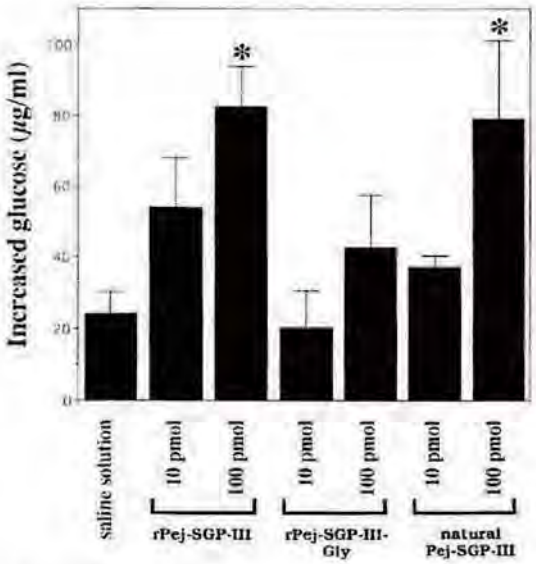

Fig. 8. Comparison of hyperglycemic activities of rPej-SGP-III, rPej-SGP-III-Gly and natural Pej-SGP-III purified from the sinus glands. The saline solution column represents the injection of saline solution only as a negative control. Results are expressed as the means ± SE of five independent bioassays. Points with asterisks (*) indicate values significantly different from that of saline solution ($P < 0.05$, Dunnett's multiple comparison test). Reprinted with permission from *Fish. Sci.*, **69**, Ohira *et al.*, Expression of a recombinant crustacean hyperglycemic hormone of the kuruma prawn *Penaeus japonicus* in methylotrophic yeast *Pichia pastoris*, 95–100, Fig. 4, © 2003, The Japanese Society of Fisheries Science.

2-1E. Preparation of recombinant CHHs

In general, recombinant proteins produced using bacterial expression systems are very useful tools for studies on the determination of their tertiary structures and the production of antibodies. The *Escherichia coli* expression system enables the production of larger amounts of recombinant proteins at lower cost than those of other expression systems, such as the baculovirus and yeast expression systems. Using the *E. coli* expression system, we have succeeded in producing a recombinant Pej-SGP-IV, an MIH in *M. japonicus*, showing molt-inhibiting activity comparable to that of the native Pej-SGP-IV (see Subsection 2-2C). Therefore, we first attempted to express a recombinant Pej-SGP-III, one of the six CHHs in *M. japonicus*, using the same *E. coli* expression system. However, the initial trial failed. Thereafter, the utility of the baculovirus expression system was also examined, but Pej-SGP-III could not be successfully produced. Since the methylotrophic yeast *Pichia pastoris* expression system has been used in the production of several peptide hormones, such as mammalian gonadotrophic hormones and human insulin (Cereghino and Cregg 2000), we examined the use of *P. pastoris* as a host organism in the expression of recombinant Pej-SGP-III (Ohira *et al.* 2003a).

A cDNA encoding Pej-SGP-III was processed by PCR and the resulting product was ligated into an expression vector. *P. pastoris* was transformed with this vector, and a recombinant Pej-SGP-III having an additional glycine residue at the C-terminus (rPej-SGP-III-Gly), a form considered to be a putative precursor of this hormone, was expressed. rPej-SGP-III-Gly secreted into the culture medium was purified by reversed-phase HPLC and its yield was about 0.4 mg from 1 liter of culture. rPej-SGP-III-Gly was subjected to an amidating reaction using a peptidylglycine α-amidating enzyme, and the amidated recombinant Pej-SGP-III (rPej-SGP-III) was purified by reversed-phase HPLC. The rPej-SGP-III showed hyperglycemic activity in an *in vivo* bioassay almost comparable to that of the native Pej-SGP-III (**Fig. 8**).

We also tried to produce other recombinant *M. japonicus* CHHs using different methods of making the recombinant Pej-SGP-III. In the case of the production of a recombinant Pej-SGP-I, the *E. coli* expression system was used (Katayama *et al.* 2002). Although biologically active recombinant Pej-SGP-I was obtained, the yield of the final product was poor (0.3 mg from 1 liter culture). This was because, the expressed recombinant Pej-SGP-I aggregated in an insoluble form, consequently yielding an inefficient refolding reaction. In order to overcome this problem, we recently introduced a new system using a Nus-tag for

doi:10.5047/absm.2013.00602.0049 © 2013 TERRAPUB, Tokyo. All rights reserved.

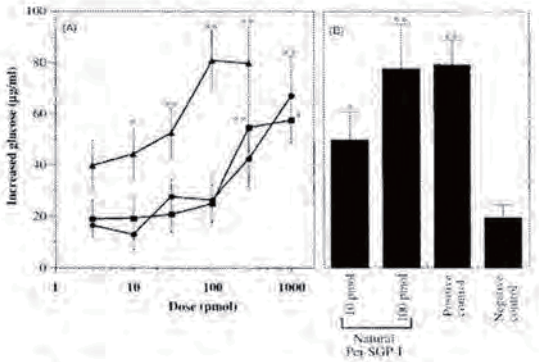

Fig. 9. Comparison of the hyperglycemic activities of recombinant and natural peptides, and sinus gland extract. (A) Dose-response curves of rPej-SGP-I-OH (●), rPej-SGP-I-Gly (■) and rPej-SGP-I-amide (▲) in terms of hyperglycemic activity. (B) Hyperglycemic activity of the natural Pej-SGP-I; negative control, injection of phosphate buffered saline (PBS); positive control, injection of the sinus gland extract (one sinus gland equivalent) of the kuruma prawn *Marsupenaeus japonicus*. Results are expressed as the means ± SE (n = 5–21). Asterisks indicate values significantly different from the negative control. $*P < 0.05$; $**P < 0.01$ using the program of Fisher's PLSD. Reprinted from *Peptides*, **23**, Katayama *et al.*, Significance of a carboxyl-terminal amide moiety in the folding and biological activity of crustacean hyperglycemic hormone, 1537–1546, © 2002, with permission from Elsevier.

Table 2. Secondary structure composition in recombinant and native peptides of Pej-SGP-I predicted from CD spectra. Reprinted from *Peptides*, **23**, Katayama *et al.*, Significance of a carboxyl-terminal amide moiety in the folding and biological activity of crustacean hyperglycemic hormone, 1537–1546, © 2002, with permission from Elsevier.

Molecule	α-Helix	β-Sheet	Turn	Random
rPej-SGP-I-Gly	29.6	0	32.7	37.7
rPej-SGP-I-OH	29.1	0	34.6	36.3
rPej-SGP-I-amide	35.3	0	41.4	23.3
Native Pej-SGP-I	42.7	0	19.7	37.6

Values indicate type of secondary structure present in terms of percentage (%).

solubilization to produce a recombinant Pej-SGP-VII (Nagai *et al.* 2009). Therefore, soluble and biologically active recombinant Pej-SGP-VII could successfully be obtained using a simpler and more efficient procedure than that previously used for the recombinant Pej-SGP-I. The yield of soluble recombinant Pej-SGP-VII attached with the Nus-tag at the N-terminal side and a Gly residue at the C-terminal end was about 160 mg from 1 liter of culture.

Recombinant CHHs of crustacean species except for *M. japonicus* were also produced by other workers using *E. coli* (Gu *et al.* 2000; Mettulio *et al.* 2004) and yeast expression systems (Treerattrakool *et al.* 2003). Injection of those recombinant CHHs elevated hemolymph glucose levels; however, it has not been determined whether their biological activities are comparable to those of native ones. Such recombinant CHHs seem to have shown lower hyperglycemic activity compared with that of recombinant *M. japonicus* CHHs, probably due to the lack of amidation at the C-terminus. In addition, their structural characteristics, including secondary structure and disulfide bond arrangement, have not yet been examined.

2-1F. Structure-activity relationship

CHH-family peptides are divided into two subtypes, types I and II, based on the structure of the mature hormone as described above. All CHH molecules are classified into type I, and MIH, MOIH and VIH molecules are classified into type II except for *Procambarus bouvieri* MIH belonging to type I (Aguilar *et al.* 1996). Most type I peptides are amidated at the C-terminus, but a few exceptions are observed. In *C. maenas*, CHH-like molecule isolated from the pericardial organ (PO-CHH) and the CHH isolated from the sinus gland (SG-CHH) share an identical N-terminal sequence, positions 1–40, but the remaining C-terminal sequences differ considerably (Dircksen *et al.* 2001). SG-CHH exhibits a remarkable hyperglycemic activity, but PO-CHH which lacks an amide moiety at the C-terminus shows no hormonal activity. In the South African spiny lobster *Jasus lalandii*, two CHHs with a C-terminal amide moiety have been isolated from the sinus gland. In addition, it was found that C-terminally truncated forms of two CHHs, lacking seven C-terminal amino acid residues and having a free C-terminus, exist concurrently in the sinus glands (Marco *et al.* 2000). The former two CHHs showed hyperglycemic activity, whereas the latter two truncated CHHs did not. Therefore, it is highly possible that the C-terminal sequence of CHH, especially the C-terminal amide moiety, is significant in conferring the hormonal activity, although no direct evidence has been obtained.

In order to examine the above hypothesis, we produced recombinant Pej-SGP-I molecules, one of the six CHHs in *M. japonicus*, with or without the C-terminal amide moiety using a bacterial expression system (Katayama *et al.* 2002). As expected, increases in hemolymph glucose levels after injection of the recombinant Pej-SGP-I with a free carboxyl-terminus (rPej-SGP-I-OH) were observed at high dosages only, whereas the recombinant Pej-SGP-I having an amidated C-terminus (rPej-SGP-I-amide) showed remarkable hyperglycemic activity, which was comparable to that of the native Pej-SGP-I (**Fig. 9**). These

doi:10.5047/absm.2013.00602.0049 © 2013 TERRAPUB, Tokyo. All rights reserved.

Fig. 10. Complete primary structure of rPej-SGP-I. Four amino acid residues at the N-terminus, Gly-Ala-Met-Gly, are derived from the nucleotide sequence of an expression vector. An additional glycine residue was attached at the C-terminus (*) in rPej-SGP-I-Gly, and the C-terminus was amidated in rPej-SGP-I-amide. Reprinted from *Peptides*, **23**, Katayama *et al.*, Significance of a carboxyl-terminal amide moiety in the folding and biological activity of crustacean hyperglycemic hormone, 1537–1546, © 2002, with permission from Elsevier.

results indicate that the C-terminal amide moiety is significant in conferring hyperglycemic activity. This was the first report that describes direct evidence for the importance of C-terminal amidation in CHH. The C-terminal amidation caused a change in the C-terminal charge from a negatively charged C-terminus to a neutral one and, therefore, it is likely that the difference between rPej-SGP-I-OH and rPej-SGP-I-amide in the C-terminal charge may cause binding affinity to the CHH receptor.

The secondary structure of rPej-SGP-I-amide as estimated by circular dichroism (CD) spectrum differed from that of rPej-SGP-I-OH (**Table 2**), indicating that the C-terminal amide moiety of CHH is also significant in the folding of the molecule to its natural conformation. The difference in hyperglycemic activity between rPej-SGP-I-OH and rPej-SGP-I-amide may be partly due to differences in secondary structure and/or C-terminal charge. The arrangements of three disulfide bonds in rPej-SGP-I-OH and rPej-SGP-I-Gly, a precursor of rPej-SGP-I-amide, were determined to be identical, and the disulfide bonds were connected between Cys^{7}–Cys^{43}, Cys^{23}–Cys^{39} and Cys^{26}–Cys^{52} (**Fig. 10**). This arrangement is identical to those of other CHH-family peptides determined thus far (Kegel *et al.* 1989; Huberman *et al.* 1993; Martin *et al.* 1993; Yasuda *et al.* 1994; Aguilar *et al.* 1995, 1996; Nagasawa *et al.* 1999; Kawakami *et al.* 2000; Katayama *et al.* 2001) and, therefore, it is likely that this arrangement of disulfide bonds is also the same as in the native Pej-SGP-I. These results indicate that the difference in conformation between rPej-SGP-I-OH and rPej-SGP-I-amide is caused not by the variation of disulfide bond arrangement, but by the conformational change of the C-terminal region.

Although the secondary structure of rPej-SGP-I-amide predicted by the CD spectrum was different from that of the native Pej-SGP-I (**Table 2**), the hyperglycemic activity of rPej-SGP-I-amide was comparable to that of the natural peptide (**Fig. 9**). Since the rPej-SGP-I-amide possessed four extra amino acid residues at the N-terminus of native Pej-SGP-I (**Fig. 10**), it is likely that the N-terminal extension of four residues causes a change in secondary structure but does not cause a significant change in biological activity. In our previous studies, recombinant Pej-SGP-IV expressed in *E. coli* exhibited an identical amino acid sequence to the native one except that the recombinant Pej-SGP-IV had an additional alanine residue at the N-terminus of the native peptide (Ohira *et al.* 1999; Katayama *et al.* 2001). It was reported that the CD spectrum of the recombinant Pej-SGP-IV was close to that of the native Pej-SGP-IV, and that the MIH activity of recombinant Pej-SGP-IV was as high as that of the native one in an *in vitro* bioassay (Ohira *et al.* 1999; Katayama *et al.* 2001). All of these results suggest that short extensions at the N-terminus of CHH-family peptides may cause slight changes in whole conformation, whereas they do not cause to affect biological activity.

All type II peptides, such as MIH, VIH and MOIH, unexceptionally have an additional glycine residue at position 12, which is lacked in all CHHs. Pej-SGP-IV carries five α-helices, and Gly^{12} is located in the short N-terminal helix (Katayama *et al.* 2003). The tertiary structure of Pej-SGP-III, one of the six CHHs in *M. japonicus*, was modeled based on the structure of Pej-SGP-IV. By comparison of tertiary and surface structures of Pej-SGP-III with those of Pej-SGP-IV, the N-terminal helix of Pej-SGP-IV was presumed to be one of the significant regions for conferring MIH activity (Katayama *et al.* 2003). In order to examine the significance of the absence of a glycine residue at position 12 in natural CHHs, we prepared a mutant rPej-SGP-I-amide (rPej-SGP-I-amide-Gly^{12}) with an additional glycine residue inserted between positions 11 and 12 (Katayama and Nagasawa 2004). rPej-SGP-I-amide-Gly^{12} had the same disulfide bond arrangement as rPej-SGP-I-amide, and exhibited a similar CD spectrum to that of rPej-SGP-I-amide, indicating that the two recombinant peptides possessed similar conformations.

The dose-response relationship of rPej-SGP-I-amide-Gly^{12} is shown in **Fig. 11**. Injection of 100 pmol of rPej-SGP-I-amide-Gly^{12} increased hemolymph glucose levels slightly, and its hyperglycemic activity reached a maximum at 300 pmol. It was demonstrated that the rPej-SGP-I-amide showed low hyperglycemic activity at 10 pmol and high activity at 100 pmol (**Fig. 9**). Therefore, the hyperglycemic activity of rPej-SGP-I-amide-Gly^{12} was lower than that of the rPej-SGP-I-amide by about one order of magnitude. Thus, these

doi:10.5047/absm.2013.00602.0049 © 2013 TERRAPUB, Tokyo. All rights reserved.

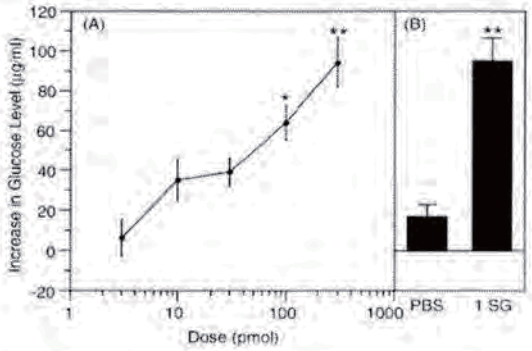

Fig. 11. (A) Dose-response relationship of Pej-SGP-I-amide-Gly[12]. (B) Negative control, injection of phosphate buffered saline (PBS); positive control, injection of sinus gland extract (one sinus gland equivalent) of *Marsupenaeus japonicus*. Results are expressed as the means ± SE (n = 7–14). Asterisks indicate values significantly different from the negative control. Symbols, (*) and (**), indicate $P < 0.01$ and $P < 0.001$, respectively, which were calculated with the program of Fisher's PLSD. Reprinted with permission from *Zool. Sci.*, **21**, Katayama *et al.*, Effect of a glycine residue insertion into crustacean hyperglycemic hormone on hormonal activity, 1121–1124, Fig. 2, © 2004, Zoological Society of Japan.

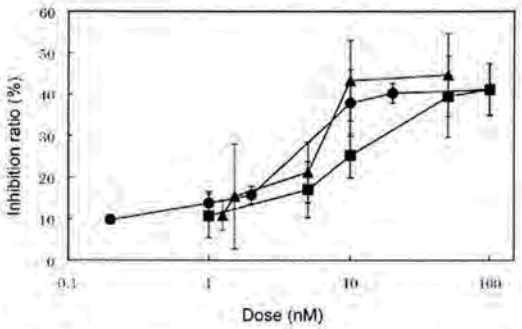

Fig. 12. Dose-response relationship of MIHs. Triangles, circles and squares show the native MIH, recombinant MIH and recombinant MIH-B, respectively. The results are expressed as the means ± SE (n = 3–8).

results suggest that the insertion of a glycine residue is one of the indices for structural and functional divergence of the CHH-family peptides.

2-2. MIH

2-2A. Bioassay and purification

In 1905, Zeleny demonstrated that eyestalk ablation shortened the molt interval of the crab *Uca pugilator* (Zeleny 1905). A molt-inhibiting factor, the so-called "MIH" was first isolated and characterized in the sinus gland located in the eyestalk of green shore crab, *C. maenas* (Webster and Keller 1986; Webster 1991). After that, MIHs were characterized from several decapod species (Webster 1991; Chung *et al.* 1996).

From the sinus gland extract of *M. japonicus*, a peptide exhibiting molt-inhibiting activity was purified by a single-step reversed-phase HPLC (Yang *et al.* 1996). Molt-inhibiting activity was measured using an *in vitro* culture of Y-organs of the crayfish, *Procambarus clarkii*, and an ecdysteroid radioimmunoassay (RIA) (Sonobe *et al.* 1991). In this work, a pair of Y-organs was dissected out of an eyestalk-ablated animal. One gland was incubated in a medium containing 1% bovine serum albmin (BSA), and the other was done in the same medium containing each peptide separated by the reversed-phase HPLC. After 6 h incubation at 25°C, ecdysteroid levels in the culture media were measured by RIA, and the inhibition ratio was calculated from the differences between the BSA and tested peptide treatments. By this method, one fraction on an HPLC chromatogram containing Pej-SGP-IV showed strong MIH activity, and therefore it was likely that this peptide might be an intrinsic MIH (**Table 1**).

The dose-response relationship of purified MIH for the inhibition of ecdysteroid secretion in *in vitro* crayfish Y-organ culture is shown in **Fig. 12** (Yang *et al.* 1996). The lowest inhibition (*ca.* 10%) was observed at a dosage level of 0.125 sinus gland equivalents in 500 μL (1.08 nM), and the inhibition was enhanced in a dose-dependent manner. Maximal inhibition (*ca.* 45%) was observed at a concentration of 1–5 sinus gland equivalents in 500 μL. This value is comparable to the effects of *C. maenas* MIH on the Y-organ culture of the same species (Webster and Keller 1986), suggesting that this purified peptide is functional in *M. japonicus*.

2-2B. Chemical structure and cDNA cloning

To determine the amino acid sequence of MIH, we firstly analyzed the N-terminal sequence using an automated protein sequencer, and the first 73 residues except for 8 residues at positions 7, 24, 27, 40, 44, 53, 69 and 71 were identified. Next, to determine these unidentified residues and the C-terminal sequence, MIH was digested with lysyl endopeptidase, and the digests were separated by reversed-phase HPLC. One of the digests was reduced by dithiothreitol and was *S*-carboxymethylated, yielding two peptides on reversed-phase HPLC. All of these fragments were analyzed on the automated protein sequencer, and the complete amino acid sequence of MIH was determined to consist of 77 amino acid residues (Yang *et al.* 1996). The C-terminal structure was confirmed by FAB mass spectral analysis of the C-terminal fragment after enzymatic digestion to be a free C-terminus. Six Cys residues exist at the positions conserved among CHH-family

doi:10.5047/absm.2013.00602.0049 © 2013 TERRAPUB, Tokyo. All rights reserved.

```
                TCCTTCGACCCCTACTCCTGGGCTTCCCTCCGTCCCTACGCTTTTACACTC 51
    ATG TAT CGG CTA GCA ATG AGG ACA TGG CTG GCG ATA GTG ATT GTA GTA 99
-28 Met Tyr Arg Leu Ala Met Arg Thr Trp Leu Ala Ile Val Ile Val Val

    GTT GGG ACA AGC CTC TTG TTC GAC ACC GCT TCG GCG AGC TTC ATA GAC 147
-12 Val Gly Thr Ser Leu Leu Phe Asp Thr Ala Ser Ala Ser Phe Ile Asp

    AAC ACC TGT AGG GGC GTG ATG GGT AAT CGT GAC ATT TAC AAG AAA GTA 195
  5 Asn Thr Cys Arg Gly Val Met Gly Asn Arg Asp Ile Tyr Lys Lys Val

    GTG CGA GTG TGT GAG GAT TGC ACT AAT ATC TTC CGA TTG CCA GGA CTG 243
 21 Val Arg Val Cys Glu Asp Cys Thr Asn Ile Phe Arg Leu Pro Gly Leu

    GAC GGC ATG TGC AGA AAT CGG TGC TTC TAC AAC GAA TGG TTC CTG ATT 291
 37 Asp Gly Met Cys Arg Asn Arg Cys Phe Tyr Asn Glu Trp Phe Leu Ile

    TGC TTG AAG GCC GCC AAC AGG GAG GAC GAG ATC GAG AAG TTC AGA GTG 339
 53 Cys Leu Lys Ala Ala Asn Arg Glu Asp Glu Ile Glu Lys Phe Arg Val

    TGG ATC AGC ATC CTG AAC GCC CGA CAG TGA GCCTGAATGTGACCAGGACCCGAT 392
 69 Trp Ile Ser Ile Leu Asn Ala Gly Gln  *

    CCCCTCCCCTCCCCAGGCCTCGCTCATATAGACCAACATTCTTGACACTTGACCAACGATTAT 455
    CATCATTAATATTCTTTATGATTTTTAAACTTATTTCGTCTCGTTATCTCTGTTACTTTACTG 518
    GTACCAGTAAATGATATGCCAGTCTGAGCCTACAAGGCTGGCGGTCATGTAAAGTATGTATAC 581
    GAAAAATTACGTGTGAAATATTCCCACTAATCTGCTCTCATTTGCTGTAATCGAATCCGGATA 644
    TCCTCTTTATTATGTACTTTATTTAATATATTGATTTGAATCTGGAAATCAAACTAAAAGAAA 707
    TATCTATTTTGTATTTTGATCTCATATGTATATTCATCGAGCGTATCTTTTCATGTCATTTGA 770
    TTGCTTCCTCATTGTTATGATGGACACGAATAAAAGTTTCTCTG(A)n                814
```

Fig. 13. Nucleotide and deduced amino acid sequences of *Marsupenaeus japonicus* MIH (Pej-SGP-IV). The numbers at the left and right sides indicate the amino acid and nucleotide numbers, respectively. Signal sequence is indicated by an underline, and the putative poly-adenylation signal is shown by a shaded box. The sequence has been deposited in the DNA Data Bank of Japan (accession No. AB004652).

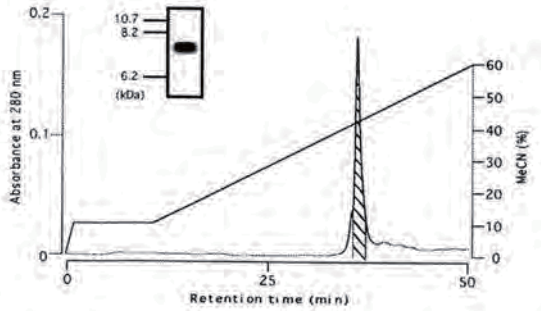

Fig. 14. Reversed-phase HPLC elution profile of the recombinant MIH after the refolding reaction. Column, TSKgel Octadecyl-4PW (4.6 × 150 mm); flow, 1.0 mL/min. A hatched peak indicates the correctly folded recombinant MIH. SDS/polyacrylamide gel electrophoresis of the hatched peak material is shown as in-set. Reprinted with permission from *Biosci. Biotechnol. Biochem.*, **63**, Ohira *et al.*, Expression of a recombinant molt-inhibiting hormone of the kuruma prawn *Penaeus japonicus* in *Escherichia coli*, 1576–1581, Fig. 4, © 1999, Japan Society for Bioscience, Biotechnology, and Agrochemistry.

peptides. *M. japonicus* MIH showed 44% sequence identity with *C. maenas* MIH (Webster 1991), and this value is higher than that between *M. japonicus* MIH and CHHs in the same species (~30%). *M. japonicus* MIH also showed high sequence identity with *P. clarkii* MIH (49%), which is consistent with the evidence that *M. japonicus* MIH possessed the molt-inhibiting activity in our bioassay system using *P. clarkii* Y-organs.

In order to clone a cDNA encoding MIH, total RNA was isolated from the eyestalk, and subjected to RT-PCR. Using a set of degenerate primers designed based on the amino acid sequence of MIH, a partial cDNA encoding MIH was obtained. This RT-PCR product was used as a probe to screen an eyestalk cDNA library, and 20 positive clones were identified. Sequence analysis of ten positive clones demonstrated that two of these clones encoded a MIH precursor. The nucleotide sequence of one of them and its deduced amino acid sequence are shown in **Fig. 13** (Ohira *et al.* 1997c). An ORF of 318 bp was found and this ORF encoded putative 105 residues protein. The sequence of the C-terminal 77 residues of the protein was identical to that of MIH, and N-terminal 28 residues were likely to constitute a signal peptide. Unlike CHH precursors, no CPRP-like sequence was found between the signal and mature peptides in the precursor of MIH.

The MIH gene was specifically expressed in the eyestalk, and no expression was observed in the hepatopancreas, abdominal muscle, brain, thoracic ganglia and abdominal ganglia by Northern blot analysis (Ohira *et al.* 1997c). We next investigated changes in levels of MIH transcripts in the eyestalk during the molt cycle. Unexpectedly, no decrease in the MIH expression level was observed at the early and late premolt stages, suggesting that the synthesis, modification and/or secretion of MIH was regulated post-transcriptionally.

Until now, MIHs have been isolated and characterized from many crustacean species (Nakatsuji *et al.* 2009). Different from the case of CHHs whose C-terminus was amidated without any exceptions, the C-terminal structures of MIHs were varied; *P. clarkii* MIH possesses shorter sequence (75 amino acid residues long) than that of *M. japonicus* and amidated terminus (Nagasawa *et al.* 1996), and *C. maenas* MIH possessed elongated C-terminus (78 residues long) (Webster 1991). These observations suggest that the C-terminal structure of MIH is not important for conferring MIH activity.

2-2C. Preparation of the recombinant MIH

In order to achieve further functional and structural analyses such as measurement of *in vivo* biological activity and tertiary structure determination, a large amount of MIH would be required. Therefore, we attempted to establish a bacterial expression system for recombinant MIH (rMIH) (Ohira *et al.* 1999).

The cDNA encoding *M. japonicus* MIH was inserted into an expression plasmid, and *E. coli* competent cells were transformed with it. Positive clones were selected on LB plates containing antibiotics, and the bacterial cells from a single colony were cultured in LB me-

doi:10.5047/absm.2013.00602.0049 © 2013 TERRAPUB, Tokyo. All rights reserved.

dium. After 2 h induction of the recombinant protein expression by addition of isopropyl-β-D-thiogalactoside (IPTG), the bacterial cells were harvested. After cell breakage by sonication, the soluble and insoluble fractions were obtained. In SDS-polyacrylamide gel electrophoresis (PAGE) analysis of these fractions, a heavily stained band corresponding to rMIH was observed only in the insoluble fraction, indicating that rMIH was expressed not as a soluble protein but in the form of inclusion bodies.

After solubilization of the inclusion bodies by 6 M guanidine-HCl, the resultant solution was applied to reversed-phase HPLC, in which four major peaks were observed. All these peak materials gave the same value in the mass spectral analysis, which coincided well with the theoretical value of rMIH. In sequence analysis, these four materials gave the same sequence, which were identical with the MIH except that these four had an additional alanine residue at the N-terminus derived from the nucleotide sequence of the expression plasmid. These results indicated that these four materials were the disulfide isomers of rMIH. These four peak materials were combined, and subjected to the *in vitro* refolding reaction.

The refolding reaction was carried out in a redox buffer containing 1.3 M urea/1 mM glutathione (reduced form, GSH)/1 mM glutathione (oxidized form, GSSG) at 4°C for overnight. After the reaction, the four peak materials were converged into one peak on the reversed-phase HPLC chromatogram (**Fig. 14**). This peak material gave the protonated ion peak at *m/z* 9135 (calculated value, 9136 for $(M+H)^+$) in mass spectral analysis and also gave the N-terminal sequence ASFID- in sequence analysis, suggesting that this peak material is rMIH which is expected to have a proper folding and correct disulfide arrangement. The yield of this peak material was about 1 mg for 1 liter of culture.

The *in vitro* molt-inhibiting activity of rMIH was examined using a *P. clarkii* Y-organ culture assay. The lowest inhibition (*ca.* 12%) was observed at a concentration of 0.2–1.0 nM. The inhibition was enhanced with increased dosage, and reached its maximum (*ca.* 41%) at the concentration of 10–20 nM (**Fig. 12**). These values are almost comparable to those of the native MIH. Although rMIH possesses an extra Ala residue at the N-terminus, this extension did not cause a significant change in biological activity.

In order to confirm the folding of rMIH, the CD spectrum of rMIH was measured. A CD spectrum of the native MIH was also measured at the same time under the same conditions. The spectral analysis indicated that rMIH possesses α-helical structure, and the helix content was calculated to be 46% (Katayama *et al.* 2001). This spectral pattern was almost the same as that of the native peptide, suggesting that rMIH and the native MIH share the same conformation. It was also similar to the CD spectra of other CHH-family peptides reported previously (Huberman *et al.* 1989; Gasparini *et al.* 1994).

Next, we examined the nature of disulfide pairing in rMIH. MIH was first digested by thermolysin, and the digests were separated by reversed-phase HPLC. The structure of one of the fragments was determined to consist of four peptide chains connected by three disulfide bonds based on mass spectral and amino acid sequence analyses. To obtain the peptide fragments containing only one disulfide bridge, this fragment was further digested sequentially with TPCK-treated trypsin and endoproteinase Asp-N, giving three double-chain fragments containing one disulfide bond. Each fragment was analyzed by MALDI-TOF mass spectrometer and a protein sequencer, establishing that the disulfide pairing occurred between Cys^7–Cys^{44}, Cys^{24}–Cys^{40} and Cys^{27}–Cys^{53}. The disulfide bond arrangement in the native MIH was also determined in the same manner, and the same results as those in the case of rMIH were obtained. This disulfide pairing is essentially the same as those in other CHH-family peptides whose disulfide bond arrangements were determined previously (Kegel *et al.* 1989; Huberman *et al.* 1993; Martin *et al.* 1993; Yasuda *et al.* 1994; Gasparini *et al.* 1994; Aguilar *et al.* 1995, 1996; Nagasawa *et al.* 1999; Kawakami *et al.* 2000), suggesting that the type II peptide share a similar conformation with those of type I CHH-family peptides.

All these results including biological assays, CD spectrum measurement and disulfide bond arrangement determination indicated that rMIH is not only biologically but also chemically identical with the native peptide except that an extra Ala residue was attached at the N-terminus in rMIH. Using this recombinant peptide, it became possible for us to conduct tertiary structure determination, *in vivo* bioassays, and screening of MIH receptor.

2-2D. Tertiary structure

We attempted to determine the tertiary structure of MIH using nuclear magnetic resonance (NMR) methods (Katayama *et al.* 2003). To measure NMR spectra, a sample solution of high concentration is required, but the solubility of rMIH in water or phosphate buffered saline (PBS) at neutral pH is poor. On the other hand, acidic solutions or aqueous organic solvents can dissolve rMIH at high concentrations above 1 mM. In particular, 30% aqueous acetonitrile dissolved rMIH in concentrations over 2 mM, and rMIH in this solution showed essentially the same CD spectrum as in PBS. Thus, we used 30% aqueous acetonitrile as the solvent for the NMR experiments.

All non-labile ^1H, ^{13}C and ^{15}N atoms of rMIH were assigned based on standard triple resonance NMR experiments. A total of 2152 restraints including 2109 distance and 43 torsion angle restraints was obtained from the NMR data and used in the structural calcula-

doi:10.5047/absm.2013.00602.0049 © 2013 TERRAPUB, Tokyo. All rights reserved.

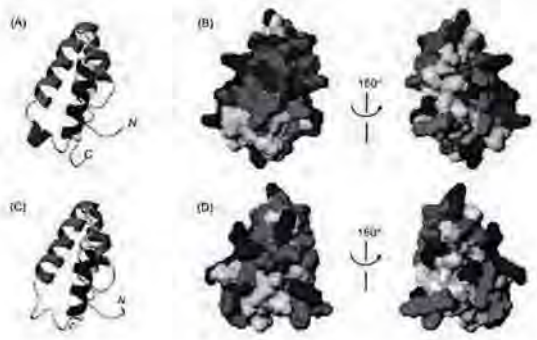

Fig. 15. (A) Ribbon model of the energy-minimized average structure of MIH. (B) Surface structure of MIH. The view angle of the left figure is the same as that of panel A, and that of the right figure is the reverse. The acidic, basic and hydrophobic residues are colored red, blue and green, respectively. (C) Ribbon model of the homology-modeled structure of Pej-SGP-III. (D) Surface structure of Pej-SGP-III. The view angle of the left figure is the same as that of panel C, and that of the right figure is the reverse. Reprinted with permission from *J. Biol. Chem.*, **278**, Katayama *et al.*, The solution structure of molt-inhibiting hormone from the Kuruma prawn *Marsupenaeus japonicus*, 9620–9623, Fig. 3, © 2003, The American Society for Biochemistry and Molecular Biology.

tions of rMIH. A set of 10 structures was selected out of 50 calculated structures based on agreement with the experimental data. In these selected structures, there were no violations greater than 0.4 Å and 2° in interproton distances and torsion angles, respectively. The pairwise RMS deviations among the 10 structures were 0.51 ± 0.09 Å for the backbone heavy atoms (N and C) and 1.24 ± 0.10 Å for all non-hydrogen atoms in the well-defined region (Asn^5–Ala^{75}). The conformation of the N-terminal (Ser^1–Asp^4) and C-terminal (Gly^{76}–Gln^{77}) regions was much less defined, because only a few restraints were obtained for these regions. In the Ramachandran ϕ–ψ plot for the well-defined region of the 10 selected structures, 99.8% of ϕ–ψ pairs were located in the favored and allowed regions.

Figure 15A shows the best-fit superposition of the backbone atoms of rMIH. The rMIH molecule consists of five α-helices ($\alpha1$: Val^{10}–Asn^{13}, $\alpha2$: Ile^{16}–Phe^{31}, $\alpha3$: Pro^{34}–Cys^{40}, $\alpha4$: Glu^{49}–Lys^{55} and $\alpha5$: Glu^{62}–Ile^{72}) and four loops between the α-helices (L1-2, L2-3, L3-4 and L4-5). The disulfide bonds linked N-terminal region and L3-4, $\alpha2$ and $\alpha3$, and $\alpha2$ and $\alpha4$. This α-helical structure is consistent with the results of CD spectral analysis.

The conformation of rMIH was stabilized by a number of hydrophobic interactions in the cluster of nine hydrophobic residues (Leu^{16}, Val^{20}, Val^{23}, Phe^{46}, Phe^{50}, Leu^{54}, Phe^{66}, Ile^{70} and Leu^{73}) and the three disulfide bonds. These hydrophobic and cysteine residues are conserved in most CHH-family peptides, suggesting that the CHH-family peptides harbor similar foldings. We searched for proteins structurally similar to MIH using the DALI server (Holm and Sander 1993), but no similar structure was found, indicating that CHH-family peptides form a novel class of folds.

The tertiary structure of Pej-SGP-III (Yang *et al.* 1995), one of the *M. japonicus* CHHs which has 32% sequence identity and 66% sequence similarity to *M. japonicus* MIH, was homology-modeled using the SWISS-MODEL server (Guex and Peitsch 1997). **Figure 15C** shows the modeled structure of the CHH. This structure is very similar to the solution structure of rMIH except that CHH lacks $\alpha1$. The solution structure of rMIH shows that the Gly residue insertion typical for type II CHH-family peptides is located at $\alpha1$, and the absence of $\alpha1$ in CHH may be due to the lack of the Gly residue. Since the C-terminal sequence of CHH is shorter than that of MIH by a few amino acid residues, the CHH lacked the C-terminal tail region present in MIH. The C-terminal tail of MIH was located sterically close to $\alpha1$, and the surface properties including electrostatic potential and hydrophobicity of these peptides were different in this terminal region. Therefore, it was presumed that the region containing $\alpha1$ and the C-terminal tail was important for molt-inhibiting activity.

As described in the previous section, it was demonstrated that the C-terminal amide moiety of CHH is significant in conferring biological activity. In addition, the C-terminally truncated CHH from the South African spiny lobster *J. lalandii*, which lacked six C-terminal amino acid residues, showed no hyperglycemic activity (Marco *et al.* 2000). These observations suggest that the functional site of CHH may be located at the C-terminal region. On the basis of our results from the NMR experiments, we proposed the hypothesis that the functionally important sites of CHH-family peptides may be located at the region containing $\alpha1$ and the C-terminal region.

2-2E. Structure-activity relationship

In order to confirm the hypothesis that the functional site of MIH is located in the region encompassing the $\alpha1$ and the C-terminus, various mutant molecules of MIH were prepared (Katayama *et al.* 2004). The amino acid residues to be mutated were selected according to the following two criteria: first, residues must reside in the region containing the $\alpha1$ helix and C terminal tail; second, residues must have a side chain exposed at the molecular surface. We selected residues exposed to the molecular surface for mutation, partly because the surface residues would directly interact with the receptor, and partly because conformational changes due to the mutations would be minimized. Thus, seven mutants, N13A (a substitution mutant at position 13

doi:10.5047/absm.2013.00602.0049 © 2013 TERRAPUB, Tokyo. All rights reserved.

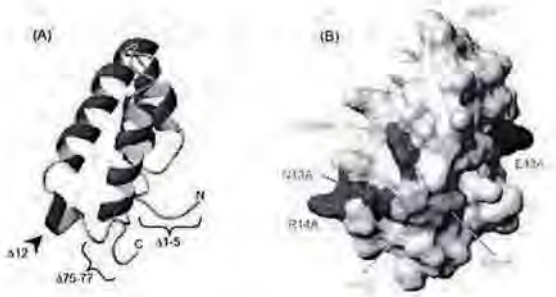

Fig. 16. (A) Ribbon model of MIH. Mutated sites of deletion mutants are indicated. (B) Surface structure of the MIH. Colors indicate the sites of various mutations. Reprinted with permission from *Biochemistry*, **43**, Katayama *et al.*, Structure-activity relationship of molt-inhibiting hormone from the kuruma prawn *Marsupenaeus japonicus*, 9629–9635, Fig. 1, © 2004, American Chemical Society.

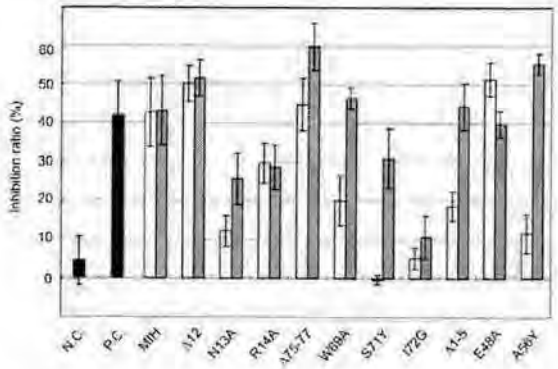

Fig. 17. Molt-inhibiting activity of the various mutants, controls and the recombinant MIH. N.C., no sample was added as the negative control; P.C., sinus gland extract of the crayfish *P. clarkii* (0.5 sinus gland equivalents) as the positive control. Mutants and the recombinant MIH were tested at 20 nM (open columns) and 200 nM (shaded columns). Results are expressed as the means ± SE (n = 3–9). Reprinted with permission from *Biochemistry*, **43**, Katayama *et al.*, Structure-activity relationship of molt-inhibiting hormone from the kuruma prawn *Marsupenaeus japonicus*, 9629–9635, Fig. 4, © 2004, American Chemical Society.

from Asn to Ala), R14A, W69A, S71Y, I72G, Δ12 (a deletion mutant of Gly[12]), and Δ75–77 (a mutant truncated three residues at the C-terminus) were designed. In addition, E48A, A56Y and Δ1–5 (a mutant truncated five residues at the N-terminus) were also designed in order to examine the influence of the putative nonfunctional position (**Fig. 16**).

These mutant peptides were expressed in *E. coli* in essentially the same manner as for rMIH. The bacterial cells were then harvested, suspended in PBS, and sonicated. Soluble and insoluble fractions obtained by centrifugation were subjected to SDS-PAGE, and heavily stained bands corresponding to recombinant mutant peptide candidates were detected only in the insoluble fractions in all mutants. These results indicated that all of the mutants were expressed in *E. coli* cells as inclusion bodies. Therefore, refolding was considered to be necessary to obtain mutant peptides with the proper conformation.

All mutants were obtained as a single peak on reversed-phase HPLC after refolding. MALDI-TOF mass spectral and N-terminal amino acid sequence analyses of each peak material showed the expected single molecular ion peak and N-terminal sequence, respectively, except for Δ1–5. The N-terminal sequence analysis of Δ1–5 gave the sequence, M/T-T/X-X/R-R/G-G/V-, indicating that the N-terminal methionine residue had only been partially removed by methionine aminopeptidase in *E. coli*. Since these two peptides could not be separated by HPLC, we used a mixture of the two Δ1–5 peptides in the following experiments. The N-terminal sequence of the other mutants, ASFIDNTXRG-, was identical to the native peptide except for the N-terminal alanine residue that was derived from the expression vector.

In order to confirm that the mutant peptides possessed the same conformation as the native peptide, the CD spectra of the mutants in PBS were recorded at room temperature. Since the solubility of S71Y in PBS was not enough for measuring CD spectrum, we could not record the CD spectrum of this mutant under the same conditions as for the other peptides. As expected, the CD spectra of the other mutants in PBS showed a pattern typical for α-helical proteins and were quite similar to the spectra of the native and recombinant molecules of MIH. Therefore, we concluded that the mutant peptides retained proper conformation regardless of the mutations.

In the dose-response relationship of the recombinant MIH, inhibition of ecdysteroid synthesis *in vitro* was observed at a concentration of 2 nM with maximum inhibition observed at 20 nM or higher (**Fig. 12**). Consequently, we assessed the molt-inhibiting activity of each mutant peptide at two concentrations, 20 and 200 nM. The results of the bioassays are shown in **Fig. 17**. Three mutants, Δ12, Δ75–77 and E48A, exhibited high molt-inhibiting activity comparable to that of rMIH at 20 and 200 nM. R14A, W69A, A56Y, and Δ1–5 showed high activity at 200 nM, but significantly lower activity than rMIH at 20 nM, indicating that the mutations in these four peptides brought about a decrease in activity by approximately one order of magnitude. Neither N13A nor S71Y exhibited activity at 20 nM with low activity at 200 nM, indicating that N13A and S71Y are less active than rMIH by more than one order of magnitude. I72G showed no activity at the two con-

doi:10.5047/absm.2013.00602.0049 © 2013 TERRAPUB, Tokyo. All rights reserved.

centrations tested, indicating that the activity of I72G is lower than that of rMIH by at least two orders of magnitude. The disulfide bond arrangement in I72G was determined to be the same as that of rMIH, indicating that the loss of activity in I72G was not due to the failure in the refolding reaction.

N13A and R14A, mutated at the α1 helix, exhibited lower activities than the recombinant MIH, although Δ12, expected to lack the helical structure of the α1 helix due to the shortened peptide chain, retained activity comparable to that of rMIH. These results suggest that the amino acid residues located at the C-terminal end of the α1 helix, but not the helical structure itself, are significant for conferring molt-inhibiting activity, which is not inconceivable because some type I CHH-family peptides show molt-inhibiting activity.

W69A, S71Y and I72G, mutated at the C-terminus, showed lower activities than rMIH, whereas Δ75–77, lacking the three C-terminal amino acid residues, was as active as rMIH. These results suggest that the residues located at the C-terminal side of the C-terminal helix (α5 helix), not including the terminal three residues, are significant for conferring molt-inhibiting activity. The C-termini of MIHs from many crustaceans show various structures; some peptides have a shortened, amidated C-terminus (Nagasawa *et al.* 1996; Marco *et al.* 2000), while others possess an extended C-terminal sequence (Webster 1991; Chung *et al.* 1996). Taken together, it is likely that a few residues at the C terminus of MIH are not recognized by its receptor.

Among the many mutants, a notable decrease in molt-inhibiting activity was observed in I72G. Since the disulfide bond arrangement in I72G was the same as that of the native MIH, it is likely that the Ile^{72} mutation caused a decrease in molt-inhibiting activity by means of reduced binding ability to its receptor but not through a conformational change in the peptide. The bulky, hydrophobic side chain of Ile^{72} may be essential for receptor binding. N13A and S71Y also exhibited very low activity. The changes in hydrophobicity in N13A and in the bulkiness and aromaticity in S71Y could affect their activities. All these results suggest that Ile^{72} is the most significant residue of the residues mutated in this study for conferring biological activity, and that Asn^{13} and Ser^{71}, both of which are sterically close to Ile^{72}, are also very important.

On the other hand, it was unexpected that the A56Y mutation within the putative non-functional region of the peptide would exhibit lower molt-inhibiting activity than that of the recombinant MIH by approximately one order of magnitude. Two reasons are considered for this contradiction. First, a functionally important site may also be located around the Ala^{56} residue, and the decrease in activity may be because the aromatic ring of Tyr directly inhibits receptor-hormone binding; second, a slight conformational change which was not detectable in the CD spectrum may have been caused by this mutation, and as a result the binding affinity for the hormone receptor may have been reduced. In the NOESY NMR spectrum of the recombinant MIH, nuclear Overhauser effects (NOEs) were detected between the side chain of the Ala^{56} residue and those of the Val^{23} and the Ile^{30} residues. Therefore, it is likely that Tyr^{56} in the A56Y mutation could not fit into the space due to its bulky side chain, causing weaker hydrophobic interactions.

The hypothesis was likewise contradicted with the decreased molt-inhibiting activity of the Δ1–5 mutation. In the crayfish *P. clarkii*, two CHHs, CHH-I and CHH-II, have been isolated from the sinus gland (Yasuda *et al.* 1994). These two CHHs have identical amino acid sequences except that CHH-II has a D-Phe, which is L-Phe in CHH-I, at the third position from the N-terminus. These peptides have both CHH and MIH activities. CHH-I exhibits hyperglycemic activity as high as CHH-II, although it displays lower molt-inhibiting activity than CHH-II by approximately one order of magnitude. These results, combined with our observations, suggest that the considerable structural change in the N-terminal region of CHH-family peptides may not affect hyperglycemic activity, but does cause a reduction in molt-inhibiting activity.

Comparing the sequence of *M. japonicus* MIH with that of *P. clarkii* MIH, the positions mutated in this study are well conserved except for Ser^{71}, which is Gly^{71} in *P. clarkii* MIH. Mutations at the conserved position among them tend to decrease MIH activity, strongly suggesting that the functional site of MIHs is located at the same position of the molecules each other. Since we used hetero-species bioassay system using *P. clarkii* Y-organs in this structure-activity relationship study, it is expected that the similar results might be obtained in structure activity relationship study of *P. clarkii* MIH.

2-2F. *In vivo* effects

In order to determine the function of MIH *in vivo*, an injection experiment using rMIH was performed (Okumura *et al.* 2005). When rMIH was injected into juvenile prawns once a day on the 2nd, 3rd, 4th, 5th, 6th and 7th days after ecdysis at the dose of 250 or 2500 ng/g-body weight (BW), the molt interval was elongated from 9.0 ± 0.4 d (means ± s.d.) in the control group to 9.2 ± 0.6 d and 9.5 ± 0.5 d in 250 and 2500 ng/g-BW groups, respectively. The molt interval differed significantly between the control and the 2500 ng/g-BW groups ($P < 0.05$). To examine the effects of MIH on the ecdysteroid level, 3 μg/g-BW of rMIH was injected to juvenile prawns at premolt stage D_1. The ecdysteroid level in the control group was increased 1.94 ± 1.09-fold, whereas the increment was signifi-

doi:10.5047/absm.2013.00602.0049 © 2013 TERRAPUB, Tokyo. All rights reserved.

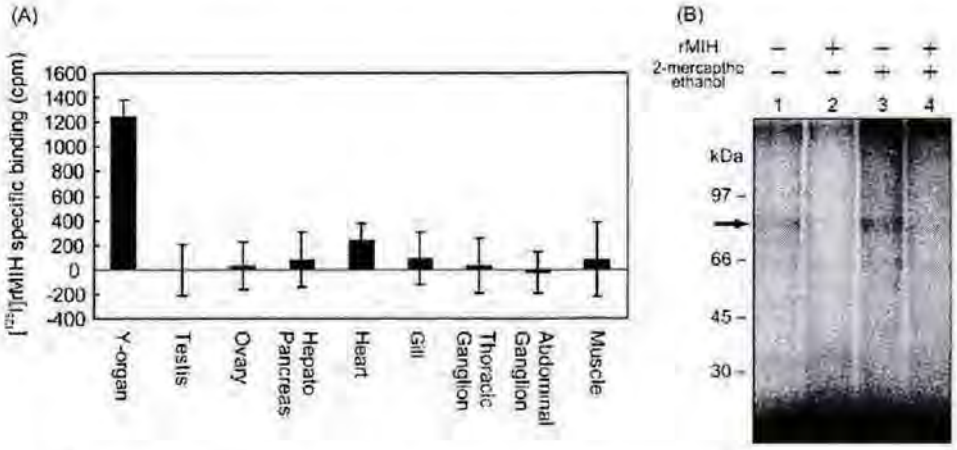

Fig. 18. (A) [^{125}I]-Recombinant MIH binding to the membrane fractions of various tissues. The results are expressed as the means ± SD. (B) Chemical cross-linking of [^{125}I]-recombinant MIH to the membrane fraction of the Y-organ. An Arrow indicates the band derived from the protein specifically binds to the recombinant MIH. Reprinted with permission of John Wiley & Sons, Inc. from *Ann. N.Y. Acad. Sci.*, **1040**, Asazuma *et al.*, Characterization of a molt-inhibiting hormone (MIH) receptor in the Y-organ of the kuruma prawn, *Marsupenaeus japonicus*, 215–218, Figs. 1 and 3, © 2005, Wiley-Liss, Inc., a Wiley Company.

cantly suppressed to 1.28 ± 0.39-fold in the test group ($P < 0.05$). To measure the biological activity of *M. japonicus* MIH *in vitro*, a hetero-species Y-organ incubation assay was used. In contrast, an *in vivo* assay was performed using the same species, and the results indicated that the MIH has an inhibitory effect on molting in this species as well.

MIH titers in the hemolymph are in the range of ~10^{-11-12} M in several species (Nakatsuji and Sonobe 2003; Chung and Webster 2005). In our injection experiments, although hormone titers may temporally increase to ~10^{-6} M, the effects on molt interval and hemolymph ecdysteroid level were not great. It has been reported that a 20-fold injection of 250 pmol/animal is required to inhibit molting in the case of the crayfish *P. clarkii* (Nakatsuji and Sonobe 2004). Considering the very short half-life of MIH in the hemolymph (Chung and Webster 2003; Nakatsuji and Sonobe 2004), it is likely that the low activity *in vivo* is due to the limited exposure of MIH to the Y-organ.

2-2G. Mode of action

In order to clarify the molecular mechanism of MIH signaling, we attempted to characterize the MIH receptor by performing a binding assay and chemical cross-linking experiments using radiolabeled rMIH (Asazuma *et al.* 2005).

The rMIH was radiolabeled with ^{125}I, and the labeled peptide was purified by reversed-phase HPLC. To survey MIH receptor distribution in *M. japonicus*, the binding capacities of [^{125}I]rMIH to the membrane fractions prepared from various tissues were compared. Non-specific binding of each membrane fraction was measured in the presence of 1000-fold amounts of non-labeled rMIH. Specific binding was calculated by subtracting non-specific binding from total binding. Significant specific binding of [^{125}I]rMIH was observed only in the membrane fraction of Y-organs, whereas no specific binding was observed in other tissues tested (**Fig. 18A**). These results strongly suggest that the MIH receptor exists specifically on the Y-organ.

To elucidate the kinetics of the MIH receptor, a saturable binding assay was carried out with various amounts of [^{125}I]rMIH ranging from 0 to 500 pM. Non-specific binding of each measuring point was determined by the count in the presence of a 10,000-fold amount of non-labeled rMIH. Scatchard analysis revealed a single population of high-affinity MIH receptors on the Y-organ membrane ($K_d = 4.76 \times 10^{-10}$ M, $B_{max} = 5.51 \times 10^{-12}$ M).

To characterize the MIH receptor, the membrane fraction from the Y-organs was incubated with [^{125}I]rMIH, and the mixture was cross-linked with a bifunctional cross-linking reagent, bis(sulfosuccinimidyl)suberate. The covalently cross-linked mixture was then analyzed by SDS-PAGE and autoradiography. A major band with the size of ~80 kDa was observed (**Fig. 18B**). On the other hand, this band disappeared when the binding reaction was carried out in the presence of an excess amount of non-labeled rMIH. These data strongly suggested that the band of 80 kDa was derived from the conjugate of [^{125}I]rMIH with the MIH receptor. In addition, this band did not change the mobility on SDS-PAGE under reducing conditions, indicating that the

doi:10.5047/absm.2013.00602.0049 © 2013 TERRAPUB, Tokyo. All rights reserved.

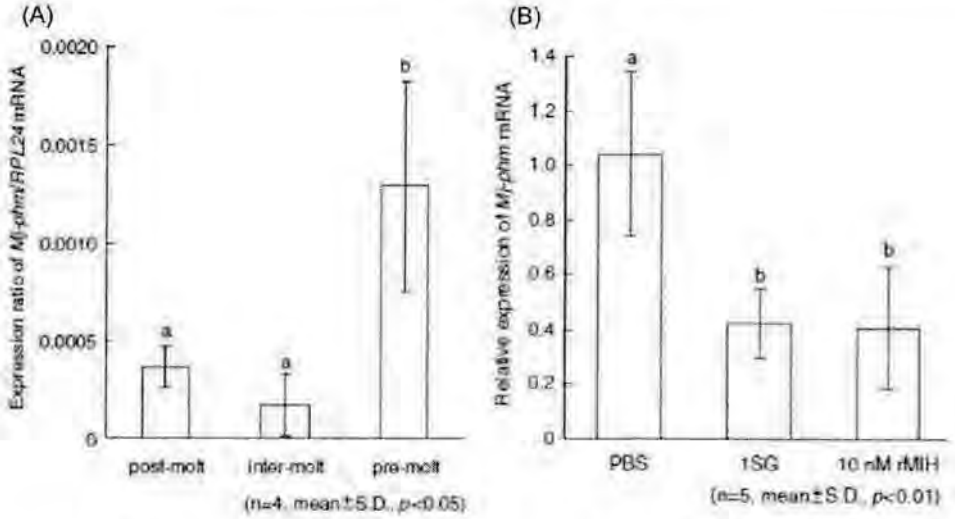

Fig. 19. (A) Expression levels of *phantom* mRNA through molting periods. Transcription levels of *phantom* and *RPL24* (a gene for 60s ribosomal protein) in the Y-organ of prawns at three different molting stages (inter-molt, pre-molt, post-molt) were analyzed using quantitative PCR. The expression levels were represented as ratios of *phantom* to *RPL24*. Different letters above the error bars indicate significant differences. Values are represented as the means ± SD ($n = 4$). (B) The expression of *phantom* in the Y-organ incubated *in vitro* with the recombinant MIH (rMIH). A pair of the Y-organs of the eyestalk-ablated prawn was incubated in a separated well with or without (control) phosphate buffered saline (PBS), sinus gland extract (SG), and 10 nM rMIH. The expression levels of *phantom* were determined by quantitative PCR. The relative expression level was represented as a percentage, control as 100%. Values are represented as the means ± SD ($n = 5$). Statistical analyses were performed using one-way ANOVA ($P < 0.05$). Reprinted with permission of John Wiley & Sons, Inc. from *Arch. Insect Biochem. Physiol.*, **72**, Asazuma *et al.*, Inhibitory effect of molt-inhibiting hormone on Phantom gene expression in the Y-organ of the kuruma prawn, *Marsupenaeus japonicus*, 220–233, Figs. 5 and 6, © 2009, Wiley-Liss, Inc., a Wiley Company.

MIH receptor on the Y-organ has a molecular mass of approximately 70 kDa and possibly is not composed of subunits linked by disulfide bonds.

It has been demonstrated that the cyclic nucleotide analogs and phosphodiesterase inhibitors mimick MIH action in the suppression of Y-organ activity in several crustacean species (Saidi *et al.* 1994; Nakatsuji *et al.* 2006, 2009). In addition, MIH treatment increased cGMP levels in Y-organ *in vitro*. Given the fact that cGMP is involved in ecdysteroidogenesis in the Y-organ, a membrane guanylate cyclase (MGC) was suggested as a candidate MIH receptor in the Y-organ (Zheng *et al.* 2006). Indeed, cDNA for MGC was recently isolated from Y-organ of the blue crab *Callinectes sapidus* which exhibits a molecular weight of 137 kDa on a Western blot analysis, thus implicating that it may be a putative receptor for MIH (Zheng *et al.* 2008). In contrast, the putative receptor of MIH in the Y-organ that was chemically cross-linked with [^{125}I]MIH revealed approximately 70 and 51 kDa proteins in *M. japonicus* and *C. sapidus*, respectively (Asazuma *et al.* 2005; Zmora *et al.* 2009). Overall, further studies are required for characterizing receptor(s) and elucidating the specific mode of actions of MIH on the inhibition of ecdysteroidogenesis in the Y-organ.

Recently, it was found that the Halloween genes encoding cytochrome P450 monooxygenases from insects were characterized as the steroidogenic enzymes catalyzing the final four steps of the ecdysteroid synthetic pathway from 5β-ketodiol to 20-hydroxyecdysone (Gilbert 2004; Truman 2005). To elucidate whether ecdysteroidogenesis in the Y-organs is regulated by MIH, the expression levels of an orthologue of a member of the Halloween genes, *phantom*, in the Y-organ of *M. japonicus* was analyzed (Asazuma *et al.* 2009). As expected, *phantom* gene expression significantly increased at the pre-molt stage, and decreased after ecdysis (**Fig. 19**). In addition, the exposure of the Y-organs to MIH significantly decreased *phantom* expression levels *in vitro*. These observations strongly suggest that the transcription of the *phantom* gene in the Y-organ is negatively regulated by MIH, although the question of how MIH regulates gene expression levels still remains unclear. In order to clarify the mechanism of MIH action on ecdysteroidogenesis, further studies are required.

2-2H. Other MIH-like peptides

Gu *et al.* cloned a fragment of a cDNA encoding an

doi:10.5047/absm.2013.00602.0049 © 2013 TERRAPUB, Tokyo. All rights reserved.

```
                    AGGTGCAGCGGCACCTGCTAGATACTTCAAGCAAATCCGCAAGCA 45
    ATG AGG GCA TGG CTG CTG TTA GCT ATC GTG GCG GCG GGA TCG TGC CTA 93
-23 Met Arg Ala Trp Leu Leu Leu Ala Ile Val Ala Ala Gly Ser Cys Leu

    TTT CCC GAA CTC TCT TCA GCC AAT ATC CTG TAC AGT AGC TGC CGA GGT 141
-7  Phe Pro Glu Leu Ser Ser Ala Asn Ile Leu Tyr Ser Ser Cys Arg Gly

    GTG ATG GGT AAC CGC GAC ATC TAC AGC AAG GTA GAG CGT GTT TGC AAC 189
10  Val Met Gly Asn Arg Asp Ile Tyr Ser Lys Val Glu Arg Val Cys Asn

    GAC TGT ACC AAT CTC TAC CGG TTG CCG CAA CTT GAC GGC TTG TGC AGA 237
26  Asp Cys Thr Asn Leu Tyr Arg Leu Pro Gln Leu Asp Gly Leu Cys Arg

    AAC CGA TGC TTC AAT AAT CAG TGG TTC CTG CTG TGC CTG AAT TCG GCG 285
42  Asn Arg Cys Phe Asn Ans Gln Trp Phe Leu Leu Cys Leu Asn Ser Ala

    AAG AGA GAA GAC GAA CTT AAT AAT TTC AGA CTA TGG ATC AGC ATC CTC 333
58  Lys Arg Glu Asp Glu Leu Asn Asn Phe Arg Leu Trp Ile Ser Ile Leu

    AAT GCC GGT CGC GAA TGG TAA ACTCTCCTCAAGGCATCCTACACATCCCCAGCCTC 389
74  Asn Ala Gly Arg Glu Trp  *

    CCGCTTCATCAAGGACACCTGACAGGACGTTGACACGGCCCCGAGGCTCCTTCCGCGCTATTA 452
    AAATTGATCATCGAAATAGACATCTCCGATCCTGATGCTTTGACGCCTGAGTTCCTTTGTGAA 515
    TACCTCTTGGTTTGGTATTTTTGTGCTCGAGGAAGACTAGGAGTGTTCGGAAACATCGTATTA 578
    AATCATGATGTTTTCCTCTTGTGTCTAACTTTATTGACGCATTACTCCTCATATATAAGTCCT 641
    GTTTTCCAAAGGTATTGGATGGAAGAGCAATTCCTTTAGATCCTGCCGGTGTGATTTCCAGT 704
    ATTATAGATTTATTGCATGTTTATCATTCACAAATTAATTGGATTCCTAATTATCCGAGTTCA 767
    ATAAGTCTTAATTTTTCGGTCGAAATAAAATTGTCTT(A)n                      804
```

Fig. 20. Nucleotide and deduced amino acid sequences of *Marsupenaeus japonicus* MIH-B. The numbers at the left and right sides indicate the amino acid and nucleotide numbers, respectively. Signal sequence is indicated by underlines, and the poly-adenylation signal is shown by a shaded box. The sequence has been deposited in the DNA Data Bank of Japan (accession No. AB162448).

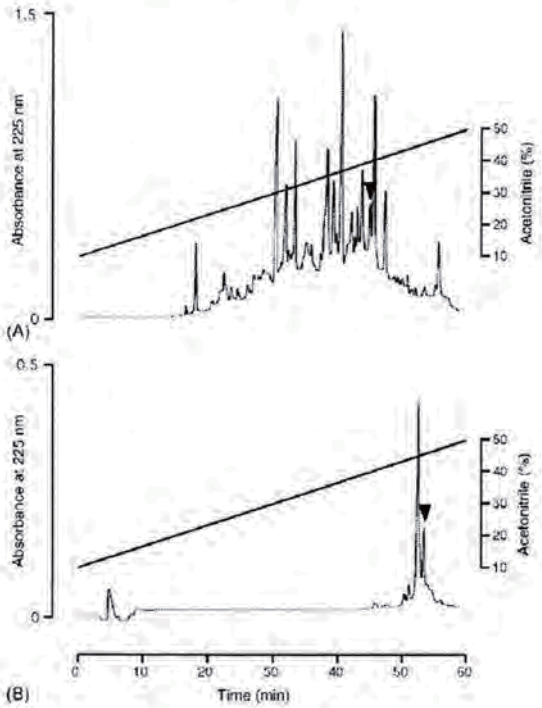

Fig. 21. Purification of the native MIH-B from the sinus gland. (A) Reverse-phase HPLC elution profile of the sinus gland extract. Separation was carried out on an Asahi-Pak ODP-50 column (4.6 × 250 mm) with a 60-min linear gradient of 10–50% acetonitrile containing 0.05% trifluoroacetic acid (TFA) at a flow rate of 0.8 mL/min. (B) Reverse-phase HPLC elution profile of the MIH-B fraction from the first HPLC. Separation was performed in the same manner as in the first HPLC except for the use of 0.05% heptafluorobutyric acid (HFBA) instead of 0.05% TFA. Arrowheads indicate the MIH-B fractions. Reprinted from *Peptides*, **26**, Ohira *et al.*, Cloning and characterization of a molt-inhibiting hormone-like peptide from the prawn *Marsupenaeus japonicus*, 259–268, © 2005, with permission from Elsevier.

MIH-like peptide named MIH-B from *M. japonicus*, but the full-length sequence of this cDNA had not yet been reported (Gu *et al.* 2002). In order to determine its nucleotide and amino acid sequences, and to analyze its biological activity, we cloned it using RT-PCR methods (Ohira *et al.* 2005).

A cDNA fragment encoding MIH-B was amplified by RT-PCR using degenerate oligonucleotide primers designed based on the partial amino acid sequence of MIH-B. Subsequently, the 5′- and 3′-regions of the cDNA were amplified by 5′- and 3′-RACE, respectively, using specific primers. In order to confirm the nucleotide sequence of the cDNA, PCR was performed to amplify the cDNA fragments including the full-length ORF. The MIH-B precursor cDNA consisted of 804 bp comprising a 5′-untranslated region (45 bp), an ORF (309 bp), a stop codon (TAA), and a 3′-untranslated region (450 bp). The 3′-untranslated region contained a consensus polyadenylation signal (AATAAA) 9 bp upstream from the poly (A) tail. The ORF of MIH-B was conceptually translated into a putative 102-residue peptide consisting of a signal peptide (23 residues) and a putative hormone portion (**Fig. 20**).

The putative hormone consisted of 79 amino acid residues containing six Cys residues which were conserved in all CHH-family peptides. The amino acid sequence of MIH-B was identical to that of the partial sequence from positions 13 to 68 previously determined by Gu *et al.* This peptide had 73% identity with MIH, and was highly homologous to MIHs characterized from other crustacean species.

The MIH-B gene was strongly expressed in the thoracic ganglia and abdominal ganglia, and weakly in the eyestalk. No expression was observed in the other tissues tested by RT-PCR analysis. This expression pattern was very similar to that of Mee-MIH-B, which is another MIH molecule in the shrimp, *Metapenaeus ensis*, having high amino acid sequence identity (66%) with *M. japonicus* MIH-B (Gu *et al.* 2002). MIH-B shares some other characteristics with Mee-MIH-B: the precursor has a shorter signal peptide (23 amino acid residues) than the other MIH precursors; the mature peptide consists of 79 amino acid residues; and the recombinant peptide shows low molt-inhibiting activity as described below. Therefore, MIH-B seems to be closely related to Mee-MIH-B in terms of not only

doi:10.5047/absm.2013.00602.0049 © 2013 TERRAPUB, Tokyo. All rights reserved.

molecular evolution but also biological function.

In order to confirm the existence of MIH-B as a peptide molecule in live prawns, we attempted to purify the peptide separately from thoracic ganglia and sinus glands. The extract of thoracic ganglia, however, included a great many proteins and peptides, making it impossible to purify MIH-B. On the other hand, MIH-B could be purified from the sinus glands by two steps of reversed-phase HPLC (**Fig. 21**). In MALDI-TOF mass spectral analysis, the purified peptide gave a protonated molecular ion peak at *m/z* 9399.0, which is coincident with the calculated mass number of MIH-B (9401.7 for $(M+H)^+$). Amino acid sequence analysis of this peptide yielded the N-terminal sequence, NILYSSXRGV-, which was identical to the putative N-terminal sequence of MIH-B. The yield of this peptide was 0.5 μg from 510 sinus glands.

In order to obtain a large quantity of MIH-B, recombinant MIH-B (rMIH-B) was expressed using an *E. coli* expression system essentially according to the methods that were used for rMIH. As in the case of rMIH, rMIH-B was expressed in the form of inclusion bodies, and it was, therefore, likely that a refolding reaction was necessary in order to obtain the peptide in its native conformation. Firstly, we attempted to conduct a refolding reaction for rMIH-B in the same redox buffer solution as was used in the refolding reaction for producing rMIH in its native conformation, but the entire product became insoluble. Next, we added acetonitrile to the reaction buffer to a final concentration of 10% in order to increase the solubility of rMIH-B. The reaction then yielded rMIH-B as a single peak on RP-HPLC. Five amino acid residues, ANILY-, could be determined by N-terminal amino acid sequence analysis of the purified peptide. This sequence was identical to that of the native peptide except for the first Ala residue, which arose from the nucleotide sequence of the expression vector. In the MALDI-TOF mass spectrum of the purified rMIH-B, a protonated molecular ion peak was observed at *m/z* 9471.5, which coincided well with the calculated value of 9472.7 for $(M+H)^+$. The yield of the refolded rMIH-B was about 2 mg from 1 liter of culture.

In order to examine the conformation of the rMIH-B, the arrangement of disulfide bonds in rMIH-B was analyzed. The recombinant MIH-B could be successively digested with trypsin and chymotrypsin, and the digests were separated by reversed-phase HPLC. Each fragment peptide was then analyzed by TOF-MS and amino acid sequence analyses. The results showed that rMIH-B had three disulfide bonds connected between Cys^7 and Cys^{44}, Cys^{24} and Cys^{40}, and Cys^{27} and Cys^{53}. This arrangement was identical with that of other CHH-family peptides reported previously (Kegel *et al.* 1989; Huberman *et al.* 1993; Martin *et al.* 1993; Yasuda *et al.* 1994; Gasparini *et al.* 1994; Aguilar *et al.* 1995, 1996; Nagasawa *et al.* 1999; Kawakami *et al.* 2000). The CD spectrum of rMIH-B showed a pattern similar to that of other CHH-family peptides reported previously (Huberman *et al.* 1989; Gasparini *et al.* 1994), which was typical for α-helix-rich proteins. All these results indicated that rMIH-B possessed the native conformation.

The dose-response relationship of rMIH-B in terms of molt-inhibiting activity was examined. rMIH-B weakly inhibited ecdysteroid synthesis by the Y-organ *in vitro* at a concentration of 2 nM (**Fig. 12**). The inhibition was enhanced with increasing peptide concentrations, and reached a maximum at a concentration of 100 nM (**Fig. 12**). These results indicated that rMIH-B was less active than rMIH by approximately one order of magnitude.

Next, we examined the hyperglycemic activity of rMIH-B. However, no elevation of hemolymph glucose level was observed with the injection of 10 or 100 pmol of rMIH-B, indicating that rMIH-B possessed no hyperglycemic activity.

As described above, the residues, Ile^{16}, Val^{20}, Val^{23}, Phe^{45}, Phe^{50}, Leu^{54}, Phe^{66}, Ile^{70} and Leu^{73}, in MIH form the hydrophobic core in the center of the molecule, and they are completely conserved in MIH-B. In addition, the surface residues around α1 helix (Asn^{13} and Arg^{14}) and the C-terminal part (Trp^{69}, Ser^{71} and Ile^{72}), which may contribute to direct binding to the MIH receptor, are also conserved. Thus, MIH-B seemed to share MIH-like molecular characteristics with MIH. The arrangement of disulfide bonds of rMIH-B was identical to that of other CHH-family peptides reported previously, and rMIH-B showed a CD spectrum similar to other CHH-family peptides, suggesting that MIH-B has a conformation similar to that of other CHH-family peptides. However, rMIH-B showed lower activity than MIH by approximately one order of magnitude. It is likely that the low molt-inhibiting activity of rMIH-B was due not to unnatural conformation, but to slight differences in the local structure of the receptor recognition site of MIH-B.

It is generally presumed that MIH exists in the eyestalks, because bilateral eyestalk ablation causes shortening of the molt interval (Zeleny 1905). Levels of *M. japonicus* MIH-B peptide in the eyestalk were very low (about 1 ng per sinus gland), and were about 40-fold lower than that of MIH. The lower activity and content of MIH-B suggest a much lower contribution to Y-organ regulation compared to MIH, and it might not act as an intrinsic MIH. Since rMIH-B showed no hyperglycemic activity *in vivo* and no vitellogenesis-inhibiting activity *in vitro* (Tsutsui *et al.* 2005a), the physiological function(s) of MIH-B is still unclear.

In an expressed sequence tag experiment using a cDNA library from *M. japonicus* eyestalk, it was demonstrated that another MIH-like gene designated "putative" MIH-C was expressed in the eyestalk (Yamano and Unuma 2006). The deduced amino acid sequence

doi:10.5047/absm.2013.00602.0049 © 2013 TERRAPUB, Tokyo. All rights reserved.

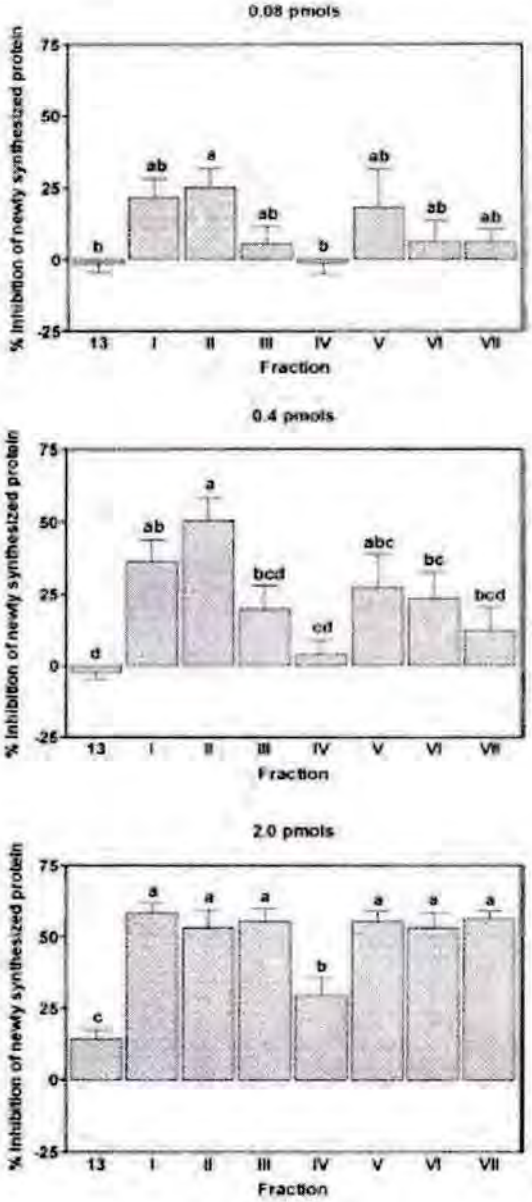

Fig. 22. Influence of *Marsupenaeus japonicus* CHH-family peptides (Fractions I–VII) and a non-CHH-family peptide (Fraction 13) on *Penaeus semisulcatus* ovarian protein synthesis. The values represent the percentage of inhibition in fragments removed from six different ovaries (means ± SE; $n = 6$). Statistical analysis of the results indicates a significant difference ($P < 0.05$) in the highest concentration (2 pmol/mL) between the inhibition values of Fraction 13 and Fraction IV and the other CHH-family peptides. Means with the same letter are not significantly different ($P > 0.05$) by analysis of the variance. Reprinted from *Gen. Comp. Endocrinol.*, **110**, Khayat *et al.*, Hyperglycaemic hormones inhibit protein and mRNA synthesis in *in vitro*-incubated ovarian fragments of the marine shrimp *Penaeus semisulcatus*, 307–318, © 1998, with permission from Elsevier.

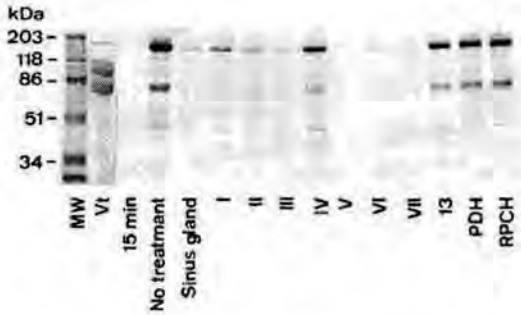

Fig. 23. Analysis of the effect of *Marsupenaeus japonicus* crude sinus gland extract (0.1 sinus gland equivalent), CHH-family peptides (Fractions I–VII) and non-CHH-family peptides (Fraction 13, PDH, and RPCH) at the highest concentration (2 pmol/mL) on *Penaeus semisulcatus* ovarian protein synthesis. Labeled proteins (30 μg) from ovarian fragment incubated *in vitro* with different peptide were separated by SDS-PAGE (10% acrylamide). Reprinted from *Gen. Comp. Endocrinol.*, **110**, Khayat *et al.*, Hyperglycaemic hormones inhibit protein and mRNA synthesis in *in vitro*-incubated ovarian fragments of the marine shrimp *Penaeus semisulcatus*, 307–318, © 1998, with permission from Elsevier.

of MIH-C shared 73% and 84% identities with those of MIH and MIH-B, respectively, and it was structurally more related to MIH-B than to MIH. The function of putative MIH-C peptide has not yet been characterized. In the *M. japonicus* genome, it is presumed that more MIH-like genes exist; along these lines, further experiments are required for understanding the molecular and functional diversity of MIHs.

2-3. VIH

2-3A. Bioassay

An *in vivo* bioassay is the most appropriate means of accurately examining VIH action; however, it is difficult to conduct such assays throughout the isolation process, because large quantities of natural hormone and lengthy procedures are required. Therefore, we have established an *in vitro* bioassay for vitellogenesis-inhibiting activity (Khayat *et al.* 1998; Tsutsui *et al.* 2005a), as described below.

In *M. japonicus*, the eight CHH-family peptides, the six CHHs (Pej-SGP-I, II, III, V, VI, VII) belonging to type I and the two MIHs (Pej-SGP-IV and MIH-B) belonging to type II, were identified from the sinus glands (see Subsections 2-1B and 2-2H). Since the two VIHs from *H. americanus* and *A. vulgare* are members of the CHH-family, the eight peptides were considered to be candidates for VIH in *M. japonicus*. Therefore, vitellogenesis-inhibitory activities of the seven of eight CHH-family peptides (Pej-SGP-I to -VII) were exam-

doi:10.5047/absm.2013.00602.0049 © 2013 TERRAPUB, Tokyo. All rights reserved.

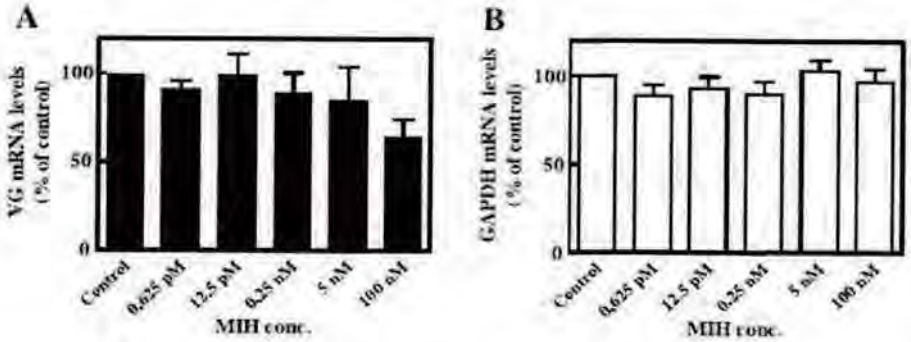

Fig. 24. The effects of MIH (Pej-SGP-IV) on vitellogenin (VG) and glyceraldehyde 3-phosphate dehydrogenase (GAPDH) mRNA levels. Relative VG mRNA levels are expressed as percentage changes relative to control values in (A). The relative GAPDH mRNA levels from the same samples are shown in (B). The results are presented as the means ± SE of five prawns each for 100, 5, and 0.25 nM, and four prawns each for 12.5 and 0.625 pM. Reprinted from *Gen. Comp. Endocrinol.*, **144**, Tsutsui *et al.*, The effects of crustacean hyperglycemic hormone-family peptides on vitellogenin gene expression in the kuruma prawn, *Marsupenaeus japonicus*, 232–239, © 2005, with permission from Elsevier.

ined using an *in vitro* incubation system with ovaries isolated from the green tiger prawn *P. semisulcatus* (Khayat *et al.* 1998). In this system, the levels of *de novo* protein synthesis in the incubated ovarian fragments were used as an index of vitellogenesis. As a result, MIH (Pej-SGP-IV) showed quite weak activity (**Fig. 22**), although this MIH is structurally more related to the known VIHs, both of which are classified into type II, than to CHHs (see Subsection 2-1B). In contrast, the six CHHs belonging to type I inhibited protein synthesis in the incubated ovarian fragments (**Fig. 22**), implying that these six CHHs are involved in the regulation of vitellogenesis. However, their effects were observed on overall protein synthesis in the ovary, and were not specific for vitellogenesis-related proteins (**Fig. 23**).

Vitellogenin (VG) is the dominant vitellogenesis-related protein. In crustaceans, VG is synthesized in the hepatopancreas and/or ovary (Chen *et al.* 1999; Yang *et al.* 2000; Tseng *et al.* 2001; Abdu *et al.* 2002; Avarre *et al.* 2003; Tsang *et al.* 2003; Tsutsui *et al.* 2004; Mak *et al.* 2005; Yang *et al.* 2005; Raviv *et al.* 2006), undergoes processing (Okuno *et al.* 2002a; Avarre *et al.* 2003), and is incorporated into developing oocytes as mature vitellin likely through receptor-mediated endocytosis (Warrier and Subramoniam 2002). In *M. japonicus*, it has been confirmed that both VG mRNA levels in the hepatopancreas and ovary, and VG protein levels in the hemolymph increase significantly during vitellogenesis (Jasmani *et al.* 2000; Tsutsui *et al.* 2000, 2005b). On the basis of this information, an *in vitro* bioassay for vitellogenesis-inhibiting activity using *M. japonicus* ovarian fragments has been established, in which VG mRNA levels in incubated ovarian fragments are used as an index of vitellogenesis (Tsutsui *et al.* 2005a). Using this assay system, it has been shown that *M. japonicus* MIH, type II peptide, had no significant effect on VG mRNA levels in the incubated ovary (**Fig. 24**), whereas Pej-SGP-III, one of the six CHHs belonging to type I, strongly reduced VG mRNA levels, but did not affect glyceraldehyde 3-phosphate dehydrogenase (GAPDH) mRNA levels (**Fig. 25**). Recently, the remaining five CHHs belonging to type I, in addition to Pej-SGP-III, were subjected to the same bioassay, and then all of them showed obvious VIH activities (Tsutsui *et al.* 2013). These results indicate that the six CHHs are probably involved not only in the control of carbohydrate metabolism but also in the regulation of vitellogenesis in *M. japonicus*. Recently, a recombinant *H. americanus* VIH was shown to have weak but significant vitellogenesis-inhibiting activity using the same assay (Ohira *et al.* 2006), as described in the next section. Moreover, VIH activities of CHH-family peptides from the whiteleg shrimp *Litopenaeus vannamei* were successfully examined by the same methods (Tsutsui *et al.* 2007). These suggest that the system is a very useful tool for the investigation of VIH not only in *M. japonicus* but also in other decapod crustaceans.

2-3B. Structure-activity relationship

H. americanus VIH was originally characterized as a type II peptide having a free C-terminus, based on the results of amino acid sequencing and mass spectrometry (Soyez *et al.* 1991). However, cDNA cloning revealed that the VIH precursor had an amidating signal sequence at the C-terminal end (De Kleijn *et al.* 1994b), and therefore it was later determined that mature *H. americanus* VIH possesses a C-terminal amide moiety (Soyez 1997). Another VIH

doi:10.5047/absm.2013.00602.0049 © 2013 TERRAPUB, Tokyo. All rights reserved.

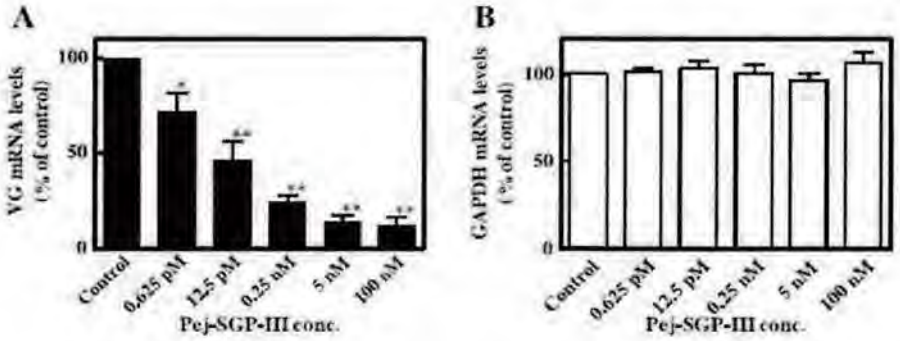

Fig. 25. The effects of Pej-SGP-III on vitellogenin (VG) and glyceraldehyde 3-phosphate dehydrogenase (GAPDH) mRNA levels. Relative VG mRNA levels are expressed as percentage changes relative to control values (means ± SE; $n = 5$). (A) Relative VG mRNA levels; (B) relative GAPDH mRNA levels from the same samples. Data were examined for significance: $*P < 0.05$; $**P < 0.01$. Reprinted from *Gen. Comp. Endocrinol.*, **144**, Tsutsui *et al.*, The effects of crustacean hyperglycemic hormone-family peptides on vitellogenin gene expression in the kuruma prawn, *Marsupenaeus japonicus*, 232–239, © 2005, with permission from Elsevier.

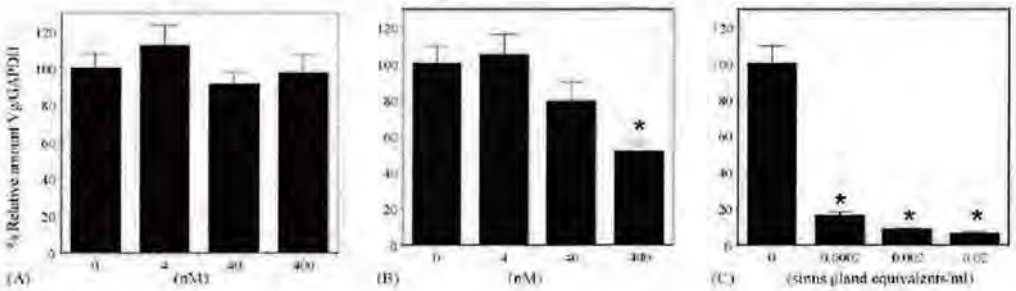

Fig. 26. The effects of rHoa-VIH-OH (A), rHoa-VIH-amide (B), and sinus gland extracts (C) on vitellogenin (VG) mRNA levels in the ovary of *Marsupenaeus japonicus*. Relative VG mRNA levels (VG/glyceraldehyde 3-phosphate dehydrogenase (GAPDH) mRNA) were expressed as a percentage change (means ± SE; $n = 5$) relative to each non-treatment group (control value = 100). Asterisks indicate values significantly different from each non-treatment group, $P < 0.05$ (*). Reprinted from *Peptides*, **27**, Ohira *et al.*, Production and characterization of recombinant vitellogenesis-inhibiting hormone from the American lobster *Homarus americanus*, 1251–1258, © 2006, with permission from Elsevier.

from *A. vulgare*, which also belongs to the type II group, has a free C-terminus in contrast to the case of *H. americanus* VIH (Gréve *et al.* 1999). In this way, whether the C-terminal amidation in VIH is necessary to confer biological activity remains a point of clarification.

In order to elucidate the above point, we produced two types of recombinant *H. americanus* VIHs (rHoa-VIHs), rHoa-VIH-amide and rHoa-VIH-OH, and assessed their vitellogenesis-inhibiting activities using a *M. japonicus* ovarian fragment incubation system (Ohira *et al.* 2006). The rHoa-VIH-amide significantly reduced vitellogenin mRNA levels in the ovary, while rHoa-VIH-OH had no effect in this assay system (**Fig. 26**). The arrangements of the three disulfide bonds in rHoa-VIH-Gly, a precursor of rHoa-VIH-amide, and rHoa-VIH-OH were identical to that of other CHH-family peptides determined thus far (Kegel *et al.* 1989; Huberman *et al.* 1993; Martin *et al.* 1993; Yasuda *et al.* 1994; Aguilar *et al.* 1995, 1996; Nagasawa *et al.* 1999; Kawakami *et al.* 2000; Katayama *et al.* 2001), and therefore, it was likely that this arrangement of disulfide bonds is also the same as that in the native *H. americanus* VIH. These results indicated that the difference in conformation between rHoa-VIH-OH and rHoa-VIH-amide is caused not by the variation of disulfide bond arrangement, but by the presence or absence of the C-terminal amide. In *M. japonicus*, the C-terminal amide moiety of CHH was important for the folding of the molecule to its natural conformation and was consequently necessary for conferring hyperglycemic activity (see Subsection 2-1F). Therefore, the C-terminal amidation of *H. americanus* VIH may also have a role in maintaining its conformation.

doi:10.5047/absm.2013.00602.0049 © 2013 TERRAPUB, Tokyo. All rights reserved.

rHoa-VIH-amide showed definite biological activity in the *in vitro* bioassay using *M. japonicus* ovary, although its efficacy was much lower than that of sinus gland extracts from *M. japonicus* (**Fig. 26**). As mentioned above, Pej-SGP-III, one of the six CHHs in *M. japonicus* belonging to the type I group with a C-terminal amide, reduced vitellogenin mRNA levels to 15% of that of the non-treatment control at only 5 nM using the same assay system (**Fig. 25**). On the other hand, Pej-SGP-IV, MIH in *M. japonicus* belonging to type II with a free C-terminus, was not effective even at 100 nM (**Fig. 24**). In another case, two C-terminally shortened CHHs with a free C-terminus from *J. lalandii*, both of which are type I peptides, showed much weaker VIH activities than those of the two CHHs having a C-terminal amide using the *P. semisulcatus* ovarian incubation system (Marco *et al.* 2002). These results suggest that the molecular characteristics required for vitellogenesis-inhibiting activity in penaeid shrimp species reside in the type I peptide with an amidated C-terminus. This postulation seems to be consistent with our present results, because rHoa-VIH-OH belonging to type II had no activity and even rHoa-VIH-amide showed very low vitellogenesis-inhibiting activity. The reason for the low activity of rHoa-VIH-amide might be due to the use of a heterologous bioassay or the presence of another VIH that is more potent. As the biological activity of native *H. americanus* VIH has also been characterized by *in vivo* studies in a different shrimp species, *Palaemonetes varians* (Soyez *et al.* 1987), it is necessary to establish a bioassay system using *H. americanus* for further examination of rHoa-VIH-amide activity.

3. Eyestalk peptide hormones II: Chromatophorotropic peptides

In 1972, Fernlund and Josefsson reported the isolation and complete structure of crustacean red pigment concentrating hormone (RPCH) from the pink shrimp *P. borealis* (Fernlund and Josefsson 1972). This shrimp RPCH was an octapeptide (pELNFSPGWamide) and showed activity of chromatophoral pigment concentration and dark-adaptation eye pigment migration. Thereafter, the primary structures of RPCH from several crustacean species were determined, revealing that all structures were identical (Gaus *et al.* 1990; Keller 1992), suggesting that only one RPCH molecule exists in crustaceans.

In 1976, crustacean pigment dispersing hormone (PDH) was purified from the sinus glands of *P. borealis* and its primary structure was determined (Fernlund 1976). This octadecapeptide with an amidated C-terminus had an effect on the light-adapting movement of pigment in the compound eye. Later, this molecule was also found to cause pigment dispersion in epidermal chromatophores and therefore has been referred

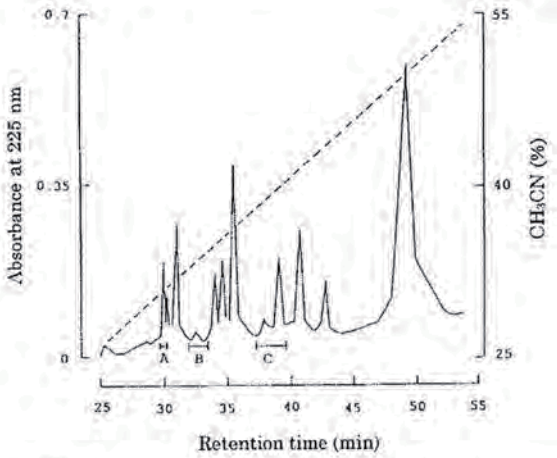

Fig. 27. Reversed-phase HPLC elution profile of extracts from 300 sinus glands of the kuruma prawn *Marsupenaeus japonicus*. Column: Asahi-Pak ODP-50 (4.6 × 150 mm). Solvent: linear gradient of 0–65% acetonitrile in 0.05% TFA for 65 min. Flow rate: 1 mL/min. Detection: absorbance at 225 nm. Temperature: 40°C. The concentration of acetonitrile is indicated by the dashed line. Fraction A showed pigment concentrating activity. Fractions B and C showed pigment dispersing activity. Reprinted from *Gen. Comp. Endocrinol.*, **114**, Yang *et al.*, Characterization of chromatophorotropic neuropeptides from the kuruma prawn *Penaeus japonicus*, 415–424, © 1999, with permission from Elsevier.

to as α-PDH (Rao and Riehm 1993). Thereafter, PDHs from several crustacean species were isolated and sequenced. Interestingly, all of them were found to differ from α-PDH of *P. borealis* at more than 6 positions out of 18 amino acid residues and were thus designated as β-PDH (Rao and Riehm 1993). The most significant difference between α- and β-PDHs is at position 3, where Gly is found in α-PDH and Glu in β-PDHs, causing β-PDH to be more potent than α-PDH. Up until now, α-PDH has only been found in species of the *Pandalus* genus.

In order to obtain more information on the structure-activity relationship of chromatophorotropic peptides, we characterized three chromatophore-regulating peptides of the kuruma prawn *M. japonicus* (Yang *et al.* 1999), as described below.

3-1. RPCH

3-1A. Purification and structure determination

Peptides were extracted from the sinus glands and fractionated by reversed-phase HPLC. RPCH activity was observed at fraction A (**Fig. 27**). Fraction A was then applied to a second reversed-phase HPLC using a different column, and the peptide showing RPCH activity could be purified (Pej-RPCH). As expected, the N-terminus was confirmed to be blocked based on N-

doi:10.5047/absm.2013.00602.0049 © 2013 TERRAPUB, Tokyo. All rights reserved.

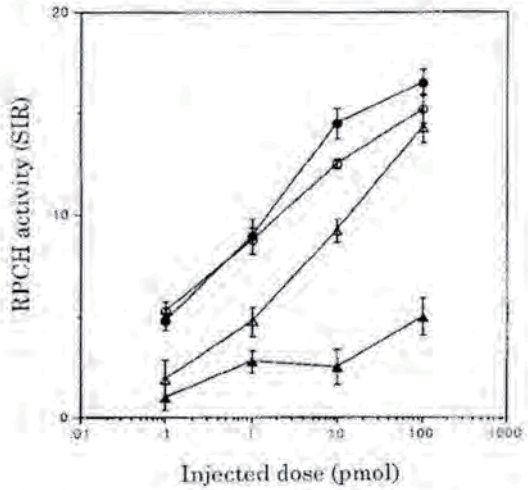

Fig. 28. Dose-response relationship of Pej-RPCH to four types of chromatophores. ○, Erythophores; ●, xanthophores; △, melanophores; ▲, leukophores. The activities are expressed as standard integrated response (SIR), and are presented as the means ± SE. Each point is derived from responses elicited by five prawns. Reprinted from *Gen. Comp. Endocrinol.*, **114**, Yang *et al.*, Characterization of chromatophorotropic neuropeptides from the kuruma prawn *Penaeus japonicus*, 415–424, © 1999, with permission from Elsevier.

Fig. 29. Summary of sequence analyses of Pej-PDH-I and Pej-PDH-II. (- - -), residues identified by amino-terminal sequence analysis. Fragments (K-I-1, K-I-2, K-II-1, and K-II-2) were generated by lysyl endopeptidase digestion of Pej-PDH-I and -II, respectively. Reprinted from *Gen. Comp. Endocrinol.*, **114**, Yang *et al.*, Characterization of chromatophorotropic neuropeptides from the kuruma prawn *Penaeus japonicus*, 415–424, © 1999, with permission from Elsevier.

terminal amino acid sequence analysis. Digestion of Pej-RPCH with Pfu pyroglutamate aminopeptidase afforded a corresponding de-blocked peptide. Amino acid sequence analysis of the de-blocked peptide unambiguously revealed the sequence of residues 2–8, LNFSPGW. To determine whether the C-terminal residue was amidated, the intact Pej-RPCH was subjected to high resolution FAB mass spectral analysis. A protonated molecular ion peak was observed at *m/z* 930.44, which coincided well with the calculated value of the amidated peptide (930.44 for $(M+H)^+$). Thus, the amino acid sequence of Pej-RPCH was determined as pELNFSPGW-NH_2.

Pej-RPCH was identical with RPCH previously determined in several crustacean species. This is in contrast to the insect AKHs, other members of the AKH/RPCH family, in which both amino acid sequences and peptide lengths vary among species. This may be due to a strict ligand-receptor interaction in the case of RPCH, which does not allow any changes in residues and peptide lengths.

3-1B. Biological activity

To examine RPCH activity, the kuruma prawns whose eyestalks were ablated one day prior to the experiment were used for an *in vivo* assay, as all types of the chromatophores were highly dispersed at this time. After the injection of peptide, the extent of concentration or dispersion was estimated using the index of Hogben and Slome (1931); maximal pigment concentration was recorded as score 1, and maximal dispersion as score 5; scores 2, 3, and 4 represented intermediate states. The observed activity was expressed in terms of Standard Integrated Response (SIR) values, as defined previously (Fingerman *et al.* 1967).

The dose-response relationships of Pej-RPCH to the four types of chromatophores (erythrophores, xanthophores, leucophores and melanophores) were shown in **Fig. 28**. The sensitivities of the four types of chromatophores to Pej-RPCH were found to be considerably different. The most sensitive response was observed in erythrophores and xanthophores, and the least sensitive response was seen in leucophores. Melanophores showed a medium-level response.

3-2. PDH

3-2A. Purification and structure determination

Pigment dispersing activity was found in fractions B and C (**Fig. 27**). These fractions were further purified separately on reversed-phase HPLC, and consequently two peptides, Pej-PDH-I and -II, were obtained from fractions B and C, respectively. Eighteen residues each were identified by the N-terminal amino acid sequence analyses of intact Pej-PDH-I and -II (**Fig. 29**). To confirm the amino acid sequences and to determine the C-terminal residues, intact Pej-PDH-I and -II were separately digested with lysyl endopeptidase and the digests were separated by reversed-phase HPLC. Amino acid sequences of the fragment peptides, K-I-1 and -2, and K-II-1 and -2, were confirmed on an automated protein sequencer (**Fig. 29**). High-resolution FAB mass spectra of both C-terminal fragments (K-I-2 and K-II-2) were analyzed to determine their C-terminal structures. Protonated molecular ion peaks for K-I-2 and K-II-2 were observed at *m/z* 535.25 and *m/z*

doi:10.5047/absm.2013.00602.0049 © 2013 TERRAPUB, Tokyo. All rights reserved.

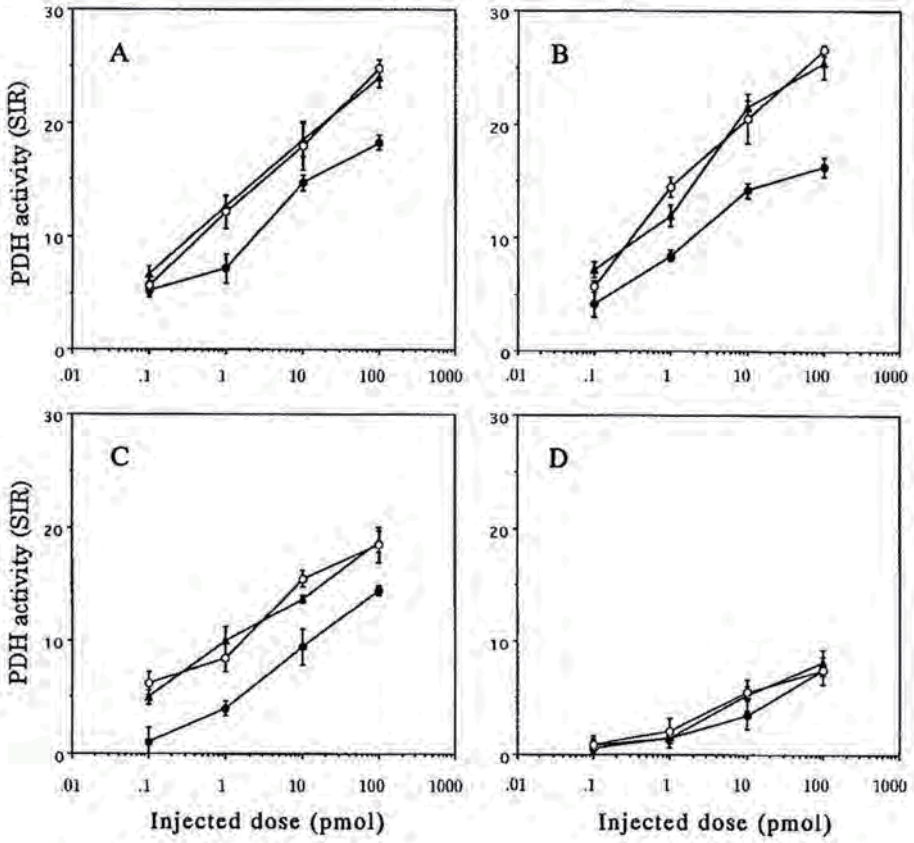

Fig. 30. Dose-response relationships of Pej-PDH-I and -II to four types of chromatophores. (A) Erythophores; (B) xanthophores; (C) melanophores; (D) leukophores. Activities are expressed as standard integrated response (SIR), elicited by Pej-PDH-I (●), Pej-PDH-II (▲), and synthetic [Ile[16]]-Pej-PDH-I (○). The results are presented as the means ± SE. Each point is derived from responses elicited by five prawns. Reprinted from *Gen. Comp. Endocrinol.*, **114**, Yang *et al.*, Characterization of chromatophorotropic neuropeptides from the kuruma prawn *Penaeus japonicus*, 415–424, © 1999, with permission from Elsevier.

595.30, respectively, and these values coincided well with the calculated values for the amidation forms of K-I-2 and K-II-2 (535.25 and 595.28, respectively), establishing the amidated C-terminus of both K-I-2 and K-II-2. Thus, the complete amino acid sequences of Pej-PDH-I and -II were determined (**Fig. 29**).

The two PDH showed considerable sequence similarity to other PDHs characterized from several crustacean species previously. Pej-PDH-I was most closely related to the PDHs of *Penaeus aztecus* (Phillips *et al.* 1988) and *Pandalus jordani* (Rao *et al.* 1989) with one residue substitution, while Pej-PDH-II was most similar to the PDHs of *C. sapidus* (Klein *et al.* 1994) and *L. vannamei* (PDH-II) (Desmoucelles-Carette *et al.* 1996) with replacement of two residues. In Pej-PDH-II, this was the first occasion in which Phe and Ile were found at positions 14 and 16 of a crustacean PDH; up until now, only Val or Leu and Asn or Thr had been found at these positions in all of the known PDHs.

3-2B. Biological activity

Prawns whose eyestalks were ablated seven days previously were injected with peptide samples to test PDH activity, as all types of the chromatophores were most concentrated. The dose-response relationships of the two PDHs to the four types of chromatophores are shown in **Fig. 30**. Pej-PDH-II was 5-, 7-, and 10-fold more potent than Pej-PDH-I for erythrophores, xanthophores, and melanophores, respectively, on the basis of the quantity of peptides required to elicit an SIR value of 10. Like RPCH, the sensitivities of four types of chromatophores to Pej-PDH-I and -II were found to differ, and the order of sensitivity was the same as that of Pej-RPCH: erythrophores = xanthophores > melanophores > leucophores.

Pej-PDH-II was more potent than Pej-PDH-I in all types of chromatophores except for leucophores. The reason for the differences in activity between the two PDHs was thought to be due to one or more differ-

doi:10.5047/absm.2013.00602.0049 © 2013 TERRAPUB, Tokyo. All rights reserved.

Fig. 31. Nucleotide and deduced amino acid sequences of the cDNAs for Pej-PDH-I (A) and -II (B) precursors in the kuruma prawn *Marsupenaeus japonicus*. Amino acid numbering starts at the N-terminal residue of each propeptide of Pej-PDH-I and -II, and the putative signal peptide is indicated by negative numbers. The shaded boxes indicate the putative dibasic cleavage site. The open boxes indicate the putative amidation signal. Each polyadenylation signal sequence is underlined. The nucleotide sequences of the cDNAs for Pej-PDH-I and -II have been deposited in the DDBJ/EMBL/GenBank databases (accession Nos. AB073367 and AB073368, respectively). With kind permission from Springer Science + Business Media: <*Mar. Biotechnol.*, Molecular cloning of cDNAs encoding two pigment-dispersing hormones and two corresponding genes from the kuruma prawn (*Penaeus japonicus*), **4**, 2002, 463–470, Ohira *et al.*, Fig. 2>.

ences in amino acid residues at position 11, 14, or 16. Previous studies on the structure-activity relationship of PDH showed that PDHs with Ile[11] and Leu[11] were equally potent (Rao and Riehm 1989). Moreover, the difference of residue at position 14, Val in Pej-PDH-I and Phe in Pej-PDH-II, was not thought to be significant enough to cause differences in activity, because these two residues have similar hydrophobic properties. We thus considered that the difference at position 16, Thr in Pej-PDH-I and Ile in Pej-PDH-II, had the greatest potential to influence activity and therefore decided to synthesize [Ile[16]]-Pej-PDH-I. As expected, this synthetic peptide showed PDH activity comparable to that of Pej-PDH-II (**Fig. 30**), even though [Ile[16]]-Pej-PDH-I had different residues at positions 11 and 14 from Pej-PDH-II. Until now, only Asn and Thr, have been found at position 16, and replacement of Asn by Thr at this position did not cause considerable change in activity (Rao and Riehm 1989). Thus, Ile[16] in Pej-PDH-II provided new information regarding the structure-activity relationship of PDH. Similar results have been reported by *P. jordani* (Rao and Riehm 1993), where α-PDH substituted by Ala at position 16 was 2-fold more potent than α-PDH with Thr, suggesting that hydrophobic residues at this position increase the activity.

3-2C. Cloning of cDNAs and corresponding genes

Until now, cDNAs encoding PDH/PDF family peptide precursors have been cloned from 4 crustacean species: the shore crab *C. maenas* (Klein *et al.* 1992), the crayfish *O. limosus* (De Kleijn *et al.* 1993), the blue crab *C. sapidus* (Klein *et al.* 1994) and the whiteleg shrimp *L. vannamei* (Desmoucelles-Carette *et al.* 1996), and from 2 insect species: the lubber grasshopper *Romalea microptera* (Davis *et al.* GenBank accession No. U42472) and the fruit fly *Drosophila melanogaster* (Park and Hall 1998). A common structure of the PDH/PDF family peptide precursors consisting of a signal peptide, a PDH/PDF precursor-related peptide (PPRP) and a PDH/PDF was demonstrated by sequence analyses of the cDNAs.

A genomic DNA for the fruit fly *D. melanogaster* PDF has been reported (Park and Hall 1998). This PDF gene has no intron and is present as a single copy per haploid genome. Until now, this has been the only instance in which gene structure of a PDH/PDF family peptide has been elucidated. Therefore, we attempted to isolate cDNAs encoding the two PDHs of *M. japonicus* and two corresponding genes (Ohira *et al.* 2002).

Two cDNAs encoding Pej-PDH-I and -II were amplified by a combination of 5′- and 3′-RACE (**Fig. 31**). The amino acid sequences of the two PDH precursors deduced from the nucleotide sequences of the cDNAs revealed that they possess a structure common to the PDH/PDF family peptide precursors. The two PDH precursors consisted of a signal peptide, a PPRP, a dibasic cleavage site, a PDH and an amidation signal. Amino acid sequences of mature peptides were highly conserved among all PDHs and PDFs, whereas PPRP exhibits lower sequence similarity among crustacean species, and sequence homology is not observed between crustaceans and insects. This observation suggests that PPRP may not have a biological function. Similar structural divergence in peptides where regions other than that corresponding to the mature peptide is observed in those of the AKH/RPCH family (Bogerd *et al.* 1995) and in those of the CHH-family (see Sub-

doi:10.5047/absm.2013.00602.0049 © 2013 TERRAPUB, Tokyo. All rights reserved.

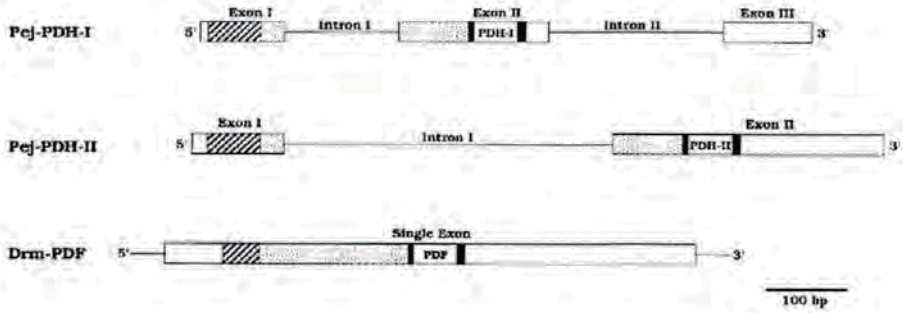

Fig. 32. Schematic representation of the organization of genes for Pej-PDH-I, -II, and *Drosophila melanogaster* PDF (Drm-PDF). Open boxes indicate the 5′- and 3′-untranslated regions. Hatched and shaded boxes indicate the signal peptide and the PDH/PDF precursor-related peptide (PPRP), respectively. Black boxes located at both sides of the mature PDH/PDF indicate the dibasic cleavage site (the N-terminal side) and the amidation signal (the C-terminal side), respectively. The nucleotide sequences of the genes for Pej-PDH-I and -II have been deposited in the DDBJ/EMBL/GenBank databases (accession Nos. AB073369 and AB073370, respectively). With kind permission from Springer Science + Business Media: <*Mar. Biotechnol.*, Molecular cloning of cDNAs encoding two pigment-dispersing hormones and two corresponding genes from the kuruma prawn (*Penaeus japonicus*), **4**, 2002, 463–470, Ohira *et al.*, Fig. 4>.

section 2-1D).

We also cloned two corresponding genes by PCR using genomic DNA derived from a single prawn as a template (**Fig. 32**). The exon/intron organization of Pej-PDH-I gene differed from that of Pej-PDH-II. The Pej-PDH-I gene consisted of three exons and two introns, while Pej-PDH-II gene consisted of two exons and a single intron. Such organization differed from that of the *D. melanogaster* PDF gene, which lacks an intron (Park and Hall 1998). These differences in exon/intron organization among the genes for the PDH/PDF family peptides are also seen in genes for CHH-family (Udomkit *et al.* 2000; Krungkasem *et al.* 2002) and in that for insulin-related peptides in insects (Kromer-Metzger and Lagueux 1994). However, the above cases seem to be exceptional, as exon/intron organization of genes for the same family peptides are generally conserved. The differences in the structure of genes for PDH/PDF family peptides may reflect their evolutionary pathway. With more information on other crustacean and insect species, it may be possible to estimate the evolutionary pathway of the PDH/PDF gene.

4. AGH

In 1954, it was first discovered by Charniaux-Cotton that the androgenic gland (AG) plays a pivotal role in crustacean sex differentiation (Charniaux-Cotton 1954). In AG-ablated *A. vulgare* males, it was demonstrated that endopodites cease to elongate and a vitellogenin gene is expressed at the same levels as in the normal females (Suzuki *et al.* 1990). On the other hand, when AGs were implanted into *A. vulgare* females, body color changed from brown, a typical color for females, into the grey-black color of the male body, and the gonads were transformed into testes with fully developed seminal vesicles (Suzuki and Yamasaki 1998). These observations strongly indicated that the AGs secrete a sex differentiation factor, AGH. In order to purify AGH, an *in vivo* bioassay system was first established by Katakura *et al.* (1975). When AG extract was injected into young *A. vulgare* females, elongation of endopodites, an external male characteristic, was observed after the ensuing molt. Using this phenomenon as an index of the AGH activity, we attempted to purify AGH as described below.

4-1. Trial for purification of AGH

At the early stage of study for purification of AGH of the terrestrial isopod, *A. vulgare* (**Fig. 33**), the whole reproductive organ was used as starting material, because it was difficult to collect only AGs due to their small size and sticky cell surface. However, since the whole reproductive organ contained various materials other than AGH, the purification could not be easily achieved. On one occasion, we thought that we had successfully isolated AGH, because the active fraction was recovered in a single UV-peak on reversed-phase HPLC after several steps of purification. This fraction was subjected to structural analysis, which showed that the fraction contained at least four peptides with closely related structures (Nagasawa *et al.* 1995). However, the activity of the purified fraction was not very high. Comparison of the specific activity of this fraction with that of later-purified AGH revealed that the activity of the former was much weaker than the latter by three orders of magnitude. Thus, it turned out that the fraction contained AGH at a ratio of only 0.1% and most

doi:10.5047/absm.2013.00602.0049 © 2013 TERRAPUB, Tokyo. All rights reserved.

Fig. 33. The terrestrial isopod *Armadillidium vulgare*.

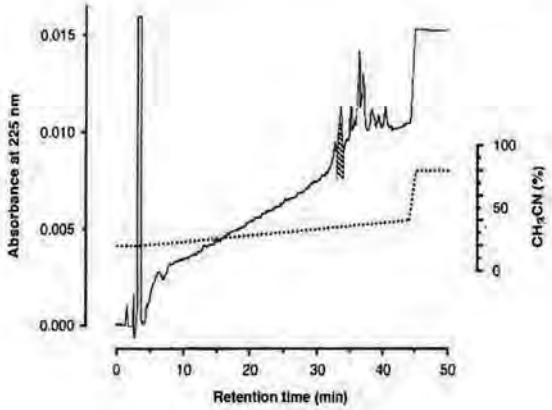

Fig. 34. Elution profile of reversed-phase HPLC at the final third step. Hatched peak material showed AGH activity. Solvent, aqueous acetonitrile containing 0.05% heptafluorobutyric acid (HFBA); column, Asahi-Pak ODP-50 (4.6 × 150 mm); flow, 1.0 mL/min. Reprinted with permission from *Zool. Sci.*, **14**, Okuno *et al.*, Purification and properties of androgenic gland hormone from the terrestrial isopod *Armadillidium vulgare*, 837–842, Fig. 4, © 1997, Zoological Society of Japan.

of the other materials were non-AGH peptides. Since the peptide thus characterized was found to be distributed only in the seminal vesicle using immunohistochemistry and an antiserum raised against a synthetic peptide fragment, we designated it as seminal vesicle-specific peptide (SVSP) (Nagasawa *et al.* 1995). Therefore, we later changed the starting material for purification of AGH from whole reproductive organs to androgenic glands only. Because of this change in strategy, AGH could thereafter be isolated successfully.

4-2. Isolation of AGH

AGH was purified from isolated androgenic glands of male *A. vulgare* by three steps of reversed-phase HPLC (Okuno *et al.* 1997). Only 160 ng of the material was finally obtained from 2,000 animals at about an 11% rate of recovery (**Fig. 34**). The elution of AGH activity by molecular sieve HPLC indicated that the molecular weight of AGH was 11,000–13,000. The purified AGH-active fraction showed masculinizing activity when 38 pg of this preparation was injected into a young female of the same species. Inactivation experiments using a crude preparation of AGH showed that AGH activity was lost by treatment with trypsin or by reductive alkylation. The AGH activity was not affected by heat treatment at 100°C for 3 min. These results indicated that AGH was a heat-stable protein with disulfide bond(s). Since sequence analysis of the final preparation thus obtained yielded two phenylthiohydantoin derivatives of amino acids at each cycle of Edman degradation, we judged that it was still impure. This was later found to be wrong, because it was clarified that AGH was really a heterodimeric peptide. It was necessary to wait for the next opportunity to analyze the N-terminal sequence of another batch of AGH, in which similar results were obtained. Thus, we concluded that AGH is a heterodimer.

At almost the same time, a French research group obtained a similar result using the same species infected by *Wolbachia* (Martin *et al.* 1998), whose AGs became enlarged possibly due to the inhibition of AG activity and possibly AGH secretion, resulting in a decrease of male characteristics in this animal, the so-called "intersex" type (Martin *et al.* 1990). Because these workers were able to obtain a high concentration of AGH in such AGs, they succeeded in the isolation of AGH from a much smaller number of animals than we used. This group postulated an overall heterodimeric structure of an AGH molecule in terms of chain length of each A and B chain, the positions of Cys residues and an *N*-glycosylation site, and the structure of its precursor molecule including the presence of C peptide, but did not reveal any amino acid residues in detail.

4-3. Cloning of a cDNA encoding AGH

Since a pair of amino acid residues with almost equimolar amounts was identified at each cycle by the N-terminal sequence analysis of native AGH, we could not determine amino acid sequences of two peptide chains consisting of AGH. On the other hand, one of the two peptides could be recovered after reductive carboxymethylation, and its N-terminal 10-residue sequence was obtained. Then, by subtraction of each amino acid residue from the doubly-identified residues for the whole molecule, the amino acid sequence of the other peptide chain could be estimated (Okuno *et al.* 1999).

A cDNA fragment encoding AGH was amplified by

doi:10.5047/absm.2013.00602.0049 © 2013 TERRAPUB, Tokyo. All rights reserved.

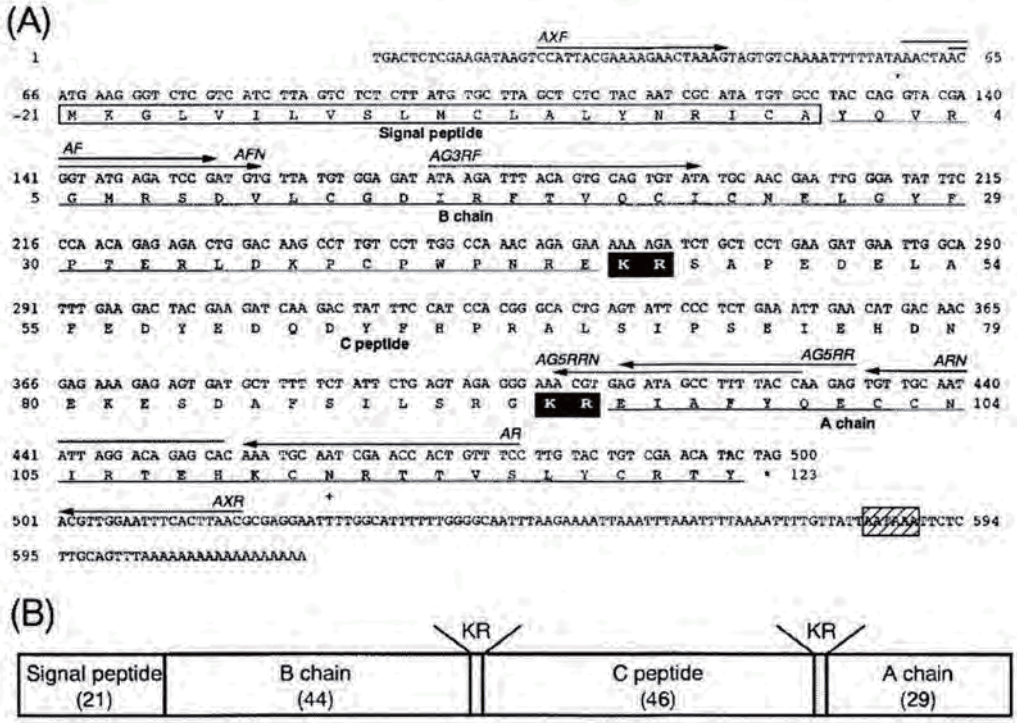

Fig. 35. The nucleotide sequence of a cDNA encoding the *A. vulgare* AGH precursor and its deduced amino acid sequence. (A) Arrows indicate the regions used as the primers for PCR. The stop codon and the putative *N*-glycosylation site are indicated by an asterisk and a symbol (+), respectively. The putative signal peptide is boxed. The A and B chains are underlined. The hatched box indicates the consensus sequence for polyadenylation signal. The filled box indicates the possible dibasic cleavage sites between B chain and C peptide, and between C peptide and A chain. The nucleotide sequence has been deposited in DDBJ, EMBL and GenBank databases under accession No. AB029615. (B) Schematic representation of the organizations of preproAGH. The numbers in parentheses indicate the number of amino acid residues in each domain of AGH. The possible cleavage sites (Lys-Arg) are indicated by KR. Reprinted from *Biochem. Biophys. Res. Commun.*, **264**, Okuno *et al.*, Characterization and cDNA cloning of androgenic gland hormone of the terrestrial isopod *Armadillidium vulgare*, 419–423, © 1999, with permission from Elsevier.

PCR using a set of primers designed based on the amino acid sequence analyzed. By combining the results obtained by 5′- and 3′ RACE, a full length cDNA covering an open reading frame was obtained (**Fig. 35**) (Okuno *et al.* 1999). An open reading frame of 432 bp encoded a preproAGH consisting of a signal peptide (21 residues), B chain (44 residues), C peptide (46 residues), and A chain (29 residues). Two dibasic processing sequences were present between the B chain and the C peptide, and between the C peptide and the A chain. The A chain possessed a putative *N*-linked glycosylation site. It was postulated that through processing including the removal of a signal peptide, disulfide bond formation, the removal of C peptide, and the addition of carbohydrate moiety, the A and B chains might form a heterodimeric glycopeptide of a mature hormone. Disulfide bond formation should proceed the removal of the C peptide. The characteristic organization of preproAGH was similar to that of insulin, although both peptide chain length and amino acid sequence differed.

4-4. Verification of the cDNA as that encoding AGH using anti-AGH antisera

In order to prove that this cloned cDNA actually encodes AGH, recombinant single-chain precursor molecules consisting of B chain, C peptide and A chain were produced using both baculovirus and bacterial expression systems (Okuno *et al.* 2002b). The former system can produce an *N*-glycosylated peptide, while the latter can yield a non-glycosylated peptide. Neither recombinant precursors containing C peptide showed AGH activity as described below. Three kinds of antisera were raised in rabbits against three antigens; a recombinant putative AGH precursor produced by the *E. coli* expression system, a synthetic peptide

doi:10.5047/absm.2013.00602.0049 © 2013 TERRAPUB, Tokyo. All rights reserved.

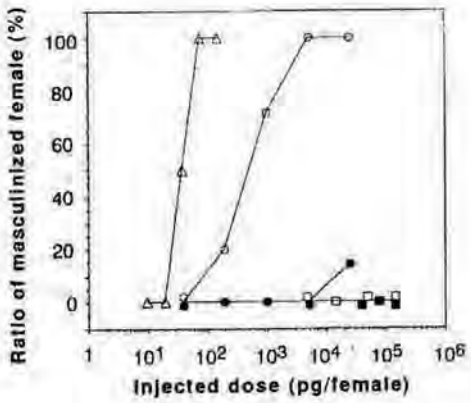

Fig. 36. Dose-response relationship of the recombinant and native AGHs. Triangles show the native AGH. Open and filled circles indicate the recombinant AGH expressed by baculovirus expression system with and without lysyl endopeptidase treatment, respectively. Open and filled squares show the recombinant AGH expressed by *E. coli* expression system with and without lysyl endopeptidase treatment, respectively. Reprinted from *Peptides*, **23**, Okuno *et al.*, Preparation of an active recombinant peptide of crustacean androgenic gland hormone, 567–572, © 2002, with permission from Elsevier.

corresponding to the N-terminal eight residues of the A chain, and a synthetic peptide corresponding to the N-terminal nine residues of the B chain. The first one was used directly for immunization, while the synthetic peptides were used as antigens after conjugation with BSA. After incubation of partially purified preparation of AGH with each of the three antisera, AGH activity decreased significantly in all cases (Okuno *et al.* 2001), strongly indicating that the cDNA encoded AGH, although it constituted indirect evidence.

In order to examine the distribution of AGH peptide, an immunohistochemical study was performed. *A. vulgare* AG showed strong immunoreactivity to all three antisera, while the testis, the seminal vesicle and the vas deferens did not (Hasegawa *et al.* 2002). These results indicated that AGH peptides are specifically localized in AG.

4-5. Preparation of biologically active recombinant AGH

The simplest method for confirming that this heterodimeric glycopeptide is the biologically active AGH is measurement of the biological activity using recombinant peptide. Along these lines, we prepared the recombinant AGHs using both *E. coli* and baculovirus expression systems (Okuno *et al.* 2002b). The recombinant AGHs were expressed as a single-chain precursor protein consisting of B chain, C peptide and A chain, and only the recombinant AGH produced by the baculovirus system possessed a carbohydrate moiety at the *N*-glycosylation site in the A chain. Both recombinant precursor proteins showed no biological activity *in vivo*, indicating that the precursor protein is inactive regardless of the *N*-linked glycan. In order to examine whether the removal of C peptide by proteolytic cleavage is essential for conferring the activity, we tried to remove the C peptide from the precursor proteins with proteases. When treated with lysyl endopeptidase at 37°C for 2 h, peptide bonds at Lys^{45}–Arg^{46} and Lys^{81}–Glu^{82} were cleaved and the peptide was partially removed, although a part of the C peptide, Glu^{82}–Arg^{94}, was still attached to the recombinant proteins. Using these double-chain recombinant proteins, the biological activity was assessed (**Fig. 36**). As expected, the digested recombinant AGH prepared by the baculovirus system showed biological activity at a dose of 0.25 ng/individual, but was less active than the native AGH by about approximately one order of magnitude. This difference may be due to the partly retained C peptide in the recombinant AGH. On the other hand, the recombinant AGH prepared by the *E. coli* system and subsequently digested by the same way showed no activity even at a dose of 440 ng/individual, indicating that the carbohydrate moiety at the A chain is essential for conferring AGH activity.

The arrangement of four disulfide bonds in the recombinant AGH prepared by the baculovirus system was determined by analyzing the structure of protease digests. The results clearly indicated that two intrachain disulfide bridges between Cys^{21}–Cys^{38} and Cys^{103}–Cys^{111} and two interchain disulfide bridges between Cys^{12}–Cys^{102} and Cys^{23}–Cys^{120} were connected. The carbohydrate structure of the recombinant AGH was also estimated to be Man_3-$GlcNAc_2$(Fuc)- by mass spectral analysis. This carbohydrate structure is typically found in glycoproteins produced by insect cells, and was different from that of the native AGH reported previously, which has a larger glycan with a sulfate group at its terminal (Martin *et al.* 1999). The weak activity of the recombinant AGH may be partly due to the difference in carbohydrate structure.

4-6. Structure-activity relationship of AGH

In order to investigate the structure-activity relationship of AGH, we synthesized the hormone by chemical means. First, we attempted to synthesize AGH by an expressed protein ligation strategy (Muir *et al.* 1998), in which 110 residues N-terminal peptide segment is expressed in an *E. coli* expression system, and the C-terminal peptide having a carbohydrate moiety is chemoselectively condensed by a native chemical ligation method (Dawson *et al.* 1994). This scheme is shown in **Fig. 37**. After the condensation reaction, disulfide bonds were formed by *in vitro* refolding reaction in a redox buffer containing reduced/oxidized forms of glutathione. The C peptide portion was cleaved off by treatment with metalloendopeptidase,

doi:10.5047/absm.2013.00602.0049 © 2013 TERRAPUB, Tokyo. All rights reserved.

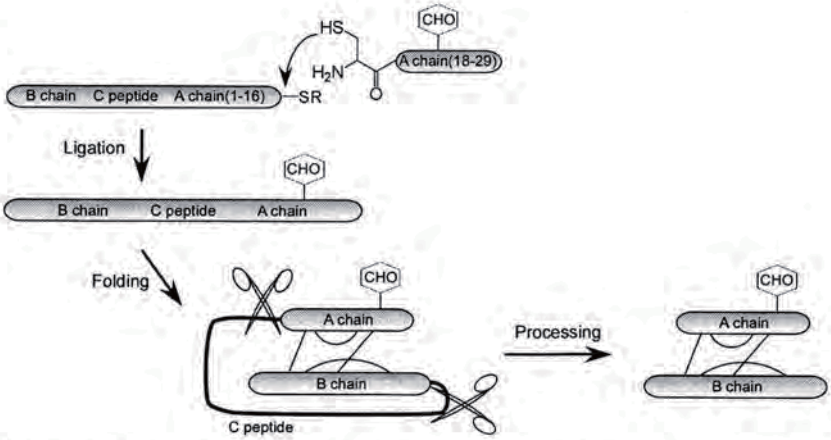

Fig. 37. Scheme for preparing the semi-synthetic AGH by the expressed protein ligation method. Reprinted with permission from *Biochemistry*, **49**, Katayama *et al.*, Correct disulfide pairing is required for the biological activity of crustacean androgenic gland hormone (AGH): Synthetic studies of AGH, 1798–1807, Graphical Abstract, © 2010, American Chemical Society.

yielding the heterodimeric glycopeptide. Unexpectedly, the semi-synthetic AGH showed no biological activity *in vivo* regardless of the carbohydrate structure (Katayama *et al.* 2010). In order to confirm the conformation of the semisynthetic AGH, the disulfide bond arrangement was determined by analyzing protease digests, establishing that four disulfides are connected between Cys^{12}–Cys^{103}, Cys^{21}–Cys^{38}, Cys^{23}–Cys^{120} and Cys^{102}–Cys^{111}. The results clearly indicated that the disulfide bond arrangement in the semisynthetic peptide is different from that in the ecombinant AGH prepared by the baculovirus expression system. These results indicated that the AGH with correct disulfide bonds could not be obtained by an *in vitro* refolding reaction, and that the native conformation is not the thermodynamically most stable form at least *in vitro*.

To confirm that the loss of biological activity resulted from disulfide bond isomerization, total chemical synthesis with selective disulfide bond formation was carried out according to the scheme shown in **Fig. 38** (Katayama *et al.* 2010). The A and B chains were separately synthesized by a 9-fluorenylmethoxycarbonyl (Fmoc)-based solid-phase peptide synthesis strategy. To form disulfide bonds selectively, three protecting groups, trityl, 4-methoxybenzyl and acetamidomethyl, were used for Cys residues, and stepwise deprotection and oxidation reactions were performed. The synthetic AGH carrying the GlcNAc moiety at the *N*-glycosylation site in the A chain showed rather weak activity *in vivo*. On the other hand, the synthetic AGH without a carbohydrate chain showed no biological activity at any dosage levels tested. These results clearly indicated that carbohydrate chain attached to the A chain and the correct disulfide pairing are essential for conferring AGH activity. Weak activity of synthetic AGH may be due in part to that the presence of GlcNAc may not be sufficient for generating complete activity, and a larger glycan moiety may be required for achieving full AGH activity.

4-7. AGH in other isopod crustacean species

Thereafter, we examined the distribution of this AGH molecule among phylogenetically close and remote species by using the anti-AGH antisera as described above. Immunohistochemical studies revealed that AGs of species belonging to Armadillidiidae, Porcellionidae and Scyphacidae families were immunostained using these antisera (Hasegawa *et al.* 2002). On the other hand, no positive signal was observed in AGs of species belonging to Tylidae and Ligiidae. These observations suggested that structural similarity of AGH might exist among some terrestrial isopods, although AGH seemed to harbor a higher degree of species specificity.

In order to clarify the molecular diversity of AGH in relation to the degree of immunostaining and hormonal activity, cDNAs encoding AGH precursors were cloned from two Porcellionidae species, *Porcellio scaber* and *Porcellio dilatatus*, by PCR techniques (Ohira *et al.* 2003b). The deduced amino acid sequences predicted from the nucleotide sequences of cDNA encoding *P. scaber* AGH consisted of a signal peptide (21 amino acid residues), a B chain (44 residues), an Arg–Arg dibasic site, a C peptide (45 residues), a Lys–Arg dibasic site, and an A chain (31 residues) (**Fig. 39**). The predicted structure of the AGH precursor protein of *P. dilatatus* was quite similar to that of *P. scaber*, except for the length of C peptide which consisted of 46 residues in *P. dilatatus*. The deduced amino acid sequences of AGH precursors of

doi:10.5047/absm.2013.00602.0049 © 2013 TERRAPUB, Tokyo. All rights reserved.

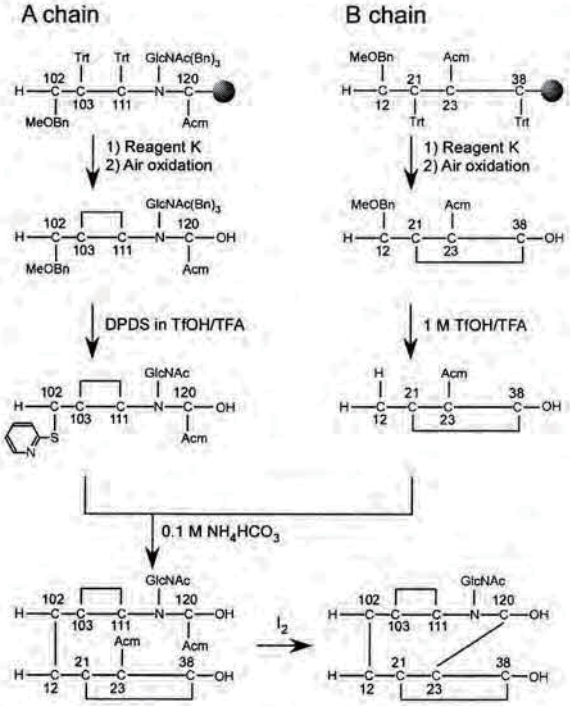

Fig. 38. Synthesis procedure for AGH by selective disulfide formation. Reprinted with permission from *Biochemistry*, **49**, Katayama *et al.*, Correct disulfide pairing is required for the biological activity of crustacean androgenic gland hormone (AGH): Synthetic studies of AGH, 1798–1807, Scheme 3, © 2010, American Chemical Society.

these two species shared high sequence identity with that of *A. vulgare* AGH (65% and 63% identity with those of *P. scaber* and *P. dilatatus*, respectively). The *N*-glycosylation site at the A chain was also conserved among these species. Such structural similarity is highly consistent with the results obtained from immunohistochemical studies (Hasegawa *et al.* 2002). In order to better understand the structural and functional diversity of AGHs in other crustacean species, further experimentation is required.

4-8. AGH of decapod crustacean species

The role of AG has also been studied in decapod crustaceans. In the giant freshwater prawn *Macrobrachium rosenbergii*, the implantation of AGs into young female prawns caused these genetic females to become phenotypic reproductive males (Nagamine *et al.* 1980). In the red-claw crayfish *Cherax quadricarinatus*, the implantation of hypertrophied AGs obtained from bilaterally deeyestalked males into immature female animals induced male-specific morphologies and inhibited female secondary sex characteristics in recipient females (Khalaila *et al.* 2001). These results indicate that the AGs in decapod species also control sexual differentiation. Recently, cDNA libraries were constructed by using suppression subtractive hybridization of the AGs of *C. quadricarinatus* and *M. rosenbergii* (Manor *et al.* 2007; Ventura *et al.* 2009). Expressed sequence tags from these libraries were sequenced and then one each AG-specific gene of *C. quadricarinatus* and *M. rosenbergii* was detected. The gene product of both animals consisted of a signal peptide, a B chain, a C peptide and an A chain. Since the organization of these gene products was the same as that of the vertebrate insulin precursor, they were named insulin-like AG factor (IAG). *C. quadricarinatus* IAG and *M. rosenbergii* IAG possessed six and eight cysteine residues, respectively, in their predicted mature peptides (A and B chains). The positions of the six cysteine residues of *C. quadricarinatus* IAG were the same as six of the eight cysteine residues in *M. rosenbergii* IAG (Manor *et al.* 2007; Ventura *et al.* 2009). Furthermore, the six cysteine residues were well-conserved within the insulin superfamily, including isopod AGHs. Therefore, the two IAG molecules have been thought to be putative AGHs in decapod species. However, *C. quadricarinatus* IAG and *M. rosenbergii* IAG showed low sequence similarities with the three isopod AGHs and shared only a little similarity with each other.

In order to obtain information of amino acid sequences of additional IAG molecules, we attempted to clone cDNAs encoding IAG precursors from three palaemonid species *Macrobrachium lar*, *Palaemon paucidens* and *Palaemon pacificus*, and a penaeid species *Marsupenaeus japonicus* (Banzai *et al.* 2011, 2012). The four IAG precursors consisted of a signal peptide, a B chain, a C peptide and an A chain (**Fig. 40**). This organization is in agreement with those of the known isopod AGH and decapod IAG precursors as mentioned above. *M. lar* IAG, *P. paucidens* IAG and *P. pacificus* IAG showed moderate sequence identities to *M. rosenbergii* IAG (72, 69 and 49%, respectively). *M. japonicus* IAG had considerable sequence similarity only to *P. monodon* IAG (68%), which was recently revealed by another research group and deposited in the GenBank database (accession No. GU208677). These results are consistent with the following phylogenetic relationship. *M. lar*, *P. paucidens*, *P. pacificus* and *M. rosenbergii* are freshwater shrimps of the family Palaemonidae, and *M. japonicus* and *P. monodon* are marine shrimps of the family Penaeidae. In isopods, however, sequence identities of AGH precursors between different families, the Armadilliidae and the Porcellionidae, are clearly higher (over 60% as described above) than those of IAG between different decapod families (around 30%). This may be due to the differences in the molecular evolutionary pathway between IAG and AGH. In order to clarify this point, further studies characterizing amino acid sequences of additional IAGs and AGHs are required.

doi:10.5047/absm.2013.00602.0049 © 2013 TERRAPUB, Tokyo. All rights reserved.

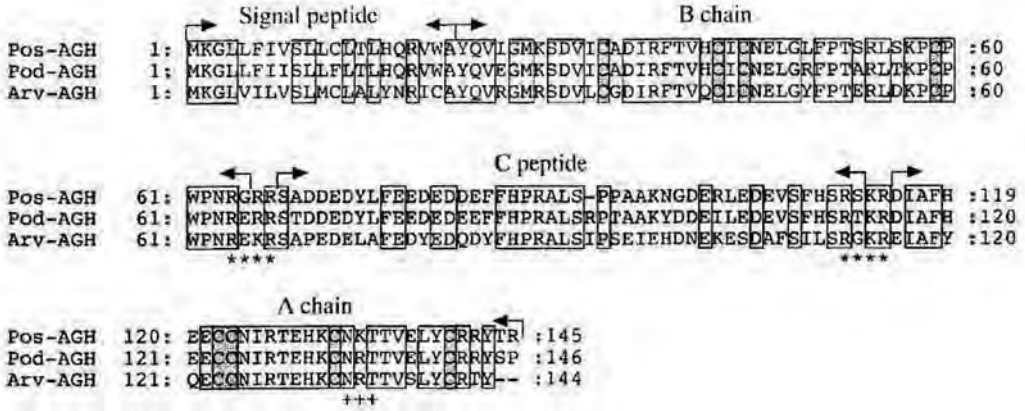

Fig. 39. Amino acid sequence alignment of *Porcellio scaber* AGH (Pos-AGH), *P. dilatatus* AGH (Pod-AGH) and *Armadillidium vulgare* AGH (Arv-AGH) precursors. Open boxes indicate the amino acids conserved among all precursors. Gray boxes indicate the positions of conserved Cys residues. The typical proteolytic cleavage motifs (R-X-K/R-R) and the putative *N*-linked glycosylation motif (N-X-S/T) are indicated by asterisks and symbols (+), respectively. Reprinted with permission from *Zool. Sci.*, **20**, Ohira *et al.*, Molecular cloning and expression analysis of cDNAs encoding androgenic gland hormone precursors from two Porcellionidae species, *Porcellio scaber* and *P. dilatatus*, 75–81, Fig. 3, © 2003, Zoological Society of Japan.

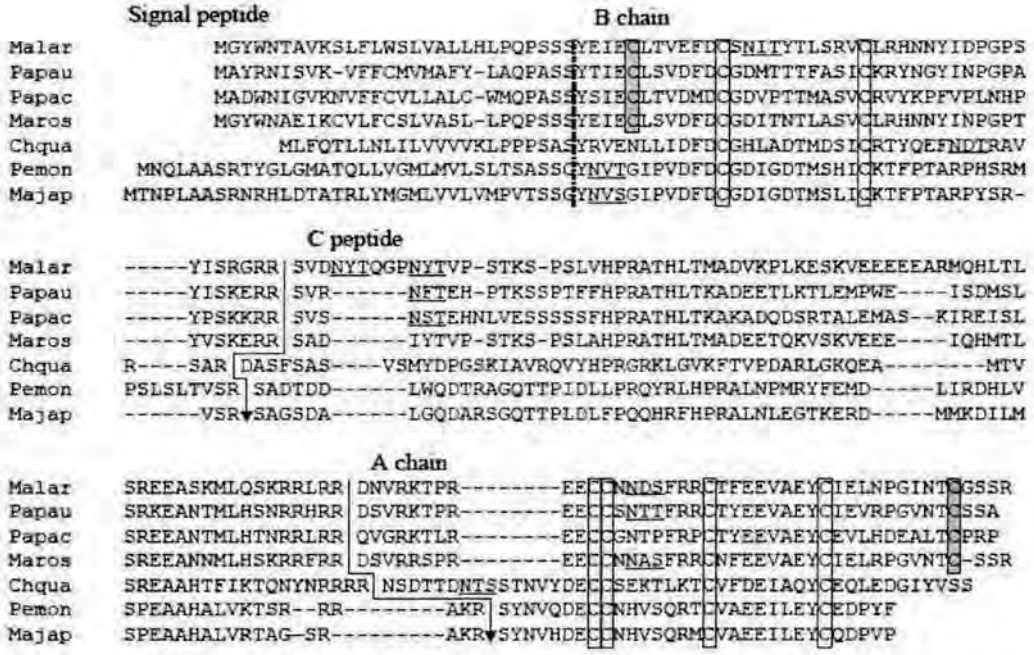

Fig. 40. Amino acid sequence alignment of *Macrobrachium lar* IAG (Malar), *Palaemon paucidens* IAG (Papau), *Palaemon pacificus* IAG (Papac), *Macrobrachium rosenbergii* IAG (Maros), *Cherax quadricarinatus* IAG (Chqua), *Penaeus monodon* IAG (Pemon), and *Marsupenaeus japonicus* IAG (Majap). Open and grey boxes indicate the positions of conserved Cys residues in all species and only in palaemonid species, respectively. The putative cleavage sites predicted by the ProP 1.0 server (http://www.cbs.dtu.dk/services/ProP/) are shown by arrows. The boundary between the signal peptide and the B chain is represented by a vertical dotted-line. Underlines indicate the putative *N*-linked glycosylation motifs (N-X-S/T). Reprinted with permission from *Jpn. Agric. Res. Q.*, **46**, Banzai *et al.*, Molecular cloning and expression analysis of cDNAs encoding insulin-like androgenic gland factor from three palaemonid species, *Macrobrachium lar*, *Palaemon paucidens* and *P. pacificus*, 105–114, Fig. 4, © 2012, Zoological Society of Japan.

doi:10.5047/absm.2013.00602.0049 © 2013 TERRAPUB, Tokyo. All rights reserved.

In isopods, AGH has a single conserved *N*-glycosylation motif (N-X-S/T) in the A chain (Okuno *et al.* 1999; Ohira *et al.* 2003b). On the other hand, the positions and the number of *N*-glycosylation motifs are not conserved among decapod IAGs (**Fig. 40**). For instance, *M. lar* IAG has one *N*-glycosylation motif in the B chain, two in the C peptide, and one in the A chain. On the other hand, *P. pacificus* IAG has only one motif in the C peptide, which indicates a mature molecule comprising the B and A chains does not possess an *N*-linked glycan moiety. Although the *N*-linked glycan in the A chain of *A. vulgare* AGH is indispensable for biological activity (Okuno *et al.* 2002b), *N*-glycosylation of the A chain of decapod IAG is not likely to be essential for conferring function. Further experiments on the purification and the structural determination of native IAG are required to clarify this issue.

IAG has been thought of as a putative AGH in decapod species as described above. In *M. rosenbergii*, silencing of the IAG gene using RNA interference methods, temporally prevented the regeneration of male-specific sexual characteristics, and led to the arrest of spermatogenesis (Ventura *et al.* 2009). This correlates well with the above hypothesis; however, as of yet, there has been no direct evidence for IAG having AGH activity. However, we are now able to easily produce a heterodimeric mature *P. pacificus* IAG with selective disulfide bond formation in its synthetic A and B chains. Because *P. pacificus* IAG is the first example of a non-glycosylated IAG in its mature form, the synthetic *P. pacificus* IAG will be useful for *in vivo* and/or *in vitro* biological studies, which are expected to provide important information for understanding IAG function in decapod crustaceans.

5. Summary and Future Perspective

Shrimp aquaculture is a significant global industry worldwide. In order to achieve further development, more efficient seed production techniques are required. Therefore, it is desirable to gain a better understanding of shrimp reproduction. However, knowledge of vitellogenesis in shrimp is still limited, and it remains difficult to control reproduction under artificial conditions for a large number of commercially important species. Therefore, at present, it is common that fully mature shrimps for commercially important species are captured from the wild and are allowed to spawn in the hatchery. However, recently it is becoming increasingly difficult to obtain sufficient numbers of wild mature shrimps, because of overfishing and/or the presence of serious shrimp viral disease in many key areas. Indeed, the development of disease-resistant strains or strains harboring certain phenotypes is now necessary. For these reasons, we have been working on the isolation of hormones regulating shrimp reproduction.

Eyestalk ablation is known to induce vitellogenesis, which permits us to presume that there exists a VIH in the eyestalks. VIHs were first isolated from the American lobster *H. americanus* (Soyez *et al.* 1991) and then from the terrestrial isopod *A. vulgare* (Gréve *et al.* 1999). Strangely enough, in the early 2,000's, VIH had not yet been isolated from shrimps. CHHs from *M. japonicus* were found to inhibit both transcription and translation in the developing ovary of another shrimp, *P. semisulcatus*, in a non-specific manner, while MIH from *M. japonicus* did not (Khayat *et al.* 1998). On the other hand, it can be presumed that the first function of VIH is vitellogenin (VG) synthesis. Recently, VG cDNAs have been cloned from several crustacean species (reviewed by Wilder *et al.*, 2010). It might be possible to develop a VIH bioassay by looking at the reduction of VG mRNA expression levels in the producing organ, e.g., the ovary or hepatopancreas in response to various factors. Along these lines, we examined the *in vitro* VIH activity of *M. japonicus* CHH-family peptides based on quantitative PCR experiments on VG gene expression. As a result, we found that CHHs from *M. japonicus* suppressed VG gene expression, while *M. japonicus* MIH and MIH-B did not (Tsutsui *et al.* 2005a, 2013). Although we have thus far isolated major CHH-family peptides, we do not know whether VIH is one of the known CHH-family peptides, or an unknown peptide. Because, other minor CHH-family peptides, putative CHH and putative MIH-C, were found in *M. japonicus* by EST analysis (Yamano and Unuma 2006). In the future, we will again search for VIH in the sinus gland extracts of the kuruma prawn *M. japonicus*. Moreover, we will analyze hemolymph levels of these peptides during vitellogenesis to elucide the real VIH molecules in *M. japonicus*.

Eyestalk ablation also causes various physiological changes, such as decrease of carbohydrate levels in hemolymph, shortening the molt-interval, and promotion of the methyl farnesoate synthesis in mandibular organs. These phenomena are known to be associated with CHH-family peptides. In our experiments, although eight CHH-family peptides have been purified and characterized from *M. japonicus* eyestalks, we have demonstrated only three functions, CHH, MIH and VIH activities. On the other hand, mandibular organ-inhibiting hormone (MOIH) was shown to be a CHH-family peptide (Wainwright *et al.* 1996). In addition, it was recently revealed that CHH-family peptides are also involved in various processes such as ion transport to the gills and water uptake for the purpose of enlarging body size after molting (Chung *et al.* 1999; Spanings-Pierrot *et al.* 2000). In order to determine the intrinsic function(s) of each peptide, further studies might be required.

doi:10.5047/absm.2013.00602.0049 © 2013 TERRAPUB, Tokyo. All rights reserved.

AGH is highly species-specific, and therefore we know the structures of only three terrestrial isopod species, which are phylogenetically very close to one another (Ohira *et al.* 2003b). As for the structure of AGH in decapod crustaceans, we know that similar to the case of isopod AGHs, IAG genes are expressed specifically in the AGs, and IAGs are presumed to belong to the insulin superfamily, strongly suggesting that IAG is an intrinsic decapod AGH. However, IAGs share little sequence similarity to isopod AGHs, and the *N*-glycosylation site which is significant for conferring AGH activity in *A. vulgare* is not conserved in decapod IAGs. In addition, direct evidence that IAG shows AGH activity has not yet been reported either *in vivo* or *in vitro*. In order to elucidate the biological activity of IAG, an assay system for AGH activity using decapod species is required.

Eyestalk hormones are involved in the control of various processes as mentioned above. Although eyestalk hormones have been studied extensively by many researchers, many problems still remain to be solved. One such unsolved problem is how AGs are regulated by the sinus glands. AG activity is thought to be under the control of a certain eyestalk hormone on the basis of finding that eyestalk ablation causes the enlargement of AG cells (Khalaila *et al.* 2002). Recently, it was reported that IAG gene expression in AG is enhanced by eyestalk ablation in *C. sapidus* (Chung *et al.* 2011). We need to further characterize sinus gland neuropeptides, both biologically and chemically, in order to clarify the endocrine mechanisms not only of sexual differentiation but also of growth and reproduction, the results of which we hope will lead to new techniques useful for shrimp aquaculture.

Acknowledgments

This work was performed in collaboration with the following researchers: Prof. K. Aida, Drs. W.-J. Yang and T.-W. Shih of Department of Aquatic Bioscience, Graduate School of Agricultural and Life Sciences, The University of Tokyo; Prof. M. Tanokura, Assoc. Prof. K. Nagata, Drs. S. Nagata, A. Okuno, H. Asazuma and C. Nagai of Department of Applied Biological Chemistry, Graduate School of Agricultural and Life Sciences, The University of Tokyo; Drs. M. N. Wilder and N. Tsutsui of Japan International Research Center for Agricultural Sciences; Prof. Y. Katakura and Assoc. Prof. Y. Hasegawa of Department of Biology, Keio University; Assoc. Prof. T. Watanabe of Ocean Research Institute, The University of Tokyo; Dr. K. Suitoh of Aichi Prefectural Sea Farming Institute; Dr. E. Lubzens of The National Institute of Oceanography, Israel Oceanographic and Limnological Research; Prof. H. Sonobe of Department of Biology, Faculty of Science, Konan University. This work was supported by Grants-in-aid for Scientific Research (Nos. 04660132, 06660127, 07044181, 07406009, 07456054, 09460055, 10556044, 11460054, 15208011, 21780186 and 23780204) from the Ministry of Education, Culture, Sports, Science and Technology of Japan.

References

Abdu U, Davis C, Khalaila I, Sagi A. The vitellogenin cDNA of *Cherax quadricarinatus* encodes a lipoprotein with calcium binding ability, and its expression is induced following the removal of the androgenic gland in a sexually plastic system. *Gen. Comp. Endocrinol.* 2002; **127**: 263–272.

Abramowitz AA, Hisaw FL, Papandrea DN. The occurrence of a diabetogenic factor in the eyestalks of crustaceans. *Biol. Bull.* 1944; **86**: 1–5.

Aguilar MB, Soyez D, Falchetto R, Arnott D, Shabanowitz J, Hunt DF, Huberman A. Amino acid sequence of the minor isomorph of the crustacean hyperglycemic hormone (CHH-II) of the Mexican crayfish *Procambarus bouvieri* (Ortmann): presence of a D-amino acid. *Peptides* 1995; **16**: 1375–1383.

Aguilar MB, Falchetto R, Shabanowitz J, Hunt DF, Huberman A. Complete primary structure of the molt-inhibiting hormone (MIH) of the Mexican crayfish *Procambarus bouvieri* (Ortmann). *Peptides* 1996; **17**: 367–374.

Asazuma H, Nagata S, Katayama H, Ohira T, Nagasawa H. Characterization of a molt-inhibiting hormone (MIH) receptor in the Y-organ of the kuruma prawn, *Marsupenaeus japonicus*. *Ann. N.Y. Acad. Sci.* 2005; **1040**: 215–218.

Asazuma H, Nagata S, Nagasawa H. Inhibitory effect of molt-inhibiting hormone on Phantom gene expression in the Y-organ of the kuruma prawn, *Marsupenaeus japonicus*. *Arch. Insect Biochem. Physiol.* 2009; **72**: 220–233.

Audsley N, McIntosh C, Phillips JE. Isolation of a neuropeptide from locust corpus cardiacum which influences ileal transport. *J. Exp. Biol.* 1992; **173**: 261–274.

Avarre JC, Michelis R, Tietz A, Lubzens E. Relationship between vitellogenin and vitellin in a marine shrimp (*Penaeus semisulcatus*) and molecular characterization of vitellogenin complimentary DNAs. *Biol. Reprod.* 2003; **69**: 355–364.

Banzai K, Ishizaka N, Asahina K, Suitoh K, Izumi S, Ohira T. Molecular cloning of a cDNA encoding insulin-like androgenic gland factor from the kuruma prawn *Marsupenaeus japonicus* and analysis of its expression. *Fish. Sci.* 2011; **77**: 329–335.

Banzai K, Izumi S, Ohira T. Molecular cloning and expression analysis of cDNAs encoding insulin-like androgenic gland factor from three palaemonid species, *Macrobrachium lar*, *Palaemon paucidens* and *P. pacificus*. *Jpn. Agric. Res. Q.* 2012 (in press).

Bogerd J, Kooiman FP, Pijnenburg MA, Hekking LH, Oudejans RC, Van der Horst DJ. Molecular cloning of three distinct cDNAs, each encoding a different adipokinetic hormone precursor, of the migratory locust, *Locusta migratoria*. Differential expression of the distinct adipokinetic hormone precursor genes during flight activity. *J. Biol. Chem.* 1995; **270**: 23038–23043.

Cereghino JL, Cregg JM. Heterologous protein expression in the methylotrophic yeast *Pichia pastoris*. *FEMS Microbiol.* 2000; **24**: 45–66.

Chang ES, Prestwich GD, Bruce MJ. Amino acid Sequence of a peptide with both molting-inhibiting and hyperglycemic activities in the lobster *Homarus*

doi:10.5047/absm.2013.00602.0049 © 2013 TERRAPUB, Tokyo. All rights reserved.

americanus. *Biochem. Biophys. Res. Commun.* 1990; **171**: 818–826.

Charniaux-Cotton H. Decouverte chez un Crustace Amphipode (*Orchestia gammarella*) d'une glande endocrine responsable de la differenciation des caracteres sexuels primaires et secondaires male. *C.R. Acad. Sci. Paris* 1954; **239**: 780–782.

Charniaux-Cotton H. Endocrinology and genetics of sex differentiation in invertebrates. *C.R. Seances Soc. Biol. Fil.* 1967; **161**: 6–9.

Chen YN, Tseng DY, Ho PY, Kuo CM. Site of vitellogenin synthesis determined from a cDNA encoding a vitellogenin fragment in the freshwater giant prawn, *Macrobrachium rosenbergii*. *Mol. Reprod. Dev.* 1999; **54**: 215–222.

Chung JS, Webster SG. Moult cycle-related changes in biological activity of moult-inhibiting hormone (MIH) and crustacean hyperglycemic hormone (CHH) in the crab, *Carcinus maenas*. *Eur. J. Biochem.* 2003; **270**: 3280–3288.

Chung JS, Webster SG. Dynamics of *in vivo* release of molt-inhibiting hormone and crustacean hyperglycemic hormone in the shore crab, *Carcinus maenas*. *Endocrinology* 2005; **146**: 5545–5551.

Chung JS, Wilkinson MC, Webster SG. Determination of the amino acid sequence of the moult-inhibiting hormone from the edible crab, *Cancer pagurus*. *Neuropeptides* 1996; **30**: 95–101.

Chung JS, Dircksen H, Webster SG. A remarkable, precisely timed release of hyperglycemic hormone from endocrine cells in the gut is associated with ecdysis in the crab *Carsinus maenas*. *Proc. Natl. Acad. Sci. USA* 1999; **96**: 13103–13107.

Chung JS, Manor R, Sagi A. Cloning of an insulin-like androgenic gland factor (*IAG*) from the blue crab, *Callinectes sapidus*: Implications for eyestalk regulation of *IAG* expression. *Gen. Comp. Endocrinol.* 2011; **173**: 4–10.

Dawson PE, Muir PW, Clark-Lewis I, Kent SB. Synthesis of proteins by native chemical ligation. *Science* 1994; **266**: 776–779.

De Kleijn DP, Van Herp F. Molecular biology of neurohormone precursors in the eyestalk of Crustacea. *Comp. Biochem. Physiol. B* 1995; **112**: 573–579.

De Kleijn DP, Coenen T, Laverdure AM, Tensen CP, Van Herp F. Localization of messenger RNAs encoding crustacean hyperglycemic hormone and gonad inhibiting hormone in the X-organ sinus gland complex of the lobster *Homarus americanus*. *Neuroscience* 1992; **51**: 121–128.

De Kleijn DP, Linck B, Klein JM, Weidemann WM, Keller R, Van Herp F. Structure and localization of mRNA encoding a pigment dispersing hormone (PDH) in the eyestalk of the crayfish *Orconectes limosus*. *FEBS Lett.* 1993; **321**: 251–255.

De Kleijn DP, Janssen KP, Martens GJ, Van Herp F. Cloning and expression of two crustacean hyperglycemic-hormone mRNAs in the eyestalk of the crayfish *Orconectes limosus*. *Eur. J. Biochem.* 1994a; **224**: 623–629.

De Kleijn DP, Sleutels FJ, Martens GJ, Van Herp F. Cloning and expression of mRNA encoding prepro-gonad-inhibiting hormone (GIH) in the lobster *Homarus americanus*. *FEBS Lett.* 1994b; **353**: 255–258.

De Kleijn DP, De Leeuw EP, Van Den Berg MC, Martens GJ, Van Herp F. Cloning and expression of two mRNAs encoding structurally different crustacean hyperglycemic hormone precursors in the lobster *Homarus americanus*. *Biochim. Biophys. Acta* 1995; **1260**: 62–66.

Desmoucelles-Carette C, Sellos D, Van Wormhoudt A. Molecular cloning of the precursors of pigment dispersing hormone in crustaceans. *Biochem. Biophys. Res. Commun.* 1996; **221**: 739–743.

Dircksen H, Böcking D, Heyn U, Mandel C, Chung JS, Baggerman G, Verhaert P, Daufeldt S, Plösch T, Jaros PP, Waelkens E, Keller R, Webster SG. Crustacean hyperglycaemic hormone (CHH)-like peptides and CHH-precursor-related peptides from pericardial organ neurosecretory cells in the shore crab, *Carcinus maenas*, are putatively spliced and modified products of multiple genes. *Biochem. J.* 2001; **356**: 159–170.

Endo H, Nagasawa H, Watanabe T. Isolation of a cDNA encoding a CHH-family peptide from the silkworm *Bombyx mori*. *Insect Biochem. Mol. Biol.* 2000; **30**: 355–361.

Fernlund P. Structure of a light-adapting hormone from the shrimp, *Pandalus borealis*. *Biochim. Biophys. Acta* 1976; **439**: 17–25.

Fernlund P, Josefsson L. Crustacean color-change hormone: amino acid sequence and chemical synthesis. *Science* 1972; **177**: 173–175.

Fingerman M, Rao KR, Bartell CK. A proposed uniform method of reporting response values for crustacean chromatophorotropins: the standard integrated response. *Experientia* 1967; **23**: 962.

Gäde G. The adipokinetic neuropeptide of Mantodea. Sequence elucidation and evolutionary relationships. *Biol. Chem. Hoppe-Seyler* 1991; **372**: 193–201.

Gasparini S, Kiyatkin N, Drevet P, Boulain JC, Tacnet F, Ripoche P, Forest E, Grishin E, Ménez A. The low molecular weight protein which co-purifies with α-latrotoxin is structurally related to crustacean hyperglycemic hormones. *J. Biol. Chem.* 1994; **269**: 19803–19809.

Gaus G, Kleinholz LH, Kegel G, Keller R. Isolation and characterization of red-pigment-concentrating hormone (RPCH) from six crustacean species. *J. Comp. Physiol. B* 1990; **160**: 373–379.

Gilbert LI. Halloween genes encode P450 enzymes that mediate steroid hormone biosynthesis in *Drosophila melanogaster*. *Mol. Cell. Endocrinol.* 2004; **215**: 1–10.

Gréve P, Sorokine O, Berges T, Lacombe C, Van Dorsselaer A, Martin G. Isolation and amino acid sequence of a peptide with vitellogenesis inhibiting activity from the terrestrial isopod *Armadillidium vulgare* (Crustacea). *Gen. Comp. Endocrinol.* 1999; **115**: 406–414.

Gu PL, Yu KL, Chan SM. Molecular characterization of an additional shrimp hyperglycemic hormone: cDNA cloning, gene organization, expression and biological assay of recombinant proteins. *FEBS Lett.* 2000; **472**: 122–128.

Gu PL, Tobe SS, Chow BK, Chu KH, He JG, Chan SM. Characterization of an additional molt inhibiting hormone-like neuropeptide from the shrimp *Metapenaeus ensis*. *Peptides* 2002; **23**: 1875–1883.

Guex N, Peitsch MC. SWISS-MODEL and the Swiss-PdbViewer: an environment for comparative protein modeling. *Electrophoresis* 1997; **18**: 2714–2723.

Hampshire F, Horn DHS. Structure of crustecdysone a crustacean moulting hormone. *Chem. Commun.* 1966; **1966**: 37–38.

Hasegawa Y, Okuno A, Nagasawa H. Immunohistochemical

doi:10.5047/absm.2013.00602.0049 © 2013 TERRAPUB, Tokyo. All rights reserved.

study of androgenic gland hormone: Localization in the male reproductive system and species specificity in the terrestrial isopods. *Gen. Comp. Endocrinol.* 2002; **125**: 218–225.

Hogben L, Slome D. The pigmentary effector system. VI. The dual character of endocrine co-ordination in amphibian colour change. *Proc. R. Soc. Lond. B* 1931; **108**: 10–53.

Holm M, Sander C. Protein structure comparison by alignment of distance matrices. *J. Mol. Biol.* 1993; **233**: 123–138.

Hoppe W, Huber R. Bestimmung des Sterin-Skeletts und seiner Orientierung mit diffuser Rontgenstreuung in Kristallen von Ecdyson. *Chem. Ber.* 1965; **98**: 2353–2360.

Huberman A, Hernandez-Arana A, Aguilar M, Rojo-Dominguez A. Secondary structure of a crustacean neuropeptide hormone family by means of CD. *Peptides* 1989; **10**: 1113–1115.

Huberman A, Aguilar MB, Brew K, Shabanowitz J, Hunt DF. Primary structure of the major isomorph of the crustacean hyperglycemic hormone (CHH-I) from the sinus gland of the Mexican crayfish *Procambarus bouvieri* (Ortmann): Interspecies comparison. *Peptides* 1993; **14**: 7–16.

Jaros PP, Keller R. Immunocytochemical identification of hyperglycemic hormone-producing cells in the eyestalk of *Carcinus maenas*. *Cell Tissue Res.* 1979; **204**: 379–385.

Jasmani S, Kawazoe I, Shih TW, Suzuki Y, Aida K. Hemolymph vitellogenin levels during ovarian development in the kuruma prawn *Penaeus japonicus*. *Fish. Sci.* 2000; **66**: 535–539.

Katakura Y, Fujimaki Y, Unno K. Partial purification and characterization of androgenic gland hormone from the isopod crustacean, *Armadillidium vulgare*. *Annot. Zool. Japon.* 1975; **48**: 203–209.

Katayama H, Nagasawa H. Effect of a glycine residue insertion into crustacean hyperglycemic hormone on hormonal activity. *Zool. Sci.* 2004; **21**: 1121–1124.

Katayama H, Ohira T, Nagata K, Nagasawa H. A recombinant molt-inhibiting hormone of the kuruma prawn has a similar secondary structure to a native hormone: determination of disulfide bond arrangement and measurements of circular dichroism spectra. *Biosci. Biotechnol. Biochem.* 2001; **65**: 1832–1839.

Katayama H, Ohira T, Aida K, Nagasawa H. Significance of a carboxyl-terminal amide moiety in the folding and biological activity of crustacean hyperglycemic hormone. *Peptides* 2002; **23**: 1537–1546.

Katayama H, Nagata K, Ohira T, Yumoto F, Tanokura M, Nagasawa H. The solution structure of molt-inhibiting hormone from the Kuruma prawn *Marsupenaeus japonicus*. *J. Biol. Chem.* 2003; **278**: 9620–9623.

Katayama H, Ohira T, Nagata S, Nagasawa H. Structure-activity relationship of molt-inhibiting hormone from the kuruma prawn *Marsupenaeus japonicus*. *Biochemistry* 2004; **43**: 9629–9635.

Katayama H, Hojo H, Ohira T, Ishii A, Nozaki T, Goto K, Nakahara Y, Takahashi T, Hasegawa Y, Nagasawa H, Nakahara Y. Correct disulfide pairing is required for the biological activity of crustacean androgenic gland hormone (AGH): Synthetic studies of AGH. *Biochemistry* 2010; **49**: 1798–1807.

Kawakami A, Kataoka H, Oka T, Mizoguchi A, Kimura-Kawakami M, Adachi T, Iwami M, Nagasawa H, Suzuki A, Ishizaki H. Molecular cloning of the *Bombyx mori* prothoracicotropic hormone. *Science* 1990; **247**: 1333–1335.

Kawakami T, Toda C, Akaji K, Nishimura T, Nakatsuji T, Ueno K, Sonobe M, Sonobe H, Aimoto S. Synthesis of a molt-inhibiting hormone of the American crayfish, *Procambarus clarkii*, and determination of the location of its disulfide linkages. *J. Biochem.* 2000; **128**: 455–461.

Kegel G, Reichwein B, Weese S, Gaus G, Peter-Katalinic J, Keller R. Amino acid sequence of the crustacean hyperglycemic hormone (CHH) from the shore crab, *Carcinus maenas*. *FEBS Lett.* 1989; **255**: 10–14.

Keller R. Crustacean neuropeptides: Structures, functions and comparative aspects. *Experientia* 1992; **48**: 439–448.

Khalaila I, Katz T, Abdu U, Yehezkel G, Sagi A. Effects of implantation of hypertrophied androgenic glands on sexual characters and physiology of the reproductive system in the female red claw crayfish, *Cherax quadricarinatus*. *Gen. Comp. Endocrinol.* 2001; **121**: 242–249.

Khalaila I, Manor R, Weil S, Granot Y, Keller R, Sagi A. The eyestalk-androgenic gland-testis endocrine axis in the crayfish, *Cherax quadricarinatus*. *Gen. Comp. Endocrinol.* 2002; **127**: 147–156.

Khayat M, Yang WJ, Aida K, Nagasawa H, Tietz A, Funkenstein B, Lubzens E. Hyperglycaemic hormones inhibit protein and mRNA synthesis in *in vitro*-incubated ovarian fragments of the marine shrimp *Penaeus semisulcatus*. *Gen. Comp. Endocrinol.* 1998; **110**: 307–318.

Klein JM, De Kleijn DPV, Keller R, Weidemann WM. Molecular cloning of crustacean pigment dispersing hormone precursor. *Biochem. Biophys. Res. Commun.* 1992; **189**: 1509–1514.

Klein JM, De Kleijn DPV, Hünemeyer G, Keller R, Weidemann WM. Demonstration of the cellular expression of genes encoding molt-inhibiting hormone and crustacean hyperglycemic hormone in the eyestalk of the shore crab *Carcinus maenas*. *Cell Tissue Res.* 1993; **274**: 515–519.

Klein JM, Mohrherr CJ, Sleutels F, Riehm JP, Rao KR. Molecular cloning of two pigment-dispersing hormone (PDH) precursors in the blue crab *Callinectes sapidus* reveals a novel member of the PDH neuropeptide family. *Biochem. Biophys. Res. Commun.* 1994; **205**: 410–416.

Kromer-Metzger E, Lagueux M. Expression of the gene encoding an insulin-related peptide in *Locusta* (*Insecta, Orthoptera*). *Eur. J. Biochem.* 1994; **221**: 427–434.

Krungkasem C, Ohira T, Yang WJ, Abdullah R, Nagasawa H, Aida K. Identification of two distinct molt-inhibiting hormone-related peptides from the giant tiger prawn *Penaeus monodon*. *Mar. Biotechnol.* 2002; **4**: 132–140.

Lacombe C, Gréve P, Martin G. Overview on the subgrouping of the crustacean hyperglycemic hormone family. *Neuropeptides* 1999; **33**: 71–80.

Leuven RS, Jaros PP, Van Herp F, Keller R. Species or group specificity in biological and immunological studies of crustacean hyperglycemic hormone. *Gen. Comp. Endocrinol.* 1982; **46**: 288–296.

Mak ASC, Choi CL, Tiu SHK, Hui JHL, He JG, Tobe SS, Chan SM. Vitellogenesis in the red crab *Charybdis*

doi:10.5047/absm.2013.00602.0049 © 2013 TERRAPUB, Tokyo. All rights reserved.

feriatus: Hepatopancreas-specific expression and farnesoic acid stimulation of vitellogenin gene expression. *Mol. Reprod. Dev.* 2005; **70**: 288–300.

Manor R, Weil S, Oren S, Glazer L, Aflalo ED, Ventura T, Chalifa-Caspi V, Lapidot M, Sagi A. Insulin and gender: an insulin-like gene expressed exclusively in the androgenic gland of the male crayfish. *Gen. Comp. Endocrinol.* 2007; **150**: 326–336.

Marco HG, Brandt W, Stoeva S, Voelter W, Gäde G. Primary structures of a second hyperglycemic peptide and of two truncated forms in the spiny lobster, *Jasus lalandii*. *Peptides* 2000; **21**: 19–27.

Marco HG, Avarre JC, Lubzens E, Gäde G. In search of a vitellogenesis-inhibiting hormone from the eyestalks of the South African spiny lobster, *Jasus lalandii*. *Invert. Reprod. Dev.* 2002; **41**: 143–150.

Martin G, Juchault P, Sorokine O, van Dorsselaer A. Purification and characterization of androgenic hormone from the terrestrial isopod *Armadillidium vulgare* Latr. (Crustacea, Oniscidea). *Gen. Comp. Endocrinol.* 1990; **80**: 349–354.

Martin G, Sorokine O, Van Dorsselaer A. Isolation and molecular characterization of a hyperglycemic neuropeptide from the sinus gland of the terrestrial isopod *Armadillidium vulgare* (crastacea). *Eur. J. Biochem.* 1993; **211**: 601–607.

Martin G, Sorokine O, Moniatte M, Van Dorsselaer A. The androgenic gland hormone of the crustacean isopod *Armadillidium vulgare*. *Ann. N.Y. Acad. Sci.* 1998; **839**: 111–117.

Martin G, Sorokine O, Moniatte M, Bulet P, Hetru C, Van Dorsselaer A. The structure of a glycosylated protein hormone responsible for sex determination in the isopod, *Armadillidium vulgare*. *Eur. J. Biochem.* 1999; **262**: 727–736.

Mettulio R, Giulianini PG, Ferrero EA, Lorenzon S, Edomi P. Functional analysis of crustacean hyperglycemic hormone by *in vivo* assay with wild-type and mutant recombinant proteins. *Regul. Pept.* 2004; **119**: 189–197.

Mordue W, Stone JV. Comparison of the biological activities of an insect and a crustacean neurohormone that are structurally similar. *Nature* 1976; **264**: 287–289.

Muir TW, Sondhi D, Cole PA. Expressed protein ligation: A general method for protein engineering. *Proc. Natl. Acad. Sci. USA* 1998; **95**: 6705–6710.

Nagai C, Asazuma H, Nagata S, Ohira T, Nagasawa H. A convenient method for preparation of biologically active recombinant CHH of the kuruma prawn, *Marsupenaeus japonicus*, using the bacterial expression system. *Peptides* 2009; **30**: 507–517.

Nagamine C, Knight AW, Maggenti A, Paxman G. Masculinization of female *Macrobrachium rosenbergii* (de Man) (Decapoda, Palaemonidae) by androgenic gland implantation. *Gen. Comp. Endcrinol.* 1980; **41**: 442–457.

Nagasawa H, Hasegawa Y, Haino-Fukushima K, Hatayama H, Yanagisawa T, Katakura Y. Isolation and structural determination of seminal vesicle-specific peptides of the terrestrial isopod, *Armadillidium vulgare*. *Biosci. Biotechnol. Biochem.* 1995; **59**: 1246–1250.

Nagasawa H, Yang WJ, Shimizu H, Aida K, Tsutsumi H, Terauchi A, Sonobe H. Isolation and amino acid sequence of a molt-inhibiting hormone from the American crayfish, *Procambarus clarkii*. *Biosci. Biotechnol. Biochem.* 1996; **60**: 554–556.

Nagasawa H, Yang WJ, Aida K, Sonobe H. Chemical and biological characterization of neuropeptides in the sinus glands of the kuruma prawn, *Penaeus japonicus*. *In*: Shimonishi Y (ed). *Peptide Science—Present and Future*. Kluwer Academic Publishers, Great Britain. 1999; 453–454.

Nakatsuji T, Sonobe H. Measurement of molt-inhibiting hormone titer in hemolymph of the American crayfish, *Procambarus clarkii*. *Zool. Sci.* 2003; **20**: 999–1001.

Nakatsuji T, Sonobe H. Regulation of ecdysteroid secretion from the Y-organ by molt-inhibiting hormone in the American crayfish, *Procambarus clarkii*. *Gen. Comp. Endocrinol.* 2004; **135**: 358–364.

Nakatsuji T, Sonobe H, Watson RD. Molt-inhibiting hormone-mediated regulation of ecdysteroid synthesis in Y-organ of the crayfish (*Procambarus clarkii*): involvement of cyclic GMP and cyclic nucleotide phosphodiesterase. *Mol. Cell. Endocrinol.* 2006; **253**: 76–82.

Nakatsuji T, Lee CY, Watson RD. Crustacean molt-inhibiting hormone: Structure, function, and cellular mode of action. *Comp. Biochem. Physiol. A* 2009; **152**: 139–148.

Ohira T. Molecular biological studies on crustacean hyperglycemic hormone-family peptides of the kuruma prawn *Penaeus japonicus*. PhD Thesis, The University of Tokyo, Tokyo, 2000.

Ohira T, Watanabe T, Nagasawa H, Aida K. Cloning and sequence analysis of a cDNA encoding a crustacean hyperglycemic hormone from the Kuruma prawn *Penaeus japonicus*. *Mol. Mar. Biol. Biotechnol.* 1997a; **6**: 59–63.

Ohira T, Watanabe T, Nagasawa H, Aida K. Molecular cloning of cDNAs encoding four crustacean hyperglycemic hormones and a molt-inhibiting hormone from the kuruma prawn *Penaeus japonicus*. *In*: Kawashima S, Kikuyama S (eds). *Proceedings of the XIII International Congress of Comparative Endocrinology*. Monduzzi Editore, Bologna. 1997b; 83–86.

Ohira T, Watanabe T, Nagasawa H, Aida K. Molecular cloning of a molt-inhibiting hormone cDNA from the kuruma prawn *Penaeus japonicus*. *Zool. Sci.* 1997c; **14**: 785–789.

Ohira T, Nishimura T, Sonobe H, Okuno A, Watanabe T, Nagasawa H, Kawazoe I, Aida K. Expression of a recombinant molt-inhibiting hormone of the kuruma prawn *Penaeus japonicus* in *Escherichia coli*. *Biosci. Biotechnol. Biochem.* 1999; **63**: 1576–1581.

Ohira T, Nagasawa H, Aida K. Molecular cloning of cDNAs encoding two pigment-dispersing hormones and two corresponding genes from the kuruma prawn (*Penaeus japonicus*). *Mar. Biotechnol.* 2002; **4**: 463–470.

Ohira T, Katayama H, Aida K, Nagasawa H. Expression of a recombinant crustacean hyperglycemic hormone of the kuruma prawn *Penaeus japonicus* in methylotrophic yeast *Pichia pastoris*. *Fish. Sci.* 2003a; **69**: 95–100.

Ohira T, Hasegawa Y, Tominaga S, Okuno A, Nagasawa H. Molecular cloning and expression analysis of cDNAs encoding androgenic gland hormone precursors from two Porcellionidae species, *Porcellio scaber* and *P. dilatatus*. *Zool. Sci.* 2003b; **20**: 75–81.

Ohira T, Katayama H, Tominaga S, Takasuka T, Nakatsuji T, Sonobe H, Aida K, Nagasawa H. Cloning and characterization of a molt-inhibiting hormone-like peptide from the prawn *Marsupenaeus japonicus*. *Peptides* 2005; **26**:

doi:10.5047/absm.2013.00602.0049 © 2013 TERRAPUB, Tokyo. All rights reserved.

259–268.

Ohira T, Okumura T, Suzuki M, Yajima Y, Tsutsui N, Wilder MN, Nagasawa H. Production and characterization of recombinant vitellogenesis-inhibiting hormone from the American lobster *Homarus americanus*. *Peptides* 2006; **27**: 1251–1258.

Okumura T, Ohira T, Katayama H, Nagasawa H. *In vivo* effects of a recombinant molt-inhibiting hormone on molt interval and hemolymph ecdysteroid level in the kuruma prawn, *Marsupenaeus japonicus*. *Zool. Sci.* 2005; **22**: 317–320.

Okuno A, Hasegawa Y, Nagasawa H. Purification and properties of androgenic gland hormone from the terrestrial isopod *Armadillidium vungare*. *Zool. Sci.* 1997; **14**: 837–842.

Okuno A, Hasegawa Y, Ohira T, Katakura Y, Nagasawa H. Characterization and cDNA cloning of androgenic gland hormone of the terrestrial isopod *Armadillidium vulgare*. *Biochem. Biophys. Res. Commun.* 1999; **264**: 419–423.

Okuno A, Hasegawa Y, Ohira T, Nagasawa H. Immunological identification of crustacean androgenic gland hormone, a glycopeptide. *Peptides* 2001; **22**: 175–181.

Okuno A, Yang WJ, Jayasankar V, Saido-Sakanaka H, Huong DTT, Jasmani S, Atmomarsono M, Subramoniam T, Tsutsui N, Ohira T, Kawazoe I, Aida K, Wilder MN. Deduced primary structure of vitellogenin in the giant freshwater prawn, *Macrobrachium rosenbergii*, and yolk processing during ovarian maturation. *J. Exp. Zool.* 2002a; **292**: 417–429.

Okuno A, Hasegawa Y, Nishiyama M, Ohira T, Kurihara M, Mastumoto S, Nagasawa H. Preparation of an active recombinant peptide of crustacean androgenic gland hormone. *Peptides* 2002b; **23**: 567–572.

Papadopoulos NM, Hess WC. Determination of neuraminic (sialic) acid, glucose and fructose in spinal fluid. *Arch. Biochem. Biophys.* 1960; **88**: 167–171.

Park JH, Hall JC. Isolation and chronobiological analysis of a neuropeptide pigment-dispersing factor gene in *Drosophila melanogaster*. *J. Biol. Rhythms.* 1998; **13**: 219–228.

Park JH, Helfrich-Forster C, Lee G, Liu L, Rosbash M, Hall JC. Differential regulation of circadian pacemaker output by separate clock genes in *Drosophila*. *Proc. Natl. Acad. Sci. USA* 2000; **97**: 3608–3613.

Phillips JM, Rao KR, Riehm JP, Morgan WT. Isolation and characterization of a pigment-dispersing hormone from the shrimp, *Penaeus aztecus*. *Soc. Neurosci. Abstr.* 1988; **14**: 534.

Rao KR, Riehm JP. The pigment-dispersing hormone family: Chemistry structure-activity relations, and distribution. *Biol. Bull.* 1989; **177**: 225–229.

Rao KR, Riehm JP. Pigment-dispersing hormones. *Ann. N.Y. Acad. Sci.* 1993; **680**: 78–88.

Rao KR, Kleinhlz LH, Riehm JP. Characterization of three forms of pigment-dispersing hormone from the shrimp, *Pandalus jordani*. *Soc. Neurosci. Abstr.* 1989; **15**: 367.

Raviv S, Parnes S, Segall C, Davis C, Sagi A. Complete sequence of *Litopenaeus vannamei* (Crustacea: Decapoda) vitellogenin cDNA and its expression in endocrinologically induced sub-adult females. *Gen. Comp. Endocrinol.* 2006; **145**: 39–50.

Rewitz KF, Gilbert LI. Daphnia Halloween genes encode cytochrome P450s mediating the synthesis of the arthropod molting hormones: evolutionary implications. *BMC Evol. Biol.* 2008; **36**: 188–199.

Rotllant G, De Kleijn D, Charmantier-Daures M, Charmantier G, Van Herp F. Localization of crustacean hyperglycemic hormone (CHH) and gonad-inhibiting hormone (GIH) in the eyestalk of *Homarus gammarus* larvae by immunocytochemistry and *in situ* hybridization. *Cell Tissue Res.* 1993; **271**: 507–512.

Saidi BN, Besse SD, Webster SG, Sedlmeier D, Lachaise F. Involvement of cAMP and cGMP in the mode of action of molt-inhibiting hormone (MIH) a neuropeptide which inhibits steroidogenesis in a crab. *Mol. Cell. Endocrinol.* 1994; **102**: 53–61.

Santos EA, Keller R. Crustacean hyperglycemic hormone (CHH) and the regulation of carbohydrate metabolism: current perspectives. *Comp. Biochem. Physiol. A* 1993; **106**: 405–411.

Schütt C, Nöthiger R. Structure, function and evolution of sex-determining systems in Dipteran insects. *Development* 2000; **127**: 667–677.

Shih TW, Suzuki Y, Nagasawa H, Aida K. Immunohistochemical localization of crustacean hyperglycemic hormones (CHHs) and a molt-inhibiting hormone (MIH) in the eyestalk of *Penaeus japonicus*. *In*: Kawashima S, Kikuyama S (eds). *Proceedings of the XIII International Congress of Comparative Endocrinology*. Monduzzi Editore, Bologna. 1997; 87–91.

Shih TW, Suzuki Y, Nagasawa H, Aida K. Immunohistochemical identification of hyperglycemic hormone- and molt-inhibiting hormone-producing cells in the eyestalk of the kuruma prawn, *Penaeus japonicus*. *Zool. Sci.* 1998; **15**: 389–397.

Sonobe H, Kamba M, Ohta K, Ikeda M, Naya Y. *In vitro* secretion of ecdysteroids by Y-organ of the crayfish, *Procambarus clarkii*. *Experientia* 1991; **47**: 949–952.

Soyez D. Occurrence and diversity of neuropeptides from the crustacean hyperglycemic hormone family in arthropods. *Ann. N.Y. Acad. Sci.* 1997; **814**: 319–323.

Soyez D, Van Deijnen JE, Martin M. Isolation and characterization of a vitellogenesis-inhibiting factor from sinus glands of the lobster, *Homarus americanus*. *J. Exp. Zool.* 1987; **244**: 479–484.

Soyez D, Le Caer JP, Noel PY, Rossier J. Primary structure of two isoforms of the vitellogenesis inhibiting hormone from the lobster *Homarus americanus*. *Neuropeptides* 1991; **20**: 25–32.

Soyez D, Van Herp F, Rossier J, Le Caer JP, Tensen CP, Lafont R. Evidence for a conformational polymorphism of invertebrate neurohormones. D-Amino acid residue in crustacean hyperglycemic peptides. *J. Biol. Chem.* 1994; **269**: 18295–18298.

Spanings-Pierrot C, Soyez D, Van Herp F, Gompel M, Skaret G, Grousset E, Charmantier G. Involvement of crustacean hyperglycemic hormone in the control of gill ion transport in the crab *Pachygrapsus marmoratus*. *Gen. Comp. Endocrinol.* 2000; **119**: 340–350.

Suzuki S, Yamasaki K. Sex reversal by implantations of ethanol-treated androgenic glands of female isopods, *Armadillidium vulgare* (Malacostraca, Crustacea). *Gen. Comp. Endocrinol.* 1998; **111**: 367–375.

Suzuki S, Yamasaki K, Katakura Y. Vitellogenin synthesis

doi:10.5047/absm.2013.00602.0049 © 2013 TERRAPUB, Tokyo. All rights reserved.

in andrectomized male of the terrestrial isopoda, *Armadillidium vulgare* (Malacostracan crustacea). *Gen. Comp. Endocrinol.* 1990; **77**: 283–291.

Tensen CP, Verhoeven AH, Gaus G, Janssen KP, Keller R, Van Herp F. Isolation and amino acid sequence of crustacean hyperglycemic hormone precursor-related peptides. *Peptides* 1991; **12**: 673–681.

Treerattrakool S, Udomkit A, Eurwilaichitr L, Sonthayanon B, Panyim S. Expression of biologically active crustacean hyperglycemic hormone (CHH) of *Penaeus monodon* in *Pichia pastoris*. *Mar. Biotechnol.* 2003; **5**: 373–379.

Truman JW. Hormonal control of insect ecdysis: endocrine cascades for coordinating behavior with physiology. *Vitam. Horm.* 2005; **73**: 1–30.

Tsang WS, Quackenbush LS, Chow BKC, Tiu SHK, He JG, Chan SM. Organization of the shrimp vitellogenin gene: evidence of multiple genes and tissue specific expression by the ovary and hepatopancreas. *Gene* 2003; **303**: 99–109.

Tseng DY, Chen YN, Kou GH, Lo CF, Kuo CM. Hepatopancreas is the extraovarian site of vitellogenin synthesis in black tiger shrimp, *Penaeus monodon*. *Comp. Biochem. Physiol. A* 2001; **129**: 909–917.

Tsutsui N, Kawazoe I, Ohira T, Jasmani S, Yang WJ, Wilder MN, Aida K. Molecular characterization of a cDNA encoding vitellogenin and its expression in the hepatopancreas and ovary during vitellogenesis in the kuruma prawn, *Penaeus japonicus*. *Zool. Sci.* 2000; **17**: 651–660.

Tsutsui N, Saido-Sakanaka H, Yang WJ, Jayasankar V, Jasmani S, Okuno A, Ohira T, Okumura T, Aida K, Wilder MN. Molecular characterization of a cDNA encoding vitellogenin in the coonstriped shrimp, *Pandalus hypsinotus* and site of vitellogenin mRNA expression. *J. Exp. Zool.* 2004; **301A**: 802–814.

Tsutsui N, Katayama H, Ohira T, Nagasawa H, Wilder MN, Aida K. The effects of crustacean hyperglycemic hormone-family peptides on vitellogenin gene expression in the kuruma prawn, *Marsupenaeus japonicus*. *Gen. Comp. Endocrinol.* 2005a; **144**: 232–239.

Tsutsui N, Kim YK, Jasmani S, Ohira T, Wilder MN, Aida K. The dynamics of vitellogenin gene expression differs between intact and eyestalk ablated kuruma prawn, *Penaeus* (*Marsupenaeus*) *japonicus*. *Fish. Sci.* 2005b; **71**: 249–256.

Tsutsui N, Ohira T, Kawazoe I, Takahashi A, Wilder MN. Purification of sinus gland peptides having vitellogenesis-inhibiting activity from the whiteleg shrimp *Litopenaeus vannamei*. *Mar. Biotechnol.* 2007; **9**: 360–369.

Tsutsui N, Nagakura-Nakamura A, Nagai C, Ohira T, Wilder MN, Nagasawa H. The *ex vivo* effects of eyestalk peptides on ovarian vitellogenin gene expression in the kuruma prawn *Marsupenaeus japonicus*. *Fish. Sci.* 2013; **79**: 33–38.

Udomkit A, Chooluck S, Sonthayanon B, Panyim S. Molecular cloning of a cDNA encoding a member of CHH/MIH/GIH family from *Penaeus monodon* and analysis of its gene structure. *J. Exp. Mar. Biol. Ecol.* 2000; **244**: 145–156.

Ventura T, Manor R, Aflalo ED, Weil S, Raviv S, Glazer L, Sagi A. Temporal silencing of an androgenic gland-specific insulin-like gene affecting phenotypical gender differences and spermatogenesis. *Endocrinology* 2009; **150**: 1278–1286.

Von Heijne G. A new method for predicting signal sequence cleavage sites. *Nucleic Acids Res.* 1986; **14**: 4683–4690.

Wainwright G, Webster SG, Wilkinson MC, Chung JS, Rees HH. Structure and significance of mandibular organ-inhibiting hormone in the crab, *Cancer pagurus*. *J. Biol. Chem.* 1996; **271**: 12749–12754.

Warrier S, Subramoniam T. Receptor mediated yolk protein uptake in the crab *Scylla serrata*: crustacean vitellogenin receptor recognizes related mammalian serum lipoproteins. *Mol. Reprod. Dev.* 2002; **61**: 536–548.

Webster SG. Amino acid sequence of putative moult-inhibiting hormone from the crab *Carcinus maenas*. *Proc. R. Soc. Lond. B* 1991; **244**: 247–252.

Webster SG, Keller R. Purification, characterization and amino acid composition of the putative moult-inhibiting hormone (MIH) of *Carcinus maenas* (Crustacea, Decapoda). *J. Comp. Physiol. B* 1986; **156**: 617–624.

Weidemann W, Gromoll J, Keller R. Cloning and sequence analysis of cDNA for precursor of a crustacean hyperglycemic hormone. *FEBS Lett.* 1989; **257**: 31–34.

Wilder MN, Okumura T, Tsutsui N. Reproductive mechanisms in Crustacea focusing on selected prawn species: vitellogenin structure, processing and synthetic control. *Aqua-BioScience Monographs* 2010; **3**: 73–110.

Yamano K, Unuma T. Expressed sequence tags from eyestalk of kuruma prawn, *Marsupenaeus japonicus*. *Comp. Biochem. Physiol. A* 2006; **143**: 155–161.

Yang F, Xu HT, Dai ZM, Yang WJ. Molecular characterization and expression analysis of vitellogenin in the marine crab *Portunus trituberculatus*. *Comp. Biochem. Physiol. B* 2005; **142**: 456–464.

Yang WJ. Structures and functions of peptide hormones in the sinus gland of the kuruma prawn *Penaeus japonicus*. PhD Thesis, The University of Tokyo, Tokyo, 1997.

Yang WJ, Aida K, Nagasawa H. Amino acid sequences of a hyperglycaemic hormone and its related peptides from the Kuruma prawn, *Penaeus japonicus*. *Aquaculture* 1995; **135**: 205–212.

Yang WJ, Aida K, Terauchi A, Sonobe H, Nagasawa H. Amino acid sequence of a peptide with molt-inhibiting activity from the kuruma prawn *Penaeus japonicus*. *Peptides* 1996; **17**: 197–202.

Yang WJ, Aida K, Nagasawa H. Amino acid sequences and activities of multiple hyperglycemic hormones from the kuruma prawn, *Penaeus japonicus*. *Peptides* 1997; **18**: 479–485.

Yang WJ, Aida K, Nagasawa H. Characterization of chromatophorotropic neuropeptides from the kuruma prawn *Penaeus japonicus*. *Gen. Comp. Endocrinol.* 1999; **114**: 415–424.

Yang WJ, Ohira T, Tsutsui N, Subramoniam T, Huong DTT, Aida K, Wilder MN. Determination of amino acid sequence and site of mRNA expression of four vitellins in the giant freshwater prawn, *Macrobrachium rosenbergii*. *J. Exp. Zool.* 2000; **287**: 413–422.

Yasuda A, Yasuda Y, Fujita T, Naya Y. Characterization of crustacean hyperglycemic hormone from the crayfish (*Procambarus clarkii*): Multiplicity of molecular forms by stereoinversion and diverse functions. *Gen. Comp. Endocrinol.* 1994; **95**: 387–398.

doi:10.5047/absm.2013.00602.0049 © 2013 TERRAPUB, Tokyo. All rights reserved.

Zeleny C. Compensatory regulation. *J. Exp. Zool.* 1905; **2**: 1–102.

Zheng J, Lee CY, Watson RD. Molecular cloning of a putative receptor quanylyl cyclase from Y-organs of the blue crab, *Callinectes sapidus*. *Gen. Comp. Endocrinol.* 2006; **146**: 329–336.

Zheng J, Nakatsuji T, Roer RD, Watson RD. Studies of a receptor guanylyl cyclase cloned from Yorgans of the blue crab (*Callinectes sapidus*), and its possible functional link to ecdysteroidogenesis. *Gen. Comp. Endocrinol.* 2008; **155**: 780–788.

Zmora N, Trant JM, Zohar JS, Chung JS. Molt-inhibiting hormone stimulates vitellogenesis at advanced ovarian developmental stages in the female blue crab, *Callinectes sapidus* 2: An ovarian stage dependent involvement. *Saline System* 2009; **5**: 6.

doi:10.5047/absm.2013.00602.0049 © 2013 TERRAPUB, Tokyo. All rights reserved.

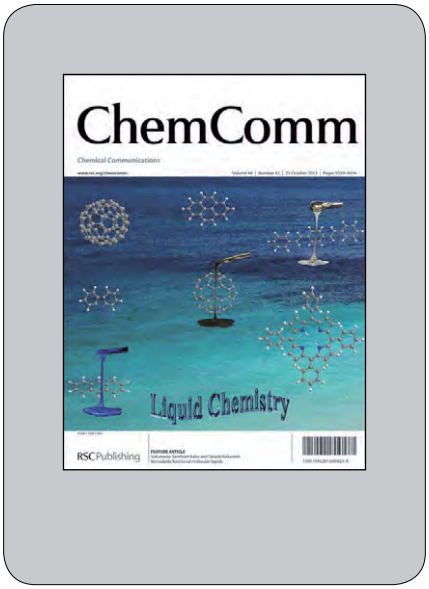

RSC Publishing

ChemComm

RSC Publishing

COMMUNICATION

View Article Online
View Journal | View Issue

Cite this: *Chem. Commun.*, 2013, **49**, 9386

Macroscopic motion of supramolecular assemblies actuated by photoisomerization of azobenzene derivatives

Yoshiyuki Kageyama,* Naruho Tanigake, Yuta Kurokome, Sachiko Iwaki, Sadamu Takeda,* Kentaro Suzuki and Tadashi Sugawara*

www.rsc.org/chemcomm

Submillimetre size self-assemblies composed of oleate and azobenzene derivatives show forceful motions such as screw-type coiling–recoiling motion by photoirradiation.

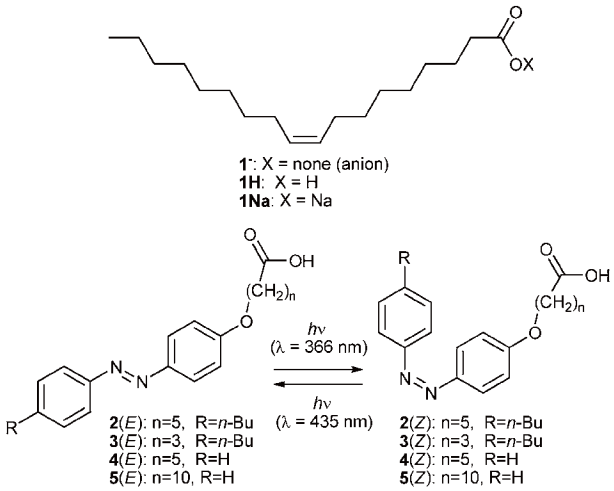

Fig. 1

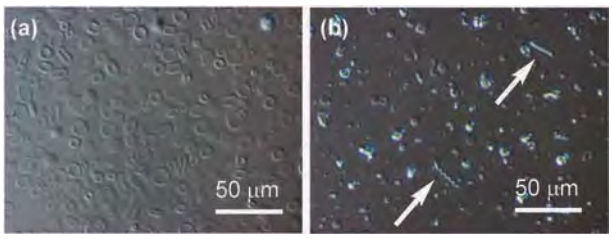

Fig. 2

1H **1⁻**

1H **1⁻**

This journal is © The Royal Society of Chemistry 2013

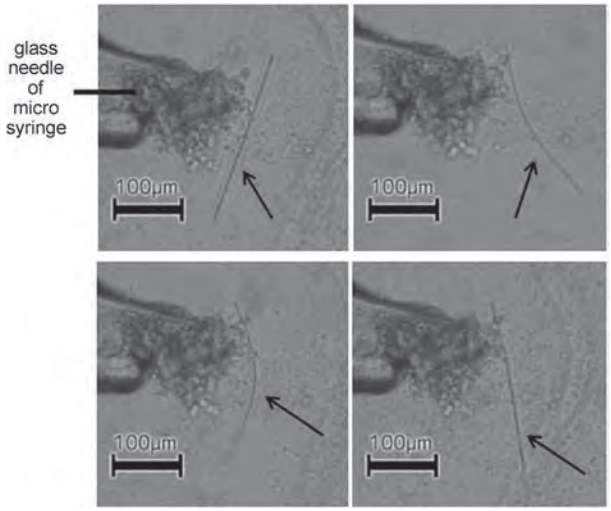

Fig. 3

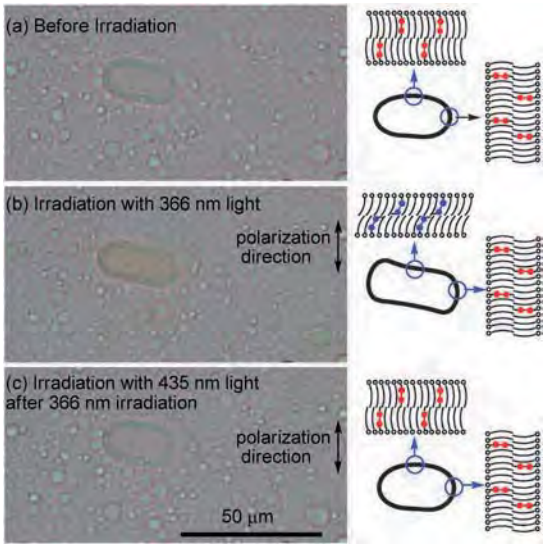

Fig. 4

2–5

trans

cis

1Na

2–5

μ

2–5

°

2–5

2–5

2

3–5

2–5

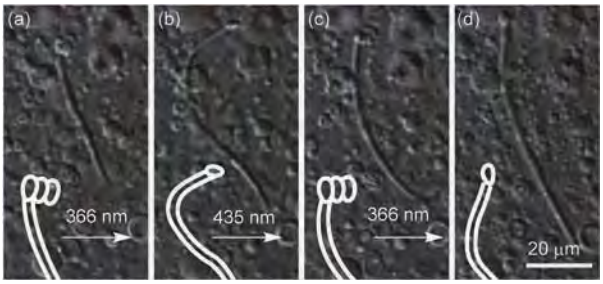

Fig. 5

2

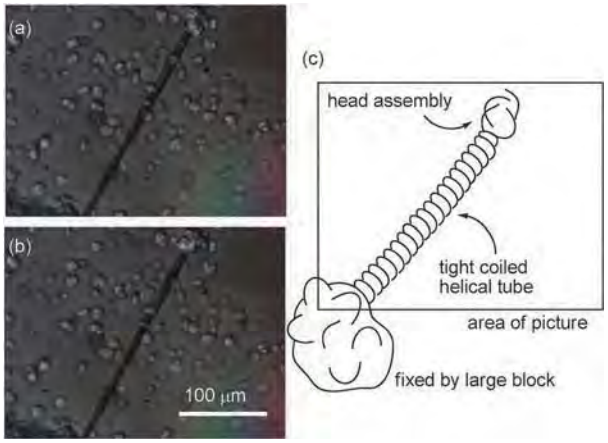

Fig. 6

3

2

2

2

Notes and references

46
3
81
7
129
2
47
425
330
45
46
2
100
288
4
243
11
12
164
17
2–5
2
72
106
2

This journal is © The Royal Society of Chemistry 2013

N_1

N_2

V

N_1 N_2

V

N_1 N_2

V

N_1 N_2

N_1 N_2

V E

N_1 N_2

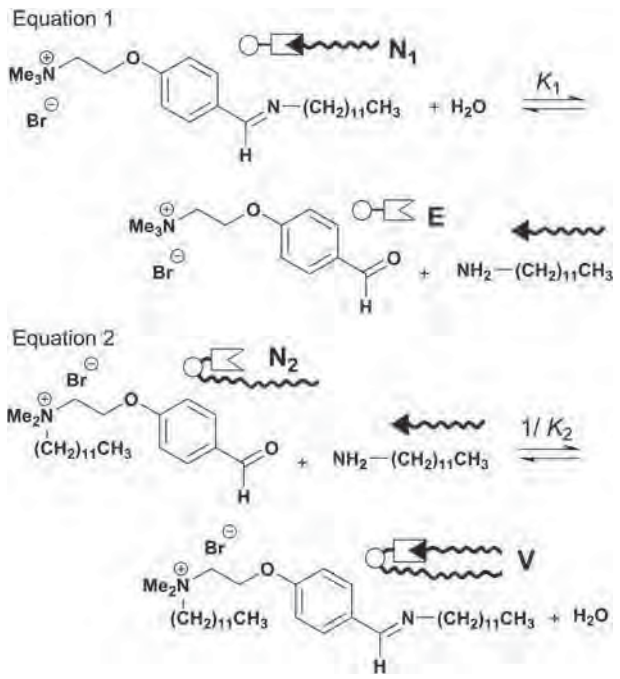

N₁ **N₂**

N₁ **N₂**

μ

N₁ **N₂**

V **E**

E

N₁

E

N₁ **N₂**

V

N₁ **N₂**

V

N₁ **N₂**

E

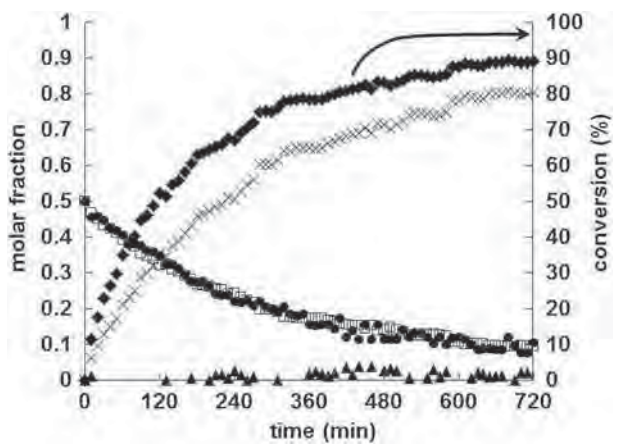

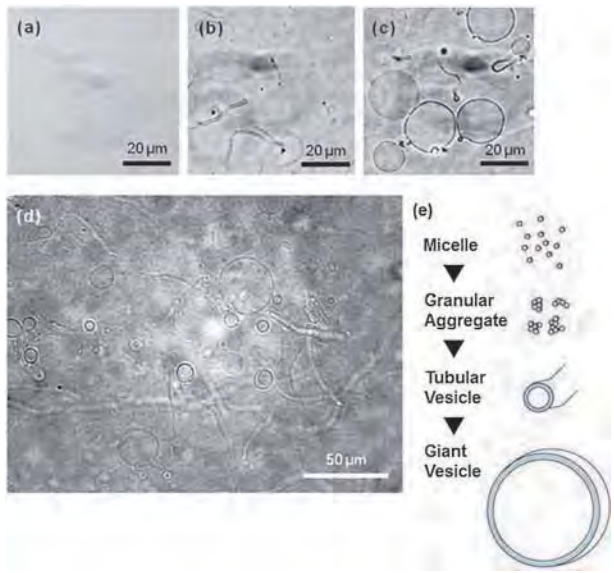

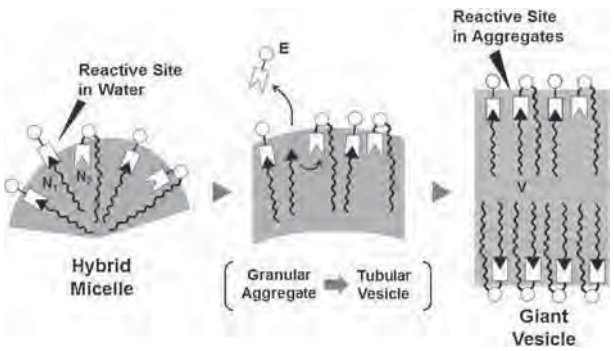

N_1 V

N_1

N_1

N_1

E

≫

N_2

V

V

V

N_1

V

N_2 V

N_1 N_2

V

N_1 V

V

E N_1

V

V

N_1

N_2

V E

18

105

90

48

47

101

9

125

20

102

27

35

7

74

8

268

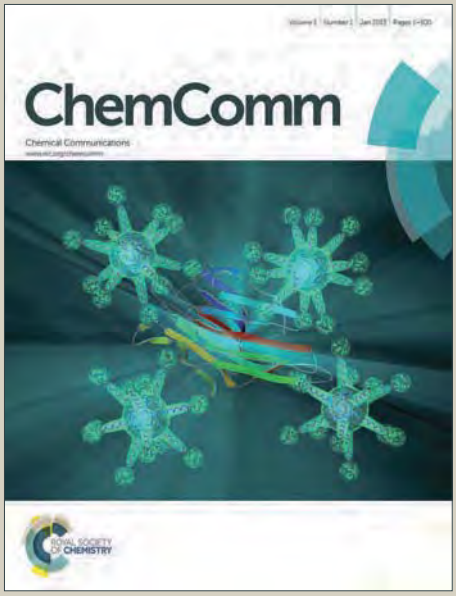

ROYAL SOCIETY OF CHEMISTRY

Publishing

Cite this: DOI: 10.1039/x0xx00000x

Received 00th January 2012,
Accepted 00th January 2012

DOI: 10.1039/x0xx00000x

www.rsc.org/

–

2–

–

–

2–

–

–/2–

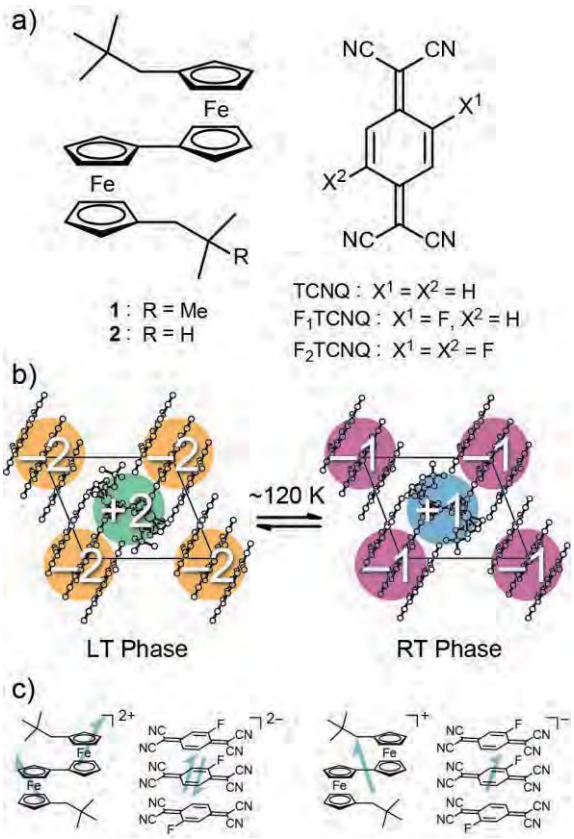

ChemComm Accepted Manuscript

T

x

3(1−

χ

≤ 0.6. The phase diagram obtained from the data is shown in

2−

2−

3−

:(1−

2−

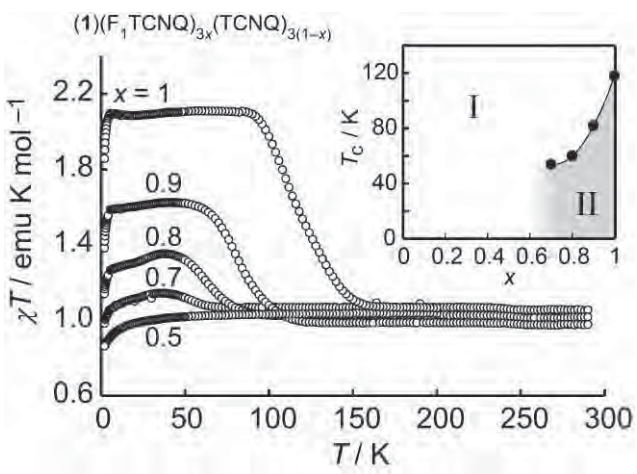

χ T

x 3(1−x x

3(1−

3−

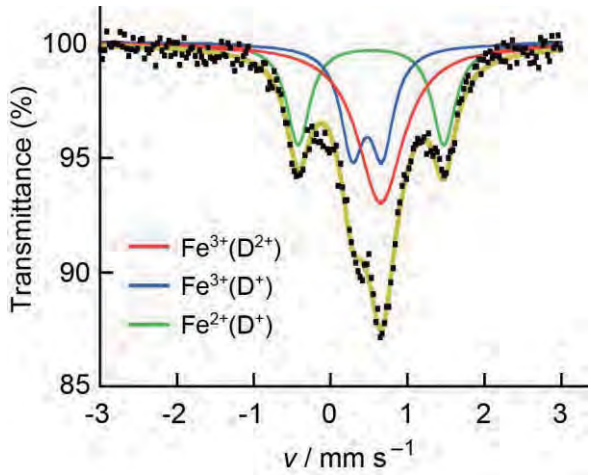

x 3(1−x x

ChemComm Accepted Manuscript

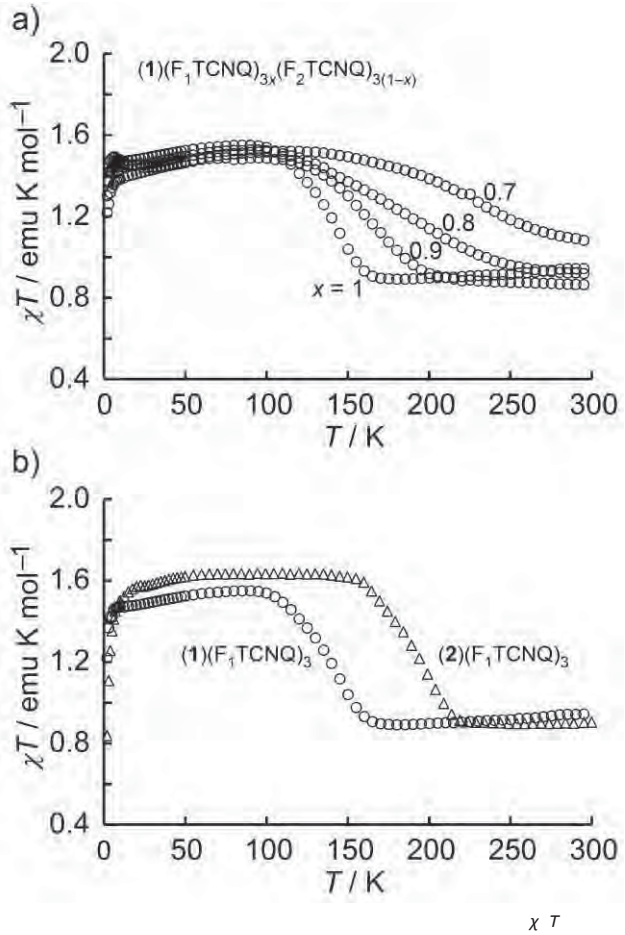

χ T

x 1−x x

3(1−

ChemComm Accepted Manuscript

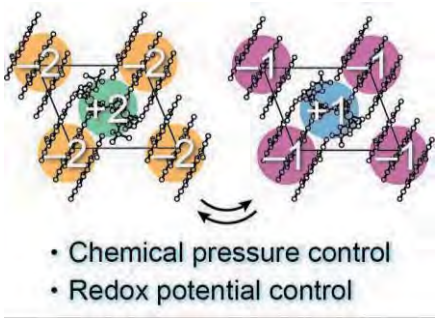

ChemComm Accepted Manuscript

Current Status and Application of Woodceramics Made from Biomass

Toshihiro OKABE, Kazuhiko KAKISHITA*, Hirotaka SIMIZU*, Kazuhiko Ogawa**, Yuko NISHIMOTO***, Akito TAKASAKI****, Toshikazu SUDA*****, Masami FUSHITANI******, Hitoshi TOGAWA*******, Minoru SATO******* and Ryouichi YAMAMOTO*******

Industrial Research Institute, Aomori Prefecture Industrial Technology Research Center, 221-10 Yamaguchi, Nogi, Aomori, 030-0142, Japan, E-mail: toshihiro_okabe@aomori-itc.or.jp
*Dept. Electrical System Eng., Polytechnic Univ., Hashimotodai, Midori-Ku, Sagamihara, Kanagawa, 252-5196, Japan,
** Polytechnic Center Hiroshima, Konan, Naka-ku, Hiroshima, Hiroshima, 730-0825, Japan
**Dept. Sci., Kanagawa University, Tsuchiya, Hiratsuka, Kanagawa, 259-1293, Japan
***Dept. Eng. Sci. & Mechanics, Shibaura Inst. of Tech., Toyosu, Koto-ku, Tokyo, 108-8548, Japan
****MitsuzawaECOTech.Lab., Mitsuzawa-minami, Kanagawa-ku, Yokohama, Kanagawa 221-0854, Japan.
*****Faculty of Agriculture, Tokyo Univ. of Agriculture and Technology, 3-5-8 Saiwai-cho, Fuchu-shi, Tokyo 183-8509, Japan
******Tokin EMC Engineering Co., Ltd., 398 Shibokuchi, Takatsu-ku, Kawasaki, Kanagawa 213-0023, Japan
*******Institute of Industrial Science, Univ. Tokyo, Komaba, Meguto-ku, Tokyo 153-8505, Japan

Woodceramics (WCMs) are the new functional carbon materials fabricated by sintering woody materials impregnated with phenolic resin. The fabrication process, properties and application of WCMs are introduced. The properties of WCMs depend on the sintering condition. WCMs have been studied as humidity and gas sensors, electrode for polymer electrolyte fuel cell (PEFC) and electromagnetic wave absorber. Electrical impedance of WCMs changes as humidity and ammonia gas concentration vary. The generated power of the PEFC with WCMs electrodes is almost the same as that of the PEFC with carbon paper electrodes. The shielding and loss properties of the electromagnetic wave absorber made from WCMs denote the same tendency of that of commercially-used electromagnetic wave absorber.
Key words: Woodceramics, Humidity Sensor, Gas Sensor, Polymer Electrolyte Fuel Cell, Electromagnetic Wave Absorber, Heat Source

1. INTRODUCTION

In Japan, forty million tons of industrial and trade waste went to final disposal and 20% of them, eight million tons were demolition scrap, totaled by the Ministry of the Environment of Japan in 2008. Of course, many of scrap is inorganic scrap like concrete scrap, therefore Government of Japan promoted the recycle use of demolition scraps, but a lot of organic waste like woody scrap were not suitable for recycle use. Faced with a protection of the global environment such as recycle of organic waste and limit emissions of carbon dioxide and other greenhouse gases, carbon materials are attracting much attention. There are many structures of carbon material such as graphite, amorphous carbon, diamond and its intermediate structures depending on raw materials and process of manufacture. However, the manufacturing process of ordinary carbon materials is complicated, expensive, and manufacture of complex shape is difficult. Therefore, the development of new carbon materials with superb functionality has been expected.

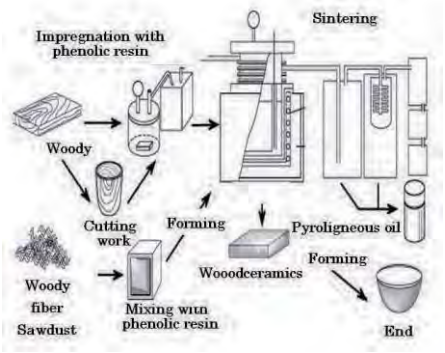

Fig.1 Fabrication process of WCMs

Woodceramics (WCMs here after) is developed with the aim of the carbon material with superb functionality and value-added using organic waste. In this paper, fabrication process, properties and some application of WCMs are introduced.

1.1 Fabrication Process of Woodceramics

Fabrication process of WCMs is shown in Fig.1 [1,2]. WCMs are fabricated by sintering woody materials impregnated with phenolic resin to form glassy carbon which reinforces the fibrous structure of non-graphitizable carbon. WCMs are processable before or after sintering, so that WCMs is suitable to both of mass and small productions. The structure of WCMs is porous as is characteristic of wood and the WCMs have the prominent characteristics of lightweight, hardness, corrosion resistance and heat resistance.

WCMs can be fabricated from waste wood, waste paper, saw dust and so on. Thermolysis products derived during sintering, wood tar and pyroligneous oil can be used as an antibacterial agent and also a medicine. From the calculation result of carbon consumption, WCMs is the carbon holding material like chipboard, whereas steel, aluminum and concrete, in contrast, are the carbon emitting materials [3-5]. WCMs sintered at 800°C holds about 170 kg/m^3 of carbon corresponding to about 42500 MJ/m^3 (12 Mwh/m^3) of fossil fuel energy.

1.2 Properties of Woodceramics

Properties of WCMs depend mainly on the sintering temperature [6-10]. Figures 2 and 3 show the sintering temperature dependence of bending strength and bending elastic modulus, respectively. The bending strength decreases in the temperature range from 300°C to 500°C and increases above 500°C. The bending elastic modulus monotonically increases with increasing sintering temperature. Electrical resistivity drastically decreases from insulator range to conductor range with increasing sintering temperature, as shown in Fig.4.

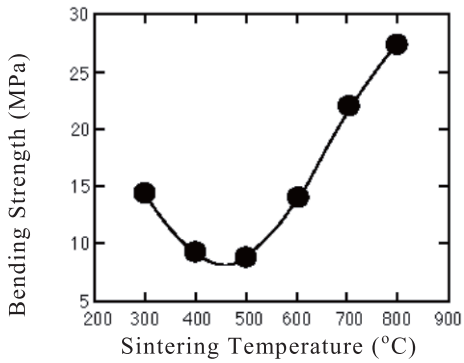

Fig.2 Sintering temperature dependence of bending strength

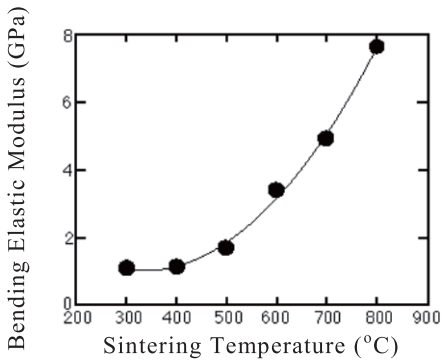

Fig.3 Sintering temperature dependence of Bending elastic modulus

2 APPLICATIONS OF WOODCERAMICS

2.1 Application of Woodceramics for Sensors

In particular, WCMs have the porous structure caused by woody fiber, so that WCMs has been developed as a humidity sensors and gas sensors [11-15]. Humidity dependence of electrical impedance for WP-WCMs (WCMs made from waste paper; postal card) and CP-WCMs (WCMs made from cotton paper) is shown

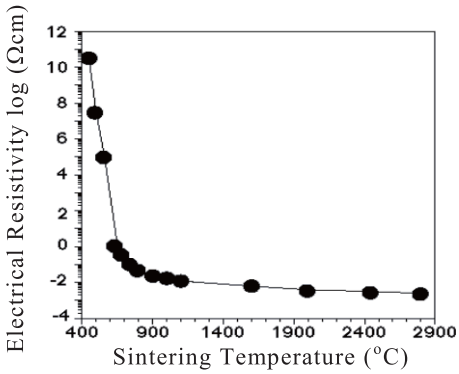

Fig.4 Sintering temperature dependence of Electrical Resistivity

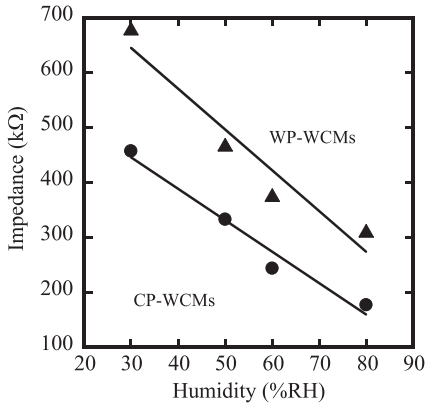

Fig.5 Humidity dependence of electrical impedance of WCMs

in Fig.5. It is obvious that the impedance linearly decreases with the increase of humidity in the range between 30%RH and 80%RH.

Although a large number of polymer sensors widely used, those are limited in usage at low temperatures and tend to have mold grown on the sensor surface by prolonged use. Using WCMs has an advantage of being able to avoid the mold. In addition, electrical impedance of WCMs shows linear change to humidity, compared with logarithmic change for polymer sensors, so that the sensitivity of humidity is the same in entire measuring range. With more research of operating temperature limit, WCMs is expected as the humidity sensors usable at high temperature.

The electrical impedance for WP-WCMs also changes with ammonia gas. Figure 6 shows impedance response to ammonia gas for various gas concentrations at working temperature of 40°C. When ammonia gas is put into the test box, the resistance increases and then saturates after 100 min from the inlet of ammonia gas. Saturated value of resistance increases as the ammonia gas concentration increases. When air or moisture is put into the test box taking over the ammonia gas, resistance does not change. The popular ceramic gas sensors need a high temperature to drive, however WCMs gas sensor can be operated at 40°C. Thus, it seems that WCMs is suitable for ammonia sensor which can be used at extremely low temperature. The impedance of WCMs

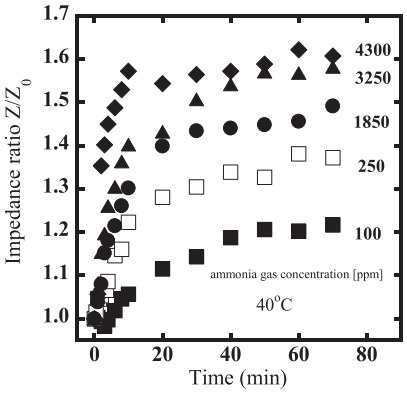

Fig.6 Impedance response to ammonia gas for various gas concentrations

also changes due to the absorption of butyl acetate gas on the surface [15].

2.2 Application of Woodceramics for Electrode of Polymer Electrolyte Fuel Cell

The application of WCMs sheet to electrode for polymer electrolyte fuel cell (PEFC) has been proposed [16-18]. The WCMs electrode was made from a paper filter. By estimating the chemical composition contained in the WCMs electrode using X-ray fluorescence analysis, we confirmed that the amount of impurities in the electrode was small. The filter paper was immersed into a methanol solution of phenolic resin for impregnation of phenolic resin. We prepared some solutions with different concentrations to investigate the influence of the degree K of the impregnation of phenolic resin to investigate the influence on the power generating performance.

Figure 7 shows the power density as a function of the current density. This figure indicates the results for K=0%, 28.2% and 42.0% together with that of carbon paper which is one of the most popular materials for PEFC electrode. As seen from this figure, the power density-current density characteristic of the PEFC has the maximum value. The maximum power density of K=28.2% was 340 mW/cm^2 and was the highest of the three. This value corresponded to 88% of that of the carbon paper. The optimum degree K of impregnation of phenolic resin may exist where the maximum power density is the highest. The generated power depends on

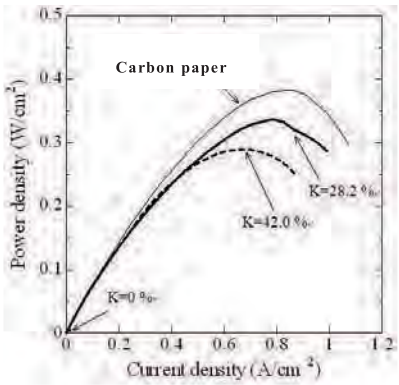

Fig.7 Relationship between power density and current density.

the electric resistivity and gas permeability of the electr ode. In the case of the electrode with too large K, the output power may be low because of bad gas permeability. On the other hand, if the electrode has too small K, the output power may also be low. That is because the mechanical strength may decrease with a decrease in K. This means that there may be the optimum K from the viewpoint of the output power. Considering of the cost reduction and low environmental impact, there is possibility of utilization of WCMs as an electrode for PEFC.

2.3 Application of Woodceramics for Electromagnetic Wave Absorber

Figure 8 (a) shows the electromagnetic wave absorber containing WCMs. After WCMs sintered at 1000°C was smashed to several micrometers powder, they were dispersed in polyvinyl alcohol (PVA) resin with polymerization degree of about 500 and then molded into the pyramid shape. Figure 9 shows electromagnetic wave reflection coefficient of electromagnetic wave absorber containing WCMs. The reflection characteristic of the electromagnetic wave absorber containing WCMs is equivalent to that of commercial absorber made of carbon material originated from oil.

Although it has been reported that WCMs are effective materials as an electromagnetic shield material [19], the technique to use WCMs as an electromagnetic loss material has been unexplored. The electromagnetic wave absorber usually has concavo-convex shape to broaden out the frequency characteristic. Recently, the technique to disperse WCMs into the concavo-convex shaped base material made with recycled pulps (Fig.9(b)) has been

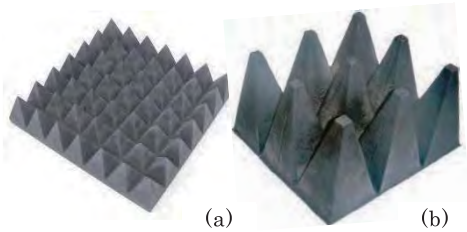

Fig.8 Electromagnetic Wave Absorber (a) using WCMs (b) using WCMs and recycling pulp for basis material[20)]

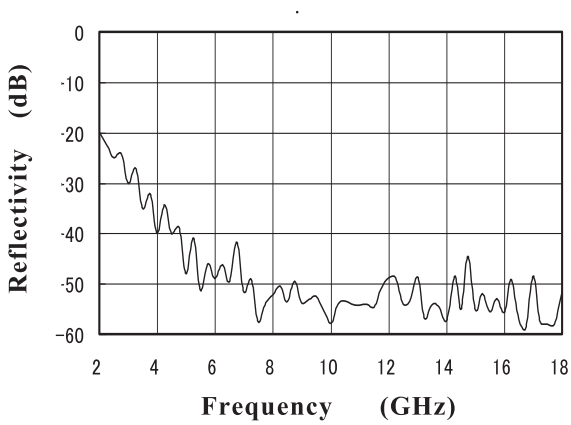

Fig.9 Electromagnetic wave reflection coefficient characteristics of electromagnetic wave absorber containing WCMs

developed [20] and it is confirmed that the reflection coefficient is so good to use as an electromagnetic wave absorber. In order to utilize WCMs as an electromagnetic loss material and to achieve reproducible result of electromagnetic characteristics, the sintering temperature, dispersion and adherability to a base material and the structure of WCMs formed on the base material are the problems that need to be solved.

2.4 Application of Woodceramics for Heat Source

Figure 10 and 11 show the far-infrared emission characterstics for WCMs sintered at 650°C. In Fig.10, the emissivity is normalized by the emissivity of black body as 100%. The spectral emissivity is about 90% of that of black body and independent of the wavelength between 5.0 μm and 25 μm. The wavelength dependence of distribution of radiated energy for WCMs at 194°C is indicated in Fig.11. It is obvious that distribution of radiated energy is very similar to that of black body. These results suggest that the WCMs is suitable for heat source for industrial use and heating.

3 CONCLUSIONS

The fabrication process, properties and some application of WCMs are introduced. The properties of WCMs depend on the sintering condition. WCMs have been studied as various applications, humidity and gas sensors, electrode for PEFC, electromagnetic wave absorber and so on. WCMs can be fabricated from the raw materials contained with carbon. Recently, WCMs fabricated from apple pomace, and excretion of barn animal has been developed.

WCMs can be fabricated from wood-based industrial waste and the thermolysis products derived during sintering can be used as an antibacterial agent and a medicine. After usage of WCMs, it can be used as active carbon, fuel and barnyard manure. WCMs are environmentally conscious composite materials (ecomaterials) designed for minimizing the environmental impacts and one of the important materials to accelerate the creation of a recycling society.

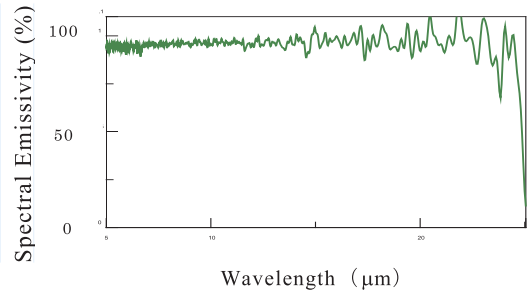

Fig.10 Wavelength dependence of spectral emissivity for WCMs.

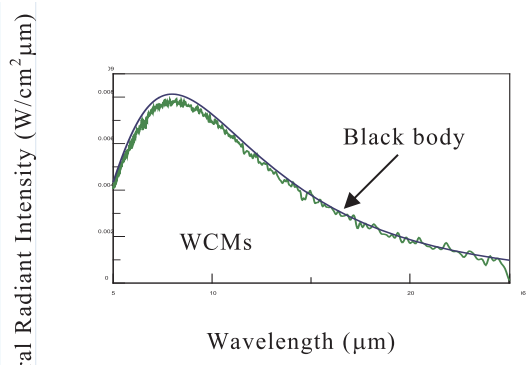

Fig.11 Wavelength dependence of spectral radiant intensity for WCMs.

References

[1] T. Okabe and K. Saito, " A manufacturing method of the woodceramics", 1992-164806, JP (1992).

[2] T. Okabe, " Wood system carbon material wood ceramics", Uchida rokakuho (1996), pp.42-111.

[3] A. H. Buchannan, *Proceeding 1990 International Timber Engineering Conference*, 931(1990).

[4]http://www.enecho.meti.go.jp/topics/hakusho/2010energyhtml/data/221-1-2.xls

[5]http://cdiac.ornl.gov/ftp/ndp030/global.1751_2007.ems

[6] T. Okabe, K. Saito and K. Hokkirigawa, *J. Porous Mater.*, 2, 215-221(1996).

[7] T. Okabe, K. Saito, M. Fushitani and M. Otsuka, *J. Porous Mater.* 2, 207-213(1996).

[8] K. Hata, K. Shibata, T. Okabe and M. Outuka, *J. Porous Mater.* 7, 483-490(2000).

[9] K. Ogawa, M. Stato, K. Hata, M. Mayuzumi, T. Okabe, M. Ogawa and M. Otsuka, *Trans. Mater. Rec. Soc. Jpn.*, 30, 1183-1186(2005).

[10] K. Shibata, K. Kasai and T. Okabe, *J. Porous Mater.* 2, 287-290(1996).

[11] T. Suda, *Kinouzairyou*, 4, 21-28(2001).

[12] K. Kakishita, S. Asai and T. Suda, *Trans. Mater. Rec. Soc. Jpn.*, 28, 1049-1051(2003).

[13] K. Kakishita and T. Suda, *Trans. Mater. Rec. Soc. Jpn.*, 29, 2427-2430(2004).

[14] K. Kakishita, and T. Suda, *Trans. Mater. Rec. Soc. Jpn.*, 30, 1187-1190(2005).

[15] H. Mito, K. Kakishita, T. Suda and M. Murakami, *Trans. Mater. Rec. Soc. Jpn.*, 33, 1221-1223(2008).

[16] H. Shimizu, K. Hashimoto, N. Watanabe, K. Kakishita, T. Suda and T. Okabe,, *Trans. Mater. Rec. Soc. Jpn.*, 31, 941-944(2006).

[17] H. Shimizu, K. Hashimoto, H. Mito, N. Watanabe, K. Kakishita, T. Suda and T. Okabe, *Trans. Mater. Rec. Soc. Jpn.*, 32, 1051-1054(2007).

[18] H. Shimizu, K. Hashimoto, H. Mito, N. Watanabe, K. Kakishita, T. Suda and T. Okabe, *Trans. Mater. Rec. Soc. Jpn.*, 32, 1055-1058(2007).

[19]T. Okabe, K. Saito, H. Togawa and Y. Kumaga, *J. Soc. Mater. Sci.*, 44, 284-287(1995).

[20]http://www.tee.tokin.jp/solution/kyushutai/eco100.html

,

,

≃

δ

δ

● :　　□ :

δ

period at 277K on tanδ

▽ :
○ :
□ :
◇ :
× :
△ :

′　　″

■ :
● :

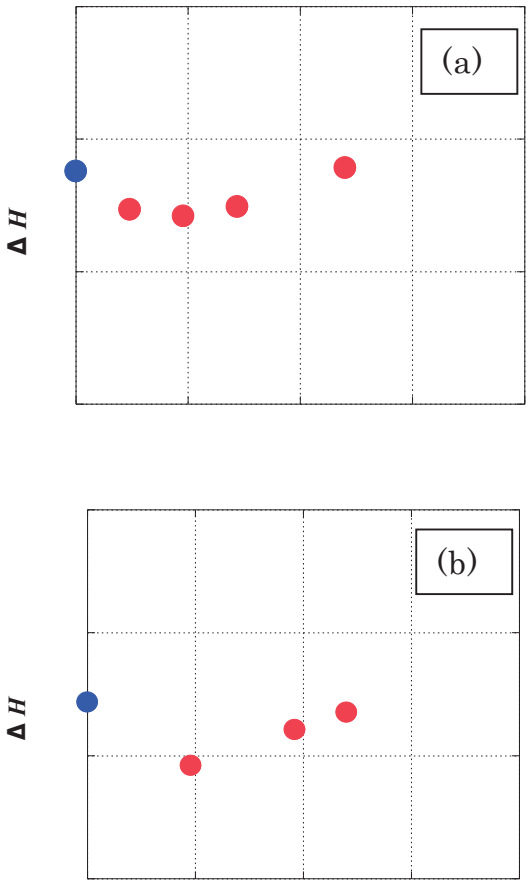
(a)
(b)
Δ H
Δ H

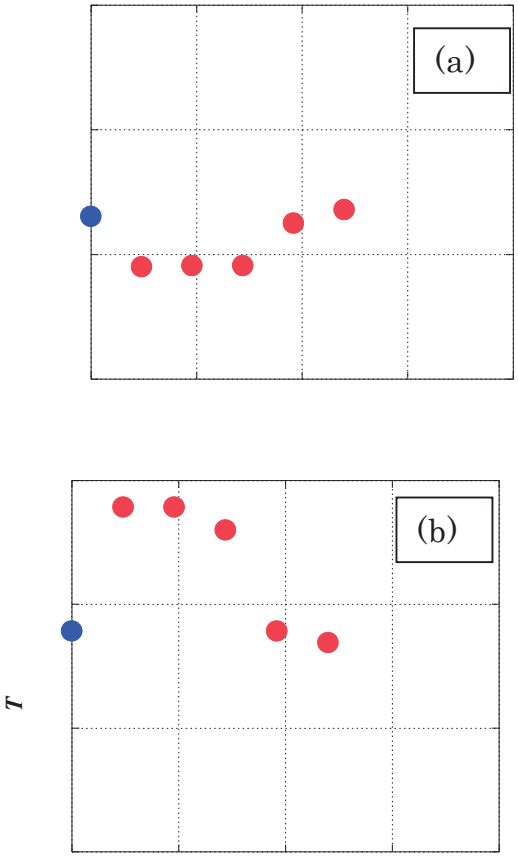
(a)
(b)
T

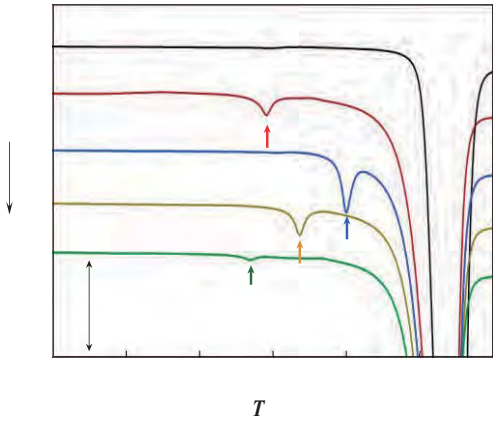
T

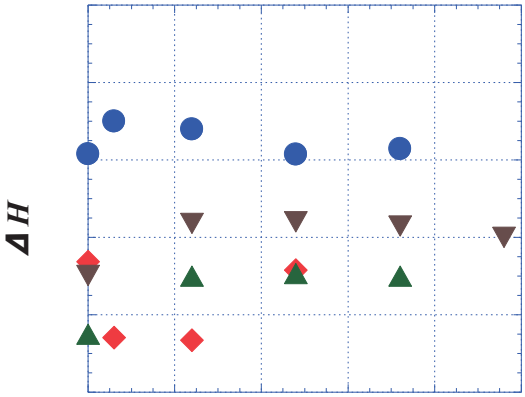
ΔH

◆ :　　● :　　▼ :　　▲ :

.

 © 2014 The Chemical Society of Japan

BCSJ Award Article

Computational Study on the Mechanism of the Electron-Transfer-Induced Repair of the (6–4) T–T Photoproduct of DNA by Photolyase: Possibility of a Radical Cation Pathway

Toshiaki Matsubara,* Nozomi Araida, Daichi Hayashi, and Hatsumi Yamada

Department o Chem stry, Facu ty o Sc ence, Kanagawa Un vers ty, 2946 Tsuch ya, H ratsuka, Kanagawa 259-1293

Rece ved October 25, 2013; E-ma : matsubara kanagawa-u.ac.jp

The oxetane and the non-oxetane mechan sms o the e ectron-trans er-dr ven repa r o the (6 4) T T photo es on o DNA by photo yase are exam ned by dens ty unct ona theory (B3LYP). We ca cu ated the rad ca cat on pathway n add t on to the rad ca an on and the neutra pathways or both mechan sms n order to assess the poss b ty o the rad ca cat on pathway, because re at ve y arge energy barr ers have been ound or the rad ca an on pathway. As a resu t, the rad ca an on pathway showed a arge energy barr er n both the oxetane and the non-oxetane mechan sms n agreement w th prev ous ca cu at ons. However, t was ound that the rad ca cat on pathway o the oxetane mechan sm has a rea st c ow energy barr er. Th s advantage o the rad ca cat on pathway was ascr bed to the pos t on o the rad ca be ore the ormat on o the oxetane and the stab ty o the oxetane n energy.

DNA s h gh y a react ve substance and s there ore read y n uenced and damaged, because the ns de o the ce s under chem ca y act ve cond t ons due to u trav o et rays, chem ca substances, and so on. In act, DNA s rout ne y damaged and var ous types o DNA es ons are known.[1] D mer zed adjacent thym nes, c ass ed as s ng e-strand damage, s a so one o such DNA es ons. A though DNA es ons can be an or g n o d seases such as cancer, damaged DNA s mmed ate y recovered through a repa r process[1] n order to ma nta n norma genet c n ormat on.

For examp e, ormed thym ne d mer s repa red by photo- yase under photo rrad at on n p ants and bacter a.[2] Many peop e have ocused on th s repa r process as a mode and have endeavored to understand ts mechan sm.[3] There ex st two orms o thym ne d mer, cyc obutane pyr m d ne d mer (CPD) and (6 4) photoproduct (F gure 1), and many exam nat ons o the repa r mechan sm have been conducted espec a y or the case o CPD. Photo yase s a avoprote n that has a chromophore co actor av n aden ne d nuc eot de (FAD) (F gure 1) p ay ng an mportant ro e as a coenzyme. A second chromophore co actor that unct ons as an antenna harvest ng b ue ght, metheny tetrahydro o ate (MTHF) or 8-hydroxy-7,8-d demethy -5-deazar bo av n (8-HDF), s a so present ns de the prote n. The FAD, wh ch s thought to be u y reduced to FADH ns de the prote n, s bur ed n the v c n ty o the act ve s te. On the other hand, the second co actor s urther deep y bur ed and a tt e ar rom FAD.

The genera y proposed mechan sm o the repa r react on o the thym ne d mer on the bas s o prev ous nd ngs or CPD

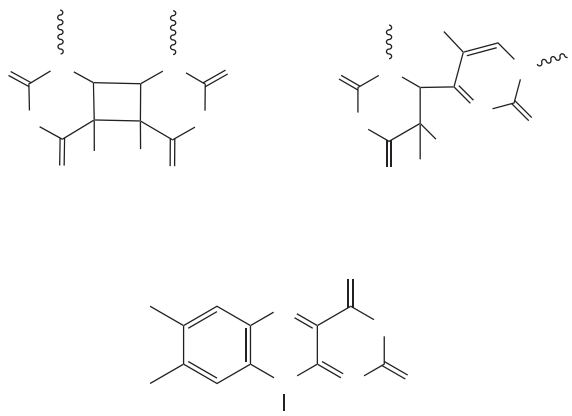

Figure 1. The structures o the DNA T T es ons, cyc o-butane pyr m d ne d mer (CPD) and (6 4) photoproduct, and the co actor av n aden ne d nuc eot de (FAD).

s d sp ayed n F gure 2A. The unct on o the photo yase or g nates n the b ue- ght harvest by the second chromophore co actor. The e ectron c state o the second co actor that absorbed the ght s enhanced to an exc ted state and th s exc tat on energy s transm tted to the other co actor FADH when the exc ted state o the second co actor returns to the ground state. The FADH , wh ch rece ved the energy, becomes an ex ted state FADH * and then unct ons as an e ectron

Pub shed on the web March 15, 2014; do :10.1246 bcsj.20130298

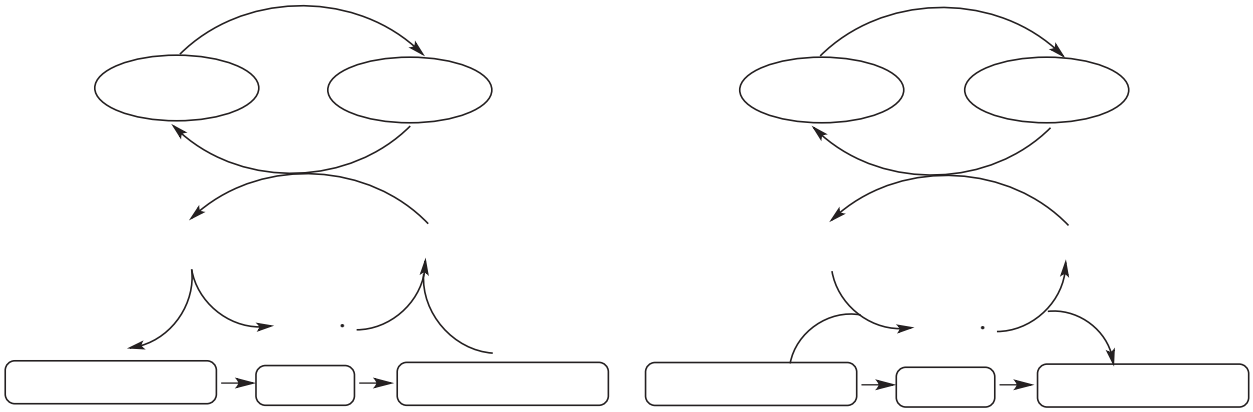

Figure 2. Mechan sm o the repa r react on o the (6 4) T T photoproduct by the photo yase proposed on the bas s o recent reports. The react on proceeds by the e ectron trans er rom the co actor FADH to the T T es on n A and rom the T T es on to the co actor FADH n B.

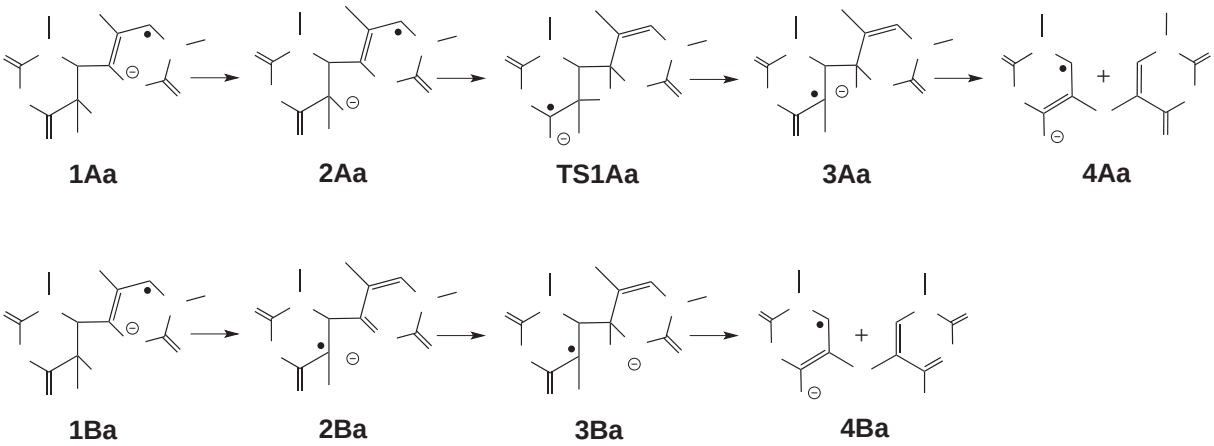

Figure 3. Convent ona y proposed mechan sms o the e ectron-trans er- nduced repa r o the (6 4) T T photoproduct o DNA.

donor. So, when an e ectron s trans erred rom the FADH * to the T T photo es on o DNA bound to the act ve s te o the photo yase, the repa r react on s commenced.

The current y proposed react on mechan sm o the sp tt ng process o the (6 4) photoproduct s presented n F gure 3.[4,5] In the past, t was genera consensus that the oxetane s eas y ormed thermochem ca y rom the (6 4) photoproduct be ore the b nd ng o the (6 4) photoproduct w th the act ve s te o the photo yase. The e ectron trans er was there ore thought to take p ace a ter the b nd ng o the oxetane w th the photo yase. However, th s assumpt on was contrad cted by a recent y reported crysta ograph c structure o a photo yase that com- b nes w th the (6 4) photoproduct,[6] wh ch shows that the e ectron trans er takes p ace not at the ntermed ate oxetane but at the start ng (6 4) photoproduct. F gure 3A d sp ays the repa r mechan sm v a the oxetane n the case o the rad ca an on. Here, the oxetane o the rad ca an on ex sts not as an equ br um structure but as a trans t on state. The repa r react on commences rom the (6 4) photoproduct **1Aa**. The hydroxy hydrogen at rst m grates to the n trogen o the other mo ety as a proton n the rst step, **1Aa** → **2Aa**. In the second step **2Aa** → **TS1Aa** → **3Aa**, the oxetane s ormed at the trans t on state **TS1Aa** and the C O bond o the oxetane s broken a ter the trans t on state to orm **3Aa**. The sp tt ng o the thym ne d mer s comp eted by the C C bond break ng n the na step, **3Aa** → **4Aa**. Another repa r mechan sm by OH trans er, wh ch does not pass through the oxetane, s presented n F gure 3B. The hydroxy group o the start ng (6 4) photoproduct **1Ba** s trans erred v a the ntermed ate **2Ba** to orm **3Ba**. The sp tt ng o the thym ne d mer s s m ar y comp eted by the C C bond break ng n the na step, **3Ba** → **4Ba**.

Domratcheva et a . have recent y reported the energy pro es or both the oxetane and the non-oxetane mechan sms ca cu- ated by dens ty unct ona theory (DFT).[5] The ca cu ated energy pro es show that both mechan sms have to pass the arge energy barr er o 25 30 kca mo 1. In contrast, the energy barr er or the sp tt ng s on y about 2 kca mo 1 n the case o CPD.[7,8] The ca cu ated arge energy barr er or the (6 4)

photoproduct does not seem to be rea st c. Hence, one wou d th nk that another rea path must ex st to escape such arge energy barr ers. Sadegh an et a . proposed such a path n the oxetane mechan sm,[9] where the e ectron trans er between the co actor FAD and the T T es on at the act ve s te occurs two t mes. However, the arge energy barr er at the oxetane tse bas ca y rema ns as t s. The contr but on o the ne ghbor ng H s res due to the repa r react on has been a so computat ona y exam ned by Faraj et a . or the non-oxetane mechan sm[10] on the bas s o a recent y proposed mechan sm.[11] The ca cu ated energy barr er o about 20 kca mo 1 s st not ow enough. Consequent y, n the present study, we exam ned the sp tt ng o the (6 4) photoproduct n the case o the rad ca cat on (F gure 2B) to search other e c ent pathways, a though the e ectron trans er rom the T T es on to the co actor FAD has been tt e cons dered except some computat ona exam nat ons or the CPD[8,12] and the (6 4) photoproduct.[13] I the co actor FAD ex sts as the u y reduced orm FADH , the exc ted FADH * ormed by an energy transm ss on rom the second co actor m ght rece ve an e ectron rom the T T es on,[3,12,14] wh ch resu ts n the ormat on o FADH•2 as presented n F gure 2B. The ormed FADH•2 returns to the FADH g v ng the e ectron back to the d ssoc ated thym ne ragments T:T(•). I the FADH• ormed under some cond t ons as prev ous y reported[3,12,15,16] contr butes to the e ectron trans er, t undergoes a am ar reduced state FADH nstead o FADH•2 . A though the var ous reduced states o the FAD have been n act exam ned by both exper ments[17] and computat ons,[7,12,13b] they are not u y c ar ed and there s yet tt e n ormat on on the e ectron-trans er mechan sm n the case o the (6 4) photoproduct.

In the present study, we there ore concentrate on the search or a pathway w th a ow energy barr er cons der ng the rad ca cat on o the (6 4) photoproduct. We conducted the ca cu a-t ons or both the oxetane and the non-oxetane mechan sms o the e ectron-trans er- nduced repa r o the (6 4) T T photoproduct at the B3LYP eve o theory n order to exam ne the poss b ty o the rad ca cat on pathway. The repa r react on was o owed by a mode system o (6 4) T T photoproduct and ts surround ng am no ac ds were approx mated by the po ar zed-cont nuum-mode (PCM), because the surround ng am no ac ds are not essent a n the d scuss on o the energy pro e o the repa r react on.[9]

Computational Method

A the ca cu at ons were per ormed us ng the Gauss an03 program package.[18] We o owed both the oxetane and the non-oxetane mechan sms o the e ectron-trans er- nduced (6 4) T T photoproduct repa r us ng a mode mo ecu e o the (6 4) T T photo es on o DNA. The env ronment o am no ac ds was approx mated by the PCM, because the surround ng am no ac ds are not essent a n the repa r react on as ment oned n the Introduct on.

The geometry opt m zat ons were per ormed by dens ty unct ona theory (DFT) at the B3LYP eve o theory, wh ch cons sts o a hybr d Becke Hartree Fock exchange and Lee Yang Parr corre at on unct ona w th non oca correct ons.[19] For the bas s set, we adopted the tr p e 6-311G used n the prev ous ca cu at on[5] n order to reproduce the structure nvo ved n the repa r react on. The energ es o the opt m zed structures were mproved us ng a h gher eve bas s set aug-cc-pVTZ.

A equ br um structures and trans t on states were den-t ed by the number o mag nary requenc es ca cu ated rom the ana yt ca Hess an matr x. The react on coord nates were o owed rom the trans t on state to the reactant and the product by the ntr ns c react on coord nate (IRC).[20] The therma correct on to the G bbs ree energy, wh ch was ca cu ated at the B3LYP 6-311G eve w th a sca e actor o 0.9614[21] or ca cu ated v brat ona requenc es at the temperature o 298.15 K, was used to ca cu ate the G bbs ree energy at the B3LYP aug-cc-pVTZ eve . The NBO ana ys s[22] was per ormed to obta n the atom c charge. The surround ng am no ac ds were taken nto account by the PCM approx mat on[23] us ng the d e ectr c constant o 5.7.[24] The ca cu at ons w th the d e ectr c constant o 80 were a so per ormed assum ng a water med um or compar son. The bas s set superpos t on error (BSSE) nc uded n the nteract on energy between two thym nes o the oxetane was corrected by the counterpo se method.[25]

We added **A** and **B** as su xes to the abe s o the equ br um and the trans t on state structures to d st ngu sh the oxetane and the non-oxetane mechan sms, and a so added **n**, **a**, and **c** to d st ngu sh the neutra , rad ca an on, and the rad ca cat on.

Results and Discussion

We exam ned a the cases o the neutra , rad ca an on, and the rad ca cat on or both the oxetane and the non-oxetane mechan sms start ng rom the (6 4) T T photoproduct a ter the e ectron trans er.

Structures Involved in the Oxetane Mechanism. The opt m zed equ br um and trans t on state structures o the repa r react on v a the oxetane are d sp ayed n F gure 4. We a so ca cu ated or the neutra n add t on to the rad ca an on and the rad ca cat on or the compar son. In the case o the neutra , the oxetane ex sts as an equ br um structure so that the T T d ssoc at on react on cons sts o two steps. The rst step s the m grat on o the OH hydrogen to the n trogen and the attack o the OH oxygen on the carbon o the other mo ety o the T T d mer n the (6 4) photoproduct **1An** to orm the oxetane **2An** through the trans t on state **TS1An**. The second step s the d ssoc at on o the C C and the C O bonds o the T<>T oxetane to orm the repa red T:T **3An** pass ng through the trans t on state **TS2An**. The mportant geometr c parameters are summar zed n Tab e 1. The d stance o the O1 C3 decreases to 1.546 Å to orm a chem ca bond n the oxetane **2An** and urther decreases to 1.248 Å to orm a C O doub e bond n the product **3An**. On the other hand, the d stance o the C1 C2 s a most constant unt **2An**, but shortened to 1.355 Å n **3An** to orm a C C doub e bond. The ormat on o the O1 C3 bond n **2An** does not pract ca y a ect the C1 C2 bond. In contrast, both C1 O1 and C2 C3 bonds are stretched by 0.06 0.07 Å n **2An** due to the ormat on o the O1 C3 bond.

In the case o the rad ca an on, a ter the m grat on o the OH hydrogen, the repa r react on essent a y proceeds by one step pass ng through the trans t on state **TS1Aa** o the oxetane (F gure 4). A though **3Aa** was ound as an equ br um structure, t d sappeared when the bas s set 6-311G s sw tched to

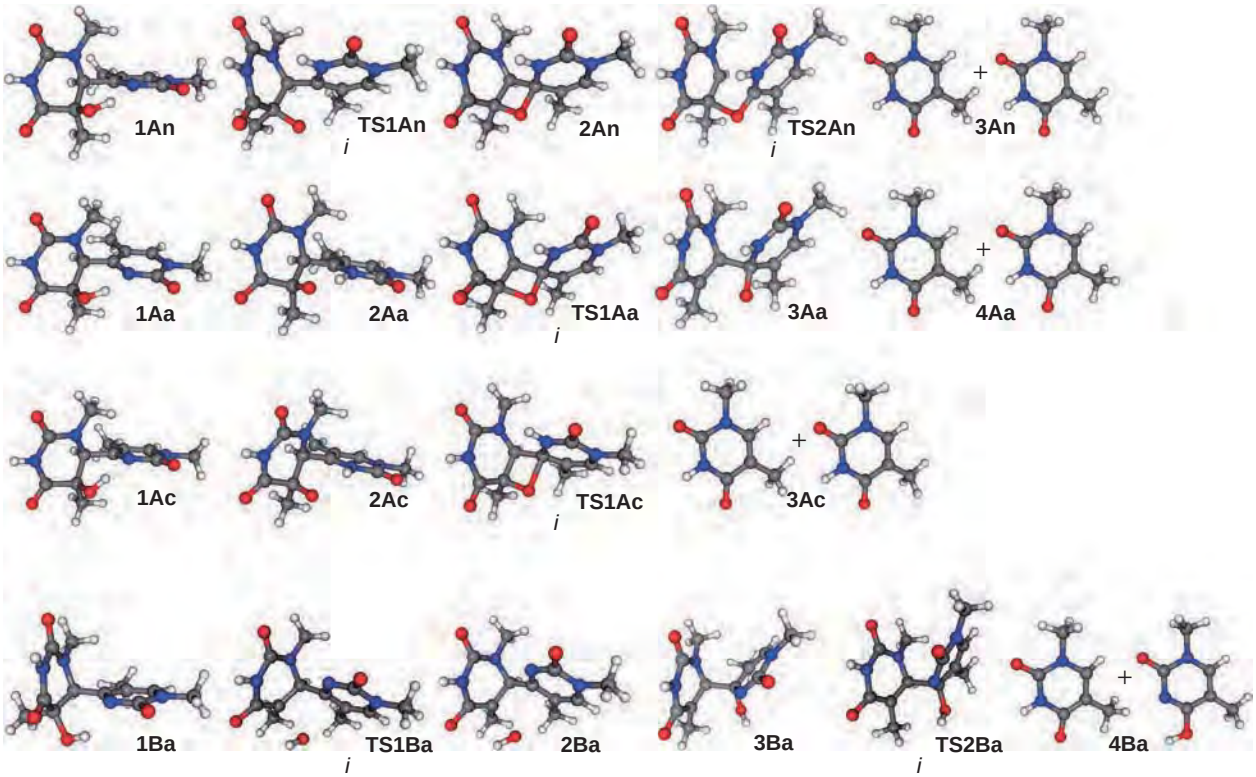

F gure 4. Opt m zed equ br um and trans t on state structures o the oxetane and the non-oxetane mechan sms n the cases o the neutra , rad ca an on, and the rad ca cat on at the B3LYP 6-311G eve . The re at ve potent a energ es (n kca mo ^{1}) together w th the mag nary requenc es (n cm ^{1}) o the trans t on states are a so presented. See Tab e 1 or the geometr c parameters.

another bas s set w th po ar zat on unct ons. The trans t on state rom **3Aa** to **4Aa** was on y 0.2 kca mo ^{1} h gher than **3Aa**. Th s resu t s the same as that o the prev ous ca cu at on.[5] The changes n the geometr c parameters re ated to the repa r react on are bas ca y s m ar to the case o the neutra as presented n Tab e 1, a though the oxetane n the trans t on state **TS1Aa** shows a re at ve y ong C1 O1 d stance o 1.695 Å and short O1 C3 d stance o 1.464 Å. The C1 C2 d stance o the sp t thym ne ragment o the rad ca an on s onger than that o the other thym ne ragment o the neutra because the rad ca s on the C2 atom (F gure 8). The repa r react on n the case o the rad ca cat on s qu te s m ar to the case o the rad ca an on as shown n F gure 4. The repa r react on proceeds by one step pass ng through the trans t on state **TS1Ac** a ter the m grat on o the OH hydrogen. However, **TS1Ac** s an ear y trans t on state so that ts structure s a tt e d erent rom oxetane. Th s s re ected n the ong O1 C3 d stance o 1.866 Å n **TS1Ac** (Tab e 1). The C1 C2 d stance o the sp t thym ne ragment o the rad ca cat on s a so onger than that o the other thym ne ragment o the neutra , because the rad ca s on the C1 atom (F gure 8) as ment oned ater.

Structures Invo ved n the Non-Oxetane Mechan sm. A though we a so o owed the non-oxetane mechan sm or three cases o the neutra , rad ca an on, and the rad ca cat on, the structures nvo ved n the repa r react on are d sp ayed on y or the case o the rad ca an on n F gure 4. The con ormat on o the start ng (6 4) T T photoproduct **1Ba** n the case o the non-oxetane mechan sm s d erent rom those o **1An**, **1Aa**, and **1Ac** n the case o the oxetane mechan sm.[5] The OH group n **1Ba** s d rected to the carbon to wh ch the OH group m grates, wh ch s re ected on the re at ve y short O1 C3 d stance o 2.782 Å (Tab e 1). The repa r react on occurs by the OH trans er, wh ch s o owed by the C C bond c eavage. S nce the trans t on state between **2Ba** and **3Ba** was very c ose to **2Ba**,[5] we cou d not nd t. The structures or the rad ca an on n F gure 4 was the same as those n the prev ous ca cu- at on.[5] As shown n Tab e 1, the O1 C3 d stance s gradua y shortened to orm a s ng e bond n **4Ba**, whereas the C2 C3 d stance s gradua y e ongated. The C1 C2 d stance becomes somewhat shorter a ter **3Ba** due to the de oca zat on o the e ectron (F gure 3).

The repa r react on n the case o the neutra and the rad ca cat on was ound to proceed by one step, where the m grat on o the OH group and the c eavage o the C C bond occurs at the same t me. To opt m ze these trans t on states n the case o the neutra and the rad ca cat on, we xed the C1 O1 and the O1 C3 d stances at the va ues p cked up rom **2Ba** and the C2 C3 d stance at the va ue p cked up rom **TS2Ba**, s nce t was hard to u y opt m ze these trans t on states. The opt m zed structures o these trans t on states were success u y obta ned w th these xed d stances and con rmed by the number o the mag nary requency and the d sp acement o the norma mode.

Energy Pro es o the Oxetane Mechan sm. The energy pro es o the oxetane mechan sm at the var ous eve s are

Tab e 1. Se ected Opt m zed Parameters (n Å) o the Equ br um and the Trans t on State Structures Invo ved n the Oxetane and the Non-Oxetane Mechan sms n the Cases o the Neutra , Rad ca An on, and the Rad ca Cat on

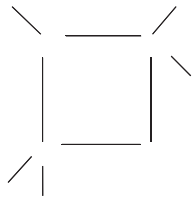

	d(C1 O1)	*d*(C2 C3)	*d*(C1 C2)	*d*(O1 C3)
Oxetane mechan sm				
Neutra				
1An	1.450	1.522	1.566	3.032
TS1An	1.488	1.558	1.545	2.200
2An	1.506	1.591	1.545	1.546
TS2An	1.841	2.252	1.440	1.383
3An			1.355	1.248
Rad ca an on				
1Aa	1.450	1.506	1.566	2.997
2Aa	1.412	1.501	1.587	2.934
TS1Aa	1.695	1.596	1.548	1.464
3Aa	2.299	1.592	1.521	1.398
4Aa[a)]			1.421 1.355	1.290 1.248
Rad ca cat on				
1Ac	1.435	1.519	1.575	2.895
2Ac	1.402	1.517	1.578	2.902
TS1Ac	1.493	1.572	1.548	1.866
3Ac[b)]			1.405 1.355	1.238 1.248
Non-oxetane mechan sm				
Rad ca an on				
1Ba	1.437	1.508	1.564	2.782
TS1Ba	2.169	1.549	1.525	2.526
2Ba	2.226	1.545	1.525	2.730
3Ba	2.858	1.626	1.491	1.515
TS2Ba	2.931	1.877	1.444	1.459
4Ba			1.421	1.369

a) The e t hand s de o the s ash s or the rad ca an on and the r ght hand s de o the s ash s or the neutra . b) The e t hand s de o the s ash s or the rad ca cat on and the r ght hand s de o the s ash s or the neutra .

presented n F gure 5. There s no s gn cant change n the eature o the energy pro e among the var ous eve s, a though the energy o the d ssoc ated T:T ragments s a ected by tak ng account o the entropy and the med um. The energy pro e o the neutra shows very arge energy barr ers n each step, suggest ng that the e ectron trans er s mportant n the repa r react on. However, the energy pro e o the rad ca an on a so has a arge energy barr er, because the oxetane s very unstab e n energy. In contrast, n the case o the rad ca cat on, the oxetane- ke trans t on state **TS1Ac** s very stab e due to the arge exotherm c ty o the react on so that the energy sur ace s qu te smooth. The trans t on state **TS1Ac** s on y 5 6 kca mo ^{1} ess stab e than the start ng (6 4) T T photoproduct **1Ac**. The energy barr er rom **2Ac** to **TS1Ac** s about 10 kca mo ^{1} when we cons der the G bbs ree energy n a d e ectr c med um. The structure o the trans t on state **TS1Ac** s ear y as ment oned above, wh ch s cons stent w th the Hammond postu ate.[26] A ter **TS1Ac**, the react on passes through the oxetane, wh ch s more stab e n energy than **1Ac**. Here, one w not ce that the stab ty o the oxetane s apparent y d erent among the neutra , rad ca an on, and the rad ca cat on, the order o the stab ty o the oxetane be ng rad ca cat on > neutra > rad ca an on. Th s s very nterest- ng, because the stab ty o the oxetane o the rad ca cat on s one o c ues to understand ng why the energy pro e o the rad ca cat on s so smooth as ment oned ater.

It shou d be a so noted here that the order o the break ng o the C C and the C O bonds o the oxetane s d erent among the neutra , rad ca an on, and the rad ca cat on. The p ots o the geometr c parameters versus the react on coord nate are presented n F gure 6. In the case o the neutra , both the C C and the C O bonds break ng occur a most concerted y. However, t s not concerted n the cases o the rad ca an on and the rad ca cat on. In the case o the rad ca an on, the C O bond s broken at rst and then the C C bond s subsequent y broken, whereas th s order s reversed n the case o the rad ca cat on, as the deta s are d scussed ater.

Energy Pro es o the Non-Oxetane Mechan sm. The energy pro es o the non-oxetane mechan sm at the var ous eve s are presented n F gure 7. It s obv ous that the OH trans er react on n the case o the neutra and the rad ca cat on s not mportant, because the trans t on states **TS1Bn** and **TS1Bc** or both cases are extreme y unstab e n energy and the energy barr ers are very arge. On the other hand, the energy barr er s reduced to ha n the case o the rad ca an on. The arge energy barr er ex sts n the rst step o the OH trans- er **1Ba** → **3Ba**. The second step o the C C bond break ng **3Ba** → **4Ba** s comb ned w th the rst step, because the tran- s t on state **TS2Ba** ound n the opt m zat on d sappeared at the h gher eve used or the energy ca cu at ons. The energy o the ntermed ate **2Ba** s c ose to that o the trans t on state **TS1Ba**, as expected rom these structures be ng s m ar to each other (F gure 4). When we ca cu ate the energy n a d e ectr c med um, both **TS1Ba** and **2Ba** are espec a y stab zed n energy. But, the energy barr er s st arge. So, we urther ca cu ated or the rst step o the OH trans er tak ng account o the ne ghbor ng H s res due n order to con rm whether th s arge energy barr er s reduced or not by the contr but on o the H s res due, accord ng to an exper menta y proposed mecha- n sm.[4] It has been thought that the nteract on o the proton rom the H s res due w th the m grat ng OH group m ght stab ze **TS1Ba** and **2Ba**. F gure S1 n the Support ng In or- mat on shows that there s no e ect o the proton rom the H s res due consequent y s nce the proton stab zes the OH group but destab zes the ent re mo ecu e. The recent ca cu at ons on the bas s o the other mechan sm[11] w th the contr but on o the H s res due have a so shown a s m ar energy barr er o about 20 kca mo ^{1}.[10] There ore, the oxetane mechan sm o the rad ca cat on s the most avorab e n energy, and the energy pro e w th the sma energy barr er o about 10 kca mo ^{1} seems to be reasonab e or the react on occurr ng n the b o og ca system.

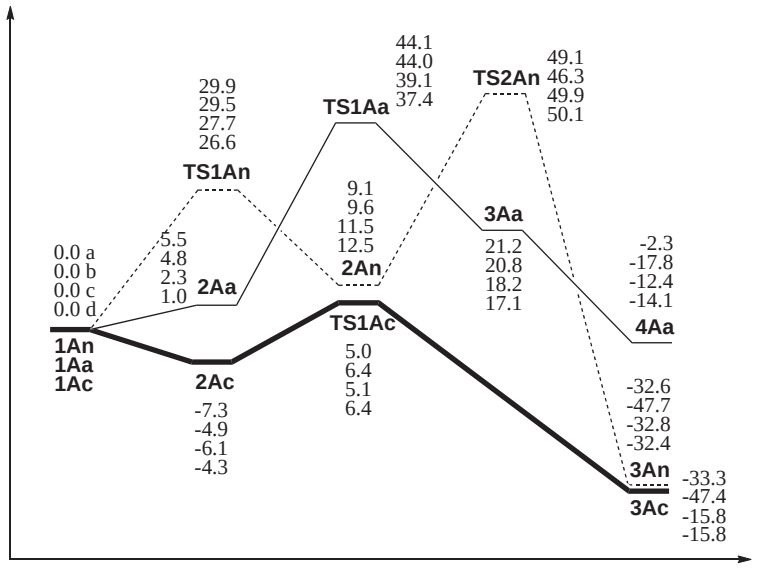

Figure 5. Energy pro es o the oxetane mechan sm n the cases o the neutra (dotted ne), rad ca an on (norma ne), and the rad ca cat on (bo d ne) at var ous eve s. a: B3LYP aug-cc-pVTZ eve , b: G bbs ree energy at the B3LYP aug-cc-pVTZ eve , c: B3LYP aug-cc-pVTZ eve n a d e ectr c med um w th a d e ectr c constant o 5.7, d: B3LYP aug-cc-pVTZ eve n a d e ectr c med um w th a d e ectr c constant o 80.

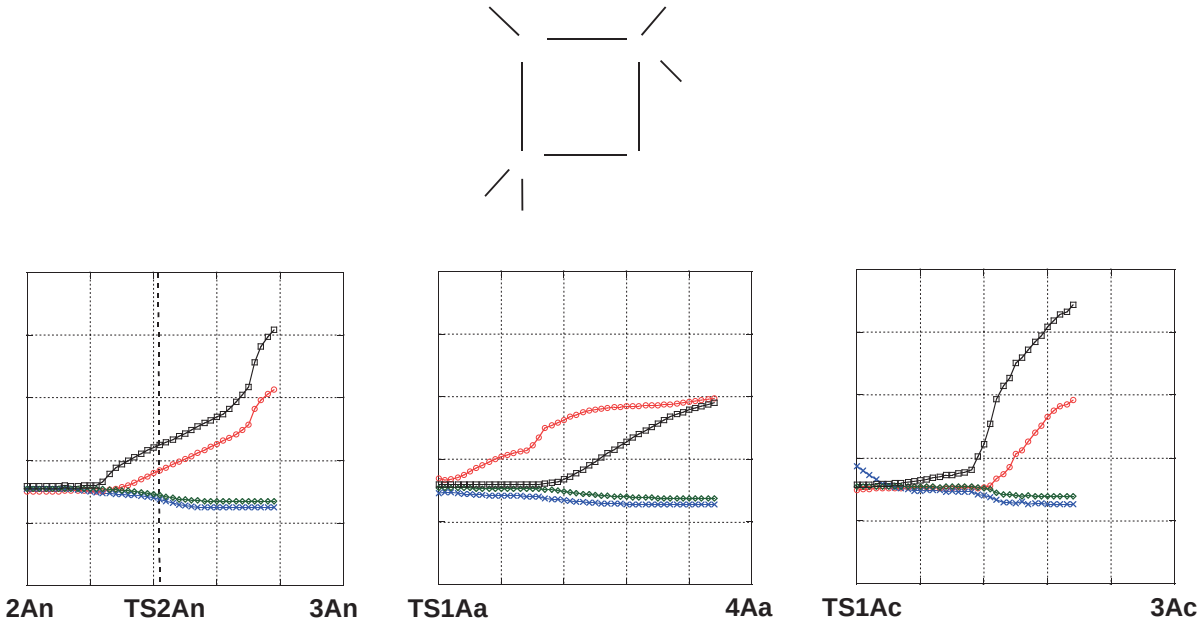

Figure 6. Changes n the geometr c parameters dur ng the d ssoc at on o the oxetane n the cases o the neutra , rad ca an on, and the rad ca cat on at the B3LYP 6-311G eve .

Reason for the Preference of the Oxetane Mechanism of the Radical Cation. In the oxetane mechan sm, t s nterest ng that the unrea st ca y arge energy barr er n the case o the rad ca an on s reduced to a moderate magn tude n the case o the rad ca cat on, a though the energy barr ers n the cases o both the rad ca an on and the rad ca cat on are ow or the repa r react on o the CPD.[7,8] The ent re energy sur ace s a so much ower or the rad ca cat on than or the rad ca an on. These resu ts are not changed by ncreas ng the ca cu at on eve and by nc ud ng the med um. Th s eature o the energy pro e o the rad ca cat on s ascr bed to the stab ty o the oxetane, as ment oned above. We there ore compared the nteract on energ es between two thym nes o the oxetane o the neutra , rad ca an on, and the rad ca cat on (Tab e 2). As a resu t, the nteract on energy was the argest n the case o the rad ca cat on, as expected.

We urther ocused on the p ace o the rad ca n order to c ar y the reason why the repa r react on by the oxetane mechan sm s ac e n the case o the rad ca cat on and s d cu t n the case o the rad ca an on. The p ace o the rad ca

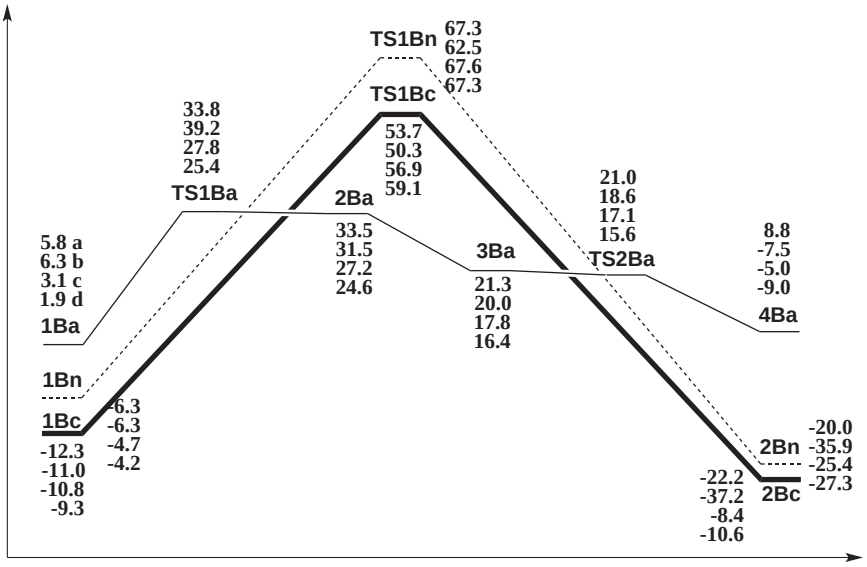

Figure 7. Energy pro es o the non-oxetane mechan sm n the cases o the neutra (dotted ne), rad ca an on (norma ne), and the rad ca cat on (bo d ne) at the var ous eve s. a: B3LYP aug-cc-pVTZ eve , b: G bbs ree energy at the B3LYP aug-cc-pVTZ eve , c: B3LYP aug-cc-pVTZ eve n a d e ectr c med um w th a d e ectr c constant o 5.7, d: B3LYP aug-cc-pVTZ eve n a d e ectr c med um w th a d e ectr c constant o 80.

Table 2. Interact on Energ es (n kca mo 1) between the Thym ne Fragments T1 and T2 o the Oxetane[a] n the Cases o the Rad ca An on, Neutra , and the Rad ca Cat on at the B3LYP 6-311G Leve

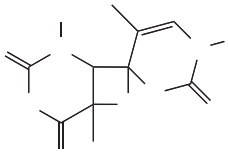

Comb nat on o the charge (T1, T2)[b]	INT[c]	BSSE corr. INT[d]
Rad ca an on		
(0, 1)	50.1	38.9
(1, 0)	56.2	46.8
Neutra		
(0, 0)	84.3	77.1
Rad ca cat on		
(0, 1)	89.0	83.2
(1, 0)	92.9	85.6

a) The opt m zed structure o the oxetane n the case o the neutra was used or a ca cu at ons o the nteract on energy. b) The comb nat on o the charge o T1 and T2 n the ca - cu at ons o the ragments. c) Interact on energy (INT) *E*(T1 T2) *E*(T1) *E*(T2). d) BSSE corrected INT INT BSSE, see the Computat ona Method or deta s.

and the negat ve or the pos t ve charge n the mo ecu e dur ng the repa r react on n the case o the rad ca an on and the rad ca cat on determ ned judg ng rom the ca cu ated sp n dens ty and Mu ken charge s presented n F gure 8. The resu t n the case o the rad ca an on s n agreement w th that prev ous y known.[5] The stretch and the shr nk o the bonds shown by the bond d stances are cons stent w th the change n the pos t on o the rad ca . On the other hand, n the case o the rad ca cat on, the pos t on o the rad ca s comp ete y d er- ent. It s noteworthy that the rad ca s on the O1 atom n **2Ac** and **TS1Ac** be ore orm ng the oxetane. The oxetane s actua y ormed a ter **TS1Ac** that s the ear y trans t on state. The va ues o the sp n dens t es and the mo ecu ar orb ta s (MOs) corre- spond ng to the rad ca n **2Aa** and **2Ac** be ore the O1 attack n both cases o the rad ca an on and the rad ca cat on are presented n F gure 9. The arge sp n dens t es are ound on the C6 atom n **2Aa** n the case o the rad ca an on wh e on the O1 atom n **2Ac** n the case o the rad ca cat on. The correspond- ng MOs suggest the ex stence o the rad ca on these atoms. The rad ca on the O1 n **2Ac** wou d make the attack o the O1 atom to orm the oxetane ac e. Name y, t wou d create a arge advantage n the ormat on o the oxetane.

It s a so thought that the pos t on o the rad ca a ects the order o the bond break ng n the sp tt ng o the oxetane. As shown n F gure 9, the bond popu at on o the C1 C2 reduced to about ha compared to that o the C5 C6 suggests that the rad ca s on the C1 C2 bond and then the C1 C2 bond s a s ng e bond n both **4Aa** n the case o the rad ca an on and **3Ac** n the case o the rad ca cat on a ter the d ssoc at on o two thym nes. The sp n dens ty shows that the rad ca ex sts on the C2 atom n **4Aa** whereas on the C1 atom n **3Ac**. The correspond ng MOs a so suggest these pos t ons o the rad ca n **4Aa** and **3Ac**. Here, we th nk the oxetane ormat on between the sp t two thym nes, the C2 C3 bond wou d be ormed at rst n the case o the rad ca an on whereas the C1 O1 bond n the case o the rad ca cat on. In other words, n the oxetane d ssoc at on, the C1 O1 bond s broken at rst n the case o the rad ca an on whereas the C2 C3 bond s broken rst n the case o the rad ca cat on. Thus, the d erence n the

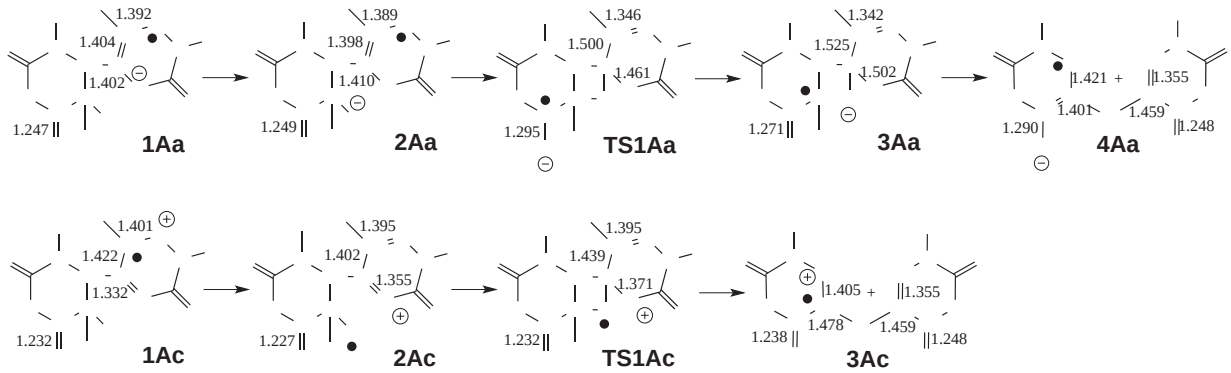

Figure 8. Rad ca and negat ve and pos t ve charges on the bas s o the sp n dens ty and the Mu ken charge and some se ected opt m zed d stances (n Å) at the B3LYP 6-311G eve o the equ br um and the trans t on state structures nvo ved n the oxetane mechan sm n the cases o the rad ca an on and the rad ca cat on.

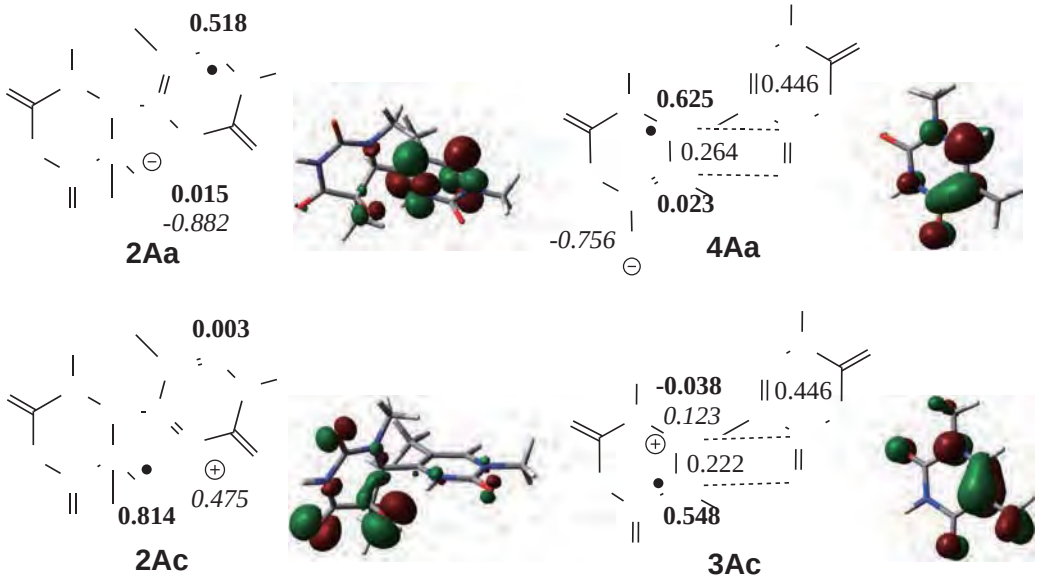

Figure 9. Sp n dens t es (bo d), NBO charges (ta c), and bond popu at ons (p a n) n **2Aa** and **2Ac** be ore the oxetane ormat on and **4Aa** and **3Ac** a ter the thym ne d mer d ssoc at on n the cases o the rad ca an on and the rad ca cat on at the B3LYP 6-311G eve . The MOs correspond ng to the rad ca n each structure are a so d sp ayed together.

pos t on o the rad ca wou d make a d erence n the order o the C–C and the C–O bond break ng o the oxetane.

The changes n the va ues o the sp n dens t es on the se ected atoms versus the react on coord nate are presented n F gure 10. In the case o the rad ca cat on, the rad ca s obv ous y on the O1 unt **TS1Ac** as shown by the arge sp n dens ty on the O1. Dur ng the ormat on o the oxetane a ter **TS1Ac**, the arge sp n dens ty on the O1 remarkab y decreases and nstead the sp n dens ty on the C5 ncreases nd cat ng the m grat on o the rad ca . The rad ca moves to C2 n the course o the C–C bond break ng and na y moves to C1 n the C–O bond break ng, as shown by the changes n the va ues o the sp n dens t es. On the other hand, n the case o the rad ca an on, the rad ca on the C4 n **TS1Aa** moves to C1 n the C–O bond break ng and then moves to C2 (or C6) n the C–C bond break ng.

Concluding Remarks

The mechan sm o the e ectron-trans er- nduced repa r reac- t on o the (6–4) T–T photo es on o DNA by the photo yase was exam ned by dens ty unct ona theory (B3LYP). The repa r react on s genera y thought to take p ace by the oxetane or the non-oxetane mechan sm a ter an e ectron trans er between the co actor FAD o the photo yase and the (6–4) T–T photo es on. A though a ot o ca cu at ons have been conducted or the rad ca an on pathway o both mechan sms, re at ve y arge energy barr ers have been ound n any case. We there ore ca cu- ated or the rad ca cat on pathway n add t on to the rad ca an on and the neutra pathways or both mechan sms to assess the poss b ty o the rad ca cat on pathway. Our ca cu at ons showed that the rad ca an on pathway has a arge energy bar- r er n both the oxetane and the non-oxetane mechan sms n

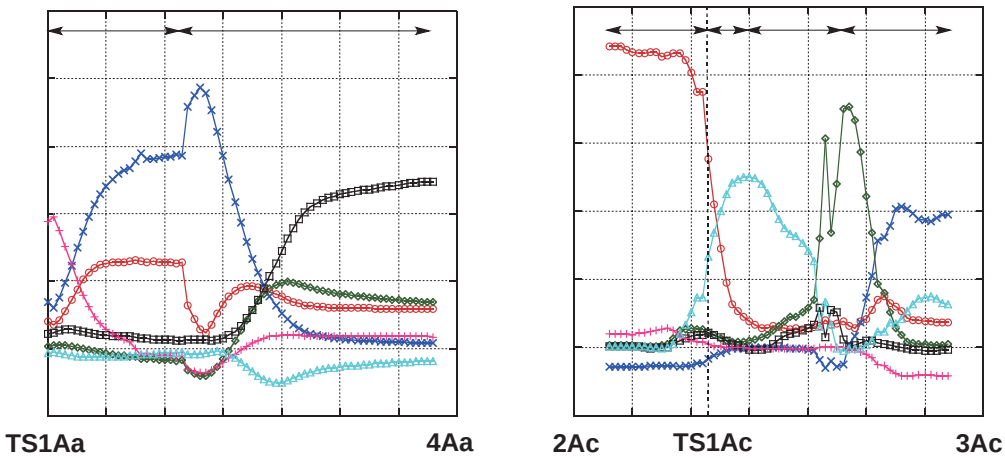

Figure 10. Changes n the sp n dens t es on the atoms dur ng the repa r react on by the oxetane mechan sm n the cases o the rad ca an on and the rad ca cat on at the B3LYP 6-311G eve . See F gure 8 or the numbered atoms.

agreement w th the prev ous ca cu at ons. However, t was ound that the rad ca cat on pathway o the oxetane mechan sm has a rea st c ow energy barr er. So, urther deta s o the state o the FADH n the am no ac d env ronment and under photo rrad at on are expected, s nce t s genera consensus that the e ectron trans er rom the (6–4) photoproduct to the FADH s un avorab e. The advantage o the rad ca cat on pathway was ascr bed to the o ow ng two th ngs, (1) the rad ca ex sts on the react ve oxygen to orm the oxetane and (2) the ormed oxetane s stab e n energy due to the strong nteract on between two thym nes. The d ssoc at on o the C–C and the C–O bonds o the oxetane n the course o the repa r react on was a so ound to take p ace stepw se n the case o the rad ca cat on, as known or the case o the rad ca an on. However, the order o the bonds d ssoc at on was reversed, the rad ca p ay ng a key ro e to determ ne th s order.

Part o the computat ons was per ormed at the Research Center or Computat ona Sc ence, Okazak , Japan.

Supporting Information

L st ngs g v ng the opt m zed Cartes an coord nates o a equ br um structures and trans t on states presented n th s paper, F gure S1: Energy pro es o the rst step o the non-oxetane mechan sm w th and w thout the contr but on o the H s res due at the B3LYP 6-311G eve . Th s mater a s ava ab e ree o charge on the Web at http://www.csj.jp/journa s/bcsj/.

References

1 a) D. Voet, J. G. Voet, *Biochemistry*, 4th ed., W ey, New York, **2011**. b) J. M. Berg, J. L. Tymoczko, L. Stryer, *Biochemistry*, 7th ed., W. H. Freeman, New York, **2012**.

2 D. L. Ne son, M. M. Cox, *Lehninger Principles of Biochemistry*, 3rd ed., Worth, New York, **2000**.

3 a) A. Sancar, *Chem. Rev.* **2003**, *103*, 2203. b) T. Care , L. T. Burgdor , L. M. Kundu, M. C chon, *Curr. Opin. Chem. Biol.* **2001**, *5*, 491.

4 J. Yamamoto, K. H tom , R. Hayash , E. D. Getzo , S. Iwa , *Biochemistry* **2009**, *48*, 9306.

5 T. Domratcheva, I. Sch cht ng, *J. Am. Chem. Soc.* **2009**, *131*, 17793.

6 M. J. Mau , T. R. M. Barends, A. F. G as, M. J. Cry e, T. Domratcheva, S. Schne der, I. Sch cht ng, T. Care , *Angew. Chem., Int. Ed.* **2008**, *47*, 10076.

7 B. Durbeej, L. A. Er ksson, *J. Am. Chem. Soc.* **2000**, *122*, 10126.

8 a) M. A da, F. Inoue, M. Kaneko, M. Dupu s, *J. Am. Chem. Soc.* **1997**, *119*, 12274. b) M. A da, M. Kaneko, M. Dupu s, n *Computational Molecular Biology* n *Theoretical and Computational Chemistry*, ed. by J. Leszczynsk , E sev er, Nether ands, **1999**, Vo . 8, pp. 211–243. do :10.1016 S1380-7323(99)80081-8.

9 K. Sadegh an, M. Boco a, T. Merz, M. Schütz, *J. Am. Chem. Soc.* **2010**, *132*, 16285.

10 a) S. Faraj , A. Dreuw, *J. Phys. Chem. Lett.* **2012**, *3*, 227. b) S. Faraj , G. Groenho , A. Dreuw, *J. Phys. Chem. B* **2013**, *117*, 10071.

11 J. L , Z. L u, C. Tan, X. Guo, L. Wang, A. Sancar, D. Zhong, *Nature* **2010**, *466*, 887.

12 C. B. Harr son, L. L. O'Ne , O. W est, *J. Phys. Chem. A* **2005**, *109*, 7001.

13 a) Y. Wang, P. P. Gaspar, J.-S. Tay or, *J. Am. Chem. Soc.* **2000**, *122*, 5510. b) O. A. Borg, L. A. Er ksson, B. Durbeej, *J. Phys. Chem. A* **2007**, *111*, 2351.

14 P. F. Hee s, R. F. Hartman, S. D. Rose, *Chem. Soc. Rev.* **1995**, *24*, 289.

15 A. A. Z eba, C. R chardson, C. Lucero, S. D. D eng, Y. M. G ndt, J. P. M. Sche v s, *J. Am. Chem. Soc.* **2011**, *133*, 7824.

16 a) M. S. Jorns, G. B. Sancar, A. Sancar, *Biochemistry* **1984**, *23*, 2673. b) Y. M. G ndt, E. Vo enbroek, K. Westpha , H. Sackett, A. Sancar, G. T. Babcock, *Biochemistry* **1999**, *38*, 3857. c) J. P. M. Sche v s, M. Ramsey, O. Soko ova, C. Tavares, C. Ceca a, K. Conne , S. Wagner, Y. M. G ndt, *J. Phys. Chem. B* **2003**, *107*, 12352.

17 a) C. Saxena, A. Sancar, D. Zhong, *J. Phys. Chem. B* **2004**, *108*, 18026. b) Y.-T. Kao, C. Saxena, L. Wang, A. Sancar, D. Zhong, *Proc. Natl. Acad. Sci. U.S.A.* **2005**, *102*, 16128.

18 M. J. Fr sch, G. W. Trucks, H. B. Sch ege , G. E. Scuser a, M. A. Robb, J. R. Cheeseman, J. A. Montgomery, Jr., T. Vreven,

K. N. Kud n, J. C. Burant, J. M. M am, S. S. Iyengar, J. Tomas , V. Barone, B. Mennucc , M. Coss , G. Sca man , N. Rega, G. A. Petersson, H. Nakatsuj , M. Hada, M. Ehara, K. Toyota, R. Fukuda, J. Hasegawa, M. Ish da, T. Nakaj ma, Y. Honda, O. K tao, H. Naka , M. K ene, X. L , J. E. Knox, H. P. Hratch an, J. B. Cross, V. Bakken, C. Adamo, J. Jaram o, R. Gomperts, R. E. Stratmann, O. Yazyev, A. J. Aust n, R. Camm , C. Pome , J. W. Ochtersk , P. Y. Aya a, K. Morokuma, G. A. Voth, P. Sa vador, J. J. Dannenberg, V. G. Zakrzewsk , S. Dappr ch, A. D. Dan e s, M. C. Stra n, O. Farkas, D. K. Ma ck, A. D. Rabuck, K. Raghavachar , J. B. Foresman, J. V. Ort z, Q. Cu , A. G. Babou , S. C ord, J. C os owsk , B. B. Ste anov, G. L u, A. L ashenko, P. P skorz, I. Komarom , R. L. Mart n, D. J. Fox, T. Ke th, M. A. A -Laham, C. Y. Peng, A. Nanayakkara, M. Cha acombe, P. M. W. G , B. Johnson, W. Chen, M. W. Wong, C. Gonza ez, J. A. Pop e, *Gaussian 03 (Revision E.01)*, Gauss an, Inc., Wa ng ord CT, **2004**.

19 a) A. D. Becke, *Phys. Rev. A* **1988**, *38*, 3098. b) C. Lee, W. Yang, R. G. Parr, *Phys. Rev. B* **1988**, *37*, 785. c) A. D. Becke, *J. Chem. Phys.* **1993**, *98*, 5648.

20 K. Fuku , S. Kato, H. Fuj moto, *J. Am. Chem. Soc.* **1975**, *97*, 1.

21 A. P. Scott, L. Radom, *J. Phys. Chem.* **1996**, *100*, 16502.

22 E. D. G enden ng, A. E. Reed, J. E. Carpenter, F. We nho d, *NBO Version 3.1*.

23 a) S. M ertu , E. Scrocco, J. Tomas , *Chem. Phys.* **1981**, *55*, 117. b) S. M ertu , J. Tomas , *Chem. Phys.* **1982**, *65*, 239.

24 a) F. Og aro, S. Cohen, S. P. de V sser, S. Sha k, *J. Am. Chem. Soc.* **2000**, *122*, 12892. b) F. Og aro, S. P. de V sser, S. Cohen, J. Kanet , S. Sha k, *ChemBioChem* **2001**, *2*, 848. c) F. Og aro, S. P. de V sser, J. T. Groves, S. Sha k, *Angew. Chem., Int. Ed.* **2001**, *40*, 2874. d) F. Og aro, S. P. de V sser, S. Sha k, *J. Inorg. Biochem.* **2002**, *91*, 554. e) S. Sha k, D. Kumar, S. P. de V sser, A. A tun, W. Th e , *Chem. Rev.* **2005**, *105*, 2279.

25 a) S. S mon, M. Duran, J. J. Dannenberg, *J. Chem. Phys.* **1996**, *105*, 11024. b) S. F. Boys, F. Bernard , *Mol. Phys.* **1970**, *19*, 553.

26 a) G. S. Hammond, *J. Am. Chem. Soc.* **1955**, *77*, 334. b) W. J. Le Nob e, A. R. M er, S. D. Hamann, *J. Org. Chem.* **1977**, *42*, 338. c) A. R. M er, *J. Am. Chem. Soc.* **1978**, *100*, 1984.

 © 2013 The Chemical Society of Japan

Computational Study of the Binding Mechanism of Complement C3b with Antigen

Toshiaki Matsubara* and Chisato Sasamoto

Department o Chem stry, Facu ty o Sc ence, Kanagawa Un vers ty, 2946 Tsuch ya, H ratsuka, Kanagawa 259-1293

Rece ved June 26, 2013; E-ma : matsubara kanagawa-u.ac.jp

The react on mechan sm o the cova ent b nd ng o comp ement component 3 (C3) w th ant gen, wh ch s gn cant y contr butes to the mmune system by enhanc ng the phagocytos s o phagocytes, s exam ned by dens ty unct ona theory (B3LYP). The cova ent b nd ng react on takes p ace by the c eavage o the hydroxy O H bond o the ant gen on the th oester bond o the C3b ormed by the act vat on o C3. We per ormed the ca cu at ons assum ng a mechan sm II that m m cs that o ser ne protease n add t on to the convent ona mechan sm I. Our ca cu at ons suggest that the convent ona mechan sm I proceeds w th tt e part c pat on o a H s res due contrary to the prev ous consensus. Mechan sm I, wh ch has a arge energy barr er o more than 30 kca mo 1, s not rea st c. On the other hand, n mechan sm II, the energy barr er s about 10 kca mo 1, due to an e c ent med at on o a H s res due by the co aborat on w th a ne ghbor ng G u res due. There ore, the cova ent b nd ng react on o the act vated C3b w th the ant gen was thought to proceed by mechan sm II we proposed rather than by the convent ona mechan sm I.

The comp ement system n b ood s compr sed o over 25 prote ns and prote n ragments synthes zed by the ver, and systemat ca y exc udes pathogen rom the body.[1] The comp ement prote n cons sts o n ne components C1 C9, and unct ons n the mmune system when act vated through one o sequent a pathways, the c ass ca comp ement pathway, the a ternat ve comp ement pathway, and the ect n pathway. The comp ement component 3 (C3), that p ays a centra ro e n the comp ement system, s act vated by a proteo yt c sp tt ng nto C3a and C3b (F gure 1). The ragment C3b s gn cant y contr butes to nnate mmun ty, serv ng as an opson z ng agent.

It has been known that the generated C3b exposes a reac- t ve th oester o the act ve s te to the com ng ant gen. The crysta ograph c structure o the C3b reg stered n the prote n data bank (PDB) w th the ID code 2HR0[2] shows that the th oester bond ormed rom Cys and G n emerges rom the ns de by a drast c movement o the th oester doma n (TED). Th s th oester bond cova ent y b nds w th the hydroxy group o the wa sur ace o ant gen. In the crysta ograph c structure o 2HR0, the mode substrate *N*-acety -L-threon ne (AcT) s actua y trapped on the th oester C S bond. Once the C3b attaches to the target ant gen, the b nd ng o the ant gen to the phagocyte s great y enhanced (F gure 1). There ore, the phagocytos s o the phagocyte, such as macrophage, n the nnate mmune system ncreases, wh ch s ca ed opson zat on. We just ocused on the cova ent b nd ng o the th oester bond o the act vated comp ement C3b w th the hydroxy group o the sur ace o the ant gen, wh ch causes th s opson zat on.

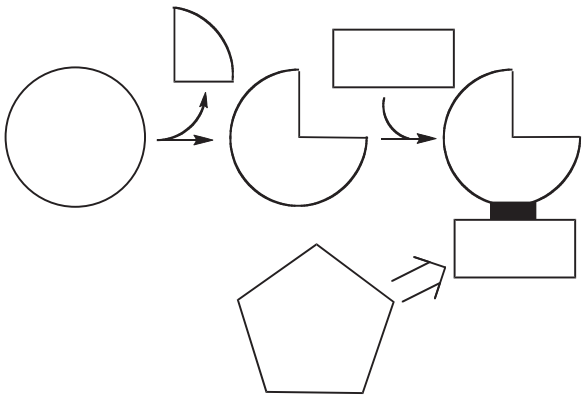

Figure 1. D agram o the opson zat on.

The convent ona y proposed cova ent b nd ng mechan sm o the th oester bond o C3b s presented n F gure 2(I). The hydroxy O H bond s broken on the th oester C S bond w th the support o H s.[3,4] In act, t has been con rmed n severa crysta ograph c structures o C3b that a H s res due ex sts n the v c n ty o the th oester bond.[2,5] Be ore break ng o the O H bond, the one e ectron pa r on the N o H s nteracts w th the pos t ve y charged carbony carbon (**B**). When the C N nteract on s converted to a cova ent bond, the C S bond s broken, where the e ectron rom the N o H s s accommodated on the S atom (**C**). The O H bond o the ncom ng ROH s hetero yt ca y broken, where the H and RO s attached to the negat ve y charged S atom and the pos t ve y charged carbony carbon, respect ve y (**D**). Thus, the hydroxy group s trapped on the th oester bond. In th s mechan sm, a H s unct ons to enhance the bas c ty o the S atom as a proton acceptor.

In add t on to the convent ona mechan sm I, we a so pro- posed a new mechan sm II (F gure 2(II)), because a G u res due has been con rmed to ex st next to the H s res due n the crysta ograph c structures[2,5] and the unct on o G u n the cova ent b nd ng mechan sm has been d scussed.[6] The mech- an sm II, wh ch m m cs the we -known mechan sm or ser ne protease,[7] seems to be p aus b e, because the th oester C S bond s broken by the ROH nuc eoph e n the current react on. The cova ent b nd ng react on through the mechan sm II s expected to be ac e, as we have computat ona y shown or the s m ar ester C O bond break ng n the degradat on o

Pub shed on the web December 15, 2013; do :10.1246 bcsj.20130181

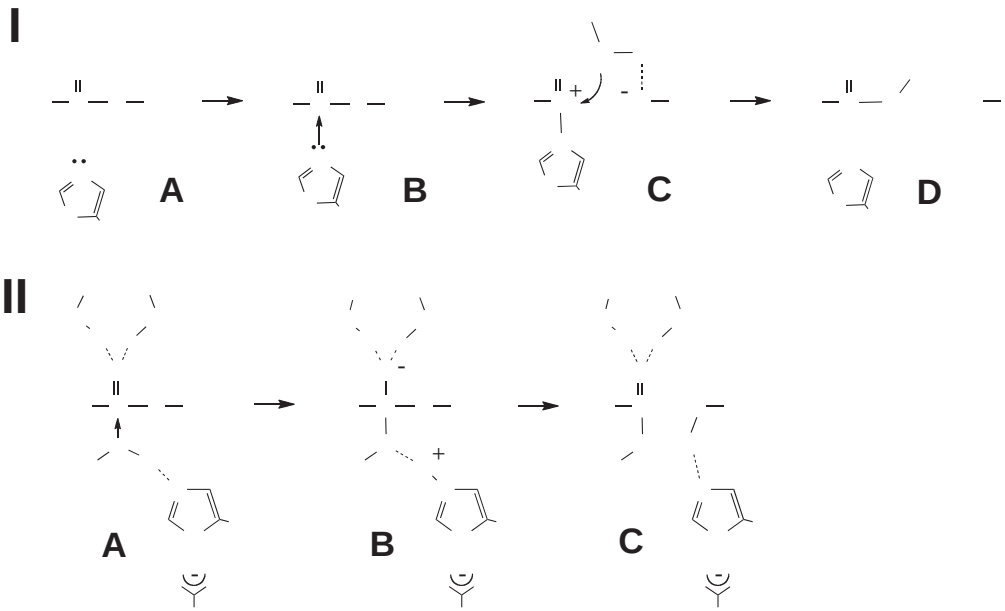

Figure 2. Convent ona y proposed cova ent b nd ng mechan sm I or the comp ement C3b (I), and a new cova ent b nd ng mechan sm II we proposed or the comp ement C3b (II). Mechan sm II m tates the rst step o the genera y known cata yt c process o ser ne protease.

b odegradab e p ast cs.[8] In mechan sm II, a G u nstead o an Asp supports the H s. As the act ve s te o the crysta ograph c structure w th the PDB ID o 2HR0, wh ch s a mode structure n th s study, s presented n F gure 3, G u1209 ex sts next to H s1104. The se ected d stance between H s1104 and G u1209 s 3.203 Å. H s1104 s a tt e ar rom G n991 n th s crysta structure a ter the react on, a though n other structures[2,5] be ore the react on H s1104 s c ose to G n991 w th the d s-tance o about 3–4 Å. The hydroxy group o the substrate AcT s trapped on the th oester bond o Cys988–G n991, and then the th oester C–S bond s broken. The negat ve charge on the carbony oxygen n the ntermed ate **B**, wh ch s known as oxyan on ho e n the case o the ser ne protease, shou d be stab zed by the pos t ve charge o the N–H hydrogen o the ma n cha n o am no ac ds. However, there s no N–H hydrogen o the ma n cha n or other pos t ve y charged atoms around the carbony oxygen. There ore, we assumed the H_2O hydrogen rom the so vent as pos t ve y charged atom to stab ze the negat ve y charged carbony oxygen as presented n F gure 2, because the c e t o the act ve s te s arge y open to the so vent and we can nd enough space or the ncom ng H_2O around the carbony oxygen.

In the present study, we conducted the ca cu at ons or the mechan sms I and II o the comp ement C3 to trap the hydroxy group o the sur ace o the ant gen at the B3LYP eve o theory n order to exam ne wh ch mechan sm s more rea st c. The react on was o owed by a mode system and ts surround ngs are taken nto account by the po ar zed-cont nuum-mode (PCM) approx mat on.

Computational Method

A ca cu at ons except B3LYP-D were per ormed us ng the Gauss an03 program package.[9] We used a mode system that cons sts o some am no ac ds part c pat ng the react ons to o ow the mechan sms I and II and ts env ronment was approx mated by the po ar zed-cont nuum-mode (PCM). We adopted methano as a mode o ant gen, as var ous a coho s have been used n exper ments to exam ne the cova ent b nd ng react v ty o C3.[4]

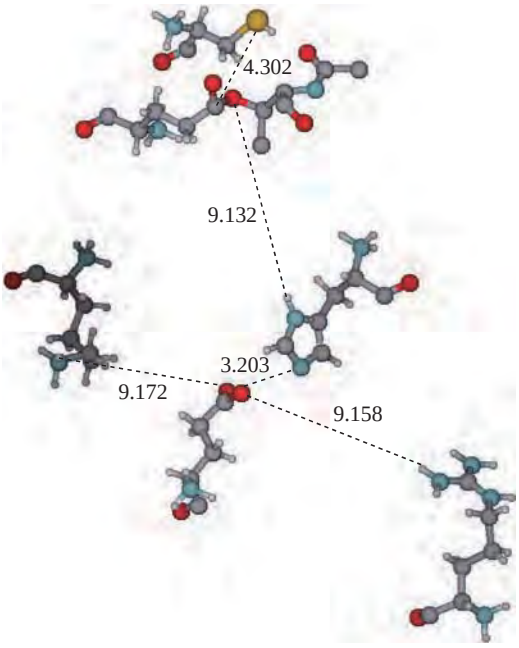

Figure 3. Act ve s te o the comp ement C3b w th the trapped substrate *N*-acety -L-threon ne res due (AcT), wh ch s abstracted rom the crysta ograh c structure reg stered n the prote n data bank (PDB) w th the ID code 2HR0.[2] On y the mportant am no ac ds are d sp ayed or c ar ty. The se ected d stances (Å) are a so presented together.

The geometry opt m zat ons were per ormed by dens ty unct ona theory (DFT) at the B3LYP eve o theory, wh ch cons sts o a hybr d Becke Hartree Fock exchange and Lee Yang Parr corre at on unct ona w th non oca correct ons[10] us ng the bas s set 6-311 G(d,p). We have just qua ed the bas s set 6-311 G(d,p) to per orm the geometry opt m zat on on the bas s o Tab es S1 and S2 o the Support ng In orma- t on. The energet cs were mproved us ng h gher eve bas s set aug-cc-pVTZ and a so the d spers on corrected B3LYP eve o theory (B3LYP-D) mp emented n the Gauss an09 program.[11]

A equ br um structures and trans t on states were u y opt m zed and dent ed by the number o mag nary requen- c es ca cu ated rom the ana yt ca Hess an matr x. The reac- t on coord nates were o owed rom the trans t on state to the reactant and the product by the ntr ns c react on coord nate (IRC) techn que.[12] The zero-po nt energy was ca cu ated at the B3LYP 6-311 G(d,p) eve w th a sca e actor o 0.9614[13] or ca cu ated v brat ona requenc es. NBO ana ys s[14] was per ormed to obta n the atom c charge. The surround ng am no ac ds were taken nto account by PCM approx mat on[15] us ng the d e ectr c constant o 5.7.[16] The ca cu at ons w th the d e ectr c constant o 80 were a so per ormed assum ng a water med um or compar son. The presented energ es are re at ve to the energy o the th oester bond w th H s and the ndependent substrate MeOH n the case o mechan sm I and o the nde- pendent th oester bond and the substrate MeOH w th H s and G u n the case o the mechan sm II. We added **O** and **N** as su xes to the abe s o the equ br um and trans t on state structures to d st ngu sh the convent ona and our proposed mechan sms, and a so added **s** and **o** to d st ngu sh the or g - na th oester and the S-subst tuted ester systems and marked w th or the system w thout H s.

Results and Discussion

Mechanism I. We at rst opt m zed the equ br um and trans t on state structures nvo ved n the convent ona mecha- n sm I. As a resu t, t was ound that the cova ent b nd ng react on proceeds by one step through the trans t on state **TS1Os** as presented n F gure 4. A H s res due part c pates tt e n th s react on **2Os** → **TS1Os** → **3Os**, wh ch s d erent rom the prev ous y pred cted react on by exper menta sts (F gure 2). Actua y, there d d not ex st an ntermed ate such as **C** n F gure 2, where a H s res due orms a cova ent bond w th the carbony carbon and the th oester C S bond s arge y stretched. In **2Os**, the C N d stance o 3.922 Å s very ong suggest ng that the nteract on o the H s w th the carbony carbon s weak. The substrate MeOH hydrogen a so weak y nteracts w th the S atom o the th oester bond as shown by the S H d stance o 2.572 Å. The MeOH come c ose to the C S bond, and then the C O bond shortens to 1.658 Å n **TS1Os**. Thereby, the C S d stance stretches to 2.526 Å. On the other hand, the MeOH O H d stance o 1.126 Å s not so stretched and the H S d stance o 1.751 Å s st ong. As shown by the ong C N d stance o 3.687 Å, the H s tt e part c pates n the react on, wh ch s d erent rom the prev ous consensus on the ro e o H s. In act, the trans t on state **TS1Os** s not stab zed by the H s, as shown by the act that stab ty o the trans - t on state **TS1Os** w th H s s s m ar to that o trans t on state **TS1Os** w thout H s (F gure 4). Thus, not the N o H s but the O o MeOH weakens the C S bond. However, the C S bond s not stretched enough so that the S atom never acts as a proton acceptor be orehand. A ter pass ng through the trans t on state **TS1Os** the MeOH hydrogen s abstracted by the S atom as a proton as d scussed ater. Thus, the convent ona mechan sm proceeds by one-step pass ng through a our-centered trans - t on state, and the H s res due mere y weak y nteracts w th the carbony carbon o the G n res due throughout and never contr butes to the react on.

The changes n the se ected geometr c parameters and NBO charges dur ng the react on are presented n F gure 5. We p otted the 65 po nts o those ga ned rom the IRC ca cu at ons aga nst the react on coord nate. The character st c o the reac- t on ment oned above s c ear y re ected n these p ots. The d stance between the carbony carbon and the MeOH oxygen s shortened enough to orm a cova ent bond whereas the C S bond s extreme y e ongated be ore reach ng the trans t on state. In accordance w th these geometr c changes, the va ue o the pos t ve charge o the C S carbon a most reaches the max mum at the trans t on state, and n contrast, the pos t ve s gn or the other S atom s changed to the negat ve s gn and the va ue o ts negat ve charge reaches the m n mum, because the C S bond s h gh y po ar zed by the approach o the MeOH oxygen to the C S carbon. A ter pass ng the trans t on state, the MeOH O H bond s sudden y stretched and ts hydrogen s abstracted as a proton by the h gh y negat ve y charged S atom. The arge pos t ve charge o the O H hydrogen, there- ore, arge y decreased a ter the trans t on state. A though the d stance between the carbony carbon and the H s n trogen gradua y decreases dur ng the react on, th s change n the ong d stance that suggests no contr but on o H s to the react on s not substant a y mportant. So, the negat ve charge o the N atom o H s s a most constant.

We per ormed s ng e po nt energy ca cu at ons or the opt m zed structures o the cova ent b nd ng react on **2Os** → **TS1Os** → **3Os** by mechan sm I at h gher eve s, B3LYP aug-cc-pVTZ and B3LYP-D aug-cc-pVTZ, to mprove the re ab ty o the energy. As the r energy pro es are d sp ayed n F gure 6, the react on s a tt e exotherm c and the energy barr er o more than 30 kca mo ^{1} s very arge. The nc u- s on o the zero-po nt correct on d d not change the energy pro e, a though the energy barr er s a tt e reduced. A though the energy pro e o the react on was a so determ ned n a d e ectr c med um tak ng account o the am no ac d env ron- ment (F gure 7), there was no remarkab e change n t. Thus, the cova ent b nd ng react on does not seem to proceed by the convent ona mechan sm I that has such arge energy barr er. We, there ore, proposed another cand date o the cova ent b nd ng mechan sm n the next sect on.

We a so exam ned the ro e o the S atom o the th oester bond by rep ac ng the S atom w th an O atom. The opt m zed structures o the S-subst tuted reactant and the trans t on state and the r re at ve energ es at the eve B3LYP 6-311 G(d,p) are presented n F gure 4. The trans t on state **TS1Os** s about 6 kca mo ^{1} destab zed n energy by th s subst tut on. Th s suggests that not the ester but the th oester bond s mportant as a react on s te. The mportance o the S atom rom a Cys res due s more obv ous n the mechan sm II as shown be ow. The trans t on state n the case o the O atom s d erent rom that n

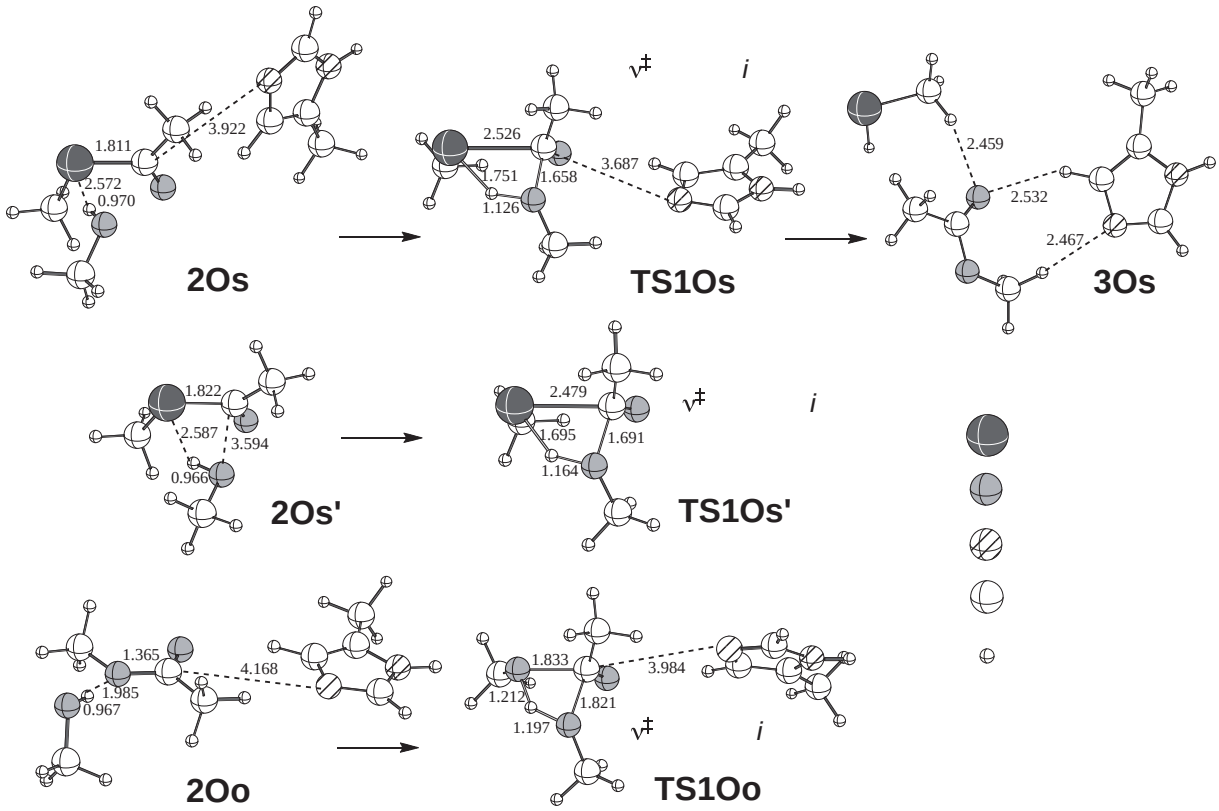

Figure 4. Opt m zed equ br um and trans t on state structures (n Å) w th the re at ve potent a energ es (n kca mo ^{1}) nvo ved n the convent ona mechan sm I at the B3LYP 6-311 G(d,p) eve . The mag nary requenc es (n cm ^{1}) are a so presented together or the trans t on states. **2Os** → **TS1Os** and **2Oo** → **TS1Oo** correspond to **2Os** → **TS1Os** w thout h st d ne and that w th ester bond nstead o th oester bond, respect ve y.

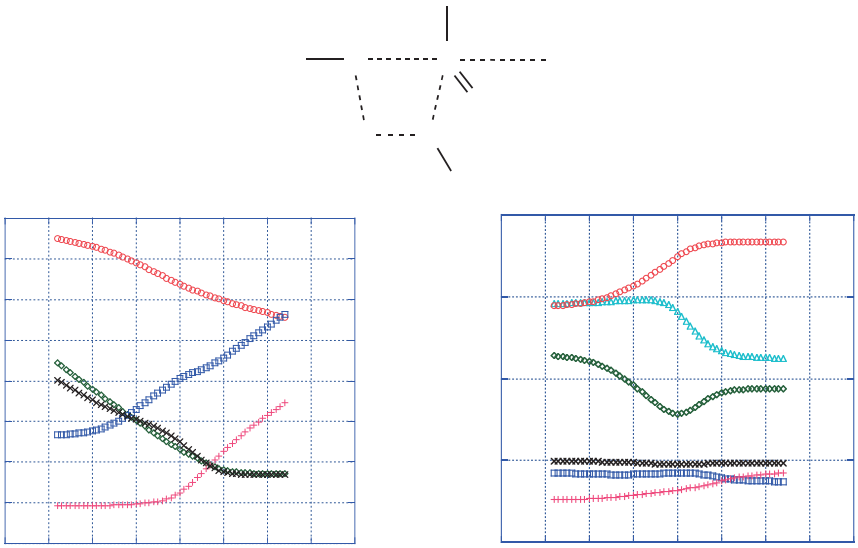

Figure 5. Changes n the se ected geometr c parameters (A) and NBO charges (B) dur ng the cova ent b nd ng react on by mechan sm I.

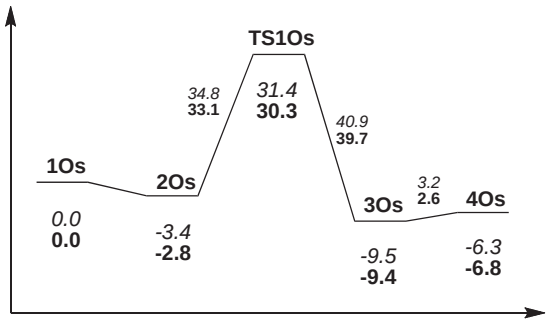

Figure 6. Energy pro es o the cova ent b nd ng react on by convent ona mechan sm I at the B3LYP aug-cc-pVTZ (p a n) and B3LYP-D aug-cc-pVTZ (ta c) eve s, and at the B3LYP-D aug-cc-pVTZ eve w th zero-po nt correct on (bo d).

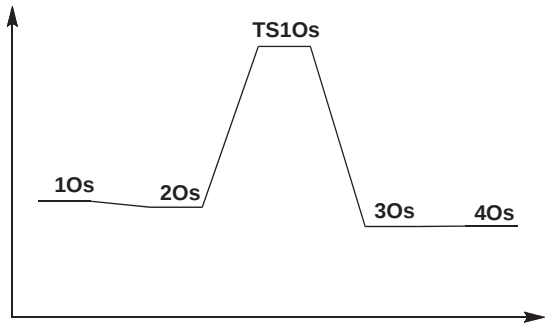

Figure 7. Energy pro es o the cova ent b nd ng react on by convent ona mechan sm I at the B3LYP 6-311 G(d,p) eve n a d e ectr c med um w th a d e ectr c constant o 5.7 or the am no ac d env ronment and o 80 or the water so vent (parenthes s).

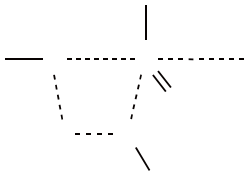

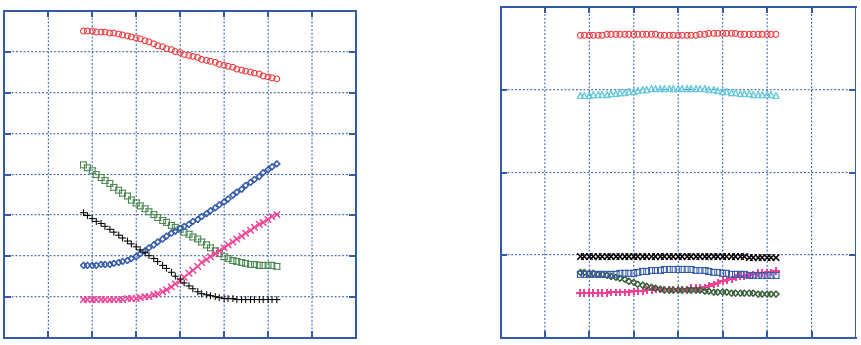

Figure 8. Changes n se ected geometr c parameters (A) and NBO charges (B) dur ng the cova ent b nd ng react on by mechan sm I n the case o an ester bond.

the case o the S atom. The O H d stance s onger by 0.071 Å whereas the O(S) H d stance s shorter by 0.539 Å or **TS1Oo** than or **TS1Os** (F gure 4), because the oxygen s a stronger proton acceptor than the su ur. As shown n F gure 8B, the oxygen s arge y negat ve y charged throughout the react on due to ts arge e ectronegat v ty (3.44 Pau ng),[17] whereas the su ur w th the sma er e ectronegat v ty (2.58 Pau ng)[17] s pos t ve y charged n the n t a stage o the react on and ts s gn o the charge s changed to negat ve dur ng the react on by the n uence o the ncom ng MeOH oxygen. The ormed C O bond s obv ous y onger, and the broken C O bond s not as stretched as n the case o the S atom. It s there ore thought that the ormat on and the break ng o the bonds s mu taneous y take p ace n contrast to the case o the S atom. Th s character st c o the react on s a so shown by F gure 8A, where geometr c parameters gradua y change throughout the react on. The N atom o the H s w th the negat ve charge s pushed away rom the carbony carbon due to the oxygen at the oppos te s te hav ng a arge negat ve charge. Th s s re ected n the stab ty o the trans t on state **TS1Oo**, be ng about 6 kca mo ^{1} ess stab e than **TS1Os**. The charge o each atom (F gure 8B), wh ch s a most constant dur ng the react on, s a so d erent rom the case o the S atom, a though the va ues o the negat ve charges o two oxygens are sw tched.

Mechanism II. The opt m zed equ br um and trans t on state structures or the mechan sm II at the B3LYP 6-311 G(d,p) eve are presented n F gure 9. The mechan sm II, where the G u res due as we as the H s res due has an mportant ro e to enhance the react v ty, m m cs a part o the react on mechan sm o ser ne protease as ment oned n the Introduct on. In **1Ns**, the nuc eoph c ty o the MeOH oxygen s enhanced by a H-bond w th the N o the H s, as shown by the negat ve charge o the MeOH oxygen o 0.471 e that s ncreased by 0.109 e compared to that o the correspond ng

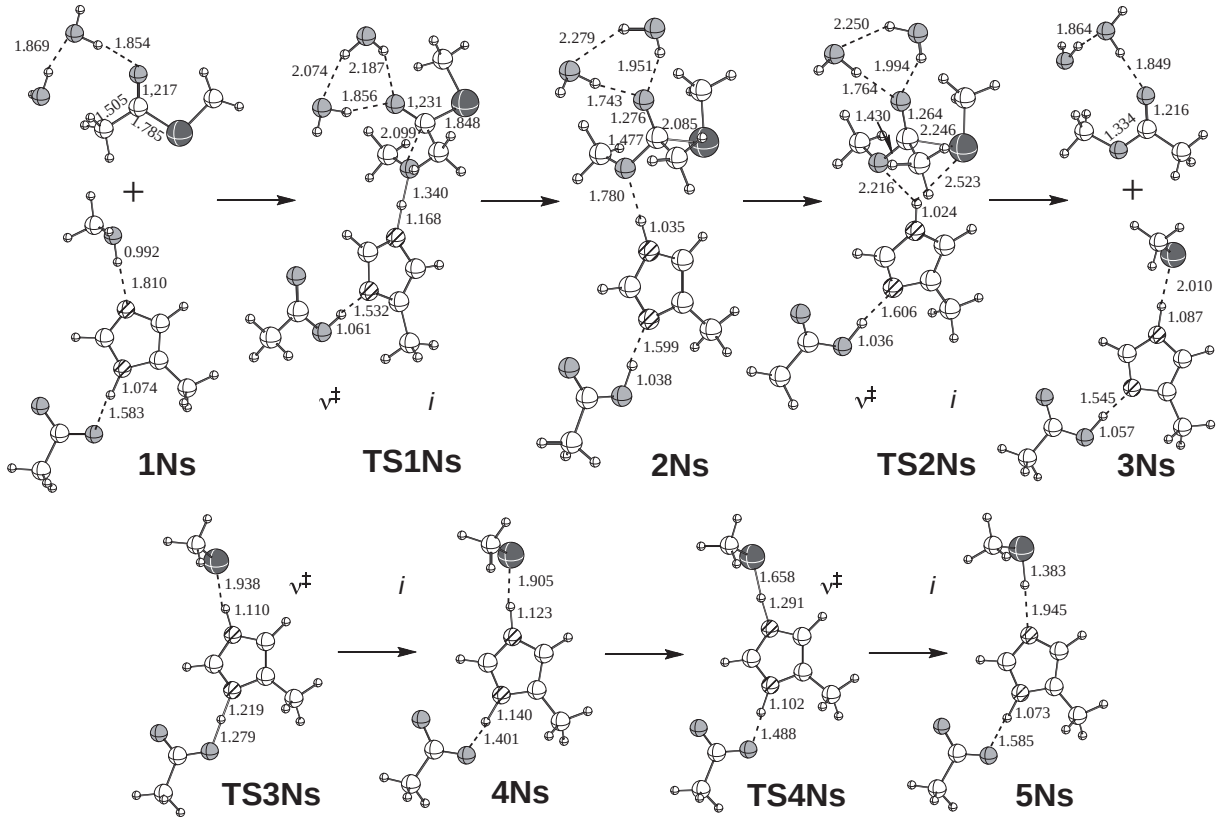

Figure 9. Opt m zed equ br um and trans t on state structures (n Å) w th the re at ve potent a energ es (n kca mo 1) nvo ved n the new mechan sm II at the B3LYP 6-311 G(d,p) eve . The mag nary requenc es (n cm 1) are a so presented together or the trans t on states.

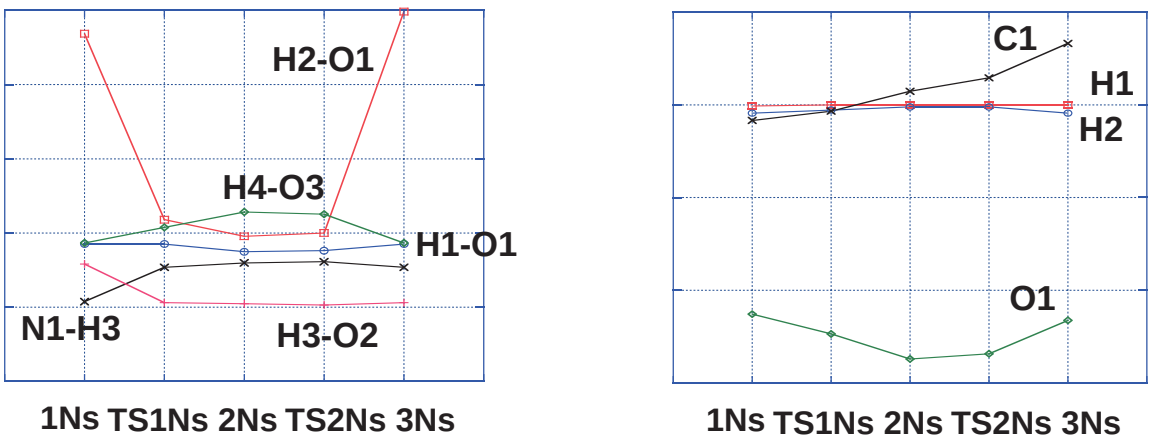

Figure 10. Changes n the se ected geometr c parameters (A) and NBO charges (B) dur ng the cova ent b nd ng react on by mechan sm II.

oxygen o the ree MeOH. The ntermed ate **2Ns** s ormed v a the trans t on state **TS1Ns** by the nuc oph c attack o the MeOH oxygen to the carbony carbon. Here, not the S o the th oester bond but the N o the H s abstracts the OH hydrogen o the MeOH as a proton.

The carbony carbon n **1Ns** takes a tetrahedra structure n the ntermed ate **2Ns** by the add t on o the MeO . A ter the add t on o the MeO , the negat ve charge o the carbony oxygen s gn cant y ncreases (F gure 10B), because the negat ve charge o the MeO s trans erred to the carbony oxygen. Th s negat ve charge o the O s stab zed n energy by ne ghbor ng pos t ve part a charges o am no ac ds n the case o the ser ne protease, orm ng an oxyan on ho e. However, as shown by the crysta ograph c structure o the act ve s te o C3b n F gure 3,

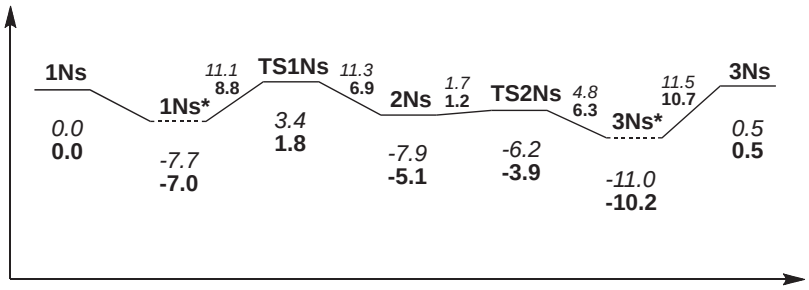

Figure 11. Energy pro es o the cova ent b nd ng react on by the new mechan sm II at the B3LYP aug-cc-pVTZ (p a n) and B3LYP-D aug-cc-pVTZ (ta c) eve s, and at the B3LYP-D aug-cc-pVTZ eve w th zero po nt correct on (bo d).

there s no su tab e am no ac d that prov des a pos t ve part a charge to the h gh y negat ve y charged oxygen n the present case. So we assumed some water mo ecu es rom the so vent nstead o am no ac ds as a prov der o the pos t ve part a charge, because the act ve s te s just open to the so vent and there s enough space around the th oester bond to accommodate some water mo ecu es. The oxyan on ho e n **2Ns** wou d be stab zed by the e ectrostat c nteract on w th the pos t ve part a charge o the hydrogen o H_2O rom the so vent. In act, as shown by F gure 10A, the carbony oxygen nteracts w th two water mo ecu es n **2Ns**, a though the correspond ng oxygen nteracts w th on y one water mo ecu e n **1Ns** and **3Ns**. A ter the trans t on state **TS2Ns**, the C S bond s broken and the carbony doub e bond s recovered. As a resu t, the MeOH s cova ent y bound to the C S carbon by the c eavage o the C S bond. The abstracted proton by the H s rom the substrate MeOH s returned to the S atom through the process, **3Ns** → **TS3Ns** → **4Ns** → **TS4Ns** → **5Ns**, where ts potent a energy pro e s a most at.

In the proton trans er between the MeOH and the H s and between the H s and the S atom, the G u supports the H s as a proton acceptor or donor. The G u contro s the bas c ty o the H s by nteract ng w th the other N H hydrogen o the H s as shown n **1Ns** and **3Ns**. In the present system, the G u actua y abstracts the N H hydrogen rom the H s as a proton to enhance the bas c ty o the H s n the **1Ns** → **TS1Ns** → **2Ns**. Th s mechan sm, where two protons trans er rom the MeOH to the H s and rom the H s to the G u, s ca ed the doub e-proton-trans er mechan sm. However, a s ng e-proton-trans er mechan sm, where on y one proton trans ers rom the MeOH to the H s, s a so cons derab e, because the act ve s te has an enough space to accommodate some water mo ecu es rom the so vent to e ectrostat ca y nteract w th the G u oxygens (There s no am no ac d to e ectrostat ca y nteract w th the G u oxygens as shown n F gure 3). There ore, the energy pro e o mechan sm II s ca cu ated a so or the case o the s ng e-proton-trans er mechan sm be ow.

The ca cu ated energy pro es or mechan sm II at the h gher eve are presented n F gure 11. Here, the c usters o **1Ns*** be ore the trans t on state **TS1Ns** and o **3Ns*** a ter the trans t on state **TS2Ns** are arb trary structures p cked up rom the energy sur ace determ ned by the IRC ca cu at on, because the u opt m zat ons o these c usters g ve unreasonab e structures as reactant and product due to ntermo ecu ar nteract ons. We do not see any s gn cant change n the energy pro e even the bas s set s mproved to aug-cc-pVTZ eve . The energy barr ers n both the rst and second steps are sma and the ent re energy pro e s qu te smooth. Both the trans t on state **TS1Ns** o the rst step and the trans t on state **TS2Ns** o the subsequent second step are arge y stab zed. They are ess stab e on y by 9.8 and 1.4 kca mo ^{1}, compared to the reactant **1Ns**. Th s wou d be ma n y ascr bed to the two reasons; the co aborat ve part c pat on o the G u to make the proton trans er v a the H s smooth and the stab zat on o the nter-med ate **2Ns** by the nteract ons w th the surround ng pos t ve part a charges. When we use the d spers on corrected B3LYP eve o theory, the ent re energy pro e except product s 3 8 kca mo ^{1} stab zed. The trans t on state **TS1Ns** at the h ghest po nt s urther stab zed by 1.6 kca mo ^{1} by the nc us on o the zero-po nt correct on. As a resu t, the energy barr er n the rst step s reduced to 9 kca mo ^{1}. However, the rst step s thought to be the rate-determ n ng step, s nce the energy barr er o about 1 kca mo ^{1} n the second step s very sma . Thus, compared to the reactant **1Ns**, the ntermed ate **2Ns** and the trans t on state **TS2Ns** s more stab e n energy, whereas the trans t on state **TS1Ns** s ess stab e but on y by about 2 kca mo ^{1}. There ore, the cova ent b nd ng react on by the mechan sm II wou d be extreme y ac e.

We a so take the surround ng am no ac ds nto account us ng a d e ectr c med um. The energy pro es at the B3LYP 6-311 G(d,p) eve n the d e ectr c med um w th the d - e ectr c constant o 5.7 are presented n F gure 12. The part o the energy pro e, **TS1Ns** → **2Ns** → **TS2Ns**, s pushed up by 9 10 kca mo ^{1} by the e ect o the am no ac d env ronment. As ment oned above, the process **1Ns** → **2Ns** proceeds by the doub e-proton-trans er mechan sm (F gure 9), where the other proton a so trans ers rom the H s to the G u when the proton trans ers rom the MeOH to the H s. However, n the case o pept de bond break ng by the ser ne protease, the s m ar process proceeds by the s ng e-proton-trans er mechan sm w thout the trans er o the other proton rom the H s to the G u,[8,18] because the bas c ty o the G u s reduced by the ex stence o pos t ve part a charges around the carboxy ate an on. The crysta o-graph c structure o the act ve s te presented n F gure 3 shows that the am no ac ds, Lys1062 and Arg1163, w th the pos t ve part a charges are about 10 Å apart rom G u. However, t s poss b e that water mo ecu es rom the so vent come nto the act ve s te and nteract w th the carboxy ate an on o the G u. In th s case, the react on w proceed by the s ng e-proton-trans er mechan sm. We there ore determ ne another energy pro e

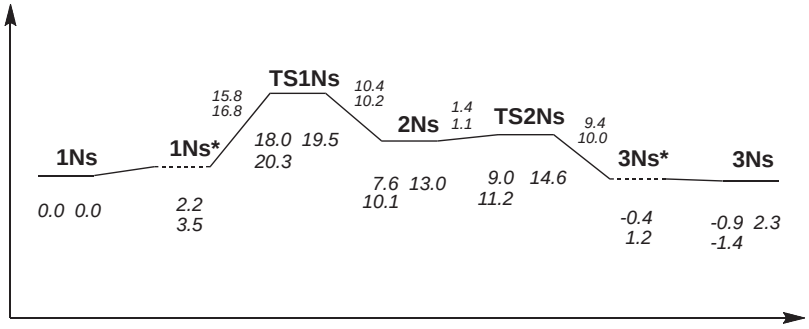

Figure 12. Energy pro es o the cova ent b nd ng react on by the new mechan sm II at the B3LYP 6-311 G(d,p) eve n a d e ectr c med um w th a d e ectr c constant o 5.7 or the am no ac d env ronment (ta c) and o 80 or the water so vent (parenthes s). The correspond ng energy pro es w thout a d e ectr c med um (p a n) and n the case o the s ng e-proton-trans er mechan sm (bracket) are a so presented. See the text or the deta .

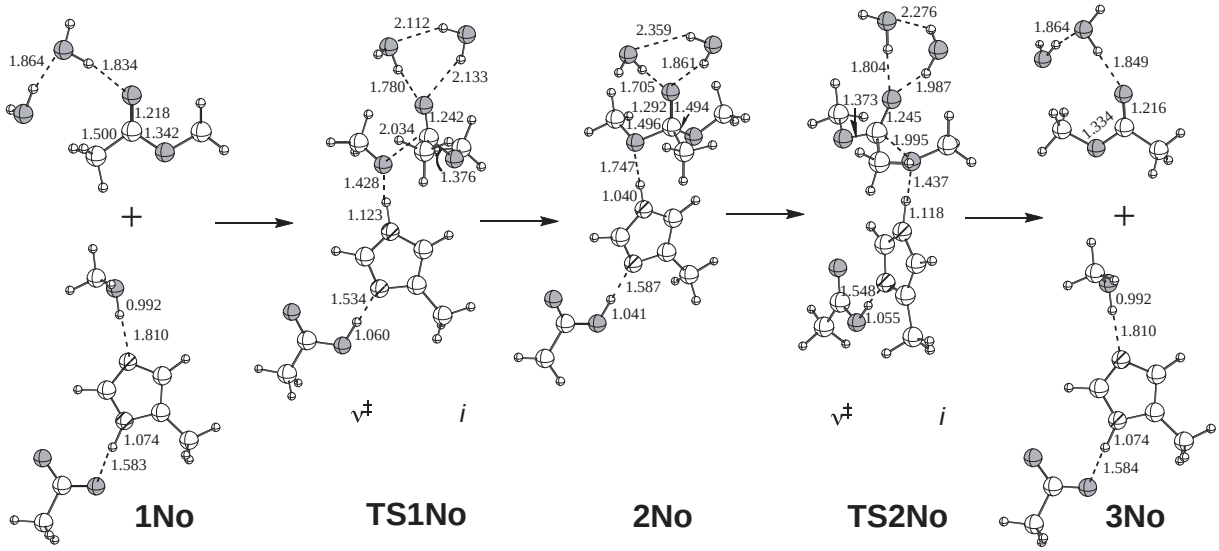

Figure 13. Opt m zed equ br um and trans t on state structures (n Å) w th the re at ve potent a energ es (n kca mo 1) nvo ved n the new mechan sm II n the case o the ester bond at the B3LYP 6-311 G(d,p) eve . The mag nary requenc es (n cm 1) are a so presented together or the trans t on states.

where the movement o the H o the H s nteract ng w th the G u s xed assum ng the s ng e-proton-trans er mechan sm. S nce the s ng e-proton-trans er mechan sm s energet ca y un avorab e, the energy pro e o **TS1Ns → 2Ns → TS2Ns** was destab zed by 5 9 kca mo 1 n the gas phase and by 2 6 kca mo 1 n the d e ectr c med um (F gure 12). However, the trans t on state **TS1Ns** st es at the ower energy so that the energy barr er o the ent re energy pro e s much sma er than the case o mechan sm I.

We exam ned the ro e o the S atom a so or the mechan sm II rep ac ng the S atom by the O atom. The opt m zed equ - br um and trans t on state structures and the r re at ve energ es or the case o the O atom at the B3LYP 6-311 G(d,p) eve s presented n F gure 13. There s no substant a d erence n the structure rom the case o the S atom, a though the MeO abstracts the proton rom the H s s mu taneous y w th ts d ssoc at on n the second step. On the other hand, n the energy pro e t shou d be noted that the ntermed ate **2No** and the trans t on state **TS2No** are destab zed by 7 8 kca mo 1 so that the trans t on state **TS2No** n the second step becomes ess stab e than the trans t on state **TS1No** n the rst step, wh ch s cons stent w th the prev ous ca cu at on or the s m ar system.[8] Name y, the second step s ac tated by the S atom o the th oester bond, wh ch suggests the mportance o the contr bu- t on o the Cys w th the S atom to the ormat on o the act ve s te.

Concluding Remarks

The comp ement component 3 (C3) s nd spensab e n the mmune system, because the act vated C3b s gn cant y enhances the phagocytos s o the phagocyte by cova ent y b nd ng w th the ant gen. In the present study, we exam ned how the C3b cova ent y b nds to the ant gen by dens ty unc- t ona theory (B3LYP) compar ng the convent ona mechan sm I to the mechan sm II we proposed that m m cs that o the ser ne protease. The ca cu at ons showed that there s no sub- stant a part c pat on o the H s n the convent ona mechan sm I, wh ch s d erent rom the prev ous consensus. The cova ent b nd ng react on there ore proceeds by one step w th the qu te arge energy barr er o more than 30 kca mo 1 n the case o

mechan sm I. In contrast, n mechan sm II, the cova ent b nd ng react on proceeds n two steps and the H s supports the reac- t on co aborat ng w th the ne ghbor ng G u. S nce the ormed ntermed ate w th the negat ve charge s stab zed n energy by the nteract on w th the pos t ve part a charge o the surround- ng mo ecu es, both energy barr ers o the rst and the second steps are sma and the energy pro e s qu te smooth. Thus, t was suggested that the cova ent b nd ng o C3b w th the ant gen takes p ace by the mechan sm II we proposed rather than the convent ona mechan sm I.

Part o the computat ons was per ormed at the Research Center or Computat ona Sc ence, Okazak , Japan.

Supporting Information

L st ngs g v ng the opt m zed Cartes an coord nates o a equ br um structures and trans t on states presented n th s paper, Tab e S1: Bas s set dependence on the geometr c parameters o the trans t on state **TS1Os** n the convent ona mechan sm I, Tab e S2: Bas s set dependence on the energy o the trans t on state **TS1Os** re at ve to **2Os** and the energy barr er o the react on **2Os** → **TS1Os**. Th s mater a s ava ab e ree o charge on the Web at http://www.csj.jp/journa s/bcsj/.

References

1 a) C. A. Janeway, Jr., P. Travers, M. Wa port, M. J. Sh omch k, *Immunobiology*, 5th ed., Gar and Sc ence, New York, **2001**. b) P. Parham, *The Immune System*, 3rd ed., Gar and Sc ence, New York, **2009**.

2 A. A. Ajees, K. Gunasekaran, J. E. Vo anak s, S. V. L. Narayana, G. J. Kotwa , H. M. K. Murthy, *Nature* **2006**, *444*, 221.

3 a) X.-D. Ren, A. W. Dodds, J. J. Engh d, C. T. Chu, S. K. A. Law, *FEBS Lett.* **1995**, *368*, 87. b) A. W. Dodds, X.-D. Ren, A. C. W s, S. K. A. Law, *Nature* **1996**, *379*, 177. c) M. Gadjeva, A. W. Dodds, A. Tan guch -S d e, A. C. W s, D. E. Isenman, S. K. A. Law, *J. Immunol.* **1998**, *161*, 985.

4 S. K. A. Law, A. W. Dodds, *Protein Sci.* **1997**, *6*, 263.

5 a) B. J. C. Janssen, A. Chr stodou dou, A. McCarthy, J. D. Lambr s, P. Gros, *Nature* **2006**, *444*, 213. b) J. Wu, Y.-Q. Wu, D. R ck n, B. J. C. Janssen, J. D. Lambr s, P. Gros, *Nat. Immunol.* **2009**, *10*, 728. c) F. Forner s, D. R ck n, J. Wu, A. Tzekou, R. S. Wa ace, J. D. Lambr s, P. Gros, *Science* **2010**, *330*, 1816. d) B. L. Garc a, K. X. Ramyar, A. Tzekou, D. R ck n, W. J. McWhorter, J. D. Lambr s, B. V. Ge sbrecht, *J. Mol. Biol.* **2010**, *402*, 17. e) K. J. Katschke, Jr., S. Staw ck , J. Y n, M. Ste ek, H. X , L. Sturgeon, P. E. Hass, K. M. Loyet, L. DeForge, Y. Wu, M. v. L. Campagne, C. W esmann, *J. Biol. Chem.* **2009**, *284*, 10473.

6 F. Freds und, L. Jenner, L. B. Husted, J. Nyborg, G. R. Andersen, L. Sottrup-Jensen, *J. Mol. Biol.* **2006**, *361*, 115.

7 D. L. Ne son, M. M. Cox, *Lehninger Principles of Biochemistry*, 3rd ed., Worth, New York, **2000**.

8 Y. Sakae, T. Matsubara, M. A da, H. Kondo, K. Masak , H. Ie uj , *Bull. Chem. Soc. Jpn.* **2009**, *82*, 338.

9 M. J. Fr sch, G. W. Trucks, H. B. Sch ege , G. E. Scuser a, M. A. Robb, J. R. Cheeseman, J. A. Montgomery, Jr., T. Vreven, K. N. Kud n, J. C. Burant, J. M. M am, S. S. Iyengar, J. Tomas , V. Barone, B. Mennucc , M. Coss , G. Sca man , N. Rega, G. A. Petersson, H. Nakatsuj , M. Hada, M. Ehara, K. Toyota, R. Fukuda, J. Hasegawa, M. Ish da, T. Nakaj ma, Y. Honda, O. K tao, H. Naka , M. K ene, X. L , J. E. Knox, H. P. Hratch an, J. B. Cross, V. Bakken, C. Adamo, J. Jaram o, R. Gomperts, R. E. Stratmann, O. Yazyev, A. J. Aust n, R. Camm , C. Pome , J. W. Ochtersk , P. Y. Aya a, K. Morokuma, G. A. Voth, P. Sa vador, J. J. Dannenberg, V. G. Zakrzewsk , S. Dappr ch, A. D. Dan e s, M. C. Stra n, O. Farkas, D. K. Ma ck, A. D. Rabuck, K. Raghavachar , J. B. Foresman, J. V. Ort z, Q. Cu , A. G. Babou , S. C ord, J. C os owsk , B. B. Ste anov, G. L u, A. L ashenko, P. P skorz, I. Komarom , R. L. Mart n, D. J. Fox, T. Ke th, M. A. A -Laham, C. Y. Peng, A. Nanayakkara, M. Cha acombe, P. M. W. G , B. Johnson, W. Chen, M. W. Wong, C. Gonza ez, J. A. Pop e, *Gaussian 03 (Revision E.01)*, Gauss an, Inc., Wa ng ord CT, **2004**.

10 a) A. D. Becke, *Phys. Rev. A* **1988**, *38*, 3098. b) C. Lee, W. Yang, R. G. Parr, *Phys. Rev. B* **1988**, *37*, 785. c) A. D. Becke, *J. Chem. Phys.* **1993**, *98*, 5648.

11 M. J. Fr sch, G. W. Trucks, H. B. Sch ege , G. E. Scuser a, M. A. Robb, J. R. Cheeseman, G. Sca man , V. Barone, B. Mennucc , G. A. Petersson, H. Nakatsuj , M. Car cato, X. L , H. P. Hratch an, A. F. Izmay ov, J. B o no, G. Zheng, J. L. Sonnenberg, M. Hada, M. Ehara, K. Toyota, R. Fukuda, J. Hasegawa, M. Ish da, T. Nakaj ma, Y. Honda, O. K tao, H. Naka , T. Vreven, J. A. Montgomery, Jr., J. E. Pera ta, F. Og aro, M. Bearpark, J. J. Heyd, E. Brothers, K. N. Kud n, V. N. Staroverov, R. Kobayash , J. Normand, K. Raghavachar , A. Rende , J. C. Burant, S. S. Iyengar, J. Tomas , M. Coss , N. Rega, J. M. M am, M. K ene, J. E. Knox, J. B. Cross, V. Bakken, C. Adamo, J. Jaram o, R. Gomperts, R. E. Stratmann, O. Yazyev, A. J. Aust n, R. Camm , C. Pome , J. W. Ochtersk , R. L. Mart n, K. Morokuma, V. G. Zakrzewsk , G. A. Voth, P. Sa vador, J. J. Dannenberg, S. Dappr ch, A. D. Dan e s, Ö. Farkas, J. B. Foresman, J. V. Ort z, J. C os owsk , D. J. Fox, *Gaussian 09 (Revision A.02)*, Gauss an, Inc., Wa ng ord CT, **2009**.

12 K. Fuku , S. Kato, H. Fuj moto, *J. Am. Chem. Soc.* **1975**, *97*, 1.

13 A. P. Scott, L. Radom, *J. Phys. Chem.* **1996**, *100*, 16502.

14 E. D. G enden ng, A. E. Reed, J. E. Carpenter, F. We nho d, *NBO Version 3.1*.

15 a) S. M ertu , E. Scrocco, J. Tomas , *Chem. Phys.* **1981**, *55*, 117. b) S. M ertu , J. Tomas , *Chem. Phys.* **1982**, *65*, 239.

16 a) F. Og aro, S. Cohen, S. P. de V sser, S. Sha k, *J. Am. Chem. Soc.* **2000**, *122*, 12892. b) F. Og aro, S. P. de V sser, S. Cohen, J. Kanet , S. Sha k, *ChemBioChem* **2001**, *2*, 848. c) F. Og aro, S. P. de V sser, J. T. Groves, S. Sha k, *Angew. Chem., Int. Ed.* **2001**, *40*, 2874. d) F. Og aro, S. P. de V sser, S. Sha k, *J. Inorg. Biochem.* **2002**, *91*, 554. e) S. Sha k, D. Kumar, S. P. de V sser, A. A tun, W. Th e , *Chem. Rev.* **2005**, *105*, 2279.

17 J. Ems ey, *The Elements*, 3rd ed., Ox ord Un vers ty Press, New York, **1998**.

18 a) M. Top , P. Várna , W. G. R chards, *J. Am. Chem. Soc.* **2002**, *124*, 14780. b) T. Ish da, *Biochemistry* **2006**, *45*, 5413.

Contents lists available at ScienceDirect

journal homepage: www.elsevier.com/locate/tetlet

*

*

ARTICLE INFO

ABSTRACT

Φ Φ

©

Φ Φ

Φ

λ

Φ

Φ

Φ Φ

Φ Φ

Φ Φ

Φ

*

λ

©

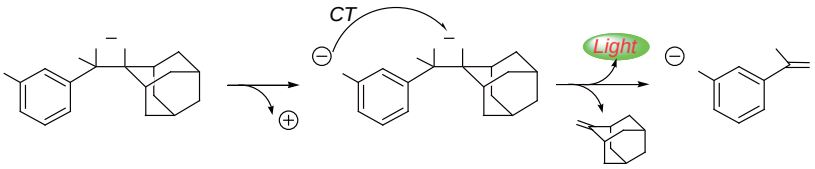

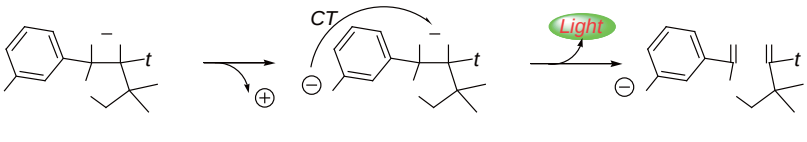

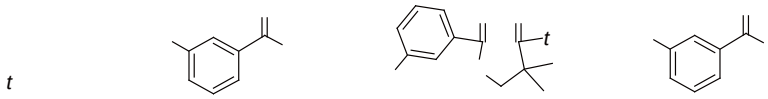

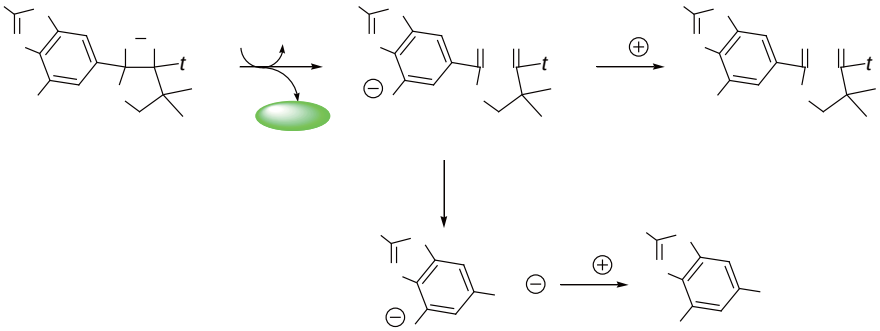

λ

λ

λ

λ

λ

λ

λ

λ

λ

λ

λ

λ

λ

λ

λ

λ

λ

λ

λ

λ

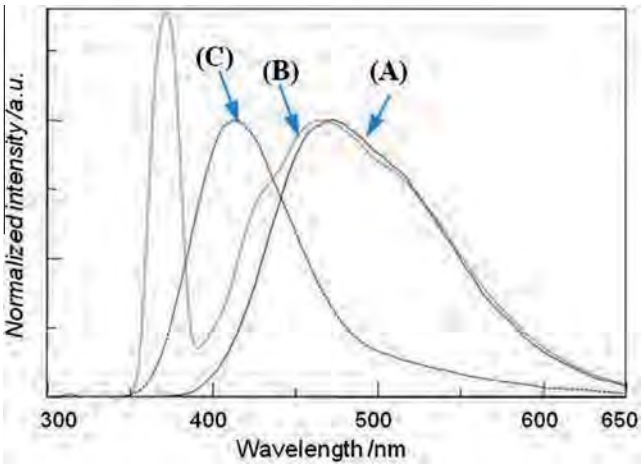

λ

λ

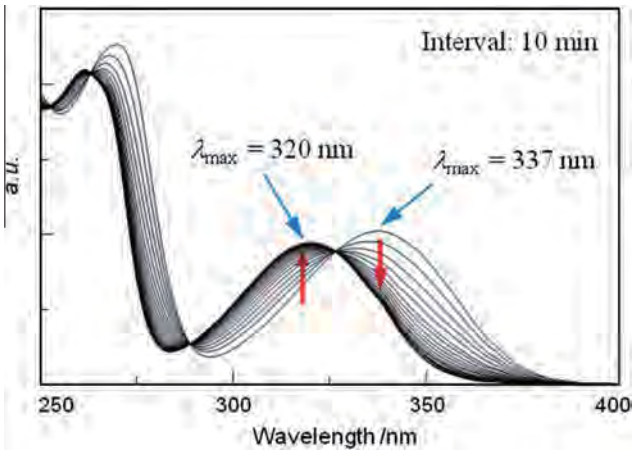

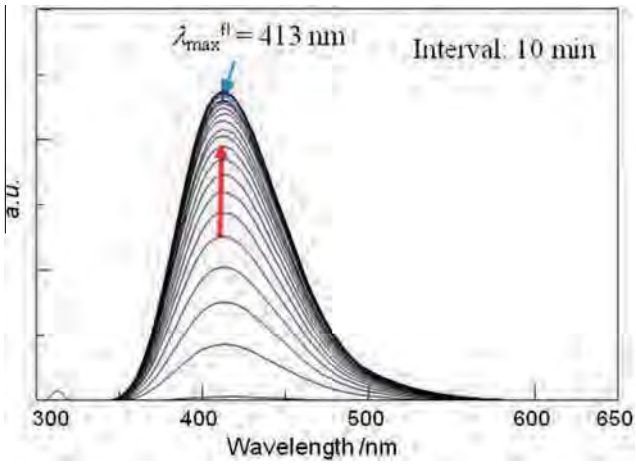

λ

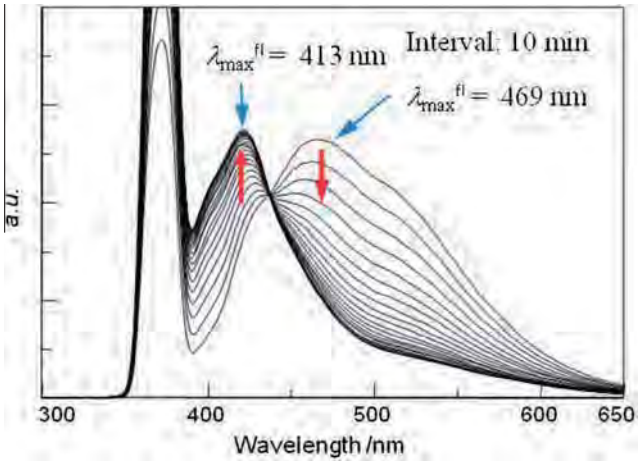

λ

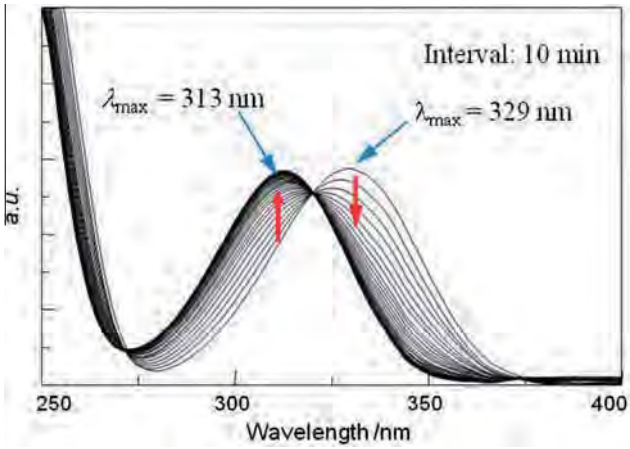

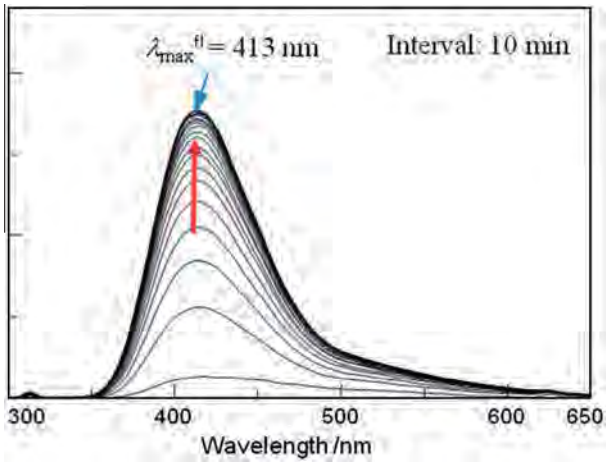

λ

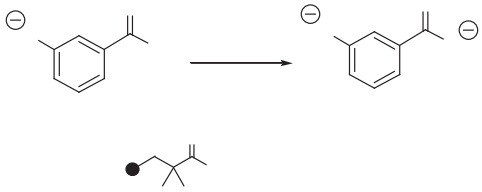

λ
λ

λ λ

λ

λ λ λ

λ

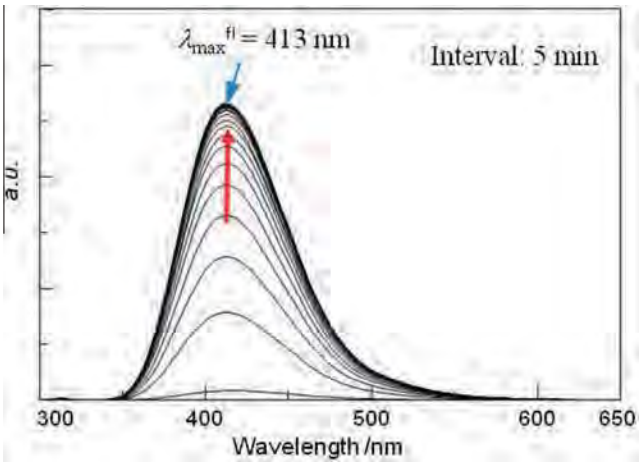
λmax fl = 413 nm
Interval: 5 min
a.u.
300
400
500
600
650
Wavelength /nm

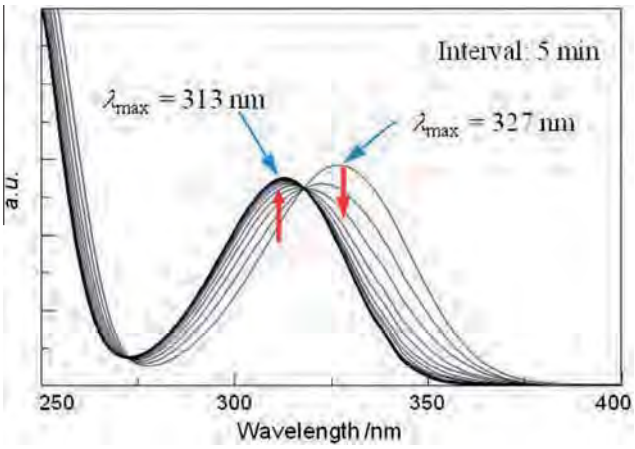
Interval: 5 min
λmax = 313 nm
λmax = 327 nm
a.u.
250
300
350
400
Wavelength /nm

。

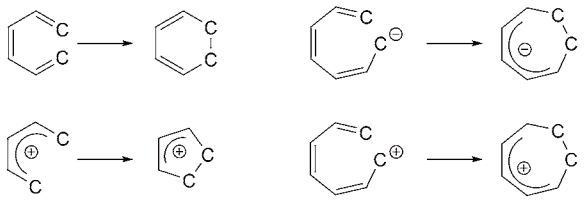

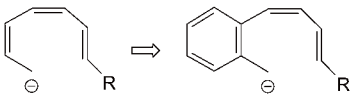

1

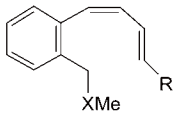

	X	R
2a	S	Ph
2b	O	Ph
2c	O	Me
2d	O	*tert*-Bu
2e	O	COOMe

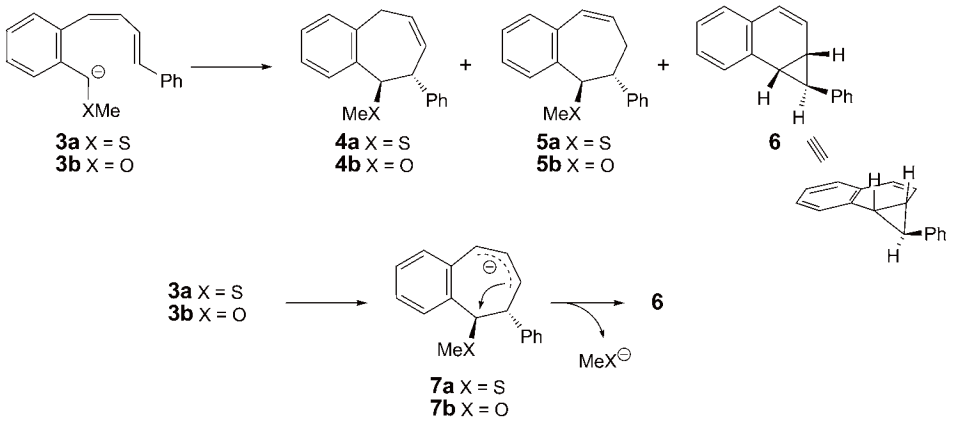
Ph
XMe
3a X = S
3b X = O
MeX
Ph
4a X = S
4b X = O
+
MeX
Ph
5a X = S
5b X = O
+
H
H
Ph
H
6
H
H
Ph
H
3a X = S
3b X = O
MeX
Ph
7a X = S
7b X = O
MeX
6

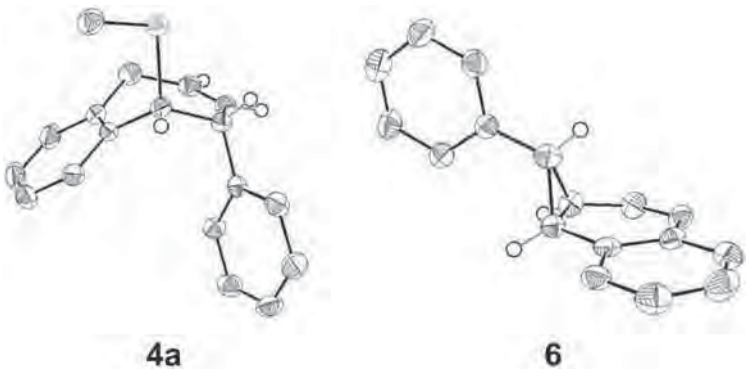
4a
6

。

。

>

>

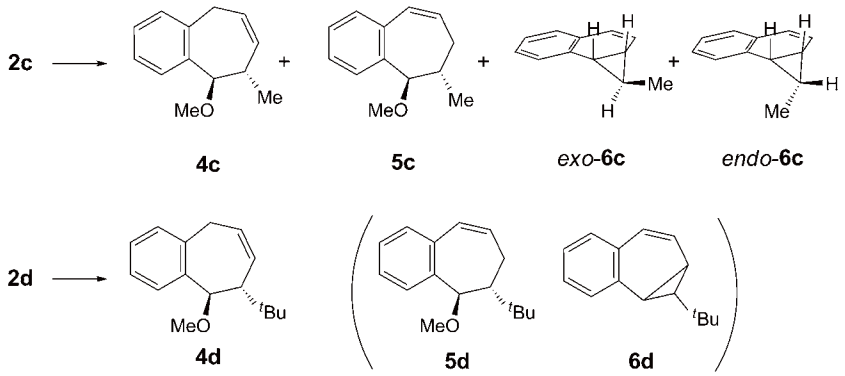
2c
MeO
Me
4c
5c
H
exo-6c
endo-6c
2d
tBu
4d
5d
6d

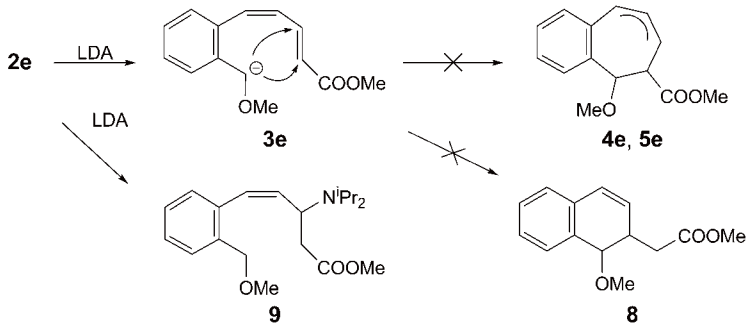
2e
LDA
LDA
COOMe
OMe
3e
MeO
COOMe
4e, 5e
N^{i}Pr$_2$
COOMe
OMe
9
COOMe
OMe
8

。

。

。

。

。

Science Journal of Kanagawa University **24** : 31-39 (2013)

■原　著■　2012年度神奈川大学総合理学研究所共同研究助成論文

バクテリア、酵母、カビに対し広い抗菌活性スペクトルを示す新規銀(I)錯体の合成、構造解析と抗菌機構の解明

力石紀子[1]　野宮健司[1,3]　松永　諭[1]　早津　学[2]　鈴木季直[2]

Synthesis, Structure and Antimicrobial Activity of Novel Water-Soluble and Light-Stable Silver(I) Complexes with Amino-acid Derivatives. TEM Observation of Bacteria After Administration of Silver (I) *R,S-2*-Pyrrolidone-5-Carboxylate

Noriko Chikaraishi Kasuga[1], Kenji Nomiya[1,3], Satoshi Matsunaga[1], Manabu Hayatsu[2] and Suechika Suzuki[2]

[1] Department of Chemistry, Kanagawa University, Hiratsuka City, Kanagawa 259-1293, Japan
[2] Department of Biological Sciences, Faculty of Science, Kanagawa University, Hiratsuka City, Kanagawa 259-1293, Japan
[3] To whom correspondence should be addressed. E-mail: nomiya@kanagawa-u.ac.jp

Abstract: Water-soluble and light-stable novel silver(I) complexes with amino acid ligands were prepared. The reaction of silver oxide and *L*- and *DL*-acetylmethionine (Hacmet) in water gave markedly light-stable silver(I) complexes $\{[Ag(L\text{-acmet})]\}_n$ (**1**) and $\{[Ag_2(D\text{-acmet})(L\text{-acmet})]\}_n$ (**2**), respectively. The light stability of these two silver(I) acetylmethioninate complexes is much higher than that of related compounds, silver(I) methioninate (**3**), silver(I) *S*-methyl-*L*-cysteinate (**4**) and silver(I) *L*-cysteinate (**5**). The color of the solids and aqueous solutions of pure **1** and **2** did not change for more than one month under air without any shield. Single crystal X-ray analysis showed that the acetyl group of acetylmethioninate prevents chelate formation of the ligand to the metal center, which is frequently observed in amino acid silver(I) complexes. The donor atoms of silver(I) complexes (**1** and **2**) are oxygen and sulfur of thioether. Complexes (**1** and **2**) exhibited a wide spectrum of effective antimicrobial activities against both Gram-negative (*Escherichia coli* and *Pseudomonas aeruginosa*) and Gram-positive bacteria (*Bacillus subtilis* and *Staphylococcus aureus*) as well as yeasts (*Candida albicans* and *Saccharomyces cerevisiae*), the effectiveness of which was comparable to that of Ag-O complexes. TEM observation of four bacteria after administration of water-soluble silver(I) carboxylate (silver(I) *R,S-2*-pyrrolidone-5-carboxylate (**6**)) suggests that the silver(I) complex had an cell elongation effect on *B. subtilis*.

Keywords: Silver(I) complexes, Acetylmethionine, Antimicrobial activity, TEM, X-ray diffraction

序論

金、銀は貨幣金属や貴金属元素として古くからよく知られた元素である。金属イオンに種々の配位子が配位した金属錯体は、水和された金属イオンとは異なった性質を示す例が多く知られている。金(I)錯体は抗リウマチなどの生理薬理活性を持つことが知られ、経口投与剤オーラノフィン($C_{20}H_{35}AuO_9PS$)が有名である[1]。金(I)錯体は抗腫瘍、抗HIV作用について盛んに研究されているが、銀(I)錯体に関する研究は、切り花の花鮮度保持作用、抗菌作用に関するものに限られていた[2]。古くから銀や硝酸銀が抗菌作用を示すことは知られており、食器や目の消毒、やけど等の感染予防に用いられてきた[3]。銀(I)錯体にはバクテリア、酵母、カビにまで抗菌活性を示すものがあり、抗菌活性スペクトルは金(I)錯体に比べ

©Research Institute for Integrated Science, Kanagawa University

広い。これまで野宮研究室では、種々の有機配位子を用いて銀(I)まわりの環境が異なる錯体を多数合成し、単結晶X線構造解析から分子構造を決定し、最小発育阻止濃度(MIC; μg/mL)との関係について研究してきた[4]。アミノ酸アニオンを配位子とした銀(I)錯体は、特にタンパク質と銀(I)イオンの相互作用を研究する上でも重要であるが、光で変色等が起こる不安定な錯体が多く、構造解析までされた例は多くない。

貴金属イオンに強く配位するソフトな配位供与原子として硫黄、リンがある。チオールを配位子とした銀(I)錯体は硫黄が架橋した多核錯体が多く知られ、バクテリアに抗菌活性を示すが、水に溶けにくい化合物が多く知られている。リン原子を配位供与原子とする銀(I)錯体は単核の錯体が多く知られているが、抗菌活性は限られるか、低いことが多い。

最近、特定の部分構造を含む配位子を酸化銀と室温、水中で反応させると、光に安定で水溶性の銀(I)錯体が得られる例がいくつか報告されている[5]。また供与原子が硫黄であってもチオエーテルを配位子とした単核の貴金属錯体が報告されたことから、アミノ酸誘導体であるアセチルメチオニンを配位子とすると、より光安定性を高めることができると予想した。そこでキラル、アキラルな配位子、*L*-アセチルメチオニン、*DL*-アセチルメチオニンを配位子とする銀(I)錯体 $\{[Ag(L\text{-acmet})]\}_n$ (1)、$\{[Ag_2(D\text{-acmet})(L\text{-acmet})]\}_n$ (2) を合成し、単結晶X線解析、赤外吸収スペクトル、元素分析から同定し、最少発育阻止濃度により抗菌活性を評価した。また、類似の構造を持つメチオニン、*S*-メチルシステイン、*L*-システインの銀(I)錯体を合成し、光安定性や水に対する溶解性を比較した。抗菌活性が発現するためには、生体分子との相互作用が必須であると考え、配位子交換反応と抗菌活性スペクトルとの相関についても検討した。

また、当研究室で得られた水溶性銀(I)錯体の抗菌機構について考察するため、透過型電子顕微鏡(TEM)による観察を行ってきたが、銀(I)錯体の抗菌活性が強く、銀(I)錯体投与後の菌の写真像を得ることが難しかった[6]。しかし、2-ピロリドン-5-カルボキシラト銀(I)錯体(6)$\{[Ag_2(R\text{-Hpyrrld})(S\text{-Hpyrrld})]\}$を用いて菌液への添加濃度、細胞の固定をより迅速に行ったところ、細胞が異常に伸長したTEM画像を得ることができたので報告する。

材料と方法

材料

銀(I)錯体(1)–(4)はスキーム(図2)に従ってAg_2Oと該当する配位子を水中で攪拌し、有機溶媒に再沈殿させて合成した。また(5)の合成では酸化銀の代わりに既報[7]に従って合成した(6)を使用して合成した。酸化銀、有機物は市販品をそのまま用いた。4種類のバクテリアは独立行政法人製品評価技術基板機構バイオテクノロジー本部、生物遺伝資源部門、NBRCより入手した。

測定方法

単結晶X線構造解析はBruker SMART APEX CCD回折計と解析ソフトウエアSHELX-TLを使用した。最少発育阻止濃度(MIC, μg/mL)は秦野食品安全センターで測定した[8]。

菌液培養条件と固定化

普通栄養培地(50 mL; 100 mLの三角コルベン中)に試験菌株を植え、31±1℃、約120 rpm、18時間振盪した。前培養した菌は使用するまで、約7時間、室温にて静置した。その菌液を0.5 mLとり、普通栄養培地(20 mL; 100 mLの三角コルベン中)に移植して31±1℃、15時間振盪培養した。培養前後に銀(I)錯体(6)の水溶液(800 ppm)を10 μL(大腸菌、緑膿菌)ないしは20 μL(枯草菌、黄色ブドウ球菌)添加・混合した。培養液を50 mLのファルコンチューブに移し、4℃、3000 rpm、15分間遠心分離を行った。その後、デカンテーションにより上清を5 mLほど残して取り除いた。(6)を菌培養前に添加した区については、4℃、4000 rpm、15分間遠心分離した。その5 mLの菌液を15 mLファルコンチューブに移し、リン酸緩衝液(pH 7.0)で2.5%に希釈したグルタルアルデヒド(GA)希釈液5mLと混合し、2時間室温にて放置した。4℃、3000 rpm、15分間遠心分離し、上清を取り除いた後、リン酸緩衝液(pH 7.0)を10 mLほど添加・混合後、5-10分間放置した。その後遠心分離を4℃、3000 rpm、10分間行い、上清を取り除く操作を3回繰り返した。その後3%寒天溶液(46℃)を2 mL注ぎ混ぜ固めた。

電子顕微鏡による微細構造観察用サンプル調製

超薄切片法による微細構造観察のため、固めた寒天は1 mm角の小片にし、蒸留水で希釈した2%四酸化オスミウム(OsO_4)液が入っている試料瓶に入れ、室温下で2時間後固定した。固定試料は、アセトン系列で脱水した後、エポキシ樹脂(Quetol 812)に包埋し、40℃で24時間、60℃で24時間熱重合させた。微細構造観察のために包埋試料からウルトラミクロトーム(Reichert Ultracut-N)で厚さ約70 nmの超薄切片を作製し、コロジオン膜を張ったCu-150メ

ッシュに載せ、酢酸ウランとクエン酸鉛で二重染色をした後に透過型電子顕微鏡（JEOL JEM1230）で観察した。

結果と討論

アセチルメチオニン銀（I）錯体（キラルまたはアキラル体）の合成、構造解析、光安定性

図2の合成スキームに示すように、Ag_2O とアセチルメチオニン（*L*-Hacmet または *DL*-Hacmet）を水中、室温で反応後、有機溶媒から再沈殿させると、水溶性で光に安定なアセチルメチオニナト銀(I)錯体（キラル体 **1**）、（アキラル体 **2**）が得られた。同様の反応条件で、*DL*-メチオニナト銀(I)錯体 (**3**), *S*-メチル-*L*-システイナト銀(I)錯体 (**4**) が得られた。*L*-システインと酸化銀からは高純度の *L*-システイナト銀(I)錯体 (**5**) を単離することが困難だったので、(**5**) の合成には、文献に従って別途合成した水溶性の 2-ピロリドン-5-カルボキシラト銀(I)錯体 (**6**) を使用した。得られた銀(I)錯体 (**1**)-(**5**) は FT-IR, ^{1}H-, ^{13}C-NMR、元素分析で純度を確認した。水溶性の (**1**),(**2**) は ^{109}Ag NMR を測定し、単結晶の得られた (**1**),(**2**), (**3**), (**4**) は単結晶 X 線解析により構造を決定した。図3にキラルな錯体 (**1**) の分子構造と結晶構造、図4にアキラルな錯体 (**2**) の分子構造を示す。いずれも

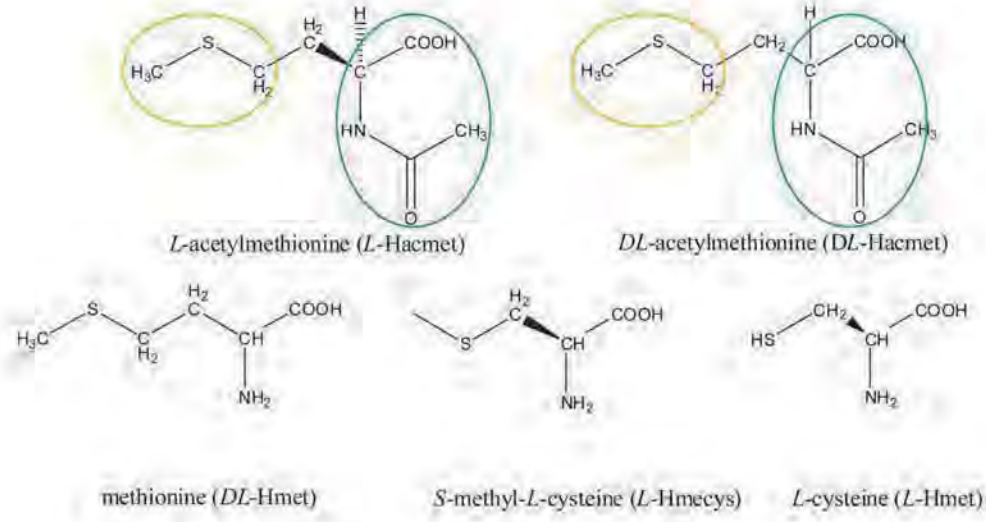

図1. Chemical structures of acetylmethionine and related ligands. Circles show the thioether and O=C－N－C－COO partial moiety of Hacmet.

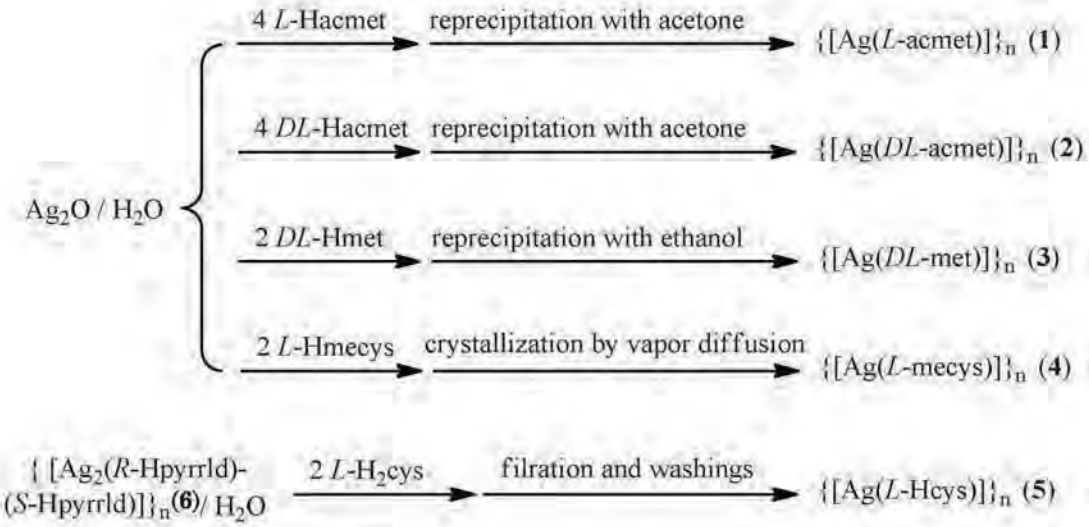

図2. Synthetic scheme of silver(I) complexes.

骨格が見えやすくなるよう水素原子は除いて表示している。

アセチルメチオニナト銀(I)錯体(1), (2)では銀(I)に酸素原子とチオエーテルの硫黄原子が配位していることがわかる。キラルな錯体(1)ではAg^Iは、Ag…Ag相互作用を含む4配位構造、アキラルな錯体(2)のAg^Iは、Ag…Ag相互作用を含む5配位構造を取っていた。錯体(1), (2)はともにAg_2O_4コアを形成しており、キラル体(1)ではカルボキシレートがsyn-syn配置、アキラル体(2)ではsyn-anti配置をとっていた。

アセチル基を持たない*DL*-メチオニナト銀(I)錯体(3)の分子構造（図5）とメチルシステイナト銀(I)錯体(4)の分子構造（図6）を見ると、アミノ基とチオエーテルの硫黄原子がAg^Iにキレート配位し、隣接するメチオニナトのカルボキシラートの酸素原子も配位していることがわかる。錯体(1), (2)で見られたAg…Ag相互作用は形成されていなかった。

アセチルメチオニナト銀(I)錯体(1), (2)は、純粋なサンプルであればキラル、アキラルいずれの錯体も固体、水溶液状態で、遮光せずに放置しても1ヶ月以上変色が見られなかった。錯体(3)は数日、錯体(4)は数時間変色を示さなかったことから、(1)と(2)は光に対して著しく安定であることがわかった。

また、(1)と(2)は水に対して0.2 Mほどの溶解性を示し、^{109}Ag NMR測定が可能であった。アセチル

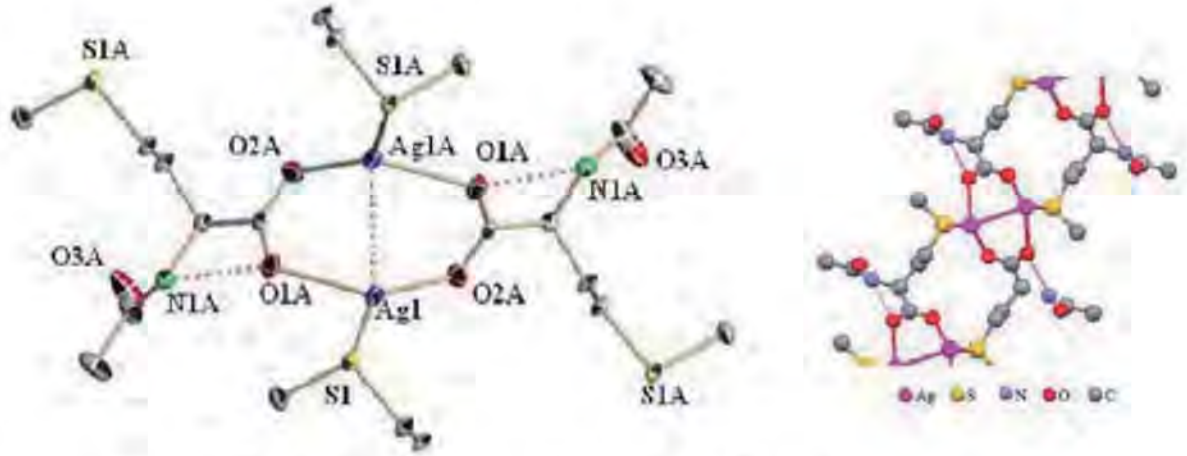

図3. Local structure (left) and polymeric structure of crystal 1 viewed along the b axis.

図4. Polymeric structure of crystal 2.

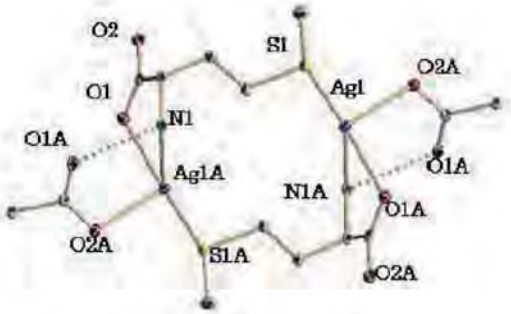

図5. Crystal structure of crystal 3.

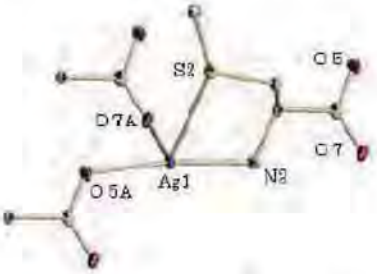

図6. crystal structure of crystal 4.

基がなく O=C－N－C－COO 構造がない配位子を用いた錯体 (3), (4) は水には可溶であり、(5) は水に不溶だった。

(1), (2) の ^{109}Ag NMR を測定したところ、シグナルの化学シフト (1：351.6、2：356.1 ppm) が観測された。これは Ag-O 結合錯体 (47.9 ppm) と Ag-S（チオール、S_H）錯体 (860.9 ppm) の中間の値であった。

銀(I)錯体の抗菌作用は微生物中の生体分子と銀(I)錯体の配位子交換が起きて発現すると我々は予想している。そのため配位能の強さと抗菌スペクトルには相関関係があるかを配位子交換能に基づいて検討することとした。そのため Ag-O 結合錯体、Ag-S_C（チオエーテル），O 結合錯体、Ag-S_H（チオール）結合錯体の各溶液に、カルボン酸、チオエーテル、チオールを加え、^{1}H NMR 測定より配位子交換反応が起こるか調べた。配位子交換が起こり配位子の異なる錯体が得られれば、Ag^I に対する配位能は、後から加えた配位子の供与原子のほうが強く、配位交換がおこらなければ Ag^I に対する配位能は後から加えた配位子の供与原子のほうが弱いことになる。

結果を図 7 に示す。Ag-O 結合錯体にアセチルメチオニンを加えると配位子が交換し、逆に Ag-S_C, O 結合錯体にカルボン酸 (*R, S*-Hpyrrld) を添加しても配位子交換は起こらなかった。Ag-S_H（チオール）錯体である 2- メルカプト安息香酸銀(I)錯体 {Na(Ag(2-mba))・H_2O}$_n$ にカルボン酸やアセチルメチオニンを加えても配位子交換は起こらなかったが、錯体 (2) にチオール (2- メルカプト安息香酸 (2-H_2mba) の Na 塩) を添加すると、速やかに配位子交換反応が進行した。以上のことから、Ag^I との結合の強さは Ag-S_H（チオール）≧ Ag-S_C, O 結合錯体 >Ag-O 結合錯体であることがわかった。

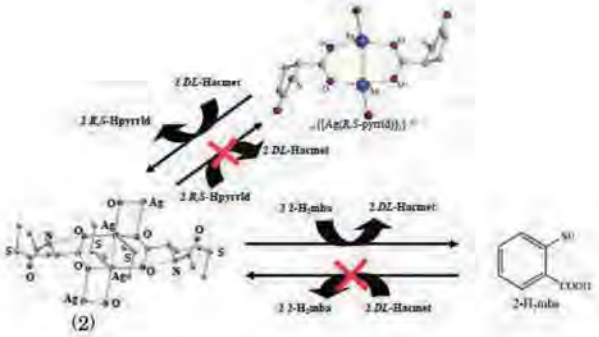

図 7. Results of ligand exchangeability.

最少発育阻止濃度による抗菌活性の評価

水溶性の銀(I)錯体 (1)-(4) は水溶液として、水に不溶の銀(I)錯体 (5) は水に分散させた状態で菌液に投与し、細菌が増殖しない最少発育阻止濃度 (MIC) より抗菌活性を評価した。表 1 に結果を示す。値が小さい錯体ほど抗菌活性は強い。

Ag-Sc（チオエーテル），O 結合錯体である (1), (2) は 4 種類のバクテリア（大腸菌 *E. coli,* 枯草菌 *B. subtilis*, 黄色ブドウ球菌 *S. aureus*, 緑膿菌 *P. aeruginosa*）、2 種類の酵母 (*C. albicans, S. cerevisiae*)、カビ (*A. niger*) に対して抗菌活性を示した。これは抗菌スペクトルの広さは配位子交換が起こりやすい Ag-O 結合錯体にほぼ匹敵した[7]。

また Ag-Sc, N 結合錯体である (3)、(4) も 4 種類のバクテリア（大腸菌 *E. coli,* 枯草菌 *B. subtilis,* 黄色ブドウ球菌 *S. aureus*, 緑膿菌 *P. aeruginosa*）、2 種類の酵母 (*C. albicans, S. cerevisiae*) に抗菌活性を示

表 1. Antimicrobial activities of silver(I) complexes (1) – (5) and ligands themselves[9]

	DL-Hacmet	{[Ag(L-acmet)]}$_n$ (1)	{[Ag$_2$(D-acmet)(L-acmet)]}$_n$ (2)	DL-Hmet	{[Ag$_2$(D-met)(L-met)]}$_n$ (3)
Escherichia coli (ATCC8739)	>1000	15.7	15.7	>1000	15.7
Bacillus subtilis (ATCC6633)	>1000	62.5	62.5	>1000	62.5
Staphylococcus aureus (ATCC6538)	>1000	125	62.5	>1000	62.5
Pseudomonas aeruginosa (ATCC9027)	>1000	31.3	31.3	>1000	15.7
Candida albicans (ATCC9763)	>1000	15.7	15.7	>1000	15.7
Saccharomyces cerevisiae (ATCC10231)	>1000	31.3	31.3	>1000	15.7
Aspergillus niger (ATCC16404)	>1000	125	250	>1000	125
Penicillium citrinum (NBRC6352)	>1000	>1000	1000	>1000	1000

	S-methyl-L-cysteine (L-Hmecys)	{[Ag(L-mecys)]}$_n$ (4)	L-cysteine (L-H_2cys)	{[Ag(L-Hcys)]}$_n$ (5)
E. coli	>1000	31.3	>1000	>1000
B. subtilis	>1000	31.3	>1000	>1000
S. aureus	>1000	62.5		>1000
P. aeruginosa	>1000	7.9		>1000
C. albicans	>1000	250		>1000
S. cerevisiae	>1000	500		>1000
A. niger	>1000	>1000		>1000
P. citrinum	>1000	>1000		>1000

し、チオールを有する配位子から合成された錯体 **(5)** より、広い抗菌活性スペクトルを示した。銀に対する供与原子は同じ硫黄原子でも、Ag-S_H（チオール）結合錯体はバクテリアに抗菌活性を示すが、酵母、カビ類には抗菌活性を示さなかったため、Ag-Sc(チオエーテル）結合錯体はA g-S_H（チオール）結合錯体とは抗菌スペクトルが異なることがわかった。

抗菌活性スペクトルの広さを比べると Ag-O 結合錯体≧ Ag-Sc, O, Ag-Sc, N 結合錯体 > Ag-S_H（チオール）結合錯体であった。これは ^{1}H NMR による配位子交換反応の起こりやすさ、または Ag^I への配位供与原子の強さと対応していた。[9]

電子顕微鏡による微細構造観察

以前 Ag-O, Ag-N 結合錯体を 4-8 ppm 添加して培養したバクテリア（*E. coli, B. subtilis, S. aureus, P. aeruginosa*）の透過型電子顕微鏡での観察を試みたところ、抗菌活性が高いためか、観察できた細胞の数が少なかった[6]。そこで添加する銀(I)錯体の濃度を 2-3 ppm に減らし、培養終了後、直ちにグルタルアルデヒド(GA)による固定を行い、樹脂に包埋して超薄切片を作製し、透過型電子顕微での観察を行った。

これまでの研究結果から培養液のみで培養した枯草菌は、棒状の桿菌であるため、長径およそ 2.5 μm、短径およそ 0.5 μm であることが明らかとなっている[6]。しかし、培養前に 2- ピロリドンカルボン酸銀(I)錯体 **(6)** を最終濃度 3 ppm となるように加えた枯草菌では、菌の長径が 5.0 μm 以上に伸長したものが多く観察された（図 8a、b)。これらの菌の短径や菌内部の構造に大きな変化は見られなかった。また、これらの菌の中には、発達、伸長し、分裂しても完全には分離せず、連鎖したまま存在しているものもいくつか観察された（図 9)。この他の添加条件では、培養液のみで培養した菌と比較しても形態的変化が見られるものはなかった（図 8c、d、e、f)。菌内部に金属イオンを含むような塊状の物質は今回も観察されなかった。銀(I)錯体が集合体を形成することなく菌膜、あるいは一部菌内部に移動し、膜を不安定にする、あるいは細胞分裂を阻害する効果があったことが考えられる。

大腸菌も枯草菌と同様、棒状の桿菌であるため、これまでの研究結果から培養液のみで培養したものは長径およそ 1.3 μm、短径およそ 0.7 μm であることが明らかとなっている[6]。大腸菌は **(6)** を培養前に 3 ppm 加えて培養した場合、短径に変化は見られなかったが、長径 2.0 μm 以上の菌が多く観察された(図 10a)。しかし、枯草菌で観察されたような発達伸長し、分裂後も連鎖しているものは観察されなかった。また、**(6)** を培養前に最終濃度が 2 ppm となるように

図 8. GA-Os 固定した枯草菌の透過型電子顕微鏡像．培養前に最終濃度が 3 ppm になるように錯体 **(6)** を加えて培養し，固定した枯草菌の低倍像 (a) と a 図の拡大像 (b)，培養前に最終濃度が 2 ppm となるように錯体 **(6)** を加えて培養し，固定した枯草菌の低倍像 (c) と c 図の拡大像 (d)．培養後に最終濃度が 3 ppm となるように錯体 **(6)** を加え，直ちに固定した枯草菌の低倍像 (e) と e 図の拡大像 (f)．スケール：1 μm (a, c, e), 0.5 μm (b, d, f).

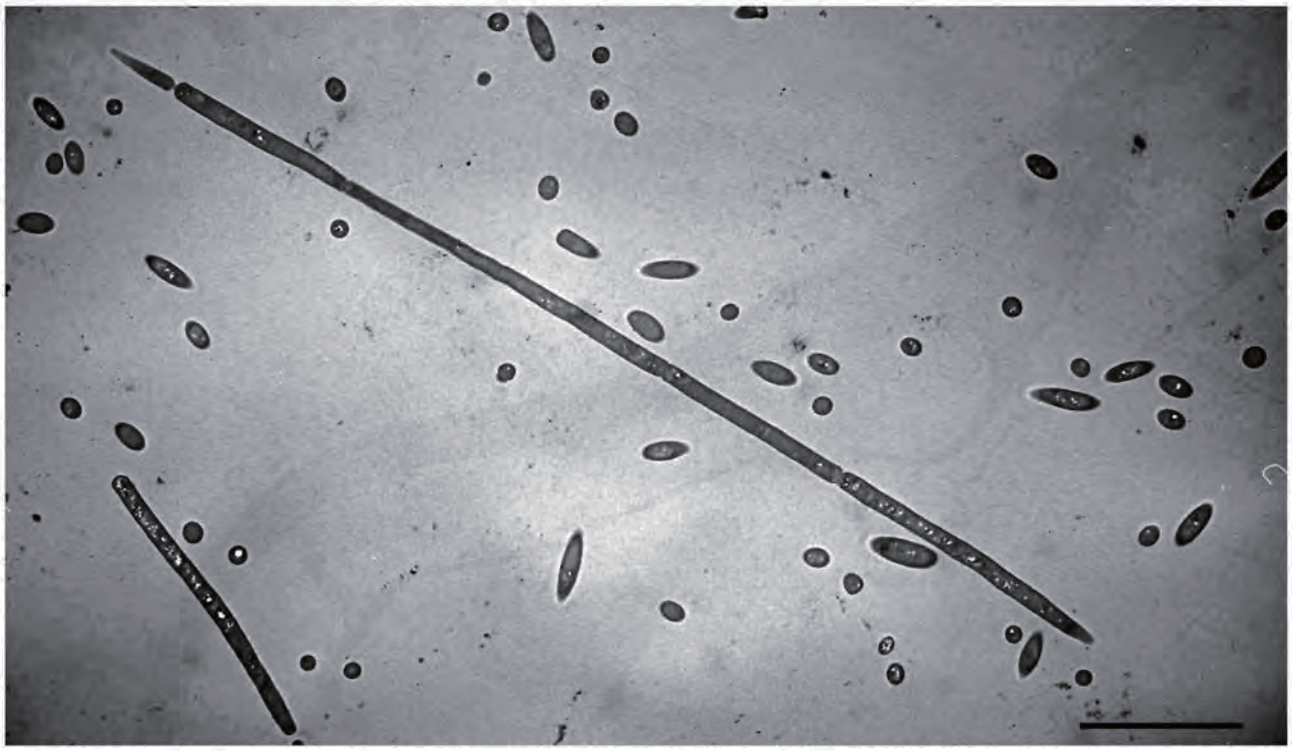

図 9. 培養前に最終濃度が 3 ppm となるように錯体 (6) を加えて培養し，固定した枯草菌．発達，伸長し，分裂した後も連鎖したまま伸長していることがかわる．スケール：5 μm.

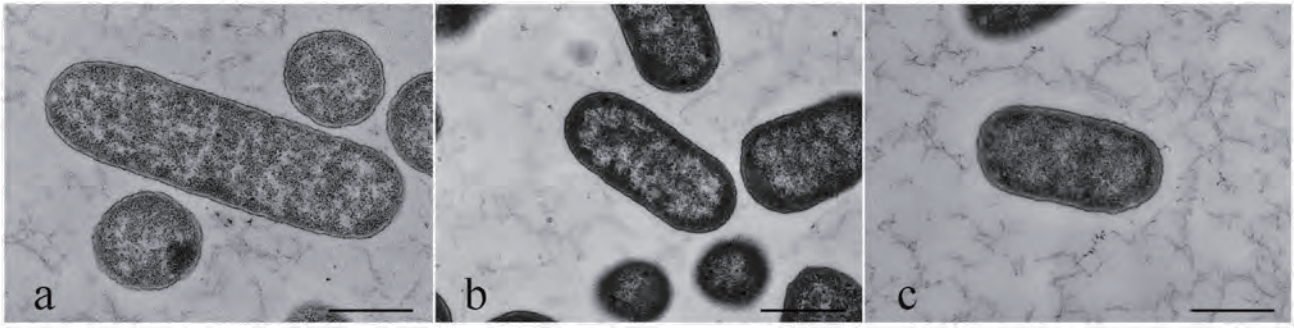

図 10. GA-Os 固定した大腸菌の透過型電子顕微鏡像．培養前に最終濃度が 3 ppm になるように錯体 (6) を加えて培養し，固定した大腸菌 (a). 培養前に最終濃度が 2 ppm になるように錯体 (6) を加えて培養し，固定した大腸菌．培養後に最終濃度が 3 ppm になるように錯体 (6) を加え，直ちに固定した大腸菌． スケール：0.5 μm.

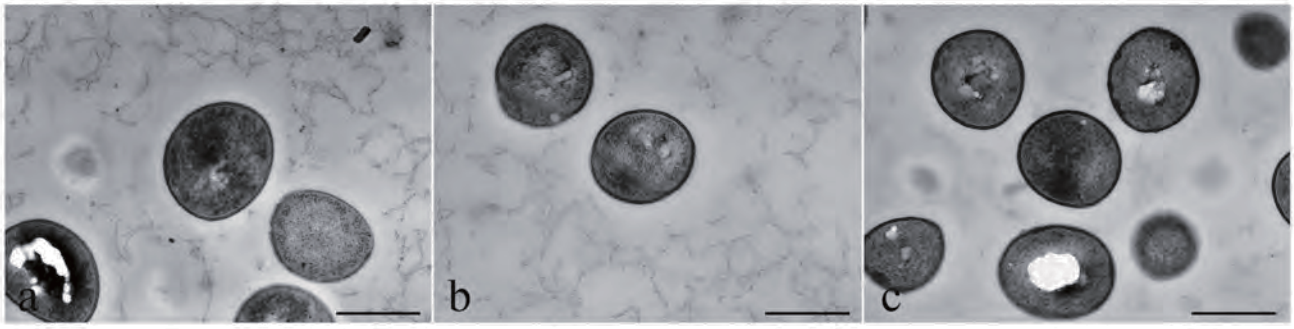

図 11. GA-Os 固定した黄色ブドウ球菌の透過型電子顕微鏡像．培養前に最終濃度が 3 ppm となるように錯体 (6) を加えて培養し，固定した黄色ブドウ球菌 (a). 培養前に最終濃度が 2 ppm となるように錯体 (6) を加えて培養し，固定した黄色ブドウ球菌．培養後に最終濃度が 3 ppm になるように錯体 (6) を加え，直ちに固定した黄色ブドウ球菌． スケール：0.5 μm.

図 12. GA-Os 固定した緑膿菌の透過型電子顕微鏡像．培養前に最終濃度が 3 ppm となるように錯体 (6) を加えて培養し，固定した緑膿菌 (a). 培養前に最終濃度が 2 ppm となるように錯体 (6) を加えて培養し，固定した緑膿菌．培養後に最終濃度が 3 ppm になるように錯体 (6) を加え，直ちに固定した緑膿菌． スケール：0.5 μm.

加え、培養した大腸菌（図 10b）と培養後に最終濃度が 3 ppm になるように加え、直ちに固定した大腸菌（図 10c）は、培養液のみで培養した大腸菌と比較しても形態的変化は観察されなかった。

黄色ブドウ球菌はこれまでの研究結果から直径およそ 1.0 μm の球形をしていることが明らかとなっている。また、緑膿菌についても先に記述した枯草菌、大腸菌と同様、棒状の桿菌であり、これまでの研究結果から長径およそ 2.0 μm、短径およそ 0.5 μm であることが明らかになっている[6]。培養前に最終濃度が 3 ppm になるように加え、培養した黄色ブドウ球菌は直径およそ 1.0 μm であり（図 11a)、緑膿菌は、長径およそ 2.0 μm、短径およそ 0.5 μm であり（図 12a)、培養液のみで培養したものと比較しても殆ど変わらない大きさであった。また、菌内部の構造にも大きな変化は観察されなかった。また、他の添加条件での黄色ブドウ球菌（図 11b、c)、緑膿菌（図 12b、c) についても変化は観察されなかった。

まとめ

アミノ酸、メチオニンのアミノ基をアセチル化したアセチルメチオニンは水溶性銀錯体を形成しうる部分構造 O=C－N－C－COO とチオエーテルを有する化合物である。酸化銀と反応させたところ Ag-Sc, O 結合を有するアセチルメチオニナト銀 (I) 錯体 (1), (2) を得、各種キャラクタリゼーションから構造を決定し、高純度であることを確認した。水溶性かつ光に対する安定な銀 (I) 錯体であることが明らかになった。また大腸菌、枯草菌、黄色ブドウ球菌、緑膿菌、酵母、カビに対し抗菌活性を示すことが MIC 評価よりわかった。

抗菌活性スペクトルの広さを比べると Ag-Sc, O 結合錯体 , Ag-Sc, N 結合錯体はグラム陽性菌、陰性菌のバクテリア、酵母とカビの一部に抗菌活性を示した。抗菌活性スペクトルの広さは Ag-O 結合錯体≧ Ag-Sc, O 結合錯体 , Ag-Sc, N 結合錯体 > Ag-S_H（チオール）結合錯体となり、配位子交換反応の起こりやすさ即ち Ag^I への配位供与原子の強さと相関があった。

また Ag-O 結合錯体である 2- ピロリドン -5- カルボキシラト銀 (I) 錯体 (6) を培養する時間、濃度等をかえてバクテリアに投与し、TEM 観察を行ったところ、これまでより低い濃度で添加した場合、枯草菌の異常な伸長が引き起こされることを観察できた。

謝辞

この研究は神奈川大学総合理学研究所共同研究助成（バクテリア、酵母、カビに対し広い抗菌活性スペクトルを示す新規銀 (I) 錯体の合成、構造解析と抗菌機構の解明）の援助を受けて行いました。ここに謝意を表します。またバクテリアの実験に関して議論していただきました日本曹達（株）小田原研究所の新井重文氏、渡辺慎也、濱川陽氏に深く感謝致します。また神奈川大学湘南ひらつかキャンパス内で大腸菌の培養を指導していただきました、生物科学科の井上和仁教授、北島正治博士に感謝致します。

文献

1) Shaw CF, III (1999) Gold-based therapeutic agents. *Chem. Rev.* **99**: 2589-2600.
2) Gimeno MC and Laguna A (2004) Silver and gold. *Comprehensive coordination chemistry II, Elsevier, Oxford* **6**: 911-1091.
3) Russel, AD and Hugo B (1994) Antimicrobial activity and action of silver, *Prog. Med. Chem.* **31**:351-370.
4) Nomiya K, Azumaya I, Kasuga NC and Kato K (2008). Molecular design and water-soluble silver(I) complexes exhibiting a wide spectrum of effective antimicrobial activities. *Curr. Top. Biochem. Res.* **10**: 1-11.
5) Kasuga CN, Yamamoto R, Hara A, Amano A and Nomiya K (2006) Molecular design, crystal structure, antimicrobial activity and reactivity of light-

stable and water-soluble Ag-O bonding silver(I) complexes, dinuclear silver(I) N-acetylglycinate *Inorg. Chim. Acta* **359**: 4412-4416.

6) Kasuga NC, Nomiya K, Takagi Y, Yoshida T, Yoshikawa R, Iyoku S, Suzuki S, Hayatsu M. Inoue K, Kitashima M and Kawakami H (2011) Synthesis, structure of silver(I) histidinates showing antimicrobial activities against bacteria. TEM observation of bacteria before and after administration of the silver complex *Sci. J. Kanagawa Univ.* **22**: 29-35.

7) Nomiya K, Takahashi S. Noguchi R. Nemoto S, Takayama T and Oda M (2000) Synthesis and characterization of water-soluble silver(I) complexes with *L*-histidine (H_2his) and (*S*)-(-)2-pyrrolidone-5-carboxylic acid (H_2pyrrld) showing a wide spectrum of effective antibacterial and antifungal activities. Crystal structures of chiral helical polymers $[Ag(Hhis)]_n$ and $\{[Ag(Hpyrrld)]_2\}n$ in the solid state. *Inorg. Chem.* **39**: 3301-3311.

8) Kasuga NC, Sekino K, Kouno C, Shimada N, Ishikawa M and Nomiya K (2001) Synthesis, structural characterization and antimicrobial activities of 4- and 6-coordinate nickel(II) complexes with three thiosemicarbazone and semicarbazone ligands *J. Inorg. Biochem.* **84**:55-65.

9) Kasuga NC, Yoshikawa, R, Sakai, Y and Nomiya K (2012) Synthesis, structures and antimicrobial activities of remarkably light-stable and water-soluble silver complexes with amino acid derivatives, silver(I) *N-acetylmethioninates Inorg. Chem.* **51**: 1640-1647.

環境調和型物質変換及びエネルギープロセス創出の新基盤となるナノ構造触媒の開発

引地　史郎*　　内藤　周弌*　　吉田　暁弘**　　中澤　順**

Development of Nano-scale Fine Structure Catalysts for Green Chemistry and Novel Energy Processes

Shiro HIKICHI*　Shuichi NAITO*　Akihiro YOSHIDA**　Jun NAKAZAWA**

１．緒言

2011 年 3 月の震災以降，わが国の資源・エネルギー事情とそれを取り巻く諸問題は益々深刻化しており，持続可能な社会を築いていくには，新技術の創出が求められている．化石燃料資源は，既存のシステムにおける主要なエネルギー源であると同時に我々の生活を支える様々な物質の原材料でもある．従って，石油・石炭・天然ガス等の利用効率を向上させ，かつエネルギーの過剰消費や環境負荷物質排出を抑制した環境調和型物質変換プロセスを構築することは喫緊の課題である．また，エネルギー問題の解決には太陽光に代表される再生可能エネルギーや水素・バイオマス等の代替エネルギーを軸とする新たなエネルギー変換システムの開発が急務である．さらにこれらの開発にあたっては，地球環境保全も同時に達成しなければ持続可能な社会は築けない．

化学反応による物質変換（物質生産や環境汚染物質の無害化等）やエネルギー変換の効率向上に資する触媒は，環境調和型物質変換および新エネルギープロセス創出を達成するために欠くべからざるものであり，その高性能化は今なお社会からの要請が多い検討課題である．また触媒にはこれまで貴金属が多用されてきたが，希少な金属資源を用い続けることは次第に困難になりつつあり，いわゆる“元素戦略”の観点からも触媒に画期的な高性能化をもたらす技術革新が求められている．そこで本研究では，持続可能な社会構築の基盤となる高性能触媒の開発を行なっている．具体的には，金属元素が持つ触媒性能を極限まで引き出すことや，天然の高性能触媒である酵素と同様に，様々な機能を併せ持つ触媒デバイスの構築を目指して，サブナノ～ナノスケールで構造が制御された触媒，すなわち“ナノ構造触媒”の開発を検討している．

現在研究開発中の新規ナノ構造触媒は，高い耐熱性と機械的強度を有し，ナノスケールで構造制御された無機酸化物多孔体を担体とし，これに分子構造や原子配列が制御された触媒活性点を構築したものである．本共同研究では，２つの研究グループが保有する技術的長所の融合により新規ナノ構造触媒の開発を目指している．内藤，吉田の研究グループはエネルギーや環境保全に関わる触媒の開発実績があり，無機酸化物多孔体の構造制御とこれを活用した触媒高性能化に関するノウハウを有している[(1)]．一方引地，中澤の研究グループは，酵素の触媒活性点に倣った金属錯体触媒の開発に携わっており，精密分子設計の手法を駆使した触媒活性点構造の制御についての研究実績を有する[(2)]．これらのバックグラウンドに基づき資源・エネルギー・環境問題の解決に資する新規触媒を開発することが本共同研究の骨子である．

２．触媒担体としての多孔体シリカゲル

固体触媒は，気相や液相中に存在する反応物に対して，固相に存在する触媒が作用することで化学反応が進行する不均一系反応に供される．すなわち固体触媒において，触媒機能を司る活性点は相界面に位置することから，界

教授　物質生命化学科

特別助教　物質生命化学科
Assistant Professor

面である担体表面の構造は触媒特性の支配因子となる．触媒が反応物と同一相に存在する均一系反応に比べ，不均一反応では触媒と反応物の衝突頻度が低くなってしまう．そのため固体触媒の担体としては単位体積あるいは単位質量あたりの表面積が大きい方が望ましい．ところで担体に微細孔が多く存在する場合，表面積は大きくなるが，分子レベルでみるとその表面構造は粗いものとなっている．このような場合，反応物がアクセスできない微細孔内部に形成された触媒活性点は機能しないため，相対的に有効な触媒活性点が減少してしまう．また担体表面に金属錯体触媒活性点を固定した，いわゆる固定化錯体触媒では，触媒活性点同士の間隔が狭まることで会合状態が生じ，反応性が変化してしまうことも懸念される．さらに有機高分子やミセル膜等の柔軟な構造を持つ担体を用いると，触媒調製や反応時に溶液中に浸すことで膨潤などによって担体自身が流動性を持ち，結果として触媒活性点構造が変化してしまうことが考えられる．従って本研究では剛直な構造を持ち，表面積も大きくかつ化学修飾が容易に行える平滑な表面構造を有する無機酸化物を担体とすることとした．このような特性を備えるものとして，メソ多孔性シリカゲルの一種である　　が挙げられる．これはハニカム様の規則的な細孔構造を有し，大表面積(～　　)および細孔直径(約　～　　)は孔内への比較的容易な物質拡散を保障する．さらに厚い細孔壁(約　　)は十分な機械的および化学的強度を有している．

そこで我々はまずこのメソ多孔性シリカ担体の有用性について検証することとした．特に担体表面の構造(　　)と触媒特性の相関を明らかにするため，大孔径かつ孔規則性の高い　　と，様々なサイズの細孔が混在する市販の多孔性アモルファスシリカゲル(　)を担体とした鉄錯体触媒を新たに開発し，その構造および触媒活性を比較した．図　のようにシリカ担体表面へ連結可能なシラノールエステル部位を有する *NNO* 型　座キレートである β−ケチミナト配位子　を合成し，表面積がほぼ同程度(　～　　)の二種類のシリカ表面に対して担持密度がほぼ等しくなるよう(　　)に固定した(　　)．なお担体表面に残留する水酸基(シラノール基と称される　　部位)は，固定した配位子に対する吸着能および金属イオンに対する配位能を有するために，均一な触媒活性点の構築を妨げる要素となりえる．そこで配位子固定後にヘキサメチルジシラザン(　　)を作用させることで，水酸基をトリメチルシリル(　　)エステルに変換し，吸着・配位能を滅失させている．なおこのトリメチルシリル化処理の有無によって，担体表面の有機官能基の配置が変化してしまうことは既に報告されている．こうして得られた配位子固定化担体に対して塩化鉄　を作用させることで固定化錯体触媒　　および　　に誘導し，金属と配位子の比率そして過酸化水素を酸化剤としたシクロヘキセン酸化に対する活性を評価した．

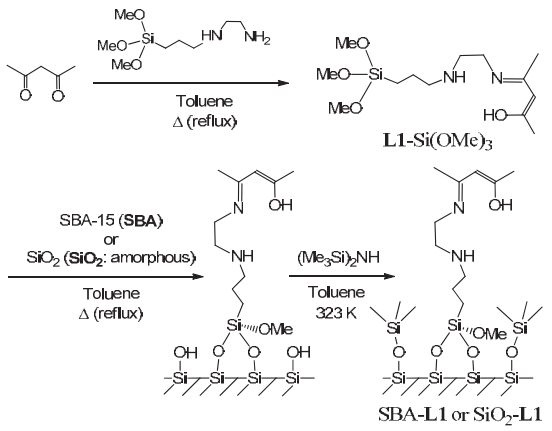

図 1．　　および　　の調製

ところで配位子の運動が制限されない溶液中において，　は鉄イオンに対して　分子結合することで熱力学的に最も安定な構造体　　が形成されるが，これは鉄イオン中心に酸化剤を活性化するための結合部位(配位座)を持たないため触媒活性を示さない．一方，調製した固定化錯体触媒における配位子対金属の比率は，　　では　であったのに対して，　　では鉄担持量が減少して約　となった．そして触媒活性(鉄原子　個あたりの触媒回転数)は，　　の　に対して　　は　であった．これらの結果は次のように解釈できる．粗い表面を有しているために担持した配位子が近接している　　では，　であることを考え併せると，溶液中と同様に配位飽和で触媒活性を持たない　　種が形成されるものと考えられる．しかし　　は　　の　割程度の活性を有していたことより，すべての鉄が　　の状態で担持されているのではなく，酸化剤結合部位を持つ触媒活性点　　も形成されており，さらに微細孔内部に位置しているために鉄が配位していない　も存在していることが考えられる．一方担体表面がより平滑な　　では，固定されている　の分散度が高いために実質的な活性点である　　錯体が相対的に多く形成され，触媒活性が高かったことが考えられる(図　)．ところで　　の触媒活性は，わずかな量(鉄とほぼ等量)の塩基を添加することにより向上するが，その活性は塩基の分子構造に依存していることも明らかに

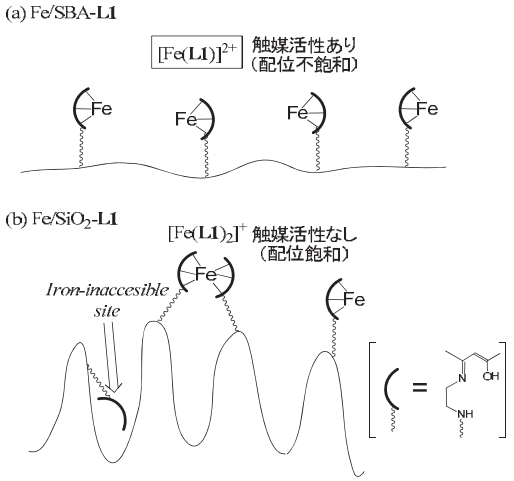

図２．　　および　　の推定構造

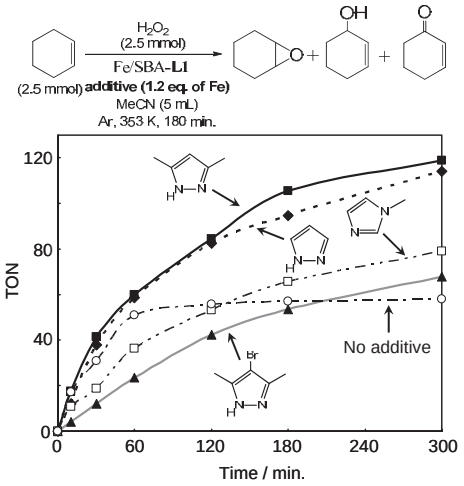

図３．塩基添加時の　　の触媒活性

なった(図　)．このことは，触媒活性点は添加した塩基や酸化剤である過酸化水素由来の　　を結合する余地を残した構造(このような状態を“配位不飽和種”という)であり，先に示した　　が活性点であることを示唆している．

３．担体表面の有機分子による化学修飾

上述のように，数値上は配位子固定密度がほぼ同じであるにもかかわらず，担体表面の構造(平滑さ)が異なることで，配位子同士の間隔が変化してしまうために担体表面に形成される錯体分子の構造が変化してしまうことが明らかになった．そしてこの結果は，平滑な表面構造を持つ　　を担体とした場合にも，配位子やその他の有機分子を固定する際には，その固定密度および分散状態を制御する必要があることを意味している．

シリカゲルを初めとする無機酸化物の表面に有機化合物を固定するには，無機酸化物担体表面に部分的に存在する水酸基に酸性物質(　　)やエステル化合物(　　)を作用させることで，水やアルコールの生成を伴って有機官能基　を担体表面に固定する方法，いわゆる　　法が一般に広く用いられている．前節で述べた固定化錯体触媒もこの方法により調製している．この方法は簡便な操作で担体の化学修飾が可能であるという利点を有するが，担体表面の　の固定密度および分散状態の制御は容易ではない．これは担体表面の水酸基の量や分布はもちろんのこと，固定しようとするエステル化合物(　　)同士の縮合もおこりえること，さらには有機官能基　の性質にも依存するためである．特に　同士が水素結合等により分子間で相互作用しやすい場合には，高分散状態を維持したままでの固定は困難となる．しかしながら，本研究で導入しようとする官能基　とは，更なる化学変換により高次機能化が図ることができるもの(配位子との連結が可能な反応性物質)や，そのもの自体が金属支持配位子となるもの，あるいは基質認識能や触媒機能を持つものであり，これらはルイスあるいはブレンステッド塩基性または酸性を有しているために本質的に分子間での相互作用を起こしやすい．このような　同士による分子間相互作用を抑制するためには，　に適切な保護基を導入することが有効である．　　らは　　にアルキルアミノ基(　　)を固定するにあたり，末端アミノ基部位を立体的にかさ高いトリチル基(　　)で保護した状態で固定し，その後脱保護を行うことにより，有機アミノ基同士が高分散状態で固定されていることを報告している　．なお導入する保護基がさほど立体的にかさ高くないフェニル基(　　)の場合には，保護基を導入せずに固定した場合よりアルキルアミノ基の固定量は減少するものの，固定されているアミノ基同士は接近していることも同時に報告されている．すなわち，保護基についても適切な分子設計を行なうことが必要である．

そこで近年　　法に替わるものとして，　　法による化学修飾メソ多孔性シリカの合成が行なわれるようになってきた．これはメソ多孔性シリカゲルが，“孔”の起源である鋳型剤の表面で，“シリカ源”となるテトラエトキシシラン　　の加水分解・脱水縮合を行うことで二酸化ケイ素　　の“壁”を形成させた後に鋳型を除去するというプロセスにより調製されていることに基づくものである．ここで鋳型剤として用いられるものはポリマーミセルである．そこで，　　に対し適当量の有機官能基を含むトリアルコキシシラン(　　)を混合したものを“シリカ源”とし，これをポリマーミセルの表面で加水分解・脱水縮合を行

うことで有機官能基　を含むメソ多孔性シリカゲルが得られる．この　　法では，　の導入量はシリカ源における　　の仕込み比により制御できると考えられる．また　　と　　が相分離することなく均質に混ざり合った状態でシリカ壁が構成されていく条件では，　の分布はランダムなものとなり，　の導入量が少ない低密度状態では分散度も高くなると考えられる．なお　　の調製に際して鋳型剤として用いられるポリマーミセルとは，疎水性と親水性部位を併せ持つ高分子(ポリ エチレンオキシド とポリ プロピレンオキシド のブロック共重合体)が水中で疎水性部位を内側に向けた状態で集合した会合体となっているものである．従ってその表面に　　と　　が集積した際，疎水性である有機官能基　はポリマーミセルの内部に向かって配向しやすく，これを縮合してから鋳型であるポリマーミセルを除去することで，細孔内壁に　が固定された構造体が得られる．ここに示した　　法により得られる化学修飾　　のうち、アルキルアジド基(　　)修飾　　の調製法は，本共同研究のメンバーのうちの　名(中澤)が確立したものであり，実際にシリカ源における仕込み比に応じた　の導入量の制御が可能であることや，その固定状態においてランダムな配置が達成されていることも明らかにされている　．

以上のような背景を踏まえ，本共同研究では　　法，　　法の両手法により官能基導入量を制御した修飾メソ多孔性シリカ担体　　を調製し，この修飾官能基　を基点に高次機能化を施すことで，新規触媒を開発した．特に　　年度の研究では，生体内機能を模倣した触媒開発に取り組んだ．

３．１．ポリペプチド修飾メソ多孔性シリカによる不斉ナノ空間反応場の構築と触媒特性の解明

α アミノ酸はタンパク質の基本構成要素であるが，生体構成要素として重要な特性のひとつに対掌性(キラリティー)がある．タンパク質を構成するアミノ酸のうち，対掌性がないグリシンを除く　　種類の必須アミノ酸では一方の対掌体(　体)のみがタンパク質の構成要素となりえる．このためタンパク質からなる空間で進行する生体内反応では，多くの場合対掌性の識別が行なわれ，例えば医薬品の場合では対掌体による生理活性の違いが生じる．従って高付加価値有用化学物質(ファインケミカルズ)の生産現場では，一方の対掌体のみを選択的に作り出す“不斉合成”に適用できる触媒，いわゆる“不斉触媒”による合成プロセスは今なお開発課題となっている．

現在既に実用に供されている不斉触媒は，均一系反応に適用される金属錯体触媒や有機分子触媒であるが，これを固体触媒化することができれば，触媒の回収や再利用性の向上により貴重な不斉源の有効利用につながる．そこで固体担体上への不斉分子触媒の固定化による不均一系不斉触媒の開発が試みられており，その固体担体の中でも特に注目されているのはメソ多孔性シリカである．これは，プロキラルな反応物(その化合物自体はキラリティーを持たないが，しかるべき反応により一段階でキラリティーを持つ化合物に変化する分子)の空間配置を制限することによって生成物の対掌体選択性が向上することが知られており　，メソ多孔性シリカが有するナノスケールの細孔は三次元構造が規定された反応場空間を構築するのに適していると考えられるためである．そこで本研究では　　のメソ細孔をポリペプチドで修飾することによって三次元不斉反応場の構築を計画した．

３．１．１．種々のポリペプチド修飾 SBA-15 の合成

メソポーラスシリカへのポリペプチドの導入は，細孔内をアミノ基で修飾した　　と活性化したアミノ酸である　　を，脱水　　またはピリジン中でリビング重合させることにより行った(図　)．　　らの報告　に倣い，かさ高い保護基を有するアミノ基修飾剤を用いて細孔内のアミノ基固定密度を低下させることで，細孔内での長鎖ポリペプチド生成を期待した．　　は，各種アミノ酸(フェニルグリシン　　，プロリン　　，アラニン　　)とトリホスゲンの反応により合成した．ペプチド修飾後の試料については　　物理吸着測定により表面積，細孔体積，細孔径を，また酸素雰囲気下での　　測定と　　元素分析より細孔内に形成したポリペプチドの数平均重合度を測定した．

各種ポリペプチドで修飾した　　の　吸着測定の結果を表　に示す．ペプチド導入前に比べて細孔径や細孔体積が減少したことから，　　の細孔内でポリペ

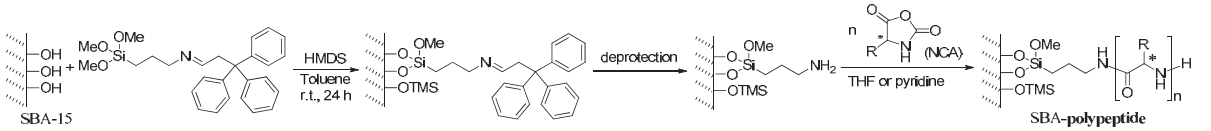

図４．ポリペプチド修飾 SBA-15 の合成

プチド鎖が伸長したことが明らかとなった．この際，　　上に存在する重合開始剤のアミノ基量に対しモノマーである　　の添加量を調節することで細孔径や細孔体積を制御できた．立体的にかさ高いフェニルグリシン由来の　　では，　（　　のモル数 アミノ基のモル数）　　の時の数平均重合度が　，　　の時となり，　　の反応率が低く，数平均重合度も低かった．一方，分子サイズの小さいアラニン由来の　　では，　　の時のポリペプチド鎖長が　，　　の時が　となり，高い　　反応率とポリペプチド鎖の伸長が観測された．また，分子サイズが両者の中間であるプロリンでは，　　の反応率及びポリペプチド鎖長は両者の中間の値となった．

表１．　　の　物理吸着測定結果

	表面積	細孔体積	細孔径
	―		―
	―		―

　　のモル数 アミノ基のモル数
　数平均重合度

３．１．２．ポリペプチド修飾 SBA-15 を用いた不斉エポキシ化反応

調製したペプチド修飾　　を用いた不斉反応の検討を行った．まず，ポリペプチド鎖末端のアミノ基に由来する塩基触媒能を期待して，様々な反応（シアノシリル化やクネーフェナーゲル反応，ニトロアルドール反応）を検討したが，いずれのポリペプチド修飾　　もこれらの反応に活性を示さなかった．そこでポリペプチドが不斉誘導剤として機能することが知られている　　エポキシ化反応に注目した．この反応は，　水溶液と有機溶媒の二相系で行われ，塩基性条件下で過酸化水素から生成する　　が電子不足のオレフィンへと求核付加することで進行する　．しかし，ペプチド修飾メソポーラスシリカを二相系の反応に用いたところ，　　の　　水溶液への溶解が起こり，反応は進行しなかった．そこで非水条件下で反応を行った．　溶媒に，基質のカルコン，　　，尿素 過酸化水素付加体（　　），数平均重合度が約　　の各ポリペプチド修飾　　を加えて室温にて反応を行ったところ，　　は溶解せず，いずれのポリペプチド修飾を用いた時も　　以上の収率でエポキシカルコンが得られた．生成物の光学活性体過剰率（　）を求めたところポリアラニン修飾　　にて　の　が観測されたが，その他のポリペプチド修飾　　ではラセミ体しか得られなかった（表　）．本反応ではポリペプチド鎖のαヘリックス構造が多点的な水素結合により基質と　　を固定し，これが不斉誘導につながることが明らかとなっている　．今回使用したポリペプチド中ではポリアラニンだけがαヘリックス構造を取りうることから，ポリアラニン修飾　　のみが高い　を示したと考えられる．なおメソポーラスシリカ細孔内へのリビング重合を用いたポリペプチド鎖の導入はすでに報告されているが　，実際にこれを用いた不斉反応を実現した例は本研究が初めてである　．

表２．　　を用いた　　エポキシ化

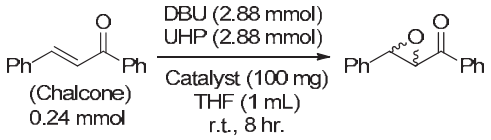

次に，ポリアラニン修飾　　と固定化していないポリアラニンの触媒特性の比較を様々なペプチド鎖長のもので行った（表　）．ポリアラニン修飾　　では，平均重合度　の時に　が最高値の　　を示したのに対し，固定していないポリアラニン（溶液状態）では，平均重合度　の時に　が最高値を示した．また，平均重合度が　の場合，　　に固定化したものでは　，固定していないものでは　と　　への固定化により　が大幅に向上した．なおアミノ基修飾　　にペプチド固相合成法の手法で　残基のアラニンを縮合させたものを合成し，同様の条件で反応を行ったところ，　はわずか　にとどまった．ポリアラニンが安定なαヘリックス構造を形成するためには，　残基程度のペプチド鎖長が必要　であることが知られており，　残基では鎖長不足のためにαヘリックスが形成できず　が大幅に低

表３．各鎖長の修飾および未修飾ポリアラニンの反応

数平均重合度　　ペプチド固相合成法にて伸長したもの

下したと考えられる．よってポリアラニン修飾
や固定していないポリアラニンにおいて，平均重合度が
であってもある程度の　が発現しているのは，重合法で合成しているために部分的に長鎖ポリペプチドが形成されているためであると推定した．また固定していないポリアラニンに比べてポリアラニン修飾　　でより高い　が観測されたことは，液相均一系での重合反応に比べ，　　に固定されているアミノ基を開始剤とした場合，細孔の入り口付近などのアクセス性が高いアミノ基上での重合反応が優先的に進行しやすく，結果としてアミノ基と　　の仕込みモル比が低くても長鎖ポリペプチドの生成量が多いことが原因と考えられる．またポリアラニン修飾　　では，鎖長が　の時最も高い　が観測され，鎖長が　以上になると　は低下した．これは，固定していないポリペプチドの場合とは異なる挙動である．本反応はペプチドが存在しない条件下で　と基質が反応し，ラセミ体を与える．したがって　細孔内で長鎖のポリペプチド鎖が形成されると，　や基質のペプチドのアクセス性が低下し，　と基質の直接反応によるラセミ体の形成が併発するため，　が低下したと考えられる．

３．１．３．ジペプチド修飾　　の合成と触媒反応

次いで，アミノ酸が本来備える酸 塩基触媒機能を　に付与することを目指して，プロリンとアスパラギン酸からなるジペプチド　　で修飾した　　の合成と，その不斉触媒能を検討した．このジペプチドは分子内に　つのイミノ基と　つのカルボキシ基を有しており，カルボキシ基のうち　つを
上への修飾に用いても，一対のイミノ基とカルボキシ基が残存する．このようなプロリン由来のイミノ基とカルボキシ基を持つオリゴペプチドは，プロリン同様にアルドール反応等に対する不斉有機分子触媒として機能することが知られている　．

は，ペプチド固相合成法の手法を応用し，アミノ基修飾　　のアミノ基に対し，ペプチド縮合剤を用いてアミノ酸を逐次的に縮合させることで合成した（図　）．得られた　　のペプチド修飾量を　元素分析により算出したところ，　　であった．

合成した　　を用いてベンズアルデヒドとアセトンのアルドール反応を行った（表　）．その結果　　において　時間で収率　（　　）で生成物が得られ，不斉触媒反応が進行した．固定化の影響を検証するため，アミノメチルポリスチレンレジンにジペプチドを修飾したもの　　，及び　　への固定化のためのリンカーを連結しているアスパラギン酸の側鎖のカルボキシ基をベンジルエステルとした　　を用いて反応の比較を行った．

は，　　と同様にアルドールを与えたが，収率はおよそ半分に低下した．これらの固定化

表４．ジペプチド修飾　　を触媒としたアルドール反応

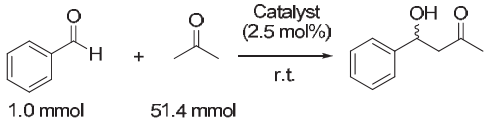

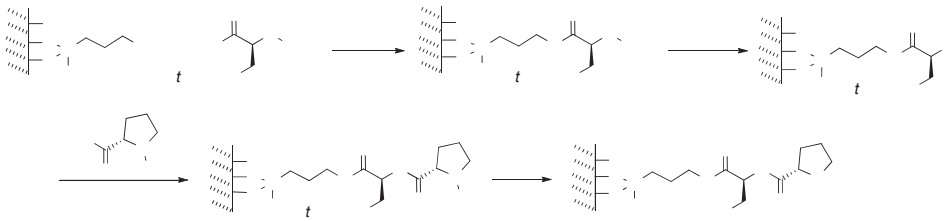

図５．ジペプチド修飾　　の合成

担体を比較すると，アミノメチルポリスチレンレジンは表面積が極めて乏しいのに対し，アミノ基修飾
は　　もの表面積を有することから，
の方が　　に比べ基質のジペプチドの接近が容易であったため高い活性を示したものと推測される．一方で，　　を触媒とした均一系反応は，収率，　共に　　の結果を上回っていた．これは　　ではシリカとジペプチドのカルボキシ基との水素結合を介した相互作用や，固体表面に固定化されたことによってジペプチドのコンフォメーションが規制されることで　の低下を招いたことが考えられる．詳細については現在検討中である．

３．２．アジド基修飾メソ多孔性シリカを用いた固定化錯体触媒

生体内における炭化水素への酸素添加反応は，主に鉄・銅などの遷移金属を活性中心とする酸素添加酵素により触媒されている．酵素の特異な反応特性は，アミノ酸やポルフィリンなどの補欠分子族によって精密に立体および電子的特性が制御された金属配位場（金属錯体）　と，その周囲を取り巻く三次元空間反応場によりもたらされる．三次元空間反応場は，基質認識能や電子伝達・雰囲気（親水性・疎水性）の制御といった反応促進や触媒安定化に関わる重要な因子である．すなわち配位子により形成される配位圏だけでなく，それを取り囲む周辺環境の構造や性質も考慮する必要があるが，これには規則的な三次元構造を有し，かつ化学修飾による親和性の制御や様々な機能の付与が可能な固体表面の活用が有効であると考えられる．また金属錯体触媒は溶液内での化学平衡や錯体分子間での不均化反応により失活してしまう場合があるが，これを防ぐには，固体表面への錯体分子の固定化が有効であると考えられる．特に液相中では不活性な配位飽和種が生成してしまうような場合でも，配位子を固体表面に適当な間隔を保って固定できれば，活性な配位不飽和錯体が担体表面で形成され，しかもその間隔を制御することで錯体触媒活性点の構造制御（単核金属種と多核金属種の創り分け）も期待できる（図　）．さらに固体の特性を活かして，同一担体上に機能の異なる金属錯体を固定化した触媒デバイスの構築も可能になると考えられる．以上の発想の下，本研究では錯体分子触媒の固定化錯体触媒への展開を検討した．

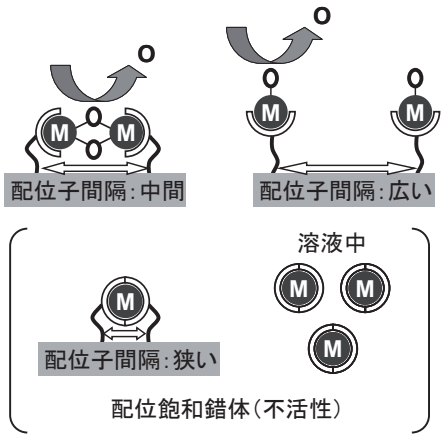

図６．配位子固定間隔に応じた錯体構造の制御

３．２．１．固定化錯体触媒の設計

錯体触媒を担体に固定することで，その触媒活性や機能が大きく変化してしまうことがある．その要因の一部として金属支持配位子部の構造・性質と，担体への固定状態が挙げられ，その解決には，①配位子と担体が安定な共有結合により連結されることや，②触媒活性点となる金属上の配位不飽和座と担体表面が直接相互作用しないこと，といった条件を満たした上で，③配位子間を適切な間隔を保って固定し，孤立した錯体触媒活性点として機能させる必要があると考えた　．

そこで本研究では有機アジド基修飾メソ多孔性シリカゲル（　　）を担体とすることを計画した．アジド基はアルキン類との　　環化付加反応（クリック反応）により　　トリアゾールに変換できる．よって金属支持配位子中に末端アルキン部位を導入できれば，　　の有機アジド基とのクリック反応によって担体上への共有結合を介した固定化が達成できる．ここで用いた　　は，テトラエトキシシラン（　　）に対して任意の量（ケイ素モル比，　；　　）のアジドプロピルトリエトキシシラン（　　）を添加したシラノールエステル混合物を，鋳型となるポリマーミセルの存在下で加水分解・脱水縮合することにより構築した　　類縁体である．この　　法により調製した
は，有機アジド基の修飾量が原料シラノールエステルの仕込み比　により制御できるだけでなく，有機アジド基の分布がランダムであるという特徴を持つ　．

この　　に固定する配位子には，末端アルキン構造への誘導が容易なビス ピリジルメチル アミン構造を基本骨格とするものを用いた．これは，アルカン水酸化触媒として機能するニッケル錯体　の金属支持配位子トリス ピリジルメチル アミン（　　）のピリジル基の　個をプロパルギル基に置換したものである．また担体固定時にクリック反応により生成するトリアゾリル基は，配位子と担体をつなぐリンカーとしての機能を担うだけ

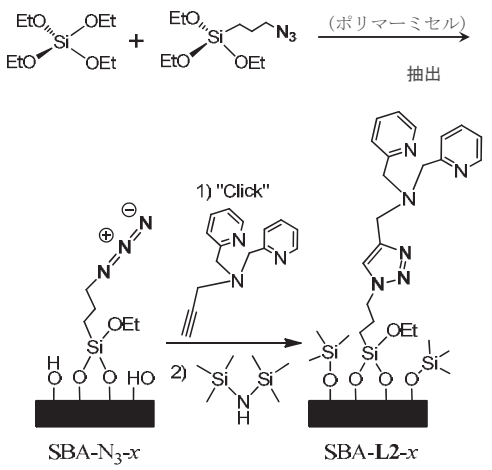

図７．　　法による　　の調製

ではなく，状況によっては金属配位基となることも想定している．なお配位子固定後の担体にヘキサメチルジシラザン(　　)を作用させることで，表面に残存している水酸基をトリメチルシリル基で不活性化した　　へと誘導した(図　)．これにニッケル　あるいはコバルト　酢酸塩を作用させることにより，対応する固定化錯体触媒　　とした　．

３．２．２．担体上の配位子固定密度と触媒特性の相関

調製した　　の配位子担持量は，調製時のアジド基仕込み比率　に応じて単調に変化していたが，配位子担持量と金属イオン固定量の比は配位子担持量に応じて異なっていた(表　)．　　における配位子担持量とニッケルイオン固定量の比は，～　ではほぼ　：　：　であったのに対して　　のものでは　：　：　に近くなった．また　では　　では　：　：　でニッケルの場合と同様であったが，　　では　：　：　でニッケル触媒と較べて金属の比率が高かった(表　)．ところで　　に替えて　　ブチルアジド　　との反応により得た配位子　　を用いて別途金属錯体を合成し，その構造解析を行なうことにより担体上に形成されている錯体種の構造について考察した．ニッケル錯体の場合，条件に応じて　：　：　である(　　図　)および　：　：　の組成からなる　　(　　図　)が得られたが，どちらの錯体においてもトリアゾリル基はニッケルに配位していないことが判明した　．一方コバルト錯体ではトリアゾリル基もコバルトイオンに結合して　　配位子が四座キレートとして機能した(　　図　)が得られた　．従って金属種により

表５．　　における配位子および金属固定量

	担持量	担持量	:
			:
			:
			:
			:
			:
			:

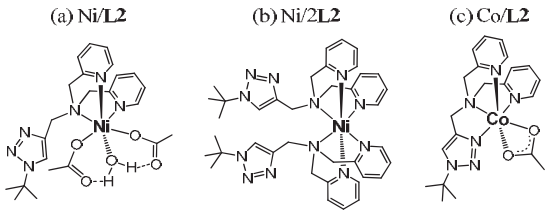

図８．　　を配位子とする錯体の分子構造

の結合様式は異なっており，　　においても同様な錯体種が担体表面に形成されているものと推測した．

これらの触媒について，　　を酸化剤とするシクロヘキサン酸化活性を比較することで，担体上の配位子固定密度が触媒活性に及ぼす影響を検討したところ，金属種により挙動が異なることが明らかになった(表　)．ニッケルを中心金属とした場合，　　等の単純な金属塩は触媒活性を示さないことが既に報告されており　，活性の発現には適切な配位子の存在が必須である．本研究で別途合成した錯体　　を触媒とした液相均一系反応は速やかに進行し，反応開始から　時間後にシクロヘキサノールの生成量が金属あたりの触媒回転数(　　)に換算して約　　回に達したところで反応が停止した．これは世界で最初に報告されたアルカン水酸化に活性を示すニッケル錯体触媒(　　を配位子とするニッケル錯体)　と同等の反応性である．一方，固定化錯体触媒では反応速度は低下していたが，特筆すべきは配位子担持量に応じて活性が異なっていたことである．　　の場合，反応生成物におけるアルコール(　)とケトン(　)およびその酸化体であるラクトン(　)の比率は，配位子担持量によらず　　や　　錯体の場合と大きく変化していないことから，反応メカニズムは同一であると考えられる．したがって配位子固定量が少ない場合(　　)には，　　と同様な孤立した錯体触媒活性点が構築されているために溶液中と同様な反応性を維持していたものの，配位子固定量が多い

表６．　　の触媒活性

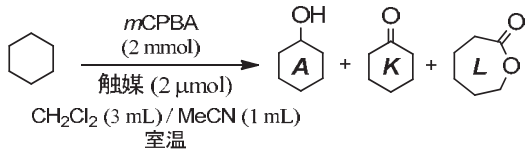

触媒	反応時間 / h	TON		
		A	*K*	*L*
none	3	8	5	0
$Ni(OAc)_2$	3	18	7	0
Ni/TPA	1	587	69	no data
Ni/**L2**$^{t\mathrm{Bu}}$	1	599	56	25
Ni/2**L2**$^{t\mathrm{Bu}}$	1	647	56	20
Ni/SBA-**L2**-0.5	3	534	17	34
Ni/SBA-**L2**-1	3	377	14	22
Ni/SBA-**L2**-2	3	261	10	11
Ni/SBA-**L2**-4	3	251	10	10
$Co(OAc)_2$	0.5	368	80	7
Co/TPA	3	~600	no data	no data
Co/**L2**$^{t\mathrm{Bu}}$	2	604	98	14
Co/SBA-**L2**-0.5	3	577	138	6
Co/SBA-**L2**-4	3	745	80	25

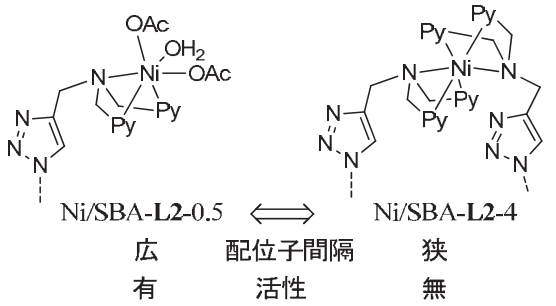

図９．　　の推定活性点構造

では，　：　が　：　に近いことから，担体表面には不活性な錯体種　　が多く形成しているものと考えられる(図　)．ところで　：　　：　である錯体　　は液相均一系反応において　　と全く同様な触媒活性を示したことから，溶液中では　　における　　は置換活性であると考えられる．しかし　　では　が担体に固定されたことで運動性が低下して平衡状態が大きく変化したために，担体表面に形成された　　は置換不活性であり触媒活性点とはなりえなかったものと推測される　．

一方，コバルトを中心金属とした場合には，ニッケル触媒とは挙動が異なった．まず大きな違いは単純なコバルト　塩が触媒活性を有することである　．均一系においてはコバルトイオンが配位子　　に保持されることにより，反応速度が顕著に低下するとともにアルコール生成物の選択性が向上した．そして固定化錯体　　においては，配位子担持量と触媒活性の相関が前述のニッケル触媒のそれとは逆の傾向を示した．興味深いことに，高担持量のもの(　　)が生成物収量・アルコール選択性ともに　　を触媒とする均一系反応よりも高かった．反応途中に触媒をろ過することにより除去した溶液では，溶出したコバルトイオンの作用により触媒反応が進行するものの，生成物に占めるアルコールの割合が減少していたことを考え併せると，担体上に高密度で存在する配位子　　がコバルトイオンの流出を抑制し，配位子　　に保持された錯体種として長時間活性を維持できた事が活性向上の要因と考えられる　．

以上に示した担体上の配位子固定密度が触媒活性に及ぼす影響の相違は，一義的には金属種に応じて安定な錯体分子構造および配位平衡が異なるためと解釈できるが，液 固界面(不均一系)と溶液状態(均一系)では平衡挙動が異なることも触媒特性の支配因子となっているものと推察される．なお固定化錯体触媒の開発と並行して，ニッケル錯体触媒による有機過酸を酸化剤とする選択的アルカン水酸化反応の機構解明も試みており，ごく最近，触媒反応が錯体反応場において進行していることを示す証拠を得ることや，触媒反応過程で生成する中間体の検出に成功した　．これらの成果は金属支持配位子の精密分子設計により位置および立体選択的なアルカン水酸化触媒が構築できる可能性を示すものであり，これと本研究の成果と組み合わせることでファインケミカルズの合成プロセスに適用可能な不斉固体酸化触媒の開発が期待できる．

４．結言

これまでの研究で，メソ多孔性シリカ担体のナノスケール細孔内部の有機官能基による化学修飾法を確立することに成功した．導入する官能基の種類や構造特性に応じて，予め調製した多孔性シリカとかさ高い官能基を有するシランカップリング剤の縮合による　　法，あるいはシリカ調製時に所望の官能基を有するシランカップリング剤を所定の割合で導入する
法により担体への官能基導入密度を制御した．導入した官能基末端を反応開始点とすることで，細孔内壁をポリペプチドで修飾した“不斉ナノ空間”を構築したところ，長鎖ポリペプチドの３次元構造に起因する基質認識能が発現して，立体選択的な酸化反応が進行することが明らかになったが，担体上でのポリペプチド鎖長の制御法を確立するには至っていない．また不斉触媒として機能するジペプチド修飾シリカの開発に成功したが，均一系有機分子触媒と同等の活性を得るには，多くの検討課題が

存在することも明らかになった．一方固定化錯体触媒については，担体への官能基導入密度に応じて，官能基末端に連結した金属錯体触媒の構造および触媒特性が変化することが明らかになり，適切な設計を行なえば溶液中での触媒活性を損なうことなく，固体触媒へと展開することが可能であることが実証できた．これらの知見は様々な有機―無機ハイブリッド材料や種々のボトムアップ型ナノ構造機能材料を設計・構築する上で有益な知見となろう．

今後は本稿で紹介した，精密有機合成の環境調和型プロセスの構築に貢献しえる触媒の更なる高性能化を推し進めるとともに，これまでに得た“ナノ構造触媒”の設計・構築に関わる知見をもとに，エネルギーや環境問題の解決に貢献しえる触媒の開発も行なっていく計画である．

参考文献

佐藤 隆介，吉田 曉弘，内藤 周弐，“種々のポリペプチド修飾メソポーラスシリカの合成と不斉触媒反応への応用”，第　触媒討論会　年　月

佐藤 隆介　吉田 曉弘　内藤 周弐 “不均一系不斉触媒調製のためのメソポーラスシリカ細孔内へのペプチド導入法の開発”，第　触媒討論会　年　月

引地 史郎 *固体物理*　引地 史郎 *触媒*

引地 史郎　中澤 順 *触媒*

■原　著■　○○○○○○○○○○○○○○○○○○○○

希ガス結晶構造と遮蔽 L-J ポテンシャル

天野　力[1,2]

序論

結晶の最密充填構造モデルとして立方最密充填　　と六方最密充填　　とがあることは良く知られている。2種の構造は充填率と配位数は等しいが、エネルギーにごくわずかの差がある。ヘリウムを除く希ガスの結晶構造として実験はもっぱら　　構造を与える　。この結果を原子間ポテンシャル、特にレナード ジョーンズ　　、以下　　と略記 ポテンシャルで解釈しようとすると問題が生じる。木原は引力項として　、斥力項として　　の形の　　ポテンシャルを用いて結晶凝集エネルギーを計算したところ、　　の方がエネルギーが低いすなわち安定であるという実験と異なる結果を得た　。次に彼は斥力項として指数関数を用いる　　ポテンシャルを用いて、谷幅の広いポテンシャルは　　構造を安定にするという結果を得た。結晶やクラスター中の原子間力は近接原子による遮蔽のため近距離力となっている、すなわちポテンシャルの谷幅は狭くなっていると考えるのが自然であろう。筆者は遮蔽効果を取り入れた　　ポテンシャルを用いる計算により、実験により予想された希ガスクラスターの正　　面体から　　への構造転移が起きる原子数が再現されることを示した　。すなわち谷幅の狭い遮蔽　　ポテンシャルがクラスターの原子間ポテンシャルとして適切であることが示された。この結果を踏まえて筆者は結晶構造においても遮蔽　　ポテンシャルは　　と比べて　　構造を安定にするであろうと予想した。遮蔽ポテンシャルとしては短距離型の引力項を持つ　　ポテンシャルと　　により提案された　　構造を安定にする切断項を持つ　　ポテンシャル　　の2種を検討した。希ガス結晶が　　より　　構造を好むという実験結果は理論的に十分には説明されていない　。

方法

遮蔽 L-J ポテンシャル

　　ポテンシャルの一般式は式　　で表される。ここで　　の場合には第　　項が斥力、第　　項が引力を

表す。大きな　、例えば　　、を持つものは遮蔽ポテンシャルすなわち近距離力で谷幅が狭いものを表し、小さな　（　　）を持つものは遠距離力で谷幅の広いポテンシャルを表す。

$$= \frac{}{-}\left\{ \left(-\right) - \left(-\right) \right\}$$

実際の計算では換算単位　ε　　ρ　　を用いる。いくつかの例を　　に示す。

以下の計算は木原に従った。格子点の初期座標は　構造では式　と　で、　構造では式　と　で与えられる。ここで　は最近接原子間距離である。

$$= \frac{}{\sqrt{}} \quad = \frac{}{\sqrt{}} \quad = \frac{}{\sqrt{}}$$

$$= \quad \pm \quad \pm \quad \pm$$

$$+ \quad + \quad =$$

$$= \frac{}{} \quad = \left[-\left\{ \frac{- \; -}{} \right\} + \quad \right] \frac{\sqrt{}}{} \quad = \frac{\sqrt{}}{\sqrt{}}$$

$$= \quad \pm \quad \pm \quad \pm$$

$$+ \quad - \quad = \qquad = \quad \pm \quad \pm \quad \pm$$

中心原子からの距離が等しい原子は同じ殻に属するものとして、順に第　殻、第　殻、第　殻、... の原子と呼ぶ。各々の殻に属する原子数は　　の場合は12, 6, 24, 12, 24, ...、　の場合は6, 12, ...となる。

ポテンシャルエネルギーの項 λ　（Tは式　のまたは　を表す）に関する　原子あたりの結合エネルギーは　　の場合は式　で与えられる。

$$-\frac{\lambda}{} \quad = -\frac{\lambda}{} \sum_{=}^{\infty} \left(-\right)$$

ここで　は　　構造のポテンシャルエネルギー定数と呼ばれる量であり、　は中心原子と　番目の殻に属する原子との距離を示す。一方項 λ　に関する　原子あたりの結合エネルギーは　　の場合は式　で与えられる。

$$-\frac{\lambda}{} \quad = -\frac{\lambda}{} \sum_{=}^{\infty} \left(-\right)$$

ここで　は　　構造のポテンシャルエネルギー定数と呼ばれる。

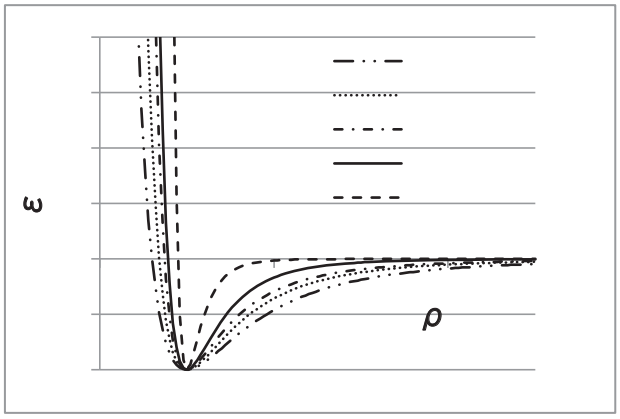

実際の計算ではポテンシャルエネルギー定数を厳密に計算できる第　項と積分近似で計算する第　項に分ける：

$$= \sum_{=}^{\infty} \left(-\right) = \sum_{=}^{\theta} \left(-\right) + \sum_{=\theta+}^{\infty} \left(-\right)$$

ここで θ はある殻数を表す。第　項を積分で近似したポテンシャルエネルギー定数を　’と表す。

$$= \sum_{=}^{\theta} \left(-\right) + \frac{\sqrt{}\pi}{- \quad {}_{\vartheta}^{-}}$$

$$_{\vartheta} = \left\{ \frac{}{\sqrt{}} \left(+ \sum_{=}^{\vartheta} \right) \right\}^{-}$$

ポテンシャルエネルギー定数を用いて凝集エネルギー（　原子あたりのポテンシャルエネルギー）は　では式（　）、　では　で与えられる：

$$= -\frac{}{-}\left\{ \left(-\right) \quad - \left(-\right) \quad \right\}$$

$$= -\frac{}{-}\left\{ \left(-\right) \quad - \left(-\right) \quad \right\}$$

それらのエネルギーを格子定数　に関して最小化した凝集エネルギーは式　と　で表される：

$$= - - \left(\frac{}{} \right)^{\frac{}{-}}$$

$$= - - \left(\frac{}{} \right)^{\frac{}{-}}$$

これらの式中の　　の代わりに近似値
’　’　’　’を用いる。

切断 L-J ポテンシャル

切断　ポテンシャルとして　　により提案された次式を用いる：

$$= \left\{\left(-\right) - \left(-\right)\right\} \left\{\frac{\quad}{\left(-\right)-\left(-\right)}\right\}$$

ここで切断距離を決める　の値は　では殻数　以上、　では殻数　以上離れた原子間力がほぼゼロになるように決められる。その値は　付近にあり、この時中心原子とゼロでない相互作用を持つ原子の総数は　では　、　では　である。この差により　構造の凝集エネルギーが低くなることが期待される。しかし、式　の関数は　でゼロでない不都合な振る舞いをするので、実際には切断関数により　の部分が強制的にゼロとしたポテンシャルが用いられる。　の値はポテンシャルの最小値が　になるようにする規格化因子である。凝集エネルギーは最近接原子間距離　の関数であるため、凝集エネルギーを最小にする　の値とその時の凝集エネルギーを数値計算により求めた。

結果

ポテンシャルエネルギー定数の近似値　’　’の値と殻数　を　に示す。　’　’の値は殻数の増加に対する小数点以下７桁の範囲の停留値であり、　はその時の殻数の最小値である。　構造の　’の値には　等　のゼータ関数法による計算値があり、それらは小数点以下　桁または　桁の範囲でこの表の値と一致している。　構造の　’の値は　に関してのみ　等　による値が報告されていて、それらは小数点以下　桁の範囲でこの表の値と一致している。　に関して木原の　’　’の値はこの表の値と小数点以下　桁まで一致している。　に関する　’の値は全く新しい。　ポテンシャル（　）に関する凝集エネルギーの値を　に示す。このうち　かつ　は遮蔽ポテンシャルである。遮蔽ポテンシャルを含む表　の全てのポテンシャルで、予想に反して　の方がエネルギーが　％低いという結果である。反対に谷幅の広いポテンシャル（　かつ　）では　の方がエネルギーが　％低い（　）。　に　型の切断　ポテンシャルを用いた計算の結果として、ポテンシャルの極小値を与える原子間距離　、凝集エネルギーの最小値を与える最近接原子間距離　、凝集エネルギーおよびその差 δ　が与えられている。切断パラメータ　、および　に関して　構造の方が　構造よりも低い凝集エネルギーを与える。

’　’

’　’

討論

遮蔽 L-J ポテンシャル

遮蔽　ポテンシャルは　構造を安定化しないという結果は木原の谷幅の狭いポテンシャルは　構造を安定化しないという結果と一致している。　で表される長距離力　ポテンシャルが　構造を安定化するという結果は木原により予見されたが、本論文で明確に示された。その計算は多数の殻数を取り入れる多量の計算を必要とするため、計算されなかったのであろう。その代わりに木原は指数関数の斥力項を持つ　ポテンシャルで谷幅を決めるパラメータ σ が $8.5<\sigma<8.675$ の範囲にある広い谷幅を持つ長距離力ポテンシャルが　構造を安定化することを示した。しかし輸送実験結果の解析によると σ の値はクリプトンに関して　が提案されている　。　谷幅の広い遠距離力ポテンシャルは　構造を安定化し、谷幅の狭い近距離力ポテンシャルは　構造を安定化するという結果は　つの構造の特徴を表している。

δ

δ

は切断型　ポテンシャルを用いて凝集エネルギーを求め、それが　構造を安定化することを示した。我々の計算も表　に示されるようにそのポテンシャルは切断パラメータと　のある範囲で　構造を安定にするものであることを支持した。しかしそのポテンシャルは　つの構造の近接原子数の違いから得られた特殊なものであり、実際のポテンシャルを表しているかどうかが問題となろう。

ゼロ点振動と３体相互作用

等はゼロ点振動の効果を木原の　ポテンシャルによる凝集エネルギーに加えても　のエネルギーの方が低いという結果は変らないと報告した　。　はゼロ点エネルギーと自由エネルギーの非調和項を取り入れた計算により　の方がエネルギーが低くなると報告した　。近年、ゼロ点振動の効果のみでも　のエネルギーが　よりも低くなるという計算結果が得られた　。　のエネルギーを下げる効果のあるのは調和振動モードの結合であり、非調和振動ではないという詳細な結果も提出された　。

は最近接原子間の３体短距離交換相互作用が　構造のエネルギーを　よりも低くするという結果を得た　。一方　は３体相互作用は　の安定化に寄与しないという結果を報告した　。　等は長距離３体相互作用が　構造のエネルギーを　よりも低くすると報告した　。　等は３体短距離交換相互作用は　の安定化を与えると報告した　。３体短距離相互作用は　のエネルギーを　に相対的に低下させるが、３体長距離相互作用は逆に増加させる。その和は　構造のエネルギーの低下を与えるが、　よりも低いエネルギーを与える程ではないという結果が得られた　。　等は完全基底系を用いた　計算によりゼロ点振動を含まなければ　が　よりも安定な構造であるという結果を得た　。

以上の考察から実験で得られた　構造の安定化を与える要因として　の切断　ポテンシャルまたはゼロ点振動、あるいはその両者が有望である。量子論ではゼロ点振動を考慮したものが真のポテンシャルエネルギーを与える。遮蔽　ポテンシャルにゼロ点振動の補正を加えたものが　構造を安定化するかどうかは今後の課題であろう。

δ

結論

木原により示されたσ値の小さい谷幅の広い　　ポテンシャル以外に、谷幅の広い遠距離　　ポテンシャル（　　）は　　構造よりも　　構造を安定にする。一般に谷幅の広いポテンシャルは　　構造を安定化すると言えるだろう。原子間力の遮蔽という自然な予想に反して、谷幅の狭い遮蔽　　ポテンシャルは　　構造の安定化を与えない。しかし遮蔽ポテンシャルのうち、切断項を持つ短距離　　ポテンシャルは切断距離を適切に選ぶことにより　　構造を安定化する。これらの結果は２種の最密充填構造の違いを表している。

２体の遮蔽　　ポテンシャルという考えは予想された結果を与えないが、結晶内では原子間力が遮蔽されているという考えは妥当であると思われる。今後は遮蔽　　ポテンシャルのエネルギーにゼロ点振動の補正を加えたものが　　構造を安定化するかどうかを調べる必要があろう。

文献

83:

→

76

107

8

32

Ⅰ

22

246

62

7

73

22

135

93

24

134

20

234

131

Science Journal of Kanagawa University **24** ：41-46 (2013)

■原　著■　2012 年度神奈川大学総合理学研究所共同研究助成論文

環境水からのホウ素及び稀少元素の分離を目的とした試薬フリーな分離濃縮システム

澤田直孝 [1]　清水秀世 [1]　武井尊也 [1]　鈴木祥弘 [2]　金沢謙一 [2]　西本右子 [1,3]

Separation and Concentration System of Boron with a Freeze and Melt Process of Environmental Water

Naotaka Sawada[1], Hideyo Shimizu[1], Takaya Takei[1], Yoshihiro Suzuki[2]
Ken'ichi Kanazawa[2] and Yuko Nishimoto[1,3]

[1] Department of Chemistry, Faculty of Science, Kanagawa University, Hiratsuka City, Kanagawa 259-1293, Japan
[2] Department of Biological Sciences, Faculty of Science, Kanagawa University, Hiratsuka City, Kanagawa 259-1293, Japan
[3] To whom correspondence should be addressed. E-mail: y24moto@kanagawa-u.ac.jp

Abstract: A separation and concentration system of boron with a freeze and melt process of environmental water, such as river water and sea water, was established. This method is applicable to relatively large-capacity environmental water without using a harmful reagent. We used sea water and river water as environmental samples. Boron in sea water or river water is concentrated by dissolving in a eutectic mixture of NaCl and the water in a freeze process. This method will be applicable to other rare metal elements.

Keywords: environmental water, melt process, freeze concentration, DSC, eutectics

序論

有害な試薬を用いずに河川水・温泉水等の環境水中のホウ素（B）を分離濃縮するシステムの構築を目的として、凍結・融解過程に注目した。ホウ素は人の健康の保護に関する環境基準として「ホウ素（B：1 mg/L 以下）」と定められている [1)]。ホウ素は温泉水の成分として、含まれていることが多く、河川への流入が問題視されている [2)]。本研究は河川水・温泉水等の環境試料に適用できるホウ素の分離濃縮システムの構築を目的とした。河川水は水道水源や工場用水源としても使用されるが、豊平川に流入する定山渓温泉のヒ素やホウ素のように温泉水の流入が問題となることは少なくない [2, 3)]。神奈川県も多くの温泉水源を有し、程度の差はあるものの流入源に近い場所で分離できれば問題の拡大は防止できる。特にホウ素の環境基準は基準値が厳しくなってから日が浅く、温泉水などに対する対策が充分間に合っているとは言いがたい。そこで有害な試薬や高価な試薬を使用しない分離・濃縮法として、凍結融解過程を利用する方法の確立を目指した。ホウ素はレアメタルの一種でもあり、分離後の有効利用が期待される。システムの構築が進めば、さらに有益な元素、稀少元素の分離濃縮への適用も考えられ、さらなる発展が予測された。現在研究開発が進んでいる分離・分析法の多くは、微量・希薄試料を対象とした高感度な手法が多い。試薬の使用料も少なく環境配慮型分析法として有用ではあるが、一方で比較的多くの試料を扱う環境試料に適用できる手法の開発は多くない。本研究では有害な試薬を用いずに、数百ｍＬ～Ｌ単位での試料の分離・濃縮を行うことを目的とした。

環境水試料としては、著者らが継続して測定を行っている相模湾の平塚市周辺の海域で採取した海水及び相模湾への流入河川である金目川及び相模川の河川水を使用した。

材料と方法

海水及び河川水の採取

河川水の試料は、金目川（上流：秦野市内、国道246 号線との交差地点付近、中流：平塚市内土屋橋付近、下流：平塚市内鼻水橋付近）、相模川（上流：

©Research Institute for Integrated Science, Kanagawa University

表 1. 金目川中流採取試料の定量結果

(ppm)

Sampling Date	Ca	Na	Si	Mg	K	Sr	B	Fe
2010.4.14	23.90	15.95	12.15	7.65	3.70	0.06	0.02	0.02
2010.8.7	25.85	16.05	13.30	8.35	3.60	0.06	0.02	0.02
2010.12.9	25.42	15.60	13.46	8.12	3.36	0.07	0.01	0.01
2011.7.15	31.88	20.33	15.23	7.96	7.06	0.07	0.03	0.01
2011.12.15	29.88	14.45	13.33	8.70	3.77	0.06	0.03	0.01
2012.7.28	26.53	15.95	13.17	7.81	3.34	0.06	0.01	0.01

表 2. 各河川水の B 濃度

(ppm)

Sampling Point	Kaname river		Sagami river		Hayakawa river		Sakawa river	
Sampling Date	2011. 12.15	2011. 12.11	2011. 12.15	2011. 12.11	2011. 12.15	2011. 12.11	2011. 12.15	2011. 12.11
Upper river	0.03	0.02	0.01	0.01	0.11	0.09	−	−
Midstream	0.03	0.02	0.02	0.01	0.29	0.38	−	−
Lower river	0.04	0.03	0.36	0.29	0.27	0.29	0.03	0.01

座間市内座袈依橋付近、中流：海老名市内海老名 IC 付近、下流：平塚市内馬入ふれあい公園付近）、早川（上流：箱根町宮城野浄水センター付近、中流：箱根町箱根湯本駅付近、下流：小田原市早川 IC 付近）、酒匂川（下流：小田原市内小田原大橋付近）で採取した。海水の試料は、相模湾の金目川河口付近と相模川河口付近の水を用いた。金目川河口及び相模川河口から 0 m, 200 m, 400 m, 800 m, 1,000 m, 2,000 m の地点の海面（水深 0 m）で採水した試料、200 m, 400 m, 800 m, 1,000 m, 2,000 m の地点の水深 5 m で採水した試料、1,000 m, 2,000 m の地点の水深 10 m, 20 m で採水した試料を使用した。

海水及び河川水の分析

採水した試料を、No.5A（ADVANTEC）と No.5C（ADVANTEC）のろ紙でろ過後、孔径 0.45 μm のシリンジフィルター（Minisart RC15, Sartorius）でろ過した。河川水は 10 倍希釈して測定試料とし、海水は 100 倍 , 1,000 倍に希釈して測定試料とした。

測定には ICP-AES(SII NT SPS3500) を使用し、キャリヤーガス：0.35 L/min、プラズマガス：14.0 L/min、補助ガス：0.40 L/min（いずれも Ar）、吸い込み量：1.70~1.90 mL/min の条件で測定した。

結果と討論

河川水及び海水の測定結果

表 1 に金目川中流での採水結果を示した。2011 年 7 月採取試料の定量結果が全体に高濃度であるが、それを除くとほぼ一定値であることがわかる。また各河川の B 濃度を表 2 に示した。相模川下流、早川中流・下流で比較的高濃度であった。相模川下流は海水の影響、早川は中流域の温泉の影響と考えられた。表 3 には 2012 年 12 月に採水した金目川河口及び相模川河口付近の海水の測定結果を示した。両地点共に河口付近を除き海水の平均濃度 [4] とほぼ同様の結果となったが、両地点共に Ca 濃度のみ高めの値を示した。これに対し 2011 年 8 月採取試料ではすべての元素でほぼ海水の平均濃度に近い値であった。また 2012 年 10 月採取試料の測定値は、12 月採取試料より約 10%低い値となっており、秋季に河川流量が最も多くなった昨年の結果と一致する [5]。

環境水の凍結・融解過程における B の濃縮

有害な試薬や高価な試薬を使用しない分離・濃縮法として、凍結融解過程を利用する方法を検討した。凍結過程では試料 200~500 mL を約 -30℃で約 1 時間保存した。凍結していない部分（水相）と凍結した部分（氷相）の体積比が 1:1 になった際に取り出し、水相と氷相を分離した。氷相は室温で完全に融解させた後に、各相に含まれる元素濃度を測定した。融解過程では試料を約 -30℃で完全に凍結するまで保存した後、凍結した試料を室温で融解させ、水相と氷相の体積比が 1:1 になった際に水相と氷相を分離した。氷相は室温で融解させた後に、各相に含まれる元素濃度を測定した。2012 年 12 月採水試料の測定結果を表 4, 5 に示した。いずれの試料でも水相に濃縮することがわかった。

表 3. 金目川及び相模川河口付近の海水の測定結果 （2012 年 12 月 13 日採取）

Sampling			Na ($\times 10^3$) ppm	Mg ($\times 10^3$) ppm	Ca ($\times 10^3$) ppm	K ($\times 10^3$) ppm	Sr ppm	B ppm
point	distance (m)	depth (m)						
Kaname River	0	0	7.35	0.95	0.43	0.29	4.7	2.8
	200	0	10.40	1.31	0.76	0.41	7.1	4.1
		5	10.66	1.34	0.71	0.41	6.8	4.1
	400	0	10.26	1.30	0.73	0.42	6.8	4.1
		5	10.67	1.33	0.79	0.44	7.3	4.5
	800	0	10.05	1.27	0.69	0.40	6.5	4.0
		5	10.68	1.34	0.77	0.43	7.2	4.2
	1000	0	10.19	1.30	0.72	0.41	6.8	3.9
		5	10.63	1.35	0.78	0.42	7.1	4.3
		10	10.65	1.35	0.77	0.41	7.1	4.3
		20	9.41	1.21	0.73	0.42	6.9	4.0
	2000	0	10.75	1.36	0.73	0.42	6.9	4.2
		5	10.85	1.35	0.76	0.42	7.0	4.0
		10	10.84	1.36	0.77	0.44	7.1	4.2
		20	10.55	1.33	0.75	0.43	7.0	4.3
average concentration of sea			10.80	1.30	0.41	0.39	7.8	4.5
Sagami River	0	0	2.40	0.31	0.12	0.11	1.8	0.8
	200	0	9.37	1.21	0.66	0.38	6.2	3.8
		5	10.51	1.34	0.76	0.42	7.0	4.3
	400	0	7.25	0.95	0.46	0.31	4.9	3.0
		5	10.81	1.38	0.78	0.44	7.0	4.3
	800	0	8.28	1.08	0.58	0.34	5.8	3.6
		5	10.88	1.38	0.79	0.44	6.9	4.3
	1000	0	9.60	1.25	0.70	0.40	6.6	4.0
		5	10.64	1.36	0.79	0.43	7.1	4.4
		10	10.85	1.38	0.79	0.44	7.1	4.3
		20	11.46	1.44	0.80	0.43	7.2	4.3
	2000	0	10.61	1.36	0.70	0.39	6.4	4.0
		5	10.50	1.32	0.73	0.41	6.7	4.0
		10	10.88	1.37	0.78	0.44	7.1	4.2
		20	10.84	1.40	0.74	0.41	6.8	4.1

B の濃縮に対する酸・塩基・塩の影響

環境水のモデル溶液として、溶液中のホウ素の濃度を 5 ppm (4.6×10^{-4} mol/L) または 1 ppm (9.3×10^{-5} mol/L)、酸 , 塩基 , 塩の濃度を 1.0×10^{-1} mol/L または 1.0×10^{-4} mol/L に調整した試料を用いた。酸として HCl と HNO_3、塩基として NaOH と KOH、塩として NaCl, KCl, $NaNO_3$, KNO_3, $NaNO_2$ を用いた。凍結・融解過程の試料分離条件は前述の河川水・海水と同様とした。凍結融解過程での B の濃度変化に対する酸 , 塩基 , 塩の影響を B 濃度 9.3×10^{-5} mol/L で酸 , 塩基 , 塩の濃度を 1.0×10^{-1} mol/L に調整して検討した結果を表 6 に、B 濃度 9.3×10^{-5} mol/L で酸 , 塩基 , 塩の濃度を 1.0×10^{-4} mol/L に調整して検討した結果を表 7 に、B 濃度 4.6×10^{-4} mol/L で酸 , 塩基 , 塩の濃度 1.0×10^{-1} mol/L に調整して検討した結果を表 8 にそれぞれ示した。凍結過程では全ての場合で水相に B が濃縮し、融解過程では酸 , 塩基 , 塩がいずれも共存しない場合にのみ氷相に B が濃縮するが、酸 , 塩基 , 塩のいずれかが共存すると水相に濃縮することがわかった。B 濃度、酸 , 塩基 , 塩の濃度、共存する酸 , 塩基 , 塩の種類によって B が濃縮する相に変化はなかった。河川水や海水では塩が共

表 4. 河川水の B 濃度 (2012 年 12 月 11 日採取)

(ppm)

		Kaname river	Sagami river	Hayakawa river	Sakawa river
Freeze process	Liquid phase	0.046	0.026	0.173	0.035
	Solid phase	0.005	0.000	0.012	0.003
Melt process	Liquid phase	0.026	0.025	0.178	0.036
	Solid phase	0.015	0.005	0.028	0.003
B concentration of river water		0.024	0.006	0.094	0.009

表 5. 海水の B 濃度 (2012 年 12 月 13 日採取)

(ppm)

			distance（depth）(m)				
			0 (0)	1000 (0)	1000 (20)	2000 (0)	2000 (20)
Estuary of Kaname river	Freeze process	Liquid phase	4.30	5.40	5.70	5.40	5.70
		Solid phase	1.80	2.85	3.25	3.15	3.10
	Melt process	Liquid phase	3.95	5.40	6.05	4.80	5.15
		Solid phase	1.55	2.45	2.65	2.75	2.45
	Boron concentration of seawater		2.80	3.90	4.00	4.20	4.30
Estuary of Sagami river	Freeze process	Liquid phase	1.70	4.65	4.40	4.90	5.55
		Solid phase	0.40	2.35	2.50	2.55	2.75
	Melt process	Liquid phase	0.50	5.00	5.95	6.10	5.95
			0.45	2.10	2.55	2.40	2.55
	Boron concentration of seawater		0.80	4.00	4.30	4.00	4.10

存しているために、水相に濃縮したと考えられた。

環境水中の凍結・融解過程における B 濃縮のメカニズム

NaCl 水溶液を冷却すると、氷が形成された後に NaCl と水の共晶が生成する。-30℃で 1 時間保持した試料では、氷は形成するが、NaCl と水の共晶は充分形成されていない。一方 -30℃で完全に凍結するまで保持した試料では氷も NaCl と水の共晶も生成するが、NaCl と水の共晶は先に融解する。海水や河川水でも同様の結果と考えられた。図 1 に相模川河口から 2000 m、水深 20 m の海水の DSC 融解曲線を示した。-23℃付近にみられる NaCl と水の共晶の融解による吸熱ピークは -30℃で 6 時間保持した試料では明瞭に観測されるが、1 時間保持した試料では不明瞭で小さい吸熱ピークとして観測される。NaCl と水の共晶には溶存気体やリン酸、アミノ酸などがとりこまれる [6,7]。B は氷が形成された後の NaCl と水の共融混合物に濃縮されたためと考えられた。そこで、NaCl 水溶液を凍結させた氷を粉砕し、B を含む溶液を滴下した。氷を通過した溶液及び溶液通過後の氷中の B 濃度を測定した。海水の塩濃度に近い 0.5 mol/L の NaCl 水溶液を凍結させた場合で、60% の B が氷中に保持された。B が氷中に保持される割合は NaCl 濃度と共に増加し、1 mol/L で約 70%、4 mol/L では約 85%が氷中に保持された。この結果は KCl, $MgCl_2$, $CaCl_2$ でも同様であった。B は中性以上の pH の水溶液中では Ca^{2+} などの共存する陽イオンと作用して、一種の錯体を形成することが知られている [8]。B が環境水中に共存する陽イオンと相互作用した形で存在し、NaCl と水の共融混合物中に濃縮されたと考えられた。

以上より、環境水を -30℃で約 1 時間凍結させた場合は、環境水中の塩と水の共晶は充分形成されず、共融混合物として存在し、その部分に B が保持される。その後さらに凍結させると B を含んだ共晶が形

表６．凍結・融解過程における水相及び氷相の B 濃度 (1)

Aqueous solution prepared with H_3BO_3			Boron concentration (mmol/L)			
			Freeze process		Melt process	
Salt	Acid	Base	Liquid phase	Solid phase	Liquid phase	Solid phase
-	-	-	0.17	0.05	0.05	0.16
-	HCl	-	0.15	0.07	0.17	0.07
-	HNO_3	-	0.16	0.08	0.15	0.05
-	-	NaOH	0.13	0.08	0.17	0.04
-	-	KOH	0.13	0.07	0.16	0.06
KNO_3	-	-	0.11	0.09	0.15	0.05
$NaNO_3$	-	-	0.12	0.08	0.15	0.05
$NaNO_2$	-	-	0.11	0.09	0.15	0.05
KCl	-	-	0.11	0.09	0.15	0.05
NaCl	-	-	0.12	0.08	0.15	0.05

(Boron concentration 9.3×10^{-5} mol/L(1 ppm)；salt, acid or base concentration 1.0×10^{-1} mol/L)

表７．凍結・融解過程における水相及び氷相の B 濃度 (2)

Aqueous solution prepared with H_3BO_3			Boron concentration (mmol/L)			
			Freeze process		Melt process	
Salt	Acid	Base	Liquid phase	Solid phase	Liquid phase	Solid phase
-	-	-	0.17	0.05	0.05	0.16
-	HCl	-	0.18	0.05	0.16	0.06
-	HNO_3	-	0.18	0.05	0.19	0.03
-	-	NaOH	0.17	0.05	0.16	0.05
-	-	KOH	0.17	0.04	0.11	0.09
KNO_3	-	-	0.19	0.04	0.13	0.07
$NaNO_3$	-	-	0.17	0.04	0.19	0.02
$NaNO_2$	-	-	0.19	0.03	0.13	0.07
KCl	-	-	0.13	0.09	0.13	0.08
NaCl	-	-	0.11	0.09	0.20	0.01

(Boron concentration 9.3×10^{-5} mol/L（1 ppm）；salt, acid or base concentration 1.0×10^{-4} mol/L)

表８．凍結・融解過程における水相及び氷相の B 濃度 (3)

Aqueous solution prepared with H_3BO_3			Boron concentration (mmol/L)			
			Freeze process		Melt process	
Salt	Acid	Base	Liquid phase	Solid phase	Liquid phase	Solid phase
-	-	-	0.56	0.34	0.23	0.67
-	HCl	-	0.58	0.37	0.65	0.29
-	HNO_3	-	0.59	0.40	0.71	0.19
-	-	NaOH	0.62	0.38	0.68	0.29
-	-	KOH	0.61	0.39	0.66	0.29
KNO_3	-	-	0.61	0.31	0.68	0.19
$NaNO_3$	-	-	0.60	0.31	0.66	0.18
$NaNO_2$	-	-	0.56	0.29	0.52	0.26
KCl	-	-	0.57	0.33	0.68	0.20
NaCl	-	-	0.56	0.32	0.59	0.19

(Boron concentration 4.6×10^{-4} mol/L(5 ppm)；salt, acid or base concentration 1.0×10^{-1} mol/L)

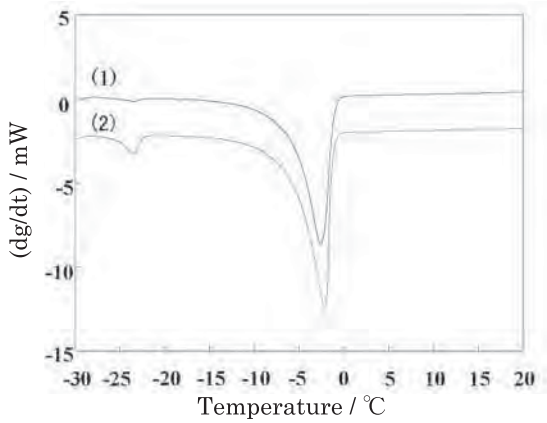

図 1 . 相模湾沿岸海水のDSC融解曲線. 河口より 2000 m, 水深 20 m, -30℃での保持時間 : (1) 1 時間、(2) 6 時間.

成し、融解過程では共晶が先に融解する。そのため、凍結過程、融解過程共に水相に濃縮すると考えられた。塩と水の共融混合物に元素が濃縮する現象はB以外にも観測されており、さらなる応用が期待できる。

謝辞

本研究の一部は、平成 24 年度大学研究成果事業化促進事業として神奈川県より業務委託を受けて実施した。また、本研究は「相模川河口域における長期環境変動のモニタリング 2」の課題名で 2012 年度神奈川大学総合理学研究所共同研究助成を受けて行った。

文献

1) 環境基本法第 3 節 , 環境基準　別表 1 . *人の健康の保護に関する環境基準* . http://www.env.go.jp/kijun/wel.html (2013 年 6 月 11 日最終確認)
2) 佐藤裕子, 大野浩一, 亀井　翼, 真柄泰基 (2002) 豊平川におけるヒ素及びホウ素の挙動と水道水管理への影響. *水道協会雑誌* 71: 22-33.
3) 辰巳健一 , 神　和夫 , 眞柄泰基 , 橘　治国 (2005) 豊平川における河川流況とヒ素の動態解析. *水環境学会誌* **28**: 101-107.
4) 国立天文台編理科年表 (2011)　平成 23 年第 84 冊 . pp. 955-956.
5) 平賀義路, 児玉壮史, 鈴木祥弘　(2012) 相模川河口域の植物プランクトンの分布への淡水流入の影響. *Sci. J. Kanagawa Univ.* **23**: 59-66.
6) Fujiwara S and Nishimoto Y (1998) Nonbiological complete differentiation on the enantiomeric isomers of amino acids and sugars by the complexes of gases with the eutectic compounds of alkali chlorides and water. *Anal. Sci.* **14**: 507-514.
7) Fujiwara S and Nishimoto Y (1991) Effect of enantiomeric isomers of amino acids on melting of oxygen adduct of eutectic compound of sodium chloride and water. *Anal. Sci.* **7**: 687-690.
8) 谷藤浩介, 清家　泰, 奥村　稔 (2009) シリカゲルによる水中ホウ素の吸着除去. *分析化学* **58**: 767-770.

Science Journal of Kanagawa University **24** : 101-104 (2013)

■報告書■ 2012年度神奈川大学総合理学研究所助成共同研究

特殊土砂分離剤の微細構造解析

張 善俊[1,4] 西本右子[2] 本城貴光[3] 久慈俊郎[3]

Fine Structure Analysis of a Special Sand Separator

Shanjun Zhang[1,4*], Yuko Nishimoto[2], Takamizu Honjyo[3] and Toshio Kuji[3]

[1] Department of Information Sciences, Kanagawa University, Hiratsuka City, Kanagawa 259-1293, Japan
[2] Department of Chemistry Sciences, School of Science, Kanagawa University, Hiratsuka City, Kanagawa 259-1293, Japan
[3] Department of Applied Chemistry, School of Engineering, Tokai University, Hiratsuka City, Kanagawa, 259-1292, Japan
[4] To whom correspondence should be addressed E-mail: zhang@info.kanagawa-u.ac.jp

Abstract: Polyelectrolytes are widely used as flocculants for water and waste-water treatment. To better control flocculation, it is important to understand the structure of the layer of polyelectrolyte adsorbed on a colloidal particle. In the present study, electrophoretic mobilities of polystyrene latex particles with adsorbed polyelectrolytes were analyzed by applying Ohshima-Kondo's theory of soft particles to reveal the structure of the adsorbed polyelectrolyte. Electrophoretic mobilities leveled off to a non-zero value in the limit of high ionic strength of solution, which is a characteristic feature of soft particles. The charge density, ZN [mol/L], in the layer and the length scale parameter of permeability, 1/λ [nm], were obtained by applying the electrophoretic theory of soft particles. It was found that the mean distance between charged segments of adsorbed polyelectrolytes estimated by ZN was almost the same as 1/λ. An experimental result is also reported.

Keywords: Polyelectrolytes, flocculation, waste-water treatment, fine structure

序論

汚泥水の浄化は近年環境対策として重要な課題である。特に、都市型土木工事さらに河川浄化は国内外で大きな問題となっている。従来汚泥浄化等の水質浄化、土砂分離剤としてゼオライトが広く使われてきた。水中の濁質成分を沈降させるために、水中の濁質成分の表面電荷を中和させながら、濁質成分同士を集塊化させる必要がある[1-4]。

本報告ではゼオライトと比較して高効率で特殊土砂分離剤を紹介しその効果と詳細な構造、組織形態を論ずる。

分離剤の構成形態

ゼオライトについて

ゼオライトの組成はアルカリ金属（Na、K）、アルカリ土類金属（Ca）を含み、水分子（H_2O）を結晶水として構造中にとり込んだ、アルミニウムの含水珪酸塩鉱物である。

このように、ゼオライトは、粘土鉱物の一種であり、規則的管状細孔と空洞を有する強い陰イオン性の骨格からなるアルカリまたはアルカリ土類金属を含む含水アルミノケイ酸塩である。我が国でも国内各地で天然の鉱物資源である天然ゼオライトを産出し、数多くのゼオライト及びその類似物質が人工的に合成されており、こうした合成ゼオライトの一部は工業的にも広く用いられています。細孔の直径は0.2～1.0 nm 程度であり、その細孔径よりも大きな分子を分離する作用を有している。この分子ふるい効果に加え、イオン交換能、吸着能などの特性をもっており、その機能を活かして吸着剤、排水処理、など幅広く利用されている[5,6]。

当該物質について

汚濁廃水の浄化処理剤としては、従来から無機系および有機系の各種凝集剤が使用されてきた。無機系凝集剤としては、硫酸アルミニウム、ポリ塩化アルミニウム（PAC）、アルミン酸ナトリウム（$NaAlO_2$）

©Research Institute for Integrated Science, Kanagawa University

等のアルミニウム化合物、硫酸鉄（$FeSO_4 \cdot 7H2O$）、塩化鉄（$FeCl_3 \cdot 6H_2O$）などの鉄化合物あるいは生石灰、消石灰などが用いられている。今回は、我々は実験的に作られた特殊な凝集剤で高い効率で土砂分離を実現しているが、その効率的な凝集原理を探るべく、その組織形態と構成を調べた。

1) 組織形態

図１は当該分離剤の SEM による表面形態観察結果である。当該分離剤は、非常に複雑なX線回折を示し、物質構造を明確に決定することはできないが、ゼオライトに見られるような細孔は認められない。大小の球状物質の集合体として認められる。しかしさらに倍率を上げ、詳細な組織形態を観察すると、非常に興味ある形態が観察される（図２）。球状物質以外ナノレベルの柱状物質が観察される。この結果から当該物質の大きな比表面積を有していることが容易に推測され、効果的な吸着能を示唆していると思われる。

2) 構成元素

表１に当該物質の EPMA 構成元素分析結果を示す。特徴的なのは Al を主体とした物質であることが分かる。この結果から酸素を除いた上位　Al、Ca、C、Si、Fe、Mg　について元素マッピングを行った（図３、４）。Al　と　Si　は同粒子内に存在し、Ca　と　Mg　は同粒子内に存在ししていることが分かる。Al-Si-O 相、Ca-Mg-O 相、Ca-C-O 相の存在を示

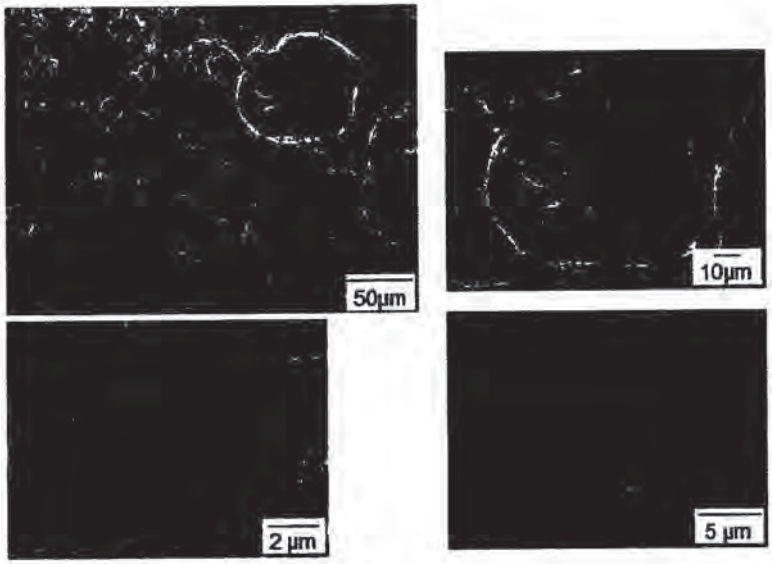

図 1. 試料の表面状態観察 -SEM.

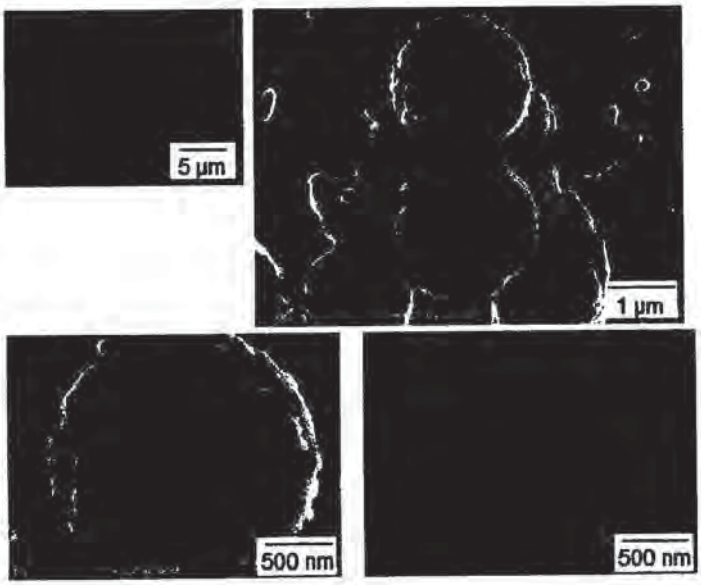

図２. 試料の表面状態観察 -SEM.

唆するX線回折結果（図4、5）と矛盾しない。

討論

濁水のコロイド画分の凝集分離にはしばしば高分子電解質が凝集剤として用いられるが，凝集現象を理解するためには高分子電解質の吸着構造の解析が必要となる．本稿では，高分子電解質が吸着したポリスチレンラテックス粒子の電気泳動移動度を溶液のイオン濃度の関数として測定し，吸着層の構造について検討した．電気泳動移動度はKClが1.0 × 10−2 mol/Lよりも高イオン濃度で一定値に収束した．この測定結果に対して，一様な電荷分布をもつ透水性の吸着層を伴うコロイド粒子の電気泳動移動度に関するOhshima-Kondoの理論を適用し，高分子吸着層の単位体積あたりの電荷密度ZN［mol/L］および透水性を特徴づける長さパラメータ1/λ［nm］を求めた．求められた1/λの値はZNから推定される電荷間の平均的な距離とほぼ等しくなることが示された．SEM観察の結果、特異な相（ex. 多孔質など）の存在は確認されなかった。X線構造解析ならびにEPMAの分析結果より粉末は主に$CaMg(CO_3)_2$相、$CaCO_3$相、Al-Si-O相より形成されている事を確認した。

表1．EPMA構成元素の定性分析

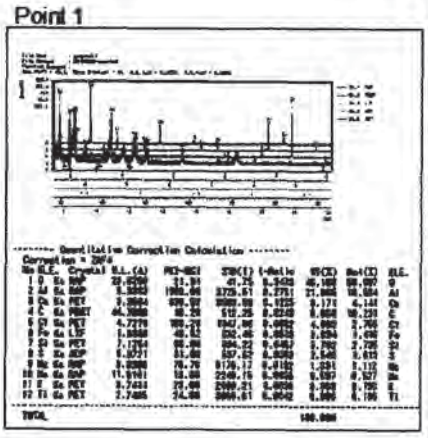

測定ビーム径 30μm, mol%

ELE	Point 1	Point 2	Point 3	Point 4
O	58.6	73.6	64.1	64.5
Al	16.5	12.6	10.2	9.5
Ca	4.1	3.4	3.0	1.2
C	10.2	-	11.1	13.0
Cl	2.8	1.5	1.8	0.2
Fe	1.4	1.5	-	0.3
Si	2.7	5.0	7.7	10.2
S	1.6	-	-	-
Mg	1.1	1.3	1.2	0.7
Na	0.5	1.5	0.6	-
K	0.2	0.2	0.1	0.2
Ti	0.1	0.2	0.3	0.3

*[-]項目は未検出

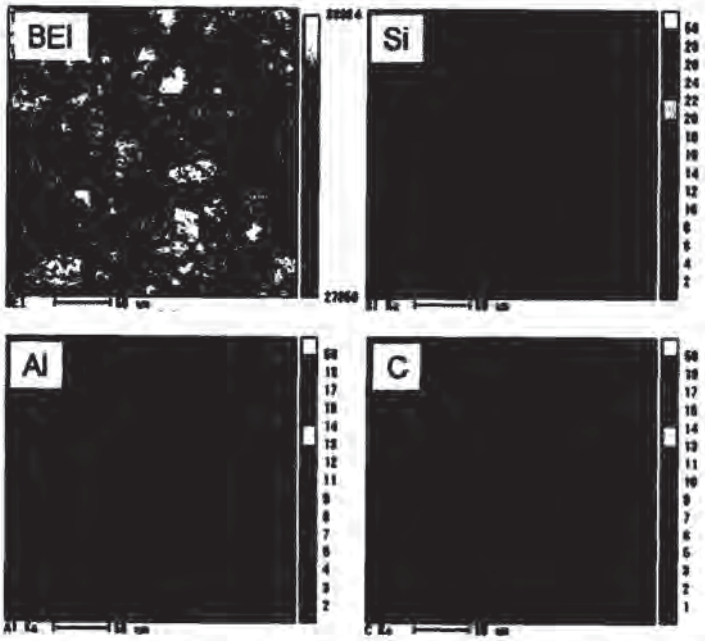

図3．元素マッピング-EPMA．両領域の間には両タイプのトライアッドが混在する領域(Mix)があり，ここでは，トライアッドの他に，ペンタッドやヘプタッドも見られる．筋線維全長に対する各領域の相対長が%で示されている．

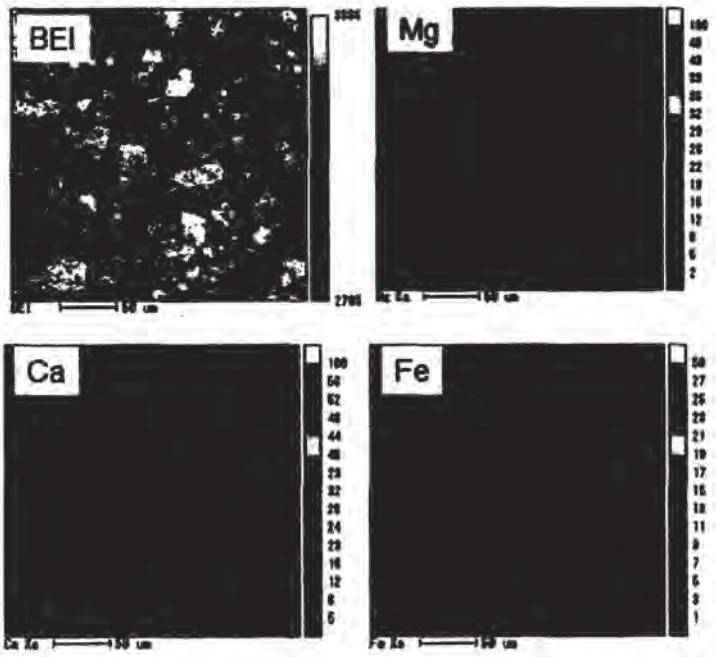

図4. 元素マッピング-EPMA.

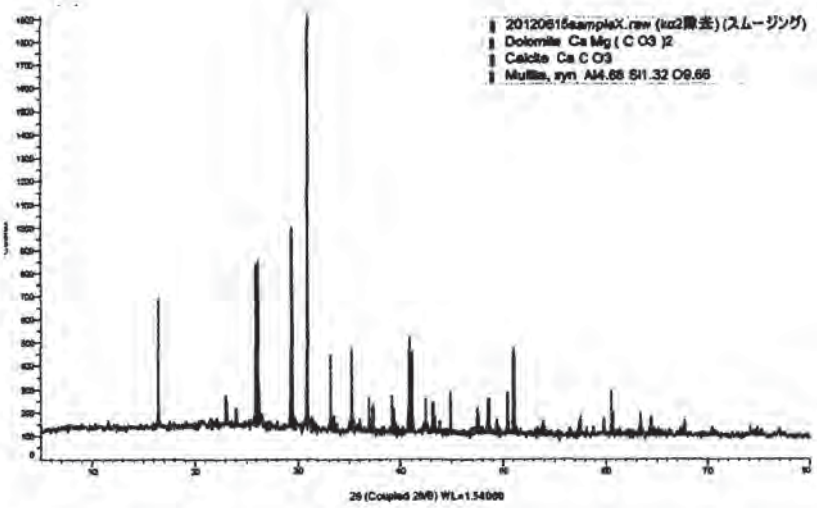

図5. X線構造解析-XRD.

謝辞

本研究は「X凝集剤の結晶構造の分析と凝集メカニズムの解明」の課題名で2012年度神奈川大学総合理学研究所共同研究助成を受けて行いました。

文献

1) 奥村　和 (2012) ゼオライトを担体とした金ナノ粒子の調製と触媒作用. *ケミカルエンジニヤリング* **57**: 849-853.
2) 松本 泰重 (1968) ゼオライト触媒の活性に及ぼす希土類カチオン濃度および吸着水量の影響. *工業化学雑誌* **71**: 1004-1006.
3) 青島政之, 佐藤　明 (2011) 強磁性棒状コロイド粒子分散系の凝集現象とレオロジー特性. *表面* **49**: 381-394.
4) Ogihara T, Kagawa H GaoQi and Mori K (2010) A study of the molecular structure of phospholipids and the aggregation of liposomes using the molecular orbital method, *Journal of computer chemistry, Japan* **9**: 43-46.
5) 鷲見栄一 (2008) 懸濁態粒子の粒径分布の現地測定 (6) 粒径分布の変化からみた凝集現象. *海洋と生物* **30**: 626-634.
6) 山本　周治, 小林孝行, 加藤和美 (2008) 電浸漬生物ろ床用素材の開発　*愛知県産業技術研究所報告書* **7**: 128-131.